Award Number: DE-FC26-07NT43098
Recipient: The Regents of the University of Colorado at Boulder

DEVELOPMENT, VERIFICATION, AND VALIDATION OF MULTIPHASE MODELS FOR POLYDISPERSE FLOWS

Final Scientific Report
18 May 2007 – 31 December 2011

Principal Investigator: **Prof. Christine M. Hrenya (University of Colorado)**
Co-principal Investigators: **Dr. Ray Cocco (PSRI)**
Prof. Rodney O. Fox (Iowa State University)
Prof. Shankar Subramaniam (Iowa State University)
Prof. Sankaran Sundaresan (Princeton University)

Prepared for:
U.S. Department of Energy
National Energy Technology Laboratory

30 March 2012

Disclaimer

Abstract

This report describes in detail the technical findings of the DOE Award entitled "Development, Verification, and Validation of Multiphase Models for Polydisperse Flows." The focus was on high-velocity, gas-solid flows with a range of particle sizes. A complete mathematical model was developed based on first principles and incorporated into MFIX. The solid-phase description took two forms: the Kinetic Theory of Granular Flows (KTGF) and Discrete Quadrature Method of Moments (DQMOM). The gas-solid drag law for polydisperse flows was developed over a range of flow conditions using Discrete Numerical Simulations (DNS). These models were verified via examination of a range of limiting cases and comparison with Discrete Element Method (DEM) data. Validation took the form of comparison with both DEM and experimental data. Experiments were conducted in three separate circulating fluidized beds (CFB's), with emphasis on the riser section. Measurements included bulk quantities like pressure drop and elutriation, as well as axial and radial measurements of bubble characteristics, cluster characteristics, solids flux, and differential pressure drops (axial only). Monodisperse systems were compared to their binary and continuous particle size distribution (PSD) counterparts. The continuous distributions examined included Gaussian, lognormal, and NETL-provided data for a coal gasifier.

Table of Contents

1. EXECUTIVE SUMMARY

This report is the final technical report for the award DE-FC26-07NT43098 entitled "Development, Verification, and Validation of Multiphase Models for Polydisperse Flows." Below is a summary of work completed under the grant for each of the major goals.

Goal I: Continuum Theory for Solid Phase

Two separate and complementary continuum theories were derived to model polydisperse solids: the kinetic theory of granular flow (KTGF) and the discrete quadrature method of moments (DQMOM). Both theories are based on first principles with no adjustable parameters. The polydisperse KTGF and DQMOM were then encoded in MFIX, and underwent a wide range of verification testing to ensure, to the best possible extent, that no coding errors were present. These verification tests included both granular and gas-solid flows, including cases where an analytical solution and/or DEM (discrete element method) data and/or simple test cases. For the case of KTGF, another set of constitutive equations were derived which rigorously incorporated the gas phase for a simplified case of monodisperse systems at low Reynolds numbers. This derivation used the acceleration model developed in Task 2 from direct numerical simulations (DNS) in the starting kinetic equation, and indicated the effect of the fluid phase on the resulting constitutive relations.

Goal II: Improved Gas-Particle Drag Laws – effect of particle size distribution

In this portion of the effort, two types of direct numerical simulations (DNS) were used to extract the drag force experienced by particles in a polydisperse suspension. These two methods, namely lattice-Boltzmann (LB) simulations and particle-resolved direct numerical simulations (PR-DNS), were used to cover the parameter space of interest to the operation of circulating fluidized beds (CFB's). Simulations were performed through assemblies of particles with zero and nonzero mean relative velocity between various species; in both cases particles had non-zero fluctuating velocities. Simulations of freely evolving suspensions were also performed. Based on the former set of simulations, a new drag law for polydisperse mixtures was obtained that is valid for low and moderate Reynolds numbers. It was found that the effect of particle velocity fluctuations on the fluid-particle drag forces was found to be only of secondary importance even at moderate Reynolds numbers. For simulations of evolving flows, it was found that clustering occurred for all cases, showing that clustering does not disappear when particle size distribution is present. The formation of clusters complicates extraction of fluid-particle drag models from such simulation data. In addition to the new polydisperse drag law, another outcome of the DNS-based simulations was an instantaneous particle acceleration model (as is used in the starting kinetic equation for derivation of continuum models) for the gas-solid interaction. It was found that the drag force (acceleration) acting on the particles has a stochastic contribution from the neighbor particles, which is described according to a Langevin model. The coefficients of this Langevin-based acceleration model are specified as functions of the solid volume fraction, mean flow Reynolds number and solid-fluid density ratio.

Goal III: Gas-Phase Instabilities: Turbulence Models for Polydisperse Systems

In the first part of this effort, the level of pseudo-turbulent kinetic energy in the gas-phase was quantified using PR-DNS of monodisperse and bidisperse gas-solid systems with particles greater that the Kolmogorov length scale. These simulations were performed for gas-solid flows of both fixed and freely evolving assemblies. In the second portion, an algebraic model is proposed for the gas-phase Reynolds stress in terms of solid volume fraction and mean flow Reynolds number. In addition a suitable scaling for dissipation of fluid-phase pseudo-turbulence was proposed.

Goal IV: Data Collection and Model Validation

Data was obtained via both DEM simulations and experiments in three fluidized beds, both low-velocity (bubbling) and high-velocity (circulating). The DEM data was used to determine how a continuous particles size distribution (PSD) could be approximated using a discrete number of particle sizes, as is used in the continuum models. The experimental data demonstrated the effect of particle size distribution, both binary and continuous, on the local flow characteristics associated with both bubbles and clusters. Measurements also included solids flux and velocity-weighted particle size distribution as function of axial and radial position. Surprisingly, the qualitative effect of increasing the widths of continuous size distributions on measured quantities (species segregation, elutriation, etc.) were often in contrast to the well-established trends of binary mixtures. Finally, a challenge problem was issued to the modeling community and spearheaded by PSRI and NETL, the results of which will be reported in a journal publication.

With regard to model predictions, grid-independent DQMOM predictions of hydrodynamic clusters were found, and the structure formation was found to be less evident than with hydrodynamic models. Simulations in axially periodic domain were performed to compare with the PSRI data obtained in this project involving the study of polydispersity and segregation. The implementation of the electrostatic model into MFIX was completed and tested with a simple channel flow problem. With regard to KTGF, a comparison of two KTGF models, using the polydisperse drag law developed here, indicated qualitatively similar gas-particle flow predictions. In addition, results from two dimensional channel flow simulations were compared with the PSRI experimental data set obtained in this project. Poor agreement was found between simulations and experimentally observed segregation profiles. This lack of agreement is traced to azimuthal variations in particle volume fraction that cannot be account for in 2D channel flow simulations.

Goal V: Project Management

The submission of this document represents the final reporting requirement of the project. All milestones were met, and the budget was fully spent.

The project resulted in 42 publications (journals and book chapters), 28 invited talks, and 53 contributed conference presentations.

2. TECHNICAL DETAILS

For each task in the project, the task description (as taken from the PMP) is shown in underlined italics for purposes of reference. The non-italicized text immediately following the task description of work completed on that task.

Goal I: Continuum Theory for the Solid Phase

Task 1.1: Derivation of KTGF (Hrenya)

The development of a kinetic theory for N particle species, which can differ in size and/or density, will be based on the Enskog equation for mixtures, and therefore will be applicable to both dilute and dense systems. The approach will follow the Boltzmann-based approach (dilute systems only) of Garzó and Dufty (2002), who are current collaborators of the PI. A rigorous Chapman-Enskog expansion about the "equilibrium" state will be followed (Chapman & Cowling, 1970), thereby precluding the need for limiting assumptions such as quasielastic collisions, equipartition of energy, etc. The resulting governing equations and corresponding constitutive relations will be applicable to a wide range of restitution coefficients.

(Hrenya reporting.) The kinetic theory for *N* particle species, which differ in size and/or density, has been derived in 2D and 3D via a Chapman-Enksog expansion about the revised Enskog equation for mixtures of inelastic grains. A brief overview of the main features of the new theory is as follows. Because the starting equation is the Enskog equation rather than the Boltzmann equation, the new theory is applicable to both dilute and dense systems. The base state used for the expansion is the homogeneous cooling state rather than the elastic (Maxwellian) base state, which makes the resulting theory applicable to a wide range of restitution coefficients. Furthermore, no limiting assumptions of a Maxwellian velocity distribution or an equipartition of energy are made as part of the derivation. Finally, due to the recognition that the timescale associated with inelastic dissipation is hydrodynamic (slow) in nature, only the mixture momentum balance and the mixture energy equation are required. Note that this form of the equations does not impose any restrictions on the resulting predictions relative to previous theories which include species momentum balances and/or species energy balances (e.g., segregation arises due to external forces as well as gradients in concentration and temperature). On the other hand, the set of governing differential equations is reduced, which is expected to lead to a significant reduction in computational requirements.

The new theory was published in *Physical Review E* in the form of two consecutive papers. In the first paper, the formal Chapman Enskog expansion is carried out, resulting in constitutive relations in the form of collision integrals, except for the few in which the collision integrals can be evaluated exactly). In the second paper, the remaining collision integrals are evaluated approximately using a truncated Sonine polynomial. The preprints of the manuscripts are attached to this report (Appendix A), in which all of the detailed calculations and resulting equations can be found. Due to the considerable length of this contribution, pointers to important pieces of information are given below for easy reference.

1) An overview of the derivation is given in Section II of the first paper.

2) A listing of equation numbers for the final form of the governing equations and constitutive relations is contained in the first paragraph of Section IV of the second paper.
3) A comprehensive discussion of the specific treatments used during the derivation process, along with a detailed comparison to previous theories, is provided in Section IV of the second paper. A more concise overview of this information is available in Tables 1 and 2 of the second paper.

Task 1.2: Development of DQMOM (Fox)

The DQMOM approach is an efficient mathematical approximation for polydisperse systems that starts with a closed transport equation for the NDF describing the system (Fox, 2003, Marchisio & Fox, 2005, Fox, et al., in preparation, Fox, in press). For gas-solid flows, a polydisperse version of the Enskog equation is the appropriate starting point. Once this equation has been closed, DQMOM will be directly applied to derive transport equations for the N number densities and N abscissas representing the properties of the system (e.g., size, density, velocity, etc.) This process results in an N-solids model where each solid has its own continuity and momentum equation (Fan, et al., 2004). However, it is different than the current N-solid model in MFIX in its treatment of the momentum equation, which is represented by N abscissas even for monodisperse particles. The DQMOM approach will also be used to represent just the polydispersity in size (density, etc.) when combined with the KTGF to treat the velocity. This combined KTGF-DQMOM approach will result in an N-solids model that is an extension of the current model in MFIX.

(Fox reporting.) A quadrature-based third-order moment closure has been developed for dilute gas-solid flows. The derivation begins with the Boltzmann equation for monosized particles and includes terms for transport, gravity, drag, and particle-particle collisions. Particle-wall collisions appear in the boundary conditions. Unlike the classical Chapman-Enskog expansion, the quadrature-based moment closure does not use expansions about the equilibrium state, and hence can be applied for arbitrary Knudsen number (including non-collisional flows far from equilibrium). The third-order closure uses two-node quadrature in each direction of velocity phase space and hence uses eight nodes for three-dimensional velocity distribution function. The key technical challenge when using quadrature-based moment methods is the inversion formula for computing the quadrature weights and abscissas from the finite set of transported moments. The method was implemented in a computer code and tested for three canonical problems: (i) Riemann shock problem, (ii) impinging particle jets, and (iii) dilute vertical gas-solid channel flow with large Stokes number particles. For the Riemann problem, we showed that the method can reproduce the classical shock structure in the limit of zero Knudsen number (i.e., the Euler equation), as well as the breakdown of the shock for increasing Knudsen number as observed in Discrete Simulation Monte Carlo (DSMC). Although it arises from rarefied gas dynamics, the Riemann problem is relevant to gas-solid flows as it will arise whenever a large solid-volume fraction gradient exists in a flow (e.g. a particle mixing layer where the initial particle temperature is uniform, the initial mean solids velocity is zero, but the solids volume fractions are different on the two sides of the mixing layer.) The impinging particle jets are a difficult problem of two-fluid models such as MFIX because in the dilute limit the particles at impact are far from equilibrium. Two-fluid models will predict so-called "delta-shocks" where the particles are all located at the shock structures, but unfortunately this behavior

in unphysical (i.e. it is not observed with DSMC). The third example is directly relevant to riser flow because it includes gravity and particle-wall interactions. Because of the high Stokes number, the particles are far from equilibrium and interact only with the mean gas-phase velocity (i.e., one-way coupling with the gas phase).

Granular Flow. The quadrature-based moment closure for granular flows with particle-particle collisions has been tested for a series of test cases. The latter were designed to test the important physics appearing in the kinetic equation (kinetic transport, collisions, and boundary conditions). By varying the average particle volume fraction, the relative importance of the collision term was investigated for both elastic and inelastic particle-particle collisions. The numerical implementation of the quadrature-based third-order moment closure was found to be robust over the entire range of Knudsen (collisions) numbers. The quadrature-based closure was shown to yield physically realistic solutions to highly non-equilibrium granular flows that cannot be accurately handled by "standard" KTGF.

Further testing of the quadrature-based moment closure was performed with particle-particle and particle-wall collisions described in detail in the manuscript by Fox (2008). The novelty of this method is that it provides a direct solution of the Boltzmann equation for the one-particle density function with collisions for the entire range of Knudsen numbers. In comparison, closures based on "equilibrium" kinetic theory approaches (e.g., the KTGF) cannot treat cases that are not dominated by collisions (i.e. the Knudsen number must be very close to zero.) The principal technical challenge is the development of a robust inversion algorithm to compute the eight weights and eight velocity abscissas from the twenty moments (in 3D) up to third order in the components of particle velocity. For collision-dominated systems, the Boltzmann equation reduces to the Euler equation for compressible inviscid flow. A robust algorithm for inverting the twenty moments must work in the Maxwell limit, as well as for deviations from this limit where the weights and abscissas deviate strongly from their Maxwellian values.

The first test considered was the classical Riemann shock problem, a standard test case for compressible flow solvers. The temperature-contour results for the quadrature-based solver are shown in Fig. 1 for three Knudsen numbers. For Kn=0, the classical solution to the Euler equation is recovered. Two non-equilibrium cases (Kn= 0.1 and 10) are shown at the same time instant. These results are in good agreement with those found using a direct Boltzmann equation solver. We should note that the results in Fig. 1 are found using the BGK collision term. Test runs using the Boltzmann collision operator have also been carried out and differ qualitatively at intermediate Knudsen numbers. It is noteworthy that using the Boltzmann collision operator is relatively straightforward in the context of quadrature, while it is quite problematic with other moment closures since the collision terms in moment equations are not closed.

Dilute Gas-Particle Flow. The second test considered is vertical gas-particle channel flow with elastic collisions. One-way coupling is assumed (due to the large Stokes number of the particles, and the gas-phase mean velocity profile is taken as an input to the simulations of the particle-phase moments. The particle-wall collisions are assumed to be elastic. We should note that the wall boundary conditions are easily implemented in terms of the weights and abscissas, which is not the case for other moment methods (e.g. Grad's 13-moment system). In the absence of particle-particle collisions (i.e. extremely low particle volume fractions), this flow reaches a steady state where the particle temperature is null (i.e. dissipation due to the drag term removes all particle velocity fluctuations.) For dilute systems, particle-particle collisions, combined with the non-uniform gas-velocity profile, lead to a non-uniform particle temperature (and number

density). The shape of the number density profile depends on the Stokes and Knudsen numbers. However, because the particle temperature is maximum near (but not at) the walls and minimum at the centerline, a core-annular profile is usually observed.

Sample results for the channel flow with an average solids volume fraction of 2 percent are shown in Fig. 2. These results were found by running a time-dependent simulation of the moment equations until the fields reached a steady state. From the weights, it can be clearly observed that Knudsen layers are formed at the channel walls because collisions are not strong enough to eliminate anisotropy generated by the boundary conditions. Likewise, note that the weights are not all equal, indicating that the velocity distribution in non-Maxwellian. This can also be observed from the diagonal anisotropy components, which are zero for the Maxwell distribution. Also note that only one off-diagonal component is non-zero (a_{uv}), which is important in determining the particle temperature distribution in the channel. Finally, one can note that the particle pressure is non-uniform for finite Knudsen numbers (but uniform for Kn=0, i.e. the Euler limit.)

The next case considered was a particle-laden 2D Taylor-Green (TG) flow with one-way coupling. For this case, at time zero the particles are uniformly distributed in the unit square. However, due to the finite Stokes number, the particles are ejected from the TG vortices (low-pressure regions). If the Stokes number is large enough, the particles will cross from the TG vortex where they started into a neighboring vortex. Depending on the particle number density, this process will result in particle-particle collisions (dilute flows) or particle trajectory crossing (very dilute flows). It is noteworthy, that only the former can be described by a two-fluid model based on the KTGF (e.g. MFIX). An example result for Kn=0 (Euler limit) is shown in Fig. 3. The particle number density reaches a steady state where all particles are clumped along the vortex boundaries. Note, however, that due to particle collisions the particle pressure at the vortex boundaries is very high, thereby stopping particles from crossing into a neighboring vortex. In contrast, for infinite Knudsen number (no collisions) the number density is determined by kinetic transport and drag only. As example result for this case is shown in Fig.4. In the absence of collisions, particle trajectory crossing is ubiquitous, leading to a discontinuous mean particle velocity field. The quadrature-based moment closure can successfully handle such non-equilibrium cases because the local velocity is described by eight velocity vectors, instead of one mean velocity vector and gradient-based fluxes. For the TG flow, the particle temperature is strongly inhomogeneous and depends on both the Stokes and Knudsen number. However, simulations with solids volume fractions as high as 10 percent still show significant non-equilibrium effects that cannot be capture using the KTGF. It is likely that the same is true for many other gas-solid flows because the particle temperature will never be large enough to overcome non-equilibrium effects at solid volume fraction even as high as 10-20 percent.

The next case considered is crossing planar particle jets with and without collisions. This case is similar to the TG flow, except that the gas phase is not present and the particle trajectory crossing is generated by the initial conditions. The particle number density in the jets determines the relative importance of collisions. For very dilute jets, the particle collisions are negligible and the particle jets simply pass through each over (Fig. 5). On the other hand, in the Euler limit (Fig. 6) particle collisions are dominant and lead to both forward- and back-scattering. We should note that a KTGF code (such as MFIX) can only predict the behavior shown in Fig. 6. In contrast, the quadrature-based moment closure can handle the entire range of particle number densities (see Fig. 7).

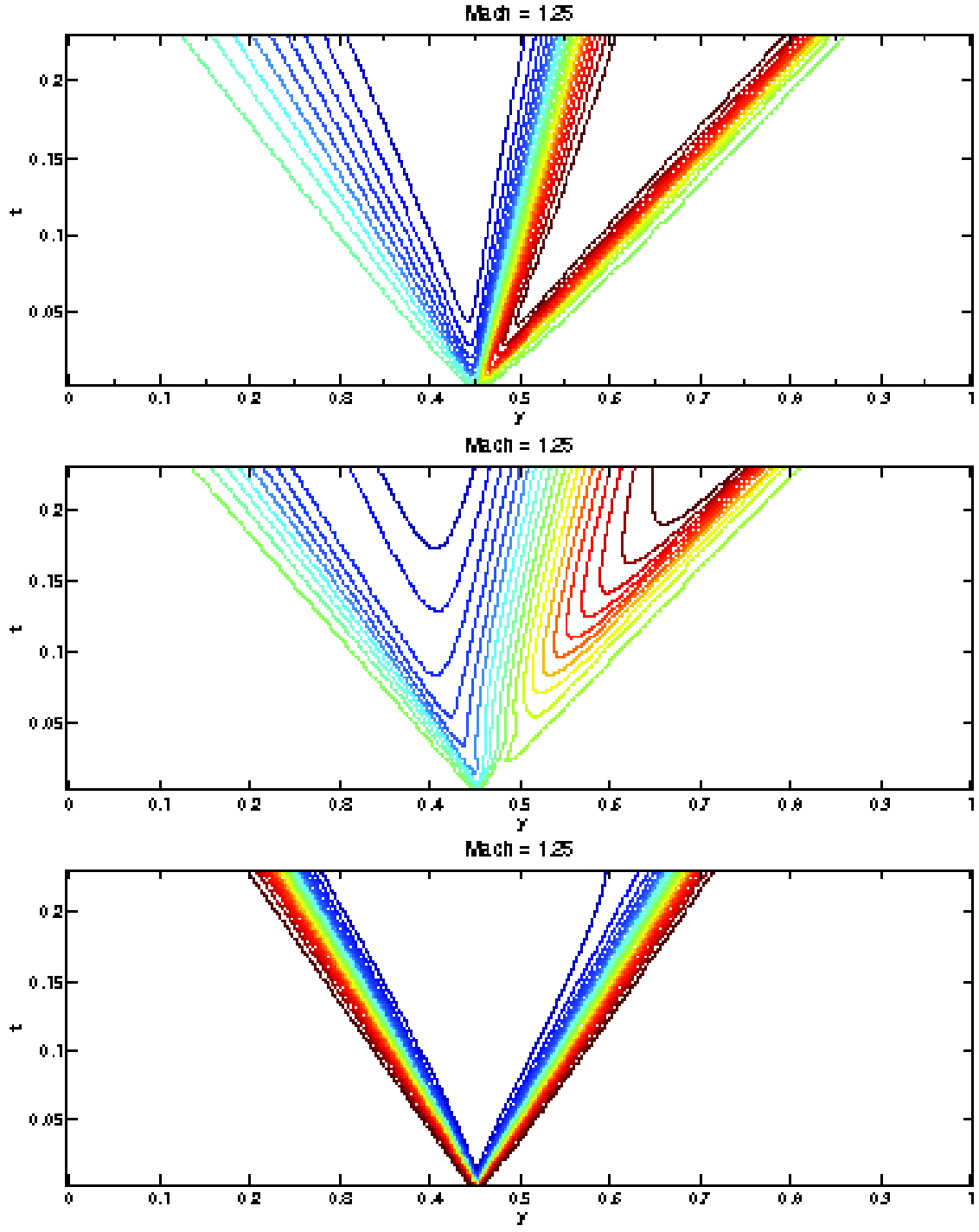

Figure 1. *Temperature contours for the Riemann shock problem at three Knudsen numbers. Top: Kn = 0. Middle: Kn = 0.1. Bottom: Kn = 10.*

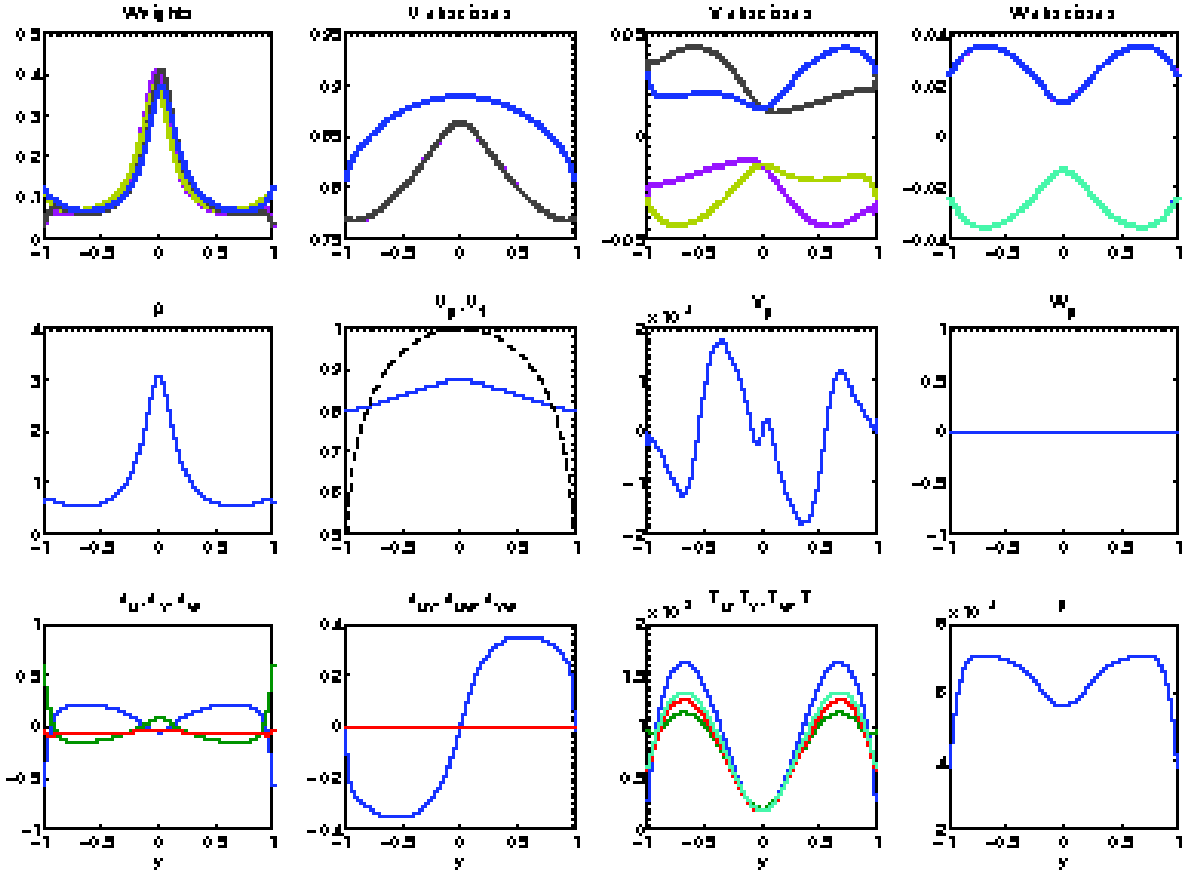

Figure 2. *Selected statistics for the vertical gas-solid channel flow at St=40.9 and an average particle volume fraction of 2 percent. Top row: weights and abscissas. Middle row: number density and mean particle velocity components. (Gas velocity is shown as a dashed curve.) Bottom row: diagonal and off-diagonal anisotropy tensor components, temperature components, and particle pressure.*

The final case that has been considered is a granular gas (i.e., possibly inelastic particle collisions) between two constant-temperature walls. This flow has been investigated by Galvin et al. (2007) using molecular dynamics and was shown to exhibit significant non-equilibrium effects. Sample results for two cases are shown in Figs. 8 and 9. We should note that the results in Figs. 8 and 9 are found with BGK collisions.

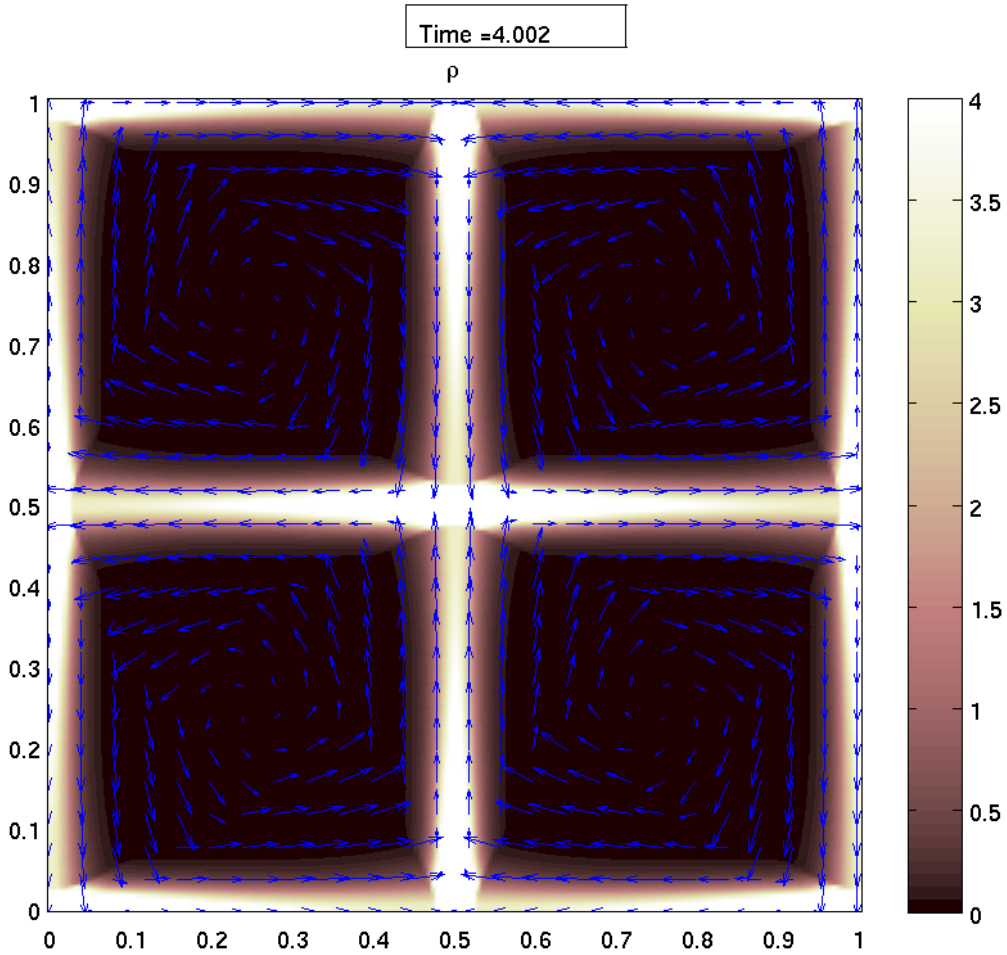

Figure 3. *Particle number distribution in TG flow in the Euler limit (Kn = 0). Mean particle velocity vectors are indicated by blue arrows. At t = 4 all particles have been ejected from the vortex centers.*

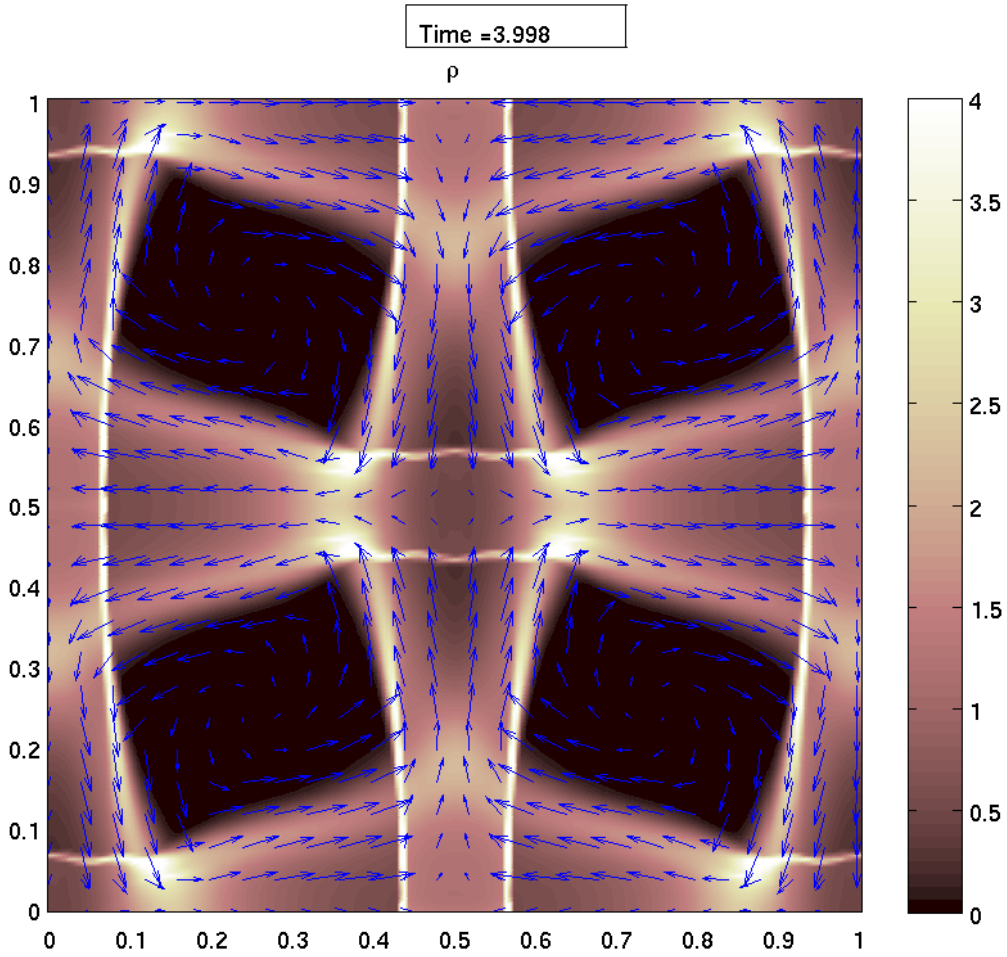

Figure 4. *Particle number distribution in TG flow in the collision-less limit. Mean particle velocity vectors are indicated by blue arrows. Extensive particle crossing is observed in this limit and the particle velocity vector field is not continuous.*

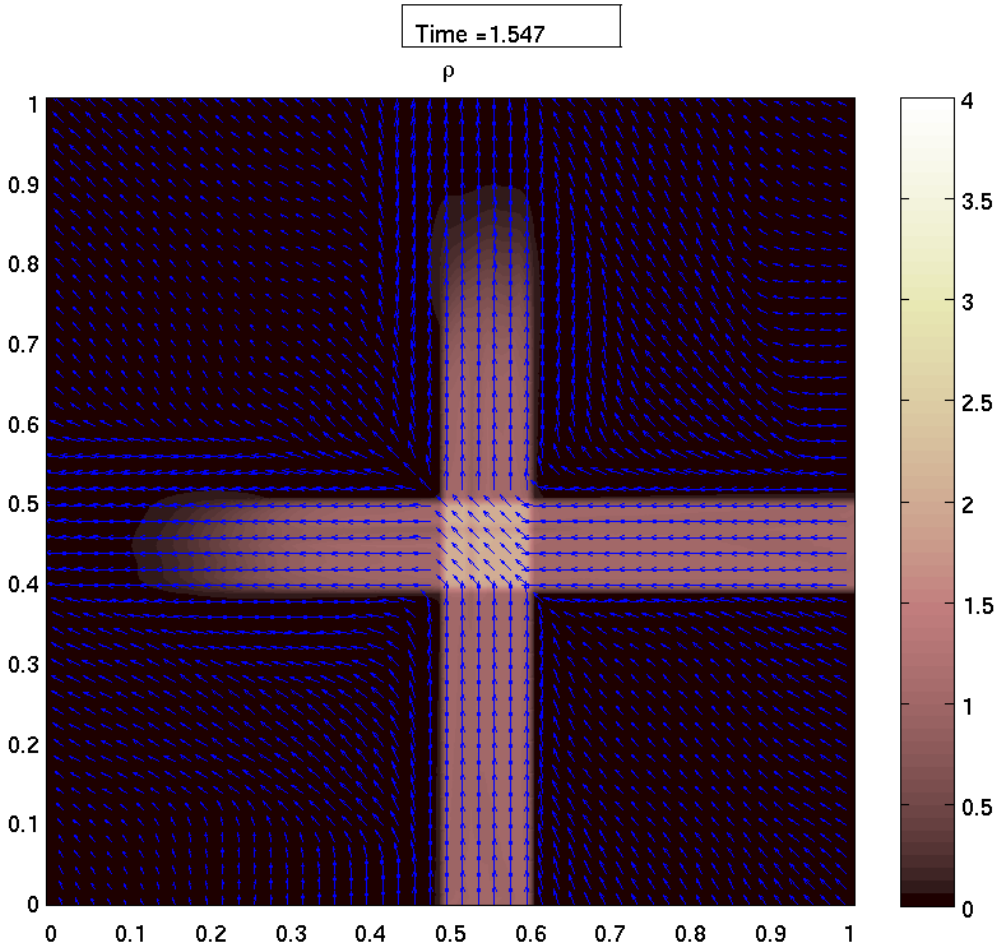

Figure 5. *Crossing planar particle jets in the collision-less limit. Mean particle velocity vectors are shown by blue arrows.*

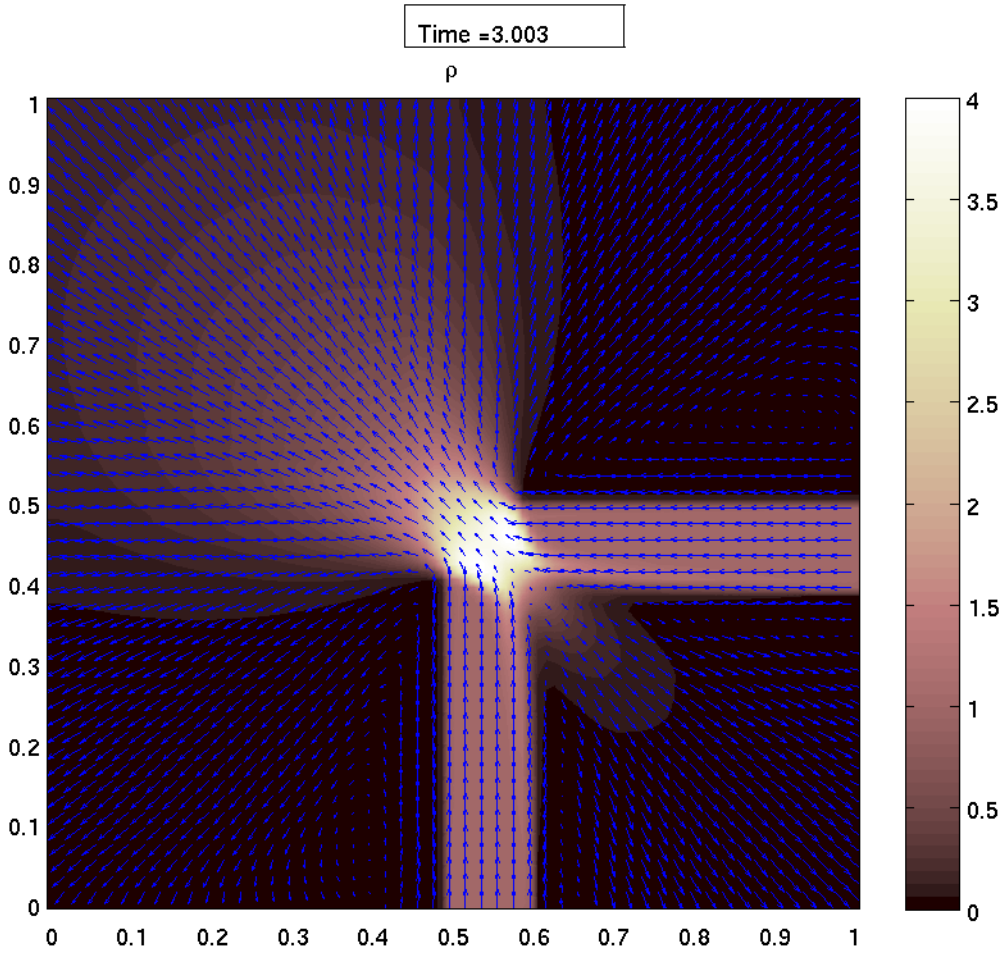

Figure 6. *Crossing planar particle jets in the Euler limit. Mean particle velocity vectors are shown by blue arrows. Both forward- and back-scattering of particles is observed.*

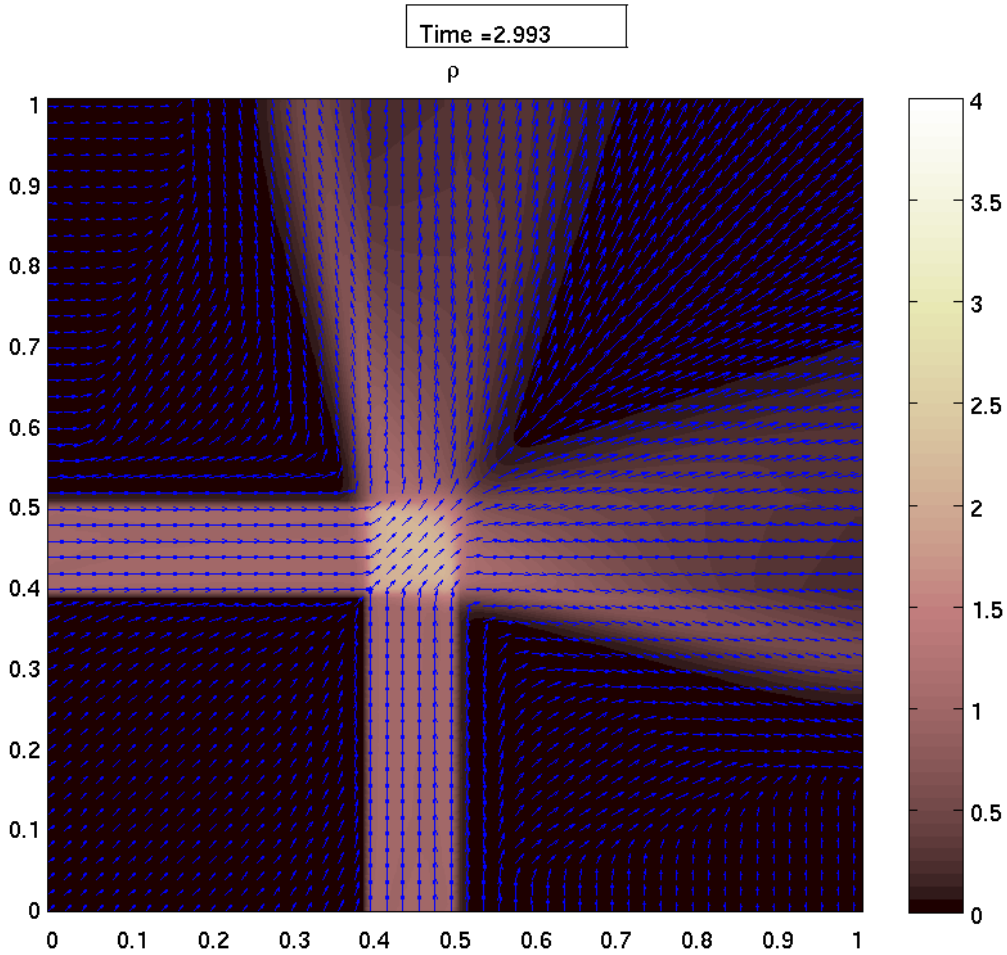

Figure 7. *Crossing planar particle jets with 1 percent solids volume fraction. Mean particle velocity vectors are shown by blue arrows. Partial scattering of particles is observed.*

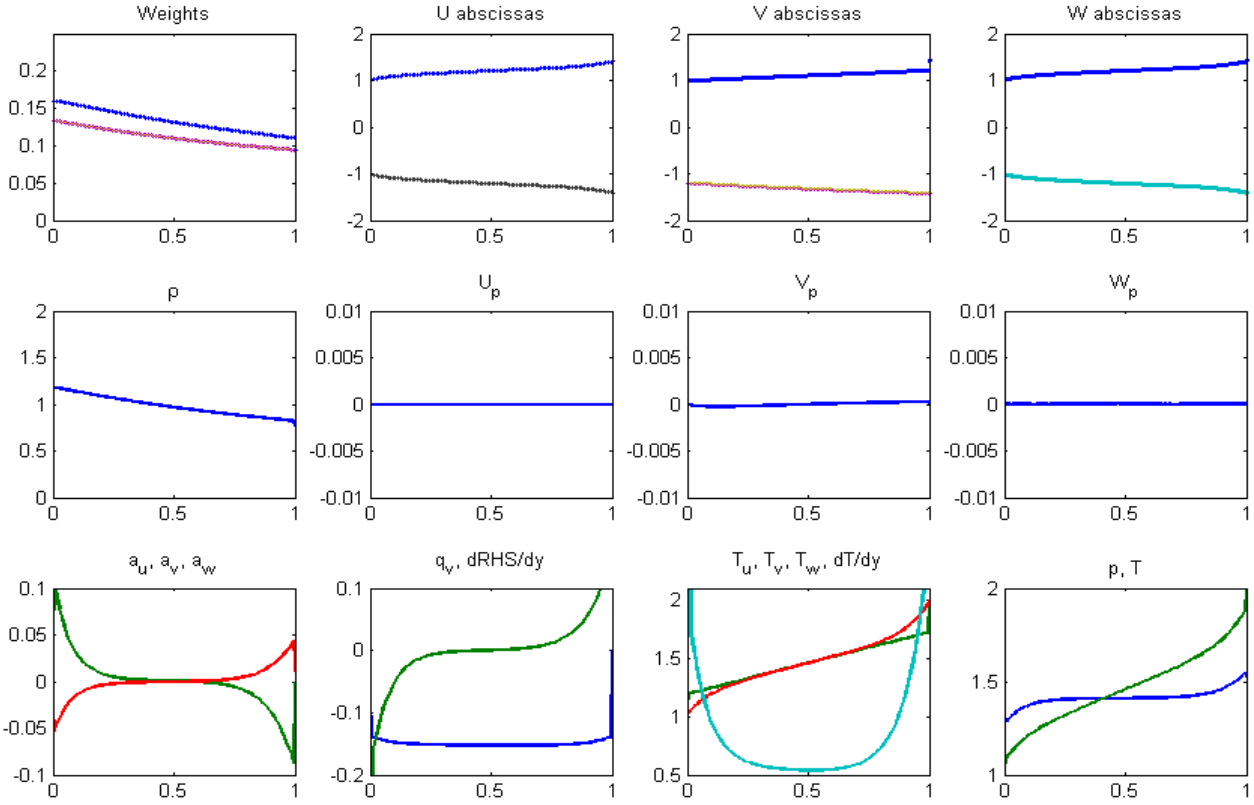

Figure 8. *Elastic granular gas with 1 percent solids between two constant-temperature walls (T_L = 1, T_R = 2). Knudsen layers are present when anisotropy components (a_i) are non-zero. Anisotropy for this case is very strong and Knudsen layers nearly reach the center of the domain.*

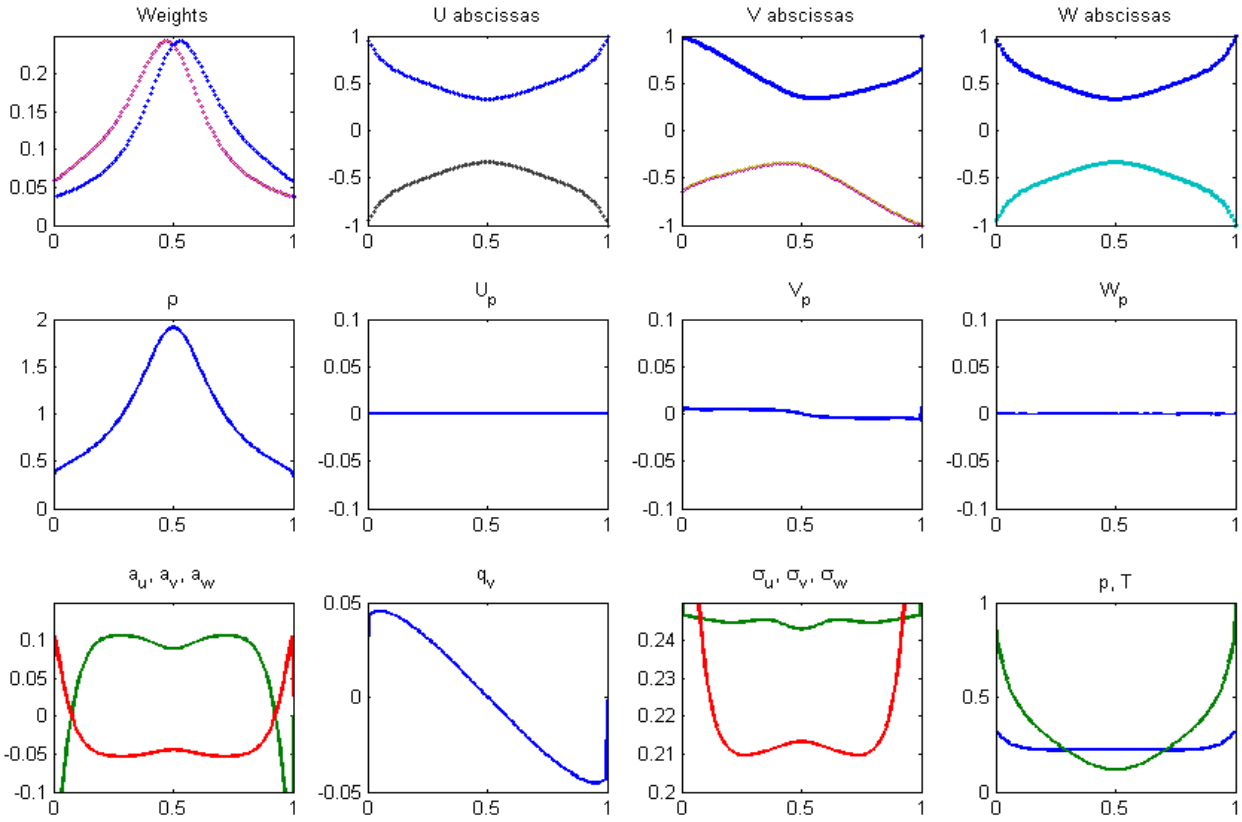

Figure 9. *Inelastic granular gas with 5 percent solids between two constant-temperature walls (T_L = 1, T_R = 1). Due to inelastic collisions, the center of the flow is anisotropic and heat flux is non-uniform. The particle number density is highest near the center where the temperature is the lowest.*

Gas-Particle Flow with Two-Way Coupling. The work then focused on the coupling of the DQMOM algorithm (Fox, 2008) with a fluid flow solver, in order to simulate cases with two-way coupling between the phases, and on the implementation and testing of second-order accurate discretization methods to calculate the spatial fluxes in the moments equations. Only the momentum coupling between the phases was taken into account in this work, considering the particulate flow dilute, and neglecting the particle-phase volume fraction inside the fluid-phase equations.

The coupling between the fluid phase solver and the moment solver was obtained by adding the momentum exchange term M_f to the fluid phase Navier-Stokes equation:

$$\frac{\partial}{\partial t}\left(\rho_f U_f\right)+\nabla\cdot\left(\rho_g U_f U_f\right)=-\nabla p+\nabla\cdot\tau_f+\rho_f g+M_f$$

The fluid phase equations of motion were solved using a second-order fully staggered algorithm, implemented into an in-house Fortran code. The drag term was treated as a source term in the fluid phase momentum equation, in analogy to what commonly done in Lagrangian solvers. The fluid phase pressure equation was solved using the FISHPACK library. The wall boundary

condition for the particles was set to be reflective, with elastic collisions between the particles and the wall. The no-slip boundary condition was adopted for the fluid phase.
The implementation of the algorithm was tested by simulating a lid-driven cavity test case, at two different Stokes numbers: St = 0.8 and St = 0.03. Figure 10 shows the comparison of the number density obtained from the simulation of a lid-driven cavity flow (Re = 100, based on the lid length and velocity) with the Eulerian quadrature-based solver with the results provided by a Lagrangian simulation. The Eulerian simulation was capable to capture the bouncing of the particles against the wall in the upper-right corner of the cavity, where particles are brought against the wall by the moving lid, and then bounce back. The capability of capturing these flow behaviours is not present in classical two-fluid models. Also the increase in the number density along the bottom border of the vortex generated by the moving lid, the higher number density in the upper-left corner, and the number density along the lid are in good agreement with what for is predicted by the Lagrangian simulation. Figure 11 shows the contour plot of the particle velocity magnitude, where the same structure of the flow noticed in Figure 12 can be identified.

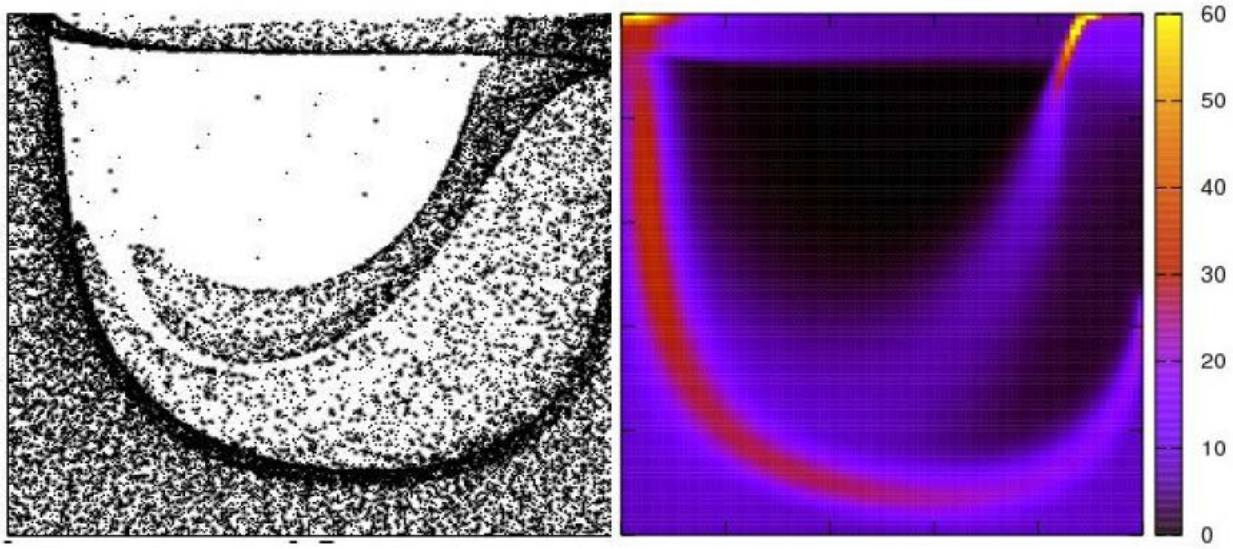

Figure 10. *Particles number density in a lid-driven cavity - Lagrangian simulation (left) and Eulerian simulation (right) - St = 0.8 - Initial volume fraction = 0.008 – 2-way coupling.*

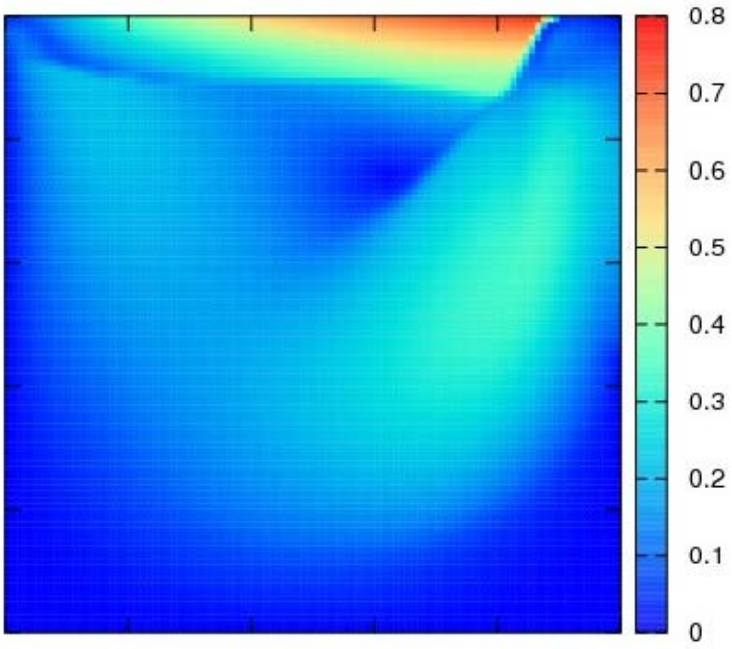

Figure 11. *Particles velocity magnitude - St = 0.8 - Initial volume fraction = 0.008 – 2-way coupling.*

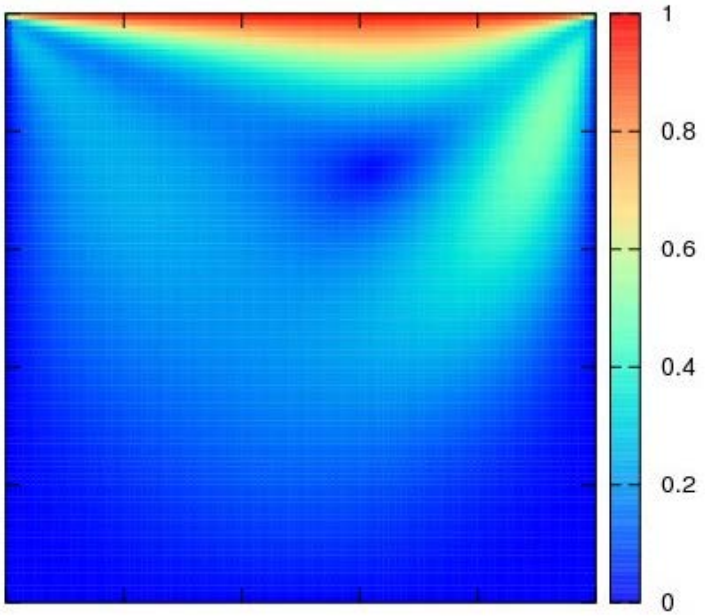

Figure 12. *Fluid velocity magnitude - St = 0.8 - Initial volume fraction = 0.008 – 2-way coupling.*

In Figure 13, the particle number density for the case of St = 0.03 is reported. Particles tend to stay uniformly distributed, with the exception of the accumulation along the left wall, were they are brought by the lid and stay trapped due to the very low velocity of the fluid phase.

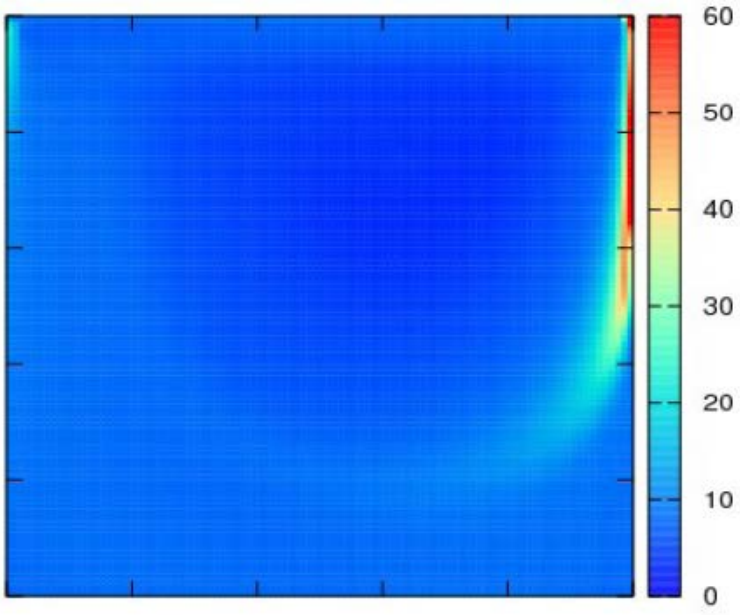

Figure 13. *Particles number density in a lid-driven cavity – 2-way coupling – Average volume fraction: 0.0001 – St = 0.03.*

In all the cases considered, the algorithm showed to be robust and efficient, without presenting particular stability issues.

The next task performed was the testing of two second-order discretization schemes to calculate the spatial fluxes in the moment equations. The first scheme is the traditional central difference scheme (CDS) with a limiter to keep the solution bounded, while the second scheme is a recently developed spectral-difference (SD) scheme. The two schemes were tested using the Riemann shock case, on two different grids: one with 200 cells and the other with 50 cells. The test performed on the refined grid made of 200 cells shows that both the second-order schemes provide almost identical results, with some more evident oscillatory behaviour for the SD scheme, as it can be noticed in Figure 14. Both second-order methods provide a sharper profile for the velocity and the pressure (Figure 15) in comparison to the first-order scheme. These results are confirmed by the simulations performed on the coarse grid (50 cells), whose results are shown in Figures 16 and 17, where the difference between the second-order methods and the first-order one is even clearer.

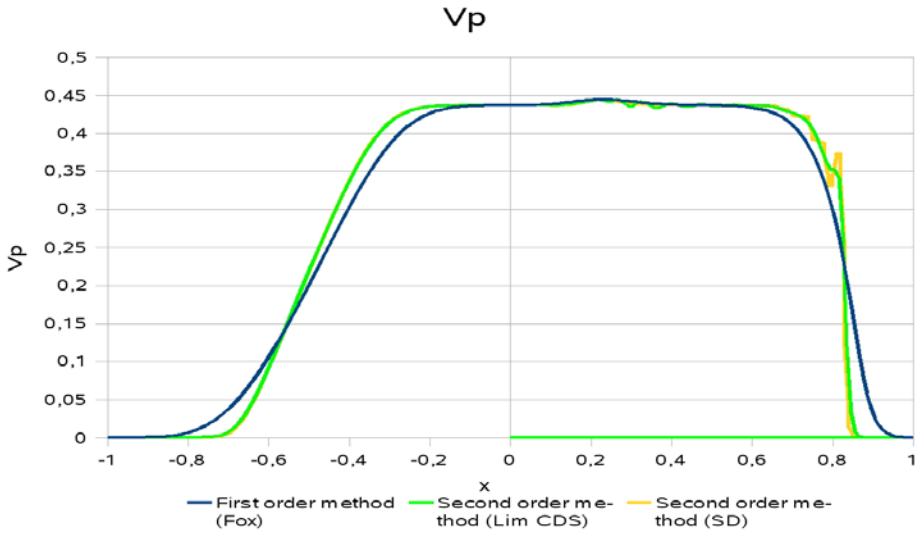

***Figure 14**. Velocity profile in the Riemann shock test case – 200 cells - Collision time: 0.015.*

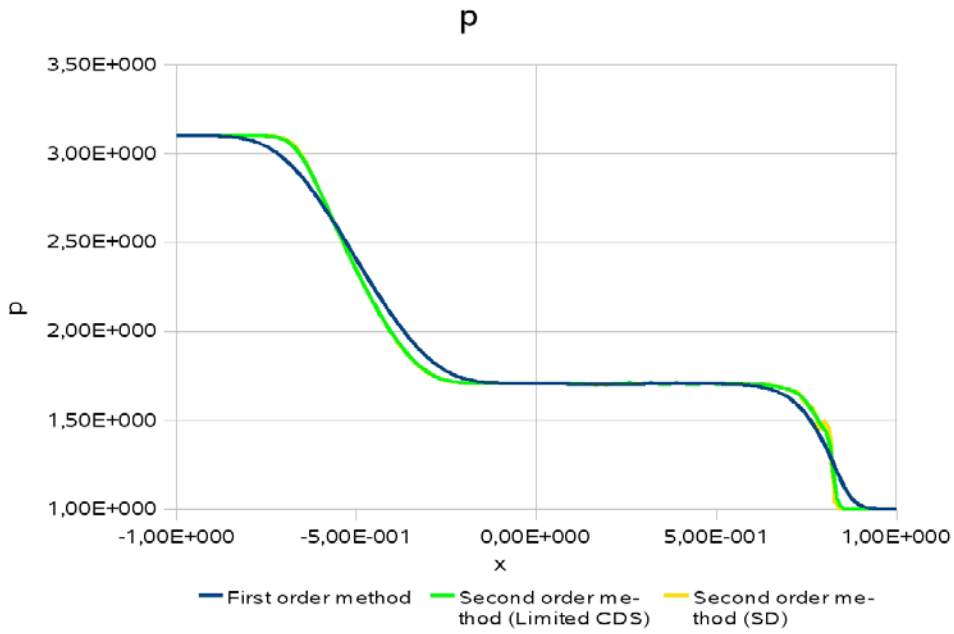

***Figure 15**. Pressure profile in the Riemann shock test case – 200 cells - Collision time: 0.015.*

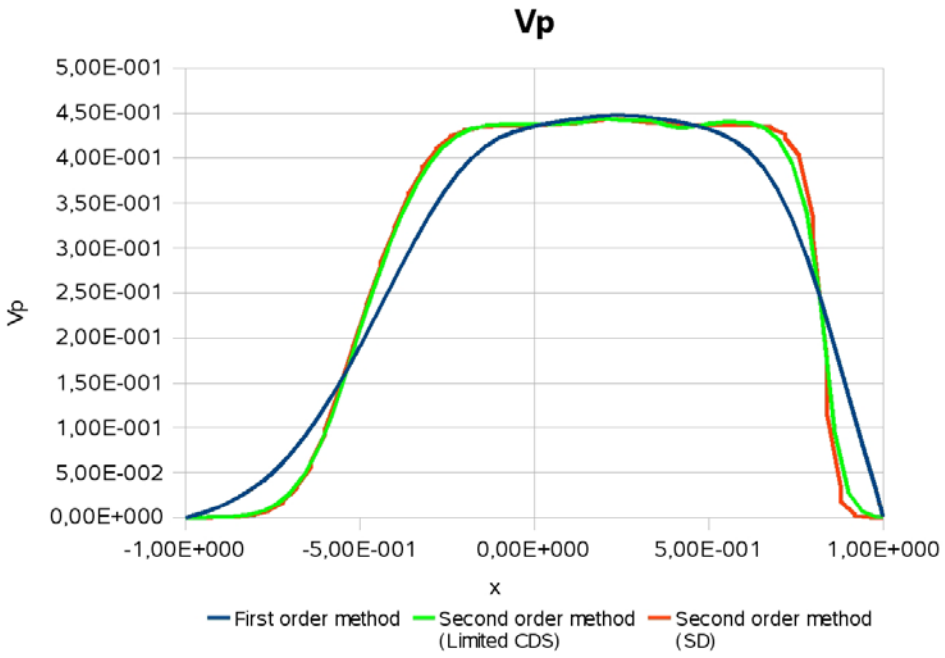

Figure 16*. Velocity profile in the Riemann shock test case – 50 cells - Collision time: 0.015.*

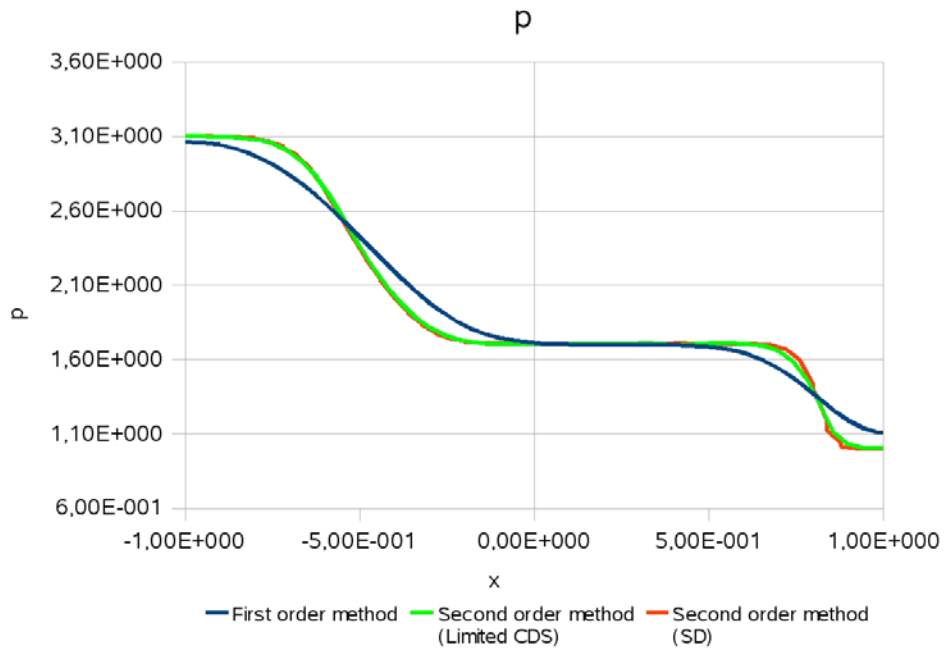

Figure 17. *Pressure profile in the Riemann shock test case – 50 cells - Collision time: 0.015.*

Polydisperse Gas-Particle Flow. The derivation of QMOM was completed, extending the algorithm presented in Fox (2008) to manage N dispersed phases. In particular the quadrature method was applied to the Boltzmann equation to consider collisions between different types of particles (Vedula and Fox, 2008). If the Boltmann equation is written in the general form for the *i*-th specie, it assumes the form:

$$\partial_t f + v_i \cdot f_i + F_i \cdot \partial_{v_i} f_i = \sum_j \frac{1}{m_j} \int_{\Re^3}\int_{\Re^2} \left(f_i\left(v_i^{'}\right) f_i\left(v_{j*}^{'}\right) - f_i\left(v_i\right) f_i\left(v_{j*}\right)\right) B_{ij}\, d\sigma dv_{j*} = I(\psi)$$

The Boltzmann collision integral (term on right-hand side) can be approximated using the quadrature method of moments, leading to

$$I_i(\psi) = \sum_j \frac{\delta_{ij}^2}{m_j} \sum_{i_k=1}^{N}\sum_{j_k=1}^{N} \tilde{p}_{i_{i_k}} \tilde{p}_{j_{j_k}} \sum_{\substack{i_1=0 \\ i_1+i_2+i_3\neq 0}}^{p}\sum_{i_2=0}^{q}\sum_{i_3=0}^{r}\sum_{j_1=0}^{i_1}\sum_{j_2=0}^{i_2}\sum_{j_3=0}^{i_3}\sum_{k_1=0}^{j_1}\sum_{k_2=0}^{j_2}\sum_{k_3=0}^{j_3} (-(1+\alpha_{ij})\mu_{ij}/m_i)^{i_1+i_2+i_3} \times$$

$$\left\{ [u]_{i_k}^{p-i_1} [v]_{i_k}^{q-i_2} [w]_{i_k}^{r-i_3} \right\}$$

$$\binom{p}{i_1}\binom{q}{i_2}\binom{r}{i_3}\binom{i_1}{j_1}\binom{i_2}{j_2}\binom{i_3}{j_3}\binom{j_1}{k_1}\binom{j_2}{k_2}\binom{j_3}{k_3} \tilde{g_{ij}}^{i_1+i_2+i_3+1}$$

$$\tilde{L}_{11}^{i_1-j_1}\tilde{L}_{12}^{i_2-j_2}\tilde{L}_{13}^{i_3-j_3}\tilde{L}_{21}^{j_1-k_1}\tilde{L}_{22}^{j_2-k_2}\tilde{L}_{23}^{j_3-k_3}\tilde{L}_{31}^{k_1}\tilde{L}_{32}^{k_2}\tilde{L}_{33}^{k_3}$$

$$\delta_{a,(i_1+i_2+i_3+k_1+k_2+k_3+1)}\ \delta_{b,(i_1+i_2+i_3-k_1-k_2-k_3+1)}$$

$$\delta_{c,(i_1+i_2+i_3-j_1-j_2-j_3)}\ \delta_{d,(j_1+j_2+j_3-k_1-k_2-k_3)}\ \ K_{a,b,c,d}.$$

where the quantity $K_{a,b,c,d}$ is given by

$$K_{a,b,c,d} = \frac{\Gamma\left(\frac{a+1}{2}\right)\Gamma\left(\frac{b+1}{2}\right)\Gamma\left(\frac{c+1}{2}\right)\Gamma\left(\frac{d+1}{2}\right)}{\Gamma\left(\frac{a+b+2}{2}\right)\Gamma\left(\frac{c+d+2}{2}\right)}$$

and Γ is Euler's gamma function.

The implementation of the collision integral was tested with a simple case of relaxation of two species to the equilibrium condition. The evolution in time of the mean velocities of the two species considered (A and B) is reported in figure 18, while the evolution of their velocity variance is reported in figure 19.

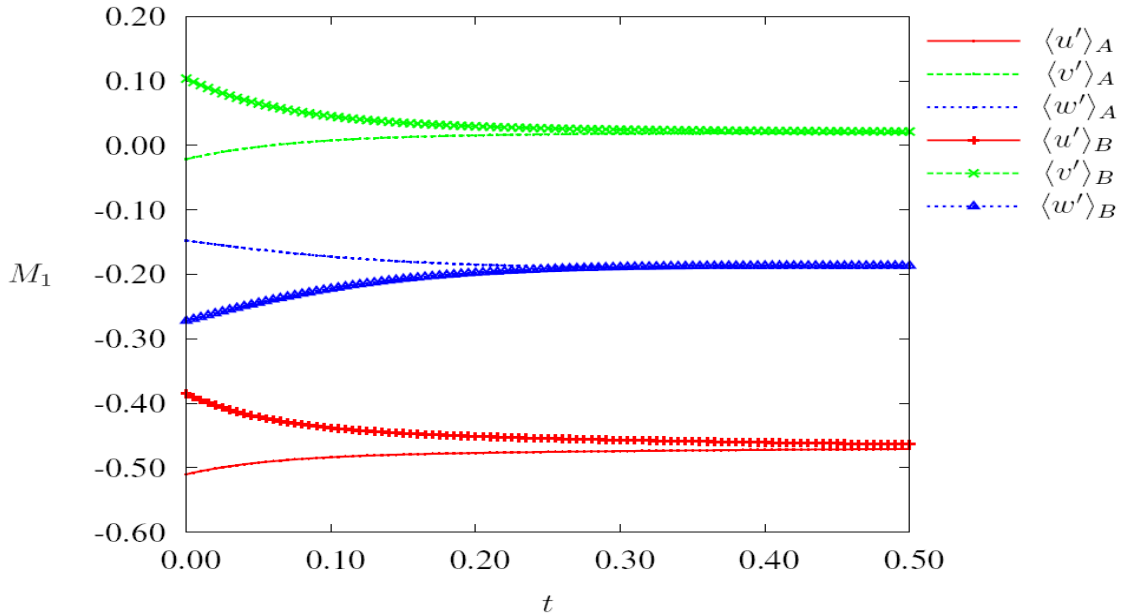

Figure 18. *Evolution of the mean velocity (first order moments) of two species A and B relaxing to the equilibrium condition.*

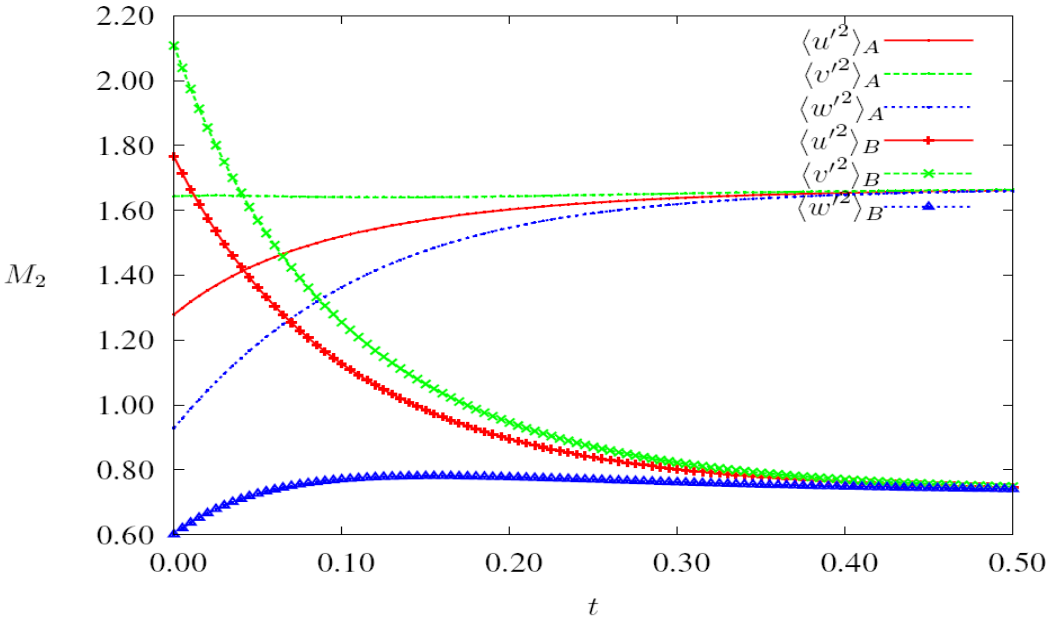

Figure 19. *Evolution of the velocity variances of two species A and B relaxing to the equilibrium condition.*

Task 1.3: Incorporation of KTGF and DQMOM into MFIX (Fox & Hrenya)

Following the derivation of the continuum models detailed above, both will be integrated into MFIX. These implementations will involve the incorporation of balance equations as well as constitutive relations. With regard to the KTGF-DQMOM approach, the basic framework of the balance equations is already in place in MFIX, and thus the bulk of the implementation effort will be focused on the coding and testing of the new constitutive relations, the form of which will be significantly more complex than existing relations. For pure DQMOM, the solid momentum equations take on a different form than those already available in MFIX (Fox, et al., in preparation), and thus the incorporation of both the balance equations and constitutive relations will be substantial tasks. For both models, code verification will begin with relatively simple systems (e.g., simple shear flow of monodisperse systems) and proceed in a stepwise manner.

(Hrenya reporting.) First, all 11 of the transport coefficients associated with the new polydisperse KTGF were programmed in Matlab and subjected to a suite of verification tests. The suite of verification tests included: (i) the reduction of the new polydisperse theory (or GHD, where GHD refers to kinetic theory of Garzo, Hrenya, & Dufty) to a previous monodisperse theory (Garzó & Dufty, 1999) for cases of $s = 1$ (where s is the number of species) and $s = 2$ species with identical properties (this test is only applicable to those transport coefficients which have a monodisperse counterpart; it does not include, for example, the diffusive species mass flux), (ii) the collapsing of predictions when the indices of unlike species for $s = 2$ were switched, and (iii) the collapsing of *dimensionless* predictions when the *dimensional* groups were changed but the *dimensionless* pi groups were kept constant, again for the case of $s = 2$. All tests were carried out over a range of input parameters, including solids fraction and restitution coefficients, to ensure robustness of the comparisons. Each of the transport coefficients passed the suite of verification tests. Additional checks include an independent check (i.e., by another person) of the hand-generated notes, and an independent, line-by-line check of the corresponding Fortran code (described below).

Following the verification testing, the Matlab codes for the calculation of the individual transport coefficients, which require inputs of material properties (particle diameters, masses, and restitution coefficients of each species) and hydrodynamic variables (granular temperature and species solids fractions), were manually converted to Fortran subroutines. These subroutines were then implemented in the MFIX framework via direct calls from MFIX, in order to reduce the amount of new/modified code (and any potential associated bugs). The incorporation of the new KTGF into MFIX was verified via comparison with output from Matlab codes and successfully tested for simple systems (e.g., simple shear flow).

It is worthwhile to mention that the current implementation of GHD in MFIX is limited to binary systems, since the I_{ilj} term appearing in the theory has not yet been extended to cases with $s > 2$. This restriction does not affect single-valued transport coefficients (e.g., shear viscosity), but rather just those associated with species pairs (e.g., ordinary diffusion coefficient D_{ij})

Although this task was focused on the incorporation of KTGF for *granular* flows, this effort was extended to *gas-solid fluidized* systems via a joint effort between Princeton, NETL (Sofiane Benyahia and Janine Galvin), and CU. This portion of the effort is reported in Task 4.6.3.

(Fox reporting.) The implementation of the third-order quadrature-based algorithm for the solution of the Boltzmann equation to describe the particle phases derived in task 1.2 into MFIX is the objective of this task. Such an implementation is based on the already existing MFIX-DEM framework, where the fluid solver is kept unchanged, and the DEM solver is replaced by the quadrature-based algorithm to manage the dispersed phases. This approach preserves the advantages of the robust fluid solver already present in MFIX without interfering with the current implementation of the standard kinetic theory of the granular flow. As a consequence of the choices presented above, the fluid phase is treated by solving its continuity and momentum equation in their full form, completely coupled with the dispersed phases through the momentum exchange term and the volume fraction. Each dispersed phase is described by directly solving one Boltzmann equation

$$\partial_t f + v_i \cdot f_i + F_i \cdot \partial_{v_i} f_i = \sum_j \frac{1}{m_j} \int_{\Re^3} \int_{\Re^2} \left(f_i\left(v_i^{'}\right) f_i\left(v_{j*}^{'}\right) - f_i\left(v_i\right) f_i\left(v_{j*}\right) \right) B_{ij} d\sigma dv_{j*} = I(\psi)$$

by means of the quadrature-based moment method, which directly provides the particle phase density (zero-order moment), from which the volume fraction is obtained, the velocity field for each particle phase (ratio of the first-order moments to the zero-order moment of each phase) and the particle-phase stress tensor.

The integration in space of the transport equations for the moments is performed using the finite volume scheme presented in Fox (2008). The value at the cell faces of the weights and abscissas, determined through the inversion algorithm of the moments, are necessary to evaluate the kinetic fluxes, which are determined according to their kinetic formulation. These face values can be calculated with a first-order upwind or with a second-order central interpolation scheme, with a limiter to keep to solution bounded. The change in the moments due to collisions can be evaluated using both a first-order Euler scheme, and a second-order Runge-Kutta scheme. A second-order Runge-Kutta method is used to integrate the moment transport equations in time, with the time step automatically determined on the basis of the Courant number, the collision time, and the drag characteristic time.

The fluid and the moments solvers exchange the information necessary to account for the interaction among the phases. In particular, the velocity field, required to calculate the drag term in the gas phase momentum equation and in the force term acting on each particle in the Boltzmann equation, and the voidage fraction, determined as the difference between the unity and the sum of the volume fractions of all the dispersed phases.
As a consequence of the choices presented above:

- The fluid phase is treated by solving its continuity and momentum equations in their full form, completely coupled with the dispersed phases through the momentum exchange term and the solids volume fraction.
- The continuity and momentum equations for each dispersed phase solved in the standard MFIX model, and the granular energy equation are not solved, because all the information they provide is obtained directly from the moments of the dispersed phase number density function.

It is worth noting that, for convenience, the zero order moment M^0 of the number density function has been scaled so that it corresponds to the volume fraction instead of to the actual

number density. The values of all variables are stored at cells centers. The value at the cell faces of the weights and abscissas, determined through the inversion algorithm of the moments, are necessary to evaluate the kinetic fluxes, which are determined according to their kinetic formulation. These face values can be reliably calculated with a first-order interpolation scheme. In the current implementation only uniform grids can be used, but the extension to non-uniform orthogonal grids is straightforward.

The change in the moments due to collisions can be evaluated using either a first-order Euler scheme, and a second-order Runge-Kutta scheme, when the Boltzmann collision operator is used. A second-order Runge-Kutta method is used to integrate the moment transport equations in time, with the time step automatically determined on the basis of:

- the dispersed phase Courant number based on the abscissas
- the collision time
- the drag characteristic time
- the fluid phase flow time

The fluid and the moments solvers exchange the information necessary to account for the interaction among the phases. In particular, the velocity field, required to calculate the drag term in the gas phase momentum equation and in the force term acting on each particle in the Boltzmann equation, and the voidage fraction, determined as the difference between unity and the sum of the volume fractions of all the dispersed phases.

Implementation in MFIX. The following diagram sums up the files added to MFIX, which are grouped in the `/model/qmomb` subdirectory, and the files changed to accommodate the implementation of QMOM.

```
mfix
`-- model
   |-- get_data.f
   |-- init_namelist.f
   |-- iterate.f
   |-- qmomk
   |   |-- qmom_boltzmann_mod.f
   |   |-- qmomk_allocate_arrays.f
   |   |-- qmomk_boundary_conditions.f
   |   |-- qmomk_collision_mod.f
   |   |-- qmomk_fluxes_mod.f
   |   |-- qmomk_gas_drag.f
   |   |-- qmomk_init_namelist.f
   |   |-- qmomk_initial_conditions.f
   |   |-- qmomk_make_arrays.f
   |   |-- qmomk_parameters_mod.f
   |   |-- qmomk_quadrature_mod.f
   |   |-- qmomk_read_restart.f
   |   |-- qmomk_time_march.f
   |   |-- qmomk_tools_mod.f
   |   |-- qmomk_write_restart.f
   |   `-- qmomknamelist.inc
```

```
|-- read_namelist.f
|-- solve_vel_star.f
`-- time_march.f
```

In particular, the `qmom_bolzmann_mod.f` module is the main module for the QMOM implementation and contains the variables declarations, while `qmomk_time_march.f` is the main QMOM routine, where all the calculations and the functions required by the QMOM algorithm are called.

For each dispersed phase, in each computational cell the following data are required:

- 8 weights (N)
- 8 abscissas for each velocity component (U_s, V_s, W_s), for a total of 24 abscissas.
- 20 moments (M)

In MFIX, the data structure is represented as follows:

```
QMOMK_N1(QMOMK_NN, DIMENSION_3, MMAX)
QMOMK_U1(QMOMK_NN, DIMENSION_3, MMAX)
QMOMK_V1(QMOMK_NN, DIMENSION_3, MMAX)
QMOMK_W1(QMOMK_NN, DIMENSION_3, MMAX)
QMOMK_M1(QMOMK_MOM, DIMENSION_3, MMAX)
```

where `QMOMK_NN` is the number of weighs and abscissas for each direction (eight), and `QMOMK_MOM` is the number of tracked moments (twenty). An identical set of arrays is used to store the previous iteration data for the Runge-Kutta 2-step method. Only weights and abscissas are stored to disk for restart purposes because they are the only necessary information to reconstruct the moments and restart the calculation. This data structure allows the algorithm to easily interact with the MFIX gas-flow solver, with the only caution of remembering that the QMOM algorithm is cell-centered, while MFIX flow solver uses a staggered arrangement of the pressure and of the velocities. As a consequence the fluid phase velocities stored at the cell faces in MFIX needs to be averaged to provide the correct value to the QMOM algorithm.

The coupling between the QMOM solver and MFIX flow solver is obtained by providing the gas phase volume fraction to the fluid solver, replacing the values stored in the `EP_g` MFIX variable at the end of each call to `QMOMK_TIME_MARCH.` The volume fraction is provided directly by the zero order moment, as a consequence of the scaling of moments discussed above. As a consequence, the fluid-phase volume fraction is given by:

$$\varepsilon_g = 1 - \sum_i M_i^0$$

The drag coupling is obtained by calculating the drag force acting on the particulate phase, as a function of the quadrature abscissas, for each velocity component:

$$D_g = \sum_{\alpha=1}^{8} \beta_\alpha \left(U_g - U_{s\alpha,} \right)$$

This quantity, changed in sign, is provided to the MFIX flow solver as an explicit source term in the gas-phase momentum equation.

This approach worked correctly in most of the considered cases but caused instabilities when the mass loading in the flow becomes high, due to the strong coupling between the fluid phase and the dispersed phase. A natural solution to this problem was already implemented in MFIX, which uses the partial elimination algorithm to decouple the multi-fluid equations. The same procedure can be adopted with QMOM, by simply considering that for each physical dispersed phase, the fluid "sees" a number of species equal to the number of weights and abscissas (eight) in the quadrature algorithm. In this way, none of the information provided by the QMOM algorithm is lost in the coupling, as it would happen if the drag coefficient were computed as a function of the particle mean velocity in the cell. In mathematical terms, using MFIX notation, the sum of the drag coefficients computed as a function of the quadrature abscissas and the sum of the products of these coefficients by the corresponding abscissa are passed to the MFIX fluid solver respectively in the *A* and *B* matrices:

$$A = \sum_{\alpha=1}^{8} \beta_{g,\alpha}$$

$$B = \sum_{\alpha=1}^{8} \beta_{g,\alpha} U_{s,\alpha}$$

where the drag coefficient is computed as

$$\beta_{g,\alpha} = \frac{\beta_{QMOM}}{V_p}$$

being β_{QMOM} the drag force acting on each particle, as used in the drag terms in the moments transport equations (Fox, 2008), and V_p the particle volume.

Verification of MFIX Implementation. The implementation was tested by simulating a gas-particle flow in a lid-driven cavity, and results were validated by comparison with Euler-Euler two-fluid and Euler-Lagrange simulations (Garg et al., 2008). The examined system is constituted by a squared box whose characteristic length is set equal to L=1. The top lid of the cavity moves so that the fluid Reynolds number based on the lid length is Re = 100. A range of Knudsen and Stokes numbers between 0.1 and 1 was considered. The definition of the Knudsen number Kn and the Stokes number St used in the calculations are

$$\mathrm{Kn} = \frac{d_p}{6\varepsilon_s L\sqrt{2}}$$

$$\mathrm{St} = \frac{\rho_p}{18\rho_g}\left(\frac{d_p}{L}\right)^2 \mathrm{Re}$$

where ρ_g, ρ_p, d_p are the gas density, the particle density, and the particle diameter respectively.

Knudsen and Stokes numbers were changed by varying the phases density ratio and the particle diameter, but keeping the average volume fraction constant. The two-fluid simulations were performed using MFIX, with Gidaspow (1994) kinetic theory and Johnson and Jackson boundary conditions, with specular collisions between particles and walls. Collisions were assumed to be perfectly elastic.

Particle volume fraction profiles are shown in figures 20, 21, 22 and 23, while the particle velocity magnitude in the case with Kn = St = 1.0 is reported in figures 24 and 25.

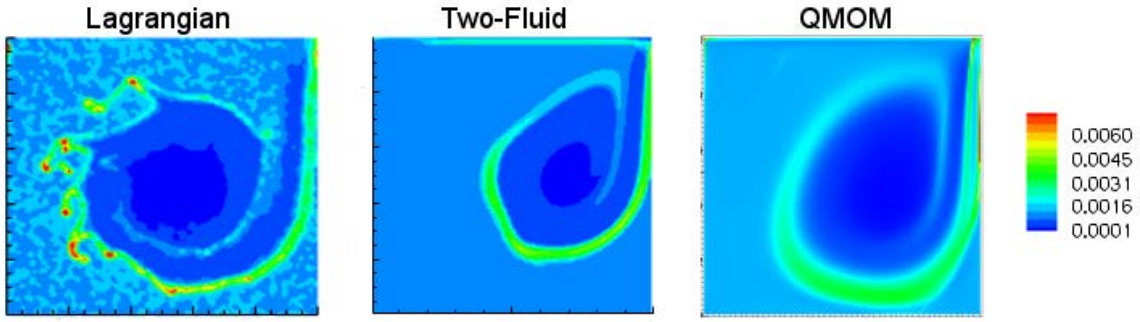

Figure 20. *Comparison of the volume fraction profiles obtained at t = 20s - Kn = 0.1 - St = 0.1*

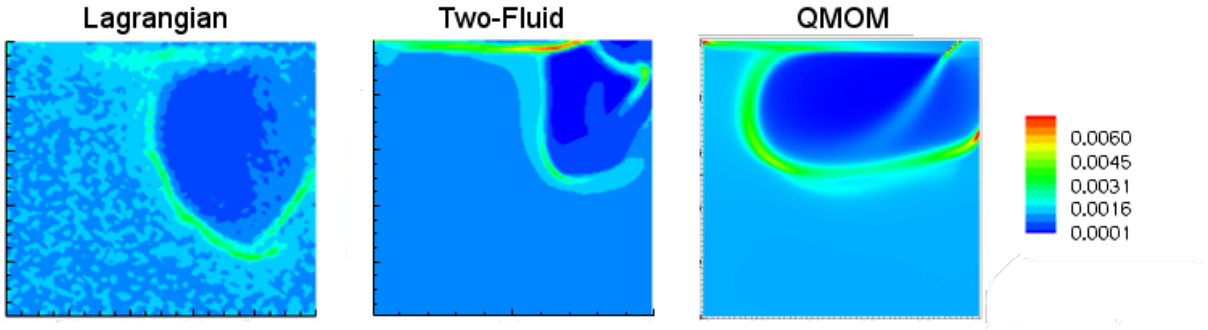

Figure 21. *Comparison of the volume fraction profiles obtained at t = 20s- Kn = 0.1 - St =1.0.*

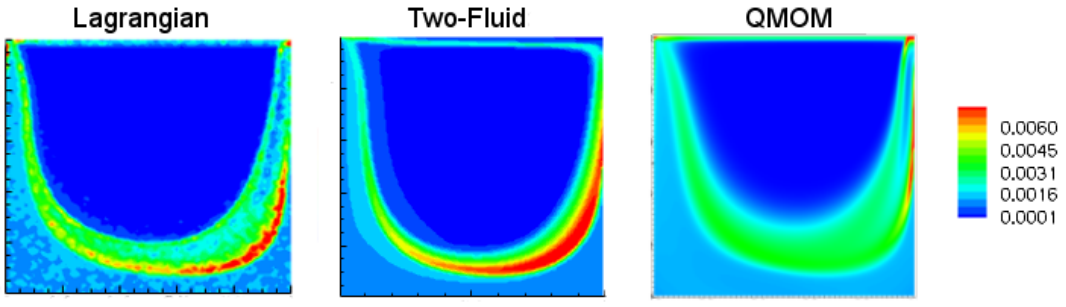

Figure 22. *Comparison of the volume fraction profiles obtained at t = 20s - Kn = 1.0 - St = 0.1.*

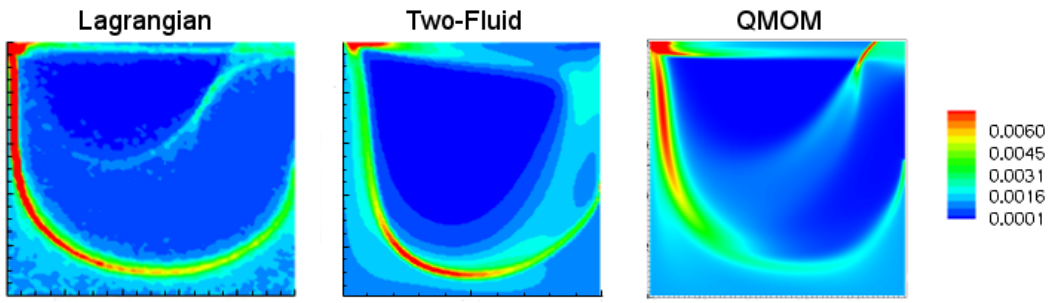

Figure 23. *Comparison of the volume fraction profiles obtained at t = 20s - Kn = 1.0 - St = 1.0.*

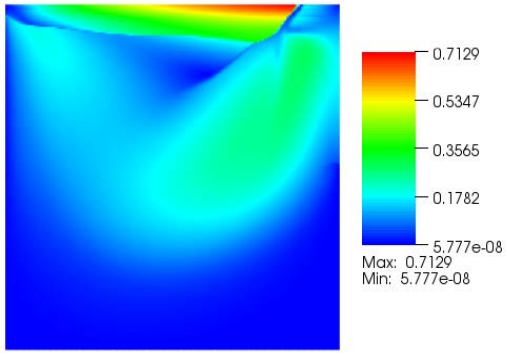

Figure 24. *Particle velocity magnitude provided by QMOM at t = 20s - Kn = 1.0 - St = 1.0.*

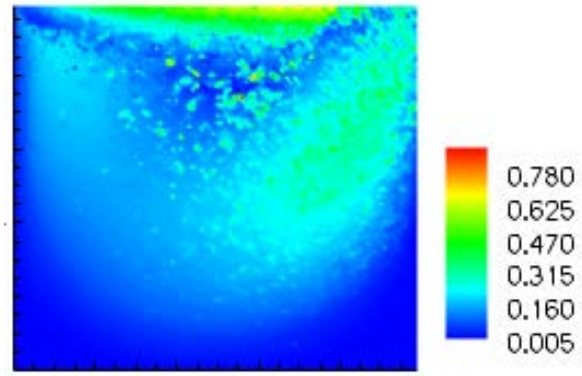

Figure 25. *Particle velocity magnitude provided by the Euler-Lagrange simulation at t = 20s - Kn = 1.0 - St = 1.0.*

The analysis of the particle volume fraction contour plots clearly shows the capabilities of the QMOM algorithm to properly predict the flow behaviour over a wide range of Stokes and Knudsen number, with good agreement with the Euler-Lagrange predictions. In comparing results with the Euler-Lagrange simulations it is necessary to remember that Euler-Lagrange results represent one realization of the flow, while both QMOM and two-fluid models provide averaged property profiles. This might explain the differences in the predictions between QMOM and Euler-Lagrange simulations, especially in the case with Kn = 0.1 and St = 0.1, where the formation of denser structures was captured by the Lagrangian calculations only. More simulations are required to obtain averaged profiles from the Euler-Lagrange code, and further studies are in progress.

It is worth to notice that QMOM captured the same structure on the right side of the cavity described by Euler-Lagrange simulations, with a zone with reduced concentration of particles surrounded by two zones with a higher particle concentration along the border of the vortex in the case of Kn = 1.0 and St = 0.1 (Figure 22). In figure 23 very good agreement between QMOM and Euler-Lagrange simulation is shown: both QMOM and the Euler-Lagrange solutions predicted particle trajectory crossing at the top corners of the cavity, while the two-fluid model was unable to properly capture it. For example, at the top-right, the particles reflected by the wall, and those going towards the wall have intersecting trajectories, but the particles do not collide with one another. As it is clear by the comparison in figure 23, this characteristic of the flow is not captured by the two-fluid model simulation, because it only computes the mean local velocity, and, as a consequence, it cannot describe situations where, at a given point, multiple velocities are defined, as in the case of crossing trajectories. In these situations discontinuities in the mean particle velocity field are present, as shown in figures 24 and 6, respectively, by the QMOM and Euler-Lagrange simulations.

The implementation of QMOM (Fox, 2008; Passalacqua et al., 2009) into MFIX has been further verified by performing a preliminary grid independence study in a 2-D channel flow of 10 cm width, with periodic boundary conditions in the direction of the flow, whose length was set to 1 m. The objective of the study is to understand the influence of the spatial discretization on the numerical solution of the moment transport equations, and, in particular, on the formation of structures at higher particle concentration.

The initial average volume fraction is 0.01, uniform in the whole computational domain. Both the fluid and the particle phase have zero velocity at the beginning of the simulation. Gravity acts along the vertical axis, in the opposite direction of the flow. A constant fluid mass flow rate is imposed, in order to have $Re_g < 1500$, to avoid the transition to turbulence of the fluid phase in a single phase flow. Three cases are considered, with grids of 40x400, 80x800 and 100x1000 cells. Results were compared to the corresponding two-fluid simulation, performed using the default model in MFIX. The contour plots of the particle phase volume fraction, taken after the flow developed in the channel are reported in Figs. 26, 27 and 28 for the three grid densities under consideration.

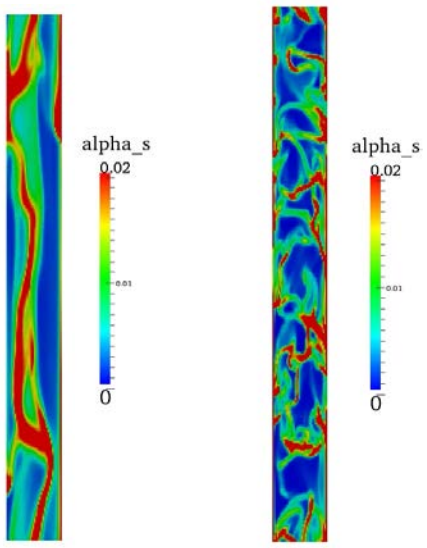

Figure 26. *QMOM (left) and two-fluid (right) predictions – Grid 40 x 400 – t = 1.20 s.*

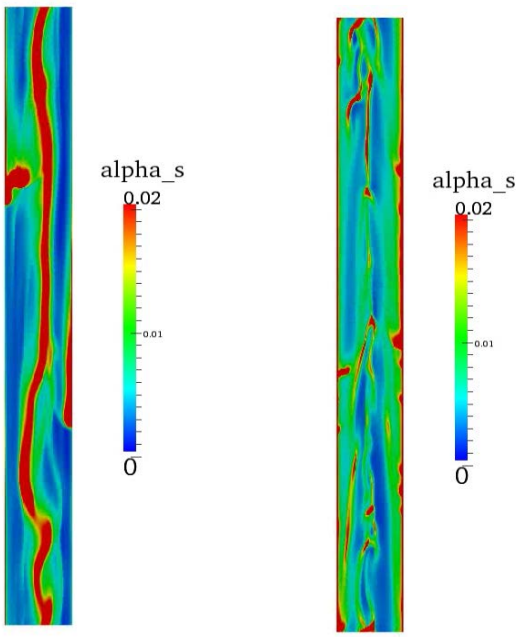

Figure 27. *QMOM (left) and two-fluid (right) predictions – Grid 80 x 800 – t = 1.20 s.*

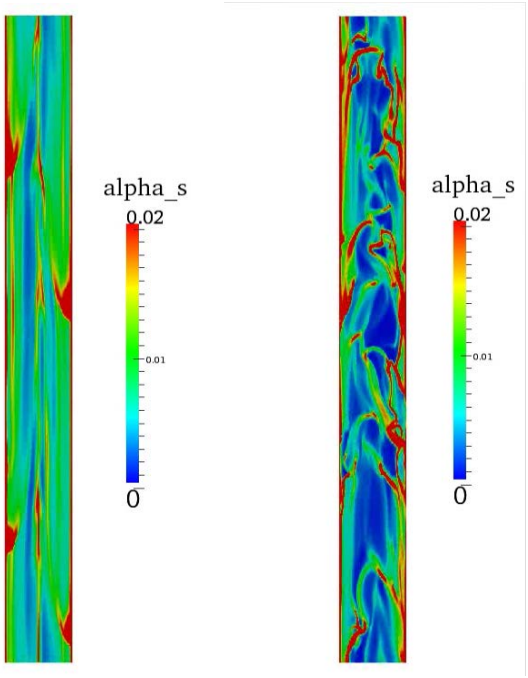

Figure 28: *QMOM (left) and two-fluid (right) predictions – Grid 100 x 1000 – t = 1.20 s.*

From the contour plots it is possible to observe that in both approaches, after a transient phase during which the flow develops, the particle phase segregates against the walls of the channel, originating the typical structure of core-annular flow, with particles falling down along the walls due to the insufficient drag force exerted by the fluid moving upward. However, significant differences can be observed in Fig. 26 with a 40 x 400 grid, where the two-fluid model prediction shows the formation of many small structures with higher particle concentration, which are not observed in QMOM predictions. Increasing the grid density to 80 x 800, as done to obtain the results reported in Fig. 28, did not significantly change the comparison: QMOM results show slightly sharper structures of the flow, but no structures of the size of the computational cell are observed, in clear opposition to what is shown in the plots obtained from the two-fluid simulations. A further increase of the grid density to 100 x 1000 computational cells confirmed what is observed in the first two cases.

As discussed in Passalacqua et al. (2009), the prediction of small structures observed in two-fluid models is due to the mathematical formulation of the equations, which are based on the hydrodynamic assumption. Such an hypothesis is not valid to describe flows with local Knudsen numbers greater than 0.1 even with the adoption of partial slip boundary conditions because the Knudsen layers extend inside the bulk of the fluid (Galvin et al., 2007). In flows like those considered in this study and typical of risers, the Knudsen number can reach values of the order of 10, clearly indicating that the regime is outside from the hydrodynamic range. Under these conditions, for finite Stokes numbers, particles trajectories can cross without collisions between particles, originating the phenomenon of particle trajectory crossing. This phenomenon can be described only by methods that account for multiple local velocities, as it happens in Lagrangian methods or in higher-order moment methods such as QMOM. If only the mean momentum equation is considered, particle trajectory crossing cannot be predicted (Desjardin et al., 2008),

leading to the formation of delta shocks in the particle concentration, which are identified with clusters, whose size and number is sensitive to the grid resolution. These structures however do not represent an actual physical entity that characterizes the particle phase, but, as clarified above, are only a consequence of the limitations of the hydrodynamic models.

Implementation of Collisional Flux. The next step consisted in the implementation in MFIX of the collisional term of the moment spatial fluxes (Fox and Vedula, 2009), in order to account for their effect, which become important for particle phase volume fractions greater than approximately 5%. The moment spatial fluxes can be written as the sum of a kinetic and collisional contribution, the latter of which originates from the collision integral. The rate of change of the moment of order γ due to collisions, in the case of finite-size particles can be written as

$$\mathbb{C}^{\gamma}_{ijk} = \frac{6}{\pi d_{\mathrm{p}}} \int_{\mathbb{R}3} \int_{\mathbb{R}3} \int_{\mathbb{S}^+} \left[(v'_{1,1})^i (v'_{1,2})^j (v'_{1,3})^k - (v_{1,1})^i (v_{1,2})^j (v_{1,3})^k \right] f^{(2)}(\mathbf{x}, \mathbf{v}_1; \mathbf{x} + d_{\mathrm{p}}\mathbf{n}, \mathbf{v}_2) \, |\mathbf{g} \cdot \mathbf{n}| \, \mathrm{d}\mathbf{n}\mathrm{d}\mathbf{v}_1\mathrm{d}\mathbf{v}_2$$

where d_{p} is the particle diameter, v is the pre-collisional particle velocity, and v' is the post-collisional particle velocity, $f^{(2)}$ is the pair distribution function, **g** is the relative velocity vector and **n** is the unit vector along the direction of the particle centres. This term can be re-written as

$$\mathbb{C}^{\gamma} = C^{\gamma} - \boldsymbol{\nabla} \cdot \mathbf{G}^{\gamma} + \mathcal{O}\left(\left(d_{\mathrm{p}}/L \right)^2 \right)$$

where the first term on the right-hand side corresponds to the rate of change of the moment for point particles, modified to introduce the radial distribution function g_0,

$$C^{\gamma} = \frac{6 g_0}{d_{\mathrm{p}}} \int_{R^3} \int_{R^3} g I^{\gamma}(\omega, \mathbf{v}_1, \mathbf{v}_1 - \mathbf{v}_2) f(\mathbf{v}_1) f(\mathbf{v}_2) \mathrm{d}\mathbf{v}_1 \mathrm{d}\mathbf{v}_2$$

and the second term is the collisional flux, with

$$\mathbf{G}^{\gamma} = 3 g_0 \int_{\mathbb{R}^3} \int_{\mathbb{R}^3} g \mathbf{F}^{\gamma}(\omega, \mathbf{v}_1, \mathbf{v}_1 - \mathbf{v}_2) f(\mathbf{v}_1) f(\mathbf{v}_2) \mathrm{d}\mathbf{v}_1 \mathrm{d}\mathbf{v}_2$$

It is worth noting that the collisional flux becomes zero in the Boltzmann limit (point particles), and it is different from zero only for finite (non-zero) size particles. Moreover, when the particle volume fraction approaches its maximum value, the collisional flux becomes very big due to the presence of the radial distribution function g_0, preventing further accumulation of particles and limiting the phase volume fraction itself. The role of collisional fluxes is shown considering two density waves moving in opposite direction, as shown in Fig. 29.

If collisional fluxes are neglected, no limitation is imposed on the particle phase volume fraction, and the density reaches a maximum value of about 0.2, when the waves collide, as shown in Fig. 30. On the other hand, when the collisional flux contribution is included, the evolution of the density profile is significantly influenced, and the maximum value of the particle concentration is limited to about 0.12, as shown in Fig. 31.

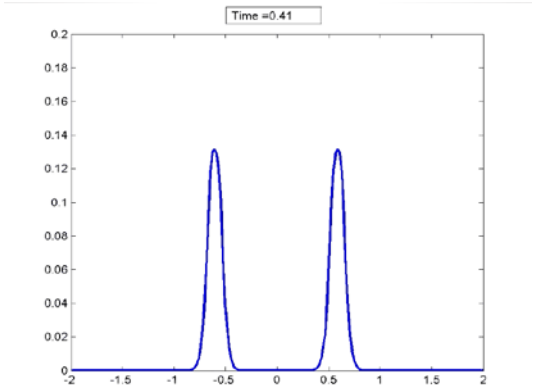

Figure 29. *Density waves moving one towards the other before colliding.*

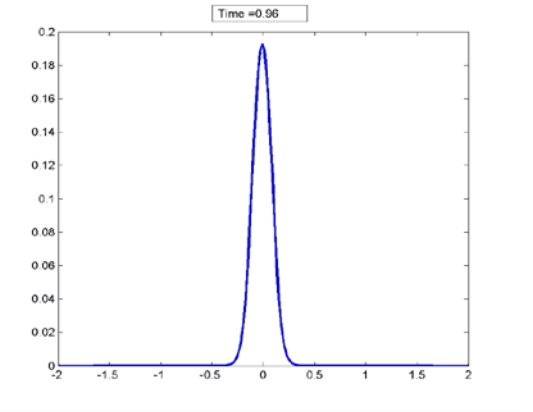

Figure 30. *Density peak without collisional fluxes.*

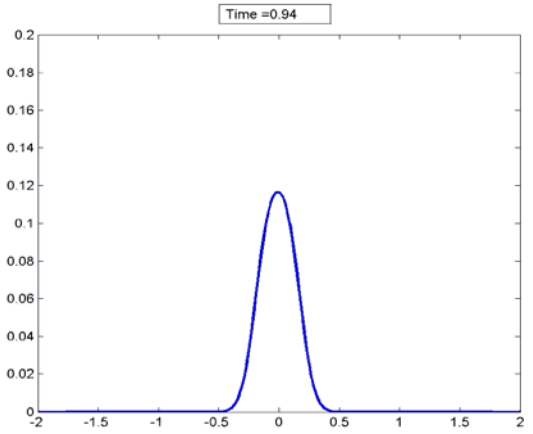

Figure 31: *Density peak with collisional fluxes.*

The implementation of collisional fluxes was verified in channel flow simulations with particle volume fractions larger than 0.01. Finally, the QMOM implementation has been slightly modified to work with the last MFIX development version.

Test Cases. The implementation of the quadrature-based moment method in MFIX was tested by performing simulations of gas-particle flows in a two-dimensional vertical channel (0.1

x 1 m) with monodisperse particles and comparing the results with two-fluid model simulations of the same case. The mass flow rate of the fluid-phase (ρ_g = 1.2 kg/m^3) was fixed so that the fluid-phase Reynolds number is 1380, well below the transition to turbulence in a single-phase flow. This choice was made to remove the direct effect of the fluid turbulence on the formation of segregated structures from the system. The desired fluid-phase Reynolds number was obtained by setting the viscosity of the fluid phase to $\mu_g = 1.74 \times 10^{-4}$ Pa s.

For the particle phase, a range of volume fractions between 0.0001 and 0.01 was considered, with a particle density of 1500 kg/m^3. The particle diameter was set to 252 μm, and the restitution coefficients for both particle-particle and particle-wall collisions were set to $e_p = e_w = 1$, which corresponds to perfectly elastic collisions.

Wall boundary conditions were set to be specularly reflective. This condition is equivalent, in the two-fluid model, to a free-slip condition for the particle phase. No-slip conditions were used at the walls for the fluid phase. Periodic conditions with constant mass flow rates were adopted in the flow direction for both phases. A uniform field for all the properties was used as the initial conditions.

Results of a channel-flow simulation with particle-phase volume fraction of 0.01 obtained with MFIX-QMOM are reported in Fig. 32, where snapshots of the time evolution of the particle-phase volume fraction are shown. The predictions of the two-fluid model for the same case are show in Fig. 33. At the beginning of the simulation, the particles, initially distributed uniformly in the channel, are accelerated towards the walls due to the mean fluid velocity gradient, where they are reflected and move towards the centre of the channel. This process leads to the formation of preferential particle-depleted vertical paths for the fluid phase, where it can accelerate. This separation however is unstable, due to the velocity gradient between the zone at low particle concentration and the one at higher particle concentration, as observed in Passalacqua et al. (2009). This leads to chaotic flow behavior, where particles tend to segregate towards the walls, originating the characteristic core-annular flow, with particles falling along the channel walls, with an oscillating upward flow in the centre.

A similar behavior is observed in the initial stages of the two-fluid model prediction, where particles are reflected by the walls and give origin to the preferential paths for the fluid phase (Fig. 33, t = 1.45 s). However, the evolution of the system from this point on proceeds with the formation of two unstable structures on the sides of the flow, which leads to particle segregation. The main difference between the MFIX-QMOM and two-fluid model predictions is, however, the abundance of fine structures at high particle concentration in the two-fluid prediction (i.e., delta-shocks), which are not predicted by the QMOM model. The formation of these structures in two-fluid models can be explained by the fact that when particle trajectory crossing occurs, models tracking only the mean momentum are unable to predict correctly all the velocity moments (Desjardin et al. 2008). In such a situation, hydrodynamic models predict a delta-shock, since they cannot represent a situation where multiple distinct local particle velocities are present. Further grid refinement will exacerbate the segregation in the two-fluid model. Although not as easily distinguished in the snapshots in Figs. 32 and 33 as in flow-field animations, there are also clear differences between the MFIX-QMOM and the two-fluid predictions in the regions near the walls. In the MFIX-QMOM simulations, the falling particles form larger ‘blobs’ that cover several grids cells away from the wall, while in the two-fluid predictions the falling particles remain much closer to the wall. We believe that these differences can be attributed to the differences in the boundary conditions for the granular temperature.

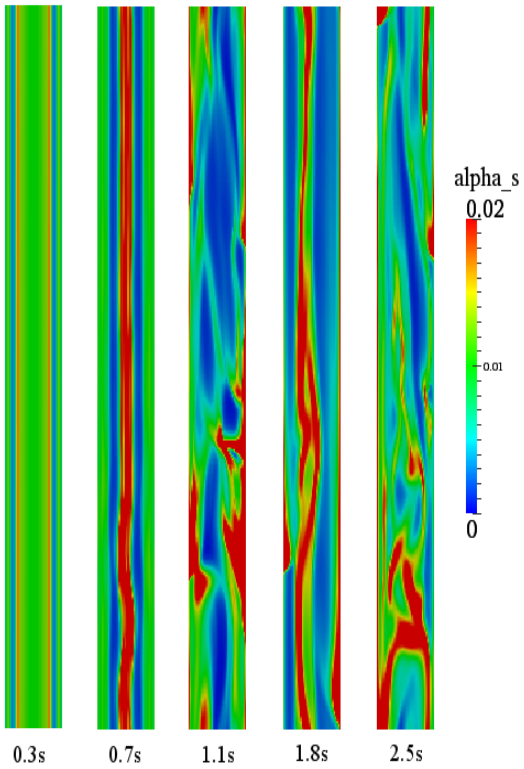

Figure 32*. Particle-phase volume-fraction evolution predicted by MFIX-QMOM with an average particle-phase volume fraction of 0.01.*

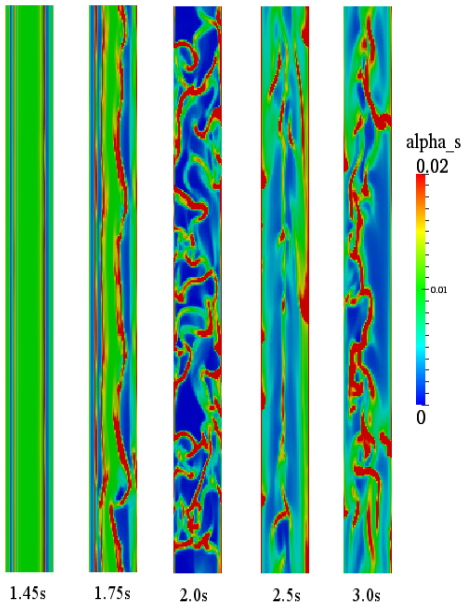

Figure 33. *Particle-phase volume-fraction evolution predicted by the two-fluid model with an average particle-phase volume fraction of 0.01.*

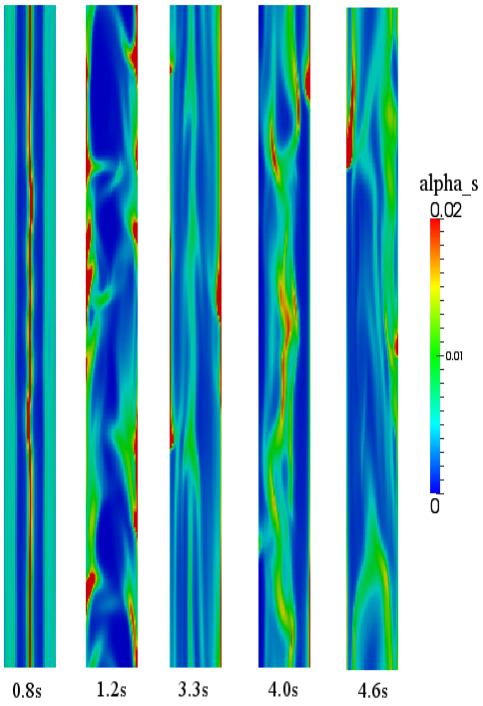

Figure 34. *Particle-phase volume-fraction evolution predicted by MFIX-QMOM with an average particle-phase volume fraction of 0.005.*

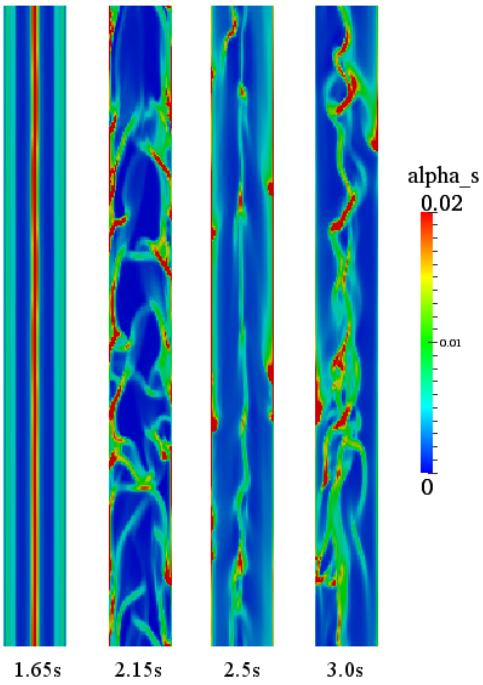

Figure 35*. Particle-phase volume-fraction evolution predicted by the two-fluid model with an average particle-phase volume fraction of 0.005.*

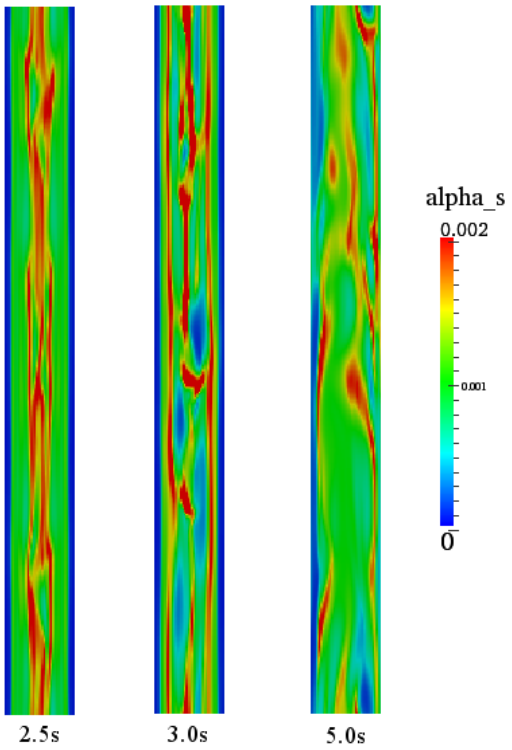

Figure 36*. Particle-phase volume-fraction evolution predicted by MFIX-QMOM with an average particle-phase volume fraction of 0.001.*

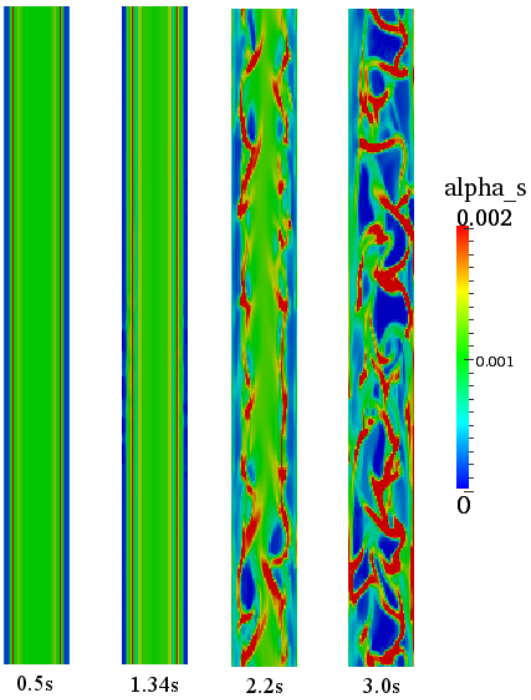

Figure 37. *Particle-phase volume-fraction evolution predicted by the two-fluid model with an average particle-phase volume fraction of 0.001.*

Similar results were observed in the case of an average particle-phase volume fraction of 0.005, reported in Fig. 34 (MFIX-QMOM) and Fig. 35 (two-fluid model). The agreement between the two predictions is consistent during the initial stages of the simulations. However, the two-fluid model still shows a tendency to predict fine structures at high particle concentration, as observed in the previous case. The effect of the particle concentration on the development of the instability that leads to particle segregation was further investigated by considering two cases with lower mass loading. Fig. 36 shows the evolution of the flow predicted by MFIX-QMOM in the case of an initial mean volume fraction of 0.001, while Fig. 37 reports the prediction of the two-fluid model in the same case. The mechanism that leads to the formation of an unstable flow is similar to that observed in the densest cases. However the transition to an unstable flow, and the consequent particle segregation phenomena, are slower and less evident, since the particle concentration is lower. The two-fluid model predicts a similar behavior to the one observed in Fig. 33, with the formation of small structures not observed in the MFIX-QMOM prediction.

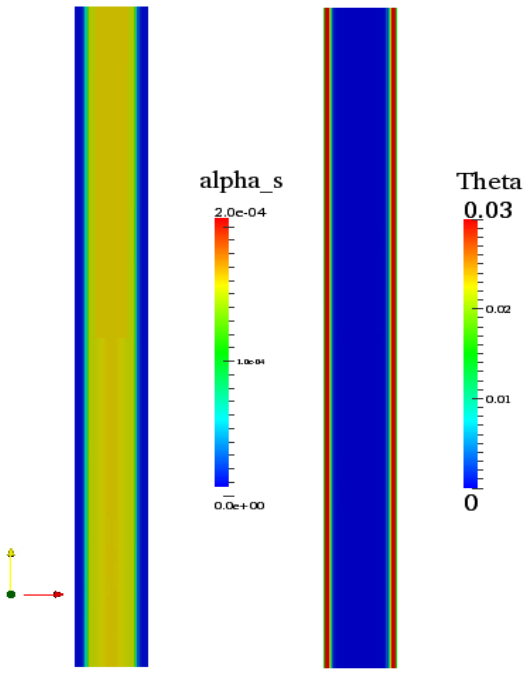

Figure 38. *Particle-phase volume fraction and granular temperature at 5 s predicted by MFIX-QMOM with an average particle-phase volume fraction of 0.0001.*

An even more dilute case, with an average particle volume fraction of 0.0001 (mass loading 0.13), was also considered. The results of the MFIX-QMOM predictions are reported in Fig. 38. For this case, after 5 s of simulation time, particles are still distributed almost uniformly across the channel, with the exception of near the walls, since in the wall zone the particle temperature is highest. We did not obtain a convergent solution using the two-fluid model with the required convergence criteria used in the other cases; as a consequence results from two-fluid models are not reported. Although we cannot confirm it directly due to the finite duration of our simulation, it appears that the case shown in Fig. 38 reaches a time-independent state where only gradients in the wall-normal direction are present.

In the zone next to walls the net particle flux is zero, and, as a consequence the mean particle velocity is zero, but the velocity variance is high due to specular reflections. As observed in Passalacqua et al. (2009), this means that the local particle Mach number of the flow, defined using of the mean particle velocity and the granular temperature (Kogan, 1969), and the local Knudsen number, are large and well outside the range of validity of hydrodynamic models (Kn < 0.1), even with the addition of partial-slip boundary conditions like those proposed by Johnson and Jackson (1987). In the cases considered in this work, the Johnson and Jackson boundary conditions degenerate into free-slip conditions, since the walls are assumed to be frictionless. It is worth noting that the Johnson and Jackson boundary conditions imply a zero granular temperature flux at the wall, when perfectly specular conditions are imposed. This implies that the two-fluid models cannot convert the velocity of particles impinging on the wall into granular temperature, even though the velocity component normal to the wall is zero. As a consequence, the maximum in the granular temperature at the walls that is observed in Fig. 38 is not captured by the two-fluid model.

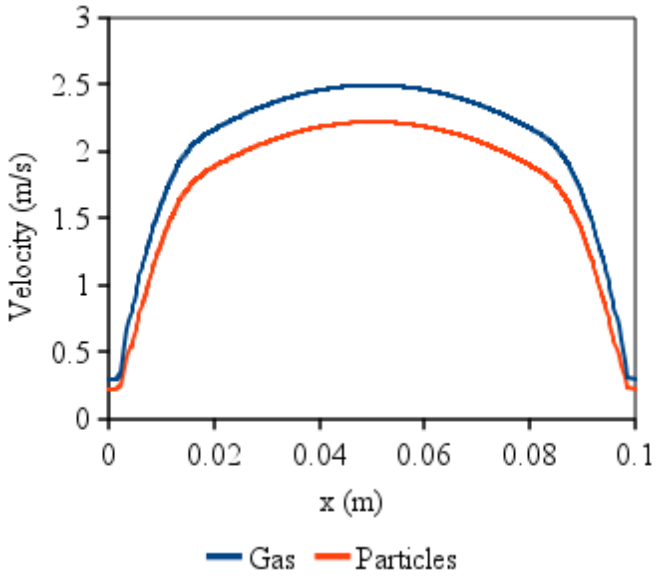

Figure 39. *Phase velocities predicted by MFIX-QMOM at 5 sec with an average particle-phase volume fraction of 0.0001.*

The vertical velocity profiles for the case in Fig. 38 are reported in Fig. 39, and show that the flow has the typical profile of a stable channel flow. For this case, the particle mass loading is small enough to not have a destabilizing effect on the fluid phase. However, it is worth noting that the velocity profiles are not perfectly parabolic, due to the presence of the particles and the momentum coupling with the particle phase. Nonetheless, no instabilities develop and both phases attain a steady state.

The relative computational cost of MFIX-QMOM with respect to the two-fluid model in MFIX is in the range of 1.5–1.9. The longest simulation was the one with the highest particle-phase volume fraction, which required 25.37 hours with the two-fluid model and 48.2 hours with MFIX-QMOM on a single core of an Intel Xeon CPU at 3.0GHz. It is worth noting that the hyperbolic nature of the QMOM model should make the MFIX-QMOM code highly scalable. In

the dilute limit, the time step is limited only by the CFL number and the kinetic-based fluxes are stable for relatively large CFL number (e.g., CFL=1 for the first-order scheme).

Riser Test Case. The third-order quadrature-based moment method in MFIX has been further tested considering a vertical channel, with a two-phase monodispersed gas-particle flow. The system under examination is constituted by a 1m channel made of two parallel walls separated by a distance of 0.1 m, with periodic boundary conditions in the direction of the flow, and gravity opposed to the flow motion. A constant mass flow rate for the fluid phase is imposed. No-slip boundary conditions were considered for the fluid phase at the walls, while specularly reflective boundary conditions were imposed both in the MFIX-QMOM and in the Euler-Lagrange simulations of the particles. Johnson and Jackson boundary conditions, with zero specularity coefficient, were adopted in the MFIX two-fluid model.

The fluid phase density is 1.2 kg m^{-3}, with a dynamic viscosity of 1.73e^{-4} Pa s, artificially increased so that the fluid Reynolds number in a single-phase flow under the same operating conditions would be under 1500 (actual Re in the channel is 1379, with a fluid mean velocity of 2 m s^{-1}). The particle density is set to 1500 kg m^{-3}, and the particle diameter is 80 μm for the case of St = 0.1, and 252.9 μm for St = 1. The channel was filled uniformly with an initial particle volume fraction equal to 0.04. Both a partially coupled (only volume fraction effects on the fluid phase) and a full coupled (volume fraction and momentum exchange with the fluid phase) were considered.

The velocity profiles in the partially coupled case are reported in figure 40, while the velocity contour plot predicted by MFIX two-fluid model is shown in figure 41. It is worth noting that all the plots reported in these figures are instantaneous snapshots. In the case of MFIX-QMOM simulations, the profiles do not change along the whole length of the channel, because the solution reaches a steady state, while in the MFIX two-fluid model no steady state is predicted. A similar behavior is present in the contour plot of the particle volume fraction (figure 42), while the two-fluid model predicts the formation of structures with higher particle concentration, as shown in figure 43.

The reason of this discrepancy was found by examining the local values of the Mach number:

$$\mathrm{Ma_p} = \frac{|\mathbf{U}_\mathrm{p}|}{\Theta^{1/2}},$$

and Knudsen number:

$$\mathrm{Kn_p} = \frac{\lambda_\mathrm{p}}{\mathrm{D}} = \sqrt{\frac{\pi}{2}}\frac{\tau_\mathrm{c}|\mathbf{U}_\mathrm{p}|}{\mathrm{D}} = \frac{\pi d_\mathrm{p}|\mathbf{U}_\mathrm{p}|}{12\sqrt{2}\mathrm{D}g_0\alpha_\mathrm{p}\Theta^{1/2}} \propto \frac{1}{\alpha_\mathrm{p}}\mathrm{Ma_p}$$

where $\mathbf{U_p}$ is the particle velocity, Θ the granular temperature, λ_p the particle mean free path, α_p the particle volume fraction, D the channel diameter, d_p the particle diameter, τ_c the collision time, g_0 the radial distribution function. In this work, the Carnahan and Starling radial distribution function has been adopted.

The profiles of the Mach and Knudsen numbers, predicted by MFIX-QMOM are reported in figure 44 (St = 0.1) and 6 (St = 1.0). The values of the local particle Knudsen number are well outside the slip regime, where rarefaction effects can be described using partial slip boundary conditions. For values of Kn > 0.1, higher-order approximations of the kinetic equation are necessary, because the rarefaction effects extend inside the bulk of the system. The origin of the

differences is clarified by considering that the particle Knudsen number is inversely proportional to the rms particle velocity, and to the particle-phase volume fraction. In the situation considered in this work, the granular temperature is relatively low, leading to a small number of collisions, even though the particle-phase volume fraction is not particularly small. Under these conditions, the two-fluid model, derived under the assumption that Kn is much smaller than 1, is invalid, and can lead to the prediction of unphysical flow behavior.

The formation of transient structures with high particle concentration in the two-fluid model, which are often confused with the particle clusters observed in gas-solid risers can be reconsidered, in light of these new observations. In order to transport the solid particles, risers operate under highly turbulent conditions, where vortical structures typical of fully developed turbulent flow are known to induce particle segregation and cluster formation. In the case with St = 0.1, the fluid flow is purposely restricted to laminar conditions, as is evident from the fluid velocity profile in the partially coupled case, which has the well-known parabolic shape. As a consequence, the phenomenon of particle segregation induced by the fluid turbulence is excluded. However, the two-fluid model still predicts the formation of time-dependent inhomogeneous structures in the flow. These structures are artifacts generated by the nature of the model when applied outside its range of validity, as demonstrated in the work of Desjardin et al. (2008), where a two-fluid model was represented by a single-node quadrature approximation of the kinetic equation. The authors showed that if only the mean momentum is considered, which is equivalent to representing the particle velocity distribution function with one node and one abscissa, in spite of observing trajectory crossing in dilute flows, a delta shock is induced in the particle-phase volume fraction because not enough information is carried about the structure of the particle velocity field. The same is true for the formation of the structures by the two-fluid model, even when the local physical conditions would not induce their formation in the solution to the original kinetic equation.

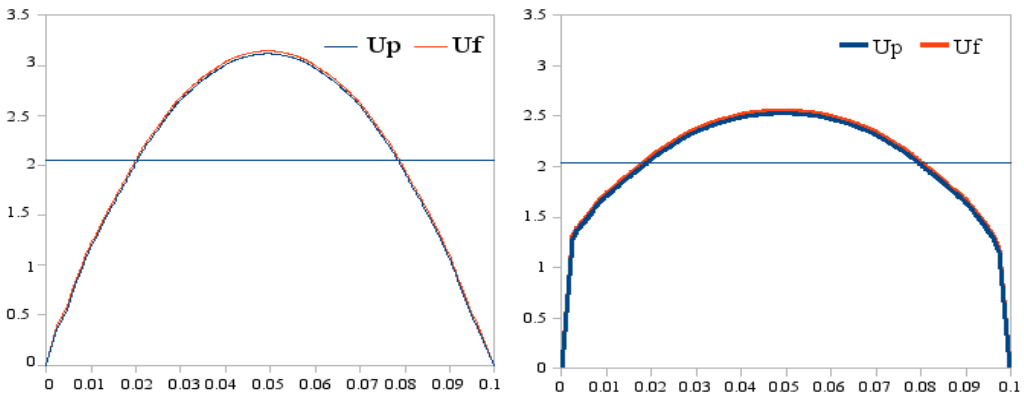

Figure 40. *Phase velocity profiles predicted by (left) MFIX-QMOM in the partially and (right) fully coupled cases. St = 0.1. Note that particle and fluid velocities nearly coincide for both cases.*

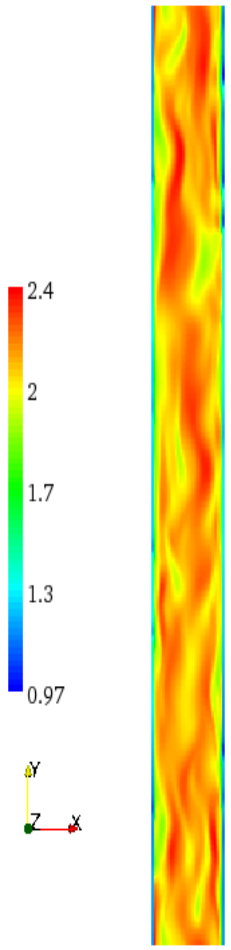

Figure 41. *Contour plot of the particle phase velocity predicted by two-fluid model. St = 0.1.*

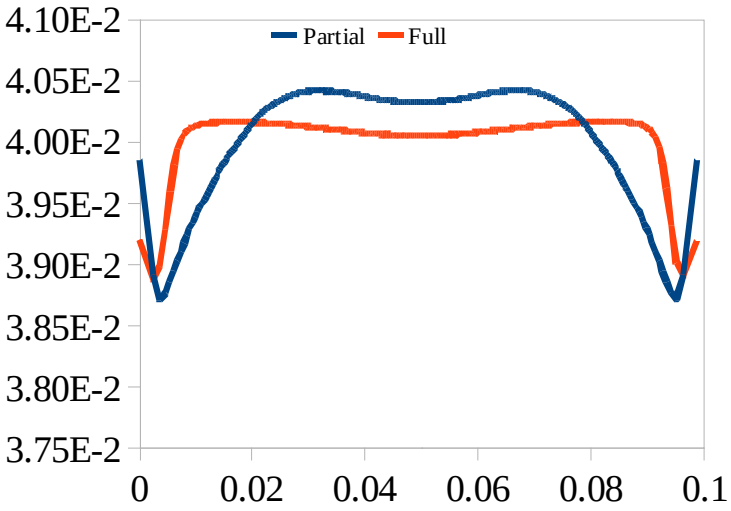

Figure 42. *Volume fraction profiles predicted by MFIX-QMOM. St = 0.1.*

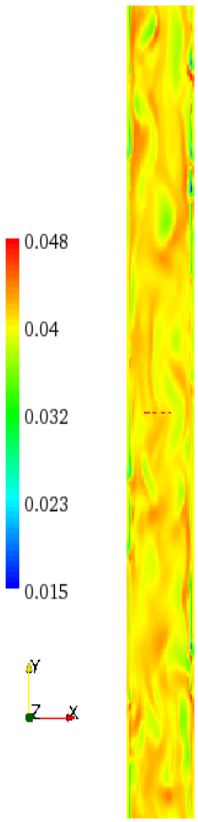

Figure 43. *Contour plot of the particle phase volume fraction predicted by the two-fluid model. St = 0.1.*

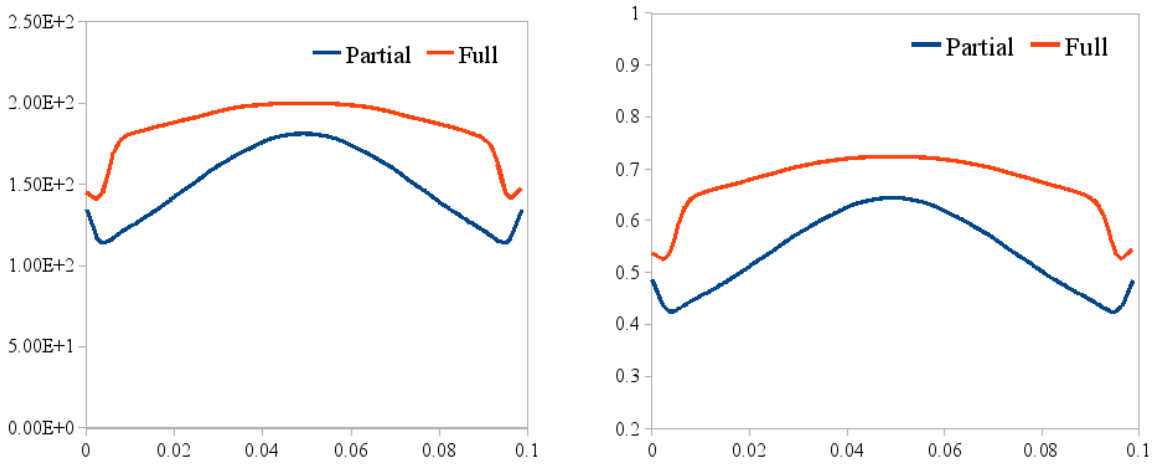

Figure 44. *Local Mach (left) and Knudsen (right) number predicted by MFIX-QMOM. St = 0.1.*

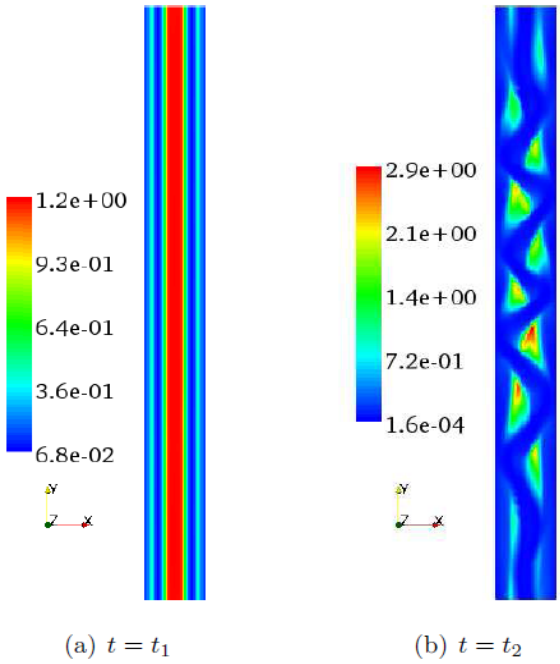

Figure 45. *Instantaneous contour plots of the particle Knudsen number at $t = t_1$ (a) and at $t = t_2$ (b), predicted by QMOM, St = 1.0.*

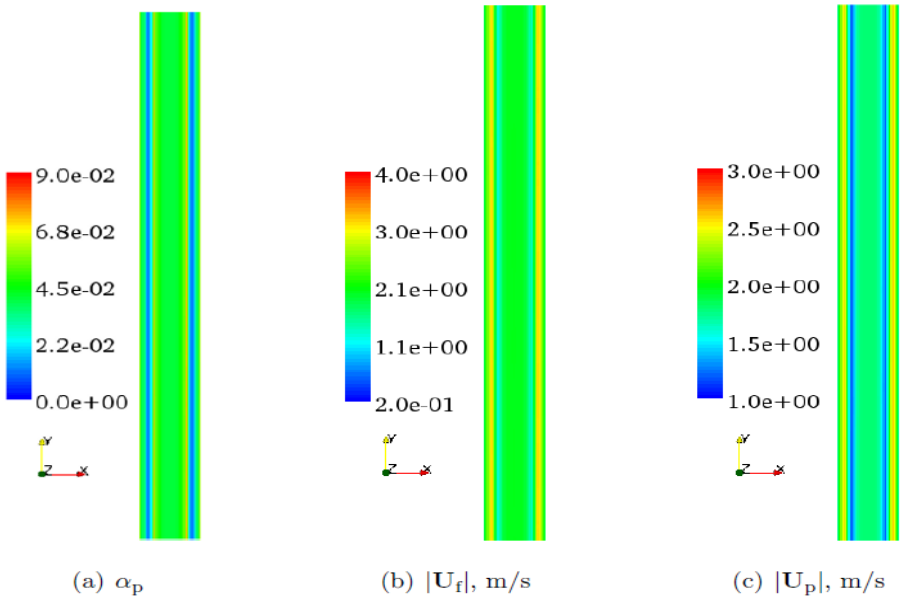

Figure 46. *Instantaneous contour plots of (a) particle volume fraction, (b) fluid-phase velocity magnitude and (c) particle-phase velocity magnitude predicted by the MFIX-QMOM simulations at time t_1, St = 1.0.*

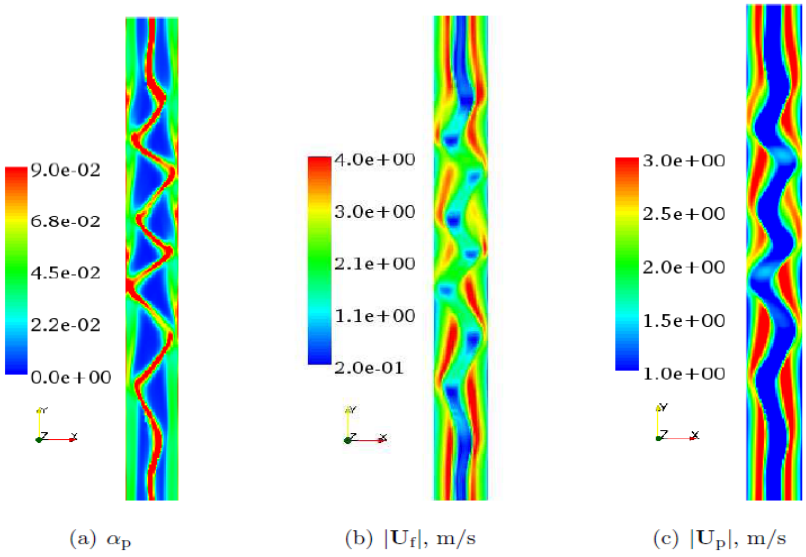

Figure 47. *Instantaneous contour plots of (a) particle volume fraction, (b) fluid-phase velocity magnitude, and (c) particle-phase velocity magnitude predicted by the MFIX-QMOM simulations at time t_2, St = 1.0.*

The results obtained in the case of St = 1 with MFIX-QMOM are reported in figures 46 and 47 for two different times t_1 = 0.66 s and t_2 = 1.06 s. The first snapshot corresponds to the phase immediately following the beginning of the simulation, when particles start to move from the walls towards the center of the channel. This leads to the formation of two stripes almost parallel to the walls, where the fluid velocity reaches its maximum value. Two bands at higher concentration of particles start to form in the internal side with respect to the channel centerline of the two stripes at higher voidage. Similar results have been obtained using Euler-Lagrange simulations as shown in figure 48. The volume fraction field predicted by the MFIX two-fluid model at the same time is reported in figure 49, where both the fields seem initially uniform, in clear disagreement with what is predicted by Euler-Lagrange and MFIX-QMOM simulations.

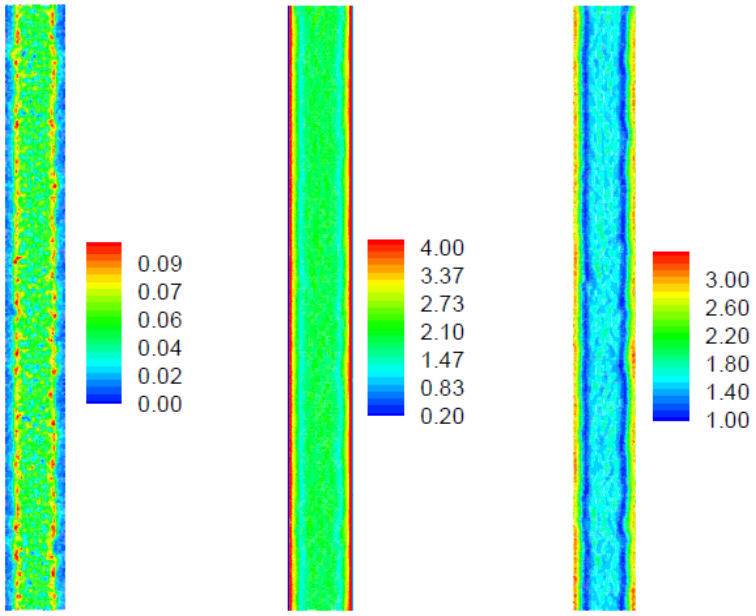

Figure 48. *Instantaneous contour plots of (a) particle volume fraction, (b) fluid-phase velocity magnitude, and (c) particle-phase velocity magnitude predicted by the Euler-Lagrange simulations at time t_1, St = 1.0.*

However, if the second snapshot obtained with two-fluid model at t = t_2 is considered, it can be noted that structures at higher particle volume fraction start to develop in the zone next to the wall, with a similar behavior to the one observed in the case with St = 0.1. Both Euler-Lagrange (figure 50) and MFIX-QMOM (figure 47) simulations predict a different process that leads to the formation of zones at higher particle concentration. Initially particles starts to move towards the center of the channel, as already discussed, then when the particle concentration in the two bands shown in figure 46 is high enough to create a consistent interface between the zone at lower particle concentration and the one at higher particle concentration, due to the velocity difference

across the interface between the two phases an instability starts to develop, which rapidly propagates to the rest of the system and, in the end, leads to the formation of structures at higher particle concentration, initiating the segregation phenomena experimentally observed in risers. Due to the intrinsic noise present in Euler-Lagrange simulations, the instability appears earlier in these than in MFIX-QMOM simulations, as a consequence the reported results for Euler-Lagrange simulations are taken at the time where corresponding structures to those observed in MFIX-QMOM simulations are present. More precisely, for the Euler-Lagrange results $t_1 = 0.19$ s and $t_2 = 0.44$ s.

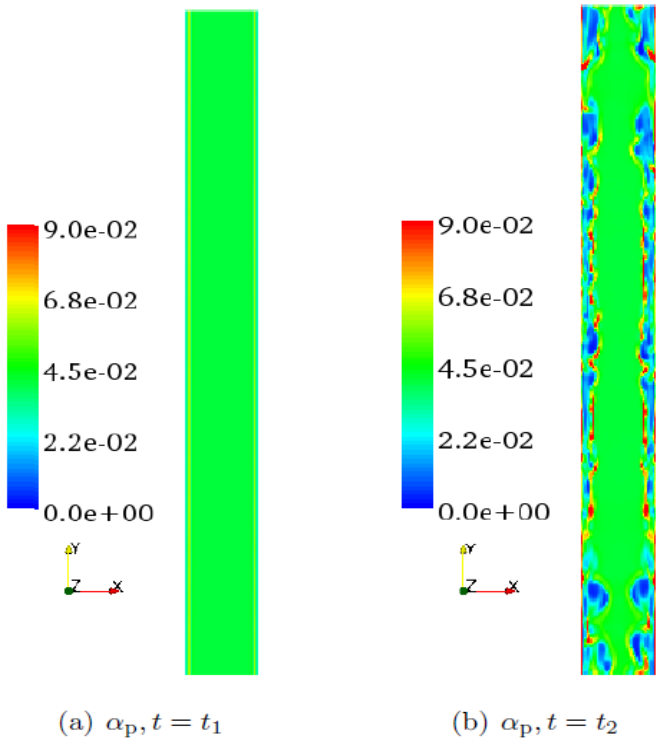

Figure 49. *Instantaneous contour plots of the particle volume fraction at (a) $t = t_1$ and at (b) $t = t_2$, predicted by MFIX two-fluid model, St = 1.0.*

The propagation of the instability seems quite significantly influenced by the introduction of the radial distribution function g_0, which makes the instability propagate more quickly when a high enough volume fraction is reached locally. However this does not affect the mechanism that leads to the instability and to the consequent segregation phenomena, because for low values of the particle volume fraction, the radial distribution function does not significantly affect the collision time.

The contour plots of figure 51 show that the Stokes number is about ten times higher than in the previous case, due to the bigger particle diameter considered, with peaks of 1.5. This means that in certain regions of the system, particles do not adapt immediately to the fluid flow, and lead to the typical conditions where particle trajectory crossing becomes significant, causing the two-fluid model to fail in the prediction of the flow behavior.

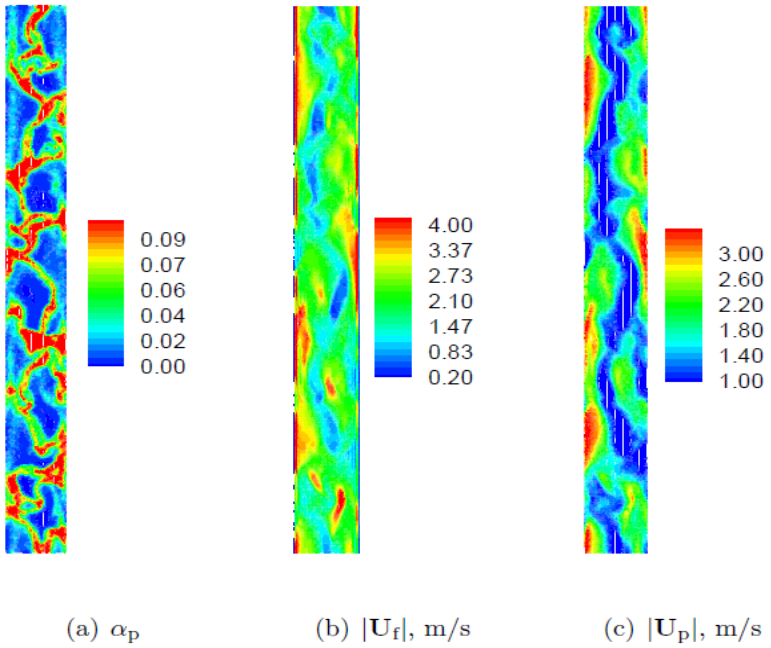

Figure 50. *Instantaneous contour plots of (a) particle volume fraction, (b) fluid-phase velocity magnitude and (c) particle-phase velocity magnitude predicted by the Euler-Lagrange simulations at time t_2, St = 1.0.*

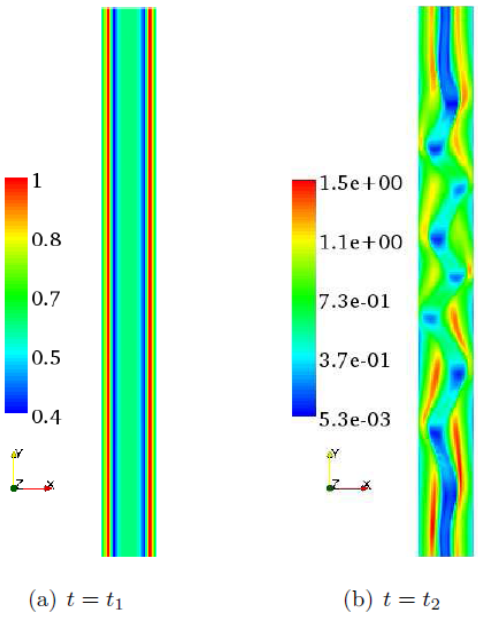

Figure 51. *Instantaneous contour plots of the Stokes number at (a) t = t_1 and at (b) t = t_2, predicted by MFIX-QMOM, St = 1.0.*

The introduction of the radial distribution function leads to significant instabilities in the solution algorithm of the moments transport equations at the base of the quadrature-based moment method. This numerical instability arises when the particle phase volume fraction locally reaches its maximum value, making the radial distribution function become very big. Currently the solution algorithm implemented in MFIX-QMOM includes g_0 explicitly in the collision time. In order to overcome this limitation, a dense flow solver was explored.

Dense Flow Solver Implementation. The quadrature-based moment method implemented in MFIX is able to compute dilute and moderately dilute gas-particle flows, but it does not impose any constraint on the maximum value of the particle phase volume fraction, which can reach values above its maximum physical limit. To enforce this limit, a particle pressure term has to be added. A direct addition of the particle pressure term to the moments transport equations might destabilize the solution procedure, as they are solved in a fully explicit manner. However, a simpler set of equations can be considered in the limit of dense particle phase. In such a limit, when the particle phase volume fraction approaches its maximum value, the kinetic equation degenerates into the Euler equation in the elastic limit, valid for Kn = 0. As a consequence, it is possible to reduce the number of moment transport equations considered in the dense case to the Euler equation itself, with a pressure defined as a function of the particle phase volume fraction and of the radial distribution function. Note that in the code time splitting is used to describe spatial transport separately from other physical phenomena. Thus, for inelastic cases, the granular energy dissipation is handled separately from the spatial fluxes. In this manner, it is possible to treat the total energy *E* as a conserved variable (i.e. as in the Euler equation) during the time split for the spatial transport.

As a starting point a one-dimensional problem was considered, and only the particle phase was taken into account, neglecting its interactions with the fluid phase. Likewise, only the spatial fluxes are considered since they are responsible for the change in volume fraction. The extension of the proposed method to three dimensions is straightforward, being widely used in aerospace engineering applications, as well as the introduction of the momentum exchange term between the phases and other physical phenomena.

The approach is explained first considering a one-dimensional single-phase flow with a bounded density due to the presence of a pressure term that opposes further increases of the density itself, by diverging when its maximum imposed value is approached.
The Euler equation in one dimension can be written as

$$\frac{\partial \mathbf{Q}}{\partial t} + \frac{\partial \mathbf{F}}{\partial x} = 0 \quad ,$$

where

$$\mathbf{Q} = \begin{pmatrix} Q_1 \\ Q_2 \\ Q_3 \end{pmatrix} = \begin{pmatrix} \rho \\ \rho u \\ E \end{pmatrix}, \quad \mathbf{F} = \begin{pmatrix} F_1 \\ F_2 \\ F_3 \end{pmatrix} = \begin{pmatrix} \rho u \\ p + \rho u^2 \\ u(E+p) \end{pmatrix},$$

with

$$E = \frac{1}{2}\left(\rho\Theta + \rho u^2\right)$$

$$p = \rho\left(\Theta + 2\alpha g_0 \Theta\left(1+e\right)\right)$$

$$g_0 = \frac{1}{1 - \left(\frac{\alpha_s}{\alpha_{s,\max}}\right)^{1/3}}$$

.

With some algebraic manipulation the flux vector **F** can be rewritten as

$$\mathbf{F} = \begin{pmatrix} F_1 \\ F_2 \\ F_3 \end{pmatrix} = \begin{pmatrix} Q_2 \\ 2Q_3 + 2g_0(Q_1)\frac{Q_1}{\rho_p}\left(2Q_3 - \frac{Q_2^2}{Q_1}\right)(1+e) \\ \frac{3Q_2Q_3}{Q_1} - \frac{Q_2^3}{Q_1^2} + 2g_0(Q_1)\frac{Q_2}{\rho_p}\left(2Q_3 - \frac{Q_2^2}{Q_1}\right)(1+e) \end{pmatrix},$$

where ρ_p is the particle density.

The Euler equation can be written in discretized form, using a time-implicit[1] scheme, as

$$\frac{\mathbf{Q}_i^{n+1} - \mathbf{Q}_i^n}{\Delta t} + \frac{\mathbf{F}_{i+1/2}^{n+1} - \mathbf{F}_{i-1/2}^{n+1}}{\Delta x} = 0,$$

and the flux term can be computed as

$$\mathbf{F}_j^{n+1} = \frac{1}{2}\left[\mathbf{F}_l^j + \mathbf{F}_r^j - \rho^j(\mathbf{J})\left(\mathbf{Q}_r^{n+1,j} - \mathbf{Q}_l^{n+1,j}\right)\right],$$

where $\rho^j(\mathbf{J})$ is the maximum eigenvalue of the Jacobian of the flux vector. Introducing a first-order interpolation scheme to find the face values of the conserved variables, we have:

$$\mathbf{Q}_{i+1/2}^r = \mathbf{Q}_{i+1}$$

$$\mathbf{Q}_{i+1/2}^l = \mathbf{Q}_i$$

$$\mathbf{Q}_{i-1/2}^r = \mathbf{Q}_i$$

$$\mathbf{Q}_{i-1/2}^l = \mathbf{Q}_{i-1}$$

.

Using the Beam and Warming scheme to linearize the discretized Euler equation we have

[1] An explict method was tested, and successfully achieved the limitation of the particle phase fraction. However the stability condition, given by the CFL condition based on the maximum eigenvalue led to very small time steps. As a consequence, an implicit method was chosen.

$$\mathbf{Q}_i^{n+1} = \mathbf{Q}_i^n + \frac{\alpha}{1+\alpha}\left(\mathbf{Q}_i^n - \mathbf{Q}_i^{n-1}\right) + \frac{\Delta t}{1+\alpha}\left[\frac{\mathrm{d}\mathbf{Q}_i^n}{\mathrm{d}t} + \beta\left(\frac{\mathrm{d}\mathbf{Q}_i^{n+1}}{\mathrm{d}t} - \frac{\mathrm{d}\mathbf{Q}_i^n}{\mathrm{d}t}\right)\right],$$

where α and β are constants that define the numerical scheme. In particular $\alpha = 0$, $\beta = 1$ gives the backward Euler scheme.

The time derivatives can be written as

$$\frac{\mathrm{d}\mathbf{Q}_i^n}{\mathrm{d}t} = -\frac{\mathbf{F}_{i+1/2}^n - \mathbf{F}_{i-1/2}^n}{\Delta x}$$
$$\frac{\mathrm{d}\mathbf{Q}_i^{n+1}}{\mathrm{d}t} = -\frac{\mathbf{F}_{i+1/2}^{n+1} - \mathbf{F}_{i-1/2}^{n+1}}{\Delta x},$$

and the flux can be expanded around t^n as

$$\mathbf{F}_{i+1/2}^{n+1} \approx \mathbf{F}_{i+1/2}^n + \frac{\partial \mathbf{F}_{i+1/2}^n}{\partial \mathbf{Q}^l}\left(\mathbf{Q}_{i+1/2}^{l,n+1} - \mathbf{Q}_{i+1/2}^{l,n}\right) + \frac{\partial \mathbf{F}_{i+1/2}^n}{\partial \mathbf{Q}^r}\left(\mathbf{Q}_{i+1/2}^{r,n+1} - \mathbf{Q}_{i+1/2}^{r,n}\right) + \mathcal{O}(\Delta t^2)$$

so that we obtain

$$\begin{aligned}\frac{\mathrm{d}\mathbf{Q}_i^{n+1}}{\mathrm{d}t} = &-\frac{\mathbf{F}_{i+1/2}^n - \mathbf{F}_{i-1/2}^n}{\Delta x} + \\ &-\frac{1}{\Delta x}\left[\hat{\mathbf{A}}_{i+1/2}^l\left(\mathbf{Q}_{i+1/2}^{l,n+1} - \mathbf{Q}_{i+1/2}^{l,n}\right) - \hat{\mathbf{A}}_{i-1/2}^l\left(\mathbf{Q}_{i-1/2}^{l,n+1} - \mathbf{Q}_{i-1/2}^{l,n}\right)\right] + \\ &-\frac{1}{\Delta x}\left[\hat{\mathbf{A}}_{i+1/2}^r\left(\mathbf{Q}_{i+1/2}^{r,n+1} - \mathbf{Q}_{i+1/2}^{r,n}\right) - \hat{\mathbf{A}}_{i-1/2}^r\left(\mathbf{Q}_{i-1/2}^{r,n+1} - \mathbf{Q}_{i-1/2}^{r,n}\right)\right]\end{aligned},$$

where the Jacobians, defined by

$$\hat{\mathbf{A}}_{i+1/2}^l = \frac{\partial \mathbf{F}_{i+1/2}^n}{\partial \mathbf{Q}^l}$$
$$\hat{\mathbf{A}}_{i+1/2}^r = \frac{\partial \mathbf{F}_{i+1/2}^n}{\partial \mathbf{Q}^r}$$

are computed at t^n:

$$\hat{\mathbf{A}}_{i+1/2}^l = \frac{1}{2}\left[\mathbf{J}(\mathbf{Q}_{i+1/2}^l) + \rho_{i+1/2}(\mathbf{J})\mathbf{I}\right]$$
$$\hat{\mathbf{A}}_{i+1/2}^r = \frac{1}{2}\left[\mathbf{J}(\mathbf{Q}_{i+1/2}^r) - \rho_{i+1/2}(\mathbf{J})\mathbf{I}\right]$$
$$\hat{\mathbf{A}}_{i-1/2}^l = \frac{1}{2}\left[\mathbf{J}(\mathbf{Q}_{i-1/2}^l) + \rho_{i-1/2}(\mathbf{J})\mathbf{I}\right]$$
$$\hat{\mathbf{A}}_{i-1/2}^r = \frac{1}{2}\left[\mathbf{J}(\mathbf{Q}_{i-1/2}^r) - \rho_{i-1/2}(\mathbf{J})\mathbf{I}\right].$$

Introducing the “delta notation”

$$\delta \mathbf{Q}_i^n = \delta \mathbf{Q}_i^{n+1} - \mathbf{Q}_i^n$$

,

a block-tridiagonal linear system is obtained

$$-\nu \hat{\mathbf{A}}_{i-1/2}^{l} \delta \mathbf{Q}_{i-1}^n + \hat{\mathbf{A}}_c \delta \mathbf{Q}_i^n + \nu \hat{\mathbf{A}}_{i+1/2}^{r} \delta \mathbf{Q}_{i+1}^n = \frac{\alpha}{1+\alpha} \delta \mathbf{Q}_i^{n-1} - \frac{\Delta t}{(1+\alpha)\,\Delta x} \left(\mathbf{F}_{i+1/2}^n - \mathbf{F}_{i-1/2}^n \right)$$

where

$$\mathbf{A}_c = \mathbf{I} + \nu \left(\mathbf{A}_{i+1/2}^{l} - \mathbf{A}_{i-1/2}^{r} \right)$$

$$\nu = \frac{\beta}{1+\alpha} \frac{\Delta t}{\Delta x}$$

.

The solution of this linear system provides the unknown vector **Q** of the original Euler equation.

The algorithm described above can be integrated with the QMOM procedure already implemented by considering that in the dense regions the distribution tends to be Maxwellian and its moments are known. As a consequence, the solution procedure can be outlined as follows:

- The moment transport equations of the QMOM approach are solved in the whole system.
- When in a cell the particle phase reaches the maximum packing limit, the algorithm switches to the solution of the Euler equation, with the implicit procedure described above, for the minimum set of cells necessary to define the problem. For example, if only a single cell has reached the particle packing limit, the Euler equation is solved, in a one dimensional problem, only locally for the set of three cells constituted by the cell where the packing has been reached, and the two neighbors, which are required to define the block-tridiagonal system.
- Once the solution of the Euler equation is obtained, the values of the volume fraction, the velocity and the granular energy are stored, the moments are locally set to Maxwellian in the cell where the particle packing limit has been reached, and the solution algorithm proceeds to the next time step.

The algorithm has been implemented in a Matlab® code, and future work will be required to verify its robustness, improve its efficiency and to extend it to multi-dimensional cases.

Task 1.4: Extension of KTGF to Multiphase Systems (Hrenya)

This development will mimic that of Task 1.1, but will also include the gas-solid drag force in the starting Enskog equation. Correspondingly, the resulting governing equations and constitutive quantities will take on a different form and include the influence of a non-conservative (drag) force.

(Hrenya reporting.) In order to gain experience with the incorporation of fluid phase into the KTGF, an idealized case was first examined: low Re, gas flow around a monodisperse suspension in which the *gas-solid interaction is described by Stokes flow*. For this idealized system, the starting kinetic equation takes the form

$$\frac{\partial}{\partial t} f + v_i \frac{\partial f}{\partial x_i} + \xi \frac{\partial}{\partial v_i}\left(v_i - U_{gi}\right) + g_i \frac{\partial}{\partial v_i} f = J \tag{1}$$

where f is the single-particle velocity distribution function, ξ is the friction coefficient for Stokes drag ($\xi = -6\pi\mu d/m$), $\mathbf{v}$ is the instantaneous particle velocity, $\mathbf{U_g}$ is the mean gas velocity, $\mathbf{g}$ is gravity, and J is the collisional operator.

The macroscopic balances for number density n, solids momentum m$\mathbf{U}$, and granular energy 3/2 nT resulting from the kinetic equation given above take the following form:

$$D_t n + n\nabla \cdot \mathbf{U} = 0 \tag{2}$$

$$D_t \mathbf{U} + \frac{1}{mn}\nabla \mathbf{P} = \xi \Delta \mathbf{U} + \mathbf{g} \tag{3}$$

$$D_t T + \frac{2}{3n}\left(\nabla \cdot \mathbf{q} + P_{ij}\nabla_j U_i\right) = -\zeta + 2\xi T \tag{4}$$

where $\mathbf{P}$ refers to the solid-phase pressure tensor, $\mathbf{q}$ is conduction of granular energy, and ζ is the cooling rate due to inelastic collisions. Note that two new terms appear due to the presence of the fluid phase. The first term on the right-hand side of the momentum balance is the drag force arising from the mean velocity difference between the two phases. The final term on the right-hand-side of the granular energy balance is a sink due to viscous drag. (It is worthwhile to note that the balances derived above differ from those reported by Koch (Koch, 1990) in that he has additional terms arising from the *fluctuating* fluid velocity. To account for such fluctuations, Koch introduces the (unphysical) concept of fluid velocity at the particle location. Our alternative to this approach is discussed below.

As mentioned above, the starting kinetic equation is simplified in that it only accounts for differences between the *mean* velocities of the gas and solid phases, further assuming a single-particle, low Re drag force. To extend this to a more realistic situation, a model for the instantaneous particle acceleration needs to be incorporated into the kinetic equation. As the name implies, this instantaneous acceleration is a function of the *instantaneous* velocities of both the gas and solid phases, rather than the corresponding mean velocities. Note that fluctuations in the particle velocity may arise from particle interactions (collisional) and/or transport across a velocity field (kinetic), whereas the gas-phase fluctuations stem from configurational and velocity changes of surrounding particles with time. For the gas phase, this instantaneous velocity can be determined rigorously by considering the distribution function for the fluid velocity (which is outside our current scope), or can come from a stochastic model. Based on the Immersed Boundary Method (IBM) simulations of Shankar Subramaniam's group at Iowa State, a generalized Langevin model is proposed for the instantaneous particle acceleration

$$A_i = -\frac{\beta}{m}\left(U_i - U_{gi}\right) - \frac{1}{m}\gamma_{ij} V_j + B_{ij} dW_j \tag{5}$$

where m is the particle mass, $\mathbf{V}$ is the particle fluctuation velocity ($\mathbf{V} = \mathbf{v} - \mathbf{U}$, where $\mathbf{v}$ is the instantaneous particle velocity, $d\mathbf{W}$ is a Wiener process increment (stochastic term), and the scalar β and the tensors $\boldsymbol{\gamma}$ and $\mathbf{B}$ are non-constant coefficients that can be extracted from the IBM simulations. Corresponding, the instantaneous particle force takes the form

$$F_i = -\beta\left(U_i - U_{gi}\right) - \gamma_{ij} V_j + mB_{ij} dW_j \tag{6}$$

With the instantaneous particle acceleration model given in Eq. (5), the one-particle velocity distribution function is given by

$$\frac{\partial}{\partial t} f + v_i \frac{\partial f}{\partial x_i} - \frac{\partial}{\partial v_i}\left\{\left[\frac{\beta}{m}\left(U_i - U_{gi}\right) + \frac{1}{m}\gamma_{ij} V_j\right] f\right\} + \frac{1}{2}\frac{\partial^2}{\partial v_i \partial v_j}\left\{B_{ik} B_{jk} f\right\} + g_i \frac{\partial}{\partial v_i} f = J \tag{7}$$

where J is the collisional operator.

Generally speaking, the coefficients extracted from IBM simulations (β, $\boldsymbol{\gamma}$ and $\mathbf{B}$) depend on constant system parameters (e.g., particle diameter, gas-phase viscosity) in addition to the dimensionless variables: (i) solids concentration (n), (ii) mean flow Reynolds number $\mathrm{Re_m} = \rho_g \sigma |\mathbf{U}\text{-}\mathbf{U_g}| / \mu_g$, and (iii) Reynolds number associated with particle velocity fluctuations $\mathrm{Re_T} = \rho_g \sigma T^{1/2} / \mu_g$, where ρ_g is the gas-phase density, σ is the particle diameter, and μ_g is the gas-phase (constant) viscosity, and $T = 1/3 \langle v^2 \rangle$ is the granular temperature.

Based on the kinetic equation shown in Eq. (6), the macroscopic balances and constitutive relations are derived in the limit of low mean Reynolds number. The macroscopic balances take the following form

$$D_t n + n\nabla \cdot \mathbf{U} = 0 \quad , \tag{8}$$

$$D_t \mathbf{U} + \rho^{-1}\nabla \cdot \mathbf{P} = -\frac{\beta}{m}\Delta\mathbf{U} + \mathbf{g} \quad , \tag{9}$$

$$D_t T + \frac{2}{3n}\left(\nabla \cdot \mathbf{q} + \mathbf{P} : \nabla\mathbf{U}\right) = -\frac{2}{3\rho}\gamma_{ij} P_{ij}^k + \frac{\rho}{3n} B_{ij} B_{ij} - \zeta T \quad . \tag{10}$$

Note that three terms arise in these balances due to the presence of the fluid phase, as expected: (i) mean drag in the momentum balance, (ii) dissipation of granular energy due to viscous effects, and (iii) source of granular energy stemming fluid-phase fluctuations.

Constitutive expressions for the cooling rate ζ, pressure tensor $\mathbf{P}$, and heat flux $\mathbf{q}$ in terms of the acceleration model parameters (β, $\boldsymbol{\gamma}$ and $\mathbf{B}$) and hydrodynamic variables n, $\mathbf{U}$, and T have also been derived via the Chapman Enskog method. The full form of these expressions is given in Sections 6 and 7 of Appendix B. The results indicate that the Langevin model for instantaneous gas-solid force matches the form of the previous analytical treatment, indicating the promise of this method for regions of the parameter space outside of those attainable by analytical methods (higher Reynolds number, etc.). The results also indicate that the effect of the gas phase on the constitutive relations for the solid-phase shear viscosity and Dufour coefficient is non-negligible, particularly in relatively dilute systems. Moreover, unlike their granular (no

gas phase) counterparts, the shear viscosity in gas-solid systems is found to be zero in the dilute limit and the Dufour coefficient is found to be non-zero in the elastic limit. See Section 8 of Appendix B for further details on these results.

Goal II: Improved Gas-Particle Drag Laws – effect of particle size distribution

Task 2.1: LBM and DTIBM simulations of fluid flow through an assembly of particle having a zero-mean velocity (Subramaniam & Sundaresan)

Simulations of fluidization of particle assemblies in small periodic domains will be carried out, covering a broad range of particle volume fractions and size distributions. In these simulations, the assembly of particles will be allowed to move randomly as granular gas (i.e. the particles respond only to inter-particle collisions, which will be treated as elastic and smooth), while the fluid flow will be maintained through an imposed pressure gradient. Such calculations have been done by Wylie et al. (2003) for uniformly sized particles, who have also developed a theory to explain the effect of this random motion on the drag force. Such simulations will be performed using various size distributions and their approximations as binary mixtures. The results will be used to construct drag force correlations.

(Subramaniam reporting.) The objectives of the task are: (i) to quantify the effect of particle velocity fluctuations on the mean drag for high particle Stokes numbers (ii) test the applicability of current drag models and (iii) provide a form of the drag law that will incorporate the effect of the fluctuating particle velocities. In order to understand the effect of fluctuations in the particle velocity on continuum multi-fluid formulation, it is important to understand the underlying theory at the level of the one-particle distribution function. The theoretical foundation that motivates the form of the drag law is presented in Appendix C.

Effect of particle velocity fluctuations on the mean drag: Drag laws for steady flow through homogeneous suspensions are obtained by integrating the conditional expectation of the acceleration as follows

$$\left\langle \mathbf{A} \;\middle|\; \mathbf{x}, \mathbf{v}, r; t \right\rangle$$

$$\left\langle \mathbf{F}^{fp} \right\rangle (\mathbf{x}, t) = \frac{1}{n} \int m \left\langle \mathbf{A} \,|\, \mathbf{x}, \mathbf{v}, r; t \right\rangle f \;\; (\mathbf{x}, \mathbf{v}, r, t) d\mathbf{v} dr, \tag{11}$$

where $\left\langle \mathbf{F}^{fp} \right\rangle$ is the average fluid-particle force, m is the particle mass (assumed equal for all particles in this expression) and n is the number density.

In order to calculate $\left\langle \mathbf{F}^{fp} \right\rangle$ from DNS, it is natural to simulate a statistically homogeneous suspension flow with freely moving particles, and to then compute volume-averaged estimates of $\left\langle \mathbf{F}^{fp} \right\rangle$ from particle acceleration data. Imposing a mean pressure gradient to balance the weight of the particles leads to a steady mean momentum balance. However, such freely moving suspensions are computationally prohibitive especially because in order to propose drag laws these simulations need to be performed over a range of solid volume fractions and mean flow Reynolds numbers (based on mean slip velocity). Furthermore, over a wide range of volume fraction and particle Stokes number, the particle configuration in individual realizations develops spatial structures due to flow instabilities. Wylie et al. (2003a) performed simulations of a suspension with particles moving along ballistic trajectories between elastic hard sphere

collisions, but the assumption that the fluid does not affect the particle motion is valid only in the limit of high Stokes number.

A convenient simplification for high Stokes number suspensions is to replace the ensemble of particle positions and velocities sampled by the system in its nonequilibrium steady state, by a set of particle configurations and velocities that would result from a granular gas simulation. Steady flow past fixed assemblies of particles in configurations (and with velocities) sampled from this set is simulated, and drag laws are obtained by averaging over this ensemble. The idea of extracting drag laws from steady flow through particle assemblies has been successfully exploited by several researchers (Hill et al. (2001); Beetstra et al. (2007)) using the lattice Boltzmann method (LBM).

The mean drag $\langle F_j \rangle$ is modeled by using a drag law that is usually formulated as a function of the mean slip $\langle W_j \rangle = \langle v_j \rangle - \langle u_j^{(f)} \rangle$. Drag correlations that are modifications of the drag law for an isolated particle in unbounded fluid are used in suspensions. Such drag laws can be expressed as

$$\langle F_j \rangle = -\beta \langle W_j \rangle.$$

In general, β is a function of the solid volume fraction, Reynolds number based on the mean slip velocity $\mathrm{Re_m}$ and Reynolds number based on the granular temperature $\mathrm{Re_T}$, i.e.,

$$\beta = \beta(\phi, \mathrm{Re_m}, \mathrm{Re}_T).$$

The mean flow Reynolds number is defined as $\mathrm{Re}_m = |\langle \mathbf{W} \rangle| d_p / \nu_f$ where d_p is the particle diameter, and the Reynolds number associated with the particle velocity fluctuations is denoted $\mathrm{Re}_T = \sqrt{T} d_p / \nu_f$, where $T = \frac{1}{3}\langle \mathbf{v}'' \cdot \mathbf{v}'' \rangle$ is the granular temperature.

In the Stokes flow regime, the drag is linear in particle velocity and hence β is independent of the slip velocity, i.e, $\beta(\phi, \mathrm{Re}_m) = \beta(\phi)$. Current drag models do not incorporate a dependence on $\mathrm{Re_T}$ and identifying the nature of this dependence is one of the objectives of this task. For finite Reynolds number based on the mean slip, the coefficient $\beta = \beta(\phi, \mathrm{Re}_m)$ i.e., drag is a nonlinear function of velocity and β depends on both the magnitude of the particle velocity and the volume fraction. For suspensions with a mean slip velocity as well as particle velocity fluctuations, the instantaneous drag experienced by a particle will have to be modeled as

$$F_i^* = -\beta(\phi, \mathrm{Re}_m) W_i$$

where $W_i = v_i - u_i^{(f)}$ is the instantaneous slip experienced by the particle. This definition of instantaneous drag raises questions on the the correct definition of $\mathbf{u}^{(f)}$, the instantaneous fluid velocity and the dependence of β on $\mathrm{Re_T}$, which is yet to be qunatified.. Wylie et al (2003, Eq. 37) wrote the instantaneous drag on a test particle as the sum of two forces: one coming from the mean drag on fixed bed and the other arising due to the viscous and fluctuating pressure forces on the test particle. This representation has the drawback that the mean and fluctuating parts of the drag cannot be identified easily.

In codes using hybrid discrete element method like MFIX-CDM, the instantaneous drag has been modeled by simply extending the drag correlations based on the mean slip velocity as

$$F_i^* = -\beta(\phi, \mathrm{Re}_m)\left(v_i - \left\langle u_i^{(f)} \right\rangle\right). \tag{12}$$

where, F_i^* is the modeled drag acting on the particle and v_j is the instantaneous velocity of the particle. In the limit $\mathrm{Re}_m \to 0$ and $\mathrm{Re}_T \to 0$, the drag is linear in the particle velocity and the mean drag is independent of particle velocity fluctuations. This result can be proved by writing the instantaneous force on the particle in the form given by Eq. (12). Without loss of generality, we can assume the mean fluid velocity $\left\langle u^{(f)} \right\rangle$ to be zero. Since the particle velocity is in the Stokes flow regime,

$$F_i^* = -\beta(\phi) v_i$$

and thus, the acceleration of the particle is $A_i^* = -\beta(\phi) v_i / m$. The mean drag acting on the suspension can be found by substituting this form for acceleration in Eq. (11) and integrating over the entire velocity space. Hence, the mean drag is

$$\begin{aligned} \left\langle \mathbf{F}^{fp} \right\rangle &= \frac{1}{n}\int \beta(\phi)\, \mathbf{v} f\ (\mathbf{x}, \mathbf{v}, r, t) d\mathbf{v} dr \\ &= \beta(\phi)\left(\frac{1}{n}\int \mathbf{v} f\ (\mathbf{x}, \mathbf{v}, r, t) d\mathbf{v} dr\right) \\ &= \beta(\phi)\langle \mathbf{v} \rangle. \end{aligned}$$

Thus, we see that when both Re_m and Re_T are in the Stokes flow regime (finite but small departures from zero), the mean drag experienced by the suspension is independent of particle velocity fluctuations.

In order to quantify the effect of particle velocity fluctuations on the mean drag, at a given mean Reynolds number Re_m we determine the Re_T at which the effect of particle velocity fluctuations on the mean drag becomes significant. For this purpose, we performed PUReIBM simulations of flow past monodisperse random arrays of spheres at Re_m values of 0.001, 20, 25, 40, 50, 75 and a solid volume fraction of 0.2. In these simulations the particles are assigned a Maxwellian velocity distribution but the particle positions are held fixed.

At a given Re_m, the change in mean drag due to Re_T is defined as

$$\Delta F\left(\phi, \mathrm{Re}_m, \mathrm{Re}_T\right) = \frac{\left|\left\langle \mathbf{F}^{fp} \right\rangle(\phi, \mathrm{Re}_m, \mathrm{Re}_T) - \left\langle \mathbf{F}^{fp} \right\rangle(\phi, \mathrm{Re}_m, 0)\right|}{\left|\left\langle \mathbf{F}^{fp} \right\rangle(\phi, \mathrm{Re}_m, 0)\right|}.$$

In the left panel of figure 52, the percentage differences in the mean drag obtained for various values of Re_m and Re_T are plotted. In order to compare the effect of the particle velocity fluctuations, percentage difference in the mean drag obtained by changing only Re_m is plotted in the right panel. This change is defined as

$$\Delta F\left(\phi, \mathrm{Re}_m, \Delta \mathrm{Re}_m\right) = \frac{\left|\left\langle \mathbf{F}^{fp} \right\rangle(\phi, \mathrm{Re}_m, \Delta \mathrm{Re}_m) - \left\langle \mathbf{F}^{fp} \right\rangle(\phi, \mathrm{Re}_m, 0)\right|}{\left|\left\langle \mathbf{F}^{fp} \right\rangle(\phi, \mathrm{Re}_m, 0)\right|}.$$

From this figure we see that at $\mathrm{Re}_m = 20$, the change in the mean drag obtained at $\mathrm{Re}_T = 2$ is comparable to the change obtained by simply changing the mean Reynolds number by 20. We also observe that the change in mean drag is increasing with the intensity of the particle velocity fluctuations.

The range of values of Re_T in these simulations were chosen fromWylie *et al.* (2003a) but experimental data of Re_T will determine the applicability of these results to gas-solid flows. In fact, recent high-speed imaging of particles performed by Cocco et al. (2010) show that the value of Re_T for gas-solid flows is indeed very low. Although the mean drag increases with increasing granular temperature, in practical gas-solid flow applications, this temperature is very small and hence the effect of particle velocity fluctuations on the mean drag can be neglected. Moreover, these results should be interpreted with caution because the simulations are for steady flow past fixed particle assemblies. If the particles are allowed to move, they will relax to lower granular temperatures (and hence lower Re_T) due to viscous dissipation (see Tenneti et al. (2010)).

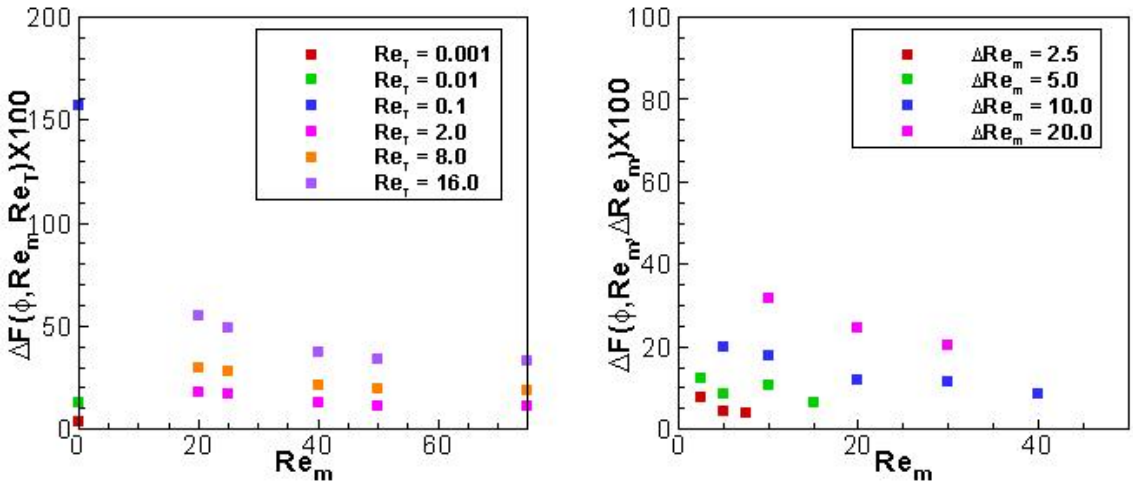

Figure 52. *In the left panel the percentage change obtained in the mean drag due to change in the level of particle velocity fluctuations, is shown for different* Re_m *at a volume fraction of 0.2. In the right panel, percentage change obtained due to the change in* Re_m *is plotted for the same volume fraction.*

<u>Effect of particle velocity fluctuations on the second moment of particle velocity</u>. The evolution equation for the second moment of velocity that appears in the particle Reynolds stress is given by Eq. A3. In statistically homogeneous flow, the key term governing the evolution of the particle Reynolds stress is the correlation of fluctuating particle acceleration with fluctuating particle velocity $\left\langle A_i'' v_j'' \right\rangle$ or equivalently $\left\langle F_i'' v_j'' \right\rangle$. The fluctuations in the acceleration are defined about the mean acceleration, i.e., $A_j'' = A_j - \left\langle A_j \right\rangle$ and similarly the fluctuations in the particle drag are defined about the mean drag, i.e. $F_j'' = F_j - \left\langle F_j \right\rangle$. In order to compute the correlation between the fluctuating drag and fluctuating particle velocity which appears in the second moment equation, an instantaneous model for the particle drag is required.

In order to validate this model, we performed PUReIBM simulations of a fixed bed of monodisperse spheres and extracted the scatter plot of fluctuating acceleration versus the

fluctuating particle velocity. Figure 53 shows that the fluctuations in drag predicted by the drag model of Eq (12) do not recover the scatter observed in the fluctuating drag obtained from our PR-DNS. In order to recover the correct acceleration distribution, we propose an instantaneous drag model which is described in the next section.

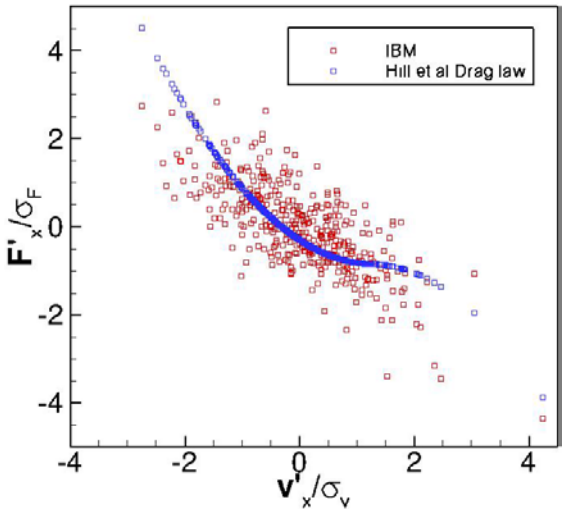

Figure 53. *Scatter plot of fluctuating drag versus the fluctuating velocity in the streamwise direction. The blue symbols are the fluctuations in drag obtained from PUReIBM simulations. The red ones are those predicted by the drag law of Hill et al. applied to the same system.*

Instantaneous drag model. We propose the following general Langevin model for the instantaneous particle drag:

$$m dv_i^* = F_i^{*(d)} dt + \Sigma_{ij}\, d\mathrm{W}_j \tag{13}$$

where $F_i^{*(d)}$ is the drift term and $d\,\mathrm{W}_j$ is a Wiener process increment. The modeled one-particle one-time distribution function f^* obeys a Fokker-Planck equation that corresponds to this generalized Langevin equation

$$\frac{\partial f^*}{\partial t} + \frac{\partial}{\partial x_i}\left(v_i f^*\right) + \frac{\partial}{\partial v_i}\left(A_i^{*(d)} f^*\right) + \frac{1}{2}\frac{\partial^2}{\partial v_i \partial v_j}\left(B_{ik} B_{jk} f^*\right) = 0 \tag{14}$$

where,

$$A_i^{*(d)} = \frac{F_i^{*(d)}}{m} \tag{15}$$

and

$$B_{ij} = \frac{\Sigma_{ij}}{m}..$$

Here, m is the mass of the particle.

The drift term $F_i^{*(d)}$ is written in terms of the mean slip velocity $\langle W_i \rangle$ and the model coefficients are functions of the mean slip. The model for instantaneous particle drag is written as

$$m dv_i^* = -\beta_{ij} \langle W_j \rangle dt - \gamma_{ij} v_j'' dt + \Sigma_{ij} d\mathrm{W}_j . \tag{16}$$

The model coefficients β_{ij}, γ_{ij} and Σ_{ij} depend on the solid volume fraction, mean flow Reynolds number Re_m, Reynolds number based on the granular temperature Re_T and the solid to fluid density ratio. These model coefficients have to be specified such that the resulting particle acceleration model predicts the correct evolution of the granular temperature. The determination of the model coefficients requires simulation of freely evolving gas-solid suspensions. These simulations and the subsequent specification of the model coefficients are described in Task 2.3.

(Supplementary material.) See Appendix C.

(Sundaresan reporting.) In this part of the project we sought to interrogate the effect of particle velocity fluctuations on the fluid-particle drag coefficient in binary systems. However, earlier work of Wylie *et al.* (2003) demonstrated that for monodisperse systems the effect of particle velocity fluctuations on the fluid-particle drag coefficient is weak, provided the Reynolds number based on the particle fluctuating velocity Re_T is smaller than the Reynolds number based on the mean slip velocity (i.e. the mean particle velocity relative to the mean velocity of the fluid) Re. To ascertain whether this limit can be realized in a gas-particle flow we performed lattice-Boltzmann simulations of a binary particle assembly falling under the action of gravity. We found that the Reynolds number based on the particle fluctuating velocity was always one order of magnitude smaller than the Reynolds number based on the mean slip velocity. It was then inferred from the study of Wylie *et al.* (2003) that given the small values of Re_T/Re there is no real need to consider the fluctuating velocity effect in models for the fluid-particle drag coefficient in gas-particle systems. Further details can be found in Holloway *et. al* (2010), which is included in this report as Appendix D.

Task 2.2: LBM and DTIBM simulations of fluid flow through an assembly of binary particle mixtures where the two types of particles have a non-zero relative velocity (Subramaniam & Sundaresan)

In the simulations outlined under Task 2.1, the mean velocity for each particle type (or bin) is zero while fluctuating velocities are nonzero. In real systems, the mean velocities of all the particle types will not be equal, and this difference plays an important role in the suspension hydrodynamics. It not only produces the particle-particle drag, captured in the kinetic theory, but also gives rise to significant corrections to the fluid-particle drag. In order to expose this correction, the influence of mean relative motion between the two types of particles in a binary mixture on the drag force will be studied. This will be done in the granular gas limit, by introducing the following small modification. After initializing the assembly with random velocities for various particles to obtain specified fluctuation energy to the collection of particles, a desired mean velocity is added to each of the two particle types, while maintaining zero mixture momentum. As the particles move around as a granular gas, they will collide and generate a drag force between the two particle types; by adding a time-dependent body force to each particle type, this drag force will be compensated for and the mean relative velocity will be maintained.

(Subramanaiam reporting.) In practical gas-solid flows with poly-disperse particles all the size classes do not necessarily have the same mean velocity. The objective of this task is to formulate a general drag law for poly-disperse suspensions that can be implemented in moment closures that arise in EE continuum models. This drag law should account for the difference in the mean velocities of the size classes.

A poly-disperse suspension is characterized by a continuous size distribution. However, this continuous distribution can be represented in terms of a finite number of size classes and higher the number of size classes, better is the representation. The theoretical basis of representing a continuous size distribution in terms of discrete size classes is given in Appendix E. To accomplish the objective of developing a poly-disperse drag law we start with a bi-disperse suspension and investigate the effect of polydispersity and Reynolds number on the mean drag.

Drag force in the discrete representation of a poly-disperse suspension. The conservation equations for the mean mass and mean momentum of each size class can be derived by taking the moments of Eq. (A1). For a statistically homogeneous system, the mean momentum conservation equation for the size class α with radius R_α is:

$$\frac{\partial}{\partial t}\left(\rho_\alpha \phi_\alpha \left\langle v_j \mid r = R_\alpha \right\rangle\right) + \frac{\partial}{\partial x_k}\left(\rho_\alpha \phi_\alpha \left\langle v_j \mid r = R_\alpha \right\rangle \left\langle v_j \mid r = R_\alpha \right\rangle\right) = \rho_\alpha \phi_\alpha \left\langle A_j \mid r = R_\alpha \right\rangle - \frac{\partial}{\partial x_k}\left(\rho_\alpha \phi_\alpha \left\langle v_j'' v_k'' \mid r = R_\alpha \right\rangle\right) \quad (17)$$

In the above equation ρ_α, ϕ_α are the density and volume fraction of the size class α respectively. The second term on the right hand side of this equation is like the Reynolds stress obtained due to fluctuations in the particle velocity which are defined about the mean velocity conditional on particle size:

$$v_j'' = v_j - \left\langle v_j \mid r = R_\alpha \right\rangle.$$

The first term on the right hand side denoted by $f_{g-\alpha,j}$ is the total force per unit volume of the suspension acting on the size class α and is related to the average force acting per particle through the expression:

$$f_{g-\alpha,j} = n_\alpha \left\langle F_j \mid r = R_\alpha \right\rangle$$

where, n_α is the number density of that size class. The quantity $\left\langle F_j \mid r = R_\alpha \right\rangle$ is extracted from the DNS and is reported as the drag force acting on the particle belonging to the size class α by Hill et al (2001) and Garg et al (2010) for mono-disperse suspensions (single size class).

The total force $f_{g-\alpha,j} = n_\alpha \left\langle F_j \mid r = R_\alpha \right\rangle$ experienced by the particles belonging to a particular size class arises due to the mean pressure gradient acting on the suspension, and the viscous stresses and the fluctuating pressure acting on the particles

$$n_\alpha \left\langle F_j \mid r = R_\alpha \right\rangle = -\phi_\alpha \frac{\partial P}{\partial x_j} + n_\alpha \left\langle F_{D,j} \mid r = R_\alpha \right\rangle.$$

Here the second term on the right hand side denotes the contributions of viscous stresses and fluctuating pressure to the total force. Drag laws for poly-disperse suspensions in the Stokes flow regime that are proposed by van der Hoef et al (2005) and Yin et al (2009) report $\left\langle F_{D,j} \mid r = R_\alpha \right\rangle$ as the drag force, whereas Hill et al (2001) and Garg et al (2010) reported $\left\langle F_j \mid r = R_\alpha \right\rangle$ that includes the mean pressure gradient term. In this work we report drag force as the average total hydrodynamic force acting per particle.

In a poly-disperse suspension, drag laws are written for each size class and the existing poly-disperse drag laws are based on the drag correlations proposed for an equivalent mono-disperse suspension. The equivalent mono-disperse suspension is defined as a suspension of equi-sized particles at a volume fraction ϕ (equal to the total volume fraction of the poly-disperse suspension) and diameter $\langle D \rangle$ where,

$$\langle D \rangle = \frac{\sum_{\alpha=1}^{M} N_\alpha D_\alpha{}^3}{\sum_{\alpha=1}^{M} N_\alpha D_\alpha{}^2}$$

is the called the Sauter mean diameter. In general, the drag force is a function of the volume fraction and the mixture mean Reynolds number, $\mathrm{Re}_m = \left| \langle \tilde{\mathbf{V}} \rangle - \langle \mathbf{u}^{(\mathbf{f})} \rangle \right| \langle D \rangle / \nu_f$ where $\langle \tilde{\mathbf{V}} \rangle$ is the mixture mass-weighted mean velocity. When there is no relative velocity between the size classes, the total force due to viscous stresses and fluctuating pressure acting per unit volume on the particles belonging to the size class α is written as

$$\mathbf{F}_\alpha = -\beta_\alpha \langle \mathbf{W} \mid r = R_\alpha \rangle,$$

where $\langle \mathbf{W} \mid r = R_\alpha \rangle = \langle \mathbf{v} \mid r = R_\alpha \rangle - \langle \mathbf{u}^{(f)} \rangle$ is the mean slip experienced by that size class and the average force per particle is obtained as $\langle \mathbf{F} \mid r = R_\alpha \rangle = \mathbf{F}_\alpha / n_\alpha$. The normalized drag acting on the size class α is defined as

$$F_\alpha(\phi, \mathrm{Re}_m) = \frac{\left| \langle \mathbf{F} \mid r = R_\alpha \rangle \right|}{3\pi\mu_f D_\alpha (1-\phi) \left| \langle \mathbf{W} \mid r = R_\alpha \rangle \right|}$$

In the Stokes flow regime, drag is only a function of the volume fraction and van der Hoef et al (2005) proposed the following drag law for a poly-disperse suspension in the Stokes flow regime

$$F_{D-\alpha}(\phi, 0) = y_\alpha F_{D-mono}(\phi, 0) \tag{18}$$

where, $y_\alpha = D_\alpha / \langle D \rangle$ is the normalized diameter and $F^*_{D-mono}(\phi, 0)$ is the normalized drag force (pressure and viscous forces only) acting on the equivalent mono-disperse suspension. van der Hoef et al proposed the following expression for the Stokes drag on a mono-disperse system

$$F^*_{D-mono}(\phi, 0) = \frac{10\phi}{(1-\phi)^2} + (1-\phi)^2 \left(1 + 1.5\sqrt{\phi}\right).$$

In the Stokes flow regime, Yin et al (2009) observed that (18) is not accurate for diameter ratios greater than 4:1 and they proposed the following modification:

$$F^*_{D-\alpha}(\phi, 0) = \frac{1}{(1-\phi)} + \left(F^*_{D-mono}(\phi, 0) - \frac{1}{(1-\phi)} \right) \left(a y_\alpha + (1-a) y_\alpha{}^2 \right),$$

where $a(\phi) = 1 - 2.66\phi + 9.096\phi^2 - 11.338\phi^3$.

At moderate Reynolds numbers Beetstra et al (2007) used LBM simulations to conclude that the drag force on a bi-disperse suspension can be written in the same form as given in (18); i.e.,

$$F^*_{D-\alpha}\left(\phi, \mathrm{Re}_m\right) = y_\alpha F^*_{D-mono}\left(\phi, \mathrm{Re}_m\right). \tag{19}$$

However, due to a confusion in their definition of drag force, they proposed their drag law for the total hydrodynamic force in the following form:

$$F_\alpha\left(\phi, \mathrm{Re}_m\right) = \left[y_\alpha\left(1-\phi\right) + \phi y_\alpha^2 \right] F\left(\phi, \mathrm{Re}_m\right) \tag{20}$$

where $F(\phi, Re_m)$ is the average total fluid-particle force per particle acting on an equivalent mono-disperse suspension.

Drag law for mono-disperse suspensions from IBM simulations. It is clear that the accuracy of poly-disperse drag law depends strongly on the accuracy of mono-disperse drag law. We performed PUReIBM simulations of flow past fixed particle assemblies of equi-sized spheres over a range of volume fractions and Reynolds numbers to assess the performance of the existing mono-disperse drag laws that are based on lattice Boltzmann simulations. We found that while PUReIBM results are in excellent agreement with existing LBM drag laws at low Reynolds numbers, there are significant differences in the drag values (~30%) at higher Reynolds numbers. To verify the accuracy of PUReIBM simulations, we compared our results with those obtained from a body-fitted solver (ANSYS-FLUENT CFD package) and found an excellent agreement. The following functional form for $F(\phi, Re_m)$ is found to fit the drag data from IBM simulations very well with an average deviation of less than 3% :

$$F\left(\phi, \mathrm{Re}_m\right) = \frac{F_{\mathrm{isol}}\left(\mathrm{Re}_m\right)}{\left(1-\phi\right)^3} + F_\phi\left(\phi\right) + F_\phi^{\mathrm{Re}_m}\left(\phi, \mathrm{Re}_m\right) \tag{21}$$

where,

$$F_{\mathrm{isol}}\left(\mathrm{Re}_m\right) = 1 + 0.15\,\mathrm{Re}_m^{\,0.687},$$

$$F_\phi\left(\phi\right) = \frac{5.81\phi}{\left(1-\phi\right)^3} + \frac{0.485\phi^{1/3}}{\left(1-\phi\right)^4},$$

and

$$F_\phi^{\mathrm{Re}_m}\left(\phi, \mathrm{Re}_m\right) = \phi^3\,\mathrm{Re}_m\left(0.95 + \frac{0.6075\phi^3}{\left(1-\phi\right)^2}\right).$$

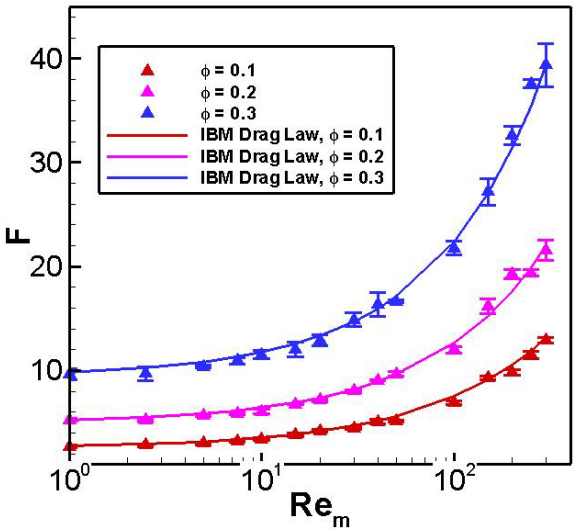

Figure 54. *Plot showing the variation of the normalized force (symbols) obtained from PUReIBM simulations of flow past fixed assemblies of mono-disperse spheres and the drag correlation (21) with the mean flow Reynolds number. The volume fractions considered in this plot are 0.1, 0.2, and 0.3.*

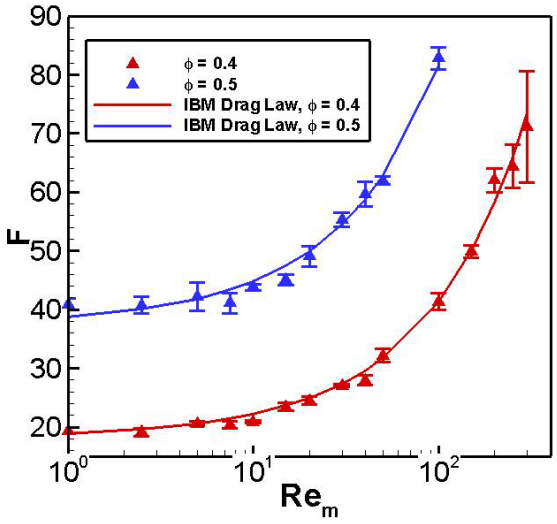

Figure 55. *Plot showing the variation of the normalized force (symbols) obtained from PUReIBM simulations of flow past fixed assemblies of mono-disperse spheres and the drag correlation (21) with the mean flow Reynolds number. The volume fractions considered in this plot are 0.4 and 0.5.*

In figures 54 and 55 the mono-disperse drag correlation given by (19) and normalized force obtained from PUReIBM simulations is plotted against the mean flow Reynolds numbers. From these figures we can see that the drag correlation given by equation (21) is a good fit for the normalized force over the range of volume fractions and mean flow Reynolds numbers for which the simulations are performed. Also, in the limit of infinite dilution ($\phi \to 0$), $F(\phi, Re_m)$ reduces to $F_{\text{isol}}(\phi, Re_m)$, the drag experienced by an isolated particle. The correlation given by the Schiller and Neumann for a single sphere in an unbounded medium is used in our correlation.

Drag on bi-disperse suspensions with no relative velocity between size classes. We performed PUReIBM simulations of flow past bi-disperse suspensions at moderate Reynolds numbers (with no relative velocity between the size classes). The objective is to verify the bi-disperse drag correlation proposed by Beetstra et al. (2007) given by equation (19) and to propose a new drag law based on the results of PUReIBM simulations. At each volume fraction, the volume fraction ratio (ϕ_2 / ϕ_1) is varied between 1 and 6 and the diameter ratio (D_2 / D_1) between 1.5 and 4.

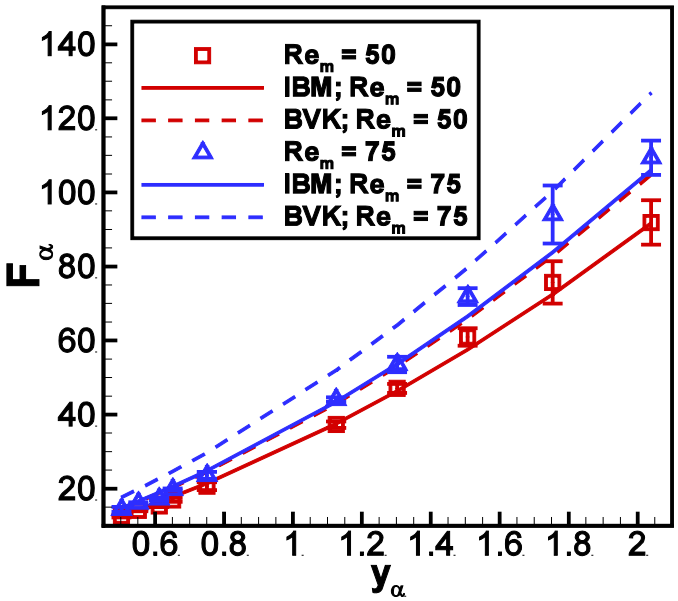

Figure 56. *Plot showing the results of PUReIBM simulations of flow past bi-disperse particle assemblies at a total volume fraction of 0.4. Normalized force is shown for two mean flow Reynolds numbers (Re_m = 50 and 75). Solid lines are obtained by substituting the PUReIBM drag correlation given by equation (21) in (20). Dashed lines are obtained by substituting the mono-disperse drag correlation given by Beetstra et al. (2007) in (20).*

The results of PUReIBM simulations of flow past bi-disperse suspensions are shown in figure 56 for a total volume fraction of 0.4 and two mean flow Reynolds numbers (50 and 75). The simulation data is compared with the drag predicted by equation (20). The solid lines are obtained by substituting equation (21) in (20) while the dashed lines are obtained by substituting the mono-disperse drag correlation of Beetstra et al. (2007) in (20). We can see that the functional form for $F_\alpha(\phi, Re_m) / F(\phi, Re_m)$ proposed by Beetstra et al (2007) seems to hold for the PUReIBM data as well. However, from the figure we can see clearly that the values of $F_\alpha(\phi, Re_m)$ from the simulations do not agree with the values predicted by the drag correlation of Beetstra et al (2007). The reason for this is the difference between the PUReIBM drag correlation and the correlation of Beetstra et al (2007) for mono-disperse suspensions.

Bi-disperse suspensions with relative velocity between size classes. When all the particles move with the same velocity (zero relative velocity between size classes), we can make a Galiliean-invariant (GI) frame transformation such that the particles are at rest in the new frame. Thus, performing fixed bed simulations is justified in the case of zero relative velocity between the size classes. However, fixed bed simulations for finite relative velocity between size classes are valid only in the limit of very low Reynolds number (Stokes flow regime). At moderate Reynolds numbers, we need to perform simulations of freely evolving suspensions to account for the finite slip between size classes. An important point to be noted is that the slip velocity between size classes is not an independent parameter.

The PUReIBM DNS code has been used to simulate freely evolving mono-disperse suspensions by solving the governing equations of motion in an accelerating frame of reference. This reference frame moves with the average velocity of the solid particles so that the particles do not travel in and out of the computational on an *average*. The frame acceleration appears as

an additional force that sets the average velocity of the solids to be zero. Viewed from the laboratory frame, the force due to the frame acceleration can be thought of as an additional time dependent body force that acts on the system to keep the average solid velocity to be zero. Tenneti et al. (2010) successfully applied this simulation methodology to perform simulations of freely evolving mono-disperse suspensions. We extended this methodology to simulate freely evolving bi-disperse suspensions with the assumption of that the density of the size classes is the same.

The governing equations of motion solved in the freely evolving bi-disperse suspensions are given in Appendix F. The average solid velocity for each size class evolves because of the force exerted by the mean pressure gradient, the fluid-particle drag force, contact force due to collisions with particles belonging to other size classes and the pseudo force due to the frame acceleration. For a mono-disperse suspension, the mean solid velocity is not influenced by the collisional forces because the total force due to collisions is zero (Newton's third law). However, for poly-disperse suspensions collisions with particles belonging to other size classes affect the average velocity. In the simulations of poly-disperse suspensions, the accelerating frame of reference moves with the mixture mean velocity such that the mean mixture momentum is zero. The slip velocity between the size classes 1 and 2 denoted $\left\langle \mathbf{W}^{(2,1)} \right\rangle$ evolves according to the following equation:

$$\frac{d}{dt}\left\langle \mathbf{W}^{(2,1)} \right\rangle = \frac{1}{\rho_p V}\left[\frac{1}{\phi_2}\mathbf{F}_{D-2} - \frac{1}{\phi_1}\mathbf{F}_{D-1}\right] + \frac{1}{\rho_p V}\left[\frac{1}{\phi_2} + \frac{1}{\phi_1}\right]\mathbf{F}^{C}{}_{2-1}.$$

This equation says that the slip velocity between the two size classes will reach a steady state because of the balance between the drag and contact forces due to collisions ($\mathbf{F}^{C}_{2-1}$) between the size classes. It is not known *a priori* if such a balance exists or not. Besides the slip velocity another important quantity to observe is the granular temperature for each size class.

To answer these questions we performed PUReIBM simulations of a bi-disperse suspension at a nominal volume fraction of 0.2 and mean slip Reynolds number of 20. We considered equal volume fractions and a diameter ratio of 2. Both size classes have the same density and the solid to fluid density ratio is taken to be 100. Figure 57 shows the evolution of the slip velocity between the size classes $\left\langle \mathbf{W}^{(2,1)} \right\rangle$.

We can see that the magnitude of the slip velocity increases in time. During this time there are no collisions between the particles because the particles slowly gain energy from the fluid. When the collisions start the slip velocity appears to reach a dynamic steady state. This steady value depends upon the mean flow Reynolds number, volume fraction, solid to fluid density ratio and the coefficient of restitution. We can also see from the figure that the granular temperature in each size class reaches a steady state. Thus, for a bi-disperse suspension once we fix the physical parameters of the problem, the slip velocity cannot be arbitrary and also one cannot provide a drag law by performing fixed bed simulations.

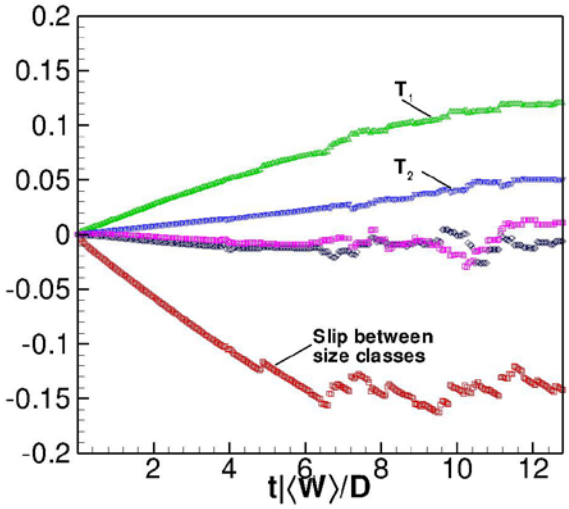

Figure 57. *Evolution of slip velocity between size classes and granular temperature for each size class for a freely evolving bi-disperse suspension (Re_m = 20, $\phi = 0.2$ and ρ_p/ρ_f = 100). Red symbols denote the streamwise component of the slip velocity while purple and black represent the cross-stream components of the slip velocity between the size classes.*

Summary. In this task, we used a Particle-resolved Uncontaminated-fluid Reconcilable Immersed Boundary Method (PUReIBM) to simulate fixed and freely evolving poly-disperse suspensions. In practical gas-solid flows with poly-disperse size distributions of particles, the mean drag is affected due to the presence of different size classes as well as the relative slip velocity between these size classes. Starting with a bi-disperse suspension; we first analyzed the drag force obtained when there is no slip velocity between the size classes. For this case, we can perform fixed bed simulations at all Reynolds numbers and a drag law for each size class is formulated in terms of the drag law for an equivalent mono-disperse suspension. We proposed a new mono-disperse drag law using the PUReIBM DNS that corrects the existing drag LBM based drag correlations of Hill et al. (2001) and Beetstra et al. (2007). This new mono-disperse drag law also corrects the drag data for bi-disperse suspensions provided by Beetstra et al. (2007). To account for the finite slip velocity between size classes, we have shown that fixed bed simulations at arbitrary slip velocities are not valid outside the Stokes flow regime and that we have to perform simulations of freely evolving suspensions. From the freely evolving simulations of bi-disperse suspensions we concluded that the steady slip velocity between the size classes cannot be chosen arbitrarily and it is determined by the physical properties of the system.

(Sundaresan reporting.) As part of Task 2.2 we first performed lattice-Boltzmann simulations of fluid-particle flows to interrogate the effect of relative velocity between particles of different types on the fluid-particle drag coefficients for the case where both particle types had the same size. Based on these results, models for the fluid-particle drag coefficients that include the effect of relative velocity between particles of different types were constructed; see Yin and Sundaresan (2009) in Appendix G for further details. We then tackled the case of a binary mixture of particles having different sizes, where we engaged in a large computational campaign and model construction; see Yin and Sundaresan (2009) in Appendix G for further details. Both

of these studies were restricted to low Reynolds number flows. In order to account for the effect of moderate Reynolds number on the fluid-particle drag force experienced by a polydisperse assembly, we performed a large number of lattice Boltzmann simulations of polydisperse gas-solid suspensions at moderate Reynolds numbers. We found that a hybrid drag force model of the form given by Yin and Sundaresan (2009) combined with the inertial correction proposed by Beetstra *et al.* (2007) for polydisperse fixed beds accurately captured our lattice Boltzmann simulation results; see Holloway *et al.* (2010) in Appendix D for further details.

Task 2.3: LBM and DTIBM simulations for freely evolving systems (Subramaniam & Sundaresan)

Simulations of fluidization of binary mixtures in periodic domains where both fluctuating motion of the particles and mean relative motion between the particles evolve naturally will then be performed. These simulations will be first done in small periodic domains to suppress evolution of inhomogeneous structures and then extended to larger domains with longer box length in the vertical direction where one-dimensional traveling waves readily form even with uniformly sized particles. Such calculations have already been performed for uniformly sized particles (Derksen & Sundaresan, submitted), indicating that one can reproduce the one-dimensional traveling waves seen experimentally by Duru et al. (2002). This study will be extended first to systems with binary mixtures and then to other size distributions. Through simulation of fully developed wave structures in such systems, we will extract data on fluid-particle and particle-particle drag forces.

These three tasks in Goal II will be carried out over a wide range of mean volume fractions, employing the LBM-based code for the lower volume fractions, the DTIBM-based code for the high volume fractions and both for an intermediate range (in order to check the results against each other).

(Subramaniam reporting.) The objective of this task is to perform simulations of freely evolving binary and other polydisperse suspensions and to propose improved particle acceleration (or drag) models. A PR-DNS approach based on PUReIBM was developed by Tenneti et al (2010) to perform simulations of freely evolving suspensions in periodic domains. In this task we performed PUReIBM simulations of freely evolving monodisperse suspensions at moderate mean flow Reynolds numbers to extract data relevant to model development.

In Task 2.1, we performed PUReIBM simulations of flow past fixed particle assemblies where the particles were assigned a Maxwellian velocity distribution. These simulations are limited to high Stokes number suspensions where it is assumed that the particles are so massive that their velocities do not change significantly due to the effect of the fluid. The principal conclusions of this task are the following:

(i) We confirmed Koch's observation (Koch, 1990) that particle velocity fluctuations correlate with particle acceleration fluctuations to generate a source in the granular temperature due to hydrodynamic effects

(ii) We showed that simple extension of mean particle acceleration models does not predict the the correct particle acceleration-velocity covariance obtained from DNS. A consequence of the use of such models in CFD codes like MFIX is that the term Φ_{gm} appearing in the granular temperature equation will be modeled incorrectly.

We propose an instantaneous particle acceleration model that will incorporate the effect of particle velocity fluctuations and hydrodynamic effects of neighboring particles. The

instantaneous particle acceleration model, its validation, and a procedure for determining its coefficients are described in the following sections.

Instantaneous particle acceleration model. We propose the following general Langevin model for the increment in the particle velocity:

$$dv_i = -\beta_{ij}\left\langle W_j \right\rangle dt - \gamma_{ij} v_j'' dt + B_{ij} d\mathsf{W}_j . \tag{22}$$

In the above equation dv_i is the increment in the particle velocity, v_i'' is the fluctuation in the particle velocity and $d\,\mathrm{W}_j$ is a Wiener process increment. The first term on the right hand side of Eq. 22 accounts for the effect of the mean slip velocity, the second term accounts for the fluctuation in the particle velocity and the last term models the effect of the hydrodynamic interaction of the neighboring particles. The coefficient γ_{ij} is the inverse of the Lagrangian particle velocity autocorrelation time. In other words it quantifies how long a particle retains the memory of its initial velocity. These coefficients are functions of volume fraction (ϕ), mean flow Reynolds number (Re_m) and particle to fluid density ratio (ρ_p/ρ_f). To extract a functional form for the Langevin model coefficients, PUReIBM simulations of freely evolving suspensions are performed over a range of parameters. Verification of the Langevin model is presented in the next section.

Verification of Langevin model. In this section, verification of the Langevin model for the instantaneous particle acceleration is presented. For this purpose we consider a simpler form for the increment of fluctuating particle velocity:

$$dv_i'' = -\gamma v_i'' dt + B d\mathsf{W}_i \tag{13}$$

As described earlier, in the above equation, γ is an inverse of the integral time scale of the particle velocity autocorrelation. The particle velocity autocorrelation function $\rho(s)$ is defined as follows:

$$\rho(s) = \frac{\left\langle v_i''(t_0)\, v_i''(t_0+s)\right\rangle}{\left\langle v_k''(t_0)\, v_k''(t_0)\right\rangle}$$

where s is the separation in time. The integral time scale for the autocorrelation function is defined as $T_L = \int_0^\infty \rho(s)\,ds$. Using this definition, we computed the integral time scale from DNS after the granular temperature reached a steady state. If a stochastic process obeys the Langevin equation with an integral time scale of T_L, then its autocorrelation function should decay exponentially, i.e., $\rho(s) = e^{-s/T_L}$. We extracted the autocorrelation function from the DNS and

compared it with the exponential function predicted by the Langevin model. This comparison is shown in figures 58 and 59. We can see that for both density ratios considered, the evolution of the autocorrelation function obtained from DNS matches with the exponential decay predicted by the Langevin model.

We established that Langevin model predicts the dynamics of a freely evolving suspension very well after the granular temperature reaches steady state. However, at a given volume fraction, mean flow Reynolds number and solid to fluid density ratio, we need to specify the coefficients as a function of the granular temperature so that we can predict the evolution of the suspension using the Langevin model. In order to do this, we have to identify the source and dissipation of granular temperature from the DNS data. In the next section, a method to identify source and dissipation of granular temperature from DNS is presented.

Identification of source and dissipation from DNS.

Using the simplified Langevin model given by Eq. 13, we can derive the evolution equation for the modeled granular temperature T^* as:

$$\frac{dT^*}{dt} = -2\gamma T^* + B^2 . \tag{24}$$

In the above equation, we can clearly identify that the source for the granular temperature is B^2 and that the dissipation is $2\gamma T^*$. For a statistically homogeneous suspension, the evolution equation for the granular temperature can be written as:

$$\frac{dT}{dt} = \frac{2}{3}\left\langle A_i'' v_i'' \right\rangle .$$

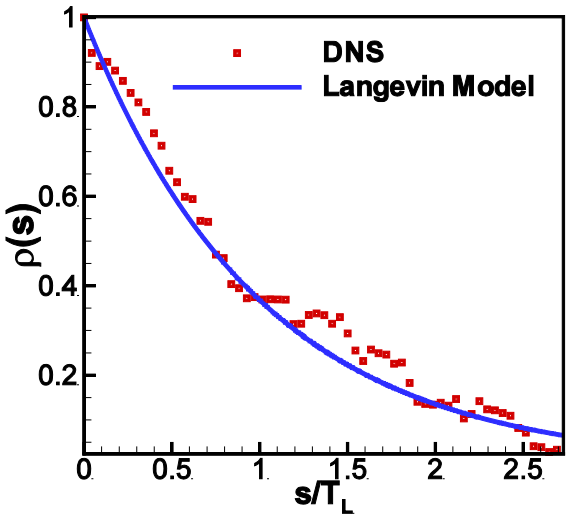

Figure 58. *Comparison of the particle velocity autocorrelation function extracted from the DNS of freely evolving suspension (volume fraction of 0.2, mean flow Reynolds number 20 and solid to fluid density ratio of 100) with the exponential decay predicted by the Langevin model.*

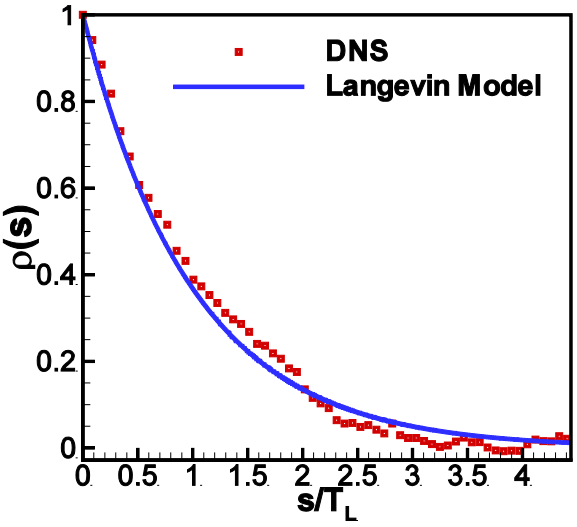

Figure 59. *Comparison of the particle velocity autocorrelation function extracted from the DNS of freely evolving suspension (volume fraction of 0.2, mean flow Reynolds number 20 and solid to fluid density ratio of 10) with the exponential decay predicted by the Langevin model.*

In the above equation, the fluctuations in the acceleration are defined about the mean acceleration, i.e. $A_j'' = A_j - \langle A_j \rangle$. Similarly the fluctuations in the particle velocity are defined about the mean velocity, i.e. $v_j'' = v_j - \langle v_j \rangle$. The instantaneous particle acceleration model should model evolution of the granular temperature correctly. In order to do this, we have to match the source and dissipation implied by the Langevin model to the source and dissipation obtained from DNS. However, given the correlation $\langle A_i'' v_i'' \rangle$, it is non-trivial to uniquely decompose it into source and dissipation. Koch (1990) derived analytical expressions for the source and dissipation in the limit of low volume fractions and low Reynolds numbers. Later, Koch and Sangani (1999) used approximate multipole expansions approach to determine the source and dissipation for dense suspensions but limited to the Stokes flow regime. Here we present a method to extract the same from the DNS at moderate Reynolds numbers.

The fluctuation in the acceleration experienced by the n^{th} particle is denoted $\mathbf{A}''^{(n)}$ and similarly, the fluctuation in the velocity is denoted $\mathbf{v}''^{(n)}$. The fluctuating acceleration can be written as:

$$A_i''^{(n)} = -\zeta^{(n)} v_i''^{(n)} + A_{R,i}''^{(n)} \tag{25}$$

In the above equation, we decomposed the fluctuating acceleration vector along a direction parallel to the particle fluctuating velocity and along a direction perpendicular to it. The component of the acceleration perpendicular to the fluctuating velocity is denoted $A_{R,i}''^{(n)}$ to represent the remainder term. It is important to note that this is not a model but an exact expression for the fluctuating particle acceleration. We can now form the estimate for the correlation $\langle A_i'' v_i'' \rangle$ as follows:

$$\langle A_i'' v_i'' \rangle_E = \frac{1}{N_p} \sum_{n=1}^{N_p} A_i''^{(n)} v_i''^{(n)} .$$

After substituting Eq. 25 into the above equation and performing some algebraic manipulations, we can write the evolution equation for the estimate of granular temperature as:

$$\frac{dT_E}{dt} = S - \Gamma \tag{26}$$

where the source is,

$$S = -\frac{2}{3}\frac{1}{N_p} \sum_{n=1}^{N_p} \zeta_-^{(n)} v_i''^{(n)} v_i''^{(n)} \tag{27}$$

and the dissipation is

$$\Gamma = \frac{2}{3}\frac{1}{N_p} \sum_{n=1}^{N_p} \zeta_+^{(n)} v_i''^{(n)} v_i''^{(n)} . \tag{28}$$

In the above expressions for source and dissipation, $\zeta_+^{(n)} = \frac{1}{2}\left(\zeta^{(n)} + \left|\zeta^{(n)}\right|\right)$ and similarly,

$$\zeta_-^{(n)} = \frac{1}{2}\left(\zeta^{(n)} - \left|\zeta^{(n)}\right|\right).$$

From these equations, it is clear that the particles whose fluctuating acceleration is aligned with the fluctuating velocity contribute to the source in granular temperature. Particles with the fluctuating acceleration aligned in a direction opposite to that of the fluctuating velocity contribute to the dissipation in granular temperature. This can be easily visualized from the scatter plot shown in figure 60. For illustration, in this figure we show the scatter plot of fluctuating particle acceleration and fluctuating particle velocity obtained from the DNS of flow past a fixed particle assembly ($\phi = 0.2$, $\mathrm{Re}_m = 20$ and $\mathrm{Re}_T = 16$). The symbols that lie in the first and the third quadrants denote the particles whose fluctuating acceleration is aligned with the fluctuating velocity. Hence, these particles contribute to the source in granular temperature. Similarly, the symbols in the second and fourth quadrants contribute to the dissipation in granular temperature.

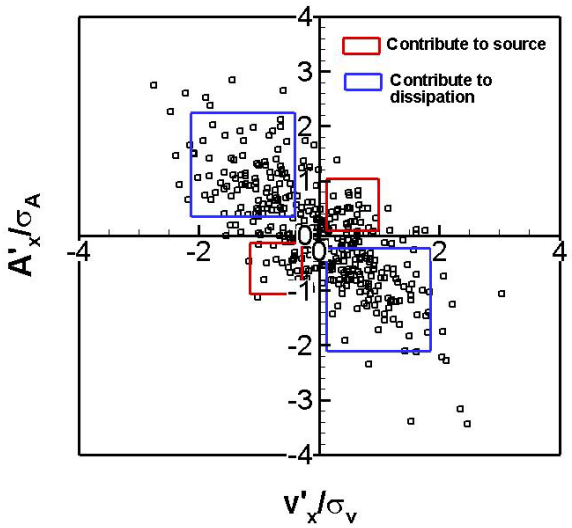

Figure 60: *Scatter plot showing the the fluctuating particle acceleration versus the fluctuating particle velocity obtained from the DNS of flow past a fixed particle assembly at a volume fraction of 0.2, mean flow Reynolds number of 20 and Reynolds number based on granular temperature of 16. From the analysis on the extraction of source and dissipation from the DNS, we can see that the symbols that lie in the first and the third quarter contribute to source and the symbols that lie in the second and the fourth quadrant contribute to the dissipation.*

Using the formulae given by Eq. 27 and Eq. 28, we extracted the source and dissipation from the DNS data and plotted them versus the granular temperature in figure 61 as a phase space plot. The source and dissipation are plotted for two sets of simulations (volume fraction of 0.2, mean flow Reynolds number of 20 and solid to fluid density ratio of 100). Triangular symbols are the data for a suspension where the particles initialized with zero granular temperature. Square symbols show the source and dissipation data for a suspension initialized with a granular temperature corresponding to Re_T = 4. We note that for the suspension with zero initial temperature, the source term is greater than dissipation at initial time, which causes the granular temperature to increase. For the case with initial granular temperature higher than the steady value, the dissipation is initially greater than the source term. We note that both suspensions reach the same steady granular temperature, and at steady state the source and dissipation are equal. Now that we have a procedure to uniquely determine the source and dissipation, the next

step is to determine the functional dependence of source and dissipation on the granular temperature. A brief outline of the specification of the model coefficients is presented in the next section.

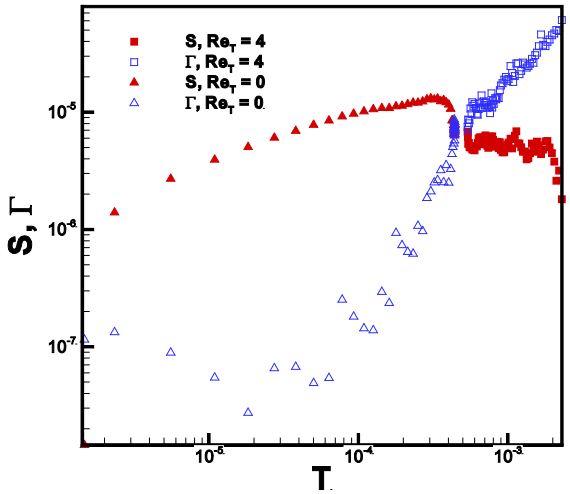

Figure 61. *Phase space plot showing the variation of source and dissipation with granular temperature. DNS data for two different suspensions is shown here. The volume fraction, mean flow Reynolds number and solid to fluid density ratio are 0.2, 20 and 100 respectvely. Triangles denote the source (filled symbols) and dissipation (hollow symbols) and dissipation for a suspension initialized with zero granular temperature. Squares denote the data for a suspension initialized with a finite granular temperature corresponding to* $Re_T = 4$.

Specification of model coefficients. To develop the functional dependence of the model coefficients on the non dimensional parameters, we performed PUReIBM simulations of freely evolving suspensions over a wide range of parameters (see Table 1). It must be noted that the statistically stationary (steady) state attained by the suspension is independent of the initial granular temperature. So in all the simulations the particles are initialized with $T = 0$.

Table 1. *Summary of the range of physical parameters used in PUReIBM simulations.*

Parameter	Range
ϕ	0.1, 0.2, 0.3, 0.4
Re_m	10, 20, 50, 75, 100
ρ_p / ρ_f	100, 800, 1000, 2000

The instantaneous particle acceleration model should model evolution of the granular temperature correctly. In order to do this, we have to match the source and dissipation implied by the Langevin model to the source (S) and dissipation (Γ) obtained from DNS. It is clear that the model coefficients γ and B can be written as follows:

$$\gamma = \frac{\Gamma\left(\phi, \mathrm{Re}_m, \rho_p / \rho_f\right)}{2T}$$

and

$$B^2 = S\left(\phi, \mathrm{Re}_m, \rho_p / \rho_f\right).$$

Clearly, source and dissipation and in turn the model coefficients are functions of the parameters. It is desirable to find a scaling for the source (and dissipation) terms as functions of the linearly independent minimal set of parameters. From the phase space plots and the evolution of the granular temperature shown in the previous quarterly report, we observe that the evolution of granular temperature for different volume fractions and Reynolds numbers is self-similar. Therefore, it is natural to analyze the dynamics of the suspension in terms of departures from the steady state values. We introduce the following scaling for temperature, source and dissipation respectively:

$$\theta = \frac{T - T_{SS}}{T_{SS}},$$

$$\hat{S} = \frac{S - S_{SS}}{S_{SS}},$$

and

$$\hat{\Gamma} = \frac{\Gamma - \Gamma_{SS}}{\Gamma_{SS}}.$$

In the above equations, $T_{SS}, S_{SS},$ and Γ_{SS} respectively, are the temperature, source and dissipation at steady state. At steady state, source and dissipation must be equal i.e. $S_{SS} = \Gamma_{SS}$. Using these definitions, the evolution equation for the granular temperature can be recast in non dimensional terms as:

$$\frac{d\theta}{ds} = \hat{S} - \hat{\Gamma}$$

where $s = \left(S_{SS} / T_{SS}\right)t$ is the non dimensional time. We can now write the Langevin model coefficients as:

$$\gamma = \frac{\Gamma}{2T} = \frac{1}{2}\left(\frac{\hat{\Gamma}(\theta)+1}{\theta+1}\right)\frac{S_{SS}\left(\phi, \mathrm{Re}_m, \rho_p / \rho_f\right)}{T_{SS}\left(\phi, \mathrm{Re}_m, \rho_p / \rho_f\right)}$$

and

$$B^2 = S = \left(\hat{S}(\theta)+1\right)S_{SS}\left(\phi, \mathrm{Re}_m, \rho_p / \rho_f\right).$$

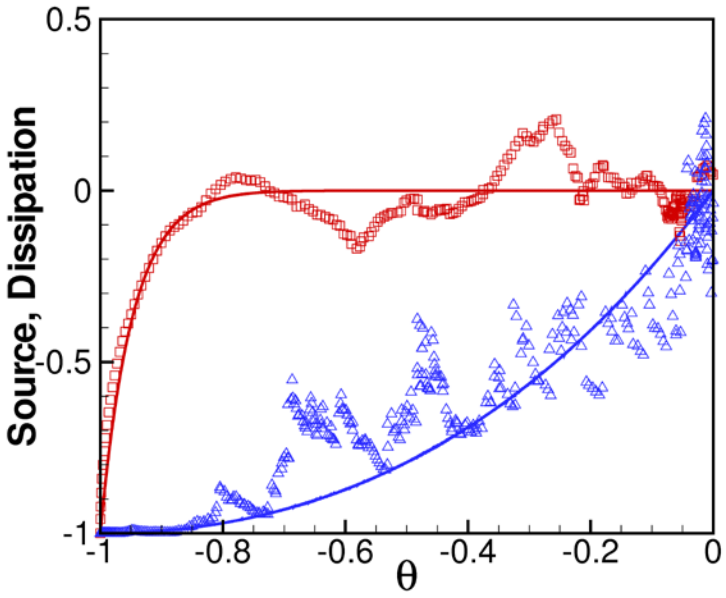

Figure 62. *Plot showing the scaling of source and dissipation with granular temperature in nondimensional phase space. Red squares denote the source and blue triangles denote dissipation. The solid lines are the curve fits for source and dissipation given by equations 29 and 30, respectively.*

Figure 62 shows the functional dependence of $\hat{S}$ and $\hat{\Gamma}$ on the non-dimensional temperature. We propose the following functional forms to model the non-dimensional source and dissipation:

$$\hat{S}(\theta) = \begin{cases} -\dfrac{e^{\theta^4} - \theta^4 - 1}{e-2}, -1 \le \theta \le 0 \\ 0, \ \theta > 0 \end{cases} \tag{29}$$

and

$$\hat{\Gamma}(\theta) = \frac{e^{\theta+1} - \theta - 2}{e-2}. \tag{30}$$

Figure 63 shows the variation of $\dfrac{T_{SS}}{\left|\langle \mathbf{W} \rangle\right|^2}$ with volume fraction and mean flow Reynolds number for a solid to fluid density ratio of 100. The steady granular temperature decreases with both volume fraction and mean flow Reynolds number. Figure 64 shows the behavior of the steady granular temperature with solid to fluid density ratio for a solid volume fraction of 0.2 and mean flow Reynolds number of 20. As expected, the steady temperature decreases with increasing inertia of the particles. Based on the data obtained from PUReIBM DNS, the following functional form is proposed for the steady value of granular temperature:

$$\frac{T_{SS}}{\left|\langle \mathbf{W} \rangle\right|^2}\left(\phi, \mathrm{Re}_m, \frac{\rho_p}{\rho_f}\right) = 2(1-\phi)^3 \exp\left(-0.02(1-\phi)\mathrm{Re}_m\right)\left(\frac{\rho_p}{\rho_f}\right)^{-1}. \tag{31}$$

In order to complete the specification of the model coefficients, we need a functional form for the steady source in terms of solid volume fraction, mean flow Reynolds number and solid to fluid density ratio. The steady source obtained from the simulations is reported using the following normalization:

$$S_{SS}^{\ *} = \frac{S_{SS} m}{3\pi\mu_f D(1-\phi)^2 \left|\langle \mathbf{W} \rangle\right|^2},$$

where m is the mass of the particle, μ_f is the dynamic viscosity of the fluid, $\langle \mathbf{W} \rangle$ is the mean slip velocity between the solid and the fluid phase, and D is the particle diameter.

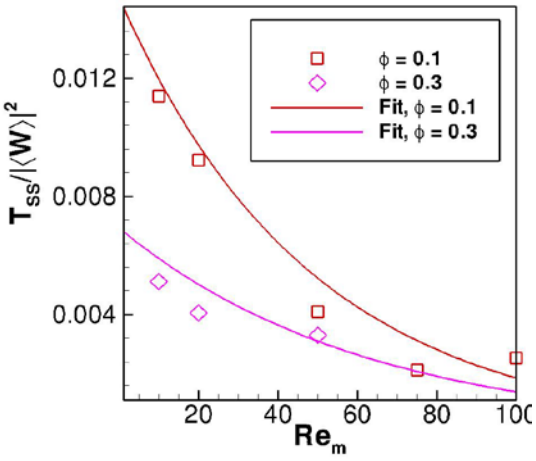

Figure 63. *Plot showing the variation of steady granular temperature with volume fraction and mean flow Reynolds number for ρ_p/ρ_f = 100. Symbols denote the data obtained from PUReIBM DNS and the solid lines indicate the fit given by Eq.(25).*

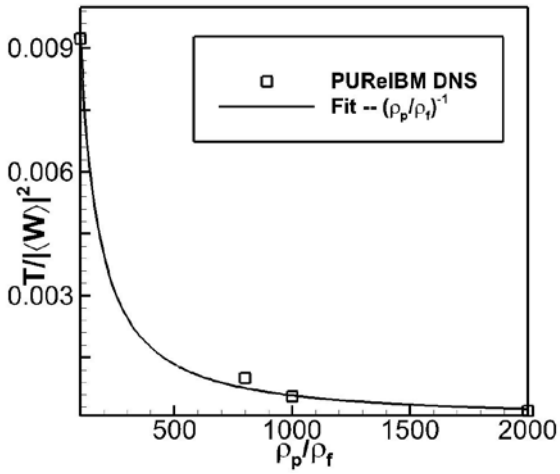

Figure 64. *Plot showing the variation of steady granular temperature with solid to fluid density ratio for a solid volume fraction of 0.1 and mean flow Reynolds number 20. Symbols denote the data obtained from PUReIBM DNS and the solid line indicates the function $(\rho_p/\rho_f)^{-1}$.*

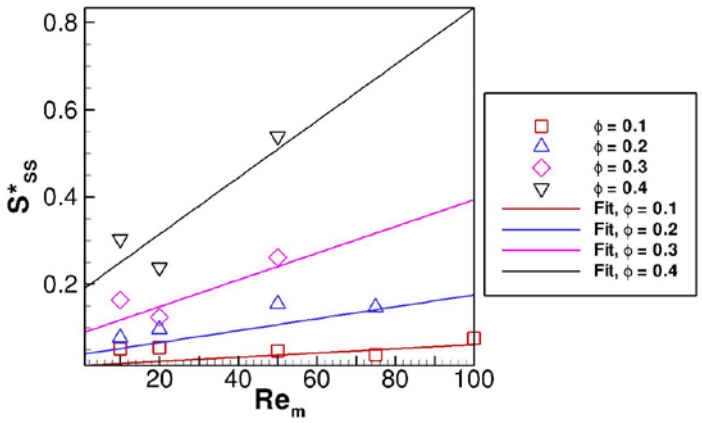

Figure 65. *Plot showing the behavior of steady source with volume fraction and Reynolds number for a solid to fluid density ratio of 100. Symbols indicate PUReIBM DNS data and solid lines indicate the fit given by Eq. (32)*

Figure 65 shows the behavior of the normalized steady source with volume fraction and mean flow Reynolds number for a solid to fluid density ratio of 100. The normalized source increases with both volume fraction and Reynolds number. This behavior can be explained by employing a simple scaling analysis. Since the source of granular temperature is caused due to the correlation of particle acceleration fluctuations and particle velocity fluctuations, the source scales as $S_{SS} \sim \sigma_A T_{SS}^{1/2}$ where σ_A is the standard deviation in the particle acceleration. This scaling implies that the normalized source scales as

$$S_{SS}^{*} = \frac{S_{SS} m}{3\pi\mu_f D(1-\phi)^2 \left|\langle \mathbf{W} \rangle\right|^2} \sim \frac{\sigma_A}{\left|\langle \mathbf{A} \rangle\right|} \frac{F(\phi, \mathrm{Re}_m)}{1-\phi} \frac{T_{SS}^{1/2}}{\left|\langle \mathbf{W} \rangle\right|},$$

where, $F(\phi, \mathrm{Re}_m)$ is the normalized mean drag per particle which increases with both solid volume fraction and mean flow Reynolds number. Although the steady granular temperature decreases with both solid volume fraction and Reynolds number, the strong dependence of the mean drag on ϕ and Re_m determines the overall behavior of normalized source. The dependence of the normalized source on the solid to fluid density ratio is determined by the dependence of steady granular temperature on ρ_p / ρ_f. In fact, the PUReIBM DNS data indicates that S_{SS}^{*} varies inversely with $\left(\rho_p / \rho_f\right)^{1/2}$. Based on the DNS data the following functional form is proposed for the normalized steady source:

$$S^{*}_{SS}\left(\phi, \mathrm{Re}_m, \frac{\rho_p}{\rho_f}\right) = \left(1 + 0.035\,\mathrm{Re}_m\right) \frac{\phi}{(1-\phi)^3} \left(\frac{\rho_p}{\rho_f}\right)^{-1/2}. \qquad (32)$$

The values of normalized source generated by the above expression are shown by solid lines in Figure 65.

(Sundaresan reporting.) In Task 2.3 we sought to examine the gas-particle flow structures that were manifested in detailed lattice Boltzmann simulations. We began our study by probing the effect of polydispersity on the average characteristics manifested by freely evolving gas-solid suspensions. Specifically, lattice Boltzmann simulations of fluidization of ternary, freely evolving, gas-solid suspensions in periodic domains were performed, and the resulting domain-averaged statistics were extracted. These were then compared with corresponding statistics obtained in simulations of monodisperse gas-solid suspensions having the same Sauter mean diameter (as the ternary case).

The simulation domain size was chosen to be a rectangular box with dimensions of 200x70x70 lattice units to suppress the formation of two-dimensional structures within the simulation domain. The axis of sedimentation was chosen to be parallel with the long side of the rectangular box. The fluid-particle assembly was allowed to fully relax and average properties were collected for comparison between monodisperse and polydisperse cases. The particle to fluid density ratio was set to 1000 for every simulation presented here.

A ternary gas-solid suspension was used for comparison with the monodisperse gas-solid suspension. As log-normal distribution of particle sizes is quite common, we started with such a distribution and identified equivalent ternary mixtures and monodisperse approximations using discrete (quadrature) method of moments. Although one could have found optimal sizes and number densities of the three types of particles in the ternary case using the method of moments, we considered a simpler case where we chose the particle sizes and determined their number densities via method of moment. Accordingly the first three moments of the discrete particle distribution function were required to be equal to those of the continuous log-normal distribution function. In all the simulations illustrated below, the mean particle diameter was 4.64 and standard deviation was 0.624, all in lattice units. The ratio of the third moment to the second moment of the particle distribution function was required to be equal to the particle diameter used in the monodisperse freely evolving suspensions. This constraint corresponds to requiring equality between the Sauter mean diameter of the ternary gas-solid suspension and the monodisperse suspension. Figure 66 illustrates a histogram of the discrete particle distribution function used for this set of simulations with the continuous particle distribution function that was approximated given by the blue line. The ternary gas-solid suspension configurations (inside the periodic domain used in flow simulations) were generated using a Monte-Carlo relaxation technique.

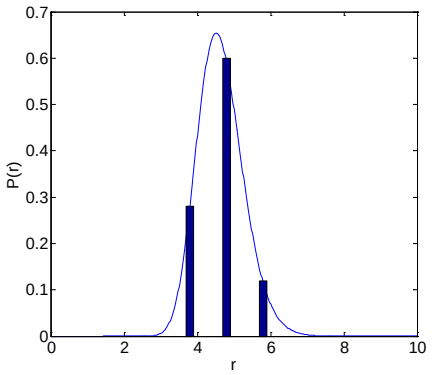

Figure 66. *Discrete particle size distribution computed using the method of moments compared with lognormal distribution.*

Freely evolving suspension simulations were performed at three different total volume fractions, namely $\phi = 0.05$, $\phi = 0.1$, and $\phi = 0.15$. At each volume fraction, several statistically steady parameters were calculated for comparison between the monodisperse and ternary suspensions. Figure 67 shows the volume weighted sedimentation velocity for both the ternary and monodisperse suspensions normalized by the terminal settling velocity of an isolated particle calculated using the Sauter mean diameter in the Schiller-Naumann relation. The volume-weighted velocity is defined as

$$\langle u \rangle = \frac{\sum_i u_i d_i^3}{\sum_i d_i^3} \tag{33}$$

where $\langle u \rangle$ is the volume weighted velocity, u_i is the average sedimentation velocity of the *i*th particle, and d_i is the diameter of the *i*th particle. The scale of the marker size indicates the uncertainty in the values given in figure 67. There is clearly very little difference between the ternary and monodisperse cases. This indicates that the Sauter mean diameter is an effective way to simplify a polydisperse system to an *equivalent* monodisperse system.

In figure 68, the dimensionless time between collisions is given for both monodisperse and polydisperse cases. The dimensionless time between collisions is given by

$$\tau_{col} = t_{col} \frac{U_t}{\langle d \rangle} \tag{34}$$

where t_{col} is the time between collisions, U_t is the sedimentation velocity calculated based on the Schiller-Naumann relation using the Sauter mean diameter $\langle d \rangle$. There seems to be fewer collisions in the polydisperse system than in the monodisperse system. This point is quite interesting and counter-intuitive; we did not pursue this point, as it was not consistent with the goal of this study. Nevertheless, it is noted that future work should gather more collisional statistics to illuminate why there seems to be fewer collisions in polydisperse suspensions.

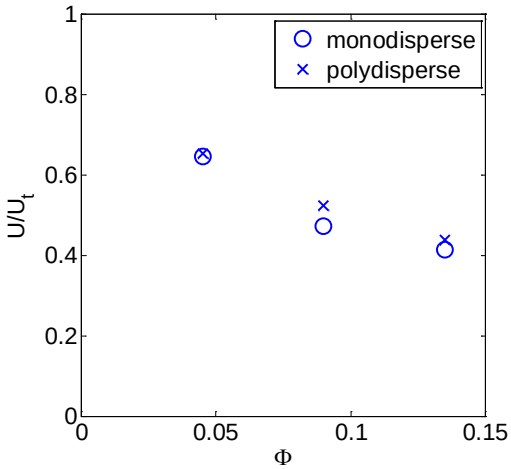

Figure 67. *Volume weighted sedimentation velocity normalized by the settling velocity of an isolated particle using Schiller-Naumann relation for both monodisperse and polydisperse cases.*

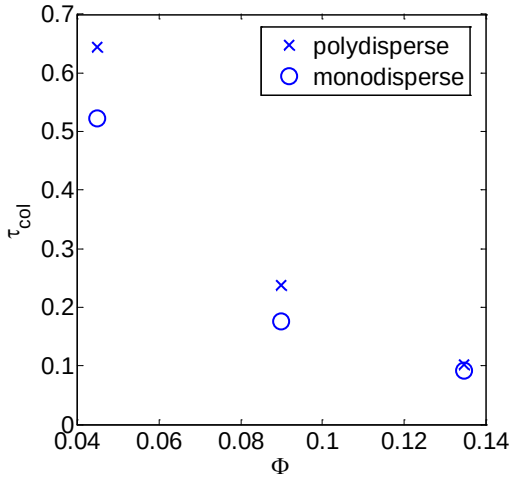

Figure 68. *Average time between collisions vs volume fraction and for monodisperse and polydisperse cases.*

It should be noted that at each volume fraction the viscous relaxation time was identical. Here we define a dimensionless viscous relaxation time as

$$\tau_{vis} = \frac{\langle d \rangle^2}{\nu} \frac{U_t}{\langle d \rangle} \tag{35}$$

where τ_{vis} is the dimensionless viscous relaxation time, ν is the kinematic viscosity of the lattice-Boltzmann fluid, and U_t is the terminal settling velocity calculated from the Schiller-Naumann relation, using the Sauter mean diameter $\langle d \rangle$. In polydisperse suspensions, as volume fraction increases, the time between successive collisions decreases dramatically, which is reasonable. However, it decreases at a faster rate in the ternary suspension than in the corresponding monodisperse case. To look at why this might be the case, the velocity distribution at each volume fraction was found for the polydisperse cases, and given below in figure 69.

$$\frac{\tau_{col}}{\tau_{vis}} = 0.895 \qquad \frac{\tau_{col}}{\tau_{vis}} = 0.398$$

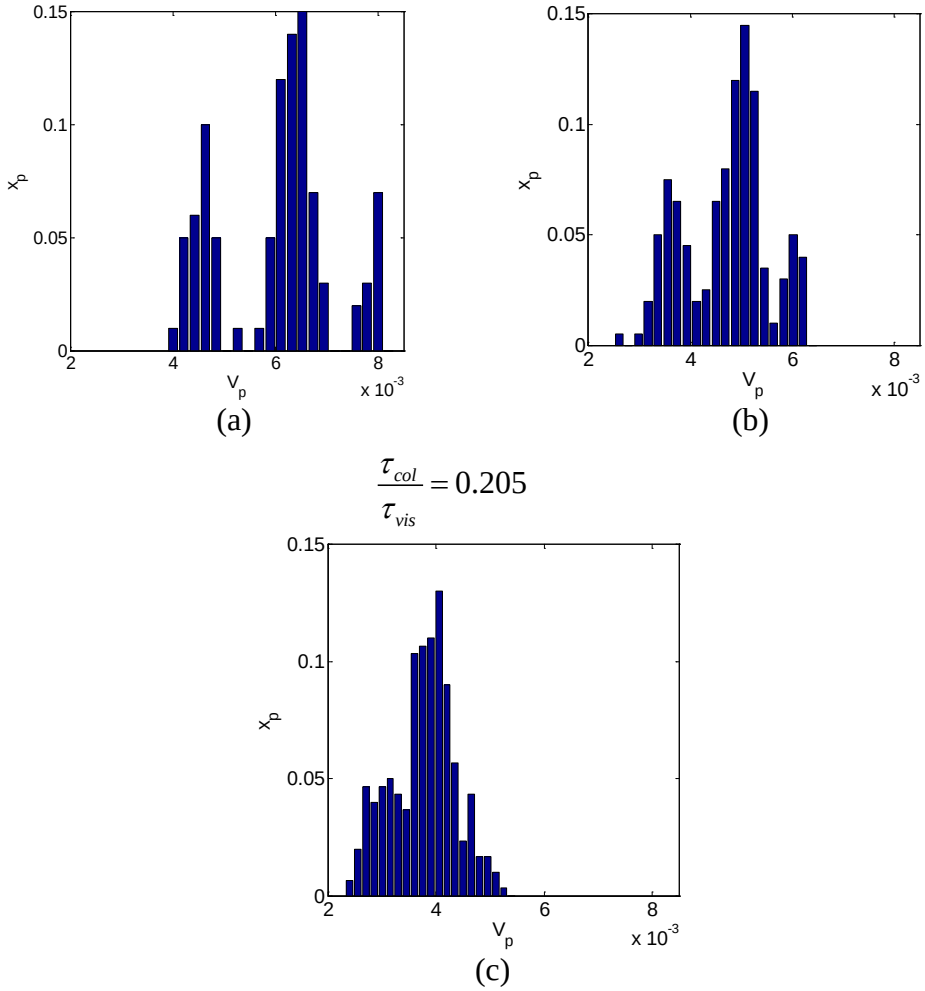

Figure 69. *In all figures x_p denotes the fraction of particles and v_p is the velocity of the particle. (a) Velocity distribution function of polydisperse gas-solid suspension at $\phi = 0.045$. (b) Velocity distribution function of polydisperse gas-solid suspension at $\phi = 0.09$. (c) Velocity distribution function at $\phi = 0.135$.*

From figure 69 it can be seen that when the ratio of the dimensionless time between successive collisions to the dimensionless viscous relaxation time is $O(1)$, the velocity distribution function of the suspension is trimodal. As the time between successive collisions decreases, the particles of species *i* are able to exchange momentum with particles of species *j*, and, as such, the velocity distribution function of the mixture tends to a unimodal shape. Therefore, in ternary suspensions the ratio of time between successive collisions to the viscous relaxation time must be significantly smaller than unity for the each species in the ternary system to interact vigorously through collisions and produce a unimodal velocity distribution. This point has been previously noted in theoretical studies of dilute bidisperse gas-solid suspensions (Kumaran, 1993).

Monodisperse gas-solid suspensions are known to exhibit spatiotemporal inhomogeneities; when the lateral dimension of the domain is small, they are known to take the

form of one-dimensional, vertically traveling waves. The existence of these waves have been documented by several researchers (Sundaresan, 2003). However, the existence of such one-dimensional travelling waves in polydisperse suspensions has remained a conjecture. This is primarily because a linear stability analysis of a polydisperse suspension is complicated by the lack of available closures for different terms in multi-fluid models. In figure 70, we give the space-time plots for the evolution of volume fraction fronts in both monodisperse and ternary cases.

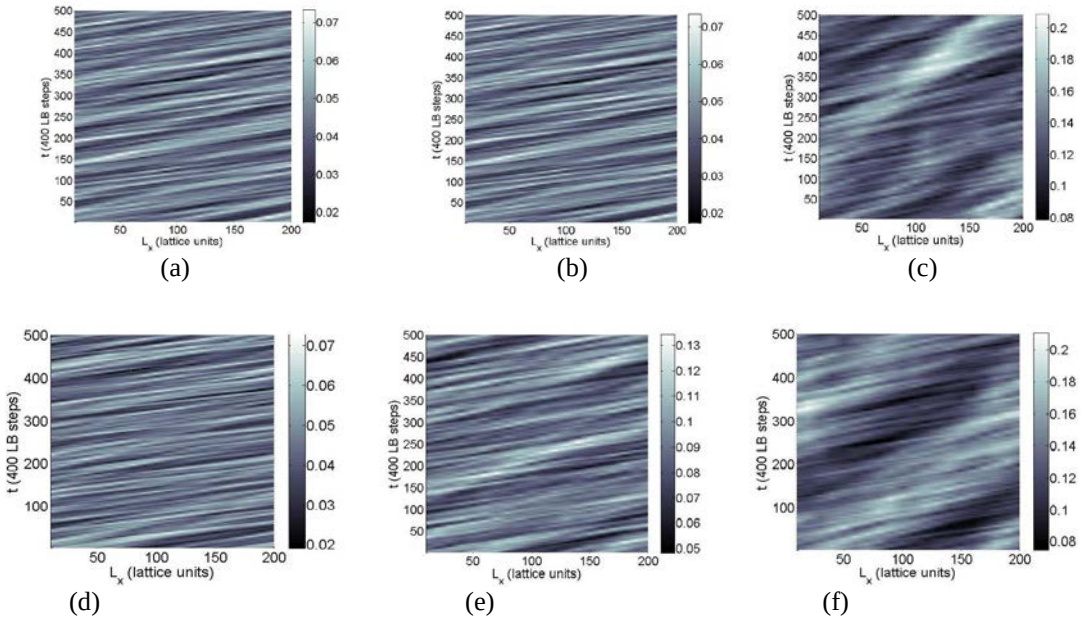

Figure 70. *(a) Space time plot of monodisperse gas-solid suspension at* ϕ = 0.045. *(b) Space time plot of monodisperse gas-solid suspension at* ϕ = 0.09. *(c) Space time plot of monodisperse gas-solid suspension at* ϕ = 0.135. *(d) Space time plot of polydisperse gas-solid suspension at* ϕ = 0.045. *(e) Space time plot of polydisperse gas-solid suspension at* ϕ = 0.09. *(f) Space time plot of polydisperse gas-solid suspension at* ϕ = 0.135.

In this work ternary freely evolving suspensions were compared with monodisperse freely evolving suspensions at the same volume fraction and Sauter mean diameter. The results show that these simulations are feasible using the current lattice Boltzmann algorithm developed by Ladd (Ladd, 1994a; b). However, the inhomogeneities manifested by these freely evolving systems (see figure 70) make extracting data useful for continuum model development difficult. Because of this limitation, we did not pursue freely evolving simulations any further in this project.

Goal III: Gas-Phase Instabilities: Turbulence Models for Polydisperse Systems (Fox & Subramaniam)

Task 3.1: Direct numerical simulations of polydisperse particles in gas-phase turbulence (Fox & Subramaniam)

The DNS-DEM code will be used to perform turbulent multiphase flow simulations for a limited range of turbulence Reynolds number $(R_\lambda = 25-50)$ *at selected volume fraction and initial nominal particle Reynolds number for bidisperse and polydisperse systems. Canonical problems include the decay of polydisperse, particle-laden turbulence in a tri-periodic box, and time permitting, the artificial forcing of the turbulence to a steady state. The settling of bidisperse spheres into initially homogeneous turbulence at finite Reynolds will also be simulated. The DNS data will be used to quantify the budget of terms in the turbulent kinetic energy evolution and the dissipation equation.*

(Subramaniam reporting.) 3.1.1: Verification of PUReIBM in single-phase turbulent flows

Approach: Prior to performing DNS of turbulent gas-solid flow using the PUReIBM code, the decay of single-phase isotropic turbulence is verified with PUReIBM. The power-law decay of isotropic turbulence suggests that turbulent kinetic energy (TKE) evolves in the form

$$k(t) = k_0 \left(\frac{t}{t_0} \right)^{-n},$$

where t_0 is a reference time, and k_0 is the magnitude of k at the reference time. To examine this behavior, an initially isotropic single-phase turbulent field is generated according to the method proposed by Rogallo (1981) with the one dimensional energy spectrum function given by Pope (2000), that is

$$E(\kappa) = C\varepsilon^{2/3}\kappa^{-5/3} f_L(\kappa L) f_\eta(\kappa\eta)$$

with C being a model constant, ε being the dissipation rate of TKE, and κ being the wave number. The functions f_L and f_η modify the energy spectrum at low and high wave numbers respectively, and are given as

$$f_L(\kappa L) = \left(\frac{\kappa L}{\left[(\kappa L)^2 + c_L^{\,2} \right]^{1/2}} \right)^{5/3+p_0},$$

$$f_\eta(\kappa\eta) = \exp\left\{ -\beta \left\{ \left[(\kappa\eta)^4 + c_\eta^{\,4} \right]^{1/4} - c_\eta \right\} \right\},$$

with L and η being the large eddy length scale and Kolmogorov length scale, respectively. The other parameters are model constants that are defined accordingly.

DNS of isotropic turbulence is performed in a cubic domain. The choice of the box length and also the grid resolution is determined by flow length scales. The domain should be large enough to accommodate sufficient number of large energetic eddies, and the grid resolution should be such that the evolution of smallest eddies being captured. The duration of an isotropic

turbulence DNS is 4 eddy turnover time scale $\tau = k/\varepsilon$ (Pope, 2000). An isotropic turbulent flow characterized by Taylor microscale Reynolds number Re_λ is generated in a cube with 256^3grid points, which satisfies the resolution requirement criteria for small and large length scales. The evolution of TKE carries on for 4 eddy turnover time scale as shown in Figure 71. The decay rate exhibits two distinct regions: i) the region were the decay rate is small due to the effect of the velocity field initialization, ii) the region where a power law decay is observed. The decay rate observed in this simulation is 1.15 which is in agreement with the value reported for decay of single-phase isotropic turbulence in literature (Pope, 2000).

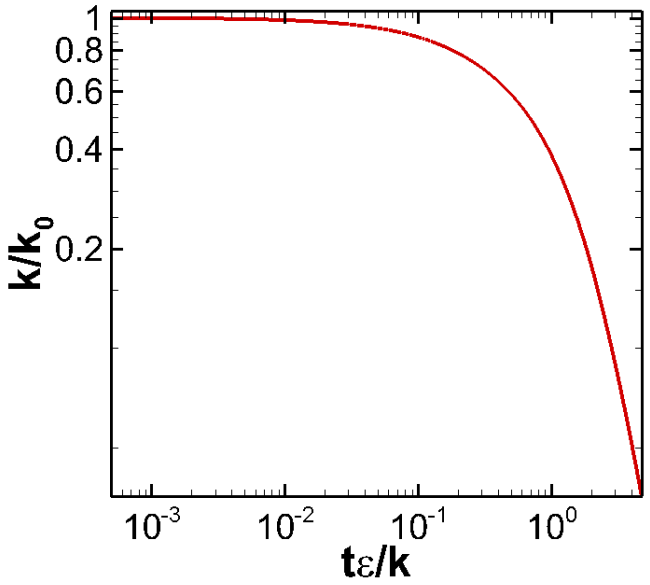

Figure 71. *The decay of k for an isotropic turbulence with* $\mathrm{Re}_\lambda = 50$.

3.1.2: Fluid-phase velocity fluctuations in monodisprese fixed particle beds

Approach: We performed PUReIBM DNS of flow past fixed assemblies of monodisperse spheres over a wide range of solids volume fraction ($0.1 \le \phi \le 0.5$) and mean flow Reynolds numbers ($0.01 \le \mathrm{Re}_m \le 300$). Then we quantify the strength of gas-phase velocity fluctuations in terms of ϕ and Re_m.

Direct numerical simulation of flow through a particle assembly using PUReIBM results in velocity and pressure fields on a regular Cartesian grid. For every realization of the gas-solid flow we compute the kinetic energy in the fluctuating motions using volume averaging:

$$k_f^{(\mu)} = \frac{1}{2V_f}\int_{V_f} I_f u_{f,i}"u_{f,i}"dv.$$

Here I_f is the fluid-phase indicator function, $\mathbf{u}_f"$ is the fluid-phase velocity fluctuations defined as $\mathbf{u}_f - \langle \mathbf{u}_f \rangle$, and μ denotes a realization or configuration of particles. The ensemble-averaged k_f represents an average over all particle configurations corresponding to the same volume

fraction and pair correlation function. Therefore, k_f obtained from a single realization is averaged over multiple independent realizations (MIS) to obtain an estimate for the ensemble averaged kinetic energy:

$$k_f = \frac{1}{\mathrm{M}} \sum_{\mu=1}^{\mathrm{M}} k_f^{(\mu)},$$

where M is the number of particle configurations used in DNS. All simulations start with the initial condition of uniform fluid velocity. Therefore, the steady state value of k_f obtained in a fixed particle assembly depends only on the solids volume fraction and the mean flow Reynolds number. Figure 72 shows the variation of k_f / E_f with solids volume fraction for different mean flow Reynolds numbers while figure 73 shows the variation of k_f / E_f with mean flow Reynolds number for different solid volume fractions. As evident from figure 72, the kinetic energy in fluctuating motions normalized by the mean energy in the gas-phase increases dramatically with volume fraction. This behavior is expected because, as the volume fraction increases, the space available to the gas decreases. Owing to conservation of mass, the velocity of the gas increases thus causing k_f / E_f to increase with volume fraction. As shown in Figure 73, at a given volume fraction, k_f / E_f decreases rapidly with increasing mean flow Reynolds number up to $\mathrm{Re}_m = 50$ and beyond $\mathrm{Re}_m = 50$ it has a weak power law dependence on Re_m. This behavior is a result of the normalization of k_f / E_f.

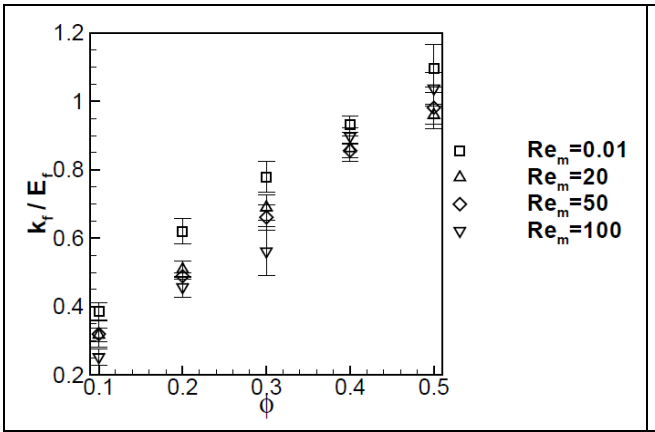

Figure 72. *The behavior of k_f/E_f with ϕ for different mean flow Reynolds numbers while.*

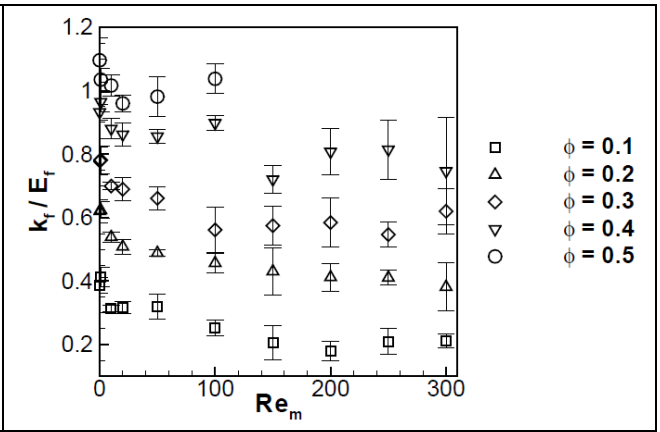

Figure 73. *The behavior of k_f/E_f with Re_m for different solid volume fractions.*

Since the fluid-phase velocity fluctuations observed originates from the presence of particles and are basically pseudo-turbulent, it is of interest to examine the effect of initial turbulent structures of the fluid phase on the steady state value of k_f in gas-solid flows, and to quantify the level of turbulent and pseudo-turbulent velocity fluctuations in the fluid phase. To address this issue we consider three types of simulations as follows:

1. Case I initialized with a pseudo-turbulent uniform laminar flow
2. Case II initialized with a specified isotropic turbulent flow

3. Case III initialized with the steady solution of Case I in addition to the initial isotropic turbulence of Case II

For the simulations, the mean slip Reynolds number is selected as 50. An isotropic turbulent field is generated with $\mathrm{Re}_\lambda = 12$ by the method described in Section 3.1.1, and the corresponding Kolmogorov length scale is selected such that the ratio d_p / η is 5. Detailed information of flow parameters is provided in Table 2. The simulations start by imposing a mean pressure gradient along the mean flow such that the Reynolds number reaches the desired value, and the results are shown in figure 74.

Table 2. *The numerical and physical parameters of turbulent/pseudo-turbulent simulations.*

	ϕ	Re_m	Re_λ	d_p / η	D_m	L / d_p
Case I: pseudo-turbulent	0.05	50	-	-	20	12.5
Case II: turbulent	0.05	50	12	5	20	12.5
Case III: Case $I_{s.s.}$+iso. turb.	0.05	50	-	-	20	12.5

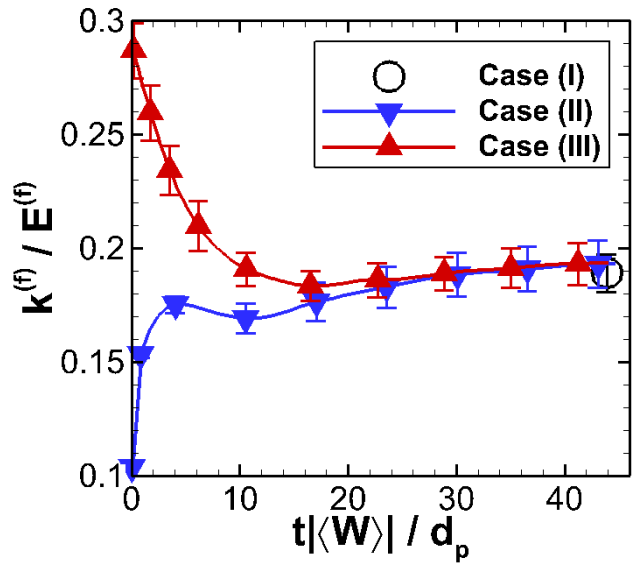

Figure 74. *Evolution of k_f normalized with mean flow energy. Symbols (∇) correspond to the simulation initialized with an isotropic turbulence. Symbols (Δ) represent simulation of perturbed velocity field. Symbol (O) shows the steady value of pseudo-turbulent simulation.*

Since the evolution of k_f for Case I is similar to other pseudo-turbulent simulations, the steady value of k_f for this case is only presented at steady state. It is also indicates that for Case II, the level of k_f starts from initial isotropic turbulence level and increases to the steady state pseudo-turbulent value. The data reveals that the velocity fluctuations arising from the particles in fluid-phase are much higher than the turbulent velocity fluctuations for $\mathrm{Re}_\lambda = 12$, and the principal contribution to the fluid-phase velocity fluctuations is pseudo-turbulent. Case III is used to

examine the relaxation of turbulence in particle-laden flows. The evolution of k_f for Case III shows that the excess amount of k_f decays and the pseudo-turbulent steady state level of k_f is recovered. These results showing both attenuation and enhancement of turbulence based on the initial level of velocity fluctuations indicate that the initial turbulent motions of the fluid-phase do not influence the steady value of k_f, and the pseudo-turbulent fluctuations are mainly due to the interaction of particles with the mean flow in gas-solid suspensions.

From these results, it is clear that the turbulent velocity fluctuations will only be important if they are of the same level as the pseudo-turbulent velocity fluctuations. Therefore, it is interesting to determine what Taylor microscale Reynolds number generates a level of initial turbulence comparable to the steady value of k_f. The equivalent Re_λ is obtained through the isotropic turbulence scaling relations $\mathrm{Re}_L = k_f^{1/2} L/\nu$, $\eta/L = \mathrm{Re}_L^{-3/4}$ and $\mathrm{Re}_\lambda = \left(20\,\mathrm{Re}_L/3\right)^{1/2}$ (Pope, 2000) with Re_L being the turbulent Reynolds number. The isotropic single-phase k is substituted by the correlation for the pseudo-turbulent k_f (discussed in section 3.2.1) which gives a final expression for Re_λ as

$$\mathrm{Re}_\lambda = \sqrt{\frac{20}{3}}\left\{\phi + 1.25\phi\left(1-\phi\right)^3 \exp\left(-\phi\,\mathrm{Re}_m^{1/2}\right)\right\}\left(\frac{\eta}{d_p}\right)^2\left(\frac{\mathrm{Re}_m}{1-\phi}\right)^2 .$$

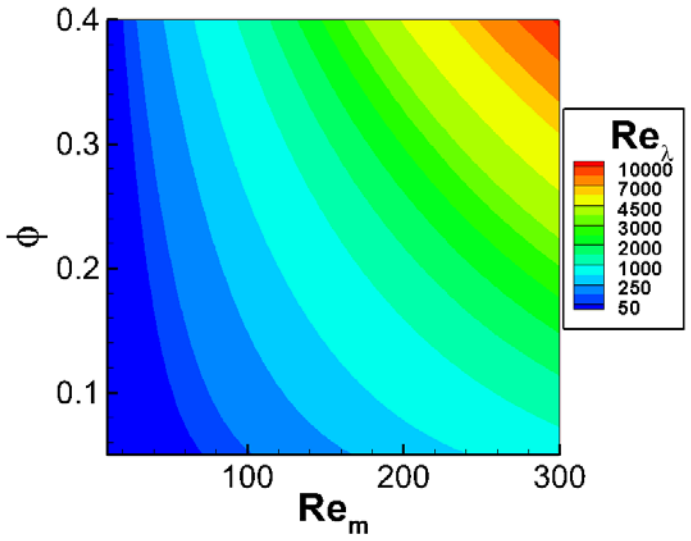

Figure 75. *The equivalent Taylor microscale turbulent Reynolds number which generates the same pseudo-turbulent level of velocity fluctuations observed in gas-solid flows. The figure corresponds to* $d_p/\eta = 5$.

To gain insight into the equivalent value of Re_λ with respect to Re_m and ϕ, a contour plot of Re_λ for $d_p/\eta = 5$ is presented in Figure 75. This figure reveals that at moderate or high Reynolds numbers the velocity fluctuations induced by particles are equivalent to high levels of single phase turbulence. The square dependence of Re_λ on Re_m indicates that the large eddies

associated with the flow structures due to the presence of particles contribute increasingly to the equivalent isotropic Re_λ. In addition, the result shows that performing a simulation initialized by a high turbulent Reynolds number that generates the same level of pseudo-turbulence is not feasible due to limitations on computational resources.

3.1.3: Fluid-phase velocity fluctuations in bidisprese fixed particle beds

Approach: Particle-resolved DNS of bidisperse gas-solid flows with fixed particle configurations are investigated to gain insight into the behavior of gas phase velocity fluctuations and interphase TKE transfer term.

In a gas-solid suspension, the particles are not exactly of the same size and there is a size distribution of particles which may affect the level of fluid-phase velocity fluctuations compared to monodisperse particle configurations. In this regard, bidisperse gas-solid flows that are the simplest polydisperse suspensions are studied over a range of particle sizes for different volume fractions and Reynolds numbers by PUReIBM and the level of fluid-phase velocity fluctuations is quantified. In this investigation, fixed particle assemblies are selected since they represent particles with high Stokes number. We consider 5 cases in this study and particle sizes normalized with Sauter mean diameter for each case is reported in Table 3.

Table 3. *The ratio of diameter of each class to Sauter mean diameter.*

	Case I	Case II	Case III	Case IV	Case V
d_1 / d_S	0.50	0.55	0.60	0.65	0.75
d_2 / d_S	1.50	1.75	2.00	1.30	1.15

These size classes are used to generate suspensions for two volume fractions being 0.3 and 0.4. In addition, for each case two different Reynolds number is considered as 50 and 75. It is worth mentioning that for each case four independent realizations are performed and the results are presented as their ensemble average at steady state.

The level of k_f is computed for simulations and are presented in figure 76 against particle size ratio. For comparison with monodisperse assemblies, corresponding data is presented at $d_2 / d_1 = 1$ as well. It is observed that the level of velocity fluctuations is highly influenced by volume fraction, and the normalized k_f is not affected by Re_m. These behaviors are similar to what is observed for monodisperse assemblies. In addition, the comparison between monodisperse and bidisperse data reveals that the level of k_f in both cases is the same (for the same volume fraction and Reynolds number) with maximum error less than 10%. To better understand the reason for the similarity of k_f, we examine the evolution equation of k_f for fixed particle assemblies, that is

$$\underbrace{\rho_f (1-\phi)\frac{d}{dt}k_f}_{\text{unsteady term}} = \underbrace{\langle W_i \rangle \left\langle \tau_{ji} n_j^{(f)} \delta\left(\mathbf{x}-\mathbf{x}^{(\mathbf{I})}\right)\right\rangle}_{\text{fluid interphase TKE transfer}} - \underbrace{2\mu_f \left\langle S_{ij} S_{ij} \right\rangle}_{\text{viscous dissipation}},$$

where ρ_f is the fluid-phase density, $\boldsymbol{\tau}$ is the stress tensor, $\mathbf{n}^{(f)}$ is the normal vector to particle surface towards the solid phase, $\delta\left(\mathbf{x}-\mathbf{x}^{(\Gamma)}\right)$ is the Dirac delta function representing fluid-solid interface, and $\mathbf{S}$ is the strain rate tensor. At steady state the terms on the right-hand-side balance each other, where interphase TKE transfer π_f is source and viscous dissipation is sink of energy (Tenneti et al). Quantification of interphase TKE transfer shown in figure 77 reveals that the difference between monodisperse and bidisperse configurations is less than 10%. Since interphase TKE transfer, representing the amount of energy fed to fluid-phase fluctuating velocities, is similar among simulated cases, the level of k_f is expected to be the same among cases with the same ϕ and Re_m. This observation suggests that a proposed model of k_f for monodisperse configurations is also applicable to bidisperse systems.

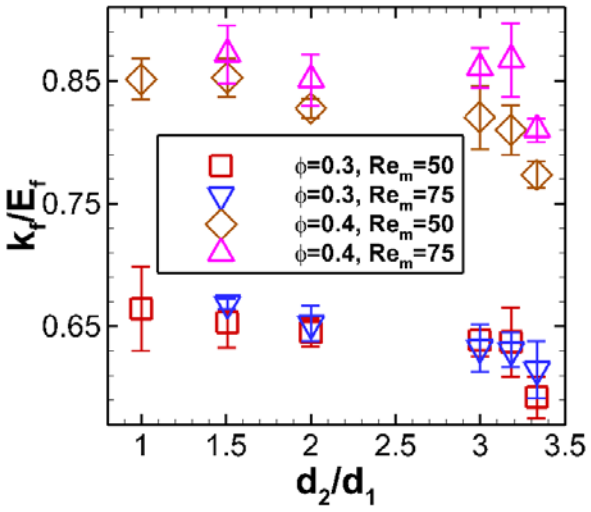

Figure 76. *Level of k_f for bidisperse gas-solid suspensions normalized by the mean flow energy.*

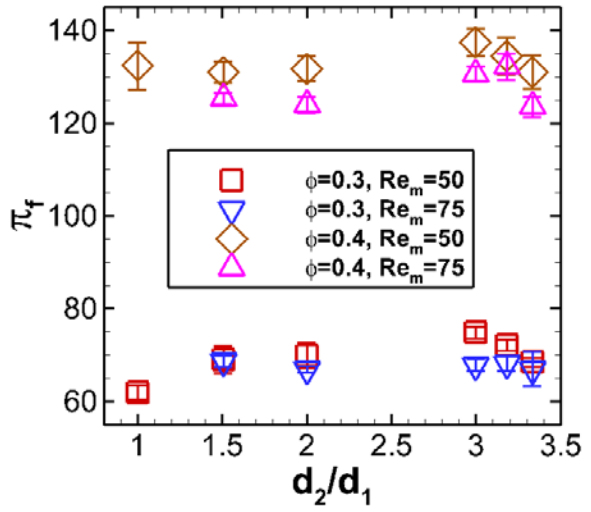

Figure 77. *Interphase TKE transfer for bidisperse gas-solid suspensions normalized with $\mu_f(|\langle\mathbf{W}\rangle|/d_s)^2$.*

3.1.4: Fluid-phase velocity fluctuations in monodisprese freely evolving suspensions

Approach: Although fixed particle beds are good approximation to fluidized beds with high Stokes number particles, in real problems the particles are free to move. We perform PUReIBM DNS of monodisperse freely evolving suspensions to investigate the influence of motion of particles under hydrodynamic and collisional forces on fluid-phase velocity fluctuations.

The simulations are carried out in an accelerating frame of reference which moves with mean particle velocities that facilitates investigation of each flow parameter separately. Accordingly, two particle to fluid density ratios are selected as 100 and 1000 to investigate the effect of particle Stokes number. The influence of the volume fraction is also studied with the choice two volume fractions 0.1 and 0.2 as well. Similarly, to investigate the effect of coefficient of restitution (COR), we select three values 1.0, 0.9, and 0.7 for this parameter. All the simulations

are performed at $\mathrm{Re}_m = 20$ with two independent realizations and are initialized with a uniform mean flow for the fluid phase and zero granular temperature for the solid phase.
The comparison of k_f for elastic cases between the two density ratios indicates that the level of fluid-phase velocity fluctuations is not influenced by particle densities as shown in figure 78. The evolution of k_f is also compared with fixed bed results of the same Reynolds number and volume fractions represented by straight lines. The difference of k_f in freely evolving suspensions from the fixed bed assemblies is less that 10% which denotes the similarity of the k_f between fixed beds and freely evolving suspensions.

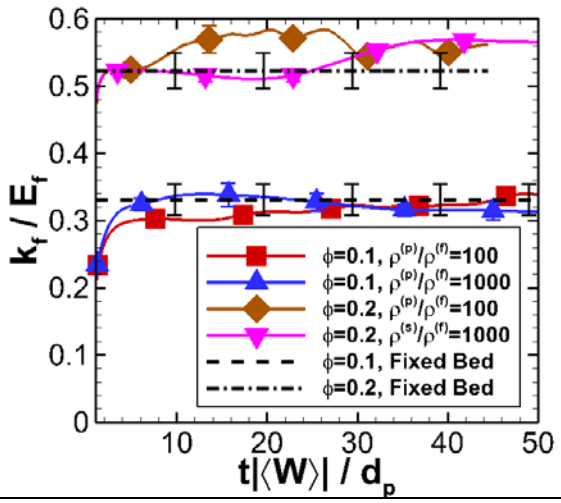

Figure 78. *Evolution of k_f for elastic particles with different volume fractions and solid to fluid density ratios.*

In addition, the comparison of k_f for particles with different CORs, presented in figure 79, indicates that k_f is not very sensitive to COR and the differences are not statistically significant, especially for the lower volume fraction. Similar to DNS of elastic particles, the level of k_f is in good agreement with fixed particle assemblies with the maximum error about 10% for the higher volume fraction.

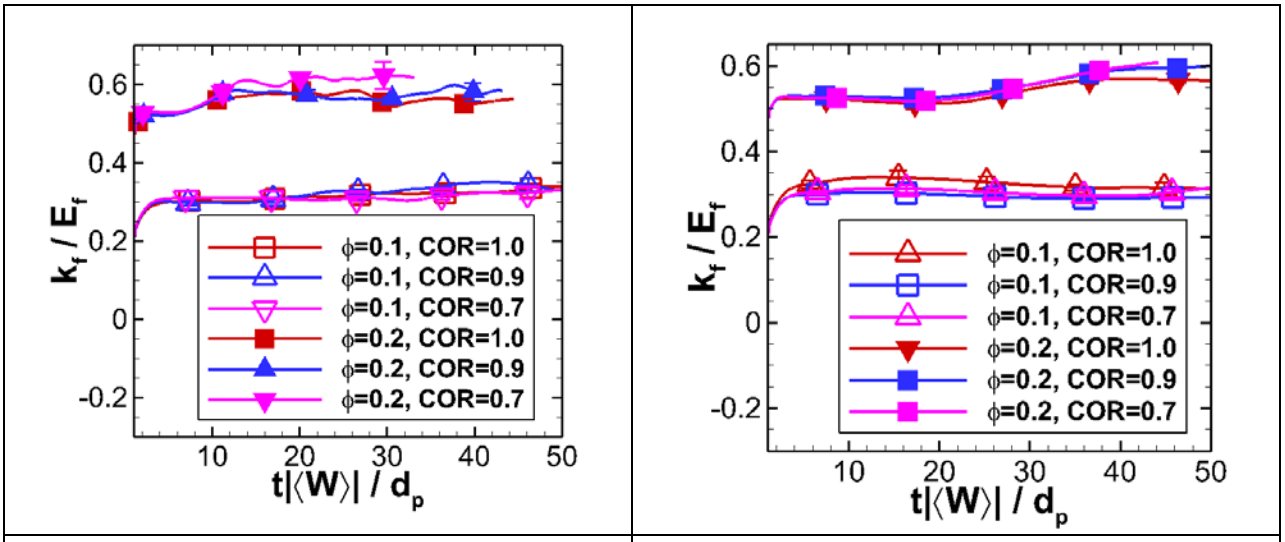

Figure 79. *Comparison of k_f among elastic and inelastic cases. Figure (a) corresponds to ρ_p/ρ_f = 100, while Figure (B) is for ρ_p/ρ_f = 1000.*

To better understand the effect of freely moving particles, specifically the inelasticity of particles on fluid-phase velocity fluctuations, it is useful to investigate the evolution equations of fluctuating energies in both fluid and solid phase. The evolution of k_f for a homogeneous suspension is

$$\underbrace{\rho_f (1-\phi)\frac{d}{dt}k_f}_{\text{unsteady term}} = \underbrace{\left\langle u_{f,i}{}'' \tau_{ji} n_j^{(f)} \delta\left(\mathbf{x}-\mathbf{x}^{(\mathbf{I})}\right)\right\rangle}_{\text{fluid interphase TKE transfer}} - \underbrace{2\mu_f \left\langle S_{ij} S_{ij} \right\rangle}_{\text{viscous dissipation}}. \tag{36}$$

The evolution equation of k_p for a homogeneous system, on the other hand, is

$$\underbrace{\rho_p \phi \frac{d}{dt}k_p}_{\text{unsteady term}} = \underbrace{\left\langle u_{p,i}{}'' \tau_{ji} n_j^{(p)} \delta\left(\mathbf{x}-\mathbf{x}^{(\mathbf{I})}\right)\right\rangle}_{\text{solid interphase TKE transfer}} - \underbrace{\Gamma_{coll}}_{\text{collisional dissipation}} \tag{37}$$

with ρ_p being the solid-phase density, and $\mathbf{n}^{(p)}$ being the normal vector to particle surface towards the fluid phase. The TKE of the two-phase mixture e_m is defined as $\rho_f (1-\phi) k_f + \rho_p \phi k_p$. The mixture TKE evolution equation is obtained by adding Eqs. (36) and (37), and using the principle of conservative interphase TKE transfer introduced by Xu and Subramaniam (2006), that is

$$\frac{d}{dt}e_m = \underbrace{\left\langle W_i \right\rangle \left\langle \tau_{ji} n_j^{(p)} \delta\left(\mathbf{x}-\mathbf{x}^{(\mathbf{I})}\right)\right\rangle}_{\Pi} - 2\mu_f \left\langle S_{ij} S_{ij} \right\rangle - \Gamma_{coll}.$$

At steady state, the terms on the right-hand-side of Eq. 36 should balance each other which are depicted in Figure 80 for simulated cases. Since the mean slip velocity is aligned with the mean interphase momentum transfer (Hill et al., 2001; Tenneti et al., 2011), the interphase TKE

transfer Π is positive and represents a source of energy, while the viscous dissipation ε_f and the collisional dissipation Γ_{coll} are sinks of energy. The viscous dissipation is computed directly from the DNS data. The collisional dissipation is however estimated from the expression given by Sangani et al. (1996) as

$$\Gamma_{coll} = \frac{24}{d_p \pi^{1/2}} (1-e) \rho_p \phi g(d_p) T^{3/2},$$

where e is the COR, $g(d_p)$ is the radial distribution function at contact, and T is the granular temperature. It is evident in figure 80 that the interphase TKE transfer and viscous dissipation balance each other with less than 5% error, and the collisional dissipation is negligible compared to aforementioned terms. Since the level of collisional dissipation in suspensions with moderate Reynolds number is not significant compared to the interphase TKE transfer and the viscous dissipation, the inelasticity of particles cannot influence the overall level of energy in the system and the level of k_f will be similar among flows with different values for COR.

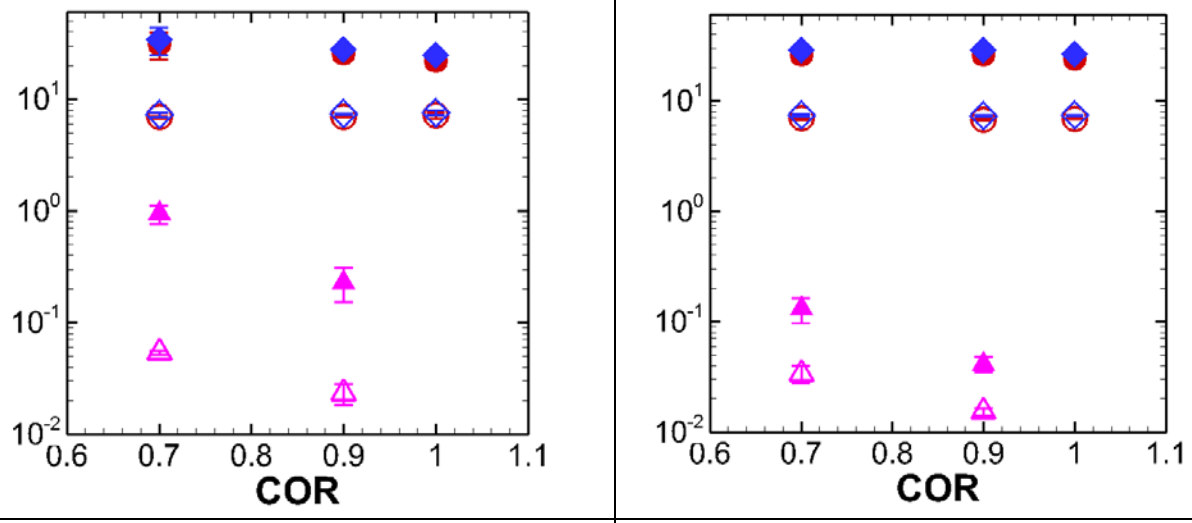

(a) **(b)**

Figure 80. *The balance of mixture energy equation terms normalized with* $\mu_f (|\langle \mathbf{W} \rangle| / d_p)^2$. *Hollow symbols correspond to* $\phi = 0.1$ *while filled symbols belong to* $\phi = 0.2$. *Interphase TKE transfer, viscous dissipation, and collisional dissipation are represented respectively by symbols (○), (◇), and (△). Figure (a) shows density ratio 100 and Figure (b) shows density ratio 1000.*

3.1.4: Fluid-phase velocity fluctuations in bidisprese freely evolving suspensions

Approach: To examine the influence of freely evolving bidisperse gas-solid suspensions, DNS PUReIBM for some selected cases are performed. These simulations are carried out over a range of particle size ratios and volume fractions. In this investigation, the particle to fluid density ratio is 1000 which represent particles with high Stokes numbers. The simulations are

performed for total solid volume fractions of 0.3 and 0.4 at a mean flow Reynolds number given as 50. The fluid phase is initialized with a uniform flow and the solid phase is initialized with zero granular temperature. Detailed information of particle size ratio d_2 / d_1 is given in Table 4.

Table 4. *Particle size ratio and volume fraction ratio of freely evolving suspensions.*

	Case I	Case II	Case III
d_2 / d_1	3	3.33	1.5

The level of k_f in these simulations, shown in figure 81, indicates that the level of fluid-phase velocity fluctuations depends strongly on total volume fraction. In addition the steady value of k_f is not significantly influenced by particle size ratios and they all represent the same level of k_f observed in fixed particle beds of the same volume fraction and Reynolds number with maximum error of 15% (except for the case $\phi = 0.4$ and $d_2 / d_1 = 1.5$ which is still converging to the fixed bed k_f value). It is worth mentioning that the simulations ran to different times and the data was extracted from the last time step. A similar analysis to monodisperse moving suspensions performed in previous section (not shown here in detail) indicates that the interphase TKE transfer and viscous dissipation balance each other and the collisional dissipation would be small due to the fact that the flow is not collision-dominated. On the hand, Figure 82 shows that interphase TKE transfer term does not change significantly with particle size ratio in comparison to fixed particle values, which justifies the similarity of k_f in these simulations.

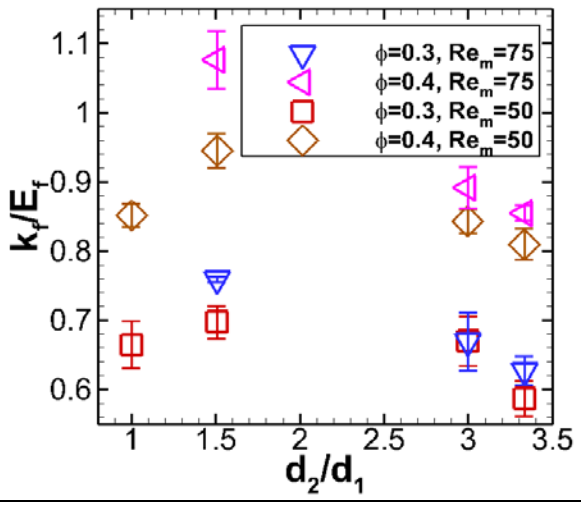

Figure 81. *The level of k_f for bidisperse gas-solid suspensions.*

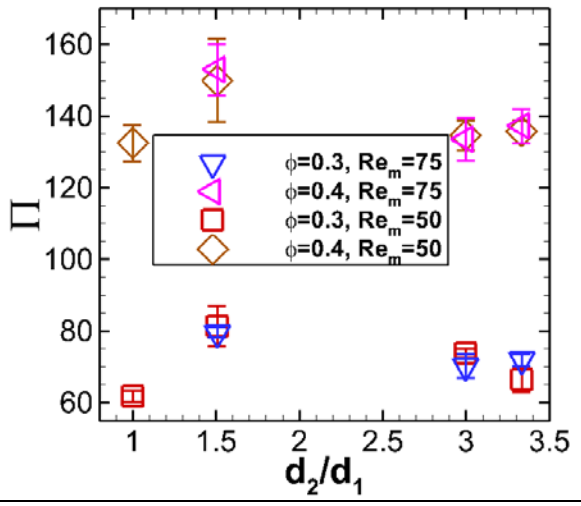

Figure 82. *Interphase TKE transfer of bidisperse gas-solid suspensions normalized with $\mu_f (|\langle \mathbf{W} \rangle| / d_S)^2$.*

Summary: In this section, level of fluid-phase velocity fluctuations in homogeneous gas-solid flows for fixed and freely evolving suspensions was reported by performing DNS using PUReIBM. It is observed that the velocity fluctuations are mainly due to the interaction of finite size particles with mean slip, and fluid-phase turbulent velocity fluctuations are not significant compared to pseudo-turbulent velocity fluctuations. The comparison between the fixed and freely evolving particles of monodisperse suspensions show that the movement of particles do not influence the level of k_f significantly for high Stokes number particles. In addition, since the flow is not collision-dominant, the energy loss through inelastic collisions is negligible and does not affect k_f. Bidisperse suspensions which are the simplest type of polydisperse flow show also similar level of k_f to monodisperse suspensions. The findings in this section reveal that the level of fluid-phase velocity fluctuations is strongly a function of total volume fraction and also a weak function of Reynolds number, and thus a single model can be used for to represent the level of k_f in gas-solid suspensions with high particle Stokes number.

Task 3.2: Multiphase turbulence model for polydisperse particles in gas-phase turbulence (Fox & Subramaniam)

The existing MFIX multiphase turbulence models (Ahmadi & Ma, 1990, Simonin, 1996) and the recently proposed EEM model (Xu & Subramaniam, 2006) will be tested in these canonical polydisperse flows. Comparison of model predictions with DNS will give insight into the accuracy of existing closures, and will lead to the development of more accurate closures, if needed.

(Subramaniam reporting.) Task 3.2.1: Eddy viscosity model for gas-solid flow

***Approach*:** In modeling the Reynolds stress tensor, the first step is to evaluate the isotropic part of the tensor, which is twice the energy of velocity fluctuations. PUReIBM DNS results reveal that the value of TKE is primarily a function of total volume fraction and Reynolds number.

The presence of finite sized particles generates high level of gas-phase velocity fluctuations even in a laminar flow regime. We performed DNS of flow past fixed assemblies of monodisperse spheres over a wide range of solid volume fractions ($0.1 \le \phi \le 0.5$) and mean flow Reynolds numbers ($0.01 \le \mathrm{Re}_m \le 300$). Based on our DNS data, we developed a correlation for k_f in terms of the solid volume fraction and mean flow Reynolds number. Figure 83 shows the data for k_f obtained from PUReIBM simulations together with the following correlation

$$\frac{k_f}{E_f} = 2\phi + 2.5\phi(1-\phi)^3 \exp\left(-\phi \,\mathrm{Re}_m^{1/2}\right),$$

which fits the data well with an average deviation of 5%. The importance of this expression is that in the limiting case of single phase flow($\phi \to 0$), the level of k_f becomes zero denoting that the origin of the stress is pseudo-turbulent and due to the presence of particles.

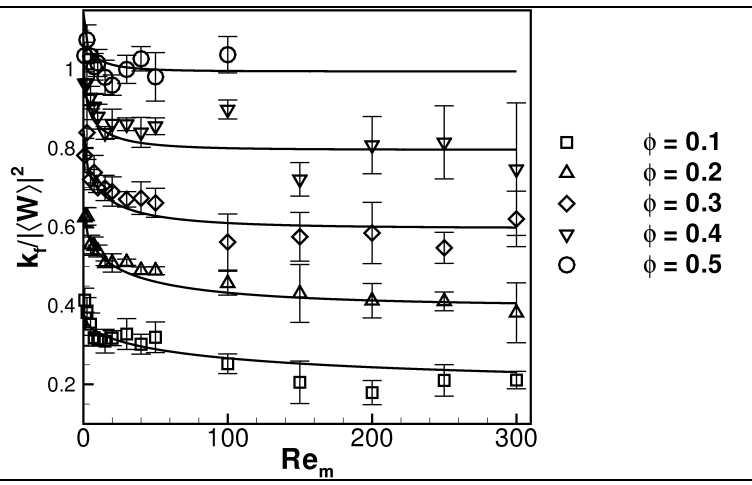

Figure 83. *Plot showing the variation of the pseudo-turbulent kinetic energy with solid volume fraction and mean flow Reynolds number. Symbols denote the data obtained from PUReIBM simulations of flow past fixed assemblies of monodisperse spheres while the lines denote the fit given by equation (1).*

In homogeneous gas-sold flows, k_f results from a balance of interphase transfer of kinetic energy and dissipation of kinetic energy. If we are able to obtain the correct scaling of dissipation with ϕ and Re_m then we can explain the dependence of k_f on ϕ and Re_m.

The evolution equation of k_f for a homogeneous suspension given in Section (3.1.3) shows that the interphase TKE transfer π_f represents a source of gas-phase velocity fluctuations. An expression for the interphase transfer of kinetic energy can be derived by

$$\pi_f = \frac{18\phi\left(1-\phi^2\right)\mu_f}{d_p^2}\ \left|\langle \mathbf{W}\rangle\right|^2 F\left(\phi,\mathrm{Re}_m\right),$$

where $F\left(\phi,\mathrm{Re}_m\right)$ is the average drag force per particle normalized by Stokes drag force $3\pi d_p\mu_f\left(1-\phi\right)\left|\langle \mathbf{W}\rangle\right|$. At steady state the source and sink of kinetic energy must balance each other, that is

$$\pi_f = \rho_f\left(1-\phi\right)\varepsilon_f.$$

All the turbulence models for multiphase flows use a Kolmogorov scaling for the dissipation term in a manner similar to single-phase turbulence models i.e., $\varepsilon_f \sim k_f^{3/2}/l_K$. While in single-phase turbulence the length scale l_K in this expression corresponds to eddies in the inertial subrange, the corresponding interpretation in gas-solids flow is not clear. Note that the validity of the Kolmogorov scaling rests on the energy cascade hypothesis with a constant dissipation rate in the inertial subrange. These assumptions may not hold in gas-solids flow. An alternative expression for the dissipation rate in single-phase turbulence is $\varepsilon_f \sim 2\nu_f k_f/l_T^2$, where l_T is the

Taylor microscale and ν_T is the kinematic viscosity of the fluid phase. This expression can be generalized to any random velocity field with a finite spatial autocorrelation length.
Using the Kolmogorov scaling for the dissipation term the following expression for l_K / d_p is obtained:

$$\frac{l_K}{d_p} = \left(\frac{k_f}{E_f}\right)^{3/2} \left(36\sqrt{2}\phi(1-\phi)^2 \frac{F(\phi, \mathrm{Re}_m)}{\mathrm{Re}_m}\right)^{-1}.$$

Similarly, using the Taylor microscale scaling for the dissipation term the expression for l_T / d_p is

$$\frac{l_T}{d_p} = \left(\frac{k_f}{E_f}\right)^{1/2} \left(18\phi(1-\phi) F(\phi, \mathrm{Re}_m)\right)^{-1/2}.$$

The variation of l_K and l_T with solid volume fraction and Reynolds number are compared in figure 84. The behavior of length scale l_K obtained by modeling the dissipation term by Kolmogorov scaling shows that this length scale increases with mean flow Reynolds number and decreases with volume fraction. The behavior of the length scale l_T obtained using a Taylor microscale scaling shows that this length scale decreases with both mean flow Reynolds number and solids volume fraction.

For laminar flow past a single sphere, the length scale on which the velocity gradients vary is of the order of the boundary layer thickness δ / d_p which varies inversely with $\sqrt{\mathrm{Re}_m}$. Thus, we expect this length scale to decrease with increasing solids volume fraction. Since the hypothesis of energy cascade probably does not hold in homogeneous gas-solid flow with finite-sized particles, the applicability of the Kolmogorov scaling is questionable, as also evidenced by the behavior of l_K with Re_m. On the other hand, the scaling of l_T indicates that the Taylor microscale is a better choice to model the dissipation term in gas-solid flows with finite sized particles. However, it must be noted that neither l_K nor l_K may correspond to the exact length scales of dissipative motions in gas-solids flow.

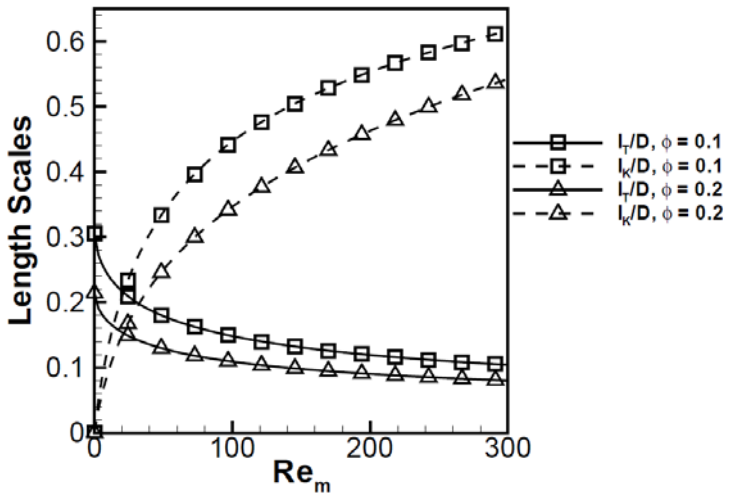

Figure 84. *Variation of dissipation length scales with Reynolds number for solid volume fractions 0.1 and 0.2. Dashed lines are obtained by modeling the dissipation term as* $k_f^{3/2}/l_K$ *while the solid lines are obtained by modeling the dissipation as* $2\nu_f k_f / l_T^2$.

In several studies the gas-phase Reynolds stress term is modeled in a fashion similar to single–phase eddy viscosity turbulence model as

$$\left\langle u_{f,i}"u_{f,j}"\right\rangle = -\nu_T\left(\frac{\partial\left\langle u_{f,i}\right\rangle}{\partial x_j}+\frac{\partial\left\langle u_{f,j}\right\rangle}{\partial x_i}\right)+\frac{2}{3}k_f\delta_{ij}.$$

In this model ν_T is the eddy viscosity for gas-solid flow that is defined as $\nu_T = C_\mu k_f^2/\varepsilon_f$ with C_μ being a model constant. Since we have quantified both k_f and ε_f using particle-resolved DNS, we can infer an eddy viscosity for gas-solid flow as a function of solid volume fraction and mean flow Reynolds number. The ratio $k_f^2/(\nu_f\varepsilon_f)$ is shown as a function of Re_m for different ϕ in figure 85. We see that the ratio $k_f^2/(\nu_f\varepsilon_f)$ increases with both solid volume fraction and mean flow Reynolds number. This dependence on the mean flow Reynolds number indicates that the transport of gas-phase Reynolds stress can become important if there are large gradients in the mean flow and solid volume fraction, as found in many multiphase flow applications.

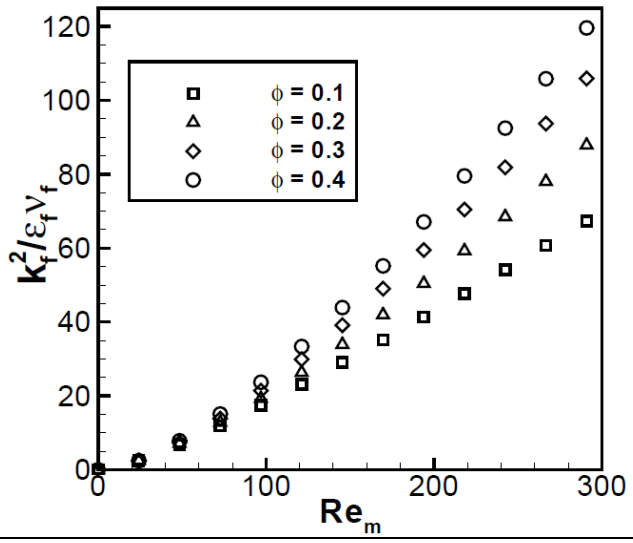

Figure 85. *Behavior of the ratio* $k_f^2/(\nu_f\varepsilon_f)$ *with mean flow Reynolds number for different solid volume fractions.*

Task 3.2.2: Reynolds stress of pseudo-turbulent fluid velocity fluctuations

***Approach*:** The eddy viscosity model can be used to model Reynolds stress and the components of the stress tensor depend on gradients of mean velocity field. However, in a homogeneous system in the absence of mean velocity gradients, eddy viscosity model predicts an isotropic Reynolds stress which is in contradiction with recent findings (Uhlmann, 2008; Xu and Subramaniam, 2010; Tenneti et al) that show the Reynolds stress is highly anisotropic. Therefore, we quantify Reynolds stress from our results and propose an algebraic model for fluid Reynolds stress in homogeneous gas-solid flows.

Any second order tensor such as fluid Reynolds stress can be characterized by isotropic and deviatoric parts. The fluid Reynolds stress is defined as

$$R_{f,ij} = \left\langle u_{f,i}"u_{f,j}" \right\rangle.$$

The trace of the tensor (a scalar quantity) is the isotropic part, and is twice the level of k_f. The deviatoric part on the other hand is a second order tensor given as

$$b_{ij} = \frac{R_{f,ij}}{2k_f} - \frac{1}{3}\delta_{ij},$$

with δ_{ij} being the Kronecker delta. A model was proposed for the isotropic part, k_f, as a function of volume fraction and Reynolds number. Now we quantify the state of anisotropy of the fluid Reynolds stress by decomposing velocity fluctuations along the streamwise (parallel to mean slip) and spanwise (perpendicular to mean slip) directions since the Reynolds stress is observed to be axisymmetric along the mean slip. The results indicate that the cross-correlation of velocity fluctuations are negligible (not shown here) and the normal component in the parallel direction is dominant compared to normal components in perpendicular direction as illustrated in figure 86.

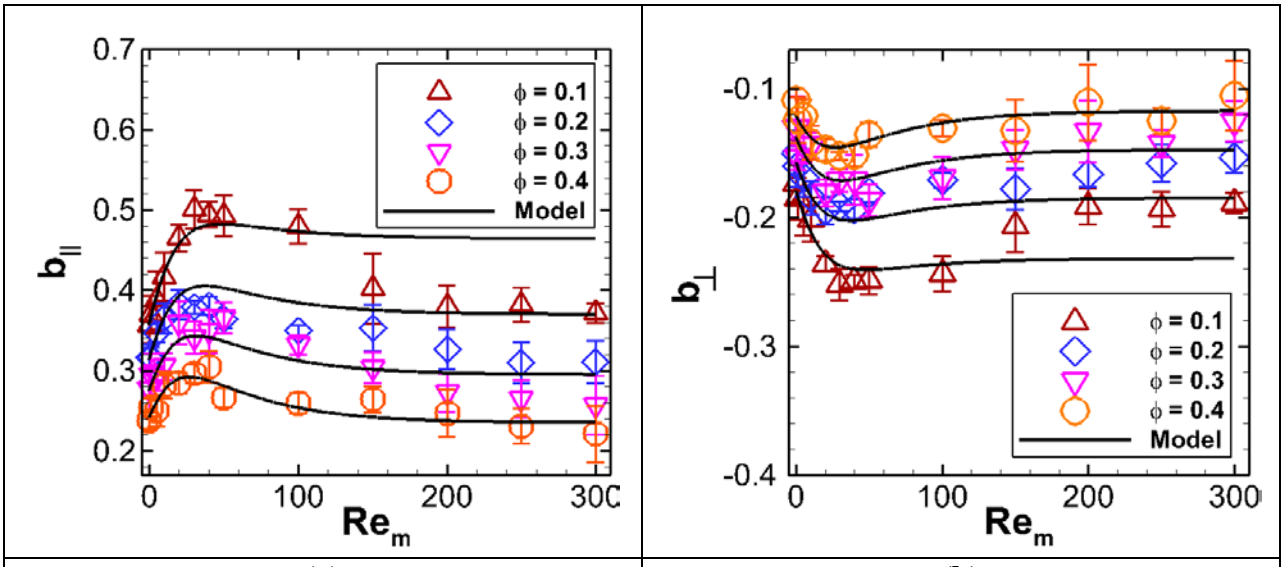

(a) **(b)**

Figure 86. *Deviatoric tensor is shown for different volume fractions and Reynolds numbers obtained from fixed bed simulations. The symbols show DNS results and the solid lines represent the suggested model. Figures (a) and (b) correspond to* $b_{||}$ *and* $b_\perp$ *, respectively.*

Figure 86 indicates that the level of anisotropy increases with Re_m from Stokes flow to moderate Reynolds numbers (ranging from 20 to 40) and then smoothly decreases. This behavior is characterized by length scales of the system, namely the eddy length scale and interparticle spacing. The eddy length scale is characterized by

$$L_{||} = \frac{1}{R_{||}(0)} \int_0^\infty R_{||}(r) dr,$$

where $R_{||}(r)$ given as

$$R_{||}(r) = \int_{V_f} \mathbf{u}_{||,f}\,''(\mathbf{x}) \cdot \mathbf{u}_{||,f}\,''(\mathbf{x}-\mathbf{r}) d\mathbf{x},$$

is the two-point velocity correlation in the parallel direction. The eddy length scale shown in Figure 87 decreases with both Re_m and ϕ due to the fact that the flow structures become finer and less spatially correlated.

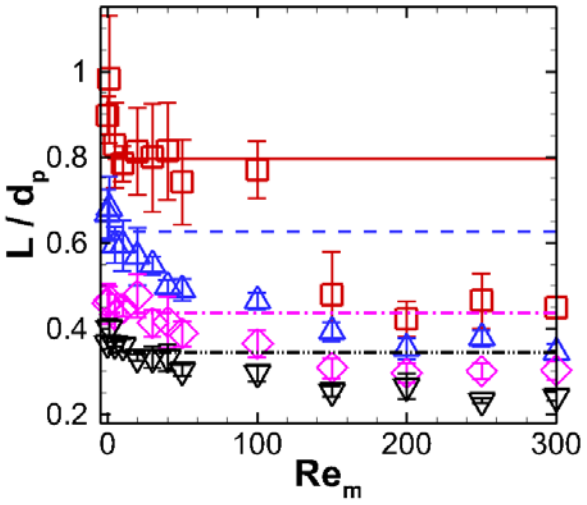

Figure 87. *Symbols show the eddy length scale. The symbols (□), (Δ), (◇), (▽) correspond to volume fractions 0.1, 02, 0.3, and 0.4, respectively. The straight lines show the interparticle spacing.*

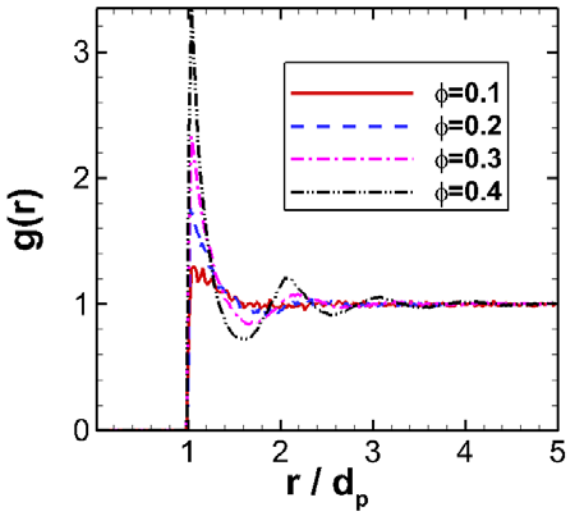

Figure 88. *Radial distribution function estimated from 100 realizations for each volume fraction.*

To compute the interparticle spacing, on the other hand, radial distribution function is used which contains all information about the particle configuration, and is given in figure 88 for different volume fractions. Since the number of particles in a spherical shell of thickness δr at separation r is $2\pi N_p n g(r) r^2 \delta r$, the interparticle spacing is estimated as

$$\frac{L_{\text{int}}}{d_p} = \frac{\int_{R_{\min}}^{R_{\max}} g(r)\, r^2 l\, f(l)\, dr}{\int_{R_{\min}}^{R_{\max}} g(r)\, r^2\, f(l)\, dr},$$

which is interpreted as a weighted average of surface to surface distance l (defined as $r - d_p$) among particles. The weight function has the form $1/l^p$ where p is selected to be 1. In addition, $R_{\min}$ is d_p where hard-core spheres come to contact, and $R_{\max}$ is where the second peak of $g(r)$ is located. The results indicate that the interparticle spacing shown as straight lines in figure 87 intersect the corresponding eddy length scales at the Reynolds number range ($20 \le \text{Re}_m \le 40$) where the anisotropy starts to decrease. The characteristics of length scales indicate that at low Reynolds numbers, flow structures formed behind particles elongate with Re_m that give rise to the increase of anisotropy. After moderate Reynolds numbers the wakes become as large as the gaps among particles and are broken up due to interaction with neighbor spheres. Thus, the anisotropy is now characterized by the interparticle spacing. The modulation of elongated structures redistributes the fluctuating velocity energy among Reynolds stress components and decreases the anisotropy.

To propose a model for the deviatoric tensor, it is only required to model the parallel component $b_{\parallel}$ due to the fact that since $b_{\perp} = -b_{\parallel}/2$ and other components are all zero (the Reynolds stress is axisymmetric). The model that best fits the data for $b_{\parallel}$ is

$$b_{\parallel} = \frac{a}{1+b\exp\left(-c\,\mathrm{Re}_m\right)}\mathrm{e}^{-d\phi/\left(1+e\exp\left(-f\,\mathrm{Re}_m\right)\right)}, \qquad \begin{cases} a = 0.523 \\ b = 0.303 \\ c = 0.114 \\ d = 3.526 \\ e = 1.809 \\ f = 0.005 \end{cases}$$

which is shown in figure 87 with solid lines. Since we have two models for both isotropic and deviatoric parts of the Reynolds stress, these models can be used as an algebraic stress model to determine the fluid Reynolds stress in homogeneous gas-solid flows in the form given as

$$\frac{R_{f,ij}}{E_f} = \left(4\phi + 5\phi\left(1-\phi\right)^3\exp\left(-\phi\,\mathrm{Re}_m^{\,1/2}\right)\right)\left(b_{ij} + \frac{1}{3}\delta_{ij}\right).$$

Summary: The level of fluid-phase velocity fluctuations is quantified over a wide range of volume fraction ($0.1 \le \phi \le 0.5$) and Reynolds number ($0.01 \le \mathrm{Re}_m \le 300$). Based on DNS data a new correlation is proposed for the level of pseudo-turbulent k_f in homogeneous gas-solid flows as a function of ϕ and Re_m. It is also observed that the dissipative length scale in these flows cannot be represented by Kolmogorov length scale since the cascade of energy hypothesis may not hold. Instead, a Taylor microscale dissipative length scale shows a better behavior since it reduces with both ϕ and Re_m and is intuitively correct. In addition, similar to single-phase eddy viscosity model, a model is proposed for turbulent eddy viscosity of gas-solid systems that can be used to model fluid Reynolds stress. However, in the absence of mean velocity gradients the eddy viscosity model predicts an isotropic Reynolds stress which in not consistent with numerical observations. Therefore, the anisotropy of Reynolds stress is quantified for DNS data that is axisymmetric along the mean slip for all cases. A model is proposed for the anisotropy of the Reynolds stress that along with the model for the level of k_f can be used to represent an algebraic stress model for the fluid Reynolds stress at steady state. The Reynolds stress representation in gas-solid flows can be further extended to dynamic models such as equilibration of energy (EoE) model where the evolution of Reynolds stress is also included.

Goal IV: Data Collection and Model Validation

Task 4.1: DEM Simluations of Granular Systems (Hrenya)

As a first step toward model validation, data from a granular system (no fluid phase) will be obtained by using discrete-element method (DEM) simulations. By initially focusing on a system in which the fluid phase plays no role, a validation of the solid-phase-only treatments (Goal I) is possible. Furthermore, by considering systems with a continuous size of distributions, the DEM data will provide a much-needed gauge as to the number of discrete sizes needed to accurately model a continuous distribution. A series of systems, characterized by an increasing level of complexity, will be simulated. Particles will be modeled as frictionless, inelastic hard spheres, which is consistent with the assumptions used in the continuum model development. The base case will be a one-dimensional, force-free system in which the two boundaries are characterized by different, but constant granular temperatures. The imposed temperature gradient will result in species segregation; concentration profiles for this system are already available for binary mixtures and continuous size distributions (Dahl & Hrenya, 2004, Galvin, et al., 2005) from an in-house DEM code. An external force (e.g., gravity) will then be added to the existing code in a direction perpendicular to the constant-temperature boundaries, which will modify the segregation profiles. Finally, simple rules will be incorporated in both the force-free and constant-force case to mimic the evolution of particle size due to reaction (e.g., shrinkage with time). A range of conditions will be examined to ensure robust data.

(Hrenya reporting.) *Overview.* As described in Task 1.1, a kinetic theory for a mixture of *s* particle components which differ in size and/or material density has been derived (Garzó, et al., 2007a, Garzó, et al., 2007b) for inelastic, smooth hard disks (two dimensions) or spheres (three dimensions). The governing equations are contained in Appendix A, so for the sake of brevity we start here by introducing the constitutive relations for mass flux ($\mathbf{j}_{0i}$), stress ($\sigma_{\alpha\beta}$), heat flux ($\mathbf{q}$), and cooling rate (ξ):

$$\mathbf{j}_{0i} = -\sum_{j=1}^{s} \frac{m_i m_j n_j}{\rho} D_{ij} \nabla \ln n_j - \rho D_i^{\,T} \nabla \ln T - \sum_{i=1}^{s} D_{ij}^{\,\mathbf{F}} \mathbf{F}_j \,, \tag{38}$$

$$\sigma_{\alpha\beta} = p\delta_{\alpha\beta} - \eta\left(\frac{\partial U_\beta}{\partial r_\alpha} + \frac{\partial U_\alpha}{\partial r_\beta} - \frac{2}{3}\delta_{\alpha\beta} \nabla \cdot \mathrm{U} \right) - \kappa \delta_{\alpha\beta} \nabla \cdot \mathrm{U} \,, \tag{39}$$

$$\mathbf{q} = -\sum_{i=1}^{s}\sum_{j=1}^{s} T^2 D_{q,ij} \nabla \ln n_j + L_{ij} \mathbf{F}_j - T \nabla \ln T \,, \tag{40}$$

$$\xi = \xi^0 + \xi_U \nabla \cdot \mathrm{U} \,. \tag{41}$$

where p is the pressure, κ is the bulk viscosity, η is the shear viscosity, λ is the thermal conductivity, $D_{q,ij}$is the Dufour coefficient, L_{ij} is a mobility coefficient, $D_{ij}$is the mutual diffusion coefficient, $D_i^{\,T}$ is the thermal diffusion coefficient, and $D_{ij}^{\,F}$ is the mobility coefficient, ξ^0 is the zeroth-order cooling rate, and ξ_U is the first-order transport coefficient for the cooling rate.

Since the newly-developed polydisperse kinetic theory is developed for *s discrete* species, the focus of this task is to determine how to best represent a *continuous* particle size distribution (PSD) using a discrete number of species. Figure 89 shows a schematic representation of a continuous PSD in which the frequency of particle size is plotted against the particle diameter. The subplots of the figure (89a, 89b, and 892c) illustrate how an increasing number of discrete species (2, 3, and 7, respectively) can be used to represent the continuous PSD. In choosing such a discrete representation, two questions are relevant: (i) What *technique* should be used to choose discrete particle sizes to represent the continuous PSD, and (ii) What *number of discrete sizes* is appropriate for an accurate representation? Regarding the first question, a representation of a continuous PSD using discrete species is pursued via the method of moments (MOM). Regarding the second question, the number of discrete species is determined by comparing the predictions obtained from all transport coefficients, over a range of parameters, using an increasing number of discrete species. The appropriate value of *s* corresponds to the point where the predictions are essentially equal upon further increase of *s*.

Discrete Representation of Continuous Size Distribution. A few common approaches to representing a continuous PSD with a discrete number of sizes are 'modal', 'sectional' and 'moment' based methods. The method of moments offers a statistically based alternative that is more efficient than compared to sectional methods in terms of computational cost and modal-based methods in terms of accuracy. Hence, the MOM approach is chosen in the current study for representing a continuous PSD.

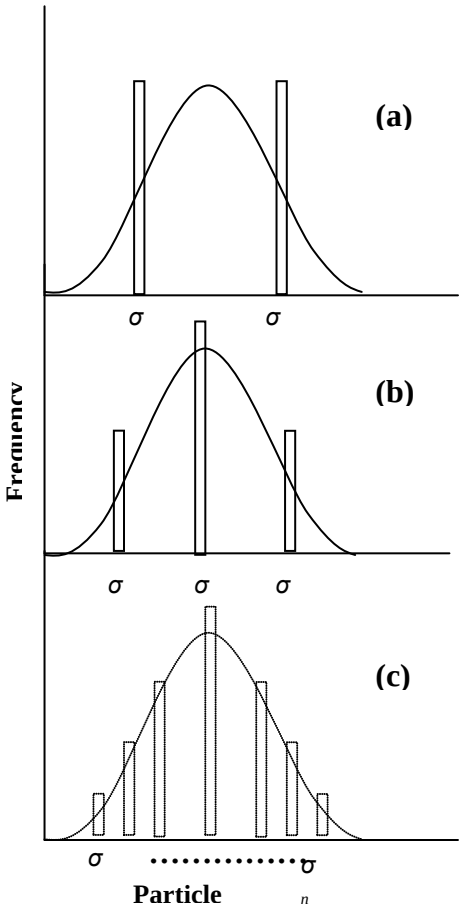

Figure 89. *Schematic representation of a continuous particle size distribution*

In the recent work by Fan and Fox (Fan & Fox, 2008), a multi-fluid model based on and Eulerian-Eulerian approach and the direct quadrature method of moments (DQMOM) were used to predict particle segregation in a gas-fluidized bed. The model predictions were compared to the segregation profiles obtained from the discrete-particle simulations of Dahl and Hrenya (Dahl & Hrenya, 2005). Their investigation shows that the predictions obtained with two discrete species (s = 2) are different than when using three discrete species (s = 3). However, their predictions for s = 3 match well with s = 4, suggesting that for a wide PSD with significant segregation, three discrete species appear sufficient to represent the system.

In the present study, the approach used to determine the value of s needed for an accurate representation of a continuous PSD differs from that of Fan and Fox (2008). In particular, the transport coefficients developed from the new polydisperse kinetic theory are evaluated, over a wide range of parametersfan (e.g., restitution coefficient, solids volume fraction), for various values of s. The resulting values are expected to differ from one another for small values of s since using a small number of discrete species provides only a "rough" approximation of the continuous PSD (Figure 89a). On the other hand, for larger values of s, the transport coefficients are expected to collapse onto the same line since they better capture the continuous nature of the distribution under consideration (Figure 89c). Accordingly, the transition between the two aforementioned behaviors provides an estimate of the value of s needed to accurately represent a continuous PSD.

Step 1. The first 2s moments of the continuous PSD of interest are calculated. The equations for calculating the moments of a Gaussian and lognormal distributions for corresponding σ_{sd} and d_{ave} are obtained from Randolph & Larsen (Randolph & Larson, 1971), where the quantities σ_{sd} and d_{ave} represent the standard deviation and mean particle diameter of the continuous PSD, respectively. For a Gaussian distribution, the moments are found by

$$\mu_j = \sum_{r=1}^{2s}\left(\sigma_{sd}{}^{j-r} d_{ave}{}^{r} \frac{j!.1.3...(j-r-1)}{(j-r)!r!}\right) \tag{42}$$

where μ_j refers to the j^{th} moment. Similarly, for a lognormal distribution, the moments are given by

$$\mu_j = d_{ave}{}^{j} \exp\left(\frac{j^2 \sigma_{sd}{}^{2}}{2}\right). \tag{43}$$

Step 2. Using the values of μ_j obtained from the first step, a product difference (PD) table is constructed. The PD table is created in a sequence of steps by setting up an upper-left triangular array of elements $P(i, j)$. The elements of first column are

$$P(i,1) = \delta_{i,1}, \tag{44}$$

where $\delta_{i,1} = 0$ for $i \neq 1$ and $\delta_{i,1} = 1$ for $i = 1$. The second column contains the moments with alternating sign:

$$P(i,2) = (-1)^{i-1} \mu_{i-1}. \tag{45}$$

The remaining elements of the array are obtained via the recursion formula

$$P(i, j) = P(1, j-1)P(i+1, j-2) - P(1, j-2)P(i+1, j-1)\,. \tag{46}$$

Only the table elements along the first row are required for the proceeding steps (McGraw, 1997). This recursion is carried out until a table of the size P (1, s +1) is achieved.

Step 3. A new vector $\alpha(s)$ is generated using the table elements beginning with $\alpha(1) = 0$ and continuing with the following equation

$$\alpha(s) = \frac{P(1, s+1)}{P(1, s)P(1, s-2)}\,. \tag{47}$$

In this portion, the algebra associated with equations (10) and (11) is handled symbolically using Maple software.

Step 4. A symmetric (upper-left) tridiagonal matrix **J** is constructed with diagonal elements a_s and off-diagonal elements b_s obtained from the α's determined in the previous step.

$$a_s = \alpha(2s) + \alpha(2s-1)\,, \text{ and}$$

$$b_s^{\,2} = \alpha(2s+1)\alpha(2s)\,. \tag{48}$$

The values of b_s are obtained as positive square root of $b_s^{\,2}$. Note that 2s elements of type a and 2(s-1) of type b are required to generate the matrix **J**.

Step 5. Once the matrix **J** is generated, the diameters (σ_s) of the discrete representation correspond to the eigenvalues and the weights (w_j) are obtained from the corresponding eigenvectors using the Christoffel and Darboux identity:

$$w_j = \mu_0 v_{j1}^{\,2}\,, \tag{49}$$

where v_{j1} is first component of the eigenvector $\mathbf{v_j}$.

Step 6. The volume fractions (ϕ_s) associated with the discrete representation are related to diameters σ_s and weights ω_s by the relation

$$\phi_s = k_v \sigma_s \omega_s\,, \tag{50}$$

where k_v is the volumetric shape factor ($k_v = \pi/6$ for spherical particles, Fan & Fox, 2007).

According to the MOM, the individual moments can be approximated by

$$\mu_j = \sum_{j=1}^{s} \omega_j \sigma_j^{\,j}\,. \tag{51}$$

As a check to the calculations above (equations 44-50), the moments obtained for Gaussian (equation 42) and lognormal (equation 43) distributions are recovered upon substitution of the diameters and weights into equation (51). The steps (1) to (6) have been carried out for s = 2-5 and the values of the corresponding weights and diameters for s = 2-4 identically match with that presented by Fan & Fox (2008) for both Gaussian and lognormal distributions.

Size Distributions Examined. In this work, four types of continuous size distributions are investigated: (i) Gaussian distributions, (ii) lognormal distributions, (iii) a bidisperse PSD of coal particles used for gasification provided by the Department of Energy National Energy Technology Laboratory (DOE NETL), and (iv) a simulant of lunar soil provided by National

Aeronautics and Space Administration Kennedy Space Center (NASA KSC). Figure 90 shows the number-based frequency distribution, f_n, for each of these size distributions. For the Gaussian and lognormal distributions, a range of distribution widths, σ/d_{ave}, where σ denotes the standard deviation of the PSD and d_{ave} denotes its arithmetic mean, are examined. Accordingly, $\sigma/d_{ave} = 0$ corresponds to the monodisperse limit. For Gaussian distributions, the maximum distribution width is σ/d_{ave} = 30% since a further increase would result in negative (unphysical) particle diameters (Dahl, et al., 2002). Due to the extended right tail of lognormal distributions, a similar limit does not exist, and here lognormal distributions with σ/d_{ave} = 0-90% are considered. Figures 90a and 90b show lognormal and Gaussian distributions, respectively, in which the average diameter (d_{ave} = 72.6 microns) is held constant, whereas Figures 90c and 90d show distributions with a constant root-mean-cube diameter (d_{rmc} = 72.6 microns). The former distributions were used in analyzing the discrete approximation of continuous PSDs, and the latter were used for direct comparison with the MD simulations of Dahl *et al*. (Dahl, et al., 2003). The PSD of coal particles provided by DOE NETL was obtained via sieving and thus was provided in a mass-based form in Figure 90e. Note that the bidisperse nature of this distribution is no longer apparent when it is converted to a number-based distribution (Figure 90f), which is used to obtain a discrete approximation. Lastly, the PSD of a simulant of lunar soil known as OB-1 and measured by NASA is shown, with the measured mass-based distribution in Figure 90g, and the associated number-based distribution in Figure 90h. For purposes of direct comparison, the bidisperse coal PSD (DOE NETL) and a lognormal distribution with the same average diameter as the OB-1 and a distribution width of σ/d_{ave} = 90% are also shown on these log-log plots. Relative distribution widths are revealed in Figures 90g and 90h. The lognormal distribution exhibits a high frequency of particles with diameters near the average diameter (d_{ave} = 0.57); however, the frequency quickly approaches zero as the particle diameter is increased. On the other hand, the lunar soil simulant distribution (OB-1) and coal PSD exhibit moderate frequencies for a larger range of particle diameters. Thus, the experimental distributions contain a larger "width" of particle diameters. Because the OB-1 distribution and the coal PSD have different average diameters, the relative width of these distributions is not so obvious. However, by approximating each experimental PSD with a lognormal distribution of appropriate width, it was determined that the lunar soil simulant distributions are much wider than the coal PSD. For the sake of brevity, the OB-1 lunar soil simulant is the only shown lunar PSD. It is worth noting that distributions of several other lunar soil simulants (OB-1, JSC-1a, LHT-2M, BP-1) and a sample of lunar soil were investigated; the resulting trends are similar to those of OB-1 and thus only the representative results of OB-1 are included below for the sake of brevity.

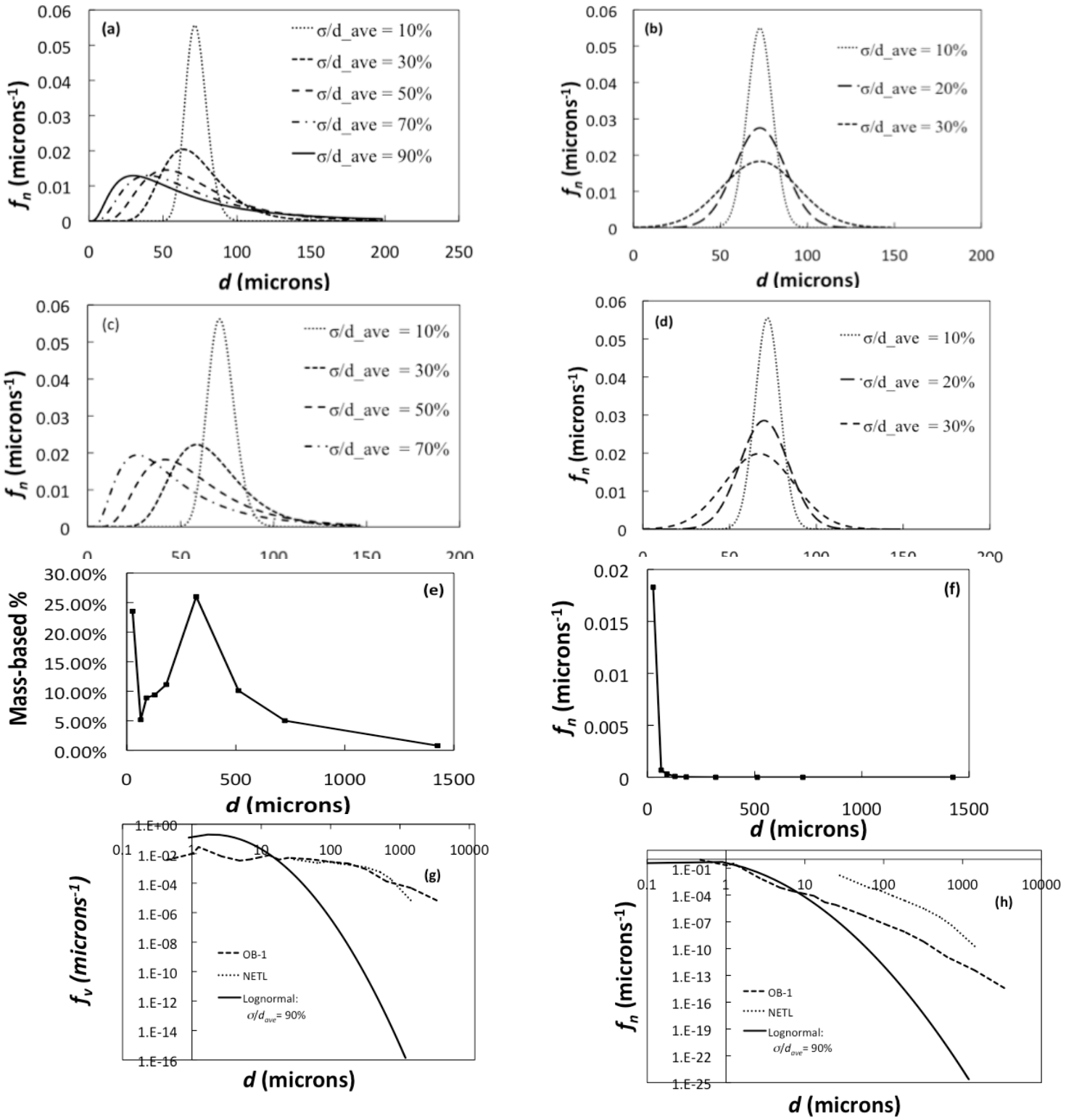

Figure 90. *Number-based frequency (f_n) for* ***(a)*** *lognormal PSD with constant d_{ave},* ***(b)*** *Gaussian PSD with constant d_{ave},* ***(c)*** *lognormal PSD with constant d_{rmc}, and* ***(d)*** *Gaussian PSD with constant d_{rmc}. Frequency distributions of coal particles in terms of a* ***(e)*** *mass and* ***(f)*** *number basis. Frequency distributions of lunar soil simulant (OB-1) in terms of a* ***(g)*** *mass and* ***(h)*** *number basis.*

Results. To determine the impact of the choice of s on the accuracy of the discrete approximations to continuous PSDs, such approximations are obtained for various values of s for each of the PSDs considered here. Then, kinetic-theory predictions of transport coefficients are evaluated using GHD theory for each of the discrete approximations. By comparing predictions for discrete distributions at various values of s, the minimum number of species (s_{min}) needed to achieve the desired accuracy can be determined. Using these values, kinetic-theory predictions of discrete distributions are then compared to MD simulations of simple shear flows with continuous size distributions. Representative results are presented below. A more comprehensive review of this task, including additional results, are given in the preprint attached in Appendix H.

Figures 91 and 92 show how the pressure and shear viscosity vs. restitution coefficient, respectively, change with the number of species for *lognormal distributions* with $\phi = 0.3$ and distribution widths of $\sigma/d_{ave} = 10\%$ (Figures 91a and 92a) and $\sigma/d_{ave} = 70\%$ (Figures 91b and 92b). Expectedly, as the number of discrete species s used to approximate the continuous distribution increases, the curves begin to collapse on one another. As described in Section II.C, once a 2% or less error is established among three consecutive approximations (e.g., s = 2, 3, 4) of a transport coefficient over the entire range of restitution coefficients shown, the minimum number of species for desired accuracy ($s_{\min}$) has been determined. For instance, Figure 91a indicates that predictions of pressure using s = 2, 3, or 4 are extremely close to one another (< 2% change). Therefore, only 2 species are deemed necessary to approximate the pressure of a lognormal PSD with $\sigma/d_{ave} = 10\%$ and $\phi = 0.3$. Comparing Figure 91a to Figure 92b, it is evident that the number of species used in the discrete approximation of a lognormal PSD has a larger effect for wider distributions. Specifically, Figure 91a shows that the monodisperse prediction of pressure agrees qualitatively and quantitatively well with the polydisperse predictions (s = 1-10) for a narrow lognormal distribution ($\sigma/d_{ave} = 10\%$). However, for the wider continuous lognormal PSD ($\sigma/d_{ave} = 70\%$) of Figure 91b, the pressure predictions for $s > 1$ are quite different quantitatively than the monodisperse counterpart (s = 1). Moreover, Figure 91b shows that pressure predicted using s = 2-10 is slightly non-monotonic, whereas the monodisperse prediction increases monotonically with restitution coefficient. Nevertheless, both discretizations require 2 particles species for the established criterion to be met for granular pressure (i.e., $s_{\min} = 2$), regardless of vast differences in distribution width. Finally, as seen when comparing the shear viscosity of different distribution widths in Figures 92a and 92b, the trends are similar to those of pressure (Figures 91a and 91b), though $s_{\min} = 3$ for $\sigma/d_{ave} = 70\%$.

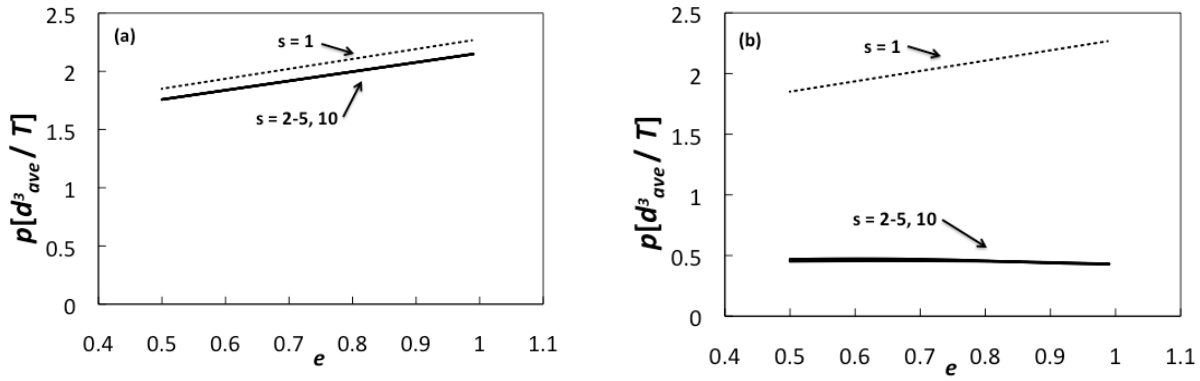

Figure 91. *Predictions of granular pressure as a function of coefficient of restitution for lognormal distributions with σ/d_{ave} of (a) 10% and (b) 70% using GHD theory. The overall volume fraction of the system is $\phi = 0.3$.*

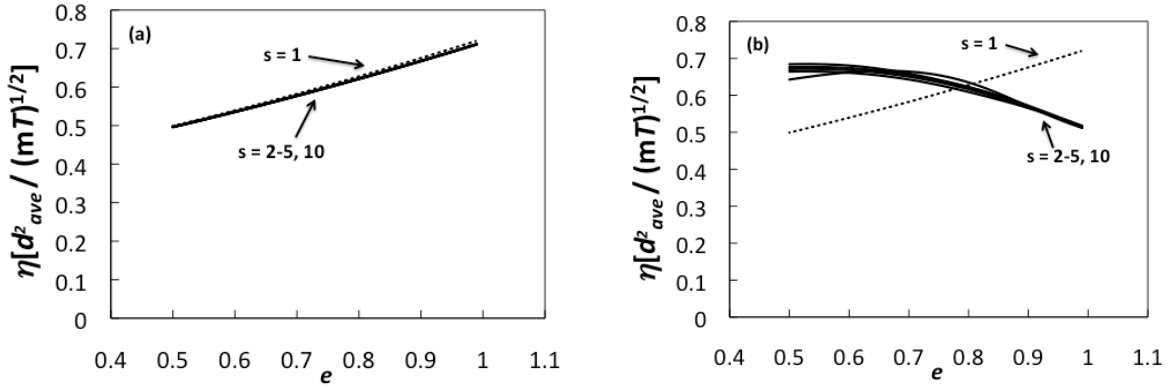

Figure 92. *Predictions of shear stress as a function of coefficient of restitution for lognormal distributions with σ/d_{ave} of (a) 10% and (b) 70% using GHD theory. The overall volume fraction of the system is $\phi = 0.3$.*

Results of dimensionless pressure and shear viscosity are also given for the *bidisperse NETL distribution of coal particles* (figure 93). When the bidisperse mass-based distribution is converted to a number-based PSD, the resulting distribution is extremely right-skewed (figure 90f), similar to a very wide lognormal distribution. Figure 93a shows that the monodisperse approximation (s = 1) of pressure is both qualitatively and quantitatively different than the polydisperse (s > 2) approximations. More notable is the discrepancy among discrete approximations for the shear viscosity (figure 93b). The predictions using s = 3 and s = 4 are almost indistinguishable; however, adding a fifth particle species causes a significant change in the prediction of shear viscosity. Predictions of this NETL distribution are obtained to s = 10 to ensure this pattern does not continue. Accordingly, the number of species required to accurately capture the pressure and shear viscosity of the NETL distribution is $s_{\min}$ = 6 for both quantities. The need for a larger number of species to accurately approximate the NETL distribution comes about from the width of the PSD. Specifically, figures 90g and 90h show the large width of the NETL distribution relative to a lognormal distribution with σ/d_{ave} = 90%. Because the frequencies associated with the NETL distribution remains moderate over a larger range of

particle diameters than those in the lognormal distribution, the coal PSD contains a larger width of particle diameters. Therefore, it is reasonable that the values of s_{min} for the NETL distribution are greater than or equal to the values of s_{min} for the Gaussian and lognormal distributions investigated here.

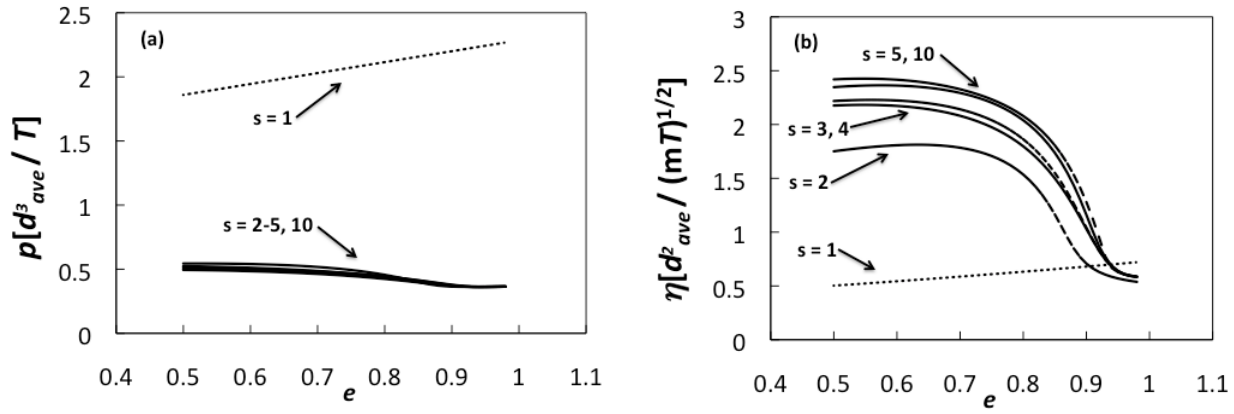

Figure 93. *Predictions of (a) granular pressure and (b) shear stress as a function of coefficient of restitution for NETL distribution of coal feedstock for gasification. The overall volume fraction of the system is ϕ = 0.3.*

For the sake of brevity, only representative results are shown above. The results obtained for the remaining transport coefficients ($\zeta^{(0)}$, ζ_u, and κ) behave in a similar fashion. A summary of these results over the parameter space evaluated is given in Table 5. Each value in Table 5 corresponds to the minimum number of species ($s_{\min}$), as determined by the 2% criterion established in Section II.B. It is important to note that the number of species required to accurately represent a continuous PSD with σ/d_{ave} = 0-90% is generally quite low ($s_{\min}$ = 1 – 5). However, the much wider distributions (i.e., lunar soil simulant) may require as many as 8 particle species ($s_{\min}$ = 8).

Another notable trend that is revealed in Table 5 is that distribution width generally has a larger effect on the number of species required for an accurate discretization ($s_{\min}$) of a given continuous PSD than does the volume fraction. More specifically, the values in Table 5 increase more within rows (varying σ/d_{ave}) than within columns (varying ϕ). To better illustrate this trend, figure 94 displays the dependency of number of discrete species required on both distribution width (Fig. 940a) and overall volume fraction (Fig. 94b). A sufficient increase in distribution width (σ/d_{ave} = 0-90%) always shows an increase to the number of species required, whereas the increases volume fraction may decrease (η) or not affect ($\zeta^{(0)}$, ζ_u , p, κ) the number of species needed. For instance, figure 94b shows that predictions for shear stress require fewer species at higher volume fractions, whereas the remaining transport coefficients require the same number of species regardless of the volume fraction (ϕ = 10^{-8} - 0.5). In sum, for all but one coefficient (η), s is independent of ϕ, though the same is not true for σ/d_{ave}.

Table 5. *Summary of minimum number of species (s_{min}) required to accurately approximate Gaussian, lognormal, bidisperse coal (NETL), and lunar soil (OB-1) size distributions with a discrete number of species.*

		Gaussian			Lognormal					NETL	OB-1
	σ/d_{ave}	10%	20%	30%	10%	30%	50%	70%	90%		
	ϕ										
Zeroth-Order Cooling Rate	0.05	2	2	3	2	2	3	4	4	5	
	0.1	2	2	2	2	2	3	4	4	5	8
	0.3	2	2	2	2	2	3	4	4	5	
	0.5	2	2	2	2	2	3	4	4	3	
First-Order Cooling Rate	0.05	1	2	2	2	2	2	4	4	6	
	0.1	1	2	2	2	2	2	4	4	6	8
	0.3	2	2	2	2	2	2	4	4	5	
	0.5	2	2	2	2	2	2	3	3	6	
Pressure	0.05	2	2	2	2	2	2	2	2	2	
	0.1	2	2	2	2	2	2	2	3	3	7
	0.3	2	2	2	2	2	2	3	4	5	
	0.5	2	2	2	2	2	2	3	4	6	
Shear Viscosity	0.05	1	2	2	1	2	4	5	5	5	
	0.1	1	2	2	1	2	4	4	4	5	8
	0.3	1	2	2	1	2	3	3	4	6	
	0.5	1	2	2	1	2	2	3	5	6	
Bulk Viscosity	0.05	2	2	2	2	2	2	4	4	5	
	0.1	1	2	2	1	2	2	4	4	5	8
	0.3	1	2	2	1	2	2	3	4	6	
	0.5	1	2	2	1	2	2	3	5	6	

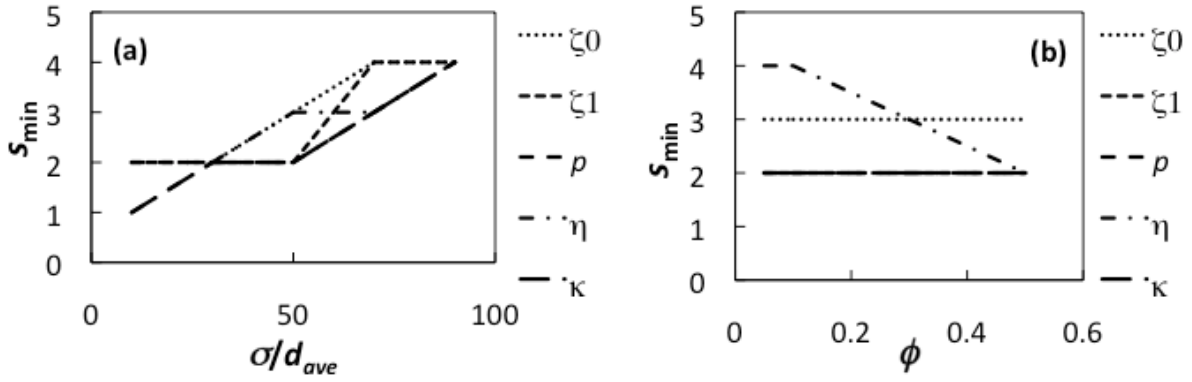

Figure 94. *Minimum number of species required (s_{min}) for a (a) lognormal distribution with a volume fraction of ϕ = 0.3 and varying σ/d_{ave} and (b) a lognormal distribution with σ/d_{ave} = 50% and varying ϕ.*

Finally, Table 5 can be used as a guide for determining how many species are needed for a specific flow system. For instance, if a specific flow geometry is dominated by the granular pressure and contains a Gaussian PSD with σ/d_{ave} = 30% and the overall volume fraction is predominantly ϕ = 0.05, only two particle species are necessary for the level of accuracy described here (2%). However, if a different flow geometry with the same PSD and overall ϕ is dominated by the zeroth-order cooling rate, three particle species are necessary for a similarly accurate approximation. Thus, in order to use these results in a practical application, some information must be known about the dominating effects of a system *a priori*. Alternatively, the

maximum value of $s_{\min}$ among all transport coefficients examined may be used as a guide. Further discussion on the pros and cons of the use of Table 5 (or a similar analysis for other distributions) as a guide for determining the appropriate number of discrete species for a given application is included in Concluding Remarks (Section IV).

Molecular dynamics (MD) simulations of lognormal and Gaussian distributions undergoing simple shear flow (SSF) have been performed by Dahl, Clelland, and Hrenya (Dahl, et al., 2003). In the current work, the simulation data is used not only to confirm for the minimum number of species ($s_{\min}$) required for an accurate discrete approximation (as reported in previous section), but also to test the accuracy of the GHD theory. The parameters used as inputs for the MD simulations are included in Table 2 of Appendix H; the outputs include both pressure and viscosity. This MD data is displayed in Figures 95 and 96 for lognormal and Gaussian distributions of various widths, respectively. Also shown in Figures 95 and 96 are the predictions obtained from GHD theory for several discrete approximations (various s) of the given continuous PSDs. Note that these predictions were obtained by first solving the energy equation (the only nontrivial equation for SSF) for granular temperature (T) using the appropriate discrete approximation, and then using this value of T to evaluate the pressure and shear viscosity. The DOE-based code MFIX (Multiphase Flow with Interphase Exchanges, www.mfix.netl.doe.gov), which contains the GHD theory, was used for these purposes.

The results displayed in Figures 95 and 96 demonstrate that the number of species required for an accurate approximation of pressure and shear viscosity is correctly predicted by the approach described in the previous section. More specifically, a value of $s = 3$ is sufficient in each case, as consistent with the values given in Table 5 (whereas smaller values of s do not achieve the desired accuracy). Figures 95 and 96 clearly show drastic differences between the monodisperse approximation and the ternary approximation ($s = 3$), where the ternary prediction using GHD theory is far more accurate. However, increasing the number of species to $s = 5$ in the discrete approximation shows little to no change at all, which further supports the predictions summarized in Table 5.

Though the monodisperse approximation of pressure and shear viscosity using GHD theory is appropriate in the monodispesre limit (i.e., $\sigma/d_{ave} = 0$), a larger number of particle species is required as the width of the PSD increases. Recall that for the MD data, the root mean cube of the continuous distribution was held constant ($d_{rmc} = 72.6$ microns). However, the dimensionless pressure and shear viscosity are plotted with respect to σ/d_{ave}. In order to maintain a constant d_{rmc} while increasing σ/d_{ave}, d_{ave} decreases accordingly, and thus the monodisperse approximations (i.e., $s = 1$) do not remain constant along the x-axis in Figures 95 and 96.

Regarding the validity of the GHD theory to predict properties of a continuous PSD, it is clear from Figures 95 and 96 that the GHD predictions using $s = 3$ and MD data are in close qualitative, as well as quantitative, agreement. From a qualitative perspective, the MD data displayed in Figures 95 and 96 indicate that the quantities behave non-monotonically with respect to the distribution width. This qualitative trend is captured by the polydisperse ($s = 3, 5$) GHD predictions, but not the monodisperse counterparts ($s=1$). Perhaps more importantly is the quantitative agreement between GHD predictions and MD data. For instance, Figure 96b shows a maximum percent difference between the $s = 3$ prediction and the MD data of 4%. For the widest distributions, GHD predictions have similar accuracy when compared to MD data as in the monodisperse limit ($\sigma/d_{ave} = 0$). Therefore, no loss of accuracy arises from the polydisperse theory itself (relative to monodisperse), nor due to the discrete approximations of continuous PSDs.

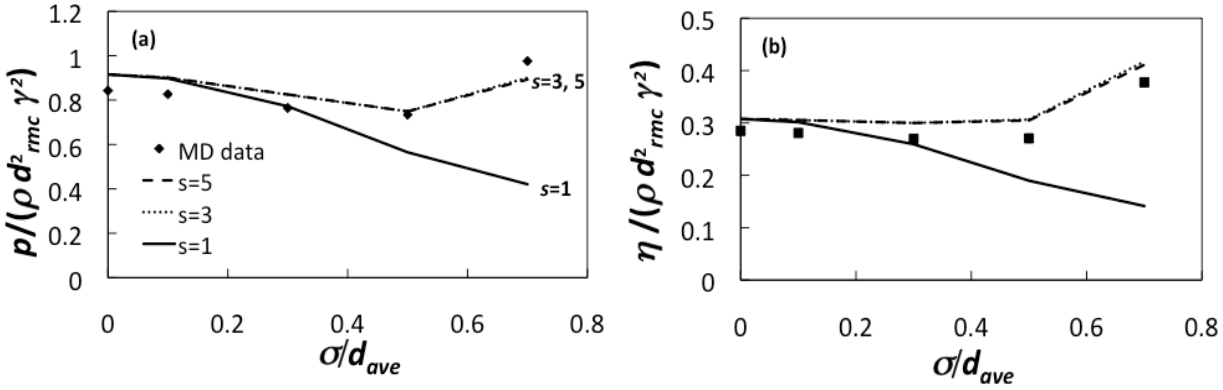

Figure 95. *Dimensionless (a) pressure and (b) shear stress as a function of σ/d_{ave} for lognormal distributions. Comparison of MD simulation data to GHD theory predictions using an increasing number of particle species. Overall volume fraction: $\phi = 0.3$, restitution coefficient: $\alpha = 0.85$.*

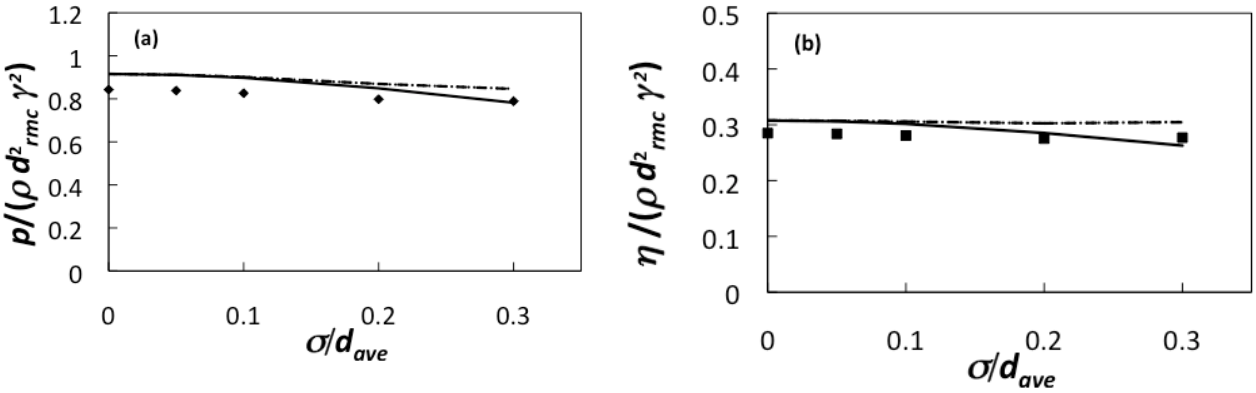

Figure 96. *Dimensionless (a) pressure and (b) shear stress as a function of σ/d_{ave} for Gaussian distributions. Comparison of MD simulation data to GHD theory predictions using an increasing number of particle species. Overall volume fraction: $\phi = 0.3$, restitution coefficient: $\alpha = 0.85$. See Figure 95a for legend.*

Task 4.2: Eulerian-DEM Simulations of Gas-Solid Systems (Subramaniam)

To assess the accuracy of the closures developed using KTGF and DQMOM in the presence of a fluid phase, simulations of a central-jet fluidized bed will be performed. The Eulerian-DEM solver in MFIX, which will be modified to incorporate the newly-developed, polydisperse drag law (Goal II), will be used. Simulations will be performed for various distributions, and the effect of an evolving particle size will be incorporated. A comparison of the continuum predictions with the Eulerian-DEM result will give a direct assessment of the accuracy of the KTGF and DQMOM closures in the presence of a fluid.

(Subramaniam reporting.) The objective of this task is to use MFX-DEM as an intermediate validation step of the drag models developed in task 2. Particle-resolved simulations of gas-solid flow performed by the Subramaniam research group in tasks 2.2 and 2.3 has resulted in the development of two new models: (i) a new model for the mean drag force at moderate

Reynolds number (ii) a new model for the instantaneous particle acceleration. The implementation and verification of these models in MFIX-DEM is described in this report.

Implementation and verification of the new model for the mean drag force

The fluid momentum equation solved in MFIX-DEM is given by

$$\frac{D}{Dt}(\varepsilon_g \rho_g \mathbf{v}_g) = \nabla . \overline{\overline{S}}_g + \varepsilon_g \rho_g \mathbf{g} - \sum_{m=1}^{M} \mathbf{I}_{gm} .$$

Statistical homogeneity of the test case leads to the following simplified momentum equation:

$$\frac{d\mathbf{v}_g}{dt} = -\frac{1}{\rho_g}\nabla P_g - \frac{\beta \mathbf{v}_g}{\varepsilon_g \rho_g} \tag{52}$$

The test case is modeled in MFIX-DEM using a single cell with an L/D ratio of 7.5 and a solid volume fraction of 0.2. The mean slip Reynolds number defined as

$$\mathrm{Re}_m = \frac{(1-\phi)\rho_g \left|\langle \mathbf{W} \rangle\right| d_p}{\mu_g}$$

was specified to be 20. The mean slip velocity $\langle \mathbf{W} \rangle$ is defined as the difference between the mean particle velocity and the mean fluid velocity $\langle \mathbf{W} \rangle = \langle \mathbf{v}^{(p)} \rangle - \langle \mathbf{u}^{(f)} \rangle$. The particles were fixed in space with zero velocities. The new IBM drag law developed in task 2.2 was used to compute the drag force on the particles.

The simplified momentum equation (52) was solved using Runge-Kutta 2nd order method in Matlab. The under-relaxation factors of the fluid momentum equations were taken as 1 in MFIX-DEM simulation as was the case in Matlab. The comparison of the results (evolution of mean slip Reynolds number) is shown in Figure 97. The graph shows that the solutions match exactly and verifies the implementation of the drag law.

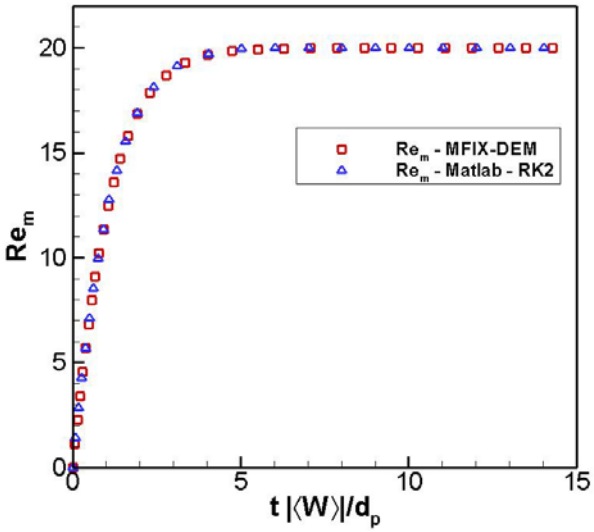

Figure 97. *Comparison of MFIX-DEM and Matlab solutions of the evolution of mean slip Reynolds number.*

Implementation and verification of the instantaneous particle acceleration model: In task 2.1 it was shown that simple extension of a class of mean particle acceleration models does not recover the joint particle acceleration-velocity statistics, leading to incorrect granular temperature evolution. Therefore, an instantaneous particle acceleration model of the Langevin equation form has been developed in task 2.3 that accounts for the particle velocity fluctuations and the hydrodynamic effects of the neighboring particles. This particle acceleration model results in a better prediction of granular temperature. The Langevin model for velocity increment of the particles is given by

$$dv_i = -\beta \left\langle W_i \right\rangle dt - \gamma\, v_i'' dt + B\, d\mathcal{W}_i$$

where dv_i is the particle velocity increment, W_j is the slip velocity, v_i'' is the fluctuating velocity of the particle, β is the interphase momentum transfer coefficient, γ and B are the Langevin model coefficients and $d\mathcal{W}_i$ is the Wiener process increment. At moderate Reynolds numbers, particle-resolved DNS is used to specify the Langevin model coefficients, while the theory of Koch (1990) and Koch and Sangani (1999) is used to specify the model coefficients in the Stokes flow regime.

Dilute suspensions in Stokes flow: In Stokes flow of highly massive particles in a dilute suspension, the steady state particle velocity distribution is shown to be an isotropic Maxwellian by Koch(1990). Koch derived analytical expressions for the source and dissipation of granular temperature in the limit of low volume fractions and low Reynolds numbers in the form of

$$\frac{dT}{dt} = -\frac{2R}{\tau}T + \frac{2S_I}{3} = -\Gamma + S, \tag{53}$$

where $R = 1 + 3\phi^{1/2}/\sqrt{2}$ is the non dimensional particle momentum relaxation rate, $S_I = \left(a\left|\left\langle \mathbf{W} \right\rangle\right|^2\right) / \left(2\pi^{1/2}\tau^2 T^{1/2}\right)$ is the source term due to hydrodynamic interactions and $\tau = m / \left(6\pi\mu_f a\right)$ is the characteristic timescale over which the velocity of a particle of mass m and radius a relaxes due to viscous forces.

The evolution equation of granular temperature implied by the Langevin model is

$$\frac{dT}{dt} = -2\gamma T + B^2 \tag{54}$$

Comparing Eq.53 and Eq.54, we get the Langevin model coefficients for the Stokes flow case with elastic particles as

$$\gamma = \frac{R}{\tau} = \frac{1}{\tau}\left(1 + \frac{3}{\sqrt{2}}\phi^{1/2}\right)$$

$$B^2 = \frac{2S_I}{3} = \frac{1}{3\sqrt{\pi}}\frac{a\left|\left\langle \mathbf{W} \right\rangle\right|^2}{\tau^2 T^{1/2}}$$

These coefficients have been used to develop an Enskog kinetic theory for monodisperse gas-solid flow in collaboration with the PI, Professor Hrenya [cite?].

The proposed particle acceleration model has been coded into MFIX-DEM and two test cases were chosen to be simulated with different initial Reynolds numbers based on granular temperature defined as

$$Re_T = \frac{\rho_g T^{1/2} d_p}{\mu_g}$$

The initial Re_T was chosen to be 0.0083 and 0.17 in the two cases respectively. The particles were initialized with velocities distributed according to a Maxwellian corresponding to these two values of initial Re_T. A single cell for the entire domain was used. The box length-to-particle diameter ratio L / d_p ratio was taken as 7.5 and the solid volume fraction ϕ was taken as 0.2. The Reynolds number based on the mean slip velocity is defined as

$$Re_m = \frac{\rho_g (1-\phi) \left| \langle \mathbf{W} \rangle \right| d_p}{\mu_g}$$

and is taken to be 0.5. The dispersed phase to carrier phase density ratio ρ_p / ρ_g is taken to be 200. The fluid was initialized with a velocity corresponding to the mean slip Reynolds number.

The evolution of mean slip Reynolds number is shown in Figure 98. The figure indicates that the mean slip velocity is recovered exactly.

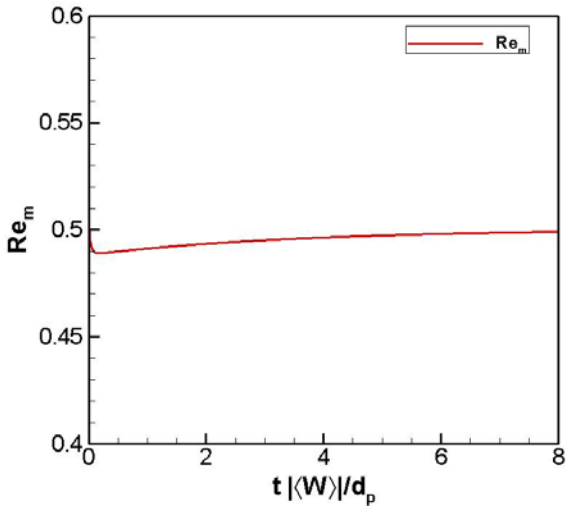

Figure 98. *Evolution of mean slip Reynolds number – Mean slip velocity is recovered exactly.*

Equation 53 was solved using Matlab with the different aforementioned initial conditions and the results were compared with the results obtained using MFIX-DEM. The comparison of the variation source and dissipation terms with granular temperature is shown in Figure 99. The plot shows that the solutions obtained using MFIX-DEM and Matlab match very well. The intersection point of the source and dissipation curves determines the steady state granular temperature.

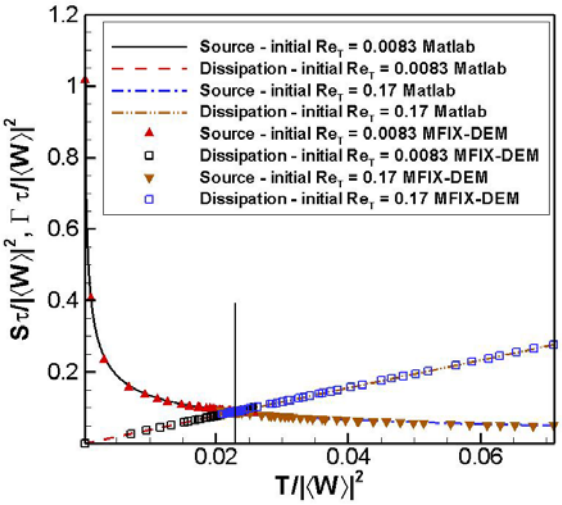

Figure 99. *Comparison of MFIX-DEM and Matlab solution - Source & Dissipation terms vs. Granular temperature.*

The comparison of the evolution of granular temperature is shown in Figure 100. The plot shows that the Matlab solution and MFIX-DEM solution match well. Also, irrespective of the initial conditions, granular temperature reaches the same steady state value.

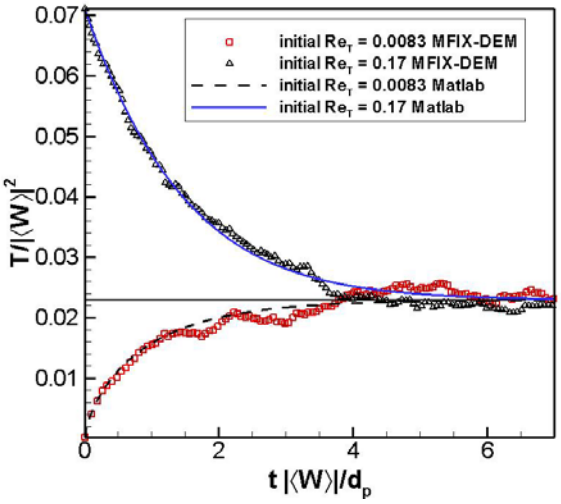

Figure 100. *Evolution of granular temperature with different initial* Re_T

Dense suspensions in Stokes flow: In Stokes flow of highly massive elastic particles in moderately dense and dense suspensions, the steady state particle velocity distribution to leading order is shown to be Maxwellian by Koch and Sangani (1999). They used the multi-pole expansion method to evaluate the source of the granular temperature due to hydrodynamic interactions. The Langevin model coefficients in this regime are given by

$$\gamma = \frac{R_{diss}(\phi)}{\tau}$$

$$B^2 = \frac{2}{3}\frac{a}{\tau^2}\frac{\left|\langle \mathbf{W} \rangle\right|^2}{T^{1/2}} S^*(\phi).$$

In the expressions given above, $R_{diss}(\phi)$ is the viscous energy dissipation in a suspension with a Maxwellian particle velocity distribution (Sangani et al., 1996), $\tau = m/(6\pi\mu_f a)$ is the characteristic timescale over which the velocity of a particle of mass m and radius a relaxes due to viscous forces, $\langle \mathbf{W} \rangle$ and S^* being the mean slip velocity and dimensionless source respectively. The non-dimensional source is expressed as

$$S^*(\phi) = \frac{1}{2\pi^{1/2}} R_s R_{drag}^2,$$

where R_s represents the energy source due to a specified mean force acting on the particles and R_{drag} is the drag coefficient. Expressions for R_{diss}, R_s and R_{drag} are given by Koch and Sangani (1999).

Two test cases with different initial granular temperatures were simulated to verify the implementation of this model. A single cell was used for the computational domain which was taken as a cubic box with periodic boundaries in all the directions. The box length-to-particle diameter ratio L/d_p was taken as 7.5 and the solid volume fraction ϕ was taken to be 0.2. The mean slip Reynolds number and the dispersed phase to carrier phase density ratio ρ_p/ρ_g were taken to be 0.5 and 200 respectively. The fluid was initialized with a velocity corresponding to the mean slip Reynolds number. A comparison between the results obtained by using MFIX-DEM and those obtained by using Matlab is shown in Figure 101. Figure 101 shows that the source and dissipation terms reach the same value irrespective of the initial conditions to give rise to the same steady-state granular temperature in both the test cases which is shown in Figure 102.

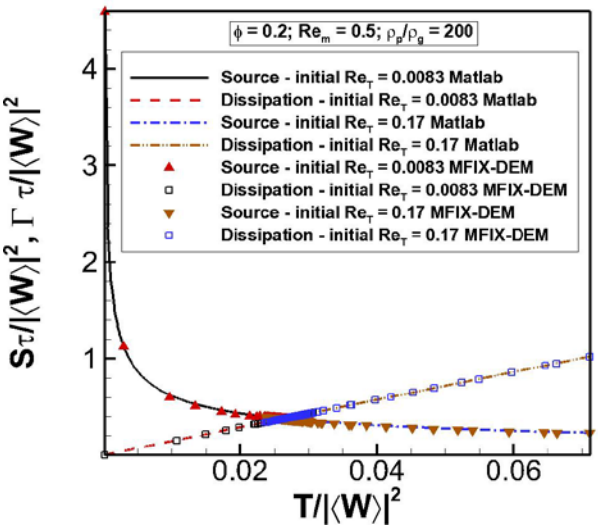

Figure 101. *Comparison of MFIX-DEM and Matlab solutions - Source & Dissipation terms vs. Granular temperature.*

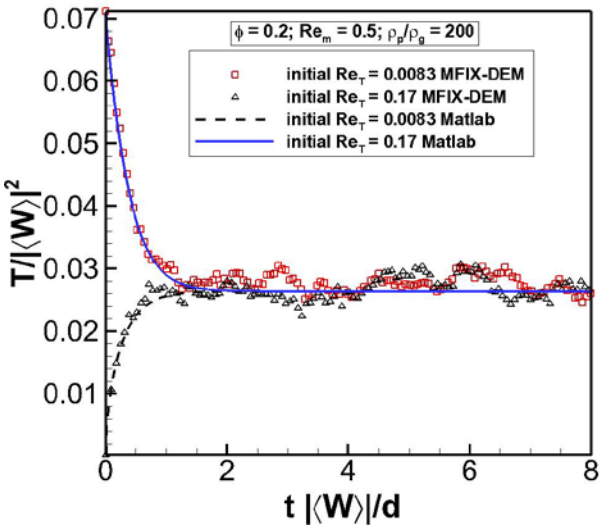

Figure 102. *Evolution of granular temperature with different initial* Re_T.

Dense suspensions at moderate Reynolds numbers: The particle acceleration model for monodisperse gas-solid suspensions at moderate Reynolds numbers proposed in Task 2.3 has been implemented in MFIX-DEM. The model coefficients are specified as the departures from their steady-state values given by the PUReIBM results. A few test cases were run using MFIX-DEM to study the effect of the initial conditions on the steady-state of the system. Figure 103 shows that the steady temperature attained by the system is not influenced by the initial conditions. It also shows that without the use of a Langevin-type particle acceleration model, the granular temperature decays to zero and emphasizes the necessity of such model.

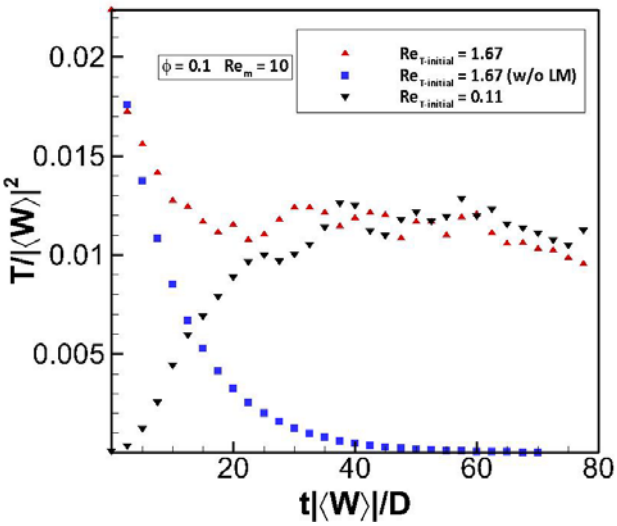

Figure 103. *Evolution of granular temperature with different initial conditions.*

Two test cases corresponding to mean slip Reynolds numbers of 10 and 20 were solved using MFIX-DEM as well as Matlab (solution of the granular temperature evolution ODE). The results are shown in Figure 104. The plots shown in Figure 104 indicate that the steady-state values predicted by the model are very close to the PUReIBM results. The difference in the evolution is due to the perturbed initial granular temperature values in MFIX-DEM and Matlab solutions. These results show that the particle acceleration model implemented in MFIX-DEM predicts the correct evolution of granular temperature over a range of the relevant physical parameters.

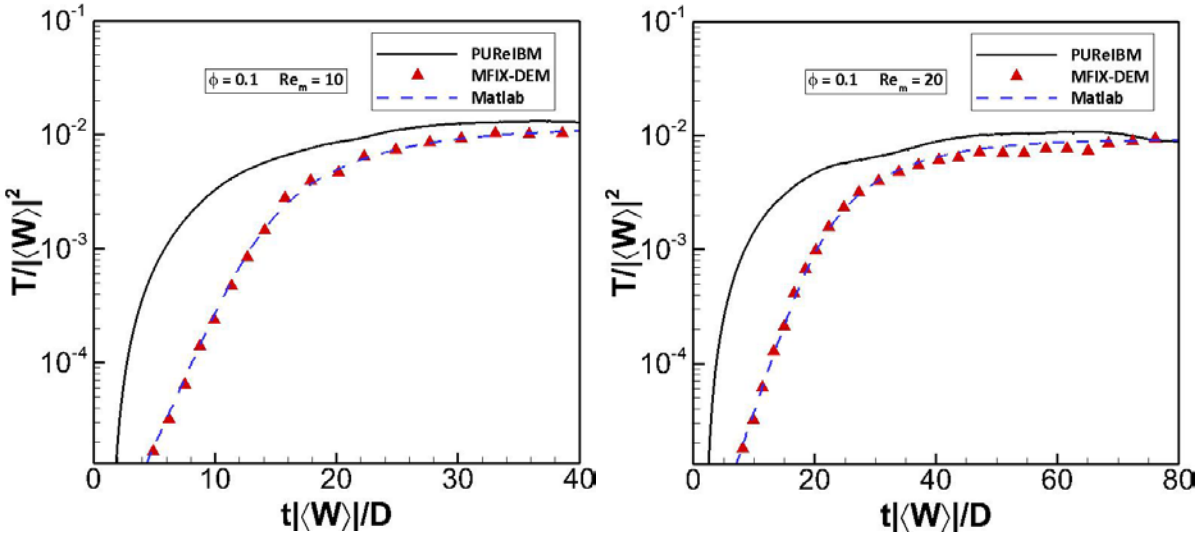

Figure 104. *Evolution of granular temperature in both the test cases: Re_m = 10, 20.*

<u>Task 4.3: Experiments in a Low-Velocity, Fluidized Bed (Hrenya and Cocco)</u>

<u>The experimental apparatus available at Colorado will be used to gather axial segregation data in a low-velocity, gas-fluidized bed. The focus will be on particles that do not evolve with time, and thus this data will provide a test of the ability of KTGF and DQMOM models to predict species segregation. To complement the existing data for a binary mixture (with differences in size and/or density), the focus here will be on particles of the same material with a continuous distribution of sizes. A range of operating conditions (e.g., gas flow rates, widths of size distributions, particle material, bed height) will be explored. Fluidization curves (pressure drop vs. gas velocity) will be generated. Bubble characteristics will be measured via an existing optical fiber probe developed by Cocco. Axial concentration profiles will be measured after the gas velocity has been suspended via layered extraction, followed by sieving. (The method is thus restricted to low gas velocities in which segregation during the free-fall of particles is effectively eliminated.)</u>

Hrenya reporting). **Task 4.3.1: Species Segregation of Continuous Particle Size Distributions**[2]

Abstract: Bubbling, gas-fluidized bed experiments involving Geldart Group B particles with continuous particle size distributions (PSDs) have been carried out. Sand of various widths of Gaussian or lognormal distributions were completely fluidized, and then axial concentration profiles were obtained from frozen-bed sectioning. Similar to previous works on binary systems, results show that mean particle diameter decreases with increasing bed height, and that wider Gaussian distributions show increased segregation extents. Surprisingly, however, lognormal distributions exhibit a non-monotonic segregation trend with respect to distribution widths. In addition, the shape of the local size distribution is largely preserved with respect to that of the overall distribution. These findings on the nature of local size distribution provide experimental confirmation of previous results for granular and gas-solid simulations. Lastly, an interesting observation is that although monodisperse Geldart Group D particles cannot be completely fluidized, their presence in lognormal distributions investigated still results in complete fluidization of all particles.

Introduction: Bubbling fluidized beds belong to the lower velocity regime of gas-solid fluidized systems that are important in numerous industries, examples of which are Union Carbide Low-density Polyethylene and Mitsui Petrochemical Polypropylene(Kunii and Levenspiel 1991). The majority of such systems are characterized by a range of particle sizes and/or densities, and the various particle species de-mix, or segregate, according to size and density (Rowe and Nienow 1976; Tang and Puri 2004; Cui and Grace 2007). Hence, an enhanced understanding of polydisperse flows will allow for an improvement of such existing operations and a more efficient design of new operations. Yet, despite the prevalence of continuous size distributions in industrial fluidized beds, most previous segregation studies have been focused on binary mixtures consisting of two particle types of different sizes and/or densities. A brief review of species segregation experiments and simulations in bubbling fluidized beds with binary mixtures has been presented by Joseph et al.(Joseph, Leboreiro et al. 2007). Comparatively, few efforts have been devoted to the investigation of continuous size distributions; these previous contributions are described below.

Experimental results have been presented on the impact of continuous size distributions on the fluid mechanical behavior of bubbling beds, with effects ranging from minimum fluidization velocity(Sun and Grace 1990; Gauthier, Zerguerras et al. 1999; Lin, Wey et al. 2002), bubble sizes(Beetstra, Nijenhuis et al. 2009), pressure fluctuations(Grace and Sun 1991), presence of particles in bubbles(Sun and Grace 1990; Sun and Grace 1994), etc. The contribution by Grace and Sun(Grace and Sun 1991) represents one of the earliest reviews on the influence of particle size distribution (PSD) on the quality of fluidization, and they summarized that a wider PSD (of Geldart Group A particles) culminates in enhanced reactor efficiency through improved inter-phase mass transfer and better gas-solid contacting. One factor impacting gas-solid interaction is the degree of species segregation, and a few efforts have reported on species segregation for continuous size distributions(Hoffmann and Romp 1991; Gauthier, Zerguerras et al. 1999; Lin and Wey 2004). Hoffman and Romp(Hoffmann and Romp 1991) investigated a Gaussian distribution of Group B particles with a distribution width of 30% (i.e., ratio of standard

[2] Chew, Wolz and Hrenya, "Axial segregation in bubbling gas-fluidized beds with Gaussian and lognormal distributions of Geldart Group B particles", AIChE Journal, 2011, 56 (12), p 3049-3061.

deviation, σ, to the average diameter, d_{ave}), under various superficial gas velocities (U_s). They found segregation of the smallest and largest particles, respectively, at the upper and lower layers of the bed, which is qualitatively similar to previous findings for binary mixtures(Hoomans, Kuipers et al. 2000; van Wachem, Schouten et al. 2001; Bokkers, Annaland et al. 2004; Joseph, Leboreiro et al. 2007). Because of the presence of more size species in a continuous distribution, concentration maxima of particles of different sizes at different heights were observed along the bed. It was also found that species segregation continues to exist for velocities significantly higher than the minimum fluidization velocity. This particular Gaussian distribution reported is also one of the distributions investigated in this work. Lin and Wey(Lin and Wey 2004) and Gauthier et al.(Gauthier, Zerguerras et al. 1999) both compared a narrow cut, a binary mixture, a uniform distribution and a Gaussian distribution to examine how different PSDs affect fluidization. Lin and Wey(Lin and Wey 2004) found that the narrow cut and Gaussian distribution exhibited the best fluidization quality, which was defined as the least amount of pressure fluctuations. Gauthier et al.(Gauthier, Zerguerras et al. 1999) further observed that Gaussian PSD and narrow cut hardly segregate, whereas binary and flat PSD mixtures always segregate. Collectively, these experimental works provide some insight on how continuous distributions segregate relative to other types of distributions. What is still missing is the impact of the width of continuous distributions on segregation behavior, which is addressed in this work.

In addition to the experimental works on continuous PSDs in bubbling beds discussed above, a number of modeling efforts supplement the experimental results. Size-segregation in gas-solid fluidized beds containing continuous PSDs has been examined via Eulerian-Lagrangian(Dahl and Hrenya 2005) and Eulerian-Eulerian(Fan and Fox 2008) simulations, with both indicating that wider distributions show more extensive segregation than narrower ones. Earlier molecular-dynamics simulations involving granular flow (i.e., no interstitial fluid) led to a similar conclusion(Dahl and Hrenya 2004). More specifically, Dahl and Hrenya(Dahl and Hrenya 2005) employed an Eulerian-Lagrangian model of a gas–solid fluidized bed to investigate the species segregation (de-mixing) behavior of both Gaussian and lognormal distributions over a range of distribution widths, restitution and friction coefficients, and gas velocities. The results indicate that: (i) the average particle diameter decreases as the height within the bed increases, (ii) the level of segregation increases with an increase in the width of the PSD, and (iii) shape of the local size distribution (i.e., Gaussian or lognormal) is found to mimic that of the overall size distribution in most regions of the fluidized bed. To date, experimental validation of points (ii) and (iii) have not been pursued, which serves as further motivation of the current work. Due to the assumptions incorporated in such simulations, experimental validation of models is important. In particular, recent work has indicated that the drag law treatment plays a crucial role in the qualitative and quantitative nature of segregation of polydisperse systems(Beetstra, van der Hoef et al. 2007; Leboreiro, Joseph et al. 2008). In the earlier DEM simulations of Dahl and Hrenya(Dahl and Hrenya 2005), however, an ad hoc treatment of the polydisperse drag law was used since more rigorous, lattice-Boltzmann-based treatments(Van der Hoef, Beetstra et al. 2005; Yin and Sundaresan 2009) were not yet available.

In an effort to build on the previous knowledge on the effect of continuous size distributions on species segregation, the objective of the current work is twofold: (i) to experimentally determine the impact of the width of the distribution on the degree of segregation, and (ii) to experimentally determine the shape of local size distributions throughout the bed. Experiments have been carried out involving both Gaussian and lognormal PSDs of Geldart Group B particles in low-velocity bubbling beds, with an emphasis on axial

concentration profiles. The results validate the trends observed in previous simulations(Dahl and Hrenya 2005) in terms of the segregation of larger particles to the bottom of the bed, a positive correlation between width of Gaussian distribution and segregation extent, and a general preservation of the shapes of local distributions. A surprising fourth finding, however, lies in the non-monotonic behavior of segregation extents with widths of lognormal distributions. Specifically, as the width of a lognormal distribution increases, the segregation extent increases and then decreases.

Finally, although not a primary focus of the current effort, interesting observations were also made for the fluidization behavior of Geldart Group D particles. Albeit the focus of this work being on Geldart group B particles, it is important to note that wide PSDs may, by necessity, span more than one Geldart group. This work presents evidence that the presence of Group B and D particles in a continuous distribution allow the Group D particles constituents to be fully fluidized even when a monodisperse suspension of the same Group D particles do not completely fluidize. The poor fluidization quality of the Group D particles is evidenced by the discrepancy between the actual bed mass and that calculated via the fluidization curve data.

Experimental Description–Experimental Apparatus: A schematic diagram of the experimental set-up for all fluidization experiments is shown in Figure 105, which is identical to that used by Joseph et al.(Joseph, Leboreiro et al. 2007). Particles are fluidized in a Plexiglas column which is 18.5 cm in diameter. A Yaskawa V7 variable frequency drive controls a Fuji Electric VFD5 regenerative blower that provides the air for fluidization. A National Instruments LabVIEW program (version 7.1) remotely controls the driver. A Mott Corporation 316 stainless steel sintered porous plate, with an average porosity of 40% and 1.6 mm thickness, serves as the distributor plate. The superficial velocity (U_s), which is reported at local atmospheric conditions (air with a 0.97 kg/m^3 density and 1.85 × 10^{-5} Pa·s viscosity), is determined based on measurements via a Lambda Square Oripac 4150-P orifice plate flow meter, which is located upstream of the plenum. Relative humidity (RH) in the unit is enhanced by an Air-O-Swiss model AOS 7144 humidifier placed at the inlet of the blower. Relative humidity (RH) is kept above 40% for all experiments to help reduce electrostatics(Ciborowski and Wlodarski 1962; Tardos and Pfeffer 1980; Guardiola, Rojo et al. 1996; Hendrickson 2006). The operating air temperature and RH in the plenum are measured by means of an Omega HX93AV-RP1 probe, with a temperature range of -4 to 171 ^{o}C and RH range of 0 to 100%, inserted into the plenum. The pressure drops across the orifice plate flow meter, across the distributor plate, and across the entire fluidized bed are measured using Orange Research 20100 Series low-differential pressure transmitters with the ± 0.2% accuracy option. Pressure drop statistics across the orifice meters are transmitted to the computer and superficial velocities computed. All temperature, relative humidity, superficial velocity and pressure data are recorded throughout the experiments.

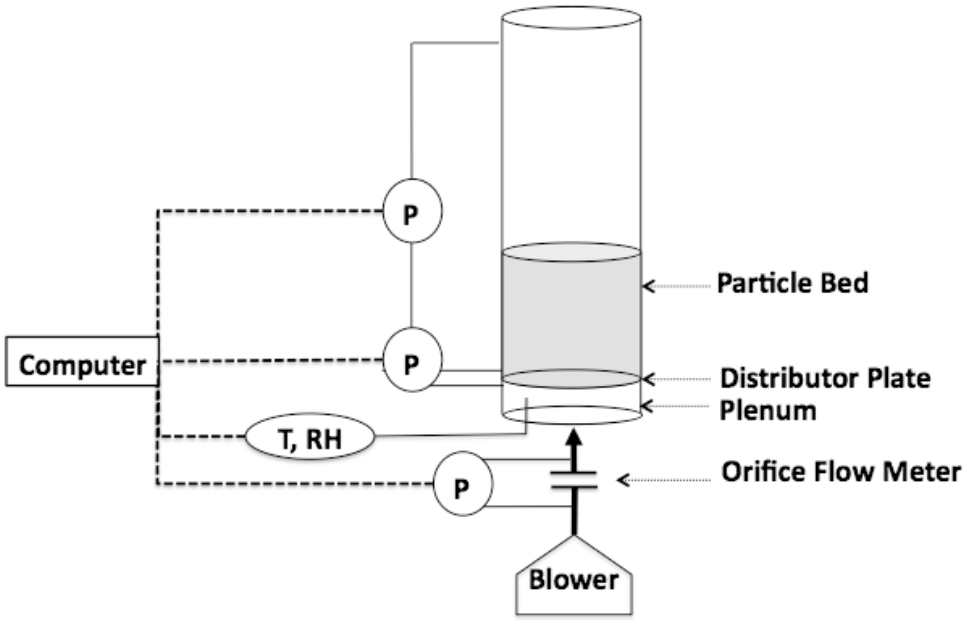

Figure 105. *Schematic of fluidized-bed experimental set-up.*

Particle Size Distributions (PSDs): Two continuous size distributions, namely Gaussian and lognormal, were examined using sand particles. The sand was acquired from US Silica Company, with a specific gravity of 2.65. Various distribution widths were examined; the distribution width is defined as the ratio of standard deviation (σ) of particle size distribution to sauter-mean particle diameter (d_{sm}). The range of σ/d_{sm} used for Gaussian distributions is 10% to 30%. These lower and upper limits are specified such that the system will not resemble a monodisperse system and will not require negatively-sized particles, respectively. The range of σ/d_{sm} used for lognormal distributions is 10% to 70%. The lower limit is 10% because it is observed that a lognormal distribution with σ/d_{sm} = 10% is similar to the Gaussian distribution with the same σ/d_{sm}, so the results for the Gaussian distribution with σ/d_{sm} = 10% will be used in the analysis for lognormal distributions too. The upper limit is established to avoid using sand particles of greater than 2.8 mm, which are scarce.

As mentioned above, this effort focuses on Geldart Group B particles fluidized by air under atmospheric conditions. For operation strictly within Geldart Group B classification(Geldart 1973), the size range of the sand particles was calculated to be 80 - 670 μm, and this is the range used for all Gaussian distributions investigated. For the wider lognormal distributions (σ/d_{sm} > 30%), however, some bigger particles in the Geldart Group D classification were required since the entire Geldart Group B range is not wide enough to contain the full distribution of particle sizes. The Sauter-mean diameter (d_{sm}) of all the Gaussian and lognormal distributions under investigation was set to 375 μm, which is the middle value of the stipulated Group B size range. In this work, d_{sm} is kept constant and the widths of the continuous PSDs (denoted σ/d_{sm}) are varied. The d_{sm} is used instead of other characteristic diameters since it is the most physically relevant. Namely, d_{sm} is the ratio of the volume-based to surface-based diameters, the former of which is proportional to the gravitational force and the latter of which is proportional to the drag force. The size distributions used in the experiments were prepared based on exact expressions

for the frequency distribution function (f_m) for Gaussian and lognormal systems:

$$f_{m,\,Gaussian}(x) = \frac{1}{\sigma\sqrt{2\pi}} \exp\left[-\frac{(x-\bar{x})^2}{2\sigma^2} \right] \tag{55}$$

where σ is the standard deviation of the mass-based PSD, x is particle diameter, and $\bar{x}$ is the arithmetic mean of the mass-based PSD. Analogously, the mass-based lognormal distribution is defined as

$$f_{m,\,lognormal}(x) = \frac{1}{x\sigma_\mu\sqrt{2\pi}} \exp\left[-\frac{(\ln(x)-\mu)^2}{2\sigma_\mu^2} \right] \tag{56}$$

whereby the natural logarithm of this distribution is a Gaussian PSD with arithmetic mean μ and standard deviation σ_μ. Correspondingly, to compute the Sauter-mean diameter (d_{sm}) (Rhodes 1998), the mass-based distributions (f_m) in Equations 55 and 56 are converted to the corresponding number-based PSDs (f_n),and then d_{sm} is determined as $\frac{\int x^3 f_n}{\int x^2 f_n}$.

Shown in Figure 106 are the Gaussian (Figure 106a) and lognormal (Figure 106b) distributions (f_m), obtained respectively by Equations 55 and 56 and denoted by lines, as well as the experimental values obtained via sieving and denoted by points. More specifically, the experimental value of f_m is determined as the ratio of the mass fraction to width of the particle size bin (as determined by the sieve cutoffs); note the division by bin width serves as a normalization to provide a straightforward means of comparison between bins of different widths(Hinds 1999). Fisherbrand U.S. Standard Brass Test Sieves, 0.20 m diameter x 0.05 m height, were used for preparing the particle size distributions (PSD). Figure 106 illustrates the close correspondence between the exact and experimental distributions. Notably, the particle sizes for all widths of Gaussian distributions investigated are contained in the Geldart Group B classification (80 - 670 μm), while up to 24% by mass of the widest lognormal distribution (σ/d_{sm} = 70%) falls in the Geldart Group D classification. As mentioned previously, due to the nature of the lognormal distribution, it is not possible to restrict all particle sizes to within Group B classification, and larger Group D particles have to be included for an accurate representation.

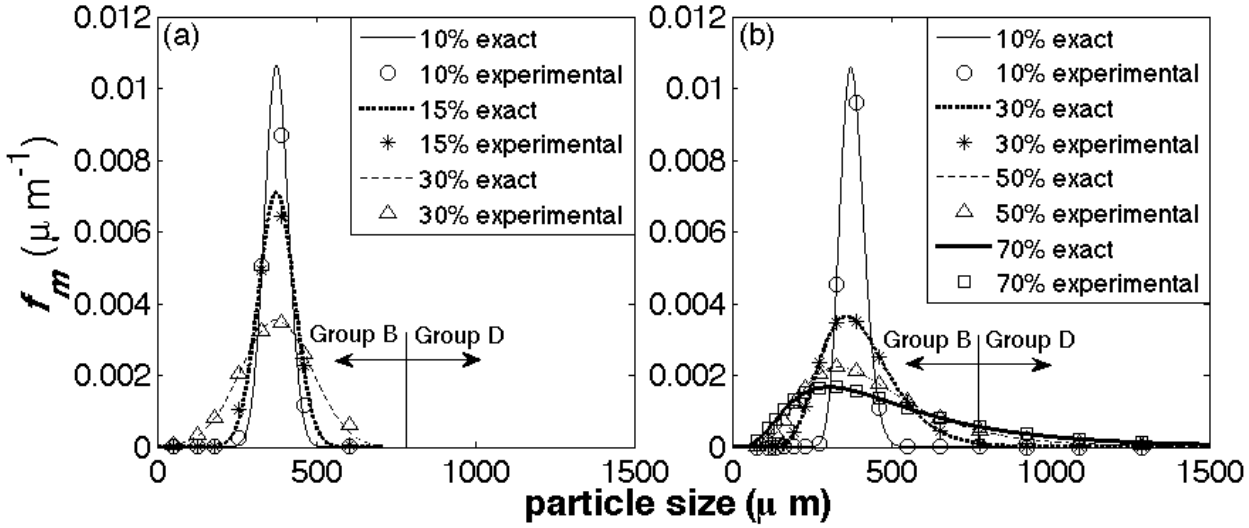

Figure 106. *Frequency distributions of (a) Gaussian with σ/d_{sm} = 10%, 15%, and 30%; and (b) lognormal with σ/d_{sm} = 10%, 30%, 50%, and 70%. The lines represent exact distributions as defined by Equations 55 and 56, while the discrete points are experimental values.*

Prior to all experiments, sand acquired from the vendor was fluidized at greater than three times the complete fluidization velocities (U_{cf}, as detailed below) for at least 100 hours. The high-velocity fluidization was necessary to smooth out the rough edges of the particles to avoid further attrition so as to preserve the integrity of PSDs during fluidization experiments. Validation tests have also been carried out to ensure reproducibility and reliability of the sieving technique used for measuring PSDs. In particular, care was taken to ensure each sieve tray was never more than half full, and an adequate sieve-shaking duration was observed depending on the loading size. For example, for a 2 kg sample, a sieve-shaking duration of 10 minutes and more gave the same sieve results, hence a sieve duration of 10 minutes was determined to be sufficient.

Axial Concentration Measurements: As a precursor to the axial concentration (or segregation) measurements, fluidization curves were first generated to determine U_{cf}, the complete fluidization (superficial) velocity, which is defined as the velocity beyond which the pressure drop across the bed remains constant. To determine U_{cf}, the particle bed of a given distribution underwent repeated cycles of defluidization-fluidization over a range of superficial velocities (U_s) to generate the fluidization curves, which are plots of pressure drop (ΔP) versus U_s. De-fluidization was always run first to ensure a repeatable initial state for subsequent fluidization, and three cycles of defluidization-fluidization were carried out for each distribution. Superficial velocities (U_s) were decreased or increased incrementally by 0.01 m/s, and held at each step for 40 s, after which pressure drop across the bed is averaged over 10 s. For all the distributions investigated, the pressure drop at which the curve plateaus for higher U_s (i.e. $U_s > U_{cf}$) is equal to the ratio of the bed weight over cross-sectional area (W/A), which provides evidence of complete fluidization. Due to some noise present in the data, a systematic method of U_{cf} determination was employed, namely defining U_{cf} as the average U_s of the first 5% of the total number of points that fall within ± 1% of the expected W/A value.

To ensure repeatable initial conditions for the segregation experiments(Joseph, Leboreiro et al. 2007), the bed was initially mixed at a high superficial velocity, specifically $U_s = 3\ U_{cf}$, before

lowering it to the desired value of 1.2 U_{cf} used in the segregation experiments. An adequate duration for this initial mixing was carefully determined: after fluidizing the bed for a stipulated duration, the PSD from an axial section at a dimensionless height (*h/H*, where *h* is the height of the axial section and *H* is the collapsed bed height) of 0.5 was measured via sieving. Because the Gaussian distribution with σ/d_{sm} = 30% was found to display the most significant segregation (described later), it was used for this portion of the investigation. At 3 U_{cf}, essentially superimposable PSDs were observed for durations ranging from 15 minutes to 1 hour, implying that 15 minutes is sufficient to generate reproducible initial conditions. Hence, the bed was allowed to initially mix at 3 U_{cf} for 15 minutes before the velocity was lowered for the subsequent segregation experiments. The same procedure was used in the investigation of binary mixtures by Joseph *et al*. (2007).

After the initial mixing period described above, the gas velocity was adjusted to the lower value, namely 1.2 U_{cf}, for which steady-state axial concentration profiles are obtained. The value of 1.2 U_{cf} was chosen because the operating U_s has to be high enough to ensure that the bed is completely fluidized and yet low enough such that subsequent bed freezing does not lead to further segregation during bed collapse. The duration required to achieve steady-state and reproducibility was also investigated. For the same reason described previously, the Gaussian distribution with σ/d_{sm} = 30% was used in this study. The bed was fluidized at 1.2 U_{cf} for various durations (namely, 30 minutes, 1 hour, 2 hours, and 60 hours). While segregation was incomplete at 30 minutes, the system appeared to have reached steady state at 1 hour and beyond. Henceforth, the air supply was quickly shut off and the plenum vented to freeze the bed after 1 hour of fluidization at 1.2 U_{cf}. Axial concentration profiles were then measured by vacuuming out axial sections of the collapsed bed and sieving the resulting samples. Radial segregation was found to be insignificant relative to variations in the axial direction, and hence only axial concentration profiles are reported(Joseph, Leboreiro *et al.*, 2007).

In summary, the procedure for the segregation experiments is as follows. (1) Load 8 kg of sand with the stipulated distribution into the column. (2) Generate a defluidization-fluidization curve in order to determine U_{cf}. (3) Mix the bed for 15 minutes at high velocity (3 U_{cf}) to generate reproducible initial conditions for the subsequent low-velocity fluidization. (4) Fluidize the bed at low velocity (1.2 U_{cf}) for a period sufficient (1 hour) for steady-state segregation to be reached. (5) Abruptly shut off the gas feed to collapse the bed. (6) Vacuum out axial sections of the bed for sieve analysis. As mentioned above, this methodology is restricted to low fluidization velocities in order to effectively eliminate the potential of segregation upon bed collapse (Joseph, Leboreiro *et al.*, 2007).

Reducing Electrostatics: During the preliminary experimental runs, some evidence of electrostatics was observed in the fluidized bed. For example, some sand particles were observed to be sticking to the inner walls of the Plexiglass column. The observation of electrostatics is not surprising, since contact charging between particles having the same chemical makeup but different sizes has been previously confirmed (Zhao, Castle et al., 2003; Hendrickson, 2006). Because the focus of the current effort is on the impact of continuous PSDs on segregation behavior (rather than electrostatic effects), efforts were made to eliminate the effect of electrostatics. Henceforth, maintaining RH at above 40% by means of a humidifier placed at the inlet of the blower was used to reduce electrostatics (Hoffmann and Romp, 1991; Guardiola, Rojo et al., 1996; Hendrickson, 2006). At higher RH, the sticky nature of the sand particle to the inner wall of the Plexiglass column appeared to have attenuated. Although Figure 107 shows that axial concentration profiles at RH ~ 25% and RH ~ 55% were similar, implying the ineffectual

role of electrostatics on the segregation profiles under examination in this work, all fluidization experiments were nonetheless carried out at RH above 40%.

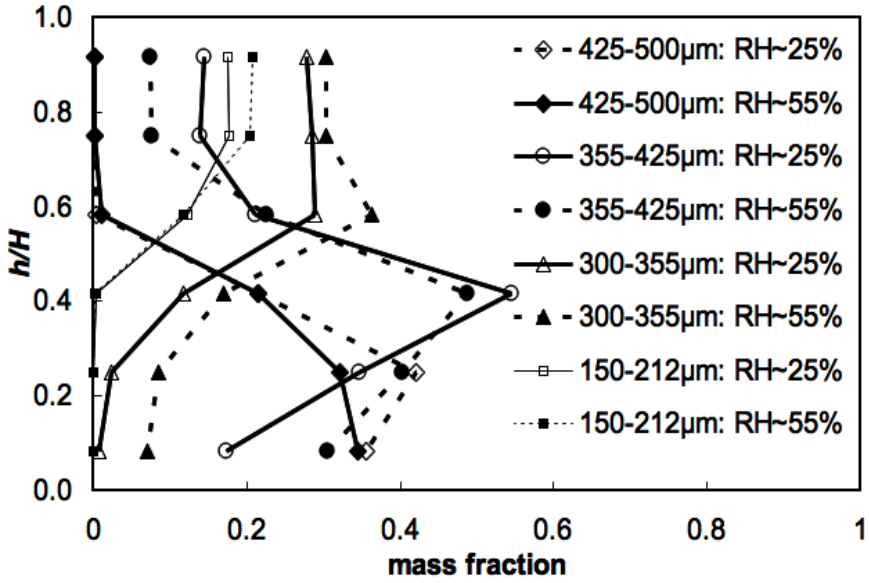

Figure 107. *Axial species concentration profiles of Gaussian distribution with σ/d_{sm} = 30% at RH ~ 25% and RH ~ 55%.*

Results & Discussion – Fluidization Curves: As a first step, fluidization curves (ΔP vs. U_s) were generated for all distributions investigated to determine the complete fluidization velocity (U_{cf}) values and the quality of fluidization. The U_{cf} values are necessary to ensure complete fluidization of all particles in the bed when carrying out segregation experiments, while also ensuring operation at low enough velocity (1.2 U_{cf}) to eliminate potential segregation during bed collapse by keeping bed expansion to a minimum. Moreover, as pointed out above, although the focus of this work is on Geldart Group B particles, Geldart Group D particles were also included in the wider lognormal distributions investigated (σ/d_{sm} = 30% to 70%) since the width of these distributions is greater than the range of diameters contained in Group B alone. Because Group D particles are known to exhibit poor fluidization quality, it was necessary to verify whether or not these bigger particles were completely fluidized in the column. For this assessment, a good test is the accurate prediction of bed weight (W) using the fluidization curves, as described below. Specifically, the weight of the particles fluidized by air was compared to the weight of particles loaded into the bed.

The fluidization curves of the narrowest and widest distributions of the Gaussian and lognormal distributions investigated are shown in Figure 108. The experimental values of U_{cf}, namely the point at which the bed pressure drop (ΔP) becomes constant with further increases in superficial gas velocity (U_s), are marked with vertical lines. As observed in Figure 108, the transition from the packed-bed region (line of non-zero slope) to the fluidized region (horizontal line) for continuous distributions is not abrupt, compared to the precipitous change (i.e., discontinuity in slope values) expected for a monodisperse distribution. Especially for the wider lognormal distributions (Figure 108c and d), the transition is a smooth elbow, due to the range of minimum fluidization velocities (U_{mf}) of the various particle sizes contained in the distribution. Accordingly, a protocol for determining U_{cf} that identifies the point of minimum U_s at which the data points are within ± 1% of the W/A value was used. For all the distributions investigated, the

experimental pressure drops (data points) plateau at the measured bed weight (*W*) divided by the cross-sectional area (*A*) (horizontal dashed line), indicating that the bed was completely fluidized beyond U_{cf}. As expected, U_{cf} values are similar, because the distributions are centered about the same mean particle size (d_{sm}); it has been reported that U_{cf} values of the continuous distributions agree with U_{mf} of the mean particle size (Sun and Grace, 1990; Gauthier, Zerguerras *et al.*, 1999). Notably, the U_{cf} value of the widest distribution investigation, specifically lognormal distribution with σ/d_{sm} = 70%, is slightly higher than the other distributions, presumably due to the presence of the largest amount of coarse Group D particles.

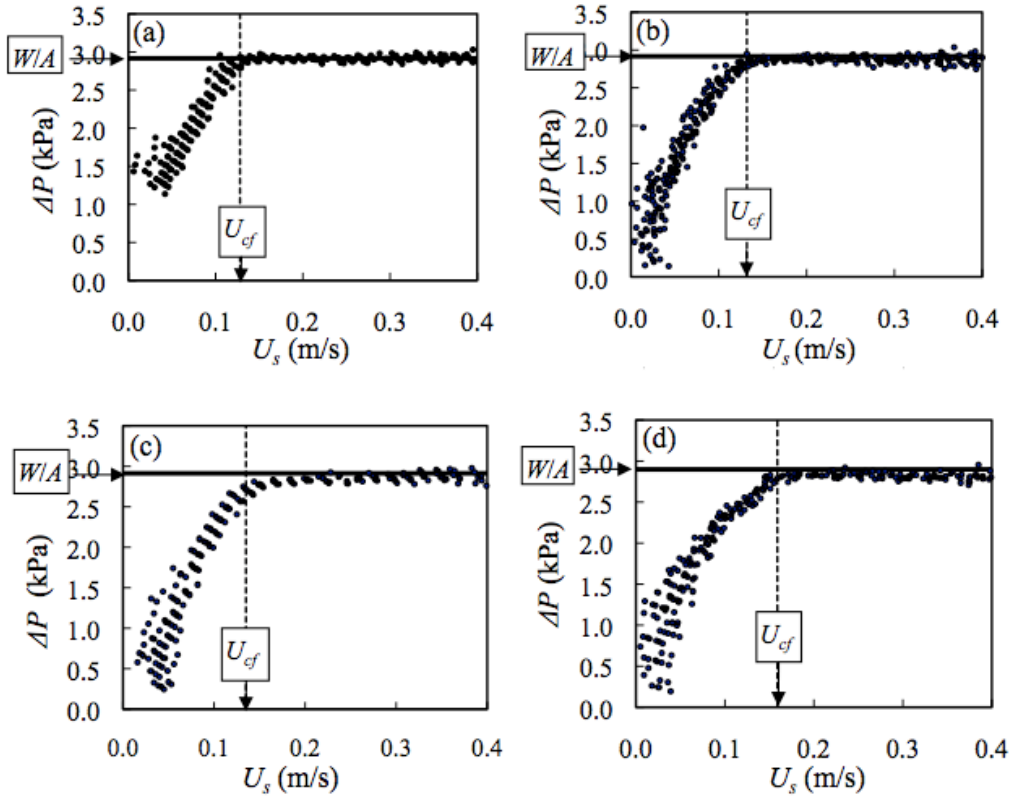

Figure 108. *Fluidization curves of Gaussian distributions with (a) σ/d_{sm} = 10% and (b) σ/d_{sm} = 30%, and lognormal distributions with (c) σ/d_{sm} = 30% and (d) σ/d_{sm} = 70%. The data points represent bed pressure drops during repeated defluidization and fluidization, while the horizontal dashed line represents the experimental bed weight over cross sectional-area (W/A).*

Interestingly, although a bed of monodisperse Group D particles do not fully fluidize, their presence in the lognormal distributions did not result in the under-prediction of *W/A*. In particular, as displayed in Figure 109, "monodisperse" Group D particles of size range 1 - 2 mm give a 13% under-prediction of *W/A*, indicating that the particles are not fully fluidized, and providing evidence that Group D particles exhibit poor fluidization quality. However, as previously shown in Figure 108c and d, the presence of the same Group D particles in lognormal distributions does not give rise to the under-prediction of *W/A*, even though they represent up to 24% by mass of the lognormal distribution with σ/d_{sm} = 70%. This observation that the presence of a wide range of particle sizes enhances fluidization of larger particles is especially noteworthy since the U_{mf} of the monodisperse Group D system, which agrees with existing empirical

correlations(Kunii and Levenspiel 1991), is about six times that of the U_{cf} of the continuous distributions contained in Figure 108. A possible explanation for the improvement of fluidization has been shown via discrete element model (DEM) simulations showing that systems with wide PSD exhibited higher particle velocities around bubbles and faster bubble growth, hence enhancing fluidization(Tagami, Mujumdar et al. 2009). As will be further elucidated in the following section, the width of a continuous distribution is an important factor in the hydrodynamics of fluidization.

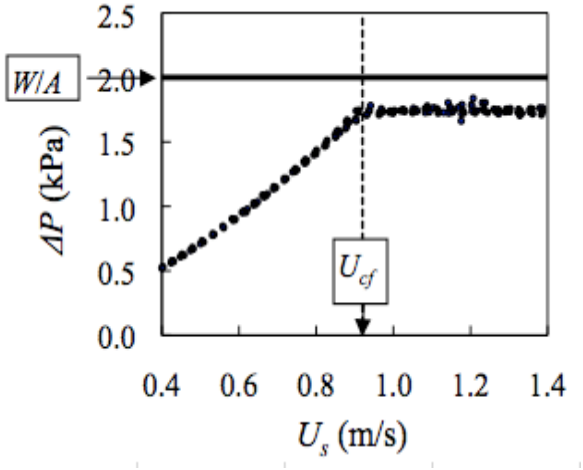

Figure 109. *Fluidization curve of monodisperse Geldart Group D sand of particle size range 1-2 mm. The data points represent repeated fluidization and defluidization, while the horizontal bold line represents the experimental W/A.*

Axial Concentration Profiles: The axial concentration profiles for the Gaussian distributions investigated are shown in Figure 110. The mass-based frequency (f_m) is on the x-axis and represents the proportion of each sieve cut for a given axial section. The dimensionless height (h/H) is on the y-axis. h/H is used for easier comparison across the distributions, because the different proportions of various partic*le sizes in different distributions result in slightly different packing heights. A vertical line on these plots implies no axial variation of concentration for a given sieve cut, thereby indicating a perfectly mixed system, while a contoured line implies segregation of different-sized particles. At least two experiments were carried out for each distribution, and the error bars represent the experimental variations, expressed as the difference between the maximum and minimum values obtained. Since the overall mass fraction of a given sieve cut changes between distributions of different widths, the appropriate comparison of the extent of segregation between the various distributions is the verticality of the lines on the axial segregation plots, rather than the absolute values of f_m. For the distribution with σ/d_{sm} = 10% (Figure 110a), it is observed that the h/H versus f_m plots for the various sieve cuts are almost vertical, indicating that the system is well-mixed. On the other hand, for the distribution with σ/d_{sm} = 30% (Figure 110c), the plots are far from vertical, indicating that comparatively extensive segregation is observed among the different sizes of sand particles. The gradual increase in segregation as the width of distribution is increased is hence apparent in Figure 110, providing experimental evidence to the DEM(Dahl and Hrenya 2005) and continuum-model(Fan and Fox 2008) simulation findings that wider distributions exhibit more extensive segregation for a gas-fluidized bed for Gaussian distributions in this range of

widths. Furthermore, Figure shows that the mass fractions of the coarser and finer particles are greater at the bottom and top of the bed, respectively, consistent with modeling and experimental (Rowe and Nienow 1976; Tang and Puri 2004; Cui and Grace 2007; Joseph, Leboreiro et al. 2007) (see references and references therein) findings of binary systems of size-segregating systems.

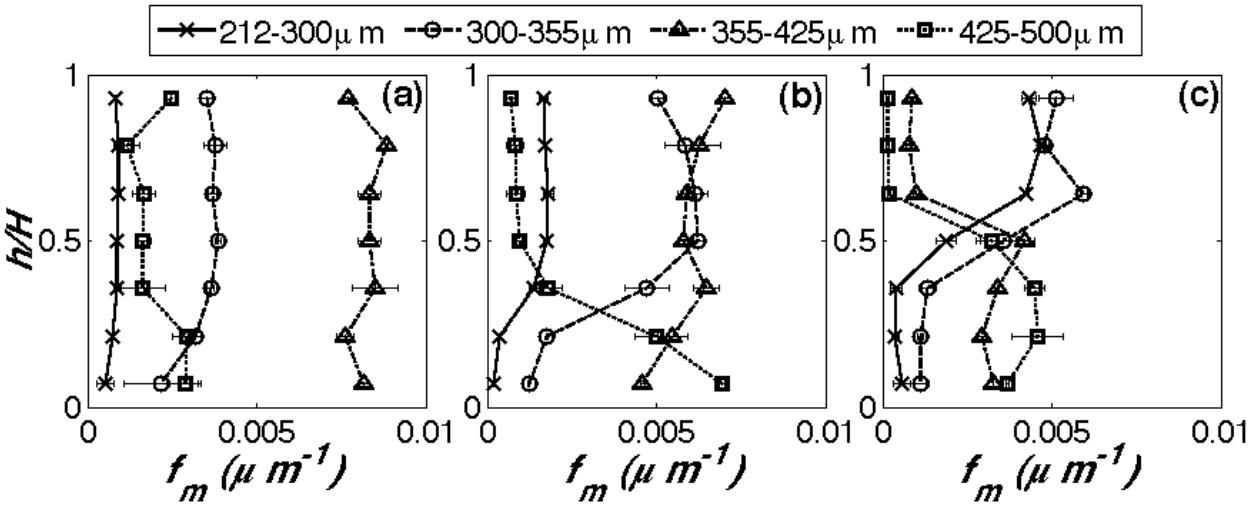

Figure 110. *Axial concentration profiles of Gaussian distributions with σ/d_{sm} = (a) 10%, (b) 15%, and (c) 30%.*

In addition to the axial concentration plots presented, the overall extent of segregation for each starting distribution can be compared using a single integrated quantity. This measure, examples of which include the mixing index (*M*) and segregation index (*s*), has been derived for binary distributions. The mixing index (*M*) takes the form(Rowe, Nienow et al. 1972; Wu and Baeyens 1998)

$$M = \frac{x}{< x >} \tag{57}$$

where *x* is the concentration of the larger particles in the topmost layer of the particle bed and <*x*> is the average concentration of the larger particles in the entire bed, such that *M* = 1 corresponds to perfect mixing and *M* = 0 implies perfect segregation. On the other hand, the segregation index (*s*) takes into account both particle sizes, and is expressed as(Goldschmidt, Link et al. 2003)

$$s = \frac{S - 1}{S_{\max} - 1} \tag{58}$$

The numerator in Equation 58 contains the ratio of the actual heights of the small and large particles which is indicative of the actual degree of segregation:

$$S = \frac{< h_{small} >}{< h_{large} >} \tag{59}$$

where $<h_{small}>$ and $<h_{large}>$ are the calculated average dimensionless heights of the small and large particles respectively. Specifically,

$$< h_{small} >= \sum_i \left(x_{small,i} * h_i \right) \tag{60}$$

$$< h_{large} >= \sum_i \left(x_{large,i} * h_i \right) \tag{61}$$

where h_i represents the dimensionless height (with respect to the bed height) of each axial section that is vacuumed out and analyzed for PSD and x_i represents the mass fraction of the species in that particular axial section.

The denominator in Equation 58 contains the associated maximum degree of segregation, which occurs when the small particles are wholly in the top portion while the large particles are all in the bottom portion:

$$<h_{small}>_{max} = x_{large} + 0.5\, x_{small} = 1 - 0.5\, x_{small} \tag{62}$$

$$<h_{large}>_{min} = 0.5\, x_{large} = 0.5\, (1 - x_{small}) \tag{63}$$

Hence, the maximum degree of segregation can be expressed as:

$$S = \frac{< h_{small} >_{\max}}{< h_{large} >_{\min}} = \frac{2 - x_{small}}{1 - x_{small}} \tag{64}$$

Accordingly, the segregation index (s) is defined in Equation 58 such that s = 1 corresponds to perfect segregation while s = 0 implies perfect mixing. Since M considers only the bigger particles and topmost layer, it is not as inclusive as s, which takes into account concentrations and averaged heights of both species in the binary mixture. Henceforth we consider only s to more accurately represent our data. Nonetheless, it is observed that M shows the same trends.

In order to quantify the extent of segregation for continuous size distributions, a new segregation index (s_{cont}) is introduced here based on an extension of the segregation index for binary mixtures (s). Specifically, the modifications made to s_{cont} are twofold: (i) the definitions of 'large' and 'small' needs to be changed, because the demarcation is not as clear-cut as in a binary distribution, and (ii) Equation 64 only works for a binary distribution, and hence was modified as described below (Equation 65). Regarding (i), 'large' and 'small' are now defined as the uppermost and lowermost sieve cuts that constitutes at least 10% by mass of the total mass of the bed, since the maximum experimental variation in the segregation data was observed to be 10% by mass. Regarding (ii), the maximum extent of overall segregation is re-defined for more general case because x_{large} is no longer simply (1- x_{small}), as was assumed in Equations 62 through 64. By lifting this assumption, a more general form of S_{max} is obtained:

$$S_{\max} = \frac{2x_{large} + x_{small}}{x_{large}} \tag{65}$$

Similar to the binary definition, the above modification for continuous distributions ensures that s_{cont} = 1 corresponds to complete segregation while s_{cont} = 0 implies complete mixing. These segregation indices (s_{cont}) and the corresponding make-up of 'large' and 'small' particles are presented in Table 6. It is worth noting that although the percentage of 'large' and 'small' particles are not constant through the various distributions due to limited sieve meshes available, effort was made to make the numbers similar for the fairest comparison possible. Results clearly show an increase in s_{cont}, which corresponds to an increase in the extent of segregation, with the width of the Gaussian distributions.

***Table 6**. Segregation indices (s_{cont}) of Gaussian distributions investigated.*

(%)	s_{cont}	mass % of 'large'	mass % of 'small'
10	0.024	16.8	25.9
15	0.175	21.2	12.5
30	0.284	18.9	28.7

Analogous axial concentration profiles and segregation indices (s_{cont}) are contained in Figure 111 and Table 7 for the lognormal distributions investigated. As evident in Figure 111, while the segregation profiles for σ/d_{sm} = 10% and 70% are vertical lines indicating well-mixed systems, those for σ/d_{sm} = 30% and 50% are contoured lines indicating segregated systems. This trend is corroborated with the data contained in Table 7, which shows quantitatively that while lognormal distributions with σ/d_{sm} = 10% and 70% have similarly low values of s_{cont}, the distribution with σ/d_{sm} = 30% has the highest s_{cont}, implying the most segregated system. This non-monotonic segregation behavior of lognormal distributions has not been previously reported in simulations or experiments. Nonetheless, non-monotonic segregation levels have been observed in binary mixtures with species of different material density (but same size), wherein segregation has been observed to be strongest for intermediate compositions, with fairly well-mixed systems at low- or high-concentrations of jetsam(Joseph, Leboreiro et al. 2007). Looking back at Figure 106b, it is apparent that the lognormal distribution with σ/d_{sm} = 70% does consist of the greatest amounts of the finest as well as largest particles. However, it is worthwhile to note that previous work on binary mixtures does not reveal a non-monotonic segregation behavior when considering species with the same material density but different sizes(Joseph, Leboreiro et al. 2007), which is most analogous to the continuous PSDs under consideration in this work.

A possible explanation may be related to the bubbling phenomenon. Rowe et al.(Rowe, Nienow et al. 1972) were the first to suggest that rising bubbles are the vehicles for particle mixing. Quantitatively, Nienow et al.(Nienow, Rowe et al. 1978) found the rate of bubbling, which has been associated with mixing behavior, as being proportional to the excess gas velocity (U_{excess}) defined as

$$U_{excess} - U_s - U_{mf \cdot small} \tag{66}$$

where $U_{mf,small}$ is the minimum fluidization velocity of the smallest particles and U_s is the operating superficial gas velocity (which in this work is 1.2 U_{cf}). When $U_{excess} < U_s$, segregation predominates, and when $U_{excess} > U_s$, mixing takes over. The slightly larger U_{cf} of the lognormal distribution with σ/d_{sm} = 70% (Figure 108d) may thus be associated with more mixing: while a wider distribution is expected to result in more segregation by virtue of the increased number of species present, the effect of mixing based on excess gas velocity (U_{excess}) may tilt the mixing-segregation balance the other way. Subsequently, some studies have shown that a wide size distribution usually give the highest reactor efficiency, while the narrow blend give the lowest(Sun and Grace 1990), possibly associated with bubbling patterns in bed(Zenz and Othmer 1960, page 278). DEM simulations(Tagami, Mujumdar et al. 2009) have also shown that systems with a wide PSD exhibit higher particle velocities around bubbles, while

experiments(Grace and Sun 1991; Beetstra, Nijenhuis et al. 2009) corroborated the enhancement of mixing through the production of smaller and faster-moving bubbles. However, it can be argued that if the lognormal distribution with σ/d_{sm} = 70% exhibits the least extent of segregation due to its greatest width, why is it that the Gaussian distribution with the greatest width of σ/d_{sm} = 30% did not similarly exhibit a well-mixed system? Grace and Sun(Grace and Sun 1991) reviewed the influence of PSD on fluidized bed reactors and asserted that fines content per se is not a sufficient parameter to characterize segregation: their nature and the overall size distribution have to be considered. Correspondingly, future work is needed to get a clearer physical picture of the mechanisms leading to the non-monotonic segregation patterns observed here.

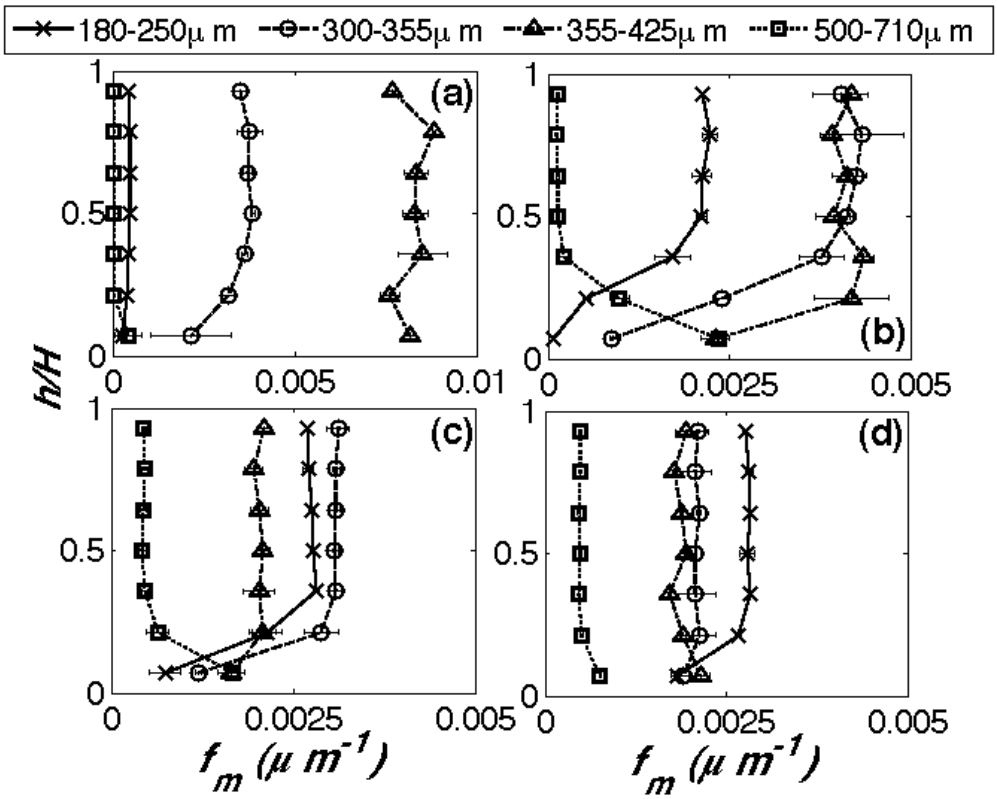

Figure 111. *Axial segregation profiles of lognormal distributions with (a) σ/d_{sm} = 10%, (b) σ/d_{sm} = 30%, (c) σ/d_{sm} = 50%, and (d) σ/d_{sm} = 70%.*

Table 7*. Segregation indices (s_{cont}) of lognormal distributions investigated.*

(%)	s_{cont}	mass % of 'large'	mass % of 'small'
10	0.024	16.8	25.9
30	0.168	13.2	13.6
50	0.074	18.1	27.6
70	0.022	19.7	19.6

The segregation extents for the various widths of Gaussian and lognormal distributions investigated (Table 6 and Table 7) are compared directly in the plot of segregation indices (s_{cont}) in Figure 112. As pointed out previously, results in this work suggest that, while the segregation extents are positively correlated with the PSD widths for Gaussian distributions, a non-monotonic behavior exists for lognormal distributions. Comparing the segregation indices (s_{cont}) shows that the lognormal distribution with σ/d_{sm} = 50% is less segregated that the Gaussian distribution with σ/d_{sm} = 30%. At first glance, this observation seems contrary to previous simulation work for fluidized beds (Dahl and Hrenya 2005; Fan and Fox 2008), which compared segregation in Gaussian distributions of σ/d_{sm} up to 30% and a lognormal distribution of σ/d_{sm} = 50%, and reported that the lognormal distribution exhibits the most extensive segregation. However, two distinctions between the previous simulations(Dahl and Hrenya 2005) and the current experimental work are worth pointing out. First, the PSDs in the simulations were number-based, whereas the PSDs in the current work are mass-based. Perhaps more importantly is a difference in particle properties. In comparing distributions of different widths, the previous simulation work(Dahl and Hrenya 2005) also incorporated a change in the restitution and friction coefficients of the particles. More specifically, the widest lognormal distribution investigated (σ/d_{rms} = 50%, where d_{rms} is the root-mean-square diameter) also had the least dissipative particles, which led to a bubble-less (and thus relatively segregated) system; the narrower distributions investigated in the simulations had more dissipative particles and correspondingly exhibited bubbling (see Hoomans et al.(Hoomans, Kuipers et al. 2000) for further discussion of relationship between particle properties and bubbling characteristics). In the current set of experiments, the same material (sand) was consistently used, and bubbles were observed in all systems. Hence, a strict comparison between the previous simulations(Dahl and Hrenya 2005) and current experiments is not warranted.

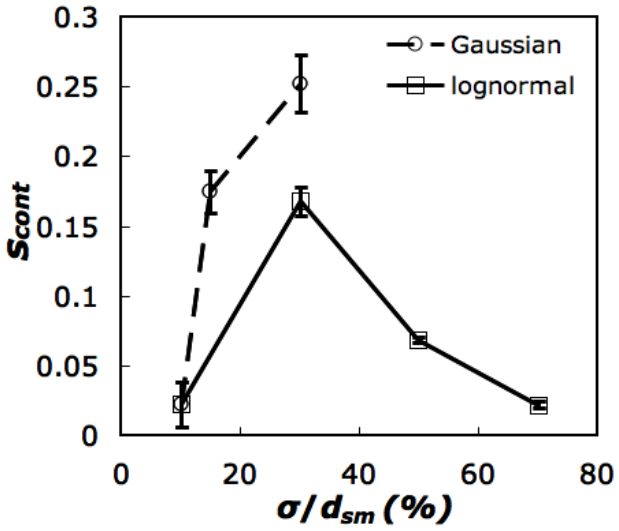

Figure 112. *Plot showing the correlation between s_{cont} and σ/d_{sm} for Gaussian and lognormal distributions.*

Shape of Local PSD: In addition to the axial concentration profiles associated with each size range given above, the shape of the size distribution (Gaussian or lognormal) at a given axial height is also of interest. Although the PSD of the entire bed mass is specified (e.g., Gaussian with σ/d_{sm} = 10%), segregation of particles may lead to different local PSDs. For the Gaussian distributions investigated, Figure 113 shows how the shapes of the local PSDs vary axially along the bed. The local PSDs are nearly superimposed for the distribution with σ/d_{sm} = 10% (Figure 113a), except for a slight rightward shift of the PSD at the bottommost axial section. This behavior further indicates a well-mixed system, as previously elucidated, implying that a system with a narrow distribution behaves similar to a monodisperse system. For the distributions with σ/d_{sm} = 15% and 30% (Figure 113b and c), the PSDs associated with various axial locations are more separated, with a rightward shift of the PSDs as the particle bed is traversed downwards, indicating again the segregation of bigger particles toward the bottom. Furthermore, for the distribution with σ/d_{sm} = 10% (Figure 113a) and 15% (Fogire 113b), the PSDs at each axial location still resemble a Gaussian distribution. However, more deviations are observed for the distribution with σ/d_{sm} = 30% (Figure 113c), especially for the two bottom-most PSDs.

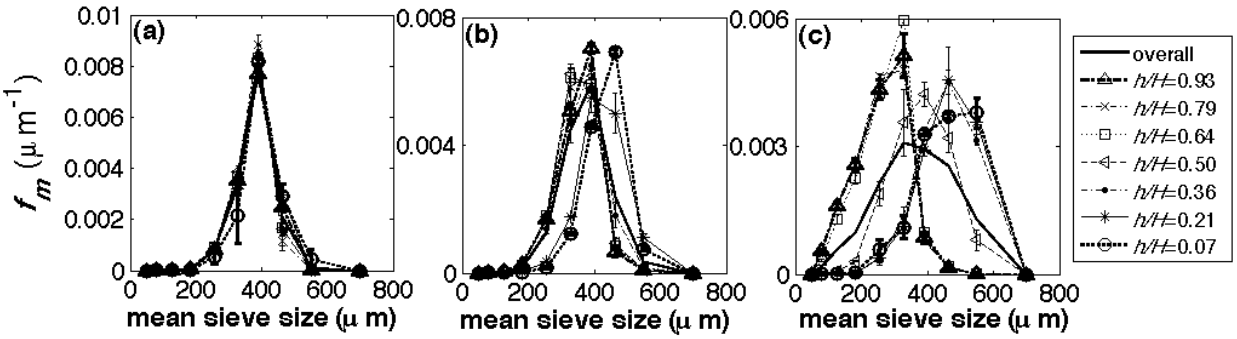

Figure 113. *Axial PSDs of Gaussian distributions with (a) σ/d_{sm} = 10%, (b) σ/d_{sm} = 15%, and (c) σ/d_{sm} = 30%.*

To better quantify how closely the shape of the local distribution mimics that of the overall distribution, comparisons between the (local) experimental PSD and an exact Gaussian PSD (as given by Equation 55) are made by minimizing the root-mean-square (rms) difference between them via changing the values of d_{sm} and σ/d_{sm}. It should be noted that the local distributions may have different d_{sm} and σ/d_{sm} but still characterized by the same shape (i.e. Gaussian or lognormal). For the Gaussian distribution with σ/d_{sm} = 10%, the statistics of the PSDs show that the d_{sm} and σ/d_{sm} for the PSD at each axial location are similar to the initial PSD with d_{sm}'s approximating 375 μm and σ/d_{sm}'s approximating 10%, further indicating a well-mixed system. Axial variations in minimized rms differences between experimentally generated and exact PSDs for each Gaussian distribution are plotted in Figure 114. As shown in Figure 114, the rms differences are less than 0.001% and 10% for all local PSDs obtained for the Gaussian distributions with σ/d_{sm} of 10% and 15%, respectively. On the other hand, rms differences average about 15% for the upper few PSDs of the Gaussian distribution with σ/d_{sm} of 30%, with rms differences as high as 40% for the two bottom-most PSDs. It seems that the wider the distribution, the larger the deviation of the local shape of the local PSD from an exact Gaussian, which is not surprising considering the increase in the number of species present in a wider distribution. Nonetheless, it can be concluded that the Gaussian shape of the PSDs at each axial section of the bed is largely preserved, which agrees with previous simulation findings in both granular and gas-fluidized systems(Dahl and Hrenya 2004; Dahl and Hrenya 2005). The observation that the bottommost PSDs no longer remain Gaussian has also been shown in DEM simulations(Dahl and Hrenya 2005), and it was postulated to be due to the bottom regions being more stagnant.

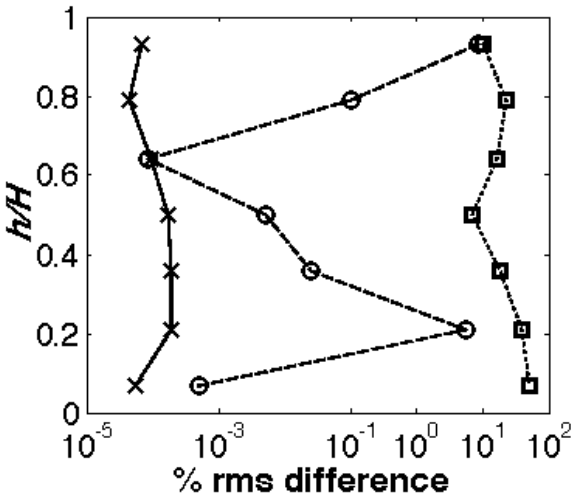

Figure 114. *Plot showing variation of the minimized rms difference between the PSD at each axial location and the equation-generated PSD for the Gaussian distributions investigated.*

For lognormal distributions, the analogous plots for variations in the local PSD are shown in Figure 115 and Figure 116. Figure 115 again shows that the shape of the local PSD at each axial location resembles the shape of the overall PSD, namely a lognormal distribution. Figure 116 further quantifies how similar each local PSD is to an exact lognormal PSD by a plot of the axial variation of the minimized rms difference between the experimentally obtained and exact lognormal PSD. The increased discrepancies for wider lognormal distributions of $\sigma/d_{sm} \geq 30\%$

are much greater than that for σ/d_{sm} = 10%. Also, it is apparent that the greatest discrepancy for lognormal distributions with σ/d_{sm} > 30% is of the bottommost PSD at h/H = 0.07. Similar to the findings for the Gaussian distribution with σ/d_{sm} = 30%, the minimized rms differences between experimentally obtained and exact PSDs for the lognormal distribution are mostly about 10%, except for the PSDs at the bottommost positions. Except for the lognormal distribution with σ/d_{sm} = 10%, it appears that the bottommost (h/H = 0.07) PSDs of all the other distributions are not lognormal, presumably due to the predominance of the coarser Group D particles in the bottommost layer of the bed. As previously mentioned, DEM simulation of gas-fluidized bed has shown similarly that the measured local PSD are not Gaussian or lognormal in regions where particles move infrequently (e.g. nearly stagnant regions of the bed near the bottom)(Dahl and Hrenya 2005).

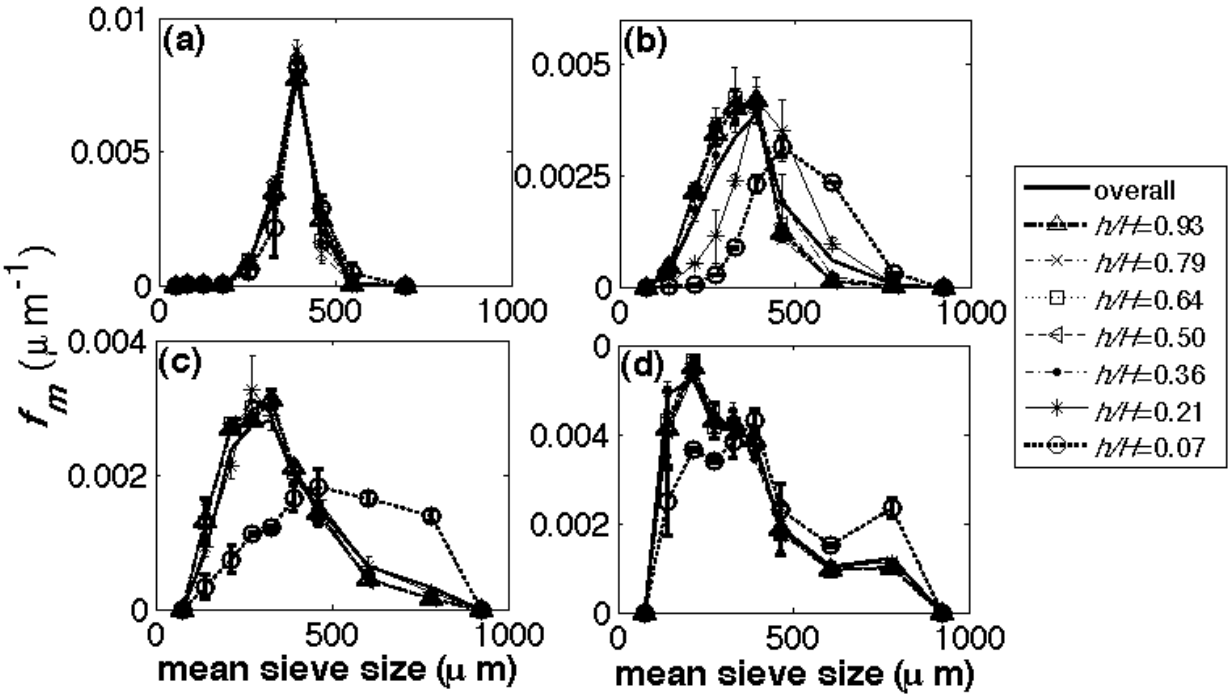

Figure 115. *Axial PSDs for the lognormal distributions with (a) σ/d_{sm} = 10%, (b) σ/d_{sm} = 30%, (c) σ/d_{sm} = 50%, and (d) σ/d_{sm} = 70%.*

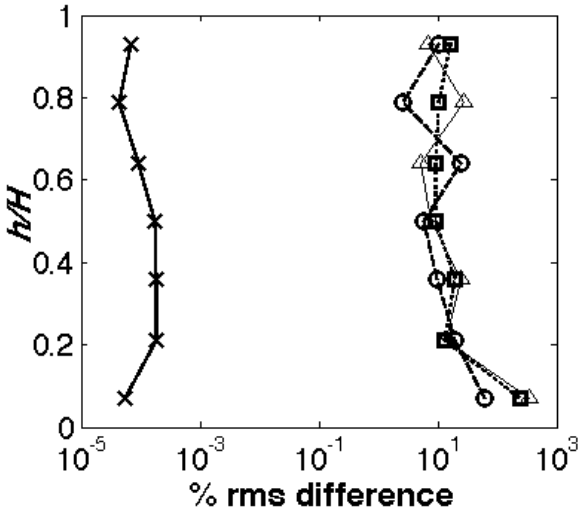

Figure 116. *Plot showing variation the minimized rms difference between the PSD at each axial location and the equation-generated PSD for the lognormal distributions investigated.*

Summary: Experiments involving low-velocity, bubbling, gas-fluidized beds have been carried out for Geldart Group B particles of various widths of Gaussian and lognormal distributions, with a focus on the axial concentration profiles. Specifically, fluidization curves were first generated to determine the velocity for complete fluidization (U_{cf}), followed by steady-state fluidization at 1.2 U_{cf}. Although only Group B particles were used in the Gaussian distributions, up to 24% by mass of the widest lognormal distribution (σ/d_{sm} = 70%) was made up of Group D particles. Due to the nature of the lognormal distribution, it is not possible to restrict all particle sizes to within Group B classification, and larger Group D particles have to be included for an accurate representation.

The complete fluidization velocity (U_{cf}) is the minimum superficial gas velocity (U_s) beyond which bed pressure drop (ΔP) equals to *W/A*. As such, *W/A* is a good indicator for quality of fluidization. Interestingly, although monodisperse Geldart Group D particles exhibited poor fluidization, as indicated by the failure of the bed pressure drop to attain *W/A*, their presence in the wider lognormal distributions did not stunt the quality of fluidization.

Results for the Gaussian (σ/d_{sm} = 10%, 15%, and 30%) and lognormal (σ/d_{sm} = 10%, 30%, 50%, and 70%) distributions investigated show that (i) increased segregation is observed for wider Gaussian distributions, whereas a non-monotonic correlation exist between segregation extents and width of lognormal distributions, (ii) similar to previous findings for binary mixtures, finer and coarser particles tend to segregate respectively to the top and bottom, (iii) the shape of the PSD (i.e., Gaussian or lognormal) at each axial section is preserved with respect to the overall PSD, except for the bottommost PSDs of the wider distributions. With the exception of the surprising finding of the non-monotonic behavior of the segregation extents with increasing widths of lognormal distributions, the experimental findings agree with previous discrete particle simulations(Dahl and Hrenya 2005) and continuum modeling(Fan and Fox 2008) of gas-solid fluidized beds with continuous size distributions. It should be noted that the nonmonotonic segregation behavior with respect to width of the lognormal distributions is not necessarily at odds with previous simulation(Dahl and Hrenya 2005) results. More specifically, bubbles were absent in the simulation of the widest lognormal distribution(Dahl and Hrenya 2005),

presumably due to a change in particle properties (restitution and friction coefficients), whereas bubbles were consistently observed in the current experiments, which all involved the same particle material (sand). More work is needed to resolve this issue definitively.

An interesting follow-up of this work is the investigation of bubbling phenomena associated with the various widths of the Gaussian and lognormal PSDs. Bubbles have been reported to be mixing agents, and may hold the key to developing a clearer physical picture to explain the non-monotonic segregation behavior with respect to the widths of the lognormal distributions. For example, DEM simulations have indicated that systems with a wide particle size distribution exhibit higher particle velocities around bubbles, resulting in faster bubble growth and its subsequent rise through the fluidized bed, thereby promoting mixing(Tagami, Mujumdar et al. 2009). Experimental evidence of this observation would be useful, because bubbling and species segregation behaviors are expected to be tightly coupled. Accordingly, the next section focuses on the investigation of bubble characteristics for the same systems presented here.

Task 4.3.2: Link between Bubbling and Species Segregation Behaviors[3]

Abstract: Experiments involving a bubbling, gas-fluidized bed with Gaussian and lognormal particle size distributions (PSDs) of Geldart Group B particles have been carried out, with a focus on bubble measurements. Previous work (Section 4.3.1) in the same systems indicated the degree of axial species segregation varies non-monotonically with respect to the width of lognormal distributions(Chew, Wolz et al. 2010). Given the widely accepted view of bubbles as 'mixing agents', the initial expectation was that bubble characteristics would be similarly non-monotonic. Surprisingly, results show that measured bubble parameters (frequency, velocity and chord length) increase monotonically with increasing width for all PSDs investigated. Closer inspection reveals a bubble-less bottom region for the segregated systems, despite the bed being fully fluidized. More specifically, results indicate that, the larger the bubble-less layer is, the more segregated the system becomes. The direct comparison between bubbling and segregation patterns performed provides a more complete physical picture of the link between the two phenomena.

Introduction*:* Results in Section 4.3.1 on continuous PSDs reveal an unexpected non-monotonic (increases then decreases) axial species segregation behavior with respect to distribution width(Chew, Wolz et al. 2010), which is a deviation from binary mixtures. Specifically, while binary mixtures have been shown to increasingly segregate with increasing disparity in size and/or density(Rowe and Nienow 1976; Tang and Puri 2004; Cui and Grace 2007; Joseph, Leboreiro et al. 2007), the trend is not so straightforward for continuous distributions. This surprising observation provides the motivation for the current effort. In particular, the objective of this work is to better understand the driving force behind the observed non-monotonic segregation behavior, with an eye toward the link between bubbling and species segregation.

Because bubble characteristics are also known to vary along the height of a bed (e.g., bubbles can grow with height), the gas-solid contact times of segregated particles at the top and the bottom of the bed may vary, thereby impacting the overall efficiency of the unit. Before discussing the role of bubbles in systems with particles of different sizes and/or material

[3] Chew and Hrenya, "Link between bubbling and segregation patterns in gas-fluidized beds with continuous size distributions", AIChE Journal, in press, 2011.

densities, a review of previous findings on bubbles in monodisperse beds is warranted. The bubbles observed in low-velocity, gas-fluidized beds can be traced to an inherent instability of the suspension(Davidson, Harrison et al. 1977; Jackson 2000; Sundaresan 2003; Yang 2003) and are believed to be the primary factor associated with solids dispersion, mixing, and reactor efficiency(Kunii and Levenspiel 1991; Kunii and Levenspiel 1991; Fan and Zhu 1998; Yang 2003). As early as 1962, Rowe et al.(Rowe, Partridge et al. 1962) used an X-ray technique to experimentally characterize bubbles in gas-fluidized beds, and the X-ray photographs of bubbles provided evidence that bubbles are primarily responsible for the axial movement of particles in the bed. Since then, detailed experimental observations of the bubbling phenomenon have sprouted(Cheremisinoff 1986; van Ommen and Mudde 2008; Mudde 2010), including, but not limited to, the volume of the wake behind the bubbles(Rowe and Partridge 1965), cloud formation around bubbles(Rowe, Partridge et al. 1964; Partridge and Rowe 1966), bubble coalescence(Clift and Grace 1971; Halow and Nicoletti 1992; Muller, Davidson et al. 2006) and breakage(Clift and Grace 1972), and exchange between the bubble and emulsion phase(Chiba and Kobayash.H 1970; Gibilaro and Rowe 1974; Basesme and Levy 1992). Generally, bubbles are commonly referred to as 'mixing agents', carrying particles efficiently upwards and allowing particles to fall through them downwards(Rowe, Partridge et al. 1962; Rowe and Partridge 1965; Rowe, Partridge et al. 1965; Rowe, Agbim et al. 1972).

For fluidized beds with particles of different sizes, studies on bubbling are scarcer. It has been reported that addition of fines (particle diameter < 45 μm) improves mixing(Rowe, Santoro et al. 1978; Yates and Newton 1986; Du, Fan et al. 2002), and electrical capacitance tomography has further verified that the enhanced mixing is brought about by the increase in the relative proportion of gas flowing interstitially and that the maximum mixing is at a fines content of 15%(Du, Fan et al. 2002). More recently, Beetstra et al.(Beetstra, Nijenhuis et al. 2009) determined experimentally the impact of fines and distribution width of Geldart Group A particles on bubbling effects, and it was found that either increasing the width of the PSD or increasing fines amount independently reduced bubble size at high velocity (10 times minimum fluidization velocity, U_{mf}) and enlarged bubble size at low velocity (1.5 U_{mf}). DEM simulations have also indicated that systems with a wider PSD exhibit higher particle velocities around bubbles, resulting in faster bubble growth and its subsequent rise through the fluidized bed(Tagami, Mujumdar et al. 2009). Collectively, these efforts shed light on how the presence of a size distribution alters the bubbling behavior.

Although a direct link between bubbling behavior and species segregation is often presumed, experimental studies with side-by-side measurements of bubble parameters and species segregation are lacking. In an effort to build on previous knowledge on the effect of continuous PSDs on species segregation and bubbling phenomena, the objective of the current work is twofold: (i) to experimentally determine the impact of the width of the PSD on bubble velocity, bubble frequency, and bubble size, and (ii) to compare the bubble measurements with species segregation measurements. The latter is of particular importance in order to determine whether bubbles also serve as the primary 'mixing agents' for polydisperse systems. A particularly good test case for this hypothesis is the species segregation results shown in Figure 112 (Chew, Wolz et al. 2010), which indicates that, while the level of segregation increases with width for Gaussian distributions, a non-monotonic behavior exists for lognormal distributions. Note that Gaussian distributions with σ/d_{sm} > 30% are not physically possible due to the introduction of negative particle diameters at wider distributions widths. Hence, with regard to objective (ii), the pertinent question is: do bubble parameters (frequency, velocity, and chord

length) in systems with Gaussian distributions behave monotonically with respect to distribution width, while the bubbles characteristics behave in a non-monotonic manner with increasing width of lognormal distributions?

In the current effort, bubbling measurements have been carried out for the same set of systems described in Task 4.3, such that a direct comparison between degree of segregation and bubbling behavior is possible. Surprisingly, the results indicate that bubble parameters (frequency, velocity and chord length) increase monotonically with an increase of PSD widths for all Gaussian and lognormal distributions examined. Accordingly, a direct correlation between measured bubble characteristics and degree of segregation does not exist. More explicitly, even though a non-monotonic correlation between degree of segregation and the width of lognormal distribution was observed, the bubbling parameters show a monotonic increase with PSD width. Nonetheless, a more careful examination of the data reveals the presence of a bubble-less layer in segregated systems. The height of this bubble-less layer is tightly coupled to the degree of segregation, thereby providing the sought-after physical link between bubbling and segregation patterns.

Experiment Description – Experimental Apparatus: The experimental setup for all bubbling experiments is identical to that used in Task 4.3.1 (Chew, Wolz et al. 2010) for the corresponding segregation experiments. As further illustrated in Figure 117, for this suite of experiments, the axial ports along the column facilitate the insertion of the fiber optic probe used for detecting bubbles. Specifically, seven ports, spaced 2.54 cm axially apart and the lowest of which is 5.08 cm above the distributor plate, are available for insertion of the fiber optic probe.

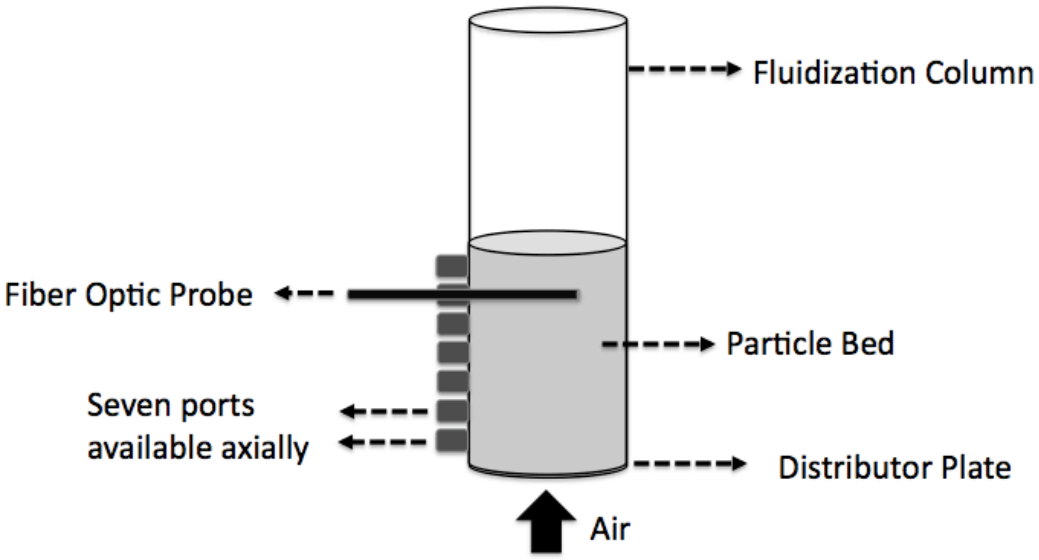

Figure 117. *Experimental set-up.*

In this section, the objective is to obtain bubble measurements for the same PSDs given in Figure 105. Accordingly, the experimental protocol is similar to that in Section 4.3.1 (Chew, Wolz et al. 2010), except that a fiber optic probe is utilized to obtain information on the bubble characteristics. At the start of each run, the fiber optic probe was inserted into one of the seven ports, and positioned such that the probe tip was flush with the inner wall of the column. Then, the prepared distribution of sand was placed in the column. Similar to Section 4.3.1, the particle

bed was mixed at high velocity (three times superficial velocity for complete fluidization (3 U_{cf})) for 15 minutes, and then fluidized at 1.2 U_{cf} for one hour to achieve a statistical steady state. Afterwards, the fiber optic probe was positioned sequentially at each of the nine radial positions to collect data for one minute. The same protocol was then repeated for the other axial locations. To obtain reasonable 95% confidence intervals of the data, each measurement was repeated ten times.

Fiber Optic Probe and Signal Analysis: With regards to the fiber optic probe, it consists of two bundles of fibers, one positioned vertically above the other. Each bundle contains three fibers: one fiber is used to transmit the light source, the second is the receiver conduit, while the third is redundant but is an important spare, as displayed in Figure 118. A higher voltage signal is obtained from the receiving fiber when light emitted from the light-source fiber is blocked, as occurs when the probe is surrounded by the emulsion (particle-rich) phase. On the other hand, a lower voltage signal is obtained when light from the emitter is relatively unobstructed, which occurs when the probe tip is surrounded by a bubble. Hence, as illustrated in the voltage traces of the bottom and top fiber bundles given in Figure 119, which is a plot of voltage measured by the probe versus time, bubbles appear as downward spikes in the voltage signal. Information about the bubbles can thus be extracted by defining a threshold voltage value ($V_{threshold}$), which serves as a demarcation between bubbles and the emulsion phase.

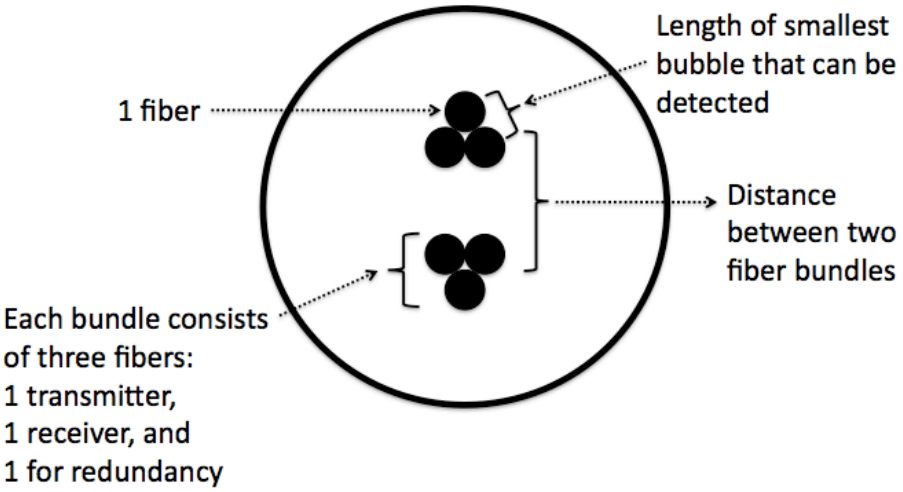

Figure 118. *Schematic of tip of fiber optic probe.*

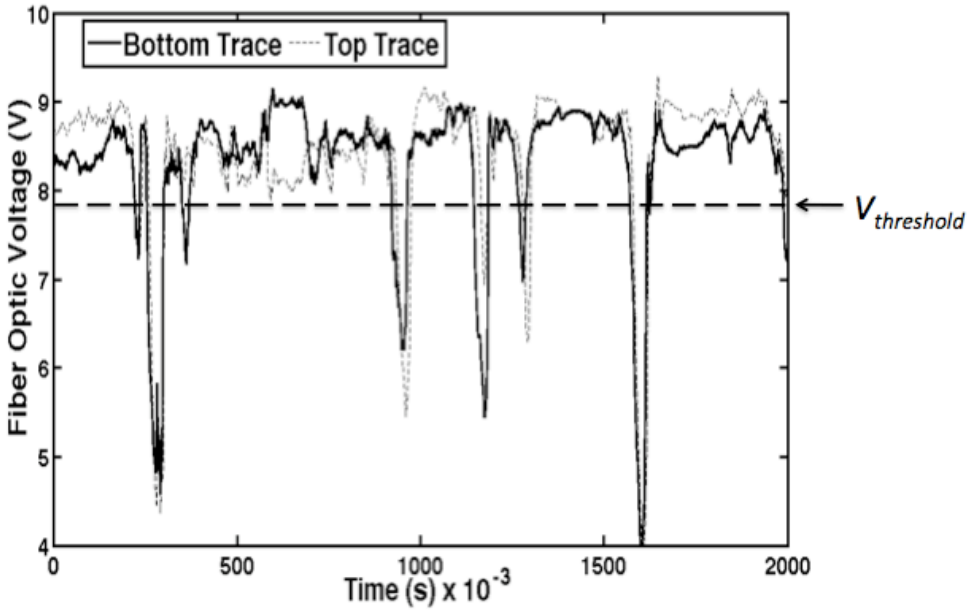

Figure 119. Example of bubble trace obtained from fiber optic probe: voltage vs. time for top and bottom bundle, where $V_{threshold}$ indicates the demarcation between bubble (below) and emulsion (above) phase.

As demonstrated in Figure 120, $V_{threshold}$ is determined by first plotting the probability density function (PDF) of the voltage trace obtained from the fiber optic probe at increments of 0.001 s. Then, the mode of the PDF and the 99th percentile of the cumulative count are determined. Finally, $V_{threshold}$ is calculated as the voltage at which the voltage difference (ΔV) between V_{mode} and $V_{99th\text{-}percentile}$ is the same as that between V_{mode} and $V_{threshold}$, namely:

$$\Delta V = V_{99th\ percentile} - V_{mode} \tag{67}$$

$$V_{threshold} = V_{mode} - \Delta V \tag{68}$$

With this value of $V_{threshold}$ at hand, a "bubble-only" trace can be obtained by eliminating the portions of the trace above $V_{threshold}$. From the bubble-only traces of the top and bottom fiber bundles, the frequency of bubbling, duration of each bubble, and bubble velocity can be found, as described below. In particular, analysis of these traces do not give bubble size per se, but instead bubble chord length, which is an indicator of bubble size(Clark and Turton 1988; Liu, Clark et al. 1998).

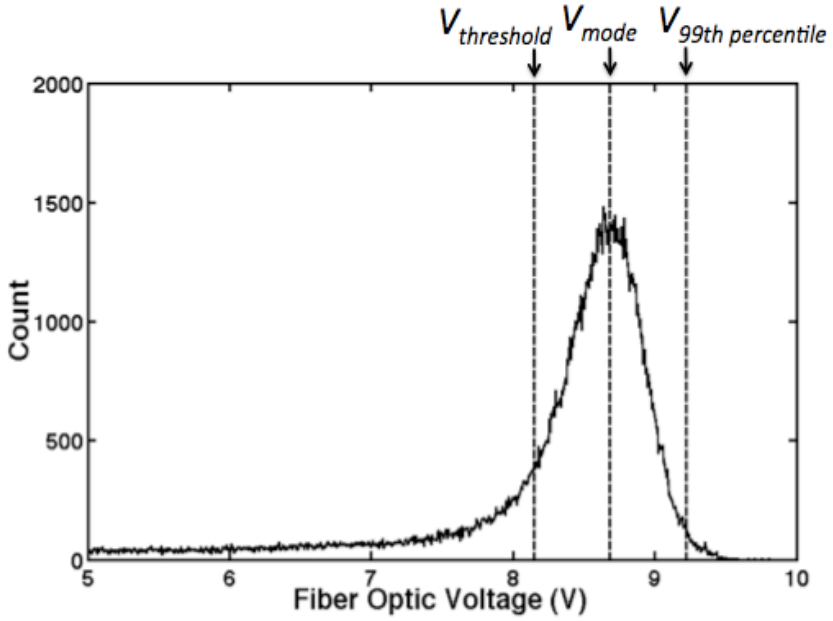

Figure 120. *Probability distribution function (PDF) of bubble trace, with* $V_{threshold}$, V_{mode}, *and* $V_{99th\text{-}percentile}$ *marked.*

With regards to bubble frequency, the number of segments of continuous data points above $V_{threshold}$ is counted, then normalized by measurement duration. As for vertical velocity of the bubble, when both the distance between the fiber bundles (Figure 118) and the time lapse between the voltage signals obtained by the bottom and top bundles are known, velocity can be derived. The distance between fiber bundles is measured to be 0.25 cm, while the time lapse is derived by cross-correlating the two signals to find where the point of strongest correlation lies. The cross-correlation formula is given as

$$\chi = \frac{\frac{1}{n}\sum_{i=1}^{n-d}(x_i - x_{mean})(y_{i+d} - y_{mean})}{\sigma_x \sigma_y} \tag{69}$$

where n is the total number of data points in each signal, d is the time lapse in units of data points being compared between the two signals, x_i and y_{i+d} are the bottom and top signal voltages respectively at time i and $i+d$, x_{mean} and y_{mean} are the mean of the bottom and top signal voltages respectively, and σ_x and σ_y are the standard deviation of each signal trace. $\chi = 1$ implies perfect correlation between the bottom and top signals, i.e. no time lapse. Dividing the distance between the fiber bundles (namely, 0.25 cm) by the time lapse derived by Equation 69 hence gives the vertical velocity of the bubbles. Then, bubble chord lengths can be obtained by multiplying the vertical velocity by durations of each segment of continuous data points above $V_{threshold}$.

Validation of fiber optic data for all bubble parameters considered here (frequency, velocity and chord lengths of bubbles) was obtained via comparison with existing correlations for monodisperse Group B particles (for example, see results of Hiraki and Kunii(Hiraki and Kunii 1969), Hilligardt and Werther(Hilligardt and Werther 1986), Mori and Wen(Mori and Wen 1975), as presented in Kunii and Levenspiel(Kunii and Levenspiel 1991), for bubble frequency, velocity, chord length respectively). It is also worth noting that previous work(Clark and Turton

1988) has shown that chord length can be used as a reliable indicator of bubble size for a given particle shape even if the bubble also has a horizontal component of velocity; for purposes of this work, however, only the direct measurement of chord length will be reported.

Results and Discussion: Experiments to obtain bubble data were carried out in an attempt to better understand the previously-reported, counter-intuitive segregation behavior displayed in Figure 112, namely the non-monotonic segregation levels observed with increases in the width of lognormal distributions. Accordingly, the experimental conditions were identical to those described in Section 4.3.1 (Chew, Wolz et al. 2010). The initial hypothesis being tested stems from the physical picture of bubbles as 'mixing agents'. In other words, would the previously observed segregation patterns correlate with bubbling characteristics – e.g., are higher bubbling frequencies observed in the more well-mixed systems? For this hypothesis to hold, bubbling parameters (some or all) should vary monotonically with PSD widths for Gaussian distributions and non-monotonically for lognormal distributions, analogous to the previously reported segregation trends (Figure 112). With this in mind, the bubbling characteristics (bubble frequency, velocity, and chord length) are presented as follows for both Gaussian and lognormal distributions of varying widths.

Before considering each bubble characteristic in turn, it is worthwhile to compare the axial and radial variations of the bubble quantities being measured. For purposes of illustration, a plot of mean bubble chord length versus dimensionless radius (r/R) is depicted in Figure 121, with error bars representing 95% confidence intervals. It is observed that mean bubble chord length increases with bed height, which is not surprising because bubbles are known to grow axially throughout a bed consisting of Geldart Group B particles (Kunii and Levenspiel 1991; Fan and Zhu 1998). Radial variation in bubble chord lengths is minimal compared to the noted axial variation, which is consistent with previous segregation results in which radial segregation was found to be negligible vis-à-vis axial segregation (Chew, Wolz et al. 2010). This consistency between bubbling and segregation results is not surprising since bubbles are often viewed as 'mixing agents'. Consequently, since radial variation of bubbling characteristics (namely, frequency, velocity, and chord length) is negligible, the focus of the following discussion will be on axial variation.

+

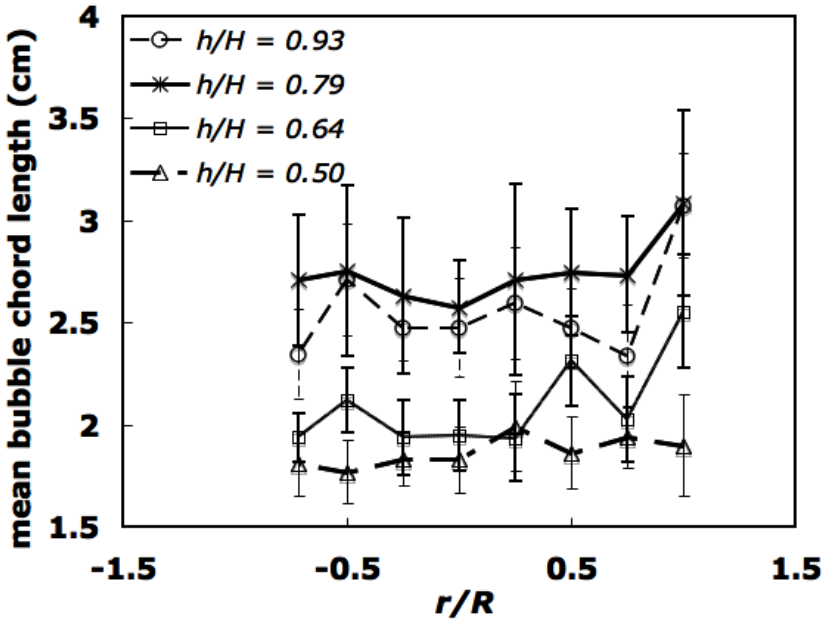

Figure 121. *Radial profiles of mean bubble size profiles at each axial position for Gaussian distribution with σ/d_{sm} = 30%.*

The bubble characteristics measured for Gaussian distributions with σ/d_{sm} = 10% – 30% are shown in Figure 122 through Figure 124, which are plots of bed height (h) versus bubble frequency, bubble velocity and bubble chord length, respectively. Error bars represent 95% confidence intervals. Analogously, Figure 125 through Figure 127 contain similar plots for lognormal distributions with σ/d_{sm} in the range of 10% to 70%. It should be noted that the larger error bars for the widest lognormal distribution of σ/d_{sm} = 70% should be expected, since biggest bubble chord lengths are found in this distribution, which implies a greater variation of chord lengths measured. Collectively, it is observed in Figure 122 through Figure 127 that bubble frequency, velocity and chord length increase monotonically with increase in PSD width for both Gaussian and lognormal PSDs. Because the previously reported degree of segregation for lognormal distributions is non-monotonic with respect to PSD width, the original anticipation that (some or all) bubble characteristics would be similarly be non-monotonic does not hold.

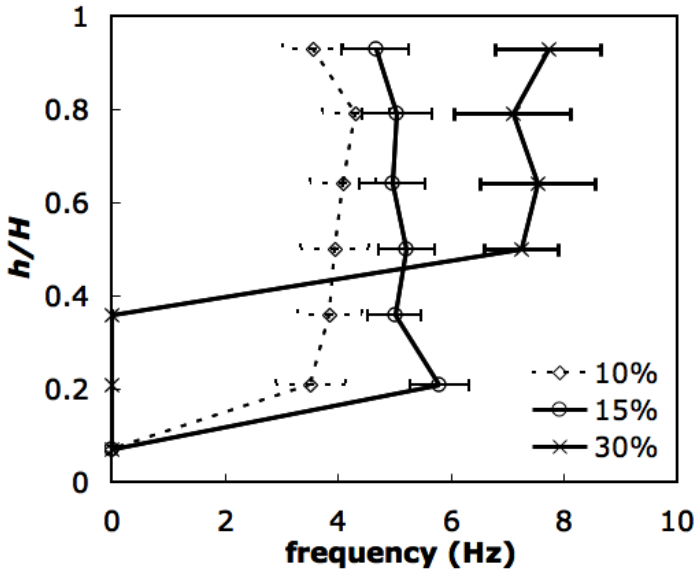

Figure 122. *Axial profiles of bubble frequency for Gaussian distributions.*

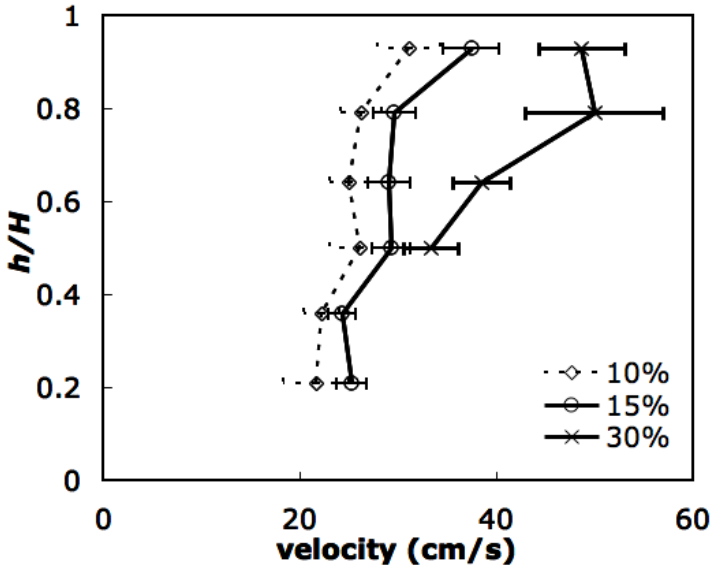

Figure 123. *Axial profiles of bubble velocity for Gaussian distributions.*

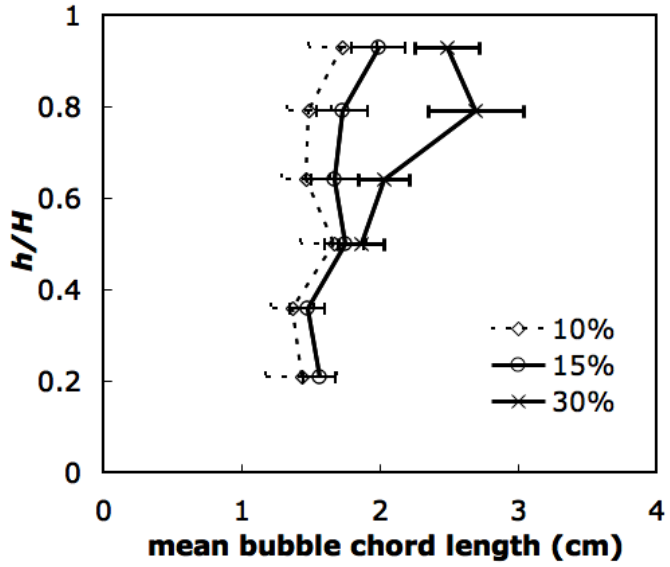

Figure 124. *Axial profiles of bubble chord length for Gaussian distributions.*

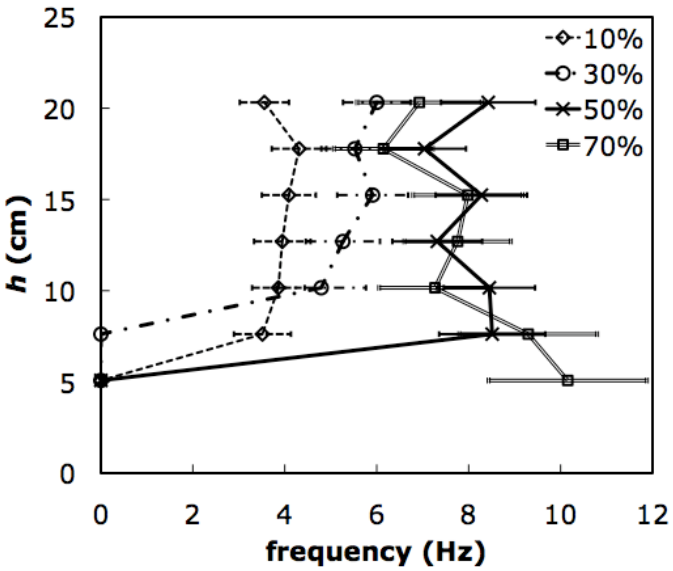

Figure 125. *Axial profiles of bubble frequency for lognormal distributions.*

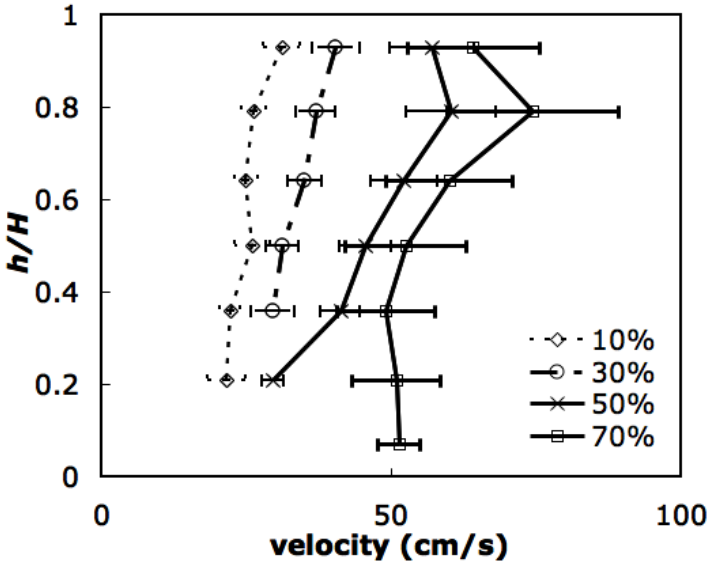

Figure 126. *Axial profiles of bubble velocity for lognormal distributions.*

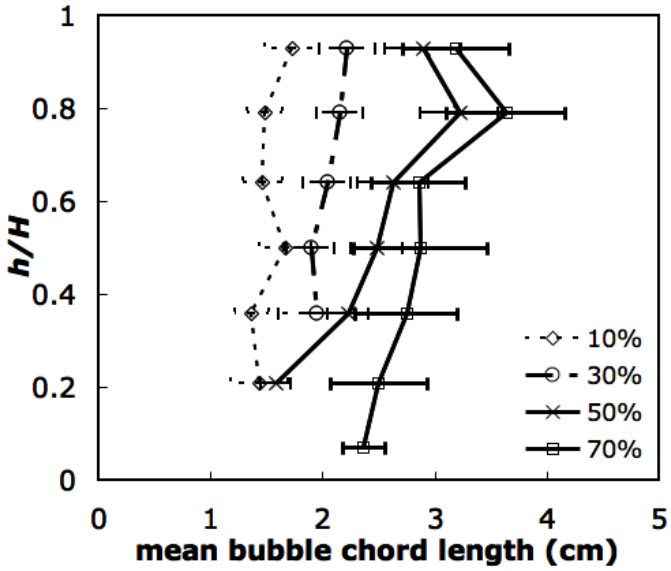

Figure 127. *Axial profiles of bubble chord length for lognormal distributions.*

Since bubbles have been known to play an important role in segregation behavior, it is worthwhile to take a more detailed look at the bubble trends to see if they are consistent with expectations. In particular, for both Gaussian PSDs and the narrower ($\sigma/d_{sm} \leq 30\%$) lognormal PSDs, the bubble characteristics vary monotonically with distribution width, as did the previously reported segregation measurements (Section 4.3.1)(Chew, Wolz et al. 2010). So the question remains: does the direction (increasing or decreasing) of the bubble trends make sense in light of the segregation data? More specifically, since bubbles are known to be 'mixing

agents', an increase in the frequency and velocity of bubbles is presumed to enhance mixing, and vice versa.

Because an increase in the width of a Gaussian PSD was found to lead to increased segregation (Figure 112), it was initially expected that bubble frequency and velocity would decrease with increasing PSD width. Surprisingly, it is observed in Figure 122 and Figure 123 that as the width of the Gaussian PSD increases, the frequency and velocity of the bubbles increase too. With regards to bubble sizes, bigger bubble sizes are expected to enhance mixing: Rowe et al.(Rowe, Agbim *et al.* 1972) asserted that the most important mechanism for transporting particles up the bed is by the bubble wake, which is approximately 20% of the volume of bubbles for the size range investigated here (Rowe and Partridge 1965). Nevertheless, Figure illustrates that bubble chord length increases with PSD width (consistent with previously reported work on Group A particles(Beetstra, Nijenhuis et al. 2009)), which thus does not seem to explain the increasing segregation extent. Hence, the results indicate that, not only is there a lack of correlation between bubbling and segregation phenomena (in particular, for lognormal distributions, bubbling is largely monotonic with an increase in width but segregation is not), but even for the distributions (Gaussian) where there is a correlation, the trends are *opposite* of expectation. A similarly puzzling observation is observed for lognormal distributions over the range in distribution widths associated with increasing extent of segregation (σ/d_{sm} = 10 – 50%). Namely, the bubble frequency, velocity, and chord length increase with distribution width (Figure 125 through Figure 127, respectively), which is seemingly contrary to the increasing levels of segregation (Figure 112).

A more careful look at the bubble measurements holds the key to understanding the link between bubbling and segregation patterns. Bubbles indeed serve as mixing agents, but the observed segregation is due instead to the *absence* of bubbles. In particular, a bubble-less layer – a bottom region of the bubbling bed where bubbles are not detected by the fiber optic probe – is observed in some systems. Specifically, the bubble-less region is where zero bubble frequency is detected, as evidenced in Figure 122 and Figure 125; the corresponding velocity and chord length are not plotted, as these parameters are not relevant in the absence of bubbles. This layer is evidenced in Figure 122 through Figure 124 for Gaussian systems. The largest bubble-less layer is observed for σ/d_{sm} = 30%, in which bubbles are not detected for the three lowest axial positions, whereas only the lowest axial position appears bubble-less for σ/d_{sm} = 10% and 15%. This trend in the bubble-less layers corresponds directly to segregation levels, which is greatest for σ/d_{sm} = 30% in the Gaussian system. A similar correspondence is noted for the lognormal systems across all distribution widths. Recall from Figure 112 that the segregation behavior is surprisingly non-monotonic with respect to PSD width for the lognormal distributions, with segregation extent peaking for the lognormal distribution with σ/d_{sm} = 30%. Figure 125 through Figure 127 illustrate that the most segregated lognormal distribution of σ/d_{sm} = 30% has the largest bubble-less layer. While bubbles are detected from the second lowermost position upwards for the more uniformly mixed lognormal distributions of σ/d_{sm} = 10%, 50% and 70%, bubbles can only be detected from the third lowermost position upwards for the lognormal distribution of σ/d_{sm} = 30%. Hence, the experimental data conclusively show that regardless of the magnitude of the bubble parameters measured in the upper layer, the larger the bubble-less layer, the more segregated a system becomes.

Two additional points are worth commenting regarding this link between the size of the bubble-less layer and the extent of segregation. First, although bubbles are not detected in the bottom layer, it is important to note that the entire bed (including the bottom layer) is known to

be completely fluidized, because the pressure drop across the bed (ΔP_{bed}) is equal to the ratio of the weight of the bed to the cross-sectional area of the column (W/A) at the operating superficial gas velocity (U_s). Second, the failure to detect bubbles can be traced to either bubbles being non-existent or bubbles being smaller than 0.1 cm, which is the separation between two fibers in each bundle (Figure 118). Regardless of the situation, however, mixing by bubbles will be ineffective in the bottom layer. More specifically, consider liquid-solid fluidized beds which do not exhibit the bubbling behavior. Such systems are known to display species segregation, which can be traced to the drag force descriptions for each species. This driving force for species segregation will also be present in gas-fluidized beds regardless of whether or not bubbles are present. When bubbles are present, however, their motion induces mixing of the various species. Accordingly, in the bottom bubble-less layer, the segregation mechanism dominates, resulting in a gradient of concentration across that layer (Figure 128). Along the same lines, in the upper bubbling layer, the mixing mechanism dominates, resulting in a well-mixed layer (note vertical nature of concentration profiles in upper layer of Figure 128).

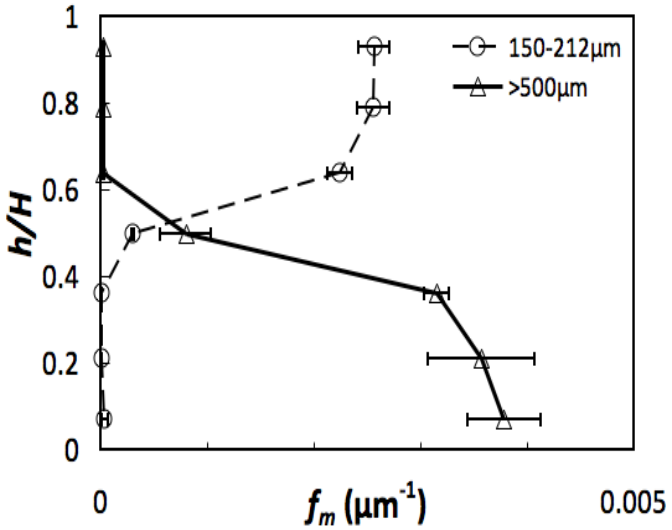

Figure 128. *Axial segregation profile of the finest and coarsest species for Gaussian distribution with σ/d_{sm} = 30%.*

Given that the presence of bubble-less layers provides a link between the observed bubbling behavior and (integrated) segregation index, it is useful to see how the axial profiles of each compare. Figure 128 is a plot of the axial segregation profiles of two different size species for the Gaussian distribution with σ/d_{sm} = 30%. The y-axis is the height of the particle bed (h), and the x-axis represents mass-based frequency (f_m), which is the mass fraction of the species normalized with respect to bin sizes. As depicted in Figure 128, two distinct layers of almost constant species concentration is observed, which has been similarly reported before for continuous PSDs(Hoffmann and Romp 1991; Chew, Wolz et al. 2010). Interestingly, but perhaps unsurprisingly, the range of heights over which the transition between the two distinct regions in Figure 128 arises (h/H ~ 0.4 – 0.6) corresponds exactly to the h range at which transition from bubble-less to bubbling regimes for σ/d_{sm} = 30% (Figure 122 through Figure 124). Other Gaussian and lognormal distributions similarly illustrate that the transition height between bubble-less and bubbling regime corresponds to the transition height between the two distinct layers in the axial segregation profiles (Section 4.3.1)(Chew, Wolz et al. 2010).

Summary. Although bubbles are widely viewed as 'mixing agents', a direct comparison between the species segregation trends in systems with continuous PSDs and corresponding bubble characteristics has been lacking. The previously-reported, non-monotonic segregation behavior(Chew, Wolz et al. 2010) (with respect to distribution width) for lognormal distributions provides a unique case study for testing the presumed link between segregation and bubble patterns. Hence, experiments involving low-velocity, bubbling, gas-fluidized beds have been carried out for Geldart Group B particles of various widths of Gaussian and lognormal distributions, with a focus of comparing axial segregation to bubble profiles.

Measured bubble parameters (frequency, velocity, and chord length) for the Gaussian (σ/d_{sm} = 10%, 15%, and 30%) and lognormal (σ/d_{sm} = 10%, 30%, 50%, and 70%) distributions are reported. A somewhat surprising initial observation is the lack of correlation between the degree of segregation and the measured bubble parameters, with respect to distribution width. In particular, although the lognormal distribution displays a non-monotonic degree of segregation as the distribution width is increased, all measured bubble parameters are found to increase over the entire range of distribution widths explored. Nonetheless, the key to understanding the segregation patterns is tied to the presence of a bubble-less layer at the bottom of the (fully-fluidized) bed. Namely, the degree of segregation is strongly tied to the height of the bubble-less layer at the bottom of the bed. For well-mixed systems (i.e., Gaussian distribution with σ/d_{sm} = 10%, and lognormal distributions with σ/d_{sm} = 10% and σ/d_{sm} = 70%), bubbles are present axially throughout most of the bed, hence enabling thorough mixing. For the most segregated systems among the Gaussian and lognormal distributions (σ/d_{sm} = 30%), the largest bubble-less bottom layer is observed, where although the entire bed is fully fluidized, bubbles are either absent or so small (< 0.1 cm) that they cannot be detected. Hence, the larger the bubble-less layer at the bottom of the bed, the more segregated the system becomes. Another new finding resulting from this work is the monotonic increase in all bubble parameters (frequency, velocity, and chord length) with respect to PSD width.

Finally, the experimental results in Task 4.3 are expected to be valuable towards the validation of discrete element models (DEM) and two-fluid models for continuous PSDs. To date, the vast majority of modeling efforts have focused on binary mixtures, and various closures (kinetic theory for collisional stresses, frictional stress, drag laws, etc.) required for adaptation to continuous PSDs remain largely untested, partly due to the lack of detailed experimental data like that reported in this work. Model validation can proceed on multiple fronts using this dataset: non-monotonic degree of species segregation with respect to PSD width, existence of a bubble-less layer, trends of bubble characteristics with widths of distributions, link between segregation and bubbling profiles, and so on.

Task 4.4: Probe Development for Clusters in a High-Velocity, Fluidized Bed (Cocco)

A probe will be developed to further capture the cluster/clumping behavior of small particles (<30 μm). Such a probe will be able to capture, in real time, the dynamic nature of particles clustering at the top of the fluidized bed and in the freeboard region.

(Cocco reporting.) This probe is described in detail in "Fiber Optic Probe" section of next task description.

Task 4.5: Experiments in a High-Velocity, Fluidized Bed (Cocco)

The large-scale (8" ID x 72') riser at PSRI will be used to characterize high-velocity, polydisperse systems. Experiments will consist of operating the riser at both a high and low particle flux, and at both a high and low superficial gas velocity. Measurements will include pressure drop profiles, solids concentration profiles, solid flux profiles, cluster characteristics, and gas residence time distribution for binary mixtures (with differences in size and/or density) and a continuous distribution of sizes.

As described above, the original (proposed) set of experiments include a full factorial design of two particle size distributions (PSDs), two gas velocities, and two overall solids fluxes in the 8" ID x 72' riser. The center point of the matrix is run in triplicate. Measurements include solids flux and concentration at 7 radial positions for 5 axial locations, in addition to gas residence time and cluster characteristics using the new probe.

To expand the data set, measurements will also be taken in additional systems, namely (i) in the 12" ID x 50' riser and (ii) in the 8" ID x 72' with an obstruction in the core region. The purpose of (i) is scale-up and the purpose of (ii) is to generate more mixing by breaking up core-annular flow, both of which will serve as new testbeds for model validation. This revised set of experiments will be performed using a half factorial design, but with the same measurements and number of PSD's as the original set of experiments. It is anticipated that some funds will also be available for a few additional experiments (not half factorial) for a third PSD. Furthermore, to offset the higher-risk associated with the new cluster probe, information on the cluster size and frequency will be extracted from the time series data obtained with the solids flux probe (whereas the data from the new probe will provide additional information, e.g., cluster stability).

(Hrenya and Cocco reporting.) **Task 4.5.1: Reverse Core-Annular Flow**[4]

Abstract: Experiments involving monodisperse Geldart Group B particles have been carried out in a pilot-scale riser of a circulating fluidized bed (CFB). Several combinations of superficial gas velocity (U_s), solids flux (G_s), average particle diameter (d_{ave}), and particle material density (ρ_s) were investigated. Surprisingly, the experiments reveal the presence of a *reverse* core-annulus profile (i.e., a dense core with a dilute annulus) under certain conditions. Specifically, for the large glass beads (d_{ave}= 650 μm, ρ_s= 2500 kg/m^3), the reverse core-annulus profile was observed near the top of the riser for all U_s and G_s combinations examined. For high-density polyethylene (HDPE) beads (d_{ave}= 650 μm, ρ_s= 900 kg/m^3) of the same d_{ave}, reverse core-annulus was observed at the top of the riser only at relatively low G_s. However, for the smaller glass beads (d_{ave} =170 μm, ρ_s=2500 kg/m^{2}s), the traditional core-annulus profile was observed for all U_s and G_s combinations. Although previous work provides possible explanations for this behavior (gas-phase turbulence, etc.), the evidence obtained in this system suggests a novel dominant factor for reverse core-annulus flow: the particle Stokes number (*St*). Lower-*St* particles are more apt to follow the gas exiting the riser while higher-*St* particles have a longer relaxation time and thus are more likely to re-enter the riser after collision with the roughened rounded-elbow exit. Accordingly, the re-direction of particles from the rounded exit elbow and back into riser due to large-scale roughness along the elbow is greater for higher-*St* particles.

[4] Chew, Hays, Findlay et al., "Reverse Core-Annular Flow of Geldart Group B Particles in Risers", submitted, Powder Technology, 2011.

Introduction: Circulating fluidized beds (CFBs) operated at much higher velocities than the bubbling fluidized beds described in Task 4.3, and find important applications in coal gasification, fluid catalytic cracking, chemical looping, and so on. The focus of the current effort (Sections 4.5.1 – 4.5.5) is on the riser section of the CFB, which refers to the high velocity, vertical section. In the riser, various flow characteristics, for example, solids concentration (Section 4.5.1), species segregation (Section 4.5.2), mass flux (Section 4.5.3), and cluster behavior (Section 4.5.4 - 5), are well-known to vary in both the axial and radial directions. Accordingly, the gas-solids contact times in different parts of the riser may vary, thereby impacting the overall efficiency of the unit. The vast majority of published work for CFBs has been for Geldart(Geldart 1973) Group A particles, in which presence of core-annulus flow (i.e., a relatively dilute core and dense annulus) and clustering instabilities are well-documented(Kunii and Levenspiel 1991; Grace, Avidan et al. 1997; Fan and Zhu 1998). Accordingly, the aim of this effort is to establish a rich experimental dataset of riser characteristics for Geldart Group B particles, and to compare the resulting behavior with that previously obtained for Group A systems.

The primary focus of this section is on solids volume fraction (Φ) profiles, because an unexpected finding is revealed therein. Notably, the current section involves three *monodisperse* materials with differences in average particle size (d_{ave}) and/or material density (ρ_s), namely (i) "large" glass beads with d_{ave} = 650 μm and ρ_s = 2500 kg/m^3, (ii) "large" HDPE (high-density polyethylene) beads with d_{ave} = 650 μm and ρ_s = 900 kg/m^3, and (iii) "small" glass beads with d_{ave} = 170 μm and ρ_s = 2500 kg/m^3. Materials (i) and (ii) (large glass and HDPE, respectively) differ in material density (ρ_s) but not size (d_{ave}), whereas materials (i) and (iii) (large glass and small glass, respectively) differ in d_{ave} but not ρ_s.

The experimental results for the Group B particles exhibit an interesting feature: a *reversal* of the core-annulus phenomenon (i.e., a dense core and dilute annulus) is observed for some of the materials at some of the operating conditions examined. Although previous researchers have made observations related to the reverse core-annulus, the source of the reversal present in this work is more nuanced, and can be explained physically in terms of the Stokes number (*St*). First, with regards to previous work, Bolio and Sinclair(Bolio, Yasuna et al. 1995) found using a kinetic-theory-based model that solids concentration along the riser axis increases with increased dilution due to the increased dominance of gas-phase turbulence effects. However, reverse core-annulus was observed in the present work at values of solids loading (*m*) higher than that of the 'dilute limit', namely *m* = 8(Tanaka, Takagi et al. 1989; Bolio, Yasuna et al. 1995), where *m* is the ratio of overall solids flux to that of the gas flux. In another kinetic-theory-based effort, Benhayia et al.(Benyahia, Syamlal et al. 2007) reported that wall roughness leads to a reverse core-annulus too, but the reversal is not as exaggerated as found in the current work. In an experimental study, Du et al.(Du, Warsito et al. 2004) observed deviation from the traditional core-annulus profile (coined a double-ring structure) during the transition to choking, which is at much higher solids concentration than in this work.

One explanation for the new finding of reverse core-annulus profile involves the Stokes number (*St*) of the material and roughness elements along the upper wall of the rounded elbow exit. Specifically, particles are re-directed from the rounded exit elbow and back into riser due to large-scale roughness along the elbow. This explanation is consistent with the dependency of the experimental observations on *St* (ratio of particle inertia to viscous effects of fluid). Namely, it is observed that the material with the highest *St* (i.e., large glass) not only displayed reversal of the core-annulus profile for all conditions investigated, but also gave the highest extent of reversal.

In other words, higher *St* particles are more likely to follow straight trajectories between collisions (and thus be re-directed back into riser after collision with roughness element along rounded elbow), whereas lower *St* materials are more apt to follow the fluid directly out of the riser.

Experimental Description – CFB system: Figure 129 shows a schematic of the circulating fluidized bed (CFB). The riser, which is the section of interest in this work, is 0.30 m in diameter and 18.3 m tall, with a rounded-elbow exit. Blowers supply air for fluidization, and the air enters the riser through a mixing pot at the bottom to ensure uniform dispersion. The air flow rate is controlled by a manual valve, and the superficial gas velocity (U_s), which is reported at local atmospheric conditions, is determined with an orifice plate located upstream of the mixing pot. The operating air temperature and relative humidity (RH) are measured by means of an Omega HX93AV-RP1 probe, with a temperature range of -4 to 171 ^{o}C and RH range of 0 to 100 %, inserted before the mixing pot. Two cyclones connected in series downstream of the riser exit enable recirculation of the solids. The solids flow rate back to the riser is controlled by a pneumatic slide valve at the bottom of the standpipe. Pressure drops across the orifice plate and along the entire riser are measured with pressure transmitters. All temperature, RH, U_s and pressure data are recorded via a DASYlab data acquisition program throughout the experiments. Ports for probe insertion are available at five approximately equally-spaced axial positions along the entire riser height, and two ports azimuthally 90^{o} apart in the horizontal plane are available at each axial position.

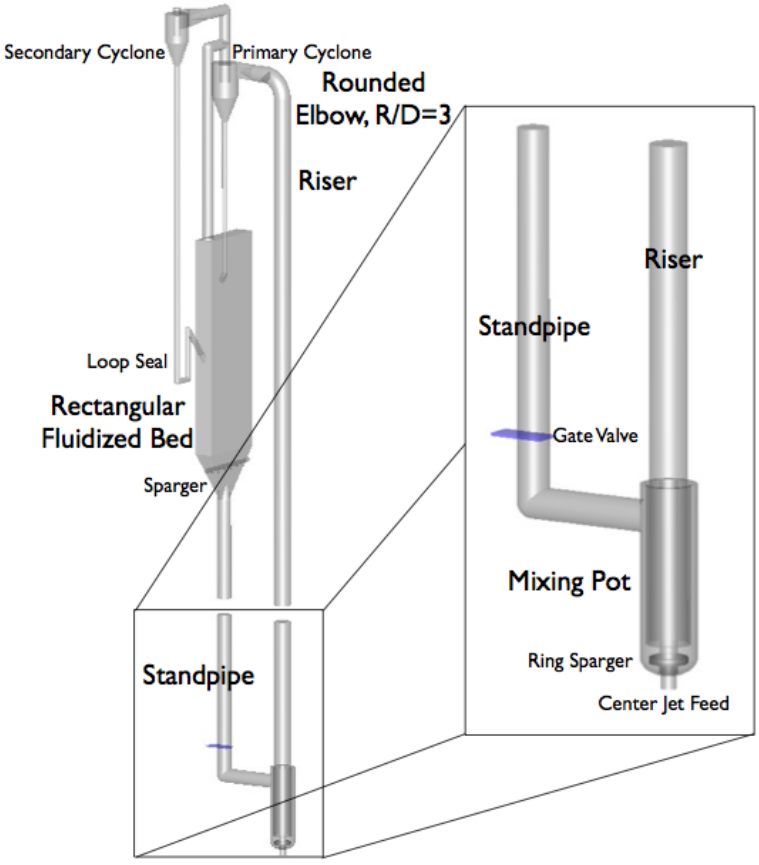

Figure 129. *Schematic of CFB at PSRI.*

Particles Investigated: The materials of interest are various sets of monodisperse particles with different material density (ρ_s) and size (d_{ave}), namely (i) "large" glass (ρ_s = 2500 kg/m^3 and d_{ave}= 650 μm) (ii) "large" high-density polyethylene, HDPE (ρ_s = 900 kg/m^3 and d_{ave}= 650 μm), and (iii) "small" glass (ρ_s = 2500 kg/m^3 and d_{ave}= 170 μm), as listed in Table 8. Materials (i) and (ii) (large glass and HDPE, respectively) differ in material density (ρ_s) but not size (d_{ave}), whereas materials (i) and (iii) (large glass and small glass, respectively) differ in d_{ave} but not ρ_s. To obtain as narrow a distribution of sizes as possible, particles procured from vendors (glass beads of both sizes from Midwest Finishing Systems and HDPE from Dyneon LLC) were sieved using the Sweco industrial sieve to obtain narrower particle size distributions (PSD's). Since the continuous nature of the Sweco sieve gives rise to an imperfect separation between the various sieve sizes, a representative sample was obtained from each drum of sieved material and then the PSD's were further analyzed using a Ro-Tap sieve-shaker. The resulting PSD for each material is depicted in Figure 130, which shows a plot of mass-based frequency (f_m, which is mass fraction of each sieve cut normalized with respect to bin size, for fairer comparison among sieve cuts of different widths) versus particle size. For each material, the width of the distribution, defined as the standard deviation (σ) normalized with respect to d_{ave}, is approximately 10%. As shown in Figure 130, the large glass and large HDPE have similar PSD's, while the small glass has a PSD that is shifted leftwards due to its smaller d_{ave}. In addition, as shown in Figure 131, the particles are approximately spherical.

Table 8. *Monodisperse materials investigated.*

	d_{ave} (μm)	ρ_s (kg/m^3)	σ/d_{ave} (%)
Large Glass	650	2500	9
Small Glass	170	2500	12
Large HDPE	650	900	11

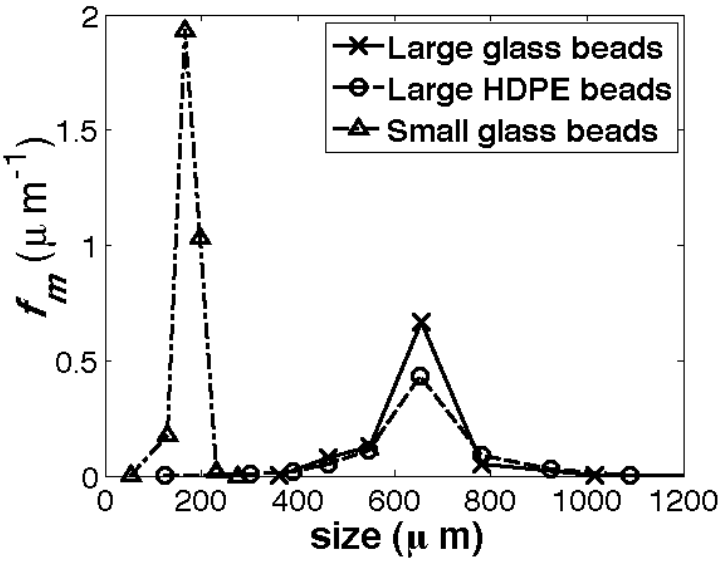

Figure 130. *PSDs of materials investigated.*

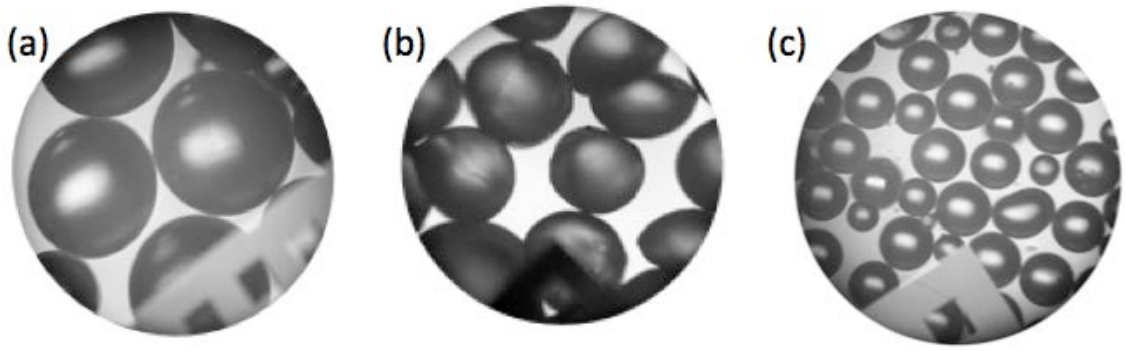

Figure 131. *Photograph taken under the microscope of (a) large glass, (b) large HDPE, and (c) small glass. The grid openings shown are of size 200 μm by 200 μm.*

Operating Conditions: In an effort to operate at the higher superficial gas velocity (U_s) and (integrated) mass flux (G_s) ranges to mimic industrial CFB's(Kunii and Levenspiel 1991), a series of range-finding experiments were carried out to maximize the range of operating values based on physical constraints. The highest limit U_s was 17 m/s, restricted by the avoidance of the generation of too much pressure on the Plexiglass fronting the rectangular fluidized bed in the recirculation loop (Figure 129). The lower limit was 13.5 m/s to allow for higher mass flux (G_s) to be investigated. As for G_s, the practical limits are 120 kg/m^{2}s and 260 kg/m^{2}s. The lower bound for G_s was restricted by sensitivity of the Pitot tube / extraction probe to detect solid volume fraction (Φ) at the higher U_s limit; On the other hand, the upper G_s bound was restricted by the lower U_s limit to deter slugging. The resulting four combinations of U_s and G_s were examined, as tabulated in Table 9. Another way to characterize these conditions is via the solid loading (m), which is a dimensionless quantity defined as the ratio of solid flux to gas flux:

$$m = \frac{G_s}{U_s \rho_g} \tag{70}$$

where ρ_g is the density of air, namely 1.2 kg/m^3. In this work, m ranges from 5.9 to 16.0 were investigated.

Table 9*. Operating conditions for monodisperse materials.*

U_s (m/s)	G_s (kg/m^{2}s)	m
13.5	120	7.4
13.5	260	16.0
17	120	5.9
17	260	12.7

Solids Concentration Measurements: To characterize the solid phase in the riser, local measurements were taken at various axial and radial positions along the riser. Instruments used include pressure transmitters, an extraction probe, a Pitot tube, a fiber optic probe, and a thermal conductivity detector for helium detection. Figure 132 shows the configuration used for the extraction probe, Pitot tube and fiber optic probe. The extraction probe and Pitot tube have

been fabricated such that probe tips are oriented 90° to the probe shaft in order to measure quantities (flux, velocity) associated with upward or downward flow while minimizing the intrusiveness of these probes. The orientation of the fiber optic probe and helium detector were used in a straight or horizontal configuration. Measurements were collected at five axial locations using two sets of 11 radial measurements that are 90° apart in the horizontal plane, as shown in Figure 132b. Two radial planes of measurements were collected to better discern the radial profile (i.e., a symmetric profile was not assumed). Only quantities derived from the Pitot tube, extraction probe and fiber optic probe will be presented in this section.

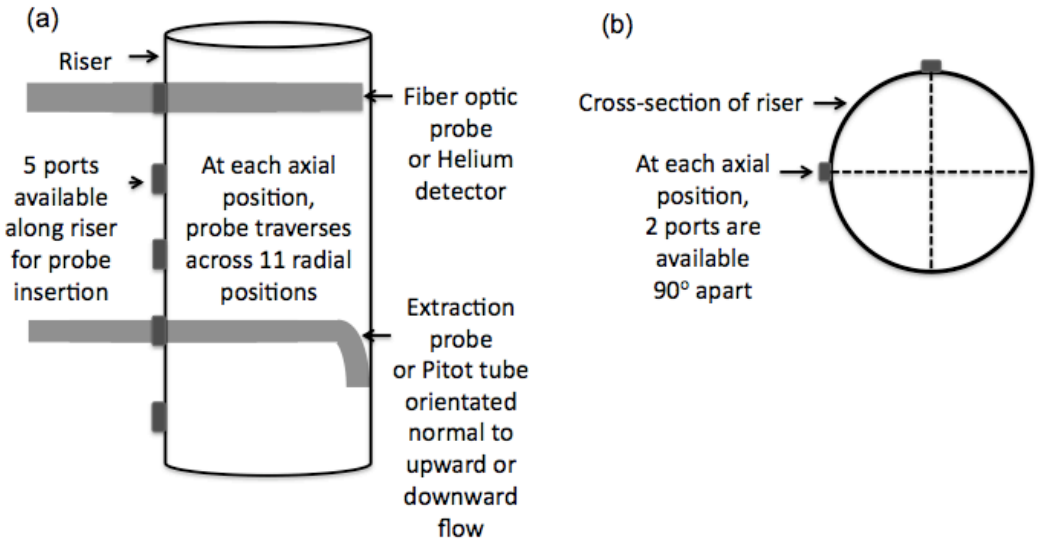

Figure 132. *Schematic illustrating (a) probe positions in the riser and (b) implementation of bi-directional measurement at each axial position.*

Pitot Tube and Extraction Probe: The solids volume fraction (Φ) profiles were obtained using a combination of the Pitot tube and extraction probe measurements. The Pitot tube is well-established as an instrument used to obtain air velocity via measurements of differential pressure between stagnant and dynamic pressures (ΔP_{pitot}), defined as:

$$\Delta P_{pitot} = \alpha \rho_g V_g^{\,2} \tag{71}$$

where α is a calibration constant specific to the Pitot tube used, and ρ_g and V_g are the air density (1.2 kg/m^3) and air velocity, respectively. To adapt this instrument for acquiring solid-phase information in the riser(van Breugel, Stein et al. 1969; Bader, Findlay et al. 1988; Azzi, Turlier et al. 1990; Harris, Davidson et al. 1994), another term is added to Equation 71:

$$\Delta P_{pitot} = \alpha[\rho_g V_g^{\,2}(1-\phi) + \rho_s V_s^{\,2}\phi] \tag{72}$$

where ρ_s and V_s are the density and velocity of the solid particles, respectively, and Φ is the solid volume fraction. An assumption and calibration are necessary(van Breugel, Stein et al. 1969; Bader, Findlay et al. 1988; Azzi, Turlier et al. 1990; Harris, Davidson et al. 1994) in implementing Equation 72. First, an assumption is made that since solid density (ρ_s) is on the order of 10^3 times greater than that of air (ρ_g), the contribution of the gas phase to ΔP_{pitot} is negligible, and hence the term accounting for the gas phase is omitted. Second, to ensure validity of the data acquired by the Pitot tube, calibration of the instrument in the air-only limit is

required using Equation 71. Specifically, the average V_g obtained by integration of the radial V_g profile measured with the Pitot tube is compared with the corresponding value of the known gas flow fed to the riser(van Breugel, Stein et al. 1969). Hence, substituting for ρ_g and average V_g, α is derived using Equation 71. It was found that the specific design of the Pitot tube used, which is fabricated in-house at PSRI, warrants a calibration constant (α) of 0.9. Therefore, Equation 72 becomes:

$$\Delta P_{pitot} = 0.9\phi\rho_s V_s^2 \tag{73}$$

Subsequently, as validation of the Pitot tube used for this work, different (integrated) air flow rates were measured accurately. Since there are two remaining unknowns (Φ and V_s) in Equation 73, extraction probe data is also needed:

$$G_r = \phi\rho_s V_s \tag{74}$$

where G_r is the local mass flux measured by the extraction probe. Solving Equations 73 and 74 simultaneously, the particle velocity (V_s) and the solids volume fraction (Φ) of the solid phase in the riser can be derived(van Breugel, Stein et al. 1969; Bader, Findlay et al. 1988; Azzi, Turlier et al. 1990; Harris, Davidson et al. 1994):

$$V_s = \frac{\Delta P_{pitot,r,upward\ flow}}{\alpha G_{r,upward\ flow}} - \frac{\Delta P_{pitot,r,downward\ flow}}{\alpha G_{r,downward\ flow}} \tag{75}$$

$$\phi = \frac{G_{r,upward\ flow} - G_{r,downward\ flow}}{V_s\rho_s} \tag{76}$$

where subscripts *upward flow* and *downward flow* refer to measurements by the probes in the upward and downward directions, respectively. Validation of the extraction probe measurements have also been carried out to ensure that (i) the radially-averaged (integrated) mass flux is consistent at all axial positions (thereby ensuring a mass balance) and (ii) the collection period is long enough; further details can be found in Chew et al.(Chew, Hays et al. 2011). An inherent assumption of Equation 76 is that the time-averaged value of solids volume fraction (Φ) can be cast in terms of the time-averaged solids flux (G_r) without any dependence on correlations of corresponding fluctuating quantities; some simulation studies have shown that this assumption is not strictly upheld in some systems(Benyahia, Syamlal et al. 2007; Benyahia 2008). Accordingly, an independent check of the solids concentration profiles determined from the Pitot tube/extraction probe is warranted, as detailed below.

Fiber Optic Probe: The fiber optic probe used in this work consists of two fibers: one fiber is used to transmit the light source, while the other is the receiver conduit. Notably, the fibers converge such that the sampling volume is reduced, in order to increase precision by reducing unnecessary scattering of the light source. The underlying principle of the fiber optic probe is such that a higher voltage signal is obtained from the receiving fiber when light emitted from the light-source fiber is blocked, as occurs when the probe is surrounded by a denser (particle-rich) phase. On the other hand, a lower voltage signal is obtained when light from the emitter is relatively unobstructed, which occurs when the probe tip is in a more dilute (gas-rich) phase.

Although numerous investigations have utilized fiber optic probes for obtaining direct measurements of solid concentration(Louge 1997; van Ommen and Mudde 2008), several works have noted the inefficacy of the fiber optic probe to give absolute concentration values due to the problematic calibration procedures involved(Matsuno, Yamaguchi et al. 1983; Herbert, Gauthier et al. 1994; Zhang, Johnston et al. 1998). Accordingly, in this work, instead of attempting to

calibrate the fiber optic probe signals to obtain absolute solid concentration values (since, for example, continual bombardment of the probe tip by glass particles may alter the baseline signal with time), a wavelet decomposition(Mallat 1998) of the raw signal is instead used as an indicator of relative solid concentration (i.e., dense phase versus dilute phase), as detailed below.

To use the fiber-optic measurements to distinguish between dense and dilute conditions, a method known as wavelet decomposition(Mallat 1998; Ren and Li 1998; Guenther and Breault 2007; Yang and Leu 2009) is implemented here via the wavelet toolbox in Matlab(Misiti, Misiti et al. 2002). More specifically, wavelet decomposition provides a means of representing different frequencies of the raw voltage signal by repeatedly breaking down the signal into higher-frequency *details* (*D*) and lower-frequency *approximations* (*A*), as illustrated in Figure 133. At the first scale of decomposition (Scale 1), the signal of *N* Hz (in this work, a data collection frequency of 100 Hz was used for large glass preliminarily and a higher 1000 Hz(Yang and Leu 2009) was subsequently used for large HDPE and small glass) is divided into the first scale of approximation (A_1) and the first scale of detail (D_1), whereby A_1 and D_1 contains the lower and higher frequency ranges, respectively. With the increase of the scale from j to $j+1$, each approximation A_j is subsequently decomposed into approximation A_{j+1} and detail D_{j+1} signals. Figure 134 further shows the detail signals at some scales, illustrating the decrease in signal frequency with the increase of scales. For the interested reader, a thorough explanation of the wavelet decomposition technique can be found in Mallat(Mallat 1989; Mallat 1998).

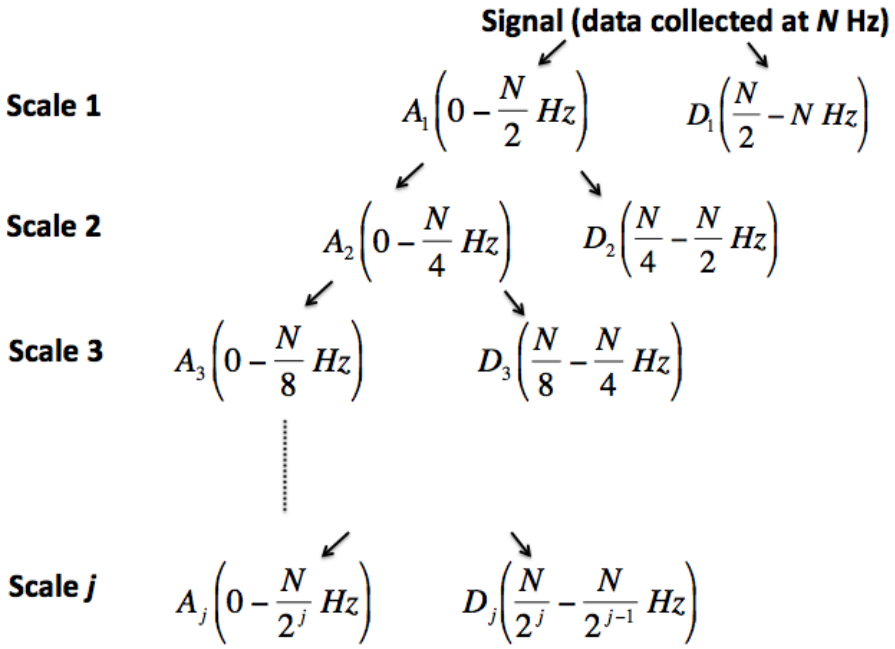

Figure 133. *Decomposition of signal into various scales via wavelet decomposition.*

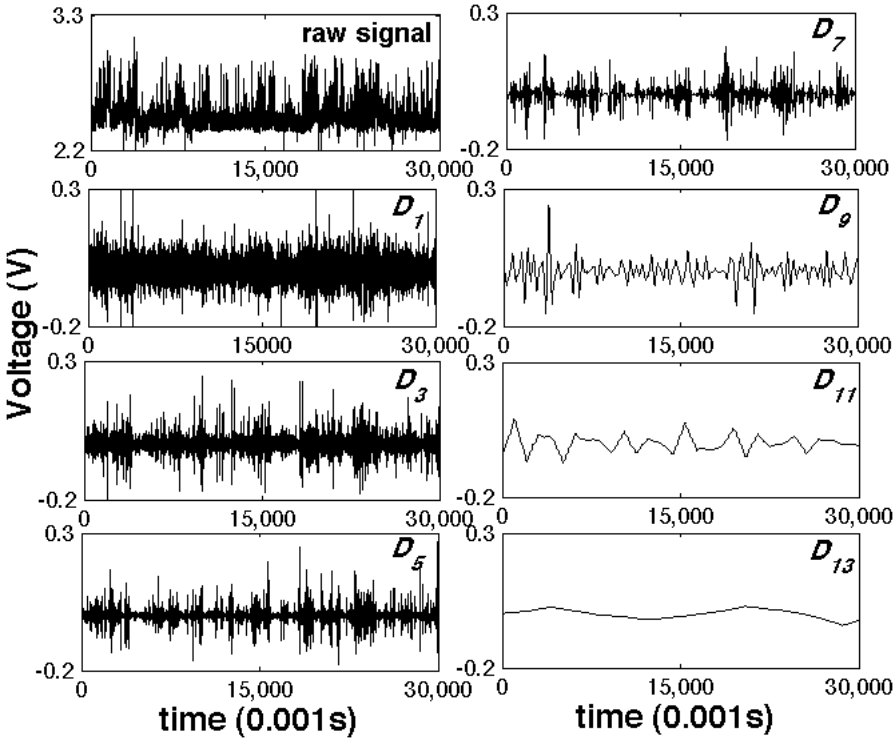

Figure 134. *Raw fiber optic trace (upper left) and corresponding details (D_j) at various scales (j) of wavelet decomposition for large HDPE at operating condition of U_s =13.5 m/s, G_s = 260 kg/m^{2}s and at h/H = 0.93 and r/R = 0.83.*

Based on the signal decomposition described above, it has been deduced that higher frequencies containing noise are represented at lower scales (micro-scale), intermediate frequencies containing particle information are represented at intermediate scales (meso-scale), and lower frequencies containing equipment effects are represented at higher scales (macro-scale)(Ren and Li 1998; Yang and Leu 2009). Based on this knowledge of the physical meaning of each scale (micro-, meso-, and macro-), the energies present at each scale can be expressed graphically, as depicted in Figure 135. The normalized relative energy of the detail signals at each scale ($\frac{E_{Dj}}{E_{J,all}}$) is calculated as(Yang and Leu 2009):

$$E_{Dj} = \sum_{t=1}^{N} \left| D_j(t) \right|^2 \tag{77}$$

$$E_{Aj} = \sum_{t=1}^{N} \left| A_j(t) - A_{j,ave} \right|^2 \tag{78}$$

$$E_{J,all} = E_{A,J} + \sum_{j=1}^{J} E_{Dj} \tag{79}$$

where E is the energy of the signal, N is the total number of data points, J is the final scale of decomposition (in this work, the largest scale of decomposition used is 13, since Figure 134 shows that negligible frequency information is present from scale 13 onwards), j is the scale of

decomposition, D is a detail signal at a specified scale j, A is an approximation signal at a specified scale j, $A_{j,ave}$ is the average value of the A_j trace, and t is time.

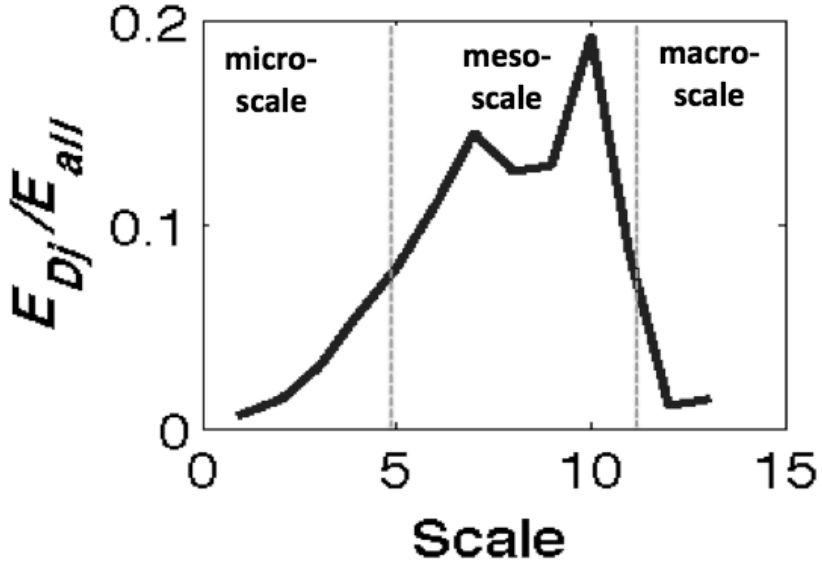

Figure 135. Normalized wavelet energy distribution for small glass under operating condition of U_s = 13.5 m/s, G_s = 260 kg/m^{2}s and at h/H = 0.47 and r/R = 0.96.

Figure 135 represents data obtained near the wall (r/R = 0.96) for the small glass system with a mass loading of m = 16.0. It is seen that most energy is contained in the meso-scale (Scales 5 - 11), which is similar to that shown by Yang and Leu(Yang and Leu 2009). The similarity of shapes is expected since both signals are collected at relatively dense flow conditions. Along the same vein, normalized wavelet energy distribution plots were generated for a background signal (absence of solids) as well as the signal collected at the riser center (presumably dilute) for the same small glass system. These results are given in Figure 136. In particular, as shown in Figure 136a, a background signal (i.e., in the absence of solids) consists only of noise. All the energies of the signal are contained in the lowest scales of an exponentially decreasing function. Figure 136b (identical to Figure 135) demonstrates that under relatively dense conditions (near the wall), the intermediate scales contain most of the energies of the signal. Finally, under relatively dilute conditions, the signal contains both noise and solids information, and therefore the dominant energies of the signal are contained in the range of low to intermediate scales, as seen in the left-skewed Gaussian plot in Figure 136c. Hence, wavelet decomposition of the fiber optic signal provides a means of identifying dense versus dilute flow conditions via the shape of the normalized wavelet energy distribution ($\frac{E_{Dj}}{E_{J,all}}$) as a function of scale.

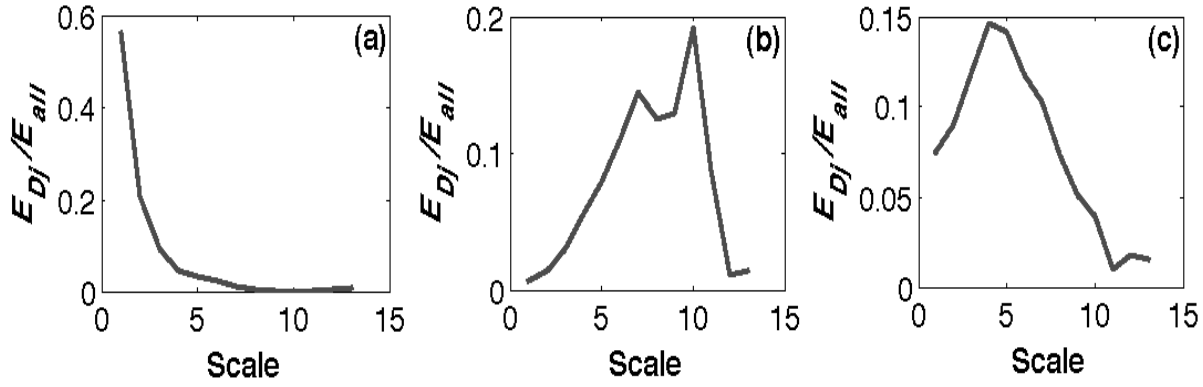

Figure 136. *Normalized wavelet energy distribution plots for (a) background signal (i.e., absence of solids at U_s = 13.5 m/s), (b) dense conditions (for small glass under operating condition of U_s = 13.5 m/s, G_s = 260 kg/m^{2}s and at h/H = 0.47 and r/R = 0.96), and (c) dilute conditions (for small glass under operating condition of U_s = 13.5 m/s, G_s = 260 kg/m^{2}s and at h/H = 0.47 and r/R = 0).*

Results and Discussion: Solid concentration information, obtained separately with both Pitot tube / extraction probe setup as well as the fiber optic probe, are highlighted below, along with the differential pressure drop measurements, since the most significant findings are revealed therein. Only the solids volume fraction profiles calculated via Equation 76 from the Pitot tube and extraction probe measurements are given below. Raw measurements obtained from the Pitot tube and extraction probe are not included here for the sake of brevity, but are available in Chew et al.(Chew, Hays et al. 2011; Chew, Hays et al. 2011) for the interested reader.

Solid volume fraction (Φ) profiles via Pitot tube and Extraction probe: Solid volume fraction plots obtained via the Pitot tube / extraction probe for each of the three monodisperse materials investigated are presented in Figure 137 through Figure 139. The subplots of each figure contain data at each of the U_s, G_s pairings given in Table 9. The vertical axis represents the solid volume fraction (Φ), while the horizontal axis represents the dimensionless radius (r/R) of the riser cross-section, where r and R are the radial position at which measurement was taken and riser diameter, respectively. The data points represent average values of the two sets of bi-directional (90^o apart) radial measurements taken at each axial position, and the error bars denote the span of the two values. The various profiles on each subplot represent measurements taken at different dimensionless heights (h/H) along the riser, as indicated in the legend. Specifically, h is the height along the riser at which measurements are taken and H is the total height of the riser.

Figure 137 shows the Φ profiles for large glass. A surprising finding for this material is that of *reverse* core-annulus (i.e., a dense core and dilute annulus) profiles at the topmost axial position (h/H = 0.92) across all four operating conditions. Lower portions of the riser, on the other hand, retain the well-known core-annulus (i.e. dilute core and dense annulus) profile. Furthermore, regarding the magnitude of this shift, Figure 137 illustrates that the U-shaped profile obtained at the lowest h/H essentially flips upside down by the highest axial position, and thus the minimum and maximum values of Φ are nearly the same in both cases, but located at different radial positions (i.e., the wall at low h/H and the center at high h/H).

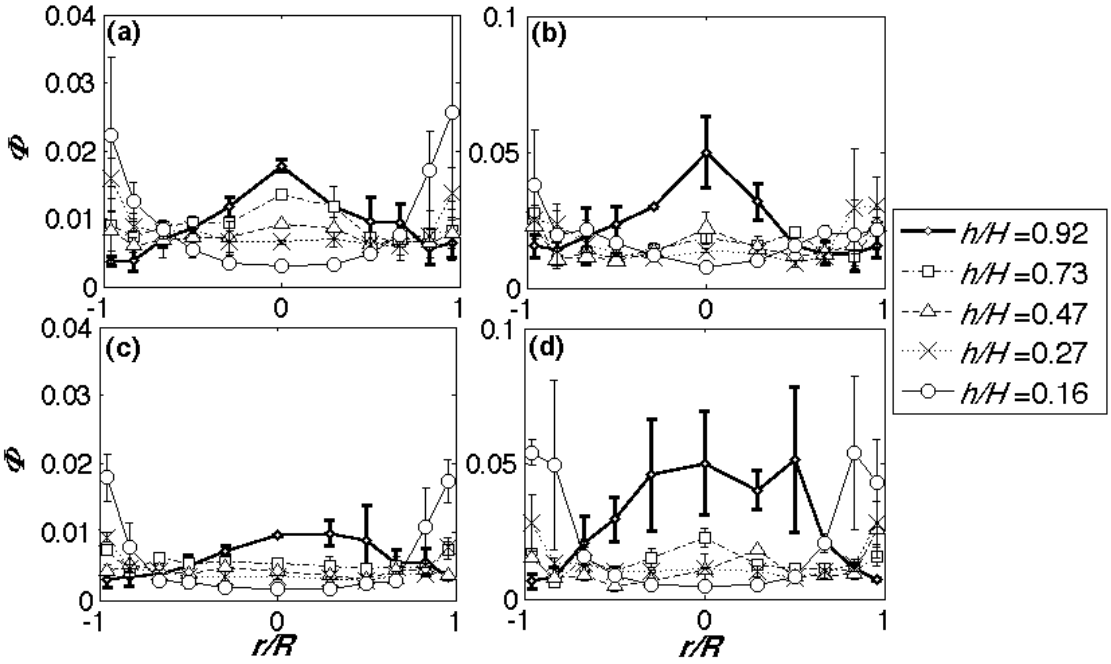

Figure 137. *Radial solid volume fraction (Φ) profiles of large glass at (a) U_s = 13.5 m/s, G_s= 120 kg/m^{2}s, m = 7.4, (b) U_s = 13.5 m/s, G_s= 260 kg/m^{2}s, m = 16.0, (c) U_s = 17 m/s, G_s= 120 kg/m^{2}s, m = 5.9, and (d) U_s = 17 m/s, G_s= 260 kg/m^{2}s, m = 12.7.*

Solid volume fraction (Φ) profiles of large HDPE for all four conditions are shown in Figure 138. Similar to the large glass system, reverse core-annulus profiles are also observed for HDPE at the topmost axial position of h/H = 0.92, but only for the low G_s (namely, 120 kg/m^{2}s) conditions (Figure 138a and c). Analogous to the large glass system (Figure 137), for conditions where reverse core-annulus is observed at the top, the lower portions of the riser still exhibit the widely acknowledged core-annulus profile (U-shape). The inversion itself is less dramatic than in the large glass case (Figure 137), as the maximum Φ observed for the profiles with the inverted U-shape is not as large as the maximum Φ observed at the wall at the bottom of the riser (Figure 138a and c). At the higher G_s (namely, 260 kg/m^{2}s) conditions (Figure 136b and d), the riser retains the traditional core-annulus profile throughout the riser, although the U-shape is flatter higher up the riser.

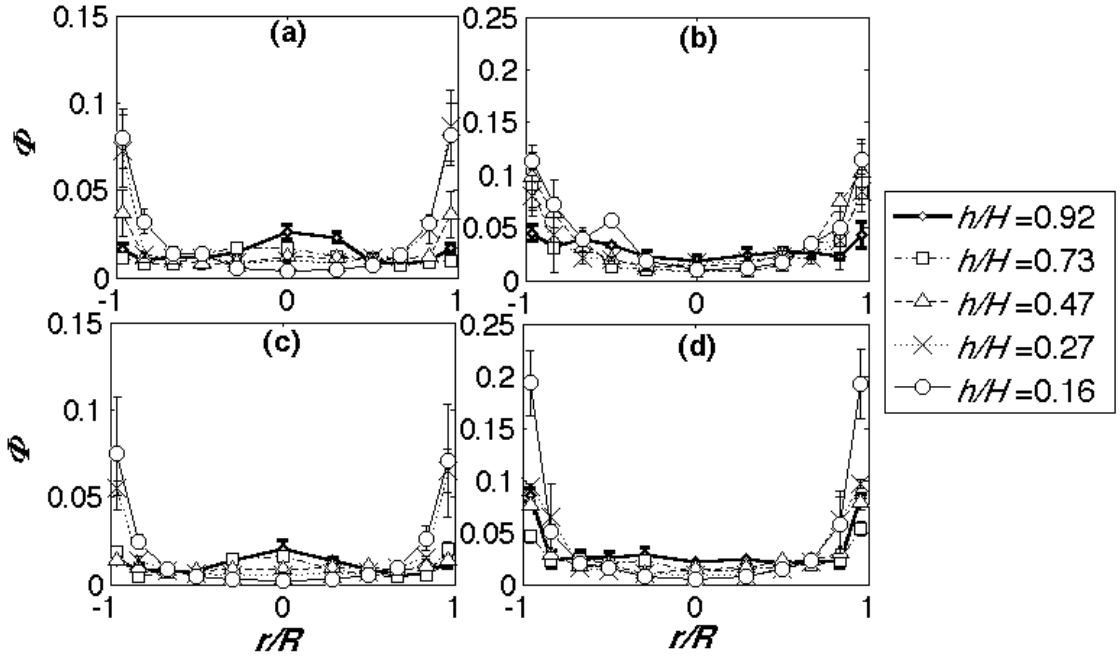

Figure 138. *Radial solid volume fraction (Φ) profiles of large HDPE at (a) U_s = 13.5 m/s, G_s = 120 kg/m^{2}s, m = 7.4, (b) U_s = 13.5 m/s, G_s = 260 kg/m^{2}s, m = 16.0, (c) U_s = 17 m/s, G_s = 120 kg/m^{2}s, m = 5.9, and (d) U_s = 17 m/s, G_s = 260 kg/m^{2}s, m = 12.7.*

The third material investigated is small glass. As shown in Figure 139, the solid volume fraction (Φ) profiles generally evolve from a U-shape at the bottom (traditional core-annulus) to approximately a flat line higher in the riser. In contrast with the previous cases of the large glass and large HDPE materials (both with d_{ave}= 650 μm), the Φ profiles do *not* exhibit a deviation from the well-known core-annulus profiles. The exaggerated reverse core-annulus (inverted U), particularly that observed for the large glass (Figure 137), however, has not been reported previously in the literature.

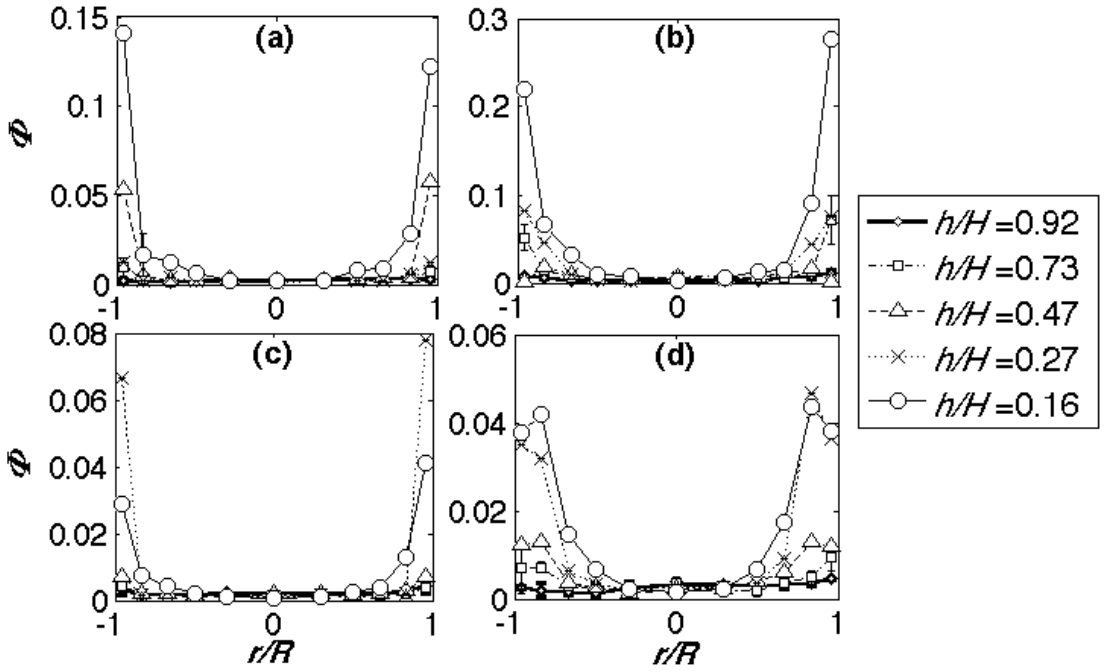

Figure 139. *Radial solid volume fraction (Φ) profiles of small glass at (a) U_s = 13.5 m/s, G_s = 120 kg/m^{2}s, m = 7.4, (b) U_s = 13.5 m/s, G_s = 260 kg/m^{2}s, m = 16.0, (c) U_s = 17 m/s, G_s = 120 kg/m^{2}s, m = 5.9, and (d) U_s = 17 m/s, G_s = 260 kg/m^{2}s, m = 12.7.*

Dense versus Dilute Flow Conditions via Fiber Optic Probe: To provide independent, supporting evidence for the reverse core-annulus phenomenon observed via the Pitot tube and extraction probe presented above, a wavelet decomposition of the fiber-optic measurements for each material was also carried out. As described below, the reverse core-annulus phenomenon is confirmed by the fiber optic data for the locations, materials, and operating conditions indicated previously by the Pitot tube/extraction probe data (Section 4.2.4.1).

Figure 140 contains the fiber optic traces collected at riser wall (subplots on left: *r/R* = 0.96) and riser center (subplots on right: *r/R* = 0.0) for the three materials for the upper region of the riser where the reverse core-annulus behavior was observed for two of the three materials (i.e., large glass beads and HDPE). For the large glass material, comparison of Figure 140a and b plotted on the same *y*-axis range reflects that a wider range of voltage and higher voltage values were obtained at *r/R* = 0.0 (Figure 140b), which indicates higher solid concentration at the center relative to the wall (Figure 140a) - i.e., reverse core-annulus. Similarly for large HDPE, a wider range of voltage and higher voltage values were obtained at *r/R* = 0.0 (Figure 140c) compared to at *r/R* = 0.96 (Fogire 140d), again providing another layer of evidence for the reverse core-annulus phenomenon observed with the Pitot tube/extraction probe. On the other hand, for small glass, a wider range of voltage and higher voltage values were obtained at *r/R* = 0.96 (Figure 140e) than *r/R* = 0.0 (Figure 140f), corroborating the traditional core-annulus profile obtained with the Pitot tube/extraction probe. Similar consistency between the fiber-optic data and the Pitot tube/extraction probe were obtained for the entire dataset, but omitted here for brevity.

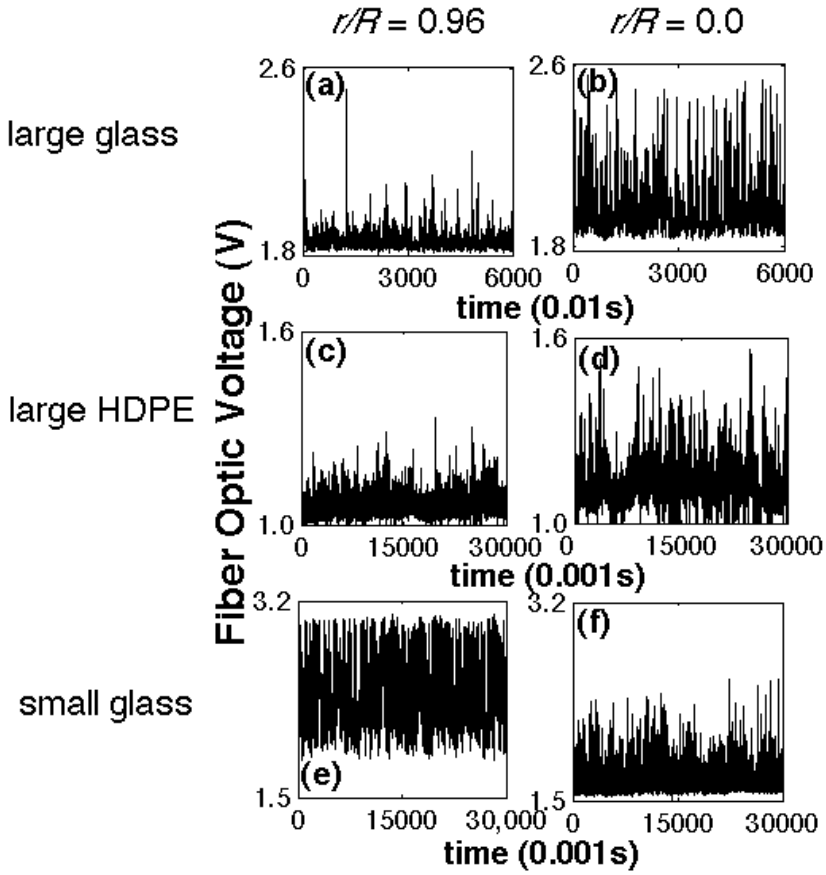

Figure 140. *Fiber optic probe voltage traces for large glass beads at U_s = 17m/s, G_s = 260kg/m^{2}s, h/H = 0.92 and at (a) r/R = 0.96 and (b) r/R = 0.0; large HDPE at U_s = 17m/s, G_s = 120kg/m^{2}s, h/H = 0.92 and at (c) r/R = 0.96 and (d) r/R = 0.0; and small glass beads at U_s = 13.5m/s, G_s = 260kg/m^{2}s, h/H = 0.27 and at (e) r/R = 0.96 and (f) r/R = 0.0.*

Keeping in mind the potential challenges involved with calibration of fiber optic voltage for absolute concentration values(Matsuno, Yamaguchi et al. 1983; Herbert, Gauthier et al. 1994; Zhang, Johnston et al. 1998), further analysis of the fiber optic data using wavelet decomposition was carried out since it gives information on relative concentration rather than absolute values. The wavelet decomposition results again confirm the presence of the reverse core-annulus phenomenon observed with the Pitot tube/extraction probe. In particular, the results are displayed in Figure 141 through Figure 143 for the same set of conditions shown in Figure 137 through Figure 139 for large glass, large HDPE and small glass, respectively. Similar to the Pitot/extraction data, the large glass and HDPE beads displayed reverse core-annulus and the small glass beads exhibited the traditional core-annulus. Note that because data acquisition frequency was lower for large glass (100Hz, instead of 1000Hz as for large HDPE and small glass), as per Figure 133, the same signal frequency information will be found in lower scales (specifically, three scales lower) for large glass than for the other two materials.

For large glass, the near-wall data exhibited in Figure 141a through Figure 141c display exponentially decreasing functions, indicating more dilute conditions near the wall (similar to Figure 136a), while the data nearer to the riser center (Figure 141d through Figure 141f) gives

rise to left-skewed Gaussian plots (similar to Figure 136c), indicating denser conditions. Hence, the wavelet analysis of the fiber optic trace supports the presence of a reverse core-annulus for large glass beads, similar to the Pitot tube/extraction probe conclusion (Figure 137d). Similarly, Figure 142 verifies the reverse core-annulus phenomenon observed for HDPE, consistent with the data from the Pitot tube/extraction probe (Figure 138a). Finally, Figure 143 confirms the traditional core-annulus observed for the small glass beads demonstrated in Figure 139b via the Pitot tube/extraction probe. This wavelet analysis was carried out across all operating conditions for each riser position and for each material investigated, and the results are uniformly consistent with the reverse and traditional core-annulus trends obtained from the Pitot tube/extraction probe, but are not shown for the sake of brevity. Accordingly, the trends reported here are verified independently through two separate measurement techniques.

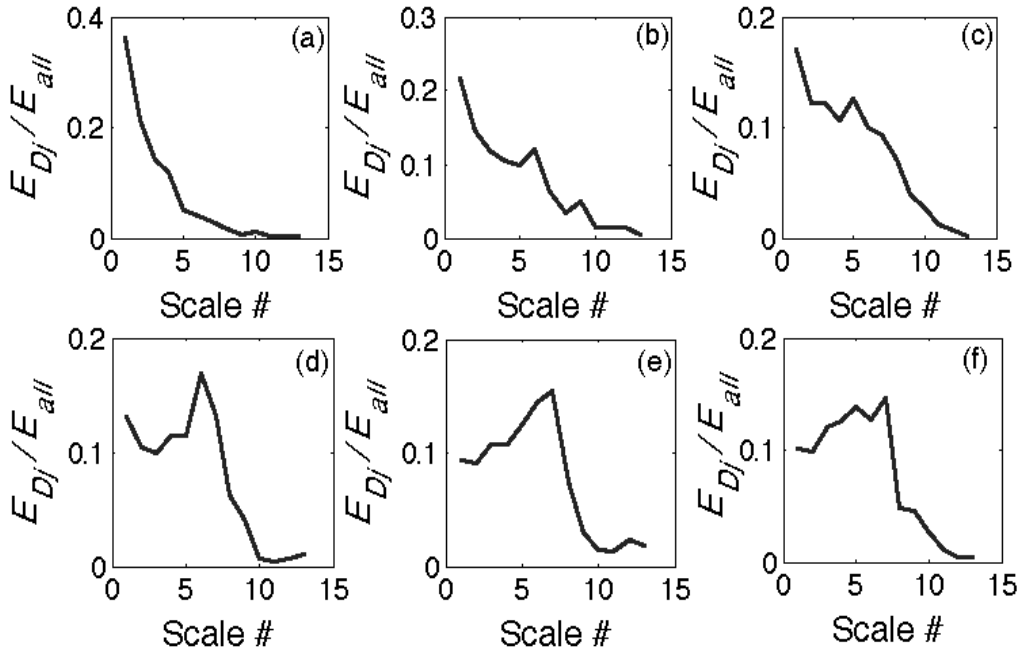

Figure 141. *Normalized wavelet energy distribution plots of fiber optic data of large glass beads under operating condition of U_s = 17m/s and G_s = 260kg/m^{2}s, at h/H = 0.92 and r/R = (a) 0.96, (b) 0.83, (c) 0.67, (d) 0.50, (e) 0.29, and (f) 0.0.*

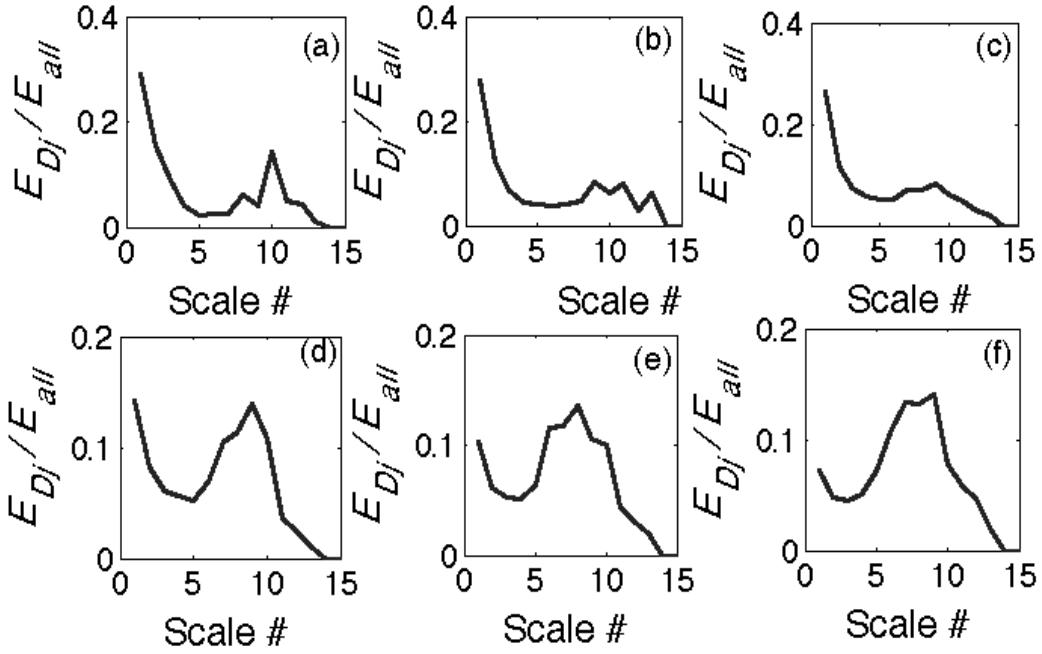

Figure 142. *Normalized wavelet energy distribution plots of fiber optic data of large HDPE at operating condition of U_s= 13.5m/s and G_s = 120kg/m^{2}s, at h/H = 0.92 and r/R = (a) 0.96, (b) 0.83, (c) 0.67, (d) 0.50, (e) 0.29, and (f) 0.0.*

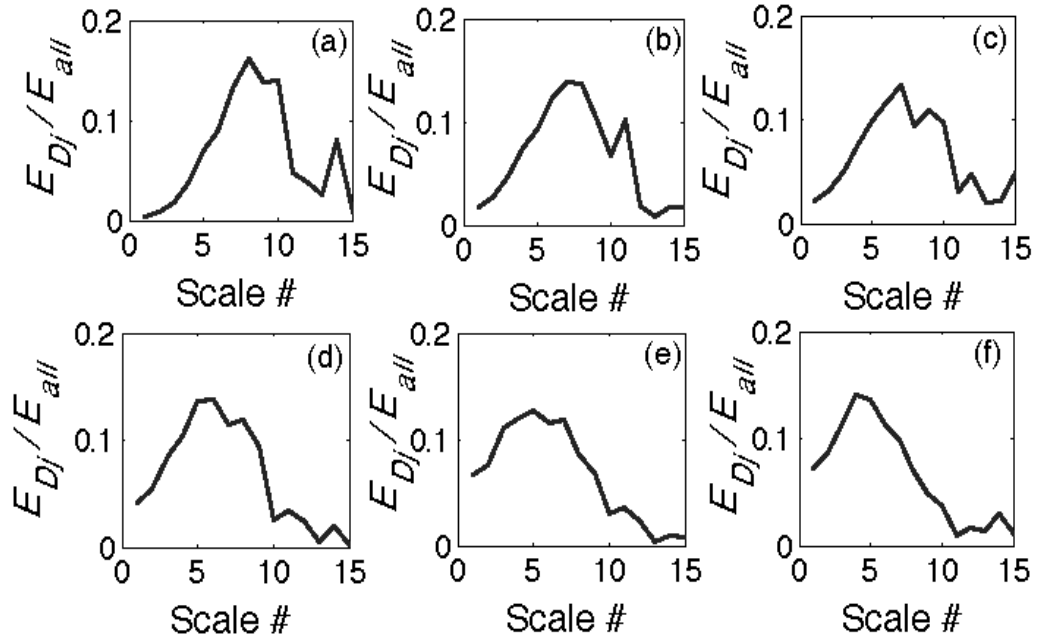

Figure 143. *Normalized wavelet energy distribution plots of fiber optic data of small glass at operating condition of U_s = 13.5m/s and G_s = 260kg/m^{2}s, at h/H = 0.47 and r/R = (a) 0.96, (b) 0.83, (c) 0.67, (d) 0.50, (e) 0.29, and (f) 0.0.*

Physical Origins of Reverse Core-annulus Flow: Collectively, Figure 137 through Figure 143 indicate the presence of a surprising deviation from the well-known core-annulus pattern at the top portion of the riser for two of the three materials. Specifically, the reverse core-annulus phenomenon is associated with the larger-sized (650 □m) of the Group B particles examined under these operating conditions. What is the origin of this unexpected deviation from the widely-reported core-annulus profile? Two hypotheses stemming from existing literature will be considered in the following paragraphs, namely (i) the impact of gas-phase turbulence associated with dilute flows (i.e., low $\bar{\phi}$, where $\bar{\phi}$ is the solid volume fraction averaged over the cross-section area), and (ii) a rough-wall effect.

Sinclair and Jackson(Sinclair and Jackson 1989) first illustrated the ability of a kinetic-theory-based model to predict core-annulus flow, though their model also predicted an unrealistic segregation of particles toward the pipe center (reverse core-annulus), which was traced to an undue sensitivity to the restitution coefficient (*e*). This unrealistic sensitivity was later eliminated by the incorporation of additional physical mechanisms: gas-phase turbulence in dilute flows (maximum *m* and $\bar{\phi}$ values of 4.2 and 0.006, respectively)(Bolio, Yasuna et al. 1995), and clustering instabilities in denser flows (minimum *m* and $\bar{\phi}$ values are 9.5 and 0.04, respectively)(Hrenya and Sinclair 1997). For the case of dilute flows ($m < 8$), both experiments(Tanaka, Takagi et al. 1989) and simulations(Tanaka and Tsuji 1991; Bolio, Yasuna et al. 1995) have revealed a mild (realistic) reverse core-annulus trend at dilute conditions. Moreover, with regards to the effect of particle size under dilute conditions, it was further found that larger particles have a higher tendency towards the reverse core-annulus phenomenon(Tanaka, Takagi et al. 1989; Bolio, Yasuna et al. 1995), which is in agreement with experimental results in this work that only the larger particles (namely, large glass and large HDPE) exhibit reverse core-annulus.

Consequently, the influence of gas-phase turbulence in dilute flow *may* serve as an explanation for the reverse core-annulus phenomenon observed in this work, because the reversal is only seen at the top of the riser where $\bar{\phi}$ is generally the lowest, as evidenced from the axial profiles of $\bar{\phi}$ exhibited in Figure 144. Nonetheless, it is worthwhile to note that the reverse core-annulus profiles in previous work were observed for dilute conditions of $\bar{\phi} < 0.01$ (whereas core-annulus was observed for higher $\bar{\phi}$values(Sinclair and Jackson 1989; Hrenya and Sinclair 1997)); in this work, a reverse core-annulus profile is observed up to $\bar{\phi} = 0.02$ (Figure 137b and d). Perhaps more importantly, the reversal of the core-annular effect is more accentuated by that observed in previous work(Tanaka, Takagi et al. 1989; Bolio, Yasuna et al. 1995), specifically in that the difference of solid concentration between wall and center was up to a factor of five in this work, whereas up to only a two-fold difference was reported before(Tanaka, Takagi et al. 1989; Bolio, Yasuna et al. 1995).Hence, the effect of gas-phase turbulence alone appears inadequate to explain the phenomenon observed, thereby suggesting that an additional effect plays a role.

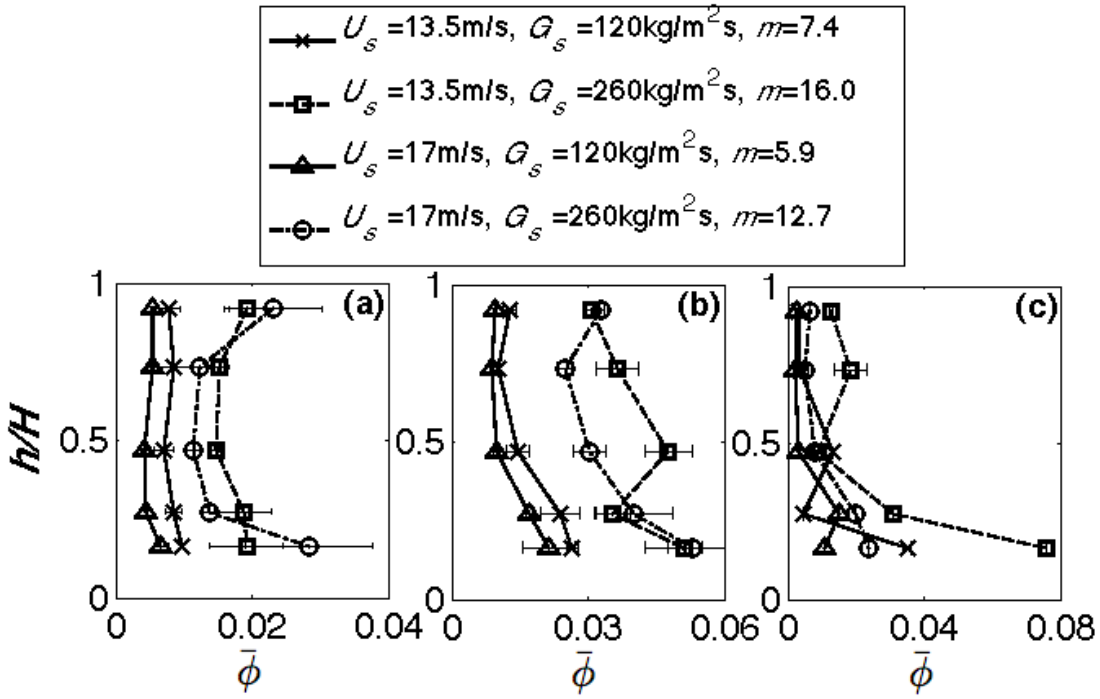

Figure 144. *$\bar{\phi}$ profiles obtained via Pitot tube/extraction probe at each operating condition for (a) large glass, (b) large HDPE, and (c) small glass.*

Along these lines, rough walls (increased friction coefficient) have been reported to not only enhance the prominence of the reversal of the traditional core-annulus profile in dilute flows(Benyahia, Syamlal et al. 2005), but in denser flow too, the traditional core-annulus profile is flattened(Zhou, Grace et al. 1996; Benyahia, Syamlal et al. 2007), thereby increasing the tendency towards reverse core-annulus. For dilute flows (m = 4), Benyahia et al.(Benyahia, Syamlal et al. 2005) found via predictions from a kinetic-theory-based model that increased friction at the walls increases the average solid volume fraction ($\bar{\phi}$) throughout the riser and also increases the prominence of the reverse core-annulus profile. With regards to denser flows, it has been corroborated experimentally(Zhou, Grace et al. 1996) that rough walls give lower voidage near the wall and more uniform Φ profile across the pipe radius, which has been observed via a kinetic-theory-based model too(Benyahia, Syamlal et al. 2007; Jin, Wang et al. 2010). To explain the effect of surface roughness, Jenkins and Louge(Jenkins and Louge 1997) reported that an increased friction coefficient increases energy of the velocity fluctuations as particles are scattered in collisions with the wall, causing an increase in granular temperature and thereby a decrease in the solids concentration. All of the above works imply that a rough wall deflects more particles toward the riser center, hence causing deviation from the traditional core-annulus profile, which may then become flat or even be reversed as the wall becomes increasingly roughened. To further build on the physical picture of the impact of rough walls on the lateral distribution of particles, a schematic is given in Figure 145. In the case of smooth walls, Figure 145a shows that upward flowing particles are more inclined to continue their vertical trajectory upwards. On the other hand, as seen in Figure 145b, diffuse particle-wall collisions resulting from rough walls imply that particles will be deflected *away* from the wall, hence understandably

reducing Φ at the wall and increasing Φ away from the wall compared to the smooth-wall case. Hence, rough walls may serve as an auxiliary explanation of the reverse core-annulus pattern observed in this work which occurs at higher solid loading than reported for the dilute flows work cited in the previous paragraph.

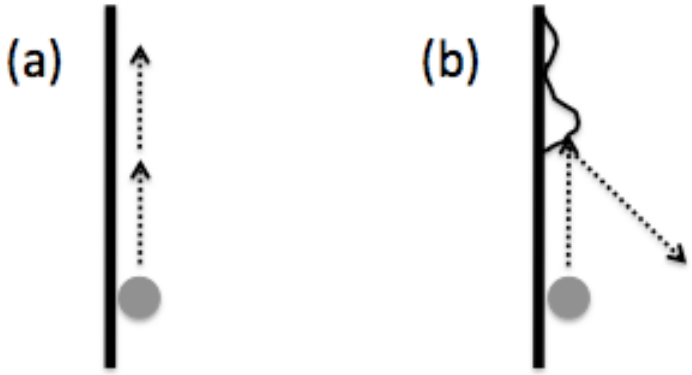

Figure 145. *(a) Straight trajectory of particle travelling along smooth wall, and (b) particle deflected away from rough wall.*

As discussed above, although either turbulence effects in dilute flows or rough walls may independently lead to reverse core-annulus, it does not appear that either effect on its own is sufficient to produce the accentuated reverse core-annulus profiles as observed in this work, especially that observed for large glass in Figure 137. First, the reverse core-annulus profiles are more exaggerated than those attributed to gas-phase turbulence in dilute flows, possibly because higher solid loading is used. Second, the vertical walls in the current setup are quite smooth, especially the section of the riser wall where the topmost measurement was taken, since a new Plexiglass section was installed at that location; thus, it is not surprising that core-annulus flow is observed in most sections of the riser. Accordingly, an alternative explanation for the observed reverse core-annulus pattern is given below.

On closer inspection, despite the smooth vertical walls, the upper wall of the elbow exit is not expected to remain smooth due to erosion by particle bombardment. Figure 146 shows clearly that the upper, curved portion of the riser exit (located above the top measurement) used in this study is very rough due to continual, head-on bombardment by particles. Based on the drawing in Figure 147b, it is surmised that the reverse core-annulus behavior observed at the top of the riser may be due to roughness associated with the rounded elbow exit. While Figure 147a shows a schematic of an elbow exit with smooth walls, Figure 147b shows the same elbow but with rough walls, serving to paint a physical picture of what may be causing higher Φ in the riser axis near the riser top. The solid arrows represent the trajectory of the particles flowing upwards from the riser into the elbow exit, and the dotted arrows represent the deflected trajectory of the particles after hitting the wall of the elbow.

For a smooth wall (Figure 147a), particle-wall collisions are specular, implying that the angles of deflection largely equal the angles of incidence. In contrast, for a rough wall (Figure 147b), particle-wall collisions are diffuse, i.e., angles of deflection arising from particle-wall collision are much more varied. As illustrated in Figure 147, particles are more likely to deflect back toward the riser when the wall of the elbow exit is rough, hence causing a region of higher Φ away from the wall near the top of the riser.

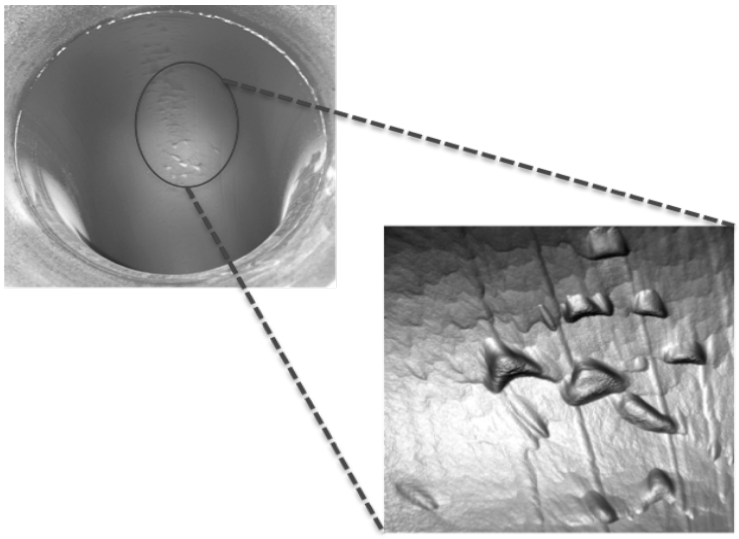

Figure 146. *Photograph of the cross-section of the elbow exit (diameter = 0.30 m) of the riser, showing the roughness elements on the upper, curved wall.*

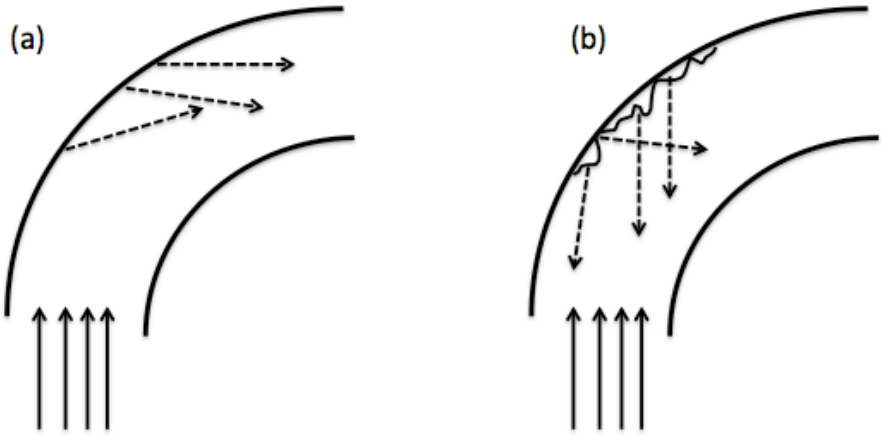

Figure 147. *Schematic of differences in particle trajectory after collision between (a) smooth wall of elbow exit, and (b) rough wall of elbow exit.*

A logical ensuing question is why the reverse core-annulus profiles exist for some materials or conditions but not others. Recall that the reverse core-annulus phenomenon was observed for all conditions for the both bigger and denser material of large glass, only at some conditions for HDPE, and was absent for small glass. These differences can be traced to the Stokes number (*St*):

$$St = \frac{\rho_s d_{ave} V_{rel}}{\mu_g} \tag{80}$$

where V_{rel} is the relative velocity between the solid and gas phases and μ_g is the viscosity of air. In physical terms, *St* is the ratio of the inertia of the solid particle to the viscous forces in the gas. More explicitly, particles with larger *St* are more likely to follow more diffuse trajectories after

collision rather than following fluid streamlines, because of greater particle inertia relative to fluid viscous forces. Hence, roughened walls are most likely to exert the greatest effect on reversing the trajectory of particles with large *St*. To ascertain the effect of particle *St* on the reverse core-annulus profiles, Table 10 lists the *St* of the various materials, with V_{rel} approximated as the terminal velocity (V_t) of a single particle. Notably, the large glass particles, which have the most exaggerated reversal of the core-annulus profiles and which were observed for all four conditions, has the largest *St* (Table 10). It has been reported that particles with higher *St* tend to have a more extensive exit effect in terms of increased $\Delta P/\Delta h$ near riser exit(Pugsley, Lapointe et al. 1997), which agrees with this work in that large glass exhibits the highest increase of $\Delta P/\Delta h$ at the riser top (Figure 148a). For HDPE, the material with the second largest *St*, reverse core-annulus was only observed for two of the four conditions. Lastly, for the smaller glass materials, their smaller *St* indicates that they are more likely to follow fluid streamlines (smaller relaxation time) and thus less likely to bounce back into riser after collision with roughness elements. It is also worthwhile to note that this relationship between large *St* and reverse core-annulus serves well to explain why existing literature largely based on the smaller Geldart Group A particles (i.e., lower *St*) largely reports traditional core-annulus profiles.

Table 10. *Stokes number (St) of the particles.*

Material	*St*
Large glass	$\frac{8.3}{\mu_g}$
Large HDPE	$\frac{1.6}{\mu_g}$
Small glass	$\frac{0.5}{\mu_g}$

Axial differential pressure ($\Delta P/\Delta h$): Axial differential pressure ($\Delta P/\Delta h$) profiles, which reflect solids concentration within the riser, of each of the three materials at all four operating conditions are depicted in Figure 148. The *y*-axis represents dimensionless height along the riser (h/H), and the *x*-axis represents $\Delta P/\Delta h$. For the large glass material depicted in Figure 148a, an increase in $\Delta P/\Delta h$ is observed at the topmost position of the riser; this phenomenon is known as 'reflux' and is due to the effect of the exit geometry(Bai, Jin et al. 1992; Martin, Derouin et al. 1992; Zhou, Grace et al. 1994; Pugsley, Lapointe et al. 1997). Interestingly, the higher $\Delta P/\Delta h$ at the top of the riser is more attenuated for the lower U_s conditions, implying that back-mixing may be more dependent on U_s than G_s. It has been reported that a sharper riser exit geometry (e.g. L-shaped or T-shaped) increases the solids holdup in the top region of the riser due to particle reflux(Bai, Jin et al. 1992; Martin, Derouin et al. 1992; Zhou, Grace et al. 1994; Pugsley, Lapointe et al. 1997; Wu, Jiang et al. 2010), but not for a more gradual exit geometry restriction such as a rounded bend(Lim, Zhu et al. 1995) consistent with this study. Based solely on the exit geometry, the rounded elbow used in this work was not expected to culminate in strong reflux of solids at the top of the riser. However, as explained in the previous section (Figure 147), in the absence of an abrupt exit, the roughened walls of the rounded exit may have the same effect in terms of a stronger reflux for particles with relatively high *St*. Radial solids concentration profiles near a T-shape(Martin, Derouin et al. 1992) and L-shape(Lackermeier and Werther

2002) exit geometry have been reported, but the traditional core-annulus profiles prevailed despite those exits being more abrupt that the rounded elbow used in this work, presumably due to the lower *St* of the materials tested.

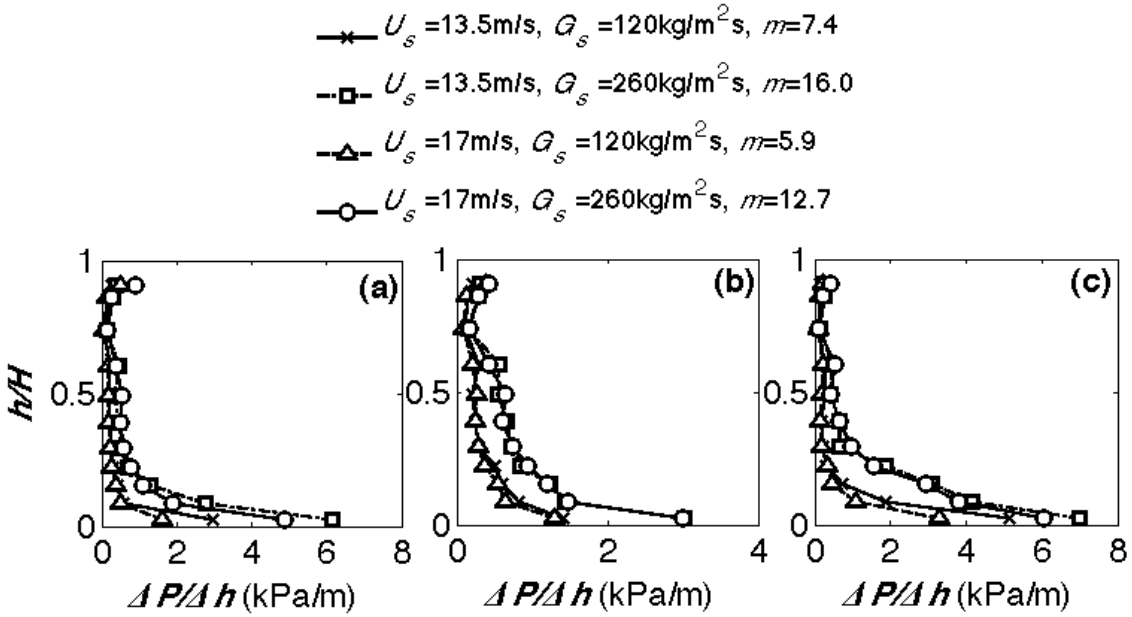

Figure 148. *Differential pressure (ΔP/Δh) profiles for (a) large glass, (b) large HDPE, and (c) small glass.*

Notably, the *ΔP/Δh* profiles in Figure 148 appear consistent with the radially-averaged solid volume fraction ($\overline{\phi}$) profiles obtained with Pitot tube / extraction probe measurements (Figure 144). Specifically, higher measurements were similarly obtained at high *h*/*H* for large glass, and higher solid loadings of 12.7 and 16.0 give distinctly higher *ΔP/Δh* and $\overline{\phi}$ in each subplot.

Summary: Experiments in a pilot-scale circulating fluidized bed (CFB) riser have been carried out for three monodisperseGeldart Group B materials of different size and material density: (i) large glass (d_{ave} = 650 μm, ρ_s = 2500 kg/m^3), (ii) large HDPE (d_{ave} = 650 μm, ρ_s = 900 kg/m^3), and (iii) smaller glass (d_{ave} = 170 μm, ρ_s = 2500 kg/m^3). Detailed solid volume fraction (Φ) profiles of the three materials are reported, providing a rich dataset towards understanding the impact of size and material density on riser flows.

Although a core-annulus solids concentration profile (i.e., dilute core and dense annulus) has been conventionally presumed, observations in this work using two independent measurement techniques indicate instead a reverse core-annulus profile (i.e., a dense core and dilute annulus) for some systems. As discussed, although either gas-phase turbulence effects in dilute flows or rough walls reported in previous works may independently lead to a slight reversal of core-annulus, it does not appear that either effect on its own is sufficient to produce the accentuated reverse core-annulus profiles observed in this work, especially that observed for large glass beads. To provide a physical picture to explain the exaggerated reverse core-annulus profile obtained at the top of the riser, it is hypothesized that roughness elements on the upper wall of the rounded elbow leads to a reversal of particles back into the riser center. More specifically, particle-wall collisions tend to be specular for smooth walls, but much more diffuse for roughened walls. Hence, particles are more likely to deflect back into the riser when the wall

of the elbow exit is rough, thereby causing a region of higher Φ away from the wall at the top of the riser.

In addition, the extent and likelihood of reverse core-annulus profiles can be linked to the Stokes number (*St*) of the material. Specifically, particles with larger *St* are more likely to follow more diffuse trajectories after collision rather than following fluid streamlines, because of greater particle inertia relative to fluid viscous forces. Hence, roughened walls are most likely to exert the greatest effect on reversing the trajectory of large-*St* particles. In particular, the larger glass beads have the highest *St*, and hence exhibit not only reverse core-annulus across all four operating conditions, but also the most pronounced reversal of the core-annulus profiles. For HDPE, the material with intermediate *St*, reverse core-annulus was only observed for two of the four conditions, namely the low G_s conditions. Lastly, for the smaller glass beads, their smaller *St* indicates that they are more likely to follow fluid streamlines and thus less likely to maintain their reversed trajectory (back into riser) after collision with roughness elements. Accordingly, the higher the *St* of the particle, the higher the tendency towards reverse core-annulus; this observation puts forth an important distinction between the larger Geldart Group B and smaller Group A particles.

Finally, the results of this work are expected to contribute towards model validation, especially in terms of the different behavior of Geldart Group A and B particles, incorporation of wall roughness and exit effects. To date, the vast majority of experimental efforts have focused on Geldart Group A particles. The unexpected reverse core-annulus behavior and its associated physical causation reported in this work contribute an interesting caveat towards validating models.

Task 4.5.2: Species Segregation[5]

Abstract: Experiments involving a gas-solid, pilot-scale circulating fluidized bed (CFB) have been carried out, with a focus on species segregation measurements in a riser. Three mixtures were considered: (i) a binary mixture with particles of different sizes (d_{ave}) but same material density (ρ_s), (ii) a binary mixture with particles of different material densities (ρ_s) but same size (d_{ave}), and (iii) a continuous particle size distribution (PSD). Local measurements of the composition (i.e., species segregation) of each mixture were obtained over a range of operating conditions. Similar to previous works, the results show that the more massive species (i.e., greater d_{ave} or ρ_s) preferentially segregates toward the wall in all cases. Several new trends were also observed. First, for the *binary* mixtures, composition of the more massive species increases with riser height at the wall under some operating conditions. The operating conditions that cause this phenomenon are mutually exclusive for the size-difference and density-difference systems. Second, for the *continuous* PSD, radial segregation is observed even when there is a net positive flux in the annular region, contrary to previous findings which indicated segregation only for conditions leading to a net downward flux in the annular region. Finally, two *qualitative differences between the binary and continuous* mixtures were noted: (i) a monotonic decrease in species segregation is observed for the binary mixtures with an increase in the solid loading (*m*), while a non-monotonic trend is observed for the continuous PSD, and (ii) while the shape of the radial segregation profile is flattest at the riser bottom for the binary mixtures, the flattest radial profile is at the riser top for the continuous PSD.

[5] Chew, Hays, Findlay et al., "Species segregation of binary mixtures and a continuous size distribution of Group B particles in riser flow", submitted, Chemical Engineering Science, 2011.

Introduction: While Section 4.5.1 focuses on monodisperse materials, this section reverts back to polydispersity, specifically with respect to species segregation (de-mixing) characteristics. Also, whereas Task 4.3 is regarding species segregation in a bubbling fluidized bed, this section concerns species segregation in a moderately dense CFB riser. Because species segregation varies along the riser, the gas-solid contact times of each species may vary and hence impact the overall efficiency of the unit. Although investigation into species segregation behavior in low-velocity bubbling fluidized beds has been fairly extensive (Rowe and Nienow 1976; Nienow and Chiba 1985; Kunii and Levenspiel 1991; Lim, Zhu et al. 1995; Joseph, Leboreiro et al. 2007), a similar effort for CFBs is lacking.

The current work is divided into two categories: *binary* mixtures (two species with particle size (d_{ave}) or material density (ρ_s) differences) and *continuous* particle size distributions (PSDs). The objectives of this experimental work are to (i) isolate the effect of d_{ave} and ρ_s on species segregation in binary mixtures, (ii) investigate a continuous PSD alongside the binary mixtures to better compare their species segregation trends, especially since qualitative differences between the two distributions have recently been observed for bubbling fluidized beds(Chew, Wolz et al. 2010; Chew and Hrenya 2011), and (iii) evaluate the impact of a wide range of operating conditions on the observed trends at all riser positions. The vast majority of previous efforts have been targeted at only binary mixtures, in which the two species have *both* size and material-density differences. With regards to axial segregation for binary mixtures, both experiments(Bai, Nakagawa et al. 1994; Nakagawa, Bai et al. 1994; Werther and Hirschberg 1997; Hirschberg and Werther 1998; Mathiesen, Solberg et al. 2000; Das, Meikap et al. 2008) and simulations(Mathiesen, Solberg et al. 2000; Zhou, Flamant et al. 2002; Lu and Gidaspow 2003; Liu, Metzger et al. 2008) have indicated that the more massive species segregates towards the bottom of the riser. As for radial segregation, both simulation results(Lu and Gidaspow 2003; Benyahia 2008; He, Deen et al. 2009) and experimental data(Hirschberg and Werther 1998; Mathiesen, Solberg et al. 2000; Das, Meikap et al. 2008) are more scarce. Nonetheless, despite differences in material properties, operating conditions and CFB riser dimensions and configurations, the more massive (i.e., higher particle mass) species have been consistently found to preferentially segregate to the wall. Compared to their binary-mixture counterparts, segregation studies on continuous PSDs are rare(Hirschberg and Werther 1998; Karri and Knowlton 1998). The trends observed to date are largely consistent with the segregation of the larger (i.e., more massive) species toward the bottom of the riser and toward the wall.

For the mixture types investigated here, the more massive species preferentially segregates toward the wall at all axial locations, as is consistent with previous experimental work(Hirschberg and Werther 1998; Karri and Knowlton 1998; Mathiesen, Solberg et al. 2000; Das, Meikap et al. 2008) and known granular temperature profiles(Lu, Liu et al. 2000; Lu, Gidaspow et al. 2001; Zhou, Flamant et al. 2002; Lu and Gidaspow 2003; Tartan and Gidaspow 2004; Biggs, Glass et al. 2008; Songprawat and Gidaspow 2010). Comparison among the three systems indicate that the greater the mass ratio between the species, the greater the extent of this radial segregation observed, which corroborates previous work(Trujillo, Alam et al. 2003; Trujillo and Herrmann 2003; Galvin, Dahl et al. 2005; Yoon and Jenkins 2006; Liu, Metzger et al. 2008). With regards to axial segregation, the composition of the more massive species generally decreases with riser height at the riser center ($r/R = 0$), consistent with previous findings that exhibited an overall decrease of composition of heavier particles with height(Nakagawa, Bai et al. 1994; Hirschberg and Werther 1998; Das, Meikap et al. 2008).

Furthermore, the observed increase in extent of axial species segregation with mass ratio is linked to increase in single-particle terminal velocity (U_t) ratios(Hirschberg and Werther 1998).

In addition to the consistent trends between the current experiments and previous findings, several new observations also emerged. First, with regards to the *binary* mixtures, a noteworthy observation involves the increase in the composition of the more massive species with riser height at the wall under some operating conditions. Interestingly, the operating conditions associated with this behavior for the size-difference binary mixture are mutually exclusive from those of the density-difference system. Second, with regards to the *continuous* PSD, while Karri and Knowlton(Karri and Knowlton 1998) found that radial segregation only exists when the annulus has a net downward, radial segregation is consistently observed in this work regardless of whether the annulus has a net upward or downward flux. Lastly, with regards to the *differences in segregation behavior between binary mixtures and continuous PSD*, two interesting observations are noted: (i) an increase in solid loading (m) correlates with a monotonic decrease in species segregation (both axial and radial) for the binary mixtures, while a non-monotonic trend is observed for the continuous PSD, and (ii) while the shape of the radial segregation profile is flatter at the riser bottom for the binary mixtures, the opposite trend is observed for the continuous PSD.

Experimental Description – Experimental Setup: Experiments were conducted in the same circulating fluidized bed (CFB) as in Section 4.5.1 (Figure 127).

Materials of Interest: The materials of interest are two binary mixtures - one with a difference in average particle diameter (d_{ave}) and the other with a difference in material density (ρ_s) - and a continuous PSD. Table 11 summarizes the basic parameters of each mixture investigated, with further details given below.

Table 11. Polydisperse materials investigated.

	Vol %	Material	d_{ave} (μm)	ρ_s (kg/m^3)	σ/d_{ave} (%)
Binary: Size-difference	50	Small Glass	170	2500	12
	50	Large Glass	650	2500	9
Binary: Density-difference	50	Large HDPE	650	900	11
	50	Large Glass	650	2500	9
Continuous PSD	100	Small Glass	170	2500	25

The continuous PSD is made up of glass beads with ρ_s = 2500 kg/m^3 and d_{ave} = 170 μm. The width of this distribution (defined as the ratio of standard deviation of mass-weighted PSD to the average particle diameter) is σ/d_{ave} = 25%. These glass beads are used as-is from the vendor (Midwest Finishing Systems). A representative sample was collected from the bulk with a sample thief and analyzed with sieve trays and a Ro-Tap sieve-shaker. The sample thief consists of two 1 m long concentric tubes with a small spacing in between to allow the tubes to rotate in opposite azimuthal directions. The inner tube is solid except for one chamber used for sample collection. The hollow outer tube has an opening that aligns with the collection chamber on the inner tube, and also has a pointed end for insertion into the drum of particles to obtain a representative sample. The resulting PSD is shown in Figure 149a, where f_m is the mass fraction of each sieve cut normalized with respect to bin size (for fairer comparison among sieve cuts of different widths).

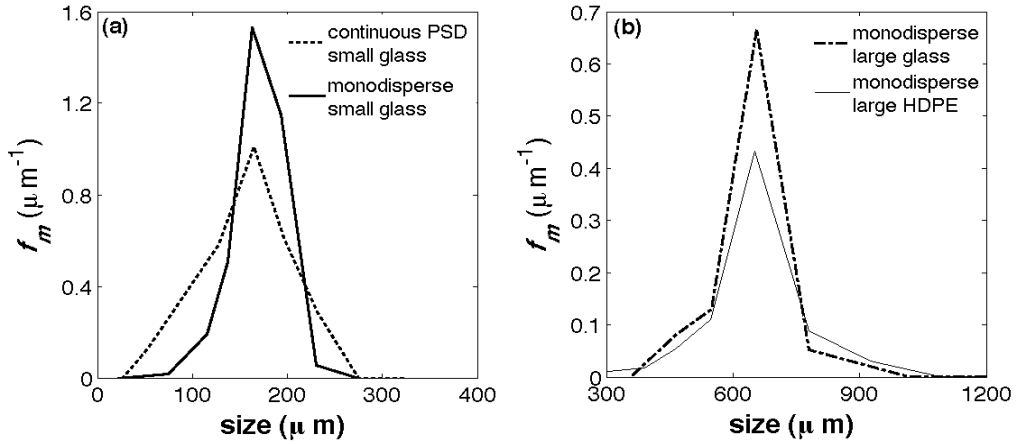

Figure 149. *PSDs of constituent materials: (a) continuous PSD of small glass with σ/d_{ave} = 25% and monodisperse small glass with σ/d_{ave} = 12%, (b) monodisperse large glass and large HDPE, each with σ/d_{ave} ~ 10%.*

Unlike the continuous PSD, the materials used to obtain the binary mixtures require processing before the experiments. As presented in Table 11, the binary mixtures are made up of various sets of monodisperse particles with different material density (ρ_s) and size (d_{ave}), namely (i) "large" glass (ρ_s = 2500 kg/m^3 and d_{ave} = 650 μm), (ii) "large" high-density polyethylene, HDPE (ρ_s = 900 kg/m^3 and d_{ave} = 650 μm), and (iii) "small" glass (ρ_s = 2500 kg/m^3 and d_{ave} = 170 μm). Glass beads of both sizes and HDPE were acquired from Midwest Finishing Systems and Dyneon LLC, respectively. It is impossible for the "monodisperse" particles to be of identical size, so here monodisperse refers to materials obtained with as narrow a distribution of sizes as possible. More specifically, the materials procured from vendors were sieved using the Sweco industrial sieve, which is a continuous sieving procedure designed to process large quantities. Due to the continuous nature of this sieve, the particles are not perfectly separated between the various sieve sizes. Accordingly, a representative sample was obtained from each drum of sieved material using the sample thief and then further analyzed using a Ro-Tap sieve-shaker. Figure 148 is a plot of mass-based frequency (f_m) versus particle diameter. For each monodisperse material, σ/d_{ave} is approximately 10%. Furthermore, all particles used are approximately spherical, as noted in a previous work(Chew, Hays et al. 2011).

Measurement Technique: To characterize the species segregation in the riser, an extraction probe was used to collect particles at various axial and radial positions along the riser. The extraction probe has an inner diameter of 0.017 m and is fabricated such that probe tip is oriented 90^o to the probe shaft in order to measure the flux associated with upward or downward flow when the shaft is inserted horizontally. Samples were collected at five approximately equally-spaced axial positions along the riser. At each axial location, two sets of 11 radial measurements that are 90^o apart in the horizontal plane were taken to determine if any asymmetries were present across the riser cross-section. For composition (species segregation) analysis, different methodologies are used for each mixture. For the size-difference binary mixture, the Sympatec HELIOS PSD analyzer, which is based on laser diffraction, was used. For the density-difference binary mixture, the species were separated via immersion in water since glass beads sink while HDPE beads float. For the continuous PSD, the Ro-Tap sieve-

shaker was utilized. Notably, volume percentage of each species can be derived with the methods and is used as a common denominator in comparing species segregation for the different mixtures.

Using the extraction probe, both the upward and downward mass flux at each local radial position (G_r) is measured by orientating the probe tip normal to the flow in the downward and upward direction, respectively. At each location, the extraction probe is used to collect particles for 20 – 30 s. The net mass flux across the cross-section of the riser at a given axial position is denoted G_s and is calculated as

$$G_s = \sum_{r=1}^{11\,radial\,positions} \left[(G_{r,upward} - G_{r,downward}) \times A_r \right] \tag{81}$$

where the subscripts upward and downward refer to the flux directions, and A_r is the annular area corresponding to that radial position. (For example, for radial position r_j, the corresponding annular area has an outer and inner radius of $(r_j+r_{j+1})/2$ and $(r_j+r_{j-1})/2$, respectively.)

To validate the extraction probe measurements, checks were made with regard to the (i) reproducibility of mass flux measurements over repeated runs and over various measurement durations, and (ii) consistency of the local mass flux integrated across the riser cross-section at each axial position, which ensures a mass balance. Reproducibility of the mass flux measurements for various measurement durations is illustrated in Figure 150a for large glass beads at U_s = 17 m/s and a target G_s = 200 kg/m^{2}s. At least two repeat measurements of G_r were carried out at various measurement durations. The results displayed in Figure 150a indicate that the scatter around the targeted G_s is about ±10% regardless of measurement duration. As a further validation of the extraction probe, Figure 150a b shows G_s measured at all axial positions for the large HDPE at U_s = 13.5 m/s and G_s = 260 kg/m^{2}s. The *y*-axis, *x*-axis and error bars represent the dimensionless riser height (*h/H;* where *h* is the height along the riser at which measurement is taken and *H* is the total height of the riser), the (radially) integrated mass flux (G_s), and the span of the two bi-directional measurements, respectively. Based on mass conservation, G_s should be consistent along the riser height, as is displayed in Figure 150a b with an acceptable tolerance of ±10%.

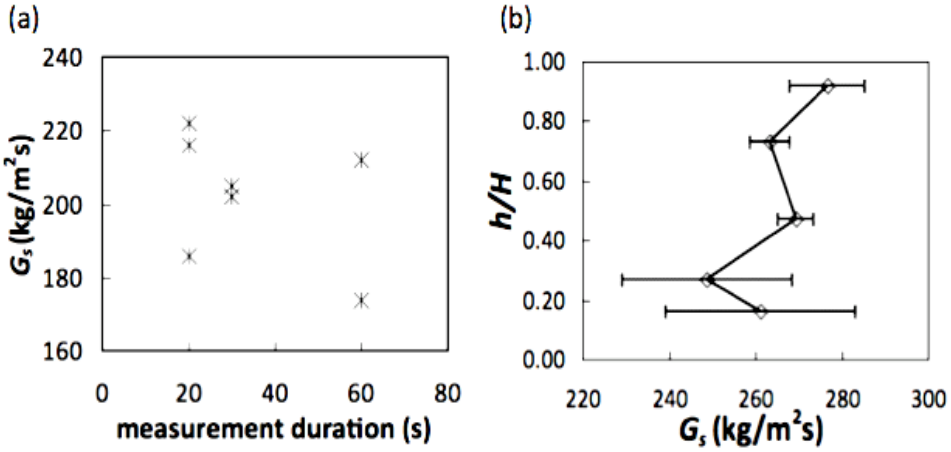

Figure 150. *(a) Reproducibility of cross-sectional mass flux over repeated measurements and various measurement durations for large glass beads at U_s = 17 m/s and G_s = 200 kg/m^{2}s. (b) Axial variation of cross-sectional mass flux for large HDPE beads at U_s = 13.5 m/s and G_s = 260 kg/m^{2}s.*

Operating Conditions: Table 12 lists the operating conditions investigated for each mixture. The ranges of superficial gas velocity (U_s) and overall mass flux (G_s) utilized were maximized based on the physical constraints of the fluidized material, experimental set-up, and instruments, as detailed below. Also listed in Table 12 is solid loading (m), which is a dimensionless quantity defined as the ratio of solid flux to gas flux, as given in Equation 70 ($m = \frac{G_s}{U_s \rho_g}$). Notably, a different set of operating conditions was used for the binary mixtures and the continuous PSD, primarily because high m leads to slugging associated with the large glass beads (highest single-particle terminal velocity, U_t, among the materials) in the binary mixtures. Accordingly, a direct comparison between the binary mixtures and the continuous PSD is not possible, and thus qualitative differences (if any) between the segregation behaviors of the two distribution types are the focus in this work.

Table 12. *Operating conditions for polydisperse materials.*

	U_s (m/s)	G_s (kg/m²s)	m
Binary Mixtures	13.5	120	7.4
	13.5	260	16.0
	17	120	5.9
	17	260	12.7
Continuous PSD	10	50	4.2
	10	300	25.0
	15	50	2.8
	15	300	16.7

For the binary mixtures, the lower U_s limit was set to 13.5 m/s to allow for higher mass flux (G_s) to be investigated, while the higher U_s limit (17 m/s) was chosen to avoid too much pressure on the Plexiglas fronting the rectangular fluidized bed in the recirculation loop (Figure 129). As for G_s, the lower bound (120 kg/m^{2}s) was restricted by the sensitivity of the Pitot tube used as part of a corollary investigation (Chew, Hays et al. 2011) at the higher U_s limit. On the other hand, the upper G_s bound (260 kg/m^{2}s) was restricted at the lower U_s limit to deter slugging. Correspondingly, four combinations ofU_s and G_s were examined for the binary mixtures (Table 12).

For the continuous PSD, the range of m was expanded since slugging was less of an issue in the absence of the larger glass beads and the Pitot tube was not used (since the momentum measurement by Pitot tube restricts its application to monodisperse materials). Accordingly, the lower G_s was set to 50 kg/m^{2}s, which is the upper limit for some industrial gas-solids reaction processes (e.g., solid fuel combustion or aluminum calcination) (Arena 1997). On the other hand, the higher G_s was set to 300 kg/m^{2}s, which is the lower limit for some industrial gas-phase reaction processes (e.g., fluid catalytic cracking (FCC) or Fischer-Tropsch synthesis) (Arena 1997). As for U_s, the lower limit was set to 10 m/s, below which slugging would prevail at the higher G_s. The upper limit was set to a conservative 15 m/s in light of the high pressure generated on the Plexiglas fronting the rectangular fluidized bed in the recirculation loop (Figure 129). Hence, four combinations of U_s and G_s were also examined for the continuous PSD (Table 12).

Results and Discussion: Local measurements of the PSD were obtained at each set of operating conditions (Table 12) and for each of the three mixtures under consideration (Table 11): size-difference binary mixture, density-difference binary mixtures, and continuous PSD. Figure 151 depicts the radial segregation profiles of the size-difference binary mixture composed of glass beads with different sizes, specifically with a d_{ave} ratio of 3.8. The subplots of each figure contain data at each of the U_s, G_s pairings given in Table 12. The vertical axis represents percentage, by volume, of the extracted sample that is composed of the larger glass beads, while the horizontal axis represents the dimensionless radius (r/R) of the riser cross-section (where r is the radius at which measurement is taken and R is the radius of the riser). The data points represent average values of the two sets of bi-directional (90^o apart) radial measurements taken at each axial position, and the error bars denote the span of the two values. Notably, the small error bars serve as verification of symmetry within the riser, which is not surprising given the design of the riser entrance region. The various profiles on each subplot represent measurements taken at different heights (h/H) along the riser, as indicated in the legend.

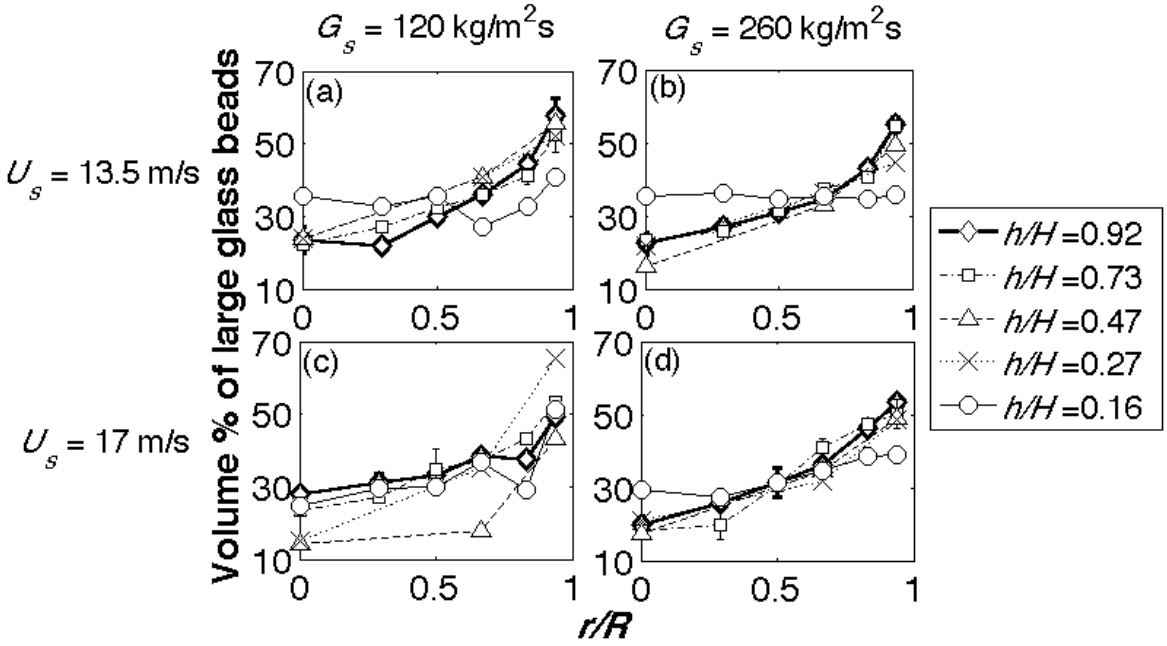

Figure 151. *Radial segregation of a size-difference binary mixture (glass beads with d_{ave} ratio of 3.8) at different axial locations and under operating conditions of (a) U_s = 13.5 m/s, G_s = 120 kg/m^{2}s, m = 7.4, (b) U_s = 13.5 m/s, G_s = 260 kg/m^{2}s, m = 16.0, (c) U_s = 17 m/s, G_s = 120 kg/m^{2}s, m = 5.9, and (d) U_s = 17 m/s, G_s = 260 kg/m^{2}s, m = 12.7.*

Based on the results contained in Figure 151, the composition of larger glass beads increases monotonically towards the wall. This phenomenon of the more massive (i.e., larger for case of size-difference mixture) species segregating preferentially toward the wall agrees with previous experimental and theoretical work(Karri and Knowlton 1998; Mathiesen, Solberg et al. 1999; Lu and Gidaspow 2003; Benyahia 2008; He, Deen et al. 2009). The physical explanation for such segregation behavior is related to the expected radial granular temperature profiles within the riser. In particular, it has been shown via both experiments(Tartan and Gidaspow

2004; Biggs, Glass et al. 2008) and kinetic-theory-based models(Lu, Liu et al. 2000; Lu, Gidaspow et al. 2001; Lu and Gidaspow 2003; Benyahia 2008; Songprawat and Gidaspow 2010) that lower granular temperature regions are found at the wall due to augmented dissipation of kinetic energy through (i) particle-wall collisions and (ii) increased particle-particle collisions due to the higher solid volume fraction expected in the annular region (i.e., core-annulus flow). The more massive species have a tendency to segregate preferentially toward the lower temperature region due to thermal diffusion(Lu and Gidaspow 2003), as is also found in granular(Hsiau and Hunt 1996; Jenkins 1998; Luding, Strauss et al. 2000; Xu, Louge et al. 2003; Dahl and Hrenya 2004; Galvin, Dahl et al. 2005; Liu, Metzger et al. 2007; Garzo and Reyes 2010) systems. Not surprisingly, a similar influence of the temperature gradient on the species segregation in bubbling fluidized beds has also been noted(van Wachem, Schouten et al. 2001; Fan and Fox 2008; Annaland, Bokkers et al. 2009).

A second observation is that, generally, the radial species segregation profile is relatively flat at the bottom of the riser (h/H = 0.16) and becomes progressively accentuated with riser height. Bearing in mind that large glass beads represent 50% by volume of the mixture, it is worthwhile to note that the composition of large glass beads is as low as 20% by volume at the riser center (r/R = 0), and increases to 60% by volume at the wall (r/R = 1). Conversely, the composition of the small glass beads is 80% and 40% at the riser center and wall, respectively. Hence, the ratio of the volume percentage at r/R = 1 to r/R = 0 for the large glass beads is 3, while the ratio of the volume percentage at r/R = 0 to r/R = 1 for the small glass beads is only 2, which indicates that the larger (more massive) species exhibits a higher extent of segregation radially.

Similar radial species segregation profiles are portrayed in Figure 152 for the density-difference binary mixture composed of large glass beads and HDPE of the same d_{ave} but different ρ_s, specifically with a ρ_s ratio of 2.8. In this system, the more massive (i.e., higher ρ_s for case of different-density systems) glass preferentially segregates to the wall at all axial positions and under all four operating conditions (though measurements closest to the wall show some variation). Compared to the size-difference system of Figure 151, the radial segregation profiles for the density-difference system (Figure 152) are significantly flatter (note the reduced range of the *y*-axis in Figure 152). For a fairer comparison between the two binary mixtures, the mass ratios between the species are calculated to be 55.9 for the *size*-difference binary mixture and 2.8 for the *density*-difference binary mixtures. Accordingly, a physical explanation for the accentuated (radial) species segregation for the *size*-difference system lies in the greater mass ratio of the two species. Previous work corroborates with this results herein in that a greater mass ratio culminates in more pronounced species segregation for both gas-solid (Trujillo, Alam et al. 2003; Liu, Metzger et al. 2008) and granular (Trujillo and Herrmann 2003; Galvin, Dahl et al. 2005; Yoon and Jenkins 2006) systems. Another observation with similarity to the size-difference case (Figure 151) is that species segregation profiles become progressively flatter lower in the riser.

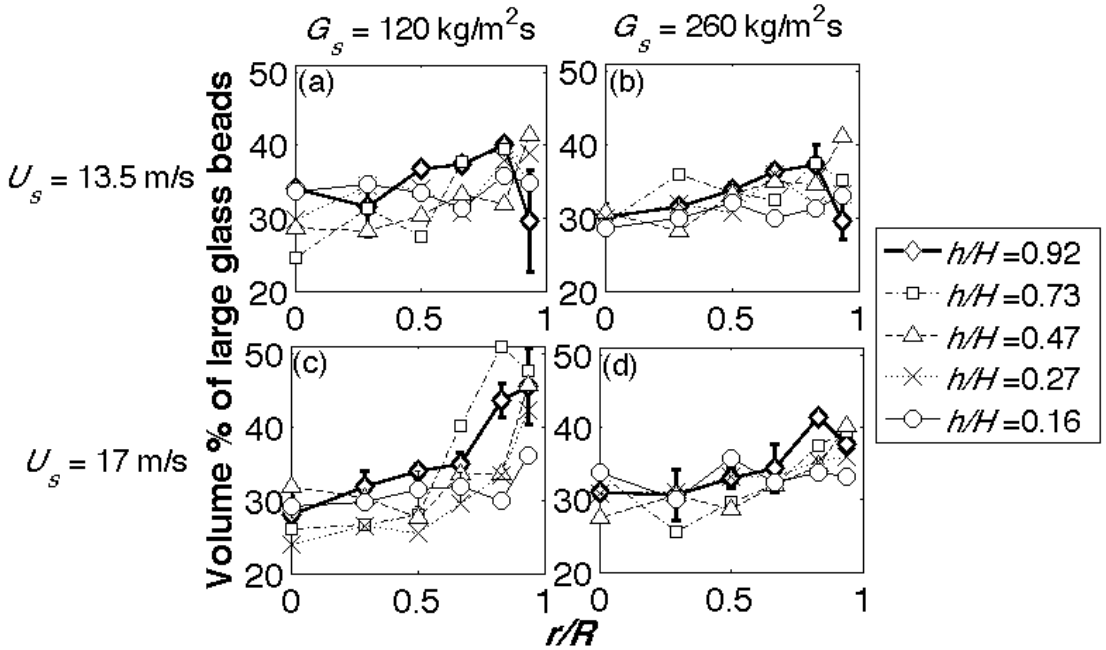

Figure 152. *Radial segregation of a density-difference binary mixture (glass beads and HDPE with ρ_s ratio of 2.8) at different axial locations and under operating conditions of (a) U_s = 13.5 m/s, G_s = 120 kg/m^{2}s, m = 7.4, (b) U_s = 13.5 m/s, G_s = 260 kg/m^{2}s, m = 16.0, (c) U_s = 17 m/s, G_s = 120 kg/m^{2}s, m = 5.9, and (d) U_s = 17 m/s, G_s = 260 kg/m^{2}s, m = 12.7.*

For a more straightforward comparison with the binary systems, the continuous PSD was analyzed in terms of two "species". Namely, particles making up the larger and smaller 50% by mass (or volume) of the initial PSD (Figure 149) are considered as the larger (d_{ave} = 188 μm for the larger half of the mass distribution) and smaller (d_{ave} = 150 μm for the smaller half of the mass distribution) species, respectively. Hence the d_{ave} ratio of the two species is 1.3. Accordingly, similar to Figure 151 and Figure 152, Figure 153 displays the radial profile of species segregation for the larger species making up the continuous PSD of glass beads. Consistent with the binary systems, it is observed that the more massive (larger) species preferentially segregate to the wall (r/R = 1), which agrees with previous work (Karri and Knowlton 1998). Although Karri and Knowlton (Karri and Knowlton 1998) also reported the segregation of larger particles toward the wall when investigating a continuous PSD, the presence of radial segregation was only observed for conditions in which the *net* annular flux was downward, whereas negligible segregation was observed at operating conditions in which the net annular flux was upward. In contrast, radial segregation is observed here for all conditions, including those with a net upward annular flux. In particular, although the net annular flux is downward only at h/H < 0.47 for all operating conditions other than at U_s = 15 m/s and G_s = 50 kg/m^{2}s (Figure 153c), radial segregation of the larger species to the wall persists. As a possible explanation for the apparent discrepancy, consider first that an annular region with a net upward flux has nonzero values of both upward and downward flux, though the former is greater in magnitude than the latter. Also, as reported in previous work (Hirschberg and Werther 1998; Das, Meikap et al. 2008), the PSD obtained for upward flux (probe tip pointing upward) at the wall consists of smaller particles than that for corresponding downward

flux (downward-pointing probe), as shown in Figure 154. Consequently, if the *net* upward flux annulus conditions that Karri and Knowlton (Karri and Knowlton 1998) operated were such that the ratio of upward flux to downward flux is relatively high, then the overall annular PSD may be shifted leftwards, and hence radial segregation effects may not significant.

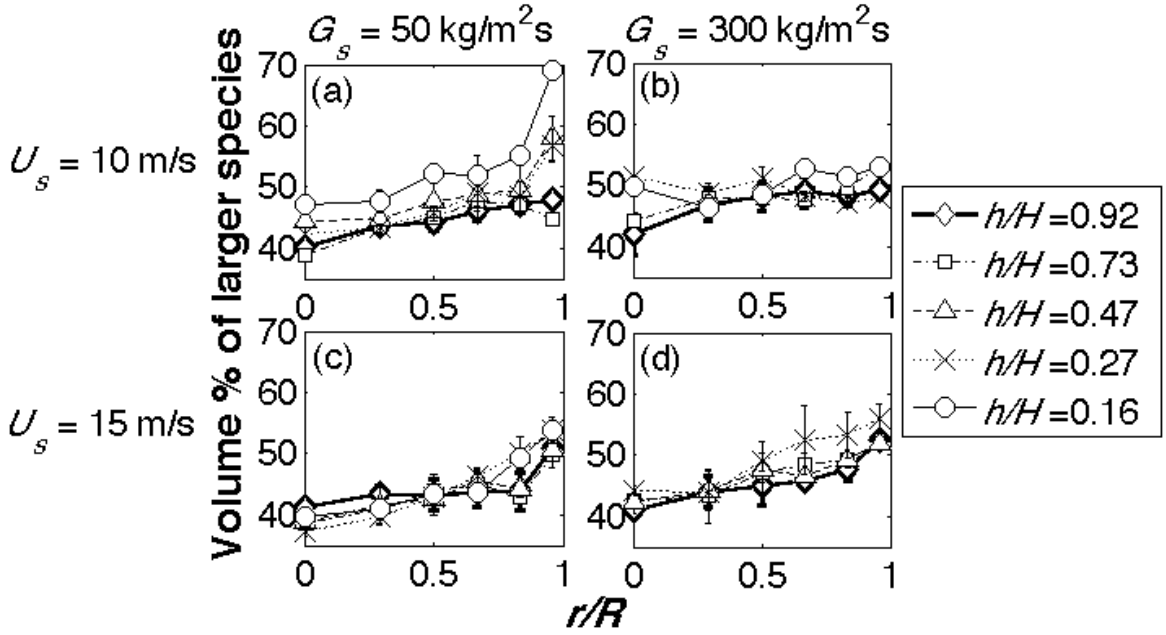

Figure 153. *Radial segregation of continuous PSD small glass at different axial locations and under operating conditions of (a) U_s = 10 m/s, G_s = 50 kg/m^{2}s, m = 4.2, (b) U_s = 10 m/s, G_s = 300 kg/m^{2}s, m = 25.0, (c) U_s = 15 m/s, G_s = 50 kg/m^{2}s, m = 2.8, and (d) U_s = 15 m/s, G_s = 300 kg/m^{2}s, m = 16.7.*

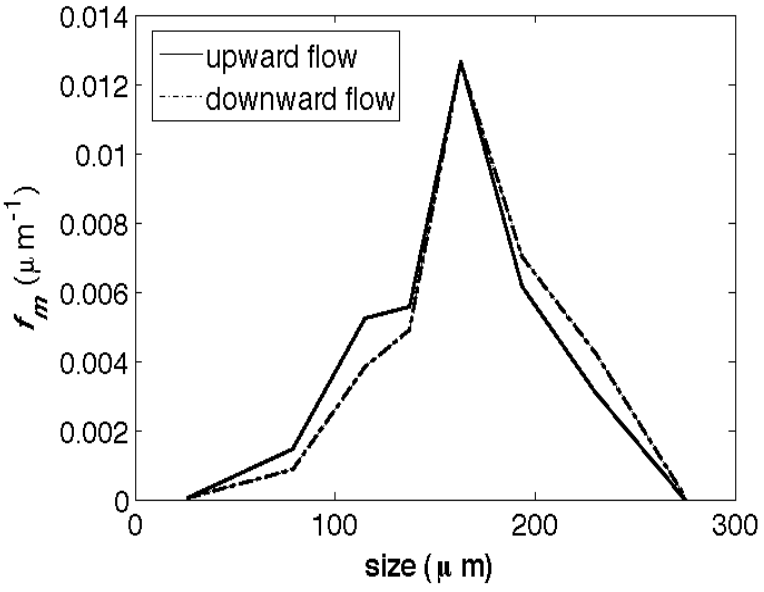

Figure 154. *PSD of upward flow versus downward flow at wall for continuous PSD of small glass under operating condition of U_s = 10 m/s, G_s = 50 kg/m^{2}s, m = 4.2, and h/H = 0.27.*

Furthermore, two other observations are noteworthy when comparing the radial segregation patterns for the continuous PSDs to those of the binary mixtures. First, the continuous PSD has a mass ratio of 2.0, which is lower than either of the binary mixtures. Thus, it is not surprising that the segregation profiles (Figure 153 are flatter than the two binary mixtures (Figure 151 and Figure 152). However, contrary to the binary systems in which the bottom-most position (*h/H*=0.16) exhibited the flattest radial profile, the flattest radial profile occurs at the top-most position (*h/H*=0.92) for this continuous PSD system. Such qualitative differences between binary-sized mixtures and continuous PSDs have not been previously documented.

Collectively, Figure 155 through Figure 157 depict the extent of *axial* segregation of the three mixtures investigated. Analogous to the *radial* segregation plots (Figure 151 through Figure 153), the subplots of each figure contain data at each of the U_s, G_s pairings given in Table 12. The vertical axis represents dimensionless height (*h/H*) along the riser, while the horizontal axis represents percentage by volume of the more massive species. The data points represent average values of the two sets of bi-directional (90^o apart) radial measurements taken at each axial position, and the error bars denote the span of the two values. The various profiles on each subplot represent measurements taken at different dimensionless radius (*r*/*R*) across the riser, as indicated in the legend. In these figures, the more vertical the plotted lines are, the lesser the extent of axial segregation.

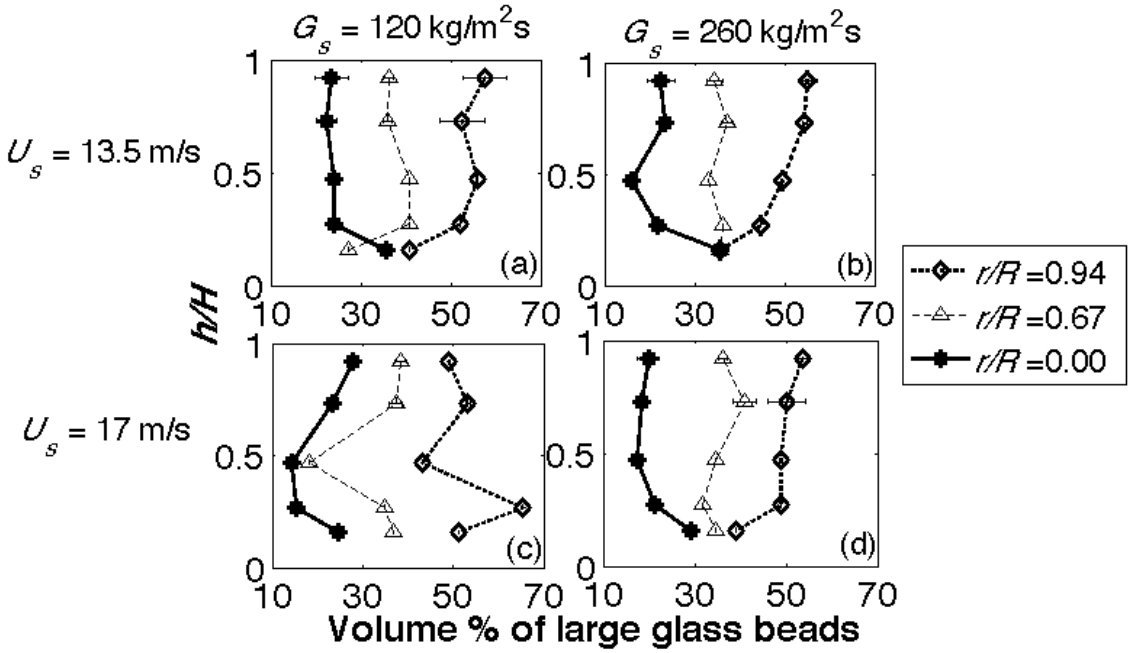

Figure 155. *Axial segregation of a size-difference binary mixture (glass beads with d_{ave} ratio of 3.8) at different radial positions and under operating conditions of (a) U_s = 13.5 m/s, G_s = 120 kg/m^{2}s, m = 7.4, (b) U_s = 13.5 m/s, G_s = 260 kg/m^{2}s, m = 16.0, (c) U_s = 17 m/s, G_s = 120 kg/m^{2}s, m = 5.9, and (d) U_s = 17 m/s, G_s = 260 kg/m^{2}s, m = 12.7.*

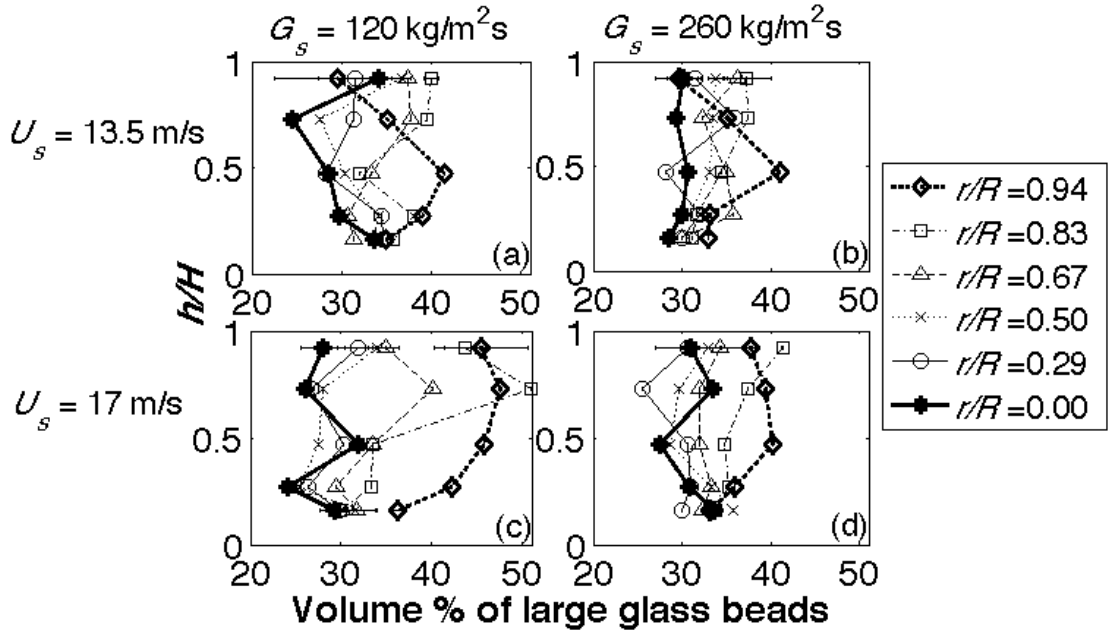

Figure 156. *Axial segregation of a density-difference binary mixture (glass beads and HDPE with density ratio of 2.8) at different radial locations and under operating conditions of (a) U_s = 13.5 m/s, G_s = 120 kg/m^{2}s, m = 7.4, (b) U_s = 13.5 m/s, G_s = 260 kg/m^{2}s, m = 16.0, (c) U_s = 17 m/s, G_s = 120 kg/m^{2}s, m = 5.9, and (d) U_s = 17 m/s, G_s = 260 kg/m^{2}s, m = 12.7.*

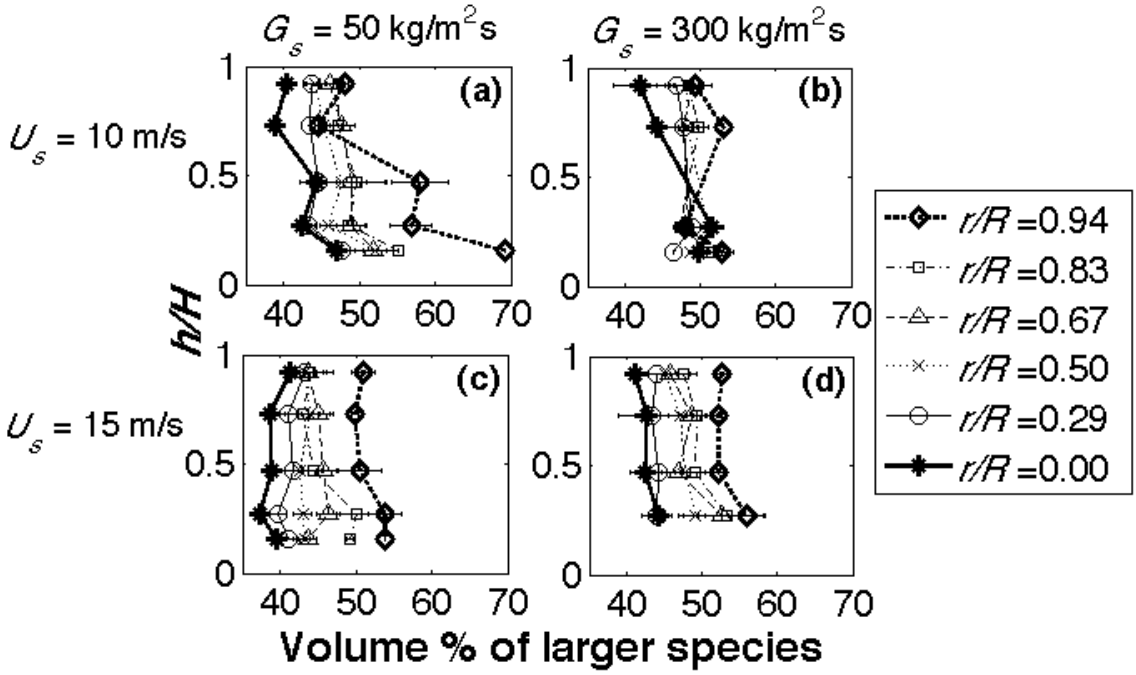

Figure 157. *Axial segregation of continuous PSD of small glass at different radial locations and under operating condition of (a) U_s = 10 m/s, G_s = 50 kg/m^{2}s, m = 4.2, (b) U_s = 10 m/s, G_s = 300* kg/m^{2}s, *m* = 25.0, (c) U_s = 15 m/s, G_s = 50 kg/m^{2}s, *m* = 2.8, and (d) U_s = 15 m/s, G_s = 300 kg/m^{2}s, *m* = 16.7.

In Figure 155, plots for the size-difference binary mixture are presented. Generally, the composition of the larger species decreases with riser height at the riser center (r/R = 0), consistent with previous findings that indicated an overall decrease of composition of coarser species with height(Nakagawa, Bai et al. 1994; Hirschberg and Werther 1998; Das, Meikap et al. 2008). However, except at the lowest *m* condition (Figure 155c), the composition of the larger species surprisingly increases with height at the wall (r/R = 1) to above 50 volume % (which is the initial mixture composition). The physical explanation for the different axial segregation trends at r/R = 0 and 1 is unclear given the combined role of drag, granular temperature gradient, and gas-phase turbulence in the vertical direction, though future modeling studies are expected to aid in this regard. Finally, the most contoured plots are observed for the lowest solid loading condition (Figure 155c), which agrees with previous work (Nakagawa, Bai et al. 1994; Hirschberg and Werther 1998; Van de Velden, Baeyens et al. 2007) in that axial segregation increases (more contoured plots) as *m* decreases.

The axial species segregation profiles for the density-difference binary mixture are illustrated in Figure 156. Consistent with Figure 155, the greatest axial variation is found for the lowest *m* condition (Figure 156c). Similar to radial segregation, noting that the *x*-axis scale in Figure 156 is approximately half that in Figure 155, less axial segregation (more vertical plots) is observed for the density-difference system than for that of size-difference. Analogous to the hypothesis that increased radial segregation can be traced to an increased mass ratio of the species, Hirschberg and Werther (Hirschberg and Werther 1998) proposed that increased single-particle-terminal-velocity (U_t) ratio of the species leads to increased axial segregation. Namely, the greater the difference in U_t of the species, the greater the difference in the driving force for elutriation (namely, U_s-U_t) of each species is expected, and hence the greater the extent of axial segregation. Notably, the size-difference and density-difference binary mixture have U_t-ratios of 4.1 and 1.9, respectively, which is consistent with the lesser axial segregation observed in the latter system (Figure 156). Another interesting observation is that, in sharp contrast to the size-difference binary mixture, the composition of the more massive species surprisingly increases with height at the wall (r/R = 1) only at the lowest *m* condition (instead of except at the lowest *m* condition for the size-difference binary mixture). The physical explanation for the difference on the impact of *m* on axial segregation at the wall (r/R = 1) for the two binary mixtures remains elusive until future modeling efforts shed more light in this regard.

Finally, Figure 157 shows the axial species segregation profiles for the continuous PSD. Generally, less axial species segregation is observed for the continuous PSD than for any of the binary mixture (Figure 155 and Figure 156), which is consistent with the U_t-based hypothesis presented earlier that the extent of axial species segregation decreases with a decrease in U_t-ratio of the species. Hence, the continuous PSD is expected to have the least axial species segregation due to its lowest U_t ratio of 1.4. On a separate note, although Karri and Knowlton (Karri and Knowlton 1998) noted negligible axial species segregation in the core (r/R = 0), the lower U_s conditions in this work display axial species segregation at r/R = 0 (Figure 157a and b), with the discrepancy presumably arising from differences in operating conditions. Specifically, Karri and Knowlton (Karri and Knowlton 1998) implemented a lower U_s (5.9 m/s) than in this work. Interestingly, axial species segregation behavior for the continuous PSD deviates from the binary mixtures on two counts. First, the most extensive axial species segregation (i.e., most contoured plots, especially at r/R = 0.94) is observed for the operating condition of U_s = 10m/s and G_s = 50 kg/m^{2}s (Figure 157a), which notably is *not* the condition with the lowest *m*. Accordingly, in contrast to the binary mixtures in which the extent of axial segregation decreases monotonically

with an increase in *m*, a non-monotonic behavior is noted for the continuous PSD. Also, another difference with the binary mixtures is that the volume % of the larger species does not increase with height under any operating condition for the continuous PSD.

Summary: A detailed experimental investigation on species segregation of Geldart Group B particles has been carried out in a pilot-scale CFB. Three mixtures were investigated: (i) a binary mixture with particles of different size but equal material density, (ii) a binary mixture with particles of different density but equal size, and (iii) a continuous size distribution of particles with equal density.

In several respects, the results observed here mimicked those previously reported. First, for all three systems and consistent with previous experimental work (Hirschberg and Werther 1998; Karri and Knowlton 1998; Mathiesen, Solberg et al. 2000; Das, Meikap et al. 2008), the more massive species preferentially segregates to the wall at all axial locations. This radial segregation behavior can be explained in terms of thermal diffusion, which drives the more massive species toward the lower granular temperature at the wall, as has been indicated from both experimental (Tartan and Gidaspow 2004; Biggs, Glass et al. 2008) and modeling (Lu, Liu et al. 2000; Lu, Gidaspow et al. 2001; Lu and Gidaspow 2003; Benyahia 2008; Songprawat and Gidaspow 2010) results. Comparison among the three mixture types indicate that the greater the mass ratio between the species, the greater the extent of radial segregation observed. Hence, the highest segregation extent is for the size-difference binary mixture followed by the density-difference binary mixture and finally the continuous PSD, with mass ratios are 55.9, 2.8 and 2.0, respectively. Again, previous work in both gas-solid(Trujillo, Alam et al. 2003; Liu, Metzger et al. 2008) and granular(Trujillo and Herrmann 2003; Galvin, Dahl et al. 2005; Yoon and Jenkins 2006) systems corroborates these trends. Second, with regards to axial segregation, the composition of the more massive species decreases with riser height at the riser center ($r/R = 0$), which is consistent with previous findings(Nakagawa, Bai et al. 1994; Hirschberg and Werther 1998; Das, Meikap et al. 2008). For axial segregation, the ratio of single-particle terminal velocity (U_t) is expected to dominate the extent of segregation(Hirschberg and Werther 1998). Consistent with this explanation, the most extensive axial segregation is observed here for size-difference binary mixture.

Beyond the consistencies with previous experimental trends, several new observations emerged from the current effort. First, for the *binary mixtures*, although the composition of the more massive species expectedly always decreases with height at $r/R = 0$ (core), an increase of the more massive species with height at $r/R = 1$ (annulus) is observed at some operating conditions. Interestingly, the operating conditions for which this behavior occurs are mutually exclusive for the size-difference and density-difference binary mixtures. Furthermore, the increase of the more massive species with height at the wall exists only for the binary mixtures and not for the continuous PSD, which was investigated under a wider range of *m*. The physical explanation for both the increase of massive species with height, and the different impact of operating conditions for the size-difference and density-difference binary mixtures is unclear at this point, but future modeling work on the effects of drag and granular temperature is expected to shed some light in this regard.

For the *continuous PSD*, two interesting findings emerged. First, while Karri and Knowlton (Karri and Knowlton 1998) found radial species segregation only for systems with a net downward annular flux, radial segregation is observed here regardless of the net direction of the annular flux. Second, while Karri and Knowlton (Karri and Knowlton 1998) observed negligible axial species segregation at $r/R = 0$, axial segregation is observed at $r/R = 0$ for the lower U_s

conditions examined in this work. One explanation for the discrepancy on the former is the different ratios of upward and downward fluxes at the annulus. On the other hand, the discrepancy for latter is presumably due to the higher U_s implemented in this work, but further work is needed in this regard for a more through understanding.

Finally, with regards to the *qualitative differences in species segregation between binary mixtures and continuous PSD*, several interesting observations are noted. First, whereas a monotonic increase in species segregation (both axial and radial) for the binary mixtures occurs with an increase in *m*, a non-monotonic trend is observed for the continuous PSD. Specifically, the greatest extent of species segregation is observed for the operating condition with the lowest *m* for both binary mixtures, whereas the greatest extent of segregation was found at an intermediate *m* condition for the continuous PSD. Second, while the shape of the radial segregation profile is flatter at the riser bottom for the binary mixtures, the opposite trend is observed for the continuous PSD. Third, while the composition of the more massive species increases with height at the wall (r/R = 1) under some operating conditions for the binary mixtures, the composition of the more massive species always decreases with height for the continuous PSD.

Collectively, the new species segregation trends reported here provide further insights into the high-velocity fluidization behavior of both binary mixtures and continuous size distributions. Perhaps more importantly, these results also reveal key qualitative differences between the segregation patterns in binary mixtures and continuous PSDs, as have previously been documented in bubbling fluidized beds ((Hoffmann and Romp 1991; Gauthier, Zerguerras et al. 1999; Lin, Wey et al. 2002) and Task 4.3(Chew, Wolz et al. 2010)). Such data is expected to be of value in the continued development and validation of polydisperse kinetic-theory-based models (for recent example, see Garzó et al. (Garzo, Dufty et al. 2007; Garzo, Hrenya et al. 2007); for recent review, see Hrenya (Hrenya 2011)). Conversely, such continuum models are expected to provide physical insight into the new segregation trends reported here.

Task 4.5.3: Mass Flux Profiles[6]

Abstract: Experiments targeted at understanding local mass flux behavior of Geldart Group B materials in the riser of a gas-solids circulating fluidized bed (CFB) have been carried out. Three monodisperse materials (with differences in particle size, d_{ave}, and/or material density, ρ_s), two binary mixtures - one with only a d_{ave} difference between the species (size-difference binary) and one with only a ρ_s difference (density-difference binary), and one continuous particle size distribution (PSD) have been investigated under four operating conditions. Results show that riser axial position has the greatest influence on mass flux behavior, especially near the riser top, where profile shapes are consistently an inverted U or V. Material type (i.e., monodisperse materials of different d_{ave} and/or ρ_s, or different types of polydispersity) and operating conditions effects are secondary, and such effects are most apparent at the riser bottom. An interesting observation involving binary mixtures is that, while the density-difference binary mixture mimics one of the constituent components, the size-difference binary mimics neither component.

[6] Chew, Hays, Findlay et al., "Impact of material property and operating conditions on mass flux profiles of monodisperse and polydisperse Group B particles in the riser", in preparation for submission in May 2011.

Introduction: In addition to the solids concentration (Section 4.5.1) and species segregation (Section 4.5.2) characteristics, understanding of other local behaviors is warranted for a complete picture of the fluidization behavior, which will aid in model validation and the design of future CFB units. Accordingly, the focus of this section (Section 4.5.3) is on the local mass flux behavior, and local cluster behaviors will be presented in Sections 4.5.4 and 4.5.5. Specifically, the objective here is to illustrate the impact of various factors, namely the local position in the riser, operating conditions, and particle materials (both monodisperse and polydisperse), on the mass flux values. Most work on local mass flux has unsurprisingly focused on fluid cracking catalyst (FCC)(van Breugel, Stein et al. 1969; Monceaux, Azzi et al. 1986; Bader, Findlay et al. 1988; Azzi, Turlier et al. 1990; Rhodes 1990; Herb, Dou et al. 1992; Miller and Gidaspow 1992; Rhodes and Laussmann 1992; Rhodes, Wang et al. 1992; Berruti, Chaouki et al. 1995; Wei, Lu et al. 1997; Mastellone and Arena 1999; Malcus, Cruz et al. 2002), which is a Geldart Group A material. However, Group A and B materials are well-known to fluidize differently(Geldart 1973). As further evidence of the different physics at play in the two groups, Section 4.5.1(Chew, Hays et al. 2011) presented a surprising reversal of the widely acknowledged core-annulus (dense core and dilute annulus) profiles for Group B materials which was traced to the higher Stokes number of Group B particles. Hence, a need exists to determine the hydrodynamic behavior of Group B particles rather than to extrapolate the behavior of their Group A counterparts.

As indicated in a review(Lim, Zhu et al. 1995), contradictory mass flux trends are present in the literature are due to non-exhaustive datasets, which provide only a limited view of the riser (i.e., comparisons are made at only two riser axial positions and/or under only a couple of operating conditions). Radial mass flux profiles have been previously reported as an inverted U-shape or inverted V-shape(van Breugel, Stein et al. 1969; Bader, Findlay et al. 1988; Azzi, Turlier et al. 1990; Herb, Dou et al. 1992; Rhodes and Laussmann 1992; Aguillon, Shakourzadeh et al. 1995; Marzocchella and Arena 1996; Coronella and Deng 1998; van der Meer, Thorpe et al. 2000; Liu, Grace et al. 2003; Salvaterra, Geldart et al. 2005; Andreux, Petit et al. 2008), but some work also showed flat or upright U-shape profiles(Qi and Farag 1993; Marzocchella and Arena 1996; Wei, Lu et al. 1997; Coronella and Deng 1998; Salvaterra, Geldart et al. 2005). Moreover, radial mass flux profiles have been shown to flatten with an increase in riser height(Bader, Findlay et al. 1988; Herb, Dou et al. 1992; Marzocchella and Arena 1996; Wei, Lu et al. 1997; Coronella and Deng 1998; Salvaterra, Geldart et al. 2005) or a decrease in solid loading (*m*, which is the ratio of mass flux to gas flux)(Herb, Dou et al. 1992; Aguillon, Shakourzadeh et al. 1995; Wei, Lu et al. 1997; Coronella and Deng 1998; Ye, Qi et al. 2009), but some other work indicate the opposite trends in that mass flux profiles flatten as riser height decreases(Salvaterra, Geldart et al. 2005) or *m* increases(Malcus, Cruz et al. 2002). In view of such contradictory trends, it seems that mass flux trends reported at certain heights and/or operating conditions may not apply to other riser heights or under other operating conditions. With regards to the effect of material type, Mastellone and Arena(Mastellone and Arena 1999) investigated the effect of particle size (one Group A, one Group B) and material density (two Group A) and indicated larger or less dense particles give flatter profiles, while smaller or more dense particles give lower wall flux. However, because data was collected at two riser heights, it is not certain if the trends attributed to material type hold at other axial positions or operating conditions. Furthermore, with regards to the concept of 'similar-profiles'(Monceaux, Azzi et al. 1986; Rhodes, Wang et al. 1992), it was shown at one axial position that normalized mass flux profiles (local solids flux divided by riser cross-sectional solids flux) become insensitive to

changes in overall mass flux (G_s) above a certain G_s. Keeping in mind the contradictory trends at different heights, it may not be possible to extrapolate 'similar profiles' for other riser heights. Apparently, the lack of an exhaustive dataset inhibits predictive understanding of the impact of various factors on local mass flux behavior in the riser, and hence a more comprehensive dataset characterizing the entire riser, and encompassing a wide range of operating conditions and different material types is worthwhile.

Notably, pertaining to polydispersity (i.e., presence of a range of particle sizes and/or material density), although polydispersity is ubiquitous in solids processing, a predictive understanding of the effects of polydispersity remains elusive (Sundaresan 2001; Muzzio, Shinbrot et al. 2002; Curtis and van Wachem 2004; Hrenya 2011). In the previous experimental studies that report radial mass flux profiles, none include an assessment of the impact of a binary mixture or continuous particle size distribution (PSD) on the mass flux. Because polydisperse systems exhibit different behavior from monodisperse systems (e.g. species segregation(Rowe and Nienow 1976; van Deemter 1980; Nienow and Chiba 1985; Fan, Chen et al. 1990; Kunii and Levenspiel 1991; Lim, Zhu et al. 1995; Werther and Hirschberg 1997; Rhodes 1998; Ottino and Khakhar 2000; Sundaresan 2001; Muzzio, Shinbrot et al. 2002; Hrenya 2011), clusters(Chew, Hays et al. 2011)) and since different behaviors have been reported among various categories of polydispersity (i.e., binary mixtures and continuous PSDs)(Hoffmann and Romp 1991; Gauthier, Zerguerras et al. 1999; Lin, Wey et al. 2002; Chew, Wolz et al. 2010; Chew, Hays et al. 2011; Chew and Hrenya 2011), investigation into the impact of the two categories of polydispersity (i.e., binary mixture and continuous PSD) on mass flux profiles is needed.

Hence, to bridge the gap in the current knowledge base, this experimental effort is aimed at collecting local mass flux measurements spanning the entire riser for various materials and various operating conditions. Specifically, the focus is on illustrating the impact of local position (radial and axial), operating conditions, and material type (i.e., various monodisperse and polydisperse materials) on mass flux behavior. With regards to material type, six materials are investigated: (i) three monodipserse materials differing in d_{ave} and/or ρ_s, (ii) two binary mixtures, namely one with only a d_{ave} difference between the species (i.e., size-difference binary) and one with only a ρ_s difference (i.e., density-difference binary), and (iii) a continuous PSD of particles with the same ρ_s.

Results show that axial position within the riser exerts the largest influence on the radial profiles of mass flux, especially near the riser top. Profile shapes are consistently inverted U- or V-shape at the topmost axial position, regardless of operating condition or material type (i.e., monodisperse materials of different d_{ave} and/or ρ_s, or different types of polydispersity). Material type and operating condition effects are secondary, and such effects are most apparent at the riser bottom. An interesting observation involving binary mixtures is that, while the density-difference binary mixture mimics one of the constituent components, the size-difference binary mimics neither component.

Experimental Description:

Experimental Set-Up: A schematic of the circulating fluidized bed (CFB) is shown in Figure 129.

Materials Investigated: Table 8 and Table 11 list the relevant parameters of the monodisperse and polydisperse materials, respectively. The particle size distributions (PSDs) are depicted in Figure 149, and photographs of the approximately spherical particles are shown in Figure 131.

Operating Conditions: The operating conditions implemented are tabulated in Table 9 and Table 12 for the monodisperse and polydisperse materials, respectively. Notably, the same set of four operating conditions were investigated for the monodisperse materials and binary mixtures, whereas a different set of four operating conditions were employed for the continuous PSD, due to constraints as explained in Section 4.5.2.

To characterize the local mass flux behavior in the riser, an extraction probe was used to collect particles at various axial and radial positions of the riser. The extraction probe has an inner diameter of 0.017 m and is fabricated (at PSRI) such that probe tip is oriented 90^o to the probe shaft in order to measure the flux associated with upward or downward flow when the shaft is inserted horizontally into the riser. Samples were collected at five approximately equally-spaced axial positions along the riser. At each axial location, two sets of 11 radial measurements that are azimuthally 90^o apart in the horizontal plane were taken to detect any asymmetries across the riser cross-section. It is worth noting that the extraction probe was operated non-isokinetically(Rhodes, Laussmann et al. 1988; Rhodes and Laussmann 1992; Aguillon, Shakourzadeh et al. 1995; Zhang, Johnsson et al. 1997; Salvaterra, Geldart et al. 2005), after checks were made to ensure that the measurements were not dependent on suction velocity. The successful implementation of non-isokinetic operation on Group B particles is expected, since the associated higher Stokes number implies that the particles are less adept at following gas streamlines.

Using the extraction probe, both the upward and downward mass flux at each radial position (G_r) is measured by orientating the probe tip normal to the flow in the downward and upward direction, respectively. At each location, the extraction probe is used to collect particles for 20 – 30 s. The net mass flux integrated across the cross-section of the riser at a given axial position is denoted G_s (which is set to agree with the imposed overall mass flux as listed in Table 9 and Table 12) and is calculated as per Equation 81 ($G_s = \sum_{r=1}^{11\ radial\ positions} \left[(G_{r,upward} - G_{r,downward}) \times A_r \right]$). To express a representative mass flux at each local position, a net mass flux normalized with respect to G_s is defined as $G_{r,net,norm}$:

$$G_{r,net,norm} = \left| \frac{G_{r,upward} - G_{r,downward}}{G_s} \right| \tag{82}$$

where the G_r is the local flux at radial position r, subscripts upward and downward refer to the flux directions, and G_s is the net mass flux integrated across the riser cross-section. The reasons for this normalization are threefold. Because of the experimental variations of approximately ±10% in G_s, this normalization is performed to present fairer comparisons between the different (i) axial locations, (ii) materials (Table 8 and Table 11) and (iii) operating conditions (Table 9

and Table 12). Extraction probe measurements validations are explained in Section 4.5.2 and illustrated in Figure 150.

Results and Discussion: Before examining the results in detail, the matrices of subplots contained in Figure 158-Figure 162 for presentation of mass flux profiles warrants explanation. Specifically, each matrix in each figure is structured to provide a straightforward comparison among measurements at different riser positions, for different materials, and under different operating conditions. Each figure contains 20 subplots: the *y*-axes represent local mass flux normalized with respect to integrated flux at axial position ($G_{r,net,norm}$, as defined in Equation 82), and the *x*-axes represent dimensionless radius (r/R, where r is the radial position at which measurement was taken and R is the riser radius) of the riser. Notably, the same ranges of *y*-axes and *x*-axes are used for within each figure for a straightforward comparison among the subplots. Each of the four columns in the matrix contains radial profiles of mass flux for a given set of operating conditions (as indicated at the top of each column). The vertical position of a subplot within a column depicts the axial position of measurements (denoted as h/H on the right-hand-side of each row, where h is the height at which measurement was taken and H is the total riser height): the bottom-most row depicts profiles at the lowest axial position (h/H = 0.16), with higher rows representing higher h/H, correspondingly the top-most row depicts profiles for the highest axial position of h/H = 0.92. Within a given subplot, each profile represents a different material, as indicated by the legend.

As per the matrix of figures described above, Figure 158 displays the radial mass flux ($G_{r,net,norm}$) profiles of the three *monodisperse* materials investigated (Table 8). Comparing the impact of axial position, type of monodisperse material, and operating conditions on the radial $G_{r,net,norm}$ profiles, Figure 158 indicates that axial position has the greatest influence on the shape of the profiles. In particular, at the riser top (h/H = 0.92), radial $G_{r,net,norm}$ profiles are inverted V-shape for all materials and operating conditions. Notably, the dominant influence of axial position relative to other effects is similar to that of cluster profile trends(Chew, Hays et al. 2011; Chew, Hays et al. 2011), although the cluster profiles are similar at the bottom-most axial position (h/H = 0.16) (Chew, Hays et al. 2011; Chew, Hays et al. 2011) whereas the mass flux profiles here (Figure 158) are similar at the top-most position (h/H = 0.92). Interestingly, near the riser top (h/H = 0.92), despite the reverse core-annulus reported for the larger materials only(Chew, Hays et al. 2011), the mass flux profiles retain the same shape for all materials, and thus solids velocity appears to have a greater influence on mass flux than solids concentration (since mass flux is a function of both solids concentration and velocity).

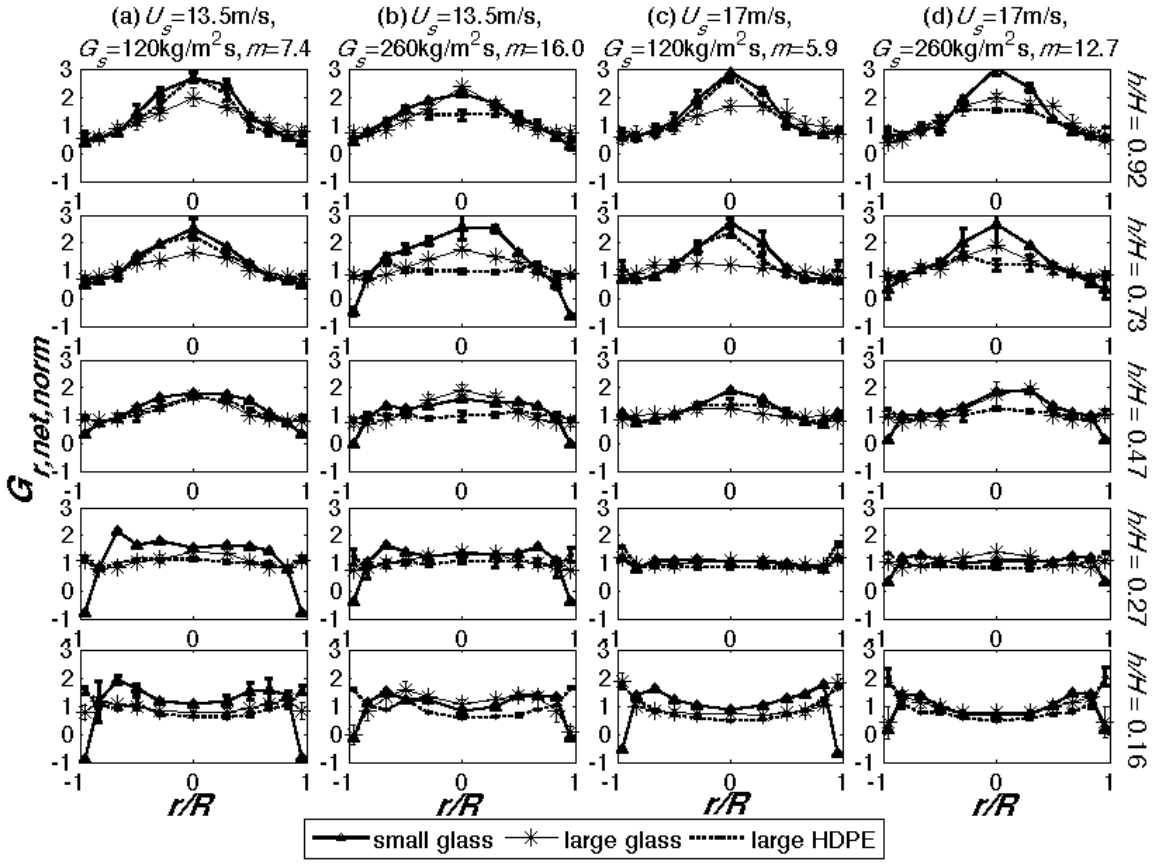

Figure 158. *Radial $G_{r,net,norm}$ profiles for all three monodisperse materials investigated at different axial positions under operating conditions of (a) U_s = 13.5 m/s, G_s = 120 kg/m^{2}s, m = 7.4, (b) U_s = 13.5 m/s, G_s = 260 kg/m^{2}s, m = 16.0, (c) U_s = 17 m/s, G_s = 120 kg/m^{2}s, m = 5.9, and (d) U_s = 17 m/s, G_s = 260 kg/m^{2}s, m = 12.7.*

When differences in the radial $G_{r,net,norm}$ profiles do exist among materials, Figure 158 reveals that these variations are most apparent (i) near the wall (r/R = 1) at low riser heights (h/H = 0.16) and (ii) near the center (r/R = 0) at high riser positions (h/H = 0.92). Interestingly, variations in cluster profiles are similarly at (i) and (ii)(Chew, Hays et al. 2011). In addition, only the larger materials (large glass and large HDPE) exhibit flat profiles at intermediate heights (h/H = 0.27 - 0.47) of the riser for all conditions, while the small-glass profiles do not flatten except at the lowest m condition (Figure 158c). With reference to previous work, Mastellone and Arena(Mastellone and Arena 1999) reported at h/H = 0.4 that larger particles give flatter profiles, and smaller particles give lower wall flux. Comparatively, while Figure 158 shows profiles for larger particles (large glass and large HDPE) to be generally flatter at all axial positions, small glass has lower wall flux only for $h/H \leq 0.47$; hence, because trends vary axially, a more complete picture of $G_{r,net,norm}$ profiles throughout the riser is necessary.

As for the impact of operating conditions on the radial $G_{r,net,norm}$ profiles, changes in operating conditions affect the various monodisperse materials differently. Interestingly, the greatest impact of operating conditions is observed at different heights for each of the monodisperse materials, with the most variations occurring at h/H = 0.16, 0.27, and 0.92 for large glass, small glass, and large HDPE, respectively. Furthermore, G_s plays a role in variations of profiles at h/H = 0.16: the larger materials (large glass and large HDPE) are similar under low

G_s conditions, but the denser materials (large glass and small glass) are similar under high G_s conditions.

To illustrate the impact of polydispersity on mass flux behavior, depicted in Figure 159 is the comparison of the mass flux ($G_{r,net,norm}$) profiles between the *density-difference binary mixture* and its constituent materials (monodisperse large glass and monodisperse large HDPE). Similar to the monodisperse materials (Figure 158), as riser height increases, radial $G_{r,net,norm}$ profile shapes for the density-difference binary mixture evolve from flat at mid-height (h/H = 0.27) to inverted V-shape at the topmost axial position (h/H = 0.92), implying axial position also has a significant influence even in the presence of polydispersity. Where a distinct variation between materials is observed, the density-difference binary mixture mimics large glass more than large HDPE, examples of which are near the wall at the riser bottom (h/H = 0.16) or near the center at the riser top (h/H = 0.92).

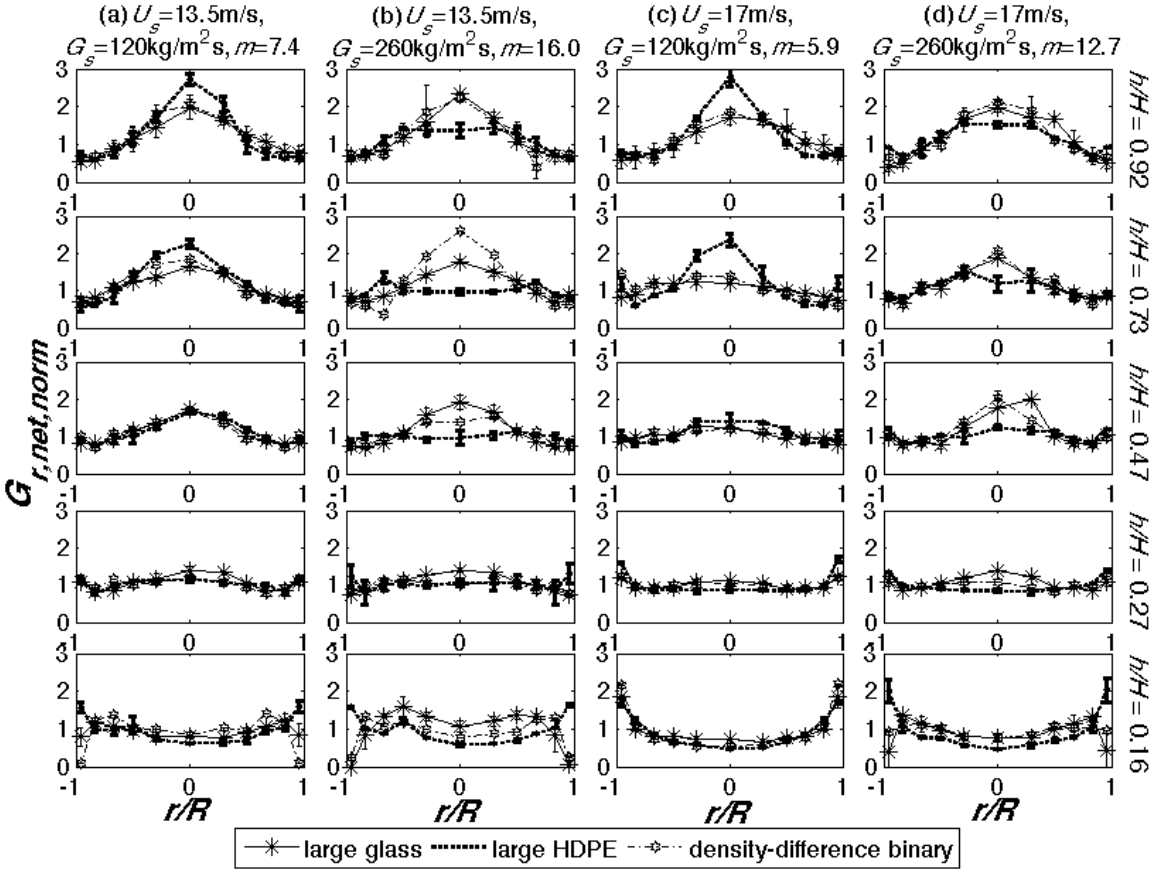

Figure 159. *Radial $G_{r,net,norm}$ profiles of density-difference binary mixture and constituent materials investigated at different axial positions under operating conditions of (a) U_s = 13.5 m/s, G_s = 120 kg/m^{2}s, m = 7.4, (b) U_s = 13.5 m/s, G_s = 260 kg/m^{2}s, m = 16.0, (c) U_s = 17 m/s, G_s = 120 kg/m^{2}s, m = 5.9, and (d) U_s = 17 m/s, G_s = 260 kg/m^{2}s, m = 12.7.*

Analogous to Figure 159, Figure 160= compares the *size-difference binary mixture* to its constituent components (in this case, large glass and small glass). Similar to the trends for the monodisperse materials in Figure 158, the size-difference binary mixture exhibit the following

characteristics: (i) $G_{r,net,norm}$ profile become inverted V-shape at the riser top (h/H = 0.92), and (ii) more material difference is observed at the riser wall (r/R = 1) at lower axial positions (h/H = 0.16), but more material difference at the riser center (r/R = 0) as riser height increases (h/H = 0.92). Notably, in contrast to the density-difference binary mixture, the size-difference binary mixture mimics neither constituent material strictly.

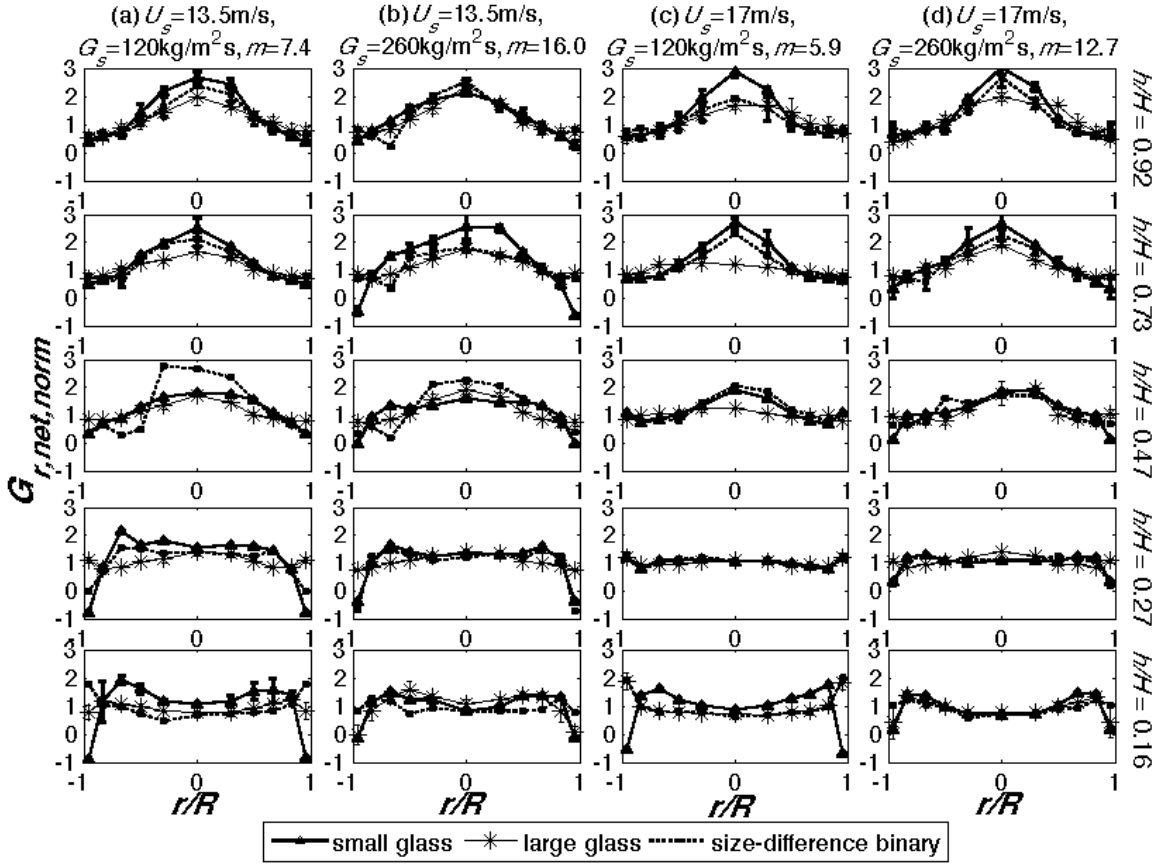

Figure 160. *Radial $G_{r,net,norm}$ profiles of size-difference binary mixture and constituent materials investigated at different axial positions under operating conditions of (a) U_s = 13.5 m/s, G_s = 120 kg/m^{2}s, m = 7.4, (b) U_s = 13.5 m/s, G_s = 260 kg/m^{2}s, m = 16.0, (c) U_s = 17 m/s, G_s = 120 kg/m^{2}s, m = 5.9, and (d) U_s = 17 m/s, G_s = 260 kg/m^{2}s, m = 12.7.*

In Figure 161, the two binary mixtures, which have a common constituent component (large glass), are directly compared. Notably, the radial profiles of $G_{r,net,norm}$ of the two binary mixtures are very similar at h/H = 0.92, which could suggest a more dominant influence of large glass (the common constituent material) relative to the other component at the top-most axial position. Interestingly, the profiles are generally more similar at the higher U_s conditions (Figure 161c and d). Where material effects are apparent particularly for the lower U_s conditions (Figure 161a and b), the binary mixtures are different at the wall (r/R = 1) at lower axial positions ($h/H \leq$ 0.27), and different at the center (r/R = 0) at intermediate heights (h/H = 0.47).

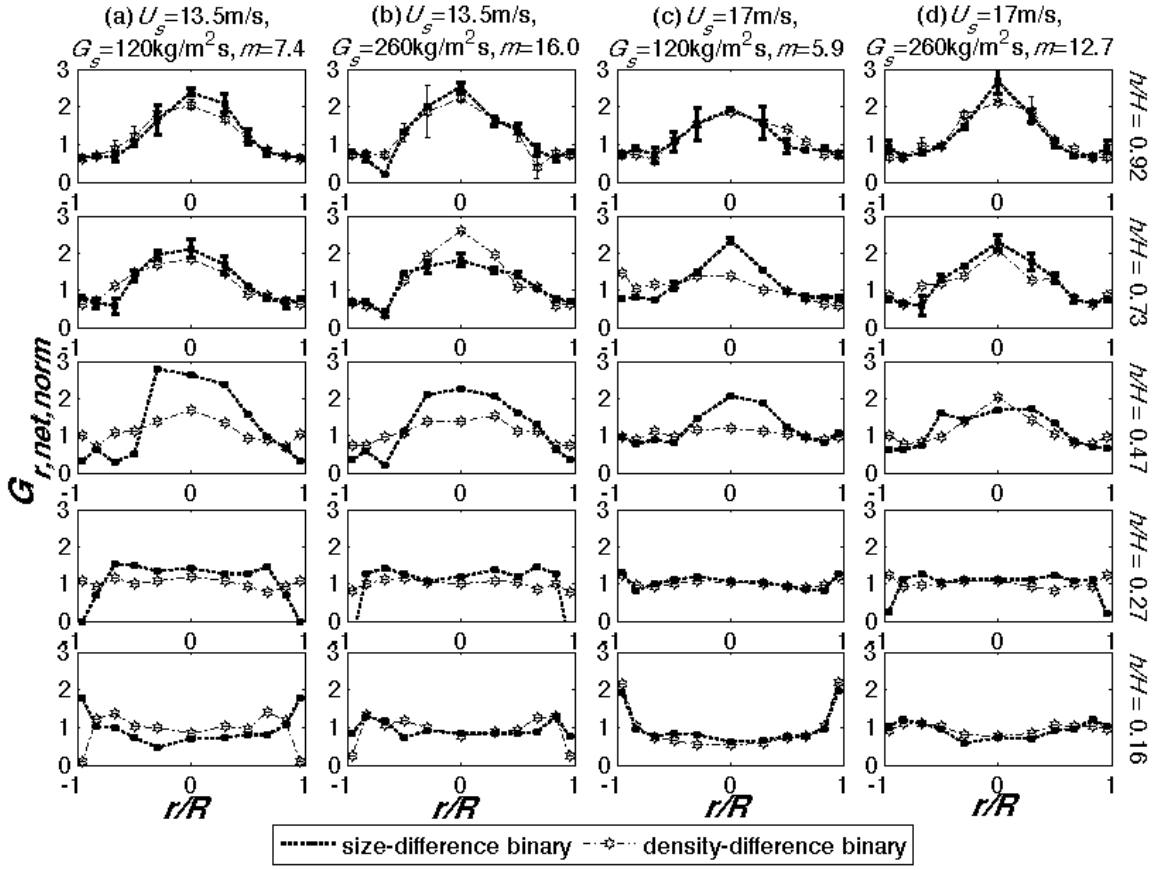

Figure 161. *Radial $G_{r,net,norm}$ profiles for size-difference and density-difference binary mixtures investigated at different axial positions under operating conditions of (a) U_s = 13.5 m/s, G_s = 120 kg/m^{2}s, m = 7.4, (b) U_s = 13.5 m/s, G_s = 260 kg/m^{2}s, m = 16.0, (c) U_s = 17 m/s, G_s = 120 kg/m^{2}s, m = 5.9, and (d) U_s = 17 m/s, G_s = 260 kg/m^{2}s, m = 12.7.*

It was initially presumed that species segregation(Chew, Hays et al. 2011) behavior would have some influence on or would be explicit in the mass flux profiles. In particular, previous species segregation results(Chew, Hays et al. 2011) on the same materials at the same operating conditions in the same riser showed that (i) the more massive (higher d_{ave} or ρ_s) species preferentially segregate to the wall, (ii) more extensive radial and axial species segregation was previously reported for the size-difference binary mixture as compared to the density-difference binary mixture, and (iii) least difference between species segregation behavior between the two binary mixtures was observed at the lower-most axial position (h/H = 0.16), since both exhibit flat species segregation profiles. Regarding (i), if higher composition of large glass is found at the wall, do the binary mixtures mimic large glass more at the wall? No - while the density-difference binary mixture (Figure 159 mimics large glass throughout the entire cross-section (i.e., not only at the wall), the size-difference binary mixture (Figure 160) does not strictly mimic large glass at the wall. Pertaining to (ii), if more extensive radial segregation was found for the size-difference binary mixture (Figure 159), it should have a higher tendency to mimic large glass at the wall than the density-difference binary mixture (Figure 160), which is not the case. Figure 161 further shows that the binary mixtures become increasingly similar with height,

despite the extent of species segregation for the size-difference binary mixture increasing more than the density-difference binary mixture with height; on the contrary, where species segregation behaviors are similar at $h/H = 0.16$, the $G_{r,net,norm}$ profiles are most different. The elusiveness of species segregation phenomenon in the $G_{r,net,norm}$ profiles should not be surprising. As noted previously from Figure 158, mass flux profiles are more dominated by solids velocity than concentration, since similar mass flux profiles of monodisperse materials are exhibited despite reverse core-annulus (i.e., dense core and dilute annulus) for the larger materials. Correspondingly, species segregation is linked to granular temperature gradient, and granular temperature is also linked to solids concentration(Lu, Liu et al. 2000; Lu, Gidaspow et al. 2001; Zhou, Flamant et al. 2002; Lu and Gidaspow 2003; Tartan and Gidaspow 2004; Biggs, Glass et al. 2008; Songprawat and Gidaspow 2010); therefore, since solids concentration has less effect on mass flux profiles, along the same vein as granular temperature, species segregation also is not apparent in mass flux profiles.

Finally, $G_{r,net,norm}$ profiles for the small glass with continuous PSD (Table 11) are portrayed in Figure 162. Because the four operating conditions implemented for this continuous PSD are different from the other materials (Table 12), a direct comparison on the effect of material is not possible. Nonetheless, the impact of axial position and operating conditions on the radial profiles are still obtainable. Similarities with results for other materials are apparent as the axial height has a greater influence on radial profiles than does the operating condition. Unlike the other materials investigated, however, at the topmost axial position ($h/H = 0.92$), profiles appear as a flatter inverted U-shape instead of the inverted V-shape for monodisperse materials (Table 8) and binary mixtures (Figure 161). In addition, the $G_{r,net,norm}$ profiles at the lowest m condition (Figure 162c) are distinctly different from the other three conditions (Figure 162a, b, and d) for $h/H \leq 0.47$, due either to (i) a behavioral difference between continuous PSD and binary mixtures (as has been noted in previous work(Chew, Wolz et al. 2010; Chew, Hays et al. 2011; Chew, Hays et al. 2011; Chew and Hrenya 2011)), or (ii) the wider range of operating conditions investigated for this material. Along the lines of "similar profiles" (Monceaux, Azzi et al. 1986; Rhodes, Wang et al. 1992), which states a critical m exists above which $G_{r,net,norm}$ profiles become similar, it is apparent that the lowest m condition (Figure 162c) in this case is below the critical m, and that the critical m lies between $m = 2.8$ (Figure 162c) and 4.2 (Figure 162a). Notably also, since the $G_{r,net,norm}$ profiles are similar for $h/H \geq 0.73$ across all four operating conditions (i.e., including $m = 2.8$ (Figure 162=c)), the magnitude of the critical m associated with the concept of "similar profiles" (investigated at $h/H = 0.4$(Rhodes, Wang et al. 1992)) decreases or disappears at higher heights, which presents another reason why an exhaustive dataset as in this work is necessary.

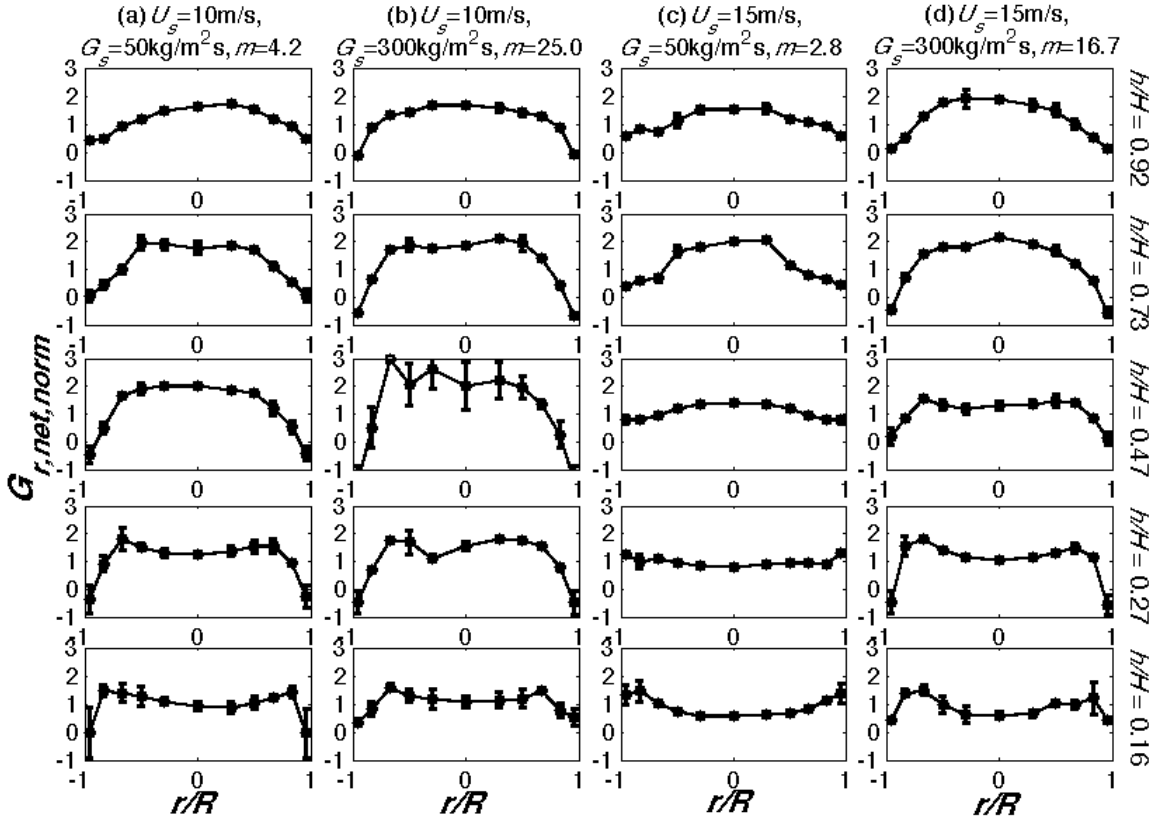

Figure 162. *Radial $G_{r,net,norm}$ profiles for continuous PSD small glass investigated at different axial positions under operating conditions of (a) U_s = 10 m/s, G_s = 50 kg/m^{2}s, m = 4.2, (b) U_s = 10 m/s, G_s = 300 kg/m^{2}s, m = 25.0, (c) U_s = 15 m/s, G_s = 50 kg/m^{2}s, m = 2.8, and (d) U_s = 15 m/s, G_s = 300 kg/m^{2}s, m = 16.7.*

Summary: An experimental suite targeted at mass flux measurements in a riser have been carried out in a pilot-scale CFB. The objective of this work is to understand the impact of (i) local riser positions (axial and radial), (ii) material type (various monodisperse materials and effect of polydispersity), and (iii) operating conditions on mass flux behavior. The particles investigated belong to Geldart Group B, and include three monodisperse materials (differing in d_{ave} and/or ρ_s), two binary mixtures (size-difference and density-difference), and a continuous PSD. Four operating conditions were implemented for each material, and local mass flux was measured at five axial positions along the riser, with two bi-directional (90 degrees azimuthally apart on the horizontal plane) sets of 11 radial positions at each axial position.

The most significant influence on mass flux profiles is the axial position in the riser (which is also the key factor for cluster trends(Chew, Hays et al. 2011; Chew, Hays et al. 2011)), especially near the riser top. Profiles shapes are inverted U- or V-shape at h/H = 0.92, regardless of material type (various monodisperse materials or various polydisperse systems) or operating conditions. Material type and operating conditions effects are secondary and inter-dependent, with effects most apparent at the bottom-most position (h/H = 0.16). As for the impact of polydispersity, the density-difference binary mixture mimics monodisperse large glass (one of the constituent components), whereas the size-difference binary mixture mimics neither constituent component. Finally, the effect of operating condition is more apparent for the

continuous PSD, but it is inconclusive whether it is due to an inherent difference between continuous PSD and binary mixtures (as has been noted in previous work(Chew, Wolz et al. 2010; Chew, Hays et al. 2011; Chew, Hays et al. 2011; Chew and Hrenya 2011)), or due to the wider range of operating conditions implemented for this material.

The mass flux characteristics presented here is part of a wider dataset of various riser characteristics (Sections 4.5.1 - 4.5.5) investigated with the same materials and operating conditions, which collectively provide a rich test-bed for validation of monodisperse and and particularly polypdisperse models(Hrenya 2011) (for recent polydisperse example, see (Garzo, Dufty et al. 2007; Garzo, Hrenya et al. 2007)).

Task 4.5.4: Cluster characteristics of monodisperse materials[7]

Abstract: Experiments in a circulating fluidized bed (CFB) riser with Geldart Group B particles have been carried out, with a focus on cluster characterization. In this section, the focus is on monodisperse materials; results for polydisperse materials are contained in Section 4.5.5(Chew, Hays et al. 2011). A fiber optic probe was used for detection of solids, and cluster identification was accomplished via wavelet decomposition. Using this threshold, three cluster characteristics were evaluated: appearance probability, duration, and frequency. Furthermore, the impact of three factors – riser position, operating condition, and material type – was examined. Results indicate that: (i) of the three factors investigated, riser position has the most dominant influence on cluster characteristics, (ii) cluster appearance probability appears to be largely a function of riser position only, and is insensitive to changes in operating condition or material type, and (iii) cluster duration and frequency are influenced by the particle material and operating condition, though only from mid-height of the riser upwards. The results presented provide a comprehensive picture of factors affecting cluster trends.

Introduction: Similar to Section 4.5.1, this section deals only with monodisperse materials (Table 8), with a specific focus on the cluster characteristics of the monodisperse materials in a moderately dense CFB riser. The next section (Section 4.5.5) will explore the impact of polydispersity on clusters. Because clusters significantly affect the performance of the fluidized bed system in terms of solids mixing, entrainment, and heat and mass transfer, an enhanced understanding of cluster behavior is warranted.

Numerous experimental results on clusters have been reported, though seemingly contradictory trends have emerged. For example, some works have indicated that overall (i.e., integrated across the riser cross-section) appearance probability of clusters decreases(Brereton and Grace 1993; Soong, Tuzla et al. 1995) or remains constant with height(Yang and Leu 2009), while other works indicate a decrease in appearance probability with height at the wall only(Wei, Yang et al. 1995; Manyele, Parssinen et al. 2002). As another example, an increase in the solid loading *m* (ratio of solids flux to air flux) has been shown to either increase(Horio, Morishita et al. 1988; Rhodes, Mineo et al. 1992; Zou, Li et al. 1994; Guenther and Breault 2007; Das, Meikap et al. 2008), decrease(Horio and Kuroki 1994; Wei, Yang et al. 1995; Sharma, Tuzla et al. 2000; Mostoufi and Chaouki 2004; Afsahi, Sotudeh-Gharebagh et al. 2009), or have no effect(Li, Zhu et al. 1995; Sharma, Tuzla et al. 2000) on cluster duration. The contradictory trends presumably stem from the lack of a complete dataset. More explicitly, most works only

[7] Chew, Hays, Findlay et al., "Cluster characteristics of Geldart Group B particles in a pilot-scale CFB riser. I. Monodisperse", in preparation for submission in May 2011.

involve one material, and/or the effect of changing operating conditions at one or two axial positions. Correspondingly, if cluster trends vary at different riser positions, over a wider range of operating conditions, or for different materials, different cluster trends may result. Therefore, the objective of the current effort is to generate a comprehensive dataset of cluster characteristics via local measurements spanning the entire riser, under various operating conditions, and for three monodisperse material types (i.e., different particle size, d_{ave}, and/or material density, ρ_s).

Notably, reports on the impact of material type on cluster characteristics have been especially scarce. Recently, Cocco et al.(Cocco, Shaffer et al. 2010) found polyethylene (PE) to exhibit increased tendency of clustering in both the bed and the freeboard compared to fluid cracking catalyst (FCC), and they attributed the difference to the higher electrostatics, lower restitution coefficient, and smoother surface associated with PE. In addition, it has been reported that coal generally has larger clusters than iron ore when compared at the same solids concentration conditions(Das, Meikap et al. 2008). Another work(Sharma, Tuzla et al. 2000) compared glass beads of different sizes (70 and 120 μm) at only one axial position, and concluded that a larger particle size increases cluster duration and decreases cluster frequency, but does not affect cluster appearance probability. However, as indicated earlier, a gap in the knowledgebase exists due to the incompleteness of the datasets. For example, it is unclear if results taken at a single axial position also hold at other axial positions.

Collectively, previous works indicate that riser position, operating condition, and material type may influence the behavior of clusters. In view of the contradictory cluster trends reported, however, the focus of the current work is to generate a more complete landscape of cluster characteristics with respect to riser position, operating condition, and material type. Namely, the salient questions are twofold. How do the local riser position (both axial and radial), operating condition (superficial gas velocity, U_s, and overall solids flux, G_s), and material type influence cluster characteristics throughout the riser? Moreover, which factor (riser position, operating condition, or material type) exerts the greatest influence on cluster behavior?

To address these questions, cluster measurements have been carried out here for three monodisperse Group B materials in a CFB riser under four operating conditions. Accordingly, a direct comparison of the impact of the various factors on cluster characteristics is possible. More specifically, a fiber optic probe was used for the detection of clusters via wavelet decomposition. Results indicate that (i) local riser position is the primary factor influencing all three cluster characteristics (appearance probability, duration, frequency), while operating conditions and material type are secondary effects, (ii) among the three cluster characteristics, appearance probability is most affected by local riser position and least affected by material type and/or operating condition, and (iii) compared to appearance probability, cluster duration and frequency is more affected by variations of material types and operating conditions (particularly near the top of the riser), although axial variation is still apparent.

Experimental Description:

Experimental Setup: The schematic of the CFB is shown in Figure 129.

Materials Investigated and Operating Conditions Implemented: The three materials considered here are monodisperse Group B particles listed in Table 8. And the operating conditions are as listed in Table 9.

Measurement Technique: The fiber optic probe used for cluster measurements was fabricated at Particulate Solid Research Incorporated (PSRI). The probe is a stainless steel tubing (outer diameter = 0.013 m) which houses two fibers, each with a diameter of 2000 μm. One fiber is used to transmit infrared from a light-emitting diode (LED) source, while the other is the receiver conduit. Notably, the two fibers are aligned to converge towards the probe tip in order to reduce the sampling volume just beyond the probe tip, thereby reducing unnecessary scattering of the light source and enhancing sensitivity(Cocco, Cleveland et al. 1995). The key operating principle of the fiber optic probe is that the receiver fiber detects a higher voltage signal when infrared emitted from the transmitter fiber is blocked and reflected back to the receiver fiber, as occurs when the probe is surrounded by a denser (particle-rich) phase. On the other hand, a lower voltage signal is obtained when infrared from the emitter is relatively unobstructed, as occurs when the probe tip is in a more dilute (gas-rich) phase. Accordingly, bubbles (gas-rich) in a bubbling fluidized bed manifest as downward spikes in a fiber-optic voltage trace, whereas clusters (particle-rich) in a riser (relatively gas-rich) manifest as upward spikes in a fiber optic voltage trace. As examples, fiber optic voltage traces in the riser of the CFB are shown for the case of background (i.e., absence of solids) in Figure 163a and in the presence of solids flow in Figure 163b, both as functions of time. Expectedly, it is observed that the presence of solids induces higher and a wider range of voltages. Hence, with a suitable threshold, cluster (i.e., flow structures denser than uniform distribution of particles) identification can be accomplished.

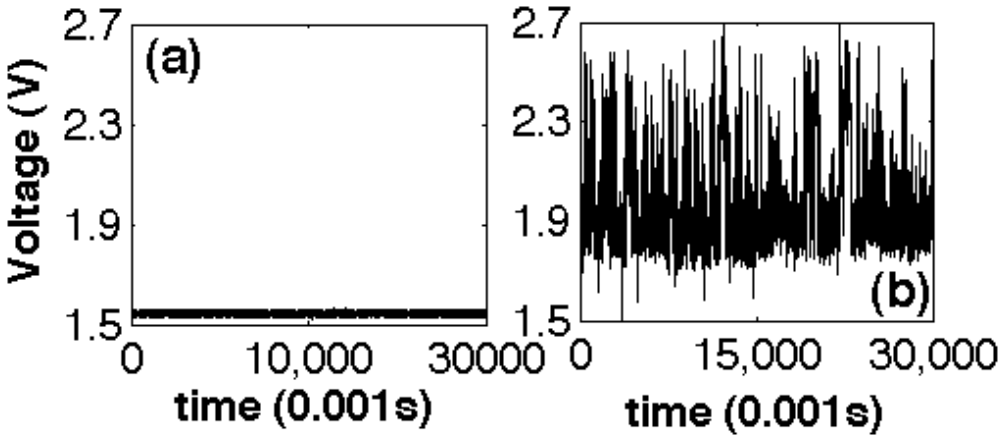

Figure 163. *Example of traces obtained in CFB by fiber optic probe for (a) background (i.e., absence of solids), and (b) large HDPE at operating condition of U_s = 13.5 m/s, G_s = 260 kg/m^{2}s at h/H = 0.47 and r/R = 0.96.*

The choice of voltage threshold for cluster detection is an important consideration. A single-value threshold(Soong, Tuzla et al. 1995; Tuzla, Sharma et al. 1998; Sharma, Tuzla et al. 2000; Manyele, Parssinen et al. 2002; Liu, Gao et al. 2005) (for example, a fixed number of standard deviations above the mean voltage) implies a time-independent demarcation between the two phases, and such a threshold has been considered inadequate due to the dynamic nature of fluidized bed systems(Ellis, Briens et al. 2003; Guenther and Breault 2007; Yang and Leu 2009). Specifically, because fluidized-bed systems have broad spectrum of solids concentration that evolve with time, identifying features like bubbles or clusters necessitates a data analysis method that takes into account the dynamic baseline of measured signals(Ren and Li 1998; Ellis, Briens et al. 2003; Guenther and Breault 2007; Yang and Leu 2009). Therefore, a critical drawback of a Fourier transform of such signals is that the time (dynamic) component is lost during analysis, and hence deficient when signal properties continuously change with time as in a fluidized bed system(Ren and Li 1998; Ellis, Bi et al. 2004). In the past decade, wavelet decomposition(Mallat 1989; Mallat 1998) has been acknowledged to be useful in its ability to extract different frequency ranges while retaining the timestamp of signals, thereby enabling classification of fluidized-bed measurement data into noise (micro-scale), flow structures like clusters or bubbles (meso-scale), and equipment (macro-scale)(Ren and Li 1998; Ellis, Briens et al. 2003; Zhao and Yang 2003; Yang and Leu 2009).

More specifically, wavelet decomposition(Mallat 1989; Mallat 1998) provides a means of extracting different frequency ranges of data signals by repeatedly breaking down the signal into higher-frequency *details* (*D*) and lower-frequency *approximations* (*A*), as illustrated in Figure 133. At the first scale of decomposition (Scale 1), the signal of *N* Hz is divided into the first scale of approximation (A_1) and the first scale of detail (D_1), whereby A_1 contains the lower half of the frequency range and D_1 contains the higher half. Combined via wavelet reconstruction (which reverses wavelet decomposition), the A_1 and D_1 signals result in the original signal. With a further increase in scale from j to $j+1$, each approximation A_j is subsequently decomposed into low-frequency A_{j+1} and high-frequency D_{j+1} signals. Figure 134 shows the approximation and detail signals at various scales, illustrating explicitly the decrease in signal frequency with the increase of scales while preserving the timeline. For the interested reader, a thorough mathematical explanation of the wavelet decomposition technique can be found in Mallat(Mallat 1989; Mallat 1998). In the current work, a data collection frequency of 100 Hz was used for large glass and a higher 1000 Hz was used for large HDPE and small glass (more details on this difference are given below), with wavelet decomposition of the signal accomplished via the wavelet toolbox in Matlab(Misiti, Misiti et al. 2002).

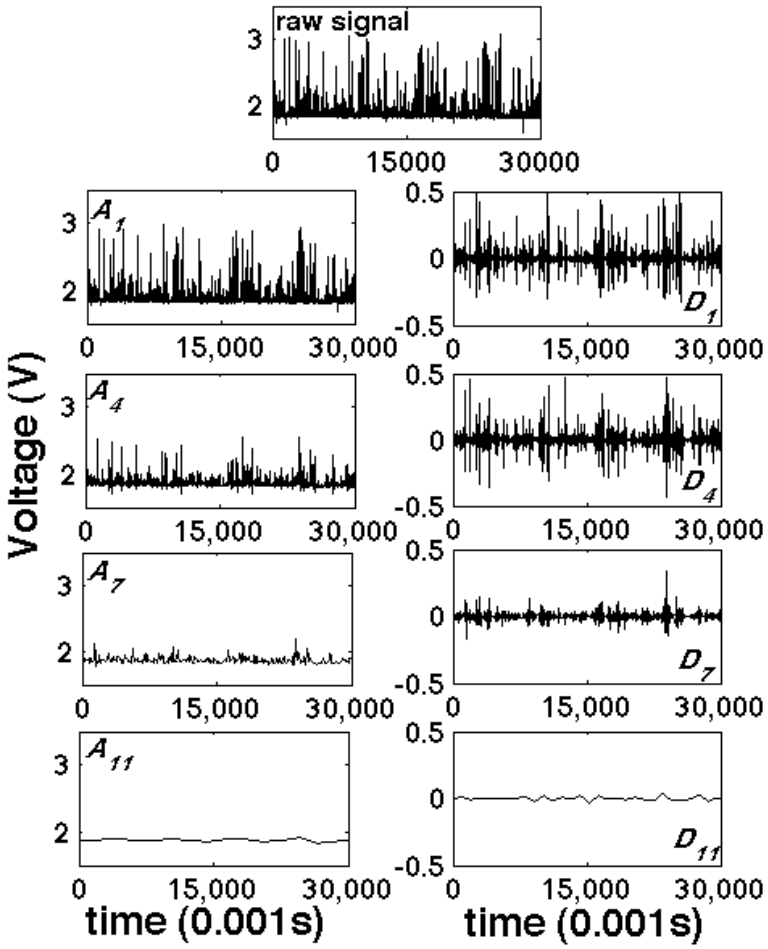

Figure 164. *Raw signal of fiber optic probe collected at 1000 Hz and corresponding approximations (A_j) and details (D_j) at various scales (j) of wavelet decomposition for small glass at operating condition of U_s = 17 m/s, G_s = 260 kg/m^{2}s at h/H = 0.16 and r/R = 0.0.*

Before discussing which wavelet decomposition scale is appropriate to use as the threshold for cluster detection, it is worth noting that efforts have been made by previous researchers towards calibrating the voltage signals obtained from fiber optic probes to obtain solids concentration traces(Louge 1997; van Ommen and Mudde 2008). Nonetheless, several works have noted the inefficacy of the fiber optic probe to give absolute concentration values due to the associated problematic calibration(Matsuno, Yamaguchi et al. 1983; Herbert, Gauthier et al. 1994; Zhang, Johnston et al. 1998). Consequently, in this work, instead of calibrating the fiber optic probe signals to obtain quantitative values (magnitudes) for solids concentration, the raw voltage traces were instead analyzed for relative changes in concentration (via wavelet analysis) in order to obtain information on clustering.

To use wavelet analysis to extract information on clusters, a threshold for cluster identification is required. More specifically, the threshold should have a physical significance based on the ability of wavelet decomposition to demarcate the different scales (micro-scale, meso-scale, macro-scale)(Ren and Li 1998; Ellis, Briens et al. 2003; Zhao and Yang 2003; Yang and Leu 2009). Since information of clusters are represented in the meso-scale (Li, Wen et al.

1996; Ren and Li 1998; Ren, Mao et al. 2001; Guenther and Breault 2007; Wu, Apostolos et al. 2007; Yang and Leu 2009), the scale corresponding to the meso-scale range is needed. Accordingly, normalized energy plots of the decomposed signals were inspected to determine the delineation among the various scales(Ren, Mao et al. 2001; Wu, Apostolos et al. 2007; Yang and Leu 2009). Specifically, the normalized relative energy of the detail signals at each scale ($\frac{E_{Dj}}{E_{J,all}}$) is calculated based on Equation 79.

The corresponding normalized wavelet energy plots are displayed in Figure 165, where the *x*- and *y*-axes depict the scale of the wavelet decomposition and the normalized wavelet energy ($\frac{E_{Dj}}{E_{J,all}}$), respectively. Notably, Figure 165 serves to illustrate the variations in the $\frac{E_{Dj}}{E_{J,all}}$ plots for different radial positions, different materials (Figure 165a versus Figure 165b), different operating conditions (Figure 165a versus Figure 165c), and at different data acquisition frequency (Figure 165b versus Figure 165d). Understanding these variations is key to the delineation of the micro-, meso- and macro-scales. Four observations are noteworthy. First, Figure 165 shows that the normalized energy ($\frac{E_{Dj}}{E_{J,all}}$) changes with radial position, with profiles skewing leftwards as the riser center (r/R = 0) is approached from the wall (r/R = 1). In particular, Figure 165a and b represent signals from the highest *m* condition (Table 9) and at a dimensionless riser height (h/H, where h is the axial position where measurement was acquired and H is the total riser height) of 0.47 for small glass and large HDPE, respectively. At the same operating condition, it is apparent that the shapes of the $\frac{E_{Dj}}{E_{J,all}}$ plots are similar at each dimensionless radius (r/R, where r is the radial position where measurement was acquired and R is the total riser radius), and that the Gaussian-shaped plots become increasingly left-skewed as r/R decreases from 0.96 to 0.0. As indicated in a previous work(Chew, Hays et al. 2011), the shapes of the $\frac{E_{Dj}}{E_{J,all}}$ plots give an indication of the relative solids concentration at each location, with increasing left-skewedness correlating with increasing dilution (i.e., profiles look more similar to background signal). Accordingly, the progression observed from the wall to the center is indicative of core-annulus flow. Second, a lower *m* condition gives plots that are more left-skewed (Figure 165a versus c), and hence the dense-dilute interpretation is further validated, since the profiles are all skewed more leftward for the lowest *m* operating condition (Figure165c). A third observation is that different materials tend to have similar energy profiles when operated at the same riser conditions (Figure 165a and b), thereby indicating that the shapes of the plots are more dependent on flow conditions and relatively independent of material. Finally, in comparing Figure 165b and d, it is apparent that a lower data acquisition frequency (Figure 165d) for the same riser location and condition shifts the energy plots leftwards, because the same features (i.e., frequency ranges) appear at lower scales when data acquisition frequency is reduced (Figure 133). For example, for a 1000 Hz signal, A_3 contains 100 Hz information, which implies frequency ranges for a 1000 Hz data are at three scales higher than that for a 100 Hz data.

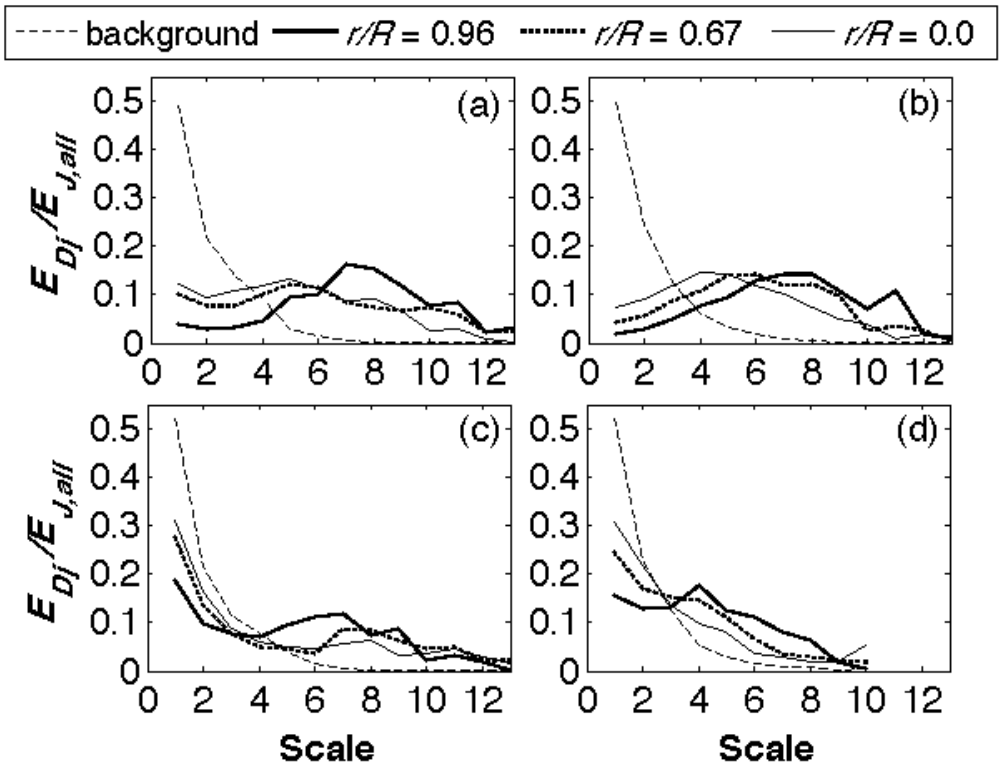

Figure 165. *Normalized energy plots at h/H = 0.47 for (a) 1000 Hz large HDPE data at highest m condition (U_s = 13.5 m/s, G_s = 260 kg/m^{2}s), (b) 1000 Hz small glass data at highest m condition (U_s = 13.5 m/s, G_s = 260 kg/m^{2}s), (c) 1000 Hz large HDPE data at lowest m condition (U_s = 17 m/s, G_s = 120 kg/m^{2}s), and (d) 100 Hz small glass data at highest m condition (U_s = 13.5 m/s, G_s = 260 kg/m^{2}s).*

With these four observations from Figure 165 in mind, delineation among the different scales (micro-, meso-, and macro-scale) can be made. Notably, the background (absence of solids) signals on Figure 165 are exponentially decreasing functions, implying most of the energy in the signal is contained in the lowest (< 5) scale, which is expected since background signal contains largely noise (micro-scale). Accordingly, the boundary between micro- (background noise) and meso-scales is the scale where the energy level of the background signal approaches zero, which is at scale 5 for both the 1000 Hz and 100 Hz data. The demarcation between meso-scale (clusters) and macro-scale (equipment) should be the scale at which the energy contained in the $\frac{E_{Dj}}{E_{J,all}}$ plots for systems with solids (not background) approach zero, which are approximately scales 11 and 8 for data collected at 1000 Hz (Figure 165a-c) and 100 Hz (Figure 165d), respectively. It is worthwhile to note that Yang and Leu (Yang and Leu 2009) used the same scale, namely 11, as the boundary between the meso-, and macro-scales for their 1000 Hz fiber-optic data.

Armed with this demarcation of the physical scales for the fiber-optic data, the scale used for cluster identification should be within the meso-scale range to filter out the noise (micro-scale) and equipment (macro-scale) influence. Referring to Figure 165, regardless of radial

position (i.e., dense or dilute conditions), the $\frac{E_{Dj}}{E_{J,all}}$ plots reflecting solids flow (i.e., except background) approach zero at the meso-/macro-scale boundary, and therefore scales 11 and 8 are physically reasonable thresholds for cluster identification for the 1000 Hz and 100 Hz data, respectively. Accordingly, for the 1000 Hz data contained in Figure 134, cluster identification involves comparing the raw signal with the corresponding A_{11} trace (i.e., threshold), and data points above the threshold are discerned as clusters(Yang and Leu 2009). Analogously, A_8 is used as the threshold for the 100-Hz data. From this comparison, the appearance probability, duration, and frequency of clusters can be obtained. First, cluster appearance probability is the ratio of the number of data points above threshold to the total number of data points. Second, cluster duration gives an approximate indication of a characteristic size of clusters (since clusters are expected to move laterally, thus not wholly captured by the probe), and is calculated as the average number of consecutive data points above the threshold. Third, cluster frequency is the number of clusters per unit time, in which the number of clusters is the number of segments of consecutive data points above the threshold. As validation of the choice of scale of threshold (namely, A_{11} for 1000 Hz data and A_8 for 100 Hz data) for cluster identification, Figure 166 shows that the radial profiles of the cluster characteristics for 1000 Hz data becomes similar beyond Scale 11 (Figure 166a - c), while those for 100 Hz data become very similar beyond Scale 8 (Figure 166d - f).

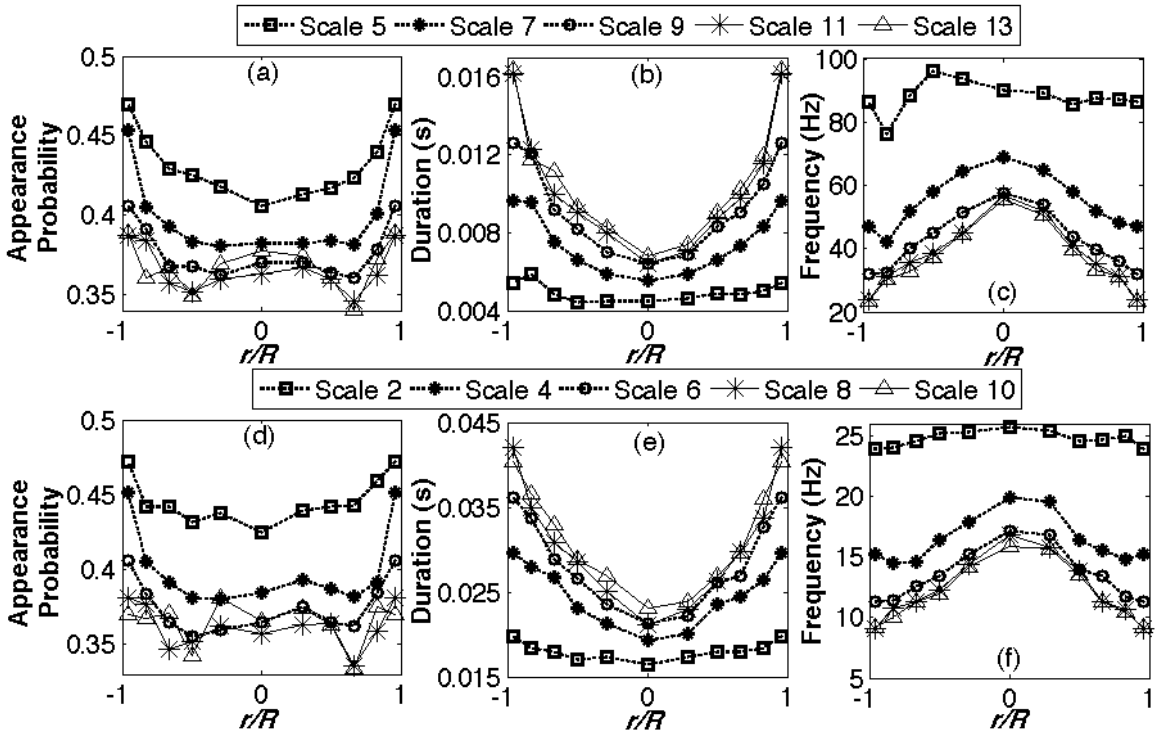

Figure 166. *Radial cluster profiles obtained with various wavelet-decomposed scales of approximation (A_j) as threshold for cluster identification for small glass collected at (a)-(c) 1000 Hz and (d)-(f) 100 Hz under operating condition of U_s = 13.5 m/s, G_s = 260 kg/m^{2}s at h/H = 0.47.*

The impact of data acquisition frequency on the three cluster characteristics is portrayed in Figure 167. The magnitudes of cluster characteristics expectedly change as data acquisition frequency changes, because higher data acquisition frequency allows finer time-specific features to be captured. For example, previous work indicates that a higher sampling frequency of 12,500 Hz give rise to cluster durations and frequencies in the ranges of 0.002 - 0.02 s and 15 - 60 Hz (Guenther and Breault 2007), respectively, whereas a lower sampling frequency of 1000 Hz lead to cluster duration and frequency ranges of 0.03 - 0.08 s and 4 - 15 Hz(Sharma, Tuzla et al. 2000; Yang and Leu 2009), respectively. The reason for this trend is that the smallest cluster duration detected by 1000 Hz data is 10^{-3} s, but 12,500 Hz data can detect clusters with a duration as small as 8 x 10^{-5} s. Figure 167 verifies that changing data acquisition frequency changes the absolute values of cluster duration and frequency, but the shapes of the radial profile and differentiation between materials are preserved. Subsequently, because large glass data was collected at 100 Hz and small glass and large HDPE data were collected at 1000 Hz, all data in this work were analyzed at 100 Hz for straightforward comparison of material (size and density of particles) effect on cluster characteristics.

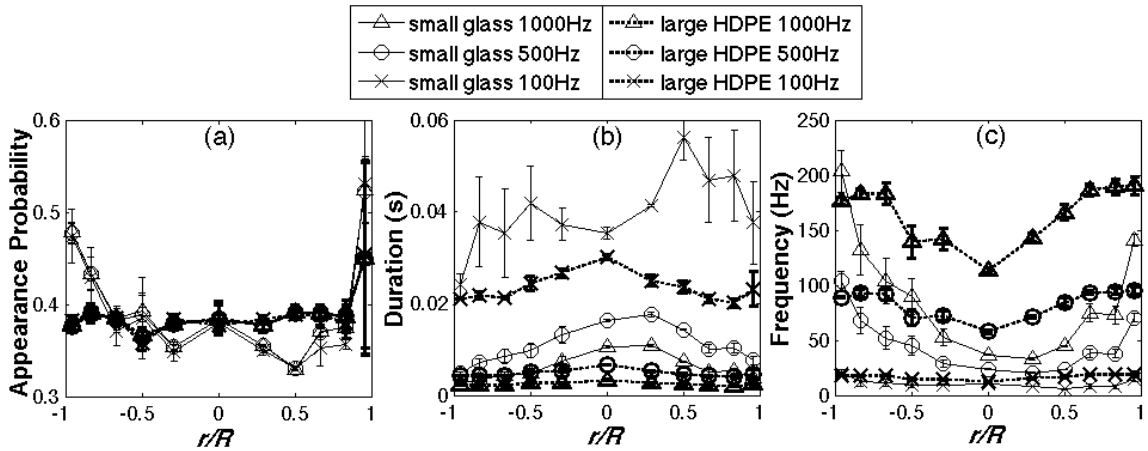

Figure 167. *Effect of frequency of data acquisition on cluster trends of small glass and large HDPE at h/H = 0.92 and operating conditions of U_s = 17 m/s, G_s = 120 kg/m^{2}s.*

Results and Discussion: Figures 168-170 collectively display the cluster characteristics – appearance probability, duration, and frequency, respectively – as functions of dimensionless radius (*r*/*R*, where *r* is the radial position at which measurement was acquired and *R* is the radius of the riser) of the riser. Each figure contains 20 subplots, with each of the four columns representing the various operating conditions listed in Table 9, and each of the five rows representing a different axial position (*h*/*H*, where *h* is the axial position at which measurement was acquired and *H* is the height of the riser) in the riser. In addition, the three profiles within each subplot depicts each of the monodisperse materials listed in Table 8. The *x*- and *y*-axes ranges are kept constant within each figure for straightfoward comparison of trends. Data for large glass is lacking for *h*/*H* = 0.16 and 0.27, but an overview of the impact of riser position, operating condition, and material type on cluster behavior is illustrated nonetheless.

Figure 168 presents the cluster *appearance probability* trends. Among the three cluster cha(8racteristics (appearance probability, duration, frequency), appearance probability is least affected by material (particle size or density) and/or operating condition, suggesting that cluster

appearance probability is dominated by the effect of local position (axial and radial) within the riser.

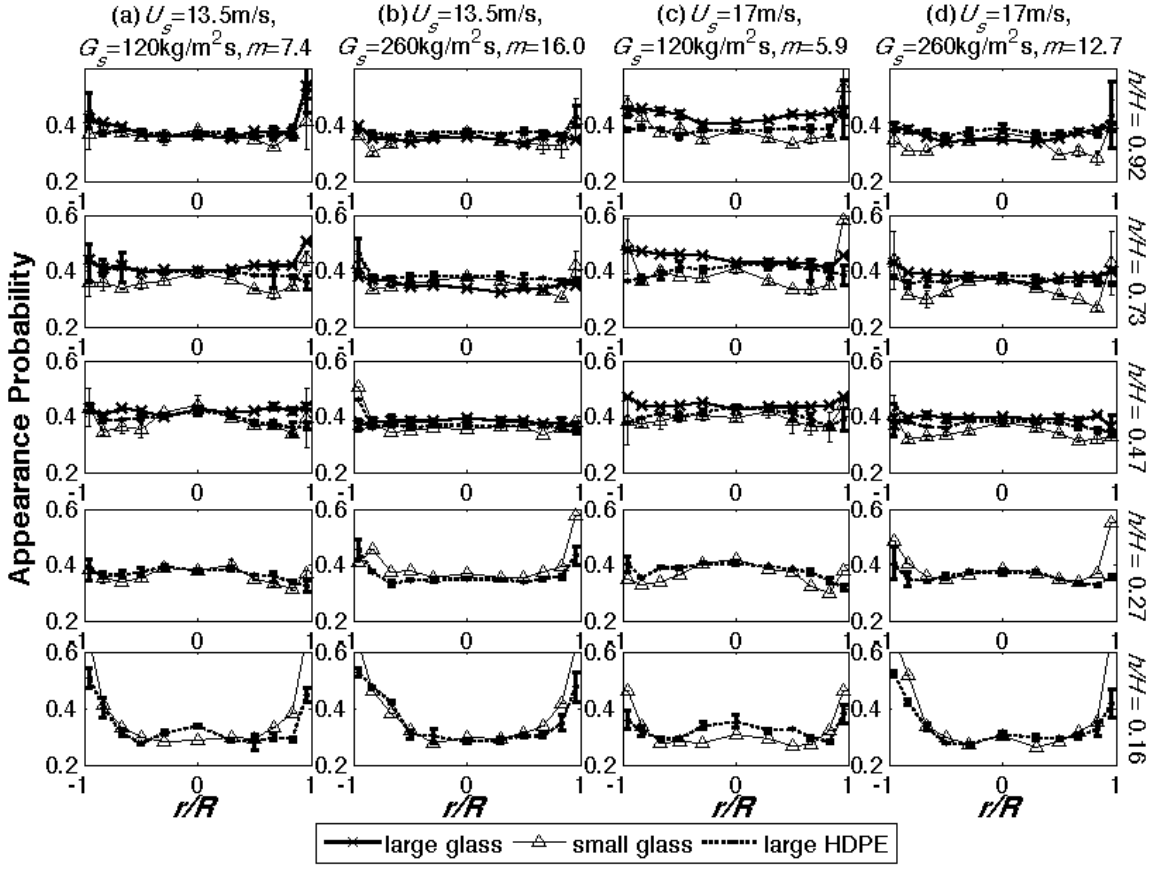

Figure 168*. Radial profiles of cluster appearance probability for different materials at various riser height and under various operating conditions.*

More specifically, as observed in Figure 168 as height increases, radial profiles generally evolve from a U-shape at the riser bottom to flatter profiles at the riser top. The evolution of profile shapes results from appearance probability decreasing with height along the wall (r/R = 1) throughout the riser height, and only mildly increasing at the center (r/R = 0) from h/H = 0.16 to 0.27. These plots present a more complete picture than previous work, which contain information only along limited or integrated sections of the riser and thus led to seemingly contradictory trends. In particular, previous works have indicated that overall (i.e., integrated across the riser cross-section) appearance probability decreases(Brereton and Grace 1993; Soong, Tuzla et al. 1995) with height or that appearance probability decreases with height only near the wall (and not at other radial positions)(Wei, Yang et al. 1995; Manyele, Parssinen et al. 2002), while others have reported that overall appearance probability remains constant with height(Yang and Leu 2009). With regards to radial variation, it is only at the bottom-most axial position (h/H = 0.16) that all materials exhibit a generally increasing appearance probability towards the wall across all conditions, corroborating with previous work which focused only on limited parts of the riser (Brereton and Grace 1993; Li, Zhu et al. 1995; Soong, Tuzla et al. 1995; Wei, Yang et al. 1995; Manyele, Parssinen et al. 2002; Yang and Leu 2009). However, Figure 168 shows that the same

trend is not strictly true for higher axial positions ($h/H \geq 0.27$). With respect to the impact of operating conditions, Figure 168 shows that the effect of the four operating conditions investigated on cluster appearance probability is generally insignificant. It is noted in previous work that cluster appearance probability increases(Brereton and Grace 1993; Zou, Li et al. 1994; Wei, Yang et al. 1995; Manyele, Parssinen et al. 2002), decreases(Li, Xia et al. 1991), or is insensitive(Li, Zhu et al. 1995) to an increase of solid loading (m); these seemingly contradictory previous results can again be traced to data obtained from only a limited portion of the riser and lacking local details. For example, comparing Figure 168c and d at h/H = 0.16 reveals that increasing m increases appearance probability at the wall (r/R = 1) but decreases apperance probbility at the center (r/R = 0), which implies that a lack of a more complete dataset may lead to opposite trends; whereas the complete landscape given in Figure 168 shows clearly that the small change due to m is insignificant compared to the greater profile variations associated with the effect of riser height. Finally, Figure 168 indicates that the role of material type (size or density of particles) on appearance probability is generally negligible.

Radial profiles of *cluster duration* are displayed in Figure 169. Compared to appearance probability (Figure 168), variations of material properties and operating conditions exert more influence on the radial profiles of cluster duration particularly near the top of the riser, although axial variation is still most apparent.

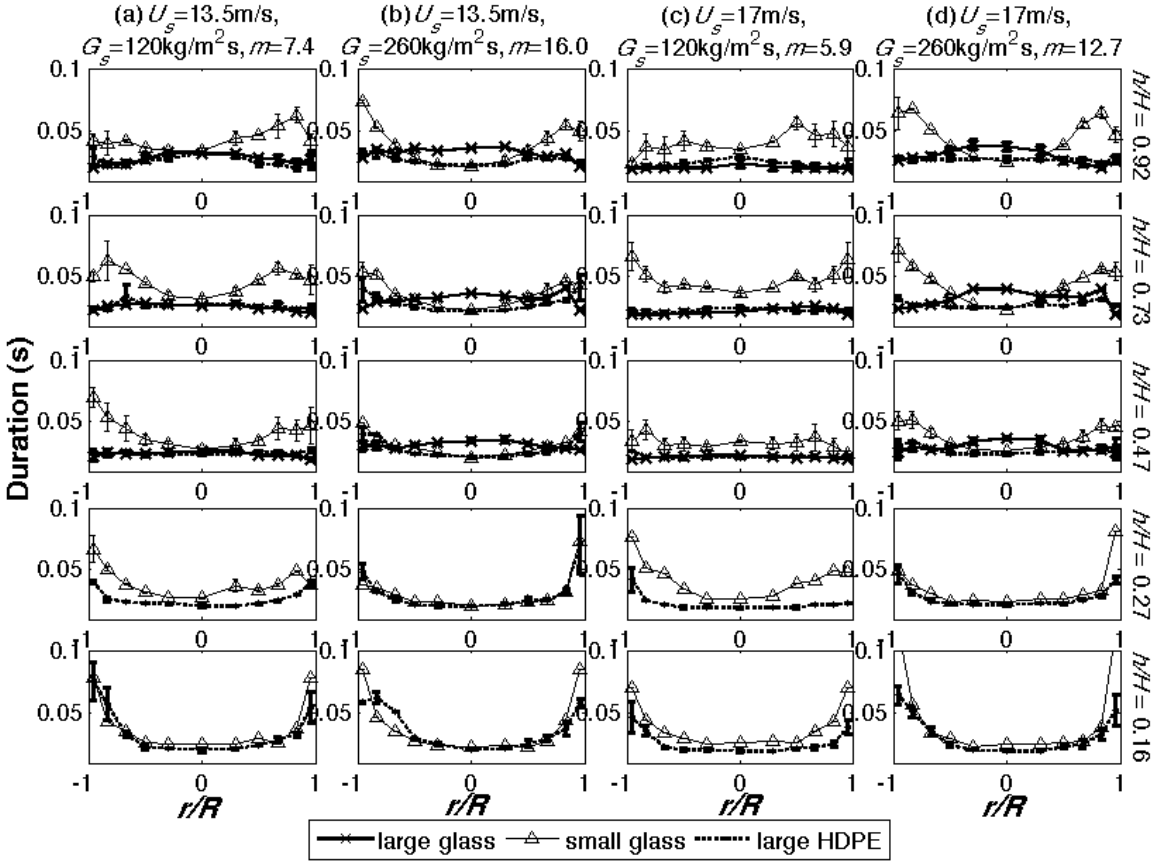

Figure 169. *Radial profiles of cluster duration for different materials at various riser height and under various operating conditions.*

With regards to influence of axial position, for $h/H \leq 0.27$, all cluster duration profiles are similarly U-shaped, implying the impact of material or operating condition is insignificant at lower riser positions. On the other hand, at higher axial positions ($h/H \geq 0.47$), variations due to material and operating conditions become evident, with the general trend that the larger materials (large glass and large HDPE) have flat profiles, while small glass tends to retain the U-shape. It is also observed that as riser height increases, cluster duration generally decreases at the wall ($r/R = 1$), agreeing with previous work which show either a general decrease of radially-integrated duration with height (Li, Zhu et al. 1995; Soong, Tuzla et al. 1995; Yang and Leu 2009) or that only wall duration decreases with height (Horio, Morishita et al. 1988; Wei, Yang et al. 1995). However, it is noted in Figure 169 that duration remains approximately constant at the center ($r/R = 0$) with height. Note that since the area at the center represents a smaller area relative to the annular area at the wall, the contributions from the riser center are drowned out when integrated radially, hence the results in this work do not necessarily contradict previous work.

As for the effect of operating conditions, similar profiles are observed at the same G_s conditions for $h/H \geq 0.27$ (i.e., Figure 169a and c are similar, while Figure 169b and d are similar). Notably, at the riser center ($r/R = 0$), changing the operating conditions results in opposite trends for the different materials. In particular, while large glass exhibits higher durations under the higher m conditions (Figure 169b and d), small glass displays the highest duration at the lowest m condition (Figure 169c). Previous works have shown that an increase in solid loading (m) either increases (Horio, Morishita et al. 1988; Rhodes, Mineo et al. 1992; Zou, Li et al. 1994; Guenther and Breault 2007; Das, Meikap et al. 2008), decreases(Horio and Kuroki 1994; Wei, Yang et al. 1995; Sharma, Tuzla et al. 2000; Mostoufi and Chaouki 2004; Afsahi, Sotudeh-Gharebagh et al. 2009), or does not affect(Li, Zhu et al. 1995; Sharma, Tuzla et al. 2000) cluster duration; with the more exhaustive dataset presented in Figure 169, different trends are indeed seen depending on riser position, operating conditions, and particle material.

Pertaining to the impact of material properties on cluster duration (Figure 169), small glass consistently exhibits the highest duration towards the wall ($r/R = 1$), which agrees with previous work (Horio, Morishita et al. 1988; Soong, Tuzla et al. 1995; Wei, Yang et al. 1995; Sharma, Tuzla et al. 2000; Manyele, Parssinen et al. 2002; Yang and Leu 2009); however, for the larger materials (large glass and large HDPE), the radial trend of increasing duration towards the wall is observed only at $h/H \leq 0.27$. Moreover, interestingly, under low G_s conditions (Figure 169a and c), large glass and large HDPE have very similar radial profiles, suggesting that particle size plays an influential role under such riser conditions. On the other hand, under high G_s conditions (Figure 169b and d), small glass and large HDPE are similar at $r/R = 0$, while large glass and large HDPE are similar at $r/R = 1$, thereby implying the dominance of different material property at different radial positions (i.e., center versus wall) under these operating conditions.

With reference to previous work, Cocco et al. (Cocco, Shaffer et al. 2010) compared cluster durations of similar-sized 70 μm FCC (fluid cracking catalyst, ρ_s = 1500 kg/m^3) and PE (polyethylene, ρ_s = 400 kg/m^3) at $r/R = 0$ and $h/H = 0.9$. It was found that the less massive PE has a higher cluster duration, which is contrary to the trend observed here of the most massive large glass having highest duration at $r/R = 0$ and $h/H = 0.92$ for the higher G_s conditions (Figure 169b and d). However, the higher duration displayed by PE has been attributed to higher electrostatics, lower restitution coefficient, and smoother surface compared to the FCC particles(Cocco, Shaffer et al. 2010). With reference to another work, Sharma et al. (Sharma, Tuzla et al. 2000) found that more massive 120 μm glass beads exhibit a higher cluster duration than 70 μm glass beads, especially at the wall at $h/H = 0.4$. This trend again looks to be different

under two of the four operating conditions (Figure 169a and d) in the current results, wherein small glass exhibits higher cluster duration (at the wall at h/H = 0.47) than other larger materials. Correspondingly, the influence of materials seems tied with operating conditions, and disparate material trends may manifest under different flow conditions. Where material impact is concerned, it is worthwhile to note that effects other than d_{ave} or ρ_s are also at play in the clustering phenomenon. In particular, clusters in gas-solids systems may arise due to the inelastic nature of particle collisions(Goldhirsch 2003) and/or gas-phase effects including the relative motion between the two phases (mean drag) and viscous damping of the granular energy by the fluid(Glasser, Sundaresan et al. 1998; Wylie and Koch 2000; Agrawal, Loezos et al. 2001). Accordingly, the differences between cluster characteristics observed here and those of previous works are likely to involve more than a simplistic d_{ave} or ρ_s effect, though such an analysis is well beyond the scope of the current effort.

The radial profiles of the final cluster parameter, namely *cluster frequency*, are displayed in Figure 170. Among the three cluster characteristics (appearance probability, duration, frequency), Figure 170 shows that the greatest influence of materials and operating conditions is exhibited in cluster frequency, even though axial position still plays an important role.

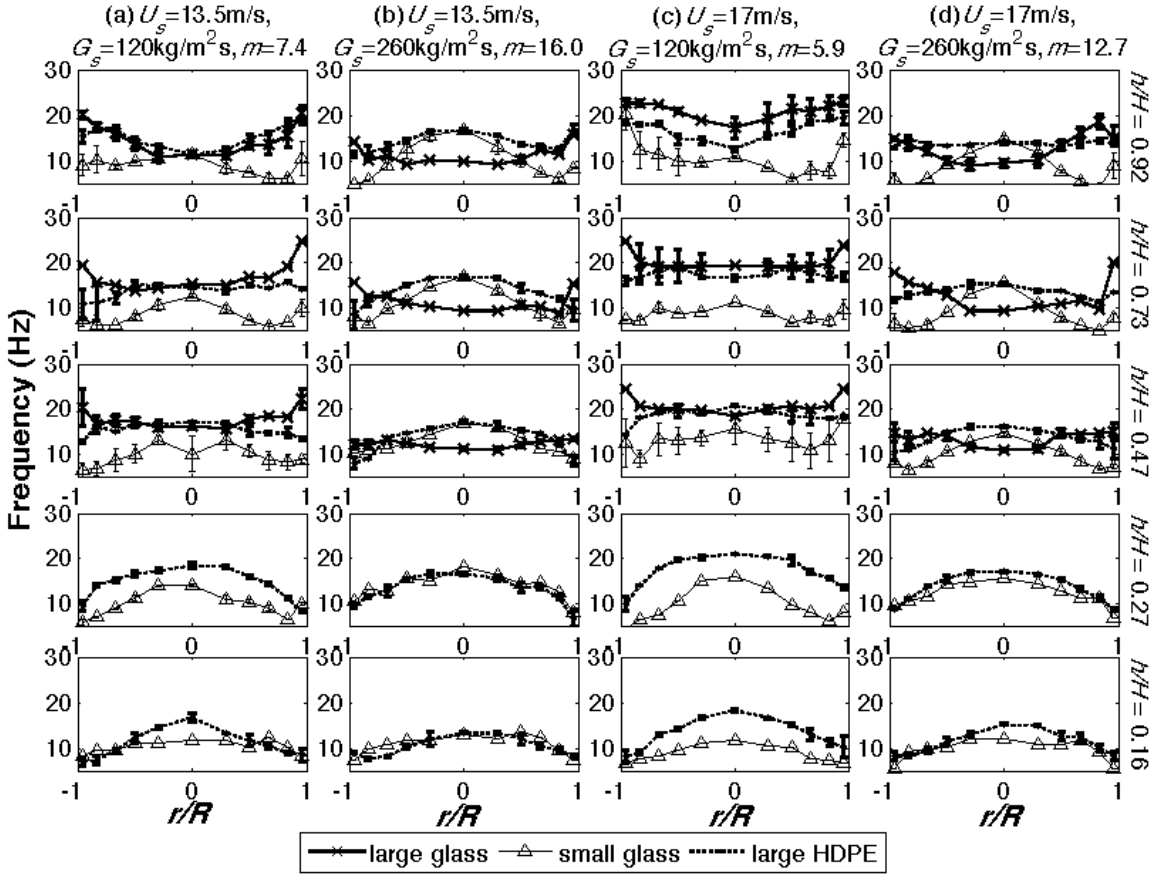

Figure 170. *Radial profiles of cluster frequency for different materials at various riser height and under various operating conditions.*

At lower axial positions ($h/H \leq 0.27$), the radial profiles of cluster frequency are inverted U-shape regardless of material and operating conditions, although more material difference is apparent at lower G_s (Figure 170a and c) than at higher G_s conditions (Figure 170b and d). Higher up in the riser ($h/H \geq 0.47$), the impact of material and operating condition variations increases, as reflected in the increasingly dissimilar profiles. Notably, similar to cluster duration (Figure 169), the trends for low G_s (Figure 170a and c) conditions are similar, while the trends for high G_s (Figure 170b and d) are similar. Regarding impact of operating condition, cluster frequency is greatest for the highest *m* (Figure 170b) for small glass (especially at the riser center), which agrees with previous work(Sharma, Tuzla et al. 2000; Manyele, Parssinen et al. 2002; Yang and Leu 2009). On the contrary, frequency is greatest for the lowest *m* condition (Figure 170c) for the larger materials (large glass and large HDPE), indicating again that the effects of operating condition and material property are coupled. Finally, with respect to impact of particle material, for $h/H \geq 0.47$, small glass generally retains the inverted U-shape observed at lower *h/H*, large glass acquires a U-shape, while profile shapes for large HDPE are more varied depending on height and operating conditions. With reference to previous work, Guenther and Breault(Guenther and Breault 2007) noted cluster frequency decreases towards the wall at all heights for Group A-B cork particles, which is generally consistent with the small glass (closest to the Group A-B boundary of the three materials investigated) trends in Figure 170. Hence, the different profile shapes higher in the riser observed for the larger materials could in part be a size effect, although other effects like restitution coefficient may come into play as pointed out earlier.

Summary: Experiments have been carried out in a pilot-scale circulating fluidized bed (CFB) riser for three monodisperse Geldart Group B materials of different size and material density (namely, large glass, large HDPE, and small glass). A fiber optic probe was used for local measurements within the riser, and a physically-based threshold for cluster identification was derived via wavelet decomposition. Using this threshold, three cluster characteristics were determined: appearance probability, duration, and frequency. Local profiles of these cluster quantities for each of the three materials and each of the four operating conditions are reported. The resulting dataset reveals the impact of local riser position, operating condition, and material type on the cluster characteristics.

Collectively, the results give way to three major findings. First, among the three factors – riser position, operating condition, and material type – investigated, riser position has the most dominant influence on the cluster characteristics (appearance probability, duration, and frequency). Second, the cluster appearance probability is largely a function of riser position only, and is insensitive to changes in operating condition or material type. Third, although differences in the cluster duration and frequency do arise from changes in the material and/or operating condition, such differences are present only from mid-height of the riser upwards

It is worthwhile to note that the material effects examined here refer to size and/or material density effects of monodisperse particles, but the origin of clusters can be traced to dissipative nature of inelastic collisions(Goldhirsch 2003) as well as gas-phase effects(Glasser, Sundaresan et al. 1998; Wylie and Koch 2000; Agrawal, Loezos et al. 2001). Correspondingly, other than material size and density effect leading to drag force instability, other effects influencing instability include restitution coefficient, friction coefficient, particle shape, etc. This dataset on clustering behavior of monodisperse materials in a CFB riser, together with that for polydisperse materials in Section 4.5.5, is expected to serve as validation data for models incorporating such

effects, and more work is needed to shed more light on the dominant physics leading to instabilities in gas-solid flows and hence clusters.

Task 4.5.5: Cluster characteristics of polydisperse materials[8]

***Abstract*:** Experiments with a focus on understanding the impact of polydispersity on clustering characteristics (namely, appearance probability, duration and frequency) of Geldart Group B particles in a circulating fluidized bed (CFB) riser have been carried out. Three mixtures are considered: (i) a density-difference binary mixture, with species of different material density (ρ_s) but same particle sizes (d_{ave}), (ii) a size-difference binary mixture, with species of different d_{ave} but same material density ρ_s, and (iii) a continuous particle size distribution (PSD). Local cluster information spanning the entire riser was obtained over a range of operating conditions using a fiber optic probe. Results show that cluster trends for the binary mixtures are similar to those reported in Section 4.5.4(Chew, Hays et al. 2011) for monodisperse materials on two counts. First, local riser position has a significant influence on all three cluster characteristics, while effects of operating condition and material type are secondary. Second, among the three cluster characteristics, cluster appearance probability is most influenced by local position, and least affected by operating condition and material type. Furthermore, the density-difference binary mixture exhibits distinctly lower cluster duration than either of its constituent components. On the other hand, for the size-difference binary mixture, cluster duration mimics one constituent component, while frequency mimics the other. Comparing the two binary mixtures at any riser location, the density-difference binary mixture has lower cluster duration and higher frequency than the size-difference binary mixture regardless of local position. Finally, with respect to the continuous PSD, which was investigated under a wider range of operating conditions, the effect of operating condition is more apparent. This deviation may be due to an inherent behavioral difference between binary mixture and continuous PSD and/or to the wider range of operating conditions examined.

Introduction: In the previous section (Section 4.5.4) on clustering in CFB risers with various monodisperse materials(Chew, Hays et al. 2011), a comprehensive picture of the impact of monodisperse material property (particle size and material density), local riser position, and operating conditions on cluster behavior was presented. The results indicate that riser local position plays a key role in influencing clusters compared to the material property and/or operating condition. Nonetheless, polydisperse systems have been known to exhibit different behaviors than their monodisperse counterparts(Sundaresan 2001; Muzzio, Shinbrot et al. 2002; Curtis and van Wachem 2004; Hrenya 2011) (e.g., mass flux profiles(Chew, Hays et al. 2011), species segregation(Rowe and Nienow 1976; Nienow and Chiba 1985; Fan, Chen et al. 1990; Kunii and Levenspiel 1991; Lim, Zhu et al. 1995; Werther and Hirschberg 1997; Rhodes 1998; Ottino and Khakhar 2000; Sundaresan 2001; Muzzio, Shinbrot et al. 2002; Hrenya 2011)), and thus the effect of polydispersity on clusters is of practical interest. In addition, different categories of polydispersity, namely binary mixtures and continuous particle size distributions (PSDs), have been reported to display qualitatively different trends in both bubbling beds(Hoffmann and Romp 1991; Gauthier, Zerguerras et al. 1999; Lin, Wey et al. 2002; Chew, Wolz et al. 2010; Chew and Hrenya 2011) and CFBs(Hirschberg and Werther 1998; Chew, Hays

[8] Chew, Hays, Findlay et al., "Cluster characteristics of Geldart Group B particles in a pilot-scale CFB riser. II. Polydisperse", in preparation for submission in May 2011.

et al. 2011; Chew, Hays et al. 2011; Chew, Parker et al. 2011), thereby motivating the investigation of both categories of polydispersity.

In an effort to build on the previous knowledge on cluster characteristics of monodisperse materials (see Section 4.5.4(Chew, Hays et al. 2011) and references therein), the objective of the current study is to experimentally investigate the effect of polydispersity on cluster characteristics in the same CFB riser as Section 4.5.4(Chew, Hays et al. 2011). Experiments have been carried out for two binary mixtures – one with only a material density, ρ_s, difference between the constituent components (density-difference binary), and one with only a particle size, d_{ave}, difference between the constituent components (size-difference binary) – as well as a continuous PSD, all belonging to Geldart Group B. Local cluster behavior is measured using a fiber optic probe and subsequent cluster identification and characterization is based on wavelet decomposition(Mallat 1989; Mallat 1998), which provides a means of delineating the different (micro, meso-, and macro) scales in fluidized bed systems(Ren and Li 1998; Ellis, Briens et al. 2003; Zhao and Yang 2003; Yang and Leu 2009). In particular, the cluster characteristics extracted from fiber optic measurements include cluster appearance probability (fraction of time that clusters are observed), cluster duration (indicator of cluster size), and frequency (number of clusters per unit time).

The results indicate similar trends between the monodisperse materials(Chew, Hays et al. 2011) and the mixtures, though some noticeable differences exist between the different categories of polydispersity examined. Regarding the former, all three cluster characteristics depend most heavily on local riser position, while the effects of operating condition and material type (monodisperse material and mixture type) are secondary. Moreover, among the three cluster characteristics, cluster appearance probability is most influenced by riser local position, and least affected by operating condition and material type. Besides these similarities, differences in the clustering trends between the binary mixtures are also apparent. First, the density-difference binary mixture exhibits distinctly lower cluster duration than either of its constituent component. On the other hand, for the size-difference binary mixture, duration mimics one constituent component, while frequency mimics the other. Second, between the two binary mixtures, the size-difference binary mixture has higher cluster duration and lower cluster frequency than the density-difference binary mixture. Finally, with respect to the continuous PSD, the effect of operating conditions is more apparent, which may be due to a difference between the mixture types (binary vs. continuous) or to the wider range of operating conditions examined.

Experiment Description:

Experimental Set-up: The CFB riser used for experiments is identical to that in Figure 129; the reader is referred to Section 4.5.1 for further details. The focus of this work is on polydisperse materials, specifically two binary mixtures - one with only a difference in particle size, d_{ave} (size-difference binary) and one with only a difference in material density, ρ_s (density-difference binary) - and one continuous (Gaussian) particle size distribution (PSD), as listed in Table 11. The binary mixtures are made up of approximately monodisperse materials, which are detailed in Table 8. Accordingly, the cluster characteristics of the binary mixtures are compared with that of the constituent monodisperse materials Section 4.5.4(Chew, Hays et al. 2011)) to illustrate the effect of their binary nature.

Operating Conditions: The operating conditions used in this investigation are listed in Table 12.

Instrumentation and Cluster Analysis: Identical to the counterpart monodisperse work in Section 4.5.4(Chew, Hays et al. 2011), data acquisition via a fiber optic probe was

implemented at 100 Hz to obtain measurements at numerous axial and radial locations throughout the riser. Wavelet analysis is used for cluster identification, and subsequent analysis is used to extract three characteristics of the clusters: appearance probability, cluster duration, and cluster frequency. For further details on these measurements and analysis, the reader is referred to Section 4.5.4(Chew, Hays et al. 2011).

Results and Discussion: The focus of this work is on understanding the impact of polydispersity on cluster characteristics. Each figure (Figure 171 through Figure 182) in this section contains 20 subplots, with each column of subplots depicting one of the four operating conditions (Table 12) investigated, and each row depicting one of the five riser axial positions (*h/H*, where *h* is the axial position at which measurements were taken, and *H* is the riser height), as indicated on the text at the right-most of the figure. While the *y*-axes denote cluster characteristics, the *x*-axes denote dimensionless radius (*r/R*, where *r* is the radial position at which measurements were taken, and *R* is the riser radius). The ranges of the axes are kept constant throughout each figure to provide more straightforward comparisons. The error bars represent the span of two repeat measurements taken at the same axial position but 90 degrees apart in the horizontal plane. Note that large glass data is lacking for $h/H \leq 0.27$, while density-difference binary mixture data is lacking for $h/H = 0.92$.

Binary Mixtures: Figures 171-173 display the cluster appearance probability of the binary mixtures. Specifically, Figure 171 compares the density-difference binary mixture with its constituent (monodisperse) components, Figure 172 compares the size-difference binary mixture with its constituent (monodisperse) components, and Figure 173 compares the two binary mixtures directly. Collectively, the three figures show that the radial profiles of appearance probability are largely a function of riser position for binary mixtures, which is consistent with the results on monodisperse systems presented in Section 4.5.4(Chew, Hays et al. 2011). In particular, the radial profiles are generally U-shaped lower (h/H = 0.16) in the riser and gradually flatten with height. In other words, neither material type (monodisperse materials, binary mixtures, etc.) nor operating condition causes significant variations in the profiles; the slight variations which are observed (e.g., Figure 171c, Figure 172d) do not follow a clear trend with local position or operating conditions. Therefore, the cluster appearance probability is most dependent on the local position in the riser.

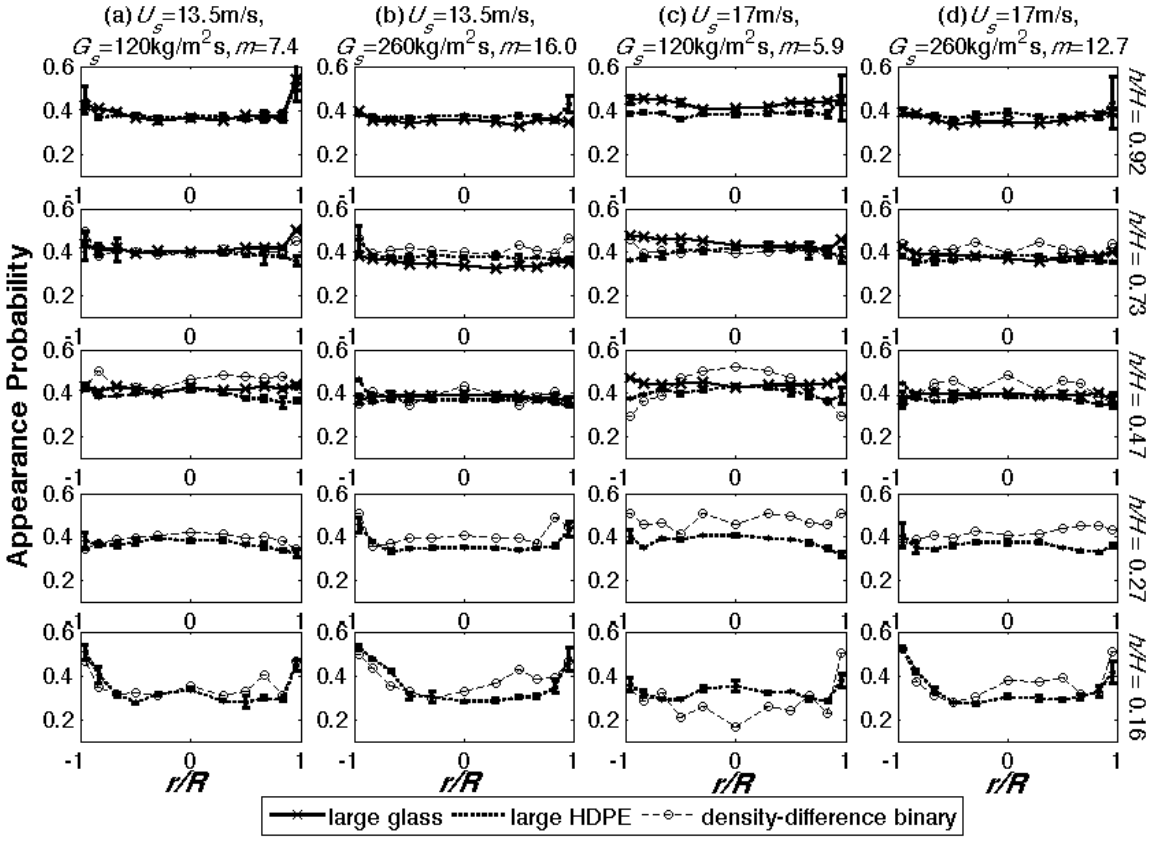

Figure 171. *Local profiles of cluster appearance probability for density-difference binary mixture and constituent monodisperse materials.*

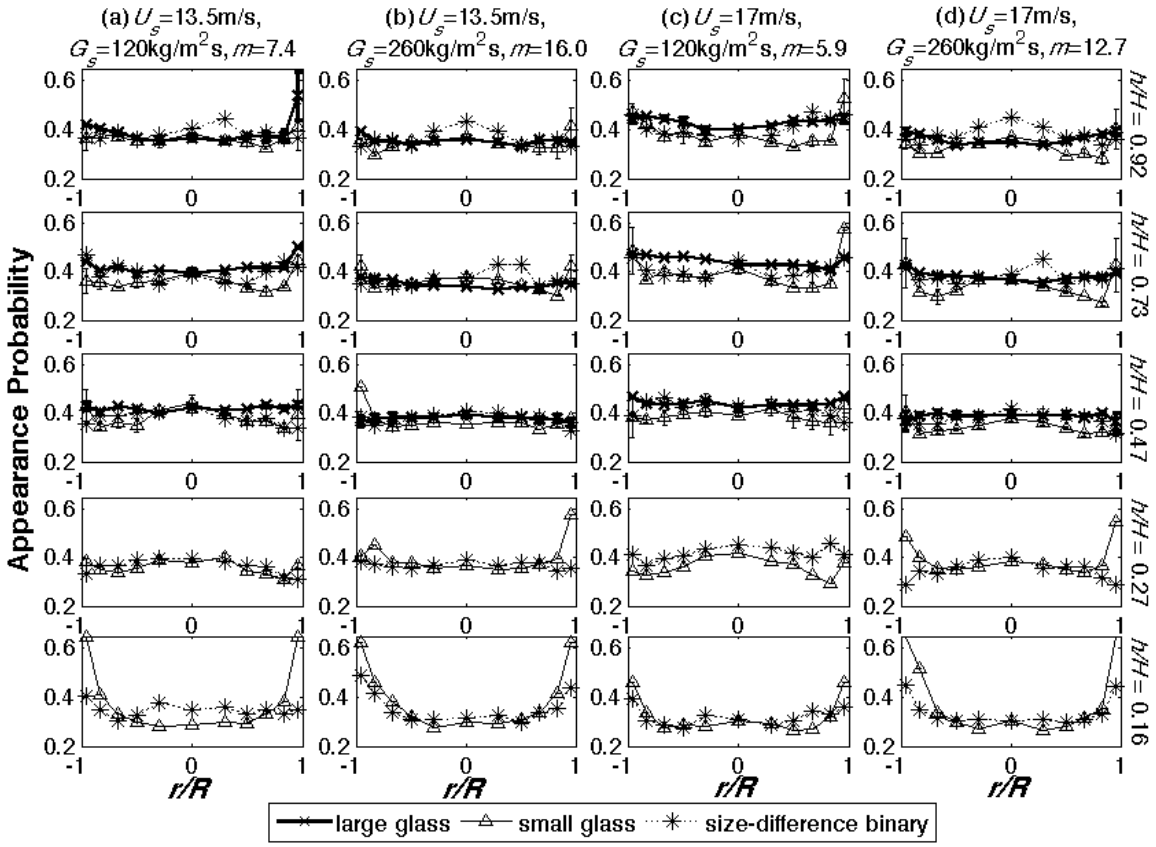

Figure 172. *Local profiles of cluster appearance probability for size-difference binary mixture and constituent monodisperse materials.*

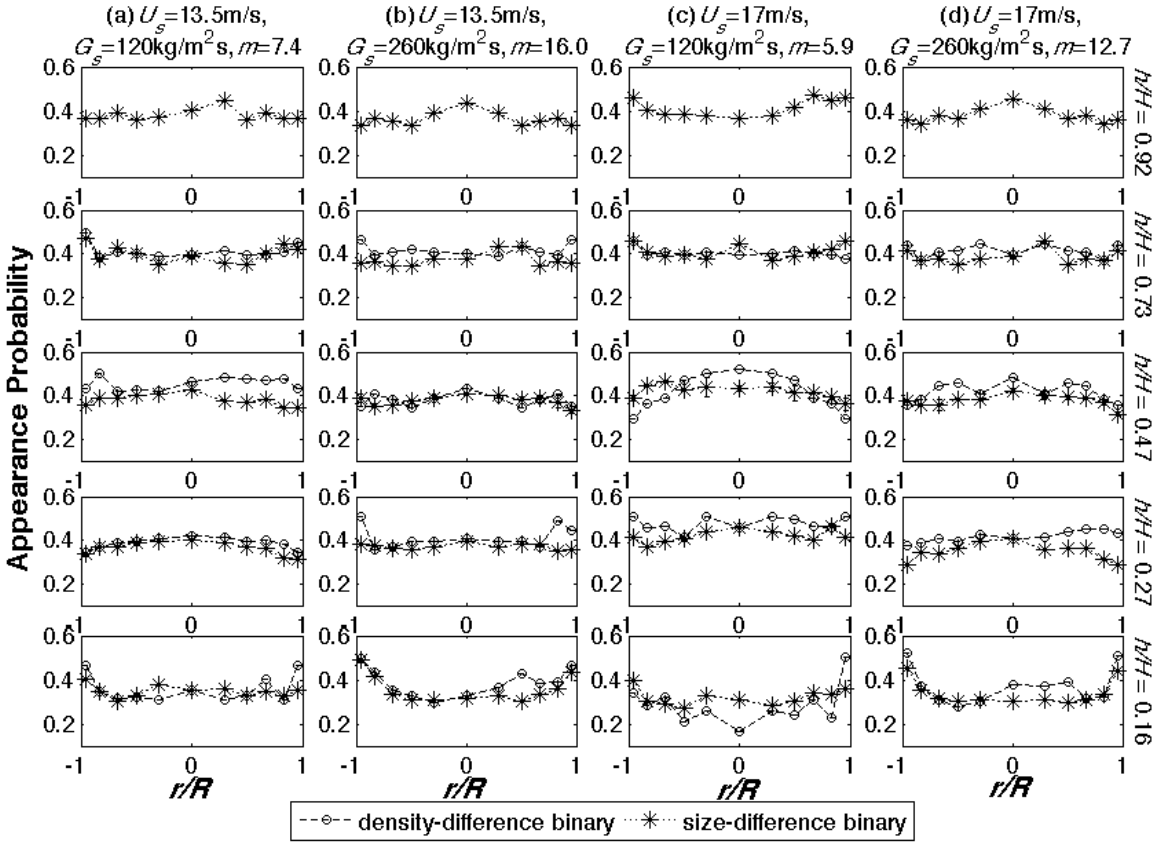

Figure 173. *Local profiles of cluster appearance probability for density-difference binary mixture and the size-difference binary mixture.*

Cluster duration profiles are presented in Figures 174-176. Analogous to previous plots, Figures 174 compares the density-difference binary mixture with its constituent (monodisperse) components, Figure 175 compares the size-difference binary mixture with its constituent (monodisperse) components, and Figure 176 compares the two binary mixtures directly. Compared to appearance probability (Figures 171-173), although the impact of local riser position remains dominant, profile variations resulting from differences in material types (monodisperse components and binary mixtures) and operating conditions are more noticeable, which is again analogous to the results presented for monodisperse systems in Section 4.5.4 (Chew, Hays et al. 2011). Interestingly, a deviation from the monodisperse cluster duration trends(Chew, Hays et al. 2011) is observed in Figure 174 and Figure 175, in that profile variations due to material type are seen at the riser bottom (h/H = 0.16). More explicitly, at this position, the binary mixtures exhibit lower cluster duration than their constituent component (Figure 174 and Figure 175), whereas profile variations between the monodisperse materials are negligible (Section 4.5.4(Chew, Hays et al. 2011)).

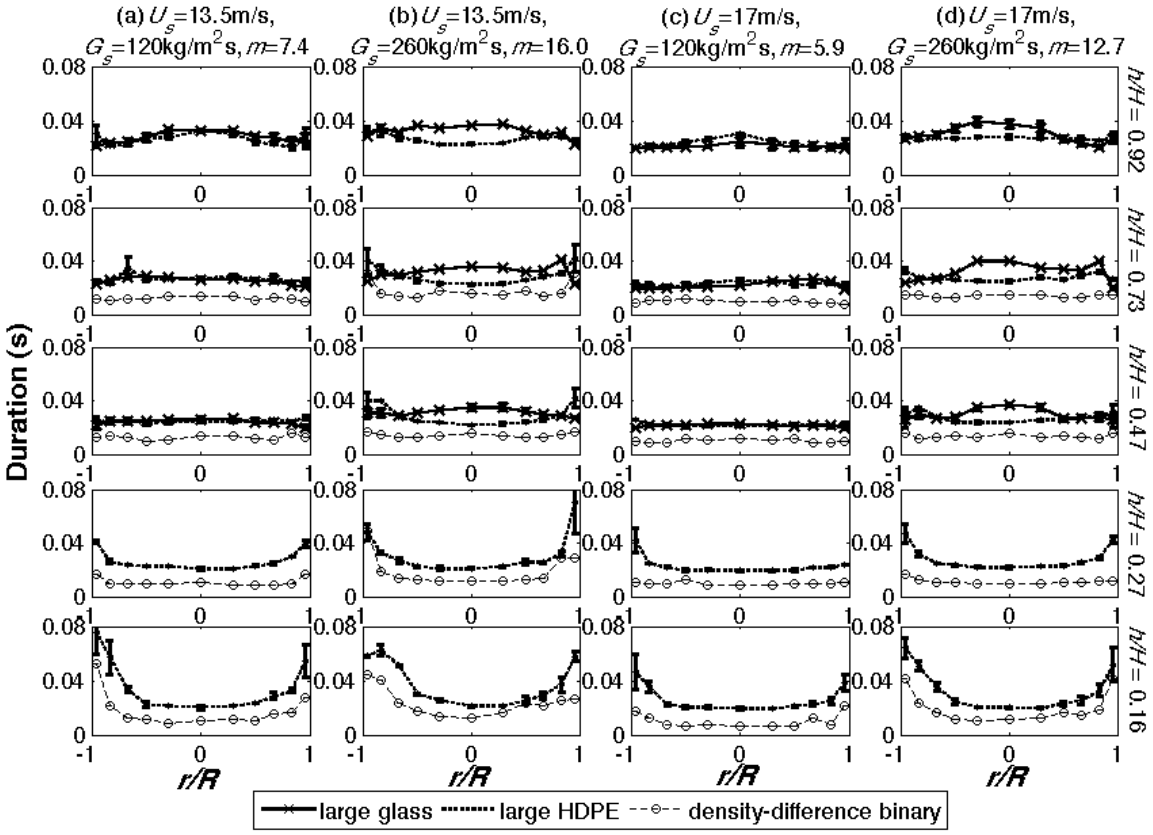

Figure 174*. Local profiles of cluster duration for density-difference binary mixture and constituent monodisperse materials.*

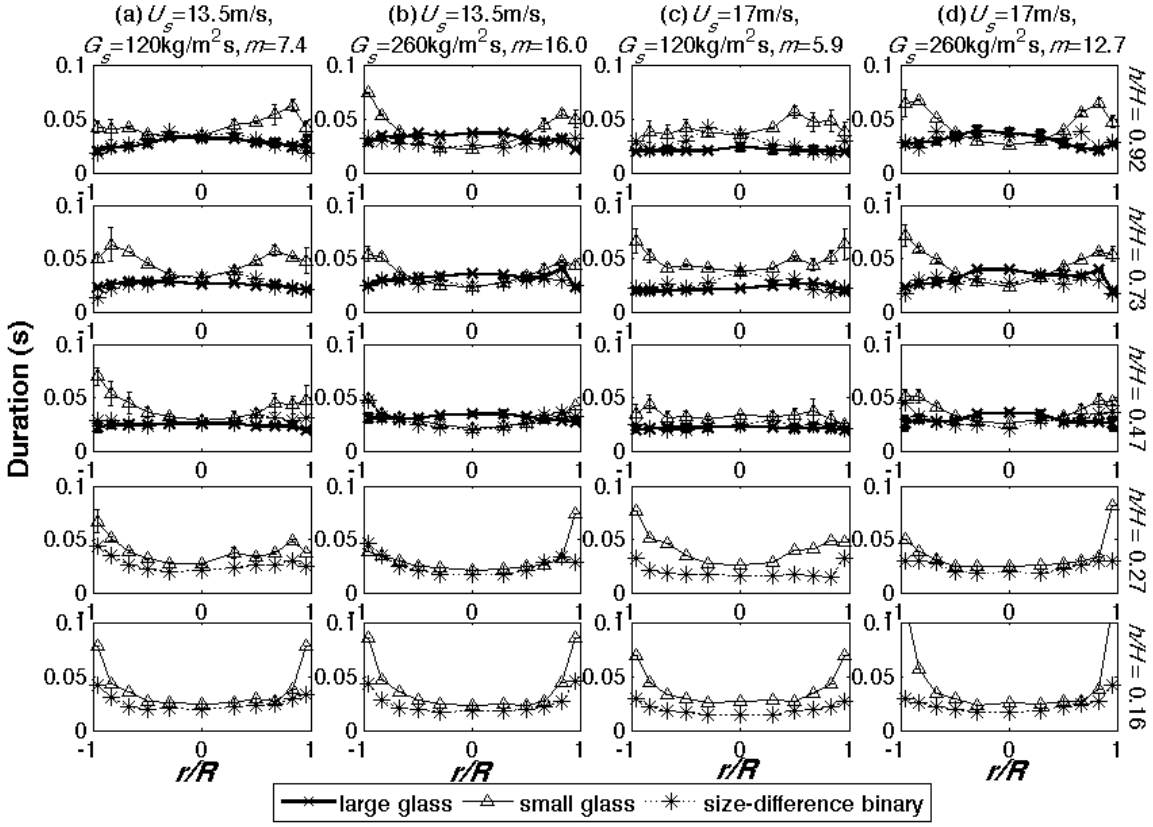

Figure 175*. Local profiles of cluster duration for size-difference binary mixture and constituent monodisperse materials.*

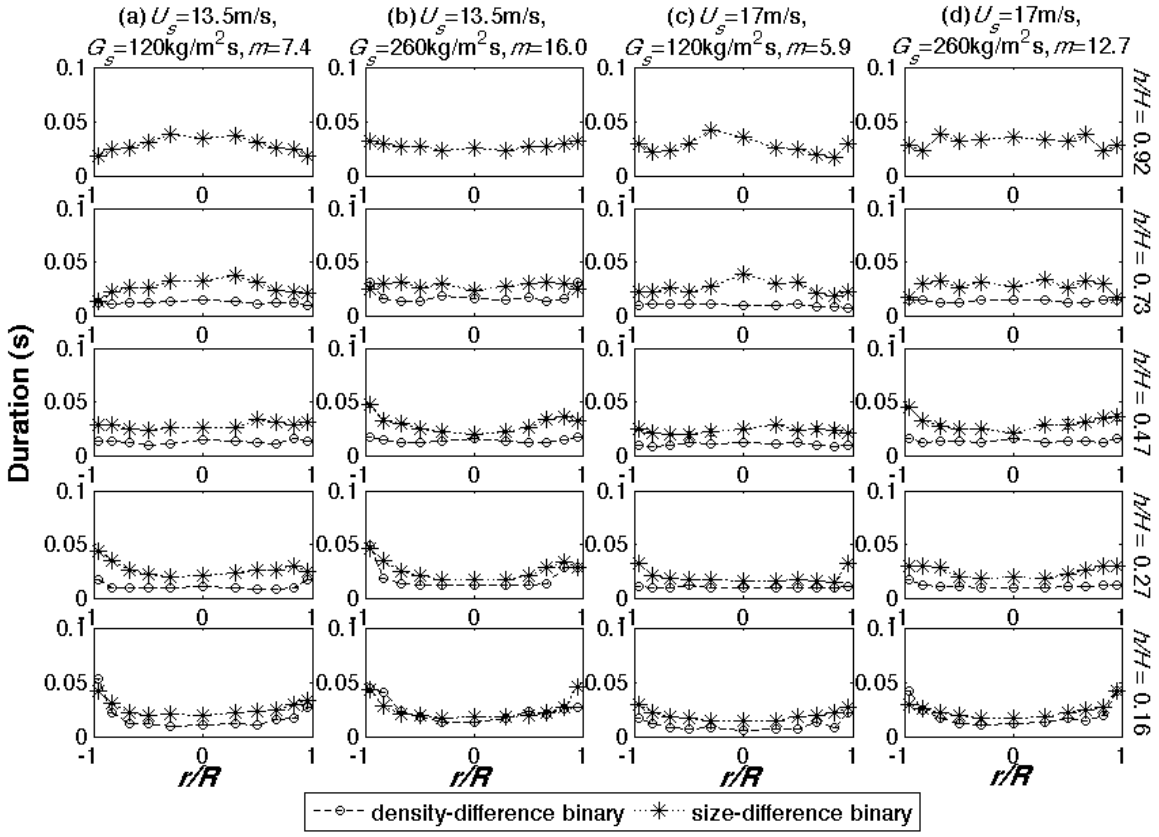

Figure 176*. Local profiles of cluster duration for density-difference and size-difference binary mixtures.*

Differences in cluster duration between the two types of binary mixtures are also noteworthy. In Figure 174, it is observed that the density-difference binary mixture generally exhibits lower cluster duration than either constituent component at all heights, which represents an interesting deviation from mass flux profiles, wherein the density-difference binary mixture mimics the large glass (i.e., higher ρ_s) component under all operating conditions(Chew, Hays et al. 2011). On the other hand, it is apparent in Figure 175 that the cluster duration profiles of the size-difference binary mixture mimics large glass (comparison not available for $h/H \leq 0.27$) more than small glass, which also is an interesting contrast from mass flux profile results(Chew, Hays et al. 2011), wherein the size-difference binary mimics neither of the constituent components. Direct comparisons between the density-difference binary and size-difference binary mixtures in Figure 176 reveal that the former generally gives lower cluster duration than the latter throughout the riser and under all operating conditions investigated (comparison not available at $h/H = 0.92$).

The third cluster characteristic, *cluster frequency*, is illustrated in Figures 177-179. Similar to both cluster appearance probability (Figures 171-173) and duration (Figures 174-176), axial position still plays the most distinctive role in affecting the radial profiles of cluster frequency. In particular, near the riser bottom ($h/H = 0.16$), profiles are similar regardless of material (type of binary mixture) or operating condition, which is consistent with results of the monodisperse materials presented in Section 4.5.4 (Chew, Hays et al. 2011). On the other hand, dissimilar to appearance probability but similar to duration, variations due to material (monodisperse or

binary) and operating conditions are apparent, though less so than axial position. Specifically, differences between materials and operating conditions are more apparent for $h/H \geq 0.47$, which again is consistent with the monodisperse results in Section 4.5.4(Chew, Hays et al. 2011).

*

Figure 177. *Local profiles of cluster frequency for density-difference binary mixture and constituent monodisperse materials.*

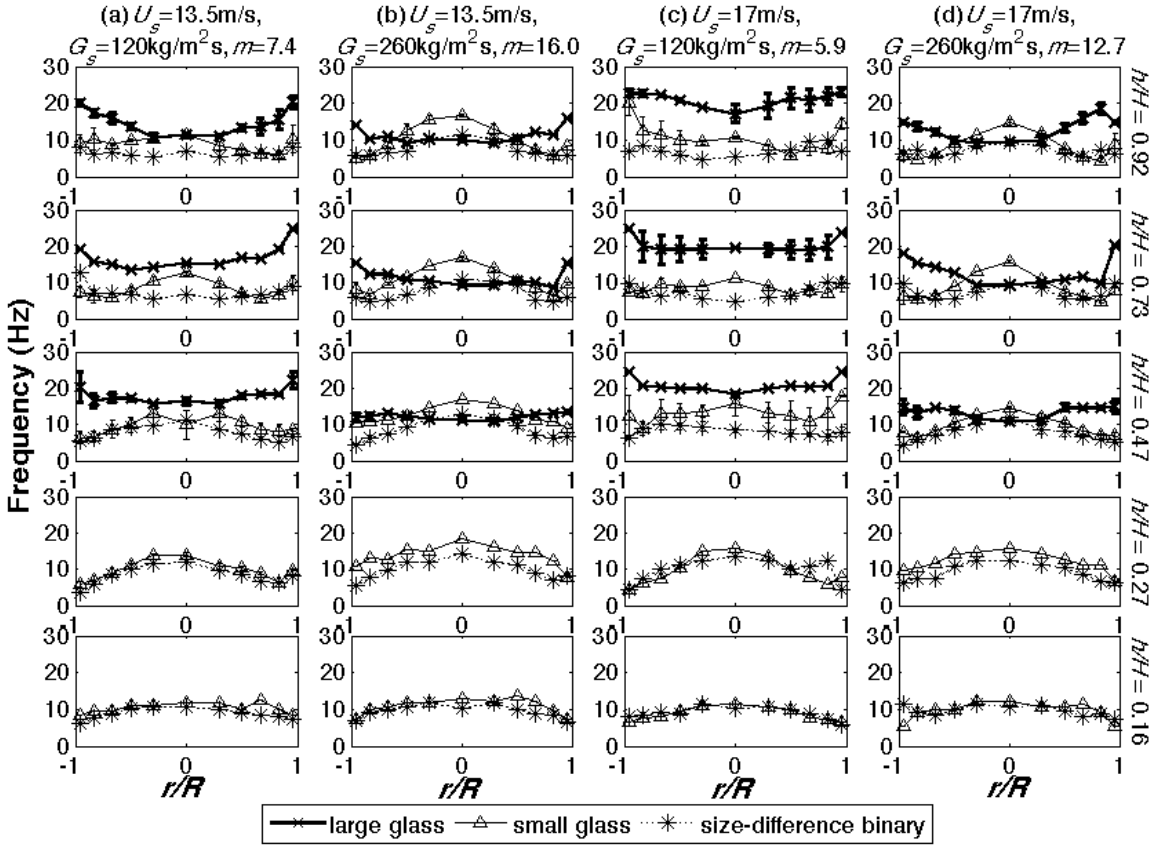

Figure 178. *Local profiles of cluster frequency for size-difference binary mixture and constituent monodisperse materials.*

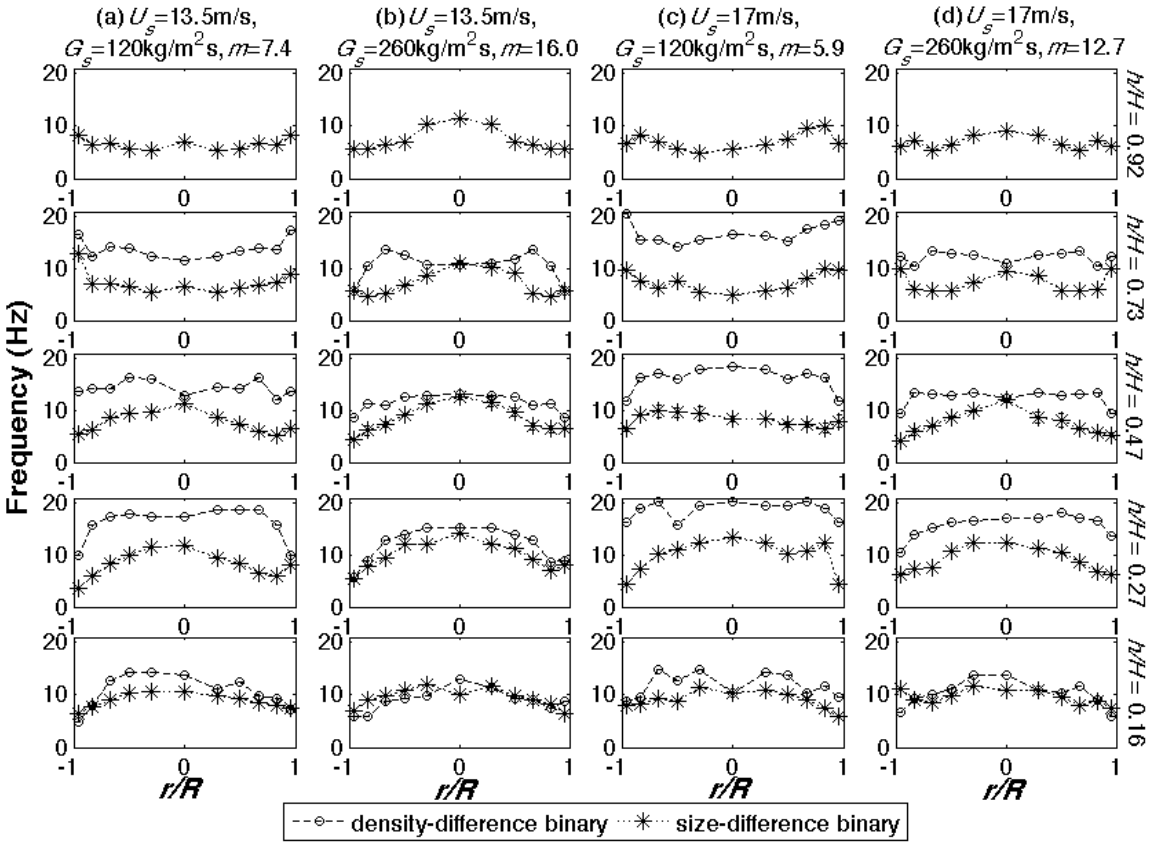

Figure 179*. Local profiles of cluster frequency for density-difference and size-difference binary mixtures.*

Since frequency profiles are similar for various materials and operating conditions for $h/H \leq 0.27$, observations on differences between the binary mixtures will focus on $h/H > 0.27$. Superimposing the cluster frequency profiles of the density-difference binary mixture with the corresponding constituent components in Figure 177 indicates that, where material variations are more apparent (Figure 177b and d), the density-difference binary mixture mimics large glass at the center ($r/R = 0$) and large HDPE at the wall ($r/R = 1$). With regards to the size-difference binary mixture, Figure 178 reveals that magnitudes of the cluster frequency for the size-difference binary mixture are generally more similar to that of small glass, which contrasts with the cluster duration trends (Figure 175), wherein the size-difference binary mixture mimics large glass more. Finally, Figure 179 shows that the cluster frequency of the size-difference binary

mixture is less than that of the density-difference mixture throughout the riser. Collectively, then, since the profiles of cluster appearance probability are similar for both binary mixtures (Figure 173), it seems that the lower cluster duration exhibited by the density-difference binary mixture (Figure 176) is balanced by higher cluster frequency (Figure 179).

Continuous PSD: It is worthwhile to note that the set of four operating conditions implemented for the continuous PSD is different from that for the binary mixtures and monodisperse materials Table 12). Hence, a direct comparison between the continuous PSD and binary mixtures or monodisperse materials (Chew, Hays et al. 2011) is not straightforward. Nonetheless, the impact of local riser position and a wider range of operating conditions (wider range of m; see Table 12) on a continuous PSD is illustrated.

Appearance probability profiles for the continuous PSD are presented in Figure 180. In contrast to Figures 171-173 (wherein axial position is the dominant influence on radial profiles, and effect of operating condition is insignificant), operating conditions play more of a role in the appearance probability profiles especially at the riser bottom (h/H = 0.16). This difference may be due to (i) an inherent difference in the nature of the distribution (continuous PSD vs. binary mixtures) and/or (ii) the wider range of operating conditions (m) implemented. In particular, it is observed that lower m gives flatter profiles and higher m gives U-shaped profiles lower in the riser (h/H = 0.16). Pertaining to (i), behavioral differences between continuous PSDs and binary mixtures have been noted before in the species segregation patterns of both bubbling beds(Hoffmann and Romp 1991; Gauthier, Zerguerras et al. 1999; Lin, Wey et al. 2002; Chew, Wolz et al. 2010; Chew and Hrenya 2011) and CFBs(Hirschberg and Werther 1998; Chew, Hays et al. 2011), and hence it is plausible that the more apparent effect of operating conditions could be due to the different type of polydispersity (i.e., continuous PSD instead of binary mixture). With regards to (ii), Figure 180a and c are at lower m than the range investigated for binary and monodisperse, while Figure 180b and d are at higher m (Table 12). Correspondingly, it is possible that when operating conditions are m = 5.9 - 16.0 (binary mixtures and monodisperse materials), appearance probability profiles are only a function of riser position; however, when operating ranges are widened (m = 2.8 - 25.0), differences in appearance probability profiles become apparent at riser bottom.

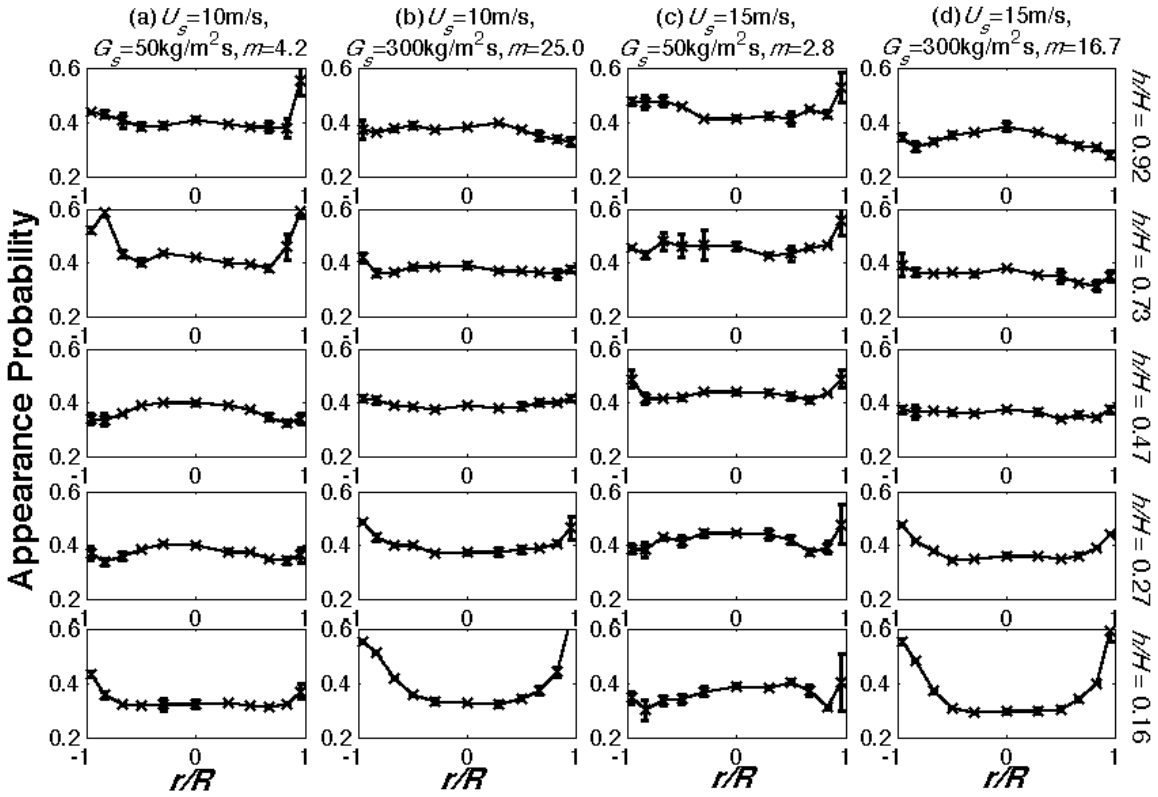

Figure 180*. Local profiles of cluster appearance probability for continuous PSD of small glass.*

Figure 181 displays the *cluster duration* profiles for the continuous PSD. As is true for cluster appearance probability, the operating conditions are seen to play more of a role on cluster duration than is observed for monodisperse materials and binary mixtures (Figures 174-178). Analogously, the difference may stem from either a behavioral difference between continuous PSD and binary mixture, or the wider range of operating conditions implemented for the continuous PSD. In contrast to the trends for cluster appearance probability (Figure 180), however, differences between operating conditions is more evident near the top of the riser. In particular, higher *m* conditions (Figure 181b and d) lead to increasingly accentuated U-shape profiles with height, whereas lower *m* (Figure 181a and c) results in an inverted U-shape. Finally, similar to trends for the monodisperse and binary mixtures, the radial profiles exhibit a U-shape near the bottom of the riser, implying that riser axial position continues to play a key role at the riser bottom, regardless of the distribution type or wider range of operating conditions.

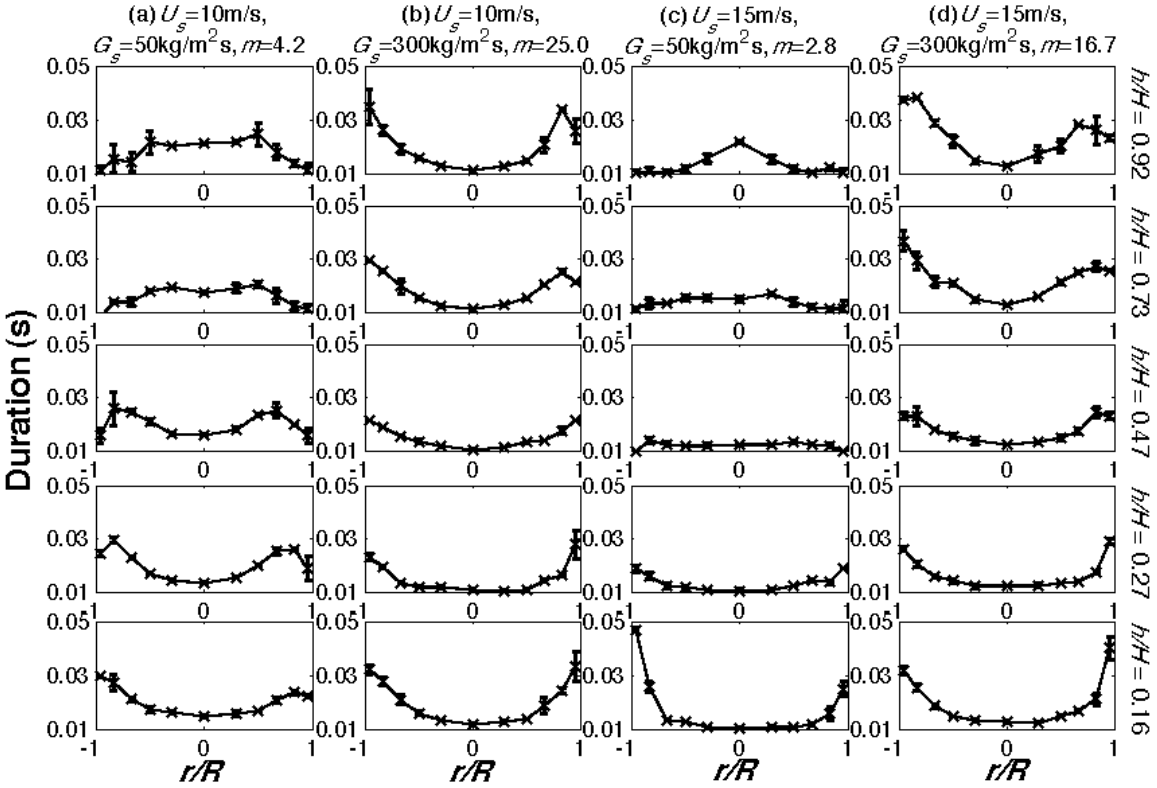

Figure 181. *Local profiles of cluster duration for continuous PSD of small glass.*

Lastly, *cluster frequency* profiles for the continuous PSD are contained in Figure 182. Again, operating conditions are seen to play more of a role on cluster frequency than is observed for monodisperse and binary mixtures. Similar to cluster duration (Figure 181), at higher axial positions ($h/H \geq 0.47$), different profile shapes manifest for different m conditions. At higher m, (Figure 182b and d), the inverted U-shapes of the frequency profiles become increasingly accentuated with riser height (for $h/H \geq 0.47$), which implies increased radial variation with height. On the other hand, at lower m (Figure 182a and c), profile shapes transform from W-shape to U-shape with height for $h/H \geq 0.47$. In other words, an interesting distinction between high and low m conditions is that higher m conditions cause the riser-center ($r/R = 0$) frequency to increase and wall frequency to decrease with height, whereas the opposite effect is brought about at low m (i.e., center frequency decreases with height, while wall frequency increases with height). The physical reasoning as to why axial trends at the riser center and riser core differs and why different m are associated with opposite axial trends is unclear, but future modeling efforts are expected to provide more understanding of these features.

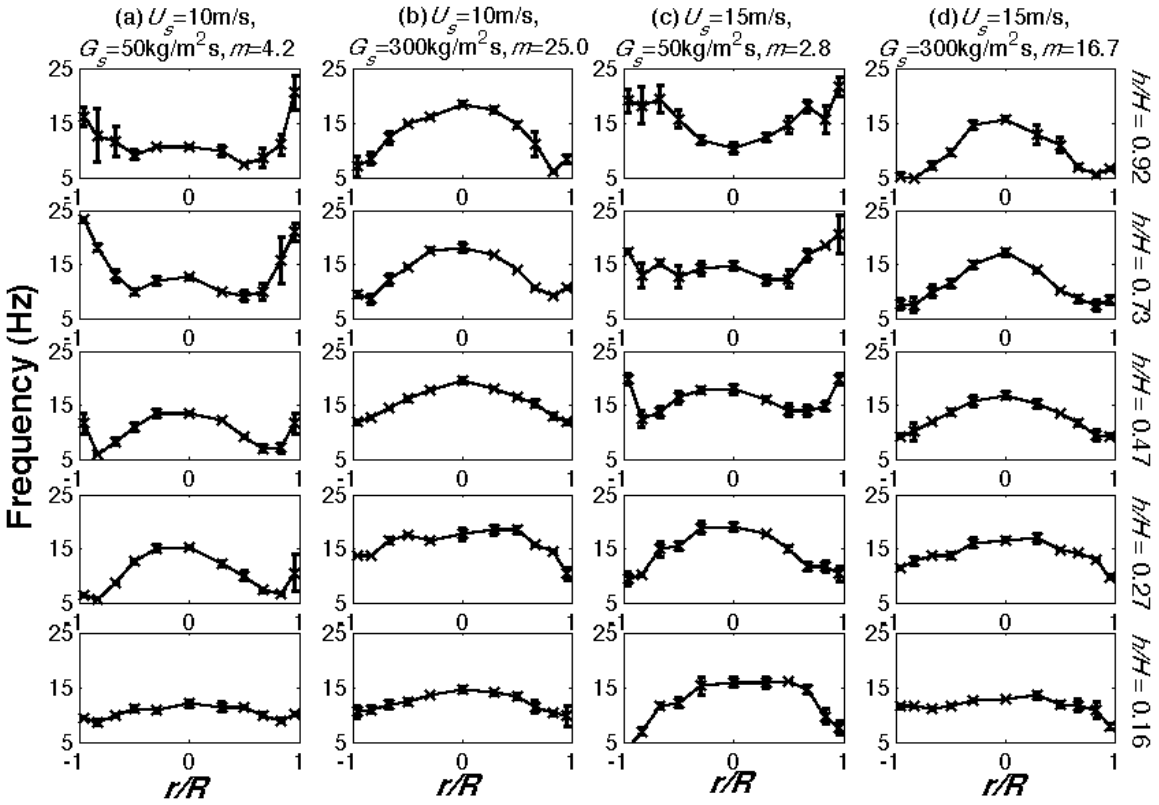

Figure 182*. Local profiles of cluster frequency for continuous PSD of small glass.*

Summary: A detailed experimental investigation on cluster characteristics of polydisperse Geldart Group B particles in a pilot-scale CFB riser has been carried out. A fiber optic probe was used for local measurements and the threshold used for cluster identification was determined via wavelet decomposition. The resulting cluster measurements include appearance probability, duration, and frequency. Three mixtures were investigated: (i) a density-difference binary mixture, (ii) a size-difference binary mixture, and (iii) a continuous size distribution of particles with equal material density.

Generally speaking, the qualitative trends of the cluster characteristics for the binary mixtures investigated here are similar to those of the monodisperse materials reported in Section 4.5.4(Chew, Hays et al. 2011), though small differences between the two types of binary mixtures are noteworthy. Regarding the former, the local riser position generally has the dominant effect on all three cluster characteristics (appearance probability, duration, and frequency). Furthermore, cluster appearance probability is most influenced by riser axial position, and least affected by operating condition and material type. Regarding differences observed between the two types of binary mixtures, for the density-difference binary mixture, cluster duration is distinctly lower than either component and neither of the three cluster characteristics mimic either component. On the other hand, for the size-difference binary mixture, cluster duration mimics the large component, while cluster frequency mimics the small component. Comparing the two binary mixtures, the density-difference binary mixture has lower cluster duration and higher cluster frequency than the size-difference binary mixture.

For the continuous PSD, similar to trends for the binary mixtures and monodisperse materials(Chew, Hays et al. 2011), the local riser position still plays a key role on cluster trends, although the impact of operating condition is more apparent for all three cluster characteristics (appearance probability, duration, and frequency). The deviation can be attributed to either inherent differences between continuous PSDs and binary mixtures, and/or a wider range of operating conditions (m = 2.8 to 25.0) examined as compared to the monodisperse and binary systems (m = 5.9 to 16.0).

The experiments reported here, which represents the first experimental dataset on clustering in polydisperse systems, provide further insight into the high-velocity fluidization behavior of both binary mixtures and continuous PSDs. It is worthwhile to note that the polydispersity effects examined here refer to the impact of having a range of particle size and/or material density, but clustering instabilities are also linked to the dissipative nature of inelastic collisions(Goldhirsch 2003), which implies other particle properties (such as restitution coefficient, friction coefficient, particle shape) may play a role as well.

The cluster measurements presented here is part of wider dataset for the same CFB unit and operating conditions; other local data available include cluster characteristics of monodisperse materials (Section 4.5.4(Chew, Hays et al. 2011)), mass flux (Section 4.5.3(Chew, Hays et al. 2011)), solids concentration (and the surprising observation of reverse core-annular flow in Section 4.5.1)(Chew, Hays et al. 2011), and species segregation (Section 4.5.2)(Chew, Hays et al. 2011). Collectively, this dataset on various flow phenomena in a moderately dense CFB riser (Task 4.5) is expected to be valuable towards validating kinetic-theory based models, especially for quantitative predictions of clustering instabilities and various forms of polydispersity (for example, refer to(Garzo, Dufty et al. 2007; Garzo, Hrenya et al. 2007) for binary mixtures and (Murray, Hrenya et al. 2010) for continuous distributions).

Task 4.6: Model Validation (all investigators)

Subtask 4.6.1: Comparison with Experimental and DEM Simulation Data (all investigators).

At this point, the fully specified model developed herein will be solved in order to compare to the data sets described above. In particular, model predictions for species concentration will first be compared against the DEM-based data for granular (Task 4.1) without particle evolution due to agglomeration, etc. In this manner, the role of the solid-solid interactions will be evaluated without a drag force present. The predicted evolution of particle properties will then be tested against the corresponding granular DEM data to determine the ability of the DQMOM approach to predict segregation without the presence of drag force. Comparisons of model predictions to the experimental data will then be performed for the case of low-velocity beds (Task 4.3). For each of the aforementioned comparisons with datasets characterized by a continuous size distribution, the models will be implemented with several different values of N in order to determine the required number of discrete sizes needed to properly represent the continuous distribution.

(Fox reporting.) The implementation of the quadrature-based moment method (Fox 2008) in MFIX was tested by performing simulations of gas-particle flows in a two-dimensional vertical channel (0.1 x 1 m) with monodisperse particles and comparing the results with two-fluid model simulations of the same case. The mass flow rate of the fluid-phase (ρ_g = 1.2 kg/m^3) was fixed so that the fluid-phase Reynolds number is 1380, well below the transition to

turbulence in a single-phase flow. This choice was made to remove the direct effect of the fluid turbulence on the formation of segregated structures from the system. The desired fluid-phase Reynolds number was obtained by setting the viscosity of the fluid phase to $\mu_g = 1.74 \times 10^{-4}$ Pa s.

For the particle phase, a range of volume fractions between 0.0001 and 0.01 was considered, with a particle density of 1500 kg/m^3. The particle diameter was set to 252 μm, and the restitution coefficients for both particle-particle and particle-wall collisions were set to $e_p = e_w = 1$, which corresponds to perfectly elastic collisions.

Wall boundary conditions were set to be specularly reflective. This condition is equivalent, in the two-fluid model, to a free-slip condition for the particle phase. No-slip conditions were used at the walls for the fluid phase. Periodic conditions with constant mass flow rates were adopted in the flow direction for both phases. A uniform field for all the properties was used as the initial conditions.

Results of a channel-flow simulation with particle-phase volume fraction of 0.01 obtained with MFIX-QMOM are reported in Figure 183, where snapshots of the time evolution of the particle-phase volume fraction are shown. The predictions of the two-fluid model for the same case are show in Figure 184. At the beginning of the simulation, the particles, initially distributed uniformly in the channel, are accelerated towards the walls due to the mean fluid velocity gradient, where they are reflected and move towards the centre of the channel. This process leads to the formation of preferential particle-depleted vertical paths for the fluid phase, where it can accelerate. This separation however is unstable, due to the velocity gradient between the zone at low particle concentration and the one at higher particle concentration, as observed in Passalacqua *et al*. (2009). This leads to chaotic flow behavior, where particles tend to segregate towards the walls, originating the characteristic core-annular flow, with particles falling along the channel walls, with an oscillating upward flow in the centre.

A similar behavior is observed in the initial stages of the two-fluid model prediction, where particles are reflected by the walls and give origin to the preferential paths for the fluid phase (Figure 184, $t = 1.45$ s). However, the evolution of the system from this point on proceeds with the formation of two unstable structures on the sides of the flow, which leads to particle segregation. The main difference between the MFIX-QMOM and two-fluid model predictions is, however, the abundance of fine structures at high particle concentration in the two-fluid prediction (i.e., delta-shocks), which are not predicted by the QMOM model. The formation of these structures in two-fluid models can be explained by the fact that when particle trajectory crossing occurs, models tracking only the mean momentum are unable to predict correctly all the velocity moments (Desjardin *et al*., 2008). In such a situation, hydrodynamic models predict a delta-shock, since they cannot represent a situation where multiple distinct local particle velocities are present. Further grid refinement will exacerbate the segregation in the two-fluid model. Although not as easily distinguished in the snapshots in Figures 183 and 184 as in flow-field animations, there are also clear differences between the MFIX-QMOM and the two-fluid predictions in the regions near the walls. In the MFIX-QMOM simulations, the falling particles form larger 'blobs' that cover several grids cells away from the wall, while in the two-fluid predictions the falling particles remain much closer to the wall. We believe that these differences can be attributed to the differences in the boundary conditions for the granular temperature.

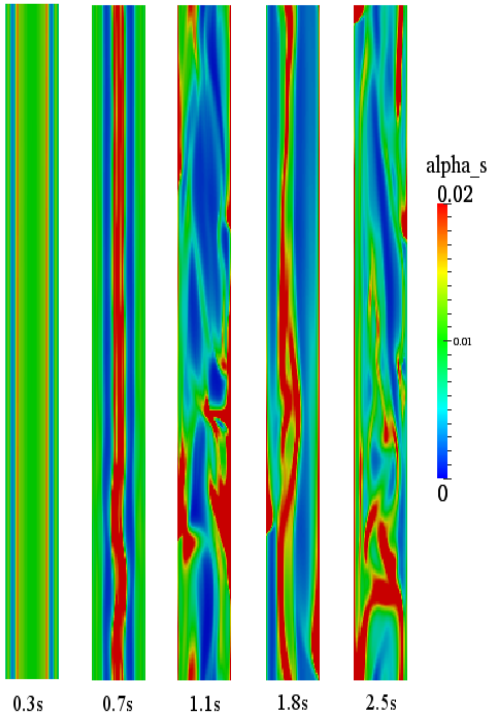

Figure 183. *Particle-phase volume-fraction evolution predicted by MFIX-QMOM with an average particle-phase volume fraction of 0.01.*

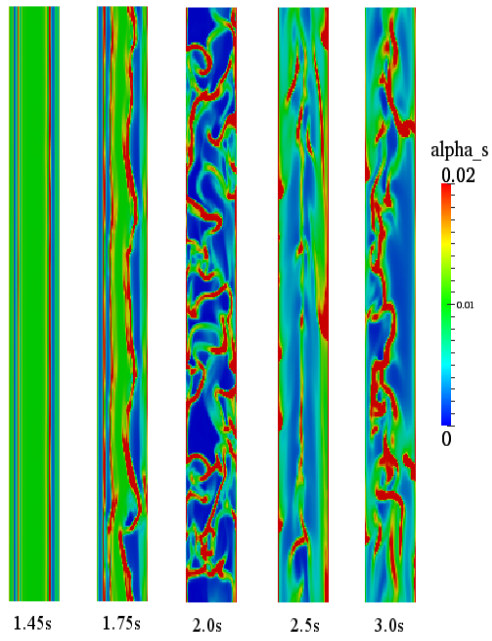

Figure 184. *Particle-phase volume-fraction evolution predicted by the two-fluid model with an average particle-phase volume fraction of 0.01.*

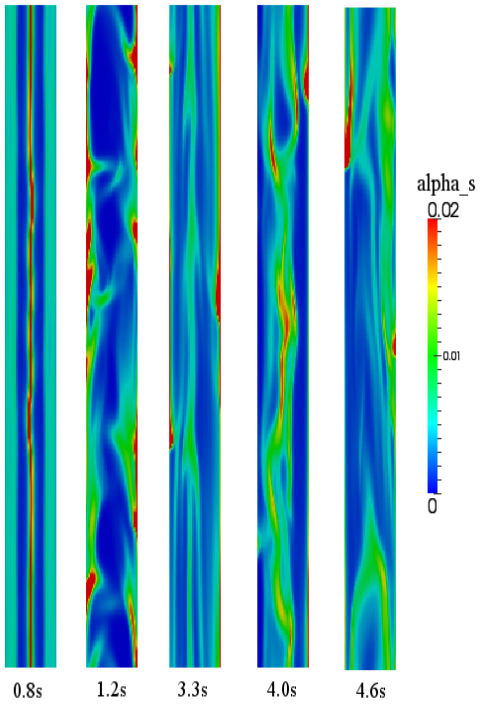

Figure 185. *Particle-phase volume-fraction evolution predicted by MFIX-QMOM with an average particle-phase volume fraction of 0.005.*

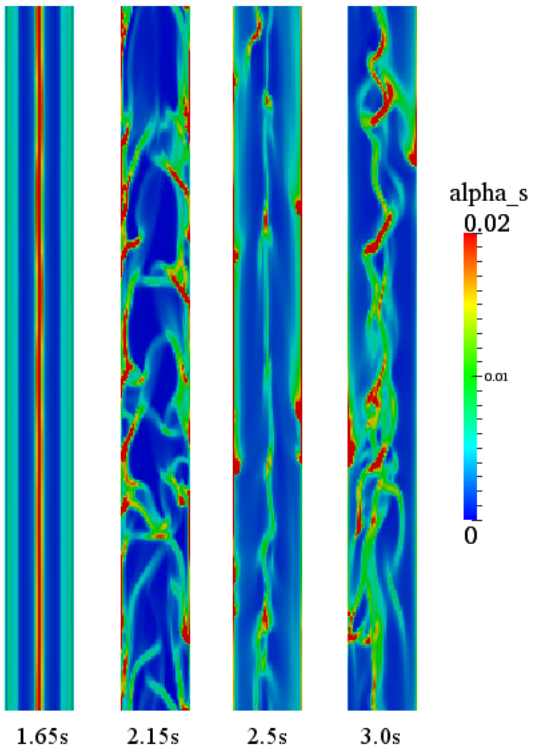

Figure 186. *Particle-phase volume-fraction evolution predicted by the two-fluid model with an average particle-phase volume fraction of 0.005.*

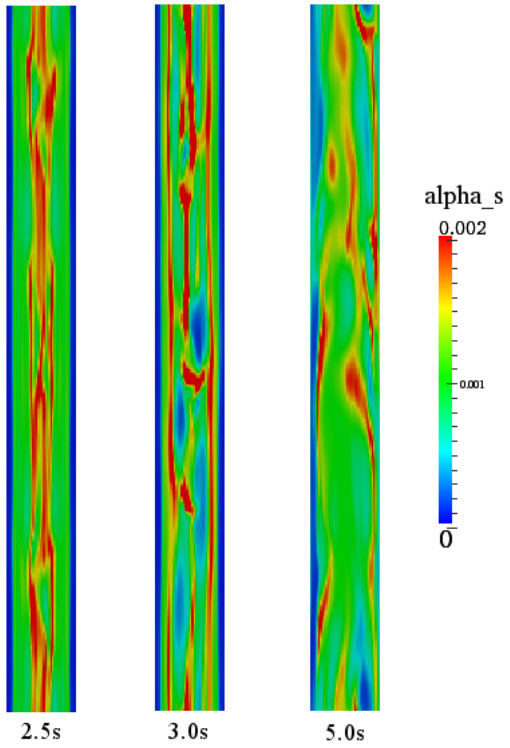

Figure 187. *Particle-phase volume-fraction evolution predicted by MFIX-QMOM with an average particle-phase volume fraction of 0.001.*

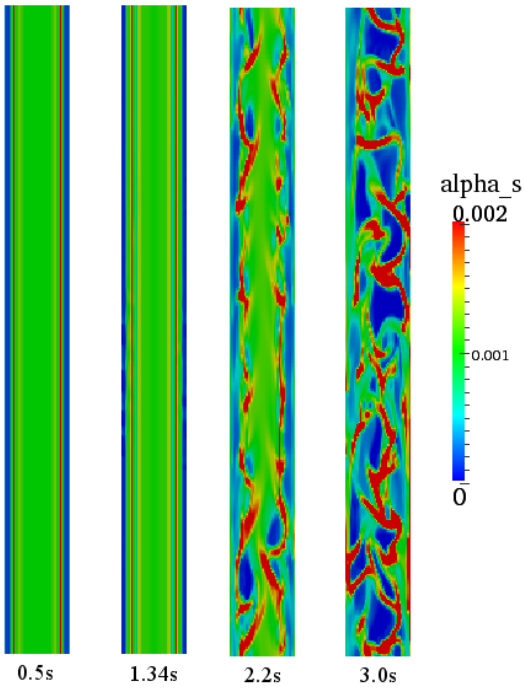

Figure 188. *Particle-phase volume-fraction evolution predicted by the two-fluid model with an average particle-phase volume fraction of 0.001.*

Similar results were observed in the case of an average particle-phase volume fraction of 0.005, reported in Figure 185 (MFIX-QMOM) and Figure 186 (two-fluid model). The agreement between the two predictions is consistent during the initial stages of the simulations. However, the two-fluid model still shows a tendency to predict fine structures at high particle concentration, as observed in the previous case. The effect of the particle concentration on the development of the instability that leads to particle segregation was further investigated by considering two cases with lower mass loading. Figure 187 shows the evolution of the flow predicted by MFIX-QMOM in the case of an initial mean volume fraction of 0.001, while Figure 188 reports the prediction of the two-fluid model in the same case. The mechanism that leads to the formation of an unstable flow is similar to that observed in the densest cases. However the transition to an unstable flow, and the consequent particle segregation phenomena, are slower and less evident, since the particle concentration is lower. The two-fluid model predicts a similar behavior to the one observed in Figure 184, with the formation of small structures not observed in the MFIX-QMOM prediction.

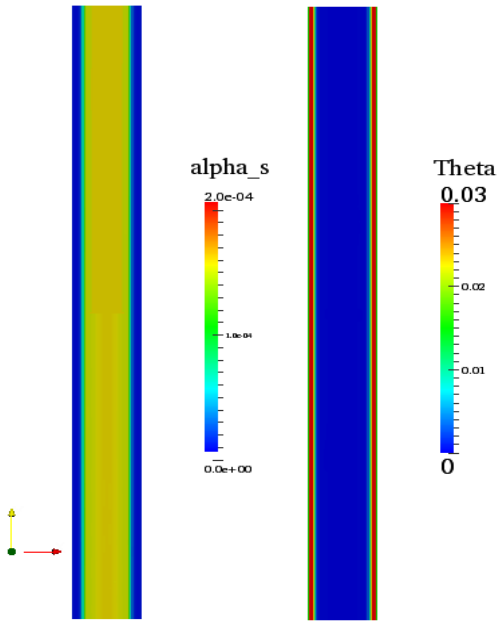

Figure 189. *Particle-phase volume fraction and granular temperature at 5 s predicted by MFIX-QMOM with an average particle-phase volume fraction of 0.0001.*

An even more dilute case, with an average particle volume fraction of 0.0001 (mass loading 0.13), was also considered. The results of the MFIX-QMOM predictions are reported in Figure 189 For this case, after 5 s of simulation time, particles are still distributed almost uniformly across the channel, with the exception of near the walls, since in the wall zone the particle temperature is highest. We did not obtain a convergent solution using the two-fluid model with the required convergence criteria used in the other cases; as a consequence results from two-fluid models are not reported. Although we cannot confirm it directly due to the finite duration of our simulation, it appears that the case shown in Figure 189 reaches a time-independent state where only gradients in the wall-normal direction are present.

In the zone next to walls the net particle flux is zero, and, as a consequence the mean particle velocity is zero, but the velocity variance is high due to specular reflections. As observed in Passalacqua *et al*. (2009), this means that the local particle Mach number of the flow, defined using of the mean particle velocity and the granular temperature (Kogan, 1969), and the local Knudsen number, are large and well outside the range of validity of hydrodynamic models (Kn < 0.1), even with the addition of partial-slip boundary conditions like those proposed by Johnson and Jackson (Johnson & Jackson, 1987). In the cases considered in this work, the Johnson and Jackson boundary conditions degenerate into free-slip conditions, since the walls are assumed to be frictionless. It is worth noting that the Johnson and Jackson boundary conditions imply a zero granular temperature flux at the wall, when perfectly specular conditions are imposed. This implies that the two-fluid models cannot convert the velocity of particles impinging on the wall into granular temperature, even though the velocity component normal to the wall is zero. As a consequence, the maximum in the granular temperature at the walls that is observed in Figure 189 is not captured by the two-fluid model.

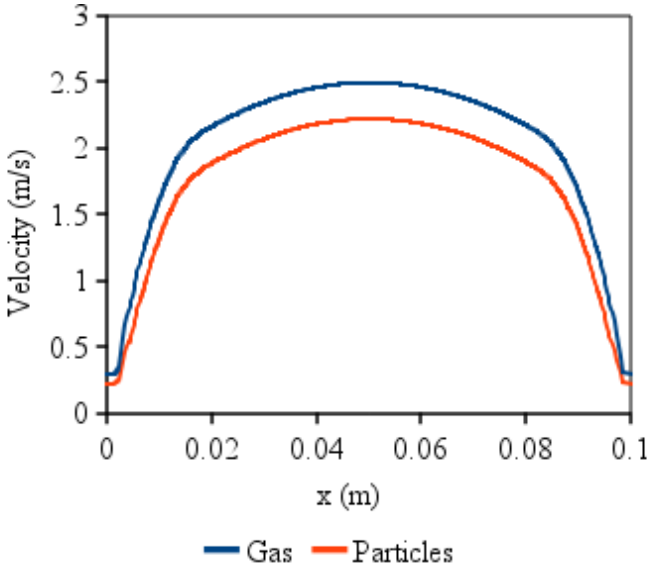

Figure 190. *Phase velocities predicted by MFIX-QMOM at 5 sec with an average particle-phase volume fraction of 0.0001.*

The vertical velocity profiles for the case in Figure 189 are reported in Figure 190, and show that the flow has the typical profile of a stable channel flow. For this case, the particle mass loading is small enough to not have a destabilizing effect on the fluid phase. However, it is worth noting that the velocity profiles are not perfectly parabolic, due to the presence of the particles and the momentum coupling with the particle phase. Nonetheless, no instabilities develop and both phases attain a steady state.

The relative computational cost of MFIX-QMOM with respect to the two-fluid model in MFIX is in the range of 1.5–1.9. The longest simulation was the one with the highest particle-phase volume fraction, which required 25.37 hours with the two-fluid model and 48.2 hours with MFIX-QMOM on a single core of an Intel Xeon CPU at 3.0GHz. It is worth noting that the hyperbolic nature of the QMOM model should make the MFIX-QMOM code highly scalable. In the dilute limit, the time step is limited only by the CFL number and the kinetic-based fluxes are stable for relatively large CFL number (e.g., CFL=1 for the first-order scheme).

Work is in progress to extend the MFIX-QMOM code discussed in this work to denser flows (Fox and Vedula, 2009), in order to create an efficient and versatile tool, able to describe gas-particle flow over the full range of particle-phase volume fractions. Although not reported here, the same approach for approximating the kinetic equation is used for polydisperse gas-particle flows by coupling a multi-component kinetic equation with the fluid solver. Such as approach naturally accounts for particle-particle collisions between like and unlike particles, as well as differences in the fluid drag depending on the particle type, and has been already implemented into MFIX, however further validation is required.

The implementation of QMOM (Fox, 2008; Passalacqua *et al.*, 2009) into MFIX has been further verified by performing a preliminary grid independence study in a 2-D channel flow of 10 cm width, with periodic boundary conditions in the direction of the flow, whose length was set to 1 m. The objective of the study is to understand the influence of the spatial discretization on the numerical solution of the moment transport equations, and, in particular, on the formation of structures at higher particle concentration such as those reported in Agrawal *et al.* (Agrawal, et al., 2001).

The initial average volume fraction is 0.01, uniform in the whole computational domain. Both the fluid and the particle phase have zero velocity at the beginning of the simulation. Gravity acts along the vertical axis, in the opposite direction of the flow. A constant fluid mass flow rate is imposed, in order to have $Re_g < 1500$, to avoid the transition to turbulence of the fluid phase in a single phase flow. Three cases are considered, with grids of 40x400, 80x800 and 100x1000 cells. Results were compared to the corresponding two-fluid simulation, performed using the default model in MFIX. The contour plots of the particle phase volume fraction, taken after the flow developed in the channel are reported in Figures 191, 192 and 193 for the three grid densities under consideration.

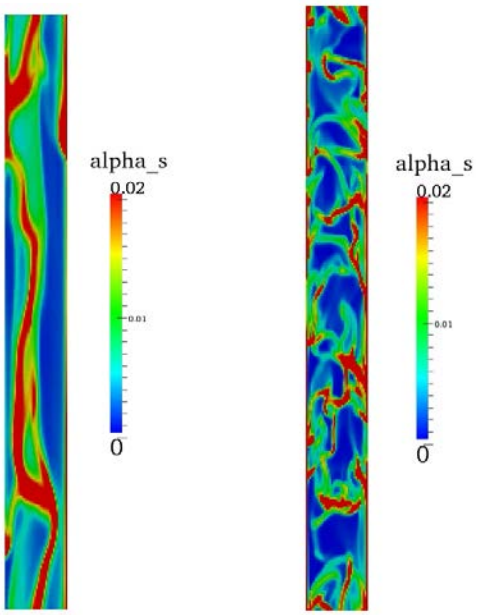

Figure 191*. QMOM (left) and two-fluid (right) predictions – Grid 40 x 400 – t = 1.20 s.*

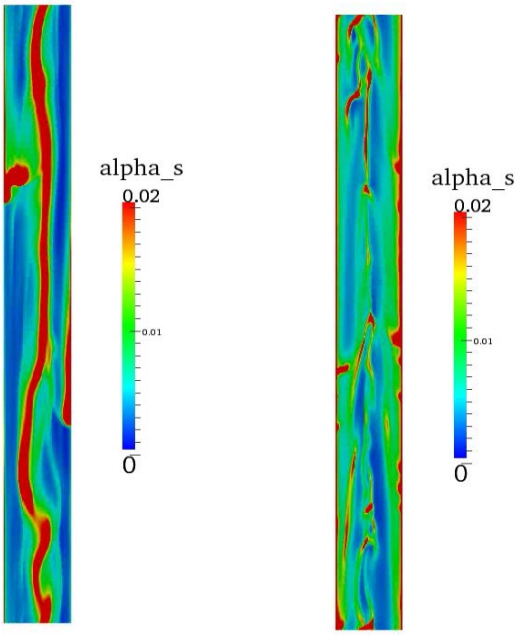

Figure 192. *QMOM (left) and two-fluid (right) predictions – Grid 80 x 800 – t = 1.20 s*

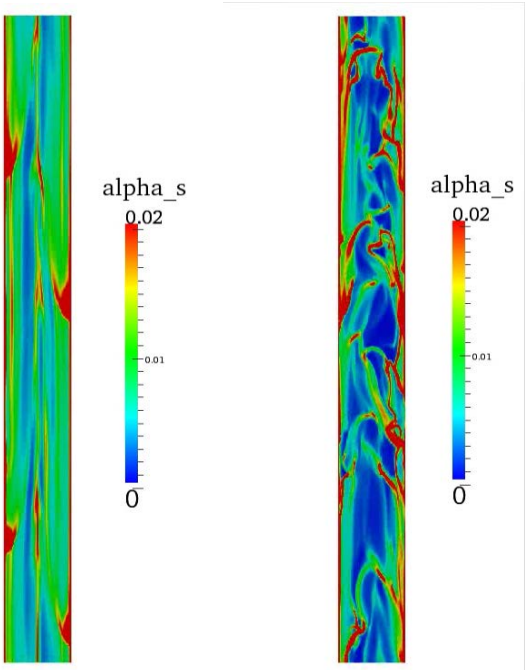

Figure 193. *QMOM (left) and two-fluid (right) predictions – Grid 100 x 1000 – t=1.20 s.*

From the contour plots it is possible to observe that in both approaches under examination, after a transient phase, during which the flow develops, the particle phase segregates against the walls of the channel, originating the typical structure of core-annular flow, with particles falling down along the walls due to the insufficient drag force exerted by the fluid moving upward. However, significant differences can be observed in Figure 191, with a 40 x 400

grid, where the two-fluid model prediction shows the formation of many small structures with higher particle concentration, which are not observed in QMOM predictions. Increasing the grid density to 80 x 800, as done to obtain the results reported in Figure 192, did not significantly change the comparison: QMOM results show slightly sharper structures of the flow, but no structures of the size of the computational cell are observed, in clear opposition to what is shown in the plots obtained from the two-fluid simulations. A further increase of the grid density to 100 x 1000 computational cells confirmed what is observed in the first two cases.

As discussed in Passalacqua *et al.* (2009), the prediction of small structures observed in two-fluid models is due to the mathematical formulation of the equations, which are based on the hydrodynamic assumption. Such an hypothesis is not valid to describe flows with local Knudsen numbers greater than 0.1 even with the adoption of partial slip boundary conditions because the Knudsen layers extend inside the bulk of the fluid (Galvin, 2007). In flows like those considered in this study and typical of risers, the Knudsen number can reach values of the order of 10, clearly indicating that the regime is outside from the hydrodynamic range. Under these conditions, for finite Stokes numbers, particles trajectories can cross without collisions between particles, originating the phenomenon of particle trajectory crossing. This phenomenon can be described only by methods that account for multiple local velocities, as it happens in Lagrangian methods or in higher-order moment methods such as QMOM. If only the mean momentum equation is considered, particle trajectory crossing cannot be predicted (Desjardin *et al.*, 2008), leading to the formation of delta shocks in the particle concentration, which are identified with clusters, whose size and number is sensitive to the grid resolution. These structures however do not represent an actual physical entity that characterizes the particle phase, but, as clarified above, are only a consequence of the limitations of the hydrodynamic models.

Another achievement is the implementation in MFIX of the collisional term of the moment spatial fluxes (Fox and Vedula, 2009), in order to account for their effect, which become important for particle phase volume fractions greater than approximately 5%. The moment spatial fluxes can be written as the sum of a kinetic and collisional contribution, the latter of which originates from the collision integral. The rate of change of the moment of order γ due to collisions, in the case of finite-size particles can be written as

$$\mathbb{C}^{\gamma}_{ijk} = \frac{6}{\pi d_{\mathrm{p}}} \int_{\mathbb{R}3} \int_{\mathbb{R}3} \int_{\mathbb{S}^+} \left[(v'_{1,1})^i (v'_{1,2})^j (v'_{1,3})^k - (v_{1,1})^i (v_{1,2})^j (v_{1,3})^k \right] f^{(2)}(\mathbf{x}, \mathbf{v}_1; \mathbf{x} + d_{\mathrm{p}}\mathbf{n}, \mathbf{v}_2) \, |\mathbf{g} \cdot \mathbf{n}| \, \mathrm{d}\mathbf{n}\mathrm{d}\mathbf{v}_1\mathrm{d}\mathbf{v}_2$$

where d_{p} is the particle diameter, v is the pre-collisional particle velocity, and v' is the post-collisional particle velocity, $f^{(2)}$ is the pair distribution function, **g** is the relative velocity vector and **n** is the unit vector along the direction of the particle centres. This term can be re-written as

$$\mathbb{C}^{\gamma} = C^{\gamma} - \boldsymbol{\nabla} \cdot \mathbf{G}^{\gamma} + \mathcal{O}\left(\left(d_{\mathrm{p}}/L \right)^2 \right)$$

where the first term on the right-hand side corresponds to the rate of change of the moment for point particles, modified to introduce the radial distribution function g_0,

$$C^{\gamma} = \frac{6 g_0}{d_{\mathrm{p}}} \int_{R^3} \int_{R^3} g I^{\gamma}(\omega, \mathbf{v}_1, \mathbf{v}_1 - \mathbf{v}_2) f(\mathbf{v}_1) f(\mathbf{v}_2) \mathrm{d}\mathbf{v}_1 \mathrm{d}\mathbf{v}_2$$

and the second term is the collisional flux, with

$$\mathbf{G}^{\gamma} = 3g_0 \int_{\mathbb{R}^3} \int_{\mathbb{R}^3} g\mathbf{F}^{\gamma}(\omega, \mathbf{v}_1, \mathbf{v}_1 - \mathbf{v}_2) f(\mathbf{v}_1) f(\mathbf{v}_2) \mathrm{d}\mathbf{v}_1 \mathrm{d}\mathbf{v}_2$$

It is worth noting that the collisional flux becomes zero in the Boltzmann limit (point particles), and it is different from zero only for finite (non-zero) size particles. Moreover, when the particle volume fraction approaches its maximum value, the collisional flux becomes very big due to the presence of the radial distribution function g_0, preventing further accumulation of particles and limiting the phase volume fraction itself. The role of collisional fluxes is shown considering two density waves moving in opposite direction, as shown in Figure 194.

If collisional fluxes are neglected, no limitation is imposed on the particle phase volume fraction, and the density reaches a maximum value of about 0.2, when the waves collide, as shown in Figure 195. On the other hand, when the collisional flux contribution is included, the evolution of the density profile is significantly influenced, and the maximum value of the particle concentration is limited to about 0.12, as shown in Figure 196.

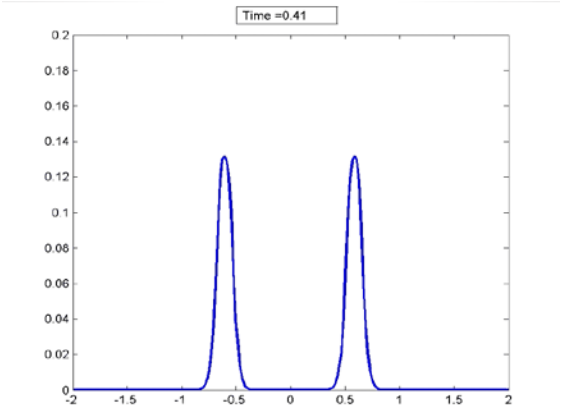

Figure 194. *Density waves moving one towards the other before colliding*

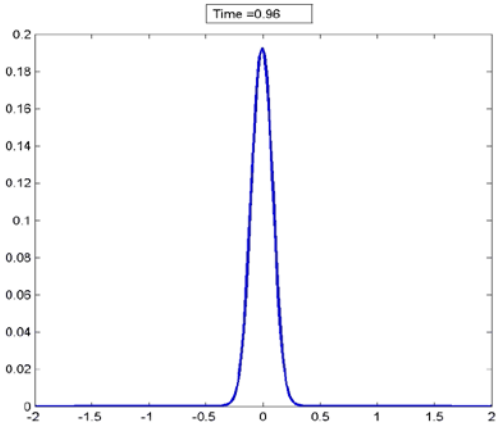

Figure 195. *Density peak without collisional fluxes*

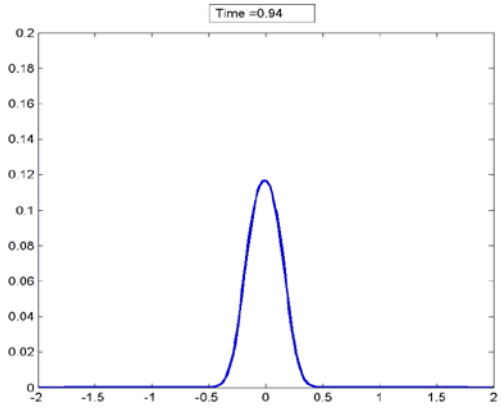

Figure 196. *Density peak with collisional fluxes*

The iterative solution procedure previously used for QMOM has been modified to implicitly include the effect of the particle pressure in the equation of the first order moment M^0, representing the particle-phase volume fraction. This modification to the solution algorithm, tested in 1-dimensional case, has proven to be very efficient in terms of computational times, and very robust in stably enforcing the particle packing limit. In particular, compared to the current implementation of QMOM into MFIX, where the time step is limited based on a Courant number defined as a function of the particle-phase speed of sound, the approach presented here led to an increase of the time-step size of up to two orders of magnitude (from 1.0×10^{-6} to 1.0×10^{-4} s), depending on the case under examination. The procedure is briefly summarized below.

The first step in the development of the improved procedure is to consider the transport equations for the zero- ($M^0 = \alpha_a$) and first-order moments ($\mathbf{M}^1 = \alpha_a \mathbf{U}_a$):

$$\frac{\partial \alpha_a}{\partial t} + \nabla \cdot (\alpha_a \mathbf{U}_a) = 0$$

and

$$\frac{\partial}{\partial t}(\alpha_a \mathbf{U}_a) + \nabla \cdot (\alpha_a \mathbf{U}_a \mathbf{U}_a + < \mathbf{Q}_a >) = < \mathbf{A}_a > + < \mathbf{P}_a >,$$

being $\langle \mathbf{A}_a \rangle$, $\langle \mathbf{P}_a \rangle$, and $\langle \mathbf{Q}_a \rangle$ respectively the average acceleration term, the collision term and the collisional contribution to the flux. We notice that

$$< \mathbf{Q}_a > = < \boldsymbol{\tau}_{a,coll} > + \mathrm{tr} < \mathbf{Q}_a > \mathbf{I},$$

where the last term represents the particle pressure p_a . We then recast the equation for the mean momentum in the form

$$\frac{\partial}{\partial t}(\alpha_a \mathbf{U}_a) + \nabla \cdot \mathbf{F} = -\nabla p_a + < \mathbf{A}_a > + < \mathbf{P}_a >,$$

where **F** is the sum of the kinetic flux and the off-diagonal part of the collisional flux. We notice than, that

$$\nabla p_{\mathrm{a}} = G(\alpha_{\mathrm{a}})\nabla\alpha,$$

where $G(\alpha_{\mathrm{a}})$ is the partial derivative of the particle pressure with respect to the phase volume fraction, given, in general, for QMOM by

$$\frac{\partial p_{\mathrm{a}}}{\partial \alpha_{\mathrm{a}}} = \frac{\partial}{\partial t}\left[\alpha_{\mathrm{a}}\Theta_{\mathrm{a}} + \frac{g_0}{3}\sum_{i=1}^{\mathrm{N}}\sum_{j=1}^{\mathrm{N}}(1+e_{ij})\alpha_{\mathrm{a},i}\alpha_{\mathrm{a},j}g_{i,j}^2\right],$$

and, in case the restitution coefficient e_{ij} does not depend on the collision velocity, and only one specie is present, by

$$\frac{\partial p_{\mathrm{a}}}{\partial \alpha_{\mathrm{a}}} = \frac{\partial}{\partial \alpha_{\mathrm{a}}}\left[\alpha\Theta_{\mathrm{a}} + 2\alpha_{\mathrm{a}}^2\Theta_{\mathrm{a}}(1+e)g_0\right]$$

which is the same expression used in hydrodynamic models with kinetic theory closures, where Θ_{a} is the granular temperature and g_0 the radial distribution function.

At this point, it is possible to reformulate the equation for the zero-order moment by first predicting the flux from the equation of the first-order moment, using information from the previous time-step, and replacing the expression for the flux in the equation for M^0, so that the force balance is directly included into it. The first step is to write the semi-discretized equation for the first-order moment, whose explicit form will clearly depend on the approach used to discretize the momentum coupling term. For simplicity, we include all the effects in a symbolic term, with the exception of the particle pressure

$$\mathbb{A}_{\mathrm{a}}\mathbf{U}_{\mathrm{a}} = \mathbb{H}_{\mathrm{a}} - \frac{1}{\rho_{\mathrm{a}}}\nabla p_{\mathrm{a}} + \mathbf{F}_{\mathrm{a}}$$

$$\mathbf{U}_{\mathrm{a}} = \frac{\mathbb{H}_{\mathrm{a}}}{\mathbb{A}_{\mathrm{a}}} - \frac{1}{\rho_{\mathrm{a}}\mathbb{A}_{\mathrm{a}}}\nabla p_{\mathrm{a}} + \frac{\mathbf{F}_{\mathrm{a}}}{\mathbb{A}_{\mathrm{a}}}$$

where $\mathbf{F}_{\mathrm{a}}$ contains all the force terms strongly dependent on the phase volume fraction, and the pressure gradient, while $\mathbf{H}_{\mathrm{a}}$ includes the remaining terms. Interpolating this velocity on cell faces gives origin to the face velocity

$$\phi_{\mathrm{a}} = (\mathbf{U}_{\mathrm{a}})_{\mathrm{f}} = \widetilde{\phi}_{\mathrm{a}} - \left(\frac{1}{\rho_{\mathrm{a}}\mathbb{A}_{\mathrm{a}}}\right)_{\mathrm{f}}|\mathbf{S}|\nabla^{\perp}p_{\mathrm{a}}$$

Observing that the equation for the zero-order moment can be written as

$$\frac{\partial \alpha_{\mathrm{a}}}{\partial t} + \nabla\cdot(\alpha_{\mathrm{a,f}}\phi_{\mathrm{a}}) = 0$$

which, substituting the expression for the face velocity, becomes

$$\frac{\partial \alpha_{\mathrm{a}}}{\partial t} + \nabla \cdot \varphi_{\mathrm{a}}^{*} = \nabla \cdot \left[\alpha_{\mathrm{a,f}} \left(\frac{G(\alpha_{\mathrm{a}})}{\rho_{\mathrm{a}} \mathbb{A}_{\mathrm{a}}} \right)_{\mathrm{f}} |\mathbf{S}| \nabla^{\perp} \alpha_{\mathrm{a}} \right]$$

where $\varphi_a^* = (\alpha_a \mathbf{U}_a)_{f.}$ It is worth noticing that, since we are interested in preserving the positive features of the kinetic flux discretization, the divergence term on the left-hand side is treated fully explicitly, as already done in QMOM, including the effect of the non-diagonal terms of the collisional stress tensor, but without adding to φ_a^* the isotropic component of that tensor, since they are accounted for in the term on the right-hand side, which is discretized explicitly.

The solution procedure is the modified as follow

- The particle-pressure derivative is updated, based on information from the previous iteration.
- The modified equation for the zero-order moment is solved. Notice that the solution at this stage avoids inconsistencies in the value of the phase fraction in the rest of the solution procedure.
- Based on the updated value of the phase volume fraction, the remaining set of equations is solved to obtain the moments of order equal or greater than one.

A convenient modification to the above procedure is to introduce under-relaxation for the equation of the zero-order moment, and perform sub-iterations on the equations for the zero- and first-order moment, until convergence, and then obtain the higher-order moments with a single solution step, using the updated, and stabilized, values of the phase volume fraction.

Before proceeding with the verification of the approach, it is worth noticing the differences and the similarities with what is currently done in MFIX. MFIX solves a volume fraction correction equation for the phase volume fraction when only one dispersed phase is present, while it explicitly introduces the particle-pressure term in the momentum equation when more than one dispersed phase is considered, stabilizing the numerical solution with adaptive time-stepping based on the evolution of solution residuals. In theory it would be possible to adopt a similar strategy for QMOM, however the following difficulties are present:

- The solution of a volume fraction correction equation would be not consistent with the approach used in the dilute regions, and it would require to define a criterion on the volume fraction, to decide when the moment equation is solved, and when the volume fraction correction is adopted. This potentially introduces inconsistencies in the solution process, while the proposed approach can be reliably used over the whole range of volume fractions, without changing the set of equations solved by the numerical algorithm.
- The approach can be extended to the case of multiple species, including the effect of the particle pressure implicitly in the equation for the zero-order moment, removing the possible source of instabilities due to the explicit treatment of the particle pressure in the momentum equation.

- The proposed method preserves the possibility of discretizing the moment spatial fluxes with their kinetic formulation, which is essential to ensure a stable solution when discontinuous fields are present.
- Finally, the proposed approach is immediately applicable to the more versatile co-located grid arrangement, which is the natural choice when using QMOM, since no variable staggering is required.

The approach has been tested considering a one-dimensional problem of particles falling on the effect of gravity. Particles are initially located at a certain distance from the bottom of the computational domain, represented by a no-slip wall. Gravity and fluid drag act on the particles, which settle on the bottom of the container. The initial stage of the simulation is shown in Figure 197, and the axial volume fraction profile after 1s of simulation is reported in Figure 198. It is possible to see that the phase is completely settled, and the concentration profile is well defined, properly showing the steep gradient at the interface without oscillations.

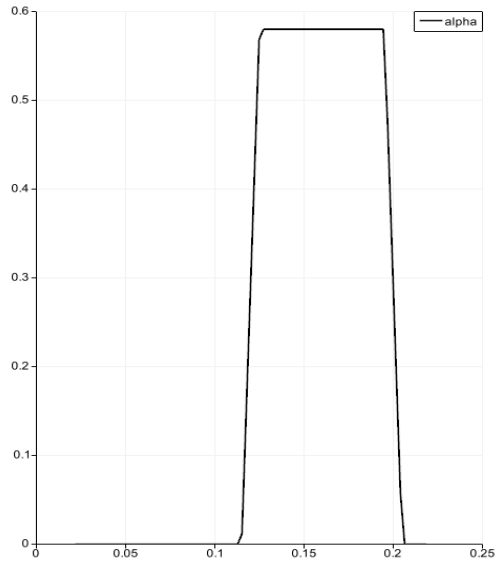

Figure 197. *Initial volume fraction profile (t = 0). Axial position on the horizontal axis.*

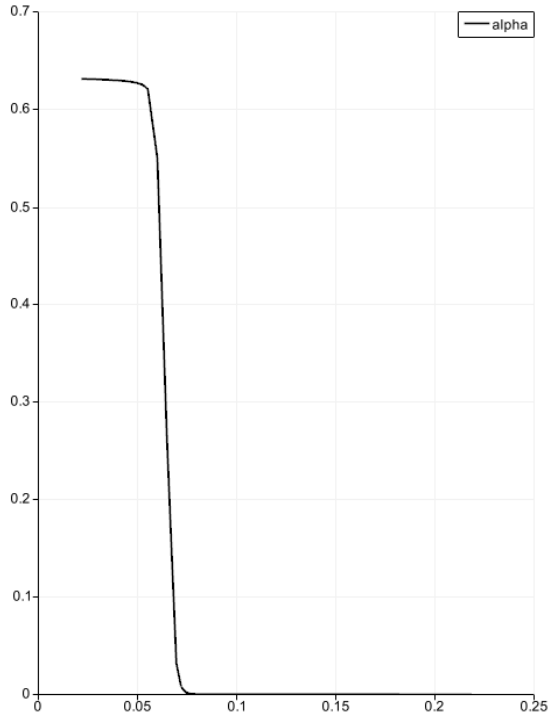

Figure 198. *Final volume fraction profile (t=1s). Axial position on the horizontal axis.*

Subtask 4.6.2: Liaison to NETL experimental effort (Cocco).

It is our understanding the NETL CFB cold flow test data for the core-annular (at least two solids), fast fluidization, and turbulent regimes already exists, including measurements of axial pressure profile, solids velocities, gas velocities, solids fractions, granular temperature, particulate turbulent kinetic energy and solids cluster size. Thus, our team will not be responsible for data collection on this facility, but will use this data for purposes of code validation. To facilitate this effort, Dr. Cocco will work with NETL personnel to survey the existing data for each of the aforementioned regimes, and make suggestions, if any, on additional tests that would be helpful for purposes of model validation.

(Cocco reporting.) PSRI and NETL discussed the various options to providing additional data sets to the modeling community as open source. The additional data will provide model developers with the data needed to validate their modeling efforts and concepts. Instead of a data dump, PSRI and NETL objective was to provide a set of data that represented current industrial concerns while gone through some sort of vetting process within the technical community. Based on the success of the previous two PSRI modeling challenge, it was decided that a third challenge problem would best meet this objective.

The goals of this third modeling challenge were to provide a vetted set of data on fluidized beds and circulating fluidized beds to the research community, provide a set of challenge problems to test the current capabilities of today's models and to us the results of these

test to depict areas where additional studies are needed. The goal did NOT include judging who has the best model.

PSRI provided the data and managed the testing procedure for hydrodynamics collected in a 3 ft diameter by 20 feet tall fluidized bed with Geldart Group A powder. NETL provided the data and managed the testing procedures for their 12 inch diameter by 50 foot tall circulating fluidized bed with Geldart Group B particles. Several operating conditions were tested. Measurements included axial pressure drop profiles, differential pressure fluctuations and bubble void fraction profiles in a fluidized bed and axial pressure drop profiles, radial particle velocity and local solids flux profiles in a circulating fluidized bed. Modelers were provided computer assisted drawings of the test facilities, particle property data, as well as data from minimum fluidization measurements to assist in setting up their simulations. In addition, modelers were given a second chance to refine their results once the data was released.

Model predictions were compared against actual experimental results and vetted in a recent workshop at the Circulating Fluid Bed X. The modelers were given detailed descriptions of the NETL and PSRI experimental facilities as well as information on the different bed materials tested. Two general types of models were submitted: Eulerian-Eulerian and Eulerian-Lagrangian. Both types of model had successes and failures indicating that good results are strongly influenced by resources such as available time, computational facilities, and experience level of the modeler. By comparing the predicted behavior the strengths and weaknesses associated with the different modeling approaches were identified and shortcomings could be targeted for future development and improvements. Details of these two problems are presented below.

Bubbling Fluidized Bed Modeling Challenge – Experimental: The bubbling fluidized bed tests were conducted in a 0.895 m inner diameter, 6.1 m tall test unit shown in Figure 199. Two air spargers were designed to provide a sufficient grid pressure drop to ensure good air distribution, while avoiding excessive pressure build-up in the plenum. For test conducted at a gas velocity of 0.3 m/s, a 76-cm-diameter PVC pipe manifold shown in Figure 200 was used. The pipe manifold had fifty, 6-mm-diameter nozzles facing downward 30° from the vertical. For tests conducted at a gas velocity of 0.6 m/s, a 10.2-cm-diameter PVC ring sparger shown in Figure 201 was used. The ring sparger had 39, 13-mm-diameter nozzles facing downward 30° from the vertical. The ring sparger was installed 0.38 m above the pipe manifold. Both air distributors were constructed of Schedule 80 grey PVC pipes and fittings. The primary cyclone of the unit had a 20-cm-diameter dipleg that returned solids onto the bed surface via an aerated trickle valve. The secondary cyclone had a 15.2-cm-diameter dipleg that returned solids to the bed via an automatic L-valve at a height of 3.35 m. A blower supplied fluidizing air and a butterfly valve installed downstream of a 76-mm-diameter orifice plate was used to control the air flow rate. Experiments were conducted for four sets of operating conditions listed in Table 13 using FCC catalyst particles of 3 and 12% fines less than 44 micron whose particle size distributions are shown in Figure 202. The particle density was 1490 kg/m3 and the particle sphericity was assumed to be 0.98. Modelers were provided computer assisted drawings of the test facility, particle property data, as well as data from minimum fluidization measurements to assist in setting up their simulations.

The measurements made at the four Test Cases are listed in Table 13 and these were (i) axial profiles of pressure drop per unit length (DP/gL), (ii) standard deviation of DP fluctuations across the entire bed at four circumferential locations, (iii) standard deviation of DP fluctuations

across bed sections of 0.6 m height at four circumferential locations, 90 apart, and, (iv) radial bubble void fraction profiles at height z = 1.52 m for the Test Cases 1 and 4.

Table 13. *Operating conditions for fluidized bubbling bed tests.*

Test Name	F44, % < 44 μm	Static Bed Height, m	Ug, m/s	Measurements
Case 1	3	3.66	0.3	A, B, C
Case 2	3	1.22	0.3	A, B
Case 3	3	2.44	0.6	A, B
Case 4	12	2.44	0.6	A, B, C
A: Axial ΔP/gL profiles, B: ΔP fluctuations across entire bed and across 61 cm tall sections of bed, C: Radial bubble void fraction profile				

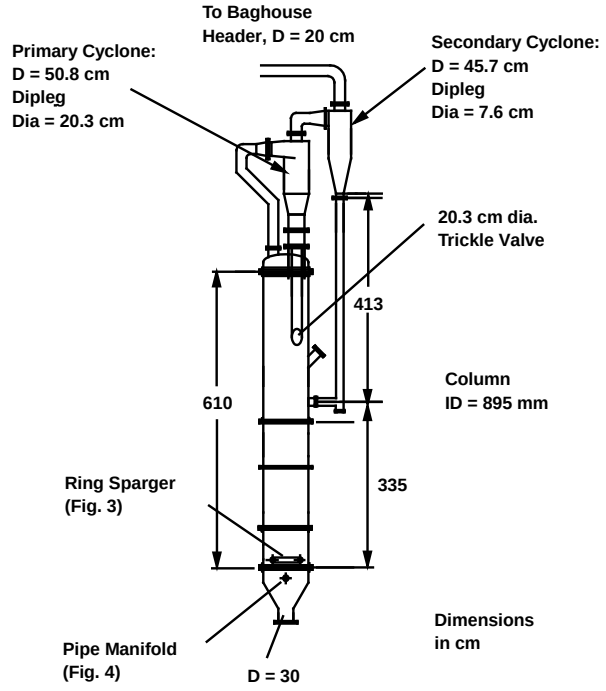

Figure 199. *Schematic drawing of the 0.9-m-diameter fluid bed unit used for the bubbling fluidized bed Test Cases 1 to 4.*

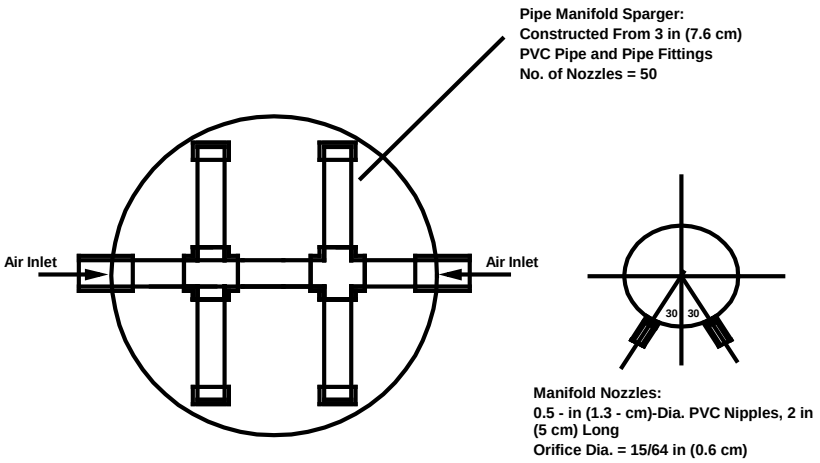

Figure 200. *Drawing of the air distributor used for bubbling fluidized bed tests cases 1 and 2.*

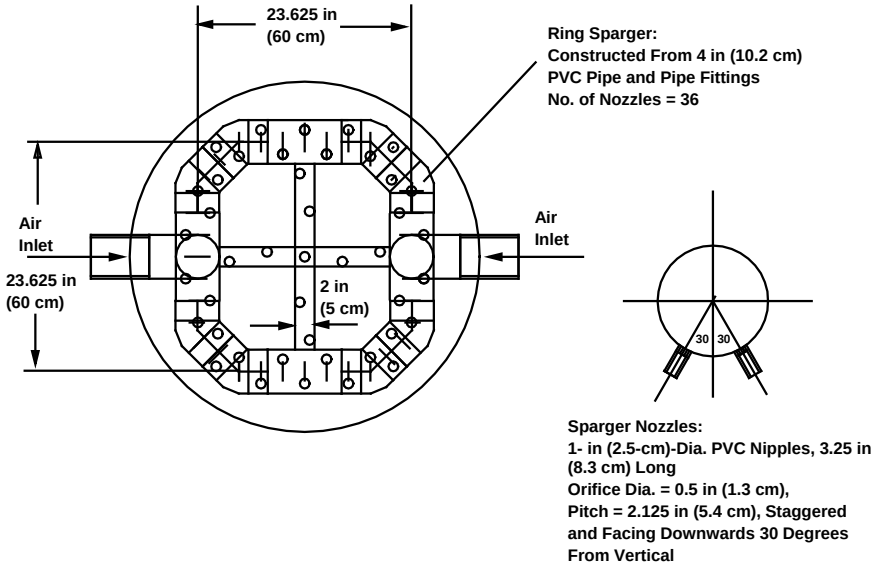

Figure 201. *Drawing of the air distributor used for bubbling fluidized bed tests cases 3 and 4.*

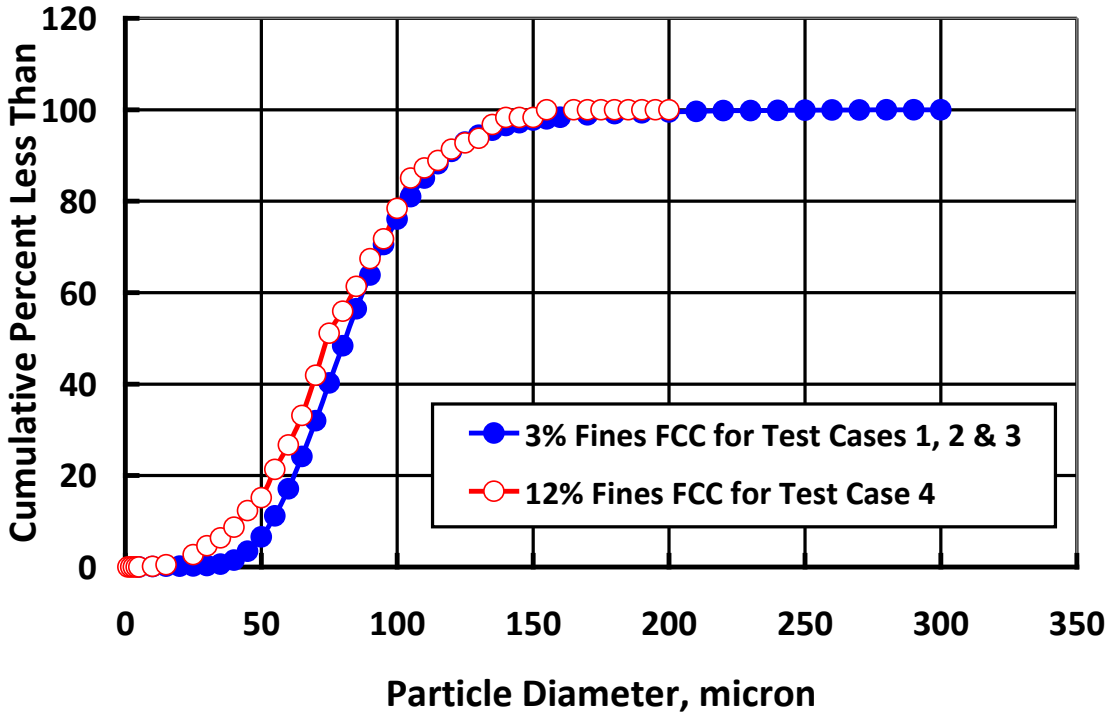

Figure 202. *Particle size distribution of solids particles used in the bubbling fluidized bed tests.*

Pressure drop fluctuations were measured across the entire column at four radial orientations (Nos. 1, 2, 3 and 4 in Figure 203) and, across 24 in (61 cm) long sections 90-degrees apart at the same four radial orientations at a mid-point elevation of 1.52 m. For Test Case 2 whose static bed height was 1.22 m, the mid-point elevation was lowered to 0.6 m. Differential pressure fluctuations were measured using 6.3 mm OD x 0.89 mm wall thickness purged steel tubes connected to high frequency pressure transducers by 6.3-mm-diameter plastic tubing. Pressure drops across vertical sections along the column height were using differential pressure transmitters connected with plastic tubing to pressure ports that were equipped with 6-mm-diameter high-porosity snubbers. Radial bubble void fraction profiles were measured with backscattered-type optical fiber bubble probes inserted in the unit (180 degrees apart as shown in Figure 203) at a height z = 1.52 m. Bubble probe and differential pressure signals were simultaneously sampled at 1000 Hz for 3 minutes by a data acquisition system. The presence of gas bypassing was inferred from the differential pressure fluctuations and bubble voidage data

The minimum fluidization tests were conducted in a 15.2-cm-inner diameter column, 1.83 m tall clear acrylic column shown in Figure 204. The tests produced plots of the pressure drop DP2, measured across a 15.2 cm section of the bed shown in Figure 205, as a function superficial gas velocity. The plots in Figure 205 are referred to as the minimum fluidization curves. The column had a porous plate distributor. The fluidizing gas was compressed air measured by a mass flowmeter. Batches of 3 and 12% fines FCC catalyst particles weighing 6.832 kg and 7.0 kg, respectively were used in the tests. Each batch was first fluidized for 3 min at Ug = 0.047 ft/s (0.0144 m/s) then DP2 was recorded by a data acquisition system for the following 2 minutes. The flowrate was then was reduced in steps and at each the bed was left 3 minutes to attain steady state before DP2 was recorded for 2 minutes. The procedure was

automated and measurements were taken until the air flow rate reached zero. Computer assisted drawings of the test facility, particle property data, as well as data from minimum fluidization measurements were made available to assist in setting up the simulations.

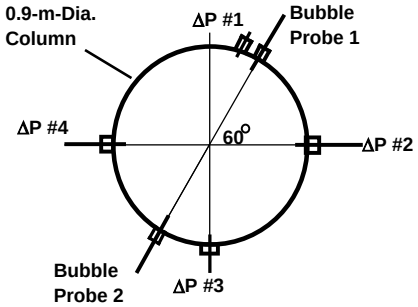

Figure 203. *Circumferential measurement locations of bubble void fraction profiles and differential pressure fluctuations (assume DP#1 to be opposite DP#3).*

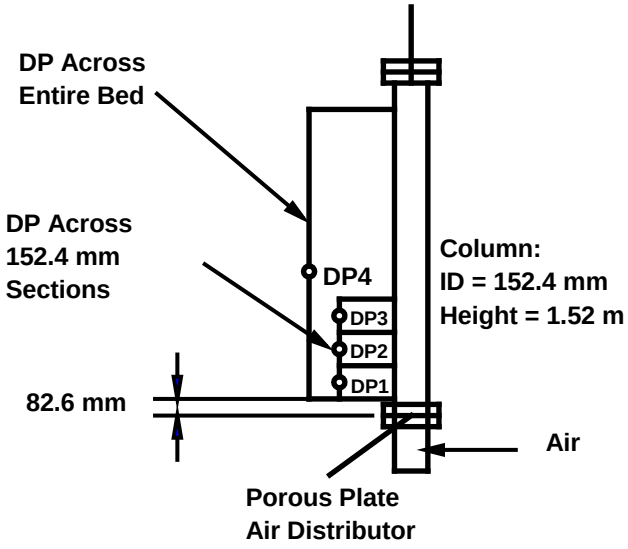

Figure 204. *Experimental set up of unit used to establish the minimum fluidization curve for materials used in bubbling fluidized bed Test Cases 1 to 4.*

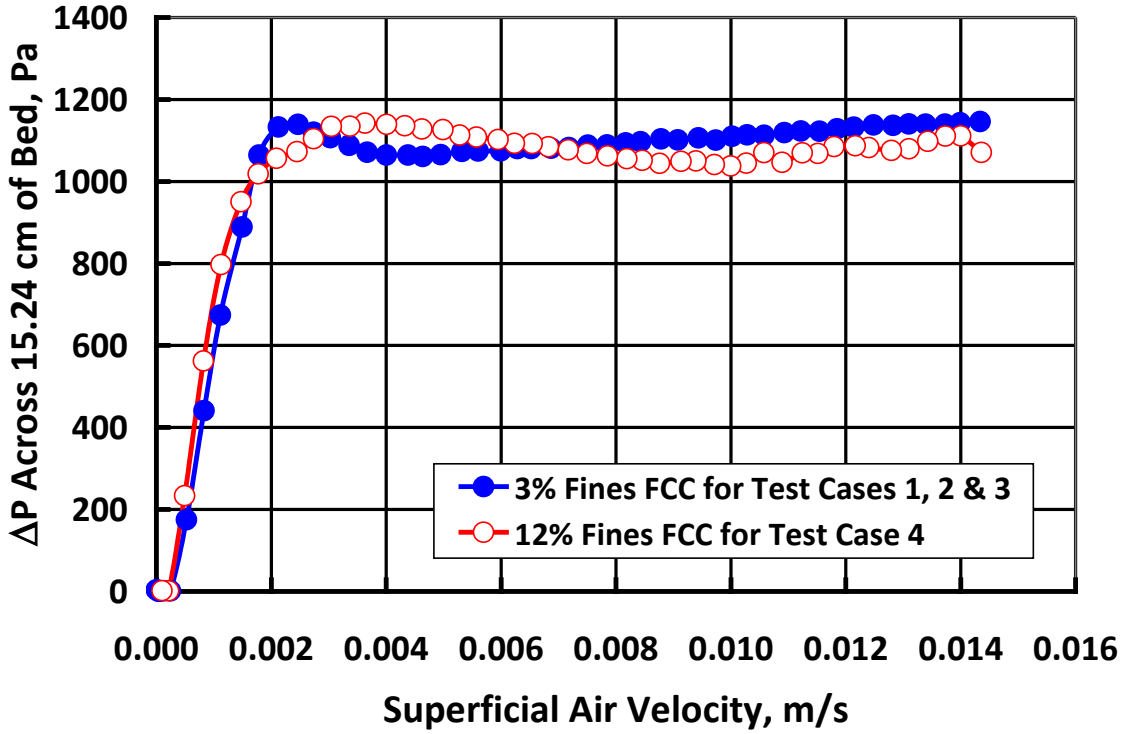

Figure 205. *Minimum fluidization curves for solids particles used in the bubbling fluidized bed tests.*

Results and Discussion: CFD modeling results for the fluidized bed challenge problem were received from three modeling groups named hereafter BFB1, BFB2 and BFB3. The key features of the BFB1, BFB2 and BFB3 models are summarized in Tables 14 and 15 (large tables are in Appendix I). BFB1 modeled only Test Case 3 but used four different modeling approaches; three Eulerian-Eulerian and one Eulerian-Lagrangian. The first Eulerian-Eulerian model assumed the solids phase consisted of 80 micron spherical particles; the second modeled the solids phase as two particulate phases of sizes 80 and 30 microns and, the third assumed a particulate phase with a size distribution and maintained a population balance. The BFB1 Eulerian-Langragian model used a particle size distribution to represent each parcel in the Lagrangian model for the particulate phase. The particle diameters, for particles in each parcel, were calculated from a Rosin-Rammler fit of the given particle size distribution. BFB2 modeled all the four Test Cases using a Eulerian-Eulerian model that treated the solids phase as consisting of monosized spherical particles of diameter equal to the Sauter mean diameter of the particle size distribution. BFB3 modeled the four Test Cases using an MP-PIC Eulerian-Lagrangian model that utilized the full particle size distribution. This paper discusses the initial modeling results as well as the refined results, which were submitted after the experimental data were made public. The refinements used in the calculations of the resubmitted results are denoted by (R) in Tables 15 and 16 and in the figures presented here.

Table 16. *Comparison of root mean square deviations of CFD model predictions from experimental data.*

	RMSD of ΔP/gΔL	RMSD of ΔP/gΔL	RMSD of ΔP/gΔL	RMSD of ΔP/gΔL
CFD Model	Case 1 FCC, 3% Fines H = 3.66 m Ug = 0.3 m/s	Case 2 FCC, 3% Fines H = 1.22 m Ug = 0.3 m/s	Case 3 FCC, 3% Fines H = 2.44 m Ug = 0.6 m/s	Case 4 FCC, 12% Fines H = 2.44 m Ug = 0.6 m/s
BFB2	**0.5775**	**0.9300**	**0.6694**	**0.6317**
BFB2 (R)	**0.3962**	**0.8351**	**0.5049**	**0.4306**
BFB3	**0.5365**	**3.8771**	**0.5986**	**3.2371**
BFB3 (R)	**0.3389**	**8.2030**	**0.4974**	**1.2454**
BFB1 (a)	-	-	**3.5099**	-
BFB1 (b)	-	-	**1.2585**	-
BFB1 (c)	-	-	**2.4426**	-
BFB1 (d)	-	-	**1.1704**	-
BFB1 (d) (R)			**1.391594**	

Table 17. *Comparison CFD models predictions on the variability of the standard deviation of DP fluctuations across four 61 cm tall sections around the column.*

	Is σΔPs significantly different at four circumferential locations around the column (= is gas bypassing present)?			
	Case 1 FCC, 3% Fines H = 3.66 m Ug = 0.3 m/s	Case 2 FCC, 3% Fines H = 1.22 m Ug = 0.3 m/s	Case 3 FCC, 3% Fines H = 2.44 m Ug = 0.6 m/s	Case 4 FCC, 12% Fines H = 2.44 m Ug = 0.6 m/s
Experiment	YES	NO (small)	YES	NO
BFB2	NO	NO	NO	NO
BFB2 (R)	NO	NO	NO	NO
BFB3	NO	NO	YES	NO
BFB3 (R)	NO	NO (small)	YES	YES
BFB1 (d)	-	-	NO	-
BFB1 (d) (R)	-	-	NO	-

Axial pressure Drop Profiles: Modeling results axial pressure drop profiles were compared to experimental data both graphically and by means of the root mean square deviation (RMSD), calculated by Equation (82).

$$\mathbf{RMSD} = \sqrt{\frac{1}{N}\sum_{i=1}^{i=N}\left(\frac{x_{CFD,i} - x_{EXPT,i}}{x_{EXPT,i}}\right)^2} \qquad (82)$$

where xCFD,i is the model prediction of the measured data xEXPT,i and N is the total number of data points. The RMSD values for the four Test Cases are shown in Table 16.

Figure 206 compares the experimental axial pressure drop profile with CFD model predictions of BFB2 for Test Case 1. The fines content was 3% fines, the static bed height was 3.66 m and the superficial gas velocity was 0.3 m/s. The initial modeling results underpredicted the data significantly whereas the refined results gave a very improved fit to the data. In the refinement the number of computational cells and the averaging time interval were increased from 7000 to 27000 and 40 s to 90 s, respectively. As shown in Table 15, the refinement caused the root mean square deviation to decrease from 0.5775 to 0.3962.

Figure 207 superimposes the initial and refined results of model BFB3 on the experimental data for Test Case 1. The refinement was to change the solids close-pack volume fraction from 0.52 to 0.625. The same was done to the other three Test Cases. The refinement changed RMSD from 0.5365 to 0.3389 and a significant improvement in the fit. Models BFB2 and BFB3 refined results are plotted in Figure 208 together with the experimental data. Both models seem to perform nearly equally but they both gave lower predictions of the height of the expanded bed height.

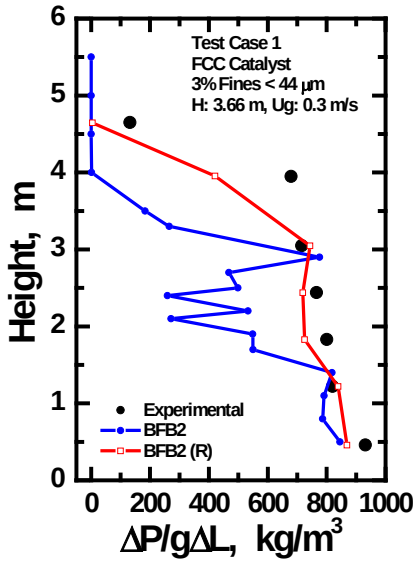

Figure 206. *Comparison of experimental axial pressure drop profile with CFD model predictions of BFB2 for Test Case 1 (3% fines FCC, H = 3.66 m and Ug = 0.3 m/s).*

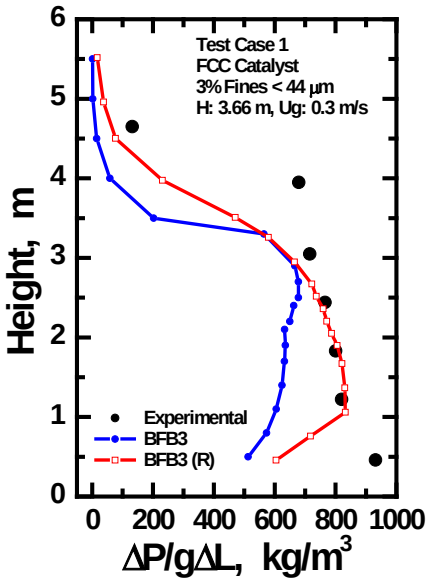

Figure 207. *Comparison of experimental axial pressure drop profile with CFD model predictions of BFB3 for Test Case 1 (3% fines FCC, H = 3.66 m and Ug = 0.3 m/s).*

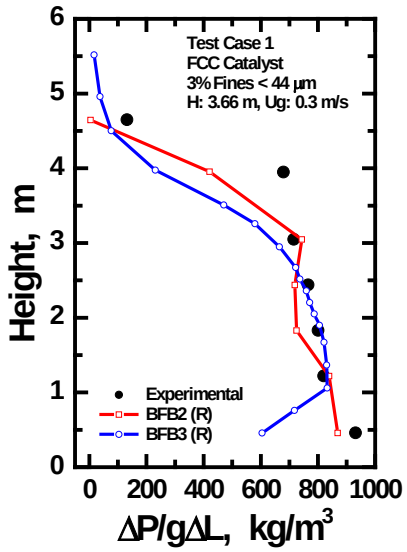

Figure 208. *Comparison of the refined CFD model predictions of BFB2 and BFB3 with experimental axial pressure drop profile for Test Case 1 (3% fines FCC, H = 3.66 m and Ug = 0.3 m/s).*

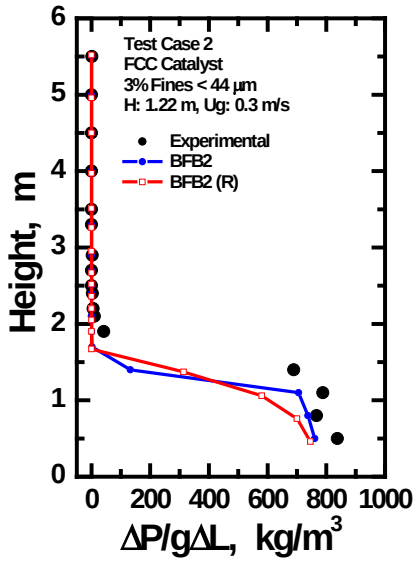

Figure 209. *Comparison of experimental axial pressure drop profile with CFD model predictions of BFB2 for Test Case 2 (3% fines FCC, H = 1.22 m and Ug = 0.3 m/s).*

Test Case 2 results of the BFB2 model are compared to experimental data in Figure 210. The static bed height and superficial gas velocity were 1.22 m and 0.3 m/s, respectively. 3% fines FCC catalyst particles were used. The RMSD for the initial and the refined modeling results were 0.9300 and 0.8351, respectively. The model captures the main features of the experimental curve. The refinement had only a slight effect. Test Case 2 results of model BFB3 are shown in Figure 211. The RMSD values were 3.8771 and 8.2030. The initial modeling results were closer to experimental values in the freeboard but underpredicted the pressure drop in the bed. The refinement shifted the curve to higher values, which made predictions better in the bed but worse in the freeboard region. It appears from Figure 212 shows that the BFB3 model does a better job in the bed whereas the BFB2 model performs better in the freeboard.

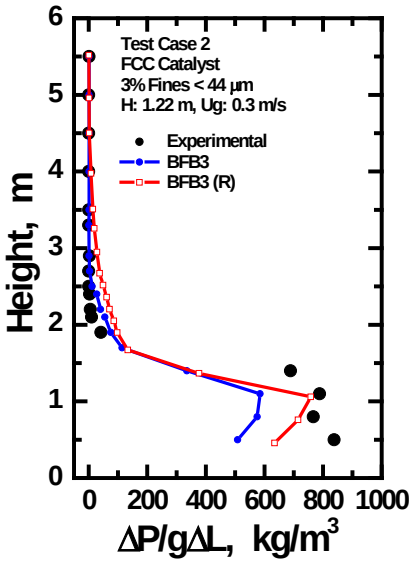

Figure 210. *Comparison of experimental axial pressure drop profile with CFD model predictions of BFB3 for Test Case 2 (3% fines FCC, H = 1.22 m and Ug = 0.3 m/s).*

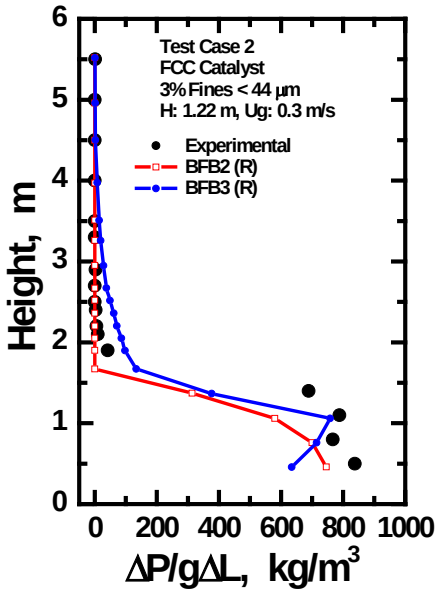

Figure 211. *Comparison of the refined CFD model predictions of BFB2 and BFB3 with experimental axial pressure drop profile for Test Case 2 (3% fines FCC, H = 1.22 m and Ug = 0.3 m/s).*

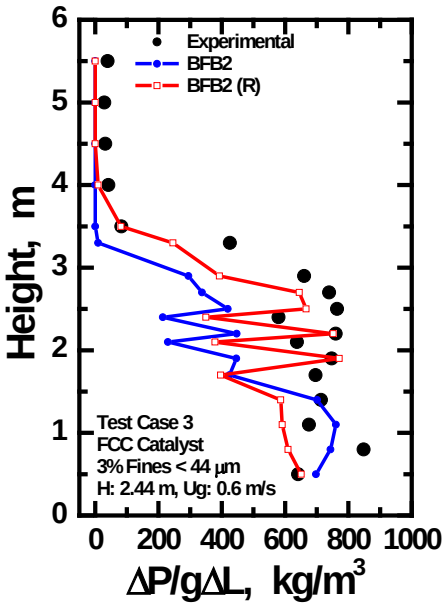

Figure 212. *Comparison of experimental axial pressure drop profile with CFD model predictions of BFB2 for Test Case 3 (3% fines FCC, H = 2.44 m and Ug = 0.6 m/s).*

Model BFB2 results for Test Case 3 are plotted with experimental data in Figure 213. The bed height was 2.44 m, 3% fines FCC catalyst particles were used and the gas velocity was 0.6 m/s. The first modeling results were significantly lower than experimental data except for the lower 1 m height of bed. The recalculated values came from 42840 computational cells instead of 8400 and that improved the RMSD value from 0.6694 to 0.5049. The fit was significantly better, but the model still underpredicted the pressure drop in nearly the whole bed height. Figure 214 gives Test Case 3 results of model BFB3. There is a much relatively good fit of the refined results with experimental data. The RMSD value dropped from 0.5986 to 0.4974.

Modeling results of BFB1 for Test Case 3 are presented in Figure 215. The Eulerian-Eulerian model that treated the solids phase particles as monosized or consisting of only two szes of particles performed very poorly. They didn't even capture the shape of the pressure drop profile. The Eulerian-Lagrangian DEM model was an improvement because it captured the profile's shape but the pressure drop predictions in the bed were significantly lower compared to experimental data. The Eulerian-Eulerian plus population balance model produced better results but still it still underpredicted the bed pressure drop even more than BFB3 and BFB2 models as seen in Figure 216. Increasing the averaging time interval from 9 s to 80 s did not improve the predictions but rather made them worse.

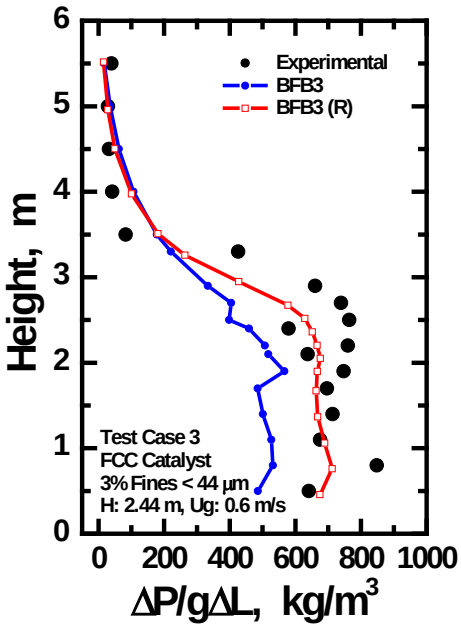

Figure 213. *Comparison of experimental axial pressure drop profile with CFD model predictions of BFB3 for Test Case 3 (3% fines FCC, H = 2.44 m and Ug = 0.6 m/s).*

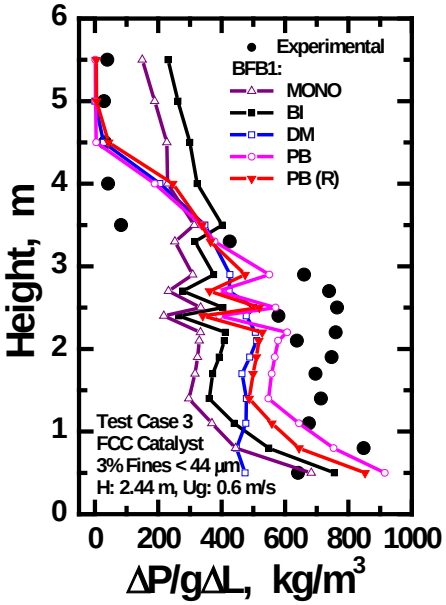

Figure 214. *Comparison of experimental axial pressure drop profile with CFD model predictions of BFB1 for Test Case 3 (3% fines FCC, H = 2.44 m and Ug = 0.6 m/s).*

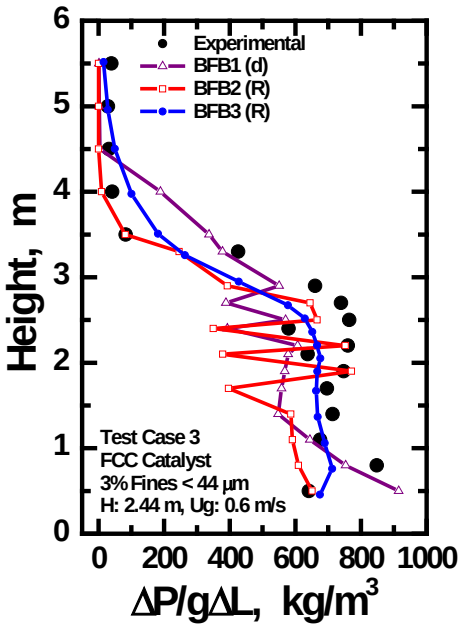

Figure 215. *Comparison of the CFD model predictions of BFB1, BFB2 and BFB3 with experimental axial pressure drop profile for Test Case 3 (3% fines FCC, H = 2.44 m and Ug = 0.6 m/s).*

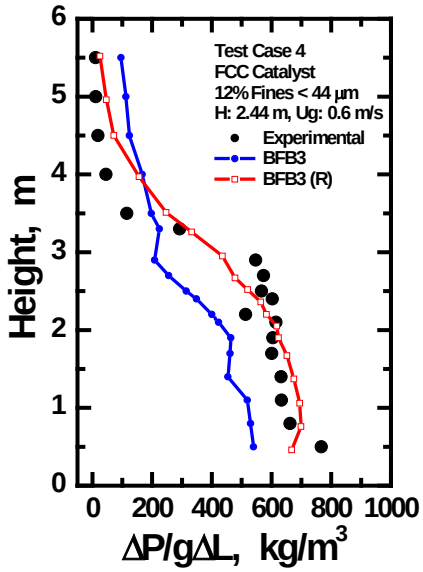

Figure 216. *Comparison of experimental axial pressure drop profile with CFD model predictions of BFB3 for Test Case 4 (12% fines FCC, H = 2.44 m and Ug = 0.6 m/s).*

Figure 217 compares experimental data to simulation results of BFB2 for Test Case 4 where the static bed height and the gas velocity were 2.44 m and 0.6 m/s, respectively and the FCC catalyst fines content was 12%. The first results captured the bed density fairly well in the lower part of the bed but dropped significantly in the upper half before recovering to the transition-to-freeboard level. The freeboard values were lower than experimental data. On the

other hand, the refined model performed poorly in the lower half of the bed but fitted the rest of the data quite well. The initial and recalculated model results had RMSD values of 0.6317 and 0.4306, respectively.

Experimental data and modeling results of model BFB3 for Test Case 4 are compared in Figure 218. The correction of the solid close-pack volume fraction gave a significantly better fit of data in the bed but the model overpredicted the pressure drops in the freeboard region. The RMSD value changed from 3.2371 to 1.2454. Results of models BFB2 and BFB3 are shown together in Figure 219. In general, former seems to give a better fit in the bed while the latter gives better predictions in the transition and the freeboard regions.

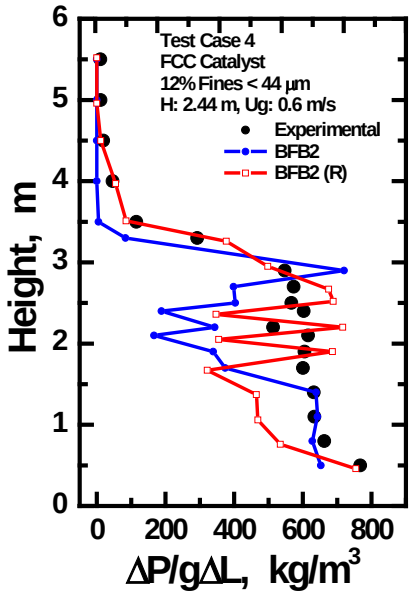

Figure 217. *Comparison of experimental axial pressure drop profile with CFD model predictions of BFB2 for Test Case 4 (12% fines FCC, H = 2.44 m and Ug = 0.6 m/s).*

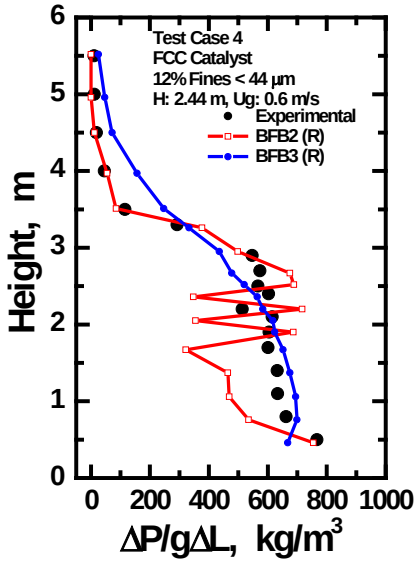

Figure 218. *Comparison of experimental axial pressure drop profile with CFD model predictions of BFB2 and BFB3 for Test Case 4 (12% fines FCC, H = 2.44 m and Ug = 0.6 m/s).*

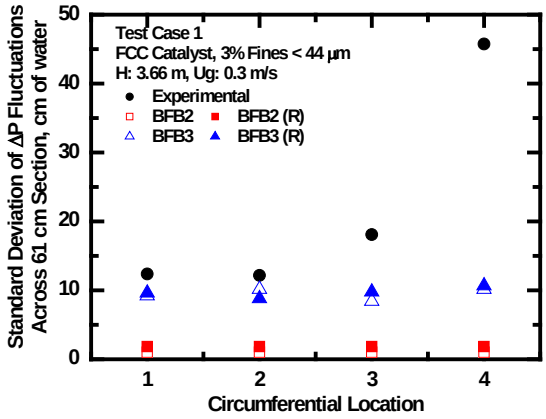

Figure 219. *Comparison of standard deviation DP fluctuations measured across the entire bed at four locations around the column with CFD model predictions of BFB3, and BFB2 for Test Case 1 (z = 1.52 m, 3% fines FCC, H = 3.66 m and Ug = 0.3 m/s).*

Differential Pressure Fluctuations and Bubble Void Fraction Profiles: Differential pressure fluctuations and bubble probe data provided means of assessing the presence or absence of gas bypassing at each of the four operating conditions. Figure 219 compares experimental versus model calculation results of the standard deviation of DP fluctuations across 61 cm tall sections of bed at four circumferential orientations spaced 90 apart for Test Case 1. The static bed height was 3.66 m, the gas velocity was 0.3 m/s and the fines content was 3% < 44 μm. The midpoint elevation of the measurement section was 1.52 m. The experimental data show a significant variation in the standard deviation of the DP fluctuations varied significantly around the bed. The standard deviation was about 45, 20 and 12 and 12 cm of water at locations 4, 3, 2 and 1, respectively. This variation suggests that gas bypassing was occurring in the bed. The magnitude and circumferential variation of DP fluctuations intensity was not captured in the modeling results of BFB2. The BFB3 model appears to be a better predictor of DP fluctuations. BFB3 results are in the same order of magnitude as the experimental data but the data varied only slightly, from about 8.8 to 10.7 cm of water, around the column. The standard deviation of DP fluctuations across the entire bed for tests case 1 did not vary significantly around the column as shown in Figure 220. BFB2 and BFB3 predictions also did not show any circumferential variations but magnitudes of the best predicted standard deviation values were nearly 50% lower than the measured values. Figure 221 compares the radial bubble void fraction profile measured at z = 1.52 m with CFD model predictions of BFB2 and BFB3 for Test Case 1. The experimental profile is significantly skewed to one side of the column indicating gas bypassing occurring on that side of the column. The two CFD models failed to capture this gas bypassing, they both predicted a constant bubble void fraction of 0.7 across the diameter of column.

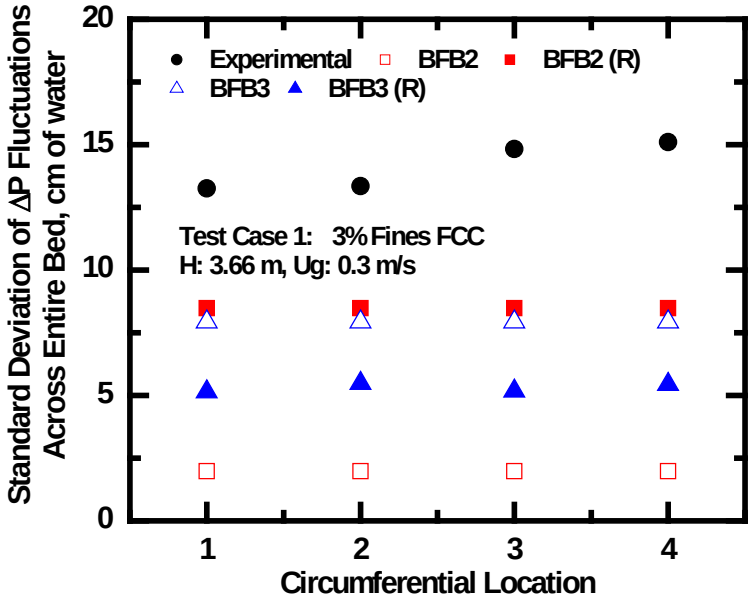

Figure 220. *Comparison of standard deviation DP fluctuations measured across the entire bed at four locations around the column with CFD model predictions of BFB3, and BFB2 for Test Case 1 (z = 1.52 m, 3% fines FCC, H = 3.66 m and Ug = 0.3 m/s).*

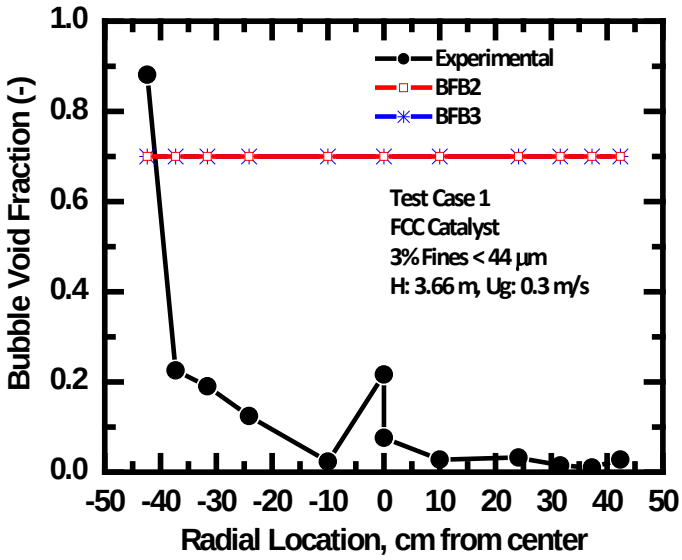

Figure 221. *Comparison of radial bubble void fraction profile measured at z = 1.52 m with CFD model predictions of BFB3, and BFB2 for Test Case 1 (3% fines FCC, H = 3.66 m and Ug = 0.3 m/s).*

Figures 222 and 223 compare the standard deviation DP fluctuations measured across 61 cm tall sections and across the entire bed, respectively, with CFD models BFB2 and BFB3 predictions for Test Case 2 (z = 0.3 m, 3% fines FCC, H = 1.22 m and Ug = 0.3 m/s). This was a test for a relatively short bed height and the DP fluctuations intensity variations were low suggesting a presence of weak gas bypassing. Bubble void fraction profiles were not measured. Both modeling groups underpredicted the local and overall DP fluctuations standard deviations by about 50% or more, with BFB3 being better than BFB2.

Test Case 3 experimental and simulation results of models BFB1, BFB2 and BFB3 are compared in Figures 224 and 225. The static bed height was 2.44 m, the fines content was 3% and the superficial gas velocity was 0.6 m/s. The standard deviation of DP fluctuations measured across 61 cm tall sections at four locations around the bed were different suggesting that gas bypassing was occurring in the column. Model BFB3 predicted some variation in the standard deviation at the four locations but models BFB1 and BFB2 did not predict any significant variation. Models BFB2 and BFB3 predictions at two locations were nearly the same as the experimental data. Predictions of model BFB1 were very low compared to experimental data. There was no significant variation in experimental or CFD modeling results for the standard deviation DP fluctuations across the entire bed at locations 1 to 4 for Test Case 3.

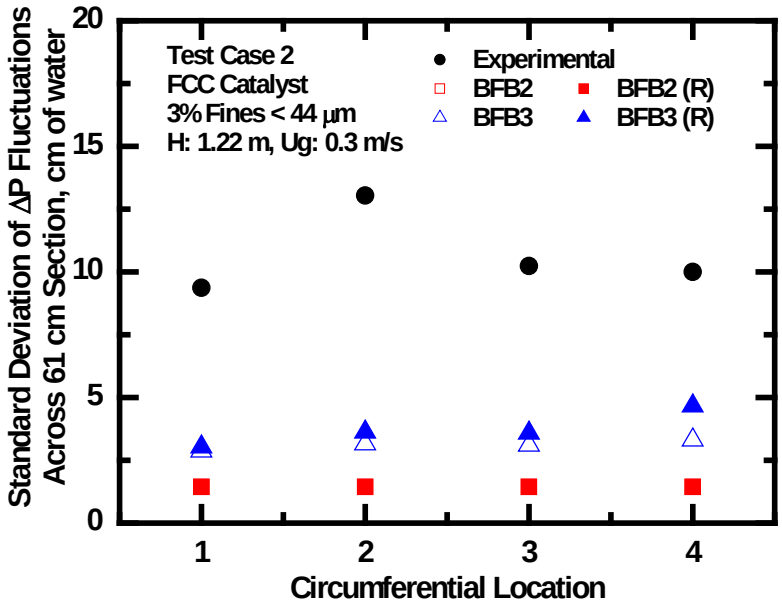

Figure 222. *Comparison of standard deviation DP fluctuations measured across 61 cm sections at four locations around the column with CFD model predictions of BFB3, and BFB2 for Test Case 2 (z = 0.3 m, 3% fines FCC, H = 1.22 m and Ug = 0.3 m/s).*

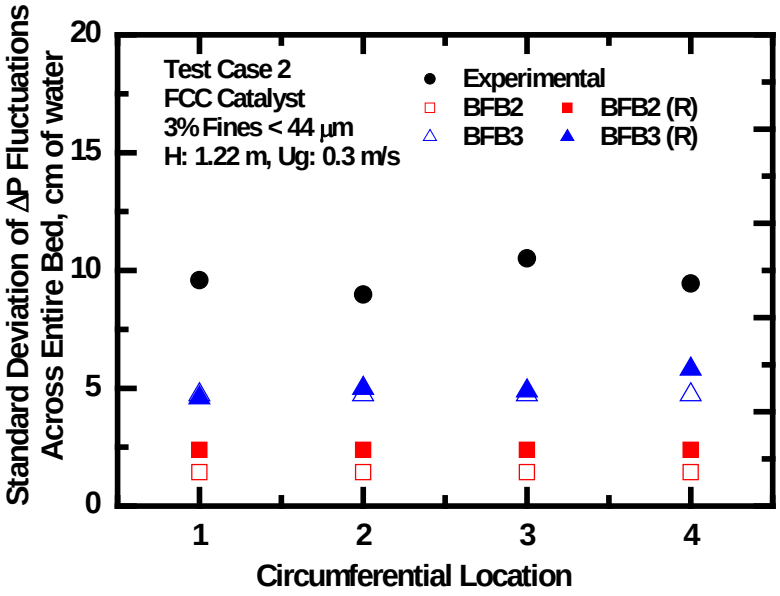

Figure 223. *Comparison of standard deviation DP fluctuations measured across the entire bed at four locations around the column with CFD model predictions of BFB3, and BFB2 for Test Case 2 (z = 0.3 m, 3% fines FCC, H = 1.44 m and Ug = 0.3 m/s.)*

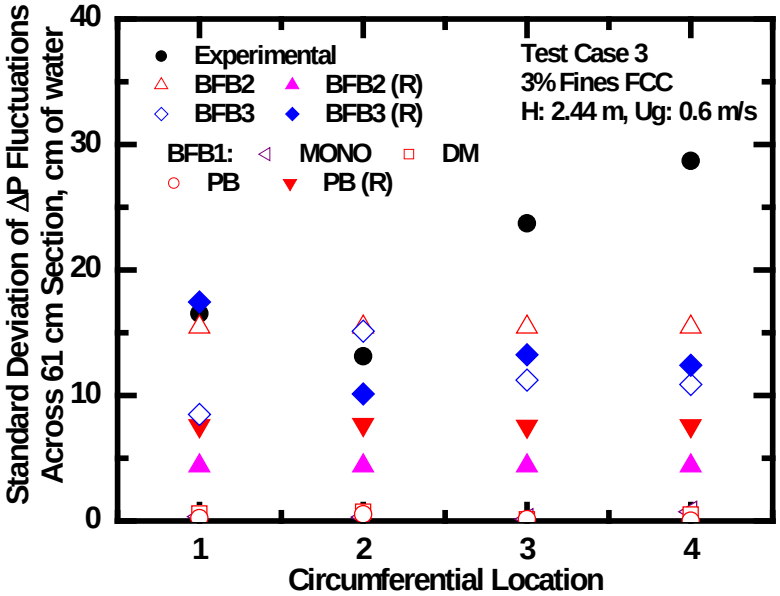

Figure 224. *Comparison of standard deviation DP fluctuations measured across 61 cm sections at four locations around the column with CFD model predictions of BFB3; BFB1; and BFB2 for Test Case 3 (z = 1.52 m, 3% fines FCC, H = 2.44 m and Ug = 0.6 m/s).*

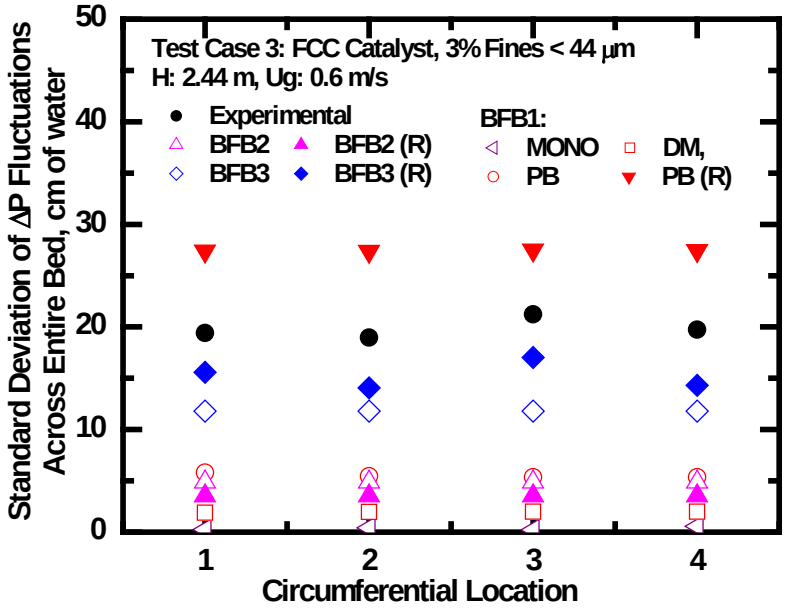

Figure 225. *Comparison of standard deviation DP fluctuations measured across the entire bed at four locations around the column with CFD model predictions of BFB3; BFB1; and BFB2 for Test Case 3 (z = 1.52 m, 3% fines FCC, H = 2.44 m and Ug = 0.6 m/s).*

Figure 226 shows the standard deviation DP fluctuations measured across bed sections of 61 cm height at four locations around the column and the corresponding CFD predictions of models BFB2 and BFB3 for Test Case 4. In test 4, z = 1.52 m, fines content = 12% and Ug = 0.6 m/s. There was no circumferential variation in the measured data which indicated that there was no gas bypassing in the bed. This is also supported by the symmetrical form of the measured radial bubble void fraction profile, as shown in Figure 228. Model BFB2 standard deviation predictions were not different at the four locations and they were lower than the experimental data. BFB2 calculated bubble void fraction profile (Figure 227) was symmetrical about the column axis but the values were greater than the measurements. Model BFB3 predicted a constant bubble void fraction of 0.7 across the bed cross section. The first submitted BFB3 simulation results of DP fluctuations standard deviation were more or less the same as the experimental data but the refined BFB3 results were higher than experimental values and they varied with measurement location suggesting gas bypassing presence in the bed.

The standard deviation of DP fluctuations across the entire bed for Test Case 4 is plotted in Figure 228. There is a very close agreement of experimental data with predictions of model BFB2 and the first simulation results of model BFB3. The refined calculations of model BFB3 gave standard deviation values, which were significantly greater than the experimental data but there was no variation with location around the bed. Table 17 summarizes the comparison of CFD models predictions on the variability of the standard deviation of DP fluctuations across four 61 cm tall sections around the column for the Test Cases. Gas bypassing was present in the bed at low fines content, tall bed heights and low gas velocities (Test Case 1 and 3). Operating with higher fines material, high gas velocity or short bed heights lower the chances of gas bypassing.

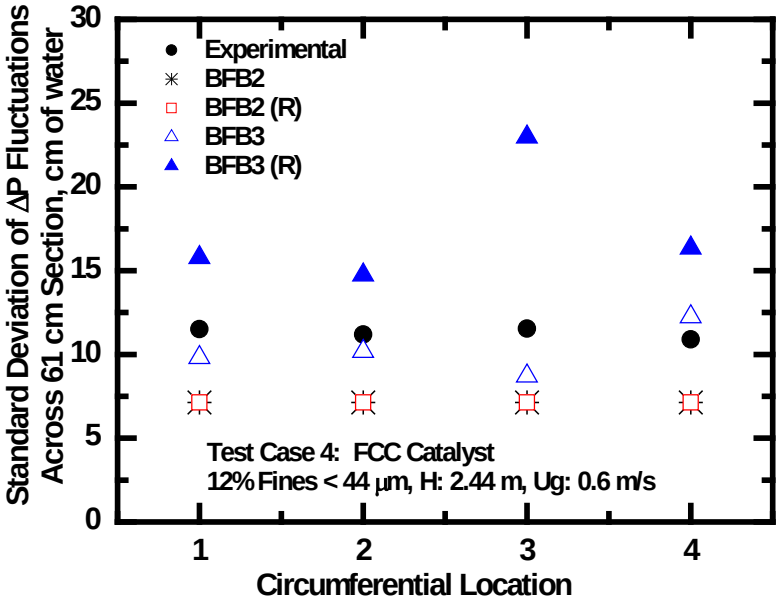

Figure 226. *Comparison of standard deviation DP fluctuations measured across 61 cm sections at four locations around the column with CFD model predictions of BFB3, and BFB2 for Test Case 4 (z = 1.52 m, 12% fines FCC, H = 2.44 m and Ug = 0.6 m/s).*

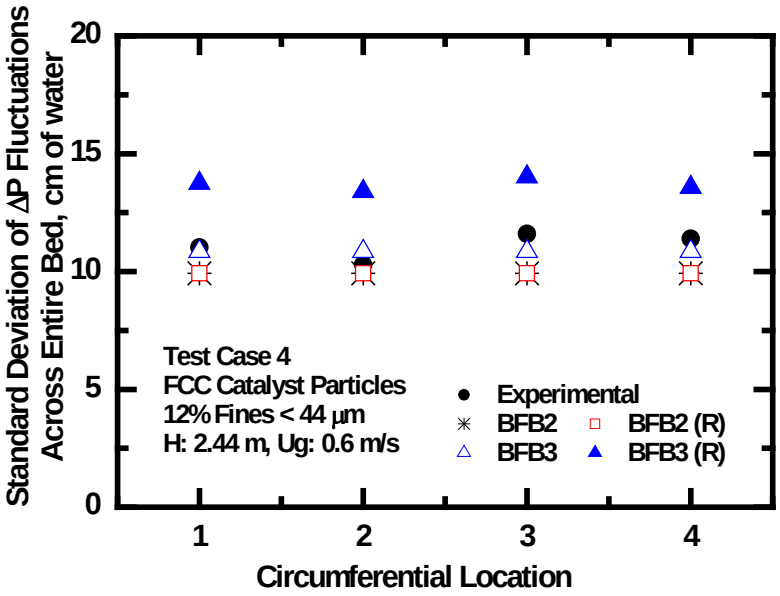

Figure 227. *Comparison of standard deviation DP fluctuations measured across the entire bed at four locations around the column with CFD model predictions of BFB3; BFB1; and BFB2 for Test Case 4 (z = 1.52 m, 12% fines FCC, H = 2.44 m and Ug = 0.6 m/s).*

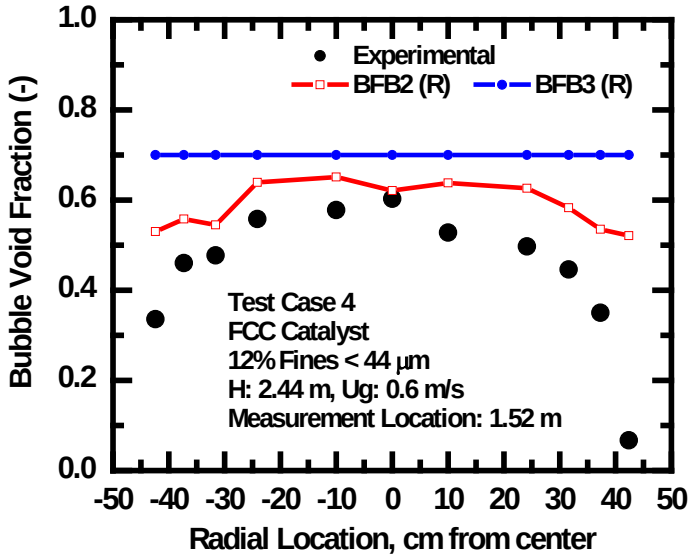

Figure 228. *Comparison of radial bubble void fraction profile measured at z = 1.52 m with CFD model predictions of BFB3, and BFB2 for Test Case 1 (3% fines FCC, H = 3.66 m and Ug = 0.3 m/s).*

Circulating Fluidized Bed Model Challenge – Experimental: The NETL riser is nominally 15 m tall, 0.3 m ID, and solids were recycled into the riser bottom via an L-valve and exited the riser through a dead-end Tee configuration, as shown in Figure 229. Fluidization particles were nominally 60 μm glass beads and 800 μm polyethylene beads with specific gravity of 2.5 and 0.9, respectively. The operator varied operating conditions by adjusting the riser flow or standpipe aeration to control the solids circulating rate. Steady state conditions were defined as holding a constant set of flow conditions and maintaining a constant response in the pressure differentials over a five-minute period. For generating the data for the Challenge Problem, the unit was operated at ~20^{o}C air as the conveying gas. Laristat was added along with increasing the relative humidity in sufficient quantities to minimize static electric discharges and particles clinging to the riser walls.

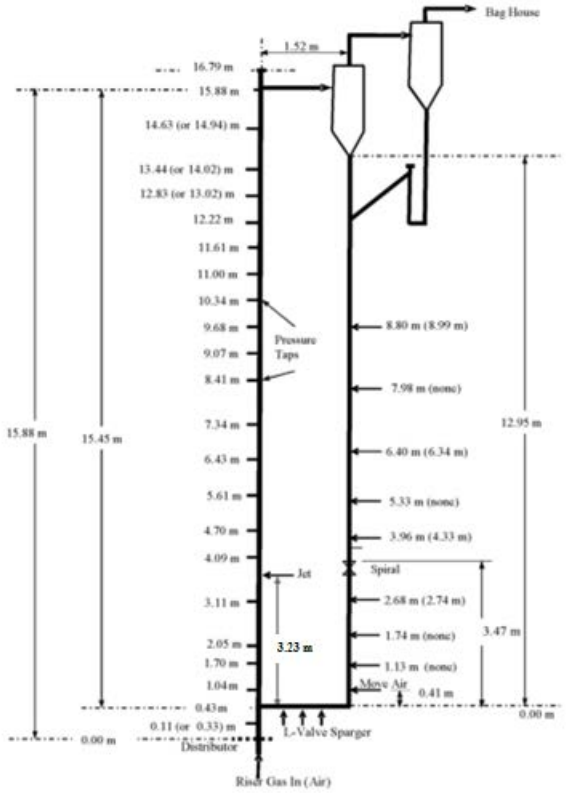

Figure 229. *Schematic of 30.48 cm ID NETL CFB facility. Values in the parentheses represent different locations for Group A tests.*

The rates of many energy conversion processes are limited by mass transport phenomena leading to the desire to use relatively small particles and high pressures. Granular materials typically used in transport reactors are characterized as Geldart Group A or Group B. Due to the different tendencies for these two materials to entrap gasses in the packed bed (Geldart, 1973), and because it is often observed that they behave different in the return loop of a CFB, it is hypothesized though never demonstrated that there may be differences in their performance in the riser of a CFB particularly when operated near the limits of dense suspension. The data obtained utilizing these bed materials were therefore posed in the Challenge Problem. The operating conditions achieved at NETL using Group A and Group B materials for this Challenge Problem are enlisted in Table 18. These are conditions that are near, but above, transition velocities for both granular materials and are relevant to many energy conversion process including refining, cracking, combustion, gasification, and gas cleanup. In previous challenge problems computational models were unable to adequately simulate similar CFB configurations, particularly the abrupt riser outlet.

Table 18. *Challenge Problem Test Conditions.*

MATERIAL	CASE	U_G (*M/SEC*)	M_S (*KG/SEC*)	F_R (*SCMS*)	F_{SL} (*SCMS*)	P_O (*KPA*)
GROUP A	**1**	**5.14±0.06**	**1.44±0.06**	**0.683±5E-3**	**0.001±2E-5**	**182±1.2**
	2	**5.14±0.02**	**9.26±0.09**	**0.682±2E-3**	**0.002±1E-5**	**167±1.7**
GROUP B	**3**	**5.71±0.05**	**5.54±0.07**	**0.476±3E-3**	**0.025±3E-3**	**100±0.4**
	4	**7.58±0.04**	**7.03±0.02**	**0.599±4E-3**	**0.089±4E-3**	**102±0.5**
	5	**7.58±0.02**	**14.00±0.21**	**0.640±4E-3**	**0.143±3E-3**	**105±0.5**
MEAS. UNCERTAINTY (% READING)		**±5**	**±10**	**±4**	**±0.05**	**±0.004**

The Group A glass bead test cases were both conducted holding the pressure at the base of the riser constant at nominally 0.85 atm. The circulation rate was varied from Case 1 to Case 2, while the gas velocity was held constant. These tests were selected out of 100 tests conducted at this elevated pressures to represent dilute and core annular flow regimes. The entire statistically designed test matrix spanned conditions from U_g = 1.3 to 7.7 m/s and M_s = 1.3 to 33 kg/s.

The Group B polyethylene bead tests were all conducted with ambient pressure at outlet of the CFB. The three test cases reported represent the star points in a composite factorial test matrix in which the factorial points were reported previously (Shadle *et al.*, 2008). This entire test matrix represents transformed dependent parameters for gas velocity and solids circulation rate such that each condition represented a fixed relative distance from the fast fluidized bed - regime transition to core annular flow. The three test cases included in this Challenge Problem include: a case near the fast fluid bed transition (Case 3), and two conditions at the same superficial gas velocity - one in core annular flow (Case 4), and the second in dense suspension up-flow (Case 5). The entire composite matrix included many of the detailed measurements described below spanned an operational range from U_g = 5.5 to 7.5 m/s and M_s = 1.4 to 14 kg/s.

Besides regular pressure, temperature and humidity measurements, advanced techniques were utilized to measure detailed flow structure within the circulating fluidized beds. Mass circulation rate was continuously recorded by measuring the rotational speed of a twisted spiral vane located in the packed region of the standpipe bed (Ludlow *et al.*, 2002, Ludlow *et al.*, 2008). This volumetric flow measurement was converted to a solids circulation using the measured packed bed density after correcting it based upon a model of the standpipe using the Ergun equation and aeration rates to simulate the measured pressure drops in the standpipe (Ludlow & Spenik, 2011).

Local particle velocities were measured using a dual fiber bundle optic, as shown in Figure 230 and positioning the tip at the desired location in the riser of the NETL cold flow CFB (Guenther & Breault, 2007, Seachman *et al.*, 2005). Each fiber bundle contains an equal number of light transmission and light reception fibers. The fiber bundles were aligned vertically in the riser to measure the axial velocities of particles and cluster moving up and down. The signals from each of the fiber optic bundles were cross-correlated to determine the particle transit times in each specified periods. The velocities were calculated knowing the translational distance. The effective spacing between the fibers was determined using a spinning wheel moving at a controlled rotational rate (Zin *et al.*, 2006).

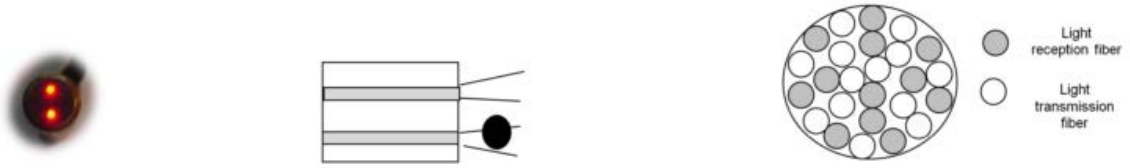

(a) Fiber probe showing light emission **(b) Particle passing through 1st bundle** **(c) Fiber arrangement in bundle**

Figure 230. *Optical fiber configuration for radial velocity measurement.*

Solid Flux was measured using a piezo probe, shown in Figure 231, which measures the impingement of particles on the surface of the transducer. Such impacts produce voltage spikes, which can be interpreted as a mass flux. One transducer is mounted at the end of a bent tube so that its active surface is pointing upward while the second is mounted on the end of a tube pointing downward. Using this arrangement, upward and downward fluxes, which can follow each other very quickly in the turbulent riser, can be measured easily (Spenik & Ludlow, 2010. A comparison was made between these measured fluxes and those measured using: 1) an extractive sampling probe and 2) using Fiber Optic probe. For the Group B polyethylene beads the extractive sampling was conducted as described by Miller and Gidaspow (1992) using a 1.9 cm ID extractive probe traversing across the entire riser diameter two directions: both in-line with and perpendicular to the recycle solids entry and gas outlet. The fiber optic probe was calibrated using the double acting isolation valves to quantify the relationship between solids loading and reflected light intensity (Zhang *et al.*, 1998) and then using the cross-correlation of the time dependent signals from each to determine the duration that it took for particles to move from one fiber to the next.

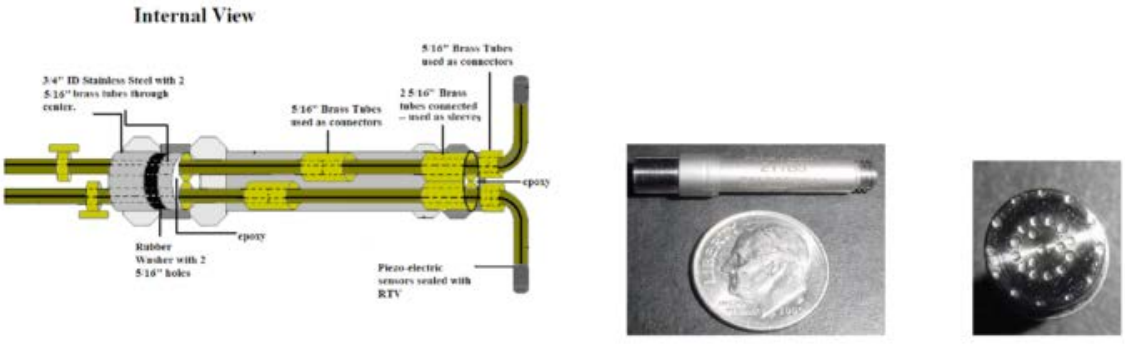

(a) Dual piezoelectric transducer probe **(b) Piezoelectric probe size** **(c) Piezoelectric probe face**

Figure 231. *Piezoelectric transducer configuration for radial solids flux measurement.*

High speed Particulate Image Velocimetry (HSPIV) measurements (Cocco *et al.*, 2010) were made at a riser elevation of 9 m for the three Challenge Problem flow conditions. HSPIV involves taking high speed videos of particle motion at frame rates on the order of 5000-50,000

frames per second. Particle motion in the high-speed videos is tracked using proprietary software developed by the NETL. From the tracked particle motion, particle trajectories and velocities are measured in two directions. By measuring the number of particles in the field-of-view, a simultaneous measurement of particle concentration is also achieved. The measurement uncertainty of an individual particle velocity of less than 1% and tracking accuracy of greater than 99.5% has been achieved with the HSPIV technique. Hence the fluctuations seen in the results are primarily due to the experimental fluctuations.

Solids tracer experiments were conducted to characterize the hydrodynamics of a particle laden jet entering a particle laden riser, as shown in Figure 232. A phosphorescent dye was added to the high density polyethylene (HDPE) beads during their manufacture to allow tracking of all particles in use during these tests (Shadle Shadle *et al.*, 2008). Experimentally, the jet consisted of a flow of gas and solids 1.9 cm in diameter which was introduced perpendicular to the riser flow at a position 3.66 m above the distributor and in the same azimuthal direction as the bulk feed of solids being recycled into the riser. Solids mass flow in the riser was measured through the use of a spiral device while gas flows were both measured and calculated. The total gas flow came from three different sources: gas used to educt the solids into the jet, gas used to assist the flow of solids down from the feed hopper to the eductor, and gas flow which resulted from the pressure driven flow through the solids feed line. In addition to measuring the mass flow of solids through the jet, the solids velocity was measured by means of simple "time of flight" experiments. The average jet velocity was reported to be 3.75 m/s for all three test cases. The value of 0.95 was found for the average solids void fraction calculated from the mass flow of solids through the jet and the jet velocity.

Finally, time dependent pressure fluctuations were measured. High speed differential pressure measurements were acquired using Setra pressure transducers. Sampling rate was set at 12,500 samples/sec for 30 seconds at each operating condition.

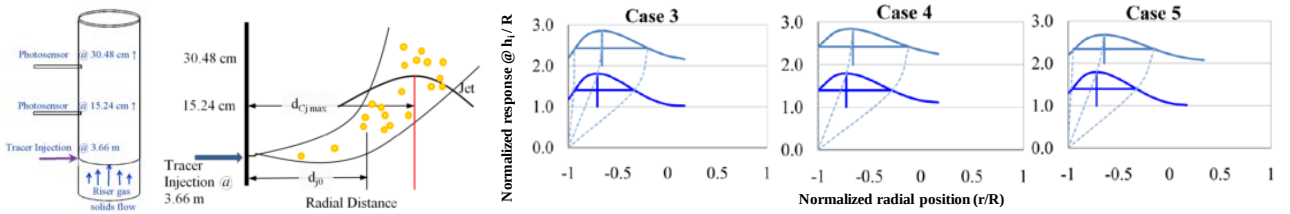

(a) Jet Injection **(b) Typical jet penetration** **(c) Normalized response of jet penetration as a function of radial position**

Figure 232. *Configuration and response of jet penetration.*

Results and Discussion: Five modelers submitted results on circulating fluidized bed. The participating modelers were software developers, graduate students at the universities and research scientists at the government organization. A summary of the modelers contributions is presented in Table 19.

Table 19. *Modeling Information for Circulating Fluidized Bed Problem.*

Modeler	Type	3D	Resolution	# of Particles (Millions)	Time to simulate 1 s (hr)	Cases Studied
CFB1	E-L(Hybrid)	x	0.2M	800 M	4.8	5
CFB2	E-E	-	12K	-	-	2
CFB3	E-E	x	76K	-	27	5
CFB4	E-L (Hybrid)	x	-	338 M	4	3
CFB5	E-E	x	3.4M		63	1

Modeler	Wall Boundary Condition	Drag	Granular Temp.	Collision Model	Gas Phase Turbulence Model	Solids Phase Turbulence Model	Solids Phase Treated as
CFB1	Turbulent wall for solids structures	Wen & Yu	-	-	LES	-	PSD
CFB2	Gas: no slip/ Solids: Johnson-Jackson	EMMS	PDE	Kinetic Models	RNG k-ε model for mixture	RNG k-ε model for mixture	Single Sphere with constant mean size
CFB3	Partial Slip Wall	Syamlal& O'Brien	Lun et. al. (1984)	None	k-ε model	None	Monodispersed with mean size
CFB4	-	Wen & Yu	NA	-	LES	None	PSD
CFB5	No Slip	Gidaspow	Algebraic form	Kinetic Models	None	Granular Temperature	Single Spherical Particle

Axial Pressure Profile and High Speed Pressure Fluctuations: The axial pressure profile is perhaps the single most important characteristic of the circulating fluidized bed riser, which reflects the macro and meso-scale features of how the solids inventory is distributed along the length of the riser. While the individual pressure transmitters varied in sensitivity to fluctuations, the process error can be evaluated by considering the deviations in second by second pressure measurements. The process variations were an order of magnitude larger than the measurement errors; however, the variation in even these process uncertainties could not readily explain the axial variation in several of adjacent transmitters, particularly those in the highly loaded mixing zone near the bottom of the riser. In order to better explain these variations it was decided to represent the process uncertainty assuming continuity along the riser height. For this reason the replicate $\Delta P/\Delta L$s were fitted using a polynomial dependence on axial location and evaluating the uncertainty from that general model. The resulting uncertainty pools the uncertainty across the entire axial profile, as shown in Figure 233.

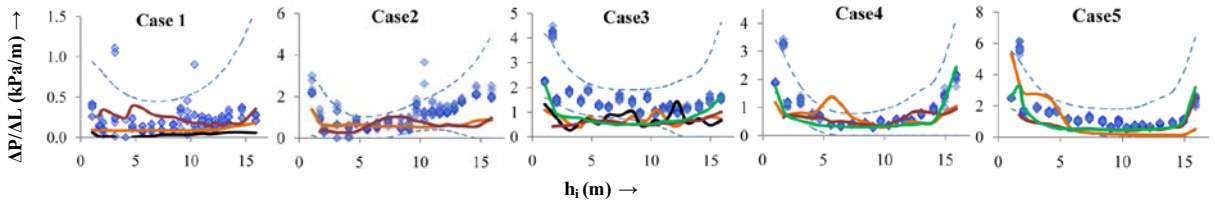

Figure 233: *Comparison of blindly modeled axial pressure profile against CFB experimental axial pressure profile.*

Regardless of the determination of uncertainty, each of these pressure profiles demonstrates the dense regions both above the solids inlet and below the riser exit, but to different degrees depending on the operating conditions. The dense region at the top of the riser for glass beads Case 2, extends furthest down into the riser, and the acceleration region at the base was shorter than any observed in the Group B profile in Figure 233. The higher solids flow Case 5 exhibited the longest mixing zone at the base and the shortest reflux zone at the top, except the very dilute glass bead Case 1.

Figure 233 also shows composite graphs with all four models overlaid on the averaged experimental data. This figure allows further graphical comparisons of the models to the data and to each other. It would appear that the simulation results were better in dilute cases, showing relatively low $\Delta P/\Delta L$ at higher solid loadings. Both CFB1 and CFB2 models underestimated the inlet condition in dilute Case 1, the overall magnitude of CFB2 being the least among three models. The CFB1 model appeared to follow inlet profile at dense condition (Case2). The opposite appeared to be true for CFB3 model at the riser exit (Case 1).

As can be seen from the leftmost graph of Figure 233, the E-E (CFB3) profile reasonably followed the experimental data starting from 10 m elevation to the top of the riser. The E-L trend seemed to match the measured profile up to 8 m from the riser bottom; however, it was unable to capture dense bed conditions near the exit (Case 2). Similarly, the CFB3 model failed to capture axial pressure profile at the top of the riser (Case 2). For these operating conditions, the E-L and E-E models consistently represented fully developed region although the E-E model predicted few humps in their axial profile.

Blindly modeled pressure profiles were also predicted within the confidence interval defined for Case 3, 4, and 5 as depicted in Figure 233. All models underestimated the axial pressure in Case 3 probably due to greatest variability in the profile itself. Moreover, the modeling results of CFB1 and CFB2 appeared unevenly distributed along the height. The CFB3 and CFB5 predictions looked similar in fully developed region except the former model could not capture the outlet conditions properly. Based on graphical comparison, it would be unfair to state that the CFB3 modeler did not capture inlet trend for Case 5 because they did not submit results at the very bottom (1.04 m). It is not clear whether their results could have followed the axial profile at the inlet. Definitely, their predictions were out of trend in other cases (Case 3 and 4). The core annular regime of Case 4 showed the lowest variability and hence, all of these models appeared to predict axial profile successfully. The E-L model (CFB1) showed a hump around 5 m while the CFB3 model could not capture the data at the very top. The CFB5

significantly predicted both inlet and outlet conditions. For Case 5, both CFB3 and CFB5 considerably modeled exit effect arising from the blind T configuration present at the riser outlet. The E-L model again shows a hump around 2 m elevation for this operating condition, as shown in Figure 233.

Table 20. *Overall ΔP_r comparison.*

CFB: ΔP_r ± 95% CL, *kPa*					
Experimental			**Test Cases**		
	Case 1	*Case 2*	*Case 3*	*Case 4*	*Case 5*
Mean (*kPa*)	3.4	18.3	22.8	13.6	20.9
± 95% CL (*kPa*)	±0.4	±0.6	±0.5	±0.4	±0.4
% Variation	12.8	3.1	2.4	2.3	2.0
% Difference between Simulations and Experimental Mean: $(\Delta P_{r,m} - \Delta P_{r,e})/\Delta P_{r,e} \cdot 100$ %					
CFB1	52	40	51	15	12
CFB2	82	-	48	-	-
CFB3	-10	47	60	14	63
CFB5	-	-	40	22	21
Error, $\tilde{E} = (\Delta P_{r,m} - \Delta P_{r,e})$ with 95% Confidence, *kPa*					
CFB1	1.8 ± 0.4	7.3 ± 0.6	11.6 ± 0.5	2.0 ± 0.4	2.5 ± 0.4
CFB2	2.8 ± 0.4	-	10.9 ± 0.5	-	-
CFB3	-0.3 ± 0.4	8.6 ± 0.6	13.7 ± 0.5	1.9 ± 0.4	13.2 ± 0.4
CFB5	-	-	9.1 ± 0.5	3.0 ± 0.4	4.4 ± 0.4

As a quantitative comparison, twenty incremental pressure drops across the riser were summed up to obtain the total pressure drop ($\Delta P_{r,m}$) from the simulation and compared it against the experimental total pressure drop ($\Delta P_{r,e}$) as a percent difference between the two Table 20. The experimental variability among replicates is also reported and they ranged from 2 to 13%. Note that the incremental pressure drops and $\Delta P_{r,e}$ values, represented the arithmetic mean of many duplicates collected at different times. Simulated $\Delta P_{r,m}$ deviated from the experimental mean ranging from -10% to 80%. The error between measured and modeled pressure drop with 95% confidence is also shown in Table 20. The 95% confidence is an interval in which the error between population mean (unknown) and the sample mean ($\Delta P_{r,e}$ in the present context) is believed to occur. The statement of confidence is *not* made directly concerning the magnitude of the modeling error, nor concerning an interval around the computational prediction (Shadle *et al.*, 2008). The reason such statements cannot be made is that the fundamental quantity that is uncertain is the *true* experimental mean. Stated differently, although there is an error in the computational result, the actual uncertain quantity is the *referent* i.e., the *true* experimental value, not the computational result. As an illustration, Case 3 is considered where the prediction from one of the E-E models is compared against the total pressure drop mean:

Population mean $\Delta P_{r,e}$ with 95% confidence = μ ~ (22.3, 23.3) kPa
Modeling error Ĕ=$(\Delta P_{r,m} - \Delta P_{r,e})$ with 95% confidence ~ (9.6, 8.6) kPa

In summary, the result of the validation metric was $E = 9.1 \pm 0.5$ kPa with 95% confidence for the total riser pressure drop. The magnitude of overall modeling error in $\Delta P_{r,m}$ was approximately 38% higher than the experimental data including its uncertainty.

Fluidized beds are known to exhibit pressure fluctuations, which can be characterized using Fourier Transform to evaluate dominant frequencies of the process. To evaluate these process fluctuations, high-speed pressure fluctuations were measured at the bottom, near the middle, and top of the riser and produced the power spectra in Figure 234.

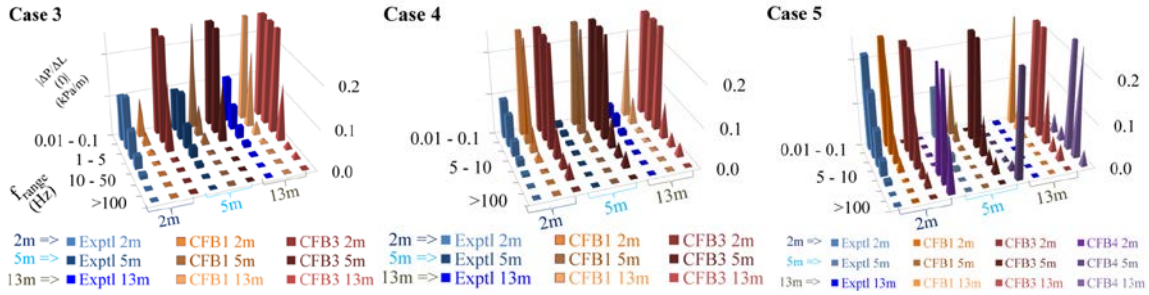

Figure 234: *Comparison of blindly modeled power spectra of high-speed pressure fluctuations against CFB experimental data.*

In all cases the amplitude drops off continuously with increasing frequency and the higher location in the riser. The decrease in amplitude was greater above 1 Hz. The case closer to fast fluidization (Case 3) and dense suspension upflow (Case 5) case had higher amplitudes than the core annular flow (Case 4). The magnitude at the two axial location were similar for these cases; however, for the core annular condition the amplitude of the pressure fluctuations was significantly less at the higher tap location. Unfortunately, for the modelers the high amplitude for the low frequency fluctuations suggests that time scales on the order of 100 seconds or more may be necessary to capture the process dynamics.

Three simulation results were submitted on the power spectra of high-speed pressure fluctuations. Amplitude variations for different axial locations were not substantially modeled for the test cases under consideration. All models showed higher magnitude response except the Eulerian-Lagrangian model for Case 5. At 2 m elevation, the E-L (CFB1) model compared favorably with the experimental amplitude. They also predicted low frequency response satisfactorily at 5 m location. The second E-L (CFB4) modeler predicted completely different behavior than typical CFB power spectra as their magnitude appeared to be significant towards higher frequency range. This seems unusual in CFB implying that the process does not show low frequency dynamics and the high frequency components engulf CFB during operations. Contrary to the magnitude response, both E-E and E-L models showed similar amplitude dependency on a signal frequency content. In the author's opinion, this is the most important result of frequency analysis since one is interested in recognizing the distribution of signal's strength at a particular range of frequencies rather than the amplitude of power itself. The application lies in filter design area of signal processing or controller design for the CFB process at dominant frequency of

interest. Mean dominant period of 8 seconds was observed for cases simulated that was commensurate with the experimental findings.

Radial Solids Velocity Profile and Solids Mass Flux Profile: The velocity profile from the fiber optic and the HSPIV are summarized in Figure 235. Also shown are the 95% confidence levels which were estimated by fitting a second order polynomial with dependence on measurement height, azimuthal angle, radial location and different techniques. The effect of height was substantial and hence separate confidence level was measured for each vertical measurement location. It should be noted that for the purpose of this error analysis the uncertainties in individual mean vertical velocity measurements (instrumental uncertainty and biases) were not included. Deviations were much more prominent when looking at the very bottom of the riser as shown in the glass bead test cases (Case 1 and 2). To characterize the process variability or experimental uncertainty in radial velocity measurement for Case 3, 4 and 5 at z = 8.88 m, velocities measured with dual multi fiber optic bundles (diamonds) and HSPIV (circles) were compared. As can be seen they matched closely.

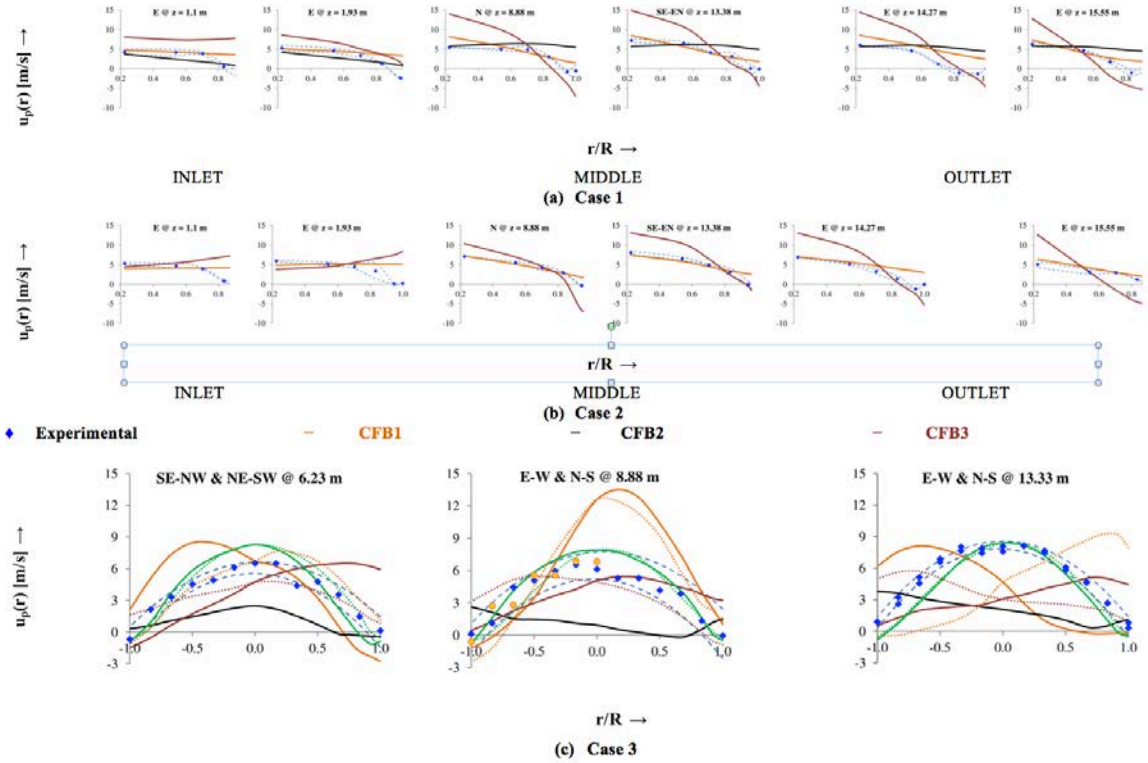

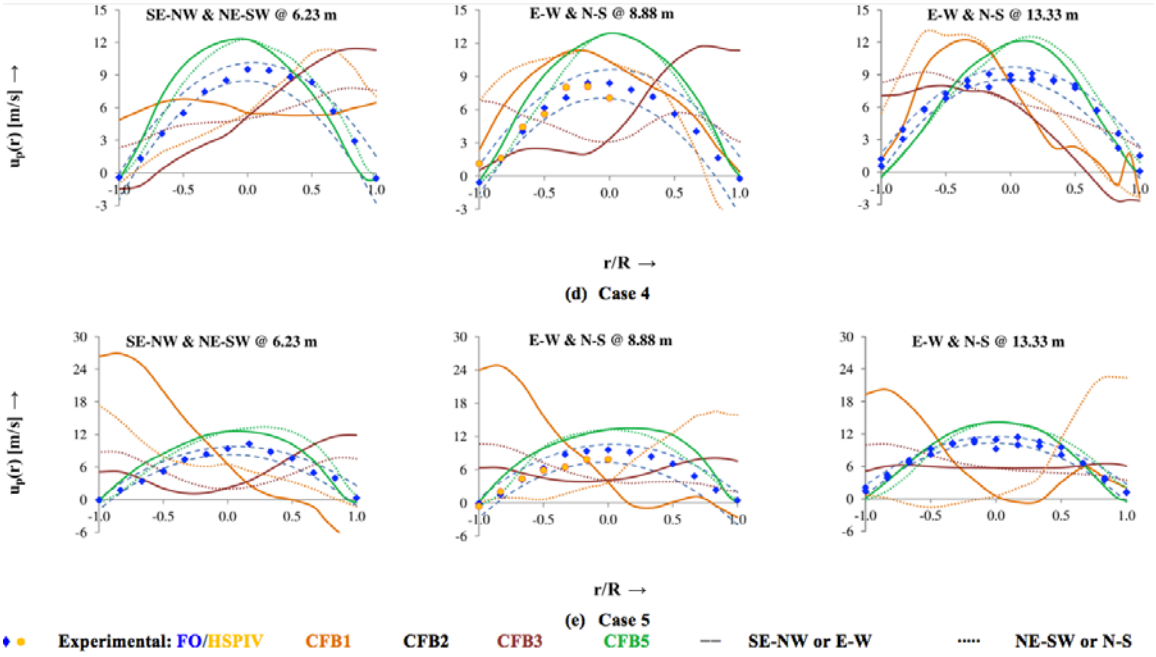

Figure 235. *Comparison of blindly modeled radial solid velocity profile against CFB experimental radial solid velocity profile.*

The comparison between experimental data and simulation results for radial velocity profile are also presented in Figure 235. The elevation is shown in ascending order from left to right. The elevation covering 1.1 m and 1.93 m interval is the INLET, that between 8 m and 13.5 m the MIDDLE and that between z = 14.27 and 15.55 m is the OUTLET. As a whole, the E-L (CFB1) profile looked linear with respect to the radius rather than curving downwards and rising up near the wall, the characteristic shown by the experiment. The E-E (CFB2) counterpart also simulated linear trend for the first test case. The magnitude of CFB2 was lower than that of the CFB1 at the INLET, and they predicted higher magnitude beyond r/R = 0.5 at the MIDDLE and OUTLET section of the riser. At every elevation, the E-L model moderately predicted radial profile throughout the azimuthal location; their results were primarily closer to the experiment near the center extending up to r/R = 0.7 or even beyond certain radial locations (e.g., Case 1 at z = 8.88 m or Case 2 at z = 15.55 m). The third E-E model (CFB3) could follow the experimental profile mostly at the MIDDLE and OUTLET section of the riser but they predicted higher magnitude than the experimental mean. For higher loading Case 2, both E-E and E-L models appeared to have difficulty predicting the radial velocity variations near the wall.

Remaining three cases achieved with Group B materials are compared in Figure 235c,d and e. In these test conditions, the statistical hypothesis could not differentiate between two radial velocity profiles measured across different radial locations. The significance of difference was quantified using t-statistics. Consistent with this statistical observation, the CFB5 model appeared to predict similar radial profiles across two azimuths although t-statistics were not performed on their modeling results. This model appropriately captured parabolic flow profile increasing with riser superficial velocity U_g at the walls but displayed higher magnitudes near the center for Case 4 and 5. In both of these test cases, the E-L profile displayed mislaid parabola showing maximum of the profile away from the riser center. For Case 3, at the middle of the

riser, radial profiles of E-L (CFB1) model were essentially similar across two azimuths albeit demonstrating higher magnitude than the experimental values. Apparently, the Euler-Lagrangian model suffered substantial deviation from the measured velocity profiles in all of these operating conditions.

Referring to Figure 235f, other E-E model (CFB3) could not display statistical similarity between their calculated radial profiles for any of three test cases. On the other hand, the model predictions of CFB2 for all radial locations were identically the same. Also, the CFB2 model displayed somewhat parabolic trend of Case 3 at 6.23 m although they calculated lower magnitude of particle velocity. Along E-W or N-S direction in the middle of the riser, their simulation began closer to the wall, then under predicted and curved upward to match the profile again at the opposite face of the wall. At the outlet, they could only match the profile at the opposite face (either West or South face of the wall but not East or North face). For all elevations in test Case 4 and 5, and at the exit condition of Case 3, both profiles of the CFB3 model appeared distorted or skewed towards either face of the riser wall. Although their simulations presented relatively undistorted profile at the bottom and middle section of the riser, their comparisons did not show any significant improvement over velocity values. Only half of their profile (E-W) corresponded the experimental profile going from the center to the West face while their N-S counterpart represented radial profile from the North face to the center.

To evaluate the quality of the local solids flux measurements, the measurements were integrated across the riser cross-section and compared to the measured solids flow rate. While the measurements agreed closely at low solids velocities, the error increased as the solids flow rate increase such that the integrated fluxes were 25% lower than the spiral flow. Even after replicate sampling data sets were obtained it was apparent that the extractive sampling was biased low compared to the spiral measurement for every test condition tested. As a result, a series of tests were conducted to identify potential problems in the accuracy of the spiral solids flow measurement. The three sources of error considered were (1) the inaccurate determination of the bed density (overestimating the density by 25%), (2) spurious noise or chatter in the encoder leading extraneous additional signals causing a higher reported rotation of the spiral, and (3) the assumption of uniform solids flow profile across the standpipe cross-section.

Drain and weigh tests confirmed the packed bed densities were accurate at least at the low flows. In any case, the packed bed would have to be fully fluidized to account for the deviations, yet this was never observed. The standpipe pressure drops over the confined moving bed were inconsistent with fluidization occurring. The drain and weigh experiments also confirmed that spurious chatter did not occur and did not contribute to the higher solids flow. Several standpipe tests were undertaken to evaluate the potential for non-uniform solids flow profile across the standpipe. Solids tracer experiments conducted by flashing a bright light at different radial locations and then tracking the time of flight of the solids to move past two downstream photo-sensors confirmed the measurements of the spiral volumetric flows and demonstrated that even under the highest flow rates there was no distinguishable velocity profile. High-speed PIV measurements taken above the spiral confirmed this conclusion. On the other hand, the extractive sampling profile did display an asymmetry such that the down-fluxes were highest in measurements taken on the side of the riser opposite from the probe entry point. This suggests that the probe was causing some interference in these sampling measurements, which were in the direction leading to a low bias. The same type of interference was observed when using the fiber optic probe to measure solids velocity. Thus, it is recommended that extractive

sampling and other intrusive probes limit their measurement to the quadrant nearest the probe entry.

Fiber optic probes are often used to measure the solids flux profile, but even when limiting the measurements to the nearest quadrant and calibrating the solids fraction using fast acting valves, this method led to significant scatter and relatively larger deviations depending upon which bundle (top or bottom) was selected for solids fraction. The fiber optic probe tended to produce integrated solids fluxes which were higher than the solids flow measured from the spiral.

The response of the piezo electric particle impact probe when integrated across the riser cross section produced solids flows that were within 10% of the measured solids flows. Like the other measurements this deviation was largest at the highest flow rates, but the integrated flows were higher than that determined by the spiral. The measurements involves determining a threshold which differentiates a particle impact from a gas pressure fluctuation, and this becomes more difficult, i.e. the signals are closer in intensity, when the solids are moving slowly. In addition, when multiple particles such as those in a cluster hit simultaneously or shield the probe from the impact of particles in their wake, then the probe will underestimate the flux. The radial solids flux profiles are presented in Figure 236. These represent net fluxes and demonstrate the significant upflow of solids flux near the wall for the dense suspension upflow case. Interestingly enough the lowest velocity Case 3 exhibited the flattest solids flux profile across the diameter of the riser. Data on the relative upflux and downflux is also available.

Figure 236 shows the comparisons of E-E and E-L models against the solids flux profile measured at the same radial locations and elevations of the riser as radial solids velocity. For Case 3, the E-L profile displayed more or less radial symmetry across the riser cross-section; the most distorted profile was exhibited in the mid section of the riser. Likewise, the model profile across the NE-SW or N-S direction appeared symmetrical and within experimental uncertainty of Case 4 (Figure 236b). Seemingly, this characteristic is opposite to what was observed in the case of velocity profile. It suggested that the E-L model was able to predict solids fraction comparatively better than the solids velocity. There was a sudden shoot observed in their results near r/R = 0.33 and relatively smaller shoot at r/R = 0.83 at the top, even then they predicted East-to-West profile (indicated by the solid orange line) within the confidence bound of Case 4. The CFB5 model showed reasonable profile in core annulus regime while they over predicted Case 3 at all elevations of the riser. At the bottom, the CFB2 model started diverging from the experimental mean when moving from SE or NE direction towards opposite face of the riser wall. This occurred mainly beyond the riser center as can be observed from Figure 236a. Their profile appeared jagged at the middle and top sections of the riser (not shown). Unfortunately, the results of CFB3 model did not look very promising in both of these test cases. At dense suspension upflow regime, the solids flux measurement showed asymmetrical profile resulting from the upflow of solids along the wall and apparently presented most difficult situation in modeling. The CFB1 model could not capture asymmetry while other E-L (CFB4) model either predicted a constant profile or linear dependency of mass flux on radial locations. As can be seen from Figure 236c and d both E-E models also showed distorted results parallel to their E-L counterpart. The CFB3 model predicted jagged profile without any sign of matching upflow of solids (z = 6.23 m) near the wall. The CFB5 model appeared to follow the NE-SW profile at 6.23 m (not shown) while moving towards SW direction but severely diverted near the wall. Few humps appeared in their flux profile in the middle and top section of the (Figure 236c and d).

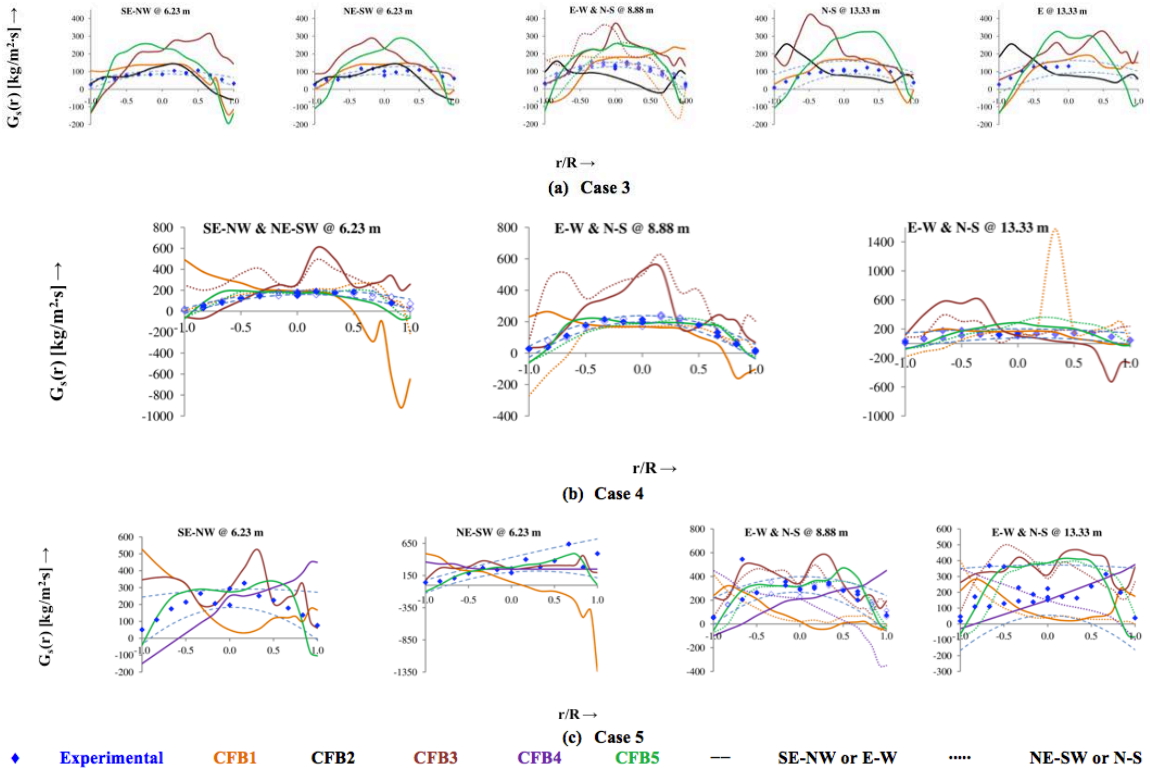

Figure 236. *Comparison of blindly modeled radial solids mass flux profile against CFB experimental radial solids mass flux profile.*

Jet Penetration: The jet penetration data is reported in Tables 21 and Figure 221. Initially, radial jet profile data was post processed by subtracting the average background signal collected during the initial 15 seconds from the "lighted" signal. The resulting data were normalized by dividing by the maximum of a signal at each position. The average voltage was plotted as a function of radial position. Each curve was fitted with a 4^{th} order polynomial. The polynomial representation allowed to mathematically fixing the maximum location of the jet concentration. Once the maximum location and its value were determined, the width of the curve at 1/2 of the maximum height was calculated.

Table 21. *Jet penetration measurements for Geldart Group B Particles.*

Height above jet (cm)			0 cm	15.24 cm above jet injection				30.48 cm above the jet injection			
Case	U_g m/s	M_s kg/s	d_{j0} cm	$d_{Cj\,max}$ cm	95% CL cm	$W_{1/2maxCj}$ cm	95% CL cm	$d_{Cj\,max}$ cm	95% CL cm	$W_{1/2maxCj}$ cm	95% CL cm
3	**5.71**	**5.54**	0.00	4.41	1.24	9.31	0.82	5.14	1.50	11.49	2.69
4	**7.58**	**7.03**	0.00	3.99	0.62	10.50	1.08	5.06	1.55	12.09	1.69
5	**7.58**	**14.00**	0.00	4.75	0.51	9.82	1.11	5.88	0.81	11.57	2.17

The results on jet penetration across a radius of CFB riser from the point of injection are depicted in Figure 238. There was relatively low penetration of solids into both densely loaded test Case 4 and 5 and moderately loaded Case 3. While there is a clear tendency for the solids continued to penetrate deeper into the riser at the higher elevation, the process variability cannot distinguish the extent of penetration. In other words, the jet penetration was statistically independent upon height. It may be thought that at any given instant the peak of jet solids concentration could be essentially the same regardless of which height above the jet the measurement was taken. More significantly, the concentration of jet solids spreads out as the jet moves up the riser as characterized by the peak width. The E-L model simulated the penetration accurately in dense suspension upflow (Case 5) while the penetration was over predicted at the lowest gas velocity Case 3 and in transport core annulus Case 4. The solids concentration, gas, and solids velocities were subjected to strong fluctuations at the jet inlet due to unstable gas-solid flow through the feed nozzle (Li & Guenther, 2011). Whether this flow condition was specified at the jet inlet or neglected in the simulation is not clear from their submitted response. Neither was it clear whether other factors such as effect of gas turbulence on solids dispersion were critical in their simulation. The E-E model could not predict any penetration for Case 3.

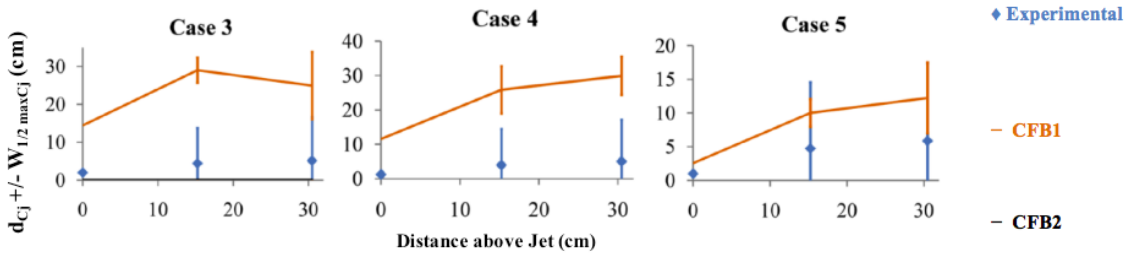

Figure 237. *Comparison of simulated jet penetration against CFB experimental jet penetration data.*

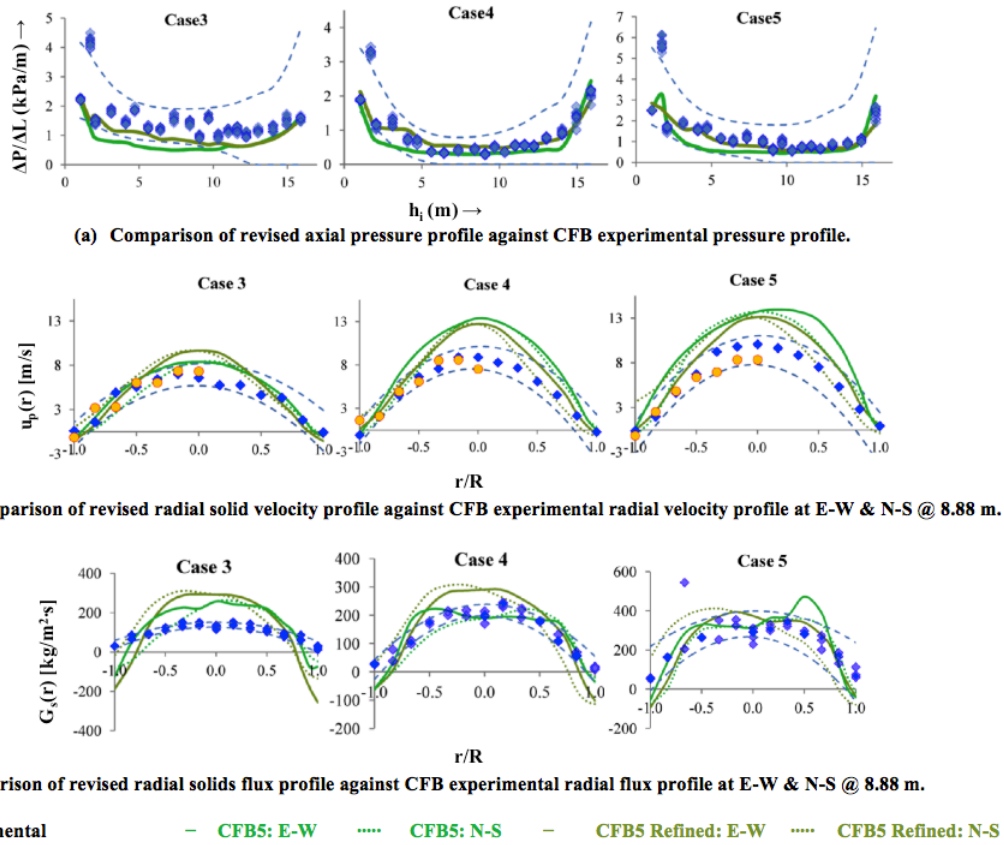

Figure 238. *Comparison of revised simulations against CFB experimental data.*

Observations: Models of fluidized bed are often transient solutions to one or another form of the Navier-Stokes equation. These are computationally intensive calculations which even on today's computers can take 30 days to resolve six seconds of simulated time. The effect is that modelers must use judgment to determine whether the simulation has reached steady state and how long to average the transient results to represent that steady state. This can be illustrated by comparing the refined profiles against the blind results submitted by the fifth modeler (CFB5) on circulating bed. They ran their simulation for a longer time going from 25 seconds to 50 seconds and the results were time averaged over the last 10 seconds for both submissions. The percentage difference between experimental mean of riser total pressure drop ($\Delta P_{r,e}$) and their refined results were improved resulting in 26%, -5% and 9% error over their blind submission.

The statement of the problem to be simulated is often a significant source of error in the simulation. For instance, during the initial release of Challenge Problem, several mistakes were identified in the description of the flow conditions in standpipe. These were readily corrected. There was also confusion among the modelers on the value of superficial gas velocity U_g reported at the bottom of the riser. This has been the topic of a recent report (Tingwen *et al.*, 2011). The riser superficial gas velocity was reported as the pressure and temperature corrected superficial gas velocity at riser process conditions. It was obtained by adding the volumetric gas flow rate given at the riser bottom, gas flow coming from the L-Valve sparger and the amount of flow coming from the standpipe at standard conditions. This gas flow rate through the L-valve was predicted from the standpipe model that was developed to correct spiral circulation rate (Tingwen *et al.*, 2011). The fifth CFB modeler believed that the improvement in their axial

pressure profile for Case 4 and 5 conditions were mainly because of the correction in their flow conditions. Initially, they used the riser superficial velocity by adding contribution from the L-Valve sparger and standpipe aerations (F_{SL}) to the composite U_g. They used the measured pressure at the bottom and exit of the riser to set the boundary conditions for their refined simulation which they believed to have small influence on their improved results. After a grid study, they used coarser grid (0.5M computational cells compared to 3.39M) to run their simulation for a longer time and produced a smoother and more symmetric radial velocity profile. These results were in closest agreement to the axial pressure profiles; however, neither coarse nor fine resolution simulations could display asymmetry in radial solids flux profile revealed by the experimental data.

The first CFB modeler did not make any adjustments to their blindly submitted models. In their opinion, their first simulations did not have enough time to reach a pseudo-steady state. As a result, they allowed their simulations to continue until it was time for the refined data submission. Unfortunately, due to lack of time parametric studies were not undertaken, the results were not adjusted and the refined results matched the blind submission quite closely.

Due to the realities of simulating 5 to 20 seconds of fluid bed performance models tended to express results related to the large temporal variations more so than the mean or time averaged values measured experimentally over 15-20 minutes. Certainly, the responses indicate that more model improvements could be gained by reducing the scope of future Challenge Problems thereby allowing more time for the model parametric sensitivity analyses.

The fluidized bed model results appeared to be less sensitive to boundary conditions. Accurate solutions appeared to be tied to capturing the particle size distribution either with Lagrangian particles or a PDF representation. Implicit and couple pressure integration is also needed to capture the subtle but important gas compression at the bottom of the bed; a precursor to gas bypassing. Finally, the some simulations had time steps that exceeded the sampling rate for the pressure fluctuations. Thus, model efficiency resulted in not capturing sub-time-step events such as pressure fluctuations due to gas bypassing.

As in previous Challenge Problems, examination of the simulation results revealed that still some improvements are required in the CFD models to achieve better outcomes. The participating models could not capture inlet and exit effects on the axial pressure profile of the CFB more than 50% of the time. One of the reasons for the mismatch was the varying bed densities at different operating conditions. The modeling discrepancies were larger in the higher solids loading, Case 2, and in a condition near fast fluidized regime, Case 3 (Table 15). Generally, the contribution of mass inventory in the riser to the pressure drop was higher from Group B materials than that from the Group A particles (Gidaspow, 1994). In experiments using same glass beads and HDPE materials, the solids flow going to the riser and the gas flows were completely cut off after steady state conditions were reached. The solids inventory in the riser were either weighed or transferred over to the standpipe. The solids inventory was computed from the pressure drop across the riser and compared against the measured inventory to understand the contribution of different factors contributing to the pressure drops. The solids inventory or weight contribution was found to be around 70% for Group A material and the rest came from wall friction term due to solids under dense transport conditions similar to Case 2. At high solids concentrations, there is a layer of moving solids near the wall and the wall supports part of the weight of solids, resulting in higher frictional contribution to the pressure drop (Shadle *et al.*, 2008). In the case of Group B materials, almost all contribution (~90%) came from the solids weight term. The solids fractions measured using an Electro-Capacitance Volumetric Tomography (ECVT) probe confirmed this observation. The solids fraction calculated from the pressure drop across the ECVT location (riser elevation between 8-11 m)

involving only the term of gravitational acceleration, and that obtained from the ECVT measurements matched closely. Whether the agreements were due to the measurement being taken in the fully developed region or whether it is generally the case for Group B materials, should be verified in future. Computational models could be used to distinguish the contribution of each factor necessary to accurately predict pressure drop across the riser. Larger magnitude of estimated at higher loading case (Case 2) and near fast fluidization case (Case 3) suggests that the participating models did not capture the contribution of solids inventory. To accurately capture the contribution of solids inventory to the momentum balance equation, additional work is needed to properly relate fundamental material properties (viscosity, strength, elasticity, grain shape, restitution coefficient etc) to their proper places in the CFD model. In the case of a wall stress, these properties may have a strong influence on the boundary conditions (Fan & Zhu, 2011, 1998). Undoubtedly, the close predictions of one or other challenge problem models (submitted blindly) to the overall pressure drop measurements at dense suspension upflow, core annulus and dilute regimes are remarkable.

The objective of comparing the CFD radial profiles to experiments was to determine whether the models could predict the radial in-homogeneities observed in real systems and in experiments. The key difficulty lies in understanding the lateral solids distribution mechanism in the riser in addition to their axial movement. The solids velocity profile pronouncedly exhibited local values of zero or values less than zero (i.e., when the solids in the annulus flow downward along the wall) for glass beads. Roughly thirty percent of time, either E-L or E-E models were able to describe solids distribution near the wall. These discrepancies between simulation results and experimental data highlight the challenges in correctly setting up the appropriate boundary conditions.

The partial slip and/or turbulent wall boundary conditions used by the three modelers resulted in poor agreements of their predictions against the experimental solids velocity near the wall (Case 1 and 2 and most of Case 3, 4 and 5). The higher solids segregation closer to the wall using the slip conditions can be attributed to dissipation of energy due to collisions between solids and wall. Moreover, there is no general turbulence model in multiphase flow that adequately relates wall slip boundary conditions and interparticle collisions to the interaction between turbulence energy and its decay rate, therefore, turbulent viscosity, and the momentum interaction between the materials (Fan & Zhu, 1998).

On the other hand, the no-slip wall boundary condition used by the fifth modeler had produced velocity profile in close agreement with the measured velocity profile for Case 3, 4 and 5, especially near the wall. This can be attributed to the exclusion of dissipation caused by the particle-wall collisions. However, their models over predicted the magnitude of the solids velocity near the center even after refinement. The sharp rise of the center velocity is caused by the fact that the thick annular region blocks the upward motion of the gas and the particles.

By conservation of mass the smaller effective flow area leads to a correspondingly larger gas, and through the drag, a larger center particle velocity (Gidaspow, 1994. Qi *et al.* (2000) reported that the particles fed into the riser got elutriated immediately, and their simulated flow became rather dilute as a whole if the drag correlation derived from Ergun equation (a hybrid (Gisaspow, 1994 of Wen and Yu (1966) and Ergun (1952) equation was used by the fifth modeler) was employed. They claimed that those drag correlations were only suitable for low gas velocity and coarse particles, in which case terminal velocity was equal or close to the superficial gas velocity.

It is obvious from Figure 238 that the distributions of radial flux across the riser cross-section are asymmetrical showing the influence of entrance and exit regions. The phenomenon arises from a strong momentum interaction between gas and solids transferring a net rate of solids from the dilute core to the denser annulus (Rhodes, 1990, Yan *et al.,* 2003). There is an

upflow of solids along the wall in a dense suspension upflow condition. Overall the predictions of the radial flux profiles from the CFD models compared only moderately with the experimental trend. As discussed in the case of radial solids velocity, several factors can be accounted for their mismatch with experimental solids flux across radial locations. Based on response obtained from the CFB3 modeler, the gas phase turbulence did not have significant influence on their voidage, velocity and pressure profiles. Their solid phase was considered to be monodisperse with the mean particle size and they planned to implement the experimental size distribution. However, they never provided answer to how sensitive their model was to the size distribution of the particulate material being used.

Conclusions: This Challenge Problem was set out to investigate the strengths and weaknesses associated with different modeling approach. The first question was "How well do the models compare to the fluidization process?" This research question also involved investigating how CFD models had improved over the past few years. In fact, the computational fluid models indeed made significant improvements within this short period of time. There were still some deficiencies such as inlet and outlet axial pressure profile agreement were out of experimental trend, unsatisfactory prediction of asymmetrical radial solids mass flux profile across the circulating bed cross-section. The fact that their modeling results came closer to the experimental reality simply by increasing the simulation time should not be underestimated. Based upon the amount of effort required to respond to this challenge problem it is clear that reducing the scope of the problem will be required to obtain a broader participation of modelers by making it a more manageable task.

Nevertheless, there is now a framework from which to build. The vision is to have a well characterized data base for model validation which can ultimately move forward towards a certification process. In this respect, NETL has already started several steps where small scale fluidized bed and 2D rectangular bed would be built, small scale tests would be devised to benchmark critical complex physics (involving low particle count thereby requiring simulation time less than two weeks on a Personal Computer), and validating flow process of interest such as reacting gas absorption and evolution in small scale (e.g., carbon capture unit), gasification of size and density fractions (e.g., drop tube furnace), granular temperature or particle-particle collisions, and particle wall impacts (e.g., high speed particle imaging).

Subtask 4.6.3: Code Validation using high-velocity data (Sundaresan and model developers).

The MFIX framework, modified to account for the new physical models developed as part of this work (KTGF, DQMOM, drag force, and gas-phase turbulence), will be compared to both simulation and experimental data obtained from high-velocity systems. The model developers will ensure code "readiness" – i.e., that it is free of bugs (checked to a reasonable extent) and convergent for a trial case (e.g., PSRI or NETL data set). At this point, the code will be transferred to Prof. Sundaresan, who will take the lead on running the code, including running on the NETL supercomputer facilities, sensitivity analyses to numerics and physics, and comparing with the validation data. It is our understanding the NETL supercomputing facilities will be available to us in order to fully resolve particle clusters.

In terms of simulation data, MFIX model predictions for segregation will be compared to the Eulerian-DEM simulations (no gas-phase turbulence) both without and with particle evolution to agglomeration (Task 4.2). These results, coupled with those of the DEM comparisons, will illustrate the ability to predict solid-solid interactions and evolution both with and without a drag force present.

In terms of experimental data, comparisons will be made with the NETL (Task 4.6.2) and PSRI (Task 4.5) data for core-annular flow, as well as NETL data for the fast fluidization and

turbulent regimes (Task 4.6.2). These cases will contain both gas-phase and solid-phase instabilities, and thus will provide a benchmark for the newly-developed turbulence models.

(Fox reporting.) A set of simulations of a gas-particle flow in an idealized system were performed using QMOM, in order to investigate the formation of grid-dependent structures at higher local particle concentration. The system under consideration is represented by a square two-dimensional domain, whose sides measure 0.1m. The fluid phase, constituted by air, moves upwards, with a constant pressure gradient. The only external force acting on the system is due to the gravitational acceleration. The average particle volume fraction in the computational domain is set to 0.05. The particle density is 1500 kg/m^3, the particle diameter is 75μm, the restitution coefficient is 0.98. The initial condition was set to ensure the average volume fraction is 0.05, however it was not set to be uniform, in order to favor the development of instabilities in the flow, reducing the computational time required to obtain a fully developed flow. It is interesting to report that, in QMOM simulations, we did not observe the onset of instabilities during the whole computed time, which was up to 15 seconds, if a uniform condition for all the variables in the system was specified. Three different cases, with different levels of grid refinement, were considered, respectively, with 128 x 128, 200 x 200 and 300 x 300 grid points in the computational domain. Simulations were performed using the standard second-order numerical schemes in MFIX for the fluid-phase, based on the SuperBee limiter. The QMOM model used in the simulations was described above. The collision model used is the standard BGK linearized model, modified to account for inelastic collisions.

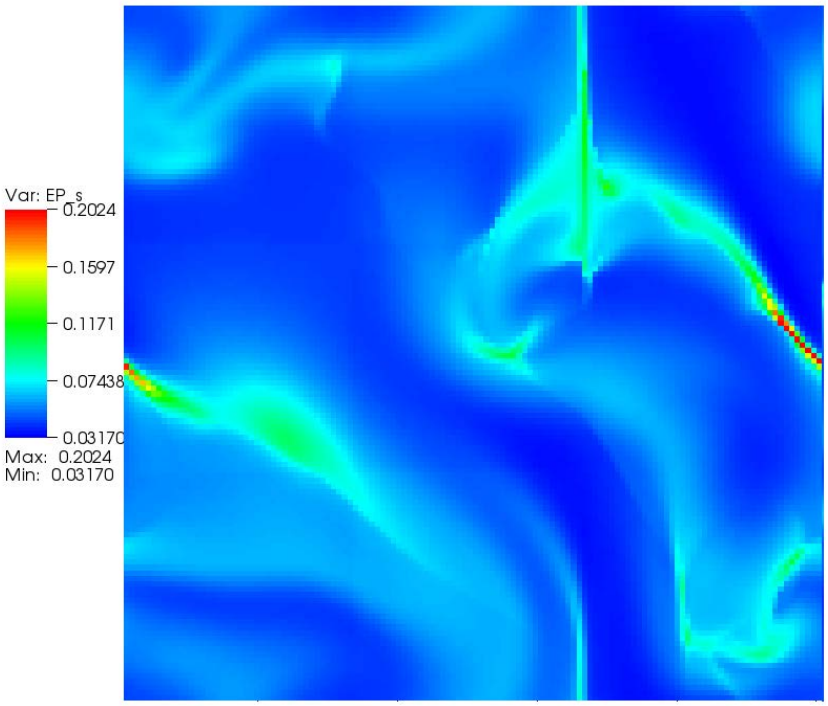

Figure 239. *Instantaneous volume fraction - 128 x 128 grid points.*

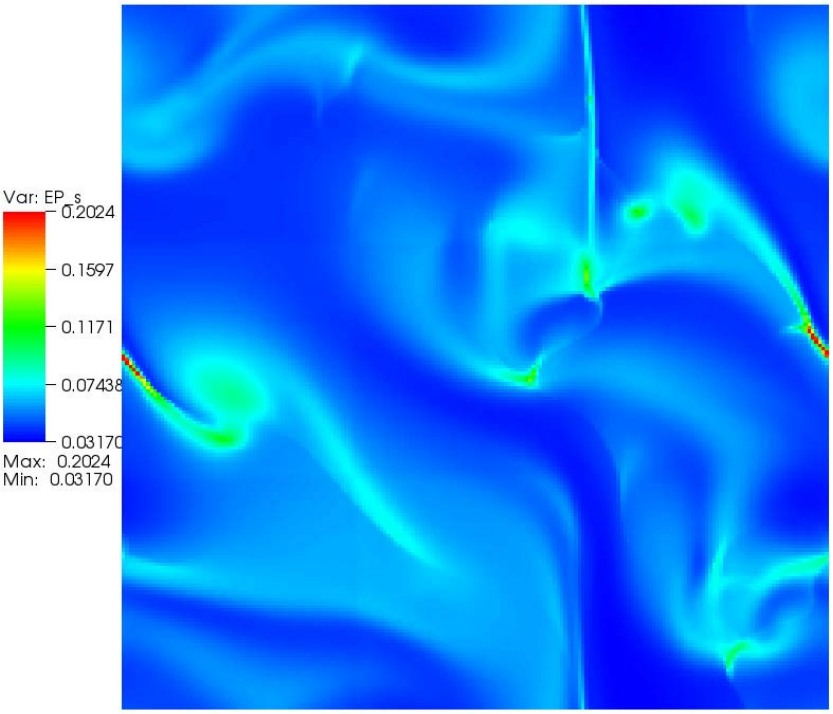

Figure 240. *Instantaneous volume fraction - 200 x 200 grid points.*

The volume fraction contour plot for the gas on the coarsest grid considered (128 x 128 grid points) is reported in Fig. 239. The diagram clearly shows the flow presents instabilities due to the interaction between the fluid and the particles. These instabilities cause the local accumulation of particles in some parts of the domain and the rarefaction of the particulate phase in other parts of the domain. Since the mean particle Stokes number is greater than unity, particles tends to segregate, as expected, in the zones with lower vorticity of the fluid phase.

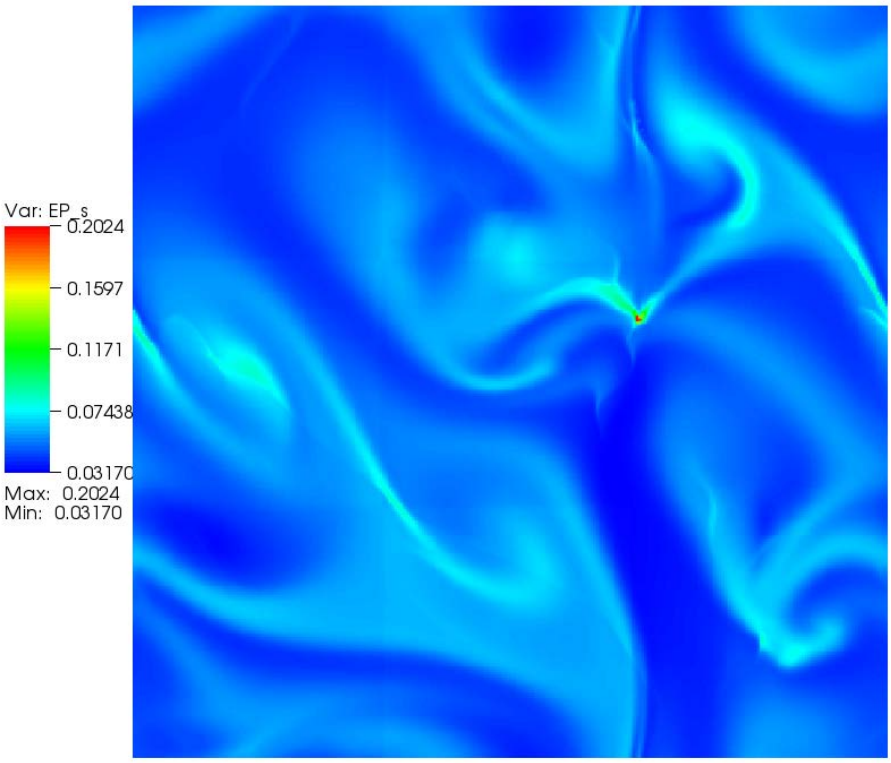

Figure 241. *Instantaneous volume fraction - 300 x 300 grid points.*

In order to investigate the effect of the spatial resolution on the numerical solution of the model, the discretization of the computational domain has been refined. The volume fraction contour plot in Fig. 240 shows the results obtained with a grid made of 200 x 200 points. The similarity with the flow represented in Fig. 239 is evident, however, as expected, sharper gradients are present, since the refined grid resolution allows them to be captured. It is interesting to observe that the major change due to the refined grid is neither on the values of the local particle concentration, which is similar in both the cases under examination, nor on the size of the observed structures, but on the resolution of the fluid vortical structures, as it can be seen observing, for example, the better definition of the vortex on the left-hand border of the periodic domain. Finally, the volume fraction contours for the most refined case considered (300 x 300 grid points) are reported in Fig. 241. In this case the shape of the structures observed is relatively different from those of Fig. 239 and 240, probably due to the better resolution of the flow, as indicated by the more defined vortical structures highlighted by the particle, however, in spite of the higher grid resolution, the simulations do not show the formation of structures in the particle-phase, whose size is strongly dependent on the grid resolution. The size of the structures observed on average in the computational domain is almost unchanged for the three grids considered in the simulations. This contrasts with the predictions obtained with traditional two-fluid model relying only on a reduced set of moments, which predict a strong dependence of the size of particle structures on the grid resolution, and can be explained in light of the intrinsic capabilities of QMOM for predicting particle trajectory crossing. A careful examination of the

figures, and, more easily, of the animations generated from the results of the simulations show, in fact, the presence of trajectory crossing, where cloud of particles hit each other, originate a locally and instantaneously higher zone of higher particle concentration, and then proceed along their path, with limited effect of collisions, which would tend to make the colliding clouds merge together. This phenomenon is particularly evident in the dilute parts of the domain, but it affects the whole behavior of the flow, since it limits the formation of the high number of small structures predicted by hydrodynamic models, which are actually delta-shocks, introduced by the mathematical formulation of the model, as explained in previous reports.

Additional simulations, with higher grid resolution will be performed to clarify this aspect. However numerical difficulties were encountered in refining the grid in MFIX on the considered computational domain, for example to 400 x 400 grid points, since the code seems to be affected by segmentation faults if the grid resolution becomes very refined.

The simulations presented in this report represent also a progress in the stabilization of QMOM in the dense limit, since local particle concentration reached values not far from the packing condition (the maximum observed value in the stored data was higher than 0.5). This stabilization was mainly obtained with an appropriate choice of the Courant number based on the particle-phase speed of sound, together with the implementation of the collisional fluxes described in previous reports. Work in the future will develop an implicit procedure, which will allow the use of larger time steps in the dense region.

Particle Pressure Solver for QMOM: The iterative solution procedure previously used for QMOM has been modified to implicitly include the effect of the particle pressure in the equation of the first order moment M^0, representing the particle-phase volume fraction. This modification to the solution algorithm, tested in 1-dimensional case, has proven to be very efficient in terms of computational times, and very robust in stably enforcing the particle packing limit. The procedure is briefly summarized below.

The first step in the development of the improved procedure is to consider the transport equations for the zero- ($M^0 = \alpha_a$) and first-order moments ($\mathbf{M}^1 = \alpha_a \mathbf{U}_a$):

$$\frac{\partial \alpha_a}{\partial t} + \nabla \cdot (\alpha_a \mathbf{U}_a) = 0$$

and

$$\frac{\partial}{\partial t}(\alpha_a \mathbf{U}_a) + \nabla \cdot (\alpha_a \mathbf{U}_a \mathbf{U}_a + < \mathbf{Q}_a >) = < \mathbf{A}_a > + < \mathbf{P}_a >,$$

being $<\mathbf{A}_a>$, $< \mathbf{P}_a >$, and $< \mathbf{Q}_a >$ respectively the average acceleration term, the collision term and the collisional contribution to the flux. We notice that

$$< \mathbf{Q}_a > = < \boldsymbol{\tau}_{a,coll} > + \mathrm{tr} < \mathbf{Q}_a > \mathbf{I},$$

where the last term represents the particle pressure p_a . We then recast the equation for the mean momentum in the form

$$\frac{\partial}{\partial t}(\alpha_a \mathbf{U}_a) + \nabla \cdot \mathbf{F} = -\nabla p_a + < \mathbf{A}_a > + < \mathbf{P}_a >,$$

where **F** is the sum of the kinetic flux and the off-diagonal part of the collisional flux. We notice than, that

$$\nabla p_{\mathrm{a}} = G(\alpha_{\mathrm{a}})\nabla\alpha,$$

where $G(\alpha_{\mathrm{a}})$ is the partial derivative of the particle pressure with respect to the phase volume fraction, given, in general, for QMOM by

$$\frac{\partial p_{\mathrm{a}}}{\partial \alpha_{\mathrm{a}}} = \frac{\partial}{\partial t}\left[\alpha_{\mathrm{a}}\Theta_{\mathrm{a}} + \frac{g_0}{3}\sum_{i=1}^{\mathrm{N}}\sum_{j=1}^{\mathrm{N}}(1+e_{ij})\alpha_{\mathrm{a},i}\alpha_{\mathrm{a},j}g_{i,j}^2\right],$$

and, in case the restitution coefficient e_{ij} does not depend on the collision velocity, and only one species is present, by

$$\frac{\partial p_{\mathrm{a}}}{\partial \alpha_{\mathrm{a}}} = \frac{\partial}{\partial \alpha_{\mathrm{a}}}\left[\alpha\Theta_{\mathrm{a}} + 2\alpha_{\mathrm{a}}^2\Theta_{\mathrm{a}}(1+e)g_0\right]$$

which is the same expression used in hydrodynamic models with kinetic theory closures, where Θ_{a} is the granular temperature and g_0 the radial distribution function.

At this point, it is possible to reformulate the equation for the zero-order moment by first predicting the flux from the equation of the first-order moment, using information from the previous time-step, and replacing the expression for the flux in the equation for M^0, so that the force balance is directly included into it. The first step is to write the semi-discretized equation for the first-order moment, whose explicit form will clearly depend on the approach used to discretize the momentum coupling term. For simplicity, we include all the effects in a symbolic term, with the exception of the particle pressure:

$$\mathbb{A}_{\mathrm{a}}\mathbf{U}_{\mathrm{a}} = \mathbb{H}_{\mathrm{a}} - \frac{1}{\rho_{\mathrm{a}}}\nabla p_{\mathrm{a}} + \mathbf{F}_{\mathrm{a}}$$

$$\mathbf{U}_{\mathrm{a}} = \frac{\mathbb{H}_{\mathrm{a}}}{\mathbb{A}_{\mathrm{a}}} - \frac{1}{\rho_{\mathrm{a}}\mathbb{A}_{\mathrm{a}}}\nabla p_{\mathrm{a}} + \frac{\mathbf{F}_{\mathrm{a}}}{\mathbb{A}_{\mathrm{a}}}$$

where $\mathbf{F}_{\mathrm{a}}$ contains all the force terms strongly dependent on the phase volume fraction, and the pressure gradient, while $\mathbf{H}_{\mathrm{a}}$ includes the remaining terms. Interpolating this velocity on cell faces gives origin to the face velocity:

$$\phi_{\mathrm{a}} = (\mathbf{U}_{\mathrm{a}})_{\mathrm{f}} = \widetilde{\phi}_{\mathrm{a}} - \left(\frac{1}{\rho_{\mathrm{a}}\mathbb{A}_{\mathrm{a}}}\right)_{\mathrm{f}}|\mathbf{S}|\nabla^{\perp}p_{\mathrm{a}}$$

Observing that the equation for the zero-order moment can be written as

$$\frac{\partial \alpha_{\mathrm{a}}}{\partial t} + \nabla\cdot(\alpha_{\mathrm{a,f}}\phi_{\mathrm{a}}) = 0$$

which, substituting the expression for the face velocity, becomes

$$\frac{\partial \alpha_{\mathrm{a}}}{\partial t} + \nabla \cdot \varphi_{\mathrm{a}}^{*} = \nabla \cdot \left[\alpha_{\mathrm{a,f}} \left(\frac{G(\alpha_{\mathrm{a}})}{\rho_{\mathrm{a}} \mathbb{A}_{\mathrm{a}}} \right)_{\mathrm{f}} |\mathbf{S}| \nabla^{\perp} \alpha_{\mathrm{a}} \right]$$

where $\varphi_a^* = (\alpha_a \mathbf{U}_a)_f$. It is worth noticing that, since we are interested in preserving the positive features of the kinetic flux discretization, the divergence term on the left-hand side is treated fully explicitly, as already done in QMOM, including the effect of the non-diagonal terms of the collisional stress tensor, but without adding to φ_a^* the isotropic component of that tensor, since they are accounted for in the term on the right-hand side, which is discretized explicitly.
The solution procedure is then modified as follow

- The particle-pressure derivative is updated, based on information from the previous iteration.
- The modified equation for the zero-order moment is solved. Notice that the solution at this stage avoids inconsistencies in the value of the phase fraction in the rest of the solution procedure.
- Based on the updated value of the phase volume fraction, the remaining set of equations is solved to obtain the moments of order equal or greater than one.

A convenient modification to the above procedure is to introduce under-relaxation for the equation of the zero-order moment, and perform sub-iterations on the equations for the zero- and first-order moment, until convergence, and then obtain the higher-order moments with a single solution step, using the updated, and stabilized, values of the phase volume fraction.

The approach has been tested considering a one-dimensional problem of particles falling due to the effect of gravity. Particles are initially located at a certain distance from the bottom of the computational domain, represented by a no-slip wall. Gravity and fluid drag act on the particles, which settle on the bottom of the container. The initial stage of the simulation is shown in Fig. 242, and the axial volume fraction profile after 1s of simulation is reported in Fig. 243. It is possible to see that the phase is completely settled, and the concentration profile is well defined, properly showing the steep gradient at the interface without oscillations.

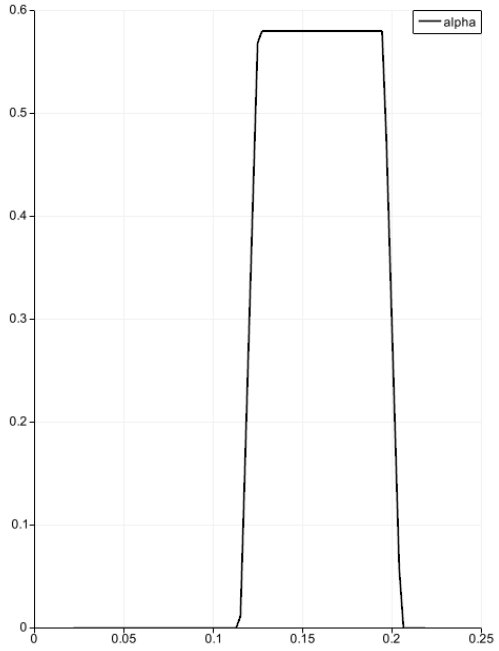

Figure 242. *Initial volume fraction profile (t = 0). Axial position on the horizontal axis.*

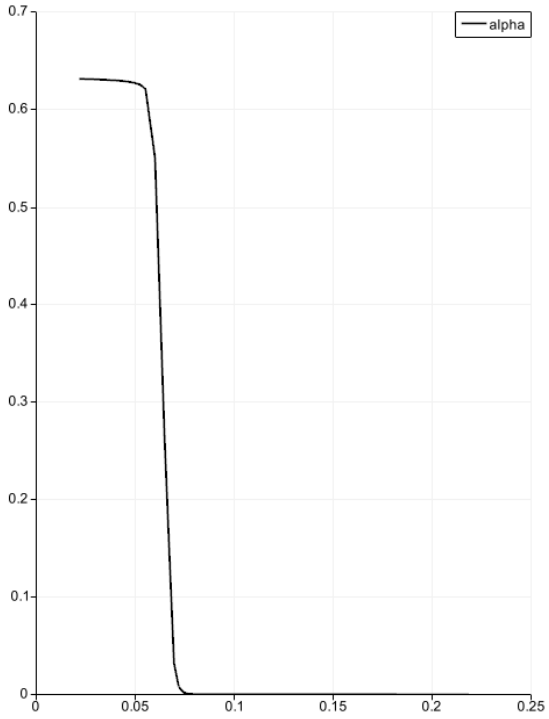

Figure 243. *Final volume fraction profile (t = 1s). Axial position on the horizontal axis.*

Polydisperse Riser Flow: The QMOM implementation into MFIX has been further validated considering a three-dimensional riser, and comparing the predictions of the model with the experimental data of He et al. (2009) in the same system. The computational domain considered in this work represents only a portion of the whole riser examined in the experiments, in the center of the column, with a height L (0.030 m), as represented by the dashed volume in Fig. 244. The other dimensions are W = 0.05 m and D = 0.015 m. The fluid phase is air at ambient temperature, while the particle phase is constituted by mono-disperse particles with diamenter of 335μm, density of 2500 kg/m^3, restitution coefficient e_p = 0.97.

Periodic boundary conditions were imposed at the top and bottom of the computational domain, while no-slip conditions were used for the fluid phase at the wall, and reflective conditions were used for the particle phase.

The fluid-phase mass flux was imposed to match the mean particle mass flux G_s of 10 kg/(m^3 s), by adapting the pressure gradient along the height of the computational domain. The grid density used in the simulations, taken from the work of He et al. (2009), is 25 grid points along W, 60 along L and 10 along D. Since the domain is periodic, averages are computed assuming the z direction to be homogeneous, and considering a symmetry plane, located at W/2, normal to the x direction. The RMS values are found by subtracting the time-averaged values from the instantaneous fields, and time averaging the square of the differences. The final RMS value are then the square root of time-averaged square differences. As convergence criterion for all the variables of the fluid-phase, a reduction of the residuals below 10^{-4} was required to consider the solution converged.

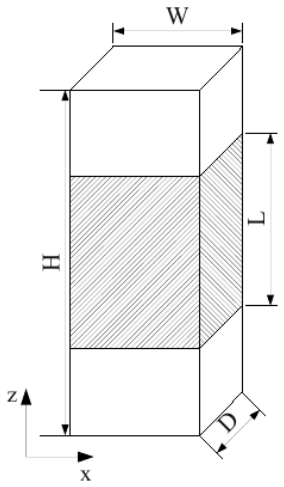

Figure 244. *Schematic representation of the riser.*

An example of the instantaneous solids volume fraction field at t = 8 s obtained in the simulation performed using the quadrature-based moment method is reported in Fig. 245.

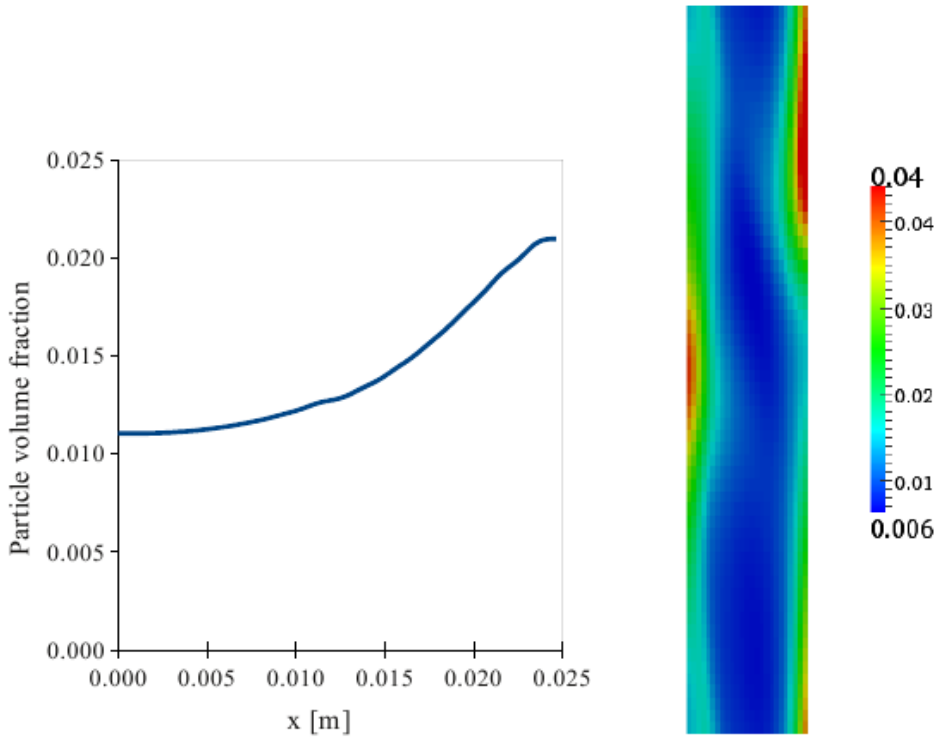

Figure 245. *Time-averaged particle volume fraction profile and instantaneous countour plot at t = 8s, across the centerline (D/2)**.***

It can be seen that particles segregated at the walls of the riser, forming ensembles at higher volume fraction, which tends to move downward, since their weight wins over the resistance exerted by the fluid. As explained in Passalacqua et al. (2010), the flow evolves from the uniform initial conditions through an intermediate state where particles, due to the reflective conditions at the walls, tend to originate two vertical stripes parallel to the walls, with lower particle concentration. In these stripes the fluid accelerates, and the difference in shear causes the flow to become unstable. The instability quickly propagates to the whole flow, leading to the segregation of particles typically observed in riser flows. The time-averaged volume fraction (experimental data is not available for this quantity), is lowest in the center of the flow and highest at the walls, which is typical of core-annular flow.

Results of the time-averaged components of the velocity obtained in the simulation performed using the quadrature-based moment method are reported in Fig. 246 and compared with the experiments of He et al. (2009). In all the reported plots, x = 0 represents the channel centerline, and x = 0.025 m indicates the channel wall. The predicted values of the axial velocity show a core-annular behavior, with negative values at the wall, indicating particles fall in that region of the system, and positive values in the center of the riser. Results are in acceptable agreement with the experimental measurements of He et al. (2009), and similar to those obtained by the same authors performing Lagrangian simulations.

The convergence of the averages is considered satisfactory, in spite of the relatively short averaging time, since the values of the time-averaged velocity along the x direction, are

approximately zero, as expected when the flow reaches the steady-state condition. Note that for the experiments, the x velocity is not exactly zero, indicating that either the flow is not fully developed at this z location in the flow or that the experimental accuracy is of the order of the measured x velocity.

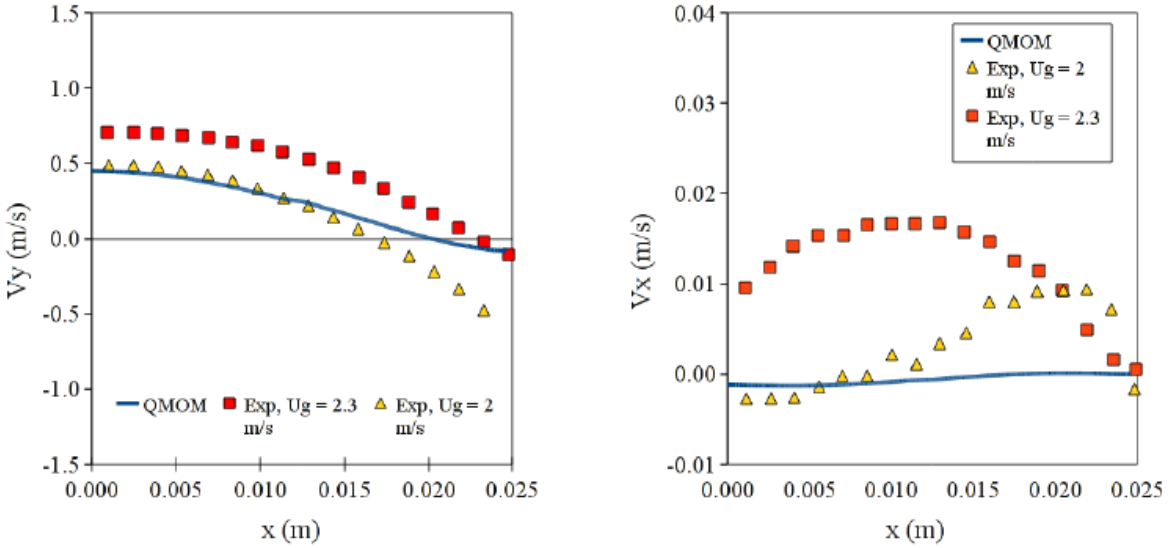

Figure 246. *Time averaged z (left) and x (right) components of the particle velocity.*

The root-mean-square (RMS) of the vertical component of the velocity of the particle phase is reported in Fig. 247 (left), and is in qualitative agreement with the experiments of He et al. (2009), but not in quantitative agreement. Both the experimental and the computational profiles show a minimum at the riser centerline, and the maximum value in proximity of the wall, but at a certain distance from it. The RMS velocity in the x direction, reported in Fig. 247 (right) is in quantitative agreement with the experimental data. Differences in the numerical predictions compared to the experimental data might depend on the simplified numerical configuration used in the simulation, where only one portion of the system is considered, and periodicity is assumed in the axial direction. Further reasons that could explain the differences are the choice of the drag law, as well as other sub-models used in the numerical model, and the systematic errors in the experimental measurements (He et al. 2009).

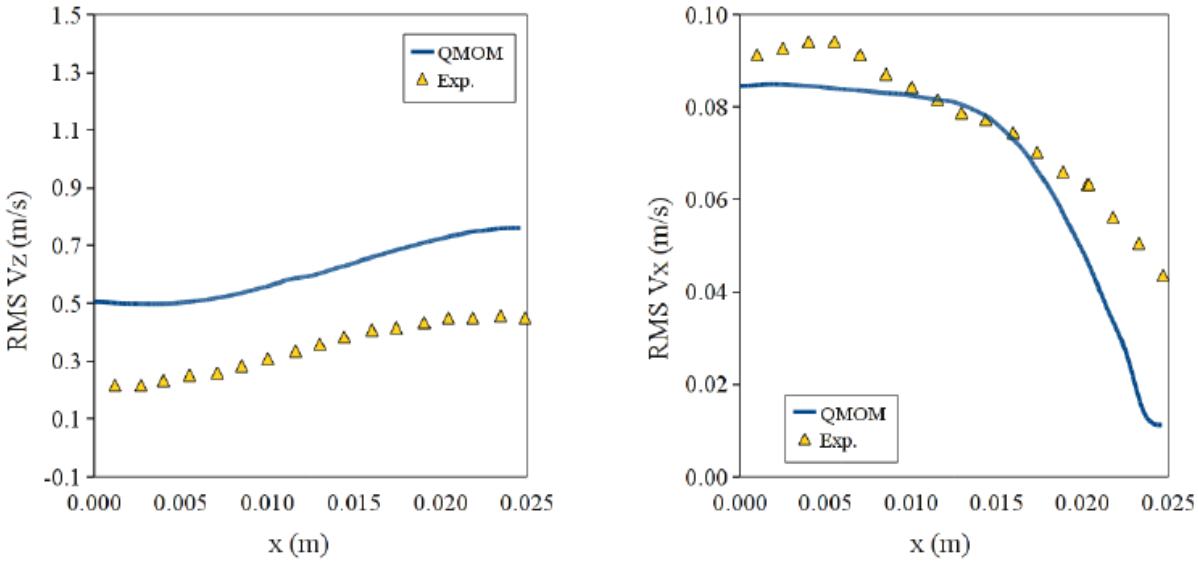

Figure 247. *RMS of the z (left) and x (right) velocity components of the particle velocity.*

The time-averaged granular temperature is reported in Fig. 248 (left). (Note that the granular temperature is not related to the RMS velocity statistics!) The values of Θ_p present a minimum at the wall of the channel, where the collision frequency is higher due to higher particle concentration, due to particle segregation, and a maximum in the core of the riser, where the flow is dilute and collisions are not predominant, as shown by the plot of the Knudsen number in Fig. 248 (right).

Before proceeding to consider the behavior of the Knudsen number in detail, it is worth noticing that the flow is in transonic conditions, meaning that there are parts of the computational domain where the particle velocity is above or equal to the local particle-phase speed of sound (Ma > 1), and other parts of the system where the particle velocity is below the the local value of the speed of sound (Ma < 1). This is evident from the values of the time-averaged local particle Mach number $Ma = |U_p|/\Theta_p^{1/2}$ in Fig. 249, which shows the Ma is approximately between 6×10^{-3} and 1.8. Under these conditions, two regimes are present in the system. Where Ma < 1, the flow is dominated by diffusive processes, regulated by the local value of the granular temperature, which has to be used to compute the characteristic velocity in this regime. When Ma > 1, the flow is dominated by convective phenomena, meaning that the transport of properties is mainly due to the convective transport of particles more than to diffusive phenomena, and the granular temperature has to be replaced by the local mean velocity magnitude in the definition of the characteristic velocity of the flow. The two zones are separated by a dashed line in Fig. 249 (left). Since the flow undergoes a transition between two different regimes, the definition of the Knudsen number is based on the mean particle velocity in the regions where Ma > 1, while it is based on the square root of the granular temperature when Ma < 1.

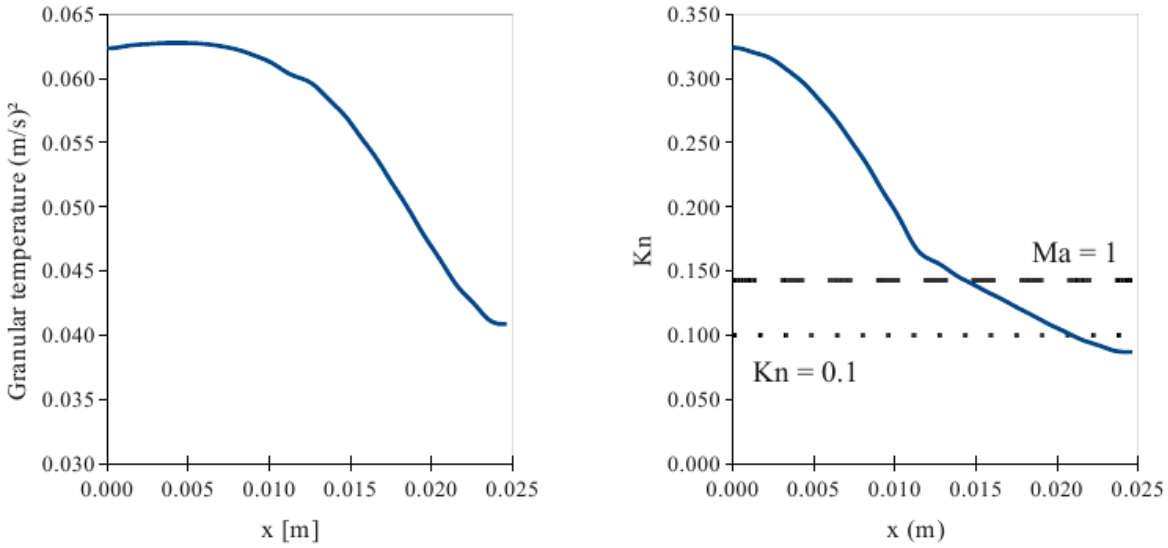

Figure 248. *Time-averaged granular temperature (left) and Knudsen number (right).*

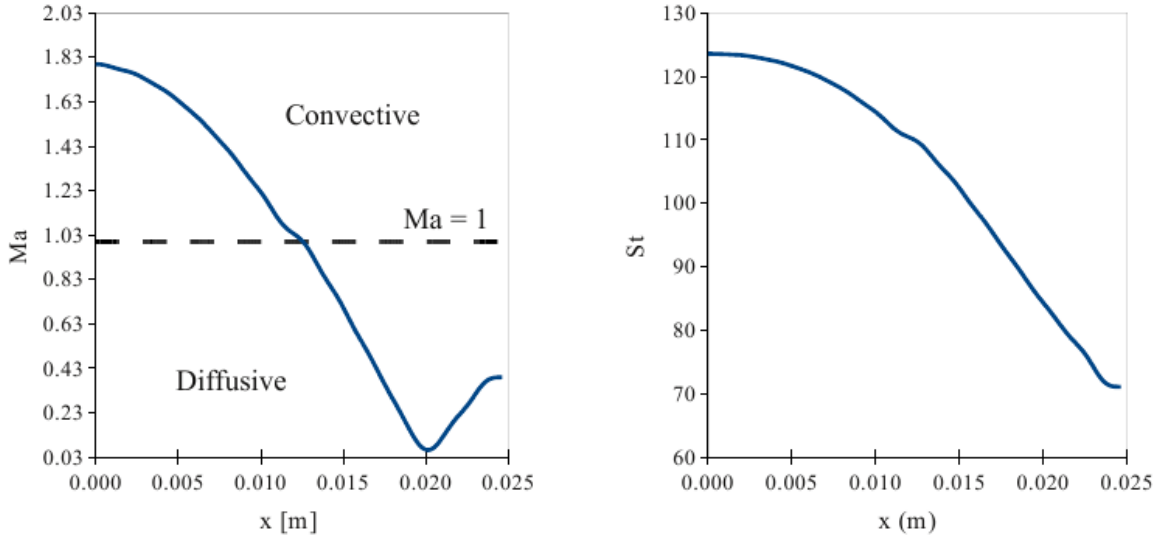

Figure 249. *Time averaged Mach number (left) and Stokes number (right).*

The values of the Knudsen number, computed assuming L = 2W D/(W + D), according to the definition of hydraulic diameter of the riser, are reported in Fig. 248 (right). The diagram shows the flow transitions from the slip regime, where 0.01 < Kn < 0.1 (Bird, 1994), in the region adjacent to the wall, to a more rarefied regime (transitional regime) in the center of the riser, where non-equilibrium phenomena are expected to happen. The two regions are separated by the dotted line. The lower value of Kn at the wall is justified by the higher particle concentration in that region of the system, which leads to higher values of the collision frequency, making the flow locally dominated by collisions. It is worth noticing that if an hydrodynamic model, derived

in the hypothesis of nearly zero Knudsen number (Continuum regime, Kn < 0.01) were used to perform the simulation, the adoption of partial slip boundary conditions would have been necessary to describe the behavior of the flow in the zone adjacent to the walls, where Kn < 0.1, however the model would have deviated from the correct behavior in the center of the riser, where higher values of the Knudsen number are present, and higher-order approximations of the kinetic equation than the hydrodynamic model are necessary. The Stokes number profile is reported in Fig. 249 (right), and reports values between 66.1 and 123.5, which indicate particles reaction to changes in the local conditions of the fluid flow are not instantaneous, but delayed and, since the flow is dilute, might lead to particle trajectory crossing. As pointed out in Desjardin et al. (2008), such phenomenon cannot be predicted by hydrodynamic models, since they only consider moments up to the second order, and define only one local velocity in each computational cell, whereas multiple local velocities are necessary to be able to capture the discontinuous velocity field that originates when particle trajectory crossing occurs. This becomes clear considering the particle velocity distribution function.

In addition to the validation work, the integration of QMOM into MFIX has been improved allowing non-uniform initial conditions and boundary conditions to be specified through the standard MFIX input file. Future work is needed to parallelize the code, enabling it to be run on DMP machines, which is a requirement to more computationally expensive validation cases, and to perform grid independence studies.

(Sundaresan reporting.) As part of subtask 4.6.3 we began by implementing the fluid-particle drag model developed in Task 2.2 into the MFIX software. This was performed at NETL by William Holloway under the supervision of Sofiane Benyahia. The implementation of the fluid-particle drag model was rigorously checked in the dilute and concentrated limits in a single cell to ensure that the limiting behavior of the drag model was correctly reproduced by the code.

Subtask 4.6.4: Effect of polydispersity on clustering (Sundaresan, Fox, and Hrenya).
The basic aim of this task is to answer the question: how does polydispersity affect clustering? More specifically, is the frequency/intensity of clustering enhanced, attenuated, or constant with a change in the particle size distribution? Also, do particles of one size tend to prefer the clustered regions while others prefer the dilute, or do they remain evenly distributed? The proposed tasks, intended for comparison with trends of PSRI data (via wavelet analysis of fiber optic probe and high-speed photography, if available), are:

(i) *3D simulations of riser flow with periodic boundaries (2D to be completed in Year 3 in conjunction with preliminary runs for INCITE proposal, as part of the existing validation task). Both KTGF (Hrenya & Sundaresan) and DQMOM (Fox) models will be pursued.*

(ii) *3D simulations of fully-developed riser flow with solid boundaries (2D to be completed in Year 3 in conjunction with preliminary runs for INCITE proposal, as part of the existing validation task). Both KTGF (Hrenya & Sundaresan) and DQMOM (Fox) models will be pursued.*

(Fox reporting.) The effort was then been concentrated in resolving a few numerical difficulties met while using the QMOM algorithm for polydisperse cases in MFIX. These difficulties were represented by sudden interruption of the numerical solution at random simulation times, and by corrupted solution with unphysical property profiles (volume fraction, velocities, …). The source of these problems was identified in an erroneous implementation of the multi-species Boltzmann collision integral, and has been corrected.

Additionally, to reduce the computational cost for bi-disperse computations, a linearized multi-species collision operator, based on the work of Andries et al. (2002) was added to MFIX. This model, even if simplified compared to the Boltzmann collision integral, maintains the fundamental properties of the collision operator:

- It ensures the number density function stays positive
- It satisfies the principle of indifferentiability, according to which, if particles of different species are identical, the behavior has to be the same of a single-specie case.
- The distribution function at equilibrium is non-isotropic Maxwellian.
- The H-theorem on the irreversible entropy growth holds.

This model has been validated showing its predictive capabilities in describing the homogenous cooling state. In particular, it was shown that the model reproduces the trend of the temperature ratio as a function of the mass ration in agreement with molecular dynamics results, while it over-estimates the value of the temperature ratio as a function of the particle diameter ratio.

A simple test case to check the implementation was considered, constituted by a square domain of 0.1 x 0.1m, with periodic boundary conditions in the horizontal and vertical directions. A constant pressure gradient, sufficient to support the suspension was applied in the vertical direction. Two species were considered, with the following properties:

Property	**Value**
Particle density [kg/m3]	2500
Particle diameter – Specie 1 [µm]	650.0×10^{-6}
Particle diameter – Specie 2 [µm]	170.0×10^{-6}
Volume fraction – Specie 1	0.05
Volume fraction – Specie 2	0.05

A snapshot of the results is shown in the following pictures, obtained with a coarse computational grid of 64 x 64 points. A snapshot of the volume fraction contours is shown for both the species considered in the simulation. The simulation proceeded without observing numerical instabilities. Results show a high numerical diffusion, which however is explained by the relatively coarse computational grid used for testing purpose, to speed up the computation.

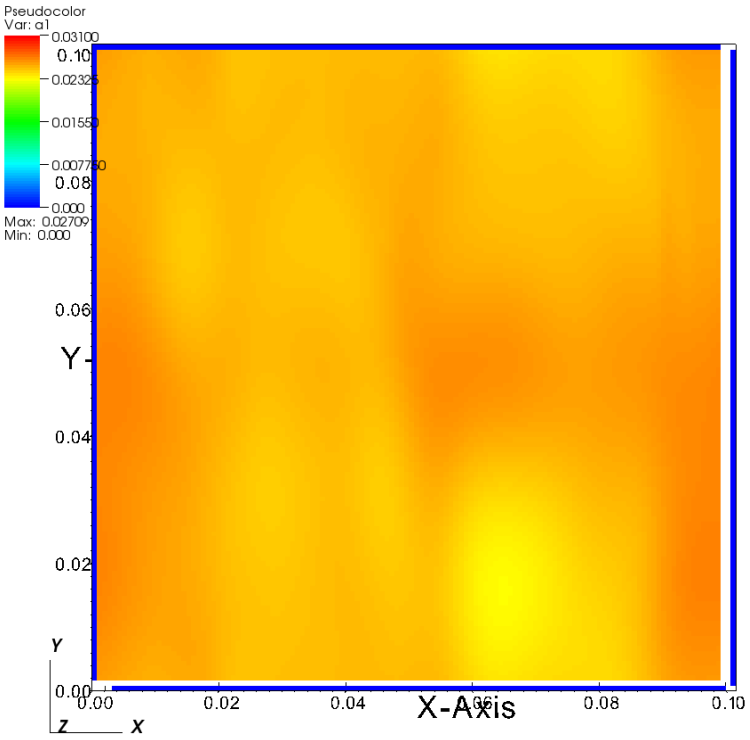

Figure 250. *Volume fraction contour plot of specie 1.*

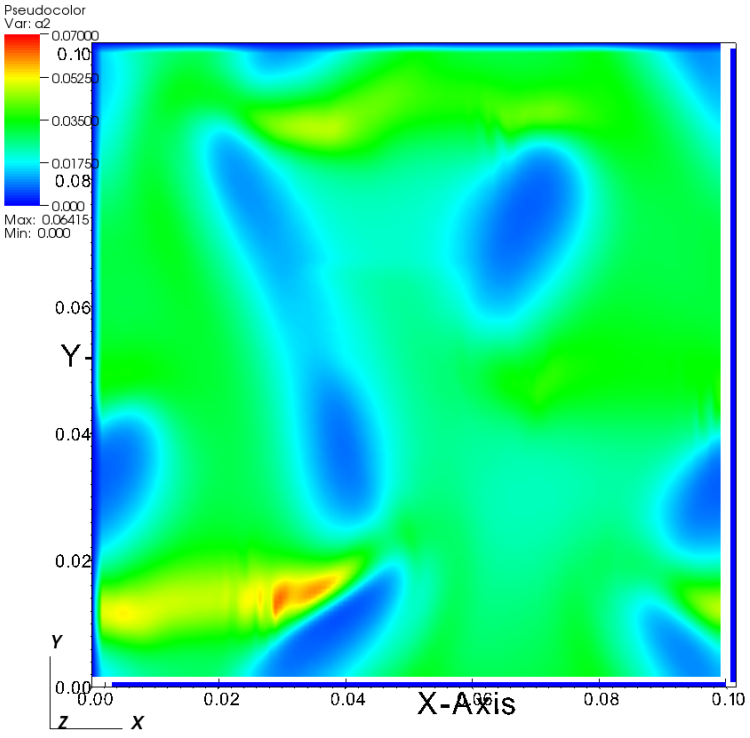

Figure 251. *Volume fraction contour plot of specie 2.*

The code validation effort proceeded with the comparison of simulations against the mono-disperse system of He et al. (2009), and on the validation of the implementation of QMOM for poly-disperse flows into MFIX against the experimental data of bi-disperse gas-particle flow provided by PSRI.

The mono-disperse case was already examined previously. We add here only the comparison with Lagrangian simulations performed by other authors on the same systems to compare with QMOM predictions. The simulated system is a three-dimensional axially-periodic channel with dimensions of 0.05m x 0.3 m x 0.015m. The fluid phase is air at ambient temperature. Particles have a density of 2500 kg/m^3, and a diameter of 335 μm. The solids mass flux is 10 kg/(m^2 s).

As it can be observed in Figure 252, QMOM simulations of the mono-disperse gas-particle flow predict the axial particle velocity in good agreement with Lagrangian simulations and experiments. The radial velocity however is under-estimated by QMOM compared to LE, the latter however shows a very noisy behavior, not always in good agreement with experiments. Figure 253 shows the particle RMS velocity. The radial RMS velocity predicted by QMOM is in good agreement with experiments, and in better agreement with experiments than the Lagrangian prediction. However, the axial RMS velocity is over-estimated by QMOM, while under-estimated by LE.

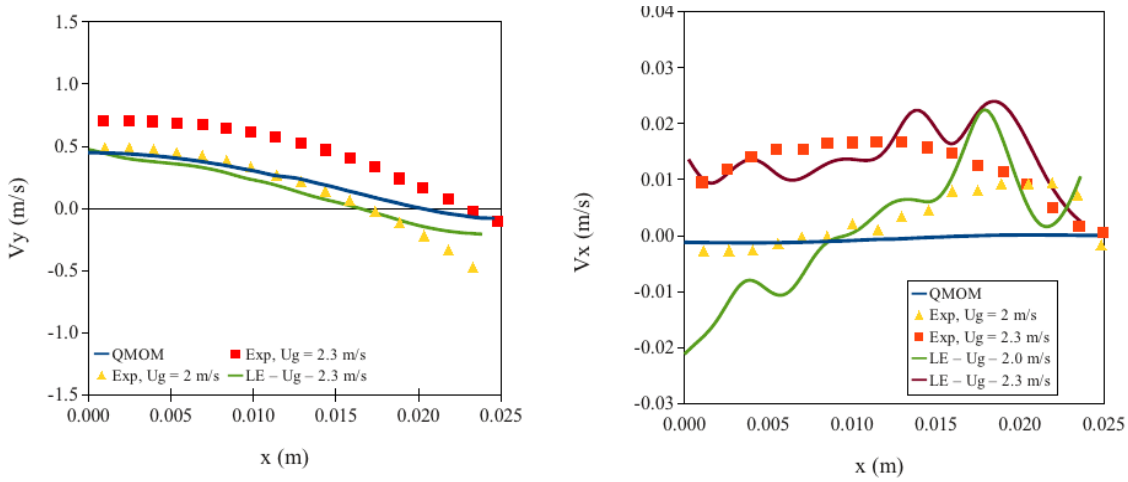

Figure 252. *Mean particle velocity.*

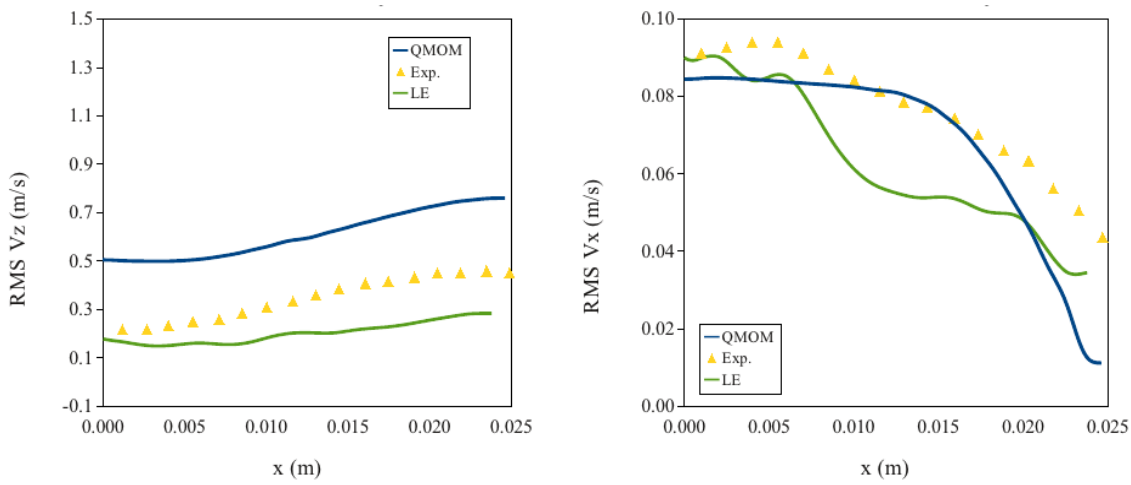

Figure 253. *Particle RMS velocity.*

The experimental system under consideration for the bi-disperse cases is constituted by a cylindrical riser, sketched in Fig. 254. The riser column is 18.3m high and has an internal diameter of 0.3m, with an elbow exit connecting to separation and recirculation systems.

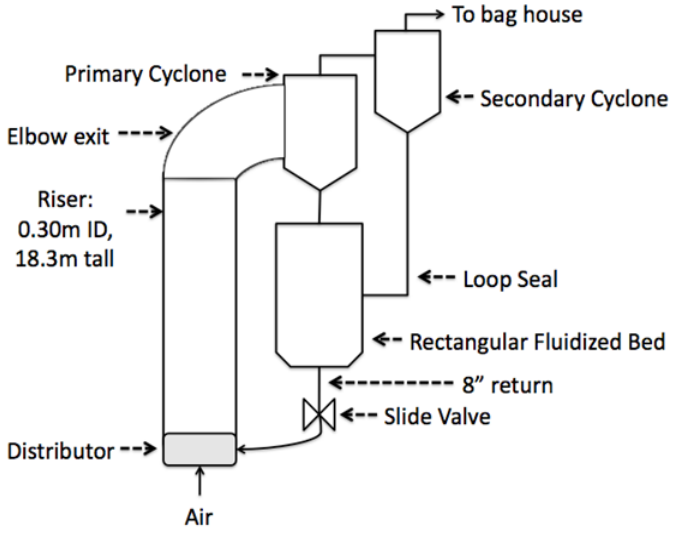

Figure 254. *Schematic representation of PSRI riser.*

The system is characterized by a geometrical structure that cannot be properly represented in the available code. Additionally, the large dimensions of the system does not allow a satisfactory spatial discretization to be obtained, in order to perform a parametric study. As a consequence, the system was simplified into a two-dimensional channel as shown in Fig. 255, where D = 0.30m, and H = 1m.

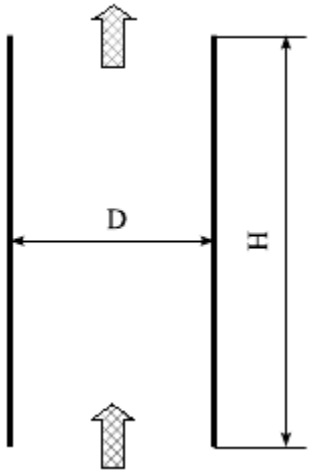

Figure 255. *Schematic representation of 2D channel.*

The bi-disperse mixture was composed by particles with density of 900 and 2500 kg/m^3, and diameter of 170 and 650µm, depending on the case. The mass loading was chosen to be equal to 16. A particle-particle restitution coefficient of 0.99 was used. The fluid velocity was set to 13.6 m/s. Six cases are being considered, as shown in Table 22, where ρ is the density, d_p the particle diameter, and φ is the phase fraction.

Table 22. *List of Test Cases.*

Case n.	ρ_{s1} [kg/m^3]	ρ_{s2} [kg/m^3]	d_{p1} [µm]	d_{p2} [µm]	φ_1/ φ
1	2500	2500	650	170	0.25
2	2500	2500	650	170	0.50
3	2500	2500	650	170	0.75
4	2500	650	650	650	0.25
5	2500	650	650	650	0.50
6	2500	650	650	650	0.75

Simulations were performed imposing a perturbed initial condition to favor the development of the flow, and using MFIX automatic time-stepping functionality. Periodic boundary conditions were adopted in the vertical direction, while reflective conditions were used to describe walls. A computational grid of 60 x 100 points was used. The simulation time was decided based on the convergence of the time-averaged solution, which depends on the case under consideration. Averaging was started after the flow was fully developed and performed over 15 seconds.

Since only a portion of the original riser is considered, only the property variation along the radius of the channel is compared against PSRI data, who reported the species segregation for different operating conditions.

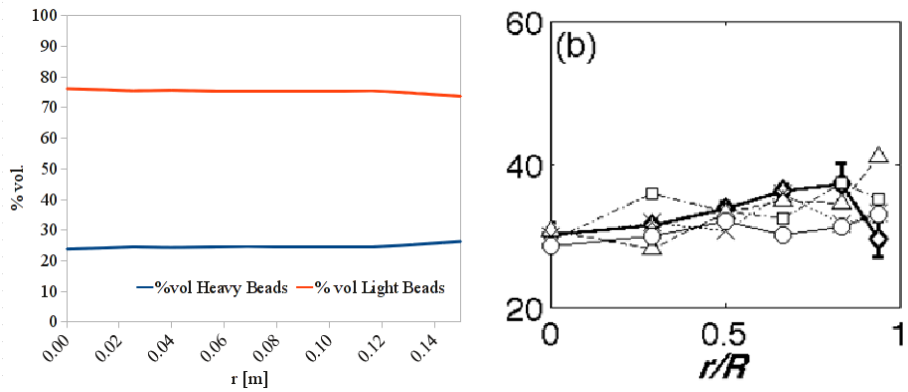

Figure 256. *Density segregation profiles: QMOM (right) and experiments (right).*

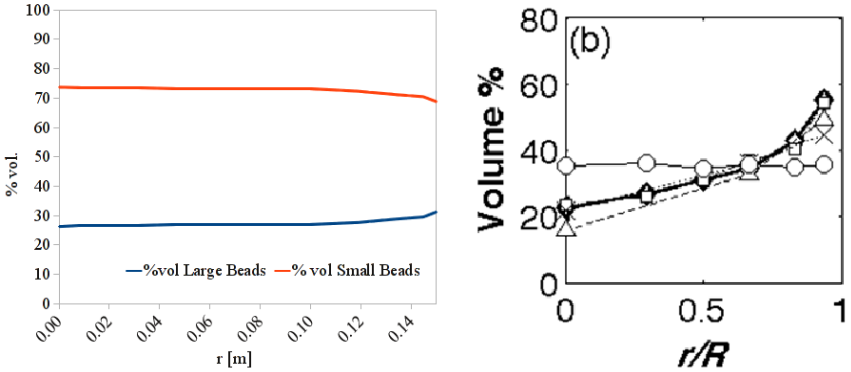

Figure 257. *Size segregation profiles: QMOM (right) and experiments (right).*

Figure 256 shows the species segregation profiles predicted by QMOM in the case of a binary mixture with density difference between the two species, compared. It can be observed that almost no species segregation is observed in QMOM simulations under these operating conditions. Only a slight increase in the percentage of the heaviest species is observed near the wall of the channel, and a lower concentration of the same species is present at the centre of the system. Size segregation profiles of each species are shown in Figure 257, which shows size segregation is predicted, however the intensity of the segregation in the simulations is significantly lower than what observed in the experiments. Only two of the six considered cases are reported, however the trends observed in Figs. 256 and 257 are very similar to those of other cases.

The effect of the computational grid, of the simplifications made to the geometrical configuration and of the model parameters must be further investigated to interpret the differences between the experimental results and the simulations.

(Sundaresan reporting.) An exploratory study was conducted where the predictions of the polydisperse kinetic theory model developed by Garzó *et al.* (2007a,b) (GHD) were compared with the polydisperse kinetic theory model of Iddir and Arastoopour (2005) (IA) for different binary particle size distributions in periodic domains using the polydisperse fluid-

particle drag model developed in Task 2.2. The GHD theory follows a *mixture*-based approach where separate continuity equations are solved for each particle phase, but a single momentum balance and a single granular energy equation are solved for the particle mixture. These are supplemented by algebraic models for the diffusive flux of each particle type relative to the particle mixture, and algebraic constraints on the individual species granular temperatures. In contrast, IA kinetic theory uses a *species*-based approach where continuity, momentum and granular energy equations are developed for each particle type. Thus, the IA theory contains a larger number of differential equations than the GHD theory. To compare these two modeling approaches, we performed simulation of gas-fluidization of binary mixtures of particles using both models; such simulations were performed in periodic domain and fine grids were employed to ensure that the domain-averaged statistics were essentially independent of grid size. It was shown that both kinetic theory model frameworks admit qualitatively similar domain-averaged statistics. Moreover, the nature of the observed clustering patterns was found to be qualitatively similar. We then proceeded to establish a theoretical criterion to indicate when the *mixture*-based GHD kinetic theory can be expected give similar predictions to the *species* framework of IA theory. A detailed description of the work discussed in this paragraph can be found in a paper that was recently published in *Chemical Engineering Science* (see Holloway *et al.* (2011) in Appendix J).

Subtask 4.6.5: Comparison with PSRI data (Sundaresan, Fox, and Hrenya).
This task is targeted at a direct comparison of KTGF (Hrenya & Sundaresan) and DQMOM (Fox) model predictions with the suite of PSRI experiments conducted in Year 3. The subtasks include:

(i) *2D and 3D simulations of fully-developed riser flow to compare with trends of PSRI measurements. For example, how do local solids flux and PSD profiles change with input parameters (gas velocity, solids flux, PSD)? This will also be extended to developing flow in order for comparison of axial trends, to the extent allowable by computational resources.*

(ii) *Since the KTGF and DQMOM models are expected to be suitable in different regions of Knudsen number (Kn), a subset of the above simulations will be extended to lower and higher Kn (and other dimensionless parameters, time permitting) to test the relative performance of these models. Note that clustering systems are expected to have a combination of Kn – low Kn in the dilute region and dense region, with high Kn across the dilute/cluster interface.*

(iii) *Time permitting, 2D and 3D simulations of riser with PSRI exit geometry will be performed, for comparison with experimental trends. For example, are experimental observed asymmetries predicted near exit? Is reverse core-annular flow predicted with larger particles, similar to experimental data?*

(Fox reporting.) The validation of QMOM continued considering the laboratory scale circulating fluidized bed studied by Mathiesen et al. (2000), who reported experimental measurements of the particle properties (velocity, volume fraction), and the predictions obtained with a conventional Euler-Euler multi-fluid model with kinetic theory closures for the particle

phase. Such a system was selected since its size allowed reasonable computational time and the adoption of a proper discretization of the computational domain. The same system was recently considered in a numerical study with Euler-Lagrange methods by He et al. (2009). The published results of the Lagrangian simulations are used in this work for comparison with the predictions with QMOM, together with the experiments of Mathiesen et al. (2000).

The circulating fluidized bed system under consideration is 0.032 m wide and 1 m tall, with a depth of 0.0012 m. He et al. (2009) showed that the system can be successfully represented with two-dimensional calculations without significant loss of accuracy in the numerical predictions, as a consequence only two-dimensional calculations were considered. Additionally, He et al. (2009) only simulated the central portion of the riser, considering only 0.3 m of the total height. The same approach is adopted here. The domain was discretized with 25 cells in the horizontal direction and 60 cells in the vertical direction. The fluid phase is air at ambient temperature (ρ_g = 1.2 kg/m^3, μ_g = 1.8 x 10^{-5} Pa s), with a mean superficial velocity of 1 m/s. Two particle types are present in the riser, both with a density of 2400 kg/m^3, but with different sizes: d_{p1} = 120 µm, and d_{p2} = 185 µm. The initial conditions are specified to be uniform, with each particle phase volume fraction fixed at 0.0125. The simulation was performed for 20 s, averaging on the last 15 seconds.

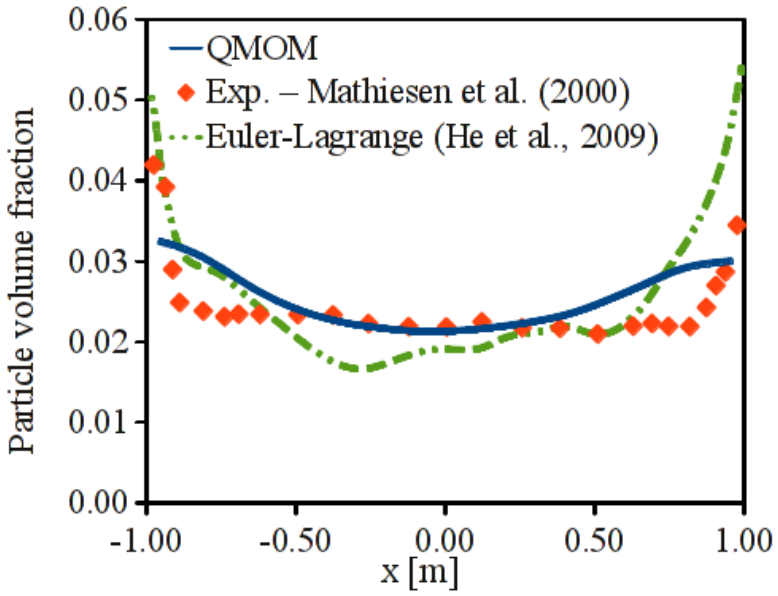

Figure 258. *Total volume fraction of the particle phase.*

Fig. 259 reports the total volume fraction of the particle phase, and compares it with the experimental measurements of Mathiesen et al. (2000) and the Euler-Lagrange simulations of He et al. (2009). The numerical simulations performed with QMOM predict particle segregation in fair agreement with the experimental data, showing the formation of a core-annular structure, as expected in riser flows. However the particle concentration at the wall is slightly under-estimated, even though experimental data are not perfectly symmetric, due to the original configuration of the experimental system, where particles are fed by means of an injection on one side of the riser.

Similar results were obtained if the volume fraction of the particles with d_{p1} = 120 µm is considered, as shown in Fig. 259, which shows the values predicted by QMOM are in good agreement with both the Euler-Lagrange predictions and the Euler-Euler predictions of Mathiesen et al. (2000). Experimental measurements were not available for this quantity.
A significantly different behavior is observed in Fig. 260, which reports the volume fraction of the heaviest particles. QMOM simulations predict almost no particle segregation, in agreement with what is observed already by Mathiesen et al. (2000) with their Euler-Euler simulations. Note that the comparison with Mathiesen's simulations can only be qualitative, since their numerical configuration is different from the numerical configuration used by He et al. (2009) and reproduced in this work. QMOM predictions however are not in agreement with the Lagrangian results provided by He et al. (2009), where significant radial segregation is observed.

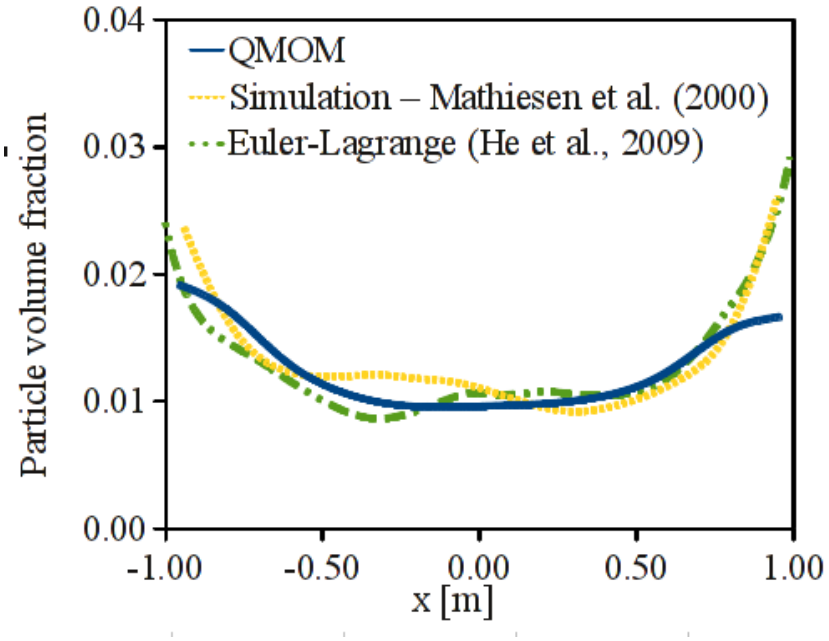

Figure 259: *Volume fraction of particles with d_{p1} = 120 µm.*

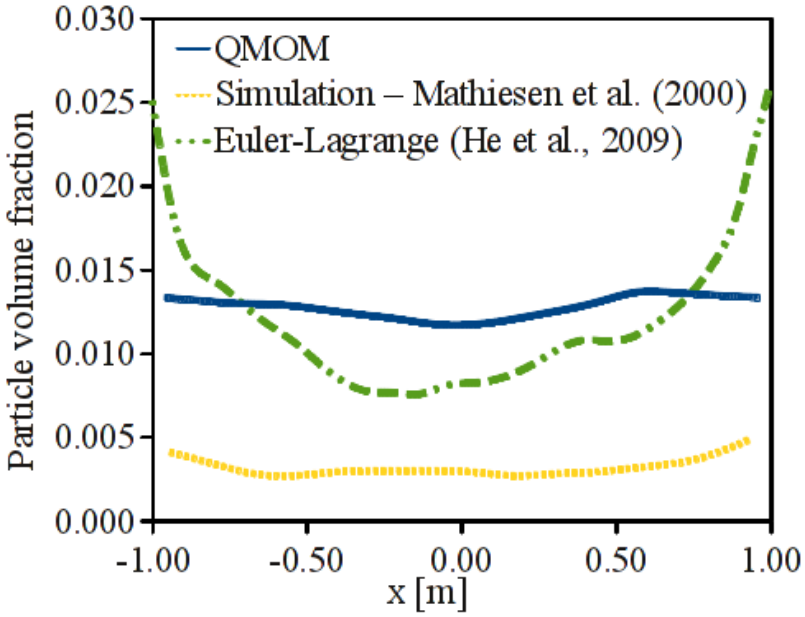

Figure 260. *Volume fraction of particles with d_{p1} = 185 µm.*

Figure 161 shows the velocity of the particles with diameter of 120 µm. QMOM predictions provide a quantitative prediction of the negative particle velocity at the wall in agreement with both the Euler-Lagrange prediction and the Euler-Euler predictions of Mathiesen et al. (2000). The predicted value of the particle velocity at the wall agrees well also with the experimental data, which, however, are not symmetric and provide two different values at the sides of the riser. QMOM over-estimates the particle velocity at the centre of the riser. This cannot be explained considering difference in the drag law, since the same correlation adopted by He at al. (2009) was used. However, He and co-workers modeled the fluid-phase turbulence with a sub-grid scale model (which would tend to flatten the mean velocity profile), while turbulence effects were neglected in the QMOM simulation.

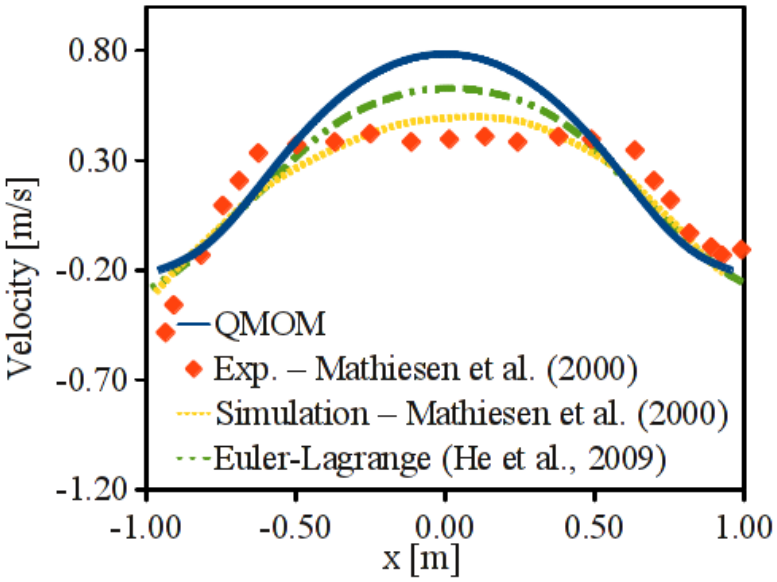

Figure 261. *Velocity of particles with d_{p1} = 120 µm.*

The velocity of particles with diameter of 185 µm is reported in Fig. 262. QMOM simulations are in agreement with the Euler-Euler simulations of Mathiesen et al. (2000), and predict the velocity near the walls and at the centre of the riser in agreement with the experiments, since the same observations done above on the asymmetry of the experimental data apply. In general however, the values of the velocity predicted by QMOM for this type of particles are under-estimated in comparison to other simulations and published results.

To conclude, QMOM simulations were performed considering the bi-disperse riser flow of Mathiesen et al. (2000). QMOM satisfactorily predicts both the volume fraction profiles and the velocity profiles in qualitative agreement with experimental data and Euler-Lagrange simulations of He et al. (2009). Quantitative agreement was observed for the total volume fraction profiles, the volume fraction profiles of the smallest particles, and the wall velocity of both particle species. Particle velocity was over-estimated at the center of the riser for the smallest particles, and under-estimated for the largest particles. No significant segregation was observed for the largest particles.

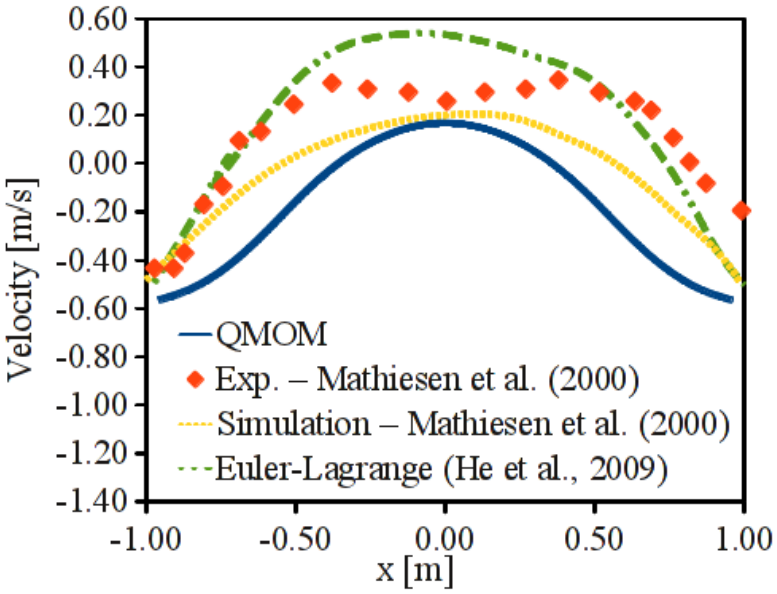

Figure 262. *Velocity of particles with d_{p1} = 185 µm.*

Electrostatic Model Implementation in MFIX

An electrostatic force was added to the acceleration term. The electrostatic model equations are

$$F_{qx} = -q_{s\alpha}\varepsilon_{s\alpha}(\nabla\varphi)_x$$

$$\nabla.(\varepsilon_m \nabla\varphi) = -\frac{\sum_{\alpha=1}^{N}\varepsilon_{s\alpha}q_{s\alpha}}{\epsilon_0}$$

As a consequence, an additional Poisson equation is solved using the PDE solver already available into MFIX.

An electrostatic separation case is simulated using a binary system in a vertical channel. The geometry is two-dimensional; with two parallel plates separated by a width of 0.1 m and height of 1.0 m. Periodic boundary conditions are applied in the flow direction, ensuring a constant mass flow rate of the gas phase. Walls are assumed to have equal and opposite non-zero electric potential. Specular reflective boundary conditions for the particle phase are assumed. The full Boltzmann collisional integral is solved to compute the collisions between the two species.

The particle density is 2400 kg/m^3, each species has a particle volume fraction equal to 0.0125, and the particle size is assumed to be the same (120µm) for both the species. The particle charge is 1.0 x 10^{-5} C/m^3 (species 1 is positively charged and species 2 is negatively charged). The potential on the left wall is set to -10000 V, while the one on the right wall is set at 10000 V.

At time zero, species 1 and species 2 are uniformly distributed. Species 1 is positively charged and species 2 is negatively charged. The left wall boundary condition has a negative and the right wall a positive electric potential. The contours of particle volume fraction at two flow times are shown in figure 263 and figure 264.

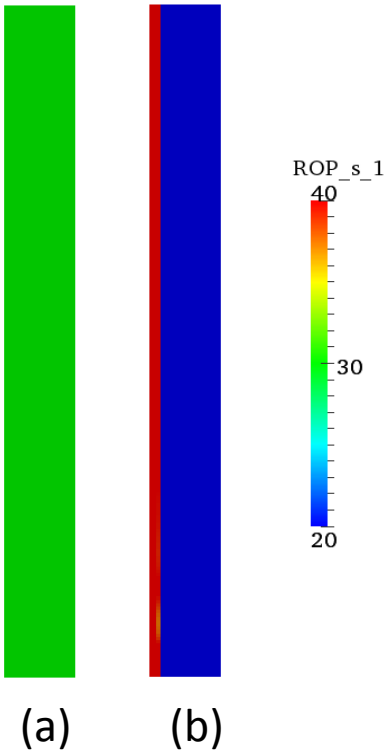

Figure 263. *Contours of species-1 volume fraction: (a) Time = 0.0 sec (b) Time = 0.15 sec.*

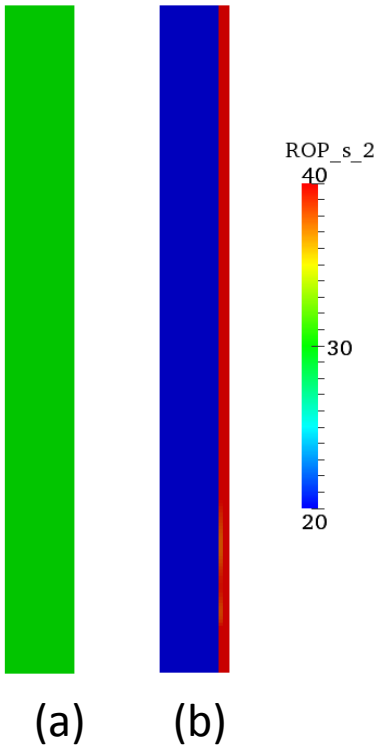

Figure 264. *Contours ofspecies-2 volume fraction: (a) Time = 0.0 sec (b) Time = 0.15 sec.*

As expected, the positively charged of species 1 segregated towards the left wall, where a negative potential is applied and similarly the negatively charged of species 2 segregated towards the right wall, where a positive potential is applied. The time for separation of the charged species is dependent upon the charge of the species and the applied potential at the wall. The simple test case illustrated that the implementation correctly captures the physical behavior of charged particles.

(Sundaresan reporting.) As part of subtask 4.6.5 we turned to the validation of the GHD polydisperse kinetic theory based model with the fluid-particle drag model developed in Task 2.2 against the experimental PSRI data set for binary systems gathered as part of Task 4.5. The large size of the PSRI riser make highly resolved full-scale simulations infeasible. Consequently, it was decided by the project team that we should perform fine scale simulations of binary gas-particle flow in axially periodic domains in order to compare the radial segregation profiles obtained from simulation with experimental results from the PSRI riser experiments with different binary particle size distributions. A list of test cases can be found in Table 23. The first three cases highlighted in red are intended to examine the species segregation behavior of differently sized particles, while the last three cases in blue are focused on interrogation of the species segregation behavior of different density particles.

Table 23. *List of two-dimensional simulations performed. Here, ρ_{si} is the density of the ith particle type, d_i is the density of the ith particle type, φ_i is the volume fraction of the ith particle type, φ is the total volume fraction, and U_s is the superficial velocity of the gas phase. In all simulations below a constant fluid density and viscosity was used, namely* $\rho_f = 1.3x10^{-3}\ g/cm^3$ *and* $\mu_f = 1.8x10^{-4}\ g/cm\ \ sec$.

	Axial length (cm)	Axial grids	Lateral length (cm)	Lateral grids	ρ_{s1} (g/cm^3)	ρ_{s2} (g/cm^3)	d_1 (cm)	d_2 (cm)	ϕ	ϕ_1	ϕ_2	U_s (cm/sec)
1	100	100	30	60	2.5	2.5	0.065	0.017	0.02	0.005	0.015	1350
2	100	100	30	60	2.5	2.5	0.065	0.017	0.02	0.01	0.01	1350
3	100	100	30	60	2.5	2.5	0.065	0.017	0.02	0.015	0.005	1350
4	100	100	30	60	2.5	0.9	0.065	0.065	0.038	0.009	0.029	1350
5	100	100	30	60	2.5	0.9	0.065	0.065	0.029	0.0145	0.0145	1350
6	100	100	30	60	2.5	0.9	0.065	0.065	0.024	0.018	0.006	1350

We have performed a set of 2D axially periodic channel flow simulations using GHD theory with the fluid-particle drag model developed in Task 2.2 (Holloway *et al.* (2010)) using free slip boundary conditions for the solid phases and a no-slip boundary condition for the gas phase. In the GHD theory model framework we have varied the coefficient of restitution to examine its impact on the observed degree of segregation. In addition, we have also performed 2D axially periodic channel flow simulation using IA kinetic theory to compare with the predictions of GHD theory. The lateral width of the channel in all cases was taken to be equal to the diameter of the riser used in the PSRI experiments. We find that bidisperse systems, be it density or size difference, exhibit core-annular flow behavior as evidenced in Figure 265 (a)-(f). It should be noted that here that the dimensionless position from the centerline of the channel is

denoted via the variable $\hat{r}\ (=r/R)$. In Figures 265 (a)-(c) we show the volume fraction profiles obtained from simulation of Case 2 (see Table 23) using GHD theory with a coefficient of restitution of 0.99 for Figure 265 (a), GHD theory with a coefficient of restitution of 0.90 for Figure 265 (b), and IA theory with a coefficient of restitution of 0.99 for Figure 265 (c). It is clear that all three different simulation results shown in Figures 265 (a)-(c) exhibit core annular flow behavior. In Figures 265 (d)-(f) we show simulation results for Case 5 (i.e. each particle species has a different density) where we have used GHD theory with a coefficient of restitution of 0.99 GHD theory with a coefficient of restitution of 0.90 for Figure 265 (e), and IA theory with a coefficient of restitution of 0.99 for Figure 265 (f). Again, a clear core-annular flow profile is evident for light and heavy particle species.

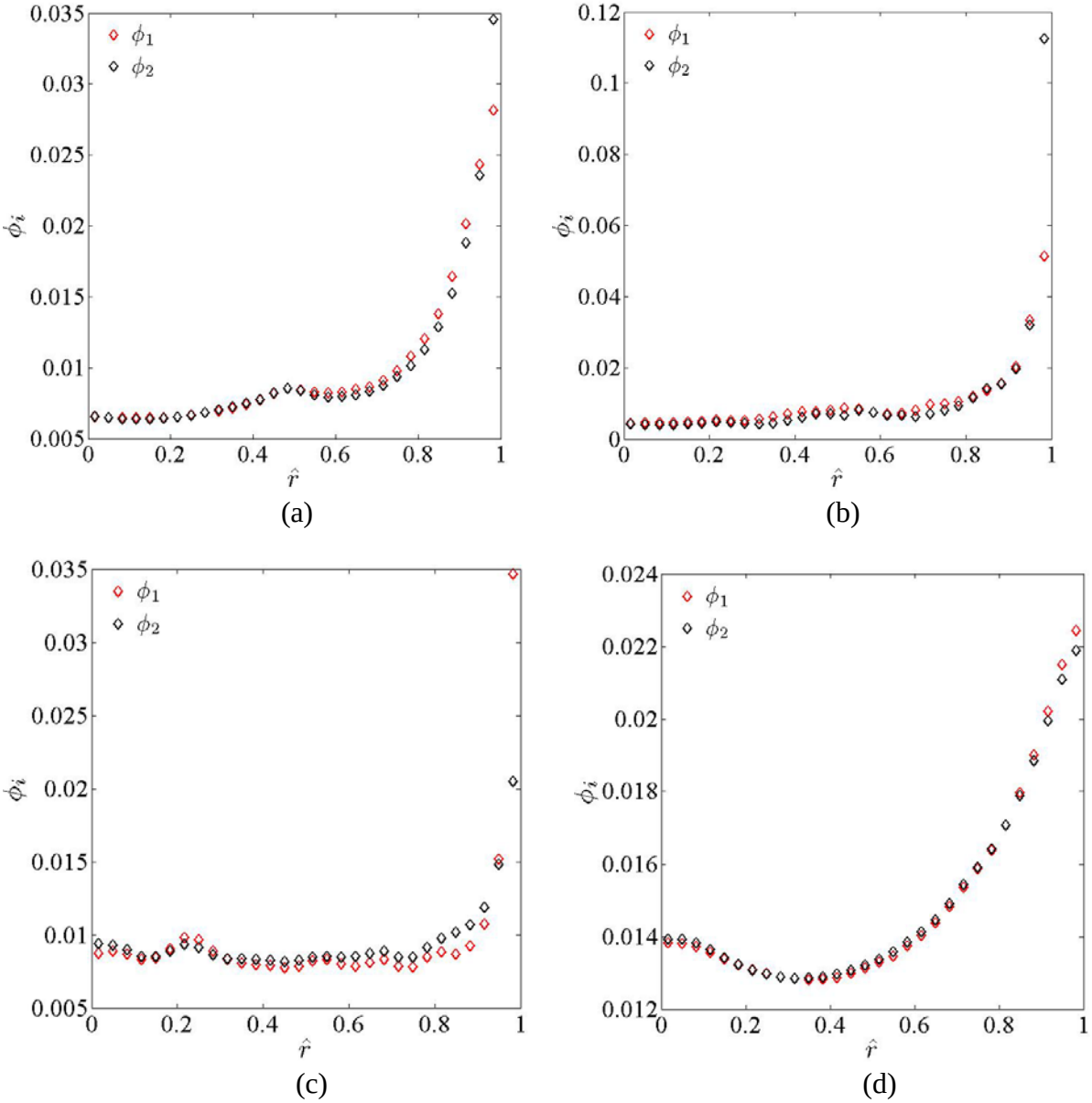

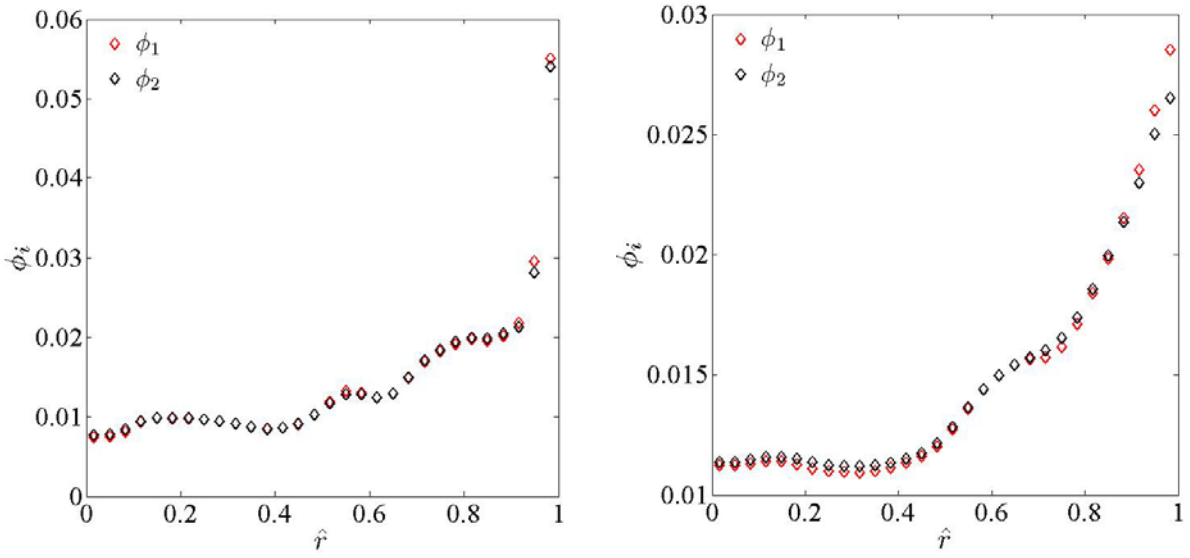

Figure 265. *Species volume fraction obtained from axially periodic two-dimensional gas-particle flow simulations is given as a function of dimensionless radial coordinate* $\hat{r}\ (=r/R)$ *for (a) Case 2 using GHD theory with a coefficient of restitution of 0.99 (see Table 23), (b) Case 2 using GHD theory with a coefficient of restitution of 0.90, (c) Case 2 using IA theory with a coefficient of restitution of 0.99, (d) Case 5 using GHD theory with a coefficient of restitution of 0.99, (e) Case 5 using GHD theory with a coefficient of restitution of 0.90, and (f) Case 5 using IA theory with a coefficient of restitution of 0.99.*

Figures 266(a)-(d) show the profiles of the volume percent of the heavy particle species. Here to be consistent with the nomenclature used in reporting the experimental measurements performed at PSRI we invoke the following definition of volume percent

$$Vol\ \% = \frac{\langle \rho_{si} \varphi_i V_i \rangle}{\sum_i^n \langle \rho_{si} \varphi_i V_i \rangle}$$

where $\langle . \rangle$ indicates a time-averaged quantity, and *n* is the number of particle species. Here, *Vol %* is based upon the heavier particle type consistent with the experimental measurements of segregation obtained in the PSRI experiment. Figures 266(a)-(d) reveal that, according to GHD theory, decreasing the coefficient of restitution enhances the degree of segregation of heavier particles toward the wall. It is also notable the GHD theory predicts a larger degree of radial segregation when the coefficient of restitution decreases in cases where particle species have different sizes or densities.

The IA and GHD theories predict qualitatively similar radial segregation profiles except near the walls in Figure 266(a) and 7 (b). We believe that this discrepancy arises as a result of insufficient sampling when we construct our time averages.

In all cases both GHD and IA theories do not capture the radial segregation profiles observed in the PSRI experimental data. One source of this discrepancy could be due to the fact that the domain-averaged volume fractions used in the simulation cases in Table 23 were deduced from pressure drop data in the PSRI riser, which has been shown to be subject to large errors (Louge and Chang (1990)). In addition, the PSRI experimental data set does not contain

individual species or total particle volume fraction data as a function of location in the riser due the experimental difficulty of measuring species particle volume fraction in bidisperse systems. As such, any method for the determination of the total volume fraction and species volume fractions that were present in this experiment *a posteriori* will be inherently subject to error.

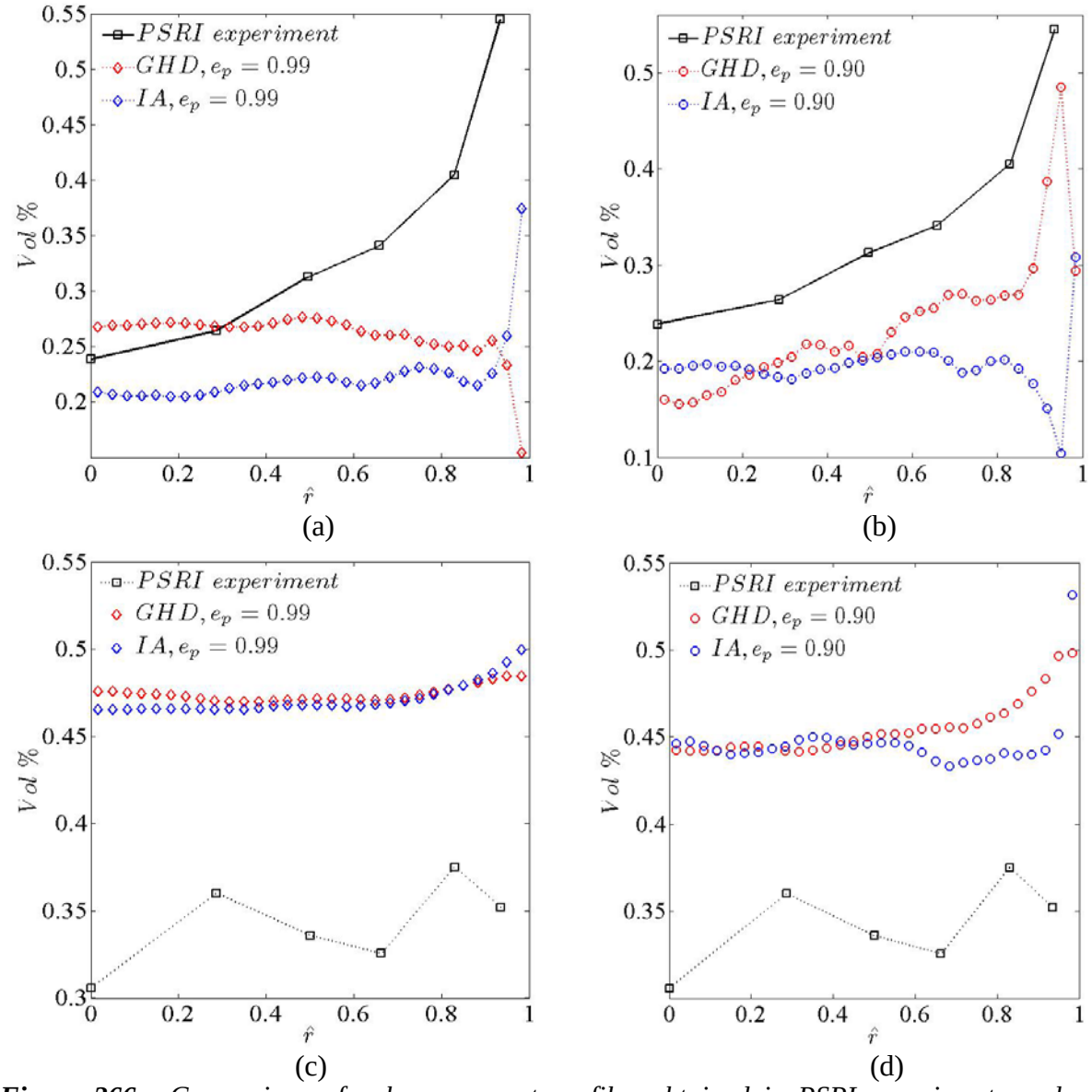

Figure 266. *Comparison of volume percent profiles obtained in PSRI experiments and results obtained from axially periodic two-dimensional gas-particle flow simulations. (a) The radial segregation profiles obtained from simulations of GHD and IA kinetic theories (using a coefficient of restitution of 0.99) of Case 2 are compared with segregation data obtained from PSRI experiments. (b) The radial segregation profiles obtained from simulations of GHD and IA kinetic theories (using a coefficient of restitution of 0.90) of Case 2 are compared with segregation data obtained from PSRI experiments. (c) The radial segregation profiles obtained from simulations of GHD and IA kinetic theories (using a coefficient of restitution of 0.99) of Case 4 are compared with segregation data obtained from PSRI experiments. (d) The radial segregation profiles obtained from simulations of GHD and IA kinetic theories (using a coefficient of restitution of 0.90) of Case 4 are compared with segregation data obtained from PSRI experiments.*

Another source of discrepancy between the experimental data and simulation results could arise as a result of the fact that our simulations presume the azimuthal variation in particle concentration has a negligible effect on the segregation profile. To test this hypothesis we performed an axially periodic cylindrical gas-particle flow calculation using 30 radial grids and 40 azimuthal grids, while limiting the number of axial grids to unity; thus, only radial and azimuthal variations in particle volume fraction are permitted. In this study the IA polydisperse kinetic theory was used because it had provided numerical simulation results that resemble experimentally observed segregation profiles more closely than GHD theory. The simulation results are shown via color plots of the particle volume fraction field that are given in a time series in Figure 267. The particle volume fraction is clearly larger at the wall consistent with core-annular flow. In addition, at late times it is observed that a concentrated cluster near the wall begins to rotate about the tube axis, with an azimuthal velocity that is roughly constant (see Figure 267). Particle volume fraction variations consistent with our observations have been reported previously in the research literature (Benyahia *et al.* (2007); Benyahia (2008)). These sustained azimuthal variations in particle volume fraction indicate that a two-dimensional simulation of the PSRI riser will not properly account for the azimuthal variations in particle concentration that are observed to exist via simulation. To interrogate the effect azimuthal particle volume fraction variations we compare the average radial variation of species volume fraction obtained from 2D simulations to those obtained from axially periodic simulations in Figures 268(a) – (b). It is clear that the azimuthal variation in particle volume fraction produces a higher concentration of particles near the wall. This serves as evidence that azimuthal particle volume fraction variations could also be responsible for the observed differences between simulation and experimental results.

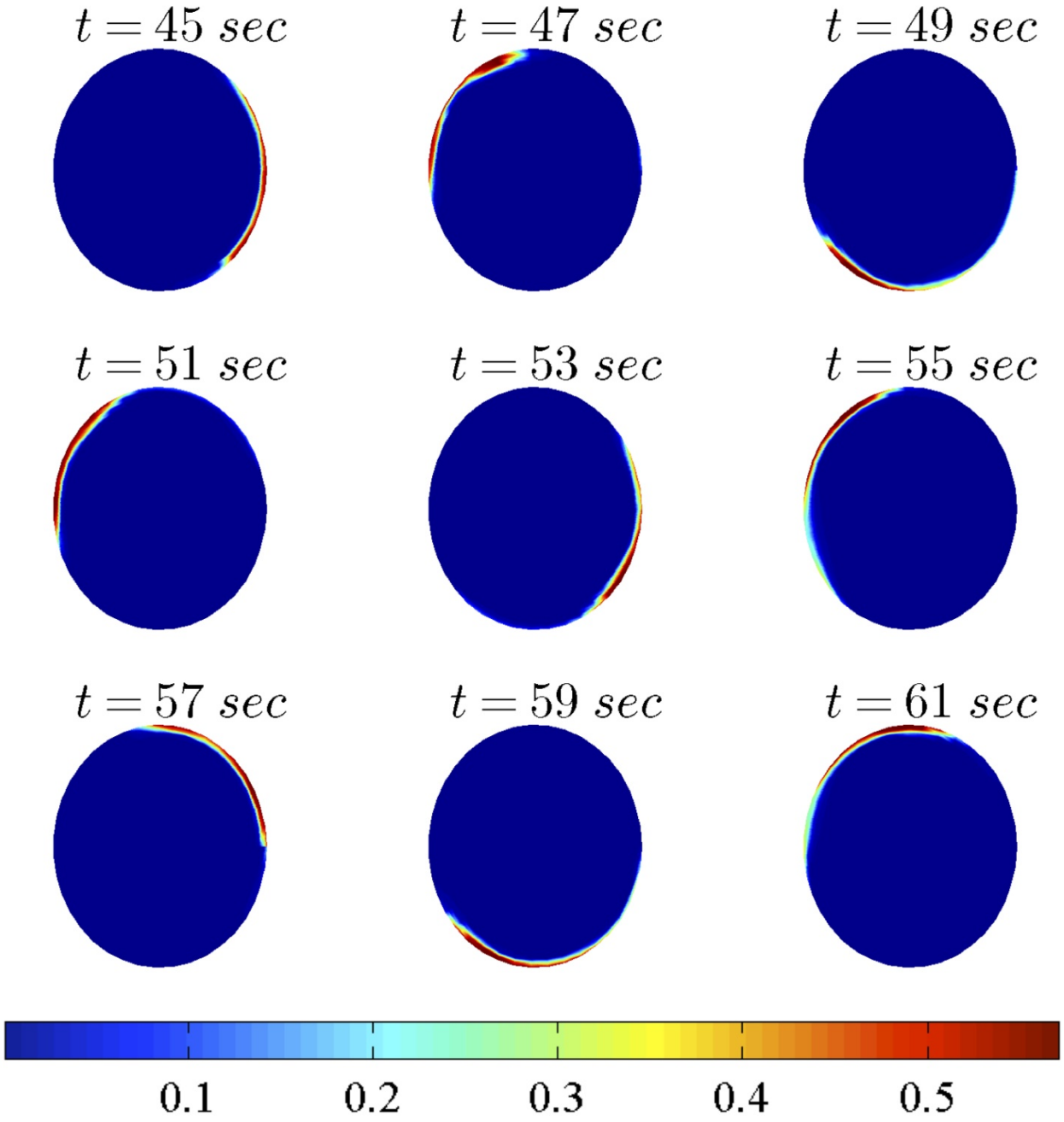

Figure 267. *Colorplots are given of the particle volume fraction ϕ field in a time progression. These simulation results are obtained from simulations of Case 2 (see Table 23).*

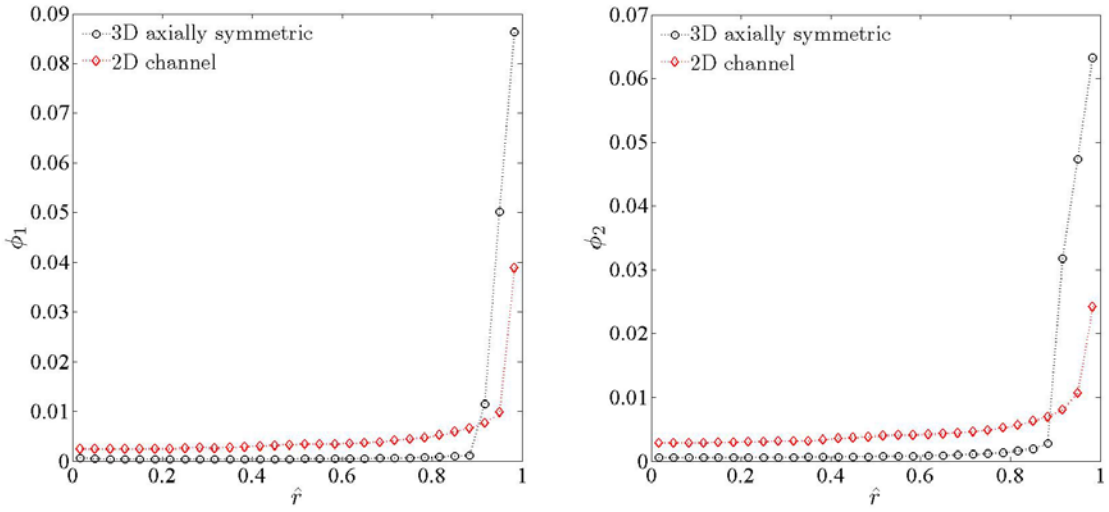

Figure 268. *Radial variation of (a) ϕ_1 and (b) ϕ_2 predicted from 3D axially symmetric and 2D channel flow simulations.*

Goal V: Project Management

Task 5.1: Project Management (Hrenya and other investigators).

This task will be led by Prof. Hrenya, with input from all investigators as needed to meet the reporting requirements. Specific requirements include

(i) Management Plan. Plan the overall work scope and coordinate with all team members and NETL. Review the contract work scope, establish key milestones and dates for deliverables, negotiate sub-award agreements, and submit final plan to DOE within 30 days after the start of the project.

(ii) Progress Reports. Submit the mandated monthly/quarterly/annual reports, and execute the requisite managerial responsibilities and coordinating efforts. Includes updates to management plan generated in Task 6.1

Final Report. Prepare and submit the final technical report.

Prior to the submission of this final report, all quarterly reports have been submitted. The submission of this final report represents the last reporting requirement. All milestones have been met, and the budgets are fully spent.

3. PRODUCT AND/OR TECHNOLOGY TRANSFER ACTIVITIES

Colorado:

Journal Publications

1) Murray, J.A., S. Benyahia, P. Metzger, and C. M. Hrenya, "Continuum representation of a continuous size distribution of particles engaged in rapid granular flow," *Physics of Fluids*, submitted.
2) Garzó, V., S. Tenneti, S. Subramaniam, and C. M. Hrenya, "Enskog kinetic theory for monodisperse gas-solid flows," *Journal of Fluid Mechanics*, submitted.

3) Chew, J.W., D. M. Parker, and C. M. Hrenya, "Elutriation and species segregation characteristics of polydisperse mixtures of Group B particles in a dilute CFB riser," *AIChE Journal*, in press.
4) Chew, J. W., R. Hays, J. G. Findlay, T. M. Knowlton, S. B. R. Karri, R. A. Cocco and C. M. Hrenya, "Reverse Core-Annular Flow of Geldart Group B Particles in Risers," *Powder Technology*, in press; invited paper for special issue.
5) Murray, J. A., C. M. Hrenya, and V. Garzó, "Enskog Theory for Polydisperse Granular Mixtures. III. Comparison of dense and dilute transport coefficients and equations of state for a binary mixture," *Powder Technology*, **22**, 24-36 (2012).
6) Chew, J. W., R. Hays, J. G. Findlay, T. M. Knowlton, S. B. R. Karri, R. A. Cocco and C. M. Hrenya, "Cluster characteristics of Geldart Group B particles in a pilot-scale CFB riser. I. Monodisperse systems," *Chemical Engineering Science*, **68**, 72-81 (2012).
7) Chew, J. W., R. Hays, J. G. Findlay, T. M. Knowlton, S. B. R. Karri, R. A. Cocco and C. M. Hrenya, "Cluster characteristics of Geldart Group B particles in a pilot-scale CFB riser. II. Polydisperse systems," *Chemical Engineering Science*, **68**, 82-93 (2012).
8) Chew, J. W., D. M. Parker, R. A. Cocco and C. M. Hrenya, "Cluster characteristics of continuous size distributions and binary mixtures of Group B particles in dilute riser flow," *Chemical Engineering Journal*, **178**, 348-358 (2011).
9) Chew, J. W. and C. M. Hrenya, "Link between bubbling and segregation patterns in gas-fluidized beds with continuous size distributions," *AIChE Journal*, **57**, 3003-3011 (2011).
10) Mitrano, P. P., S. R. Dahl, D. J. Cromer, M. S. Pacella, and C. M. Hrenya, "Instabilities in the homogeneous cooling of a granular gas: A quantitative assessment of kinetic-theory predictions," *Physics of Fluids*, **23**, art. no. 093303, 8 pages (2011).
11) Chew, J. W., R. Hays, J. G. Findlay, T. M. Knowlton, S. B. R. Karri, R. A. Cocco and C. M. Hrenya, "Impact of material property and operating conditions on mass flux profiles of monodisperse and polydisperse Group B particles in a CFB riser," *Powder Technology*, **214**, 89-98 (2011).
12) Chew, J. W., R. Hays, J. G. Findlay, T. M. Knowlton, S. B. R. Karri, R. A. Cocco and C. M. Hrenya, "Species segregation of binary mixtures and a continuous size distribution of Group B particles in riser flow," *Chemical Engineering Science*, **66**, 4595-4604 (2011).
13) Holloway, W., S. Benyahia, C. M. Hrenya, and S. Sundaresan, "Meso-scale structures of bidisperse mixtures of particles fluidized by a gas," *Chemical Engineering Science*, **66**, 4403-4420 (2011).
14) Passalacqua, A., J. E. Galvin, P. Vedula, C. M. Hrenya, and R. O. Fox, "A quadrature-based kinetic model for dilute non-isothermal granular flows," *Communications in Computational Physics*, **10**, 216-252 (2011).
15) Hrenya, C. M., "Kinetic theory for granular materials: Polydispersity," in *Computational Gas-Solids Flows and Reacting Systems: Theory, Methods and Practice*, S. Pannala, M. Syamlal, and T. O'Brien (eds.), IGI Global, Hershey, PA (2011).
16) Chew, J. W., J. Wolz, and C. M. Hrenya, "Axial segregation in bubbling gas-fluidized beds with Gaussian and lognormal Distributions of Geldart group B particles," *AIChE Journal*, **56**, 3049-3061 (2010).
17) Tenneti S., R. Garg, C. M. Hrenya, R. O. Fox and S. Subramaniam, "Direct numerical simulation of gas-solid suspensions at moderate Reynolds number: Quantifying the coupling between hydrodynamic forces and particle velocity fluctuations," *Powder Technology*, **203**, 57-69 (2010).

18) Hrenya, C. M., "Extraction of transport coefficients from molecular dynamics simulations: A perspective," *Industrial & Engineering Chemistry Research*, **49**, 5304-5409 (2010); invited paper for special issue honoring Dimitri Gidaspow.

Invited Talks

1) Keynote: "Polydisperse Gas-Solid Fluidization: Segregation, Bubbles, and Clusters," 6th Sino-U.S. Chemical Engineering Conference, Beijing, China (Nov 2011).
2) "Experiments in Gas-Solid Fluidized Beds using Continuous Particle Size Distributions," ZCAM Workshop on Granular and Active Fluids, Zaragoza, Spain (Sep 2011).
3) "Polydispersity Model Development & Validation: Report on Findings," DOE NETL 2010 Workshop on Multiphase Flow Science, Pittsburgh, PA (Aug 2011).
4) "Segregation in Rapid Flows: Continuum and DEM," Granular Flows Summer School, University of Maryland, MD (Jun 2011).
5) "An Overview of Modeling Activities for Solids Flows," Hemlock Semiconductor Corporation, Midland, MI (Mar 2011).
6) "Experiments and Model Development for Polydisperse, Gas-Fluidized Systems," DOE NETL 2010 Workshop on Multiphase Flow Science, Pittsburgh, PA (May 2010).
7) "Enskog-based Hydrodynamic Description of Gas-Solid Suspensions," Southern Workshop on Granular Materials, Vina del Mar, Chile (Dec 2009).
8) "Molecular Dynamics-Driven Transport Coefficients for Granular Flows: A Perspective," Festschrift Session for Professor Dimitri Gidaspow's 75th Birthday, Annual Meeting of the American Institute of Chemical Engineers, Nashville, TN (Nov 2009).
9) "Benefits and Shortfalls of Modeling Tools for Solids Flows," UOP / Honeywell Invitational Lecture Series, Chicago, IL (May 2009).
10) "Kinetic Theory of Polydisperse Granular Flows and Validation Data," DOE NETL Workshop on Multiphase Flow Science, Morgantown, WV (Apr 2009).

Contributed Conference Presentations

1) Mitrano, P.P., A. Hilger and C. M. Hrenya, "Instabilities in a Freely Cooling Granular Gas: A Quantitative Comparison of DEM simulations and Kinetic-Theory-based models," 64th Annual Meeting of American Physical Society Division of Fluid Dynamics, Baltimore, MD (Nov 2011).
2) Chew, J. W., D.M. Parker and C. M. Hrenya, "Elutriation and Species Segregation Characteristics of Polydisperse Mixtures of Group B Particles In a Dilute CFB Riser," Annual Meeting of the American Institute of Chemical Engineers, Minneapolis, MN (Oct 2011).
3) Chew, J. W., R. C. Hays, D. M. Parker, J. G. Findlay, T. M. Knowlton, S. B. R. Karri, R. A. Cocco and C. M. Hrenya, "Cluster Characteristics of Polydisperse Group B Particles In a CFB Riser," Annual Meeting of the American Institute of Chemical Engineers, Minneapolis, MN (Oct 2011).
4) Murray, J. A. and C. M. Hrenya, "Discrete Approximation of a Continuous Size Distribution for Use In Kinetic-Theory Predictions of Solids Flows," Annual Meeting of the American Institute of Chemical Engineers, Minneapolis, MN (Oct 2011).
5) Mitrano, P.P., S. R. Dahl and C. M. Hrenya, "Impact of Friction On Instabilities In the Homogenous Cooling of Granular Materials," Annual Meeting of the American Institute of Chemical Engineers, Minneapolis, MN (Oct 2011).

6) Cromer, D. J., S. R. Dahl, P. P. Mitrano, M. S. Pacella, and C. M. Hrenya, "Predicting the Critical Length Scale for Clustering Instabilities in the Homogenous Cooling of Inelastic Particles," Annual Meeting of the American Institute of Chemical Engineers, Salt Lake City, UT (Nov 2010).
7) Chew, J. W. and C. M. Hrenya, "Linking Bubble Characteristics and Species Segregation in Bubbling Gas-Fluidized Beds," Annual Meeting of the American Institute of Chemical Engineers, Salt Lake City, UT (Nov 2010).
8) Murray, J. A., C. M. Hrenya and V. Garzo, "Extension of Kinetic Theory for Granular Binary Mixtures to Moderately Dense Flows," Annual Meeting of the American Institute of Chemical Engineers, Salt Lake City, UT (Nov 2010).
9) Chew, J. W., C. M. Hrenya, R. A. Cocco, R. C. Hays, J. G. Findlay, S. B. R. Karri, and T. M. Knowlton, "Observation of Reverse Core-Annulus Behavior in Risers and Its Relation to Stokes Number," Annual Meeting of the American Institute of Chemical Engineers, Salt Lake City, UT (Nov 2010)
10) Chew, J., J. Wolz, and C. M. Hrenya, "Linking bubbling and species segregation patterns in low-velocity fluidized beds (poster)," NETL 2010 Workshop on Multiphase Flow Science, Pittsburgh, PA (May 2010).
11) Chew, J. W., C. M. Hrenya, R. A. Cocco, J. G. Findlay, S. B. R. Karri, T. M. Knowlton, "Observations of reverse core-annular flow in risers with Geldart group B particles," Sixth World Congress of Particle Technology 6, Nuremberg, Germany (Apr 2010).
12) Pacella, M., D. Cromer, and C. M. Hrenya, "Determination of a Critical Length Scale for Clustering Instability in Granular Systems (poster)," Annual Meeting of the American Institute of Chemical Engineers, Nashville, TN (Nov 2009).
13) Chew, J., C. M. Hrenya, R. A. Cocco, J. G. Findlay, T. M. Knowlton, "Riser-Flow Measurements of Polydisperse Geldart Group B Particles," Annual Meeting of the American Institute of Chemical Engineers, Nashville, TN (Nov 2009).
14) Chew, J., J. Wolz, C. M. Hrenya, "Axial Segregation in Bubbling, Gas-Fluidized Beds with Continuous Size Distributions," Annual Meeting of the American Institute of Chemical Engineers, Nashville, TN (Nov 2009).
15) Chew, J., J. Wolz, C. M. Hrenya, "Experiments on the Local Segregation Patterns of Gas-Fluidized Beds with Continuous Size Distributions (poster)," Powders & Grains 2009, Golden, CO (Jul 2009).
16) Viswanathan, H., C. M. Hrenya, R. O. Fox, "Representation of a Continuous Particle Size Distribution Using a New Polydisperse Kinetic Theory," Annual Meeting of the American Institute of Chemical Engineers, Philadelphia, PA (Nov 2008).

Iowa State (Fox): During the course of this project, 1 book chapter and 14 journal papers were produced, along with 18 invited talks and 26 conference contributed presentations.

Book Chapters

1) Passalacqua, A., P. Vedula, R. O. Fox, Quadrature-based moment methods for polydisperse gas-solid flows. In S. Pannala, M. Syamlal, T. O'Brien (Ed.), Computational gas-solids flows and reacting systems: theory, methods and practice, In press, IGI Global, Hershey, USA.

Journal Publications

1) De Chaisemartin, S., L. Freret, D. Kah, F. Laurent, R. O. Fox, J. Reveillon, and M. Massot, "Eulerian models for turbulent spray combustion with polydispersity and droplet crossing," *Comptes Rendus Mecanique* **337**, 438-448, 2009.
2) Kah, D., F. Laurent, L. Freret, S. de Chaisemartin, R. O. Fox, J. Reveillon, and M. Massot, "Eulerian quadrature-based moment models for dilute polydisperse evaporating sprays," *Flow, Turbulence, and Combustion*, 85, 649-676 (2010).
3) Fox, R. O., "Higher-order quadrature-based moment methods for kinetic equations," *Journal of Computational Physics* **228**, 7771-7791, 2009.
4) Fox, R. O., "Optimal moment sets for the multivariate direct quadrature method of moments," *Industrial & Engineering Chemistry Research* **48**, 9686-9696, 2009.
5) Liu, H., Z. Wang, and R. O. Fox, "A level set approach for dilute non-collisional fluid-particle flows," *Journal of Computational Physics*,230, 920-936 (2011).
6) Desjardin, O., R. O. Fox, P. Villedieu, "A quadrature-based moment method for dilute fluid-particle flows", Journal of Computational Physics, 227, 2514 – 2539, 2008.
7) Fox, R. O., "A quadrature-based third-order moment method for dilute gas-particle flows", Journal of Computational Physics 227, 6313, 2008.
8) Fox, R. O., F. Laurent, and M. Massot, "Numerical simulation of spray coalescence in an Eulerian framework: direct quadrature method of moments and multi-fluid method", Journal of Computational Physics 227, 3058, 2008.
9) Fox, R. O., & P. Vedula, 2009, "Quadrature-based moment method for moderately dense polydisperse gas-particle flows", Ind. Eng. Chem. Res., 49 (11), pp 5174–5187.
10) Passalacqua, A., R. O. Fox, "Implementation of an iterative solution procedure for multi-fluid gas-particle flow models on unstructured grids", Powder Technology, 213, pp. 174-187, 2011.
11) Vikas, V., Z. J. Wang, A. Passalacqua, R. O. Fox, "Realizable high-order finite-volume schemes for quadrature-based moment method", Journal of Computational Physics, Vol. 230, Issue 13, pp. 5328-5352, 2011.
12) Passalacqua, A., J. Galvin, P. Vedula, C.M. Hrenya, R. O. Fox, "A quadrature-based kinetic model for dilute non-isothermal granular flows", Communications in Computational Physics, 10, pp. 216-252, 2011.
13) Passalacqua, A., R. O. Fox, "Advanced continuum modelling of gas-particle flows beyond the hydrodynamic limit", Applied Mathematical Modelling, Volume 35, Issue 4, pp. 1616-1627, 2011.
14) Passalacqua, A., R. O. Fox, R. Garg, S. Subramaniam, "A fully coupled quadrature-based moment method for dilute to moderately dilute fluid-particle flows", Chemical Engineering Science, Vol. 65, pp. 2267-2283, 2010.

Invited Talks

1) Fox, R. O., "A quadrature-based moment method for polydisperse gas-solid flows," Departmental Seminar, Ecole Centrale, Paris, France, 2009.
2) Fox, R. O., "CFD modeling of chemical reactors: Current capabilities and future directions," ChE Distinguished Lecturer Series, University of Utah, Salt Lake City, UT, 2009.
3) Fox, R. O., "CFD modeling of chemical reactors: Current capabilities and future directions," Departmental Seminar, Chemical Engineering, University of Minnesota, Minneapolis, MN, 2009.

4) Fox, R. O., "Kinetic models for multiphase flow, kinetic description of multiscale phenomena," CSCAMM, University of Maryland, College Park, MD, 2009.
5) Fox, R. O., "Multiphase CFD for fluid-particle flows: Beyond the two-fluid model," Keynote Speaker, CFD2009: The 7th International Conference on CFD in the Minerals and Process Industries, Melbourne, Australia, 2009.
6) Fox, R. O., "Quadrature-based moment methods for multiphase chemically reacting flows," Symposium in Honor of Prof. S. B. Pope, Cornell University, Ithaca, NY, 2009.
7) Fox, R. O., "Quadrature-based moment methods for polydisperse gas-solid flows," The 5th Sino-US Conference of Chemical Engineering, Beijing, China, 2009.
8) Fox, R. O., "Quadrature-based moment methods," International Workshop on Mathematics in Chemical Kinetics and Engineering 2009, Ghent, Belgium, 2009.
9) Fox, R. O., "Advanced reactive multiphase flows," Keynote Speaker, 3rd Latin American CFD Workshop Applied to the Oil Industry, Rio de Janeiro, Brazil, 2008.
10) Fox, R. O., "CFD modeling of chemical reactors: Current capabilities and future directions," Departmental Seminar, Chemical Engineering, The Ohio State University, Columbus, OH, 2008.
11) Fox, R. O., "CFD modeling of chemical reactors: Polydisperse multiphase flows," ArcelorMittal, Mezieres-les-Metz, France, 2008.
12) Fox, R. O., "Quadrature-based moment methods for dilute gas-solid flows," Departmental Seminar, Chemical Engineering, Illinois Institute of Technology, Chicago, IL, 2008.
13) Fox, R. O., "Quadrature-based moment methods for simulation of collisional gas-particle flows," Departmental Seminar, Ecole Centrale, Paris, France, 2008.
14) Fox, R. O., "Models for polydisperse multiphase flows," Plenary Lecture, 45th European Two-Phase Flow Group Meeting, IMFT, Toulouse, France, 2007.
15) Fox, R. O., "Quadrature-based moment methods for Boltzmann-like equations," Computational and Mathematical Aspects of Material and Fluids, Iowa State University, Ames, IA, 2007.
16) Fox, R. O., "Quadrature-based moment methods for Boltzmann-like equations," Reaction Engineering International, Salt Lake City, UT, 2007.
17) Fox, R. O., "Quadrature-based moment methods for polydisperse multiphase flows," Departmental Seminar, Fluid Mechanics, IMFT, Toulouse, France, 2007.
18) Fox, R. O., "Quadrature-based moment methods for polydisperse multiphase flows," CFD Group, CERFACS, Toulouse, France, 2007.

Contributed Conference Presentations

1) Passalacqua, A., R. O. Fox, "Numerical simulation of turbulent gas-particle flow in a riser using a quadrature-based moment method", 7th International Conference on Multiphase Flow (ICMF), Tampa, Florida, May 30th – June 4th, 2010.
2) Vikas, V., Z. J. Wang, A. Passalacqua, R. O. Fox, "A fully coupled fluid-particle solver using quadrature-based moment method with higher-order realizable schemes on unstructured grids", 7th International Conference on Multiphase Flow (ICMF), Tampa, Florida, May 30th – June 4th, 2010.
3) Vikas, V., Z. J. Wang, A. Passalacqua, R. O. Fox, "Development of High-Order Realizable Finite-Volume Schemes for Quadrature-Based Moment Method", 48th AIAA Aerospace Sciences Meeting, AIAA, Orlando, Florida, January 4th – 8th, 2010.

4) Passalacqua, A., R. O. Fox, "Multiphase CFD for gas-particle flows: beyond the two-fluid model", Seventh International Conference on CFD in the Minerals and Process Industry, CSIRO, Melbourne, Australia, December 9th – 11th, 2009.
5) Passalacqua, A., L. Marmo, CFD modelling of gas-solid flow in risers, ANIMP Multiphase Flow Engineering Section 9th International Conference "Multiphase Flow in Industrial Plants" Rome, Italy, September 20th-21st, 2004.
6) Passalacqua, A., R. O. Fox, "Continuum Description Of Poly-disperse Multiphase Fluid-particle Flows With Quadrature-based Moment Methods", 48th Annual Technical Conference of Society of Engineering Sciences, Northwestern University, Evanston, IL, October 12-14, 2011.
7) Passalacqua, A., R. O. Fox, "Implementation of an iterative solution procedure for multi-fluid gas-particle flow models on unstructured grids – Multi-fluid models in OpenFOAM", NETL 2011 Workshop on Multiphase Flow Science, Airport Marriott Station Square, Pittsburgh, PA, August 16th – 18th , 2011.
8) Passalacqua, A., C. Yuan, R. O. Fox, P. Vedula, V. Vikas, Z. J. Wang, "Advanced quadrature-based models for gas-particle flows", ASME 2010 3rd Joint US-European Fluids Engineering Summer Meeting, Open forum fluid-particle interactions in turbulence, August 1st-5th, Montreal, Canada, FEDSM-ICNMM2010-31320.
9) Fox, R. O., A. Passalacqua, C. Yuan, V. Vikas, Z. J. Wang, "Quadrature-based moment methods for gas-particle flows", 2010 SIAM Annual Meeting, Numerical Methods for Kinetic Equations and Related Models, Pittsburgh, PA, July 12th –16th , 2010.
10) Passalacqua, A., R. O. Fox, "Fully three-dimensional simulations of riser flows with a third-order quadrature-based moment method", NETL 2010 Workshop on Multiphase Flow Science, Pittsburgh Airport Marriot Hotel, Coraopolis, PA, May 4th – 6th, 2010
11) Passalacqua, A., J. Galvin, P. Vedula, C. M. Hrenya, R. O. Fox, "A quadrature-based kinetic model for a dilute non-isothermal granular gas", 62nd Annual Meeting of the APS Division of Fluid Dynamics, Minneapolis, November 22nd – 24th, 2009.
12) Passalacqua, A., R. Garg, S. Subramaniam, R. O. Fox, "A fully coupled third-order quadrature-based moment method for the simulation of gas-particle flows", AIChE Annual Meeting, Nashville, TN, 8th–13rd November, 2009.
13) Passalacqua, A., P. Vedula, C. M. Hrenya, R. O. Fox, "A kinetic model for a non-isothermal granular gas with bi-disperse particles", AIChE Annual Meeting, Nashville, TN, 8th–13rd November, 2009.
14) Passalacqua, A., R. O. Fox, "A quadrature-based moment method for gas-particle flows", Kinetic FRG: Annual Meeting (FRG2009), CSCAMM – CSIC building, University of Maryland, College Park, MD, September 21st-25th, 2009.
15) Passalacqua, A., R. O. Fox, "Development of a quadrature-based moment method for polydisperse flows and incorporation in MFIX", NETL 2009 Workshop on Multiphase Flow Science, Euro-Suites Hotel, Morgantown, WV, April 22nd-23rd, 2009.
16) Passalacqua, A., P. Vedula, R. O. Fox, "Solution of the Boltzmann equation for fluid flows in microchannels at finite Knudsen numbers with a third-order quadrature-based moment method", AIChE Annual Meeting, Philadelphia, November 16th-21st, 2008.
17) Passalacqua, A., P. Vedula, C. M. Hrenya, R. O. Fox, "A kinetic-based model for a non-isothermal granular gas with mono- and bi-dispersed particles", AIChE Annual Meeting, Philadelphia, November 16th-21st, 2008.

18) Freret, L., F. Laurent, S. de Chaisemartin, D. Kah, R. O. Fox, P. Vedula, J. Reveillon, O. Thomine, and M. Massot, "Turbulent combustion of polydisperse evaporating sprays with droplet crossing: Eulerian modeling of collisions at finite Knudsen and validation," in *Proceedings of the 2008 Summer Program*, Center for Turbulence Research, Stanford, CA, pp. 277-288, 2008.
19) Laurent, F., M. Massot, and R. O. Fox, "Numerical simulation of polydisperse, dense liquid sprays in an Eulerian framework: direct quadrature of moment method and multi-fluid method," in *Proceedings of 6th International Conference on Multiphase Flow* (ICMF 2007), Leipzig, Germany, pp. 1-15, 2008.
20) Le Lostec, N., R. O. Fox, O. Simonin, and P. Villedieu, "Numerical description of dilute particle-laden flows by a quadrature-based moment method," in *Proceedings of the 2008 Summer Program, Center for Turbulence Research*, Stanford, CA, pp. 209-221, 2008.
21) Desjardins, O., R. O. Fox, and P. Villedieu, "A quadrature-based moment method for dilute gas-particle flows," in *Proceedings of 6th International Conference on Multiphase Flow* (ICMF 2007), Leipzig, Germany, pp. 1-9, 2007.
22) R. Garg, A. Passalacqua, S. Subramaniam, R. O. Fox, Comparison of Euler-Euler and Euler-Lagrange simulations of finite-Stokes-numbers gas-particle flows in a lid-driven cavity, AIChE Annual Meeting, Philadelphia, November 16th -21st, 2008.
23) Vedula, P., and R. O. Fox, "Turbulence modeling based on a collisional Boltzmann equation," Annual Meeting of American Physical Society Division of Fluid Dynamics, Salt Lake City, UT, 2007.
24) Vedula, P., and R. O. Fox, "Turbulence modeling based on a collisional Boltzmann equation," Annual Meeting of American Physical Society Division of Fluid Dynamics, Salt Lake City, UT, 2007.
25) Fox, R. O., and P. Vedula, "A quadrature-based kinetic equation solver for arbitrary Knudsen numbers," Annual Meeting of American Physical Society Division of Fluid Dynamics, Salt Lake City, UT, November 2007.
26) Vedula, P., and R. O. Fox, "Analysis of non-equilibrium multi-species mixing based on Boltzmann kinetic equation," Annual Meeting of American Physical Society Division of Fluid Dynamics, San Antonio, TX, 2008.

Iowa State (Subramaniam):
Journal Publications

1) Mehrabadi, M., Tenneti, S., Subramaniam, S., "Fluid-phase velocity fluctuations in fixed particle beds and freely evolving suspensions," In preparation.
2) Tenneti, S., Garg, R., Subramaniam, S., "Quantification of gas–phase velocity fluctuations in statistically homogeneous gas–solid flow using particle–resolved direct numerical simulation," In review.
3) Tenneti, S., Garg, R., Subramaniam, S., "Drag law for monodisperse gas-solid systems using particle-resolved direct numerical simulation of flow past fixed assemblies of spheres," *International Journal of Multiphase Flow*, 2011. 37(9): p. 1072-1092.
4) Tenneti, S., Garg, R., Hrenya, C. M., Fox, R. O., Subramaniam, S., "Direct numerical simulation of gas-solid suspensions at moderate Reynolds number: Quantifying the coupling between hydrodynamic forces and particle velocity fluctuations," *Powder Technology*, 2010. 203(1): p. 57-69.

Princeton (Sundaresan): During the course of this project, 5 journal papers were produced, along with 8 conference contributed oral presentations and 3 conference contributed poster presentations.

Journal Publications

1) Yin, X., and S. Sundaresan, "Drag Law for Bidisperse Gas-Solid Suspensions Containing Equally Sized Spheres," *Industrial and Engineering Chemistry Research*, **48**, 227-241, (2008).
2) Yin, X., and S. Sundaresan, "Fluid-particle drag in low-Reynolds-number polydisperse gas-solid suspensions," *AIChE Journal*, **55**, 1352-1368, (2009).
3) Holloway, W., X. Yin, and S. Sundaresan, "Fluid-particle drag in inertial polydisperse gas-solid suspensions," *AIChE Journal*, **56**, 1995-2004, (2010).
4) Holloway, W., S. Benyahia, C. M. Hrenya, and S. Sundaresan. Meso-scale structures of bidisperse mixtures of particles fluidized by a gas," *Chem. Eng. Sci.*, **66**, 4403-4420, (2011).
5) Holloway, W., J. Sun, and S. Sundaresan, "Effect of microstructural anisotropy on the fluid-particle drag force and the stability of the uniformly fluidized state," *J. Fluid Mech.* (in revision)

Contributed Conference Oral Presentations

1) Yin, X. and S. Sundaresan, "Fluid-particle drag in binary Stokes gas-solid suspensions," Annual Meeting of the American Institute of Chemical Engineers, Salt Lake City, UT (November 2007).
2) Yin, X., W. Holloway, and S. Sundaresan, "Fluid-Particle Drag in Bidisperse Gas-Solid Suspensions," Annual Meeting of the American Institute of Chemical Engineers, Philadelphia, PA (November 2008).
3) Holloway, W., X. Yin, and S. Sundaresan, "Fluid-particle drag in polydisperse gas-solid suspensions," National Energy Technology Laboratory Multiphase Flow Workshop, Morgantown, WV (April 2009).
4) Holloway, W., J. Sun, and S. Sundaresan, "Fluid-particle drag in sheared particle configurations," Annual Meeting of the American Institute of Chemical Engineers, Nashville, TN (November 2009).
5) Holloway, W., S. Benyahia, C. M. Hrenya, and S. Sundaresan, "Meso-scale structures in binary gas-solid flows," National Energy Technology Laboratory Multiphase Flow Workshop, Pittsburgh, PA (April 2010).
6) Holloway, W., J. Sun, and S. Sundaresan, "Effect of microstructural anisotropy on the fluid-particle drag force," Graduate Student Symposium, Princeton University, Princeton, NJ (October 2010).
7) Holloway, W., S. Benyahia, C. M. Hrenya, and S. Sundaresan, "Meso-scale structures in binary gas-solid flows," Annual Meeting of the American Institute of Chemical Engineers, Salt Lake City, UT (November 2010).
8) Holloway, W., J. Sun, and S. Sundaresan, "Effect of microstructural anisotropy on the fluid-particle drag force," Annual Meeting of the American Physical Society, Division of Fluid Dynamics, Long Beach, CA (November 2010).

Contributed Conference Poster Presentations

1) Holloway, W., X. Yin, and S. Sundaresan. Fluid-particle drag in polydisperse gas-solid suspensions. Annual Meeting of the American Institute of Chemical Engineers, Nashville, TN (November 2009).
2) Holloway, W., X. Yin, and S. Sundaresan. Fluid-particle drag in polydisperse gas-solid suspensions. Graduate Student Symposium, Princeton University, Princeton, NJ (November 2009).
3) Holloway, W., J. Sun, and S. Sundaresan. Fluid-particle drag in sheared particle configurations. National Energy Technology Laboratory Multiphase Flow Workshop, Pittsburgh, PA (April 2010).

4. NOMENCLATURE

A	area of fluidization column
$\mathbf{A}_f$	Frame acceleration
$\mathrm{A}_{(\mathrm{n})}$	acceleration of the n^{th} particle
$\mathbf{A}'^{(\mathrm{n})}$	fluctuation in the acceleration of the n^{th} particle
A_j	approximation trace at the j^{th} scale of wavelet decomposition
A_{j}	j^{th} component of the particle acceleration vector
$b_{\parallel}$	anisotropy along the mean slip
b_{ij}	anisotropy of fluid-phase Reynolds stress
$b_{\perp}$	anisotropy perpendicular to the mean slip
c_L	low wave number adjusting function constant
c_η	high wave number adjusting function constant
C	energy spectrum function constant
C_μ	eddy viscosity model constant
$\langle d \rangle$	Sauter mean diameter
d_{ave}	average diameter of PSD
d_{ave}	average particle diameter
d_i	diameter of the *i*th particle species
d_1, d_2	particle diameter
d_p	particle diameter
d_S	Sauter mean diameter
D_{gs}	momentum exchange source term
D_i^T	thermal diffusion coefficient
D_j	detail trace at the j^{th} scale of wavelet decomposition
D_m	particle grid resolution
$\langle D \rangle$	Sauter mean diameter in a polydisperse suspension
d_p	particle diameter

D_α	diameter of the particles belonging to the size class α
D_{ij}	mutual diffusion coefficient
$D_{ij}^{\ F}$	mobility coefficient
$D_{q,ij}$	Dufour coefficient
$d\mathsf{W}_j$	Wiener process increment
e	coefficient of restitution
e_m	two-phase mixture energy
E	energy spectrum function
E_f	mean flow kinetic energy
f	single-particle velocity distribution function
$\mathbf{f}_{g-\alpha}$	total gas-solid force per unit volume acting on the particles belonging to the size class α
f_i	number density function
f_L	low wave number adjusting function of energy spectrum function
f_η	high wave number adjusting function of energy spectrum function
f_m	mass-based frequency
$f(r)$	weight function
F_α	normalized drag fluid-particle force acting on the particles belonging to the size class α in a polydisperse suspension
$\mathbf{F}^C_{\alpha-\beta}$	total contact force acting on the size class α due to collisions with particles belonging to the size class β
$\mathbf{F}_{D-\alpha}$	total force due to viscous and fluctuating pressure contributions acting on the size class α
F_i	force acting on the particle.
$\mathrm{F_i}$	instantaneous drag force acting on a particle
$\mathrm{F_i^*}$	modeled instantaneous drag force acting on a particle
Fq	electrostatic force
$\mathrm{F_x}$	streamwise component of force
$\left\langle \mathbf{F}_D \mid r = R_\alpha \right\rangle$	average force per particle due to viscous and fluctuating pressure contributions
$\left\langle \mathbf{F} \mid r = R_\alpha \right\rangle$	average gas-solid force per particle acting on a particle belonging to the size class
$F\left(\phi, \mathrm{Re}_m\right)$	drag force per particle
g	gravitational acceleration
$\mathbf{g}$	gravity
g_{ij}	relative velocity
$\langle \mathbf{g} \rangle$	mean pressure gradient
$g(r)$	radial distribution function
$G_{r,net,norm}$	local normalized net mass flux
G_s	overall mass flux

h	height at which measurement was taken
H	height of particle bed
I_f	fluid-phase indicator function
J	collisional operator
k	turbulent kinetic energy
k_f	kinetic energy of fluid-phase velocity fluctuations
k_0	reference k
k_p	kinetic energy of solid-phase velocity fluctuations
Kn	Knudsen number
l	surface to surface distance
l_K	dissipation length scale corresponding Kolmogorov scaling
l_T	dissipation length scale corresponding Taylor microscale scaling
L	large eddy length scale
L_{ij}	mobility coefficient
L_{int}	interstitial distance
$L_{\|\|}$	eddy length scale
L	Characteristic length scale
$\mathbf{L}$	transformation matrix
m	mass of the particle
m	solid loading, i.e., ratio of mass flux to gas flux
m_i, m_j	particle mass
M	number of realizations
M	number of size classes
M_f	momentum exchange term in the fluid-phase momentum equation
M_i^0	zero order moment of the i-th specie
n	number density
$\mathbf{n}^{(s)}$	normal vector to particle surface towards the fluid phase
$\mathbf{n}^{(f)}$	normal vector to particle surface towards the solid phase
N	number of weights and abscissas
n	power decay of k
$\mathbf{P}$	solid-phase pressure tensor
p	pressure
p	solid-phase pressure
p, q, r	indexes of the moments (for example m_{111} has $p = q = r = 1$)
p_i	quadrature weights N the number of weights
p_0	energy spectrum function constant
$\mathbf{q}$	conduction of granular energy
q	electric charge
r	radius at which measurement was taken
r	channel half-width
$\tilde{r}$	dimensionless radial position
R	radius of column

R	radius of riser
R	radius of the particle
Re	Reynolds number
Re_{λ}	Taylor microscale turbulent Reynolds number
Re_{L}	turbulent Reynolds number
Re_{m}	mean slip Reynolds number
$R_{f,ij}$	fluid-phase Reynolds stress
$R_{\parallel}$	two-point velocity correlation along the mean slip
s	number of discrete species
s_{cont}	segregation index of continuous size distribution
s_{min}	minimum number of discrete species needed to represent continuous PSD
$_{sm}$	Sauter-mean diameter
S	source in the granular temperature
S_{SS}	steady state source in the granular temperature
S_{ij}	strain rate tensor (task 3)
$\hat{S}$	non dimensional source in the granular temperature
S^{*}_{SS}	normalized steady state source in the granular temperature
$\mathrm{S_{ij}}$	source term in the second moment evolution equation (task 2)
St	Stokes number
t	time
t_0	reference time
t_{col}	dimensional time between successive collisions
T	granular temperature
$\mathrm{T_{ij}}$	component of the second moment of particle velocity in Koch's (1999) notation
T_{SS}	steady state granular temperature
$\mathbf{u}_f$	fluid-phase instantaneous velocity
$u_{f,i}$"	fluid-phase velocity fluctuations
u_i	sedimentation velocity of species *i*
$u_{p,i}$"	solid-phase velocity fluctuations
u, v, w	velocity components
$\langle u \rangle$	volume-weighted sedimentation velocity
$\langle \mathbf{u}^{(s)} \rangle$	mixture mean solid velocity
U_{cf}	superficial gas velocity for complete fluidization
U_f	fluid-phase velocity
$\mathbf{U_g}$	mean gas velocity
U_g	Gas velocity
U_s	superficial gas velocity
$U_{s\alpha}$	Abscissa at node α

U_t	terminal settling velocity of an isolated particle using Schiller-Naumann relation and Sauter mean diameter
$\mathbf{v}$	instantaneous particle velocity
v_{t_i}	terminal settling velocity of an isolated particle of species *i*
V	volume of the computational domain
V_f	fluid-phase volume
$\mathrm{V}_{(n)}$	velocity of the nth particle
$\mathbf{V}^{(n,\alpha)}$	velocity of the nth particle belonging to the size class α
$V_{99th\text{-}percentile}$	99th percentile of voltages in trace
V_i	axial particle velocity
$\mathrm{v_i}$	ith component of the particle velocity in a continuum description
v_i	velocity of the i-th specie
$\mathrm{v_i}''$	ith component of the particle fluctuating velocity. Fluctuation defined about the conditional mean velocity
$\left\langle \mathbf{v} \middle\| r = R_\alpha \right\rangle$	mean velocity of solids belonging to the size class α
V_{mode}	mode of voltages in trace
Vol %	ratio of the flux of a particle of type *i* compared to the particle mixture
V_p	particle volume
$V_{threshold}$	threshold voltage
W	weight of bed
$\left\langle \mathbf{W} \right\rangle$	mean-slip velocity
$\left\langle \mathbf{W}^{(2,1)} \right\rangle$	mean slip velocity between size classes 2 and 1
$\mathbf{x}$	position
$\mathbf{x}^{(\mathrm{I})}$	fluid-solid interface position
$\mathrm{X}_{(n)}$	position of the nth particle
y_α	normalized diameter of the size class α

Greek Symbols

α	index of the size class
β	high wave number adjusting function constant in task 3
β_{ij}	coefficient tensor multiplying the mean slip velocity in the Langevin model (task 2
β_g, β_{QMOM}	drag coefficient
$\boldsymbol{\gamma}$	coefficient tensor multiplying the fluctuating velocity in the Langevin model (task 2)
Γ	Euler's gamma function
Γ_{coll}	collisional dissipation
Γ_{ij}	dissipation term in the second moment evolution equation
δ	particle diameter

δ	boundary layer thickness
δ	Dirac delta function
δ_{ij}	Kronecker delta
$\Delta P/\Delta h$	differential pressure drop across particle bed
ΔP_{bed}	pressure drop across particle bed
Δx	grid cell size
ε	dissipation of k
ε_f	dissipation of k_f
ε_g	gas volume fraction
ε_s	particle phase volume fraction
ζ	cooling rate due to inelastic collisions
η	shear viscosity
η	Komogorov length scale
κ	wave number
κ	bulk viscosity
λ	thermal conductivity
μ_f	dynamic viscosity of the fluid phase
μ_{ij}	reduced mass: $m_i\, m_j /(m_i + m_j)$
ν	fluid kinematic viscosity
ν_f	kinematic viscosity of the fluid phase
ν_T	pseudo-turbulent eddy viscosity
ξ	friction coefficient for Stokes drag ($\xi = -6\pi\mu d/m$)
ξ^0	zeroth-order cooling rate
ξ_U	first-order transport coefficient for the cooling rate
π_f	interphase TKE transfer
Π	interphase TKE transfer of two-phase mixture energy evolution equation
ρ_α	density of the particles belonging to the size class α
ρ_f	fluid-phase density
ρ_g	gas density
ρ_p	particle density
ρ_s	material density
ρ_{s_i}	density of the *i*th particle phase
σ	standard deviation of the mass-based particle size distribution
σ	standard deviation of PSD
$\mathbf{\Sigma}$	tensor whose components are the source terms in the second moment equation
τ	eddy turnovet time scale
τ_{col}	dimensionless time between successive collisions
τ_f	fluid stress tensor
τ_{ij}	stress tensor
τ_{vis}	dimensionless viscous relaxation time

ϕ	solid volume fraction
ϕ_i	volume fraction of the *i*th particle species
ϕ	total solids volume fraction
φ	electric potential
Φ	solid volume fraction
χ	cross-correlation coefficient

Acronyms

BGK	Bhatnagar-Gross-Krook.
BVP	boundary-value problem.
COR	coefficient of restitution
DNS	direct numerical simulation
DQMOM	direct quadrature method of moments.
GHD	kinetic theory of Garzo, Hrenya, and Dufty
HDPE	high density polyethylene
HKL	Hill, Koch and Ladd (2001)
IVP	initial-value problem.
LBM	lattice Boltzmann method
MIS	multiple independent simulation
PBE	population balance equation.
PR-DNS	particle-resolved direct numerical simulation
PSD	particle size distribution
PUReIBM	particle-resolved uncontaminated-fluid reconcilable immersed boundary method
QMOM	quadrature method of moments.
RH	relative humidity
TG	Taylor-Green.

5. REFERENCES

Afsahi, F. A., R. Sotudeh-Gharebagh, et al. (2009). "Clusters Identification and Characterization in a Gas-Solid Fluidized Bed by the Wavelet Analysis." Canadian Journal of Chemical Engineering **87**(3): 375-385.

Agrawal, K., Loezos, P. N., Syamlal M. & Sundaresan, S., 2001, The role of meso-scale structures in rapid gas-solid flows, J. Fluid. Mech, 445, 151 – 185.

Aguillon, J., K. Shakourzadeh, et al. (1995). "Comparative-Study of Nonisokinetic Sampling Probes for Solids Flux Measurement in Circulating Fluidized-Beds." Powder Technology **83**(1): 79-84.

Ahmadi, G., & Ma, D. (1990). A Thermodynamical Formulation for Dispersed Multiphase Turbulent Flows.1. Basic Theory. *Int. J. Multiphase Flow, 16*(2), 323-340.

Andreux, R., G. Petit, et al. (2008). "Hydrodynamic and solid residence time distribution in a circulating fluidized bed: Experimental and 3D computational study." Chemical Engineering and Processing **47**(3): 463-473.

Annaland, M. V., G. A. Bokkers, et al. (2009). "Development of a multi-fluid model for poly-disperse dense gas-solid fluidised beds, Part II: Segregation in binary particle mixtures." Chemical Engineering Science **64**(20): 4237-4246.

Arena, U. (1997). Gas Mixing. Circulating Fluidized Beds, Chapter 3. J. R. Grace, A. A. Avidan and T. M. Knowlton. London ; New York, Blackie Academic & Professional**:** xvi, 585 p.

Azzi, M., P. Turlier, et al. (1990). Use of a momentum probe and gammadensitometry to study local properties of fast fluidized beds. 3rd International Conference on Circulating Fluidized Beds, Nagoya, Japan.

Bader, R., J. Findlay, et al. (1988). Gas/solids flow patterns in a 30.5-cm-diameter circulating fluidized bed. Circulating Fluidized Bed Technology II. P. Basu and J. F. Large, Pergamon Press**:** 123-137.

Bai, D. R., N. Nakagawa, et al. (1994). "Axial Distribution of Solid Holdups in Binary Solids Circulating Fluidized-Beds." Journal of Chemical Engineering of Japan **27**(3): 271-275.

Bai, D. R., Y. Jin, et al. (1992). "The Axial Distribution of the Cross-Sectionally Averaged Voidage in Fast Fluidized-Beds." Powder Technology **71**(1): 51-58.

Basesme, E. A. and E. K. Levy (1992). "Solids Exchange between the Bubble Wake and the Emulsion Phase in a 2-Dimensional Gas-Fluidized Bed." Powder Technology **72**(1): 45-50.

Beetstra, R., J. Nijenhuis, et al. (2009). "The Influence of the Particle Size Distribution on Fluidized Bed Hydrodynamics Using High-Throughput Experimentation." AIChE Journal **55**(8): 2013-2023.

Beetstra, R., M. A. van der Hoef, et al. (2007). "Numerical study of segregation using a new drag force correlation for polydisperse systems derived from lattice-Boltzmann simulations." Chemical Engineering Science **62**(1-2): 246-255.

Beetstra, R., van der Hoef, M. A., & Kuipers, J. A. M. (2007). Drag force of intermediate Reynolds number flow past mono- and bidisperse arrays of spheres. *AIChE Journal*, *53*(2), 489-501.

Benyahia, S. (2008). "A time-averaged model for gas-solids flow in a one-dimensional vertical channel." Chemical Engineering Science **63**(9): 2536-2547.

Benyahia, S. (2008). "Verification and validation study of some polydisperse kinetic theories." Chemical Engineering Science **63**(23): 5672-5680.

Benyahia, S., M. Syamlal, et al. (2005). "Evaluation of boundary conditions used to model dilute, turbulent gas/solids flows in a pipe." Powder Technology **156**(2-3): 62-72.

Benyahia, S., M. Syamlal, et al. (2007). "Study of the ability of multiphase continuum models to predict core-annulus flow." AIChE Journal **53**(10): 2549-2568.

Berruti, F., J. Chaouki, et al. (1995). "Hydrodynamics of Circulating Fluidized-Bed Risers - a Review." Canadian Journal of Chemical Engineering **73**(5): 579-602.

Biggs, M. J., D. Glass, et al. (2008). "Granular temperature in a gas fluidized bed." Granular Matter **10**: 63-73.

Bokkers, G. A., M. V. S. Annaland, et al. (2004). "Mixing and segregation in a bidisperse gas-solid fluidised bed: a numerical and experimental study." Powder Technology **140**(3): 176-186.

Bolio, E. J., J. A. Yasuna, et al. (1995). "Dilute Turbulent Gas-Solid Flow in Risers with Particle-Particle Interactions." AIChE Journal **41**(6): 1375-1388.

Brereton, C. M. H. and J. R. Grace (1993). "Microstructural Aspects of the Behavior of Circulating Fluidized-Beds." Chemical Engineering Science **48**(14): 2565-2572.

Chapman, S., & Cowling, T. G. (1970). *The Mathematical Theory of Non-Uniform Gases* (3rd ed.). Cambridge: Cambridge University Press.

Cheremisinoff, N. P. (1986). "Review of Experimental Methods for Studying the Hydrodynamics of Gas Solid Fluidized-Beds." Industrial & Engineering Chemistry Process Design and Development **25**(2): 329-351.

Chew, J. W. and C. M. Hrenya (2011). "Link between bubbling and segregation patterns in gas-fluidized beds with continuous size distributions." AIChE Journal **in press**.

Chew, J. W., D. M. Parker, et al. (2011). "Elutriation and Species Segregation Characteristics of Polydisperse Mixtures of Group B particles in a dilute CFB Riser." submitted, AIChE J.

Chew, J. W., J. R. Wolz, et al. (2010). "Axial Segregation in Bubbling Gas-Fluidized Beds with Gaussian and Lognormal Distributions of Geldart Group B Particles." AIChE Journal **56**(12): 3049-3061.

Chew, J. W., R. Hays, et al. (2011). "Cluster characteristics of Geldart Group B particles in a pilot-scale CFB riser. I. Monodisperse Systems." submitted, Chemical Engineering Science.

Chew, J. W., R. Hays, et al. (2011). "Impact of material property and operating conditions on mass flux profiles of monodisperse and polydisperse Group B particles in the riser." in preparation for submission in May.

Chew, J. W., R. Hays, et al. (2011). "Reverse Core-Annular Flow of Geldart Group B Particles in Risers." submitted, Powder Technology.

Chew, J. W., R. Hays, et al. (2011). "Species segregation of binary mixtures and continous size distribution of Group B particles in riser flow." submitted, Chemical Engineering Science.

Chiba, T. and Kobayash.H (1970). "Gas Exchange between Bubble and Emulsion Phases in Gas-Solid Fluidized Beds." Chemical Engineering Science **25**(9): 1375-1385.

Ciborowski, J. and A. Wlodarski (1962). "On Electrostatic Effects in Fluidized Beds." Chemical Engineering Science **17**(1): 23-32.

Clark, N. N. and R. Turton (1988). "Chord Length Distributions Related to Bubble-Size Distributions in Multiphase Flows." International Journal of Multiphase Flow **14**(4): 413-424.

Clift, R. and J. R. Grace (1971). "Bubble Coalescence in Fluidized Beds - Comparison of 2 Theories." AIChE Journal **17**(1): 252-254.

Clift, R. and J. R. Grace (1972). "Mechanism of Bubble Break-up in Fluidized-Beds." Chemical Engineering Science **27**(12): 2309-2310.

Cocco, R. A., J. Cleveland, et al. (1995). "Simultaneous in-situ determination of particle loadings and velocities in a gaseous medium." AIChE Symposium Series **308**: 147.

Cocco, R., F. Shaffer, et al. (2010). "Particle clusters in and above fluidized beds." Powder Technology **203**(1): 3-11.

Cocco, R., F. Shaffer, R. Hays, S.B. Reddy Karri, and T. Knowlton, Particle Clusters In and Above Fluidized Beds, *Powder Technology*, 203(1), pp. 3-11, 2010.

Cocco, R., Shaffer, F., Hays, R., Karri, S. B. R., & Knowlton, T. (2010). Particle clusters in and above fluidized beds. *Powder Technology, 203*(1), 3-11.

Coronella, C. J. and J. X. Deng (1998). "A novel method for isokinetic measurement of particle flux within the riser of a circulating fluidized bed." Powder Technology **99**(3): 211-219.

Cui, H. P. and J. R. Grace (2007). "Fluidization of biomass particles: A review of experimental multiphase flow aspects." Chemical Engineering Science **62**(1-2): 45-55.

Curtis, J. S. and B. van Wachem (2004). "Modeling particle-laden flows: A research outlook." AIChE Journal **50**(11): 2638-2645.

Dahl, S. R. & Hrenya, C. M. 2004 Size segregation in rapid, granular flows with continuous size distributions. *Phys. Fluids* **16**, 1-13.

Dahl, S. R. and C. M. Hrenya (2005). "Size segregation in gas-solid fluidized beds with continuous size distributions." Chemical Engineering Science **60**(23): 6658-6673.

Dahl, S. R., Clelland, R. & Hrenya, C. M. 2002 The effects of continuous size distributions on the rapid flow of inelastic particles. *Phys. Fluids* **14**, 1972.

Dahl, S. R., Clelland, R. & Hrenya, C. M. 2003 Three-dimensional, rapid shear flow of particles with continuous size distributions. *Powder Tech.* **138**, 7.

Das, M., B. C. Meikap, et al. (2008). "Characteristics of axial and radial segregation of single and mixed particle system based on terminal settling velocity in the riser of a circulating fluidized bed." Chemical Engineering Journal **145**(1): 32-43.

Das, M., B. C. Meikap, et al. (2008). "Prediction of cluster diameter for a wide range of particles for gas-solid dispersed phase in a fast fluidized-bed reactor." Asia-Pacific Journal of Chemical Engineering **3**(2): 223-229.

Davidson, J. F., D. Harrison, et al. (1977). "Liquid-Like Behavior of Fluidized-Beds." Annual Review of Fluid Mechanics **9**: 55-86.

Derksen, J. J. & Sundaresan, S. submitted Dns of dense suspensions: Wave instabilities in liquid-fluidized beds. *J. Fluid Mech.*

Desjardin, O., Fox, R. O. & Villedieu, P. 2008 A quadrature-based moment method for dilute fluid-particle flows. *J. Comp. Phys.* **227**, 2534.

Desjardin, O., Fox, R. O. & Villedieu, P., 2008, A quadrature-based moment method for dilute fluid-particle flows, J. Comput. Phys., 227, 2514 – 2539.

Du, B., L. S. Fan, et al. (2002). "Gas and solids mixing in a turbulent fluidized bed." AIChE Journal **48**(9): 1896-1909.

Du, B., W. Warsito, et al. (2004). "ECT studies of the choking phenomenon in a gas-solid circulating fluidized bed." AIChE Journal **50**(7): 1386-1406.

Duru, P., M.Nicolas, HInch, J., & Guazzelli, E. (2002). Constitutive laws in liquid-fluidized beds. *J. Fluid Mech., 452*, 371-404.

Ellis, N., H. T. Bi, et al. (2004). "Influence of probe scale and analysis method on hydrodynamic properties of gas-fluidized beds." Chemical Engineering Science **59**: 1841-1851.

Ellis, N., L. A. Briens, et al. (2003). "Characterization of dynamic behavior in gas-solid turbulent fluidized bed using chaos and wavelet analyses." Chemical Engineering Journal **96**(1-3): 105-116.

Ergun, S, *Fluid through Packed Columns*, Chem. Eng. Prog., 48, pp. 89-94, 1952.

Euler-Lagrange simulations of finite-Stokes-numbers gas-particle flows in a lid-driven cavity, AIChE Annual Meeting, November 16th – 21st, Philadelphia.

Fan, L. S. and C. Zhu (1998). Principles of Gas-Solid Flows, Chapter 9, Cambridge University Press.

Fan, L. S. and C. Zhu (1998). Principles of Gas-Solid Flows. New York, Cambridge University Press.

Fan, L. S. and C. Zhu, *Principles of Gas-Solid Flows*, Cambridge University Press, 1998.

Fan, L. T., Y. M. Chen, et al. (1990). "Recent Developments in Solids Mixing." Powder Technology **61**(3): 255-287.

Fan, R. and R. O. Fox (2008). "Segregation in polydisperse fluidized beds: Validation of a multi-fluid model." Chemical Engineering Science **63**(1): 272-285.

Fan, R., Marchisio, D. L., & Fox, R. O. (2004). Application of the direct quadrature method of moments to polydisperse gas-solid fludized beds. *Powder Tech., 139*, 7-20.

Fox, R. O. (2003). *Computational Models for Turbulent, Reacting Flows*. Cambridge: Cambridge University Press.

Fox, R. O. (in press). Bivariate direct quadrature method of moments for coagulation and sintering of particle populations. *J. Aerosol Sci.*

Fox, R. O. 2008 A quadrature-based third-order moment method for dilute gas-particle flows. *J. Comp. Phys.* **227**, 6313.

Fox, R. O., F. Laurent, and M. Massot, Numerical simulation of spray coalescence in an Eulerian framework: direct quadrature method of moments and multi-fluid method, Journal of Computational Physics 227, 3058 (2008).

Fox, R. O., Laurent, F. & Massot, M. (In preparation) Application of the direct quadrature method of moments to polydisperse dense liquid sprays. *J. Comp. Phys.*

Fox, R.O. & Vedula., 2009, Quadrature-based moment method for moderately dense polydisperse gas-particle flows, Ind. Eng. Chem. Res., 49 (11), pp 5174–5187.

Galvin, J. E., Dahl, S. R., & Hrenya, C. M. (2005). On the role of non-equipartition in the dynamics of rapidly-flowing, granular mixtures. *J. Fluid Mech., 528*, 207-232.

Galvin, J. E., Hrenya, C. M., and Wildman, R. D. (2007) On the role of the Knudsen layer in rapid granular flows, J. Fluid. Mech., 585, 73–92.

Garg, R., Passalacqua, A., Subramaniam, S., & Fox. R. O. 2008, Comparison of Euler-Euler and

Garzó, V. & Dufty, J. 1999 Dense fluid transport for inelastic hard spheres. *Phys. Rev. E* **59**, 5895.

Garzó, V. & Dufty, J. W. 2002 Hydrodynamics for a granular binary mixture at low density. *Phys. Fluids* **14**, 1476.

Garzó, V. and F. V. Reyes (2010). "Segregation by thermal diffusion in granular shear flows." Journal of Statistical Mechanics-Theory and Experiment: P07024.

Garzó, V., & Dufty, J. W. (2002). Hydrodynamics for a granular binary mixture at low density. *Phys. Fluids, 14*(4), 1476-1490.

Garzó, V., C. M. Hrenya, et al. (2007). "Enskog theory for polydisperse granular mixtures. II. Sonine polynomial approximation." Physical Review E **76**(3): 031304.

Garzó, V., Dufty, J. W., Hrenya, C.M. 2007a Enskog theory for polydisperse granular mixtures. I. Navier-Stokes order transport. *Phys. Rev E.* **14**, 1476.

Gauthier, D., S. Zerguerras, et al. (1999). "Influence of the particle size distribution of powders on the velocities of minimum and complete fluidization." Chemical Engineering Journal **74**(3): 181-196.

Gauthier, D., S. Zerguerras, et al. (1999). "Influence of the particle size distribution of powders on the velocities of minimum and complete fluidization." Chemical Engineering Journal **74**(3): 181-196.

Geldart, D. (1973). "Types of Gas Fluidization." Powder Technology **7**(5): 285-292.

Geldart, D., Types of Gas Fluidization, *Powder Technology*, 7(5), pp. 285-292, 1973.

Gibilaro, L. G. and P. N. Rowe (1974). "Model for a Segregating Gas Fluidized-Bed." Chemical Engineering Science **29**(6): 1403-1412.

Gidaspow, D. (1994), Multiphase flow and fluidization, New York, USA: Academic Press.

Gidaspow, D., *Multiphase Flow and Fluidization: Continuum and Kinetic Theory Descriptions*, Academic Press, 1994.

Glasser, B. J., S. Sundaresan, et al. (1998). "From bubbles to clusters in fluidized beds." Physical Review Letters **81**(9): 1849-1852.

Goldhirsch, I. (2003). "Rapid granular flows." Annual Review of Fluid Mechanics **35**: 267-293.

Goldschmidt, M. J. V., J. M. Link, et al. (2003). "Digital image analysis measurements of bed expansion and segregation dynamics in dense gas-fluidised beds." Powder Technology **138**(2-3): 135-159.

Grace, J. R. and G. Sun (1991). "Influence of Particle-Size Distribution on the Performance of Fluidized-Bed Reactors." Canadian Journal of Chemical Engineering **69**(5): 1126-1134.

Grace, J. R., A. A. Avidan, et al. (1997). Circulating fluidized beds. London ; New York, Blackie Academic & Professional.

Guardiola, J., V. Rojo, et al. (1996). "Influence of particle size, fluidization velocity and relative humidity on fluidized bed electrostatics." Journal of Electrostatics **37**(1-2): 1-20.

Guenther, C. and R. Breault (2007). "Wavelet analysis to characterize cluster dynamics in a circulating fluidized bed." Powder Technology **173**(3): 163-173.

Guenther, C. and R. Breault, Wavelet Analysis to Characterize Cluster Dynamics in a Circulating Fluidized Bed, *Powder Technology*, 173(3), pp. 163-173, 2007.

Halow, J. S. and P. Nicoletti (1992). "Observations of Fluidized-Bed Coalescence Using Capacitance Imaging." Powder Technology **69**(3): 255-277.

Harris, B. J., J. F. Davidson, et al. (1994). Axial and radial variation of flow in circulating fluidized bed risers. International conference on circulating fluidized bed IV.

He, Y.; Deen, N.; Van Sint Annaland, M.; Kuipers, J. A. M. (2009) Gas-solid turbulent flow in a circulating fluidized bed riser: Experimental and numerical study of mono-disperse particle systems. Ind. Eng. Chem. Res, 8091 – 8097.

He, Y.; Deen, N.; Van Sint Annaland, M.; Kuipers, J. A. M. Gas-solid turbulent flow in a circulating fluidized bed riser: Numerical study of binary particle systems. Ind. Eng. Chem. Res. 2009, 8098 – 8108.

Hendrickson, G. (2006). "Electrostatics and gas phase fluidized bed polymerization reactor wall sheeting." Chemical Engineering Science **61**(4): 1041-1064.

Herb, B., S. Dou, et al. (1992). "Solid Mass Fluxes in Circulating Fluidized-Beds." Powder Technology **70**(3): 197-205.

Herbert, P. M., T. A. Gauthier, et al. (1994). "Application of Fiber Optic Reflection Probes to the Measurement of Local Particle-Velocity and Concentration in Gas-Solid Flow." Powder Technology **80**(3): 243-252.

Hill, R. J., Koch, D. L., & Ladd, A. J. C. (2001). Moderate-Reynolds-number flows in ordered and random arrays of spheres. *Journal of Fluid Mechanics*, *448*, 243-278.

Hilligardt, K. and J. Werther (1986). "Local bubble gas hold-up and expansion of gas/solid fluidized beds." German chemical engineering **9**(4): 215-221.

Hinds, W. C. (1999). Aerosol technology: Properties, behavior, and measurement of airborne particles. New York, Wiley.

Hiraki, I. and D. Kunii (1969). "Behavior of bubbles in fluidized beds." Chem. Eng., Tokyo **33**: 681.

Hirschberg, B. and J. Werther (1998). "Factors affecting solids segregation in circulating fluidized-bed riser." AIChE Journal **44**(1): 25-34.

Hoffmann, A. C. and E. J. Romp (1991). "Segregation in a Fluidized Powder of a Continuous Size Distribution." Powder Technology **66**(2): 119-126.

Holloway, W., Benyahia, S., Hrenya, C. M. & Sundaresan, S. 2011 Meso-scale structures of bidisperse mixtures of particles fluidized by a gas. *Chem. Eng. Sci.*, **66**, 4403-4420.

Holloway, W., Yin, X., & Sundaresan, S. 2010 Fluid-particle drag in inertial polydisperse gas-solid suspensions. *AIChE J.*, **56**, 1995-2004.

Hoomans, B. P. B., J. A. M. Kuipers, et al. (2000). "Granular dynamics simulation of segregation phenomena in bubbling gas-fluidised beds." Powder Technology **109**(1-3): 41-48.

Horio, M. and H. Kuroki (1994). "3-Dimensional Flow Visualization of Dilutely Dispersed Solids in Bubbling and Circulating Fluidized-Beds." Chemical Engineering Science **49**(15): 2413-2421.

Horio, M., K. Morishita, et al. (1988). Solid distribution and movement in circulating fluidized beds. Circulating fluidized bed technology II. P. Basu and J. F. Large. Oxford, Pergamon Press**:** 147-154.

Hrenya, C. M. (2011). Kinetic theory for granular materials: Polydispersity. Computational Gas-Solids Flows and Reacting Systems: Theory, Methods and Practice. S. Pannala, M. Syamlal and T. O'Brien. Hershey, PA, IGI Global**:** 475.

Hrenya, C. M. and J. L. Sinclair (1997). "Effects of particle-phase turbulence in gas-solid flows." AIChE Journal **43**(4): 853-869.

Hsiau, S. S. and M. L. Hunt (1996). "Granular thermal diffusion in flows of binary-sized mixtures." Acta Mechanica **114**(1-4): 121-137.

Iddir, H. & Arastoopour, H. 2005 Modeling of multitype particle flow using the kinetic theory approach. *AIChE J.*, **51**, 1620-1632.

in dilute granular flows. Proceedings of the 21st International Symposium on Rarefied Gas Dynamics, Cepadues-Editions, Toulouse, France.

Jackson, R. (2000). The Dynamics of Fluidized Particles, Chapter 5, Cambridge University Press.

Jenkins, J. T. (1998). Particle segregation in collisional flows of inelastic spheres. Physics of dry granular media. H. J. Herrmann, J. P. Hovi and S. Luding. Dordrecht ; Boston, Mass, Kluwer Academic**:** 645-658.

Jenkins, J. T. and M. Y. Louge (1997). "On the flux of fluctuation energy in a collisional grain flow at a flat, frictional wall." Physics of Fluids **9**(10): 2835-2840.

Jin, B. S., X. F. Wang, et al. (2010). "Modeling on High-Flux Circulating Fluidized Bed with Geldart Group B Particles by Kinetic Theory of Granular Flow." Energy & Fuels **24**: 3159-3172.

Johnson, P. C. & Jackson, R. 1987 Frictional-collisional constitutive relations for granular materials, with application to plane shearing. *J. Fluid Mech.* **176**, 67.

Joseph, G. G., J. Leboreiro, et al. (2007). "Experimental segregation profiles in bubbling gas-fluidized beds." AIChE Journal **53**(11): 2804-2813.

Karri, S. B. R. and T. M. Knowlton (1998). "Flow direction and size segregation of annulus solids in a riser." Fluidization IX: 189-196.

Koch, D. L. 1990 Kinetic theory for a monodisperse gas-solid suspension. *Phys. Fluids A* **2**, 1711.

Kogan, M. N., 1969 *Rarified Gas Dynamics*. Plenum Press, NewYork.

Kumaran, V., Tsao, H. K., Koch, D. 1993 Velocity distribution-functions for a sedimenting bidisperse gas-solid suspension. *Int. J. Multiphase Flow*, **19**,665-681.

Kunii, D. and O. Levenspiel (1991). Fluidization engineering. Boston, Butterworth-Heinemann.

Lackermeier, U. and J. Werther (2002). "Flow phenomena in the exit zone of a circulating fluidized bed." Chemical Engineering and Processing **41**(9): 771-783.

Leboreiro, J., G. G. Joseph, et al. (2008). "The influence of binary drag laws on simulations of species segregation in gas-fluidized beds." Powder Technology **184**(3): 275-290.

Li, H. Z., Q. S. Zhu, et al. (1995). "The Cluster-Size Distribution and Motion Behavior in a Fast Fluidized-Bed." Powder Technology **84**(3): 241-246.

Li, H. Z., Y. S. Xia, et al. (1991). "Microvisualization of Clusters in a Fast Fluidized-Bed." Powder Technology **66**(3): 231-235.

Li, J. H., L. X. Wen, et al. (1996). "Structure heterogeneity, regime multiplicity and nonlinear behavior in particle-fluid systems." Chemical Engineering Science **51**(11): 2693-2698.

Li, T. and C. Guenther, A CFD Study of Gas-Solid Jet in a CFB Riser Flow, *AICHE J.*, Vol. 0, 2011.

Lim, K. S., J. X. Zhu, et al. (1995). "Hydrodynamics of gas-solid fluidization." International Journal of Multiphase Flow **21**: 141-193.

Lin, C. L. and M. Y. Wey (2004). "Statistical and power spectral analysis of quality of fluidization for different particle size distributions at high temperature." Advanced Powder Technology **15**(1): 79-96.

Lin, C. L., M. Y. Wey, et al. (2002). "The effect of particle size distribution on minimum fluidization velocity at high temperature." Powder Technology **126**(3): 297-301.

Liu, J. Z., J. R. Grace, et al. (2003). "Novel multifunctional optical-fiber probe: I. Development and validation." AIChE Journal **49**(6): 1405-1420.

Liu, W. D., N. N. Clark, et al. (1998). "Relationship between bubble size distributions and chord-length distribution in heterogeneously bubbling systems." Chemical Engineering Science **53**(6): 1267-1276.

Liu, X. H., S. Q. Gao, et al. (2005). "Characterizing particle clustering behavior by PDPA measurement for dilute gas-solid flow." Chemical Engineering Journal **108**(3): 193-202.

Liu, X., M. Metzger, et al. (2007). "Couette flow with a bidisperse particle mixture." Physics of Fluids **19**(7): -.

Liu, X., M. Metzger, et al. (2008). "Granular and gas-particle flows in a channel with a bidisperse particle mixture." Chemical Engineering Science **63**(23): 5696-5713.

Louge, M. (1997). Experimental techniques. Circulating fluidized beds. J. R. Grace, A. A. Avidan and T. M. Knowlton. London ; New York, Blackie Academic & Professional**:** xvi, 585 p.

Louge, M., Chang, H. 1990 Pressure and voidage gradients in vertical gas-solid risers. *Powder Tech.*, **60**, 197-201.

Lu, H. L. and D. Gidaspow (2003). "Hydrodynamics of binary fluidization in a riser: CFD simulation using two granular temperatures." Chemical Engineering Science **58**(16): 3777-3792.

Lu, H. L., D. Gidaspow, et al. (2001). "Kinetic theory of fluidized binary granular mixtures." Physical Review E **6406**(6): 061301.

Lu, H. L., W. T. Liu, et al. (2000). "Kinetic theory of fluidized binary granular mixtures with unequal granular temperature." Physica A **284**(1-4): 265-276.

Luding, S., O. Strauss, et al. (2000). Segregation of polydisperse granular media in the presence of a temperature gradient. Lutam symposium on segregation in granular flows, Kluwer Academic Publishers.

Ludlow, J. C. and J. Spenik, Apparatus and Method for Determining Solids Circulation Rate, U.S. Patent S-116,774, 2011.

Ludlow, J. C. R. Panday, and L. J. Shadle, Standpipe Models for Diagnostics and Control of a Circulating Fluidized Bed, submitted to R. Breault, Ed., Special Issue of *Powder Technology*, 2011.

Ludlow, J. C., E. R. Monazam, and L. J. Shadle, Improvement of Continuous Solids Circulation Rate Measurement in a Cold Flow Circulating Fluidized Bed, *Powder Technology*, 182(3), pp. 379-387, 2008.

Ludlow, J. C., L. O. Lawson, and L. J. Shadle, Development of a Spiral Device for Measuring the Solids Flow in a Standpipe, 7th International Circulating Fluid Bed Conference, Niagara Falls, Canada, 2002.

Malcus, S., E. Cruz, et al. (2002). "Radial solid mass flux profiles in a high-suspension density circulating fluidized bed." Powder Technology **125**(1): 5-9.

Mallat, S. G. (1989). "A Theory for Multiresolution Signal Decomposition - the Wavelet Representation." Ieee Transactions on Pattern Analysis and Machine Intelligence **11**(7): 674-693.

Mallat, S. G. (1998). A wavelet tour of signal processing. San Diego, Academic Press.

Manyele, S. V., J. H. Parssinen, et al. (2002). "Characterizing particle aggregates in a high-density and high-flux CFB riser." Chemical Engineering Journal **88**(1-3): 151-161.

Marchisio, D. L. & Fox, R. O. 2005 Solution of population balance equations using the direct quadrature method of moments. *J. Aerosol Sci.* **36**, 43.

Martin, M. P., C. Derouin, et al. (1992). "Catalytic Cracking in Riser Reactors - Core-Annulus and Elbow Effects." Chemical Engineering Science **47**(9-11): 2319-2324.

Marzocchella, A. and U. Arena (1996). "Hydrodynamics of a circulating fluidized bed operated with different secondary air injection devices." Powder Technology **87**(3): 185-191.

Mastellone, M. L. and U. Arena (1999). "The effect of particle size and density on solids distribution along the riser of a circulating fluidized bed." Chemical Engineering Science **54**(22): 5383-5391.

Mathiesen, V., T. Solberg, et al. (1999). "Experimental and computational study of multiphase gas/particle flow in a CFB riser." AIChE Journal **45**(12): 2503-2518.

Mathiesen, V.; Solberg, T.; Hjertager, B. H. (2000) An experimental and computational study of multiphase flow behavior in a circulating fluidized bed. Int. J. Multiphase Flow, 387 – 419.

Matsuno, Y., H. Yamaguchi, et al. (1983). "The Use of Optic Fiber Probes for the Measurement of Dilute Particle Concentrations - Calibration and Application to Gas-Fluidized Bed Carryover." Powder Technology **36**(2): 215-221.

Miller, A. and D. Gidaspow (1992). "Dense, Vertical Gas-Solid Flow in a Pipe." AIChE Journal **38**(11): 1801-1815.

Miller, A. and D. Gidaspow, Dense, Vertical Gas-Solid Flow in a Pipe, *AICHE J.*, 38, pp. 1801-1815, 1992.

Misiti, M., Y. Misiti, et al. (2002). Matlab Wavelet Toolbox Users Guide Version 2. Natick, MA, The MathWorks, Inc.

Monceaux, L., M. Azzi, et al. (1986). Overall and local characterization of flow regimes in a circulating fluidized bed. Circulating Fluidized Bed Technology. P. Basu. Oxford, Pergamon press**:** 185-191.

Mori, S. and C. Y. Wen (1975). "Estimation of Bubble Diameter in Gaseous Fluidized-Beds." AIChE Journal **21**(1): 109-115.

Mostoufi, N. and J. Chaouki (2004). "Flow structure of the solids in gas-solid fluidized beds." Chemical Engineering Science **59**(20): 4217-4227.

Mudde, R. F. (2010). "Time-resolved X-ray tomography of a fluidized bed." Powder Technology **199**(1): 55-59.

Muller, C. R., J. F. Davidson, et al. (2006). "Real-time measurement of bubbling phenomena in a three-dimensional gas-fluidized bed using ultrafast magnetic resonance imaging." Physical Review Letters **96**(15): 154504.

Murray, J. A., C. M. Hrenya, et al. (2010). Extension of Kinetic Theory for Granular Binary Mixtures to Moderately Dense Flows. AIChE Annual Meeting. Salt Lake City, UT.

Muzzio, F. J., T. Shinbrot, et al. (2002). "Powder technology in the pharmaceutical industry: the need to catch up fast." Powder Technology **124**(1-2): 1-7.

Nakagawa, N., D. R. Bai, et al. (1994). "Segregation of Particles in Binary Solids Circulating Fluidized-Beds." Journal of Chemical Engineering of Japan **27**(2): 194-198.

Nienow, A. W. and T. Chiba (1985). Fluidization of dissimilar materials. Fluidization. J. F. Davidson, R. Clift and D. Harrison. Orlando, FL, Academic Press**:** 733.

Nienow, A. W., P. N. Rowe, et al. (1978). "Quantitative-Analysis of Mixing of 2 Segregating Powders of Different Density in a Gas-Fluidized Bed." Powder Technology **20**(1): 89-97.

Oberkampf, W. L. and M. F. Barone, Measures of Agreement between Computation and Experiment: Validation Metrics, *Journal of Computational Physics*, 217, pp. 5-36, 2006.

Ottino, J. M. and D. V. Khakhar (2000). "Mixing and segregation of granular materials." Annual Review of Fluid Mechanics **32**: 55-91.

Partridge, B. A. and P. N. Rowe (1966). "Analysis of Gas Flow in a Bubbling Fluidised Bed When Cloud Formation Occurs." Transactions of the Institution of Chemical Engineers and the Chemical Engineer **44**(9): T349-358.

Passalacqua A., Vedula P., Fox R. O. 2008 Solution of the Boltzmann Equation for Fluid Flows In Microchannels at Finite Knudsen Numbers with a Third-Order Quadrature-Based Moment Method, Submitted to AIChE Annual Meeting.

Passalacqua A., Vedula P., Hrenya C.M., Fox R. O. 2008 A Kinetic-Based Model for a Non-Isothermal Granular Gas with Mono- and Bi-Dispersed Particles, Submitted to AIChE Annual Meeting.

Passalacqua, A., Fox, R. O., Garg, R., Subramaniam, S. 2009 A fully coupled quadrature-based moment method for dilute to moderately dilute fluid-particle flows, *Chemical Engineering Science*, doi:10.1016/j.ces.2009.09.002.

Passalacqua, A., Fox, R. O., Garg, R., Subramaniam, S., 2009, A fully coupled quadrature-based moment method for dilute to moderately dilute fluid-particle flows, Chem. Eng. Sci., doi:10.1016/j.ces.2009.09.002.

polydisperse gas-particle flows, Ind. Eng. Chem. Res., 49 (11), pp 5174–5187.

Pope, S. P. 2000 Turbulent flows. Cambridge University Press, Cambridge.

Pugsley, T., D. Lapointe, et al. (1997). "Exit effects in circulating fluidized bed risers." Canadian Journal of Chemical Engineering **75**(6): 1001-1010.

Qi, C. M. and I. H. Farag (1993). "Radial Particle-Flux and Momentum-Transfer in the Circulating Fluidized-Bed." Chemical Engineering Communications **124**: 15-27.

Qi, H., C. You, A. Boemer, and U. Renz, Eulerian Simulation of Gas-Solid Two Phase Flow in a CFB-Riser under Consideration of Cluster Effect, in D. Xu, and S. Mori, Eds., *Fluidization 2000: Science and Technology*, Xi'an Publishing House, Xi'an, pp. 231-237, 2000.

Randolph, A. D. & Larson, M. A. 1971 *Theory of particulate processes*. Academic Press, New York.

Ren, J. and J. Li (1998). "Wavelet analysis of dynamic behavior in fluidized beds." Fluidization IX: 629-636.

Ren, J. Q., Q. M. Mao, et al. (2001). "Wavelet analysis of dynamic behavior in fluidized beds." Chemical Engineering Science **56**(3): 981-988.

Rhodes, M. (1998). Introduction to particle technology. West Sussex, England, John Wiley & Sons Ltd.

Rhodes, M. J. (1990). "Modeling the Flow Structure of Upward-Flowing Gas Solids Suspensions." Powder Technology **60**(1): 27-38.

Rhodes, M. J. and P. Laussmann (1992). "Characterizing Nonuniformities in Gas-Particle Flow in the Riser of a Circulating Fluidized-Bed." Powder Technology **72**(3): 277-284.

Rhodes, M. J., Modeling the Flow Structure of Upward-Flowing Gas-Solids Suspensions, *Powder Technology*, 60, pp. 27-38, 1990.

Rhodes, M. J., P. Laussmann, et al. (1988). Measurement of radial and axial solids flux variations in the riser of a circulating fluidized bed. Circulating fluidized bed technology II. P. Basu and J. F. Large. Oxford, Pergamon Press**:** 155-164.

Rhodes, M. J., X. S. Wang, et al. (1992). "Similar Profiles of Solids Flux in Circulating Fluidized-Bed Risers." Chemical Engineering Science **47**(7): 1635-1643.

Rhodes, M., H. Mineo, et al. (1992). "Particle Motion at the Wall of a Circulating Fluidized-Bed." Powder Technology **70**(3): 207-214.

Rogallo, R. S. 1981 Numerical experiments in homogenous turbulence. NASA Technical Memorandum. 81315.

Rowe, P. N. and A. W. Nienow (1976). "Particle Mixing and Segregation in Gas-Fluidized Beds - Review." Powder Technology **15**(2): 141-147.

Rowe, P. N. and B. A. Partridge (1965). "An X-Ray Study of Bubbles in Fluidised Beds." Transactions of the Institution of Chemical Engineers and the Chemical Engineer **43**(5): T157-T175.

Rowe, P. N., A. J. Agbim, et al. (1972). "Mechanisms by Which Particles Segregate in Gas Fluidized-Beds - Binary-Systems of near-Spherical Particles." Transactions of the Institution of Chemical Engineers and the Chemical Engineer **50**(4): 310-323.

Rowe, P. N., A. W. Nienow, et al. (1972). "Preliminary Quantitative Study of Particle Segregation in Gas Fluidized-Beds - Binary-Systems of near Spherical Particles." Transactions of the Institution of Chemical Engineers and the Chemical Engineer **50**(4): 310-323.

Rowe, P. N., B. A. Partridge, et al. (1962). "Bubbles in Fluidized Beds." Nature **195**(4838): 278-279.

Rowe, P. N., B. A. Partridge, et al. (1964). "Cloud Formation around Bubbles in Gas Fluidized Beds." Chemical Engineering Science **19**(12): 973-985.

Rowe, P. N., B. A. Partridge, et al. (1965). "Mechanisms of Solids Mixing in Fluidised Beds." Transactions of the Institution of Chemical Engineers and the Chemical Engineer **43**(9): T271-T286.

Rowe, P. N., B. A. Partridge, et al. (1965). "Mechanisms of Solids Mixing in Fluidised Beds." Transactions of the Institution of Chemical Engineers and the Chemical Engineer **43**(9): T271-T286.

Rowe, P. N., L. Santoro, et al. (1978). "Division of Gas between Bubble and Interstitial Phases in Fluidized-Beds of Fine Powders." Chemical Engineering Science **33**(1): 133-140.

Sakiz, M. & Simonin, O. 1998 Numerical experiments and modelling of non-equilibrium effects

Salvaterra, A., D. Geldart, et al. (2005). "Solid flux in a circulating fluidized bed riser." Chemical Engineering Research & Design **83**(A1): 24-29.

Sangani, A. S., Mo, G., Tsao, H. K. W., Koch, D. L. 1996 Simple shear flows of dense gas–solid suspensions at finite Stokes numbers. *J. Fluid Mech*. **313**, 309-341.

Seachman, S. M., P. C. Yue, E. M. Taylor, and L. J. Shadle, Solids Fractions and Flow Characteristics in a CFB as Measured with a Fiber Optic Probe, AIChE Annual Meeting, Cincinnati, OH, Session 03006 Circulating Fluidized Beds, MS# 32940, p.10, 2005.

Shadle, L. J., J. C. Ludlow, J. Spenik , S.M. Seachman, and C. Guenther in J. Werther, W. Nowak, K-E Wirth, and E-U Hartge, Eds., *Circulating Fluidized Bed Technology IX*, TuTech Innovation GmbH, Hamburg, Germany, pp. 307-312, 2008.

Shadle, Lawrence J., Christopher J. Ludlow, James L. Spenik , Steven M. Seachman, and Chris Guenther (2008) "Jet Penetration into a Riser Operated in Dense Suspension Upflow: Experimental and Model Comparisons", Circulating Fluidized Bed Technology IX, eds. J. Werther, W. Nowak, K-E Wirth, and E-U Hartge, TuTech Innovation GmbH, Hamburg, Germany, p. 307-312.

Sharma, A. K., K. Tuzla, et al. (2000). "Parametric effects of particle size and gas velocity on cluster characteristics in fast fluidized beds." Powder Technology **111**(1-2): 114-122.

Simonin, O. (1996). *Continuum modeling of dispersed turbulent two-phase flows. Part I: General model description.* Paper presented at the von Karman Institute of Fluid Dynamics Lecture Series.

Sinclair, J. L. and R. Jackson (1989). "Gas-Particle Flow in a Vertical Pipe with Particle-Particle Interactions." AIChE Journal **35**(9): 1473-1486.

Songprawat, S. and D. Gidaspow (2010). "Multiphase flow with unequal granular temperatures." Chemical Engineering Science **65**(3): 1134-1143.

Soong, C. H., K. Tuzla, et al. (1995). Experimental determination of cluster size and velocity in circulating fluidized beds. Proceedings of the 8th Engineering Foundation Conference on Fluidization. J. F. Large and C. Laguerie. NY, Engineering Foundation**:** 219-227.

Spenik, J. and J.C. Ludlow, Use of Piezoelectric Pressure Transducers to Determine Local Solids Mass Flux in the Riser of a Cold Flow Circulating Fluidized Bed, *Powder Technology*, 203, pp. 86-90, 2010.

Sun, G. and J. R. Grace (1994). "Experimental-Determination of Particle Dispersion in Voids in a Fluidized-Bed." Powder Technology **80**(1): 29-34.

Sun, G. G. and J. R. Grace (1990). "The Effect of Particle-Size Distribution on the Performance of a Catalytic Fluidized-Bed Reactor." Chemical Engineering Science **45**(8): 2187-2194.

Sundaresan, S. (2001). "Some outstanding questions in handling of cohesionless particles." Powder Technology **115**(1): 2-7.

Sundaresan, S. (2003). "Instabilities in fluidized beds." Annual Review of Fluid Mechanics **35**: 63-88.

Tagami, N., A. Mujumdar, et al. (2009). "DEM simulation of polydisperse systems of particles in a fluidized bed." Particuology **7**(1): 9-18.

Tanaka, T. and Y. Tsuji (1991). "Numerical Simulation of Gas-Solid Two-Phase Flow in a Vertical Pipe: On the Effect of Inter-Particle Collision." Gas-Solid Flows, ASME FED **121**: 123-128.

Tanaka, T., Y. Takagi, et al. (1989). "Measurements of gas-solid two-phase flow in a vertical pipe." Transactions of JSME (Ser. B) **55**(516): 2302-2309.

Tang, P. and V. M. Puri (2004). "Methods for minimizing segregation: A review." Particulate Science and Technology **22**(4): 321-337.

Tardos, G. and R. Pfeffer (1980). "A Method to Measure Electrostatic Charge on a Granule in a Fluidized-Bed." Chemical Engineering Communications **4**(6): 665-671.

Tartan, M. and D. Gidaspow (2004). "Measurement of granular temperature and stresses in risers." AIChE Journal **50**(8): 1760-1775.

Tenneti, S., Garg, R., Hrenya, C. M., Fox, R. O., & Subramaniam, S. (2010). Direct numerical simulation of gas-solid suspensions at moderate Reynolds number: Quantifying the coupling between hydrodynamic forces and particle velocity fluctuations. *Powder Technology, 203*(1), 57-69.

Tenneti, S., Garg, R., Subramaniam, S., Quantification of gas–phase velocity fluctuations in statistically homogeneous gas–solid flow using particle–resolved direct numerical simulation. *In review*.

Tingwen, Li, Grace, John; Shadle, Lawrence; (2011): On the superficial gas velocity in deep gas-solids fluidized beds CHEMICAL ENGINEERING SCIENCE (66) 22, p. 5735-5738

Trujillo, L. and H. J. Herrmann (2003). "Hydrodynamic model for particle size segregation in granular media." Physica A-Statistical Mechanics and Its Applications **330**(3-4): 519-542.

Trujillo, L., M. Alam, et al. (2003). "Segregation in a fluidized binary granular mixture: Competition between buoyancy and geometric forces." Europhysics Letters **64**(2): 190-196.

Tuzla, K., A. K. Sharma, et al. (1998). "Transient dynamics of solid concentration in downer fluidized bed." Powder Technology **100**(2-3): 166-172.

Uhlmann, M., 2008 Interface-resolved direct numerical simulation of vertical particulate channel flow in the turbulent regime. *Physics of Fluids* **20(5)**.

van Breugel, J. W., J. J. M. Stein, et al. (1969). "Isokinetic sampling in dense gas-solid stream." Proceedings of the Institution of Mechanical Engineers **184**(3c): 18-23.

Van de Velden, M., J. Baeyens, et al. (2007). "Solids mixing in the riser of a circulating fluidized bed." Chemical Engineering Science **62**(8): 2139-2153.

van Deemter, J. J. (1980). Mixing patterns in large-scale fluidized beds. Fluidization. J. R. Grace and J. M. Matsen. New York, Plenum Press**:** xviii, 605 p.

Van der Hoef, M. A., R. Beetstra, et al. (2005). "Lattice-Boltzmann simulations of low-Reynolds-number flow past mono- and bidisperse arrays of spheres: results for the permeability and drag force." Journal of Fluid Mechanics **528**: 233-254.

van der Meer, E. H., R. B. Thorpe, et al. (2000). "Flow patterns in the square cross-section riser of a circulating fluidised bed and the effect of riser exit design." Chemical Engineering Science **55**(19): 4079-4099.

van Ommen, J. R. and R. F. Mudde (2008). "Measuring the Gas-Solids Distribution in Fluidized Beds-A Review." International Journal of Chemical Reactor Engineering **6**: Review R3.

van Wachem, B. G. M., J. C. Schouten, et al. (2001). "CFD modeling of gas-fluidized beds with a bimodal particle mixture." AIChE Journal **47**(6): 1292-1302.

Wei, F., F. B. Lu, et al. (1997). "Mass flux profiles in a high density circulating fluidized bed." Powder Technology **91**(3): 189-195.

Wei, F., G. Q. Yang, et al. (1995). "The Characteristics of Cluster in a High-Density Circulating Fluidized-Bed." Canadian Journal of Chemical Engineering **73**(5): 650-655.

Wen, C. Y. and Y. H. Yu, *Mechanics of Fluidization*, Chem. Eng. Prog. Symp. Ser., 62 (62), pp. 100-111, 1966.

Werther, J. and B. Hirschberg (1997). Solids motion and mixing. Circulating fluidized beds. J. R. Grace, A. A. Avidan and T. M. Knowlton. London, UK, Blackie Academic and Professional**:** 585.

Wu, B., K. Apostolos, et al. (2007). "Multiresolution analysis of pressure fluctuations in a gas-solids fluidized bed: Application to glass beads and polyethylene powder systems." Chemical Engineering Journal **131**(1-3): 23-33.

Wu, S. Y. and J. Baeyens (1998). "Segregation by size difference in gas fluidized beds." Powder Technology **98**(2): 139-150.

Wu, X. Z., F. Jiang, et al. (2010). "CFD simulation of smooth and T-abrupt exits in circulating fluidized bed risers." Particuology **8**(4): 343-350.

Wylie, J. J. and D. L. Koch (2000). "Particle clustering due to hydrodynamic interactions." Physics of Fluids **12**(5): 964-970.

Wylie, J. J., Koch, D. L. & Ladd, J. C. 2003 Rheology of suspensions with high particle inertia and moderate fluid inertia. *J. Fluid Mech.* **480**, 95.

Wylie, J. J., Koch, D. L., & Ladd, A. J. C. (2003a). Rheology of suspensions with high particle inertia and moderate fluid inertia. *Journal of Fluid Mechanics, 480,* 95-118.

Xu, H., M. Louge, et al. (2003). "Solutions of the kinetic theory for bounded collisional granular flows." Continuum Mechanics and Thermodynamics **15**(4): 321-349.

Xu, Y. & Subramaniam, S. 2006 A multiscale model for dilute turbulent gas-particle flows based on the equilibration of energy concept. *Phys. Fluids* **18**.

Xu, Y. & Subramaniam, S. 2007 Consistent modeling of interphase turbulent kinetic energy transfer in particle-laden turbulent flows. *Phys. Fluids* 19.

Xu, Y., & Subramaniam, S. (2006). A multiscale model for dilute turbulent gas-particle flows based on the equilibration of energy concept. *Phys. Fluids, 18*(3).

Xu, Y., & Subramaniam, S. (2010). A multiscale model for dilute turbulent gas-particle flows based on the equilibration of energy concept. *Phys. Fluids, 18*(3).

Yan, A., J. H. Pärssinen, and J-X. Zhu, Flow Properties in the Entrance and Exit Regions of a High Flux Circulating Fluidized Bed Riser, *Powder Technology*, 131, pp. 256-263, 2003.

Yang, T. Y. and L. P. Leu (2009). "Multiresolution Analysis on Identification and Dynamics of Clusters in a Circulating Fluidized Bed." AIChE Journal **55**(3): 612-629.

Yang, W. (2003). Handbook of Fluidization and Fluid-Particle Systems, Chapters 1-2. New York, Marcel Dekker, Inc.

Yates, J. G. and D. Newton (1986). "Fine Particle Effects in a Fluidized-Bed Reactor." Chemical Engineering Science **41**(4): 801-806.

Ye, S., X. B. Qi, et al. (2009). "Direct Measurements of Instantaneous Solid Flux in a Circulating Fluidized Bed Riser using a Novel Multifunctional Optical Fiber Probe." Chemical Engineering & Technology **32**(4): 580-589.

Yin, X., & Sundaresan, S. 2008 Drag Law for Bidisperse Gas-Solid Suspensions Containing Equally Sized Spheres. *Ind. Eng. Chem. Res.,* **48**, 227-241.

Yin, X., & Sundaresan, S. Fluid-particle drag in low-Reynolds-number polydisperse gas-solid suspensions. *AIChE J.*, **55**, 1352-1368.

Yoon, D. K. and J. T. Jenkins (2006). "The influence of different species' granular temperatures on segregation in a binary mixture of dissipative grains." Physics of Fluids **18**(7): 073303.

Zenz, F. and D. Othmer (1960, page 278). Fluidization and Fluid-Particle Systems. New York, Reinhold Publishing Corp.

Zhang, H., P. M. Johnston, et al. (1998). "A novel calibration procedure for a fiber optic solids concentration probe." Powder Technology **100**(2-3): 260-272.

Zhang, H.,P. Johnston, J. Zhu, H. de Lasa, and M. Bergougnou, A Novel Calibration Procedure for a Fiber Optic Solids Concentration Probe, *Powder Technology*, 100, pp. 260-272, 1998.

Zhang, W. N., F. Johnsson, et al. (1997). "Momentum probe and sampling probe for measurement of particle flow properties in CFB boilers." Chemical Engineering Science **52**(4): 497-509.

Zhao, G. B. and Y. R. Yang (2003). "Multiscale resolution of fluidized-bed pressure fluctuations." AIChE Journal **49**(4): 869-882.

Zhao, H. L., G. S. P. Castle, et al. (2003). "Bipolar charging of poly-disperse polymer powders in fluidized beds." Ieee Transactions on Industry Applications **39**(3): 612-618.

Zhou, H. S., G. Flamant, et al. (2002). "Lagrangian approach for simulating the gas-particle flow structure in a circulating fluidized bed riser." International Journal of Multiphase Flow **28**(11): 1801-1821.

Zhou, J., J. R. Grace, et al. (1994). "Voidage Profiles in a Circulating Fluidized-Bed of Square Cross-Section." Chemical Engineering Science **49**(19): 3217-3226.

Zhou, J., J. R. Grace, et al. (1996). "Influence of wall roughness on the hydrodynamics in a circulating fluidized bed." AIChE Journal **42**(4): 1153-1156.

Zinn, A., E. R. Monazam, J. Spenik, and J. C. Ludlow, REM Laser Probe Contract Results and Summary, DOE/NETL-2006/1229, 2006.

Zou, B., H. Z. Li, et al. (1994). "Cluster Structure in a Circulating Fluidized-Bed." Powder Technology **78**(2): 173-178.

APPENDIXES

Appendix A: "Enskog Theory for Polydisperse Granular Mixtures. I. Navier-Stokes Order Transport," by Garzo, Dufty, and Hrenya
"Enskog Theory for Polydisperse Granular Mixtures II. Sonine Polynomial Approximation," by Garzo, Hrenya, and Dufty

Appendix B: "Enskog Kinetic Theory for Monodisperse Gas-solid Flows," by Garzo, Tenneti, Subramaniam, and Hrenya

Appendix C: Iowa State – Task 2.1

Appendix D: "Fluid-Particle Drag in Inertial Polydisperse Gas–Solid Suspensions," by Holloway, Yin, and Sundaresan

Appendix E: Iowa State – Task 2.2

Appendix F: Iowa State – Governing Equations

Appendix G: **"**Drag Law for Bidisperse Gas-Solid Suspensions Containing Equally Sized Spheres," by Yin and Sundaresan

Appendix H: **"**Continuum Representation of a Continuous Size Distribution of Particles Engaged in Rapid Granular Flow," by Murray, Benyahia, Metzger, and Hrenya

Appendix I: Tables 14 and 15 (PSRI)

Appendix J: **"**Fluid-Particle Drag in Low-Reynolds-Number Polydisperse Gas–Solid Suspensions," by Yin and Sundaresan

Appendix K: "Meso-scale Structures of Bidisperse Mixtures of Particles Fluidized by a Gas," by Holloway, Benyahia, Hrenya, and Sundaresan

Appendix L: **"**Effect of Microstructural Anisotropy on the Fluid-particle Drag Force and the Stability of the uniformly Fluidized State," by Holloway, Sun, and Sundaresan

Enskog Theory for Polydisperse Granular Mixtures. I. Navier-Stokes order Transport

Vicente Garzó*
Departamento de Física, Universidad de Extremadura, E-06071 Badajoz, Spain

James W. Dufty†
Department of Physics, University of Florida, Gainesville, Florida 32611

Christine M. Hrenya ‡
Department of Chemical and Biological Engineering, University of Colorado, Boulder, CO 80309

(Dated: February 6, 2008)

A hydrodynamic description for an s-component mixture of inelastic, smooth hard disks (two dimensions) or spheres (three dimensions) is derived based on the revised Enskog theory for the single-particle velocity distribution functions. In this first portion of the two-part series, the macroscopic balance equations for mass, momentum, and energy are derived. Constitutive equations are calculated from exact expressions for the fluxes by a Chapman–Enskog expansion carried out to first order in spatial gradients, thereby resulting in a Navier-Stokes order theory. Within this context of small gradients, the theory is applicable to a wide range of restitution coefficients and densities. The resulting integral-differential equations for the zeroth- and first-order approximations of the distribution functions are given in exact form. An approximate solution to these equations is required for practical purposes in order to cast the constitutive quantities as algebraic functions of the macroscopic variables; this task is described in the companion paper.

I. INTRODUCTION

Flows of polydisperse particles (mixtures) are ubiquitous in nature and industry alike. Examples of the former include pyroclastic flows, landslides, pollutant transport, and planetary rings. Examples of the latter include pneumatic conveying of grains, ores, and chemicals; fluidized-bed operation for power production and catalytic cracking; mixing of pharmaceutical powders (medication and binder) and poultry feedstock (grains and vitamins). A non-uniform particle distribution may be a property of the starting material itself, or it may be intentionally utilized in order to improve process performance. For an example of the latter, the addition of fines to a relatively monodisperse material has been shown to (i) decrease attrition in high-speed conveying lines [1], (ii) increase conversion in high-velocity, fluidized-bed reactors [2] and (iii) improve heat transfer efficiency in a circulating fluidized bed (CFB) combustor [3]. Polydisperse materials are also known to exhibit counter-intuitive behaviors that have no monodisperse counterpart. For example, agitation of polydisperse materials via vibration, free-fall, or flow down an incline leads to segregation among unlike particles (de-mixing). Enhancing or suppressing this segregation tendency may be critical to process performance, depending on whether the desired outcome is a separated or well-mixed state, respectively.

In the current effort, attention is restricted to rapid flows, in which particle collisions are assumed to be both binary and instantaneous in nature. For monodisperse systems, kinetic-theory-based treatments have been successful at predicting not only rapid granular flows (in which the role of the interstitial fluid is assumed negligible), but have also been incorporated into models of high-velocity, gas-solid systems. In particular, kinetic-theory-based descriptions are now standard components in both commercial and open-source CFD (computational fluid dynamics) software packages for multiphase flows such as Fluent$^{\mathrm{R}}$ and MFIX (http://www.mfix.org/), respectively. Nonetheless, the development and application of kinetic-theory-based descriptions for polydisperse systems is in its infancy relative to their monodisperse counterparts, as has been highlighted in several recent review articles and perspectives [4, 5, 6, 7]. The main challenge associated with the derivation of kinetic-theory-based descriptions for mixtures is the increased complexity associated with the additional hydrodynamic fields and associated transport coefficients, and in particular with the accurate evaluation of the collisions integrals. Correspondingly, many of the early contributions resorted to assumptions which are only strictly true in the limit of perfectly elastic spheres in a uniform steady state: a Maxwellian (single-particle) velocity distribution [8, 9, 10] or an equipartition of energy [11, 12, 13, 14]. However, the presence of a non-Maxwellian velocity distribution in granular flows is well-documented [15, 16, 17, 18, 19, 20, 21, 22], and has been shown to have a significant impact on some transport coefficients [23]. Moreover, a non-equipartition

* Electronic address: vicenteg@unex.es
† Electronic address: dufty@phys.ufl.edu
‡ Electronic address: hrenya@colorado.edu

of energy between unlike particles is widely established [24, 25, 26, 27, 28, 29, 30, 31, 32] , and has been shown to significantly contribute to the driving force for segregation [33] and to lead to a reversal of the segregation direction [34, 35, 36] in certain systems. A more recent theory [37] involves the lifting of both of these assumptions, except in the evaluation of collision integrals involving two unlike particles, in which case a Maxwellian velocity distribution is assumed for each particle type. Two current theories exist that do not involve either of these assumptions [38, 39], though both are based on the Boltzmann equation and thus are limited to dilute flows. Another key difference between existing polydisperse theories is the base state used in the Chapman–Enskog (CE) expansion. Some theories [8, 9, 10, 11, 12, 13, 14, 37, 39] assume an expansion about a perfectly elastic (molecular equilibrium) base state, and thus are restricted to nearly-elastic systems. However, in the CE method the base state must not be chosen a priori, but rather it is determined as the solution to the kinetic equation to zeroth order in the gradient expansion. This solution is found to correspond to the *local* homogeneous cooling state (HCS) and was used in Ref. [38] as the reference state to determine the Navier-Stokes transport coefficients of a dilute mixture, without any restriction on the level of inelasticity.

The objective of the current effort is twofold. First, a kinetic-theory-based description for the flow of an s-component mixture in d dimensions is derived which (i) incorporates non-Maxwellian and non-equipartition effects, (ii) is applicable to a wide range of restitution coefficients, and (iii) is applicable to both dilute and (moderately) dense flows. In particular, a CE expansion of the revised Enskog theory for inelastic, hard spheres is carried out for both disks ($d = 2$) and spheres ($d = 3$) up to the Navier-Stokes order. Second, the derivation of the resulting theory is critically compared and contrasted to that of existing theories, in an effort to clearly reveal the implications of various treatments on both the governing equations and constitutive relations. For this reason, the derivation is presented in a detailed and somewhat pedagogical fashion. This work takes the form of two self-contained, companion papers. In this first paper, the results of the exact analysis are given. The follow-on paper details the leading order approximations needed for the explicit evaluation of all properties derived here: the distribution functions, the "equations of state" (cooling rate and pressure), and the transport coefficients. In addition, the methodology used to obtain these results is critically compared there to that of previous theories.

A confusing issue in the granular community is the context of the Navier-Stokes hydrodynamic equations in freely cooling granular gases derived in this paper. The expressions for the Navier-Stokes transport coefficients are not limited to weak inelasticity and so the calculations provided here apply even for strong dissipation. The Navier-Stokes hydrodynamic equations may or may not be limited with respect to inelasticity, depending on the particular states analyzed. The CE method assumes that the relative changes of the hydrodynamic fields over distances of the order of the mean free path are small. For ordinary (elastic) gases this can be controlled by the initial or boundary conditions. However, in the case of granular fluids the situation is more complicated since in some cases (e.g., steady states such as the simple shear flow problem [40]) the boundary conditions imply a relationship between dissipation and gradients so that both cannot be chosen independently. In these cases, the Navier-Stokes approximation only holds for nearly elastic particles [40]. However, the transport coefficients characterizing the Navier-Stokes hydrodynamic equations are nonlinear functions of the coefficients of restitution, regardless the applicability of those equations.

In spite of the above cautions, the Navier-Stokes approximation is relevant to describe a wide class of granular flows. One of them corresponds to spatial perturbations of the HCS for an isolated system. Computer simulations have confirmed the accuracy of the Navier-Stokes hydrodynamic equations with their associated transport coefficients to quantitatively describe cluster formation [41]. The same kinetic theory results apply to driven systems as well. This is so since the reference state is a *local* HCS whose parameters change throughout the system to match the physical values in each cell. Another examples of good agreement between theory and simulation [42] and experiments [43, 44] include the application of the Navier-Stokes hydrodynamics to describe density/temperature profiles in vertical vibrated gases, supersonic flow past at wedge in real experiments [45], and nonequipartition and size segregation in agitated granular mixtures [27, 28, 46]. In summary, the Navier-Stokes hydrodynamics with the constitutive equations obtained in this paper constitute an important and useful description for many different physical situations, although more limited than for elastic gases.

II. OVERVIEW OF DERIVATION

The theoretical basis for a hydrodynamic description of molecular gases is most completely established at low density using the Boltzmann kinetic equation. There, the CE solution and its prediction of transport coefficients is well-established from both computer simulation and experiment [47]. For a moderately dense gas there is no accurate and practical generalization of the Boltzmann equation except for the idealized hard sphere fluid. In that case, the Enskog kinetic equation describes the dominant positional corrections to the Boltzmann equation due to excluded volume effects of other particles on a colliding pair [47]. The neglected velocity correlations are important only at much higher densities. The derivation of hydrodynamics and evaluation of transport coefficients based on the Enskog

kinetic equation leads to an accurate and unique description of moderately dense gases. The generalization to mixtures requires a revision of the original Enskog theory for thermodynamic consistency (revised Enskog theory, or RET) [48], and its application to hydrodynamics and mixture transport coefficients was accomplished twenty years ago [49]. As noted above, for granular (dissipative) gases, there remains an open problem of predicting transport properties at moderate densities, as occur in current experiments and simulations. This problem is addressed here in its full generality using the extension of this revised Enskog theory to inelastic collisions without limits on the number of components, densities, temperature, or degree of dissipation. This subsumes all previous analyses for both molecular and granular gases, which are recovered in the appropriate limits.

Due to the extreme length of the derivation, an outline of the steps involved is given here for easy reference.

- *Section III.* The starting point of the derivation process is the revised Enskog kinetic equations for mixtures of inelastic, hard spheres. These equations for the single-particle, position and velocity distribution functions of each species, $\{f_i\}$, take the form of nonlinear, integro-differential equations, where the integral portion arises from the collision operator.

- *Section IV.* The macroscopic variables of interest (number density $\{n_i\}$, etc.) are defined exactly in terms of moments of $\{f_i\}$ (e.g., $n_i(\mathbf{r}) = \int d\mathbf{v} f_i(\mathbf{r},\mathbf{v},t)$, where $\mathbf{v}$ is the velocity of species i). Thus, the macroscopic balance equations can be obtained by appropriate manipulation of the Enskog kinetic equations (e.g., multiplication by $d\mathbf{v}$ followed by integration over the velocity to obtain the species mass balance). At this stage, all of the constitutive quantities (cooling rate, stress tensor, conduction, and mass flux) appearing in the macroscopic balances are integral functionals of $\{f_i\}$, which depend explicitly on space and time only through their dependence on $\{f_i\}$.

- *Section V.* In order to obtain a hydrodynamic description (one in which the constitutive quantities are determined entirely by the macroscopic or hydrodynamic variables), the concept of a normal solution is introduced. These are special solutions to the Enskog equations for which the $\{f_i\}$ depend on space and time only through an implicit *functional* dependence on the macroscopic fields (or equivalently as explicit *functions* of these local fields and their gradients at the spatial point of interest).

- *Section VI.* An exact analytical solution for $\{f_i\}$ is not a practical objective in the most general case, and thus attention is restricted to states with small spatial gradients. In this case the gradients provide a small parameter, allowing a small spatial gradients, or small Knudsen number, expansion (i.e., the CE expansion). The analysis is carried out here to first (Navier-Stokes) order: $f_i = f_i^{(0)} + f_i^{(1)}$, where $f_i^{(0)}$ is the zeroth order solution and $f_i^{(1)}$ is the first-order correction (zero- and first-order in gradients, respectively). The kinetic equations then become integral-differential equations for the determination of $f_i^{(0)}$ and $f_i^{(1)}$.

- *Section VII.* Correspondingly, the constitutive equations are identified as functions of the hydrodynamic variables and their gradients through their dependence on $\{f_i\}$, with coefficients of the gradients defining the transport coefficients. Hence, all equations of state (pressure and reference state cooling rate) and all transport coefficients, which are integrals involving $f_i^{(0)}$, inherit this dependence on the hydrodynamic variables and their gradients. The coefficients are determined from solutions to the integral equations.

This completes the derivation reported in this manuscript. Up until this point, the results are exact for Navier-Stokes order hydrodynamics (first order in spatial gradients) of the RET. This determines the form of the Navier-Stokes hydrodynamics, but more explicit dependence of the transport coefficients on the macroscopic variables requires a corresponding explicit solution to the integral equations for $f_i^{(0)}$ and $f_i^{(1)}$. One approximate method, known to be accurate for ordinary fluids, is detailed in the follow-on paper [50], resulting in constitutive quantities that are algebraic functions of the macroscopic variables.

III. REVISED ENSKOG KINETIC THEORY

The system considered is a mixture of $\{N_i\}$ smooth hard disks ($d = 2$) or spheres ($d = 3$) of masses $\{m_i\}$ and diameters $\{\sigma_i\}$, where the subscript i labels one of the s mechanically different species and d is the dimension. In general, collisions among all pairs are inelastic and are characterized by independent constant normal restitution coefficients $\{\alpha_{ij} = \alpha_{ji}\}$, where α_{ij} is the restitution coefficient for collisions between particles of species i and j, $0 < \alpha_{ij} \leq 1$. The macroscopic (or hydrodynamic) properties of interest (number densities, flow velocity, and energy density) are determined from the single particle position and velocity distribution functions $f_i(\mathbf{r}_1, \mathbf{v}_1; t)$, for $i = 1, ..s$,

where $f_i(\mathbf{r}_1,\mathbf{v}_1;t)d\mathbf{r}_1d\mathbf{v}_1$ is proportional to the probability to find a particle of species i in the position and velocity element $d\mathbf{r}_1d\mathbf{v}_1$ at time t. The fundamental description of any system is based on the probability density for *all* constituent particles and the Liouville equation for its time evolution; this is equivalent to solving the collective equations of motion for all particles in the system and becomes computationally prohibitive for a large number of particles. However, for the macroscopic fields only the reduced distribution functions $\{f_i\}$, obtained from the integration of the probability density over all except one particle's position and velocity for each of the species, are required for calculation of the macroscopic properties. The equations for these reduced distribution functions resulting from the partial integrations of the Liouville equation, give rise to the BBGKY hierarchy equations. The first level of this hierarchy gives the time dependence of $\{f_i\}$ [51, 52]

$$\left(\partial_t+\mathbf{v}_1\cdot\nabla_{\mathbf{r}_1}+m_i^{-1}\mathbf{F}_i(\mathbf{r}_1)\cdot\nabla_{\mathbf{v}_1}\right)f_i(\mathbf{r}_1,\mathbf{v}_1;t)=C_i(\mathbf{r}_1,\mathbf{v}_1;t), \tag{3.1}$$

where

$$\begin{aligned} C_i(\mathbf{r}_1,\mathbf{v}_1;t) \;=\; & \sum_{j=1}^{s}\sigma_{ij}^{d-1}\int d\mathbf{v}_2\int d\widehat{\boldsymbol{\sigma}}\Theta(\widehat{\boldsymbol{\sigma}}\cdot\mathbf{g}_{12})(\widehat{\boldsymbol{\sigma}}\cdot\mathbf{g}_{12}) \\ & \times\left(\alpha_{ij}^{-2}f_{ij}(\mathbf{r}_1,\mathbf{v}_1'',\mathbf{r}_1-\boldsymbol{\sigma}_{ij},\mathbf{v}_2'';t)-f_{ij}(\mathbf{r}_1,\mathbf{v}_1,\mathbf{r}_1+\boldsymbol{\sigma}_{ij},\mathbf{v}_2;t)\right). \end{aligned} \tag{3.2}$$

The left sides of these equations describe changes in the distribution functions due to motion in the presence of external conservative forces $\mathbf{F}_i(\mathbf{r}_1)$. The right side describes changes due to collisions among the particles. The function $f_{ij}(\mathbf{r}_1,\mathbf{v}_1,\mathbf{r}_2,\mathbf{v}_2;t)d\mathbf{r}_1d\mathbf{v}_1d\mathbf{r}_2d\mathbf{v}_2$ is proportional to the joint probability of finding a particle of species i in $d\mathbf{r}_1d\mathbf{v}_1$ and one of species j in $d\mathbf{r}_2d\mathbf{v}_2$. The position $\mathbf{r}_2$ in these functions appears only for $\mathbf{r}_2=\mathbf{r}_1\pm\boldsymbol{\sigma}_{ij}$, where $\boldsymbol{\sigma}_{ij}=\widehat{\boldsymbol{\sigma}}\sigma_{ij}$ and $\sigma_{ij}\equiv(\sigma_i+\sigma_j)/2$; this means that the two particles are at contact. The vector $\widehat{\boldsymbol{\sigma}}$ is a unit vector directed along the line of centers from the sphere of species j to that of species i at contact and the integration $d\widehat{\boldsymbol{\sigma}}$ is over a solid angle for this contact sphere. The Heaviside step function Θ assures that the relative velocities $\mathbf{g}_{12}=\mathbf{v}_1-\mathbf{v}_2$ are such that a collision takes place, and the "restituting" (pre-collisional) velocities $\mathbf{v}_1''$ and $\mathbf{v}_2''$ are related to the post-collisional velocities by

$$\mathbf{v}_1''=\mathbf{v}_1-\mu_{ji}\left(1+\alpha_{ij}^{-1}\right)(\widehat{\boldsymbol{\sigma}}\cdot\mathbf{g}_{12})\widehat{\boldsymbol{\sigma}},\qquad \mathbf{v}_2''=\mathbf{v}_2+\mu_{ij}\left(1+\alpha_{ij}^{-1}\right)(\widehat{\boldsymbol{\sigma}}\cdot\mathbf{g}_{12})\widehat{\boldsymbol{\sigma}} \tag{3.3}$$

where $\mu_{ij}=m_i/(m_i+m_j)$. It is convenient for the discussion here to write that equation in a more symbolic form by introducing the notation

$$X(\mathbf{v}_1'',\mathbf{v}_2'')=b_{ij}^{-1}X(\mathbf{v}_1,\mathbf{v}_2), \tag{3.4}$$

so that b_{ij}^{-1} is a general substitution operator that changes the argument of a function to its precollision velocities given by (3.3). Then, changing variables $\widehat{\boldsymbol{\sigma}}\to-\widehat{\boldsymbol{\sigma}}$ in the second term on the right side of (3.1) and noting that $b_{ij}^{-1}\widehat{\boldsymbol{\sigma}}\cdot\mathbf{g}_{12}=-\alpha_{ij}^{-1}\widehat{\boldsymbol{\sigma}}\cdot\mathbf{g}_{12}$ gives the equivalent form [51, 52]

$$\begin{aligned} \left(\partial_t+\mathbf{v}_1\cdot\nabla_{\mathbf{r}_1}+m_i^{-1}\mathbf{F}_i(\mathbf{r}_1)\cdot\nabla_{\mathbf{v}_1}\right)f_i(\mathbf{r}_1,\mathbf{v}_1;t) \;=\; & -\sum_{j=1}^{s}\sigma_{ij}^{d-1}\int d\mathbf{v}_2\int d\widehat{\boldsymbol{\sigma}}(\alpha_{ij}^{-1}b_{ij}^{-1}+1)(\widehat{\boldsymbol{\sigma}}\cdot\mathbf{g}_{12}) \\ & \times\Theta(-\widehat{\boldsymbol{\sigma}}\cdot\mathbf{g}_{12})f_{ij}(\mathbf{r}_1,\mathbf{v}_1,\mathbf{r}_1-\boldsymbol{\sigma}_{ij},\mathbf{v}_2;t). \end{aligned} \tag{3.5}$$

This demonstrates that the two particle distributions f_{ij} appear only on the contact hemisphere given by $\Theta(-\widehat{\boldsymbol{\sigma}}\cdot\mathbf{g}_{12})$, correponding to particles that are directed toward each other and hence have a change in their velocities.

Equation (3.1) becomes a kinetic theory (i.e., closed equations for the set of f_i) only after specifying f_{ij} on the right side as a functional of the set of f_i (the alternative of making approximations at higher levels of the BBGKY hierarchy has not been productive in general for molecular gases). As indicated above, this is required for f_{ij} only when the particles are at contact and on that hemisphere for which the relative velocities are directed toward each other. In this restricted context, the Enskog kinetic theory results from a neglect of velocity correlations, i.e. the Enskog approximation

$$f_{ij}(\mathbf{r}_1,\mathbf{v}_1,\mathbf{r}_2,\mathbf{v}_2;t)\to\chi_{ij}\left(\mathbf{r}_1,\mathbf{r}_2\mid\{n_i\}\right)f_i(\mathbf{r}_1,\mathbf{v}_1;t)f_j(\mathbf{r}_2,\mathbf{v}_2;t). \tag{3.6}$$

Spatial correlations arising from volume exclusion effects are retained through the factor $\chi_{ij}\left(\mathbf{r}_1,\mathbf{r}_2\mid\{n_i\}\right)$. In the special case of a uniform system, it is simply related to the nonequilibrium pair correlation function $g_{ij}\left(|\mathbf{r}_1-\mathbf{r}_2|;\{n_i\}\right)$ (probability density to find a particle of species i at $\mathbf{r}_1$ and j at $\mathbf{r}_2$) by [53]

$$g_{ij}\left(\sigma_{ij};\{n_k\}\right)=\frac{1+\alpha_{ij}}{2\alpha_{ij}}\chi_{ij}\left(\sigma_{ij};\{n_k\}\right) \tag{3.7}$$

This relationship is proved in Appendix A and provides some partial interpretation for χ_{ij}. It is important to note that these correlation functions are *functionals* of the actual species densities $\{n_i\}$ (defined below in Eq. (4.1)). This functional dependence is what distinguishes the RET from the original "standard" Enskog theory (SET), where the g_{ij} are *functions* of the species densities at the single position of interest, $\mathbf{r}_1$. Some partial justification for the approximation (3.6) for ordinary atomic fluids is given in Appendix A, where it is known to provide accurate results for moderately dense gases, and reasonable estimates even for dense gases. Its use for granular gases is justified largely from expectations based on these results for ordinary fluids.

Substitution of the Enskog approximation (3.6) into the exact first level hierarchy equations (3.1) defines the RET for the distribution functions $\{f_i\}$

$$\left(\partial_t + \mathbf{v}_1 \cdot \nabla + m_i^{-1}\mathbf{F}_i(\mathbf{r}_1) \cdot \nabla_{\mathbf{v}_1}\right) f_i(\mathbf{r}_1, \mathbf{v}_1; t) = \sum_{j=1}^{s} J_{ij}\left[\mathbf{r}_1, \mathbf{v}_1 \mid f(t)\right] \ . \tag{3.8}$$

The collision operators $\{J_{ij}\left[\mathbf{r}_1, \mathbf{v}_1 \mid f(t)\right]\}$ are given by

$$\begin{aligned} J_{ij}\left[\mathbf{r}_1, \mathbf{v}_1 \mid f(t)\right] \ \equiv \ & \sigma_{ij}^{d-1} \int d\mathbf{v}_2 \int d\widehat{\boldsymbol{\sigma}} \Theta(\widehat{\boldsymbol{\sigma}} \cdot \mathbf{g}_{12})(\widehat{\boldsymbol{\sigma}} \cdot \mathbf{g}_{12}) \\ & \times \left[\alpha_{ij}^{-2} \chi_{ij}\left(\mathbf{r}_1, \mathbf{r}_1 - \boldsymbol{\sigma}_{ij} \mid \{n_i\}\right) f_i(\mathbf{r}_1, \mathbf{v}_1''; t) f_j(\mathbf{r}_1 - \boldsymbol{\sigma}_{ij}, \mathbf{v}_2''; t)\right. \\ & \left. - \chi_{ij}\left(\mathbf{r}_1, \mathbf{r}_1 + \boldsymbol{\sigma}_{ij} \mid \{n_i\}\right) f_i(\mathbf{r}_1, \mathbf{v}_1; t) f_j(\mathbf{r}_1 + \boldsymbol{\sigma}_{ij}, \mathbf{v}_2; t)\right]. \end{aligned} \tag{3.9}$$

The corresponding Boltzmann equations for a dilute mixture follow from this result since $\chi_{ij}\left(\mathbf{r}_1, \mathbf{r}_1 - \boldsymbol{\sigma}_{ij} \mid \{n_i\}\right) \to 1$ at low density. Furthermore, on length scales of the order of the mean free path or greater, the different centers $(\mathbf{r}_1, \mathbf{r}_2 = \mathbf{r}_1 \pm \boldsymbol{\sigma}_{ij})$ of the colliding pair in Eq. (3.9) can be neglected ($\mathbf{r}_1 \approx \mathbf{r}_2$) since the diameters of the particles are small compared to the mean free path at low density. As will be shown below, a nonzero distance between the particle centers gives rise to the collisional contributions to the transport coefficients, which are not present in dilute systems. These two modifications to f_{ij} result in the usual Boltzmann description for a granular mixture. The results obtained here therefore encompass earlier work on granular mixtures at low density [38]. In the elastic limit, $\alpha_{ij} \to 1$, these equations become the Enskog theory for mixtures of dense molecular gases studied in Ref. [49].

As happens for elastic collisions, the inelastic Enskog equation provides a semiquantitative description of the hard sphere system that neglects the velocity correlations between the particles that are about to collide (molecular chaos assumption). The Enskog approximation is expected to be valid for short times since as the system evolves corrections to the Enskog equation due to multiparticle collisions, including recollision events ("ring" collisions) should be incorporated. The latter are expected to be stronger for fluids with inelastic collisions where the colliding pairs tend to be more focused. Therefore, some deviations from molecular chaos have been observed in molecular dynamics (MD) simulations [54, 55, 56] of granular fluids as the density increases. Although the existence of these correlations restricts the range of validity of the Enskog equation, there is substantial evidence in the literature for the validity of the Enskog theory at moderate densities and higher restitution coefficients especially at the level of macroscopic properties (such as transport coefficients). In the case of molecular dynamics (MD) simulations, the Enskog theory compares quite well with simulations for the radial distribution function [53], the self-diffusion coefficient [57, 58], the kinetic temperatures of a binary mixture in homogeneous cooling state [59], and the rheological properties of a mixture under simple shear flow [60, 61]. The agreement between MD and Enskog equation is good for moderate densities (solid volume fraction up to 0.15) and even conditions of strong dissipation (restitution coefficients $\alpha_{ij} > 0.7$). For higher densities the α range is more limited but the Enskog theory still captures the relevant qualitative features. The Enskog transport coefficients for a monocomponent gas [62] have also been tested against NMR experiments of a system of mustard seeds vibrated vertically [43, 44]. The average value of the coefficient of restitution of the grains used in this experiment is $\alpha = 0.87$, which lies outside of the quasielastic limit ($\alpha \approx 0.99$). Comparison between theory and experiments shows that the Enskog kinetic theory successfully models the density and granular temperature profiles away from the vibrating container bottom and quantitatively explains the temperature inversion observed in experiments [63]. All these results clearly show the applicability of the Enskog theory for densities outside the Boltzmann limit and values of dissipation beyond the quasielastic limit. In this context, one can conclude that the Enskog equation provides a unique basis for the description of dynamics across a wide range of densities, length scales, and degrees of dissipation. No other theory with such generality exists.

IV. MACROSCOPIC BALANCE EQUATIONS

In the previous section, the Enskog assumption (3.6) was used to obtain a closed set of kinetic equations (3.8) for a moderately dense mixture of inelastic hard spheres. The result takes the form of nonlinear, integral-differential

equations for the distribution function f_i, which contains information on a *microscopic* scale. In this section, this theory will be used to obtain the corresponding description on the *macroscopic* (or hydrodynamic) scale. First, the relevant macroscopic variables will be identified and defined. Next, the corresponding balance equations will be derived. Finally, expressions for the equations of state (pressure and cooling rate) and fluxes will be presented as integral expressions containing f_i.

The variables of interest for a macroscopic description of the mixture are the number densities for all species, $\{n_i(\mathbf{r},t)\}$ (or equivalently, the mass densities $\{\rho_i(\mathbf{r},t) = m_i n_i(\mathbf{r},t)\}$), the total energy density, $e(\mathbf{r},t)$, and the total momentum, $\mathbf{p}(\mathbf{r},t)$. These are expected to be the $s+1+d$ slow variables that dominate the dynamics for long times through a closed autonomous set of equations, the hydrodynamic equations. The reasoning behind this is that these are the densities for global conserved quantities in molecular fluids, and therefore have decay times set by the wavelength of the excitations. Long wavelength (space scales large compared to the mean free path) phenomena therefore persist at long times (compared to a mean free time) after which the complex transient microscopic dynamics has become negligible. For granular fluids, the energy is not conserved but is characterized by a cooling rate at long wavelengths. Still, this cooling rate may be slow compared to the transient dynamics and thus the energy remains a relevant slow variable. This is confirmed by MD simulations showing a rapid approach to this cooling law after only a few collisions [59].

These macroscopic variables will be referred to collectively as the hydrodynamic fields. They are defined without approximation in terms of moments of the distribution functions

$$n_i(\mathbf{r},t) \equiv \int d\mathbf{v} f_i(\mathbf{r},\mathbf{v};t), \qquad i = 1,..s, \tag{4.1}$$

$$e(\mathbf{r},t) \equiv \sum_{i=1}^{s} \int d\mathbf{v} \frac{1}{2} m_i v^2 f_i(\mathbf{r},\mathbf{v};t) \tag{4.2}$$

$$\mathbf{p}(\mathbf{r},t) \equiv \sum_{i=1}^{s} \int d\mathbf{v} m_i \mathbf{v} f_i(\mathbf{r},\mathbf{v};t) \tag{4.3}$$

The time dependence occurs entirely through the distribution function and hence is determined from the Enskog kinetic equations (3.8). However, rather than solving the kinetic equation to determine this complete time dependence it is useful for the purposes of deriving the simpler hydrodynamic description to first obtain the balance equations. These equations express the time derivative of the hydrodynamic fields in terms of local fluxes and sources due to collisions or the external force. These equations and the identification of the fluxes follow in detail from the form of the collision operators in (3.2) as shown in Appendix B (in fact they are obtained there exactly from the first hierarchy equation (3.1) without the Enskog approximation (3.6) and hence are exact). The results for the balance equations are

$$\partial_t n_i(\mathbf{r},t) + m_i^{-1} \nabla \cdot \mathbf{j}_i(\mathbf{r},t) = 0, \tag{4.4}$$

$$\partial_t e(\mathbf{r},t) + \nabla \cdot \mathbf{s}(\mathbf{r},t) = -w(\mathbf{r},t) + \sum_{i=1}^{s} m_i^{-1} \mathbf{F}_i(\mathbf{r}) \cdot \mathbf{j}_i(\mathbf{r},t), \tag{4.5}$$

$$\partial_t p_\beta(\mathbf{r},t) + \partial_{r_\gamma} t_{\gamma\beta}(\mathbf{r},t) = \sum_{i=1}^{s} n_i(\mathbf{r},t) F_{i\beta}(\mathbf{r}). \tag{4.6}$$

The explicit expressions for $\mathbf{j}_i$, $\mathbf{s}$, w and $t_{\gamma\beta}$ are contained in Appendix B and not shown here since they are cast in a more convenient form below.

The mass fluxes $\{\mathbf{j}_i(\mathbf{r},t)\}$, energy flux $\mathbf{s}(\mathbf{r},t)$, and momentum flux $t_{\beta\gamma}(\mathbf{r},t)$ describe the rate of transport of the hydrodynamic fields through a given cross sectional area. They consist of parts due to pure convection and parts due to collision. To identify the convective (kinetic) parts, the local flow field $\mathbf{U}(\mathbf{r},t)$ is defined in terms of the momentum density by

$$\mathbf{p}(\mathbf{r},t) \equiv \rho(\mathbf{r},t)\mathbf{U}(\mathbf{r},t), \qquad \rho(\mathbf{r},t) = \sum_{i=1}^{k} m_i n_i(\mathbf{r},t), \tag{4.7}$$

where the second equation defines the mass density. Also, the energy density is written in terms of the internal energy density $e_0(\mathbf{r},t)$ in the local rest frame, plus the energy due to flow

$$e(\mathbf{r},t) = e_0(\mathbf{r},t) + \frac{1}{2}\rho(\mathbf{r},t)\,U^2(\mathbf{r},t)\,. \tag{4.8}$$

In terms of $\mathbf{U}(\mathbf{r},t)$ the fluxes become

$$\mathbf{j}_i(\mathbf{r},t) = \rho_i(\mathbf{r},t)\,\mathbf{U}(\mathbf{r},t) + \mathbf{j}_{0i}(\mathbf{r},t)\,, \tag{4.9}$$

$$s_\beta(\mathbf{r},t) = \left(e_0(\mathbf{r},t) + \frac{1}{2}\rho(\mathbf{r},t)\,U^2(\mathbf{r},t)\right)U_\beta(\mathbf{r},t) + P_{\beta\gamma}(\mathbf{r},t)\,U_\gamma(\mathbf{r},t) + q_\beta(\mathbf{r},t)\,, \tag{4.10}$$

$$t_{\beta\gamma}(\mathbf{r},t) = \rho(\mathbf{r},t)\,U_\beta(\mathbf{r},t)\,U_\gamma(\mathbf{r},t) + P_{\beta\gamma}(\mathbf{r},t)\,. \tag{4.11}$$

The first terms on the right sides describe convective transport, while the diffusion fluxes $\mathbf{j}_{0i}(\mathbf{r},t)$, heat flux $\mathbf{q}(\mathbf{r},t)$, and pressure tensor $P_{\beta\gamma}(\mathbf{r}_1,t)$ describe the residual transport for each fluid element in its local rest frame. Before giving their forms more explicitly, it is instructive to insert (4.9)–(4.11) into (4.4)–(4.6) to get the equivalent form for the balance equations

$$D_t n_i + n_i \nabla\cdot\mathbf{U} + m_i^{-1}\nabla\cdot\mathbf{j}_{0i} = 0, \tag{4.12}$$

$$D_t e_0 + (e_0\delta_{\gamma\beta} + P_{\gamma\beta})\,\partial_{r_\gamma}U_\beta + \nabla\cdot\mathbf{q} = -w(\mathbf{r},t) + \sum_{i=1}^{s} m_i^{-1}\mathbf{F}_i(\mathbf{r})\cdot\mathbf{j}_{0i}(\mathbf{r},t)\,, \tag{4.13}$$

$$\rho D_t U_\beta + \partial_{r_\gamma}P_{\gamma\beta} = \sum_{i=1}^{s} n_i(\mathbf{r},t)\,F_{i\beta}(\mathbf{r})\,, \tag{4.14}$$

where $D_t = \partial_t + \mathbf{U}\cdot\nabla$ is the material derivative.

The independent hydrodynamic fields are now $\{n_i(\mathbf{r},t)\}$, $e_0(\mathbf{r},t)$, and $\mathbf{U}(\mathbf{r},t)$. The remaining quantities in the balance equations are the energy loss rate $w(\mathbf{r},t)$, the mass fluxes $\{\mathbf{j}_{0i}(\mathbf{r},t)\}$, the heat flux $\mathbf{q}(\mathbf{r},t)$, and the pressure tensor $P_{\beta\gamma}(\mathbf{r}_1,t)$. These quantities, which are defined in terms of the distribution functions, are obtained by the explicit forms for $\mathbf{j}_i$, $\mathbf{s}$, w, and $t_{\gamma\beta}$ given in Appendix B together with Eqs. (4.9)–(4.11).

Specifically, the energy loss rate is due to inelastic collisions

$$\begin{aligned} w(\mathbf{r},t) \;\equiv\; & \frac{1}{4}\sum_{i,j=1}^{s}\left(1-\alpha_{ij}^2\right)m_i\mu_{ji}\sigma_{ij}^{d-1}\int d\mathbf{v}_1\int d\mathbf{v}_2\int d\widehat{\boldsymbol{\sigma}} \\ & \times\Theta(\widehat{\boldsymbol{\sigma}}\cdot\mathbf{g}_{12})(\widehat{\boldsymbol{\sigma}}\cdot\mathbf{g}_{12})^3 f_{ij}(\mathbf{r}_1,\mathbf{v}_1,\mathbf{r}_1+\boldsymbol{\sigma}_{ij},\mathbf{v}_2;t), \end{aligned} \tag{4.15}$$

whereas the diffusion flux arises from convective (kinetic) transport

$$\mathbf{j}_{0i}(\mathbf{r}_1,t) \equiv m_i\int d\mathbf{v}_1\mathbf{V}_1 f_i(\mathbf{r}_1,\mathbf{v}_1;t), \tag{4.16}$$

where $\mathbf{V}_1 = \mathbf{v}_1 - \mathbf{U}(\mathbf{r},t)$ is the velocity in the local rest frame. The heat flux has both "kinetic" and "collisional" transfer contributions

$$\mathbf{q}(\mathbf{r}_1,t) \equiv \mathbf{q}^k(\mathbf{r}_1,t) + \mathbf{q}^c(\mathbf{r}_1,t)\,, \tag{4.17}$$

with

$$\mathbf{q}^k(\mathbf{r}_1,t) = \sum_{i=1}^{s}\int d\mathbf{v}_1\frac{1}{2}m_i V_1^2\mathbf{V}_1 f_i(\mathbf{r}_1,\mathbf{v}_1;t), \tag{4.18}$$

$$\mathbf{q}^c(\mathbf{r}_1,t) = \sum_{i,j=1}^{k}\frac{1}{8}(1+\alpha_{ij})\,m_j\mu_{ij}\sigma_{ij}^d\int d\mathbf{v}_1\int d\mathbf{v}_2\int d\widehat{\boldsymbol{\sigma}}\,\Theta(\widehat{\boldsymbol{\sigma}}\cdot\mathbf{g}_{12})$$
$$\times(\widehat{\boldsymbol{\sigma}}\cdot\mathbf{g}_{12})^2\left[(1-\alpha_{ij})\,(\mu_{ji}-\mu_{ij})\,(\widehat{\boldsymbol{\sigma}}\cdot\mathbf{g}_{12})+4\widehat{\boldsymbol{\sigma}}\cdot\mathbf{G}_{ij}\right)$$
$$\times\widehat{\boldsymbol{\sigma}}\int_0^1 dx f_{ij}(\mathbf{r}_1-x\boldsymbol{\sigma}_{ij},\mathbf{v}_1,\mathbf{r}_1+(1-x)\,\boldsymbol{\sigma}_{ij},\mathbf{v}_2;t), \tag{4.19}$$

where $\mathbf{G}_{ij}=\mu_{ij}\mathbf{V}_1+\mu_{ji}\mathbf{V}_2$ is the center-of-mass velocity.

Similarly, the pressure tensor has both kinetic and collisional contributions

$$P_{\gamma\beta}(\mathbf{r}_1,t)\equiv P_{\gamma\beta}^k(\mathbf{r}_1,t)+P_{\gamma\beta}^c(\mathbf{r}_1,t), \tag{4.20}$$

where

$$P_{\gamma\beta}^k(\mathbf{r}_1,t)=\sum_{i=1}^{s}\int d\mathbf{v}_1 m_i V_{1\beta}V_{1\gamma}f_i(\mathbf{r}_1,\mathbf{v}_1;t), \tag{4.21}$$

$$P_{\gamma\beta}^c(\mathbf{r}_1,t) = \frac{1}{2}\sum_{i,j=1}^{s}m_j\mu_{ij}\,(1+\alpha_{ij})\,\sigma_{ij}^d\int d\mathbf{v}_1\int d\mathbf{v}_2\int d\widehat{\boldsymbol{\sigma}}\,\Theta(\widehat{\boldsymbol{\sigma}}\cdot\mathbf{g}_{12})(\widehat{\boldsymbol{\sigma}}\cdot\mathbf{g}_{12})^2$$
$$\times\widehat{\sigma}_\beta\widehat{\sigma}_\gamma\int_0^1 dx f_{ij}(\mathbf{r}_1-x\boldsymbol{\sigma}_{ij},\mathbf{v}_1,\mathbf{r}_1+(1-x)\,\boldsymbol{\sigma}_{ij},\mathbf{v}_2;t). \tag{4.22}$$

Equations (4.12)–(4.14) together with the definitions (4.15)–(4.22) represent the macroscopic balance equations for a granular mixture, without restrictions on the densities or degrees of dissipation. In the case of a three-dimensional system ($d=3$), the above equations reduce to previous results [64] derived for hard spheres. When the approximate form (3.6) is used in the first hierarchy equation and in these expressions for the cooling rate and fluxes, the Enskog theory results.

For historical consistency with the usual constitutive equations for a ordinary fluid, the temperature $T(\mathbf{r},t)$ is used in the following instead of the internal energy density $e_0(\mathbf{r},t)$, with the definition

$$e_0(\mathbf{r},t)\equiv\frac{d}{2}n(\mathbf{r},t)\,T(\mathbf{r},t). \tag{4.23}$$

As a definition, this amounts only to a change of variables and there are no thermodynamic implications involved in the use of this temperature for a granular fluid. The corresponding hydrodynamic equation for $T(\mathbf{r},t)$ follows directly from (4.13)

$$\frac{d}{2}n(D_t+\zeta)\,T+P_{\gamma\beta}\partial_{r_\gamma}U_\beta+\nabla\cdot\mathbf{q}-\frac{d}{2}T\sum_{i=1}^{s}m_i^{-1}\nabla\cdot\mathbf{j}_{0i}=\sum_{i=1}^{s}m_i^{-1}\mathbf{F}_i\cdot\mathbf{j}_{0i}. \tag{4.24}$$

To obtain these results the continuity equation has been used

$$D_t\rho+\rho\nabla\cdot\mathbf{U}=0. \tag{4.25}$$

This follows from the definitions of ρ and $\mathbf{U}$ and the conservation laws for the $\{n_i(\mathbf{r},t)\}$. A related consequence is

$$\sum_{i=1}^{s}\mathbf{j}_{0i}=0, \tag{4.26}$$

so that only $s-1$ dissipative mass fluxes are independent. Finally, the "cooling rate" ζ has been introduced in (4.24) by the definition

$$\zeta = \frac{2}{dnT}w=\frac{1}{2dnT}\sum_{i,j=1}^{s}\left(1-\alpha_{ij}^2\right)m_i\mu_{ji}\sigma_{ij}^{d-1}\int d\mathbf{v}_1\int d\mathbf{v}_2\int d\widehat{\boldsymbol{\sigma}},$$
$$\times\Theta(\widehat{\boldsymbol{\sigma}}\cdot\mathbf{g}_{12})(\widehat{\boldsymbol{\sigma}}\cdot\mathbf{g}_{12})^3 f_{ij}(\mathbf{r}_1,\mathbf{v}_1,\mathbf{r}_1+\boldsymbol{\sigma}_{ij},\mathbf{v}_2;t). \tag{4.27}$$

V. CONCEPT OF A NORMAL SOLUTION AND HYDRODYNAMICS

The form of the equations of state and fluxes given in the previous section, (4.16)–(4.22) and (4.27), are cast as functionals of the distributions $\{f_i\}$, which depend explicitly on space and time. As a result, the macroscopic balance equations are not entirely expressed in terms of the hydrodynamic fields, and thus do not comprise a closed set of equations. If these distributions can instead be expressed as functionals of the hydrodynamic fields (*normal* solution), then $\zeta(\mathbf{r},t)$, $\{\mathbf{j}_{0i}(\mathbf{r},t)\}$, $\mathbf{q}(\mathbf{r},t)$, and $P_{\beta\gamma}(\mathbf{r}_1,t)$ also will become functionals of the hydrodynamic fields through (4.16)–(4.22) and (4.27). Such expressions are called "constitutive relations". They provide the missing link between the balance equations and a closed set of equations for the hydrodynamic fields alone. Such a closed set of equations defines "hydrodynamics" in its most general sense.

It is seen, therefore, that any derivation of hydrodynamics proceeds first by construction of normal solutions to the kinetic equations. More precisely, a normal solution is one whose space and time dependence occurs entirely through the hydrodynamic fields, denoted

$$f_i(\mathbf{r}_1,\mathbf{v}_1;t)=f_i(\mathbf{v}_1\mid\{y_\beta(\mathbf{r}_1,t)\}), \tag{5.1}$$

where $\{y_\beta(\mathbf{r}_1,t)\}$ denotes generically the set of hydrodynamic fields

$$y_\beta\Leftrightarrow\{T,\mathbf{U},\{n_i(\mathbf{r},t)\}\}. \tag{5.2}$$

Therefore, the space and time derivatives of the kinetic equation are given by

$$(\partial_t+\mathbf{v}_1\cdot\nabla_{\mathbf{r}})f_i(\mathbf{v}_1\mid\{y_\beta(\mathbf{r}_1,t)\})=\int d\mathbf{r}\frac{\delta f_i(\mathbf{v}_1\mid\{y_\beta(t)\})}{\delta y_\eta(\mathbf{r};t)}(\partial_t+\mathbf{v}_1\cdot\nabla_{\mathbf{r}})y_\eta(\mathbf{r};t). \tag{5.3}$$

Furthermore, the balance equations for the hydrodynamic fields (4.12)–(4.14) can be used to express $\partial_t y_\eta(\mathbf{r};t)$ in (5.3) in terms of space derivatives of the hydrodynamic fields. For such a solution for f_i, Eqs. (4.16)–(4.22) and (4.27) give directly by integration the desired constitutive relations.

The determination of $f_i(\mathbf{v}_1\mid\{y_\beta(\mathbf{r}_1,t)\})$ from the kinetic equations (3.8) is a very difficult task in general, and further restriction on the class of problems considered is required at this point to make progress. Any *functional* of the fields can be represented equivalently as a local *function* of the fields *and* all of their gradients. In many cases, gradients of high degree are small and may be negligible so that the normal distribution becomes

$$f_i(\mathbf{v}_1\mid\{y_\beta(\mathbf{r}_1,t)\})\rightarrow f_i(\mathbf{v}_1;\{y_\beta(\mathbf{r}_1,t),\nabla_{\mathbf{r}_1}y_\beta(\mathbf{r}_1,t),\cdots\}) \tag{5.4}$$

This representation does not imply that the low degree gradients are small, and f_i may be a non-linear function of the relevant gradients. This occurs in many important applications for granular fluids [40]. In the limiting case where the low-degree gradients can be controlled by boundary or initial conditions and made small, a further Taylor series expansion can be given

$$\begin{aligned}f_i(\mathbf{v}_1\mid\{y_\beta(\mathbf{r}_1,t)\}) &\rightarrow f_i^{(0)}(\mathbf{v}_1;\{y_\beta(\mathbf{r}_1,t)\})+f_i^{(1)}(\mathbf{v}_1;\{y_\beta(\mathbf{r}_1,t)\})+\cdots\\ &\rightarrow f_i^{(0)}(\mathbf{v}_1;\{y_\beta(\mathbf{r}_1,t)\})+\mathbf{Y}_{i\alpha}(\mathbf{v}_1;\{y_\beta(\mathbf{r}_1,t)\})\cdot\nabla_{\mathbf{r}_1}y_\alpha(\mathbf{r}_1,t)+\cdots\end{aligned} \tag{5.5}$$

It follows that the leading order distributions have the exact properties

$$n_i(\mathbf{r},t)\equiv\int d\mathbf{v}f_i^{(0)}(\mathbf{v};\{y_\beta(\mathbf{r},t)\}),\qquad i=1,..s, \tag{5.6}$$

$$\frac{d}{2}n(\mathbf{r},t)T(\mathbf{r},t)\equiv\sum_{i=1}^{s}\int d\mathbf{v}\frac{1}{2}m_iV^2f_i^{(0)}(\mathbf{v};\{y_\beta(\mathbf{r},t)\}), \tag{5.7}$$

$$\rho(\mathbf{r},t)\mathbf{U}(\mathbf{r},t)\equiv\sum_{i=1}^{s}\int d\mathbf{v}m_i\mathbf{v}f_i^{(0)}(\mathbf{v};\{y_\beta(\mathbf{r},t)\}), \tag{5.8}$$

and the corresponding moments of all higher order terms in (5.5) must vanish. Generalization of this type of gradient expansion for the normal solution to include a class of nonlinear gradients in the reference state has been discussed recently [65, 66].

As is standard for molecular gases, the gradient expansion will be taken with respect to the reference local HCS, i.e. that resulting from the neglect of all gradients in the functional but evaluated at the value of the fields at the chosen point and time $\{y_\beta(\mathbf{r}_1,t)\}$. This point is crucial in our analysis since most of the previous results have taken elastic Maxwell distributions as the base state. Note that in the CE method the form of $f_i^{(0)}$ comes from the solution to the kinetic equation to zeroth order in gradients and cannot be chosen a priori. Accordingly, $f_i^{(0)}(\mathbf{v}_1;\{y_\beta(\mathbf{r}_1,t)\}) \to f_i^{(0)}(V_1;\{y_\beta(\mathbf{r}_1,t)\})$, where $V=|\mathbf{v}-\mathbf{U}(\mathbf{r},t)|$ is homogeneous and isotropic with respect to its velocity dependence. This symmetry implies that the leading (zero) order contributions to (4.16) and (4.17) for the vector fluxes $\{\mathbf{j}_{0i}(\mathbf{r},t)\}$ and $\mathbf{q}(\mathbf{r},t)$ must vanish, and this contribution to the pressure tensor $P_{\gamma\beta}$ must be isotropic (proportional to $\delta_{\gamma\beta}$). Similar symmetry considerations to the first order contribution (linear in the gradients) determines the exact structure of the constitutive equation to this order. Based on these symmetry considerations, the constitutive quantities are known to take the forms

$$\zeta(\mathbf{r},t) \to \zeta^{(0)}(\{y_\beta(\mathbf{r},t)\}) + \zeta_U(\{y_\beta(\mathbf{r},t)\})\nabla\cdot\mathbf{U}(\mathbf{r},t), \tag{5.9}$$

$$\begin{aligned}\mathbf{j}_{0i}(\mathbf{r},t) \;\to\; & -\sum_{j=1}^{s} m_i m_j \frac{n_j(\mathbf{r},t)}{\rho(\mathbf{r},t)} D_{ij}(\{y_\beta(\mathbf{r},t)\})\nabla \ln n_j(\mathbf{r},t) \\ & -\rho(\mathbf{r},t)\, D_i^T(\{y_\beta(\mathbf{r},t)\})\nabla \ln T(\mathbf{r},t) - \sum_{j=1}^{s} D_{ij}^F(\{y_\beta(\mathbf{r},t)\})\mathbf{F}_j(\mathbf{r}),\end{aligned} \tag{5.10}$$

$$\begin{aligned}\mathbf{q}(\mathbf{r},t) \;\to\; & -\lambda(\{y_\beta(\mathbf{r},t)\})\nabla T(\mathbf{r},t) \\ & -\sum_{i,j=1}^{s}\left(T^2(\mathbf{r},t)\, D_{q,ij}(\{y_\beta(\mathbf{r},t)\})\nabla \ln n_j(\mathbf{r},t) + L_{ij}(\{y_\beta(\mathbf{r},t)\})\mathbf{F}_j(\mathbf{r})\right),\end{aligned} \tag{5.11}$$

$$\begin{aligned}P_{\gamma\lambda}(\mathbf{r},t) \;=\; & p(\{y_\beta(\mathbf{r},t)\})\delta_{\gamma\lambda} - \eta(\{y_\beta(\mathbf{r},t)\})\left(\partial_{r_\gamma}U_\lambda(\mathbf{r},t) + \partial_{r_\lambda}U_\gamma(\mathbf{r},t) - \frac{2}{d}\nabla\cdot\mathbf{U}(\mathbf{r},t)\right) \\ & -\kappa(\{y_\beta(\mathbf{r},t)\})\nabla\cdot\mathbf{U}(\mathbf{r},t).\end{aligned} \tag{5.12}$$

The unknown quantities in these constitutive equations (5.9)–(5.12) include the cooling rate $\zeta^{(0)}(\{y_\beta(\mathbf{r},t)\})$, the hydrostatic granular pressure $p(\{y_\beta(\mathbf{r},t)\})$, and the transport coefficients ζ_U, D_{ij}, D_i^T, D_{ij}^F, $D_{q,ij}$, L_{ij}, η, and κ. These quantities can be expressed as explicit functions of the hydrodynamic variables once $f_i^{(0)}$ and $f_i^{(1)}$ are known. The equations governing the solution of $f_i^{(0)}$ and $f_i^{(1)}$ are found using the CE method, as described below.

VI. CHAPMAN–ENSKOG NORMAL SOLUTION

The CE method is a procedure for constructing an approximate normal solution. It is perturbative, using the spatial gradients as the small expansion parameter. More precisely, the small parameter is Knudsen number (Kn), defined as the gradient of the hydrodynamic fields relative to their local value times the mean free path. This means that the conditions for the solution are restricted to small variations of the hydrodynamic fields over distances of the order of the mean free path. In the presence of an external force it is necessary to characterize the magnitude of this force relative to the gradients as well. Here, it is assumed that the magnitude of the force is first order in perturbation expansion. This allows comparison with the results of Ref. [49] for the elastic case.

The perturbation is carried out by considering the Enskog kinetic equations successively at each order in the gradients. As described below, the zeroth order equation is first obtained for $f_i^{(0)}$. Next, the first order equation for $f_i^{(1)}$ is obtained. This expansion leads to integral-differential equations for the determination of $f_i^{(0)}$ and $f_i^{(1)}$, which are solved explicitly in the follow-on paper [50].

As detailed in Appendix C, to zeroth order in the gradients, the kinetic equation (3.8) becomes

$$(\partial_t T)\,\partial_T f_i^{(0)}(\mathbf{v}_1;\{y_\beta(\mathbf{r}_1,t)\}) = \sum_{j=1}^{s} J_{ij}^{(0)}\left[\mathbf{v}_1 \mid f^{(0)}(t)\right], \tag{6.1}$$

where

$$J_{ij}^{(0)}\left[\mathbf{v}_1 \mid f^{(0)}(t)\right] \equiv \chi_{ij}^{(0)}\left(\sigma_{ij};\{n_i\left(\mathbf{r}_1,t\right)\}\right)\sigma_{ij}^{d-1}\int d\mathbf{v}_2\int d\widehat{\boldsymbol{\sigma}}\Theta(\widehat{\boldsymbol{\sigma}}\cdot\mathbf{g}_{12})(\widehat{\boldsymbol{\sigma}}\cdot\mathbf{g}_{12})$$
$$\times\left[\alpha_{ij}^{-2}f_i^{(0)}(V_1'';\{y_\beta\left(\mathbf{r}_1,t\right)\})f_j^{(0)}(V_2'';\{y_\beta\left(\mathbf{r}_1,t\right)\})\right.$$
$$\left.-f_i^{(0)}(V_1;\{y_\beta\left(\mathbf{r}_1,t\right)\})f_j^{(0)}(V_2;\{y_\beta\left(\mathbf{r}_1,t\right)\})\right]. \tag{6.2}$$

All spatial gradients are neglected at this lowest order. Equation (6.1) determines the velocity dependence of $f_i^{(0)}(V_1;\{y_\beta\left(\mathbf{r}_1,t\right)\})$; the space and time dependence is local and entirely through the fields $\{y_\beta\left(\mathbf{r}_1,t\right)\}$ at the space and time point of interest. This has been exploited by writing the time dependence of $f_i^{(0)}$ in terms of the time dependence of the fields, and recognizing that all time derivatives of the latter are proportional to space gradients, except the temperature, through the balance equations

$$\partial_t n_i = 0, \quad \partial_t T = -\zeta^{(0)}T, \quad \partial_t \mathbf{U} = \mathbf{0}. \tag{6.3}$$

Here, $\zeta^{(0)}$ is the cooling rate (4.27) to zeroth order in the gradients

$$\zeta^{(0)} = \frac{1}{2dnT}\sum_{i,j=1}^{s}\left(1-\alpha_{ij}^2\right)m_i\mu_{ji}\chi_{ij}^{(0)}\left(\sigma_{ij};\{n_i\left(\mathbf{r}_1,t\right)\}\right)\sigma_{ij}^{d-1}\int d\mathbf{v}_1\int d\mathbf{v}_2\int d\widehat{\boldsymbol{\sigma}}$$
$$\times\Theta(\widehat{\boldsymbol{\sigma}}\cdot\mathbf{g}_{12})(\widehat{\boldsymbol{\sigma}}\cdot\mathbf{g}_{12})^3 f_i^{(0)}(V_1;\{y_\beta\left(\mathbf{r}_1,t\right)\})f_j^{(0)}(V_2;\{y_\beta\left(\mathbf{r}_1,t\right)\}). \tag{6.4}$$

Similarly, the functional dependence of $\chi_{ij}^{(0)}\left(\mathbf{r}_1,\mathbf{r}_2 \mid \{n_i\}\right)$ on the compositions to zeroth order in the gradients has the functional dependence on the densities replaced by $\{n_i\} \to \{n_i\left(\mathbf{r}_1,t\right)\}$, at the point of interest. The result is translational and rotational invariant $\chi_{ij}^{(0)}\left(\mathbf{r}_1,\mathbf{r}_2 \mid \{n_i\}\right) \to \chi_{ij}^{(0)}\left(|\mathbf{r}_1-\mathbf{r}_2|;\{n_i\left(\mathbf{r}_1,t\right)\}\right)$, a *function* of the densities. Finally, gradients in the distribution functions of the collision operators must be neglected, e.g. $f_i^{(0)}(\mathbf{v}_1;\{y_\beta\left(\mathbf{r}_1+\boldsymbol{\sigma}_{ij},t\right)\}) \to f_i^{(0)}(\mathbf{v}_1;\{y_\beta\left(\mathbf{r}_1,t\right)\})$.

A further simplification of these equations for the lowest order distribution functions occurs when they are written in terms of the corresponding dimensionless forms $\{\phi_i\}$

$$f_i^{(0)}(V;\{y_\beta\}) = n_i v_0^{-d}(T)\phi_i\left(V^*;\{n_i^*\}\right), \tag{6.5}$$

with the definitions

$$\mathbf{V}^* = \frac{\mathbf{V}}{v_0(T)}, \quad v_0(T) = \sqrt{\frac{2T}{m}}, \quad n_i^* = n_i\sigma_i^d, \quad m = \frac{1}{s}\sum_{i=1}^{s}m_i. \tag{6.6}$$

The solution depends on the flow field only through the relative velocity $\mathbf{V}$. Furthermore, since there is no external energy scale the temperature can occur only through the scaling of the dimensionless velocity through the thermal velocity $v_0(T)$. Equation (6.1) now takes the dimensionless form

$$-\frac{1}{2}\zeta^*\nabla_{\mathbf{V}^*}\cdot\left(\mathbf{V}^*\phi_i\right) = \sum_j J_{ij}^{(0)*}\left(V^* \mid \phi_i\right), \tag{6.7}$$

where $\nabla_{\mathbf{V}^*} \equiv \partial/\partial\mathbf{V}^*$ and

$$\zeta^* = \frac{\ell}{v_0}\zeta^{(0)}, \quad J_{ij}^{(0)*} = \frac{\ell}{n}v_0^{d-1}J_{ij}^{(0)}, \quad \ell = \frac{1}{n\sigma^{d-1}}, \quad n = \sum_{i=1}^{s}n_i, \quad \sigma = \frac{1}{s}\sum_{i=1}^{s}\sigma_i. \tag{6.8}$$

The solution to this equation is a universal function of the magnitude of the velocity V^* and is otherwise independent of the temperature and flow field. For a one component fluid it is independent of the density as well. However, for mixtures it is parameterized by the dimensionless species densities through the factors $\chi_{ij}^{(0)}\left(\sigma_{ij};\{n_i^*\}\right)$. Equation (6.1) has the same form as the corresponding dimensionless Enskog equations for a strictly *homogeneous* state. The latter is called the HCS. Here, however, the state is not homogeneous because of the requirements (5.6)–(5.8). Instead it is a *local* HCS. As said before, an important point to recognize is that the occurrence of this local HCS as the reference

state is not an assumption of the CE expansion but rather a consequence of the kinetic equations to lowest order in the gradient expansion.

The analysis to first order in the gradients is similar and the details are given in Appendix C. The result has the form (5.5)

$$\begin{aligned} f_i^{(1)} \;\rightarrow\; & \boldsymbol{\mathcal{A}}_i(\mathbf{V}) \cdot \nabla \ln T + \sum_{j=1}^{s} \boldsymbol{\mathcal{B}}_i^j(\mathbf{V}) \cdot \nabla \ln n_j \\ & + \mathcal{C}_{i,\gamma\eta}(\mathbf{V}) \frac{1}{2}\left(\partial_\gamma U_\eta + \partial_\eta U_\gamma - \frac{2}{d}\delta_{\gamma\eta}\nabla\cdot\mathbf{U}\right) \\ & + \mathcal{D}_i(\mathbf{V})\nabla\cdot\mathbf{U} + \sum_{j=1}^{s} \boldsymbol{\mathcal{E}}_i^j(\mathbf{V})\cdot\mathbf{F}_j. \end{aligned} \tag{6.9}$$

The contributions from the flow field gradients have been separated into independent traceless and diagonal components, as follows from fluid symmetry. The velocity dependence of the gradient contributions is contained in the functions $\boldsymbol{\mathcal{A}}_i(\mathbf{V}), \boldsymbol{\mathcal{B}}_i^j(\mathbf{V}), \mathcal{C}_{i,\gamma\eta}(\mathbf{V}), \mathcal{D}_i(\mathbf{V})$, and $\boldsymbol{\mathcal{E}}_i^j(\mathbf{V})$. The kinetic equations determine these functions as the solutions to the integral equations

$$\left(\left(\mathcal{L} - \frac{1}{2}\zeta^{(0)}\right)\boldsymbol{\mathcal{A}}\right)_i = \mathbf{A}_i, \tag{6.10}$$

$$\left(\mathcal{L}\boldsymbol{\mathcal{B}}^j\right)_i - n_j \frac{\partial \zeta^{(0)}}{\partial n_j}\boldsymbol{\mathcal{A}}_i = \mathbf{B}_i^j, \tag{6.11}$$

$$\left(\left(\mathcal{L} + \frac{1}{2}\zeta^{(0)}\right)\mathcal{C}_{\gamma\eta}\right)_i = C_{i,\gamma\eta}, \tag{6.12}$$

$$\left(\left(\mathcal{L} + \frac{1}{2}\zeta^{(0)}\right)\mathcal{D}\right)_i = D_i, \tag{6.13}$$

$$\left(\left(\mathcal{L} + \zeta^{(0)}\right)\boldsymbol{\mathcal{E}}^j\right)_i = \mathbf{E}_i^j. \tag{6.14}$$

The linear operator $\mathcal{L}$ is given by

$$\left(\mathcal{L}X\right)_i = \frac{1}{2}\zeta^{(0)}\nabla_{\mathbf{V}}\cdot(\mathbf{V}X_i) + \left(LX\right)_i, \tag{6.15}$$

$$\left(LX\right)_i = -\sum_{j=1}^{s}\left(J_{ij}^{(0)}\left[\mathbf{v}_1 \mid X_i, f_j^{(0)}\right] + J_{ij}^{(0)}\left[\mathbf{v}_1 \mid f_i^{(0)}, X_j\right]\right), \tag{6.16}$$

and the inhomogeneous terms are defined by

$$A_{i,\gamma}(\mathbf{V}) = \frac{1}{2}V_\gamma\nabla_{\mathbf{V}}\cdot\left(\mathbf{V}f_i^{(0)}\right) - \frac{p}{\rho}\partial_{V_\gamma}f_i^{(0)} + \frac{1}{2}\sum_{j=1}^{k}\mathcal{K}_{ij,\gamma}\left[\nabla_{\mathbf{V}}\cdot\left(\mathbf{V}f_j^{(0)}\right)\right], \tag{6.17}$$

$$\begin{aligned} B_{i,\gamma}^j(\mathbf{V}) \;=\; & -V_\gamma n_j \partial_{n_j} f_i^{(0)} - \rho^{-1}(\partial_{V_\gamma} f_i^{(0)}) n_j (\partial_{n_j} p) \\ & - \sum_{\ell=1}^{s}\mathcal{K}_{i\ell,\gamma}\left[\left(n_j\partial_{n_j} + \frac{1}{2}\left(n_\ell \frac{\partial \ln \chi_{i\ell}^{(0)}}{\partial n_j} + I_{i\ell j}\right)\right) f_\ell^{(0)}\right], \end{aligned} \tag{6.18}$$

$$C_{i,\gamma\beta}\left(\mathbf{V}\right) = \frac{1}{2}\left(V_\gamma\partial_{V_\beta}f_i^{(0)} + V_\beta\partial_{V_\gamma}f_i^{(0)} - \frac{2}{d}\delta_{\beta\gamma}\mathbf{V}\cdot\nabla_{\mathbf{V}}f_i^{(0)}\right) + \frac{1}{2}\sum_{j=1}^{s}\left(\mathcal{K}_{ij,\gamma}[\partial_{V_\beta}f_j^{(0)}] + \mathcal{K}_{ij,\beta}[\partial_{V_\gamma}f_j^{(0)}] - \frac{2}{d}\delta_{\beta\gamma}\mathcal{K}_{ij,\lambda}[\partial_{V_\lambda}f_j^{(0)}]\right), \tag{6.19}$$

$$D_i(\mathbf{V}) = \frac{1}{d}\mathbf{V}\cdot\nabla_{\mathbf{V}}f_i^{(0)} - \frac{1}{2}\left(\zeta_U + \frac{2}{nTd}p\right)\nabla_{\mathbf{V}}\cdot\left(\mathbf{V}f_i^{(0)}\right) + \sum_{j=1}^{s}\left(n_j\partial_{n_j}f_i^{(0)} + \frac{1}{d}\mathcal{K}_{ij,\gamma}\left[\partial_{V_\gamma}f_j^{(0)}\right]\right), \tag{6.20}$$

$$\mathbf{E}_i^j(\mathbf{V}) = -\left(\nabla_{\mathbf{V}}f_i^{(0)}\right)\frac{1}{m_j}\left(\delta_{ij} - \frac{n_jm_j}{\rho}\right), \tag{6.21}$$

where the operator $\mathcal{K}_{ij,\gamma}[X]$ is defined by Eq. (C16).

This completes the construction of the normal solution to the revised Enskog equations up through first order in the gradients. Equation (6.7) determines the $f_i^{(0)}$ through the definition (6.5); solution to the linear integral equations (6.10)–(6.14) determines the $f_i^{(1)}$ through the definition (6.9). The unknown fluxes and cooling rate of the hydrodynamic equations can then be calculated with these solutions. This is made explicit in the next section.

VII. CONSTITUTIVE EQUATIONS AND TRANSPORT COEFFICIENTS

The forms for the constitutive equations to first order in the gradients are given by Eqs. (5.9)–(5.12). The explicit representations for the coefficients in these equations are given in terms of the solutions to the integral equations for $f_i^{(0)}$ and $f_i^{(1)}$ of the previous section. Details of the simplification of these expressions in terms of $f_i^{(0)}$ and $f_i^{(1)}$ are given in Appendix F and only the final results are presented here.

Recall that the results below are based on the assumption that the external force is of the same magnitude as $f_i^{(1)}$; a force of different magnitude would result in different constitutive relations.

A. Cooling Rate

The cooling rate is calculated from Eq. (4.27), resulting in the form (5.9)

$$\zeta \to \zeta^{(0)} + \zeta_U\nabla\cdot\mathbf{U}, \tag{7.1}$$

with

$$\zeta^{(0)} = \frac{B_3}{2dnT}\sum_{i,j=1}^{s}\left(1-\alpha_{ij}^2\right)\frac{m_im_j}{m_i+m_j}\chi_{ij}^{(0)}\sigma_{ij}^{d-1}\int d\mathbf{v}_1\int d\mathbf{v}_2 f_i^{(0)}(V_1)f_j^{(0)}(V_2)\,g_{12}^3, \tag{7.2}$$

and

$$\zeta_U = -\frac{d+2}{dnT}B_4\sum_{i,j=1}^{s}\left(1-\alpha_{ij}^2\right)\mu_{ji}\chi_{ij}^{(0)}\sigma_{ij}^d n_in_jT_i^{(0)} + \frac{B_3}{dnT}\sum_{i,j=1}^{s}\left(1-\alpha_{ij}^2\right)\frac{m_im_j}{m_i+m_j}\chi_{ij}^{(0)}\sigma_{ij}^{d-1}\int d\mathbf{v}_1\int d\mathbf{v}_2\; g_{12}^3 f_i^{(0)}(\mathbf{V}_1)\mathcal{D}_j(\mathbf{V}_2). \tag{7.3}$$

The constant B_n is defined by

$$B_n \equiv \pi^{(d-1)/2}\frac{\Gamma\left(\frac{n+1}{2}\right)}{\Gamma\left(\frac{n+d}{2}\right)}. \tag{7.4}$$

Also in (7.3) the species temperatures $\left\{T_i^{(0)}\right\}$ have been defined by

$$\frac{d}{2}n_i T_i^{(0)} = \int d\mathbf{v}\frac{1}{2}m_i V^2 f_i^{(0)}(\{n_i\}, T, V). \tag{7.5}$$

There is no special significance to these quantities other than naming the integral on the right side, which is a specified function of the hydrodynamic fields $\{n_i\}$ and the global temperature T through $f_i^{(0)}$.

B. Mass Fluxes

The mass fluxes are determined from the definition of (4.16) leading to the form (5.10) to first order in the gradients

$$\mathbf{j}_{0i} \to -\sum_{j=1}^{s} m_i m_j \frac{n_j}{\rho} D_{ij}\nabla \ln n_j - \rho D_i^T \nabla \ln T - \sum_{j=1}^{s} D_{ij}^F \mathbf{F}_j. \tag{7.6}$$

The transport coefficients are identified as

$$D_i^T = -\frac{m_i}{\rho d}\int d\mathbf{v}\mathbf{V}\cdot\boldsymbol{\mathcal{A}}_i(\mathbf{V}), \tag{7.7}$$

$$D_{ij} = -\frac{\rho}{m_j n_j d}\int d\mathbf{v}\mathbf{V}\cdot\boldsymbol{\mathcal{B}}_i^j(\mathbf{V}), \tag{7.8}$$

$$D_{ij}^F = -\frac{m_i}{d}\int d\mathbf{v}\mathbf{V}\cdot\boldsymbol{\mathcal{E}}_i^j(\mathbf{V}). \tag{7.9}$$

C. Energy Flux

The energy flux to first order in the gradients is given by (5.11)

$$\mathbf{q} \to -\lambda\nabla T - \sum_{i,j=1}^{s}\left(T^2 D_{q,ij}\nabla \ln n_j + L_{ij}\mathbf{F}_j\right). \tag{7.10}$$

There are both kinetic and collisional transfer contributions according to Eq. (4.17), $\mathbf{q} \equiv \mathbf{q}^k + \mathbf{q}^c$. The kinetic contributions to the transport coefficients are identified as

$$\lambda^k = \sum_{i=1}^{s}\lambda_i^k = -\frac{1}{dT}\sum_{i=1}^{s}\int d\mathbf{v}\frac{1}{2}m_i V^2\mathbf{V}\cdot\boldsymbol{\mathcal{A}}_i(\mathbf{V}), \tag{7.11}$$

$$D_{q,ij}^k = -\frac{1}{dT^2}\int d\mathbf{v}\frac{1}{2}m_i V^2\mathbf{V}\cdot\boldsymbol{\mathcal{B}}_i^j(\mathbf{V}), \tag{7.12}$$

$$L_{ij}^k = -\frac{1}{d}\int d\mathbf{v}\frac{1}{2}m_i V^2\mathbf{V}\cdot\boldsymbol{\mathcal{E}}_i^j(\mathbf{V}). \tag{7.13}$$

For convenience below, the partial thermal conductivities λ_i^k have been introduced in Eq. (7.11). The collision transfer contributions are obtained from (4.19) to first order in the gradients. These are calculated in Appendix F with the results

$$\begin{aligned}\lambda^c \;=\; &\sum_{i,j=1}^{s}\frac{1}{8}(1+\alpha_{ij})\,m_j\mu_{ij}\sigma_{ij}^d\chi_{ij}^{(0)}\left\{2B_4(1-\alpha_{ij})(\mu_{ij}-\mu_{ji})\,n_i\left[\frac{2}{m_j}\lambda_j^k + (d+2)\frac{T_i^{(0)}}{m_i m_j T}\rho D_j^T\right]\right.\\ &\left.+\frac{8B_2}{2+d}n_i\left[\frac{2\mu_{ij}}{m_j}\lambda_j^k - (d+2)\frac{T_i^{(0)}}{m_i m_j T}(2\mu_{ij}-\mu_{ji})\,\rho D_j^T\right] - T^{-1}C_{ij}^T\right\},\end{aligned} \tag{7.14}$$

$$
\begin{aligned}
D_{q,ij}^{c} &= \sum_{p=1}^{s}\frac{1}{8}\left(1+\alpha_{ip}\right)m_{p}\mu_{ip}\sigma_{ip}^{d}\chi_{ip}^{(0)}\left\{2B_{4}\left(1-\alpha_{ip}\right)\left(\mu_{ip}-\mu_{pi}\right)\right.\\
&\times n_{i}\left[\frac{2}{m_{p}}D_{q,pj}^{k}+(d+2)\frac{T_{i}^{(0)}}{T^{2}}\frac{m_{j}n_{j}}{\rho m_{i}}D_{pj}\right]\\
&\left.+\frac{8B_{2}}{d+2}n_{i}\left[\frac{2\mu_{pi}}{m_{p}}D_{q,pj}^{k}-(d+2)\left(2\mu_{ip}-\mu_{pi}\right)\frac{T_{i}^{(0)}}{T^{2}}\frac{n_{j}m_{j}}{m_{i}\rho}D_{pj}\right]-T^{-2}C_{ipj}^{T}\right\},
\end{aligned}
\tag{7.15}
$$

$$
\begin{aligned}
L_{ij}^{c} &= \sum_{p=1}^{s}\frac{1}{8}\left(1+\alpha_{ip}\right)m_{p}\mu_{ip}\sigma_{ip}^{d}\chi_{ip}^{(0)}\left\{2B_{4}\left(1-\alpha_{ip}\right)\left(\mu_{ip}-\mu_{pi}\right)\right.\\
&\times n_{i}\left[\frac{2}{m_{p}}L_{pj}^{k}+(d+2)\frac{T_{i}^{(0)}}{m_{i}m_{p}}D_{pj}^{F}\right]\\
&\left.+\frac{8B_{2}}{d+2}n_{i}\left[\frac{2\mu_{pi}}{m_{p}}L_{pj}^{k}-(d+2)\left(2\mu_{ip}-\mu_{pi}\right)\frac{T_{i}^{(0)}}{m_{i}m_{p}}D_{pj}^{F}\right]\right\},
\end{aligned}
\tag{7.16}
$$

where the coefficients C_{ij}^{T} and C_{ipj}^{T} are given by Eqs. (F27) and (F28). These expressions also depend on the transport coefficients of the mass fluxes, D_{i}^{T}, D_{ij}, and D_{ij}^{F} given by Eqs. (7.7), (7.8), and (7.9), respectively, and on the kinetic contributions λ_{i}^{k}, $D_{q,ij}^{k}$, and L_{ij}^{k}.

D. Momentum Flux

The pressure tensor is evaluated from Eqs. (4.20)–(4.22). To zeroth order in the gradients, one gets the pressure p as

$$
p\left(\{n_{i}\},T\right)=\frac{1}{d}P_{\gamma\gamma}^{(0)}\equiv p^{k}\left(\{n_{i}\},T\right)+p^{c}\left(\{n_{i}\},T\right)=\frac{1}{d}P_{\gamma\gamma}^{(0)k}+\frac{1}{d}P_{\gamma\gamma}^{(0)c},
\tag{7.17}
$$

where

$$
p=p^{k}+p^{c},
\tag{7.18}
$$

$$
p^{k}=nT,\qquad p^{c}=B_{2}\sum_{i,j=1}^{s}\mu_{ji}\left(1+\alpha_{ij}\right)\sigma_{ij}^{d}\chi_{ij}^{(0)}n_{i}n_{j}T_{i}^{(0)}.
\tag{7.19}
$$

Similarly the shear viscosity is $\eta=\eta^{k}+\eta^{c}$ where

$$
\eta^{k}=\sum_{i=1}^{s}\eta_{i}^{k},\quad \eta_{i}^{k}=-\frac{1}{(d+2)(d-1)}\sum_{i=1}^{s}\int d\mathbf{v}m_{i}V_{\lambda}V_{\gamma}\mathcal{C}_{i,\lambda\gamma}\left(\mathbf{V}\right),
\tag{7.20}
$$

$$
\eta^{c}=\frac{2B_{2}}{(d+2)}\sum_{i,j=1}^{s}\mu_{ij}\left(1+\alpha_{ij}\right)\chi_{ij}^{(0)}n_{i}\sigma_{ij}^{d}\eta_{j}^{k}+\frac{d}{d+2}\kappa^{c}.
\tag{7.21}
$$

Finally, the bulk viscosity is $\kappa=\kappa^{k}+\kappa^{c}$ where

$$
\kappa^{k}=0,\quad \kappa^{c}=\frac{B_{3}\left(d+1\right)}{2d^{2}}\sum_{i,j=1}^{s}m_{j}\mu_{ij}\left(1+\alpha_{ij}\right)\chi_{ij}^{(0)}\sigma_{ij}^{d+1}\int d\mathbf{v}_{1}\int d\mathbf{v}_{2}f_{i}^{(0)}(\mathbf{V}_{1})f_{j}^{(0)}(\mathbf{V}_{2})g_{12}.
\tag{7.22}
$$

VIII. DISCUSSION

The most complete and accurate description of mixtures for ordinary fluids is based on the revised Enskog kinetic equations for hard spheres. The explicit construction of solutions to those equations by the CE expansion to first order in the gradients was given more that twenty years ago in Ref. [49]. These solutions, together with the macroscopic balance equations obtained from the kinetic equations, provide a self-consistent derivation of Navier-Stokes hydrodynamics for mixtures and the identification of expressions for all the Navier-Stokes parameters (equations of state, transport coefficients). In the context of the chosen kinetic theory, the analysis and the expressions for these parameters are exact. At this formal level questions of principle could be addressed, prior to the introduction of subsequent approximations for practical evaluations. For example, it was shown that application of the analysis to the original and revised Enskog theories leads to qualitatively different Navier-Stokes hydrodynamics, only one of which is consistent with irreversible thermodynamics. Since no approximations were involved this was sufficient to reject the Enskog kinetic theory in favor of its revised version [48].

The present work is simply an extension of that in Ref. [49] to *inelastic* hard sphere granular mixtures. Modification of the collisions to account for inelasticity leads to significant differences from ordinary fluids in detail, but the formal structure of the CE expansion remains the same. Similarly, granular Navier-Stokes hydrodynamics results exactly from the CE solution to first order in the gradients and the corresponding modified balance equations. The form of these hydrodynamic equations and expressions for the transport coefficients are exact, as in the ordinary fluid case. The primary motivation for this analysis is to provide the basis for practical applications, as noted in the Introduction, and described in the following paper. However, at the formal level, important fundamental questions can be addressed and clarified as well.

The existence of hydrodynamics for granular fluids has been questioned, due to the many known differences from ordinary fluids: there is no equilibrium or even stationary reference state; the temperature is not a hydrodynamic field (failure of energy conservation), or conversely, multiple temperature fields could be required for mixtures (failure of equilibrium state equipartition for the corresponding granular HCS). In the end, qualitative discussions must be resolved by controlled analysis. Here, the validity of the RET for some range of densities and degree of dissipation has been assumed as a mesoscopic basis for possible macroscopic dynamics in a granular mixture. As shown in the text, sufficient conditions are the macroscopic balance equations (verified) and a normal solution to the kinetic equations. The normal solution is defined in terms of a chosen set of hydrodynamic fields, and the question of hydrodynamics reduces to its existence. The details of the Appendices give the explicit construction of this solution to first order in the gradients, together with a proof of the existence of solutions to the associated integral equations. It can be concluded from this that a closed set of hydrodynamic equations for the species densities, flow velocity, and a single temperature exist for sufficiently small gradients.

This conclusion is consistent with the observations that the reference state is not equilibrium, depends on the cooling temperature, energy loss can be large at strong dissipation, and the kinetic temperatures of species are different. None of these facts compromises implementation of the CE expansion for solution to the kinetic equation. The parameters of the resulting Navier-Stokes equations incorporate such effects through the integral equations that determine them, and their dependence on the time dependent fields. This in turn affects the solutions to the Navier-Stokes equations under different physical conditions, and is responsible for some of the observed peculiarities of granular fluids. Clearly, it is important to get the details of the Navier-Stokes equations accurately before concluding that any observed experimental phenomenon is hydrodynamic or not. This is another primary motivation for the present work.

These details entail solution to the equation for the reference state and solution to the integral equations for the transport coefficients, to determine them as functions of the hydrodynamic fields (temperature, flow field, and species densities) and the system parameters (restitution coefficients, masses, particle sizes). There has been considerable study of the reference state, as an expansion about a Gaussian for relatively small velocities (asymptotic forms for large velocities are known as well). The integral equations can be solved approximately as truncated expansions in a complete set of polynomials with Gaussian weight factors. For ordinary fluids the leading approximation is generally quite accurate, and the following paper gives its extension to the granular mixture. Still, there are open questions about this approximation for strong dissipation and large mechanical disparity (e.g., mass ratio). Previous results obtained for granular mixtures at low-density [67, 68] and for the shear viscosity of a heated granular mixture at moderate density [64] have shown the accuracy of the above approximation, even for strong dissipation.

An accurate solution to the integral equations will predict the transport coefficients as functions of the dissipation. There is only one correct result for this dependence, given by the formulas obtained here. However, its measurement in a given experiment or simulation can entangle and affect this dependence of the transport coefficients due to higher order gradients beyond the Navier-Stokes limit. It may be tempting to compare experimental or simulation data to a corresponding Navier-Stokes solution, adjusting the transport coefficients for a best fit and reporting these as the "measured" values. This can be misleading for granular fluids under conditions where the size of the gradients increase with the degree of dissipation. For such states, strong dissipation can require additional terms in the constitutive

equations beyond those of Navier-Stokes order [40, 69, 70]. This does not mean that the results obtained here are not correct at strong dissipation, only that they must be distinguished carefully from other effects of the same order. A careful tabulation of the Navier-Stokes results given here (e.g., via Monte Carlo simulation) is required for an accurate analysis of experiments of current interest. It is an interesting new feature of granular fluids that hydrodynamic states beyond Navier-Stokes order may be the norm rather than the exception.

IX. ACKNOWLEDGMENTS

V. G. acknowledges partial support from the Ministerio de Ciencia y Tecnología (Spain) through Grant No. FIS2007–60977. C.M.H. is grateful to the National Science Foundation for providing financial support of this project through grant CTS-0318999 with additional support provided by the American Chemical Society Petroleum Research Fund (Grant 43393-AC9) and the Engineering and Physical Sciences Research Council (Grant EP/DO30676/1). C. M. H. and J. W. D. are also grateful to the organizers and participants of the Granular Physics Workshop at the Kavli Institute of Theoretical Physics (with partial support from the National Science Foundation under grant PHY99-07949), which provided a starting forum for much of this work.

APPENDIX A: RET AND SPATIAL CORRELATIONS AT CONTACT

In the case of ordinary fluids, the Enskog approximation can be understood as a short time, or Markovian approximation. This follows if the initial distribution has the Enskog form

$$f_{ij}(\mathbf{r}_1,\mathbf{v}_1,\mathbf{r}_1-\boldsymbol{\sigma}_{ij},\mathbf{v}_2;t=0)=f_i(\mathbf{r}_1,\mathbf{v}_1,t=0)f_j(\mathbf{r}_1-\boldsymbol{\sigma}_{ij},\mathbf{v}_2;t=0)\chi_{ij}\left(\mathbf{r}_1,\mathbf{r}_1-\boldsymbol{\sigma}_{ij}\mid\{n_k\}\right). \tag{A1}$$

In fact, this is a quite plausible class of initial conditions since correlations in that case are generally induced by the interparticle structure that is independent of the velocities. Then at finite times, it is assumed that $f_{ij}(\mathbf{r}_1,\mathbf{v}_1,\mathbf{r}_1-\boldsymbol{\sigma}_{ij},\mathbf{v}_2;t)$ becomes a functional of f_i

$$f_{ij}(\mathbf{r}_1,\mathbf{v}_1,\mathbf{r}_1-\boldsymbol{\sigma}_{ij},\mathbf{v}_2;t)=F_{ij}(\mathbf{r}_1,\mathbf{v}_1,\mathbf{r}_1-\boldsymbol{\sigma}_{ij},\mathbf{v}_2;t\mid f_i(t)). \tag{A2}$$

The Enskog approximation corresponds to evaluating this functional at $t=0$

$$f_{ij}(\mathbf{r}_1,\mathbf{v}_1,\mathbf{r}_1-\boldsymbol{\sigma}_{ij},\mathbf{v}_2;t)\to F_{ij}(\mathbf{r}_1,\mathbf{v}_1,\mathbf{r}_1-\boldsymbol{\sigma}_{ij},\mathbf{v}_2;t=0\mid f_i(t)). \tag{A3}$$

Thus for the special class of initial conditions the Enskog approximation is asymptotically exact at short times, and assumes that the generator for dynamics at later times is the same as that initially. This idea provides a simple mean field theory for particles with continuous potentials of interaction, but is more realistic for hard spheres where there is instantaneous momentum transport at the initial time. The presence of inherent velocity correlations for granular fluids suggests that the form (A1) is less justified than in the ordinary fluid case. However, it is noted that velocity correlations are present for any nonequilibrium state even with elastic collisions and it is known that the Enskog equation still provides a good approximation in these latter cases.

An important exact boundary condition for hard spheres is given by [53]

$$\Theta(\widehat{\boldsymbol{\sigma}}\cdot\mathbf{g}_{12})f_{ij}(\mathbf{r}_1,\mathbf{v}_1,\mathbf{r}_1-\boldsymbol{\sigma}_{ij},\mathbf{v}_2;t)=\alpha_{ij}^{-2}b_{ij}^{-1}\Theta(-\widehat{\boldsymbol{\sigma}}\cdot\mathbf{g}_{12})f_{ij}(\mathbf{r}_1,\mathbf{v}_1,\mathbf{r}_1-\sigma_{ij},\mathbf{v}_2;t). \tag{A4}$$

This equation implies that the distribution of particles that have collided is the same as those about to collide, but with their velocities changed according to the collision rules. In general the two particle distribution function can be written as

$$\begin{aligned} f_{ij}(\mathbf{r}_1,\mathbf{v}_1,\mathbf{r}_1-\boldsymbol{\sigma}_{ij},\mathbf{v}_2;t) &= \Theta(-\widehat{\boldsymbol{\sigma}}\cdot\mathbf{g}_{12})f_{ij}(\mathbf{r}_1,\mathbf{v}_1,\mathbf{r}_1-\boldsymbol{\sigma}_{ij},\mathbf{v}_2;t) \\ &\quad+\Theta(\widehat{\boldsymbol{\sigma}}\cdot\mathbf{g}_{12})f_{ij}(\mathbf{r}_1,\mathbf{v}_1,\mathbf{r}_1-\boldsymbol{\sigma}_{ij},\mathbf{v}_2;t). \end{aligned} \tag{A5}$$

If the Enskog approximation (A3) is introduced in the first term on the right side of (A5), then the corresponding approximation on the right side of Eq. (A5) gives the approximate two particle distribution function at contact as

$$\begin{aligned} f_{ij}(\mathbf{r}_1,\mathbf{v}_1,\mathbf{r}_1-\boldsymbol{\sigma}_{ij},\mathbf{v}_2;t) &\to \Theta(-\widehat{\boldsymbol{\sigma}}\cdot\mathbf{g}_{12})\chi_{ij}\left(\mathbf{r}_1,\mathbf{r}_1-\boldsymbol{\sigma}_{ij}\mid\{n_k\}\right)f_i(\mathbf{r}_1,\mathbf{v}_1;t)f_j(\mathbf{r}_1-\boldsymbol{\sigma}_{ij},\mathbf{v}_2;t) \\ &+ \alpha_{ij}^{-2}b_{ij}^{-1}\Theta(-\widehat{\boldsymbol{\sigma}}\cdot\mathbf{g}_{12})\chi_{ij}\left(\mathbf{r}_1,\mathbf{r}_1-\boldsymbol{\sigma}_{ij}\mid\{n_k\}\right)f_i(\mathbf{r}_1,\mathbf{v}_1;t) \\ &\quad\times f_j(\mathbf{r}_1-\boldsymbol{\sigma}_{ij},\mathbf{v}_2;t) \\ &= \Theta(-\widehat{\boldsymbol{\sigma}}\cdot\mathbf{g}_{12})\chi_{ij}\left(\mathbf{r}_1,\mathbf{r}_1-\boldsymbol{\sigma}_{ij}\mid\{n_k\}\right)f_i(\mathbf{r}_1,\mathbf{v}_1;t)f_j(\mathbf{r}_1-\boldsymbol{\sigma}_{ij},\mathbf{v}_2;t) \\ &\quad+\alpha_{ij}^{-2}\Theta(\widehat{\boldsymbol{\sigma}}\cdot\mathbf{g}_{12})\chi_{ij}\left(\mathbf{r}_1,\mathbf{r}_1-\boldsymbol{\sigma}_{ij}\mid\{n_k\}\right)f_i(\mathbf{r}_1,\mathbf{v}_1'';t) \\ &\quad\times f_j(\mathbf{r}_1-\boldsymbol{\sigma}_{ij},\mathbf{v}_2'';t). \end{aligned} \tag{A6}$$

Since $\mathbf{v}_1''$ and $\mathbf{v}_2''$ are functions of both $\mathbf{v}_1$ and $\mathbf{v}_2$ there are velocity correlations on the complementary hemisphere, even when they are neglected on the precollision hemisphere.

An important consequence of (A6) is the relationship of $\chi_{ij}\left(\mathbf{r}_1, \mathbf{r}_1 - \boldsymbol{\sigma}_{ij} \mid \{n_i\}\right)$ to the pair correlation function $g_{ij}\left(\mathbf{r}_1, \mathbf{r}_1 - \boldsymbol{\sigma}_{ij} \mid \{n_k\}\right)$ defined by

$$n_i\left(\mathbf{r}_1\right) n_j\left(\mathbf{r}_1 - \boldsymbol{\sigma}_{ij}\right) g_{ij}\left(\mathbf{r}_1, \mathbf{r}_1 - \boldsymbol{\sigma}_{ij} \mid \{n_k\}\right) = \int d\mathbf{v}_1 \int d\mathbf{v}_2 \; f_{ij}(\mathbf{r}_1, \mathbf{v}_1, \mathbf{r}_1 - \boldsymbol{\sigma}_{ij}, \mathbf{v}_2; t) \tag{A7}$$

Use of the approximation (A6) gives the result

$$\begin{aligned} n_i\left(\mathbf{r}_1\right) n_j\left(\mathbf{r}_1 - \boldsymbol{\sigma}_{ij}\right) g_{ij}\left(\mathbf{r}_1, \mathbf{r}_1 - \boldsymbol{\sigma}_{ij} \mid \{n_k\}\right) \;=\; & \frac{1+\alpha_{ij}}{\alpha_{ij}} \chi_{ij}\left(\mathbf{r}_1, \mathbf{r}_1 - \boldsymbol{\sigma}_{ij} \mid \{n_k\}\right) \int d\mathbf{v}_1 \int d\mathbf{v}_2 \\ & \times \Theta(-\widehat{\boldsymbol{\sigma}} \cdot \mathbf{g}_{12}) f_i(\mathbf{r}_1, \mathbf{v}_1; t) f_j(\mathbf{r}_1 - \boldsymbol{\sigma}_{ij}, \mathbf{v}_2; t), \end{aligned} \tag{A8}$$

where a change of variables has been made in the integration of the second term in (A6)

$$\int d\mathbf{v}_1 \int \; d\mathbf{v}_2 X(\mathbf{v}_1'', \mathbf{v}_2'') = \alpha_{ij} \int d\mathbf{v}_1'' \int d\mathbf{v}_2'' \; X(\mathbf{v}_1'', \mathbf{v}_2''). \tag{A9}$$

For a uniform system, $g_{ij}\left(\mathbf{r}_1, \mathbf{r}_2 \mid \{n_k\}\right) \to g_{ij}\left(|\mathbf{r}_1 - \mathbf{r}_2|; \{n_k\}\right)$ and this expression reduces to

$$g_{ij}\left(\sigma_{ij}; \{n_k\}\right) = \frac{1+\alpha_{ij}}{2\alpha_{ij}} \chi_{ij}\left(\sigma_{ij}; \{n_k\}\right) \tag{A10}$$

Equation (A10) is the result quoted in the text and provides the interpretation for $\chi_{ij}\left(\mathbf{r}_1, \mathbf{r}_1 - \boldsymbol{\sigma}_{ij} \mid \{n_k\}\right)$. For elastic collisions $\chi_{ij}\left(\sigma_{ij}; \{n_k\}\right)$ is indeed the pair correlation function at contact. The Enskog theory in that case takes $\chi_{ij}\left(\mathbf{r}_1, \mathbf{r}_1 - \boldsymbol{\sigma}_{ij} \mid \{n_k\}\right)$ to be the pair correlation function for an equilibrium nonuniform fluid whose densities are equal to those for the actual nonequilibrium state being considered. This assumption is based on the fact that structural correlations for hard spheres are entirely due to excluded volume effects which should be similar for equilibrium and nonequilibrium states. It is reasonable to extend this choice for $\chi_{ij}\left(\mathbf{r}_1, \mathbf{r}_1 - \boldsymbol{\sigma}_{ij} \mid \{n_k\}\right)$ to granular fluids as well. Its accuracy can be judged by measuring (via MD simulation) the pair correlation given by (A10) with this choice on the right side. This has been done for the one component fluid, indicating reasonable results over a range of values for the restitution coefficient [53].

APPENDIX B: BALANCE EQUATIONS AND FLUXES

The macroscopic balance equations follow from the definitions (4.1)–(4.3) and the first hierarchy equation (3.1)

$$\partial_t n_i + \nabla_{\mathbf{r}_1} \cdot \int d\mathbf{v}_1 \mathbf{v}_1 f_i = \int d\mathbf{v}_1 C_i, \tag{B1}$$

$$\partial_t e + \nabla_{\mathbf{r}_1} \cdot \sum_{i=1}^{s} \int d\mathbf{v}_1 \frac{1}{2} m_i v_1^2 \mathbf{v}_1 f_i - \sum_{i=1}^{s} \mathbf{F}_i \cdot \int d\mathbf{v}_1 \mathbf{v}_1 f_i = \sum_{i=1}^{s} \int d\mathbf{v}_1 \frac{1}{2} m_i v_1^2 C_i, \tag{B2}$$

$$\partial_t p_\beta + \partial_{r_{1\gamma}} \sum_{i=1}^{s} \int d\mathbf{v}_1 m_i v_{1\gamma} v_{1\beta} f_i - \sum_{i=1}^{s} n_i F_{i\beta} = \sum_{i=1}^{s} \int d\mathbf{v}_1 m_i v_{1\beta} C_i. \tag{B3}$$

The integrals over the collisional contribution C_i are analyzed below with the results

$$\int d\mathbf{v}_1 C_i = 0, \tag{B4}$$

$$\sum_{i=1}^{s} \int d\mathbf{v}_1 \frac{1}{2} m_i v_1^2 C_i = -\nabla \cdot \mathbf{s}^c - w, \tag{B5}$$

$$\sum_{i=1}^{s}\int d\mathbf{v}_1 m_i v_{1\beta} C_i = -\partial_{r_\gamma} t^c_{\gamma\beta}. \tag{B6}$$

Use of these expressions in (B1)–(B3) gives the balance equations (4.4)–(4.6) of the text with

$$\mathbf{j}_i = m_i \int d\mathbf{v}_1 \mathbf{v}_1 f_i, \tag{B7}$$

$$\mathbf{s} = \sum_{i=1}^{s}\int d\mathbf{v}_1 \frac{1}{2} m_i v_1^2 \mathbf{v}_1 f_i + \mathbf{s}^c, \tag{B8}$$

$$t_{\gamma\beta} = \sum_{i=1}^{s}\int d\mathbf{v}_1 m_i v_{1\gamma} v_{1\beta} f_i + t^c_{\gamma\beta}. \tag{B9}$$

The terms w, $\mathbf{s}^c$, and $t^c_{\gamma\beta}$ arising from the collisional contribution C_i are identified by further analysis of the left sides of (B5) and (B6). To do so consider the general expression for some arbitrary function $\psi_i(\mathbf{v}_1)$

$$\begin{aligned}\int d\mathbf{v}_1 \psi_i C_i \;=\; & \sum_{j=1}^{s}\sigma_{ij}^{d-1}\int d\mathbf{v}_1\int d\mathbf{v}_2\int d\widehat{\boldsymbol{\sigma}}\,\Theta(\widehat{\boldsymbol{\sigma}}\cdot\mathbf{g}_{12})(\widehat{\boldsymbol{\sigma}}\cdot\mathbf{g}_{12})\psi_i(\mathbf{v}_1)\\ & \times\left[\alpha_{ij}^{-2} f_{ij}(\mathbf{r}_1,\mathbf{v}_1'',\mathbf{r}_1-\boldsymbol{\sigma}_{ij},\mathbf{v}_2'';t) - f_{ij}(\mathbf{r}_1,\mathbf{v}_1,\mathbf{r}_1+\boldsymbol{\sigma}_{ij},\mathbf{v}_2;t)\right].\end{aligned} \tag{B10}$$

The restituting velocities are functions of the given velocities, $\mathbf{v}_1'' = \mathbf{v}_1''(\mathbf{v}_1,\mathbf{v}_2)$, $\mathbf{v}_2'' = \mathbf{v}_2''(\mathbf{v}_1,\mathbf{v}_2)$, defined by (3.3). These relations can be inverted to get

$$\mathbf{v}_1 = \mathbf{v}_1'' - \mu_{ji}(1+\alpha_{ij})(\widehat{\boldsymbol{\sigma}}\cdot\mathbf{g}_{12}'')\widehat{\boldsymbol{\sigma}}, \qquad \mathbf{v}_2 = \mathbf{v}_2'' + \mu_{ij}(1+\alpha_{ij})(\widehat{\boldsymbol{\sigma}}\cdot\mathbf{g}_{12}'')\widehat{\boldsymbol{\sigma}}. \tag{B11}$$

Therefore, in the first term of (B10) it is possible to change integration variables from $d\mathbf{v}_1 d\mathbf{v}_2$ to $d\mathbf{v}_1'' d\mathbf{v}_2''$, with a Jacobian α_{ij} to get

$$\begin{aligned}&\int d\mathbf{v}_1\int d\mathbf{v}_2\int d\widehat{\boldsymbol{\sigma}}\,\Theta(\widehat{\boldsymbol{\sigma}}\cdot\mathbf{g}_{12})(\widehat{\boldsymbol{\sigma}}\cdot\mathbf{g}_{12})\psi_i(\mathbf{v}_1)\,\alpha_{ij}^{-2} f_{ij}(\mathbf{r}_1,\mathbf{v}_1'',\mathbf{r}_1-\boldsymbol{\sigma}_{ij},\mathbf{v}_2'';t)\\ =\;& \int d\mathbf{v}_1''\int d\mathbf{v}_2''\int d\widehat{\boldsymbol{\sigma}}\,\Theta(-\widehat{\boldsymbol{\sigma}}\cdot\mathbf{g}_{12}'')(-\widehat{\boldsymbol{\sigma}}\cdot\mathbf{g}_{12}'')\psi_i(\mathbf{v}_1(\mathbf{v}_1'',\mathbf{v}_2''))\,f_{ij}(\mathbf{r}_1,\mathbf{v}_1'',\mathbf{r}_1-\boldsymbol{\sigma}_{ij},\mathbf{v}_2'';t)\\ =\;& \int d\mathbf{v}_1\int d\mathbf{v}_2\int d\widehat{\boldsymbol{\sigma}}\,\Theta(\widehat{\boldsymbol{\sigma}}\cdot\mathbf{g}_{12})(\widehat{\boldsymbol{\sigma}}\cdot\mathbf{g}_{12})\psi_i(\mathbf{v}_1'(\mathbf{v}_1,\mathbf{v}_2))\,f_{ij}(\mathbf{r}_1,\mathbf{v}_1,\mathbf{r}_1+\boldsymbol{\sigma}_{ij},\mathbf{v}_2;t),\end{aligned} \tag{B12}$$

where use has been made of $(\widehat{\boldsymbol{\sigma}}\cdot\mathbf{g}_{12}) = -\alpha_{ij}(\widehat{\boldsymbol{\sigma}}\cdot\mathbf{g}_{12}'')$. In the last line the dummy variables $(\mathbf{v}_1'',\mathbf{v}_2'')$ have been relabelled $(\mathbf{v}_1,\mathbf{v}_2)$, and a change of integration from $\widehat{\boldsymbol{\sigma}}$ to $-\widehat{\boldsymbol{\sigma}}$ has been performed. Accordingly $\mathbf{v}_1(\mathbf{v}_1'',\mathbf{v}_2'')$ has been relabelled $\mathbf{v}_1'(\mathbf{v}_1,\mathbf{v}_2)$ with (B11) becoming in this notation

$$\mathbf{v}_1' = \mathbf{v}_1 - \mu_{ji}(1+\alpha_{ij})(\widehat{\boldsymbol{\sigma}}\cdot\mathbf{g}_{12})\widehat{\boldsymbol{\sigma}}, \qquad \mathbf{v}_2' = \mathbf{v}_2 + \mu_{ij}(1+\alpha_{ij})(\widehat{\boldsymbol{\sigma}}\cdot\mathbf{g}_{12})\widehat{\boldsymbol{\sigma}}. \tag{B13}$$

This is the direct scattering law, which differs from the restituting scattering law (3.3) for $\alpha_{ij}\neq 1$. With this transformation the integral (B10) is

$$\begin{aligned}\int d\mathbf{v}_1\psi_i C_i \;=\; & \sum_{j=1}^{s}\sigma_{ij}^{d-1}\int d\mathbf{v}_1\int d\mathbf{v}_2\int d\widehat{\boldsymbol{\sigma}}\,\Theta(\widehat{\boldsymbol{\sigma}}\cdot\mathbf{g}_{12})(\widehat{\boldsymbol{\sigma}}\cdot\mathbf{g}_{12})\\ & \times(\psi_i(\mathbf{v}_1')-\psi_i(\mathbf{v}_1))\,f_{ij}(\mathbf{r}_1,\mathbf{v}_1,\mathbf{r}_1+\boldsymbol{\sigma}_{ij},\mathbf{v}_2;t).\end{aligned} \tag{B14}$$

The special choice $\psi_i(\mathbf{v}_1)=1$ proves (B4) above.

Next, consider the sum of (B14) over all species

$$\begin{aligned}\sum_{i=1}^{s}\int d\mathbf{v}_1\psi_i C_i \;=\; & \sum_{i,j=1}^{s}\sigma_{ij}^{d-1}\int d\mathbf{v}_1\int d\mathbf{v}_2\int d\widehat{\boldsymbol{\sigma}}\,\Theta(\widehat{\boldsymbol{\sigma}}\cdot\mathbf{g}_{12})(\widehat{\boldsymbol{\sigma}}\cdot\mathbf{g}_{12})\\ & \times[\psi_i(\mathbf{v}_1')-\psi_i(\mathbf{v}_1)]\,f_{ij}^{(2)}(\mathbf{r}_1,\mathbf{v}_1,\mathbf{r}_1+\boldsymbol{\sigma}_{ij},\mathbf{v}_2;t)\\ =\; & \frac{1}{2}\sum_{i,j=1}^{k}\sigma_{ij}^{d-1}\int d\mathbf{v}_1\int d\mathbf{v}_2\int d\widehat{\boldsymbol{\sigma}}\,\Theta(\widehat{\boldsymbol{\sigma}}\cdot\mathbf{g}_{12})(\widehat{\boldsymbol{\sigma}}\cdot\mathbf{g}_{12})\\ & \times\{[\psi_i(\mathbf{v}_1')-\psi_i(\mathbf{v}_1)]\,f_{ij}(\mathbf{r}_1,\mathbf{v}_1,\mathbf{r}_1+\boldsymbol{\sigma}_{ij},\mathbf{v}_2;t)\\ & +[\psi_j(\mathbf{v}_2')-\psi_j(\mathbf{v}_2)]\,f_{ji}(\mathbf{r}_1,\mathbf{v}_2,\mathbf{r}_1-\boldsymbol{\sigma}_{ij},\mathbf{v}_1;t)\}.\end{aligned} \tag{B15}$$

The second equality is obtained from the first by taking half the sum of the first plus an equivalent form obtained by interchanging $\mathbf{v}_1$ and $\mathbf{v}_2$, interchanging i and j, and changing $\widehat{\boldsymbol{\sigma}}$ to $-\widehat{\boldsymbol{\sigma}}$. To simplify this further, note the relation $f_{ji}(\mathbf{r}_1,\mathbf{v}_2,\mathbf{r}_1-\boldsymbol{\sigma}_{ij},\mathbf{v}_1;t)=f_{ij}(\mathbf{r}_1-\boldsymbol{\sigma}_{ij},\mathbf{v}_1,\mathbf{r}_1,\mathbf{v}_2;t)$ and arrange terms as

$$\begin{aligned}\sum_{i=1}^{s}\int d\mathbf{v}_1\psi_i C_i &= \frac{1}{2}\sum_{i,j=1}^{s}\sigma_{ij}^{d-1}\int d\mathbf{v}_1\int d\mathbf{v}_2\int d\widehat{\boldsymbol{\sigma}}\,\Theta(\widehat{\boldsymbol{\sigma}}\cdot\mathbf{g}_{12})(\widehat{\boldsymbol{\sigma}}\cdot\mathbf{g}_{12})\\ &\times\ \left\{\left[\psi_i\left(\mathbf{v}_1'\right)+\psi_j\left(\mathbf{v}_2'\right)-\psi_i\left(\mathbf{v}_1\right)-\psi_j\left(\mathbf{v}_2\right)\right]f_{ij}(\mathbf{r}_1,\mathbf{v}_1,\mathbf{r}_1+\boldsymbol{\sigma}_{ij},\mathbf{v}_2;t)\right.\\ &+\ \left.\left[\psi_i\left(\mathbf{v}_1'\right)-\psi_i\left(\mathbf{v}_1\right)\right]\left[f_{ij}(\mathbf{r}_1,\mathbf{v}_1,\mathbf{r}_1+\boldsymbol{\sigma}_{ij},\mathbf{v}_2;t)-f_{ij}(\mathbf{r}_1-\boldsymbol{\sigma}_{ij},\mathbf{v}_1,\mathbf{r}_1,\mathbf{v}_2;t)\right]\right\}.\end{aligned} \tag{B16}$$

The first term of the integrand represents a collisional effect due to scattering with a change in the velocities. The second term is a collisional effect due to the spatial difference of the colliding pair. This second effect is called "collisional transfer". It can be written as a divergence through the identity

$$\begin{aligned}f_{ij}(\mathbf{r}_1,\mathbf{v}_1,\mathbf{r}_1+\boldsymbol{\sigma}_{ij},\mathbf{v}_2;t) &- f_{ij}(\mathbf{r}_1-\boldsymbol{\sigma}_{ij},\mathbf{v}_1,\mathbf{r}_1,\mathbf{v}_2;t)\\ &= \int_0^1 dx\frac{\partial}{\partial x}f_{ij}(\mathbf{r}_1-x\boldsymbol{\sigma}_{ij},\mathbf{v}_1,\mathbf{r}_1+(1-x)\,\boldsymbol{\sigma}_{ij},\mathbf{v}_2;t)\\ &= \nabla_{\mathbf{r}_1}\cdot\boldsymbol{\sigma}_{ij}\int_0^1 dx\ f_{ij}(\mathbf{r}_1-x\boldsymbol{\sigma}_{ij},\mathbf{v}_1,\mathbf{r}_1+(1-x)\,\boldsymbol{\sigma}_{ij},\mathbf{v}_2;t).\end{aligned} \tag{B17}$$

Using the identity (B17), Eq. (B16) can be finally written as

$$\begin{aligned}\sum_{i=1}^{s}\int d\mathbf{v}_1\psi_i C_i &= \frac{1}{2}\sum_{i,j=1}^{s}\sigma_{ij}^{d-1}\int d\mathbf{v}_1\int d\mathbf{v}_2\int d\widehat{\boldsymbol{\sigma}}\,\Theta(\widehat{\boldsymbol{\sigma}}\cdot\mathbf{g}_{12})(\widehat{\boldsymbol{\sigma}}\cdot\mathbf{g}_{12})\\ &\times\ \left\{\left[\psi_i\left(\mathbf{v}_1'\right)+\psi_j\left(\mathbf{v}_2'\right)-\psi_i\left(\mathbf{v}_1\right)-\psi_j\left(\mathbf{v}_2\right)\right]f_{ij}(\mathbf{r}_1,\mathbf{v}_1,\mathbf{r}_1+\boldsymbol{\sigma}_{ij},\mathbf{v}_2;t)\right.\\ &+\ \left.\nabla_{\mathbf{r}_1}\cdot\boldsymbol{\sigma}_{ij}\left[\psi_i\left(\mathbf{v}_1'\right)-\psi_i\left(\mathbf{v}_1\right)\right]\int_0^1 dx\ f_{ij}(\mathbf{r}_1-x\boldsymbol{\sigma}_{ij},\mathbf{v}_1,\mathbf{r}_1+(1-x)\,\boldsymbol{\sigma}_{ij},\mathbf{v}_2;t)\right\}.\end{aligned} \tag{B18}$$

Now, apply this result to the case $\psi_i=m_i\mathbf{v}_1$. Since the total momentum is conserved in all pair collisions, $\psi_i\left(\mathbf{v}_1'\right)+\psi_j\left(\mathbf{v}_2'\right)-\psi_i\left(\mathbf{v}_1\right)-\psi_j\left(\mathbf{v}_2\right)=0$ for this case and (B18) gives (B6) with

$$\begin{aligned}t_{\gamma\beta}^{c} &\equiv -\frac{1}{2}\sum_{i,j=1}^{s}\sigma_{ij}^{d}\int d\mathbf{v}_1\int d\mathbf{v}_2\int d\widehat{\boldsymbol{\sigma}}\,\Theta(\widehat{\boldsymbol{\sigma}}\cdot\mathbf{g}_{12})(\widehat{\boldsymbol{\sigma}}\cdot\mathbf{g}_{12})\widehat{\sigma}_\gamma\\ &\quad\times\left(m_i v_{1\beta}'-m_i v_{1\beta}\right)\int_0^1 dx\,f_{ij}(\mathbf{r}_1-x\boldsymbol{\sigma}_{ij},\mathbf{v}_1,\mathbf{r}_1+(1-x)\,\boldsymbol{\sigma}_{ij},\mathbf{v}_2;t)\\ &= \frac{1}{2}\sum_{i,j=1}^{s}m_i\mu_{ji}\left(1+\alpha_{ij}\right)\sigma_{ij}^{d}\int d\mathbf{v}_1\int d\mathbf{v}_2\int d\widehat{\boldsymbol{\sigma}}\,\Theta(\widehat{\boldsymbol{\sigma}}\cdot\mathbf{g}_{12})(\widehat{\boldsymbol{\sigma}}\cdot\mathbf{g}_{12})^2\widehat{\sigma}_\gamma\widehat{\sigma}_\beta\\ &\quad\times\int_0^1 dx\ f_{ij}(\mathbf{r}_1-x\boldsymbol{\sigma}_{ij},\mathbf{v}_1,\mathbf{r}_1+(1-x)\,\boldsymbol{\sigma}_{ij},\mathbf{v}_2;t).\end{aligned} \tag{B19}$$

The analysis leading to (B6) follows from (B16) in a similar way with $\psi_i=m_i v_1^2/2$. However, since energy is not conserved in pair collisions the first term on the right side does not vanish. Instead, it represents the collisions energy loss w

$$\begin{aligned}w &= -\sum_{i,j=1}^{s}\frac{1}{4}\sigma_{ij}^{d-1}\int d\mathbf{v}_1\int d\mathbf{v}_2\int d\widehat{\boldsymbol{\sigma}}\,\Theta(\widehat{\boldsymbol{\sigma}}\cdot\mathbf{g}_{12})(\widehat{\boldsymbol{\sigma}}\cdot\mathbf{g}_{12})\\ &\quad\left(m_i v_1'^2+m_j v_2'^2-m_i v_1^2-m_j v_2^2\right)f_{ij}(\mathbf{r}_1,\mathbf{v}_1,\mathbf{r}_1+\boldsymbol{\sigma}_{ij},\mathbf{v}_2;t)\\ &= \frac{1}{4}\sum_{i,j=1}^{s}\left(1-\alpha_{ij}^2\right)m_i\mu_{ji}\sigma_{ij}^{d-1}\int d\mathbf{v}_1\int d\mathbf{v}_2\int d\widehat{\boldsymbol{\sigma}}\,\Theta(\widehat{\boldsymbol{\sigma}}\cdot\mathbf{g}_{12})(\widehat{\boldsymbol{\sigma}}\cdot\mathbf{g}_{12})^3\\ &\quad\times f_{ij}(\mathbf{r}_1,\mathbf{v}_1,\mathbf{r}_1+\boldsymbol{\sigma}_{ij},\mathbf{v}_2;t).\end{aligned} \tag{B20}$$

The second term on the right side of (B18) gives the collisional transfer contribution to the flux

$$\begin{aligned}\nabla\cdot\mathbf{s}^c &= -\nabla_{\mathbf{r}_1}\cdot\sum_{i,j=1}^{s}\frac{1}{4}m_i\sigma_{ij}^d\int d\mathbf{v}_1\int d\mathbf{v}_2\int d\widehat{\boldsymbol{\sigma}}\,\Theta(\widehat{\boldsymbol{\sigma}}\cdot\mathbf{g}_{12})(\widehat{\boldsymbol{\sigma}}\cdot\mathbf{g}_{12})\widehat{\boldsymbol{\sigma}}\\ &\quad\left(v_1'^2-v_1^2\right)\int_0^1 dx\; f_{ij}(\mathbf{r}_1-x\boldsymbol{\sigma}_{ij},\mathbf{v}_1,\mathbf{r}_1+(1-x)\,\boldsymbol{\sigma}_{ij},\mathbf{v}_2;t)\\ &= \nabla_{\mathbf{r}_1}\cdot\sum_{i,j=1}^{s}\frac{1}{4}\left(1+\alpha_{ij}\right)m_i\mu_{ji}\sigma_{ij}^d\int d\mathbf{v}_1\int d\mathbf{v}_2\int d\widehat{\boldsymbol{\sigma}}\;\Theta(\widehat{\boldsymbol{\sigma}}\cdot\mathbf{g}_{12})(\widehat{\boldsymbol{\sigma}}\cdot\mathbf{g}_{12})^2\widehat{\boldsymbol{\sigma}}\\ &\quad\times\left[\mu_{ji}\left(1-\alpha_{ij}\right)(\widehat{\boldsymbol{\sigma}}\cdot\mathbf{g}_{12})+2\widehat{\boldsymbol{\sigma}}\cdot(\mu_{ij}\mathbf{v}_1+\mu_{ji}\mathbf{v}_2)\right]\\ &\quad\times\int_0^1 dx\; f_{ij}(\mathbf{r}_1-x\boldsymbol{\sigma}_{ij},\mathbf{v}_1,\mathbf{r}_1+(1-x)\,\boldsymbol{\sigma}_{ij},\mathbf{v}_2;t).\end{aligned}\tag{B21}$$

This confirms (B5) and identifies $\mathbf{s}^c$, which has the equivalent form (obtained by taking half the sum of forms with i and j interchanged)

$$\begin{aligned}\mathbf{s}^c &= \sum_{i,j=1}^{s}\frac{1}{8}\left(1+\alpha_{ij}\right)m_i\mu_{ji}\sigma_{ij}^d\int d\mathbf{v}_1\int d\mathbf{v}_2\int d\widehat{\boldsymbol{\sigma}}\,\Theta(\widehat{\boldsymbol{\sigma}}\cdot\mathbf{g}_{12})(\widehat{\boldsymbol{\sigma}}\cdot\mathbf{g}_{12})^2\\ &\quad\times\widehat{\boldsymbol{\sigma}}\left[\left(1-\alpha_{ij}\right)\left(\mu_{ji}-\mu_{ij}\right)(\widehat{\boldsymbol{\sigma}}\cdot\mathbf{g}_{12})+4\widehat{\boldsymbol{\sigma}}\cdot(\mu_{ij}\mathbf{v}_1+\mu_{ji}\mathbf{v}_2)\right]\\ &\quad\times\int_0^1 dx\; f_{ij}(\mathbf{r}_1-x\boldsymbol{\sigma}_{ij},\mathbf{v}_1,\mathbf{r}_1+(1-x)\,\boldsymbol{\sigma}_{ij},\mathbf{v}_2;t).\end{aligned}\tag{B22}$$

APPENDIX C: CHAPMAN–ENSKOG SOLUTION

As described in the text a normal solution to the kinetic equation is a non-local functional of the hydrodynamic fields $f_i(\mathbf{v}_1\mid\{y_\beta(t)\})$. This is equivalent to a function of the fields at a point and all their derivatives at that point

$$f_i(\mathbf{r}_1,\mathbf{v}_1\mid\{y_\beta(t)\})=f_i(\mathbf{v}_1;\{y_\beta(\mathbf{r}_1,t)\};\{\partial_{\mathbf{r}_1}y_\beta(\mathbf{r}_1,t);..\}).\tag{C1}$$

If the gradients are small, this function can be expanded in the appropriate dimensionless small parameter

$$f_i(\mathbf{v}_1\mid\{y_\beta(t)\})=f_i^{(0)}(\mathbf{v}_1;\{y_\beta(\mathbf{r}_1,t)\})+f_i^{(1)}(\mathbf{v}_1;\{y_\beta(\mathbf{r}_1,t)\};\{\partial_{\mathbf{r}_1}y_\beta(\mathbf{r}_1,t)\})+\cdots\tag{C2}$$

where $f_i^{(0)}$ is a function of the fields alone, $f_i^{(1)}$ is a function of the fields and linear in their gradients, and so on. Thus the kinetic equation can be solved perturbatively by requiring that contributions from common order in this gradient expansion vanish.

To perform this ordering it is necessary to expand the collision operators of (3.9)

$$\begin{aligned}J_{ij}[\mathbf{r}_1,\mathbf{v}_1\mid f(t)] &\equiv \sigma_{ij}^{d-1}\int d\mathbf{v}_2\int d\widehat{\boldsymbol{\sigma}}\Theta(\widehat{\boldsymbol{\sigma}}\cdot\mathbf{g}_{12})(\widehat{\boldsymbol{\sigma}}\cdot\mathbf{g}_{12})\\ &\quad\times\left[\alpha_{ij}^{-2}\chi_{ij}(\mathbf{r}_1,\mathbf{r}_1-\boldsymbol{\sigma}_{ij}\mid\{n_i\})\,f_i(\mathbf{r}_1,\mathbf{v}_1'';t)f_j(\mathbf{r}_1-\boldsymbol{\sigma}_{ij},\mathbf{v}_2'';t)\right.\\ &\quad\left.-\chi_{ij}(\mathbf{r}_1,\mathbf{r}_1+\boldsymbol{\sigma}_{ij}\mid\{n_i\})\,f_i(\mathbf{r}_1,\mathbf{v}_1;t)f_j(\mathbf{r}_1+\boldsymbol{\sigma}_{ij},\mathbf{v}_2;t)\right].\end{aligned}\tag{C3}$$

For the purposes here it is sufficient to go up through first order. The distribution functions evaluated at $\mathbf{r}_1\pm\boldsymbol{\sigma}_{ij}$ become

$$\begin{aligned}&f_i(\mathbf{v}_1;\{y_\beta(\mathbf{r}_1\pm\boldsymbol{\sigma}_{ij},t)\};\{\partial_{\mathbf{r}_1}y_\beta(\mathbf{r}_1\pm\boldsymbol{\sigma}_{ij},t);\cdots\})\to(1\pm\boldsymbol{\sigma}_{ij}\cdot\nabla_{\mathbf{r}_1})\,f_i^{(0)}(\mathbf{v}_1;\{y_\beta(\mathbf{r}_1,t)\})\\ &+f_i^{(1)}(\mathbf{v}_1;\{y_\beta(\mathbf{r}_1,t)\};\{\partial_{\mathbf{r}_1}y_\beta(\mathbf{r}_1,t)\})\\ =\;& f_i^{(0)}(\mathbf{v}_1;\{y_\beta(\mathbf{r}_1,t)\})\pm\left(\partial_{y_\beta}f_i^{(0)}(\mathbf{v}_1;\{y_\beta(\mathbf{r}_1,t)\})\right)\boldsymbol{\sigma}_{ij}\cdot\nabla_{\mathbf{r}_1}y_\beta(\mathbf{r}_1,t)\\ &+f_i^{(1)}(\mathbf{v}_1;\{y_\beta(\mathbf{r}_1,t)\};\{\partial_{\mathbf{r}_1}y_\beta(\mathbf{r}_1,t)\}).\end{aligned}\tag{C4}$$

The functional expansion of $\chi_{ij}(\mathbf{r}_1,\mathbf{r}_1\pm\sigma_{ij}\mid\{n_i\})$ to this order is obtained by a functional expansion of all species densities about their values at $\mathbf{r}_1$

$$\chi_{ij}(\mathbf{r}_1,\mathbf{r}_1\pm\sigma_{ij}\mid\{n_i(t)\})=\chi_{ij}^{(0)}(\sigma_{ij}\mid\{n_k(\mathbf{r}_1,t)\})\tag{C5}$$

$$+\sum_{\ell=1}^{s}\int d\mathbf{r}'\frac{\delta\chi_{ij}\left(\mathbf{r}_1,\mathbf{r}_1\pm\boldsymbol{\sigma}_{ij}\mid\{n_i\}\right)}{\delta n_\ell(\mathbf{r}',t)}\mid_{\delta n=0}\left(n_\ell(\mathbf{r}')-n_\ell(\mathbf{r}_1)\right)+..$$

$$\rightarrow\chi_{ij}^{(0)}\left(\sigma_{ij};\{n_k\left(\mathbf{r}_1,t\right)\}\right)+\sum_{\ell=1}^{s}\left(\nabla_{\mathbf{r}_1}n_\ell(\mathbf{r}_1;t)\right)\cdot\int d\mathbf{r}'\left(\mathbf{r}'-\mathbf{r}_1\right)\frac{\delta\chi_{ij}\left(\mathbf{r}_1,\mathbf{r}_1\pm\boldsymbol{\sigma}_{ij}\mid\{n_i\}\right)}{\delta n_\ell(\mathbf{r}',t)}\mid_{\delta n=0}. \tag{C6}$$

The arrow denotes the leading terms of a Taylor series for $\left(n_\ell(\mathbf{r}')-n_\ell(\mathbf{r}_1)\right)$. The integral can be simplified by noting at $\delta n=0$ the functional integral has translational invariance

$$\frac{\delta\chi_{ij}\left(\mathbf{r}_1,\mathbf{r}_1\pm\boldsymbol{\sigma}_{ij}\mid\{n_i\}\right)}{\delta n_\ell(\mathbf{r}',t)}\mid_{\delta n=0}=F_{ij\ell}\left(\mathbf{r}_1-\mathbf{r}',\mathbf{r}_1\pm\boldsymbol{\sigma}_{ij}-\mathbf{r}'\right) \tag{C7}$$

so

$$\int d\mathbf{r}'\left(\mathbf{r}'-\mathbf{r}_1\right)\frac{\delta\chi_{ij}\left(\mathbf{r}_1,\mathbf{r}_1\pm\boldsymbol{\sigma}_{ij}\mid\{n_i\}\right)}{\delta n_\ell(\mathbf{r}',t)}\mid_{\delta n=0}=\int d\mathbf{r}'\left(\mathbf{r}'\pm\frac{1}{2}\boldsymbol{\sigma}_{ij}\right)\frac{\delta\chi_{ij}\left(\mp\frac{1}{2}\boldsymbol{\sigma}_{ij},\pm\frac{1}{2}\boldsymbol{\sigma}_{ij}\mid\{n_i\}\right)}{\delta n_\ell(\mathbf{r}',t)}\mid_{\delta n=0} \tag{C8}$$

$$=\pm\frac{1}{2}\boldsymbol{\sigma}_{ij}\frac{\partial\ln\chi_{ij}^{(0)}\left(\sigma_{ij};\{n_\ell\left(\mathbf{r}_1\right)\}\right)}{\partial n_\ell\left(\mathbf{r}_1\right)}+\int d\mathbf{r}'\mathbf{r}'\frac{\delta\chi_{ij}\left(\mp\frac{1}{2}\boldsymbol{\sigma}_{ij},\pm\frac{1}{2}\boldsymbol{\sigma}_{ij}\mid\{n_i\}\right)}{\delta n_\ell(\mathbf{r}',t)}\mid_{\delta n=0} \tag{C9}$$

The expansion for $\chi_{ij}\left(\mathbf{r}_1,\mathbf{r}_1\pm\boldsymbol{\sigma}_{ij}\mid\{n_i\left(t\right)\}\right)$ becomes

$$\begin{aligned}\chi_{ij}\left(\mathbf{r}_1,\mathbf{r}_1\pm\boldsymbol{\sigma}_{ij}\mid\{n_i\left(t\right)\}\right) &= \chi_{ij}^{(0)}\left(\sigma_{ij};\{n_k\left(\mathbf{r}_1,t\right)\}\right)\left[1\pm\frac{1}{2}\boldsymbol{\sigma}_{ij}\cdot\sum_{\ell=1}^{s}\nabla_{\mathbf{r}_1}\ln n_\ell(\mathbf{r}_1;t)\right.\\ &\times\left.\left(n_\ell\left(\mathbf{r}_1\right)\frac{\partial\ln\chi_{ij}^{(0)}\left(\sigma_{ij};\{n_\ell\left(\mathbf{r}_1\right)\}\right)}{\partial n_\ell\left(\mathbf{r}_1\right)}+I_{ij\ell}(\sigma_{ij};\{n_k\left(\mathbf{r}_1,t\right)\})\right)\right].\end{aligned} \tag{C10}$$

The last line defines $I_{ij\ell}(\sigma_{ij};\{n_k\left(\mathbf{r}_1,t\right)\})$ as

$$I_{ij\ell}(\sigma_{ij};\{n_k\})\equiv\frac{2n_\ell(\mathbf{r}_1,t)}{\chi_{ij}^{(0)}\left(\sigma_{ij};\{n_k\}\right)\sigma_{ij}}\int d\mathbf{r}'\left(\widehat{\boldsymbol{\sigma}}_{ij}\cdot\mathbf{r}'\right)\frac{\delta\chi_{ij}\left(-\frac{1}{2}\boldsymbol{\sigma}_{ij},+\frac{1}{2}\boldsymbol{\sigma}_{ij}\mid\{n_i\}\right)}{\delta n_\ell(\mathbf{r}',t)}\mid_{\delta n=0}. \tag{C11}$$

These results give the expansion of $J_{ij}\left[\mathbf{r}_1,\mathbf{v}_1\mid f_i\right]$ to first order in the gradients

$$\sum_{j=1}^{s}J_{ij}\left[\mathbf{r}_1,\mathbf{v}_1\mid f\right]\rightarrow\sum_{j=1}^{s}J_{ij}^{(0)}\left[\mathbf{v}_1\mid f_i^{(0)},f_j^{(0)}\right]-\left(Lf^{(1)}\right)_i \tag{C12}$$

$$-\sum_{j=1}^{s}\mathcal{K}_{ij,\gamma}[\mathbf{v}_1\mid\partial_{y_\beta}f_j^{(0)}(t)]\partial_\gamma y_\beta\left(\mathbf{r}_1,t\right) \tag{C13}$$

$$-\sum_{j,\ell=1}^{s}\left(n_\ell\frac{\partial\ln\chi_{ij}^{(0)}\left(\sigma_{ij};\{n_k\}\right)}{\partial n_\ell}+I_{ij\ell}(\sigma_{ij};\{n_k\})\right)\mathcal{K}_{ij,\gamma}[\mathbf{v}_1\mid f_j^{(0)}(t)]\partial_\gamma\ln n_\ell(\mathbf{r}_1;t) \tag{C14}$$

with the definitions $\partial_\gamma X\equiv\partial X/\partial r_\gamma$,

$$\begin{aligned}J_{ij}^{(0)}\left[\mathbf{v}_1\mid g_i,f_j\right] &\equiv \chi_{ij}^{(0)}\left(\sigma_{ij};\{n_i\left(\mathbf{r}_1,t\right)\}\right)\sigma_{ij}^{d-1}\int d\mathbf{v}_2\int d\widehat{\boldsymbol{\sigma}}\Theta(\widehat{\boldsymbol{\sigma}}\cdot\mathbf{g}_{12})(\widehat{\boldsymbol{\sigma}}\cdot\mathbf{g}_{12})\\ &\times\left[\alpha_{ij}^{-2}g_i(\mathbf{V}_1'')f_j(\mathbf{V}_2'')-g_i(\mathbf{V}_1)f_j(\mathbf{V}_2)\right],\end{aligned} \tag{C15}$$

$$\mathcal{K}_{ij,\gamma}[X_j] = \sigma_{ij}^d \chi_{ij}^{(0)} \int d\mathbf{v}_2 \int d\widehat{\boldsymbol{\sigma}} \Theta(\widehat{\boldsymbol{\sigma}}\cdot\mathbf{g}_{12})(\widehat{\boldsymbol{\sigma}}\cdot\mathbf{g}_{12})\widehat{\sigma}_\gamma \times \left[\alpha_{ij}^{-2} f_i^{(0)}(\mathbf{r}_1,\mathbf{V}_1'';t)X_j(\mathbf{r}_1,\mathbf{V}_2'') + f_i^{(0)}(\mathbf{r}_1,\mathbf{V}_1;t)X_j(\mathbf{r}_1,\mathbf{V}_2)\right]. \tag{C16}$$

Finally, L is a linear operator defined over s dimensional vectors $\{X_i\}$ whose components are labelled by the species

$$(LX)_i = -\sum_{j=1}^{s}\left(J_{ij}^{(0)}\left[\mathbf{v}_1 \mid X_i, f_j^{(0)}\right] + J_{ij}^{(0)}\left[\mathbf{v}_1 \mid f_i^{(0)}, X_j\right]\right). \tag{C17}$$

It remains to choose the magnitude of the external forces $\mathbf{F}_i$ to consistently order this expansion. To be specific, and for comparison with Ref. [49] it is assumed here to be of first order in the gradients.

1. Zeroth Order

At lowest order all gradients of the hydrodynamic fields are neglected, and (3.8) becomes

$$\partial_t^{(0)} f_i^{(0)}(\mathbf{v}_1;\{y_\beta(\mathbf{r}_1,t)\}) = \sum_{j=1}^{s} J_{ij}^{(0)}\left[\mathbf{v}_1 \mid f_i^{(0)}(\{y_\beta(\mathbf{r}_1,t)\}), f_j^{(0)}(\{y_\beta(\mathbf{r}_1,t)\})\right]. \tag{C18}$$

The notation $\partial_t^{(0)}$ for the time derivative means that the balance equations are to be used to zeroth order in the gradients

$$\begin{aligned}\partial_t^{(0)} f_i^{(0)}(V_1;\{y_\beta(\mathbf{r}_1,t)\} &= \left(\partial_{y_\beta} f_i^{(0)}(V_1;\{y_\beta(\mathbf{r}_1,t)\})\right)\partial_t^{(0)} y_\beta(\mathbf{r}_1,t)\\ &= -\zeta^{(0)}(\{y_\beta(\mathbf{r}_1,t)\})T\partial_T f_i^{(0)}(V_1;\{y_\beta(\mathbf{r}_1,t)\}).\end{aligned} \tag{C19}$$

Use of (C19) in (C18) gives the zeroth order equation (6.1) of the text.

2. First Order

The kinetic equation for contributions of first order in the gradients is

$$\begin{aligned}\partial_t^{(0)} f_i^{(1)} + \left(Lf^{(1)}\right)_i &= -\left(\partial_t^{(1)} + \mathbf{v}_1\cdot\nabla_{\mathbf{r}_1} + m_i^{-1}\mathbf{F}_i\cdot\nabla_{\mathbf{v}_1}\right) f_i^{(0)} - \sum_{j=1}^{s}\mathcal{K}_{ij,\gamma}[\mathbf{v}_1 \mid \partial_{y_\beta} f_j^{(0)}]\partial_\gamma y_\beta\\ &\quad -\frac{1}{2}\sum_{j,\ell=1}^{s}\mathcal{K}_{ij,\gamma}\left[\mathbf{v}_1\right|\left(n_\ell\frac{\partial\ln\chi_{ij}^{(0)}}{\partial n_\ell} + I_{ij\ell}\right) f_j^{(0)}\left]\partial_\gamma\ln n_\ell,\right.\end{aligned} \tag{C20}$$

where $\nabla_{\mathbf{r}} \equiv \partial/\partial\mathbf{r}$ and $\nabla_{\mathbf{V}} \equiv \partial/\partial\mathbf{V}$. The first term on the right side of (C20) can be expressed explicitly in terms of the gradients, where now $\partial_t^{(1)}$ means that the balance equations are to be used with only terms of first order in the gradients

$$\begin{aligned}\left(\partial_t^{(1)} + \mathbf{v}_1\cdot\nabla_{\mathbf{r}_1} + m_i^{-1}\mathbf{F}_i\cdot\nabla_{\mathbf{V}_1}\right) f_i^{(0)} &= m_i^{-1}\mathbf{F}_i\cdot\nabla_{\mathbf{V}_1} f_i^{(0)} + \left(\partial_{y_\beta} f_i^{(0)}\right)\left(D_t^{(1)} + \mathbf{V}_1\cdot\nabla_{\mathbf{r}_1}\right) y_\beta\\ &= \left(m_i^{-1}\mathbf{F}_i - \rho^{-1}\sum_{j=1}^{s} n_j\mathbf{F}_j\right)\cdot\nabla_{\mathbf{V}_1} f_i^{(0)}\\ &\quad -\left(\nabla_{\mathbf{V}_1} f_i^{(0)}\right)\cdot\left(-\rho^{-1}\nabla_{\mathbf{r}_1} p + \mathbf{V}_1\cdot\nabla_{\mathbf{r}_1}\mathbf{U}\right)\\ &\quad -\left(\partial_T f_i^{(0)}\right)\left(\left(T\zeta_U + \frac{2}{nd}p\right)\nabla\cdot\mathbf{U} - \mathbf{V}_1\cdot\nabla_{\mathbf{r}_1} T\right)\\ &\quad +\sum_{j=1}^{s}\left(\partial_{n_j} f_i^{(0)}\right)\left(-n_j\nabla\cdot\mathbf{U} + \mathbf{V}_1\cdot\nabla_{\mathbf{r}_1} n_j\right).\end{aligned} \tag{C21}$$

In (C21), $D_t^{(1)} \equiv \partial_t^{(1)} + \mathbf{U}\cdot\nabla$ and use has been made of the fact that $f_i^{(0)}$ depends on $\mathbf{U}$ only through the combination $\mathbf{V}_1 = \mathbf{v}_1 - \mathbf{U}$, so that

$$\nabla_{\mathbf{U}} f_i^{(0)} = -\nabla_{\mathbf{V}_1} f_i^{(0)}. \tag{C22}$$

The pressure gradient can be expressed in terms of the temperature and density gradients

$$\nabla_{\mathbf{r}_1} p = \frac{p}{T}\nabla_{\mathbf{r}_1} T + \sum_{j=1}^{s} \left(\partial_{n_j} p\right) \nabla_{\mathbf{r}_1} n_j, \tag{C23}$$

to give

$$\begin{aligned}
\left(\partial_t^{(1)} + \mathbf{v}_1\cdot\nabla_{\mathbf{r}_1} + m_i^{-1}\mathbf{F}_i\cdot\nabla_{\mathbf{v}_1}\right) f_i^{(0)} \;=\; & m_i^{-1}\mathbf{F}_i\cdot\nabla_{\mathbf{V}_1} f_i^{(0)} - \rho^{-1}\sum_{j=1}^{s} n_j \nabla_{\mathbf{V}_1} f_i^{(0)}\cdot\mathbf{F}_j \\
& + \left(\frac{p}{\rho T}\nabla_{\mathbf{v}_1} f_i^{(0)} + \mathbf{V}_1\partial_T f_i^{(0)}\right)\cdot\nabla_{\mathbf{r}_1} T \\
& + \sum_{j=1}^{s}\left(\rho^{-1}\partial_{n_j} p\nabla_{\mathbf{v}_1} f_i^{(0)} + \mathbf{V}_1\partial_{n_j} f_i^{(0)}\right)\cdot\nabla_{\mathbf{r}_1} n_j \\
& - \left(\left(\zeta_U + \frac{2}{nTd}p\right) T\partial_T f_i^{(0)} + \sum_{j=1}^{s} n_j\partial_{n_j} f_i^{(0)}\right)\nabla\cdot\mathbf{U} \\
& - V_{1\gamma}(\partial_{V_{1\eta}} f_i^{(0)})\partial_\gamma U_\eta.
\end{aligned} \tag{C24}$$

Equations (C20) for the first order distributions, $f_i^{(1)}$, now become

$$\begin{aligned}
\partial_t^{(0)} f_i^{(1)} + \left(Lf^{(1)}\right)_i \;=\; & \mathbf{A}_i\left(\mathbf{V}_1;\{n_i\}\right)\cdot\nabla\ln T + \sum_{j=1}^{s}\mathbf{B}_i^j\left(\mathbf{V}_1;\{n_i\}\right)\cdot\nabla\ln n_j \\
& + C_{i,\gamma\eta}\left(\mathbf{V}_1;\{n_i\}\right)\frac{1}{2}\left(\partial_\gamma U_\eta + \partial_\eta U_\gamma - \frac{2}{d}\delta_{\gamma\eta}\nabla\cdot\mathbf{U}\right) \\
& + D_i\left(\mathbf{V}_1;\{n_i\}\right)\nabla\cdot\mathbf{U} + \sum_{j=1}^{s}\mathbf{E}_i^j\left(\mathbf{V}_1;\{n_i\}\right)\cdot\mathbf{F}_j.
\end{aligned} \tag{C25}$$

The functions of velocity on the right side of (C25) are identified as

$$A_{i,\gamma}\left(\mathbf{V}\right) = \frac{1}{2}V_\gamma\nabla_{\mathbf{V}}\cdot\left(\mathbf{V}f_i^{(0)}\right) - \frac{p}{\rho}\partial_{V_\gamma} f_i^{(0)} + \frac{1}{2}\sum_{j=1}^{k}\mathcal{K}_{ij,\gamma}\left[\nabla_{\mathbf{V}}\cdot\left(\mathbf{V}f_j^{(0)}\right)\right], \tag{C26}$$

$$\begin{aligned}
B_{i,\gamma}^j\left(\mathbf{V}\right) \;=\; & -V_\gamma n_j\partial_{n_j} f_i^{(0)} - \rho^{-1}(\partial_{V_\gamma} f_i^{(0)})n_j(\partial_{n_j} p) \\
& - \sum_{\ell=1}^{s}\mathcal{K}_{i\ell,\gamma}\left[\left(n_j\partial_{n_j} + \frac{1}{2}\left(n_\ell\frac{\partial\ln\chi_{i\ell}^{(0)}}{\partial n_j} + I_{i\ell j}\right)\right) f_\ell^{(0)}\right],
\end{aligned} \tag{C27}$$

$$\begin{aligned}
C_{i,\gamma\beta}\left(\mathbf{V}\right) \;=\; & \frac{1}{2}\left(V_\gamma\partial_{V_\beta} f_i^{(0)} + V_\beta\partial_{V_\gamma} f_i^{(0)} - \frac{2}{d}\delta_{\beta\gamma}\mathbf{V}\cdot\nabla_{\mathbf{V}} f_i^{(0)}\right) \\
& + \frac{1}{2}\sum_{j=1}^{s}\left(\mathcal{K}_{ij,\gamma}[\partial_{V_\beta} f_j^{(0)}] + \mathcal{K}_{ij,\beta}[\partial_{V_\gamma} f_j^{(0)}] - \frac{2}{d}\delta_{\beta\gamma}\mathcal{K}_{ij,\lambda}[\partial_{V_\lambda} f_j^{(0)}]\right),
\end{aligned} \tag{C28}$$

$$\begin{aligned}
D_i(\mathbf{V}) \;=\; & \frac{1}{d}\mathbf{V}\cdot\nabla_{\mathbf{V}} f_i^{(0)} - \frac{1}{2}\left(\zeta_U + \frac{2}{nTd}p\right)\nabla_{\mathbf{V}}\cdot\left(\mathbf{V}f_i^{(0)}\right) \\
& + \sum_{j=1}^{s}\left(n_j\partial_{n_j} f_i^{(0)} + \frac{1}{d}\mathcal{K}_{ij,\gamma}\left[\partial_{V_\gamma} f_j^{(0)}\right]\right),
\end{aligned} \tag{C29}$$

$$\mathbf{E}_i^j(\mathbf{V}) = -\left(\nabla_{\mathbf{V}} f_i^{(0)}\right) \frac{1}{m_j}\left(\delta_{ij} - \frac{n_j m_j}{\rho}\right). \tag{C30}$$

Upon deriving (C26)–(C30), use has been made of the relations

$$T\partial_T f_i^{(0)} = -\frac{1}{2}\nabla_{\mathbf{V}} \cdot \left(\mathbf{V} f_i^{(0)}\right), \qquad \partial_{U_\beta} f_i^{(0)} = -\partial_{V_\beta} f_i^{(0)}. \tag{C31}$$

The tensor derivative of the flow field $\partial_\gamma U_\eta$ has been expressed in terms of its independent trace and traceless parts, using the spherical symmetry of $f_i^{(0)}$, e.g.

$$\begin{aligned}\left(V_\gamma \partial_{V_\eta} f_i^{(0)}\right)\partial_\gamma U_\eta &= \widehat{V}_\gamma \widehat{V}_\eta (V\partial_V) f_i^{(0)} \left(\partial_\gamma U_\eta\right) = \widehat{V}_\gamma \widehat{V}_\beta (V\partial_V f_i^{(0)}) \frac{1}{2}\left(\partial_\gamma U_\eta + \partial_\eta U_\gamma\right) \\ &= \widehat{V}_\gamma \widehat{V}_\eta (V\partial_V f_i^{(0)}) \frac{1}{2}\left(\partial_\gamma U_\eta + \partial_\eta U_\gamma - \frac{2}{d}\delta_{\gamma\eta}\nabla\cdot\mathbf{U}\right) \\ &\quad + \frac{1}{d}(V\partial_V f_i^{(0)})\nabla\cdot\mathbf{U},\end{aligned} \tag{C32}$$

and a similar analysis of the contribution from $\sum_{j=1}^s \mathcal{K}_{ij,\gamma}[\mathbf{v} \mid \partial_{V_\beta} f_j^{(0)}]$. Equation (C25) is an inhomogeneous, linear integral equation, where the inhomogeneity (the right side) is a linear combination of the the external force and the gradients of the hydrodynamic fields. The coefficients of these fields are specified functions of the velocity $\mathbf{V}$. Since by definition $f_i^{(1)}$ is proportional to the external force and the gradients of the hydrodynamic fields, it must have the form

$$\begin{aligned} f_i^{(1)} \;\to\; & \boldsymbol{\mathcal{A}}_i(\mathbf{V})\cdot\nabla\ln T + \sum_{j=1}^s \boldsymbol{\mathcal{B}}_i^j(\mathbf{V})\cdot\nabla\ln n_j \\ & + \mathcal{C}_{i,\gamma\eta}(\mathbf{V})\frac{1}{2}\left(\partial_\gamma U_\eta + \partial_\eta U_\gamma - \frac{2}{d}\delta_{\gamma\eta}\nabla\cdot\mathbf{U}\right) \\ & + \mathcal{D}_i(\mathbf{V})\nabla\cdot\mathbf{U} + \sum_{j=1}^s \boldsymbol{\mathcal{E}}_i^j(\mathbf{V})\cdot\mathbf{F}_j. \end{aligned} \tag{C33}$$

The unknown functions of the peculiar velocity, $\boldsymbol{\mathcal{A}}_i, \boldsymbol{\mathcal{B}}_i^j, \mathcal{C}_{i,\gamma\eta}, \mathcal{D}_i$, and $\boldsymbol{\mathcal{E}}_i^j$ are determined by solving Eq. (C25). By dimensional analysis, $\boldsymbol{\mathcal{A}}_i(\mathbf{V}) = v_0^{-d}\ell^{1-d}\boldsymbol{\mathcal{A}}_i^*(\mathbf{V}^*)$, $\boldsymbol{\mathcal{B}}_i^j(\mathbf{V}) = v_0^{-d}\ell^{1-d}\boldsymbol{\mathcal{B}}_i^{j*}(\mathbf{V}^*)$, $\mathcal{C}_{i,\gamma\eta}(\mathbf{V}) = v_0^{-(d+1)}\ell^{1-d}\mathcal{C}_{i,\gamma\eta}^*(\mathbf{V}^*)$, $\mathcal{D}_i(\mathbf{V}) = v_0^{-(d+1)}\ell^{1-d}\mathcal{D}_i^*(\mathbf{V}^*)$, and $\boldsymbol{\mathcal{E}}_i^j(\mathbf{V}) = m^{-1}v_0^{-(d+2)}\ell^{1-d}\boldsymbol{\mathcal{E}}_i^{j*}(\mathbf{V}^*)$, where ℓ is an effective mean free path and $\boldsymbol{\mathcal{A}}_i^*(\mathbf{V}^*)$, $\boldsymbol{\mathcal{B}}_i^{j*}(\mathbf{V}^*)$, $\mathcal{C}_{i,\gamma\eta}^*(\mathbf{V}^*)$, $\mathcal{D}_i^*(\mathbf{V}^*)$, and $\boldsymbol{\mathcal{E}}_i^{j*}(\mathbf{V}^*)$ are dimensionless functions of the reduced velocity $\mathbf{V}^* = \mathbf{V}/v_0$, $v_0 = \sqrt{2T/m}$ being a thermal speed. Consequently,

$$\partial_t^{(0)}\boldsymbol{\mathcal{A}}_i(\mathbf{V}) = -\zeta^{(0)}T\partial_T\boldsymbol{\mathcal{A}}_i(\mathbf{V}) = \frac{1}{2}\zeta^{(0)}\nabla_{\mathbf{V}}\cdot\left(\mathbf{V}\boldsymbol{\mathcal{A}}_i(\mathbf{V})\right), \tag{C34}$$

$$\partial_t^{(0)}\boldsymbol{\mathcal{B}}_i^j(\mathbf{V}) = -\zeta^{(0)}T\partial_T\boldsymbol{\mathcal{B}}_i^j(\mathbf{V}) = \frac{1}{2}\zeta^{(0)}\nabla_{\mathbf{V}}\cdot\left(\mathbf{V}\boldsymbol{\mathcal{B}}_i^j(\mathbf{V})\right), \tag{C35}$$

$$\partial_t^{(0)}\mathcal{C}_{i,\gamma\eta}(\mathbf{V}) = -\zeta^{(0)}T\partial_T\mathcal{C}_{i,\gamma\eta}(\mathbf{V}) = \frac{1}{2}\zeta^{(0)}\mathcal{C}_{i,\gamma\eta} + \frac{1}{2}\zeta^{(0)}\nabla_{\mathbf{V}}\cdot\left(\mathbf{V}\mathcal{C}_{i,\gamma\eta}(\mathbf{V})\right), \tag{C36}$$

$$\partial_t^{(0)}\mathcal{D}_i(\mathbf{V}) = -\zeta^{(0)}T\partial_T\mathcal{D}_i(\mathbf{V}) = \frac{1}{2}\zeta^{(0)}\mathcal{D}_i + \frac{1}{2}\zeta^{(0)}\nabla_{\mathbf{V}}\cdot\left(\mathbf{V}\mathcal{D}_i(\mathbf{V})\right), \tag{C37}$$

$$\partial_t^{(0)}\boldsymbol{\mathcal{E}}_i^j(\mathbf{V}) = -\zeta^{(0)}T\partial_T\boldsymbol{\mathcal{E}}_i^j(\mathbf{V}) = \zeta^{(0)}\boldsymbol{\mathcal{E}}_i^j(\mathbf{V}) + \frac{1}{2}\zeta^{(0)}\nabla_{\mathbf{V}}\cdot\left(\mathbf{V}\boldsymbol{\mathcal{E}}_i^j(\mathbf{V})\right). \tag{C38}$$

In addition,

$$\partial_t^{(0)}\nabla\ln T = \nabla\partial_t^{(0)}\ln T = -\nabla\zeta^{(0)} = -\frac{1}{2}\zeta^{(0)}\nabla\ln T - \sum_{j=1}^s n_j\frac{\partial\zeta^{(0)}}{\partial n_j}\nabla\ln n_j. \tag{C39}$$

Since the external force and gradients of the fields are all independent, Eq. (C25) can be separated into independent equations for the coefficients of each. This leads to the set of linear, inhomogeneous integral equations

$$\left(\left(\mathcal{L}-\frac{1}{2}\zeta^{(0)}\right)\boldsymbol{\mathcal{A}}\right)_i=\mathbf{A}_i, \tag{C40}$$

$$\left(\mathcal{L}\boldsymbol{\mathcal{B}}^j\right)_i-n_j\frac{\partial\zeta^{(0)}}{\partial n_j}\boldsymbol{\mathcal{A}}_i=\mathbf{B}_i^j, \tag{C41}$$

$$\left(\left(\mathcal{L}+\frac{1}{2}\zeta^{(0)}\right)\mathcal{C}_{\gamma\eta}\right)_i=C_{i,\gamma\eta}, \tag{C42}$$

$$\left(\left(\mathcal{L}+\frac{1}{2}\zeta^{(0)}\right)\mathcal{D}\right)_i=D_i, \tag{C43}$$

$$\left(\left(\mathcal{L}+\zeta^{(0)}\right)\boldsymbol{\mathcal{E}}^j\right)_i=\mathbf{E}_i^j. \tag{C44}$$

The linear operator $\mathcal{L}$ is

$$\left(\mathcal{L}X\right)_i=\frac{1}{2}\zeta^{(0)}\nabla_{\mathbf{V}}\cdot\left(\mathbf{V}X_i\right)+\left(LX\right)_i. \tag{C45}$$

Notice that (C40) can be used in (C41) to give the equivalent representation for the latter

$$\left(\mathcal{L}\left(\boldsymbol{\mathcal{B}}^j-\left(2n_j\partial_{n_j}\ln\zeta^{(0)}\right)\boldsymbol{\mathcal{A}}\right)\right)_i=\mathbf{B}_i^j-\left(2n_j\partial_{n_j}\ln\zeta^{(0)}\right)\mathbf{A}_i. \tag{C46}$$

This completes the CE solution up through first order in the gradients and first order in the external force. Once (6.1) has been solved for $f_i^{(0)}$ the integral equations for $\boldsymbol{\mathcal{A}}_i$, $\boldsymbol{\mathcal{B}}_i^j$, $\mathcal{C}_{i,\gamma\eta}$, $\mathcal{D}_i$, and $\boldsymbol{\mathcal{E}}_i^j$ can be solved for $f_i^{(1)}$. Then, the cooling rate, heat flux, and pressure tensor can be calculated as linear functions of the gradients and the external force, and the explicit forms for the transport coefficients identified.

APPENDIX D: AN EIGENVALUE PROBLEM FOR $\mathcal{L}$

To simplify and interpret the linear integral equations defining the first order solutions $\left\{f_i^{(1)}\right\}$ it is useful to identify a special set of eigenvalues and eigenfunctions for the operator $\mathcal{L}$. Consider the equation for $f_i^{(0)}$

$$-\zeta^{(0)}T\partial_T\,f_i^{(0)}=\sum_{j=1}^{s}J_{ij}^{(0)}\left[\mathbf{r}_1,\mathbf{v}_1\mid f_i^{(0)},f_j^{(0)}\right]. \tag{D1}$$

Since the temperature occurs through the form (6.10), the temperature derivatives can be expressed as velocity derivatives

$$\frac{1}{2}\zeta^{(0)}\nabla_{\mathbf{V}}\cdot\left(\mathbf{V}f_i^{(0)}\right)=\sum_{j=1}^{s}J_{ij}^{(0)}\left[\mathbf{r}_1,\mathbf{v}_1\mid f_i^{(0)},f_j^{(0)}\right]. \tag{D2}$$

Noting that $\zeta^{(0)}\propto\sqrt{T}$, the derivative of this equation with respect to T gives directly

$$\left(\mathcal{L}T\partial_T f^{(0)}\right)_i=\frac{1}{2}\zeta^{(0)}T\partial_T f_i^{(0)}. \tag{D3}$$

where use has been made of (C34), i.e. $T\partial_T f_i^{(0)}=-\nabla_{\mathbf{V}}\cdot\left(\mathbf{V}f_i^{(0)}\right)/2$. An equivalent dimensionless form is

$$\left(\mathcal{L}\nabla_{\mathbf{V}}\cdot\left(\mathbf{V}f^{(0)}\right)\right)_i=\frac{1}{2}\zeta^{(0)}\nabla_{\mathbf{V}}\cdot\left(\mathbf{V}f_i^{(0)}\right). \tag{D4}$$

In a similar way, differentiation of (D2) with respect to each component of the flow velocity gives

$$\left(\mathcal{L}\partial_{U_\gamma} f^{(0)}\right)_i = -\frac{1}{2}\zeta^{(0)}\partial_{U_\gamma} f_i^{(0)}. \tag{D5}$$

Finally, differentiate (D2) with respect to each of the species densities and noting that the density dependence of all quantities occurs only through the $f^{(0)}$'s and the χ_{ij}'s, one gets

$$\begin{aligned}\left(\mathcal{L}\partial_{n_\ell} f^{(0)}\right)_i &= \left(\partial_{n_\ell}\sum_{j=1}^{s} J_{ij}^{(0)}\left[f_i^{(0)}, f_j^{(0)}\right]\right)|_{f^{(0)}} - \frac{1}{2}\left(\partial_{n_\ell}\zeta^{(0)}\right)\nabla_{\mathbf{V}}\cdot\left(\mathbf{V}f_i^{(0)}\right)\\ &= \frac{1}{2}\left(\partial_{n_\ell}\zeta^{(0)}\,|_{f^{(0)}} - \partial_{n_\ell}\zeta^{(0)}\right)\nabla_{\mathbf{V}}\cdot\left(\mathbf{V}f_i^{(0)}\right)\\ &= -\partial_{n_\ell}\ln\zeta^{(0)}\,|_{\chi_{ij}^{(0)}}\ \frac{1}{2}\zeta^{(0)}\nabla_{\mathbf{V}}\cdot\left(\mathbf{V}f_i^{(0)}\right).\end{aligned} \tag{D6}$$

This last form can be simplified by taking into account (D4) to get

$$\left(\mathcal{L}\left(\partial_{n_\ell} f^{(0)} + \partial_{n_\ell}\ln\zeta^{(0)}\,|_{\chi_{ij}^{(0)}}\ \nabla_{\mathbf{V}}\cdot\left(\mathbf{V}f^{(0)}\right)\right)\right)_i = 0. \tag{D7}$$

In summary, there are $s+d+1$ eigenvalues and eigenfunctions of the operator $\mathcal{L}$. Equations (D4) and (D5) identify these for the eigenvalue $\zeta^{(0)}/2$ and the d–fold degenerate value $-\zeta^{(0)}/2$, respectively. Equation (D7) identifies the eigenfunctions for the s– fold degenerate eigenvalue 0. In dimensionless form this eigenvalue problem is written as

$$\left(\mathcal{L}\Psi^{(m)}\right)_i = \lambda^{(m)}\Psi_i^{(m)}. \tag{D8}$$

The eigenvectors are

$$\begin{aligned}\Psi_i^{(\ell)} &= n_\ell\partial_{n_\ell} f_i^{(0)} - 2n_\ell\partial_{n_\ell}\ln\zeta^{(0)}\,|_{\chi_{ij}^{(0)}}\ \Psi_i^{(s+1)}, \qquad \ell = 1,..,s,\\ \Psi_i^{(s+1)} &= -\frac{1}{2}\nabla_{\mathbf{V}}\cdot\left(\mathbf{V}f_i^{(0)}\right), \qquad \Psi_i^{(\gamma)} = -v_0\partial_{V_\gamma} f_i^{(0)},\end{aligned} \tag{D9}$$

with the corresponding eigenvalues

$$\lambda^{(m)} \Leftrightarrow \left(0,..,0,\frac{1}{2}\zeta^{(0)},-\frac{1}{2}\zeta^{(0)},-\frac{1}{2}\zeta^{(0)},-\frac{1}{2}\zeta^{(0)}\right). \tag{D10}$$

These eigenvalues are the same as those of the linearized hydrodynamic equations in the long wavelength limit. This provides a direct link between hydrodynamics and the spectrum of the linearized Enskog operator. In addition to this physical interpretation, the eigenvalues and eigenfunctions allow a practical formulation of the integral equations, as follows.

1. Biorthogonal set

Define a scalar product by

$$(a,b) = \sum_{i=1}^{s}\int d\mathbf{V} a_i^{\dagger}(\mathbf{V})\, b_i(\mathbf{V}), \tag{D11}$$

where the dagger denotes complex conjugation. A biorthogonal basis set is then defined by the eigenfunctions $\Psi_i^{(m)}$ above, and

$$\psi_{\alpha i} = \left(\frac{\delta_{i1}}{n_i},..\frac{\delta_{is}}{n_i},\left(\frac{2m_i}{dm}V^{*2}-1\right),\frac{m_i}{\rho}\mathbf{V}^*\right), \tag{D12}$$

where $\mathbf{V}^* = \mathbf{V}/v_0$. The orthonormality condition

$$\sum_{i=1}^{s}\int d\mathbf{V}^*\psi_{\alpha i}(\mathbf{V}^*)\,\Psi_{\beta i}(\mathbf{V}^*) = \delta_{\alpha\beta} \tag{D13}$$

is easily verified. An associated projection operator is given by

$$(\mathcal{P}X)_i = \sum_\alpha \Psi_{\alpha i}(\mathbf{V}^*) \sum_j \int d\mathbf{V}^* \psi_{\alpha j}(\mathbf{V}^*) X_j(\mathbf{V}^*). \tag{D14}$$

It follows from (D14) that $\mathcal{P}^2 = \mathcal{P}$. The corresponding orthogonal projection is

$$\mathcal{Q} = 1 - \mathcal{P}. \tag{D15}$$

Consider the quantity $(\mathcal{P}\mathcal{L}X)_i$

$$\begin{aligned}(\mathcal{P}\mathcal{L}X)_i &= \sum_\alpha \Psi_{\alpha i}(\mathbf{V}^*) \sum_j \int d\mathbf{V}^* \psi_{\alpha j}(\mathbf{V}^*) (\mathcal{L}X)_j \\ &= \Psi_i^{(s+1)}(\mathbf{V}^*) \sum_{j=1}^s \frac{2m_j}{dm} \int d\mathbf{V}^* V^{*2} (\mathcal{L}X)_j. \end{aligned} \tag{D16}$$

Only the projection onto $\Psi_i^{(s+1)}$ contributes due to conservation of species number and momentum. It follows then that

$$(\mathcal{P}\mathcal{L}\boldsymbol{\mathcal{A}})_i = 0, \qquad \left(\mathcal{P}\mathcal{L}\boldsymbol{\mathcal{B}}^j\right)_i = 0, \qquad \left(\mathcal{P}\mathcal{L}\boldsymbol{\mathcal{E}}^j\right)_i = 0, \qquad (\mathcal{P}\mathcal{L}\mathcal{C})_i = 0. \tag{D17}$$

The terms with $\boldsymbol{\mathcal{A}}, \boldsymbol{\mathcal{B}}^j$, and $\boldsymbol{\mathcal{E}}^j$ vanish from symmetry since these all vectors; the last equality follows because $\mathcal{C}$ has zero trace. Next, note that

$$\zeta_U \nabla \cdot \mathbf{U} = \zeta^{(1)} = \frac{2}{dnT} \sum_{i=1}^s \int d\mathbf{v}_1 \frac{1}{2} m_i v_1^2 (\mathcal{L}\mathcal{D})_i - \frac{2}{dnT} \sum_{i,j=1}^s \int d\mathbf{v}_1 \frac{1}{2} m_i v_1^2 \mathcal{K}_{ij,\eta} \left[\partial_{V_\eta} f_j^{(0)}\right], \tag{D18}$$

or equivalently

$$\begin{aligned}\Psi_i^{s+1} \zeta_U &= \Psi_{2i} \sum_{j=1}^k \int d\mathbf{v}_1 \psi_j^{s+1} \mathcal{L}_j[\mathcal{D}] - \Psi_i^{s+1} \frac{2m}{dnT} \sum_{j=1}^k \int d\mathbf{v}_1 \frac{1}{2mdv_0} m_j v_1^2 \sum_p \mathcal{K}_{jp,\eta}[\partial_{V_\eta^*} f_j^{(0)}] \\ &= \Psi_{2i} \sum_{j=1}^k \int d\mathbf{v}_1 \psi_{2j} \mathcal{L}_j[\mathcal{D}] - \mathcal{P} \frac{1}{dv_0} \mathcal{K}_\eta \left[\partial_{V_\eta^*} f^{(0)}\right] \\ &= \mathcal{P}\mathcal{L}_j[\mathcal{D}] + \mathcal{P} \frac{1}{dv_0} \mathcal{K}_\eta \left[\partial_{V_\eta^*} f^{(0)}\right]. \end{aligned} \tag{D19}$$

This can be used to eliminate the explicit occurrence of the transport coefficient ζ_U in the integral equation (C43). Finally, two additional identities are needed for the proofs of Appendix E

$$-\partial_{V_\gamma^*} f_i^{(0)} \frac{p - nT}{v_0^2 \rho} = \mathcal{P} \sum_{j=1}^k \frac{1}{2v_0} \mathcal{K}_{ij,\gamma}[\nabla_{\mathbf{V}^*} \cdot \left(\mathbf{V}^* f_j^{(0)}\right)], \tag{D20}$$

$$\left(\nabla_{\mathbf{V}*} f_i^{(0)}\right) \left(v_0^2 \rho\right)^{-1} n_j \partial_{n_j} (p - nT) = -\mathcal{P} \sum_{\ell=1}^k \frac{1}{v_0} \mathcal{K}_{i\ell}[\left(n_j \partial_{n_j} + \frac{1}{2} I_{i\ell j}\right) f_\ell^{(0)}]. \tag{D21}$$

APPENDIX E: SOLUBILITY CONDITIONS AND UNIQUENESS

The results of Appendix D allow proof that the integral equations have solutions and that they are unique. These equations have the generic form

$$(\mathcal{L} - \lambda)\mathcal{X} = X, \tag{E1}$$

where λ is one of the eigenvalues (D10). Let relation $\mathcal{X}$ be a solution to (E1). Then adding any solution to the corresponding homogeneous integral equation also gives a solution

$$\mathcal{X}' = \mathcal{X} + c\Psi, \tag{E2}$$

where $(\mathcal{L} - \lambda)\,\Psi = 0$. However, the property

$$\left(\mathcal{P} f^{(1)}\right)_i = \sum_\alpha \Psi_{\alpha i}\left(\mathbf{V}\right) \sum_j \int d\mathbf{v} \psi_{\alpha j}\left(\mathbf{V}\right) f_j^{(1)}\left(\mathbf{V}\right) = 0 \tag{E3}$$

follows from the fact that the average densities, temperature, and flow velocity are given exactly by the first order term $f_i^{(0)}$, so that contributions to these averages from all higher order terms must vanish. Equivalently, (E3) implies

$$\mathcal{P}\begin{pmatrix} \boldsymbol{\mathcal{A}} \\ \boldsymbol{\mathcal{B}}^j \\ \mathcal{C} \\ \mathcal{D} \\ \boldsymbol{\mathcal{E}}^j \end{pmatrix} = 0. \tag{E4}$$

Consequently, the solution to (E1) with the condition (E4) is unique.

To show that solutions exist the integral equations are written in the equivalent form

$$\left(\mathcal{Q}\left(\mathcal{L} - \frac{1}{2}\zeta^*\right)\boldsymbol{\mathcal{A}}\right)_i = \mathcal{Q}\mathbf{A}_i, \tag{E5}$$

$$\left(\mathcal{Q}\mathcal{L}\left(\boldsymbol{\mathcal{B}}^j - 2n_j \frac{\partial \ln \zeta^{(0)}}{\partial n_j}\boldsymbol{\mathcal{A}}\right)\right)_i = \mathcal{Q}\left(\mathbf{B}_i^j - 2n_j \frac{\partial \ln \zeta^*}{\partial n_j}\mathbf{A}_i\right), \tag{E6}$$

$$\left(\mathcal{Q}\left(\mathcal{L} + \frac{1}{2}\zeta^{(0)}\right)\mathcal{C}_{\gamma\eta}\right)_i = \mathcal{Q}C_{i,\gamma\eta}, \tag{E7}$$

$$\left(\mathcal{Q}\left(\mathcal{L} + \frac{1}{2}\zeta^*\right)\mathcal{D}\right)_i = \mathcal{Q}D_i, \tag{E8}$$

$$\left(\mathcal{Q}\left(\mathcal{L} + \zeta^*\right)\boldsymbol{\mathcal{E}}^j\right)_i = \mathcal{Q}\mathbf{E}_i^j. \tag{E9}$$

These equations are the same as (C40)–(C44). The appearance of the factors of $\mathcal{Q}$ simply represent a convenient rearrangement of those equations, using the identities of Appendix D. They show that the relevant linear operator is $\mathcal{Q}\left(\mathcal{L} - \lambda\right)$ where λ is one of the eigenvalues (D10). The orthogonal projection $\mathcal{Q}$ identifies the left eigenfunctions with zero eigenvalue as being those of the biorthogonal set $\psi_{\alpha i}$ in (D12). According to the Fredholm alternative [71], solutions to these equations exist if and only if the inhomogeneity is orthogonal to the null space of the left eigenfunctions. Here, all the inhomogeneities on the right sides of (E5)–(E9) appear explicitly orthogonal to this null space. Hence, solutions exist and are unique.

APPENDIX F: DETAILS OF THE CONSTITUTIVE EQUATIONS

The cooling rate, and fluxes of mass, momentum, and energy are given exactly as explicit integrals of solutions to the kinetic equation. Once the CE solution is obtained, approximately to first order in the gradients, these expressions give the cooling rate and fluxes in the form of the constitutive equations (5.9)–(5.12). The objective of this Appendix is to simplify these expressions to the extent possible without making any approximations. This is accomplished in most cases by performing solid angle integrations using the results

$$\int d\widehat{\boldsymbol{\sigma}}\Theta(\widehat{\boldsymbol{\sigma}}\cdot\mathbf{g})(\widehat{\boldsymbol{\sigma}}\cdot\mathbf{g})^n = \pi^{(d-1)/2}\frac{\Gamma\left(\frac{n+1}{2}\right)}{\Gamma\left(\frac{n+d}{2}\right)}g^n \equiv B_n g^n, \tag{F1}$$

$$\int d\widehat{\boldsymbol{\sigma}}\Theta(\widehat{\boldsymbol{\sigma}}\cdot\mathbf{g})(\widehat{\boldsymbol{\sigma}}\cdot\mathbf{g})^n\widehat{\boldsymbol{\sigma}}=B_{n+1}g^n\widehat{\mathbf{g}}, \tag{F2}$$

$$\int d\widehat{\boldsymbol{\sigma}}\Theta(\widehat{\boldsymbol{\sigma}}\cdot\mathbf{g})(\widehat{\boldsymbol{\sigma}}\cdot\mathbf{g})^n\widehat{\sigma}_k\widehat{\sigma}_\ell=\frac{B_n}{n+d}g^n\left(n\widehat{g}_k\widehat{g}_\ell+\delta_{k\ell}\right), \tag{F3}$$

$$\int d\widehat{\boldsymbol{\sigma}}\Theta(\widehat{\boldsymbol{\sigma}}\cdot\mathbf{g})(\widehat{\boldsymbol{\sigma}}\cdot\mathbf{g})^n\widehat{\sigma}_k\widehat{\sigma}_\ell\widehat{\sigma}_m=g^n\frac{B_{n+1}}{n+d+1}\left[(n-1)\,\widehat{g}_k\widehat{g}_\ell\widehat{g}_m+\widehat{g}_m\delta_{k\ell}+\widehat{g}_k\delta_{m\ell}+\widehat{g}_\ell\delta_{km}\right], \tag{F4}$$

where d is the dimension ($d\geq 2$), and $\Gamma(x)$ is the usual Gamma function

$$\Gamma(x+1)=x\Gamma(x), \qquad \Gamma\left(\frac{1}{2}\right)=\sqrt{\pi}, \qquad \Gamma(1)=1. \tag{F5}$$

In addition, for the sake of convenience, henceforth we will use the notation $\mathbf{g}_{12}\equiv\mathbf{g}$.

To get the collisional transfer contributions to the fluxes, one has to consider the following expansion

$$\begin{aligned}\int_0^1 dx \quad & f_{ij}(\mathbf{r}_1-x\boldsymbol{\sigma}_{ij},\mathbf{v}_1,\mathbf{r}_1+(1-x)\,\boldsymbol{\sigma}_{ij},\mathbf{v}_2;t)=\int_0^1 dx\chi_{ij}\left(\mathbf{r}_1-x\boldsymbol{\sigma}_{ij},\mathbf{r}_1+(1-x)\,\boldsymbol{\sigma}_{ij}\mid\{n_i\}\right)\\
&\times f_i(\mathbf{r}_1-x\boldsymbol{\sigma}_{ij},\mathbf{v}_1;t)f_j(\mathbf{r}_1+(1-x)\,\boldsymbol{\sigma}_{ij},\mathbf{v}_2;t)\\
&\to\chi_{ij}^{(0)}\left(\sigma_{ij};\{n_i\}\right)f_i^{(0)}(\mathbf{v}_1;t)f_j^{(0)}(\mathbf{v}_2;t)\\
&+\frac{1}{2}\chi_{ij}^{(0)}\left(\sigma_{ij};\{n_i\}\right)\left[f_i^{(0)}(\mathbf{v}_1;t)\partial_{y_\beta}f_j^{(0)}(\mathbf{v}_2;t)-f_j^{(0)}(\mathbf{v}_2;t)\partial_{y_\beta}f_i^{(0)}(\mathbf{v}_1;t)\right]\boldsymbol{\sigma}_{ij}\cdot\nabla y_\beta\\
&+\chi_{ij}^{(0)}\left[f_i^{(0)}(\mathbf{v}_1;t)f_j^{(1)}(\mathbf{r}_1,\mathbf{v}_2;t)+f_i^{(1)}(\mathbf{v}_1;t)f_j^{(0)}(\mathbf{r}_1,\mathbf{v}_2;t)\right]\\
&+f_i^{(0)}(\mathbf{v}_1;t)f_j^{(1)}(\mathbf{r}_1,\mathbf{v}_2;t)\delta\chi_{ij},\end{aligned} \tag{F6}$$

where $\delta\chi_{ij}$ is defined by

$$\delta\chi_{ij}=\sum_{\ell=1}^s\left(\nabla_{\mathbf{r}_1}n_\ell(\mathbf{r}_1;t)\right)\cdot\int_0^1 dx\int d\mathbf{r}'\left(\mathbf{r}'-\mathbf{r}_1\right)\frac{\delta\chi_{ij}\left(\mathbf{r}_1-x\boldsymbol{\sigma}_{ij},\mathbf{r}_1+(1-x)\,\boldsymbol{\sigma}_{ij}\mid\{n_i\}\right)}{\delta n_\ell(\mathbf{r}',t)}\mid_{\delta n=0} \tag{F7}$$

The functional derivative is evaluated at $\delta n=0$ and so it depends only on differences of pairs of coordinates, as in (C7). A change of variables then makes the dependence on x explicit

$$\begin{aligned}\int d\mathbf{r}'\left(\mathbf{r}'-\mathbf{r}_1\right) \quad & \frac{\delta\chi_{ij}\left(\mathbf{r}_1-x\boldsymbol{\sigma}_{ij},\mathbf{r}_1+(1-x)\,\boldsymbol{\sigma}_{ij}\mid\{n_i\}\right)}{\delta n_\ell(\mathbf{r}',t)}\mid_{\delta n=0}=\int d\mathbf{r}''\left(\mathbf{r}''+\frac{1}{2}\boldsymbol{\sigma}_{ij}-x\boldsymbol{\sigma}_{ij}\right)\\
&\times\frac{\delta\chi_{ij}\left(-\frac{1}{2}\sigma_{ij},\frac{1}{2}\boldsymbol{\sigma}_{ij}\mid\{n_i\}\right)}{\delta n_\ell(\mathbf{r}'',t)}\mid_{\delta n=0}\\
=&-\left(x-\frac{1}{2}\right)\boldsymbol{\sigma}_{ij}\frac{\partial\chi_{ij}^{(0)}\left(\sigma_{ij}\mid\{n_i\}\right)}{\partial n_\ell(\mathbf{r}'',t)}\mid_{\delta n=0}+\int d\mathbf{r}''\mathbf{r}''\frac{\delta\chi_{ij}\left(-\frac{1}{2}\sigma_{ij},\frac{1}{2}\sigma_{ij}\mid\{n_i\}\right)}{\delta n_\ell(\mathbf{r}'',t)}\mid_{\delta n=0}\\
=&-\frac{\chi_{ij}^{(0)}}{n_\ell}\boldsymbol{\sigma}_{ij}\left[\left(x-\frac{1}{2}\right)n_\ell\frac{\partial\ln\chi_{ij}^{(0)}(\sigma_{ij};\{n_k\})}{\partial n_\ell}-\frac{1}{2}I_{ij\ell}(\sigma_{ij};\{n_k\})\right],\end{aligned} \tag{F8}$$

where $I_{ij\ell}(\sigma_{ij};\{n_k\})$ is defined in (C7). Finally, then

$$\delta\chi_{ij}=\frac{1}{2}\chi_{ij}^{(0)}\sum_{\ell=1}^s\left(\nabla_{\mathbf{r}_1}\ln n_\ell(\mathbf{r}_1;t)\right)\cdot\boldsymbol{\sigma}_{ij}\left(I_{ij\ell}(\sigma_{ij};\{n_k\})\right). \tag{F9}$$

1. Cooling rate

Since ζ is a scalar, the only gradient contributions are proportional to $\nabla\cdot\mathbf{U}$, and (4.27) to first order in the gradients becomes

$$\zeta=\zeta^{(0)}+\zeta_U\nabla\cdot\mathbf{U}, \tag{F10}$$

with

$$\zeta^{(0)}=\frac{1}{2dnT}\sum_{i,j=1}^{s}\left(1-\alpha_{ij}^2\right)m_i\mu_{ji}\chi_{ij}^{(0)}\sigma_{ij}^{d-1}\int d\mathbf{v}_1\int d\mathbf{v}_2\int d\widehat{\boldsymbol{\sigma}}\Theta(\widehat{\boldsymbol{\sigma}}\cdot\mathbf{g})(\widehat{\boldsymbol{\sigma}}\cdot\mathbf{g})^3 f_i^{(0)}(\mathbf{V}_1)f_j^{(0)}(\mathbf{V}_2), \tag{F11}$$

$$\begin{aligned}\zeta_U &= \frac{1}{2dnT}\sum_{i,j=1}^{s}\left(1-\alpha_{ij}^2\right)m_i\mu_{ji}\chi_{ij}^{(0)}\sigma_{ij}^{d-1}\int d\mathbf{v}_1\int d\mathbf{v}_2\int d\widehat{\boldsymbol{\sigma}}\Theta(\widehat{\boldsymbol{\sigma}}\cdot\mathbf{g})(\widehat{\boldsymbol{\sigma}}\cdot\mathbf{g})^3\\ &\times\left[\frac{1}{d}f_j^{(0)}(\mathbf{V}_2)\boldsymbol{\sigma}_{ij}\cdot\nabla_{\mathbf{V}_1}f_i^{(0)}(\mathbf{V}_1)+2f_i^{(0)}(\mathbf{V}_1)\mathcal{D}_j(\mathbf{V}_2)\right].\end{aligned} \tag{F12}$$

Performing the solid angle integrals gives

$$\zeta^{(0)}=\frac{B_3}{2dnT}\sum_{i,j=1}^{s}\left(1-\alpha_{ij}^2\right)\frac{m_im_j}{m_i+m_j}\chi_{ij}^{(0)}\sigma_{ij}^{d-1}\int d\mathbf{v}_1\int d\mathbf{v}_2 g^3 f_i^{(0)}(\mathbf{V}_1)f_j^{(0)}(\mathbf{V}_2), \tag{F13}$$

$$\begin{aligned}\zeta_U &= \frac{B_4}{2d^2nT}\sum_{i,j=1}^{s}\left(1-\alpha_{ij}^2\right)\frac{m_im_j}{m_i+m_j}\chi_{ij}^{(0)}\sigma_{ij}^{d}\int d\mathbf{v}_1\int d\mathbf{v}_2\, g^2 f_j^{(0)}(\mathbf{V}_2)\left(\mathbf{g}\cdot\nabla_{\mathbf{V}_1}f_i^{(0)}(\mathbf{V}_1)\right)\\ &+\frac{B_3}{dnT}\sum_{i,j=1}^{s}\left(1-\alpha_{ij}^2\right)\frac{m_im_j}{m_i+m_j}\chi_{ij}^{(0)}\sigma_{ij}^{d-1}\int d\mathbf{v}_1\int d\mathbf{v}_2\, g^3 f_i^{(0)}(\mathbf{V}_1)\mathcal{D}_j(\mathbf{V}_2).\end{aligned} \tag{F14}$$

Finally, an integration by parts in the first term of the velocity integrals gives the result quoted in the text

$$\begin{aligned}\zeta_U &= -\frac{d+2}{2dnT}B_4\sum_{i,j=1}^{s}\left(1-\alpha_{ij}^2\right)\frac{m_im_j}{m_i+m_j}\chi_{ij}^{(0)}\sigma_{ij}^{d}n_in_j\left(\frac{T_i^{(0)}}{m_i}+\frac{T_j^{(0)}}{m_j}\right)\\ &+\frac{B_3}{dnT}\sum_{i,j=1}^{s}\left(1-\alpha_{ij}^2\right)\frac{m_im_j}{m_i+m_j}\chi_{ij}^{(0)}\sigma_{ij}^{d-1}\int d\mathbf{v}_1\int d\mathbf{v}_2\, g^3 f_i^{(0)}(\mathbf{V}_1)\mathcal{D}_j(\mathbf{V}_2),\end{aligned} \tag{F15}$$

where the species temperatures are defined by

$$\frac{d}{2}n_iT_i^{(0)}=\int d\mathbf{v}\frac{1}{2}m_iV^2f_i^{(0)}(\mathbf{V}). \tag{F16}$$

In the case of mechanically equivalent particles, Eq. (F15) reduces to previous results obtained for a monocomponent gas [62, 72].

2. Mass Flux

The mass fluxes are determined from the definition of (4.16)

$$\begin{aligned}\mathbf{j}_{0i}\left(\mathbf{r}_1,t\right) &\to m_i\int d\mathbf{v}\mathbf{V}f_i^{(1)}(\mathbf{r}_1,\mathbf{v};t)\\ &= \frac{1}{d}\int d\mathbf{v}m_i\mathbf{V}\cdot\left(\boldsymbol{\mathcal{A}}_i\left(\mathbf{V}\right)\nabla\ln T+\sum_{j=1}^{s}\left(\boldsymbol{\mathcal{B}}_i^j\left(\mathbf{V}\right)\nabla\ln n_j+\boldsymbol{\mathcal{E}}_i^j\left(\mathbf{V}\right)\mathbf{F}_j\right)\right),\end{aligned} \tag{F17}$$

where the contribution from $f_i^{(0)}$ vanishes. The transport coefficients according to (5.10) are identified as

$$D_i^T=-\frac{m_i}{\rho d}\int d\mathbf{v}\mathbf{V}\cdot\boldsymbol{\mathcal{A}}_i\left(\mathbf{V}\right), \tag{F18}$$

$$D_{ij}=-\frac{\rho}{m_jn_jd}\int d\mathbf{v}\mathbf{V}\cdot\boldsymbol{\mathcal{B}}_i^j\left(\mathbf{V}\right), \tag{F19}$$

$$D_{ij}^F=-\frac{m_i}{d}\int d\mathbf{v}\mathbf{V}\cdot\boldsymbol{\mathcal{E}}_i^j\left(\mathbf{V}\right). \tag{F20}$$

3. Energy Flux

The energy flux to first order in the gradients is obtained from Eqs. (4.18) and (4.19) as

$$\mathbf{q} = \mathbf{q}^k + \mathbf{q}^c. \tag{F21}$$

The kinetic contribution is

$$\begin{aligned}
\mathbf{q}^k &= \sum_{i=1}^{s} \int d\mathbf{v}_1 \frac{1}{2} m_i V_1^2 \mathbf{V}_1 f_i^{(1)}(\mathbf{r}_1, \mathbf{v}_1; t) \\
&= \frac{1}{d} \sum_{i=1}^{s} \int d\mathbf{v}_1 \frac{1}{2} m_i V_1^2 \mathbf{V}_1 \cdot \boldsymbol{\mathcal{A}}_i(\mathbf{V}_1) \nabla \ln T \\
&\quad + \frac{1}{d} \sum_{i,j=1}^{s} \int d\mathbf{v}_1 \frac{1}{2} m_i V_1^2 \mathbf{V}_1 \cdot \left(\boldsymbol{\mathcal{B}}_i^j(\mathbf{V}_1) \nabla \ln n_j + \boldsymbol{\mathcal{E}}_i^j(\mathbf{V}_1) \mathbf{F}_j \right).
\end{aligned} \tag{F22}$$

The contributions proportional to derivatives of the flow velocity vanish from symmetry. The collisional transfer contribution is

$$\begin{aligned}
\mathbf{q}^c &= \sum_{i,j=1}^{s} \frac{1}{8}(1+\alpha_{ij}) m_j \mu_{ij} \sigma_{ij}^d \chi_{ij}^{(0)} \int d\mathbf{v}_1 \int d\mathbf{v}_2 \int d\widehat{\boldsymbol{\sigma}}\, \Theta(\widehat{\boldsymbol{\sigma}} \cdot \mathbf{g}) (\widehat{\boldsymbol{\sigma}} \cdot \mathbf{g})^2 \widehat{\boldsymbol{\sigma}} \\
&\quad \times \left[-(1-\alpha_{ij})(\mu_{ij} - \mu_{ji})(\widehat{\boldsymbol{\sigma}} \cdot \mathbf{g}) + 4(\mathbf{G}_{ij} \cdot \widehat{\boldsymbol{\sigma}}) \right] \Big[f_i^{(0)}(\mathbf{V}_1) f_j^{(1)}(\mathbf{V}_2) + f_i^{(1)}(\mathbf{V}_1) f_j^{(0)}(\mathbf{V}_2) \\
&\quad - \frac{1}{2} f_j^{(0)}(\mathbf{V}_2) \partial_{y_\beta} f_i^{(0)}(\mathbf{V}_1) \boldsymbol{\sigma}_{ij} \cdot \nabla y_\beta + \frac{1}{2} f_i^{(0)}(\mathbf{V}_1) \partial_{y_\beta} f_j^{(0)}(\mathbf{V}_2) \boldsymbol{\sigma}_{ij} \cdot \nabla y_\beta \Big],
\end{aligned} \tag{F23}$$

where $\mathbf{G}_{ij} \equiv \mu_{ij} \mathbf{V}_1 + \mu_{ji} \mathbf{V}_2$. The contribution from $\delta\chi_{ij}$ in (F9) vanishes from symmetry. The angular integrals can be performed to get

$$\begin{aligned}
q_\gamma^c &= \sum_{i,j=1}^{s} \frac{1}{8}(1+\alpha_{ij}) m_j \mu_{ij} \sigma_{ij}^d \chi_{ij}^{(0)} \int d\mathbf{v}_1 \int d\mathbf{v}_2 \Big\{ -B_4 (1-\alpha_{ij})(\mu_{ij} - \mu_{ji}) g^2 g_\gamma \\
&\quad + \frac{4B_2}{2+d} \left[2(\mathbf{G}_{ij} \cdot \mathbf{g}) g_\gamma + g^2 G_{ij,\gamma} \right] \left(f_i^{(0)}(\mathbf{V}_1) f_j^{(1)}(\mathbf{V}_2) + f_i^{(1)}(\mathbf{V}_1) f_j^{(0)}(\mathbf{V}_2) \right) \\
&\quad + \frac{B_3}{3+d} \Big[-(1-\alpha_{ij})(\mu_{ij} - \mu_{ji}) g^3 (3\widehat{g}_\gamma \widehat{g}_\eta + \delta_{\gamma\eta}) + 4g^2 ((\mathbf{G}_{ij} \cdot \widehat{\mathbf{g}})(\widehat{g}_\gamma \widehat{g}_\eta + \delta_{\gamma\eta}) \\
&\quad + \widehat{g}_\gamma G_{ij,\eta} + \widehat{g}_\eta G_{ij,\gamma}) \Big] \frac{1}{2} \left[f_i^{(0)}(\mathbf{V}_1) \partial_{y_\beta} f_j^{(0)}(\mathbf{V}_2) - f_j^{(0)}(\mathbf{V}_2) \partial_{y_\beta} f_i^{(0)}(\mathbf{V}_1) \right] \partial_\eta y_\beta \Big\}.
\end{aligned} \tag{F24}$$

Interchanging the labels i, j and $\mathbf{v}_1, \mathbf{v}_2$ it is seen that the contributions from $f_i^{(1)}$ and $f_j^{(1)}$ are the same. For the same reason the contributions from $\partial_{y_\beta} f_i^{(0)}$ and $-\partial_{y_\beta} f_j^{(0)}$ are the same. The first terms of the integrand give velocity moments of $f_j^{(1)}$ of degree one and three, which are proportional to the (partial) mass and kinetic energy fluxes. Finally, the only contributions from $\partial_{y_\beta} f_i^{(0)}$ are those that are scalar functions of the velocities, i.e. those proportional to temperature and species density gradients. The final result is therefore

$$\begin{aligned}
\mathbf{q}^c &= \sum_{i,j=1}^{s} \frac{1}{8}(1+\alpha_{ij}) m_j \mu_{ij} \sigma_{ij}^d \chi_{ij}^{(0)} \left[2B_4 (1-\alpha_{ij})(\mu_{ij} - \mu_{ji}) n_i \left(\frac{2}{m_j} \mathbf{q}_j^k + (d+2) \frac{T_i^{(0)}}{m_i m_j} \mathbf{j}_{0j}^{(1)} \right) \right. \\
&\quad \left. + \frac{8B_2}{2+d} n_i \left(\frac{2\mu_{ji}}{m_j} \mathbf{q}_j^k - (d+2) \frac{T_i^{(0)}}{m_i m_j} (2\mu_{ij} - \mu_{ji}) \mathbf{j}_{0j}^{(1)} \right) + C_{ij}^T \nabla \ln T + \sum_{p=1}^{s} C_{ijp}^T \nabla \ln n_p \right],
\end{aligned} \tag{F25}$$

where $\mathbf{j}_{0i}^{(1)}$ is defined by Eq. (F17) and the partial kinetic energy flux is

$$\mathbf{q}_i^k = \int d\mathbf{v}\ \frac{m_i}{2} V^2 \mathbf{V} f_i^{(1)}(\mathbf{V}). \tag{F26}$$

The constants C_{ij}^T and C_{ijp}^T are

$$C_{ij}^T = \frac{B_3}{d} \int d\mathbf{v}_1 \int d\mathbf{v}_2 \left[-(1-\alpha_{ij})(\mu_{ij}-\mu_{ji}) g^3 + 4g(\mathbf{g}\cdot\mathbf{G}_{ij}) \right] f_i^{(0)}(\mathbf{V}_1) T\partial_T f_j^{(0)}(\mathbf{V}_2), \tag{F27}$$

$$C_{ijp}^T = \frac{B_3}{d} \int d\mathbf{v}_1 \int d\mathbf{v}_2 \left[-(1-\alpha_{ij})(\mu_{ij}-\mu_{ji}) g^3 + 4g(\mathbf{g}\cdot\mathbf{G}_{ij}) \right] f_i^{(0)}(\mathbf{V}_1) n_p \partial_{n_p} f_j^{(0)}(\mathbf{V}_2). \tag{F28}$$

The expression of C_{ij}^T can be simplified when one takes into account the relation

$$T\partial_T f_j^{(0)}(\mathbf{V}) = -\frac{1}{2}\nabla_{\mathbf{V}} \cdot \left(\mathbf{V} f_j^{(0)}(\mathbf{V}) \right), \tag{F29}$$

and integrates by parts in (F27). The result is

$$\begin{aligned} C_{ij}^T \ =\ & -\frac{2B_3}{d} \int d\mathbf{v}_1 \int d\mathbf{v}_2 f_i^{(0)}(\mathbf{V}_1) f_j^{(0)}(\mathbf{V}_2) \left\{ gG_{ij}^2 + g^{-1}(\mathbf{g}\cdot\mathbf{G}_{ij})^2 + (1+\mu_{ji}) g(\mathbf{g}\cdot\mathbf{G}_{ij}) \right. \\ & \left. + \mu_{ji}\mu_{ij} g^3 + \frac{3}{4}(1-\alpha_{ij})(\mu_{ji}-\mu_{ij}) \left[g(\mathbf{g}\cdot\mathbf{G}_{ij}) + g^3 \right] \right\}. \end{aligned} \tag{F30}$$

On the other hand, no significant further simplification of Eq. (F28) is possible until $f_i^{(0)}$ is specified in detail.

The heat flux is seen to have the form (5.11),

$$\mathbf{q}(\mathbf{r},t) \to -\lambda \nabla T - \sum_{i,j=1}^{s} \left(T^2 D_{q,ij} \nabla \ln n_j + L_{ij} \mathbf{F}_j \right), \tag{F31}$$

so the transport coefficients now can be identified

$$\lambda = \lambda^k + \lambda^c, \qquad D_{q,ij} = D_{q,ij}^k + D_{q,ij}^c, \qquad L_{ij} = L_{ij}^k + L_{ij}^c. \tag{F32}$$

The kinetic parts are,

$$\lambda^k = \sum_{i=1}^{s} \lambda_i^k = -\frac{1}{dT} \sum_{i=1}^{s} \int d\mathbf{v} \frac{m_i}{2} V^2 \mathbf{V} \cdot \boldsymbol{\mathcal{A}}_i(\mathbf{V}), \tag{F33}$$

$$D_{q,ij}^k = -\frac{1}{dT^2} \int d\mathbf{v} \frac{m_i}{2} V^2 \mathbf{V} \cdot \boldsymbol{\mathcal{B}}_i^j(\mathbf{V}), \tag{F34}$$

$$L_{ij}^k = -\frac{1}{d} \int d\mathbf{v} \frac{m_i}{2} V^2 \mathbf{V} \cdot \boldsymbol{\mathcal{E}}_i^j(\mathbf{V}), \tag{F35}$$

while the collisional transport parts are given by Eqs. (7.14)–(7.16).

4. Momentum Flux

The momentum flux to first order in the gradients is obtained from (4.20)–(4.22)

$$P_{\gamma\lambda} \equiv P_{\gamma\lambda}^k + P_{\gamma\lambda}^c, \tag{F36}$$

where

$$P_{\gamma\lambda}^k \to \sum_{i=1}^s \int d\mathbf{v}_1 m_i V_{1\gamma} V_{1\lambda} \left(f_i^{(0)}(\mathbf{V}_1) + f_i^{(1)}(\mathbf{V}_1) \right)$$
$$= \delta_{\gamma\lambda} nT + \sum_{i=1}^s \int d\mathbf{v}_1 m_i V_{1\lambda} V_{1\gamma} f_i^{(1)}(\mathbf{V}_1), \tag{F37}$$

$$P_{\gamma\lambda}^c = \frac{1}{2} \sum_{i,j=1}^s m_j \mu_{ij} (1+\alpha_{ij}) \sigma_{ij}^d \chi_{ij}^{(0)} \int d\mathbf{v}_1 \int d\mathbf{v}_2 \int d\widehat{\boldsymbol{\sigma}}\, \Theta(\widehat{\boldsymbol{\sigma}} \cdot \mathbf{g}) (\widehat{\boldsymbol{\sigma}} \cdot \mathbf{g})^2 \widehat{\sigma}_\lambda \widehat{\sigma}_\gamma$$
$$\times \Big[f_i^{(0)}(\mathbf{V}_1) f_j^{(0)}(\mathbf{V}_2) + 2 f_i^{(0)}(\mathbf{V}_1) f_j^{(1)}(\mathbf{V}_2)$$
$$- \frac{1}{2} \left(f_j^{(0)}(\mathbf{V}_2) \partial_{y_\beta} f_i^{(0)}(\mathbf{V}_1) - f_i^{(0)}(\mathbf{V}_1) \partial_{y_\beta} f_j^{(0)}(\mathbf{V}_2) \right) \boldsymbol{\sigma}_{ij} \cdot \nabla y_\beta \Big]. \tag{F38}$$

A contribution to (F38) proportional to the density gradients from the expansion of $\chi_{ij}(\mathbf{r}_1 - x\boldsymbol{\sigma}_{ij}, \mathbf{r}_1 + (1-x)\boldsymbol{\sigma}_{ij})$ vanishes from symmetry. For similar reasons, the only gradients contributing to both (F37) and (F38) are those from the flow field. The terms proportional to $\mathcal{D}_i$ in (C33) also do not contribute due to the orthogonality condition (E4). The solid angle integrations can be performed with the results

$$P_{\gamma\lambda}^k \to \delta_{\gamma\lambda} nT + \frac{1}{2} \sum_{i=1}^s \int d\mathbf{v}_1 m_i V_{1\lambda} V_{1\gamma} \mathcal{C}_{i,\beta\mu}(\mathbf{V}_1) \left(\partial_\beta U_\mu + \partial_\mu U_\beta - \frac{2}{d} \delta_{\beta\mu} \nabla \cdot \mathbf{U} \right), \tag{F39}$$

$$P_{\gamma\lambda}^c = \delta_{\gamma\lambda} \frac{B_2}{2d} \sum_{i,j=1}^s m_j \mu_{ij} (1+\alpha_{ij}) \sigma_{ij}^d \chi_{ij}^{(0)} n_i n_j \left(\frac{T_i^{(0)}}{m_i} + \frac{T_j^{(0)}}{m_j} \right)$$
$$+ \frac{B_2}{d+2} \sum_{i,j=1}^s \mu_{ij} (1+\alpha_{ij}) \chi_{ij}^{(0)} n_i \sigma_{ij}^d \int d\mathbf{v}_2 m_j V_{2\gamma} V_{2\lambda} \mathcal{C}_{j,\beta\mu}(\mathbf{V}_2) \left(\partial_\beta U_\mu + \partial_\mu U_\beta - \frac{2}{d} \delta_{\beta\mu} \nabla \cdot \mathbf{U} \right)$$
$$+ \frac{1}{2} \frac{B_3}{3+d} \sum_{i,j=1}^s m_j \mu_{ij} (1+\alpha_{ij}) \chi_{ij}^{(0)} \sigma_{ij}^d \int d\mathbf{v}_1 \int d\mathbf{v}_2 f_j^{(0)}(V_2) \left(\partial_{V_{1\ell}} f_i^{(0)}(V_1) \right)$$
$$\times g^2 \left(\widehat{g}_\lambda \widehat{g}_\gamma \widehat{g}_\mu + \widehat{g}_\mu \delta_{\lambda\gamma} + \widehat{g}_\gamma \delta_{\mu\lambda} + \widehat{g}_\lambda \delta_{\gamma\mu} \right) \partial_\mu U_\ell. \tag{F40}$$

An integration by parts in the velocity integral, and use of fluid symmetry gives, finally

$$P_{\gamma\lambda}^c = \delta_{\gamma\lambda} \frac{B_2}{2d} \sum_{i,j=1}^s m_j \mu_{ij} (1+\alpha_{ij}) \sigma_{ij}^d \chi_{ij}^{(0)} n_i n_j \left(\frac{T_i^{(0)}}{m_i} + \frac{T_j^{(0)}}{m_j} \right)$$
$$+ \frac{B_2}{d+2} \sum_{i,j=1}^s \mu_{ij} (1+\alpha_{ij}) \chi_{ij}^{(0)} n_i \sigma_{ij}^d \int d\mathbf{v}_2 m_j V_{2\gamma} V_{2\lambda} \mathcal{C}_{j,\beta\mu}(\mathbf{V}_2) \left(\partial_\beta U_\mu + \partial_\mu U_\beta - \frac{2}{d} \delta_{\beta\mu} \nabla \cdot \mathbf{U} \right)$$
$$- \frac{B_3 (d+1)}{2d(d+2)} \sum_{i,j=1}^s m_j \mu_{ij} (1+\alpha_{ij}) \chi_{ij}^{(0)} \sigma_{ij}^d \int d\mathbf{v}_1 \int d\mathbf{v}_2 f_i^{(0)}(\mathbf{V}_1) f_j^{(0)}(\mathbf{V}_2) g$$
$$\times \left[\left(\partial_\lambda U_\gamma + \partial_\gamma U_\lambda - \frac{2}{d} \delta_{\gamma\lambda} \nabla \cdot \mathbf{U} \right) + \frac{d+2}{d} \delta_{\gamma\lambda} \nabla \cdot \mathbf{U} \right]. \tag{F41}$$

The pressure tensor therefore has the form (5.12), and the pressure, shear viscosity, and bulk viscosity are identified in terms of their kinetic and collisional transfer contributions. Their expressions are given by Eqs. (7.18)–(7.22), respectively.

---

[1] T. M. Knowlton, J. W. Carson, G. E. Klinzing, and W. C. Yang, Chem. Eng. Prog. **90**, 44 (1994).

[2] M. Pell and S. P. Jordan, AIChE Symp. Ser. **84**, 68 (1988).
[3] Y. Y. Lee, in *Circulating Fluidized Beds*, edited by J. Grace, A. Avidan, and T. Knowlton (Blackie Academic & Professional, New York, 1997), pp. 417–440.
[4] J. M. Ottino and D. V. Khakhar, Annu. Rev. Fluid Mech. **32**, 55 (2000).
[5] S. Sundaresan, Powder Technol. **115**, 2 (2001).
[6] F. J. Muzzio, T. Shinbrot, and B. J. Glasser, Powder Technol. **124**, 1 (2002).
[7] J. S. Curtis and B. van Wachem, AIChE J. **50**, 2638 (2004).
[8] J. T. Jenkins and F. Mancini, J. Appl. Mech.-Trans. ASME **54**, 27 (1987).
[9] L. Huilin, D. Gidaspow, and E. Manger, Phys. Rev. E **64**, 061301 (2001).
[10] M. F. Rahaman, J. Naser, and P. J. Witt, Powder Technol. **138**, 82 (2003).
[11] J. T. Jenkins and F. Mancini, Phys. Fluids A **1**, 2050 (1989).
[12] P. Zamankhan, Phys. Rev. E **52**, 4877 (1995).
[13] B. O. Arnarson and J. T. Willits, Phys. Fluids **10**, 1324 (1998).
[14] J. T. Willits and B. O. Arnarson, Phys. Fluids **11**, 3116 (1999).
[15] C. S. Campbell, Annu. Rev. Fluid Mech. **22**, 57 (1990).
[16] A. Goldshtein and M. Shapiro, J. Fluid Mech. **282**, 75 (1995).
[17] I. Goldhirsch and M. L. Tan, Phys. Fluids **8**, 1752 (1996).
[18] S. E. Esipov and T. Pöschel, J. Stat. Phys. **86**, 1385 (1997).
[19] T. P. C. van Noije and M. H. Ernst, Gran. Matt. **1**, 57 (1998).
[20] J. J. Brey, D. Cubero, and M. J. Ruiz-Montero, Phys. Rev. E **59**, 1256 (1999).
[21] W. Losert, D. G. W. Cooper, J. Delour, A. Kudrolli, and J. P. Gollub, Chaos **9**, 682 (1999).
[22] A. Kudrolli and J. Henry, Phys. Rev. E **62**, R1489 (2000).
[23] V. Garzó, J. M. Montanero, and J. W. Dufty, Phys. Fluids **18**, 083305 (2006).
[24] V. Garzó and J. W. Dufty, Phys. Rev. E **60**, 5706 (1999).
[25] J. M. Montanero and V. Garzó, Gran. Matt. **4**, 17 (2002).
[26] A. Barrat and E. Trizac, Gran. Matt. **4**, 57 (2002).
[27] R. D. Wildman and D. J. Parker, Phys. Rev. Lett. **88**, 064301 (2002).
[28] K. Feitosa and N. Menon, Phys. Rev. Lett. **88**, 198301 (2002).
[29] R. Clelland and C. M. Hrenya, Phys. Rev. E **65**, 031301 (2002).
[30] S. R. Dahl, R. Clelland, and C. M. Hrenya, Phys. Fluids **14**, 1972 (2002).
[31] M. Alam and S. Luding, J. Fluid Mech. **476**, 69 (2003).
[32] D. Paolotti, C. Cattuto, U. M. B. Marconi, and A. Puglisi, Gran. Matt. **5**, 75 (2003).
[33] J. E. Galvin, S. R. Dahl, and C. M. Hrenya, J. Fluid Mech. **528**, 207 (2005).
[34] J. J. Brey, M. J. Ruiz-Montero, and F. Moreno, Phys. Rev. Lett. **95**, 0978001 (2005).
[35] D. K. Yoon and J. T. Jenkins, Phys. Fluids **18**, 073303 (2006).
[36] V. Garzó, Europhys. Lett. **75**, 521 (2006).
[37] H. Iddir and H. Arastoopour, AIChE J. **51**, 1620 (2005).
[38] V. Garzó and J. W. Dufty, Phys. Fluids **14**, 1476 (2002).
[39] D. Serero, I. Goldhirsch, S. H. Noskowicz, and M. L. Tan, J. Fluid Mech. **554**, 237 (2006).
[40] A. Santos, V. Garzó, and J. W. Dufty, Phys. Rev. E **69**, 061303 (2004).
[41] J. J. Brey, M. J. Ruiz-Montero, and D. Cubero, Europhys. Lett. **48**, 359 (1999).
[42] J. J. Brey, M. J. Ruiz-Montero, F. Moreno, and R. García-Rojo, Phys. Rev. E **65**, 061302 (2002).
[43] X. Yang, C. Huan, D. Candela, R. W. Mair, and R. L. Walshorth, Phys. Rev. Lett. **88**, 044301 (2002).
[44] C. Huan, X. Yang, D. Candela, R. W. Mair, and R. L. Walshorth, Phys. Rev. E **69**, 041302 (2004).
[45] E. C. Rericha, C. Bizon, M. D. Shattuck, and H. L. Swinney, Phys. Rev. Lett. **88**, 014302 (2002).
[46] M. Schröter, S. Ulrich, J. Kreft, J. B. Swift, and H. L. Swinney, Phys. Rev. E **74**, 011307 (2006).
[47] J. Ferziger and H. Kaper, *Mathematical Theory of Transport Processes in Gases* (North Holland, Amsterdam, 1972).
[48] H. van Beijeren and M. H. Ernst, Physica **68**, 437 (1973).
[49] M. López de Haro, E. G. D. Cohen, and J. M. Kincaid, J. Chem. Phys. **78**, 2746 (1983).
[50] V. Garzó, C. M. Hrenya, and J. W. Dufty, *Enskog theory for polydisperse granular mixtures II. Sonine polynomial approximation*, preprint cond-mat/0702110 (2007).
[51] J. J. Brey, J. W. Dufty, and A. Santos, J. Stat. Phys. **87**, 1051 (1997).
[52] T. P. C. van Noije and M. H. Ernst, in *Granular Gases*, edited by T. Pöschel and S. Luding (Springer, New York, 2001).
[53] J. F. Lutsko, Phys. Rev. E **63**, 061211 (2001).
[54] S. McNamara and S. Luding, Phys. Rev. E **58**, 2247 (1998).
[55] R. Soto and M. Mareschal, Phys. Rev. E **63**, 041303 (2001).
[56] I. Pagonabarraga, E. Trizac, T. P. C. van Noije, and M. H. Ernst, Phys. Rev. E **65**, 011303 (2002).
[57] J. J. Brey, M. J. Ruiz-Montero, D. Cubero, and R. García-Rojo, Phys. Fluids **12**, 876 (2000).
[58] J. F. Lutsko, J. J. Brey, and J. W. Dufty, Phys. Rev. E **65**, 051304 (2002).
[59] S. R. Dahl, C. M. Hrenya, V. Garzó, and J. W. Dufty, Phys. Rev. E **66**, 041301 (2002).
[60] J. F. Lutsko, Phys. Rev. E **70**, 061101 (2001).
[61] J. M. Montanero, V. Garzó, M. Alam, and S. Luding, Gran. Matt. **8**, 103 (2006).
[62] V. Garzó and J. W. Dufty, Phys. Rev. E **59**, 5895 (1999).
[63] T. W. Martin, J. M. Huntley, and R. D. Wildman, J. Fluid Mech. **535**, 325 (2005).

[64] V. Garzó and J. M. Montanero, Phys. Rev. E **68**, 041302 (2003).
[65] J. F. Lutsko, Phys. Rev. E **73**, 021302 (2006).
[66] V. Garzó, Phys. Rev. E **73**, 021304 (2006).
[67] J. M. Montanero and V. Garzó, Phys. Rev. E **67**, 021308 (2003).
[68] V. Garzó and J. M. Montanero, Phys. Rev. E **69**, 021301 (2004).
[69] N. Sela and I. Goldhirsch, J. Fluid Mech. **361**, 41 (1998).
[70] C. M. Hrenya, J. E. Galvin, and R. D. Wildman (in preparation).
[71] N. Dunford and J. Schwartz, *Linear Operators* (Interscience Publishers, New York, 1967).
[72] J. F. Lutsko, Phys. Rev. E **72**, 021306 (2005).

Enskog Theory for Polydisperse Granular Mixtures II. Sonine Polynomial Approximation

Vicente Garzó*
Departamento de Física, Universidad de Extremadura, E-06071 Badajoz, Spain

Christine M. Hrenya ‡
Department of Chemical and Biological Engineering, University of Colorado, Boulder, CO 80309

James W. Dufty†
Department of Physics, University of Florida, Gainesville, Florida 32611
(Dated: February 6, 2008)

The linear integral equations defining the Navier-Stokes (NS) transport coefficients for polydisperse granular mixtures of smooth inelastic hard disks or spheres are solved by using the leading terms in a Sonine polynomial expansion. Explicit expressions for all the NS transport coefficients are given in terms of the sizes, masses, compositions, density and restitution coefficients. In addition, the cooling rate is also evaluated to first order in the gradients. The results hold for arbitrary degree of inelasticity and are not limited to specific values of the parameters of the mixture. Finally, a detailed comparison between the derivation of the current theory and previous theories for mixtures is made, with attention paid to the implication of the various treatments employed to date.

I. INTRODUCTION

In the first portion [1] of this two-paper effort on the development of a kinetic-theory-based description of mixtures, a rigorous Chapman-Enskog (CE) expansion of the revised Enskog theory (RET) for an s -component mixture of inelastic hard spheres was carried out to first (Navier-Stokes) order in spatial gradients. The expansion was performed about a homogeneous cooling state (HCS), which is the zeroth-order solution of the kinetic equation for the single-particle velocity distribution function f_i of species i. Unlike previous theories for mixtures which derive from expansions about an elastic base state [2, 3, 4, 5, 6, 7, 8, 9, 10], this CE expansion does not impose any constraints on the level of dissipation. The resulting theory is thus expected to be applicable to a wide range of restitution coefficients. Furthermore, because the derivation used the RET as its starting point (as opposed to the Boltzmann equation as used in Ref. [11]), the results are expected to be applicable to dilute and moderately dense systems. The theory is not expected to be applicable to systems dense enough for ring collisions to play a significant role, since such velocity correlations are not accounted for in the RET.

This formally exact analysis for Navier-Stokes order hydrodynamics, reported in the companion paper, resulted in integral-differential equations for the zeroth-order $f_i^{(0)}$ and first-order $f_i^{(1)}$ distribution functions as well as integral expressions (in terms of $f_i^{(0)}$ and $f_i^{(1)}$) for each of the equations of state (cooling rate and pressure) and the transport coefficients $\{D_{ij}, D_i^T, D_{ij}^F, \eta, \kappa, \lambda, D_{q,ij}, L_{ij}\}$. Of these, only the pressure could be directly evaluated and cast in algebraic expressions of the macroscopic (hydrodynamic) variables. Hence, in this second part of the work, approximate methods are used to obtain algebraic equations for the kinetic and collisional contributions to the cooling rate and transport coefficients. In particular, the equations for $f_i^{(0)}$ have previously been solved [12] via a combination of scaling arguments and an approximation to the distribution function based on leading-order Sonine polynomials. Recent results derived for binary granular mixtures at low-density [11, 13] have shown that the influence of the non-Gaussian (higher-order) corrections of $f_i^{(0)}$ to the transport coefficients is in general negligible, except for quite large values of dissipation and velocities. For this reason, we use leading order in the Sonine polynomial expansion (Maxwellians) at different temperatures to evaluate integrals over the distributions $f_i^{(0)}$. The solutions for the $f_i^{(1)}$ are also found using a truncated polynomial expansion. These forms for $f_i^{(0)}$ and $f_i^{(1)}$ are then used to obtain practical expressions for the cooling rate and transport coefficients. Namely, the resulting, algebraic constitutive equations depend explicitly on the hydrodynamic variables only and not on the distribution functions of the mixture. Collision integrals are reduced to Gaussian forms and evaluated using standard integration techniques; a computer package of symbolic

* Electronic address: vicenteg@unex.es
‡ Electronic address: hrenya@colorado.edu
† Electronic address: dufty@phys.ufl.edu

calculations (Mathematica) was used to check their analytical evaluation. Wherever possible, limiting values of the equations of state and transport coefficients were verified by comparison with previously published works in the cases of mechanically equivalent particles [14, 15], binary mixtures at low-density [11, 16], and simple shear flow states for binary mixtures at moderate density [17]. All analytic calculations of both papers were performed independently and cross-checked.

Finally, as mentioned in the Introduction of the companion paper, a myriad of treatments has appeared in the literature for the derivation of kinetic-theory-based descriptions of granular mixtures. To help put the current effort in the context of previous contributions, Sec. VI contains a breakdown of the theoretical contributions to date, along with a critical discussion of the ramifications of each treatment.

II. EULER ORDER PARAMETERS

The hydrodynamic equations to first order in the spatial gradients (Euler order) have as unknown (phenomenological) parameters the pressure and the cooling rate,

$$p = p(T, \{n_i\}), \qquad \zeta(T, \{n_i\}) = \zeta^{(0)}(T, \{n_i\}) + \zeta_U(T, \{n_i\}) \nabla \cdot \mathbf{U}. \tag{2.1}$$

The pressure $p(T, \{n_i\})$ has been evaluated exactly in the previous paper [1] [Eqs. (7.18) and (7.19)] with the result

$$p(T, \{n_i\}) = nT + \frac{\pi^{d/2}}{d\Gamma\left(\frac{d}{2}\right)} \sum_{i=1}^{s} \sum_{j=1}^{s} \mu_{ji} \sigma_{ij}^d \chi_{ij}^{(0)} n_i n_j (1 + \alpha_{ij}) T_i, \tag{2.2}$$

where henceforth, for the sake of convenience, we will use the notation $T_i \equiv T_i^{(0)}$ with $T_i^{(0)}$ defined by Eq. (7.5) of Ref. [1]. Detailed forms for the functions $\chi_{ij}^{(0)}$ are discussed in Appendix C. The leading order cooling rate, $\zeta^{(0)}(T, \{n_i\})$, also is given there by Eq. (7.2) as an integral over $f_i^{(0)}$. For reasons just mentioned above, these integrals are performed using the leading order Sonine approximation for $f_i^{(0)}$

$$f_i^{(0)}(\mathbf{V}) \to f_{i,M}(\mathbf{V}) = n_i \left(\frac{m_i}{2\pi T_i}\right)^{d/2} \exp\left(-\frac{m_i V^2}{2T_i}\right), \tag{2.3}$$

and $\mathbf{V} = \mathbf{v} - \mathbf{U}$ is the peculiar velocity. The result is [14, 16]

$$\begin{aligned} \zeta^{(0)}(T, \{n_i\}) &= \zeta_i^{(0)}(T, \{n_i\}) \\ &= \frac{4\pi^{(d-1)/2}}{d\Gamma\left(\frac{d}{2}\right)} v_0 \sum_{j=1}^{s} \chi_{ij}^{(0)} n_j \mu_{ji} \sigma_{ij}^{d-1} \left(\frac{\theta_i + \theta_j}{\theta_i \theta_j}\right)^{1/2} (1 + \alpha_{ij}) \left[1 - \frac{\mu_{ji}}{2}(1 + \alpha_{ij}) \frac{\theta_i + \theta_j}{\theta_j}\right], \end{aligned} \tag{2.4}$$

where $n = \sum_i n_i$ is the total density, $v_0(t) = \sqrt{2T/m}$ is a thermal velocity, $m = (\sum_j m_j)/s$, $\mu_{ij} = m_i/(m_i + m_j)$, and $\theta_i = m_i T/m T_i$. The $\zeta_i^{(0)}(T, \{n_i\})$ are species cooling rates, measuring the decrease of kinetic energy of each species. This is an implicit definition of $\zeta^{(0)}(T, \{n_i\})$. The equality of cooling rates for all i gives $s-1$ equations for the species temperatures T_i in terms of T. A final equation is given by the condition that the total kinetic energy is the sum of species energies $nT = \sum_{i=1}^{s} n_i T_i$. With the species temperatures determined as functions of T and $\{n_i\}$, Eq. (2.4) gives the cooling rate $\zeta^{(0)}(T, \{n_i\})$. In all of the following expressions, it is understood that the $T_i(T, \{n_i\})$ have been determined in this way.

At first order in gradients, there is a contribution to the cooling rate from $\nabla \cdot \mathbf{U}$. The proportionality coefficient ζ_U is a new transport coefficient for granular fluids. Two different contributions can be identified

$$\zeta_U = \zeta^{(1,0)} + \zeta^{(1,1)}. \tag{2.5}$$

The coefficient $\zeta^{(1,0)}$ is given by an integral over $f_i^{(0)}$ and its velocity derivative. It has been evaluated explicitly in Appendix F of Ref. [1] with the result

$$\zeta^{(1,0)} = -\frac{3}{nT} \frac{\pi^{d/2}}{d^2 \Gamma\left(\frac{d}{2}\right)} \sum_{i=1}^{s} \sum_{j=1}^{s} n_i n_j \mu_{ji} \sigma_{ij}^d \chi_{ij}^{(0)} (1 - \alpha_{ij}^2) T_i. \tag{2.6}$$

The second term of Eq. (2.5), $\zeta^{(1,1)}$, is given by

$$\zeta^{(1,1)} = \frac{1}{nT}\frac{\pi^{(d-1)/2}}{d\Gamma\left(\frac{d+3}{2}\right)}\sum_{i=1}^{s}\sum_{j=1}^{s}\sigma_{ij}^{d-1}\chi_{ij}^{(0)}m_j\mu_{ij}(1-\alpha_{ij}^2)\int d\mathbf{v}_1\int d\mathbf{v}_2\, g^3 f_i^{(0)}(\mathbf{V}_1)\mathcal{D}_j(\mathbf{V}_2), \tag{2.7}$$

where the unknown functions $\mathcal{D}_i(\mathbf{V})$ are the solutions to the linear integral equations

$$\left(\left(\mathcal{L}+\frac{1}{2}\zeta^{(0)}\right)\mathcal{D}\right)_i + \frac{1}{2}\zeta^{(1,1)}(\mathcal{D}_i)\nabla_{\mathbf{V}}\cdot\left(\mathbf{V}f_i^{(0)}\right) = \overline{D}_i. \tag{2.8}$$

Here, $\nabla_{\mathbf{V}} \equiv \partial/\partial\mathbf{V}$ and the linear operator $\mathcal{L}$ is

$$\left(\mathcal{L}X\right)_i = \frac{1}{2}\zeta^{(0)}\nabla_{\mathbf{V}}\cdot(\mathbf{V}X_i) + \left(LX\right)_i, \tag{2.9}$$

where L is the linearized Enskog collision operator

$$\left(LX\right)_i = -\sum_{j=1}^{s}\left(J_{ij}^{(0)}\left[\mathbf{v}_1 \mid X_i, f_j^{(0)}\right] + J_{ij}^{(0)}\left[\mathbf{v}_1 \mid f_i^{(0)}, X_j\right]\right), \tag{2.10}$$

$$\begin{aligned} J_{ij}^{(0)}\left[\mathbf{v}_1 \mid X_i, f_j\right] \;\equiv\; & \chi_{ij}^{(0)}\left(\sigma_{ij};\{n_i\left(\mathbf{r}_1,t\right)\}\right)\sigma_{ij}^{d-1}\int d\mathbf{v}_2\int d\widehat{\boldsymbol{\sigma}}\Theta(\widehat{\boldsymbol{\sigma}}\cdot\mathbf{g}_{12})(\widehat{\boldsymbol{\sigma}}\cdot\mathbf{g}_{12}) \\ & \times\left[\alpha_{ij}^{-2}X_i(\mathbf{V}_1'')f_j(\mathbf{V}_2'') - X_i(\mathbf{V}_1)f_j(\mathbf{V}_2)\right], \end{aligned} \tag{2.11}$$

and $\mathbf{v}_1'', \mathbf{v}_2''$ are the precollision velocities associated with $\mathbf{v}_1, \mathbf{v}_2$ for the colliding pair of species i and j. The same linear operator $\mathcal{L}$ appears below in the definitions of all other transport coefficients as well. The inhomogeneity of Eq. (2.8), $\overline{D}_i(T,\{n_i\})$, is given by

$$\begin{aligned} \overline{D}_i \;=\; & \left(\frac{1}{d}\left(1-\frac{p}{nT}\right) - \frac{1}{2}\zeta^{(1,0)}\right)\nabla_{\mathbf{V}}\cdot\left(\mathbf{V}f_i^{(0)}\right) - f_i^{(0)} + \sum_{j=1}^{s} n_j\frac{\partial f_i^{(0)}}{\partial n_j} \\ & + \frac{1}{d}\sum_{j=1}^{s}\mathcal{K}_{ij,\beta}[\partial_{V_\beta}f_j^{(0)}], \end{aligned} \tag{2.12}$$

and the operator $\mathcal{K}_{ij,\beta}$ is given by (B1) of Appendix B. An approximate solution to this integral equation is obtained by using $f_i^{(0)}$, p, $\zeta^{(0)}$, and $\zeta^{(1,0)}$ as determined above, and the leading order term in an expansion of $\mathcal{D}_i(\mathbf{V})$ in a complete set of Sonine polynomials

$$\mathcal{D}_i(\mathbf{V}) \to e_{i,D}f_{i,M}(\mathbf{V})F_i(\mathbf{V}). \tag{2.13}$$

The lowest order Sonine polynomial contributing in this case is

$$F_i(\mathbf{V}) = \left(\frac{m_i}{2T_i}\right)^2 V^4 - \frac{d+2}{2}\frac{m_i}{T_i}V^2 + \frac{d(d+2)}{4}, \tag{2.14}$$

as determined by the fact that $\mathcal{D}_i(\mathbf{V})$ is a scalar and orthogonal to 1 and V^2. Finally, $e_{i,D}$ is the projection of $\mathcal{D}_i$ along F_i

$$e_{i,D} = \frac{2}{d(d+2)}\frac{1}{n_i}\int d\mathbf{v}\;\mathcal{D}_i(\mathbf{V})F_i(\mathbf{V}). \tag{2.15}$$

Note that the polynomials are defined for each species in terms of the weight factor $f_{i,M}(\mathbf{V})$ characterized by the mass and temperature of that species [11]. The coefficients $e_{i,D}$ are determined by substituting (2.13) into the integral equation (2.8), multiplying by $F_i(\mathbf{V})$, and integrating over $\mathbf{V}$ (this assures that the integral equation is exactly satisfied in the subspace spanned F_i) to get the algebraic equations

$$\sum_{j=1}^{s}\left(\psi_{ij} - \frac{3}{2}\zeta^{(0)}\delta_{ij}\right)e_{j,D} = \overline{e}_{i,D}. \tag{2.16}$$

The collision frequencies ψ_{ij} are defined by

$$\psi_{ii} = -\frac{2}{d(d+2)}\frac{1}{n_i}\left(\sum_{j=1}^{s}\int d\mathbf{v}\, F_i J_{ij}^{(0)}[f_{i,M}F_i, f_j^{(0)}] + \int d\mathbf{v}\, F_i J_{ii}^{(0)}[f_i^{(0)}, f_{i,M}F_i]\right), \tag{2.17}$$

$$\psi_{ij} = -\frac{2}{d(d+2)}\frac{1}{n_i}\int d\mathbf{v}\, F_i J_{ij}^{(0)}[f_i^{(0)}, f_{j,M}F_j], \quad (i\neq j). \tag{2.18}$$

The inhomogeneity on the right-hand side of (2.16) is computed in Appendix B with the result

$$\begin{aligned}
\overline{e}_{i,D} &= \frac{1}{d}\sum_{j=1}^{s}\int d\mathbf{v}\, F_i(\mathbf{V})\mathcal{K}_{ij,\gamma}[\partial_{V_\gamma} f_j^{(0)}] \\
&= \frac{\pi^{d/2}}{4d\Gamma\left(\frac{d}{2}\right)}\sum_{j=1}^{s} n_i n_j \chi_{ij}^{(0)}\sigma_{ij}^d \mu_{ji}(1+\alpha_{ij})\left[8(d+2)(\mu_{ij}-1)\right. \\
&\quad +4(13+2d+9\alpha_{ij})\mu_{ji} - 48\mu_{ji}^2\theta_j^{-1}(\theta_i+\theta_j)(1+\alpha_{ij})^2 \\
&\quad \left.+15\mu_{ji}^3\theta_j^{-2}(\theta_i+\theta_j)^2(1+\alpha_{ij})^3\right].
\end{aligned} \tag{2.19}$$

The explicit form of the collision frequencies ψ_{ij} are displayed in Appendix A, so the coefficients $e_{i,D}$ can be determined by solving the algebraic Eqs. (2.16) with all coefficients determined.

Finally, $\zeta^{(1,1)}$ is given in terms of $e_{i,D}$ by substitution of Eq. (2.13) into (2.7), with the result

$$\zeta^{(1,1)} = e_{i,D}\frac{3\pi^{(d-1)/2}}{4d\Gamma\left(\frac{d}{2}\right)}\frac{v_0^3}{nT}\sum_{i=1}^{s}\sum_{j=1}^{s}\sigma_{ij}^{d-1}\chi_{ij}^{(0)} m_j\mu_{ij}(1-\alpha_{ij}^2)\theta_i^{-3/2}\theta_j^{1/2}(\theta_i+\theta_j)^{-1/2}. \tag{2.20}$$

III. NAVIER-STOKES ORDER TRANSPORT COEFFICIENTS

The hydrodynamic equations to second order in the spatial gradients have contributions to the mass flux, pressure tensor, and heat flux from the Chapman-Enskog expansion proportional to gradients of the species densities, temperature, and flow velocity and to an external applied force (of the same order of magnitude as the gradients). For fluid symmetry, this leads to $(s-1)(2s+1)$ transport coefficients for the mass flux, the shear and bulk viscosity for the pressure tensor, and $2s^2+1$ coefficients for the heat flux. The mass flux coefficients are determined from integral equations in the same way as $\zeta^{(1,1)}$, just described. The pressure tensor and heat fluxes have "kinetic" and "collisional" transfer parts, i.e. of the forms

$$\omega = \omega^k + \omega^c.$$

The contributions ω^k are determined from integral equations like that for $\zeta^{(1,1)}$; the collisional transfer contributions have been reduced in the previous paper to specific integrals over $f_i^{(0)}$ and can be computed explicitly by using the multi-temperature Maxellians (2.3). The analysis is similar to that for the cooling rate and many of the details are transferred to the Appendices.

A. Mass Flux

To first order in the spatial gradients, the mass flux $\mathbf{j}_{0i}^{(1)}$ is given by

$$\mathbf{j}_{0i}^{(1)} = -\sum_{j=1}^{s}\frac{m_i m_j n_j}{\rho}D_{ij}\nabla\ln n_j - \rho D_i^T\nabla\ln T - \sum_{j=1}^{s}D_{ij}^F\mathbf{F}_j, \tag{3.1}$$

where $\rho = \sum_i \rho_i = \sum_i m_i n_i$ is the total mass density of the mixture, D_{ij} are the mutual diffusion coefficients, D_i^T are the thermal diffusion coefficients and D_{ij}^F are the mobility coefficients. These transport coefficients are defined as

$$D_{ij} = -\frac{\rho}{dm_j n_j}\int d\mathbf{v}\,\mathbf{V}\cdot\boldsymbol{\mathcal{B}}_i^j(\mathbf{V}), \tag{3.2}$$

$$D_i^T = -\frac{m_i}{d\rho}\int d\mathbf{v}\,\mathbf{V}\cdot\boldsymbol{\mathcal{A}}_i(\mathbf{V}), \tag{3.3}$$

$$D_{ij}^F = -\frac{m_i}{d}\int d\mathbf{v}\,\mathbf{V}\cdot\boldsymbol{\mathcal{E}}_i^j(\mathbf{V}). \tag{3.4}$$

The functions $\mathcal{A}_i(\mathbf{V})$, $\mathcal{B}_i^j(\mathbf{V})$, and $\boldsymbol{\mathcal{E}}_i^j(\mathbf{V})$ verify the linear integral equations

$$\left(\left(\mathcal{L}-\frac{1}{2}\zeta^{(0)}\right)\boldsymbol{\mathcal{A}}\right)_i = \mathbf{A}_i, \tag{3.5}$$

$$\left(\mathcal{L}\boldsymbol{\mathcal{B}}^j\right)_i - n_j\frac{\partial\zeta^{(0)}}{\partial n_j}\boldsymbol{\mathcal{A}}_i = \mathbf{B}_i^j, \tag{3.6}$$

$$\left(\left(\mathcal{L}+\zeta^{(0)}\right)\boldsymbol{\mathcal{E}}^j\right)_i = \mathbf{E}_i^j, \tag{3.7}$$

where the linear operator $\mathcal{L}$ and the inhomogeneous terms $\mathbf{A}_i$, $\mathbf{B}_i^j$, and $\mathbf{E}_i^j$ are given by Eqs. (6.16), (6.17), and (6.20) of the preceding paper [1]. The approximate solutions to these equations are obtained in the same manner as that for (2.8). The leading order Sonine polynomial in all of these cases is $\mathbf{V}$, since all are vectors

$$\boldsymbol{\mathcal{A}}_i(\mathbf{V}) \to -\frac{\rho}{n_iT_i}D_i^T f_{i,M}(\mathbf{V})\mathbf{V}, \tag{3.8}$$

$$\boldsymbol{\mathcal{B}}_i^j(\mathbf{V}) \to -\frac{m_im_jn_j}{\rho n_iT_i}D_{ij} f_{i,M}(\mathbf{V})\mathbf{V}, \tag{3.9}$$

$$\boldsymbol{\mathcal{E}}_i^j(\mathbf{V}) \to -\frac{1}{n_iT_i}D_{ij}^F f_{i,M}(\mathbf{V})\mathbf{V}, \tag{3.10}$$

The coefficients are now projections of $\boldsymbol{\mathcal{A}}_i$, $\boldsymbol{\mathcal{B}}_i^j$, and $\boldsymbol{\mathcal{E}}_i^j$ along $\mathbf{V}$, which are identified in terms of the transport coefficients through Eqs. (3.2)–(3.4). Multiplication of Eqs. (3.5)–(3.7) by $m_i\mathbf{V}$ and integrating over the velocity yields the algebraic equations determining all mass flux transport coefficients

$$\sum_{j=1}^s(\nu_{ij}-\zeta^{(0)}\delta_{ij})D_j^T = -\frac{1}{d\rho}\int d\mathbf{v}\,m_i\mathbf{V}\cdot\mathbf{A}_i(\mathbf{V}), \tag{3.11}$$

$$\sum_{\ell=1}^s\left(\nu_{i\ell}-\frac{1}{2}\zeta^{(0)}\delta_{i\ell}\right)\frac{m_\ell}{m_i}D_{\ell j} - \frac{\rho^2}{m_im_j}\frac{\partial\zeta^{(0)}}{\partial n_j}D_i^T = -\frac{1}{d}\frac{\rho}{m_im_jn_j}\int d\mathbf{v}\,m_i\mathbf{V}\cdot\mathbf{B}_i^j(\mathbf{V}), \tag{3.12}$$

$$\sum_{\ell=1}^s\left(\nu_{i\ell}+\frac{1}{2}\zeta^{(0)}\delta_{i\ell}\right)\frac{m_\ell}{m_i}D_{\ell j}^F = -\frac{1}{d}\int d\mathbf{v}\,m_i\mathbf{V}\cdot\mathbf{E}_i^j(\mathbf{V}). \tag{3.13}$$

The new collision frequencies ν_{ij} are

$$\nu_{ii} = -\frac{1}{dn_iT_i}\sum_{j\neq i}^s\int d\mathbf{v}\,m_i\mathbf{V}\cdot J_{ij}^{(0)}[f_{i,M}\mathbf{V}, f_j^{(0)}], \tag{3.14}$$

$$\nu_{ij} = -\frac{1}{dn_jT_j}\int d\mathbf{v}\,m_i\mathbf{V}\cdot J_{ij}^{(0)}[f_i^{(0)}, f_{j,M}\mathbf{V}], \quad (i\neq j). \tag{3.15}$$

Note that the self-collision terms of ν_{ii} arising from $J_{ii}^{(0)}[f_{i,M}\mathbf{V}, f_i^{(0)}]$ do not occur in (3.14) since these conserve momentum for species i. The above collision frequencies were already evaluated in the Boltzmann limit (except for

the factors $\chi_{ij}^{(0)}$) [11, 16]. The details will not repeated here and only the results are quoted in Appendix A. The integrals on the right hand side of Eqs. (3.11), (3.12), and (3.13) can be performed using the definitions of $\mathbf{A}_i$, $\mathbf{B}_i^j$, and $\mathbf{E}_i^j$. The result is

$$\int d\mathbf{v}\, m_i \mathbf{V}\cdot\mathbf{A}_i = dp\frac{\rho_i}{\rho}\left(1-\frac{\rho n_i T_i}{\rho_i p}\right)+\frac{1}{2}\sum_{j=1}^{s}\int d\mathbf{v}\, m_i V_\gamma \mathcal{K}_{ij,\gamma}[\nabla_{\mathbf{V}}\cdot(\mathbf{V}f_j^{(0)})], \tag{3.16}$$

$$\begin{aligned}\int d\mathbf{v}\, m_i \mathbf{V}\cdot\mathbf{B}_i^j \;=\; & -dn_j\frac{\partial}{\partial n_j}(n_iT_i)+d\frac{\rho_i}{\rho}n_j\frac{\partial p}{\partial n_j}\\ & -\sum_{\ell=1}^{s}\int d\mathbf{v}\, m_i V_\gamma \mathcal{K}_{i\ell,\gamma}\left[\left(n_j\partial_{n_j}+\frac{1}{2}\left(n_j\partial_{n_j}\ln\chi_{i\ell}^{(0)}+I_{i\ell j}\right)\right)f_\ell^{(0)}\right],\end{aligned} \tag{3.17}$$

$$\int d\mathbf{v}\, m_i \mathbf{V}\cdot\mathbf{E}_i^j = d\frac{n_i m_i}{m_j}\left(\delta_{ij}-\frac{n_j m_j}{\rho}\right). \tag{3.18}$$

The integrals appearing in Eqs. (3.16) and (3.17) that involve the operator $\mathcal{K}_{ij,\gamma}[X]$ have been evaluated in Appendix B. They are given by Eqs. (A18), (B6), and (B7). With these results, Eqs. (3.11), (3.12), and (3.13) become

$$\sum_{j=1}^{s}(\nu_{ij}-\zeta^{(0)}\delta_{ij})D_j^T = -\frac{p\rho_i}{\rho^2}\left(1-\frac{\rho n_i T_i}{\rho_i p}\right)+\frac{\pi^{d/2}}{d\Gamma\left(\frac{d}{2}\right)}\frac{n_i}{\rho}\sum_{j=1}^{s}n_j\mu_{ij}\chi_{ij}^{(0)}\sigma_{ij}^d T_j(1+\alpha_{ij}), \tag{3.19}$$

$$\begin{aligned}\sum_{\ell=1}^{s}\left(\nu_{i\ell}-\frac{1}{2}\zeta^{(0)}\delta_{i\ell}\right)\frac{m_\ell}{m_i}D_{\ell j} \;=\; & \frac{\rho^2}{m_i m_j}\frac{\partial\zeta^{(0)}}{\partial n_j}D_i^T+\frac{\rho}{m_i m_j}\frac{\partial}{\partial n_j}(n_iT_i)-\frac{n_i}{m_j}\frac{\partial p}{\partial n_j}\\ & +\frac{\pi^{d/2}}{d\Gamma\left(\frac{d}{2}\right)}\frac{\rho n_i}{m_j}\sum_{\ell=1}^{s}\chi_{i\ell}^{(0)}\,\sigma_{i\ell}^d\,\mu_{\ell i}(1+\alpha_{i\ell})\left\{\left(\frac{T_i}{m_i}+\frac{T_\ell}{m_\ell}\right)\right.\\ & \left.\times\left[\delta_{j\ell}+\frac{1}{2}\frac{n_\ell}{n_j}\left(n_j\frac{\partial}{\partial n_j}\ln\chi_{i\ell}^{(0)}+I_{i\ell j}\right)\right]+\frac{n_\ell T_\ell}{m_\ell}\frac{\partial}{\partial n_j}\ln\gamma_\ell\right\},\end{aligned} \tag{3.20}$$

$$\sum_{\ell=1}^{s}\left(\nu_{i\ell}+\frac{1}{2}\zeta^{(0)}\delta_{i\ell}\right)\frac{m_\ell}{m_i}D_{\ell j}^F = -\frac{n_i m_i}{m_j}\left(\delta_{ij}-\frac{n_j m_j}{\rho}\right), \tag{3.21}$$

where $\gamma_i \equiv T_i/T$ is the temperature ratio. An explicit form for $I_{i\ell j}$ is chosen in Appendix C. The solution of the set of algebraic equations (3.19)–(3.21) gives the dependence of the coefficients D_{ij}, D_i^T, and D_{ij}^F on the restitution coefficients α_{ij} and the composition, the density, and the sizes and masses of the constituents of the mixture.

B. Pressure Tensor

The constitutive equation for the pressure tensor $P_{\alpha\beta}^{(1)}$, proportional to the velocity gradients, is

$$P_{\alpha\beta}^{(1)} = -\eta\left(\partial r_\alpha U_\beta+\partial r_\beta U_\alpha-\frac{2}{d}\delta_{\alpha\beta}\nabla\cdot\mathbf{u}\right)-\kappa\delta_{\alpha\beta}\nabla\cdot\mathbf{u}. \tag{3.22}$$

Here, η is the shear viscosity coefficient and κ is the bulk viscosity. The coefficient η has kinetic and collisional contributions while κ only has a collisional contribution κ^c (and so, vanishes for dilute gases)

$$\eta = \eta^k+\eta^c, \qquad \kappa = \kappa^c. \tag{3.23}$$

The collisional transfer contributions have been analyzed in the preceding paper [1] [Eqs. (7.21) and (7.22)]. These expressions reduce to those previously derived in the monodisperse case [14, 15], and in the case of binary mixtures of

hard spheres [17]. The integrals over $f_i^{(0)}(\mathbf{V})$ are easily performed in the multi-temperature Maxwellian approximation (2.3) with the results

$$\kappa^c = \frac{\pi^{(d-1)/2}}{d^2\Gamma\left(\frac{d}{2}\right)}\sum_{i=1}^{s}\sum_{j=1}^{s}\frac{m_i m_j}{m_i+m_j}n_i n_j v_0 \sigma_{ij}^{d+1}\chi_{ij}^{(0)}(1+\alpha_{ij})\left(\frac{\theta_i+\theta_j}{\theta_i\theta_j}\right)^{1/2}, \tag{3.24}$$

$$\eta^c = \frac{2\pi^{d/2}}{\Gamma\left(\frac{d}{2}\right)}\frac{1}{d(d+2)}\sum_{i=1}^{s}\sum_{j=1}^{s}n_j\sigma_{ij}^d\chi_{ij}^{(0)}\mu_{ji}(1+\alpha_{ij})\eta_i^k + \frac{d}{d+2}\kappa^c. \tag{3.25}$$

1. *Kinetic contribution η^k*

As noted above, there is no kinetic part of the bulk viscosity, $\kappa^k = 0$, so κ is given entirely by (3.24). The kinetic contribution to the shear viscosity, η^k, is defined by

$$\eta^k = \sum_{i=1}^{s}\eta_i^k = -\frac{1}{(d-1)(d+2)}\sum_{i=1}^{s}\int d\mathbf{v}\; m_i V_\alpha V_\beta \mathcal{C}_{i,\alpha\beta}(\mathbf{V}). \tag{3.26}$$

The second equality identifies the partial contribution η_i^k of the species i to the shear viscosity η^k in terms of $\mathcal{C}_{i,\alpha\beta}(\mathbf{V})$, which is the solution to the integral equation

$$\left(\left(\mathcal{L}+\frac{1}{2}\zeta^{(0)}\right)\mathcal{C}_{\alpha\beta}\right)_i = C_{i,\alpha\beta}, \tag{3.27}$$

where $C_{i,\alpha\beta}$ is given by Eq. (6.18) in the preceding paper [1]. It is symmetric and traceless so the leading Sonine approximation for the function $\mathcal{C}_{i,\alpha\beta}(\mathbf{V})$ is

$$\mathcal{C}_{i,\alpha\beta}(\mathbf{V}) \to -f_{i,M}(\mathbf{V})\frac{\eta_i^k}{n_i T_i^2}R_{i,\alpha\beta}(\mathbf{V}), \tag{3.28}$$

where

$$R_{i,\alpha\beta}(\mathbf{V}) = m_i\left(V_\alpha V_\beta - \frac{1}{d}V^2\delta_{\alpha\beta}\right). \tag{3.29}$$

The partial contributions η_i^k are obtained by multiplying the integral equation (3.27) with $R_{i,\alpha\beta}$ and integrating over the velocity to get the set of equations:

$$\sum_{j=1}^{s}(\tau_{ij}-\frac{1}{2}\zeta^{(0)}\delta_{ij})\eta_j^k = n_i T_i - \frac{1}{(d-1)(d+2)}\sum_{j=1}^{s}\int d\mathbf{v}\, R_{i,\alpha\beta}\mathcal{K}_{ij,\alpha}[\partial_{V_\beta}f_j^{(0)}], \tag{3.30}$$

The collision frequencies τ_{ii} are

$$\tau_{ii} = -\frac{1}{(d-1)(d+2)}\frac{1}{n_i T_i^2}\left(\sum_{j=1}^{s}\int d\mathbf{v}\, R_{i,\alpha\beta}J_{ij}^{(0)}[f_{i,M}R_{i,\alpha\beta}, f_j^{(0)}] + \int d\mathbf{v}\, R_{i,\alpha\beta}J_{ii}^{(0)}[f_i^{(0)}, f_{i,M}R_{i,\alpha\beta}]\right), \tag{3.31}$$

$$\tau_{ij} = -\frac{1}{(d-1)(d+2)}\frac{1}{n_j T_j^2}\int d\mathbf{v}\, R_{i,\alpha\beta}J_{ij}^{(0)}[f_i^{(0)}, f_{j,M}R_{j,\alpha\beta}], \quad (i\neq j). \tag{3.32}$$

The explicit forms of τ_{ii} and τ_{ij} are displayed in Appendix A, and the integral appearing on the right hand side of Eq. (3.30) has been evaluated in Appendix B with the result

$$\begin{aligned}\int d\mathbf{v}\, R_{i,\alpha\beta}\mathcal{K}_{ij,\alpha}[\partial_{V_\beta}f_j^{(0)}] \;=\; & -\frac{\pi^{d/2}}{\Gamma\left(\frac{d}{2}\right)}\frac{d-1}{d}m_i n_i n_j \mu_{ji}\sigma_{ij}^d\chi_{ij}^{(0)}(1+\alpha_{ij}) \\ & \times\left[\mu_{ji}(3\alpha_{ij}-1)\left(\frac{T_i}{m_i}+\frac{T_j}{m_j}\right) - 4\frac{T_i-T_j}{m_i+m_j}\right].\end{aligned} \tag{3.33}$$

In the case of a three-dimensional system ($d = 3$), Eq. (3.33) reduces to the one previously derived for hard spheres [17]. In addition, for identical particles previous results [12, 15] obtained for monodisperse gases are also recovered.

With the right side of Eqs. (3.30) now determined the algebraic equations

$$\sum_{j=1}^{s}(\tau_{ij}-\frac{1}{2}\zeta^{(0)}\delta_{ij})\eta_j^k = n_iT_i+\frac{m_in_in_j\mu_{ji}}{d(d+2)\Gamma\left(\frac{d}{2}\right)}\pi^{d/2}\sigma_{ij}^d\chi_{ij}^{(0)}(1+\alpha_{ij}) \times\left[\mu_{ji}(3\alpha_{ij}-1)\left(\frac{T_i}{m_i}+\frac{T_j}{m_j}\right)-4\frac{T_i-T_j}{m_i+m_j}\right], \tag{3.34}$$

can be solved to determine the partial contributions η_i^k. Their sum then gives the kinetic contribution to the shear viscosity, η^k. Finally, adding this to the collisional transfer contribution of (3.25) gives the total shear viscosity.

C. Heat Flux

The constitutive equation for the heat flux $\mathbf{q}^{(1)}$ has contributions proportional to gradients of the densities and the temperature, and terms proportional to an applied force (taken to have the same order of magnitude as the gradients)

$$\mathbf{q}^{(1)} = -\sum_{i=1}^{s}\sum_{j=1}^{s}\left(T^2D_{q,ij}\nabla\ln n_j+L_{ij}\mathbf{F}_j\right)-T\lambda\nabla\ln T, \tag{3.35}$$

where λ is the thermal conductivity coefficient and $D_{q,ij}$ are the Dufour coefficients. As in the case of the shear viscosity, the transport coefficients $D_{q,ij}$, L_{ij} and λ have kinetic and collisional contributions

$$D_{q,ij}=D_{q,ij}^k+D_{q,ij}^c, \qquad L_{ij}=L_{ij}^k+L_{ij}^c, \qquad \lambda=\lambda^k+\lambda^c. \tag{3.36}$$

The collisional transfer contributions λ^c, $D_{q,ij}^c$, and L_{ij}^c are given in the preceding paper by Eqs. (7.14)–(7.16)

$$\lambda^c = \sum_{i=1}^{s}\sum_{j=1}^{s}\frac{1}{8}(1+\alpha_{ij})m_j\mu_{ij}\sigma_{ij}^d\chi_{ij}^{(0)}\left\{2B_4(1-\alpha_{ij})(\mu_{ij}-\mu_{ji})n_i\left[\frac{2}{m_j}\lambda_j^k+(d+2)\frac{T_i}{m_im_jT}\rho D_j^T\right] +\frac{8B_2}{2+d}n_i\left[\frac{2\mu_{ij}}{m_j}\lambda_j^k-(d+2)\frac{T_i}{m_im_jT}(2\mu_{ij}-\mu_{ji})\rho D_j^T\right]-T^{-1}C_{ij}^T\right\}, \tag{3.37}$$

$$D_{q,ij}^c = \sum_{p=1}^{s}\frac{1}{8}(1+\alpha_{ip})m_p\mu_{ip}\sigma_{ip}^d\chi_{ip}^{(0)}\{2B_4(1-\alpha_{ip})(\mu_{ip}-\mu_{pi}) \times n_i\left[\frac{2}{m_p}D_{q,pj}^k+(d+2)\frac{T_i}{T^2}\frac{m_jn_j}{\rho m_i}D_{pj}\right] +\frac{8B_2}{d+2}n_i\left[\frac{2\mu_{pi}}{m_p}D_{q,pj}^k-(d+2)(2\mu_{ip}-\mu_{pi})\frac{T_i}{T^2}\frac{n_jm_j}{\rho m_i}D_{pj}\right]-T^{-2}C_{ipj}^T\right\}, \tag{3.38}$$

$$L_{ij}^c = \sum_{p=1}^{s}\frac{1}{8}(1+\alpha_{ip})m_p\mu_{ip}\sigma_{ip}^d\chi_{ip}^{(0)}\{2B_4(1-\alpha_{ip})(\mu_{ip}-\mu_{pi}) \times n_i\left[\frac{2}{m_p}L_{pj}^k+(d+2)\frac{T_i}{m_im_p}D_{pj}^F\right] +\frac{8B_2}{d+2}n_i\left[\frac{2\mu_{pi}}{m_p}L_{pj}^k-(d+2)(2\mu_{ip}-\mu_{pi})\frac{T_i}{m_im_p}D_{pj}^F\right]\right\}. \tag{3.39}$$

The constants, B_k, are defined by Eq. (A19) of Appendix A, and

$$C_{ij}^T = -\frac{2B_3}{d}\int d\mathbf{v}_1\int d\mathbf{v}_2f_i^{(0)}(\mathbf{V}_1)f_j^{(0)}(\mathbf{V}_2)\left\{gG_{ij}^2+g^{-1}(\mathbf{g}\cdot\mathbf{G}_{ij})^2+(1+\mu_{ji})g(\mathbf{g}\cdot\mathbf{G}_{ij}) +\mu_{ji}\mu_{ij}g^3+\frac{3}{4}(1-\alpha_{ij})(\mu_{ji}-\mu_{ij})\left[g(\mathbf{g}\cdot\mathbf{G}_{ij})+g^3\right]\right\}, \tag{3.40}$$

$$C_{ipj}^T = \frac{B_3}{d}\int d\mathbf{v}_1 \int d\mathbf{v}_2 \left[-(1-\alpha_{ip})(\mu_{ip}-\mu_{pi})\, g^3 + 4g\,(\mathbf{g}\cdot\mathbf{G}_{ip})\right] f_i^{(0)}(\mathbf{V}_1) n_j \partial_{n_j} f_p^{(0)}(\mathbf{V}_2), \tag{3.41}$$

where $\mathbf{G}_{ip} = \mu_{ip}\mathbf{V}_1 + \mu_{pi}\mathbf{V}_2$. In the first Sonine approximation these integrals have the explicit forms

$$\begin{aligned} C_{ij}^T &= -\frac{2\pi^{(d-1)/2}}{d\Gamma\left(\frac{d}{2}\right)} n_i n_j v_0^3 (\theta_i+\theta_j)^{-1/2}(\theta_i\theta_j)^{-3/2} \\ &\times \left\{2\beta_{ij}^2 + \theta_i\theta_j + (\theta_i+\theta_j)\left[(\theta_i+\theta_j)\mu_{ij}\mu_{ji} + \beta_{ij}(1+\mu_{ji})\right]\right\} \\ &-\frac{3\pi^{(d-1)/2}}{2d\Gamma\left(\frac{d}{2}\right)} n_i n_j v_0^3 (1-\alpha_{ij})(\mu_{ji}-\mu_{ij}) \left(\frac{\theta_i+\theta_j}{\theta_i\theta_j}\right)^{3/2} \left[\mu_{ji} + \beta_{ij}(\theta_i+\theta_j)^{-1}\right], \end{aligned} \tag{3.42}$$

$$\begin{aligned} C_{ipj}^T &= \frac{4\pi^{(d-1)/2}}{d\Gamma\left(\frac{d}{2}\right)} n_i n_p v_0^3 (\theta_i+\theta_p)^{-1/2}(\theta_i\theta_p)^{-3/2} \left\{\delta_{jp}\beta_{ip}(\theta_i+\theta_p)\right. \\ &\left. -\frac{1}{2}\theta_i\theta_p\left[1 + \frac{\mu_{pi}(\theta_i+\theta_p) - 2\beta_{ip}}{\theta_p}\right]\frac{\partial \ln \gamma_p}{\partial \ln n_j}\right\} \\ &+\frac{\pi^{(d-1)/2}}{d\Gamma\left(\frac{d}{2}\right)} n_i n_p v_0^3 (1-\alpha_{ip})(\mu_{pi}-\mu_{ip}) \left(\frac{\theta_i+\theta_p}{\theta_i\theta_p}\right)^{3/2} \left(\delta_{jp} + \frac{3}{2}\frac{\theta_i}{\theta_i+\theta_p}\frac{\partial \ln \gamma_p}{\partial \ln n_j}\right), \end{aligned} \tag{3.43}$$

where $\beta_{ip} \equiv \mu_{ip}\theta_p - \mu_{pi}\theta_i$. With these expressions, the collisional contributions to the heat flux are explicitly known. For mechanically equivalent particles, all the above expressions for the collision transfer contributions reduce again to the previous results obtained for monocomponent gases [14, 15].

1. Kinetic contributions

The kinetic parts of the transport coefficients λ^k, $D_{q,ij}^k$, L_{ij}^k are defined respectively as

$$\lambda^k = -\frac{1}{dT}\sum_{i=1}^s \int d\mathbf{v}\, \frac{m_i}{2} V^2 \mathbf{V}\cdot\boldsymbol{\mathcal{A}}_i(\mathbf{V}), \tag{3.44}$$

$$D_{q,ij}^k = -\frac{1}{dT^2}\int d\mathbf{v}\, \frac{m_i}{2} V^2 \mathbf{V}\cdot\boldsymbol{\mathcal{B}}_i^j(\mathbf{V}), \tag{3.45}$$

$$L_{ij}^k = -\frac{1}{d}\int d\mathbf{v}\, \frac{m_i}{2} V^2 \mathbf{V}\cdot\boldsymbol{\mathcal{E}}_i^j(\mathbf{V}). \tag{3.46}$$

where $\boldsymbol{\mathcal{A}}_i(\mathbf{V})$, $\boldsymbol{\mathcal{B}}_i^j(\mathbf{V})$, and $\boldsymbol{\mathcal{E}}_i^j(\mathbf{V})$ are again the solutions to (3.5)–(3.7). The leading Sonine approximations of (3.8)–(3.10) are not adequate to determine the general leading order for these transport coefficients, since the coefficients D_i^T, D_{ij}, and D_{ij}^F vanish for a simple one component fluid. This would imply a vanishing thermal conductivity λ as well. Consequently, it is necessary to include here the next (second order) Sonine polynomial

$$\boldsymbol{\mathcal{A}}_i(\mathbf{V}) \to f_{i,M}(\mathbf{V})\left[-\frac{\rho}{n_i T_i}\mathbf{V}D_i^T - \frac{2}{d+2}\frac{T m_i}{n_i T_i^3}\lambda_i \mathbf{S}_i(\mathbf{V})\right], \tag{3.47}$$

$$\boldsymbol{\mathcal{B}}_i^j(\mathbf{V}) \to f_{i,M}(\mathbf{V})\left[-\frac{m_i m_j n_j}{\rho n_i T_i}\mathbf{V}D_{ij} - \frac{2}{d+2}\frac{T^2 m_i}{n_i T_i^3} d_{q,ij}\mathbf{S}_i(\mathbf{V})\right], \tag{3.48}$$

$$\boldsymbol{\mathcal{E}}_i^j(\mathbf{V}) \to f_{i,M}(\mathbf{V})\left[-\frac{1}{n_i T_i}\mathbf{V}D_{ij}^F - \frac{2}{d+2}\frac{m_i}{n_i T_i^3}\ell_{ij}\mathbf{S}_i(\mathbf{V})\right], \tag{3.49}$$

where the next order polynomial $\mathbf{S}_i(\mathbf{V})$ is

$$\mathbf{S}_i(\mathbf{V}) = \left(\frac{1}{2}m_i V^2 - \frac{d+2}{2}T_i\right)\mathbf{V}. \tag{3.50}$$

In the above equations, it is understood that the transport coefficients D_i^T, D_{ij}, and D_{ij}^F are given by Eqs. (3.19)–(3.21), respectively. The coefficients λ_i, $d_{q,ij}$, and ℓ_{ij} are the projections along $\mathbf{S}_i$:

$$\lambda_i = -\frac{1}{dT}\int d\mathbf{v}\ \mathbf{S}_i(\mathbf{V})\cdot\boldsymbol{\mathcal{A}}_i(\mathbf{V}), \tag{3.51}$$

$$d_{q,ij} = -\frac{1}{dT^2}\int d\mathbf{v}\ \mathbf{S}_i(\mathbf{V})\cdot\boldsymbol{\mathcal{B}}_i^j(\mathbf{V}), \tag{3.52}$$

$$\ell_{ij} = -\frac{1}{d}\int d\mathbf{v}\ \mathbf{S}_i(\mathbf{V})\cdot\boldsymbol{\mathcal{E}}_i^j(\mathbf{V}). \tag{3.53}$$

In terms of λ_i, $d_{q,ij}$ and ℓ_{ij}, the transport coefficients λ^k, $D_{q,ij}^k$, and L_{ij}^k become

$$\lambda^k = \sum_{i=1}^s \lambda_i + \frac{d+2}{2T}\frac{\rho T_i}{m_i}D_i^T, \tag{3.54}$$

$$D_{q,ij}^k = d_{q,ij} + \frac{d+2}{2T^2}\frac{m_j n_j T_i}{\rho}D_{ij}. \tag{3.55}$$

$$L_{ij}^k = \ell_{ij} + \frac{d+2}{2}\frac{T_i}{m_i}D_{ij}^F. \tag{3.56}$$

Since D_i^T, D_{ij}, and D_{ij}^F are known from the analysis above it remains to determine λ_i, $d_{q,ij}$ and ℓ_{ij}. The algebraic equations determining them are obtained by substituting (3.47)–(3.49) into the integral equations (3.5)–(3.7), multiplying Eq. (3.5) by $\mathbf{S}_i(\mathbf{V})$ and integrating over the velocity. The results are

$$\sum_{j=1}^s(\gamma_{ij} - 2\zeta^{(0)}\delta_{ij})\lambda_j = \overline{\lambda}_i, \tag{3.57}$$

$$\sum_{\ell=1}^s\left(\gamma_{i\ell} - \frac{3}{2}\zeta^{(0)}\delta_{i\ell}\right)d_{q,\ell j} = \overline{d}_{q,ij} \tag{3.58}$$

$$\sum_{k=1}^s\left(\gamma_{ik} - \frac{1}{2}\zeta^{(0)}\delta_{ik}\right)\ell_{kj} = \overline{\ell}_{ij}, \tag{3.59}$$

with the inhomogeneities given by

$$\begin{aligned}\overline{\lambda}_i &= -\frac{d+2}{2}\frac{\rho}{T_i}\frac{n_i T_i^3}{T m_i}\sum_{j=1}^s\frac{\omega_{ij}-\zeta^{(0)}\delta_{ij}}{n_j T_j}D_j^T + \frac{d(d+2)}{2d}\frac{n_i T_i^2}{m_i T}\\ &\quad -\frac{1}{2Td}\sum_{j=1}^s\int d\mathbf{v}\, S_{i,\beta}(\mathbf{V})\mathcal{K}_{ij,\beta}[\nabla_{\mathbf{V}}\cdot(\mathbf{V}f_j^{(0)})],\end{aligned} \tag{3.60}$$

$$\begin{aligned}\overline{d}_{q,ij} &= -\frac{d+2}{2}\frac{n_i n_j T_i^3}{m_i T^2}\left(\frac{m_j}{\rho T_i}\sum_{\ell=1}^s m_\ell\frac{\omega_{i\ell}-\zeta^{(0)}\delta_{i\ell}}{n_\ell T_\ell}D_{\ell j} + \frac{\partial\zeta^{(0)}}{\partial n_j}\lambda_i - \frac{1}{T_i}\frac{\partial\ln T_i}{\partial n_j}\right)\\ &\quad +\frac{1}{dT^2}\sum_{\ell=1}^s\int d\mathbf{v}\, S_{i,\gamma}\left(\mathcal{K}_{i\ell,\gamma}[n_j\partial_{n_j}f_\ell^{(0)}] + \frac{1}{2}\left(n_\ell\partial_{n_j}\ln\chi_{i\ell}^{(0)} + I_{i\ell j}\right)\mathcal{K}_{i\ell,\gamma}[f_\ell^{(0)}]\right),\end{aligned} \tag{3.61}$$

$$\overline{\ell}_{ij}=-\frac{d+2}{2}\frac{n_iT_i^2}{m_i}\sum_{k=1}^{s}\frac{\omega_{ik}-\zeta^{(0)}\delta_{ik}}{n_kT_k}D_{kj}^F. \tag{3.62}$$

Use has been made of the results

$$\int d\mathbf{v}\,\mathbf{S}_i\cdot\mathbf{A}_i(\mathbf{V})=-\frac{d(d+2)}{2}\frac{n_iT_i^2}{m_i}+\frac{1}{2}\sum_{j=1}^{s}\int d\mathbf{v}\,S_{i,\beta}(\mathbf{V})\mathcal{K}_{ij,\beta}[\nabla_{\mathbf{V}}\cdot(\mathbf{V}f_j^{(0)})], \tag{3.63}$$

$$\begin{aligned}\int d\mathbf{v}\,\mathbf{S}_i\cdot\mathbf{B}_i^j(\mathbf{V}) &= -\frac{d(d+2)}{2}\frac{n_in_jT_i}{m_i}\frac{\partial T_i}{\partial n_j}\\ &\quad-\sum_{\ell=1}^{s}\int d\mathbf{v}\,S_{i,\beta}(\mathbf{V})\mathcal{K}_{i\ell,\beta}\left[\left(n_j\partial_{n_j}+\frac{1}{2}\left(n_\ell\frac{\partial\ln\chi_{i\ell}^{(0)}}{\partial n_j}+I_{i\ell j}\right)\right)f_\ell^{(0)}\right],\end{aligned} \tag{3.64}$$

$$\int d\mathbf{v}\,\mathbf{S}_i(\mathbf{V})\cdot\mathbf{E}_i^j(\mathbf{V})=0. \tag{3.65}$$

The collision frequencies introduced here are

$$\gamma_{ii}=-\frac{2}{d(d+2)}\frac{m_i}{n_iT_i^3}\left(\sum_{j=1}^{s}\int d\mathbf{v}\,\mathbf{S}_i\cdot J_{ij}^{(0)}[f_{i,M}\mathbf{S}_i,f_j^{(0)}]+\int d\mathbf{v}\,\mathbf{S}_i\cdot J_{ii}^{(0)}[f_i^{(0)},f_{i,M}\mathbf{S}_i]\right), \tag{3.66}$$

$$\gamma_{ij}=-\frac{2}{d(d+2)}\frac{m_j}{n_jT_j^3}\int d\mathbf{v}\,\mathbf{S}_i\cdot J_{ij}^{(0)}[f_i^{(0)},f_{j,M}\mathbf{S}_j],\quad(i\neq j). \tag{3.67}$$

$$\omega_{ii}=-\frac{2}{d(d+2)}\frac{m_i}{n_iT_i^2}\left(\sum_{j=1}^{s}\int d\mathbf{v}\,\mathbf{S}_i\cdot J_{ij}^{(0)}[f_{i,M}\mathbf{V},f_j^{(0)}]+\int d\mathbf{v}\,\mathbf{S}_i\cdot J_{ii}^{(0)}[f_i^{(0)},f_{i,M}\mathbf{V}]\right), \tag{3.68}$$

$$\omega_{ij}=-\frac{2}{d(d+2)}\frac{m_i}{n_iT_i^2}\sum_{j=1}^{s}\int d\mathbf{v}\,\mathbf{S}_i\cdot J_{ij}^{(0)}[f_i^{(0)},f_{j,M}\mathbf{V}].\quad(i\neq j). \tag{3.69}$$

The explicit expressions for the above collision frequencies are also displayed in Appendix A.

The inhomogeneous terms (3.60) and (3.61) involve integrals over the operator $\mathcal{K}_{ij,\gamma}$. These are evaluated in Appendix B

$$\begin{aligned}\int d\mathbf{v}\quad S_{i,\gamma}(\mathbf{V})\mathcal{K}_{ij,\gamma}[\nabla_{\mathbf{V}}\cdot(\mathbf{V}f_j^{(0)})] &= -\frac{\pi^{d/2}}{\Gamma\left(\frac{d}{2}\right)}n_in_j\mu_{ij}\chi_{ij}^{(0)}\sigma_{ij}^dT_j(1+\alpha_{ij})\left\{\frac{T_i}{m_i}\left[(d+2)(\mu_{ij}^2-1)\right.\right.\\ &\left.\left.+(2d-5-9\alpha_{ij})\mu_{ij}\mu_{ji}+(d-1+3\alpha_{ij}+6\alpha_{ij}^2)\mu_{ji}^2\right]+6\frac{T_j}{m_j}\mu_{ji}^2(1+\alpha_{ij})^2\right\},\end{aligned} \tag{3.70}$$

$$\begin{aligned}\int d\mathbf{v}\quad S_{i,\gamma}(\mathbf{V})\mathcal{K}_{ij,\gamma}[f_j^{(0)}] &= \frac{\pi^{d/2}}{2\Gamma\left(\frac{d}{2}\right)}m_in_in_j\chi_{ij}^{(0)}\sigma_{ij}^d\mu_{ji}(1+\alpha_{ij})\\ &\times\left\{\left[(d+8)\mu_{ij}^2+(7+2d-9\alpha_{ij})\mu_{ij}\mu_{ji}+(2+d+3\alpha_{ij}^2-3\alpha_{ij})\mu_{ji}^2\right]\frac{T_i^2}{m_i^2}\right.\\ &+3\mu_{ji}^2(1+\alpha_{ij})^2\frac{T_j^2}{m_j^2}+\left[(d+2)\mu_{ij}^2+(2d-5-9\alpha_{ij})\mu_{ij}\mu_{ji}+(d-1+3\alpha_{ij}+6\alpha_{ij}^2)\mu_{ji}^2\right]\\ &\left.\times\frac{T_iT_j}{m_im_j}-(d+2)\left(\frac{T_i}{m_i}+\frac{T_j}{m_j}\right)\frac{T_i}{m_i}\right\},\end{aligned} \tag{3.71}$$

$$\int d\mathbf{v}\,S_{i,\gamma}(\mathbf{V})\mathcal{K}_{i\ell,\gamma}[n_j\partial_{n_j}f_\ell^{(0)}]=\int d\mathbf{v}\,S_{i,\gamma}(\mathbf{V})\left(\mathcal{K}_{i\ell,\gamma}[\delta_{\ell j}f_\ell^{(0)}]-\frac{1}{2}\mathcal{K}_{i\ell,\gamma}[\nabla_{\mathbf{V}}\cdot(\mathbf{V}f_\ell^{(0)})]\frac{\partial\ln\gamma_\ell}{\partial\ln n_j}\right). \tag{3.72}$$

This completely determines the parameters of the integral equations (3.57)–(3.59). Their solution determines λ_i, $d_{q,ij}$ and ℓ_{ij}, and hence the transport coefficients λ^k, $D_{q,ij}^k$, and L_{ij}^k through Eqs. (3.54)–(3.56). In the special case of mechanically equivalent particles, this description reduces to those previously obtained for a monodisperse gas [14, 15].

IV. SUMMARY AND DISCUSSION

First, a brief summary of the results obtained in the two papers presented here is given. The revised Enskog kinetic equation was used as the basis for deriving exact balance equations for the hydrodynamic fields. The pressure, cooling rate, mass flux, momentum flux, and energy flux were determined from the kinetic theory as linear combinations of the gradients of these fields and an applied force. These are the constitutive equations that convert the exact balance equations into closed equations for the hydrodynamic fields (Navier-Stokes equations, at this order of gradients). The coefficients in these equations are the pressure, leading order cooling rate, and the transport coefficients. Formally exact expressions for these coefficients were obtained in the first paper, expressed as integrals over solutions to integral equations via the Chapman-Enskog method for constructing a solution to the kinetic equation. In the present paper, these exact expressions were evaluated using approximate solutions to the integral equations. The approximation consists of expanding the unknown functions in a complete set of polynomials, and truncating that expansion to convert the integral equations to algebraic equations that can be solved by standard matrix methods. Here, the detailed forms for those equations or their solutions have been given in terms of the hydrodynamic fields and other parameters of the problem. The result is a complete description of the hydrodynamic equations to Navier-Stokes order with all parameters determined explicitly from the theory. Due to the complexity of the analysis it may be useful to give the specific location of the final results. The pressure is given by Eq. (2.2) and the lowest order cooling rate by Eq. (2.4). The equivalence of all species cooling rates determine the species temperatures as well (to this order in the gradients). The only transport coefficient for the cooling rate to first order is given by (2.20) and the solution to the algebraic equations (2.16). The transport coefficients characterizing the mass flux are the solutions to the algebraic equations (3.19)–(3.21). The momentum flux has two transport coefficients, the shear and bulk viscosities. These are given by Eqs. (3.23)–(3.26) and the solutions to the algebraic equations (3.34). Finally, the transport coefficients for the heat flux are given by Eqs. (3.36)–(3.39), (3.54)–(3.56), and the solutions to the algebraic equations (3.57)–(3.59). Detailed forms for the collision frequencies and other input functions are presented in the Appendices. These explicit "constitutive relations" together with the exact macroscopic balance equations for species mass densities, flow velocity, and temperature (Eqs. (4.12), (4.14), and (4.24) of the previous paper) complete the practical description of Navier-Stokes hydrodynamics for a moderately dense, multi-component granular mixture based on the revised Enskog kinetic equation.

In the remainder of this Discussion the relationship to several previous works on kinetic-theory-based descriptions of granular mixtures in the literature is considered. These contributions, which are abbreviated according to the initials of authors and the final two digits of the publication year, are listed in Tables I and II. To help put the current effort in the context of previous works, Tables I and II also list the applicability of each contribution (dimensionality and number of species), the starting kinetic equation (Boltzmann or Enskog), and the specific mechanics and assumptions used in the derivation process: the standard Enskog theory (SET) vs. the revised Enskog theory (RET), pair correlation function $\chi_{ij}^{(0)}$, solution method, order and base state of expansion, single particle velocity distribution function [Maxwellian (M) and non-Maxwellian (nM)], energy distribution [energy equipartition (EE) and non-energy equipartition (nEE)], and hydrodynamic variables. In the subsections below, each of these various treatments are detailed and their implications are discussed.

Dimensionality

The number contained in Table I refers to the dimensionality of the particles. Namely, 2D refers to circular particles (disks) that are constrained to motion in a plane, while 3D refers to spherical particles that can move in all three dimensions. Although systems of practical importance are three-dimensional, two-dimensional theories have appeared in the literature for purposes of comparing with molecular-dynamics (MD) simulations. Specifically, early MD simulations were performed in two dimensions due to computational constraints, whereas three-dimensional simulations are now common. The WA99 theory is applicable to 2D only, the JM87 and GHD theories are derived for both 2D and 3D, while all remaining theories JM89, Z95, H06, GD02, R03, IA05, and S06 are for 3D systems.

Number of Species

Most mixture theories to date have been targeted at binary mixtures, in which the two species can differ in size, mass, restitution coefficient, and density (JM87, JM89, WA99, H01, GD02, R03, and S06). Some recent theories have been derived for a more general system of s distinct species (Z95, IA05, and GHD).

Kinetic Theory

Two kinetic theories have been used in the development of hydrodynamic equations for mixtures, namely the Boltzmann equation and the Enskog equation for hard spheres. The difference between these two equations stems

from the treatment of the two-particle distribution function f_{ij}. For the Boltzmann equation, f_{ij} is assumed equal to the product of the two single-particle distribution functions ($f_{ij} = f_i f_j$). This lack of spatial and pre-collisional velocity correlations between the two particles restricts the Boltzmann equation to dilute systems. The Enskog equation, on the other hand, accounts for positional correlations (but not pre-collisional velocity correlations) via the equilibrium pair correlation function at contact χ_{ij}, namely $f_{ij} = \chi_{ij} f_i f_j$ (the Enskog approximation). More specifically, χ_{ij} accounts for excluded volume effects encountered in denser flows, and thus the corresponding Enskog kinetic theory is applicable to moderately dense flows. The Enskog approximation is expected to deteriorate at higher densities as ring collisions and their associated velocity correlations become important. The prevalence of such correlations has also been found to depend on the restitution coefficient; namely, velocity correlations have been observed to increase as the restitution coefficient decreases. Thus, theories based on the Enskog equation are applicable to both dilute and moderately dense flows (JM87, JM89, Z95, WA99, H01, R03, IA05, and GHD), while theories using the Boltzmann equation as a starting point are restricted to dilute flows (GD02 and S06).

From a practical perspective, the upper limit of concentration that a given kinetic theory should be applied to depends on the desired level of accuracy. As a quick gauge to the range of validity of the Boltzmann equation, the limiting case of a monodisperse system is considered using the theories of Garzó and Dufty [14] and Lutsko [15], which are based on the Enskog equation and thus are applicable to both dilute and dense flows. According to these theories, the dense collisional contributions to the pressure (absent in the Boltzmann equation) are 4% and 18% for solids volume fractions of 0.01 and 0.05, respectively, at $\alpha = 0.9$. A similar estimate of the range of validity of the Enskog equation is not available, since the impact of velocity correlations on granular hydrodynamics has not been extensively studied.

SET vs. RET

For those contributions listed in Table I that employ the Enskog equation, two different approaches are possible – the SET and the RET. As mentioned previously, the difference between SET and RET traces to the choice of the pair correlation function, $\chi_{ij}^{(0)}$. In SET, $\chi_{ij}^{(0)}$ is a *function* of concentration (i.e., depends on local value only) at a single position of interest, whereas for RET $\chi_{ij}^{(0)}$ is treated as a *functional* of concentration (i.e., depends on the local value and its gradient) at the two particle centers. In SET, the location (e.g., midpoint) at which to evaluate $\chi_{ij}^{(0)}$ for mixtures is unclear [18]. Regardless of the choice, however, the resulting diffusion force is found to be inconsistent with irreversible thermodynamics, unlike in RET [19].

The implications of the SET vs. RET treatment on the resulting theory depends on the type system being examined. For the case of monodisperse systems, SET and RET lead to the same Navier-Stokes transport coefficients [19, 20, 21, 22] but different inhomogeneous equilibrium states [19, 20, 21]. For mixtures, however, different Navier-Stokes transport coefficients are obtained from SET and RET. More specifically, although the fluxes appearing in the momentum and energy balances are the same for SET and RET [$\mathbf{q}$ and $P_{\gamma\beta}$ in Eqs. (4.13) and (4.14) in the companion paper], the diffusion flux [$\mathbf{j}_{0i}$ in Eq. (4.12) in companion paper] takes on different forms [23]. Although the quantitative impact of such differences on segregation predictions has not been investigated in detail, it is clear that RET is the appropriate approach since it is consistent with irreversible thermodynamics. The Enskog-based theories of JM89, Z95, WA99, and GHD use RET, whereas JM87, H01, R03, and IA05 utilize SET.

Pair Correlation Function

As noted in Table I, various forms of the pair correlation function $\chi_{ij}^{(0)}$ have been used in conjunction with mixtures. Its explicit forms can be found in the references displayed in the table.

Solution Method

With the exception of Zamankhan [4], all of the efforts to date on mixtures have implemented a Chapman-Enskog (CE) expansion to solve the kinetic equation. By definition, the CE expansion involves a perturbative expansion about low Knudsen numbers (where Kn is defined as the ratio of the mean free path to the characteristic length of the mean-flow gradients) or "small gradients," and thus is not applicable to systems in which free-molecular (non-continuum) effects play a non-negligible role. The Grad moment method, as was employed by Zamankhan [4] does not contain similar restrictions, though the derivation is necessarily more complex and thus has not been performed without resorting to other simplifying assumptions (e.g., equipartition of energy).

Order of Chapman-Enskog Expansion

For each of the entries in Table I that employ the CE expansion to solve the kinetic theory equation, all expansions are carried out to first order in spatial gradients – i.e., to the Navier Stokes (NS) order. Nonetheless, evidence of higher-order effects has been noted in a range of granular flows, and Burnett-order effects (second order in spatial gradients) in particular have been shown to be linked to the anisotropy in the stress tensor [24]. Examples of systems in which significant higher-order effects have been identified include the upper region of an open-ended, vibro-fluidized bed [25, 26], the vanishing heap of a vibrated, granular material [27], dilute flow around an immersed cylinder [28], simple shear flow [29], the Knudsen layer adjacent to a thermal (energy-providing) boundary [30], and in the continuum interior of a thermally-driven granular gas [31]. For the case of monodisperse systems, several theories[24, 32, 33, 34] and boundary conditions[25, 26, 35] have been developed that account for such higher order effects in a limited class of systems (dilute, sheared flow, open boundary, etc.). Analogous work has not been reported for mixtures [36, 37], however, and thus the incorporation of higher-order effects does not serve as a differentiator between those theories listed in Table II that employ the CE expansion. Nonetheless, the possible presence of such higher-order effects should be kept in mind when comparing these theories with experiments and simulations for purposes of validation.

Base State of Chapman-Enskog Expansion

As described in the companion paper, hydrodynamics results from a "normal solution" to the kinetic equation, whose space and time dependence occurs only through the hydrodynamic fields. The CE expansion is a systematic method for constructing this normal solution as an expansion in powers of the Knudsen number, or spatial gradients of the fields. At zeroth order in these fields, the kinetic theory determines the form of the distribution function to be the "local equilibrium" Maxwellian for molecular fluids. However, in the presence of dissipation the kinetic theory requires a different solution at zeroth order, the "local homogeneous cooling" (HCS) distribution. The HCS distribution agrees with the local Maxwellian only for $\alpha = 1$. It is possible to make an expansion in both Knudsen number and $(1 - \alpha)$, in which case the lowest order term is indeed the Maxwellian. Such a double expansion is necessarily limited to asymptotically weak dissipation. The theories of JM87, JM89, WA99, H01, R03, IA05, and S06 are of this type with the corresponding implicit limitation. The theories of GD02 and GHD, on the other hand, expand only in the Knudsen number, with HCS as the leading order solution and hence no a priori limitation on the degree of dissipation. Quantitatively, the difference between the two types of expansions has been examined in monodisperse systems via a comparison of the dissipation rate obtained in MD simulations [31]. As an example, at a volume fraction of 0.3 and $\alpha = 0.75$, an error of 23% is obtained when using a theory [38] based on an expansion about $\alpha = 1$, while an error of 7% is obtained when using a theory [14] based on an expansion about the HCS. For both theories, the level of mismatch is found to increase with concentration and dissipation levels.

Order of Sonine polynomial expansion

To make the analytical evaluation of the collision integrals possible, a truncated Sonine polynomial expansion is employed. All theories listed in Table I employ the lowest, non-zero order of the polynomial expansion (leading term), except for the weak dissipation theory of S06 which carries out the expansion to third order. Nonetheless, the transport coefficients of S06 agree with those of GD02 in the common domain of validity, namely in the nearly elastic limit [10].

The accuracy of a given Sonine polynomial approximation can be tested via comparison with discrete simulation Monte Carlo (DSMC) results. DSMC provides a numerical solution of the starting kinetic (Boltzmann or Enskog) equation for a specific system, and thus provides a check for the existence of a normal solution, the order of the gradient expansion (e.g., Navier Stokes), and the truncated Sonine polynomial. For dilute granular mixtures, good agreement between DSMC and the theory of Garzó and Dufty [11] was found for the shear viscosity, even for strong dissipation [39]. This agreement for the shear viscosity is also present for moderately dense systems [17]. A similar comparison was carried out for the diffusion coefficient for a system with an impurity [40]. The agreement is again excellent, except when the size or mass disparity is large, in which case the second Sonine approximation leads to a significant improvement over the first Sonine approximation.

Single Particle Velocity Distribution

In an effort to simplify the evaluation of collision integrals, some previous works have assumed that the single particle velocity distribution function is Maxwellian (M). Strictly speaking, such an assumption is valid only for perfectly elastic spheres in equilibrium [41]. Numerous experimental, theoretical, and simulation studies of inelastic, monodisperse systems have indicated that the distribution function departs from Maxwellian [42, 43, 44, 45, 46, 47, 48, 49]. For the case of perfectly elastic mixtures, an estimate of the impact of this effect is given by Willits and Arnarson [6], who compare the shear viscosity predictions of two theories with that of MD simulations. For this particular system, the

only effective difference between the two theories is that one contains a Maxwellian assumption and the other does not. For disks with a diameter ratio of 1.25 and over a range of solids fractions from 0.05 to 0.4, the non-Maxwellian (nM) theory exhibits very good agreement with the simulations. The Maxwellian-based predictions, on the other hand, are significantly lower in value since the Maxwellian assumption precludes the kinetic contribution to the shear stress and simplifies its collisional counterpart. Although similar studies on the impact of non-Maxwellian effects on other constitutive quantities are not available, it is clear that a non-Maxwellian treatment is critical for the accurate prediction of shear stress. Of the mixture theories presented in Table I, those of JM87, H01, and R03 are based on a Maxwellian assumption, while those of JM89, WA99, Z95, GD02, S06, and GHD incorporate non-Maxwellian effects. The theory of IA05 takes a hybrid approach, in which collision integrals involving unlike particles are evaluated based on Maxwellian distributions, whereas collisions integrals involving like particles account for non-Maxwellian effects.

Energy Distribution

Similar to the assumption of a Maxwellian velocity distribution, the assumption of an equipartition of energy (EE) has also been made periodically in an effort to simplify the evaluation of collision integrals. Again, an equipartition of energy between unlike particles is only expected for a perfectly elastic system in equilibrium. Numerous theoretical [12, 39, 50], simulation [51, 52, 53, 54, 55, 56], and experimental [57, 58, 59] studies of granular materials provide evidence that an equipartition of energy does not exist, and that the level of non-equipartition of energy (nEE) increases as the restitution coefficient decreases (dissipation increases) and as the mass ratio gets further from unity. The impact of such non-equipartition has recently been evaluated in the context of species segregation. In particular, Galvin, Dahl and Hrenya [60] have found that the driving forces for species segregation that arise from non-equipartition are significant over a moderate range of parameters for the case of a thermally-driven system. Furthermore, for the case of an intruder particle in the presence of gravity, both Brey et al.[61], Garzó [62], and Yoon and Jenkins[63] have found that the direction of species segregation may reverse due to non-equipartition effects. Together, these studies indicate the importance of non-equipartition in a variety of systems. The mixture theories of JM87, H01, GD02, R03, IA05, and GHD include the effects of non-equipartition, while those of JM89, WA99, Z95, and S06 do not account for non-equipartition.

Hydrodynamic Variables

The appropriate choice of hydrodynamic variables to include in a hydrodynamic theory depends on the timescale associated with a given variable [64]. First consider the case of a molecular gas, in which two timescales are relevant – the "kinetic" time scale and the "hydrodynamic" time scale. The kinetic time scale is "fast" and representative of the time between collisions (i.e., mean free time). The hydrodynamic time scale is "slow" and is set by the gradients in the system; this is the timescale over which macroscopic variables change.

It is important to note that the velocity distribution function f_i (and thus the Boltzmann and Enskog equations) carries information with it on the kinetic time scale. However, the macroscopic variables (n_i, U, and T for the case of a molecular gas) correspond to velocity moments of f_i that are *collisional invariants* – i.e., n_i, U, and T are conserved upon collision. As a result, they will stay constant over a time on the order of a mean free path, and vary in time over the much longer hydrodynamic time scale. It is this property which defines the appropriate (minimum set of) hydrodynamic variables needed to describe a system.

To illustrate the above point, consider the time evolution of mixture temperature (T) and species temperature (T_i), again for the case of a molecular gas with more than one species present:

$$\frac{DT}{Dt} = (\text{energy flux})$$
$$\frac{DT_i}{Dt} = (\text{energy flux}) + \left(\begin{array}{l} \text{collisional exchange (source/sink)} \\ \text{between unlike species} \end{array} \right)$$

Note that T is a collisional invariant (the total energy is conserved upon collision and thus no "source" term is present), but that T_i is not a collisional invariant since the energy associated with a given species can change upon collision with another species. Also note that the time scale of the flux term is set by gradients (e.g., Fourier's law), whereas the time scale of the source term is collisional in nature and thus relatively "fast." Hence, the mixture temperature T is characterized by one (slow) timescale and the species temperature is characterized by two (slow and fast) timescales. The corresponding physical picture is the following: each species is expected to have a rapid relaxation after a few collisions to a distribution near local equilibrium (local mixture temperature), and then all temperatures evolve according to the slow hydrodynamic mode. Thus, the relevant hydrodynamic (macroscopic) variable is T since it is associated with a conserved quantity; all other variables (T_i) are enslaved to it. Thus, solving a separate balance for T_i is superfluous – indeed this is not done for molecular gases.

Next, consider a granular system in which the particles engage in dissipative collisions. Three timescales need to be considered, as illustrated by the balances below:

$$\frac{DT}{Dt} = (\text{energy flux}) + \left(\begin{array}{l} \text{inelastic} \\ \text{dissipation} \\ \text{(sink)} \end{array} \right)$$

$$\frac{DT_i}{dt} = (\text{energy flux}) + \left(\begin{array}{l} \text{inelastic} \\ \text{dissipation} \\ \text{(sink)} \end{array} \right) + \left(\begin{array}{l} \text{collisional exchange (source/sink)} \\ \text{between unlike species} \end{array} \right)$$

As with the molecular systems, the energy flux is characterized by a slow (hydrodynamic) time scale and the collisional exchange between species is characterized by a fast (kinetic) time scale. In the granular system, inelastic dissipation also occurs, and its corresponding time scale is not as obvious. More specifically, the dissipation rate depends not only on the collisional frequency (kinetic time scale), but also on the value of restitution coefficient. As α approaches unity, the dissipation rate goes to zero, and the time scale becomes large (hydrodynamic time scale). In other words, it is unclear *a priori* whether this term is characterized by a fast or slow timescale.

The previous observation leads to the question: for moderate (smaller) values of α, does the time scale become fast enough to approach the kinetic time scale or is there still a separation of time scales? If the latter is assumed (that the time scale associated with inelastic dissipation is much longer than that of the kinetic time scale), Garzó and Dufty [12] have shown that in a HCS two-component system, (i) the cooling rates associated with mixture and species temperatures are equal and (ii) the ratio of species temperature (T_1/T_2) remains constant – i.e., all temperatures decay at the same rate but their ratios remain constant. Further note that T_1/T_2 is not equal to one for unlike particles – i.e., a non-equipartition of energy is predicted. To test this assumption of the separation of timescales, MD simulations of a binary mixture in HCS were performed by Dahl et al. [54]. The simulation results indicate that a constant value of T_1/T_2 is achieved after only a few collisions, and this behavior was confirmed over a wide range of parameters.

As a result of the aforementioned finding that the timescale associated with inelastic dissipation is hydrodynamic (slow) in nature, the physical picture is analogous to that of a molecular system Namely, each species has a rapid relaxation to a local "equilibrium" state (now characterized by a constant value of non-equipartition) – HCS – and is then enslaved to slow (hydrodynamic) evolution. Thus, the relevant hydrodynamic variables are the same – n_i, $\mathbf{U}$, and T – and the balance of additional variables (such as T_i) would be superfluous.

The practical implications of using n_i, $\mathbf{U}$, and T as the hydrodynamic variables in granular flows are twofold. First, only a single balance for T is needed, instead of separate balance for each T_i. The reduction in the number of governing equations is expected to lead to a considerable decrease in computational overhead. Second, the level of non-equipartition is in a state of local "equilibrium" due to the fast time time scale of T_i, and thus T_1/T_2 depends on local values of flow field variables and particle properties (mixture composition, α, etc.). Hence, even though a non-equipartition of energy is indeed present, it does not appear explicitly in the transport coefficients. Instead, its dependency on the flow field variables is incorporated into the transport coefficients – i.e., the effect of non-equipartition is *implicitly* contained in the transport coefficients. It can be solved for explicitly once the flow field variables have been solved for using, for example, the relation derived by Garzó and Dufty [12].

Of the non-equipartition theories listed in Table II, GD02 and GHD use T as the hydrodynamic variable for the granular energy field, whereas the other non-equipartition theories use T_i (JM87, H01, R03, IA05). The choice of hydrodynamic variable(s) is a non-issue for theories which invoke an equipartition assumption (JM89, Z95, WA99, S06) since they inherently assume $T = T_i$ and thus use T as the energy variable. (It is worthwhile to note that S06 defines temperature differently than others, namely $T_S = 3T$. Furthermore, IA06 uses a species temperature $T_{i,IA}$, which is defined in terms of velocity fluctuations relative the mean species velocity, rather than the mass-averaged velocity used for T.)

Recapitulation

Unlike previous Enskog-based (dense) theories, the current effort is based on an expansion about the homogeneous cooling state and employs n_i, U, and T as the hydrodynamic variables. The former extends the range of validity to strong dissipation levels while the latter results in fewer balance equations, thereby reducing the computational cost. This approach was first put forth by Garzó and Dufty [11] who instead used the Boltzmann equation as their starting kinetic equation; the current work thus extends the domain of applicability from dilute to moderately dense flows.

TABLE I: Hydrodynamic Descriptions of Granular Mixtures

References	**Abbrev.**	**Dimension**	**Number of Species**	**Kinetic Theory**	**SET vs. RET**	**Pair Correlation Function** $\chi_{ij}^{(0)}$
[2]	JM87	2D and 3D	2	Enskog	SET	2D [2], 3D [65]
[3] and [5]	JM89	3D	2	Enskog	RET	3D [65]
[4]	Z95	3D	s	Enskog	RET	[66]
[6] and [67]	WA99	2D	2	Enskog	RET	2D [2]
[7]	H01	3D	2	Enskog	RET	[65]
[11]	GD02	3D	2	Boltzmann	–	–
[8]	R03	3D	2	Enskog	SET	[68]
[9]	IA05	3D	s	Enskog	SET	[69]
[10]	S06	3D	2	Boltzmann	–	–
current work	GHD	2D and 3D	s	Enskog	RET	2D [70], 3D [71]

TABLE II: Hydrodynamic Descriptions of Granular Mixtures

Ref.	**Solution Method**	**Chapman-Enskog Expansion Order**	**Chapman-Enskog Expansion Base State**	**Sonine Expansion Order**	**Single Particle Velocity Distribution**	**Energy Distributon**	**Hydro-dynamic Variables**
JM87	CE	NS	$\alpha = 1$	1st	M	nEE	n_i, $\mathbf{U}_i$, T_i
JM89	CE	NS	$\alpha = 1$	1st	nM	EE	n_i, $\mathbf{U}_i$, T
Z95	Grad's method	–	–	–	nM	EE	13 moments
WA99	CE	NS	$\alpha = 1$	1st	nM	EE	n_i, $\mathbf{U}_i$, T
H01	CE	NS	$\alpha = 1$	1st	M	nEE	n_i, $\mathbf{U}_i$, T_i
GD02	CE	NS	HCS	1st	nM	nEE	n_i, $\mathbf{U}_i$, T
R03	CE	NS	$\alpha = 1$	1st	M	nEE	n_i, $\mathbf{U}_i$, T_i
IA05	CE	NS	$\alpha = 1$	1st	M/nM	nEE	n_i, $\mathbf{U}_i$, $T_{i,IA}$
S06	CE	NS	$\alpha = 1$	3rd	nM	EE	n_i, $\mathbf{U}_i$, T_s
GHD	CE	NS	HCS	1st	nM	nEE	n_i, $\mathbf{U}_i$, T

Acknowledgments

V. G. acknowledges partial support from the Ministerio de Ciencia y Tecnología (Spain) through Grant No. FIS2007–60977. C.M.H. is grateful to the National Science Foundation for providing financial support of this project through grant CTS-0318999 with additional support provided by the American Chemical Society Petroleum Research Fund (Grant 43393-AC9) and the Engineering and Physical Sciences Research Council (Grant EP/DO30676/1). C. M. H. and J. W. D. are also grateful to the organizers and participants of the Granular Physics Workshop at the Kavli Institute of Theoretical Physics (with partial support from the National Science Foundation under grant PHY99-07949), which provided a starting forum for much of this work.

APPENDIX A: COLLISION FREQUENCIES

In this Appendix we display the expressions for the collision frequencies appearing in the evaluation of the kinetic contributions to the transport coefficients and in the first order contributions to the cooling rate. As noted in the main text, most of these frequencies (those corresponding to the transport coefficients) have been obtained in the low-density limit (except for the factors $\chi_{ij}^{(0)}$) [16] for arbitrary dimensions by considering the Maxwellian approximation for the zeroth-order distribution functions $f_i^{(0)}$. Their expressions are

$$\nu_{ii}=\frac{2\pi^{(d-1)/2}}{d\Gamma\left(\frac{d}{2}\right)}\sum_{j\neq i}^{s}n_j\sigma_{ij}^{d-1}\chi_{ij}^{(0)}\mu_{ji}v_0(1+\alpha_{ij})\left(\frac{\theta_i+\theta_j}{\theta_i\theta_j}\right)^{1/2}, \tag{A1}$$

$$\nu_{ij}=-\frac{2\pi^{(d-1)/2}}{d\Gamma\left(\frac{d}{2}\right)}n_i\sigma_{ij}^{d-1}\chi_{ij}^{(0)}\mu_{ij}v_0(1+\alpha_{ij})\left(\frac{\theta_i+\theta_j}{\theta_i\theta_j}\right)^{1/2}, \tag{A2}$$

$$\begin{aligned}\tau_{ii} &= \frac{2\pi^{(d-1)/2}}{d(d+2)\Gamma\left(\frac{d}{2}\right)}v_0\left\{n_i\sigma_i^{d-1}\chi_{ii}^{(0)}(2\theta_i)^{-1/2}(3+2d-3\alpha_{ii})(1+\alpha_{ii})\right.\\ &+2\sum_{j\neq i}^{s}n_j\chi_{ij}^{(0)}\sigma_{ij}^{d-1}\mu_{ji}(1+\alpha_{ij})\theta_i^{3/2}\theta_j^{-1/2}\left[(d+3)\beta_{ij}\theta_i^{-2}(\theta_i+\theta_j)^{-1/2}\right.\\ &\left.\left.+\frac{3+2d-3\alpha_{ij}}{2}\mu_{ji}\theta_i^{-2}(\theta_i+\theta_j)^{1/2}+\frac{2d(d+1)-4}{2(d-1)}\theta_i^{-1}(\theta_i+\theta_j)^{-1/2}\right]\right\},\end{aligned} \tag{A3}$$

$$\begin{aligned}\tau_{ij} &= \frac{4\pi^{(d-1)/2}}{d(d+2)\Gamma\left(\frac{d}{2}\right)}v_0n_i\chi_{ij}^{(0)}\sigma_{ij}^{d-1}\mu_{ij}\theta_j^{3/2}\theta_i^{-1/2}(1+\alpha_{ij})\\ &\times\left[(d+3)\beta_{ij}\theta_j^{-2}(\theta_i+\theta_j)^{-1/2}+\frac{3+2d-3\alpha_{ij}}{2}\mu_{ji}\theta_j^{-2}(\theta_i+\theta_j)^{1/2}\right.\\ &\left.-\frac{2d(d+1)-4}{2(d-1)}\theta_j^{-1}(\theta_i+\theta_j)^{-1/2}\right],\end{aligned} \tag{A4}$$

$$\begin{aligned}\omega_{ii} &= \frac{\pi^{(d-1)/2}}{\Gamma\left(\frac{d}{2}\right)}\frac{2}{d\sqrt{2}}\sigma_i^{d-1}n_i\chi_{ii}^{(0)}v_0\theta_i^{-1/2}(1-\alpha_{ii}^2)\\ &+\frac{\pi^{(d-1)/2}}{\Gamma\left(\frac{d}{2}\right)}\frac{2}{d(d+2)}\sum_{j\neq i}^{s}n_j\chi_{ij}^{(0)}\sigma_{ij}^{d-1}v_0\mu_{ji}(1+\alpha_{ij})(\theta_i+\theta_j)^{-1/2}\theta_i^{1/2}\theta_j^{-3/2}A_{ij},\end{aligned} \tag{A5}$$

$$\omega_{ij}=\frac{\pi^{(d-1)/2}}{\Gamma\left(\frac{d}{2}\right)}\frac{2}{d(d+2)}n_j\chi_{ij}^{(0)}\sigma_{ij}^{d-1}v_0\mu_{ji}(1+\alpha_{ij})(\theta_i+\theta_j)^{-1/2}\theta_i^{1/2}\theta_j^{-3/2}C_{ij}, \tag{A6}$$

$$\begin{aligned}\gamma_{ii} &= \frac{\pi^{(d-1)/2}}{\Gamma\left(\frac{d}{2}\right)}\frac{8}{d(d+2)}\sigma_i^{d-1}n_i\chi_{ii}^{(0)}v_0(2\theta_i)^{-1/2}(1+\alpha_{ii})\left[\frac{d-1}{2}+\frac{3}{16}(d+8)(1-\alpha_{ii})\right]\\ &+\frac{\pi^{(d-1)/2}}{\Gamma\left(\frac{d}{2}\right)}\frac{1}{d(d+2)}\sum_{j\neq i}^{s}n_j\chi_{ij}^{(0)}\sigma_{ij}^{d-1}v_0\mu_{ji}(1+\alpha_{ij})\left(\frac{\theta_i}{\theta_j(\theta_i+\theta_j)}\right)^{3/2}\left[E_{ij}-(d+2)\frac{\theta_i+\theta_j}{\theta_i}A_{ij}\right],\end{aligned} \tag{A7}$$

$$\gamma_{ij}=-\frac{\pi^{(d-1)/2}}{\Gamma\left(\frac{d}{2}\right)}\frac{1}{d(d+2)}n_i\chi_{ij}^{(0)}\sigma_{ij}^{d-1}v_0\mu_{ij}(1+\alpha_{ij})\left(\frac{\theta_j}{\theta_i(\theta_i+\theta_j)}\right)^{3/2}\left[F_{ij}+(d+2)\frac{\theta_i+\theta_j}{\theta_j}C_{ij}\right]. \tag{A8}$$

In the above equations, $v_0=\sqrt{2T/m}$ is the thermal velocity, $\theta_i=m_iT/mT_i$, and we have introduced the dimensionless quantities

$$
\begin{aligned}
A_{ij} &= (d+2)(2\beta_{ij}+\theta_j)+\mu_{ji}(\theta_i+\theta_j)\left\{(d+2)(1-\alpha_{ij})-[(11+d)\alpha_{ij}-5d-7]\beta_{ij}\theta_i^{-1}\right\}\\
&+3(d+3)\beta_{ij}^2\theta_i^{-1}+2\mu_{ji}^2\left(2\alpha_{ij}^2-\frac{d+3}{2}\alpha_{ij}+d+1\right)\theta_i^{-1}(\theta_i+\theta_j)^2-(d+2)\theta_j\theta_i^{-1}(\theta_i+\theta_j),
\end{aligned}
\tag{A9}
$$

$$
\begin{aligned}
C_{ij} &= (d+2)(2\beta_{ij}-\theta_i)+\mu_{ji}(\theta_i+\theta_j)\left\{(d+2)(1-\alpha_{ij})+[(11+d)\alpha_{12}-5d-7]\beta_{ij}\theta_j^{-1}\right\}\\
&-3(d+3)\beta_{ij}^2\theta_j^{-1}-2\mu_{ji}^2\left(2\alpha_{ij}^2-\frac{d+3}{2}\alpha_{ij}+d+1\right)\theta_j^{-1}(\theta_i+\theta_j)^2+(d+2)(\theta_i+\theta_j),
\end{aligned}
\tag{A10}
$$

$$
\begin{aligned}
E_{ij} &= 2\mu_{ji}^2\theta_i^{-2}(\theta_i+\theta_j)^2\left(2\alpha_{ij}^2-\frac{d+3}{2}\alpha_{ij}+d+1\right)[(d+2)\theta_i+(d+5)\theta_j]\\
&-\mu_{ji}(\theta_i+\theta_j)\left\{\beta_{ij}\theta_i^{-2}[(d+2)\theta_i+(d+5)\theta_j][(11+d)\alpha_{ij}-5d-7]\right.\\
&\left.-\theta_j\theta_i^{-1}[20+d(15-7\alpha_{ij})+d^2(1-\alpha_{ij})-28\alpha_{ij}]-(d+2)^2(1-\alpha_{ij})\right\}\\
&+3(d+3)\beta_{ij}^2\theta_i^{-2}[(d+2)\theta_i+(d+5)\theta_j]+2\beta_{ij}\theta_i^{-1}[(d+2)^2\theta_i+(24+11d+d^2)\theta_j]\\
&+(d+2)\theta_j\theta_i^{-1}[(d+8)\theta_i+(d+3)\theta_j]-(d+2)(\theta_i+\theta_j)\theta_i^{-2}\theta_j[(d+2)\theta_i+(d+3)\theta_j],
\end{aligned}
\tag{A11}
$$

$$
\begin{aligned}
F_{ij} &= 2\mu_{ji}^2\theta_j^{-2}(\theta_i+\theta_j)^2\left(2\alpha_{ij}^2-\frac{d+3}{2}\alpha_{ij}+d+1\right)[(d+5)\theta_i+(d+2)\theta_j]\\
&-\mu_{ji}(\theta_i+\theta_j)\left\{\beta_{ij}\theta_j^{-2}[(d+5)\theta_i+(d+2)\theta_j][(11+d)\alpha_{ij}-5d-7]\right.\\
&\left.+\theta_i\theta_j^{-1}[20+d(15-7\alpha_{ij})+d^2(1-\alpha_{ij})-28\alpha_{ij}]+(d+2)^2(1-\alpha_{ij})\right\}\\
&+3(d+3)\beta_{ij}^2\theta_j^{-2}[(d+5)\theta_i+(d+2)\theta_j]-2\beta_{ij}\theta_j^{-1}[(24+11d+d^2)\theta_i+(d+2)^2\theta_j]\\
&+(d+2)\theta_i\theta_j^{-1}[(d+3)\theta_i+(d+8)\theta_j]-(d+2)(\theta_i+\theta_j)\theta_j^{-1}[(d+3)\theta_i+(d+2)\theta_j],
\end{aligned}
\tag{A12}
$$

where $\beta_{ij}\equiv\mu_{ij}\theta_j-\mu_{ji}\theta_i$.

It only remains to evaluate the collision frequencies ψ_{ij} needed to get the first order contribution $\zeta^{(1,1)}$ to the cooling rate. These frequencies have not been previously determined in the Boltzmann limit. To compute them, we use the property

$$
\begin{aligned}
\int d\mathbf{v}_1 h(\mathbf{v}_1)J_{ij}^{(0}[\mathbf{V}_1|\Phi_i,\Phi_j] &= \chi_{ij}^{(0)}\sigma_{ij}^{d-1}\int d\mathbf{v}_1\int d\mathbf{v}_2\Phi_i(\mathbf{v}_1)\Phi_j(\mathbf{v}_2)\\
&\times\int d\widehat{\boldsymbol{\sigma}}\,\Theta(\widehat{\boldsymbol{\sigma}}\cdot\mathbf{g})(\widehat{\boldsymbol{\sigma}}\cdot\mathbf{g})\left[h(\mathbf{V}_1^{'})-h(\mathbf{V}_1)\right],
\end{aligned}
\tag{A13}
$$

with

$$
\mathbf{V}_1'=\mathbf{V}_1-\mu_{ji}(1+\alpha_{ij})(\widehat{\boldsymbol{\sigma}}\cdot\mathbf{g})\widehat{\boldsymbol{\sigma}}\,.
\tag{A14}
$$

To determine ψ_{ij}, let us consider first the integral

$$
I_\psi=\int d\mathbf{v}\,\left(\frac{m_iV^2}{2T_i}\right)^2\,J_{ij}^{(0)}[f_i^{(0)},f_{j,M}F_j].
\tag{A15}
$$

Use of Eqs. (A13) and (A14) gives

$$
I_\psi=\chi_{ij}^{(0)}\sigma_{ij}^{d-1}\frac{m_i^2}{4T_i^2}\int d\mathbf{v}_1\int d\mathbf{v}_2 f_i^{(0)}(\mathbf{V}_1)f_{j,M}(\mathbf{V}_2)F_j(\mathbf{V}_2)\int d\widehat{\boldsymbol{\sigma}}\,\Theta(\widehat{\boldsymbol{\sigma}}\cdot\mathbf{g})(\widehat{\boldsymbol{\sigma}}\cdot\mathbf{g})\left(V_1'^4-V_1^4\right)\,.
\tag{A16}
$$

The collision rule (A14) yields

$$V_1'^4 - V_1^4 = 2\mu_{ji}^2(1+\alpha_{ij})^2(\widehat{\boldsymbol{\sigma}}\cdot\mathbf{g})^2\left[2(\widehat{\boldsymbol{\sigma}}\cdot\mathbf{V}_1)^2 + V_1^2 + \frac{\mu_{ji}^2}{2}(1+\alpha_{ij})^2(\widehat{\boldsymbol{\sigma}}\cdot\mathbf{g})^2\right]$$
$$-4\mu_{ji}(1+\alpha_{ij})(\widehat{\boldsymbol{\sigma}}\cdot\mathbf{g})(\widehat{\boldsymbol{\sigma}}\cdot\mathbf{V}_1)\left[V_1^2 + \mu_{ji}^2(1+\alpha_{ij})^2(\widehat{\boldsymbol{\sigma}}\cdot\mathbf{g})^2\right]. \tag{A17}$$

The integration over the solid angle in (A16) leads to

$$\int d\widehat{\boldsymbol{\sigma}}\,\Theta(\widehat{\boldsymbol{\sigma}}\cdot\mathbf{g})(\widehat{\boldsymbol{\sigma}}\cdot\mathbf{g})\left(V_1'^4 - V_1^4\right) = \frac{4B_3}{d+3}\mu_{ji}^2(1+\alpha_{ij})^2 g\left[3(\mathbf{V}_1\cdot\mathbf{g})^2 + \frac{d+5}{2}g^2V_1^2 + \mu_{ji}^2(1+\alpha_{ij})^2g^4\right]$$
$$-\frac{4B_3}{d+3}\mu_{ji}(1+\alpha_{ij})g(\mathbf{V}_1\cdot\mathbf{g})\left[(d+3)V_1^2 + 4\mu_{ji}^2(1+\alpha_{ij})^2g^2\right], \tag{A18}$$

where

$$B_k \equiv \int d\widehat{\boldsymbol{\sigma}}\,\Theta(\widehat{\boldsymbol{\sigma}}\cdot\mathbf{g})\,(\widehat{\boldsymbol{\sigma}}\cdot\widehat{\mathbf{g}})^k = \pi^{(d-1)/2}\frac{\Gamma\left(\frac{k+1}{2}\right)}{\Gamma\left(\frac{k+d}{2}\right)}. \tag{A19}$$

Therefore, the integral (A16) can be written as

$$I_\psi = \frac{B_3}{d+3}\chi_{ij}^{(0)}\sigma_{ij}^{d-1}n_in_j(\theta_i\theta_j)^{d/2}v_0\mu_{ji}(1+\alpha_{ij})\theta_i^2\Delta_jI_\psi^*(\theta_i,\theta_j), \tag{A20}$$

where we have taken the Maxwellian form for $f_i^{(0)}$ and have introduced the dimensionless integral

$$I_\psi^*(\theta_i,\theta_j) = \pi^{-d}\int d\mathbf{c}_1\int d\mathbf{c}_2\; e^{-(\theta_ic_1^2+\theta_jc_2^2)}x$$
$$\times\left\{4\mu_{ji}(1+\alpha_{ij})\left[3(\mathbf{c}_1\cdot\mathbf{x})^2 + \frac{d+5}{2}g^2c_1^2 + \mu_{ji}^2(1+\alpha_{ij})^2x^4\right]\right.$$
$$\left.-4(\mathbf{c}_1\cdot\mathbf{x})\left[(d+3)c_1^2 + 4\mu_{ji}^2(1+\alpha_{ij})^2x^2\right]\right\}, \tag{A21}$$

and the operator

$$\Delta_j \equiv \theta_j^2\frac{\partial^2}{\partial\theta_j^2} + (d+2)\theta_j\frac{\partial}{\partial\theta_j} + \frac{d(d+2)}{4}. \tag{A22}$$

In addition, $\mathbf{c}_i \equiv \mathbf{V}_1/v_0$ and $\mathbf{x} \equiv \mathbf{g}/v_0$. The integral (A21) can be performed by the change of variables $\{\mathbf{c}_1,\mathbf{c}_2\} \to \{\mathbf{x},\mathbf{y}\}$ where $\mathbf{y} \equiv \theta_i\mathbf{c}_1 + \theta_j\mathbf{c}_2$ and the Jacobian is $(\theta_i+\theta_j)^{-d}$. With this change the integrations can be done quite efficiently by using a computer package of symbolic calculations. A lengthy and careful algebra gives

$$I_\psi^*(\theta_i,\theta_j) = (d+3)\frac{\Gamma\left(\frac{d+3}{2}\right)}{\Gamma\left(\frac{d}{2}\right)}(\theta_i\theta_j)^{-d/2}(\theta_i\theta_j)^{-5/2}(\theta_i+\theta_j)^{-1/2}$$
$$\times\left\{-2\theta_j^2\left[(d+3)\theta_j + (d+2)\theta_i\right] + \mu_{ji}(1+\alpha_{ij})\theta_j(\theta_i+\theta_j)\right.$$
$$\times\left[(11+d)\theta_j + \frac{d^2+5d+6}{d+3}\theta_i\right]$$
$$\left.-8\mu_{ji}^2(1+\alpha_{ij})^2\theta_j(\theta_i+\theta_j)^2 + 2\mu_{ji}^3(1+\alpha_{ij})^3(\theta_i+\theta_j)^3\right\}. \tag{A23}$$

Use of (A20) in (A23) leads to the final expression for I_ψ :

$$I_\psi = \frac{\pi^{(d-1)/2}}{4\Gamma\left(\frac{d}{2}\right)}n_in_j\chi_{ij}^{(0)}\sigma_{ij}^{d-1}v_0\mu_{ji}(1+\alpha_{ij})\theta_i^{3/2}\theta_j^{-3/2}(\theta_i+\theta_j)^{-5/2}$$
$$\times\left\{\left[(d-1)\theta_j + (d+2)\theta_i\right]\left[2\theta_j + 3\mu_{ji}(1+\alpha_{ij})(\theta_i+\theta_j)\right]\right.$$
$$\left.-24\mu_{ji}^2(1+\alpha_{ij})^2(\theta_i+\theta_j)^2 + 30\mu_{ji}^3(1+\alpha_{ij})^3\theta_j^{-1}(\theta_i+\theta_j)^3\right\}. \tag{A24}$$

Following similar mathematical steps as made before for I_ψ, one obtains

$$\int d\mathbf{v}\frac{m_iV^2}{2T_i}J_{ij}^{(0)}[f_i^{(0)},f_{j,M}F_j] = \frac{\pi^{(d-1)/2}}{4\Gamma\left(\frac{d}{2}\right)}n_in_j\chi_{ij}^{(0)}\sigma_{ij}^{d-1}v_0\mu_{ji}\left(1+\alpha_{ij}\right)\theta_i^{3/2}\theta_j^{-3/2}\left(\theta_i+\theta_j\right)^{-3/2} \times\left[2\theta_j+3\mu_{ji}\left(1+\alpha_{ij}\right)\left(\theta_i+\theta_j\right)\right]. \tag{A25}$$

Combining Eqs. (A24) and (A25), one gets the result

$$\begin{aligned}\int d\mathbf{v}F_i(V)J_{ij}^{(0)}[f_i^{(0)},f_{j,M}F_j] &= \frac{\pi^{(d-1)/2}}{4\Gamma\left(\frac{d}{2}\right)}n_in_j\chi_{ij}^{(0)}\sigma_{ij}^{d-1}v_0\mu_{ji}\left(1+\alpha_{ij}\right)\theta_i^{3/2}\theta_j^{-3/2}(\theta_i+\theta_j)^{-5/2}\\ &\times\{[(d-1)\theta_j+(d+2)\theta_i]\left[2\theta_j+3\mu_{ji}\left(1+\alpha_{ij}\right)\left(\theta_i+\theta_j\right)\right]\\ &-24\mu_{ji}^2\left(1+\alpha_{ij}\right)^2\left(\theta_i+\theta_j\right)^2+30\mu_{ji}^3\left(1+\alpha_{ij}\right)^3\theta_j^{-1}\left(\theta_i+\theta_j\right)^3\\ &-(d+2)\left(\theta_i+\theta_j\right)\left[2\theta_j+3\mu_{ji}\left(1+\alpha_{ij}\right)\left(\theta_i+\theta_j\right)\right]\}.\end{aligned} \tag{A26}$$

The remaining integrals needed to determine the collision frequencies ψ_{ii} and ψ_{ij} can be also obtained by performing identical mathematical steps. Their expressions are

$$\begin{aligned}\int d\mathbf{v}F_i(\mathbf{V})J_{ij}^{(0)}[f_{i,M}F_i,f_j^{(0)}] &= \frac{\pi^{(d-1)/2}}{4\Gamma\left(\frac{d}{2}\right)}n_in_j\chi_{ij}^{(0)}\sigma_{ij}^{d-1}v_0\mu_{ji}\left(1+\alpha_{ij}\right)\left(\theta_i\theta_j\right)^{-1/2}(\theta_i+\theta_j)^{-5/2}\\ &\times\left\{-2\left[(45+15d)\theta_j^3+3(38+13d)\theta_i\theta_j^2\right.\right.\\ &\left.+8(11+4d)\theta_i^2\theta_j+8(2+d)\theta_i^3\right]\\ &+3\mu_{ji}\left(1+\alpha_{ij}\right)\left(\theta_i+\theta_j\right)\left[(55+5d)\theta_j^2+9(10+d)\theta_i\theta_j+4(8+d)\theta_i^2\right]\\ &-24\mu_{ji}^2\left(1+\alpha_{ij}\right)^2\left(\theta_i+\theta_j\right)^2\left(5\theta_j+4\theta_i\right)+30\mu_{ji}^3\left(1+\alpha_{ij}\right)^3\left(\theta_i+\theta_j\right)^3\\ &\left.+(d+2)\theta_j\left(\theta_i+\theta_j\right)\left[2(4\theta_i+3\theta_j)-3\mu_{ji}\left(1+\alpha_{ij}\right)\left(\theta_i+\theta_j\right)\right]\right\},\end{aligned} \tag{A27}$$

$$\int d\mathbf{v}F_i(\mathbf{V})J_{ii}^{(0)}[f_i^{(0)},f_{i,M}F_i] = \frac{3\sqrt{2}}{64}\frac{\pi^{(d-1)/2}}{\Gamma\left(\frac{d}{2}\right)}n_i^2\chi_{ii}^{(0)}\sigma_i^{d-1}\left(1+\alpha_{ij}\right)v_0\theta_i^{-1/2} \times\left[10\alpha_{ii}^3+22\alpha_{ii}^2+11\alpha_{ii}-3\right], \tag{A28}$$

$$\int d\mathbf{v}F_i(\mathbf{V})J_{ii}^{(0)}[f_{i,M}F_i,f_i^{(0)}] = \frac{\sqrt{2}}{64}\frac{\pi^{(d-1)/2}}{\Gamma\left(\frac{d}{2}\right)}n_i^2\chi_{ii}^{(0)}\sigma_i^{d-1}\left(1+\alpha_{ij}\right)v_0\theta_i^{-1/2} \times\left[30\alpha_{ii}^3-126\alpha_{ii}^2+177\alpha_{ii}+16d(3\alpha_{ii}-7)-137\right]. \tag{A29}$$

The expressions for the frequencies ψ_{ii} and ψ_{ij} can be easily obtained from Eqs. (A27)–(A30) when one takes into account their definitions (2.17) and (2.18).

In the case of mechanically equivalent particles ($\chi_{ij}^{(0)}=\chi^{(0)}$, $\sigma_i=\sigma$, and $\alpha_{ij}=\alpha$), Eqs. (A28) and (A29) yield

$$\int d\mathbf{v}F(\mathbf{V})\left(J^{(0)}[f^{(0)},f_MF(\mathbf{V})]+J^{(0)}[f_MF(\mathbf{V}),f^{(0)}]\right) = \frac{\pi^{(d-1)/2}}{8\Gamma\left(\frac{d}{2}\right)}\chi^{(0)}\sigma^{d-1}n_in_j\frac{1+\alpha}{2} \times\left(30\alpha^3-30\alpha^2+105\alpha+24d\alpha-56d-73\right). \tag{A30}$$

This expression coincides with the one previously derived for a monodisperse granular gas [15].

APPENDIX B: COLLISION INTEGRALS

In this Appendix, we provide some of the mathematical steps to compute the different collision integrals involving the operator $\mathcal{K}_{ij,\gamma}[X]$. This operator is defined as

$$\mathcal{K}_{ij,\gamma}[X_j] = \sigma_{ij}^d\chi_{ij}^{(0)}\int d\mathbf{v}_2\int d\widehat{\boldsymbol{\sigma}}\Theta(\widehat{\boldsymbol{\sigma}}\cdot\mathbf{g}_{12})(\widehat{\boldsymbol{\sigma}}\cdot\mathbf{g}_{12})\widehat{\sigma}_\gamma \times\left[\alpha_{ij}^{-2}f_i^{(0)}(\mathbf{V}_1'')X_j(\mathbf{V}_2'')+f_i^{(0)}(\mathbf{V}_1)X_j(\mathbf{V}_2)\right]. \tag{B1}$$

To simplify all these type of integrals, we use the property

$$\int d\mathbf{v}_1 h(\mathbf{V}_1)\mathcal{K}_{ij,\gamma}[X_j(\mathbf{V}_2)] = -\chi_{ij}^{(0)}\sigma_{ij}^d \int d\mathbf{v}_1 \int d\mathbf{v}_2 f_i^{(0)}(\mathbf{V}_1)X_j(\mathbf{V}_2) \times \int d\widehat{\boldsymbol{\sigma}}\,\Theta(\widehat{\boldsymbol{\sigma}}\cdot\mathbf{g})(\widehat{\boldsymbol{\sigma}}\cdot\mathbf{g})\widehat{\sigma}_\gamma\left[h(\mathbf{V}_1')-h(\mathbf{V}_1)\right], \tag{B2}$$

where $\mathbf{V}_1'$ is defined by Eq. (A14).

Let us start with the collision integrals appearing in the evaluation of the mass flux. One of them is

$$I_D \equiv \int d\mathbf{v}_1 m_i V_{1,\gamma}\mathcal{K}_{ij,\gamma}[\nabla_{\mathbf{V}_2}\cdot(\mathbf{V}_2 f_j^{(0)})]. \tag{B3}$$

Use of the identity (B2) in (B3) gives

$$I_D = B_2\sigma_{ij}^d\chi_{ij}^{(0)}m_i\mu_{ji}(1+\alpha_{ij})\int d\mathbf{V}_1 \int d\mathbf{V}_2 f_i^{(0)}(\mathbf{V}_1)\nabla_{\mathbf{V}_2}\cdot\left(\mathbf{V}_2 f_j^{(0)}(\mathbf{V}_2)\right) g^2. \tag{B4}$$

The integral (B4) can be exactly evaluated and the result is

$$I_D = -2dB_2 n_i n_j \sigma_{ij}^d \chi_{ij}^{(0)}\mu_{ij}(1+\alpha_{ij})T_j. \tag{B5}$$

The remaining integrals corresponding to the mass flux can be computed by using similar mathematical steps as those made before for I_D. The results are

$$\int d\mathbf{v}_1 m_i V_{1,\beta}\mathcal{K}_{ij,\beta}[f_j^{(0)}] = dB_2 n_i n_j \sigma_{ij}^d\chi_{ij}^{(0)}m_i\mu_{ji}(1+\alpha_{ij})\left(\frac{T_i}{m_i}+\frac{T_j}{m_j}\right), \tag{B6}$$

$$\begin{aligned}\int d\mathbf{v}_1 m_i V_{1,\beta}\mathcal{K}_{i\ell,\beta}[n_j\partial_{n_j}f_\ell^{(0)}] &= \int d\mathbf{v}_1 m_i V_{1,\beta}\left(\mathcal{K}_{i\ell,\beta}[\delta_{j\ell}f_\ell^{(0)}]-\frac{1}{2}\mathcal{K}_{i\ell,\beta}[\nabla_{\mathbf{V}_2}\cdot(\mathbf{V}_2 f_\ell^{(0)})]n_j\partial_{n_j}\ln\gamma_\ell\right)\\ &= dB_2 n_i n_j\sigma_{i\ell}^d\chi_{i\ell}^{(0)}m_i\mu_{\ell i}(1+\alpha_{i\ell})\left[\delta_{j\ell}\left(\frac{T_i}{m_i}+\frac{T_\ell}{m_\ell}\right)\right.\\ &\left.+\frac{n_\ell T_\ell}{n_j m_\ell}\frac{\partial\ln\gamma_\ell}{\partial\ln n_j}\right].\end{aligned} \tag{B7}$$

The collision integral involved in the evaluation of the pressure tensor is of the form

$$\begin{aligned}I_\eta &\equiv \int d\mathbf{v}_1 m_i V_{1,\gamma}V_{1,\beta}\mathcal{K}_{ij,\gamma}[\partial_{V_\beta}f_j^{(0)}]\\ &= \chi_{ij}^{(0)}\sigma_{ij}^d m_i\int d\mathbf{v}_1\int d\mathbf{v}_2 f_i(\mathbf{V}_1)\left(\partial_{V_{2,\beta}}f_j^{(0)}(\mathbf{V}_2)\right)\\ &\times\int d\widehat{\boldsymbol{\sigma}}\,\Theta(\widehat{\boldsymbol{\sigma}}\cdot\mathbf{g})(\widehat{\boldsymbol{\sigma}}\cdot\mathbf{g})\widehat{\sigma}_\alpha\left(V_{1,\gamma}'V_{1,\beta}'-V_{1,\gamma}V_{1,\beta}\right),\end{aligned} \tag{B8}$$

where the identity (B2) has been used. The scattering rule (A14) gives

$$\begin{aligned}V_{1,\gamma}'V_{1,\beta}'-V_{1,\gamma}V_{1,\beta} &= -\mu_{ji}(1+\alpha_{ij})(\widehat{\boldsymbol{\sigma}}\cdot\mathbf{g})\left[G_{ij,\gamma}\widehat{\sigma}_\beta+G_{ij,\beta}\widehat{\sigma}_\gamma+\mu_{ji}(g_\gamma\widehat{\sigma}_\beta+g_\beta\widehat{\sigma}_\gamma\right.\\ &\left.-\mu_{ji}(1+\alpha_{ij})(\widehat{\boldsymbol{\sigma}}\cdot\mathbf{g})\widehat{\sigma}_\gamma\widehat{\sigma}_\beta\right],\end{aligned} \tag{B9}$$

where $\mathbf{G}_{ij}=\mu_{ij}\mathbf{V}_1+\mu_{ji}\mathbf{V}_2$. Substitution of Eq. (B9) into (B8) allows the angular integral to be performed with the result

$$\begin{aligned}\int d\widehat{\boldsymbol{\sigma}}\,\Theta(\widehat{\boldsymbol{\sigma}}\cdot\mathbf{g})(\widehat{\boldsymbol{\sigma}}\cdot\mathbf{g})\widehat{\sigma}_\gamma\left(V_{1,\gamma}'V_{1,\beta}'-V_{1,\gamma}V_{1,\beta}\right) &= -\frac{B_2}{d+2}\mu_{ji}(1+\alpha_{ij})\left[(d+3)g^2G_{ij,\beta}\right.\\ &+\left.\mu_{ji}(1+d-3\alpha_{ij})g^2g_\beta+2(\mathbf{g}\cdot\mathbf{G}_{ij})g_\beta\right].\end{aligned} \tag{B10}$$

With this result the integral I_η becomes

$$
\begin{aligned}
I_\eta &= -\frac{dB_2}{d+2} n_i n_j \chi_{ij}^{(0)} \sigma_{ij}^d m_i \mu_{ji} (1+\alpha_{ij}) \int d\mathbf{v}_1 \int d\mathbf{v}_2 f_i^{(0)}(\mathbf{V}_1) f_j^{(0)}(\mathbf{V}_2) \\
&\times \left[(d+2)\mu_{ji}(3\alpha_{ij}-1) g^2 - 4(d+2)(\mathbf{g}\cdot\mathbf{G}_{ij}) \right] \\
&= -dB_2 n_i n_j \chi_{ij}^{(0)} \sigma_{ij}^d m_i \mu_{ji} (1+\alpha_{ij}) m_i \left[\mu_{ji} \left(\frac{T_i}{m_i} + \frac{T_j}{m_j} \right) (3\alpha_{ij}-1) - 4 \frac{T_i - T_j}{m_i + m_j} \right].
\end{aligned}
\tag{B11}
$$

From Eq. (B11) it is easy to get the expression (3.34).

To evaluate the collision integrals appearing in the determination of the heat flux one needs the partial results

$$
\begin{aligned}
\mathbf{S}_i(\mathbf{V}_1^{'}) - \mathbf{S}_i(\mathbf{V}_1) &= \frac{m_i}{2}(1+\alpha_{ij})\mu_{ji}(\widehat{\boldsymbol{\sigma}}\cdot\mathbf{g}) \left\{ \left[(1-\alpha_{ij}^2)\mu_{ji}^2 (\widehat{\boldsymbol{\sigma}}\cdot\mathbf{g})^2 - G_{ij}^2 - \mu_{ji}^2 g^2 \right.\right. \\
&\left. -2\mu_{ji}(\mathbf{g}\cdot\mathbf{G}_{ij}) + 2(1+\alpha_{ij})\mu_{ji}(\widehat{\boldsymbol{\sigma}}\cdot\mathbf{g})(\widehat{\boldsymbol{\sigma}}\cdot\mathbf{G}_{ij}) + (d+2)\frac{T_i}{m_i} \right] \widehat{\boldsymbol{\sigma}} \\
&\left. - \left[(1-\alpha_{ij})\mu_{ji}(\widehat{\boldsymbol{\sigma}}\cdot\mathbf{g}) + 2(\widehat{\boldsymbol{\sigma}}\cdot\mathbf{G}_{ij}) \right] (\mathbf{G}_{ij} + \mu_{ji}\mathbf{g}) \right\},
\end{aligned}
\tag{B12}
$$

$$
\begin{aligned}
\int d\widehat{\boldsymbol{\sigma}}\, \Theta(\widehat{\boldsymbol{\sigma}}\cdot\mathbf{g})(\widehat{\boldsymbol{\sigma}}\cdot\mathbf{g}) \quad & \widehat{\boldsymbol{\sigma}}\cdot\left[\mathbf{S}_i(\mathbf{V}_1^{'}) - \mathbf{S}_i(\mathbf{V}_1) \right] = -\frac{3}{2}\frac{B_2}{d+2}(1+\alpha_{ij})\mu_{ji} \\
&\times \left\{ \frac{1}{3}\mu_{ji}^2 \left[(d+2) - 3\alpha_{ij}(1-\alpha_{ij}) \right] g^4 + \frac{d+4}{3} g^2 G_{ij}^2 \right. \\
&\left. + \frac{1}{3}\mu_{ji}(7+2d-9\alpha_{ij}) g^2 (\mathbf{g}\cdot\mathbf{G}_{ij}) + \frac{4}{3}(\mathbf{g}\cdot\mathbf{G}_{ij})^2 - \frac{(d+2)^2}{3}\frac{T_i}{m_i} g^2 \right\}.
\end{aligned}
\tag{B13}
$$

The corresponding integrals associated with the heat flux can be explicitly evaluated by using Eqs. (B12) and (B13) and the same mathematical steps as before. After a lengthy algebra, one gets the expressions (3.70), (3.71), and (3.72).

Let us consider now the integral appearing in the evaluation of the cooling rate. To do that, we compute first the collision integral

$$
I_\zeta = \int d\mathbf{v} V^4 \mathcal{K}_{ij,\gamma}[\partial_{V_\gamma} f_j^{(0)}].
\tag{B14}
$$

In order to evaluate it we use Eq. (A17) and the angular integrations

$$
\begin{aligned}
\int d\widehat{\boldsymbol{\sigma}}\, \Theta(\widehat{\boldsymbol{\sigma}}\cdot\mathbf{g})(\widehat{\boldsymbol{\sigma}}\cdot\mathbf{g})\widehat{\sigma}_\beta \left(V_1'^4 - V_1^4 \right) &= \frac{3B_2}{(d+2)(d+4)}\mu_{ji}(1+\alpha_{ij}) \\
&\times \left\{ 4\mu_{ji}(1+\alpha_{ij}) \left[2(\mathbf{V}_1\cdot\mathbf{g})^2 g_\beta + 2(\mathbf{V}_1\cdot\mathbf{g}) g^2 V_{1,\beta} \right.\right. \\
&\left. + \frac{1}{2}(d+6) g^2 V_1^2 g_\beta \right] + 5\mu_{ji}^3 (1+\alpha_{ij})^3 g^4 g_\beta \\
&- \frac{4}{3}(d+4) V_1^2 \left[2(\mathbf{V}_1\cdot\mathbf{g}) g_\beta + g^2 V_{1,\beta} \right] \\
&\left. - 4\mu_{ji}^2 (1+\alpha_{ij})^2 g^2 \left[4(\mathbf{V}_1\cdot\mathbf{g}) g_\beta + g^2 V_{1,\beta} \right] \right\}.
\end{aligned}
\tag{B15}
$$

With these results, the integral I_ζ becomes

$$\begin{aligned} I_\zeta &= -3dB_2 n_i n_j \chi_{ij}^{(0)} \sigma_{ij}^d m_i \mu_{ji}(1+\alpha_{ij}) \int d\mathbf{v}_1 \int d\mathbf{v}_2 f_i^{(0)}(\mathbf{V}_1) f_j^{(0)}(\mathbf{V}_2) \\ &\times \Big\{ \mu_{ji}(1+\alpha_{ij}) \left[2(d+4) g^2 V_1^2 + 8(\mathbf{V}_1\cdot\mathbf{g})^2 + 5\mu_{ji}^2(1+\alpha_{ij})^2 g^4 - 16\mu_{ji}(1+\alpha_{ij}) g^2 (\mathbf{V}_1\cdot\mathbf{g}) \right] \\ &\quad -\frac{8}{3}(d+2) V_1^2 (\mathbf{V}_1\cdot\mathbf{g}) \Big\} \\ &= -3dB_2 n_i n_j \chi_{ij}^{(0)} \sigma_{ij}^d \mu_{ji}(1+\alpha_{ij}) \left\{ \frac{T_i^2}{m_i^2} \left[\mu_{ji}(1+\alpha_{ij}) \left(16 + 2d - 16\mu_{ji}(1+\alpha_{ij}) \right. \right. \right. \\ &\quad \left. \left. \left. +5\mu_{ji}^2(1+\alpha_{ij})^2 \right) - \frac{8}{3}(d+2) \right] + 5\mu_{ji}^3 (1+\alpha_{ij})^3 \frac{T_j^2}{m_j^2} \right. \\ &\quad \left. + \frac{2}{d+2} \frac{T_i T_j}{m_i m_j} \mu_{ji}(1+\alpha_{ij}) \left[d(d+4) + 4 - 8(d+2)\mu_{ji}(1+\alpha_{ij}) + 5(d+2)\mu_{ji}^2(1+\alpha_{ij})^2 \right] \right\}. \end{aligned} \tag{B16}$$

The final expression (2.19) can be easily obtained from Eqs. (B11) and (B16).

Finally, note that the integrals C_{ij}^T and C_{ipj}^T defined by Eqs. (3.40) and (3.41), respectively, can be easily computed by using the change of variables written below Eq. (A22). After some algebra and using the Maxwellian approach for the distributions $f_i^{(0)}$ one gets the results (3.42) and (3.43).

APPENDIX C: CHOICE OF $\chi_{ij}^{(0)}$ AND $I_{i\ell j}$

This Appendix deals with the choice of the pair correlation function $\chi_{ij}^{(0)}$ and the functional derivative $I_{i\ell j}$. A good approximation for $\chi_{ij}^{(0)}$ in two dimensions ($d=2$) is given by [72]

$$\chi_{ij}^{(0)} = \frac{1}{1-\phi} + \frac{10-\phi}{16} \frac{\beta}{(1-\phi)^2} \frac{\sigma_i\sigma_j}{\sigma_{ij}} - \frac{1}{16} \frac{\beta^2}{\phi(1-\phi)} \left(\frac{\sigma_i\sigma_j}{\sigma_{ij}} \right)^2, \tag{C1}$$

where $\phi = \sum_{i=1}^s \phi_i$ is the total solid volume fraction, $\phi_i = n_i \pi \sigma_i^2/4$ is the species volume fraction of component i and $\beta = \pi(\sum_{i=1}^s n_i\sigma_i)/4$. In the case of hard-spheres ($d=3$) we take the following approximation for $\chi_{ij}^{(0)}$ [71]

$$\chi_{ij}^{(0)} = \frac{1}{1-\phi} + \frac{3}{2} \frac{\beta}{(1-\phi)^2} \frac{\sigma_i\sigma_j}{\sigma_{ij}} + \frac{1}{2} \frac{\beta^2}{(1-\phi)^3} \left(\frac{\sigma_i\sigma_j}{\sigma_{ij}} \right)^2, \tag{C2}$$

where now $\phi_i = n_i\pi\sigma_i^3/6$ and $\beta = \pi(\sum_{i=1}^s n_i\sigma_i^2)/6$.

The parameter $I_{i\ell j}$ is chosen to recover the results derived by López de Haro *et al.* [73] for ordinary polydisperse mixtures in the context of the RET. To do that, for the sake of simplicity, we assume that the temperature, the pressure and the flow velocity are homogeneous so that only the spatial gradients associated with the partial densities will be considered. In this simple case, for elastic collisions ($\alpha_{ij}=1$), the first-order distribution function is given by $f_i^{(1)} = \sum_{j=1}^s \boldsymbol{\mathcal{B}}_i^j \cdot \nabla \ln n_j$ where $\boldsymbol{\mathcal{B}}_i^j(\mathbf{V})$ verifies the integral equation

$$\left(\boldsymbol{\mathcal{L}} \boldsymbol{\mathcal{B}}^j \right)_{i,\gamma} = -V_\gamma n_j \partial_{n_j} f_i^{(0)} - \sum_{\ell=1}^s \left(\mathcal{K}_{i\ell,\gamma}[n_j\partial_{n_j} f_\ell^{(0)}] + \frac{1}{2} \left(n_\ell \partial_{n_j} \ln \chi_{i\ell}^{(0)} + I_{i\ell j} \right) \mathcal{K}_{i\ell,\gamma}[f_\ell^{(0)}] \right). \tag{C3}$$

In the elastic case, $n_j\partial_{n_j} f_\ell^{(0)} = \delta_{j\ell} f_\ell^{(0)}$ and the linear operator $\boldsymbol{\mathcal{K}}_{i\ell}[f_\ell^{(0)}]$ can be explicitly written as

$$\mathcal{K}_{i\ell,\gamma}[f_\ell^{(0)}] = 2B_2 n_\ell \chi_{i\ell}^{(0)} \sigma_{i\ell}^d V_\gamma f_i^{(0)}(\mathbf{V}). \tag{C4}$$

With this result, Eq. (C3) becomes

$$-\left(\boldsymbol{\mathcal{L}} \boldsymbol{\mathcal{B}}^j \right)_{i,\gamma} = V_\gamma f_i^{(0)} \delta_{ij} + 2B_2 \sum_{\ell=1}^s n_\ell \chi_{i\ell}^{(0)} \sigma_{i\ell}^d \left[\delta_{j\ell} + \frac{1}{2} \left(n_\ell \partial_{n_j} \ln \chi_{i\ell}^{(0)} + I_{i\ell j} \right) \right] V_\gamma f_i^{(0)}. \tag{C5}$$

Comparison with the results derived by López de Haro *et al.* [73] allow us to identify $I_{ij\ell}$ to be defined through the relation

$$\sum_{\ell=1}^{s} n_\ell \chi_{i\ell}^{(0)} \sigma_{i\ell}^d \left(n_\ell \partial_{n_j} \ln \chi_{i\ell}^{(0)} + I_{i\ell j} \right) = \frac{n_j}{B_2} \left[\frac{1}{T} \left(\frac{\partial \mu_i}{\partial n_j} \right)_{T, n_{k \neq j}} - \frac{1}{n_i} \delta_{ij} - 2 B_2 \chi_{ij}^{(0)} \sigma_{ij}^d \right], \tag{C6}$$

where μ_i is the chemical potential of species i.

[1] V. Garzó, J. W. Dufty, and C. M. Hrenya, *Enskog theory for polydisperse granular mixtures I. Navier–Stokes order transport*, preprint cond-mat/0702109 (2007).
[2] J. T. Jenkins and F. Mancini, J. Appl. Mech.-Trans. ASME **54**, 27 (1987).
[3] J. T. Jenkins and F. Mancini, Phys. Fluids A **1**, 2050 (1989).
[4] P. Zamankhan, Phys. Rev. E **52**, 4877 (1995).
[5] B. O. Arnarson and J. T. Willits, Phys. Fluids **10**, 1324 (1998).
[6] J. T. Willits and B. O. Arnarson, Phys. Fluids **11**, 3116 (1999).
[7] L. Huilin, D. Gidaspow, and E. Manger, Phys. Rev. E **64**, 061301 (2001).
[8] M. F. Rahaman, J. Naser, and P. J. Witt, Powder Technol. **138**, 82 (2003).
[9] H. Iddir and H. Arastoopour, AIChE J. **51**, 1620 (2005).
[10] D. Serero, I. Goldhirsch, S. H. Noskowicz, and M. L. Tan, J. Fluid Mech. **554**, 237 (2006).
[11] V. Garzó and J. W. Dufty, Phys. Fluids **14**, 1476 (2002).
[12] V. Garzó and J. W. Dufty, Phys. Rev. E **60**, 5706 (1999).
[13] V. Garzó, J. M. Montanero, and J. W. Dufty, Phys. Fluids **18**, 083305 (2006).
[14] V. Garzó and J. W. Dufty, Phys. Rev. E **59**, 5895 (1999).
[15] J. F. Lutsko, Phys. Rev. E **72**, 021306 (2005).
[16] V. Garzó and J. M. Montanero, J. Stat. Phys. (in press) and preprint cond-mat/0604552.
[17] V. Garzó and J. M. Montanero, Phys. Rev. E **68**, 041302 (2003).
[18] L. Barajas, L. S. Garcia-Colín, and E. Piña, J. Stat. Phys. **7**, 161 (1973).
[19] H. van Beijeren and M. H. Ernst, Physica **68**, 437 (1973).
[20] H. van Beijeren and M. H. Ernst, Physica **70**, 225 (1973).
[21] H. van Beijeren and M. H. Ernst, J. Stat. Phys. **21**, 125 (1979).
[22] M. López de Haro and V. Garzó, Physica A **197**, 98 (1993).
[23] B. O. Arnarson and J. T. Jenkins, in *Traffic and granular flow '99: Social, traffic, and granular dynamics*, edited by D. Helging, H. J. Herrmann, M. Schreckenberg, and D. E. Wolf (Springer, 2000).
[24] N. Sela and I. Goldhirsch, J. Fluid Mech. **361**, 41 (1998).
[25] J. J. Brey, M. J. Ruiz-Montero, and F. Moreno, Phys. Rev. E **63**, 061305 (2001).
[26] T. W. Martin, J. M. Huntley, and R. D. Wildman, J. Fluid Mech. **535**, 325 (2005).
[27] R. P. Behringer, E. van Doorn, R. R. Hartley, and H. K. Pak, Gran. Matt. **4**, 9 (2002).
[28] C. R. Wassgren, J. A. Cordova, R. Zenit, and A. Karion, Phys. Fluids **15**, 3318 (2003).
[29] A. Santos, V. Garzó, and J. W. Dufty, Phys. Rev. E **69**, 061303 (2004).
[30] J. E. Galvin, C. M. Hrenya, and R. D. Wildman, J. Fluid Mech. (in press).
[31] C. M. Hrenya, J. E. Galvin, and R. D. Wildman (in preparation).
[32] V. Kumaran, J. Fluid Mech. **340**, 319 (1997).
[33] D. Risso and P. Cordero, Phys. Rev. E **65**, 021304 (2002).
[34] V. Kumaran, Phys. Rev. Lett. **95**, 108001 (2005).
[35] I. Goldhirsch, Chaos **9**, 659 (1999).
[36] J. M. Montanero and V. Garzó, Physica A **310**, 17 (2002).
[37] J. F. Lutsko, Phys. Rev. E **70**, 061101 (2004).
[38] J. T. Jenkins, in *Physics of dry granular media*, edited by H. J. Hermann, J. P. Hovi, and S. Luding (Kluwer, 1998).
[39] J. M. Montanero and V. Garzó, Phys. Rev. E **67**, 021308 (2003).
[40] V. Garzó and J. M. Montanero, Phys. Rev. E **69**, 021301 (2004).
[41] S. Chapman and T. G. Cowling, *The Mathematical Theory of Non-Uniform Gases* (Cambridge University Press, Cambridge, 1970).
[42] C. S. Campbell, Annu. Rev. Fluid Mech. **22**, 57 (1990).
[43] A. Goldshtein and M. Shapiro, J. Fluid Mech. **282**, 75 (1995).
[44] I. Goldhirsch and M. L. Tan, Phys. Fluids **8**, 1752 (1996).
[45] S. E. Esipov and T. Pöschel, J. Stat. Phys. **86**, 1385 (1997).
[46] T. P. C. van Noije and M. H. Ernst, Gran. Matt. **1**, 57 (1998).
[47] J. J. Brey, D. Cubero, and M. J. Ruiz-Montero, Phys. Rev. E **59**, 1256 (1999).
[48] W. Losert, D. G. W. Cooper, J. Delour, A. Kudrolli, and J. P. Gollub, Chaos **9**, 682 (1999).
[49] A. Kudrolli and J. Henry, Phys. Rev. E **62**, R1489 (2000).

[50] A. Barrat and E. Trizac, Gran. Matt. **4**, 57 (2002).
[51] R. Clelland and C. M. Hrenya, Phys. Rev. E **65**, 031301 (2002).
[52] S. R. Dahl, R. Clelland, and C. M. Hrenya, Phys. Fluids **14**, 1972 (2002).
[53] J. M. Montanero and V. Garzó, Gran. Matt. **4**, 17 (2002).
[54] S. R. Dahl, C. M. Hrenya, V. Garzó, and J. W. Dufty, Phys. Rev. E **66**, 041301 (2002).
[55] M. Alam and S. Luding, J. Fluid Mech. **476**, 69 (2003).
[56] D. Paolotti, C. Cattuto, U. M. B. Marconi, and A. Puglisi, Gran. Matt. **5**, 75 (2003).
[57] K. Feitosa and N. Menon, Phys. Rev. Lett. **88**, 198301 (2002).
[58] R. D. Wildman and D. J. Parker, Phys. Rev. Lett. **88**, 064301 (2002).
[59] M. Schröter, S. Ulrich, J. Kreft, J. B. Swift, and H. L. Swinney, Phys. Rev. E **74**, 011307 (2006).
[60] J. E. Galvin, S. R. Dahl, and C. M. Hrenya, J. Fluid Mech. **528**, 207 (2005).
[61] J. J. Brey, M. J. Ruiz-Montero, and F. Moreno, Phys. Rev. Lett. **95**, 0978001 (2005).
[62] V. Garzó, Europhys. Lett. **75**, 521 (2006).
[63] D. K. Yoon and J. T. Jenkins, Phys. Fluids **18**, 073303 (2006).
[64] J. Ferziger and H. Kaper, *Mathematical Theory of Transport Processes in Gases* (North Holland, Amsterdam, 1972).
[65] G. A. Mansoori, N. F. Carnahan, K. E. Starling, and T. W. Leland, J. Chem. Phys. **54**, 1523 (1971).
[66] N. F. Carnahan and K. E. Starling, J. Chem. Phys. **51**, 635 (1969).
[67] M. Alam, J. Willits, B. Arnarson, and S. Luding, Phys. Fluids **11**, 4085 (2002).
[68] V. Mathiesen, T. Solberg, and B. H. Hjertager, Powder Technol. **112**, 34 (2000).
[69] J. L. Lebowitz, Phys. Rev. **133**, A895 (1964).
[70] S. Luding and A. Santos, J. Chem. Phys. **121**, 8458 (2004).
[71] T. Boublik, J. Chem. Phys. **53**, 471 (1970).
[72] A. Santos, S. B. Yuste, and M. L. de Haro, J. Chem. Phys. **117**, 5785 (2002).
[73] M. López de Haro, E. G. D. Cohen, and J. M. Kincaid, J. Chem. Phys. **78**, 2746 (1983).

Enskog kinetic theory for monodisperse gas-solid flows

V. GARZÓ[1], S. TENNETI[2], S. SUBRAMANIAM[2], and C. M. HRENYA[3]

[1]Departamento de Física, Universidad de Extremadura, E-06071 Badajoz, Spain, email: vicenteg@unex.es

[2]Department of Mechanical Engineering, Iowa State University, Ames, IA 50011,
[3] Department of Chemical and Biological Engineering, University of Colorado, Boulder, CO 80309,
email: hrenya@colorado.edu

(Received 13 March 2012)

The Enskog kinetic theory is used as a starting point to model a suspension of solid particles in a viscous gas. Unlike previous efforts for similar suspensions, the gas-phase contribution to the instantaneous particle acceleration appearing in the Enskog equation is modeled using a Langevin equation, which can be applied to a wide parameter space (high Reynolds number, etc.). Attention here is limited to low Reynolds number flow, however, in order to assess the influence of the gas phase on the constitutive relations, which was assumed negligible in a previous analytical treatment. The Chapman-Enskog method is used to derive the constitutive relations needed for the conservation of mass, momentum and granular energy. The results indicate that the Langevin model for instantaneous gas-solid force matches the form of the previous analytical treatment, indicating the promise of this method for regions of the parameter space outside of those attainable by analytical methods (higher Reynolds number, etc.). The results also indicate that the effect of the gas phase on the constitutive relations for the solid-phase shear viscosity and Dufour coefficient is non-negligible, particularly in relatively dilute systems. Moreover, unlike their granular (no gas phase) counterparts, the shear viscosity in gas-solid systems is found to be zero in the dilute limit and the Dufour coefficient is found to be non-zero in the elastic limit.

1. Introduction

The kinetic-theory-based description of rapid *granular* flows (i.e., those in which the role of the interstitial fluid is neglected) has been an active area of research for the past several decades (Campbell 1990; Goldhirsch 2003; Brilliantov & Pöschel 2004). Sinclair & Jackson (1989) first extended this analogy to rapid *gas-solid* flows in vertical tubes to explain the ubiquitous "core-annulus" flow, in which the solids are observed to have a higher concentration near the pipe wall (annulus), while the center of the pipe (core) remains relatively dilute. This extension of the kinetic-theory analogy to gas-solid systems is appropriate for relatively massive particles (i.e., high Stokes number) engaging in nearly instantaneous collisions. Such systems occur in a wide range of engineering operations, including the riser section of a circulating fluidized bed, pneumatic conveying systems, bubbling fluidized beds, etc. Correspondingly, the further development and application of kinetic-theory-based models to high-velocity, gas-solid systems have mushroomed over the last twenty years (Gidaspow 1994; Jackson 2000; Koch & Hill 2001; Gidaspow & Jiradilok 2009; Pannala *et al.* 2010). Important research thrusts have included, but are

not limited to, the effects of gas-phase turbulence, clustering instabilities, polydispersity, cohesion, non-spherical particles, and friction.

The aim of the current effort is on the fluid-solid interaction force, $\mathbf{F}_{\text{fluid}}$, present in high-velocity gas-solid flows. Particular emphasis is put on the incorporation of $\mathbf{F}_{\text{fluid}}$ into the continuum description of the solid-phase (which can later be coupled with gas-phase mass and momentum balances for a complete description of the gas-solid system). Before describing related previous works, it is worthwhile to introduce the physical picture associated with this interaction force. Mathematically, this fluid-solid force is the sum of normal ($\mathbf{F}_n$) and tangential ($\mathbf{F}_t$) forces experienced by the particle at its surface. For the case of fluid flow in z-direction around a stationary sphere, the z-component of this interaction force is given as

$$\begin{aligned} F_{\text{fluid},z} &= F_{n,z} + F_{t,z} \\ &= \int_0^{2\pi}\int_0^{\pi} \left(-p|_{r=R}\cos\theta\right) R^2 \sin\theta d\theta d\varphi + \int_0^{2\pi}\int_0^{\pi} \left(\tau_{r\theta}|_{r=R}\sin\theta\right) R^2 \sin\theta d\theta d\varphi, \end{aligned} \tag{1.1}$$

where p is the fluid pressure, $\boldsymbol{\tau}$ is the (Newtonian) fluid stress, and R is the particle radius. Accordingly, $\mathbf{F}_{\text{fluid}}$ depends on both the pressure and velocity-gradient fields at the particle surface. As an illustration of the former, the pressure field is given in figure 1b, which shows a single motionless particle suspended in mean (far-away) fluid flow (or, equivalently, a sphere moving in the same direction as mean fluid flow). For this simple case, the fluid-solid force on the particle is typically expressed as $\mathbf{F}_{\text{fluid}} = \beta(\mathbf{U}_g - \mathbf{U})$, where β is a drag coefficient that depends on the particle Reynolds number, $\mathbf{U}_g$ is the mean gas velocity and $\mathbf{U}$ is the (mean) particle velocity. A slightly more complex situation is depicted in Figure 1c, where the particle is now moving in a different direction than the mean fluid flow, as indicated by the arrow, but still unaffected by neighbor particle effects. The presence of such particle motion leads to a change in the pressure field (and velocity-gradient field, not shown) at the particle surface, thereby causing a change in $\mathbf{F}_{\text{fluid}}$ (Eq. (1.1)). An even more complex scenario is shown in figure 1d, where the presence of surrounding, moving particles causes a continual change in the pressure (and velocity) field around the particle of interest, resulting in a dynamic gas-solid interaction force. Accordingly, the fluid-solid force experienced by a single particle can be decomposed into the contributions arising from mean slip velocity between the solid and the gas-phase (figure 1b), instantaneous particle velocity fluctuations with respect to mean velocity of the solid–phase (figure 1c) and the contribution due to neighbor particle effects (figure 1d). It is worthwhile to note that this last system (figure 1d) best captures the interactions occurring in the practical gas-solid systems mentioned above (fluidized beds, etc.).

Early efforts to incorporate the effects of $\mathbf{F}_{\text{fluid}}$ into the continuum description of gas-solids flows took a relatively straightforward approach, while more recent studies have continued to increase the level of rigor. In particular, the first gas–solid models described the solid phase according to the mass, momentum, and granular energy balances developed for granular (no fluid) systems, with the only modification being the addition of a (mean) drag force onto the momentum balance. This drag force was typically described using empirical relations obtained via settling experiments (Richardson & Zaki 1954; Wen & Yu 1966; Gidaspow 1994), in which the force is a function of the relative mean velocity between the two phases and the solids volume fraction ϕ [i.e., $\mathbf{F}_{\text{fluid}} = \beta(\mathbf{U}_g - \mathbf{U})$, where β is a function of $\mathbf{U}_g - \mathbf{U}$ and ϕ]. It is worthwhile to note that with this approach, the granular energy balance does not contain any new terms arising from fluid-phase effects, nor do any of the constitutive relations for the solid phase (stress, heat flux, or

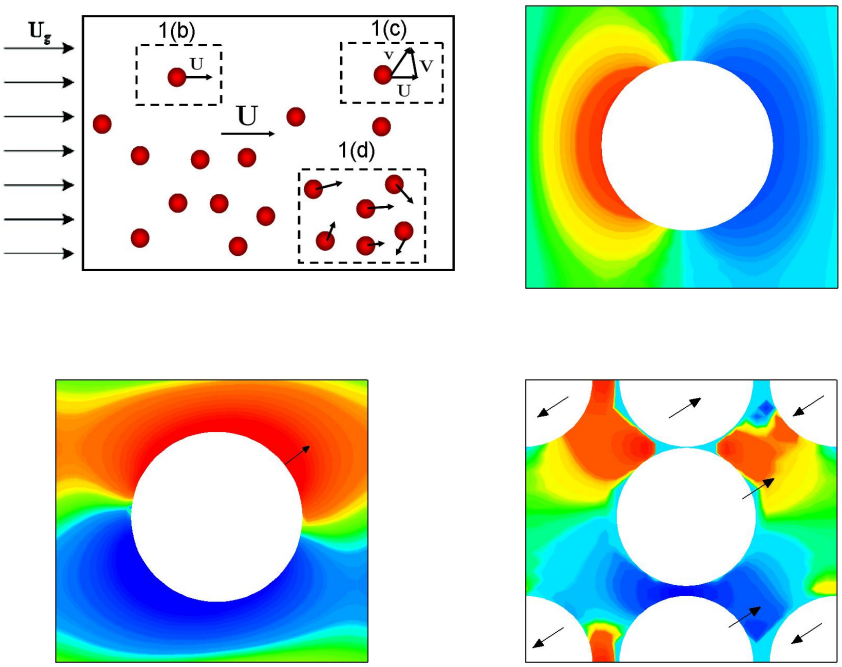

FIGURE 1. (color online) Illustration of different contributions to the instantaneous gas-solid force in a suspension with a mean fluid velocity $\mathbf{U}_g$ and a mean particle velocity $\mathbf{U}$ is shown in top left panel (a). Pressure contours are shown for (b) a single particle far away from its neighbors and moving with a velocity equal to the mean particle velocity (top right panel), (c) a particle moving in a different direction than the mean fluid flow and far from its neighbors (bottom left panel), and (d) a collection of particles moving in different directions (bottom right panel). The pressure contours are obtained from particle–resolved direct numerical simulations (PR–DNS) for a gas-solid suspension that corresponds to a solid volume fraction of 0.2 and mean flow Reynolds number 0.01.

collisional cooling rate) incorporate fluid-phase effects. As an example, see the pioneering gas-solid model proposed by Sinclair & Jackson (1989), who used the governing balances of Anderson & Jackson (1967) and the granular theory of Lun & Savage (2003). A more exact approach has since been adopted, in which fluid-phase effects are incorporated at the starting point of the derivation for the solid-phase balances and their constitutive equations, namely the kinetic equation (e.g., Boltzmann or Enskog kinetic equation):

$$\partial_t f + \mathbf{v}\cdot\nabla f + \frac{\partial}{\partial \mathbf{v}}\cdot\left[\left(\frac{\mathbf{F}_{\text{fluid}}}{m}\right) f\right] + \mathbf{g}\cdot\frac{\partial f}{\partial \mathbf{v}} = J[f,f], \tag{1.2}$$

where f is the one–particle velocity distribution function, $\mathbf{v}$ is the instantaneous particle velocity, m is the particle mass, $\mathbf{g}$ is the gravity vector, and $J[f,f]$ is the collisional operator. It is important to note here that $\mathbf{F}_{\text{fluid}}(\mathbf{r},\mathbf{v},t)$ is a function of the instantaneous particle velocity and can vary in both time and space. Strictly speaking, then, $\mathbf{F}_{\text{fluid}}$ is an instantaneous force rather than a mean force - where a mean force is one which depends on the hydrodynamic, or mean, fields. Although not strictly correct, the treatment of $\mathbf{F}_{\text{fluid}}$ as a mean force is considerably easier since it can be taken outside the differential in Eq. (1.2). Along these lines and following from the earlier discussion surrounding

Figure 1, different approximations for $\mathbf{F}_{\text{fluid}}$ have been made, leading to differences in the balance equations appearing in the literature.

Consider first the simplest case, where $\mathbf{F}_{\text{fluid}}$ is approximated as a mean force , namely $\mathbf{F}_{\text{fluid}} = \beta(\mathbf{U}_g - \mathbf{U})$, where β is a function of hydrodynamic (mean) variables (Figure 1a). For this treatment, a mean drag force will appear in the solid-phase momentum balance, consistent with the treatment described in the previous paragraph (Sinclair & Jackson 1989), but no terms appear in the granular energy equation. Next, consider an approximation which accounts for the fluctuation in the particle velocity (Figure 1b) in the following manner: $\mathbf{F}_{\text{fluid}} = \beta(\mathbf{U}_g - \mathbf{v})$ and thus is a function of the instantaneous particle velocity $\mathbf{v}$, though β remains a function of the hydrodynamic (mean) fields only. In this case, an additional sink term (which is proportional to β) arises in the granular energy balance due to viscous drag (for example, see Koch (1990)). In a third and improved approximation, fluctuations in both phases are considered in the fluid-force relation (Figure 1c), namely $\mathbf{F}_{\text{fluid}} = \beta(\mathbf{v}_g - \mathbf{v})$, where $\mathbf{v}_g$ is the instantaneous gas velocity and with β again typically treated as a function of mean variables. This treatment leads to an additional source term in the granular energy balance arising from fluid-dynamic interactions (for example, see Gidaspow (1994)). However, this approximation leads to a single point fluid-particle velocity covariance that Xu & Subramaniam (2006) have shown to be inconsistent for finite particle size.

In addition to the aforementioned impact of the $\mathbf{F}_{\text{fluid}}$ treatment on the *balance* equations, the form of $\mathbf{F}_{\text{fluid}}$ will also impact the constitutive relations for the solid-phase quantities (shear stress, heat flux, and collisional cooling rate), as these are also derived from the kinetic equation (1.2). The incorporation of such effects into the constitutive relations has received less attention in the literature. Several groups (Ma & Ahmadi 1988; Balzer *et al.* 1995; Lun & Savage 2003) have derived the constitutive relations using a description of $\mathbf{F}_{\text{fluid}}$ which depends on the instantaneous fluid ($\mathbf{v}_g$) and solid ($\mathbf{v}$) velocities. With regard to $\mathbf{v}_g$, it is worth noting that these works have included velocity fluctuations arising from fluid-phase turbulence. Other groups (Zaichik *et al.* 2009; Simonin *et al.* 2006; Février *et al.* 2005) have also incorporated the effect of turbulent gas–phase velocity fluctuations on the one-particle velocity distribution function in the regime of dilute, sub–Kolmogorov size particles. The type of fluctuations depicted in Figure 1c, on the other hand, do not require the presence of turbulent instabilities. More specifically, for the system of Figure 1c, the presence of numerous particles moving in different directions will lead to continually-changing fluid–dynamic interactions between particles (i.e., fluctuations in the fluid velocity and pressure fields) even at low Reynolds number. Finally, and perhaps more importantly, a common assumption in works that incorporate gas- and/or solid-phase fluctuations is that the basic form of the mean fluid force [$\mathbf{F}_{\text{fluid}} = \beta(\mathbf{U}_g - \mathbf{U})$] also holds for its instantaneous counterpart by simply replacing the mean hydrodynamic fields with instantaneous ones [e.g., $\mathbf{F}_{\text{fluid}} = \beta(\mathbf{v}_g - \mathbf{v})$]. Recent findings by Tenneti *et al.* (2010*b*), however, indicate that such treatments are not appropriate. Figure 2 shows a plot of the streamwise component of fluctuations in particle acceleration $\mathbf{A}''$ versus the streamwise component of fluctuations in particle velocity $\mathbf{V}$. The fluctuations in the particle acceleration and velocity are defined with respect to their corresponding mean values. The particle acceleration fluctuations are normalized by the standard deviation in the particle acceleration distribution σ_A, while the fluctuations in the particle velocity are normalized by the standard deviation in the particle velocity distribution σ_V. Square symbols are the particle acceleration fluctuations obtained from particle–resolved direct numerical simulation (PR–DNS) of a freely evolving gas–solid suspension. Triangles are the fluctuations in the particle acceleration predicted by using a model for the fluid–particle force of the form $\mathbf{F}_{\text{fluid}} = \beta\,(\mathbf{U}_g - \mathbf{v})$. It is clear

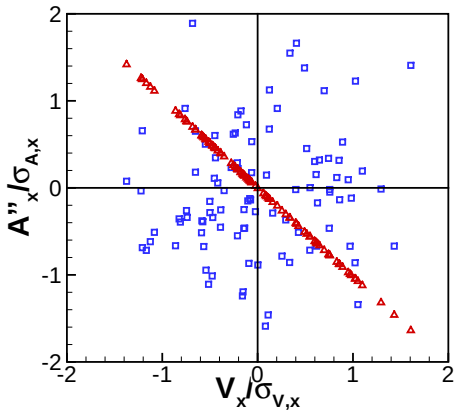

FIGURE 2. (color online) Scatter plot of streamwise component of particle acceleration fluctuations $\mathbf{A}''$ (normalized by the standard deviation in the particle acceleration distribution σ_A) versus the streamwise component of particle velocity fluctuations $\mathbf{V}$ (normalized by the standard deviation in the particle acceleration distribution σ_v). Square symbols (□) denote the fluctuations in the particle acceleration obtained from PR–DNS of a freely evolving gas–solid suspension corresponding to a solid volume fraction of 0.2, mean flow Reynolds number of 1.0 and solid to fluid density ratio of 1000. Upper triangles (△) denote the fluctuations in the particle acceleration predicted by using a model for the fluid–particle force of the form $\mathbf{F}_{\text{fluid}} = \beta\,(\mathbf{U}_g - \mathbf{v})$.

that the joint statistics of the particle acceleration and particle velocity that are crucial for the accurate prediction of the evolution of granular temperature are not well captured by this simplified class of instantaneous models for $\mathbf{F}_{\text{fluid}}$. Although the model $\mathbf{F}_{\text{fluid}} = \beta\,(\mathbf{U}_g - \mathbf{v})$ results in a sink of granular temperature, it does not account for the source in granular temperature that is responsible for points in quadrants I and III of the fluctuating particle acceleration–velocity scatter plot (see Tenneti *et al.* (2010*a*) for details). Moreover, the scatter observed in the particle acceleration fluctuations suggests a stochastic contribution to the fluid–particle force that arises due to the effect of the neighbor particles. For the limiting case of Stokes flow, Koch and co-workers (Koch 1990; Koch & Sangani 1999) were able to correctly describe the acceleration–velocity correlation via analytical means (Koch 1990) and through the use of multipole expansions (Koch & Sangani 1999). Extensions of analytical approaches beyond the Stokes limit are difficult since the governing Navier-Stokes equations become nonlinear (Koch & Hill 2001). A further assumption of their analysis was that the influence of gas-phase effects on constitutive relations for the solid phase are negligible at sufficiently large Stokes number; such effects appeared in the balance equations only.

A long-term objective of this effort, then, is to develop a framework in which (i) an accurate instantaneous model for $\mathbf{F}_{\text{fluid}}$ is developed over a wide range of conditions, and (ii) the resulting $\mathbf{F}_{\text{fluid}}$ model is used to derive solid-phase balance equations and constitutive relations which fully incorporate gas-phase effects. With regard to (i), the instantaneous gas-solid force is modeled using a Langevin equation because the particle velocity autocorrelation decays exponentially for a range of mean flow Reynolds numbers (see Fig. 3). With regard to (ii), the Langevin model for $\mathbf{F}_{\text{fluid}}$ is then used in the kinetic equation (1.2) to derive the balance equations and constitutive relations. As a first step in this direction, this two-part process is carried out here for low Reynolds numbers. It is important to note that the methodology itself is not restricted to this limit; instead, the focus here is to demonstrate proof-of-concept by (i) comparing the Langevin model

for $\mathbf{F}_{\text{fluid}}$ with previous results for the Stokes limit (Koch 1990; Koch & Sangani 1999), and (ii) use this model to assess the influence of gas-phase effects on the constitutive relations, which were neglected in the analytical treatment. For future extensions to higher Reynolds numbers, the coefficients in the Langevin model can be obtained from PR–DNS as described by Tenneti *et al.* (2010*a*) (see also Tenneti *et al.* (2011)).

2. Fluid–solid force ($\mathbf{F}_{\text{fluid}}$) model

As mentioned above, to develop a closed kinetic equation for the one-particle velocity distribution function $f(\mathbf{v})$ (Eq. (1.2)), a description of the instantaneous particle force $\mathbf{F}_{\text{fluid}}$ is needed. As the name implies, this instantaneous force is a function of the instantaneous velocities of both the gas and solid phases ($\mathbf{v}_g$ and $\mathbf{v}$, respectively), rather than solely the corresponding mean velocities ($\mathbf{U}_g$ and $\mathbf{U}$). However, consideration of $\mathbf{v}_g$ and $\mathbf{v}$ for finite particle size would require consideration of two–point statistics (Sundaram & Collins 1999; Xu & Subramaniam 2006). Note that fluctuations in the particle velocity may arise from particle interactions (collisional) and/or gas-solid interactions. Although in the special case of Stokes flow the fluid–dynamic interaction arising from neighbor particles can be treated analytically (Koch 1990) for the general case of finite fluid inertia, this is not feasible.

Therefore, a generalized Langevin model is proposed for the instantaneous impulse as follows

$$m d\mathbf{v} = \mathbf{F}_{\text{fluid}} dt = -\beta\,(\mathbf{U} - \mathbf{U}_g)\,dt - \boldsymbol{\gamma}\cdot\mathbf{V} dt + m\mathbf{B}\cdot d\mathbf{W}, \tag{2.1}$$

where $\mathbf{V} = \mathbf{v} - \mathbf{U}$ is the particle fluctuation (or *peculiar*) velocity, the vector $d\mathbf{W}$ is a Wiener process increment (stochastic term), and the scalar β and the tensors $\boldsymbol{\gamma}$ and $\mathbf{B}$ are the model coefficients. The first term on the right-hand-side represents the portion of the drag force arising from the mean motion of particle and solid phase; the second term is traced to fluctuations in the particle velocity; the third term is a stochastic model for the change in particle momentum due to shear stress and pressure contributions at the particle surface that arise from the fluid velocity and pressure disturbances caused by neighbor particles. This is one way to extend the analysis of Koch (1990) for point particles in Stokes flow regime to gas-solid flows with finite fluid inertia and finite particle size. Regarding this third term, note that the instantaneous velocity for the gas phase can be determined rigorously by considering the distribution function for the fluid velocity (in addition to that of the particle velocity, Eq. (1.2)), though such an approach would involve two-point distributions (Sundaram & Collins 1999) which is outside of the current scope and thus a stochastic model is adopted here. In the following section we outline the assumptions made in this work and justify their validity for the range of physical parameters considered here.

3. Assumptions and their range of validity

The assumptions that are used in this work are relevant to the range of dimensionless physical parameters encountered in a circulating fluidized bed (CFB). The relevant independent set of dimensionless parameters are the solid volume fraction ϕ, the mean flow Reynolds number Re_{m}, the Reynolds number associated with the particle velocity fluctuations Re_{T}, and the ratio of the densities of the solid and the gas ρ_s/ρ_g. The mean flow Reynolds number is defined as

$$\text{Re}_{\text{m}} = \frac{(1-\phi)\rho_g \sigma |\Delta\mathbf{U}|}{\mu_g}, \tag{3.1}$$

where, $\Delta\mathbf{U} = \mathbf{U} - \mathbf{U}_g$, σ is the particle diameter and ρ_g, μ_g are the mass density and dynamic viscosity of the gas, respectively. The Reynolds number associated with the particle velocity fluctuations is defined as

$$\mathrm{Re_T} = \frac{\rho_g \sigma}{\mu_g}\sqrt{\frac{T}{m}}, \tag{3.2}$$

where T is the granular temperature (cf. Eq. (4.10)) and m is the mass of the particle. It is worth noting that some previous works (Koch 1990) on gas-solid suspensions in the Stokes flow regime cast their results in terms of a Stokes number St (rather than $\mathrm{Re_m}$ and/or $\mathrm{Re_T}$). Here, for a three-dimensional system, we define the two relevant Stokes numbers as

$$\mathrm{St_m} = \frac{m|\Delta\mathbf{U}|}{6\pi\mu_g R^2}, \tag{3.3}$$

$$\mathrm{St_T} = \frac{m\sqrt{T/m}}{6\pi\mu_g R^2}, \tag{3.4}$$

where $R = \sigma/2$ is the radius of a particle. Thus, the relationship between the Stokes numbers and corresponding Reynolds numbers are

$$\mathrm{St_m} = \frac{1}{9(1-\phi)}\frac{\rho_s}{\rho_g}\mathrm{Re_m}, \tag{3.5}$$

$$\mathrm{St_T} = \frac{1}{9}\frac{\rho_s}{\rho_g}\mathrm{Re_T}, \tag{3.6}$$

where $\rho_s = 6m/(\pi\sigma^3)$ is the mass density of a particle. Whereas $\mathrm{Re_m}$ and $\mathrm{Re_T}$ are measures of the *fluid* inertia (related to mean and fluctuating components of particle motion, respectively) to viscous effects, the Stokes numbers $\mathrm{St_m}$ and $\mathrm{St_T}$ are measures of *particle* inertia to fluid viscous effects. The results presented in this paper (cf. §8) will give ranges for each of these parameters for purposes of greater physical understanding (even though they are not independent quantities).

The most important assumption in this work is that the instantaneous impulse can be modeled using a Langevin equation (cf. Eq. (2.1)). The assumption that is implicit in using this model is that the change in particle momentum due to neighbor particle effects occurs on time scales much smaller than those associated with drag due to the mean slip and particle velocity fluctuations. The validity of the Langevin model can be justified by examining the decay of particle velocity autocorrelation function that is computed from PR–DNS (that accounts for all fluid–dynamic interactions exactly). The particle velocity autocorrelation function $\rho(s)$ is defined as

$$\rho(s) = \frac{\langle V_i(t_0)\, V_i(t_0+s)\rangle}{\langle V_k(t_0)\, V_k(t_0)\rangle}, \tag{3.7}$$

where $\mathbf{V}$ denotes fluctuation in the particle velocity (or peculiar velocity) around the mean velocity computed from PR–DNS and s is the separation in time. The angular brackets $\langle\cdots\rangle$ in Eq. (3.7) denote an average over all particle configurations and velocities. The integral time scale for the autocorrelation function is

$$T_L = \int_0^\infty \rho(s)\, ds. \tag{3.8}$$

If a stochastic process obeys the Langevin equation with an integral time scale of T_L, then its autocorrelation function should decay exponentially (Gardiner 1985), i.e., $\rho(s) =$

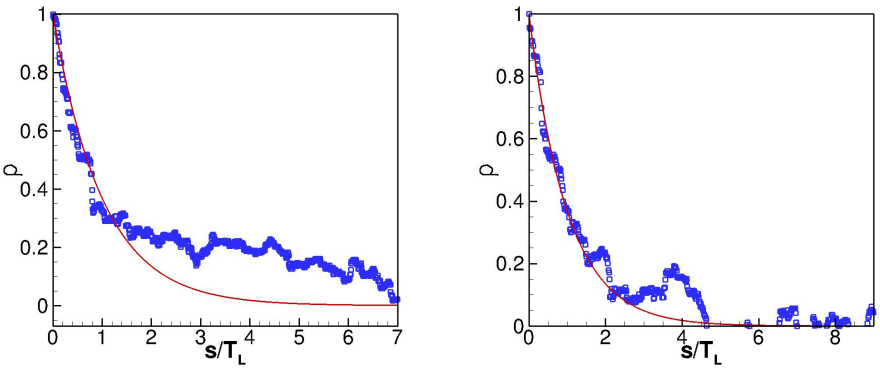

FIGURE 3. (color online) Decay of the particle velocity autocorrelation function. Figure 3(a) compares the particle velocity autocorrelation function computed from PR–DNS (symbols) of freely evolving suspension (volume fraction of 0.2, mean flow Reynolds number 1.0 and solid to fluid density ratio of 1000) with the exponential decay predicted by the Langevin model (solid line). Figure 3(b) is the same as Fig. 3(a) for a suspension with a solid volume fraction of 0.35.

e^{-s/T_L}. The velocity autocorrelation function computed from PR–DNS of freely evolving gas–solid suspensions and the exponential decay predicted by the Langevin model are compared in Fig. 3. The good agreement of the decay of the velocity autocorrelation function obtained from PR–DNS with the exponential decay indicates that the use of Langevin model is appropriate.

Although the quantities $\boldsymbol{\gamma}$ and $\mathbf{B}$ in Eq. (2.1) are given as tensors in the most general case, as a first approximation, we take $\gamma_{ij} = \gamma\delta_{ij}$ and $B_{ij} = B\delta_{ij}$ to obtain a distribution function which is isotropic in velocity space for the homogeneous flow and additionally provide analytical expressions for all the transport coefficients and the collisional cooling rate. We verify this assumption of isotropy by computing the state of anisotropy of the particle–phase Reynolds stress (RS), defined as the average $\langle V_i V_j \rangle$, from PR–DNS. The invariants of the deviatoric part of the normalized particle–phase RS, $\xi_{\rm RS}$ and $\eta_{\rm RS}$, are plotted on the Lumley plane (Lumley & Newman 1977) to characterize the state of anisotropy. In the three-dimensional case, the deviatoric part of the normalized particle–phase RS is defined as

$$b_{ij} = \frac{\langle V_i V_j \rangle}{\langle V_k V_k \rangle} - \frac{1}{3}\delta_{ij}, \tag{3.9}$$

and the invariants are defined following Lumley & Newman (1977) as $6\eta_{\rm RS}^2 = b_{ij}b_{ij}$ and $6\xi_{\rm RS}^3 = b_{ij}b_{jk}b_{ki}$. The state of anisotropy of the particle–phase RS is studied by plotting $\eta_{\rm RS}$ versus $\xi_{\rm RS}$. The origin of this plane denotes an isotropic state, while the point (1/3, 1/3) denotes a one–component axisymmetric state of the particle–phase RS. The evolution of the invariants obtained from PR–DNS for $\phi = 0.35$, $\rho_s/\rho_g = 1000$ and two different Reynolds numbers ($\mathrm{Re_m} = 1.0$ and $\mathrm{Re_m} = 0.5$) is plotted in Fig. 4. The results show that the state of anisotropy in the solid–phase is small for the range of physical parameters considered in this work and hence the assumption of isotropic coefficients is justified. The results also indicate that the effect of collisions rapidly isotropizes the anisotropy introduced by fluid–dynamic interactions in the particle–phase RS. It is also worthwhile to note that this assumption is consistent for a homogeneous system, since the homogeneous (zeroth order) solution to the kinetic equation (1.2) will be isotropic

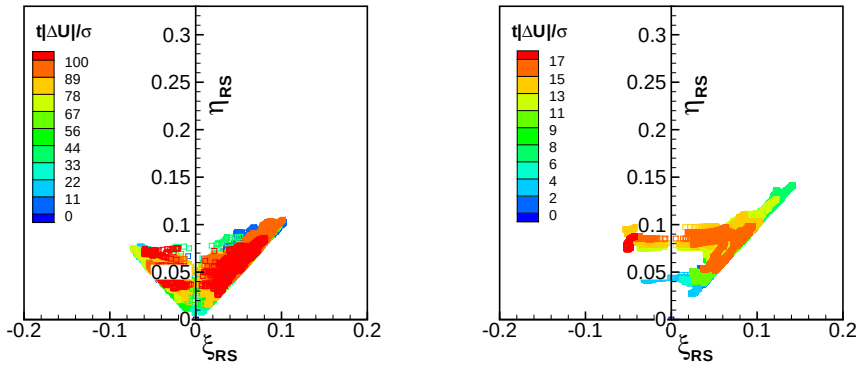

FIGURE 4. Evolution of the invariants of the deviatoric part of the normalized particle–phase RS in time. Blue symbols denote earlier time and red symbols denote later time. These results are obtained from PR–DNS of freely evolving suspensions corresponding to a solid volume fraction of 0.35 and solid to fluid density ratio of 1000 for the following mean flow Reynolds numbers: (a) 1.0 and (b) 0.5.

as no spatial gradients exist for a homogenous system. The description for general forms for $\boldsymbol{\gamma}$ and $\mathbf{B}$ is an interesting problem to be addressed in the future.

The final assumption made in this work is related to the Chapman–Enskog expansion (see §5 for further details), which is essentially a perturbation method about a small Knudsen number. The Knudsen number Kn is defined as the ratio of the mean free path of the particles to a length scale that characterizes the distance over which gradients in the hydrodynamic variables occur. The mean free path is a function of the solid volume fraction only, while the length scale associated with the gradients depends on the specific gas–solid flow system. Since the results in this work are applicable to any geometry and flow situation, assessment of this low–Kn assumption is not possible *a priori*.

4. Kinetic equation for gas-solid flows

We consider a suspension of solid particles of mass m and diameter σ immersed in a gas. Under rapid flow conditions, particles are usually modeled as a gas of inelastic hard spheres. In the simplest model, the spheres are completely smooth so that the inelasticity of collisions is characterized by a (constant) coefficient of normal restitution $0 < \alpha \leqslant 1$. As described in §2, the influence of gas phase on particles is accomplished by the inclusion of three new quantities (see Eq. (2.1)) in the instantaneous particle force: β, γ and B.

Under the above conditions and in the presence of the gravitational force $m\mathbf{g}$, the Enskog kinetic equation (Brey *et al.* 1997; Brilliantov & Pöschel 2004) for the one-particle velocity distribution function $f(\mathbf{r}, \mathbf{v}, t)$ of grains reads

$$\partial_t f + \mathbf{v}\cdot\nabla f - \frac{\beta}{m}\Delta\mathbf{U}\cdot\frac{\partial f}{\partial \mathbf{V}} - \frac{\gamma}{m}\frac{\partial}{\partial \mathbf{V}}\cdot\mathbf{V}f - \frac{1}{2}\xi\frac{\partial^2}{\partial V^2}f + \mathbf{g}\cdot\frac{\partial f}{\partial \mathbf{V}} = J_{\mathrm{E}}\left[\mathbf{r}, \mathbf{v}|f, f\right], \quad (4.1)$$

where

$$\begin{aligned} J_{\mathrm{E}}\left[\mathbf{r}, \mathbf{v}_1|f, f\right] = \sigma^{d-1}\int d\mathbf{v}_2 \int d\widehat{\boldsymbol{\sigma}}\,\Theta(\widehat{\boldsymbol{\sigma}}\cdot\mathbf{g}_{12})(\widehat{\boldsymbol{\sigma}}\cdot\mathbf{g}_{12}) \\ \times\left[\alpha^{-2}\chi(\mathbf{r}, \mathbf{r}-\boldsymbol{\sigma})f(\mathbf{r}, \mathbf{v}_1'; t)f(\mathbf{r}-\boldsymbol{\sigma}, \mathbf{v}_2'; t)\right. \\ \left.-\chi(\mathbf{r}, \mathbf{r}+\boldsymbol{\sigma})f(\mathbf{r}, \mathbf{v}_1; t)f(\mathbf{r}+\boldsymbol{\sigma}, \mathbf{v}_2; t)\right] \end{aligned} \quad (4.2)$$

is the Enskog collision operator. Here, d is the dimensionality of the system ($d = 2$ for disks and $d = 3$ for spheres), $\boldsymbol{\sigma} = \sigma\widehat{\boldsymbol{\sigma}}$, $\widehat{\boldsymbol{\sigma}}$ being a unit vector pointing in the direction from the center of particle 1 to the center of particle 2, σ is the particle diameter, Θ is the Heaviside step function, $\mathbf{g}_{12} = \mathbf{v}_1 - \mathbf{v}_2$ and $\chi[\mathbf{r}, \mathbf{r} + \boldsymbol{\sigma}|\{n(t)\}]$ is the equilibrium pair correlation function at contact as a functional of the nonequilibrium density field $n(\mathbf{r}, t)$ defined by

$$n(\mathbf{r}, t) = \int d\mathbf{v} f(\mathbf{r}, \mathbf{v}, t). \tag{4.3}$$

For the case of spheres ($d = 3$) considered in this work, the Carnahan-Starling approximation (Carnahan & Starling 1969) for χ is given by

$$\chi(\phi) = \frac{1 - \frac{1}{2}\phi}{(1 - \phi)^3}. \tag{4.4}$$

The primes on the velocities in Eq. (4.2) denote the initial values $\{\mathbf{v}_1', \mathbf{v}_2'\}$ that lead to $\{\mathbf{v}_1, \mathbf{v}_2\}$ following a binary collision:

$$\mathbf{v}_1' = \mathbf{v}_1 - \frac{1}{2}\left(1 + \alpha^{-1}\right)(\widehat{\boldsymbol{\sigma}} \cdot \mathbf{g}_{12})\widehat{\boldsymbol{\sigma}}, \quad \mathbf{v}_2' = \mathbf{v}_2 + \frac{1}{2}\left(1 + \alpha^{-1}\right)(\widehat{\boldsymbol{\sigma}} \cdot \mathbf{g}_{12})\widehat{\boldsymbol{\sigma}}. \tag{4.5}$$

Moreover, in Eq. (4.1), $B^2 \equiv \xi$ and

$$\mathbf{U}(\mathbf{r}, t) = \frac{1}{n}\int d\mathbf{v}\mathbf{v} f(\mathbf{r}, \mathbf{v}, t) \tag{4.6}$$

is the mean particle velocity. As said before, the scalar coefficients β, γ, and ξ appearing in Eq. (4.1) are associated with the instantaneous gas-solid force. Recall that β appears in the mean portion of this drag force (first term on right-hand-side of Eq. (2.1)), and the terms γ and ξ are associated with the fluctuating solid velocity and particle momentum change caused by neighbor particles, respectively (Abbas *et al.* 2009).

The macroscopic balance equations for the system are obtained when one multiplies the Enskog equation (4.1) by $\{1, m\mathbf{V}, mV^2\}$ and integrates over velocity. After some lengthy algebra one gets

$$D_t n + n\nabla \cdot \mathbf{U} = 0\,, \tag{4.7}$$

$$D_t \mathbf{U} + (mn)^{-1}\nabla \cdot \mathsf{P} = -\frac{\beta}{m}\Delta\mathbf{U} + \mathbf{g}\,, \tag{4.8}$$

$$D_t T + \frac{2}{dn}\left(\nabla \cdot \mathbf{q} + \mathsf{P} : \nabla\mathbf{U}\right) = -\frac{2T}{m}\gamma + m\xi - \zeta T\,. \tag{4.9}$$

In the above equations, $D_t = \partial_t + \mathbf{U} \cdot \nabla$ is the material derivative and

$$T(\mathbf{r}, t) = \frac{1}{dn}\int d\mathbf{v} m V^2 f(\mathbf{r}, \mathbf{v}, t) \tag{4.10}$$

is the granular temperature. This quantity is a measure of the mean square fluctuating particle velocity. The collisional cooling rate ζ is proportional to $1 - \alpha^2$ and is due to dissipative collisions. The pressure tensor $\mathsf{P}(\mathbf{r}, t)$ and the heat flux $\mathbf{q}(\mathbf{r}, t)$ have both *kinetic* and *collisional transfer* contributions, i.e., $\mathsf{P} = \mathsf{P}^k + \mathsf{P}^c$ and $\mathbf{q} = \mathbf{q}^k + \mathbf{q}^c$. The kinetic, or streaming, contributions stem from the particles carrying momentum and granular energy with them as they travel from one part of the domain to another, while the collisional contributions arise from a transfer of momentum and granular energy between particles as they collide. The kinetic contributions P^k and $\mathbf{q}^k$ are given, respectively, by

$$\mathsf{P}^k(\mathbf{r}, t) = \int d\mathbf{v} m\mathbf{V}\mathbf{V} f(\mathbf{r}, \mathbf{v}, t), \quad \mathbf{q}^k(\mathbf{r}, t) = \int d\mathbf{v}\frac{m}{2}V^2\mathbf{V} f(\mathbf{r}, \mathbf{v}, t), \tag{4.11}$$

and the collisional transfer contributions are (Brey *et al.* 1997; Garzó & Dufty 1999)

$$\mathsf{P}^c(\mathbf{r},t) = \frac{1+\alpha}{4} m\sigma^d \int d\mathbf{v}_1 \int d\mathbf{v}_2 \int d\widehat{\boldsymbol{\sigma}}\, \Theta(\widehat{\boldsymbol{\sigma}}\cdot\mathbf{g}_{12})(\widehat{\boldsymbol{\sigma}}\cdot\mathbf{g}_{12})^2 \widehat{\boldsymbol{\sigma}}\widehat{\boldsymbol{\sigma}} \times \int_0^1 dx\; f^{(2)}\left[\mathbf{r}-x\boldsymbol{\sigma}, \mathbf{r}+(1-x)\boldsymbol{\sigma}, \mathbf{v}_1, \mathbf{v}_2; t\right], \tag{4.12}$$

$$\mathbf{q}^c(\mathbf{r},t) = \frac{1+\alpha}{4} m\sigma^d \int d\mathbf{v}_1 \int d\mathbf{v}_2 \int d\widehat{\boldsymbol{\sigma}}\, \Theta(\widehat{\boldsymbol{\sigma}}\cdot\mathbf{g}_{12})(\widehat{\boldsymbol{\sigma}}\cdot\mathbf{g}_{12})^2 (\mathbf{G}_{12}\cdot\widehat{\boldsymbol{\sigma}})\widehat{\boldsymbol{\sigma}} \times \int_0^1 dx\; f^{(2)}\left[\mathbf{r}-x\boldsymbol{\sigma}, \mathbf{r}+(1-x)\boldsymbol{\sigma}, \mathbf{v}_1, \mathbf{v}_2; t\right]. \tag{4.13}$$

Here, $\mathbf{G}_{12} = \frac{1}{2}(\mathbf{V}_1 + \mathbf{V}_2)$ is the velocity of center of mass and

$$f^{(2)}(\mathbf{r}_1, \mathbf{r}_2, \mathbf{v}_1, \mathbf{v}_2, t) \equiv \chi(\mathbf{r}_1, \mathbf{r}_2 | n(t)) f(\mathbf{r}_1, \mathbf{v}_1, t) f(\mathbf{r}_2, \mathbf{v}_2, t). \tag{4.14}$$

Finally, the collisional cooling rate is given by

$$\zeta(\mathbf{r},t) = \frac{\left(1-\alpha^2\right)}{4dnT} m\sigma^{d-1} \int d\mathbf{v}_1 \int d\mathbf{v}_2 \int d\widehat{\boldsymbol{\sigma}} \Theta(\widehat{\boldsymbol{\sigma}}\cdot\mathbf{g}_{12})(\widehat{\boldsymbol{\sigma}}\cdot\mathbf{g}_{12})^3 f^{(2)}(\mathbf{r}, \mathbf{r}+\boldsymbol{\sigma}, \mathbf{v}_1, \mathbf{v}_2; t). \tag{4.15}$$

For a statistically homogeneous suspension undergoing elastic collisions ($\alpha = 1$), $\zeta = 0$ and the granular energy equation (4.9) becomes

$$\frac{dT}{dt} = -\frac{2T}{m}\gamma + m\xi. \tag{4.16}$$

Comparing this equation with the granular energy equation given for spheres ($d = 3$) by Koch & Sangani (1999)

$$\frac{3}{2}\frac{dT}{dt} = -\Gamma_{\text{vis}} + S, \tag{4.17}$$

one sees that there is a one-to-one correspondence between the coefficients γ and ξ and the dissipation Γ_{vis} and source S in Koch & Sangani (1999), respectively. Therefore, for Stokes flow we can use the existing analytical closure from Koch (1990) for solid volume fraction $\phi \leqslant 0.1$. For $\phi > 0.1$, Koch & Sangani (1999) used simulations based on multipole expansions to propose source and dissipation terms as a function of solid volume fraction. It must be noted that the correlation used for the drag coefficient does not include the effect of forces like buoyancy, shear lift, spin lift, etc. Accordingly, these coefficients depend on constant parameters (particle mass and diameter, gas viscosity) as well as the hydrodynamic (mean) variables (solids concentration, gas and solid velocities, and granular temperature); explicit dependencies are given in §8.

The macroscopic balance equations (4.7)–(4.9) are not entirely expressed in terms of the hydrodynamic fields due to the presence of the collisional cooling rate ζ, the pressure tensor P and the heat flux $\mathbf{q}$ which are given as functionals of the distribution function $f(\mathbf{r}, \mathbf{v}, t)$. However, if this distribution function can be expressed as functionals of the hydrodynamic fields, then the collisional cooling rate and the fluxes will also become functional of the hydrodynamic fields through Eqs. (4.11)–(4.13) and (4.15). Such expressions are called *constitutive* relations and are the link between the exact balance equations and a closed set of equations for the fields n, $\mathbf{U}$ and T. This hydrodynamic description can be derived by looking for a *normal* solution to the Enskog equation by means of the Chapman-Enskog (CE) method (Chapman & Cowling 1970) adapted to inelastic collisions, as detailed in §5.

It is worthwhile to note that the macroscopic equations given in Eqs. (4.7)–(4.9) differ from their granular (no gas phase) counterparts (Garzó & Dufty 1999) via the appearance of three additional terms arising from the presence of the gas phase, and more specifically the instantaneous drag force (Eq. (2.1)). The first of these contains β and appears in the momentum balance (Eq. (4.8)); this term represents the mean drag force between the two phases. The other two terms stemming from the gas phase appear in the granular energy balance (Eq. (4.9)); the term containing γ represents the sink due to viscous drag while the term containing ξ represents the source arising from the change in particle momentum due to neighbor particles. Similar effects of the gas phase on the constitutive expressions for the pressure tensor P, the heat flux $\mathbf{q}$ and the collisional cooling rate ζ will be presented in §6 and §7.

5. Chapman-Enskog solution

The CE method assumes the existence of a normal solution such that all space and time dependence of the distribution function occurs through the hydrodynamic fields

$$f(\mathbf{r},\mathbf{v},t) = f\left[\mathbf{v}|n(\mathbf{r},t),T(\mathbf{r},t),\mathbf{U}(\mathbf{r},t)\right] \ . \tag{5.1}$$

The notation on the right hand side indicates a functional dependence on the density, temperature and flow velocity. For small spatial variations (i.e., low Knudsen numbers), this functional dependence can be made local in space through an expansion in gradients of the hydrodynamic fields. To generate it, f is written as a series expansion in a formal parameter ϵ measuring the nonuniformity of the system,

$$f = f^{(0)} + \epsilon\, f^{(1)} + \epsilon^2\, f^{(2)} + \cdots \ , \tag{5.2}$$

where each factor of ϵ means an implicit gradient of a hydrodynamic field. The uniformity parameter ϵ is related to the Knudsen number Kn defined as the ratio of the mean free path of the particles to a length scale that characterizes the distance over which gradients in the hydrodynamic variables occur. Note that while the strength of the gradients can be controlled by the initial or the boundary conditions in the case of elastic collisions, the problem is more complicated for granular fluids since in some cases (e.g., steady states such as the simple shear flow (Goldhirsch 2003; Santos *et al.* 2004)) there is an intrinsic relation between dissipation and some hydrodynamic gradient. In these situations the Navier-Stokes approximation (first order in the expansion) only applies for nearly elastic systems (Goldhirsch 2003). Here, however we consider situations where the spatial gradients are sufficiently small (low Knudsen number) (Hrenya *et al.* 2008). Moreover, in ordering the different level of approximations in the kinetic equation, one has to characterize the magnitude of the external forces relative to the gradients as well. The scaling of the forces depends on the conditions of interest. Here, we assume that the external forces (gravity and drag forces) do not induce any flux in the system and only modify the form of the transport coefficients. As a consequence, g, β, γ and ξ are taken to be of zeroth order in gradients.

According to the expansion (5.2) for the distribution function, the Enskog collision operator and time derivative are also given in the representations

$$J_{\mathrm{E}} = J_{\mathrm{E}}^{(0)} + \epsilon J_{\mathrm{E}}^{(1)} + \cdots \ , \quad \partial_t = \partial_t^{(0)} + \epsilon\partial_t^{(1)} + \cdots \ . \tag{5.3}$$

The coefficients in the time derivative expansion are identified by a representation of the fluxes and the collisional cooling rate in the macroscopic balance equations as a similar series through their definitions as functionals of f. This is the usual CE method (Chapman & Cowling 1970; Garzó & Santos 2003) for solving kinetic equations. The

main difference here with respect to previous works (Garzó & Dufty 1999; Brey *et al.* 1998) is that the reference state $f^{(0)}$ has a time dependence associated with the fluid phase terms γ and ξ apart from the one associated with the collisional cooling rate that is not proportional to the gradients. As a consequence, terms from the time derivative $\partial_t^{(0)}$ are not zero as expected. In addition, given that collisional dissipation and gradients are uncoupled, the different approximations $f^{(k)}$ are nonlinear functions of α, regardless of the applicability of the corresponding hydrodynamic equations truncated at that order.

To summarize, the Chapman-Enskog expansion is carried out up to first order (Navier-Stokes order), resulting in constitutive equations which are proportional to the first order spatial derivatives in the hydrodynamic fields. This first order expansion is strictly valid for small Knudsen number Kn. Because the length scale for variations of the hydrodynamic fields depends on the local flow field, the assumption of small Kn (also known as the "small gradient" assumption) may be valid for some flow geometries and invalid for others. Since our results are presented below in a general form (prior to the application for any specific flow geometry), assessment of this low Knudsen assumption is not possible *a priori*. Nonetheless, it is worth noting that for ordinary fluids, the Navier-Stokes hydrodynamic equations work well beyond their range of validity expected from a strict application of their assumptions. The same has also been found to be true for granular fluids; namely, the range of applicability of the Navier-Stokes description, based on comparisons with experimental data, is often much wider than expected (Rericha *et al.* 2002; Wildman *et al.* 2008).

6. Local homogeneous state. Zeroth-order solution

To zeroth-order in ϵ, the Enskog equation (4.1) becomes

$$\partial_t^{(0)} f^{(0)} - \frac{\beta}{m}\Delta\mathbf{U}\cdot\frac{\partial f^{(0)}}{\partial\mathbf{V}} - \frac{\gamma}{m}\frac{\partial}{\partial\mathbf{V}}\cdot\mathbf{V}f^{(0)} - \frac{1}{2}\xi\frac{\partial^2}{\partial V^2}f^{(0)} + \mathbf{g}\cdot\frac{\partial f^{(0)}}{\partial\mathbf{V}} = J_{\mathrm{E}}^{(0)}[f^{(0)},f^{(0)}], \quad (6.1)$$

where

$$J_{\mathrm{E}}^{(0)}\left[f^{(0)},f^{(0)}\right] \equiv \chi\sigma^{d-1}\int d\mathbf{v}_2\int d\widehat{\boldsymbol{\sigma}}\Theta(\widehat{\boldsymbol{\sigma}}\cdot\mathbf{g}_{12})(\widehat{\boldsymbol{\sigma}}\cdot\mathbf{g}_{12}) \times\left[\alpha^{-2}f^{(0)}(v_1')f^{(0)}(v_2') - f^{(0)}(v_1)f^{(0)}(v_2)\right]. \quad (6.2)$$

Here, $\chi\equiv\chi[\mathbf{r},\mathbf{r}+\boldsymbol{\sigma}|n(t)]|_{n=n(t)}$ is the pair functional evaluated with all density fields at the local point $\mathbf{r}$. The collision operator (6.2) can be recognized as the Boltzmann operator for inelastic collisions multiplied by the factor χ. Note that in Eq. (6.1) all spatial gradients are neglected at this lowest order. Moreover, as discussed before, upon writing Eq. (6.1) it has been assumed that the gravity field and the external parameters accounting for the effects of gas-phase are taken to be of zeroth-order in spatial gradients. The macroscopic balance equations at this order are

$$\partial_t^{(0)} n = 0, \quad \partial_t^{(0)}\mathbf{U} = -\frac{\beta}{m}\Delta\mathbf{U} + \mathbf{g}, \quad (6.3)$$

$$\partial_t^{(0)} T = -\frac{2T}{m}\gamma + m\xi - \zeta^{(0)}T, \quad (6.4)$$

where $\zeta^{(0)}$ is determined by Eq. (4.15) to zeroth order, namely, by using the distribution $f^{(0)}$. Since $f^{(0)}$ qualifies as a *normal* solution, then

$$\partial_t^{(0)} f^{(0)} = \frac{\partial f^{(0)}}{\partial n}\partial_t^{(0)} n + \frac{\partial f^{(0)}}{\partial U_i}\partial_t^{(0)} U_i + \frac{\partial f^{(0)}}{\partial T}\partial_t^{(0)} T$$
$$= \left(\frac{\beta}{m}\Delta\mathbf{U} - \mathbf{g}\right)\cdot\frac{\partial f^{(0)}}{\partial \mathbf{V}} - \left(\frac{2\gamma}{m} - \frac{m}{T}\xi + \zeta^{(0)}\right) T\frac{\partial f^{(0)}}{\partial T}, \tag{6.5}$$

where in the last step we have taken into account that $f^{(0)}$ depends on $\mathbf{U}$ through its dependence on $\mathbf{V}$. Substitution of Eq. (6.5) into Eq. (6.1) yields

$$-\left(\frac{2}{m}\gamma - \frac{m}{T}\xi + \zeta^{(0)}\right) T\frac{\partial f^{(0)}}{\partial T} - \frac{\gamma}{m}\frac{\partial}{\partial \mathbf{V}}\cdot\mathbf{V} f^{(0)} - \frac{1}{2}\xi\frac{\partial^2}{\partial V^2} f^{(0)} = J_{\mathrm{E}}^{(0)}[f^{(0)}, f^{(0)}]. \tag{6.6}$$

Since the solution to Eq. (6.6) is isotropic in $\mathbf{V}$, dimensional analysis requires that $f^{(0)}$ has the scaled form

$$f^{(0)}(\mathbf{V}) = n v_0^{-d}\Psi\left(\frac{V}{v_0}\right), \tag{6.7}$$

where Ψ is an unknown function of $\mathbf{V}/v_0$, where $v_0 = \sqrt{2T/m}$ is the thermal speed. Therefore, according to Eq. (6.7), the temperature dependence of $f^{(0)}$ can occur only through v_0 and the dimensionless velocity V/v_0 so that

$$T\frac{\partial f^{(0)}}{\partial T} = -\frac{1}{2}\frac{\partial}{\partial \mathbf{V}}\cdot\mathbf{V} f^{(0)}. \tag{6.8}$$

Taking into account Eqs. (6.7) and (6.8), the Enskog equation (6.6) for the zeroth-order distribution function becomes finally

$$\frac{1}{2}\left(\zeta^{(0)} - \frac{m\xi}{T}\right)\frac{\partial}{\partial \mathbf{V}}\cdot\mathbf{V} f^{(0)} - \frac{1}{2}\xi\frac{\partial^2}{\partial V^2} f^{(0)} = J_{\mathrm{E}}^{(0)}[f^{(0)}, f^{(0)}]. \tag{6.9}$$

Note that Eq. (6.9) is independent of the parameters β and γ. In fact, when $\xi = 0$, one recovers the kinetic equation defining the homogeneous cooling state (HCS), whose solution has been previously worked out by several authors (van Noije & Ernst 1998; Montanero & Santos 2000; Pöschel & Brilliantov 2006; Santos & Montanero 2009).

In terms of the (scaled) distribution Ψ, Eq. (6.9) can be rewritten as

$$\frac{1}{2}\left(\zeta^* - \xi^*\right)\frac{\partial}{\partial \mathbf{c}}\cdot\mathbf{c}\Psi - \frac{1}{4}\xi^*\frac{\partial^2}{\partial c^2}\Psi = J_{\mathrm{E}}^*[\Psi, \Psi], \tag{6.10}$$

where $\mathbf{c} = \mathbf{V}/v_0$,

$$\zeta^* = \frac{\ell\zeta^{(0)}}{v_0}, \quad \xi^* = \frac{m\xi\ell}{T v_0}, \quad J_{\mathrm{E}}^* = \frac{\ell}{n} v_0^{d-1} J_{\mathrm{E}}^{(0)}, \tag{6.11}$$

and $\ell = 1/(n\sigma^{d-1})$ is the (local) mean free path for hard spheres. In the case of elastic particles ($\alpha = 1$), $\zeta^* = 0$ and the solution of Eq. (6.10) is a Maxwellian distribution Koch (1990):

$$\Psi(\mathbf{c}) = \pi^{-d/2} e^{-c^2}. \tag{6.12}$$

However, if the particles collide inelastically ($\alpha < 1$), the exact form of $\Psi(\mathbf{c})$ is not known, even in the dry granular case ($\xi^* = 0$). However, a very good approximation can be obtained from an expansion in Sonine polynomials (van Noije & Ernst 1998). In particular, since the distribution function is isotropic the zeroth order pressure tensor

and heat flux are found from Eqs. (4.11)–(4.13) to be

$$P_{ij}^{(0)} = p\,\delta_{ij}, \quad \mathbf{q}^{(0)} = \mathbf{0}, \tag{6.13}$$

where the hydrostatic pressure p is

$$p = nT\left[1 + 2^{d-2}(1+\alpha)\chi\phi\right], \tag{6.14}$$

where

$$\phi = \frac{\pi^{d/2}}{2^{d-1}d\Gamma\left(\frac{d}{2}\right)} n\sigma^d \tag{6.15}$$

is the solid volume fraction. Note that the presence of the gas phase does not enter the constitutive relation for pressure.

The deviation of $\Psi(c)$ from its Maxwellian form is measured through the kurtosis or fourth-cumulant (van Noije & Ernst 1998)

$$a_2 = \frac{4}{d(d+2)}\langle c^4\rangle - 1, \tag{6.16}$$

where

$$\langle c^k\rangle = \int d\mathbf{c}\; c^k \Psi(c). \tag{6.17}$$

In order to determine a_2, we multiply both sides of Eq. (6.10) by c^4 and integrate over velocity. The result is

$$\frac{d(d+2)}{2}\left[\zeta^*(1+a_2) - \xi^* a_2\right] = \mu_4, \tag{6.18}$$

where

$$\mu_k = -\int d\mathbf{c}\; c^k\; J_{\mathrm{E}}^*[\Psi,\Psi]. \tag{6.19}$$

Upon writing Eq. (6.18) use has been made of the partial result

$$\int d\mathbf{c}\; c^p\; \frac{\partial^2\Psi}{\partial c^2} = p(p+d-2)\langle c^{p-2}\rangle \tag{6.20}$$

with $p = 4$ and $\langle c^2\rangle = \frac{d}{2}$.

Equation (6.18) is still exact. To get an approximate expression for the quantities $\zeta^* = (2/d)\mu_2$ and μ_4, we consider the first Sonine approximation for Ψ, then we insert this expansion into Eq. (6.19) and neglects terms nonlinear in a_2. The results are

$$\mu_2 \to \mu_2^{(0)} + \mu_2^{(1)} a_2, \quad \mu_4 \to \mu_4^{(0)} + \mu_4^{(1)} a_2, \tag{6.21}$$

where (van Noije & Ernst 1998)

$$\mu_2^{(0)} = \frac{\pi^{(d-1)/2}}{\sqrt{2}\Gamma\left(\frac{d}{2}\right)}\chi(1-\alpha^2), \quad \mu_2^{(1)} = \frac{3}{16}\mu_2^{(0)}, \tag{6.22}$$

$$\mu_4^{(0)} = \left(d + \frac{3}{2} + \alpha^2\right)\mu_2^{(0)}, \tag{6.23}$$

$$\mu_4^{(1)} = \left[\frac{3}{32}(10d + 39 + 10\alpha^2) + \frac{d-1}{1-\alpha}\right]\mu_2^{(0)}, \tag{6.24}$$

and in Eq. (6.22), Γ refers to Gamma function. With the use of the approximations (6.21)

and retaining only linear terms in a_2, the solution to Eq. (6.18) is

$$a_2 = -\frac{\mu_4^{(0)} - (d+2)\mu_2^{(0)}}{\mu_4^{(1)} - (d+2)\left(\frac{19}{16}\mu_2^{(0)} - \frac{d}{2}\xi^*\right)}. \tag{6.25}$$

In terms of a_2, the zeroth-order expression $\zeta^{(0)}$ for the collisional cooling rate can be written as

$$\zeta^{(0)} = \frac{2}{d}\frac{\pi^{(d-1)/2}}{\Gamma\left(\frac{d}{2}\right)}(1-\alpha^2)\chi\left(1+\frac{3}{16}a_2\right)n\sigma^{d-1}\sqrt{\frac{T}{m}}. \tag{6.26}$$

Note that the effects of the interstitial gas on the zeroth-order collisional cooling rate $\zeta^{(0)}$ is only through the dependence of the kurtosis a_2 on ξ^* (Eq. (6.25)).

7. First order solution. Navier-Stokes transport coefficients

The analysis to first order in the expansion parameter is similar to the one worked out by Garzó & Dufty (1999) and Lutsko (2005) in the dry granular case. We only display here the final expressions for the fluxes and the collisional cooling rate with some details being given in the Appendices A and B. The form of the first-order velocity distribution function $f^{(1)}$ is given by

$$\begin{aligned} f^{(1)} = &\boldsymbol{\mathcal{A}}(\mathbf{V})\cdot\nabla\ln T + \boldsymbol{\mathcal{B}}(\mathbf{V})\cdot\nabla\ln n \\ &+\mathcal{C}_{ij}(\mathbf{V})\frac{1}{2}\left(\partial_i U_j + \partial_j U_i - \frac{2}{d}\delta_{ij}\nabla\cdot\mathbf{U}\right) + \mathcal{D}(\mathbf{V})\nabla\cdot\mathbf{U}, \end{aligned} \tag{7.1}$$

where the quantities $\boldsymbol{\mathcal{A}}(\mathbf{V})$, $\boldsymbol{\mathcal{B}}(\mathbf{V})$, $\mathcal{C}_{ij}(\mathbf{V})$ and $\mathcal{D}(\mathbf{V})$ are the solutions of the linear integral equations (A 18)–(A 21), respectively. With the distribution function $f^{(1)}$ determined by Eq. (7.1), the pressure tensor, the heat flux and the collisional cooling rate can be calculated to first order in the spatial gradients. It is worthwhile to note that the spatial dependence of ξ with respect to $|\Delta\mathbf{U}|$ (see below Eq. (8.2)) has been neglected in these calculations (unlike the spatial dependence with respect to the density n and the granular temperature T). This assumption traces to the applications which motivate this work. Namely, in circulating fluidized beds (CFBs), the solids concentration and granular temperature vary considerably in space, whereas the relative velocity $\Delta\mathbf{U}$ remains relatively constant ($\sim$ terminal velocity of single particle). Accordingly, $\Delta\mathbf{U}$ is treated as a constant here, which also has the benefit of greatly simplifying the calculations. It is also important to remark that our results have been derived systematically from the inelastic Enskog equation by the CE procedure and consequently, there is no *a priori* any limitation on the degree of inelasticity. Thus, the results apply to a wide range of values of the coefficient of restitution. Moreover, since the transport coefficients and the collisional cooling rate are given in terms of the solutions of the coupled linear integral equations (A 18)–(A 21), for practical purposes these integral equations have been solved by truncated expansions in Sonine polynomials.

The forms of the collisional contributions to the momentum and heat fluxes are exactly the same as the ones obtained in the absence of the gas phase (Garzó & Dufty 1999; Lutsko 2005) except that a_2 depends on ξ^*. Thus, we will focus here our attention in the evaluation of the kinetic parts of the transport coefficients and the collisional cooling rate. Some technical details of this calculation are provided in the Appendix B. Let us consider each flux separately.

7.1. *Pressure tensor*

To first order, the pressure tensor is given by

$$P_{ij}^{(1)} = -\eta\left(\partial_i U_j + \partial_j U_i - \frac{2}{d}\delta_{ij}\nabla\cdot\mathbf{U}\right) - \lambda\delta_{ij}\nabla\cdot\mathbf{U}, \tag{7.2}$$

where η is the shear viscosity and λ is the bulk viscosity. While the shear viscosity has kinetic and collisional contributions, the bulk viscosity has only a collisional contribution. The shear viscosity is

$$\eta = \eta_k + \eta_c. \tag{7.3}$$

The collisional contribution η_c to the shear viscosity η is given by (Garzó & Dufty 1999; Lutsko 2005)

$$\eta_c = \frac{2^{d-1}}{d+2}\phi\chi(1+\alpha)\eta_k + \frac{d}{d+2}\lambda, \tag{7.4}$$

and the bulk viscosity is

$$\lambda = \frac{2^{2d+1}}{\pi(d+2)}\phi^2\chi(1+\alpha)\left(1-\frac{a_2}{16}\right)\eta_0. \tag{7.5}$$

Here,

$$\eta_0 = \frac{d+2}{8}\frac{\Gamma\left(\frac{d}{2}\right)}{\pi^{(d-1)/2}}\sigma^{1-d}\sqrt{mT} \tag{7.6}$$

is the low density value of the shear viscosity in the elastic limit. The kinetic part η_k of the shear viscosity is

$$\eta_k = \frac{nT}{\nu_\eta - \frac{1}{2}\left(\zeta^{(0)} - \frac{m}{T}\xi - \frac{2}{m}\gamma\right)}\left[1 - \frac{2^{d-2}}{d+2}(1+\alpha)(1-3\alpha)\phi\chi\right], \tag{7.7}$$

where the collision frequency ν_η is (Garzó *et al.* 2007*c*)

$$\nu_\eta = \frac{3\nu_0}{4d}\chi\left(1-\alpha+\frac{2}{3}d\right)(1+\alpha)\left(1+\frac{7}{16}a_2\right). \tag{7.8}$$

Here, $\nu_0 = nT/\eta_0$. The shear viscosity can be finally written as

$$\eta = \eta_k\left[1 + \frac{2^{d-1}}{d+2}\phi\chi(1+\alpha)\right] + \frac{d}{d+2}\lambda. \tag{7.9}$$

Thus, in addition to the presence of a_2 (which depends on ξ) in Eq. (7.5) for the bulk viscosity, gas-phase effects appear explicitly on the kinetic part η_k of the shear viscosity via the appearance of γ and ξ in Eq. (7.7) and implicitly via the appearance of ν_η, which also depends on a_2 (see Eq. (7.8)).

7.2. *Heat Flux*

The constitutive form for the heat flux in the Navier-Stokes approximation is

$$\mathbf{q}^{(1)} = -\kappa\nabla T - \mu\nabla n, \tag{7.10}$$

where κ is the thermal conductivity and μ is the Dufour coefficient, which is not present in the granular case (no gas phase) when particles collide elastically ($\alpha = 1$).

The thermal conductivity κ is given by

$$\kappa = \kappa_k + \kappa_c. \tag{7.11}$$

The collisional contribution κ_c to the thermal conductivity κ is (Garzó & Dufty 1999; Lutsko 2005)

$$\kappa_c = 3\frac{2^{d-2}}{d+2}\phi\chi(1+\alpha)\kappa_k + \frac{2^{2d+1}(d-1)}{(d+2)^2\pi}\phi^2\chi(1+\alpha)\left(1+\frac{7}{16}a_2\right)\kappa_0, \tag{7.12}$$

where

$$\kappa_0 = \frac{d(d+2)}{2(d-1)}\frac{\eta_0}{m} \tag{7.13}$$

is the thermal conductivity coefficient of an elastic dilute gas. The expression of the kinetic part κ_k is

$$\kappa_k = \frac{d-1}{d}\kappa_0\nu_0\left(\nu_\kappa + \frac{1}{2}\frac{m\xi}{T} - 2\zeta^{(0)} - \frac{2T}{m}\gamma_T + m\xi_T\right)^{-1} \times\left\{1+2a_2+3\frac{2^{d-3}}{d+2}\phi\chi(1+\alpha)^2\left[2\alpha-1+a_2(1+\alpha)\right]\right\}, \tag{7.14}$$

where

$$\gamma_T \equiv \frac{\partial\gamma}{\partial T}, \quad \xi_T \equiv \frac{\partial\xi}{\partial T}, \tag{7.15}$$

and the collision frequency ν_κ is given by (Garzó *et al.* 2007*c*)

$$\nu_\kappa = \nu_0\frac{1+\alpha}{d}\chi\left[\frac{d-1}{2}+\frac{3}{16}(d+8)(1-\alpha)+\frac{296+217d-3(160+11d)\alpha}{256}a_2\right]. \tag{7.16}$$

The (combined) thermal conductivity κ can be finally written as

$$\kappa = \kappa_k\left[1+3\frac{2^{d-2}}{d+2}\phi\chi(1+\alpha)\right] + \frac{2^{2d+1}(d-1)}{(d+2)^2\pi}\phi^2\chi(1+\alpha)\left(1+\frac{7}{16}a_2\right)\kappa_0. \tag{7.17}$$

The Dufour coefficient is given by

$$\mu = \mu_k + \mu_c, \tag{7.18}$$

where the expression for the collisional contribution μ_c is (Garzó & Dufty 1999; Lutsko 2005)

$$\mu_c = 3\frac{2^{d-2}}{d+2}\phi\chi(1+\alpha)\mu_k. \tag{7.19}$$

The kinetic contribution μ_k is given by

$$\mu_k = \frac{\kappa_0\nu_0 T}{n}\left[\nu_\kappa - \frac{3}{2}\left(\zeta^{(0)}-\frac{m\xi}{T}\right)\right]^{-1}\left\{\frac{\kappa_k}{\kappa_0\nu_0}\left[\frac{2n}{m}\gamma_n - \frac{\rho}{T}\xi_n + \zeta^{(0)}\left(1+\phi\partial_\phi\ln\chi\right)\right] + \frac{d-1}{d}a_2 + 3\frac{2^{d-2}(d-1)}{d(d+2)}\phi\chi(1+\alpha)\left(1+\frac{1}{2}\phi\partial_\phi\ln\chi\right) \times\left[\alpha(\alpha-1)+\frac{a_2}{6}(10+2d-3\alpha+3\alpha^2)\right]\right\}, \tag{7.20}$$

where

$$\gamma_n \equiv \frac{\partial\gamma}{\partial n}, \quad \xi_n \equiv \frac{\partial\xi}{\partial n}. \tag{7.21}$$

The (combined) Dufour coefficient μ can be written as

$$\mu = \mu_k\left[1+3\frac{2^{d-2}}{d+2}\phi\chi(1+\alpha)\right]. \tag{7.22}$$

In the granular case (no gas phase and so, $\beta = \gamma = \xi = 0$), the Dufour coefficient vanishes for elastic collisions ($\alpha = 1$). On the other hand, Eq. (7.22) shows that $\mu \neq 0$ when the gas phase is accounted for even for elastic collisions. In this case ($\alpha = 1$), $a_2 = 0$ and the Dufour coefficient μ is given by Eq. (7.22) with

$$\mu_k = \frac{\kappa_k T}{n}\left(\nu_\kappa + \frac{3}{2}\frac{m\xi}{T}\right)^{-1}\left(\frac{2n}{m}\gamma_n - \frac{\rho}{T}\xi_n\right), \tag{7.23}$$

where κ_k is given by Eq. (7.14) with $\alpha = 1$, and $a_2 = \zeta^{(0)} = 0$.

Again, similar to the pressure tensor, gas-phase effects appear implicitly in the thermal conductivity and Dufour coefficients via the appearance of the cumulant a_2 (which depends on ξ) in Eqs. (7.14), (7.17), and (7.20). Furthermore, such effects are explicit in the kinetic contributions to the thermal conductivity and the Dufour coefficient (see Eqs. (7.14) and (7.20)) through the terms containing γ and ξ.

7.3. *Collisional cooling rate*

The collisional cooling rate ζ is given by

$$\zeta = \zeta^{(0)} + \zeta_U \nabla \cdot \mathbf{U}, \tag{7.24}$$

where $\zeta^{(0)}$ is defined in Eq. (6.26). At first order in gradients, the proportionality constant ζ_U is a new transport coefficient for granular fluids. This coefficient is given by

$$\zeta_U = \zeta_{10} + \zeta_{11}, \tag{7.25}$$

where

$$\zeta_{10} = -3\frac{2^{d-2}}{d}\chi\phi(1-\alpha^2), \tag{7.26}$$

$$\zeta_{11} = \frac{27(d+2)^2\,2^{d-8}}{32d^2}\phi\chi^2(1-\alpha^2)\frac{\left(1+\frac{3a_2}{128}\right)\left[\frac{\omega}{2(d+2)} - (1+\alpha)\nu_0\left(\frac{1}{3}-\alpha\right)\frac{a_2}{2}\right]}{\nu_\gamma - \frac{\gamma}{m} - \frac{3m\xi}{2T} + \frac{3}{2}\zeta^{(0)}}. \tag{7.27}$$

In the above expression, the collision frequencies ω and ν_γ are given by (Garzó & Dufty 1999; Lutsko 2005)

$$\omega = (1+\alpha)\nu_0\left\{(1-\alpha^2)(5\alpha-1) - \frac{a_2}{6}\left[15\alpha^3 - 3\alpha^2 + 3(4d+15)\alpha - (20d+1)\right]\right\}, \tag{7.28}$$

$$\nu_\gamma = -\frac{1+\alpha}{192}\chi\nu_0\left[30\alpha^3 - 30\alpha^2 + (105+24d)\alpha - 56d - 73\right]. \tag{7.29}$$

The presence of the gas phase impacts ζ_{11} via the explicit appearance of γ and ξ (see Eq. (7.27)) as well as an implicit dependency via the cumulant a_2.

8. Results and Discussion

8.1. *Drag model: Low mean flow Reynolds numbers*

The expressions derived in §6 and §7 for the (reduced) transport coefficients and the collisional cooling rate depend on the coefficient of restitution α, the solid volume fraction ϕ along with the external parameters γ and ξ and their derivatives with respect to the density n and the granular temperature T. Thus, to show the explicit forms of η, λ, κ, μ and ζ_U, one has to provide relations for γ and ξ. As described in §4, these quantities are derived from the Stokes flow closures for the source and dissipation of granular energy given by Koch (1990) and Koch & Sangani (1999). Recall that attention here is limited to low mean flow Reynolds numbers in order to compare with previous analytical results

(Koch 1990; Koch & Sangani 1999) and to assess the impact of the gas phase on the constitutive relations, the latter of which was neglected in the analytical treatment.

We consider here the physical case of hard spheres ($d = 3$). For the case of low mean flow Reynolds numbers, the expressions of γ and ξ are given by

$$\gamma = \frac{m}{\tau} R_{\rm diss}(\phi), \tag{8.1}$$

$$\xi = \frac{1}{6\sqrt{\pi}} \frac{\sigma |\Delta \mathbf{U}|^2}{\tau^2 \sqrt{\frac{T}{m}}} S^*(\phi), \tag{8.2}$$

where $\tau = m/(3\pi\mu_g\sigma)$ is the characteristic time scale over which the velocity of a particle of mass m and diameter σ relaxes due to viscous forces. Here, μ_g is the gas viscosity.

In the case of dilute suspensions ($0 \leqslant \phi \leqslant 0.1$), the expressions for the functions $R_{\rm diss}(\phi)$ and $S^*(\phi)$ are (Koch 1990)

$$R_{\rm diss}(\phi) = 1 + 3\sqrt{\frac{\phi}{2}}, \quad S^*(\phi) = 1. \tag{8.3}$$

For moderately dense suspensions ($0.1 \leqslant \phi \leqslant 0.4$), the functions $R_{\rm diss}(\phi)$ and $S^*(\phi)$ can be well approximated by (Sangani *et al.* 1996; Koch & Sangani 1999)

$$\begin{aligned} R_{\rm diss}(\phi) = 1 + 3\sqrt{\frac{\phi}{2}} + \frac{135}{64}\phi \ln \phi \\ + 11.26\phi\left(1 - 5.1\phi + 16.57\phi^2 - 21.77\phi^3\right) - \phi\chi(\phi) \ln \epsilon_m, \end{aligned} \tag{8.4}$$

$$S^*(\phi) = \frac{R_{\rm drag}^2}{\chi(\phi)\left(1 + 3.5\sqrt{\phi} + 5.9\phi\right)}, \tag{8.5}$$

where the function $R_{\rm drag}$ is given by

$$R_{\rm drag}(\phi) = \frac{1 + 3\sqrt{\frac{\phi}{2}} + \frac{135}{64}\phi \ln \phi + 17.14\phi}{1 + 0.681\phi - 8.48\phi^2 + 8.16\phi^3}. \tag{8.6}$$

In Eq. (8.4), $\epsilon_m\sigma$ can be interpreted as a length scale characterizing the importance of non-continuum effects on the lubrication force between two smooth particles at close contact. Typical values of the factor ϵ_m are in the range 0.01–0.05. However, given that this term only contributes to $R_{\rm diss}(\phi)$ through a weak logarithmic factor, its explicit value does not play a significant role in the final results. Here, we take the typical value $\epsilon_m = 0.01$.

According to Eqs. (8.1) and (8.2), the derivatives of γ and ξ with respect to n and T are given by

$$n\gamma_n = \gamma\phi\partial_\phi \ln R_{\rm diss}(\phi), \quad \gamma_T = 0, \tag{8.7}$$

$$T\xi_T = -\frac{1}{2}\xi, \quad n\xi_n = \xi\phi\partial_\phi \ln S^*(\phi). \tag{8.8}$$

In particular, $n\xi_n = 0$ for a dilute suspension since $S^*(\phi) = 1$. To make a connection with the ranges of dimensionless parameters which are of practical relevance for the gas-solid flows, it is convenient to express the reduced parameters $\gamma^* \equiv (\gamma\ell)/(mv_0)$ and $\xi^* \equiv (m\xi\ell)/(Tv_0)$ in terms of the mean flow Reynolds number $\mathrm{Re_m}$ and the Reynolds number associated with particle velocity fluctuations $\mathrm{Re_T}$.

The expressions of γ^* and ξ^* as functions of $\mathrm{Re_m}$ and $\mathrm{Re_T}$ can be easily obtained when

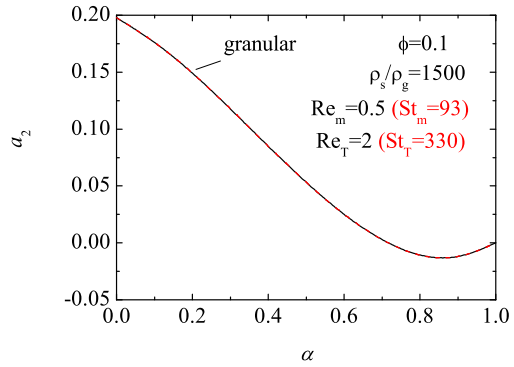

FIGURE 5. (color online) Fourth cumulant a_2 versus α for hard spheres with ϕ=0.1, $\rho_s/\rho_g = 1500$, $\mathrm{Re_m} = 0.5$ ($\mathrm{St_m} = 93$), and $\mathrm{Re_T} = 2$ ($\mathrm{St_T} = 330$). The dashed line corresponds to the results obtained in the granular case (no gas phase).

one takes into account Eqs. (3.1), (3.2), (8.1), and (8.2). The result is

$$\gamma^* = \frac{3\pi}{\sqrt{2}\phi}\frac{\rho_g}{\rho_s}\frac{R_{\mathrm{diss}}(\phi)}{\mathrm{Re_T}}, \tag{8.9}$$

$$\xi^* = \frac{9}{2}\sqrt{2\pi}\left(\frac{\rho_g}{\rho_s}\right)^2 \frac{\mathrm{Re_m^2}}{\phi(1-\phi)^2\mathrm{Re_T^4}} S^*(\phi). \tag{8.10}$$

8.2. *Impact of gas phase on the constitutive relations*

To assess the influence of the gas phase on the constitutive relations derived in §5 and §6 for the continuum equations given by Eqs. (4.7)–(4.9), the zeroth and first-order contribution to these relations ($\zeta^{(0)}$, ζ_U, η, λ, κ, and μ) have been examined for spheres (d=3) over a wide dimensionless parameter space: $\{\phi, \alpha, \rho_s/\rho_g, \mathrm{Re_m}, \mathrm{Re_T}\}$. Here, we consider a range of dimensionless parameters relevant to operate in a CFB: $\phi = 0-0.5$, $\alpha = 0.5-1$, $\rho_s/\rho_g = 800-2500$, $\mathrm{Re_m} = 0.1-1$ (Stokes flow), and $\mathrm{Re_T} = 0.5-5$.

It is worthwhile to note that the results presented below are not specific to any one flow system (e.g., simple shear flow), but instead are applicable generally. In other words, all the transport coefficients are displayed as a function of the full set of dimensionless parameters, which depend on both material properties (particle mass, radius, ...) and hydrodynamic variables (granular temperature, mean relative velocity between gas and solids, ...) alike. Finally, since a primary contribution of this paper is to assess the effect of the gas phase on transport properties, the transport coefficients plotted below are non-dimensionalized with respect to their "dry" values (those obtained when the interstitial fluid is neglected).

Recall that the gas-phase effects appear in the collisional cooling rate and transport coefficients explicitly via the appearance of γ and ξ and/or implicitly via the appearance of the kurtosis a_2, which depends on ξ via Eq. (6.25). Hence, it is worthwhile to first consider the effect of the gas phase on a_2, as is displayed in figure 5 for the representative case of $\phi = 0.1$, $\mathrm{Re_m} = 0.5$, $\mathrm{Re_T} = 2$, and $\rho_s/\rho_g = 1500$. It is observed that the gas phase plays a negligible role on the kurtosis a_2 since both curves (granular case and gas-solid suspension) are practically indistinguishable. Accordingly, it follows that the quantities that only have an implicit dependence on the gas phase through the appearance of a_2 also display a negligible role of the gas phase. These quantities include the zeroth-order

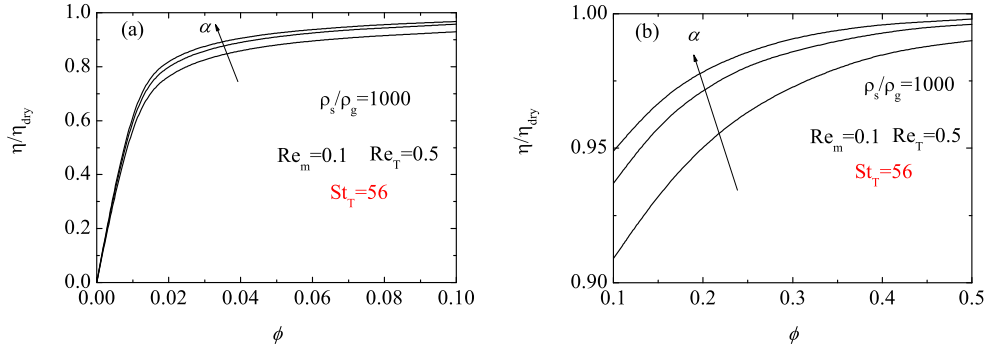

FIGURE 6. Plot of the ratio η/η_{dry} versus the volume fraction ϕ for a dilute (panel (a)) and a moderately dense (panel (b)) suspension for $\rho_s/\rho_g = 1000$, $\text{Re}_m = 0.1$, $\text{Re}_\text{T} = 0.5$ ($\text{St}_\text{T} = 56$) and three different values of the coefficient of restitution α: From the bottom to the top, α=0.5, 0.7 and 0.9.

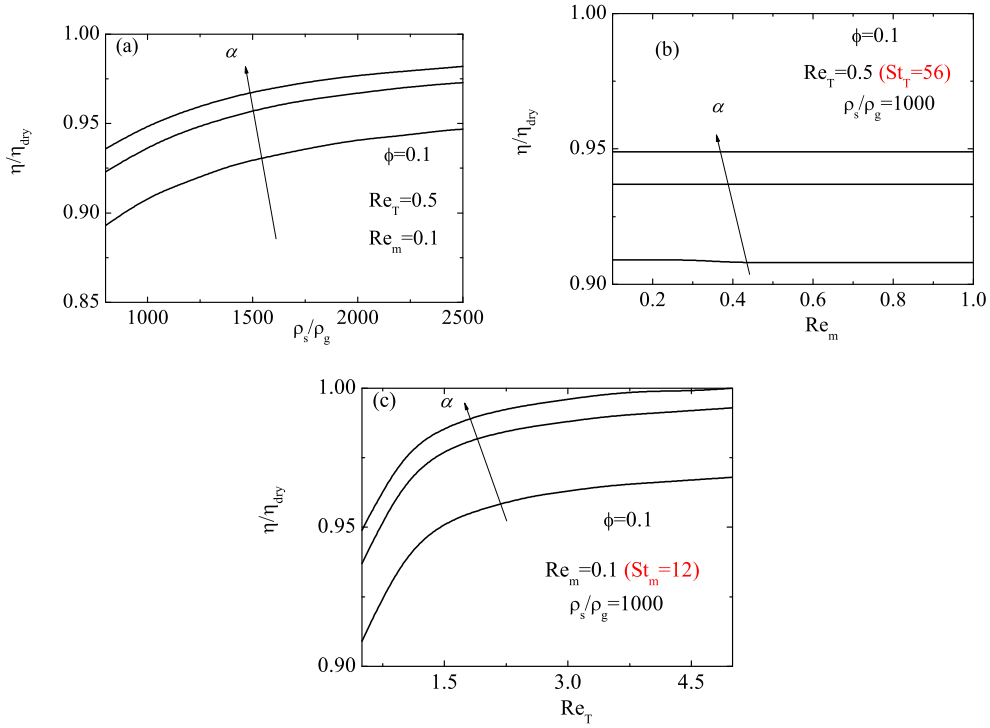

FIGURE 7. Plot of the ratio η/η_{dry} for $\phi = 0.1$ and three different values of the coefficient of restitution α: From the bottom to the top, α=0.5, 0.7 and 0.9. In the panel (a) η/η_{dry} is plotted versus ρ_s/ρ_g for $\text{Re}_\text{m} = 0.1$ and $\text{Re}_\text{T} = 0.5$, in the panel (b) η/η_{dry} is plotted versus Re_m for $\rho_s/\rho_g = 1000$ and $\text{Re}_\text{T} = 0.5$ ($\text{St}_\text{T} = 56$) and in the panel (c) η/η_{dry} is plotted versus Re_T for $\rho_s/\rho_g = 1000$ and $\text{Re}_\text{m} = 0.1$ ($\text{St}_\text{m} = 12$).

collisional cooling rate $\zeta^{(0)}$ (Eq. (6.26)) and the bulk viscosity (Eq. (7.5)), which are not shown for the sake of brevity. It is also worthwhile to note that although the first-order contribution to the collisional cooling rate ζ_U (Eqs. (7.25)–(7.27)) and the thermal conductivity κ (Eqs. (7.14) and (7.17)) also contain an explicit dependency on γ and ξ,

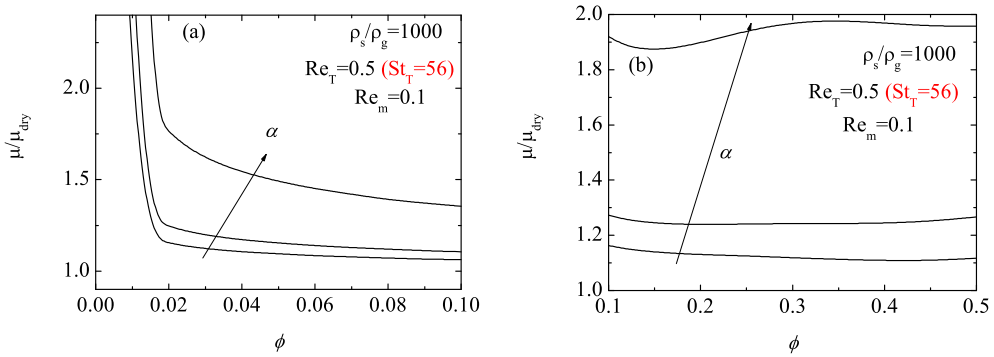

FIGURE 8. Plot of the ratio $\mu/\mu_{\rm dry}$ versus the volume fraction ϕ for a dilute (panel (a)) and a moderately dense (panel (b)) suspension for $\rho_s/\rho_g = 1000$, $\mathrm{Re}_m = 0.1$, $\mathrm{Re}_\mathrm{T} = 0.5$ ($\mathrm{St}_\mathrm{T} = 56$) and three different values of the coefficient of restitution α: From the bottom to the top, α=0.5, 0.7 and 0.9.

the gas phase shows a similarly negligible impact ($< 0.1\%$) over the range of parameters examined. Again, these plots are not shown for the sake of brevity.

Thus, of the six constitutive quantities derived, the two for which the gas phase does exert a considerable influence are the shear viscosity η and the Dufour coefficient μ. Henceforth, the subscript dry refers to the value of the corresponding quantity in the absence of gas phase (i.e., when $\beta = \gamma = \xi = 0$). The shear viscosity is displayed in figures 6 and 7. Here, the shear viscosity is shown as a function of the solid fraction ϕ for both the dilute and dense expressions (figures 6a and 6b, respectively), the density ratio ρ_s/ρ_g (figure 7a), the mean Reynolds number Re_m (figure 7b), and the Reynolds number based on particle velocity fluctuations Re_T (figure 7c). For each figure, only the quantity displayed along the abscissa is varied while all others are kept constant. Note also from figure 6 that the dilute- and dense-phase expressions for $\eta/\eta_{\rm dry}$ are roughly similar in value at the boundary of $\phi = 0.1$ used between the two sets of expressions.

Regarding the dependency of shear viscosity on concentration (figures 6a and 6b), it is observed that the dampening influence of the gas phase increases ($\eta/\eta_{\rm dry}$ decreases further below unity) as the system becomes more dilute (ϕ decreases), with this effect being stronger at stronger dissipation levels (lower α). The physical explanation for this behavior traces to the increased mean free path of the particles in dilute systems, over which the gas phase serves to buffer the kinetic transport of particles. From a mathematical perspective, recall that the collisional contributions to the transport coefficients were only modified by the presence of the gas phase via the appearance of a_2, which is negligibly changed by the inclusion of a gas phase (see figure 5). On the other hand, the kinetic contribution to the shear viscosity, which dominates at more dilute conditions, has an additional dependence on the gas phase via the explicit appearance of γ and ξ (see Eq. (7.7)). It is also worthwhile to point out that the shear viscosity $\eta \to 0$ in the dilute limit, as previously reported by Tsao & Koch (1995) and Sangani *et al.* (1996). The same is not true for the granular counterpart $\eta_{\rm dry}$, which is well-known to take on a finite value in the dilute limit. Again, this behavior can be traced to the buffering effect (viscous forces) of the interstitial gas which serves to continually reduce the random component of particle motion in the dilute limit (gas-phase sink of granular temperature much larger than gas-phase source).

Regarding the dependency of the shear viscosity on the other system parameters, figure 7a demonstrates an increased influence of the gas phase on shear viscosity as ρ_s/ρ_g

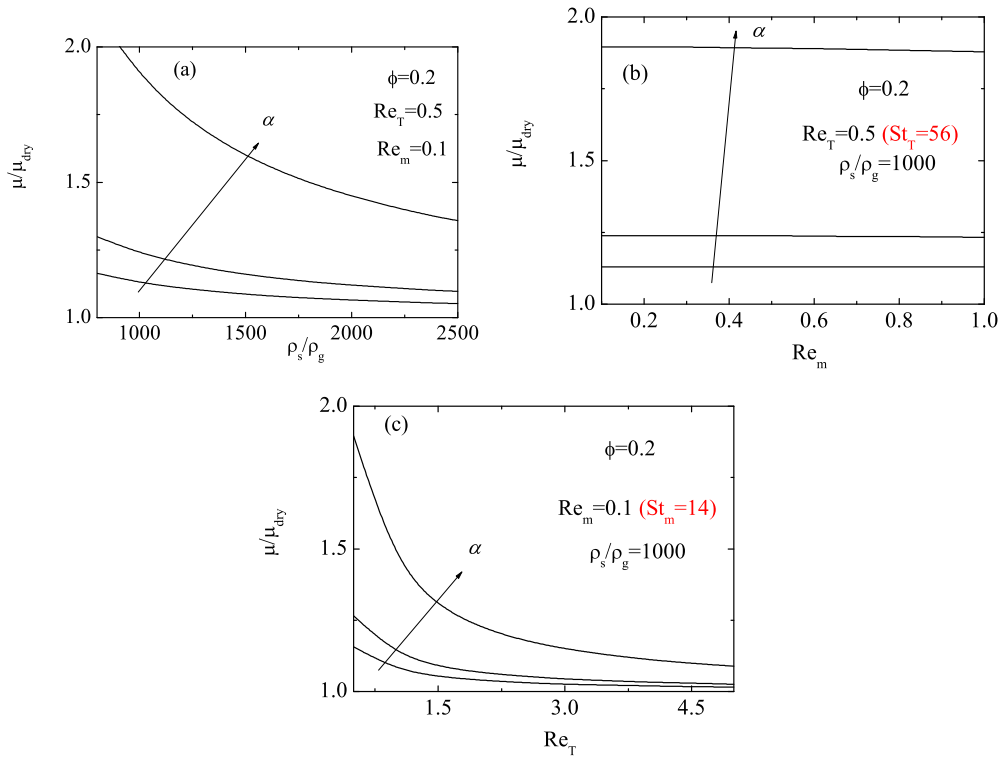

FIGURE 9. Plot of the ratio $\mu/\mu_{\rm dry}$ for $\phi = 0.2$ and three different values of the coefficient of restitution α: From the bottom to the top, α=0.5, 0.7 and 0.9. In the panel (a) $\mu/\mu_{\rm dry}$ is plotted versus ρ_s/ρ_g for $\mathrm{Re_m} = 0.1$ and $\mathrm{Re_T} = 0.5$, in the panel (b) $\eta/\eta_{\rm dry}$ is plotted versus $\mathrm{Re_m}$ for $\rho_s/\rho_g = 1000$ and $\mathrm{Re_T} = 0.5$ ($\mathrm{St_T} = 56$) and in the panel (c) $\mu/\mu_{\rm dry}$ is plotted versus $\mathrm{Re_T}$ for $\rho_s/\rho_g = 1000$ and $\mathrm{Re_m} = 0.1$ ($\mathrm{St_m} = 14$).

decreases, which can be explained by the decreased role of particle inertia relative to gas-phase viscous forces. As displayed in figure 7b, however, the shear viscosity is essentially independent of $\mathrm{Re_m}$ over the small range of (low) $\mathrm{Re_m}$ investigated here. However, as illustrated in figure 7c, the gas phase displays a larger impact on the shear viscosity for lower $\mathrm{Re_T}$ due to the decreased role of random particle motion. At the other extreme of higher $\mathrm{Re_T}$, the granular limit ($\eta/\eta_{\rm dry} \to 1$) is approached, as expected. Finally, for all of these system parameters (figures 7a–7c), the gas-phase effect on shear viscosity is again more pronounced for higher dissipation levels (lower α).

As discussed previously, the Reynolds numbers $\mathrm{Re_m}$ and $\mathrm{Re_T}$ can be converted to Stokes numbers $\mathrm{St_m}$ and $\mathrm{St_T}$ via Eqs. (3.5) and (3.6), respectively. In figures 7, the relevant Stokes numbers both cover the range of $\mathcal{O}(10)$-$\mathcal{O}(100)$, though results are observed to be more sensitive to the value of $\mathrm{St_T}$ than $\mathrm{St_m}$ (i.e., figure 7c compared to figure 7b). In figure 7c, the x-axis corresponds to the value of $\mathrm{St_T} \sim 80 - 500$. At the higher $\mathrm{St_T}$ (higher $\mathrm{Re_T}$ of figure 7c), the shear viscosity results approach those of the dry granular limit, as expected (fluid phase becomes negligible). However, the differences are non-negligible for $\mathrm{St_T}$ of $\mathcal{O}(10)$ (lower $\mathrm{Re_T}$ in figure 7c). This observation is particularly true for more dilute systems, as illustrated in figure 6a. In this figure, the Stokes number is constant at $\mathrm{St_T} \sim 60$, yet the shear viscosity η varies greatly from its dry counterpart $\eta_{\rm dry}$. For example, η is about 40% of $\eta_{\rm dry}$ at the volume fraction $\phi = 0.01$. Since the core of a CFB riser is often characterized by solid volume fractions on the order of a few percent,

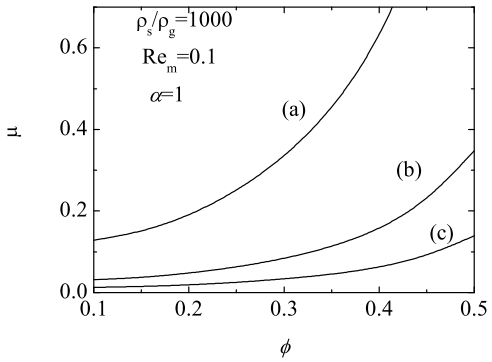

FIGURE 10. Plot of the Dufour coefficient μ versus ϕ for hard spheres with α=1 (elastic collisions), $\mathrm{Re_m} = 0.5$, $\rho_s/\rho_g = 1000$, and three different values of the Reynolds number $\mathrm{Re_T}$: (a) $\mathrm{Re_T} = 0.5$ ($\mathrm{St_T} = 56$), (b) $\mathrm{Re_T} = 2$ ($\mathrm{St_T} = 222$), and (c) $\mathrm{Re_T} = 5$ ($\mathrm{St_T} = 556$)

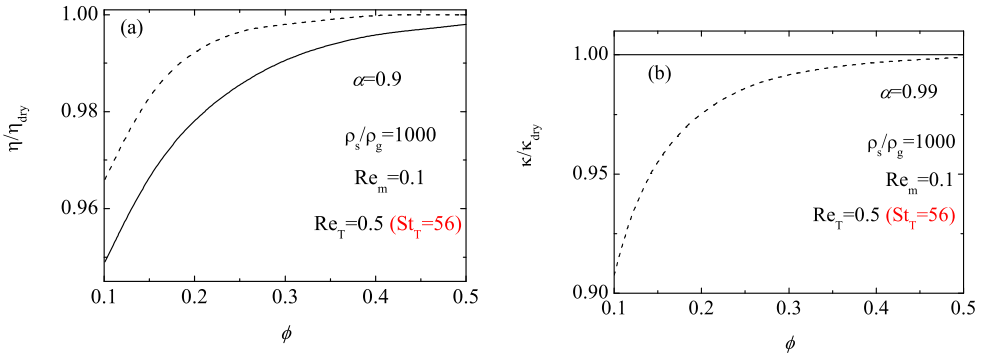

FIGURE 11. Plot of the ratios η/η_{dry} (panel (a)) and $\kappa/\kappa_{\mathrm{dry}}$ (panel (b)) as a function of the solid fraction ϕ for $\mathrm{Re_m} = 0.1$, $\mathrm{Re_T} = 0.5$ ($\mathrm{St_T} = 56$) and different values of the coefficient of restitution α. The solid lines are the results derived here while the dashed lines are based on the model used by Agrawal *et al.* (2001).

gas-phase modifications to the shear viscosity are not negligible for practical systems, even at finite St.

Now switching to the Dufour coefficient μ, the influence of the gas phase is presented in figures 8 and 9 over the similar ranges of system parameters. However, it is important to recall that $\mu = 0$ in the granular case when $\alpha = 1$. When $\alpha \neq 1$, $\mu_{\mathrm{dry}} \neq 0$ but its magnitude is small for weak dissipation (for instance, $\mu_{\mathrm{dry}} \simeq 0.207$ for $\alpha = 0.9$ and $\phi = 0.2$). In stark contrast to the shear viscosity (figures 6 and 7), the gas phase serves to increase the Dufour coefficient relative to its dry counterpart (i.e., $\mu/\mu_{\mathrm{dry}} > 1$), and these effects are more noticeable at lower dissipation levels (higher α). Nonetheless, similar to the shear viscosity, the influence of the gas phase is greater at more dilute conditions since the kinetic contributions dominate over their collisional counterparts (figures 8a and 8b). Also similar is the increased role of the gas phase for lower density ratios due to the decreased role of particle inertia (figure 9a). Finally, the impact of $\mathrm{Re_T}$ and $\mathrm{Re_m}$ on the Dufour coefficient is analogous to that of the shear viscosity, where the influence of the gas phase is relatively independent of $\mathrm{Re_m}$ (see figure 9b) over the range of low $\mathrm{Re_m}$ considered, but does depend on $\mathrm{Re_T}$ (see figure 9c).

The behavior of the Dufour coefficient in the elastic limit ($\alpha = 1$) is further explored in

figure 10. Recall for the dry granular case (no gas phase), $\mu = 0$ at $\alpha = 1$, so the discovery of a non-zero value for the gas-solid suspension may appear surprising. However, the appearance of a non-zero Dufour coefficient is also observed in granular mixtures (i.e., more than one solid species) at the elastic limit (see, for example, (Garzó *et al.* 2007*a*,*b*)), so the gas phase plays an analogous role to an additional solid species in this regard. As illustrated in figure 10, μ increases with solid fraction but decreases with $\mathrm{Re_T}$; note that this trend cannot be compared with that of figure 8 directly since the latter is non-dimensionalized with the dry case and figure 10 is not to avoid division by zero.

Although the previous analytical works of Koch and co-workers in the Stokes flow limit (Koch 1990; Sangani *et al.* 1996; Koch & Sangani 1999) ignore the impact of the gas phase on the solid-phase constitutive relations, other groups have included such effects (Ma & Ahmadi 1988; Balzer *et al.* 1995; Lun & Savage 2003). Expressions including such effects for the shear viscosity and thermal conductivity are given by Agrawal *et al.* (2001), and are compared with those derived here in figures 11a and 11b, respectively. For the shear viscosity (figure 11a), the qualitative nature of the gas-phase influence is similar in that it is more apparent at dilute conditions, though the expression derived here shows a stronger gas-phase influence. On the other hand, for the case of the thermal conductivity (figure 11b), the expression derived here displays essentially no impact from the gas phase, whereas previous expressions show a dampening of the thermal conductivity relative to the (dry) granular case. It is worth noting, however, that this comparison is not apples-to-apples due to two key differences between the previous treatments and the current one. Namely, as described in §1, the previous treatments have incorporated the effects of gas-phase turbulence and have used a form of the instantaneous drag force that mimics the form of the mean force, neither of which is implemented in our expressions.

Finally, our predictions for the shear viscosity and the steady granular temperature are compared in figures 12 and 13, respectively, with the numerical simulations performed by Sangani *et al.* (1996). The shear viscosity and the (steady) granular temperature were obtained from simulations in the simple shear flow state, and thus $\mathrm{Re_m} = 0$. Consistent with this work (Sangani *et al.* 1996), the results here are plotted against a Stokes number $\mathrm{St_{shear}}$ based on the shear rate $\dot{\gamma} \equiv \partial U_x/\partial y$. This Stokes number is defined as (Sangani *et al.* 1996)

$$\mathrm{St_{shear}} = \frac{m\dot{\gamma}}{3\pi\sigma\mu_g}. \tag{8.11}$$

The reduced shear viscosity μ_s is defined as

$$\mu_s = \frac{4\eta}{\rho_s\phi\dot{\gamma}\sigma^2}, \tag{8.12}$$

while the (steady) granular temperature θ is

$$\theta = \frac{4T}{m\sigma^2\dot{\gamma}^2}. \tag{8.13}$$

In the simple shear flow state, the granular temperature T is determined by applying the steady state condition to the balance equation of the temperature. The shear viscosity μ_s and the square root of temperature $\sqrt{\theta}$ are plotted in figures 12 and 13, respectively, as functions of $\mathrm{St_{shear}}/R_{\mathrm{diss}}$ for hard spheres with $\alpha = 1$ (Note that the reduced shear viscosity μ_s is also defined differently than shown in Sangani *et al.* (1996); the results presented here correct the error contained in the original publication (Koch 2012)). It is apparent that our theoretical predictions slightly overestimate the shear viscosity and granular temperature for dilute conditions ($\phi = 0.01$ in figures 12a and 13a) while exhibiting close agreement at more moderate volume fractions ($\phi = 0.1$ in figures 12b 13b). This

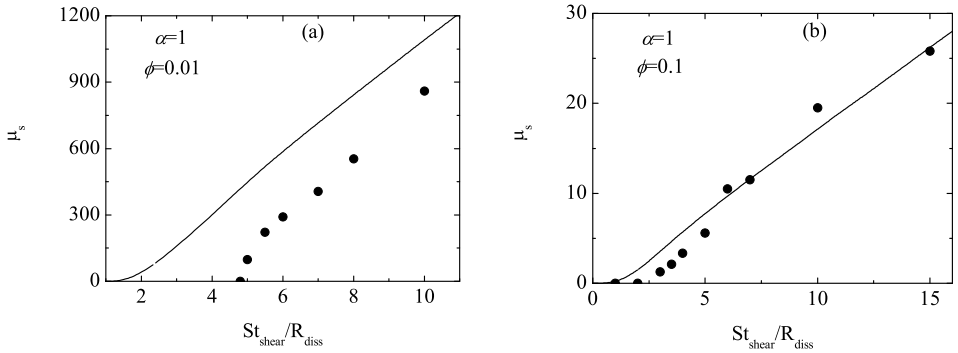

FIGURE 12. Plot of reduced shear viscosity $\mu_s = 4\eta/(\rho_s\phi\dot{\gamma}\sigma^2)$ as a function of $\mathrm{St}_{\mathrm{shear}}/R_{\mathrm{diss}}$ in the case of hard spheres with $\alpha = 1$ for two different values of the solid volume fraction: $\phi = 0.01$ (panel (a)) and $\phi = 0.1$ (panel (b)). The solid lines are the theoretical results and the circles are the simulation results obtained by Sangani *et al.* (1996).

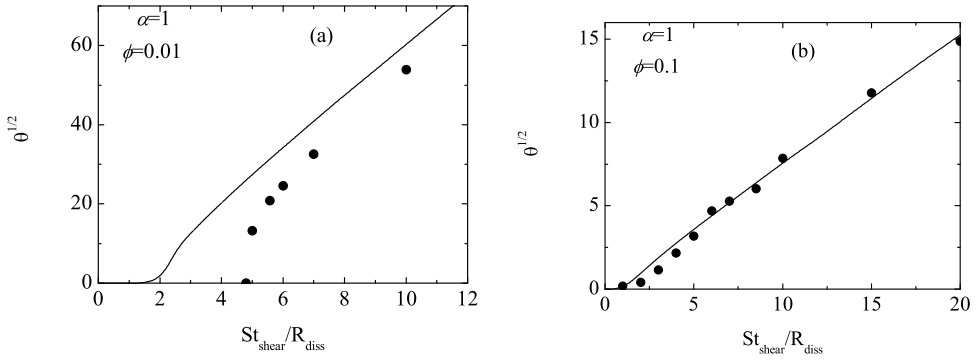

FIGURE 13. Plot of the square root of granular temperature $\sqrt{\theta} = \sqrt{4T/m}(\dot{\gamma}\sigma)^{-1}$ as a function of $\mathrm{St}_{\mathrm{shear}}/R_{\mathrm{diss}}$ in the case of hard spheres with $\alpha = 1$ for two different values of the solid volume fraction: $\phi = 0.01$ (panel (a)) and $\phi = 0.1$ (panel (b)). The solid lines are the theoretical results and the circles are the simulation results obtained by Sangani *et al.* (1996).

observation can be explained via the assumption of low Knudsen number Kn used in our derivation. In particular, previous work in granular systems (no fluid phase) has shown that the simple shear flow state contains higher-order effects (beyond Navier-Stokes order; see Santos *et al.* (2004)) and that such effects become more important in dilute flows (Hrenya *et al.* 2008). Nonetheless, the agreement here is encouraging and bodes well for the extension of the PR–DNS-based acceleration model used here to higher Re_{m}, and its subsequent incorporation into Navier-Stokes-order hydrodynamics, especially considering the complexities associated with deriving higher-order hydrodynamics and associated boundary conditions.

9. Summary

In this work, a rigorous incorporation of the gas phase into the starting kinetic (Enskog) equation has been demonstrated via an instantaneous model for the drag force. A unique aspect of this work is the use of a Langevin model for the instantaneous gas-phase force on a particle. The coefficients of the Langevin model are related to the dissipation

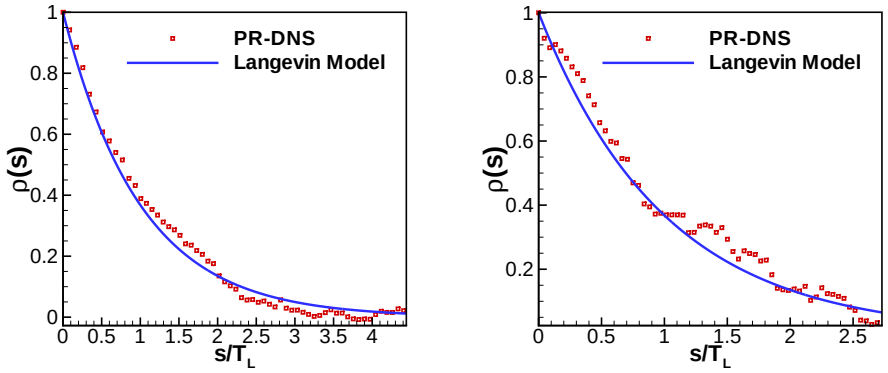

FIGURE 14. Plots showing the verification of the Langevin model. Figure 14(a) compares the particle velocity autocorrelation function extracted from PR–DNS of freely evolving suspension (volume fraction of 0.2, mean flow Reynolds number 20 and solid to fluid density ratio of 100) with the exponential decay predicted by the Langevin model. Figure 14(b) is the same as Fig. 14(a) for a suspension with solid to fluid density of 10.

and source of granular energy and can be obtained from analytical expressions (for Stokes flow and $\phi < 0.1$ (Koch 1990)) or from simulations (multipole expansions for Stokes flow and $\phi > 0.1$ (Koch & Sangani 1999)) or from PR–DNS (for higher Reynolds numbers). For proof-of-concept purposes, attention here is limited to low Reynolds number in order to allow for direct comparisons with previous analytical treatments. It is found that the additional terms appearing in the balance equations due to the presence of the gas phase are the same regardless of treatment. Furthermore, the Chapman-Enskog method is used to derive Navier-Stokes order constitutive relations for balance equations. The results indicate a non-negligible influence of the gas phase on the shear viscosity and the Dufour coefficient, whereas such effects had been ignored in previous analytical treatments for Stokes flow. Specifically, the presence of the gas phase lowers the shear viscosity and increases the Dufour coefficient relative to the granular (no gas phase) case, with the degree of influence larger in more dilute systems. This non-negligible influence persists even for finite Stokes number of $\mathcal{O}(10)$. Moreover, the shear viscosity in gas-solid suspensions is found to approach to zero in the dilute limit (consistent with previous findings of Tsao & Koch (1995) and Sangani *et al.* (1996) for simple shear flow), unlike its granular counterpart which takes on a finite value in the same limit. Also, the Dufour coefficient in gas-solid systems is found to be non-zero in the elastic limit, which is not the case for (dry) granular systems but is the case for granular mixtures (i.e., more than one solid species).

The Langevin model for the instantaneous gas-solid force is applicable to a much wider parameter space than that explored here, including higher Reynolds numbers, polydisperse systems, etc. For instance figure 14 shows that the decay of the particle velocity autocorrelation function $\rho(s)$ (cf. Eq. 3.7) computed from PR–DNS of freely evolving gas–solid suspension at a mean flow Reynolds number of 20 matches with the exponential decay predicted by the Langevin equation. Therefore, fluid–solid force models of the form given by equation 2.1 can be extended seamlessly to gas–solid systems at higher Reynolds numbers. The model coefficients for such systems are attainable via PR–DNS, which are not limited to a narrow parameter space as is their analytical counterpart. Such work is expected to be important for a wide range of practical applications and

physical phenomenon, such as systems in which the interstitial gas has been shown to have an impact on the stability of the homogeneous state (Koch 1990; Garzó 2005) or on species segregation (Möbius *et al.* 2001; Yan *et al.* 2003; Naylor *et al.* 2003; Sánchez *et al.* 2004; Möbius *et al.* 2005; Wylie *et al.* 2008; Zeilstra *et al.* 2008; Idler *et al.* 2009; Clement *et al.* 2010).

The work of V. G. has been supported by the Spanish Government through Grant No. FIS2010-16587, partially financed by FEDER funds and by the Junta de Extremadura (Spain) through Grant No. GR10158. C.M.H. and S. S. are grateful for the funding support provided by the Department of Energy (DE-FC26- 07NT43098). C.M.H. would also like to acknowledge funding from the National Science Foundation (CBET-0318999).

Appendix A. Chapman-Enskog method

The velocity distribution function $f^{(1)}$ obeys the kinetic equation

$$\left(\partial_t^{(0)}+\mathcal{L}\right) f^{(1)}-\left(\frac{\beta}{m}\Delta\mathbf{U}-\mathbf{g}\right)\cdot\frac{\partial f^{(1)}}{\partial\mathbf{V}}-\frac{\gamma}{m}\frac{\partial}{\partial\mathbf{V}}\cdot\mathbf{V}f^{(1)}-\frac{1}{2}\xi\frac{\partial^2}{\partial V^2}f^{(1)}$$
$$=-\left(\partial_t^{(1)}+\mathbf{v}\cdot\nabla\right) f^{(0)}-J_{\mathrm{E}}^{(1)}[f]. \tag{A 1}$$

Here, $J_{\mathrm{E}}^{(1)}[f]$ means the first order contribution to the expansion of the Enskog collision operator and $\mathcal{L}$ is the linear operator

$$\mathcal{L}f^{(1)}=-\left(J_{\mathrm{E}}^{(0)}[f^{(0)},f^{(1)}]+J_{\mathrm{E}}^{(0)}[f^{(1)},f^{(0)}]\right). \tag{A 2}$$

The macroscopic balance equations to first order in the gradients are

$$D_t^{(1)}n=-n\nabla\cdot\mathbf{U},\quad D_t^{(1)}U_i=-(mn)^{-1}\nabla_i p,\quad D_t^{(1)}T=-\frac{2p}{dn}\nabla\cdot\mathbf{U}-\zeta^{(1)}T, \tag{A 3}$$

where $D_t^{(1)}\equiv\partial_t^{(1)}+\mathbf{U}\cdot\nabla$. Use of Eqs. (A 3) in (A 1) and taking into account the form of $J_{\mathrm{E}}^{(1)}[f]$ obtained by Garzó & Dufty (1999) for a dry granular gas, one gets

$$\left(\partial_t^{(0)}+\mathcal{L}\right) f^{(1)}-\left(\frac{\beta}{m}\Delta\mathbf{U}-\mathbf{g}\right)\cdot\frac{\partial f^{(1)}}{\partial\mathbf{V}}-\frac{\gamma}{m}\frac{\partial}{\partial\mathbf{V}}\cdot\mathbf{V}f^{(1)}-\frac{1}{2}\xi\frac{\partial^2}{\partial V^2}f^{(1)}$$
$$=\mathbf{A}\cdot\nabla\ln T+\mathbf{B}\cdot\nabla\ln n+C_{ij}\frac{1}{2}\left(\partial_i U_j+\partial_j U_i-\frac{2}{d}\delta_{ij}\nabla\cdot\mathbf{U}\right)+D\nabla\cdot\mathbf{U}, \tag{A 4}$$

where the expressions of $\mathbf{A}$, $\mathbf{B}$, C_{ij}, and D are the same as those obtained by Garzó & Dufty (1999). They are given by

$$A_i(\mathbf{V})=\frac{1}{2}V_i\nabla_{\mathbf{V}}\cdot\mathbf{V}f^{(0)}-\frac{p}{\rho}\frac{\partial}{\partial V_i}f^{(0)}+\frac{1}{2}\mathcal{K}_i\left[\nabla_{\mathbf{V}}\cdot\left(\mathbf{V}f^{(0)}\right)\right], \tag{A 5}$$

$$B_i(\mathbf{V})=-V_i f^{(0)}-\frac{p}{\rho}\left(1+\phi\frac{\partial}{\partial\phi}\ln p^*\right)\frac{\partial}{\partial V_i}f^{(0)})-\left(1+\frac{1}{2}\phi\frac{\partial}{\partial\phi}\ln\chi\right)\mathcal{K}_i\left[f^{(0)}\right], \tag{A 6}$$

$$C_{ij}(\mathbf{V})=V_i\frac{\partial}{\partial V_j}f^{(0)}+\mathcal{K}_i\left[\frac{\partial}{\partial V_j}f^{(0)}\right], \tag{A 7}$$

$$D=\frac{1}{d}\nabla_{\mathbf{V}}\left(\mathbf{V}\cdot f^{(0)}\right)-\frac{1}{2}\left(\zeta_U+\frac{2}{d}p^*\right)\nabla_{\mathbf{V}}\cdot\left(\mathbf{V}f^{(0)}\right)+\frac{1}{d}\mathcal{K}_i\left[\partial_{V_i}f^{(0)}\right]. \tag{A 8}$$

Here, $\nabla_{\mathbf{V}} \equiv \partial/\partial \mathbf{V}$,

$$p^* \equiv \frac{p}{nT} = 1 + 2^{d-2}(1+\alpha)\chi\phi, \tag{A 9}$$

ϕ is defined by Eq. (6.15), ζ_U is defined by Eqs. (7.24) and (7.25) and $\mathcal{K}_i$ is the operator

$$\mathcal{K}_i[X] = \sigma^d \chi \int d\mathbf{v}_2 \int d\widehat{\boldsymbol{\sigma}} \Theta(\widehat{\boldsymbol{\sigma}}\cdot\mathbf{g}_{12})(\widehat{\boldsymbol{\sigma}}\cdot\mathbf{g}_{12})\widehat{\sigma}_i \left[\alpha^{-2} f^{(0)}(\mathbf{v}_1'') X(\mathbf{v}_2'') + f^{(0)}(\mathbf{v}_1) X(\mathbf{v}_2)\right], \tag{A 10}$$

where $\mathbf{v}_1'' = \mathbf{v}_1 - \frac{1}{2}(1+\alpha^{-1})(\widehat{\boldsymbol{\sigma}}\cdot\mathbf{g}_{12})\widehat{\boldsymbol{\sigma}}$ and $\mathbf{v}_2'' = \mathbf{v}_2 + \frac{1}{2}(1+\alpha^{-1})(\widehat{\boldsymbol{\sigma}}\cdot\mathbf{g}_{12})\widehat{\boldsymbol{\sigma}}$.

The solution to Eq. (A 4) can be written in the form (7.1). The unknown functions of the peculiar velocity, $\boldsymbol{\mathcal{A}}$, $\boldsymbol{\mathcal{B}}$, $\mathcal{C}_{ij}$, and $\mathcal{D}$ appearing in $f^{(1)}$ are determined by solving Eq. (A 4). By dimensional analysis, $\boldsymbol{\mathcal{A}}(\mathbf{V}) = v_0^{-d}\ell^{1-d}\boldsymbol{\mathcal{A}}^*(\mathbf{V}^*)$, $\boldsymbol{\mathcal{B}}(\mathbf{V}) = v_0^{-d}\ell^{1-d}\boldsymbol{\mathcal{B}}^*(\mathbf{V}^*)$, $\mathcal{C}_{ij}(\mathbf{V}) = v_0^{-(d+1)}\ell^{1-d}\mathcal{C}_{ij}^*(\mathbf{V}^*)$, and $\mathcal{D}(\mathbf{V}) = v_0^{-(d+1)}\ell^{1-d}\mathcal{D}^*(\mathbf{V}^*)$, where $\ell = 1/n\sigma^{d-1}$ is the mean free path for hard spheres and $\boldsymbol{\mathcal{A}}^*(\mathbf{V}^*)$, $\boldsymbol{\mathcal{B}}^*(\mathbf{V}^*)$, $\mathcal{C}_{ij}^*(\mathbf{V}^*)$, and $\mathcal{D}_i^*(\mathbf{V}^*)$ are dimensionless functions of the reduced velocity $\mathbf{V}^* = \mathbf{V}/v_0$, $v_0 = \sqrt{2T/m}$ being the thermal speed. Consequently,

$$\begin{aligned}\partial_t^{(0)}\boldsymbol{\mathcal{A}}(\mathbf{V}) &= (\partial_t^{(0)}T)\partial_T\boldsymbol{\mathcal{A}}(\mathbf{V}) = -\frac{1}{2T}\nabla_{\mathbf{V}}\cdot(\mathbf{V}\boldsymbol{\mathcal{A}}(\mathbf{V}))(\partial_t^{(0)}T)\\ &= -\frac{1}{2T}\nabla_{\mathbf{V}}\cdot(\mathbf{V}\boldsymbol{\mathcal{A}}(\mathbf{V}))\left(m\xi - \frac{2T}{m}\gamma - \zeta^{(0)}T\right),\end{aligned} \tag{A 11}$$

$$\begin{aligned}\partial_t^{(0)}\boldsymbol{\mathcal{B}}(\mathbf{V}) &= (\partial_t^{(0)}T)\partial_T\boldsymbol{\mathcal{B}}(\mathbf{V}) = -\frac{1}{2T}\nabla_{\mathbf{V}}\cdot(\mathbf{V}\boldsymbol{\mathcal{B}}(\mathbf{V}))(\partial_t^{(0)}T)\\ &= -\frac{1}{2T}\nabla_{\mathbf{V}}\cdot(\mathbf{V}\boldsymbol{\mathcal{B}}(\mathbf{V}))\left(m\xi - \frac{2T}{m}\gamma - \zeta^{(0)}T\right),\end{aligned} \tag{A 12}$$

$$\begin{aligned}\partial_t^{(0)}\mathcal{C}_{ij}(\mathbf{V}) &= (\partial_t^{(0)}T)\partial_T\mathcal{C}_{ij}(\mathbf{V}) = -\frac{1}{2T}\left[\nabla_{\mathbf{V}}\cdot(\mathbf{V}\mathcal{C}_{ij}(\mathbf{V})) + \mathcal{C}_{ij}\right](\partial_t^{(0)}T)\\ &= -\frac{1}{2T}\left[\nabla_{\mathbf{V}}\cdot(\mathbf{V}\mathcal{C}_{ij}(\mathbf{V})) + \mathcal{C}_{ij}\right]\left(m\xi - \frac{2T}{m}\gamma - \zeta^{(0)}T\right),\end{aligned} \tag{A 13}$$

$$\begin{aligned}\partial_t^{(0)}\mathcal{D}(\mathbf{V}) &= (\partial_t^{(0)}T)\partial_T\mathcal{D}(\mathbf{V}) = -\frac{1}{2T}\left[\nabla_{\mathbf{V}}\cdot(\mathbf{V}\mathcal{D}(\mathbf{V})) + \mathcal{D}\right](\partial_t^{(0)}T)\\ &= -\frac{1}{2T}\left[\nabla_{\mathbf{V}}\cdot(\mathbf{V}\mathcal{D}(\mathbf{V})) + \mathcal{D}\right]\left(m\xi - \frac{2T}{m}\gamma - \zeta^{(0)}T\right).\end{aligned} \tag{A 14}$$

In addition,

$$\begin{aligned}\partial_t^{(0)}\nabla\ln T &= \nabla\partial_t^{(0)}\ln T = \nabla\left(\frac{m\xi}{T} - \frac{2}{m}\gamma - \zeta^{(0)}\right)\\ &= -\left[\frac{2n}{m}\gamma_n - \frac{\rho}{T}\xi_n + \zeta^{(0)}\left(1 + \phi\partial_\phi\ln\chi\right)\right]\nabla\ln n\\ &\quad -\left(\frac{2T}{m}\gamma_T + \frac{m}{T}\xi - m\xi_T + \frac{1}{2}\zeta^{(0)}\right)\nabla\ln T,\end{aligned} \tag{A 15}$$

where

$$\gamma_n \equiv \frac{\partial\gamma}{\partial n}, \quad \gamma_T \equiv \frac{\partial\gamma}{\partial T}, \tag{A 16}$$

$$\xi_n \equiv \frac{\partial\xi}{\partial n}, \quad \xi_T \equiv \frac{\partial\xi}{\partial T}. \tag{A 17}$$

Upon deriving Eqs. (A 14), use has been made of the explicit form of $\zeta^{(0)}$. Since the gradients of the fields are all independent, Eq. (A 4) can be separated into independent equations for each coefficient. This leads to the following set of linear, inhomogeneous integral equations:

$$\frac{1}{2}\left(\frac{2\gamma}{m}-\frac{m\xi}{T}+\zeta^{(0)}\right)\frac{\partial}{\partial\mathbf{V}}\cdot(\mathbf{V}\boldsymbol{\mathcal{A}})-\left(\frac{2T}{m}\gamma_T+\frac{m}{T}\xi-m\xi_T+\frac{1}{2}\zeta^{(0)}\right)\boldsymbol{\mathcal{A}} - \left(\frac{\beta}{m}\Delta\mathbf{U}-\mathbf{g}\right)\cdot\frac{\partial}{\partial\mathbf{V}}\boldsymbol{\mathcal{A}} -\frac{\gamma}{m}\frac{\partial}{\partial\mathbf{V}}\cdot\mathbf{V}\boldsymbol{\mathcal{A}}+\frac{1}{2}\xi\frac{\partial^2}{\partial V^2}\boldsymbol{\mathcal{A}}+\mathcal{L}\boldsymbol{\mathcal{A}}=\mathbf{A}, \tag{A 18}$$

$$\frac{1}{2}\left(\frac{2\gamma}{m}-\frac{m\xi}{T}+\zeta^{(0)}\right)\frac{\partial}{\partial\mathbf{V}}\cdot(\mathbf{V}\boldsymbol{\mathcal{B}})-\left(\frac{\beta}{m}\Delta\mathbf{U}-\mathbf{g}\right)\cdot\frac{\partial}{\partial\mathbf{V}}\boldsymbol{\mathcal{B}}-\frac{\gamma}{m}\frac{\partial}{\partial\mathbf{V}}\cdot\mathbf{V}\boldsymbol{\mathcal{B}}+\frac{1}{2}\xi\frac{\partial^2}{\partial V^2}\boldsymbol{\mathcal{B}} +\mathcal{L}\boldsymbol{\mathcal{B}}=\mathbf{B}+\left[\frac{2n}{m}\gamma_n-\frac{\rho}{T}\xi_n+\zeta^{(0)}\left(1+\phi\partial_\phi\ln\chi\right)\right]\boldsymbol{\mathcal{A}}, \tag{A 19}$$

$$\frac{1}{2}\left(\frac{2\gamma}{m}-\frac{m\xi}{T}+\zeta^{(0)}\right)\left[\mathcal{C}_{ij}+\frac{\partial}{\partial\mathbf{V}}\cdot(\mathbf{V}\mathcal{C}_{ij})\right]-\left(\frac{\beta}{m}\Delta\mathbf{U}-\mathbf{g}\right)\cdot\frac{\partial}{\partial\mathbf{V}}\mathcal{C}_{ij}-\frac{\gamma}{m}\frac{\partial}{\partial\mathbf{V}}\cdot\mathbf{V}\mathcal{C}_{ij} +\frac{1}{2}\xi\frac{\partial^2}{\partial V^2}\mathcal{C}_{ij}+\mathcal{L}\mathcal{C}_{ij}=C_{ij}, \tag{A 20}$$

$$\frac{1}{2}\left(\frac{2\gamma}{m}-\frac{m\xi}{T}+\zeta^{(0)}\right)\left[\mathcal{D}+\frac{\partial}{\partial\mathbf{V}}\cdot(\mathbf{V}\mathcal{D})\right]-\left(\frac{\beta}{m}\Delta\mathbf{U}-\mathbf{g}\right)\cdot\frac{\partial}{\partial\mathbf{V}}\mathcal{D}-\frac{\gamma}{m}\frac{\partial}{\partial\mathbf{V}}\cdot\mathbf{V}\mathcal{D} +\frac{1}{2}\xi\frac{\partial^2}{\partial V^2}\mathcal{D}+\mathcal{L}\mathcal{D}=D. \tag{A 21}$$

Equations (A 18)–(A 21) reduce to the ones previously obtained for dry granular fluids (no gas phase) (Garzó & Dufty 1999; Lutsko 2005) when $\beta=\gamma=\xi=0$.

Appendix B. Kinetic contributions and collisional cooling rate

In this Appendix we give some details on the evaluation of the kinetic contributions to the transport coefficients η, κ and μ and the first-order contribution ζ_U to the collisional cooling rate.

Let us start with the shear viscosity η. Its kinetic part η_k is given by

$$\eta_k=-\frac{1}{(d-1)(d+2)}\int d\mathbf{v}D_{ij}\mathcal{C}_{ij}(\mathbf{V}), \tag{B 1}$$

where $D_{ij}=m(V_iV_j-\frac{1}{d}V^2\delta_{ij})$. To obtain it, we multiply (A 19) by D_{ij} and integrate over velocity to get

$$-\frac{1}{2}\left(\frac{2\gamma}{m}-\frac{m\xi}{T}+\zeta^{(0)}\right)\eta_k+\frac{2\gamma}{m}\eta_k+\nu_\eta\eta_k=nT-\frac{1}{(d-1)(d+2)}\int d\mathbf{V}D_{ij}(\mathbf{V})\mathcal{K}_i\left[\frac{\partial}{\partial V_j}f^{(0)}\right], \tag{B 2}$$

where

$$\nu_\eta=\frac{\int d\mathbf{v}D_{ij}(\mathbf{V})\mathcal{L}\mathcal{C}_{ij}(\mathbf{V})}{\int d\mathbf{v}D_{ij}(\mathbf{V})\mathcal{C}_{ij}(\mathbf{V})}, \tag{B 3}$$

and use has been made of the results

$$\int d\mathbf{V} D_{ij} \frac{\partial}{\partial V_\ell} \mathcal{C}_{ij} = 0, \quad \int d\mathbf{V} D_{ij} \frac{\partial}{\partial V_\ell} V_\ell \mathcal{C}_{ij} = 2(d-1)(d+2)\eta_k, \tag{B 4}$$

$$\int d\mathbf{V} D_{ij} \frac{\partial^2}{\partial V^2} \mathcal{C}_{ij} = 0. \tag{B 5}$$

The first identity in Eq. (B 4) and Eq. (B 5) follow from the solubility conditions of the Chapman-Enskog method:

$$\int d\mathbf{v} \{1, \mathbf{v}, v^2\} f^{(1)}(\mathbf{V}) = \{0, \mathbf{0}, 0\}. \tag{B 6}$$

The collision integral of the right hand side of Eq. (B 2) has been evaluated in previous works (Garzó & Dufty 1999; Lutsko 2005). Thus, the kinetic part η_k is given by

$$\eta_k = \frac{nT}{\nu_\eta - \frac{1}{2}\left(\zeta^{(0)} - \frac{m}{T}\xi - \frac{2}{m}\gamma\right)} \left[1 - \frac{2^{d-2}}{d+2}(1+\alpha)(1-3\alpha)\phi\chi\right]. \tag{B 7}$$

In order to get an explicit expression for η_k, one has to consider the leading terms in a Sonine polynomial expansion of the distribution function. Here, we have considered a recent modified version of the standard method (Garzó *et al.* 2007*c*, 2009) that yields good agreement with computer simulations even for quite strong values of dissipation (Montanero *et al.* 2007). The final form of η_k is given by Eq. (7.7).

The kinetic parts κ_k and μ_k of the transport coefficients characterizing the heat flux are defined, respectively, as

$$\kappa_k = -\frac{1}{dT} \int d\mathbf{v} \mathbf{S}(\mathbf{V}) \cdot \boldsymbol{\mathcal{A}}(\mathbf{V}), \tag{B 8}$$

$$\mu_k = -\frac{1}{dn} \int d\mathbf{v} \mathbf{S}(\mathbf{V}) \cdot \boldsymbol{\mathcal{B}}(\mathbf{V}), \tag{B 9}$$

where

$$\mathbf{S}(\mathbf{V}) = \left(\frac{m}{2}V^2 - \frac{d+2}{2}T\right)\mathbf{V}. \tag{B 10}$$

We obtain first the kinetic part κ_k. It is obtained by multiplying Eq. (A 18) by $\mathbf{S}(\mathbf{V})$ and integrating over $\mathbf{V}$. The result is

$$-\frac{3}{2}\left(\frac{2\gamma}{m} - \frac{m\xi}{T} + \zeta^{(0)}\right)\kappa_k - \left(\frac{2T}{m}\gamma_T + \frac{m}{T}\xi - m\xi_T + \frac{1}{2}\zeta^{(0)}\right)\kappa_k + \left(\frac{3\gamma}{m} + \nu_\kappa\right)\kappa_k = -\frac{1}{dT}\int d\mathbf{V}\mathbf{S}(\mathbf{V})\cdot\mathbf{A}, \tag{B 11}$$

where

$$\nu_\kappa = \frac{\int d\mathbf{v}\mathbf{S}(\mathbf{V})\cdot\mathcal{L}\boldsymbol{\mathcal{A}}(\mathbf{V})}{\int d\mathbf{v}\mathbf{S}(\mathbf{V})\boldsymbol{\mathcal{A}}(\mathbf{V})}, \tag{B 12}$$

and use has been made of the results

$$\int d\mathbf{V} S_i \frac{\partial}{\partial V_\ell} \mathcal{A}_i = 0, \quad \int d\mathbf{V} S_i \frac{\partial}{\partial V_\ell} V_\ell \mathcal{A}_i = 3dT\kappa_k, \tag{B 13}$$

$$\int d\mathbf{V} S_i \frac{\partial^2}{\partial V^2} \mathcal{A}_i = 0. \tag{B 14}$$

The right hand side of Eq. (B 11) has been already evaluated for dry granular fluids

(Garzó & Dufty 1999; Lutsko 2005) so that the final form of κ_k can be easily obtained from Eq. (B 11). It is given by Eq. (7.17). The evaluation of μ_k follows similar mathematical steps as those made in the calculation of κ_k. Its explicit form can be written as

$$\mu_k = \frac{\kappa_0\nu_0 T}{n}\left[\nu_\mu - \frac{3}{2}\left(\zeta^{(0)} - \frac{m\xi}{T}\right)\right]^{-1}\left\{\kappa_k^*\nu_0^{-1}\left[\frac{2n}{m}\gamma_n - \frac{\rho}{T}\xi_n + \zeta^{(0)}\left(1+\phi\partial_\phi \ln\chi\right)\right]\right.$$
$$+\frac{d-1}{d}a_2 + 3\frac{2^{d-2}(d-1)}{d(d+2)}\phi\chi(1+\alpha)\left(1+\frac{1}{2}\phi\partial_\phi\ln\chi\right)$$
$$\left.\times\left[\alpha(\alpha-1)+\frac{a_2}{6}(10+2d-3\alpha+3\alpha^2)\right]\right\}, \tag{B 15}$$

where

$$\nu_\mu = \frac{\int d\mathbf{v}\mathbf{S}(\mathbf{V})\cdot\mathcal{L}\boldsymbol{\mathcal{B}}(\mathbf{V})}{\int d\mathbf{v}\mathbf{S}(\mathbf{V})\boldsymbol{\mathcal{B}}(\mathbf{V})}. \tag{B 16}$$

As in the case of the shear viscosity, to get the explicit forms of ν_κ and ν_μ one has consider the leading terms in the (modified) Sonine polynomial expansion (Garzó *et al.* 2007*c*, 2009). To leading order the results yield $\nu_\kappa = \nu_\mu$ where μ_κ is given by Eq. (7.22).

We consider finally the first-order contribution ζ_U to the collisional cooling rate. It is given by Eq. (7.25) where ζ_{11} is defined as

$$\zeta_{11} = \frac{1}{2nT}\frac{\pi^{(d-1)/2}}{d\Gamma\left(\frac{d+3}{2}\right)}\sigma^{d-1}\chi m(1-\alpha^2)\int d\mathbf{V}_1\int d\mathbf{V}_2\, g_{12}^3 f^{(0)}(\mathbf{V}_1)\mathcal{D}(\mathbf{V}_2), \tag{B 17}$$

where the unknown functions $\mathcal{D}(\mathbf{V})$ are the solutions to the linear integral equation (A 21). An approximate solution to this integral equation (A 21) can be obtained by taking the leading Sonine approximation

$$\mathcal{D}(\mathbf{V}) \to e_D f_M(\mathbf{V})F(\mathbf{V}), \tag{B 18}$$

where

$$F(\mathbf{V}) = \left(\frac{m}{2T}\right)^2 V^4 - \frac{d+2}{2}\frac{m}{T}V^2 + \frac{d(d+2)}{4}. \tag{B 19}$$

The coefficient e_D is given by

$$e_D = \frac{2}{d(d+2)}\frac{1}{n}\int d\mathbf{V}\ \mathcal{D}(\mathbf{V})F(\mathbf{V}). \tag{B 20}$$

Substitution of Eq. (B 19) into Eq. (B 17) gives

$$\zeta_{11} = \frac{3(d+2)}{32d}\chi(1-\alpha^2)\left(1+\frac{3}{128}a_2\right)\nu_0 e_D. \tag{B 21}$$

The coefficient e_D is determined by substituting Eq. (B 22) into the integral equation (A 21), multiplying by $F(\mathbf{V})$ and integrating over $\mathbf{V}$. The result is

$$-\frac{3}{2}\left(\frac{2\gamma}{m} - \frac{m\xi}{T} + \zeta^{(0)}\right)e_D + 4\frac{\gamma}{m}e_D + \nu_\gamma e_D = \frac{2}{d(d+2)}\frac{1}{n}\int d\mathbf{V}F(\mathbf{V})D(\mathbf{V}), \tag{B 22}$$

where the term $\zeta_{11}a_2$ has been been neglected in accord with the present approximation. Moreover, the terms proportional to a_2 coming from ν_γ and $\zeta^{(0)}$ must be also neglected by consistency. In Eq. (B 22), we have introduced the collision frequency

$$\nu_\gamma = \frac{\int d\mathbf{V}F(\mathbf{V})\mathcal{L}[f_M(V)F(\mathbf{V})]}{\int d\mathbf{V}f_M(V)F(\mathbf{V})F(\mathbf{V})}. \tag{B 23}$$

As before, the right hand side of Eq. (B 22) has been previously evaluated for dense

dry granular fluids (Garzó & Dufty 1999; Lutsko 2005). Taking into these results, the expression for e_D can be written as

$$e_D = \left(\nu_\gamma - \frac{\gamma}{m} - \frac{3m\xi}{2T} + \frac{3}{2}\zeta^{(0)}\right)^{-1} \frac{9(d+2)2^{d-8}}{d^2}\phi\chi\left[\frac{\omega\nu_0^{-1}}{2(d+2)} - (1+\alpha)\left(\frac{1}{3}-\alpha\right)\frac{a_2}{2}\right], \tag{B 24}$$

where ω^* and ν_γ are given by Eqs. (7.28) and (7.29), respectively. With this result one gets the expression (7.27) for ζ_{11}.

Appendix C. Another theory for suspensions

In this Appendix we display the explicit expressions for η and κ used by Agrawal *et al.* (2001). They can be written as $\eta = \eta_0\eta^*$ and $\kappa = \kappa_0\kappa^*$ where the (reduced) coefficients η^* and κ^* are given by

$$\eta^* = 1.2\left\{\frac{\mu_0}{\chi\delta(2-\delta)}\left(1+\frac{8}{5}\phi\delta\chi\right)\left[1+\frac{8}{5}\delta(3\delta-2)\phi\chi\right] + \frac{768}{25\pi}\delta\phi^2\chi\right\}, \tag{C 1}$$

$$\kappa^* = \frac{\lambda_0}{\chi}\left\{\left(1+\frac{12}{5}\phi\delta\chi\right)\left[1+\frac{12}{5}\delta^2(4\delta-3)\phi\chi\right] + \frac{64}{25\pi}(41-33\delta)\delta^2\phi^2\chi^2\right\}. \tag{C 2}$$

Here, we have introduced the quantities

$$\mu_0 = (1+2\beta^*)^{-1}, \quad \beta^* = \frac{5\sqrt{\pi}}{128}\frac{C_D F(\phi)}{\phi\chi}\frac{\rho_g}{\rho_s}\frac{Re_m}{Re_T}, \tag{C 3}$$

$$\lambda_0 = \frac{8}{\delta(41-33\delta)+36\beta^*}, \tag{C 4}$$

$$\delta = \frac{1+\alpha}{2}, \quad F(\phi) = (1-\phi)^{2.65}, \tag{C 5}$$

$$C_D = (24/Re_m)(1+0.15Re_m^{0.687}), Re_m < 1000, \quad C_D = 0.44, Re_m \geqslant 1000. \tag{C 6}$$

REFERENCES

Abbas, M., Climent, E. & Simonin, O. 2009 Shear-induced self-diffusion of inertial particles in a viscous fluid. *Phys. Rev. E* **79** (3), 036313.

Agrawal, K., Loezos, P. N., Syamlal, M. & Sundaresan, S. 2001 The role of meso-scale structures in rapid gas-solid flows. *J. Fluid Mech.* **445**, 151–185.

Anderson, T. B. & Jackson, R. 1967 A fluid mechanical description of fluidized beds. *I & EC Fund.* **6**, 527.

Balzer, G., Boelle, A. & Simonin, O. 1995 Eulerian gas-solid flow modelling of dense fluidized beds. In *Computational gas-solid flows and reacting systems: Theory, methods and practice. Fluidization VIII* (ed. J.F. Large & C. Lagurie). Engineering Foundation.

Brey, J. J., Dufty, J. W. & Santos, A. 1997 Dissipative dynamics for hard spheres. *J. Stat. Phys.* **87**, 1051–1066.

Brey, J. J., Dufty, J. W., Santos, A. & Kim, C. S. 1998 Hydrodynamics for granular flows at low density. *Phys. Rev. E* **58**, 4638–4653.

Brilliantov, N. & Pöschel, T. 2004 *Kinetic Theory of Granular Gases*. Oxford University Press.

Campbell, C. S. 1990 Rapid granular flows. *Annu. Rev. Fluid Mech.* **22**, 57–92.

Carnahan, N. F. & Starling, K. E. 1969 Equation of state for nonattracting rigid spheres. *J. Chem. Phys.* **51**, 635–636.

Chapman, S. & Cowling, T. G. 1970 *The Mathematical Theory of Nonuniform Gases*. Cambridge University Press.

Clement, C. P., Pacheco-Martínez, H. A., Swift, M. R. & King, P. J. 2010 The water-enhanced Brazil nut effect. *Europhys. Lett.* **91**, 54001.

Février, P., Simonin, O. & Squires, K. D. 2005 Partitioning of particle velocities in gas–solid turbulent flows into a continuous field and a spatially uncorrelated random distribution: theoretical formalism and numerical study. *J. Fluid. Mech.* **533**, 1–46.

Gardiner, C. W. 1985 *Handbook of Stochastic Methods*, 2nd edn. Berlin: Springer.

Garzó, V. 2005 Instabilities in a free granular fluid described by the Enskog equation. *Phys. Rev. E* **72**, 021106.

Garzó, V. & Dufty, J. W. 1999 Dense fluid transport for inelastic hard spheres. *Phys. Rev. E* **59**, 5895–5911.

Garzó, V., Dufty, J. W. & Hrenya, C. M. 2007*a* Enskog theory for polydisperse granular mixtures. I. Navier-Stokes order transport. *Phys. Rev. E* **76**, 031303.

Garzó, V., Hrenya, C. M. & Dufty, J. W. 2007*b* Enskog theory for polydisperse granular mixtures II. Sonine polynomial approximation. *Phys. Rev. E* **76**, 031304.

Garzó, V. & Santos, A. 2003 *Kinetic Theory of Gases in Shear Flows. Nonlinear Transport*. Kluwer Academic Publishers.

Garzó, V., Santos, A. & Montanero, J. M. 2007*c* Modified Sonine approximation for the Navier-Stokes transport coefficients of a granular gas. *Physica A* **376**, 94–107.

Garzó, V., Vega Reyes, F. & Montanero, J. M. 2009 Modified Sonine approximation for granular binary mixtures. *J. Fluid Mech.* **623**, 387–411.

Gidaspow, D. 1994 *Multiphase flow and fluidization*. Academic Press, San Diego.

Gidaspow, D. & Jiradilok, V. 2009 *Computational techniques: The multiphase cfd approach to fluidization and green energy technologies*. Nova Publishers, New York.

Goldhirsch, I. 2003 Rapid granular flows. *Annu. Rev. Fluid Mech.* **35**, 267.

Hrenya, C. M., Galvin, J. E. & Wildman, R. D. 2008 Evidence of higher-order effects in thermally driven granular flows. *J. Fluid Mech.* **598**, 429–450.

Idler, V., Sánchez, I., Paredes, R., Gutiérrez, G., Reyes, L. I. & Botet, R. 2009 Three-dimensional simulations of a vertically vibrated granular bed including interstitial air. *Phys. Rev. E* **79**, 051301.

Jackson, R. 2000 *The dynamics of fluidized particles*. Cambridge University Press, New York.

Koch, D. 2012 personal communication .

Koch, D. L. 1990 Kinetic theory for a monodisperse gas-solid suspension. *Phys. Fluids A* **2**, 1711.

Koch, D. L. & Hill, R. J. 2001 Inertial effects in suspensions and porous-media flows. *Annu. Rev. Fluid Mech.* **33**, 619–647.

Koch, D. L. & Sangani, A. S. 1999 Particle pressure and marginal stability limits for a homogeneous monodiperse gas-fluidized bed: Kinetic theory and numerical simulations. *J. Fluid Mech.* **400**, 229.

Lumley, J. L. & Newman, G. R. 1977 The return to isotropy of homogeneous turbulence. *J. Fluid Mech.* **82**, 161–178.

Lun, C. K. K. & Savage, S. B. 2003 Kinetic theory for inertia flows of dilute turbulent gas-solids mixtures. In *Granular gas dynamics* (ed. T. Pöschel & N. Brilliantov), p. 263. Springer.

Lutsko, J. 2005 Transport properties of dense dissipative hard-sphere fluids for arbitrary energy loss models. *Phys. Rev. E* **72**, 021306.

Ma, D. & Ahmadi, G. 1988 A kinetic model for rapid granular flow of nearly elastic particles including interstitial fluid effects. *Powder Tech.* **56**, 191.

Möbius, M. E., Cheng, X., Eshuis, P., Karczmar, G. S., Nagel, S. R. & Jaeger, H. M. 2005 Effect of air on granular size separation in a vibrated granular bed. *Phys. Rev. E* **72**, 011304.

Möbius, M. E., Lauderdale, B. E., Nagel, S. R. & Jaeger, H. M. 2001 Size separation of granular particles. *Nature (London)* **414**, 270.

Montanero, J. M. & Santos, A. 2000 Computer simulation of uniformly heated granular fluids. *Granular Matter* **2**, 53–64.

Montanero, J. M., Santos, A. & Garzó, V. 2007 First-order Chapman-Enskog velocity distribution function in a granular gas. *Physica A* **376**, 75–93.

Naylor, M. A., Swift, M. R. & King, P. J. 2003 Air-driven Brazil nut effect. *Phys. Rev. E* **68**, 012301.

van Noije, T. P. C. & Ernst, M. H. 1998 Velocity distributions in homogeneous granular fluids: the free and heated case. *Granular Matter* **1**, 57–64.

Pannala, S., Syamlal, M. & O'Brien, T. 2010 In *Computational gas-solid flows and reacting systems: Theory, methods and practice.* (ed. S. Pannala, M. Syamlal & T. O'Brien). Hershey: IGI Global.

Pöschel, T. & Brilliantov, N. 2006 Breakdown of the Sonine expansion for the velocity distribution of granular gases. *Europhys. Lett.* **74**, 424.

Rericha, E. C., Bizon, C., Shattuck, M. D. & Swinney, H. L. 2002 Shocks in supersonic sand. *Phys. Rev. Lett.* **88**, 014302.

Richardson, J. F. & Zaki, W. N. 1954 Sedimentation and fluidisation: Part 1. *Trans. Inst. Chem. Eng. London* **32**, 35.

Sánchez, P., Swift, M. R. & King, P. J. 2004 Stripe formation in granular mixtures due to the differential influence of drag. *Phys. Rev. Lett.* **93**, 184302.

Sangani, A. S., Mo, G., Tsao, H-K & Koch, D. L. 1996 Simple shear flows of dense gas-solid suspensions at finite Stokes numbers. *J. Fluid Mech.* **313**, 309–341.

Santos, A. & Montanero, J. M. 2009 The second and third Sonine coefficients of a freely cooling granular gas revisited. *Granular Matter* **11**, 157–168.

Santos, V., Garzó, V. & Dufty, J. W. 2004 Inherent rheology of a granular fluid in uniform shear flow. *Phys. Rev. E* **69**, 061303.

Simonin, O., Zaichik, L. I., Alipchenkov, V. M. & Février, P. 2006 Connection between two statistical approaches for the modelling of particle velocity and concentration distributions in turbulent flow: The mesoscopic Eulerian formalism and the two-point probability density function method. *Phys. Fluids* **18** (12), 125107.

Sinclair, J. L. & Jackson, R. 1989 Gas-particle flow in a vertical pipe with particle-particle interactions. *AIChE J.* **35**, 1473.

Sundaram, S. & Collins, L. R. 1999 A numerical study of the modulation of isotropic turbulence by suspended particles. *J. Fluid Mech.* **379**, 105–143.

Tenneti, S., Fox, R. O. & Subramaniam, S. 2010*a* Instantaneous particle acceleration model for gas-solid suspensions at moderate Reynolds numbers. In *Proceedings of the International Conference on Multiphase Flow*.

Tenneti, S., Fox, R. O. & Subramaniam, S. 2011 Stochastic acceleration model for inertial particles in gas-solid suspensions at moderate Reynolds numbers. In preparation.

Tenneti, S., Garg, R., Hrenya, C. M., Fox, R. O. & Subramaniam, S. 2010*b* Direct numerical simulation of gas-solid suspensions at moderate Reynolds number: Quantifying the coupling between hydrodynamic forces and particle velocity fluctuations. *Powder Tech.* **203**, 57.

Tsao, H-K & Koch, D. L. 1995 Simple shear flows of dilute gas-solid suspensions. *J. Fluid Mech.* **296**, 211–245.

Wen, C. Y. & Yu, Y. H. 1966 Mechanics of fluidization. *Chem. Eng. Prog. Symp. Ser.* **62**, 100.

Wildman, R., Martin, T. W., Huntley, J. M., Jenkins, J. T., Viswanathan, H., Fen, X. & Parker, D. J. 2008 Experimental investigation and kinetic-theory-based model of a rapid granular shear flow. *J. Fluid Mech.* **602**, 63–79.

Wylie, J. J., Zhang, Q., Xu, H. Y. & Sun, X. X. 2008 Drag-induced particle segregation with vibrating boundaries. *Europhys. Lett.* **81**, 54001.

Xu, Y. & Subramaniam, S. 2006 A multiscale model for dilute turbulent gas-particle flows based on the equilibration of energy concept. *Phys. Fluids* **18**, 033301.

Yan, X., Shi, Q., Hou, M., Lu, K. & Chan, C. K. 2003 Effects of air on the segregation of particles in a shaken granular bed. *Phys. Rev. Lett.* **91**, 014302.

Zaichik, L. I., Simonin, O. & Alipchenkov, V. M. 2009 An Eulerian approach for large eddy simulation of particle transport in turbulent flows. *J. of Turbulence* **10** (4), 1–21.

Zeilstra, M. A., van der Hoef, M. A. & Kuipers, J. A. M. 2008 Simulations of density segregation in vibrated beds. *Phys. Rev. E* **77**, 031309.

Appendix C: Theory (Iowa State – Task 2.1)

A Lagrangian-Eulerian (LE) description is employed to describe the multiphase flow. The starting point for the LE description is the one-particle distribution function or the droplet distribution function (used in spray terminology). The evolution equation of the ddf is rigorously derived by Subramaniam (2001).

Consider a particle-laden flow where for simplicity we consider spherical particles. At time t, the n^{th} particle is characterized by its position vector $\mathbf{X}_{(n)}(t)$, its velocity vector $\mathbf{V}_{(n)}(t)$. It is assumed that the size and shape of the particles do not change and hence the particle property vector is a 7-dimensional random vector whose components are the location $\mathbf{X}$, velocity $\mathbf{V}$ and particle size characterized by the radius r. The governing equations of motion for the particle are:

$$\frac{d\mathbf{X}_{(n)}}{dt} = \mathbf{V}_{(n)} \tag{C1}$$

$$\frac{d\mathbf{V}_{(n)}}{dt} = \mathbf{A}_{(n)} \quad , \tag{C2}$$

where, $\mathbf{A}_{(n)}$ is the acceleration experienced by the n^{th} particle. This acceleration can depend on the particle velocity, size and fluid flow statistics.

The evolution equation for the one-particle distribution function $f(\mathbf{x},\mathbf{v},r;t)$ can be derived (Subramaniam 2001):

$$\frac{\partial f}{\partial t} + \frac{\partial}{\partial x_i}\left(v_i f\right) + \frac{\partial}{\partial v_i}\left(\left\langle A_i \,|\mathbf{x},\mathbf{v},r;t\right\rangle f\right) = \dot{f}_{\text{coll}} \quad , \tag{C3}$$

where, $\dot{f}_{\text{coll}}$ is the collisional term that depends on higher order statistics.

The evolution equation of the one-particle distribution function is written in a simpler form as:

$$\frac{\partial f}{\partial t} + \frac{\partial}{\partial x_i}\left(v_i f\right) + \frac{\partial}{\partial v_i}\left(\left\langle A_i \,|\mathbf{x},\mathbf{v},r;t\right\rangle f\right) = 0 \ . \tag{C4}$$

This simpler form is useful when analyzing static particle assemblies. The mean mass, momentum and the second moment equations for a monodisperse suspension can be derived from equation (4).

The mean momentum conservation equation is

$$\frac{\partial}{\partial t}\left(n\rho r^3\left\langle v_j\right\rangle\right) + \frac{\partial}{\partial x_k}\left(n\rho r^3\left\langle v_j\right\rangle\left\langle v_k\right\rangle\right) = n\rho r^3\left\langle A_j\right\rangle - \frac{\partial}{\partial x_k}\left(n\rho r^3\left\langle v_j'' v_k''\right\rangle\right), \tag{C5}$$

where ρ is the thermodynamic density of the particles. In Eq. (5), we note that the second term on the right hand side of is the particle Reynolds stress arising from fluctuations in the particle velocity. The particle velocity fluctuations are defined about the mean velocity as follows:

$$v_j'' = v_j - \left\langle v_j\right\rangle \tag{C7}$$

The evolution equation for the second moment of velocity that appears in the particle Reynolds stress is:

$$\frac{\partial}{\partial t}\left(n\rho r^3\left\langle v_i'' v_j''\right\rangle\right) + \frac{\partial}{\partial x_k}\left(n\rho r^3\left\langle v_i'' v_j''\right\rangle\left\langle v_k\right\rangle\right) = n\rho r^3\left(-\left\langle v_i'' v_k''\right\rangle\frac{\partial}{\partial x_k}\left(\left\langle v_j\right\rangle\right) - \left\langle v_j'' v_k''\right\rangle\frac{\partial}{\partial x_k}\left(\left\langle v_i\right\rangle\right)\right) \tag{C8}$$

$$-\frac{\partial}{\partial x_k}\left(n\rho r^3\left\langle v_i'' v_j'' v_k''\right\rangle\right) + n\rho r^3\left(\left\langle A_i'' v_j''\right\rangle + \left\langle A_j'' v_i''\right\rangle\right)$$

AIChE

Fluid-Particle Drag in Inertial Polydisperse Gas–Solid Suspensions

William Holloway, Xiaolong Yin, and Sankaran Sundaresan
Dept. of Chemical Engineering, Princeton University, Princeton, NJ 08544

DOI 10.1002/aic.12127
Published online December 22, 2009 in Wiley InterScience (www.interscience.wiley.com).

In this article, we extend the low Reynolds number fluid-particle drag relation proposed by Yin and Sundaresan for polydisperse systems to include the effect of moderate fluid inertia. The proposed model captures the fluid-particle drag results obtained from lattice-Boltzmann simulations of bidisperse and ternary suspensions at particle mixture Reynolds numbers ranging from $0 \leq Re_{mix} \leq 40$, over a particle volume fraction range of $0.2 \leq \phi \leq 0.4$, volume fraction ratios of $1 \leq \phi_i/\phi_j \leq 3$, and particle diameter ratios of $1 \leq d_i/d_j \leq 2.5$. © 2009 American Institute of Chemical Engineers *AIChE J,* 56: 1995–2004, 2010

Keywords: fluid-particle drag force, polydisperse mixtures, lattice-Boltzmann simulation, multi-fluid model, moderate inertia, fluidized bed

Introduction

Analysis of large scale gas-particle flows, which are widely encountered in the chemical process industry, is commonly done using averaged equations of motion where the individual particle phase(s) and the fluid are treated as interpenetrating continua.[1–3] These equations contain several terms—the fluid-particle drag force, the particle and fluid-phase effective stresses, etc.—which require constitutive relations. Among these, the fluid-particle drag plays a dominant role in gas–solid fluidized beds in balancing the gravitational force acting on the particles.[2–8] A number of constitutive relations for the fluid-particle drag in monodisperse suspensions (i.e., particles of the same size/density) can be found in the literature.[1–3,9–14] Polydispersity (differences in particle size and/or density) is common in most industrial scale devices; addition of fines is known to affect the quality of fluidization,[15] and segregation is an important consideration in polydisperse fluidized beds.[16–18] Indeed, a substantial amount of recent research has been devoted to the formulation of fluid-particle drag relations for polydisperse fixed beds and suspensions (for example see following references, and the references cited therein).[7,8,12,19] Beetstra et al.[19] provide expressions for fluid-particle drag in polydisperse fixed beds over a range of Reynolds numbers, while Yin and Sundaresan[7,8] limit themselves to Stokes flow conditions, but allow for relative motion (in the local average sense) between the various types of particles.

This study builds on the earlier studies by Yin and Sundaresan[7,8] and considers the effect of moderate inertia on the fluid-particle drag in polydisperse systems, allowing for relative motion between the different types of particles. Towards this end, we have carried out lattice-Boltzmann simulations of fluid flow through assemblies of polydisperse particles in periodic domains, and extracted the fluid-particle drag force under conditions where fluid inertia has a non-negligible effect. We find that the results can be captured reasonably well by a new drag force model for polydisperse suspensions that combines the expressions proposed by Yin and Sundaresan[7,8] for Stokes flow of suspensions and the inertial correction developed by Beetstra et al.[19] for monodisperse fixed beds. We restrict our attention to large Stokes number and moderate Reynolds numbers based on the local-average slip velocity between the fluid and the different types of particles; these conditions are indeed satisfied by most gas-fluidized beds. Strictly speaking, the fluid-particle drag force will also depend on the Reynolds number based on the fluctuating velocities of the particles[20]; however, in fluidized suspensions, the fluctuating velocities of the particles tend to be considerably smaller than the local-average fluid-particle slip velocity, and so their effect on the drag force in only weak.[20] With this in mind, we have not engaged in a

Correspondence concerning this article should be addressed to S. Sundaresan at sundar@princeton.edu.

systematic study of the effect of particle velocity fluctuations on the fluid particle drag in polydisperse systems.

This article is organized as follows: we first present the fluid-particle drag relations proposed by Beetstra et al.[19] for polydisperse fixed beds and Yin and Sundaresan[7,8] for polydisperse suspensions under Stokes flow conditions, and propose an extension of the Yin and Sundaresan[7,8] expressions to account for the effect of moderate fluid inertia. We then outline the lattice-Boltzmann simulation procedure and present the results for polydisperse suspensions with relative motion between the different particle types at moderate fluid inertia. These simulation results are then used to validate the proposed drag force model. The article then concludes with a summary of the main results.

Fluid-Particle Interaction Force in Polydisperse Systems

Fixed beds

The total fluid-particle interaction force per unit volume of a polydisperse *fixed* bed acting on particle of type i, $\mathbf{f}_{\text{Di-fixed}}$, is usually expressed as

$$\mathbf{f}_{\text{i-fixed}} = -\phi_i \nabla P + \mathbf{f}_{\text{Di-fixed}}; \qquad \mathbf{f}_{\text{Di-fixed}} = -\beta_i \Delta \mathbf{U} \tag{1}$$

where P is the local-average fluid pressure, ϕ_i is the volume fraction of particles of type i, $\mathbf{f}_{\text{Di-fixed}}$ is the fluid-particle drag force *per unit volume* of the bed, β_i is the volume-specific friction coefficient for particles of type i, and $\Delta\mathbf{U}$ is the difference between the local average velocities of the particle and fluid phases. It is convenient to express the fixed-bed friction coefficient β_i as [7,8,12,19]

$$\beta_i = \frac{18\phi_i(1-\phi)\mu}{d_i^2} F^*_{\text{Di-fixed}} \tag{2}$$

where ϕ is the total particle phase volume fraction, d_i is the diameter of the ith particle species, μ is the fluid viscosity; $F^*_{\text{Di-fixed}}$ is a dimensionless fluid-particle drag on a particle of type i in a polydisperse fixed bed ($F^*_{\text{Di-fixed}}$ is nondimensionalized by the Stokes drag, namely $3\pi\mu d_i\ (1-\phi)\ \Delta U$). Yin and Sundaresan[8] recently proposed the following expression for $F^*_{\text{Di-fixed}}$ for Stokes flow through polydisperse fixed beds (particle diameter ratios up to 4:1):

$$F^*_{\text{Di-fixed}} = \left(\frac{1}{1-\phi}\right) + \left(F^*_{\text{D-fixed}} - \frac{1}{1-\phi}\right)\left(a y_i + (1-a) y_i^2\right) \tag{3}$$

where $y_i = d_i/\langle d\rangle$; $\langle d\rangle$ is the Sauter mean diameter

$$\langle d\rangle = \sum_i n_i d_i^3 \Big/ \sum_i n_i d_i^2; \tag{4}$$

$F^*_{\text{D-fixed}}$ is the dimensionless fluid particle drag force in a monodisperse fixed bed[12]

$$F^*_{\text{D-fixed}} = \frac{10\phi}{(1-\phi)^2} + (1-\phi)^2\left(1 + 1.5\sqrt{\phi}\right) \tag{5}$$

and a is a cubic polynomial of volume fraction:

$$a = 1 - 2.66\phi + 9.096\phi^2 - 11.338\phi^3. \tag{6}$$

To account for the effects of moderate fluid inertia on the monodisperse fixed bed drag force, Beetstra et al.[19] modified Eq. 5 as

$$F^*_{\text{D-fixed}} = \left(\frac{10\phi}{(1-\phi)^2} + (1-\phi)^2\left(1 + 1.5\sqrt{\phi}\right)\right)(1 + \chi_{\text{BVK}}). \tag{7}$$

where χ_{BVK} represents the inertial correction:

$$\chi_{\text{BVK}} = \frac{0.413\text{Re}}{240\phi + 24(1-\phi)^4(1+1.5\sqrt{\phi})} \times \frac{(1-\phi)^{-1} + 3\phi(1-\phi) + 8.4\text{Re}^{-0.343}}{1 + 10^{3\phi}\text{Re}^{\frac{-(1+4\phi)}{2}}}. \tag{8}$$

Here, Re is the Reynolds number, defined as follows

$$\text{Re} = \frac{|\Delta U|(1-\phi)d}{\nu} \tag{9}$$

where ν is the fluid kinematic viscosity.

Polydisperse suspensions with particle–particle relative motion

Stokes Flow Regime. For high Stokes number, low Reynolds number suspensions with particle–particle relative motion, Yin and Sundaresan[7,8] proposed the following drag force model:

$$\mathbf{f_i} = -\phi_i \nabla P + \mathbf{f_{Di}}; \quad \mathbf{f_{Di}} = -\beta_i \Delta \mathbf{U}_i - \sum_{i \neq j} \beta_{ij}\left(\Delta \mathbf{U}_j - \Delta \mathbf{U}_i\right) \tag{10}$$

For one-dimensional flow, the drag force expression can be written as

$$f^*_{\text{Di}} = -\beta^*_i \text{Re}_i - \sum_{j \neq i} \beta^*_{ij}\ \text{sgn}\left(\Delta U_j - \Delta U_i\right)\text{Re}_{ji}, \tag{11}$$

where, f^*_{Di} is the dimensionless fluid-particle drag force *per unit volume* suspension experienced by particles of type i; $\beta^*_i = \frac{\rho_f \langle d\rangle^3}{\mu^2}\beta_i$ is the dimensionless fixed bed friction coefficient for particles of type i (with ρ_f denoting the fluid density and the dimensional friction coefficient β_i being given by Eqs. 2–6); $\beta^*_{ij} = \frac{\rho_f \langle d\rangle^3}{\mu^2}\beta_{ij}$ is the (dimensionless) fluid-mediated particle–particle drag friction coefficient; sgn $(\Delta U_j - \Delta U_i)$ is the signum function of $\Delta U_j - \Delta U_i$; Re_i and Re_{ji} are given as

$$\text{Re}_i = \frac{\langle d\rangle |\Delta U_i|}{\nu}, \quad \text{Re}_{ji} = \frac{\langle d\rangle \left|\Delta U_j - \Delta U_i\right|}{\nu}. \tag{12}$$

Note that the signum function is used in Eq. 11 to account for the change in sign of the fluid mediated particle–particle drag when the velocities of different particle types relative to one another change sign, while still retaining a positive definite form of Re_{ji}. For β^*_{ij}, Yin and Sundaresan[8] proposed:

$$\beta_{ij}^{*} = -2\alpha_{ij}\frac{\phi_i\phi_j}{\frac{\phi_i}{\beta_i^{*}}+\frac{\phi_j}{\beta_j^{*}}} \tag{13}$$

where α_{ij} is a parameter that depends on the ratio of the lubrication cutoff distance λ (discussed later in this article) to the smaller particle diameter of i and j species:

$$\alpha_{ij} = 1.313\log_{10}\left(\frac{\min(d_i,d_j)}{\lambda}\right) - 1.249. \tag{14}$$

Modification to Account for the Effect of Moderate Fluid Inertia. This study is concerned with extending the model proposed by Yin and Sundaresan[8] for Stokes flow regime to account for moderate inertia. It will be demonstrated in this article that a simple modification, which includes the inertial correction for fixed beds proposed by Beetstra et al.,[19,21] presented later, is able to capture drag force results extracted from our lattice-Boltzmann simulations. Specifically, the modified model consists of Eqs. 2–4, 6, 10, 12–14, and the following:

$$F_{\text{D-fixed}}^{*} = \left(\frac{10\phi}{(1-\phi)^2} + (1-\phi)^2\left(1+1.5\sqrt{\phi}\right)\right)\left(1+\chi_{\text{BVK}}^{*}\right) \tag{15}$$

where χ_{BVK}^{*} is given by:

$$\chi_{\text{BVK}}^{*} = \frac{0.413\text{Re}_{\text{mix}}}{240\phi + 24(1-\phi)^4(1+1.5\sqrt{\phi})} \times \frac{(1-\phi)^{-1} + 3\phi(1-\phi) + 8.4\text{Re}_{\text{mix}}^{-0.343}}{1+10^{3\phi}\text{Re}_{\text{mix}}^{\frac{-(1+4\phi)}{2}}}. \tag{16}$$

These two equations differ from Eqs. 7 and 8 slightly, with Re being replaced by Re_{mix}:

$$\text{Re}_{\text{mix}} = \frac{|\Delta U_{\text{mix}}|(1-\phi)\langle d\rangle}{\nu}; \quad \Delta U_{\text{mix}} = \frac{\sum_i \phi_i \Delta U_i}{\sum_i \phi_i}. \tag{17}$$

Effect of Particle Velocity Fluctuations. Strictly speaking, whenever fluid inertia plays a non-negligible role, the fluid-particle drag force is not independent of fluctuating particle motions.[20] For monodisperse suspensions, Wylie et al.[20] have modeled the effect of particle velocity fluctuations on the fluid-particle drag in a large-Stokes-number, moderate-Reynolds-number monodisperse suspension; toward this end, they define a Reynolds number based on particle velocity fluctuations as $\text{Re}_T = dT^{0.5}/\nu$ where the granular temperature $T = (1/3)(\langle(\Delta U)^2\rangle - \langle\Delta U\rangle^2)$ and the angle brackets indicate ensemble averages. They found that the effect of particle velocity fluctuations on the fluid-particle drag is very small provided Re_T is much smaller than the Reynolds number based on mean flow velocity and particle diameter (Re_m). Figure 1 illustrates the variation of the fluid-particle drag with particle velocity fluctuations scaled by the fluid-particle drag in the absence of particle velocity fluctuations plotted with Re_T/Re_m for $\text{Re}_m = 20$ and two different values of particle volume fractions, as given by the theory of Wylie et al.[20] It is clear that when Re_T/Re_m is small the effect of particle velocity fluctuations on the fluid-particle drag is small. In Figure 2, we present results on the Re_m/Re_T ratio obtained from a lattice-Boltzmann simulation of a collection of bidisperse particles in a periodic domain, sedimenting freely under the action of gravity. (Details of the lattice-Boltzmann simulation methodology are discussed later.) The two curves correspond to the two types of particles in the mixture. It is clear that Re_m/Re_T is much larger than unity for both particle types. The results from the study by Wylie et al. for monodisperse systems (presented in Figure 1) then suggest that in polydisperse systems such as those occurring in gas-fluidized beds, the effect of particle velocity fluctuations on the fluid-particle drag is quite small. With this in mind, we have not explored the Re_T-dependence of fluid-particle drag in the present study.

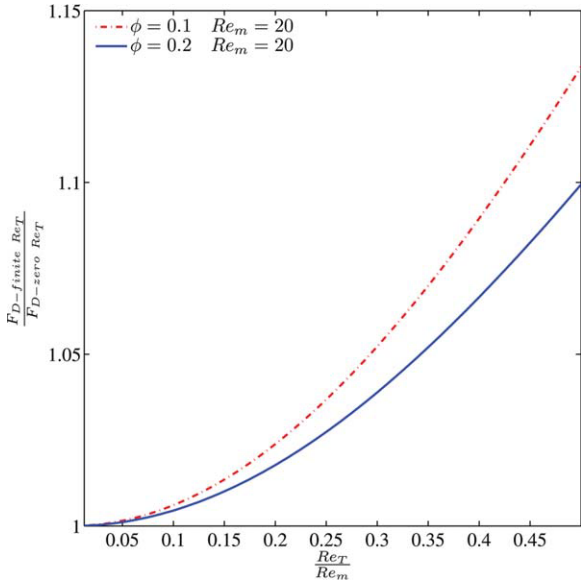

Figure 1. The effect of particle velocity fluctuations on the fluid-particle drag force in a suspension of uniformly sized spherical particles.

The Reynolds number associated with the mean slip velocity, $\text{Re}_m = 20$. Re_T refers to the Reynolds number associated with the particle velocity fluctuations. The ordinate shows the fluid-particle drag force in the presence of particle velocity fluctuations scaled with respect to that obtained in the absence of velocity fluctuations (i.e., a random fixed bed). The results are obtained using the model proposed by Wylie et al.[20] The two curves correspond to two different particle volume fractions. [Color figure can be viewed in the online issue, which is available at www.interscience.wiley.com.]

Lattice-Boltzmann Simulations

To generate the computational data needed to develop and verify the fluid-particle drag force model, we simulated fluid flow through assemblies of particles using the lattice-Boltzmann scheme developed by Ladd,[22–24] which has been used in a number of earlier studies.[7,8,12,19,20,25,26] Ladd's code has been used by a number of investigators to study particle-laden flows, and we have used the same code. As details about the method are readily available in the literature, we

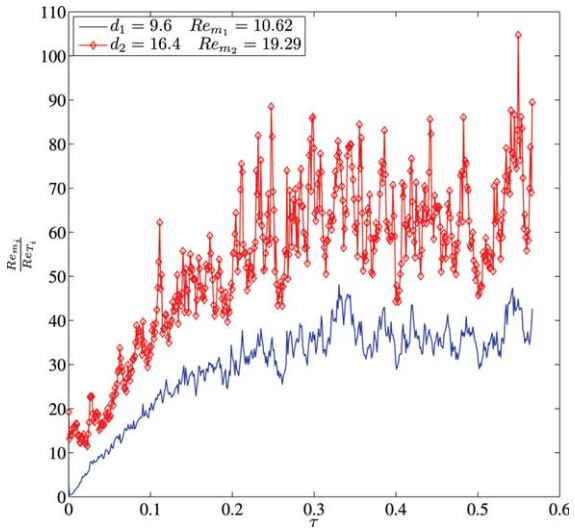

Figure 2. The evolution of Re_m/Re_t as a function of $\tau = tv/\langle d \rangle^2$ in a freely evolving, bidisperse, sedimenting, suspension, where t is time in lattice units, v is the fluid kinematic viscosity, and $\langle d \rangle$ is the Sauter mean diameter of the mixture.

The diameters of the two particles indicated in the figure are multiples of the lattice spacing. The Re_m values indicated in the figure are the statistical average values in the plateau region. The volume fraction of each particle type is the same. The collisions between the particles are elastic. The simulation was carried out in a cubic periodic box of dimension $L = 110$ lattice spacing, containing 144 Type 1 and 29 Type 2 particles. The particle density to fluid density ratio is 1000. $d_1 = 9.6$ and $d_2 = 16.4$, giving a total particle volume fraction of $\phi = 0.1$. A gravitational force $g\langle d \rangle^3/v^2 = 0.897$ is applied in the x-direction, and balanced by a pressure gradient equal to the weight of the suspension per unit volume. [Color figure can be viewed in the online issue, which is available at www.interscience.wiley.com.]

provide only a brief outline of the computational procedure. The 3-D lattice-Boltzmann method used in this study employs at 19-point quadrature in velocity space, the so-called D3Q19 model, with fluid density $\rho_f = 36$ (lattice units [l.u.]). To access a range of Re_m values, various fluid viscosity values ($\mu_f = 0.03$ and 0.36 [l.u.]) were used, while still maintaining low fluid velocities (<0.02 in [l.u.]) to ensure numerical stability. The particle sizes used in this study varied with the smallest particle diameter being ~10 lattice units. The effect of lattice resolution has been addressed by comparing and extrapolating simulation results obtained using different lattice resolutions.

When the separation between particles becomes smaller than the lattice spacing, the hydrodynamic (lubrication) interaction between the particles cannot be resolved in the simulations and are added explicitly.[27] For perfectly spherical, approaching particle pairs, the lubrication force would diverge near contact; in reality, such a divergence is removed by particle surface roughness, or non-continuum effects. To model this effect, it is implemented in the simulations that the lubrication force saturates at a value corresponding to a user specified separation known as the lubrication cut-off distance (λ). Yin and Sundaresan[8] found that the off-diagonal friction coefficient depended systematically on the value of λ (see Eqs. 13 and 14). In our simulations, we used a value of $\lambda = 0.01$ (l.u.) for our lattice-Boltzmann simulations performed at a fluid viscosity of $\mu_f = 0.36$ (l.u.). In our simulations performed at a fluid viscosity of $\mu_f = 0.03$ (l.u.), we assigned a value of λ so that every lattice resolution had an identical $\lambda/\min(d_i,d_j)$ ratio equal to 0.001.

Our simulations began by placing a binary mixture of spheres in a cubic periodic simulation domain whose sides are 10–15 times larger than the diameter of the smaller particle. A large number of Monte Carlo movements of these particles were then executed to ensure that the particle microstructure obeyed that of a binary hard sphere configuration.[8] Subsequently, each particle type was assigned its desired (local average) velocity (ΔU_1 and ΔU_2); this induced fluid flow in the interstices of the particle assembly, whose evolution was followed via lattice-Boltzmann method. To ensure that the average fluid velocity approached zero, a pressure gradient was imposed on the fluid phase. This provides a means of specifying ΔU_1 and ΔU_2 before the simulation instead of extracting the values after the simulation by subtracting the resulting fluid velocity. Once a steady state was reached, the total fluid-particle interaction force F_i (ensemble averaged fluid-particle interaction force per particle) was obtained by integrating the traction due to the fluid over the surfaces of all the like particles. The fluid-particle drag was then isolated by removing the contribution due to the imposed pressure gradient (see Eq. 10). The number of particles used in each simulation varied depending on the total particle volume fraction, fluid viscosity, and volume fraction ratios of each species; see Tables 1–3 for lists of performed simulations. Typically 8–12 independent realizations of each flow situation were performed to obtain good statistical averages of the fluid-particle drag on each particle type in the mixture for chosen Re_1 and Re_2 values.

Strictly speaking, the linear and angular velocities and positions of all the particles will change as the fluid flow evolves, and they should be updated by invoking Newton's laws. It is then not possible to maintain a specified relative velocity (in a local average sense) between the two particle types, as it will also evolve in time. This consideration led us to the so-called *frozen* particle simulations, where the particles were given specified velocities, and the positions and velocities were not updated in time. Such an approach is justifiable in Stokes flow,[8] but is only an approximation when fluid inertia is significant. Frozen particle simulations are attractive for several reasons:

(a) Freely evolving sedimentation of high-Stokes-number suspensions are inherently unstable and form inhomogeneous microstructure.[6,28,29] Figure 3 illustrates the formation of inhomogeneous, time-dependent microstructure in a freely evolving ternary suspension simulation. The areas of dark shading indicate areas high in volume fraction while lighter shading indicates regions of lower volume fraction. (We observed such inhomogeneous structures in simulations involving sedimentation of monodisperse and bidisperse suspensions as well. Thus, the origin of these structures is not polydispersity, although polydispersity can certainly be expected to affect the details.)

(b) In some freely evolving simulations where the relative velocity between the different particle phases is large, the

Table 1. List of Bidisperse Suspension Simulations Performed at a Total Volume Fraction of $\phi = 0.2$

N_1	N_2	$\frac{d_2}{d_1}$	ϕ_1	ϕ_2	Re_1	Re_{21}	δ	f^*_{D1}	f^*_{D2}
763	763	1.00	0.10	0.10	1.16	0.50	−1	7.96	3.12
763	763	1.00	0.10	0.10	2.31	1.00	−1	15.98	6.28
763	763	1.00	0.10	0.10	5.78	2.50	−1	40.76	16.21
763	763	1.00	0.10	0.10	11.55	5.00	−1	94.94	43.86
763	763	1.00	0.10	0.10	1.00	2.00	−1	9.66	−9.65
763	763	1.00	0.10	0.10	2.00	4.00	−1	19.35	−19.32
763	763	1.00	0.10	0.10	5.00	10.00	−1	49.12	−49.11
763	763	1.00	0.10	0.10	10.00	20.00	−1	101.23	−101.08
175	175	1.00	0.10	0.10	26.62	13.33	−1	269.96	68.97
175	175	1.00	0.10	0.10	22.79	5.67	−1	206.12	120.83
175	175	1.00	0.10	0.10	56.97	14.16	−1	824.59	565.40
95	36	2.00	0.05	0.15	35.34	13.74	1	290.24	689.42
191	24	2.00	0.10	0.10	2.45	1.87	1	22.30	22.13
191	24	2.00	0.10	0.10	28.86	12.42	1	358.72	295.77
191	24	2.00	0.10	0.10	13.34	5.32	1	135.11	98.66
186	36	2.50	0.05	0.15	5.12	3.70	1	33.36	72.89
382	24	2.50	0.10	0.10	4.38	3.32	1	43.08	37.48
382	24	2.50	0.10	0.10	14.99	19.21	1	7.96	3.12

N_i, d_j/d_i, ϕ_i, Re_i, Re_{ji}, $\delta = \mathrm{sgn}(\Delta U_j - \Delta U_i)$, and f^*_{Di} represent the particle number, diameter ratio, volume fraction, Reynolds number of particles of type i, Reynolds number based on the magnitude of the relative velocity between particles of type j and i, the sign of the relative velocity between particles of type j and i, and the dimensionless fluid-particle drag force experienced by a particle of type i, respectively, in the simulation domain. The fluctuation velocities were zero in all the simulations.

different types of particles tend to segregate. Extracting data on drag force from simulations with such inhomogeneities is very difficult, as the local average volume fractions and local relative velocities in any selected region within the periodic domain are all changing with time.

Frozen particle simulations suppress such inhomogeneities and allow us to compute fluid-particle drag in homogeneous mixtures.

To test the adequacy of frozen particle simulation technique for moderate-Reynolds-number suspensions, we

Table 2. List of Bidisperse Suspension Simulations Performed at a Total Volume Fraction of $\phi = 0.3$

N_1	N_2	$\frac{d_2}{d_1}$	ϕ_1	ϕ_2	Re_1	Re_{21}	δ	f^*_{D1}	f^*_{D2}
1144	1144	1.00	0.15	0.15	1.26	0.50	−1	20.07	8.18
1144	1144	1.00	0.15	0.15	2.52	1.00	−1	40.23	16.43
1144	1144	1.00	0.15	0.15	6.30	2.50	−1	102.05	42.07
1144	1144	1.00	0.15	0.15	12.61	5.00	−1	211.85	89.09
1144	1144	1.00	0.15	0.15	1.09	0.67	−1	22.52	−13.09
1144	1144	1.00	0.15	0.15	2.17	1.35	−1	45.08	−26.18
1144	1144	1.00	0.15	0.15	5.43	3.37	−1	113.51	−65.52
1144	1144	1.00	0.15	0.15	1.00	2.00	−1	23.75	−23.72
1144	1144	1.00	0.15	0.15	2.00	4.00	−1	47.54	−47.50
1144	1144	1.00	0.15	0.15	5.00	10.00	−1	119.71	−119.58
1144	1144	1.00	0.15	0.15	10.00	20.00	−1	244.87	−244.54
1144	1144	1.00	0.08	0.23	0.96	0.41	−1	12.11	−16.82
1144	1144	1.00	0.08	0.23	1.91	0.83	−1	24.24	−33.65
1144	1144	1.00	0.08	0.23	4.78	2.07	−1	60.93	−84.38
1144	1144	1.00	0.08	0.23	9.57	4.13	−1	123.89	−170.51
1144	1144	1.00	0.08	0.23	0.83	0.35	1	13.02	−31.84
1144	1144	1.00	0.08	0.23	1.65	0.69	1	26.05	−63.81
1144	1144	1.00	0.08	0.23	4.13	1.74	1	65.42	−161.51
1144	1144	1.00	0.08	0.23	8.26	3.47	1	132.66	−334.59
1144	1144	1.00	0.08	0.23	1.22	0.50	−1	10.31	13.22
1144	1144	1.00	0.08	0.23	2.43	1.00	−1	20.65	26.50
1144	1144	1.00	0.08	0.23	6.09	2.50	−1	52.17	67.25
1144	1144	1.00	0.08	0.23	12.17	5.00	−1	107.34	139.68
261	261	1.00	0.15	0.15	13.32	6.69	−1	238.35	58.69
261	261	1.00	0.15	0.15	11.40	2.83	−1	187.06	106.56
261	261	1.00	0.15	0.15	22.80	5.67	−1	424.40	249.74
261	261	1.00	0.15	0.15	45.60	2.75	−1	1124.20	980.51
261	261	1.00	0.15	0.15	26.63	13.37	−1	545.12	143.36
287	36	2.00	0.07	0.23	31.41	10.57	1	452.82	1131.90
287	36	2.00	0.15	0.15	15.05	9.41	−1	357.20	18.60
287	36	2.00	0.15	0.15	22.46	13.00	1	522.72	495.49
287	36	2.00	0.15	0.15	4.29	4.00	1	73.97	100.50
287	54	2.50	0.08	0.23	6.03	3.68	1	69.56	182.89
574	36	2.50	0.15	0.15	17.91	19.20	1	307.35	602.51
574	36	2.50	0.15	0.15	5.08	3.32	1	81.40	106.01

See Table 1 for definition of symbols.

Table 3. List of Bidisperse Suspension Simulations Performed at a Total Volume Fraction of $\phi = 0.4$

N_1	N_2	$\frac{d_2}{d_1}$	ϕ_1	ϕ_2	Re_1	Re_{21}	δ	f^*_{D1}	f^*_{D2}
1526	1526	1.00	0.20	0.20	1.39	0.50	−1	45.54	19.21
1526	1526	1.00	0.20	0.20	6.97	2.50	−1	230.66	98.07
1526	1526	1.00	0.20	0.20	13.94	5.00	−1	475.01	205.31
1526	1526	1.00	0.20	0.20	1.13	0.76	−1	50.24	−28.64
1526	1526	1.00	0.20	0.20	2.26	1.53	−1	100.55	−57.29
1526	1526	1.00	0.20	0.20	5.66	3.81	−1	252.63	−143.35
1526	1526	1.00	0.20	0.20	11.31	7.63	−1	513.37	−287.58
1526	1526	1.00	0.20	0.20	1.00	2.00	−1	52.59	−52.57
1526	1526	1.00	0.20	0.20	2.00	4.00	−1	105.27	−105.21
1526	1526	1.00	0.20	0.20	5.00	10.00	−1	264.49	−264.35
1526	1526	1.00	0.20	0.20	10.00	20.00	−1	537.42	−537.16
1526	1526	1.00	0.20	0.20	56.98	14.16	−1	2958.50	1500.60
1526	1526	1.00	0.20	0.20	26.62	13.33	−1	1095.60	188.30
1526	1526	1.00	0.10	0.30	0.93	0.37	−1	26.33	−37.05
1526	1526	1.00	0.10	0.30	1.87	0.74	−1	52.68	−74.14
1526	1526	1.00	0.10	0.30	4.67	1.84	−1	132.11	−185.82
1526	1526	1.00	0.10	0.30	9.34	3.68	−1	266.95	−374.74
1526	1526	1.00	0.10	0.30	0.74	0.53	−1	27.89	−70.98
1526	1526	1.00	0.10	0.30	1.47	1.05	−1	55.82	−142.17
1526	1526	1.00	0.10	0.30	3.68	2.63	−1	139.98	−358.78
1526	1526	1.00	0.10	0.30	7.37	5.26	−1	282.54	−737.08
1526	1526	1.00	0.10	0.30	1.33	0.50	−1	23.20	30.75
1526	1526	1.00	0.10	0.30	2.66	1.00	−1	46.46	61.61
1526	1526	1.00	0.10	0.30	6.64	2.50	−1	117.08	155.72
1526	1526	1.00	0.10	0.30	13.29	5.00	−1	239.34	320.85
191	72	2.00	0.10	0.30	33.50	9.61	1	822.50	2227.80
382	48	2.00	0.20	0.20	11.39	6.48	1	357.27	483.58
382	48	2.00	0.20	0.20	33.39	18.68	1	1327.50	1750.80
382	48	2.00	0.20	0.20	6.68	3.74	1	209.30	275.27
382	72	2.50	0.10	0.30	7.27	3.68	1	156.08	436.63
764	48	2.50	0.20	0.20	5.95	3.32	1	198.29	231.38
764	48	2.50	0.20	0.20	21.44	19.21	1	771.13	1285.10

See Table 1 for definition of symbols.

compared the fluid-particle drag results obtained from frozen simulations where the particle positions were not updated in time with those obtained from simulations where the particles were allowed to move but treated as elastic granular gas (as in Wylie et al.[20]), (i.e., the particles do not respond to fluid-particle drag, but execute elastic collisions). In these test simulations, all the particles were of the same size and computations were done at various grid resolutions. Both types of simulations had the same Re_m, Re_T, and particle volume fraction. The hydraulic radius of the interstitial region is given by,

$$r_h = \frac{\langle d \rangle (1-\phi)}{6\phi}. \tag{18}$$

As resolution increases, the particle diameter-to-lattice spacing ratio, d, and the hydraulic radius-to-lattice spacing ratio, r_h, increase. In Figure 4, we have plotted the fluid-particle drag obtained from both granular gas and frozen simulations as a function of r_h^{-2} for two different combinations of Re_m and Re_T. It is clear that the two approaches yield different estimates for the fluid-particle drag force at any finite grid resolution; this difference decreases as the value of r_h^{-2} decreases (which is equivalent to increasing resolution). It is also clear that the fluid-particle drag varies linearly with r_h^{-2} as already noted by van der Hoef et al.[12] and Beetstra et al.[19]; when the fluid-particle drag results are extrapolated to infinite resolution, the difference between frozen and granular gas simulations becomes small. Therefore, in our work we have performed frozen particle simulations at a minimum of two different

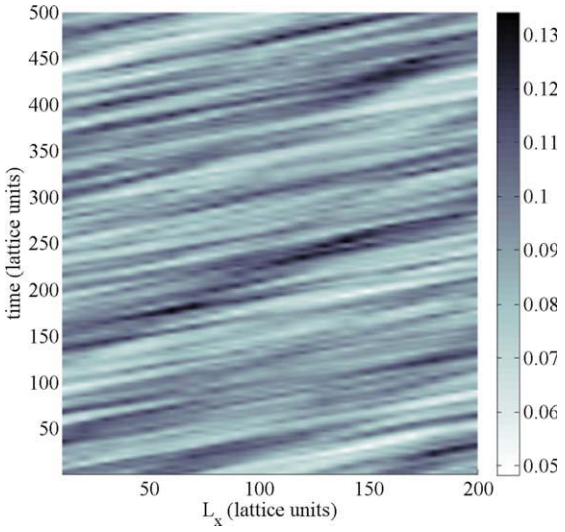

Figure 3. Space-time plot of volume fraction in a freely evolving ternary suspension.

The vertical axis is time, and the horizontal axis is the position in the simulation domain. The variations in the gray scale indicate variations in volume fraction with the darker regions corresponding to regions of higher volume fraction. This simulation was performed in a $200 \times 70 \times 70$ periodic box. The particle diameters used in this simulation were $d_1 = 7.6$, $d_2 = 9.6$, and $d_3 = 11.6$, with respective particle numbers of $N_1 = 56$, $N_2 = 120$, and $N_3 = 24$, giving a total particle volume fraction of $\phi = 0.1$. A gravitational force $g\langle d \rangle^3/\nu^2 = 1.11 \times 10^{-2}$ is applied in the x-direction, and balanced by a pressure gradient equal to the weight of the suspension per unit volume. [Color figure can be viewed in the online issue, which is available at www.interscience.wiley.com.]

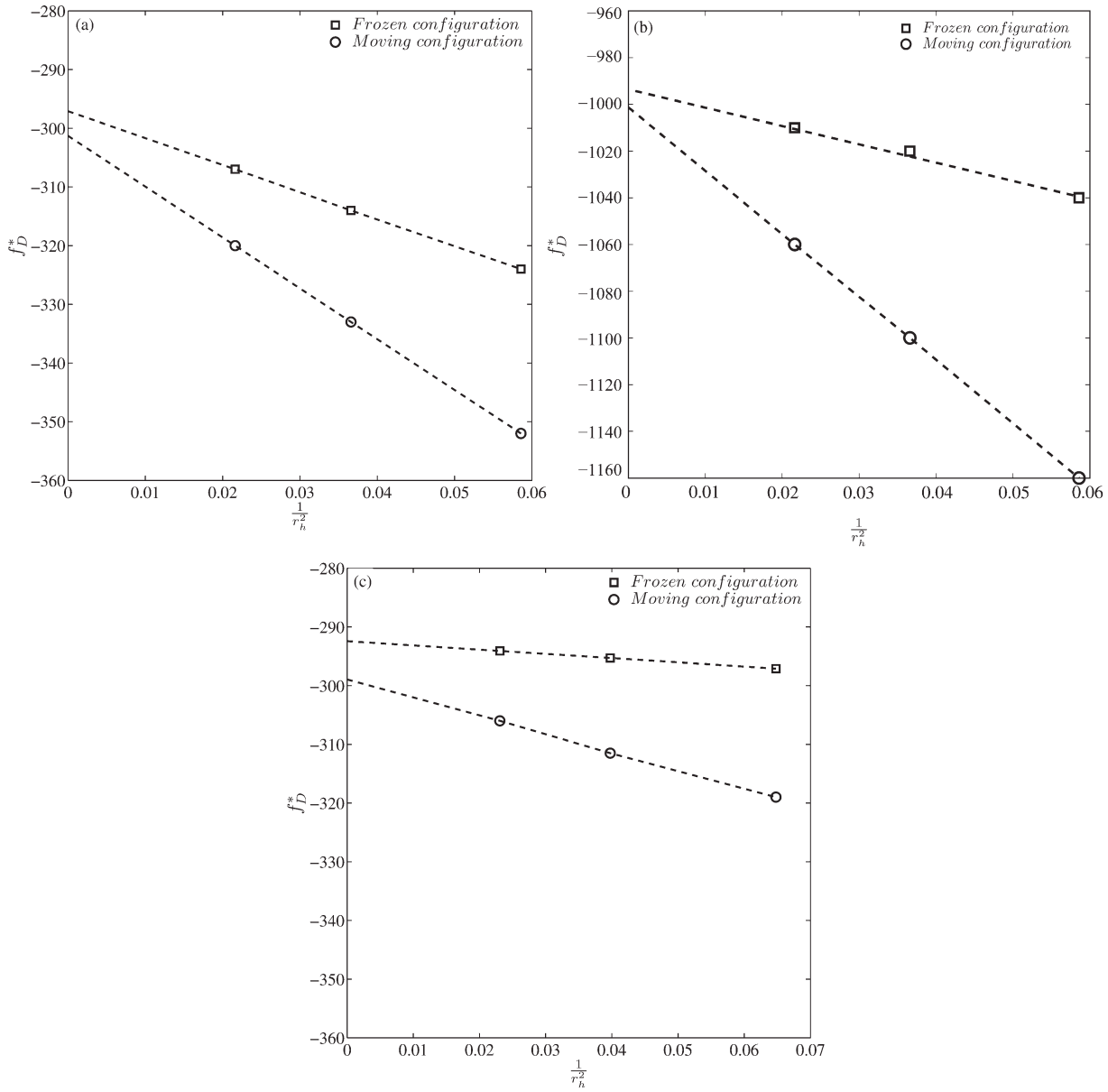

Figure 4. Dimensionless fluid-particle drag force as a function of grid resolution.

Shown are results obtained from frozen particle simulations and those obtained from simulations where the particles were allowed to move as granular gas. All the particles were of the same size. Both types of simulations had the same Re_m, Re_T, and particle volume fraction. (a) $\mathrm{Re}_m = 7$, $\mathrm{Re}_T = 0.6$; $\mu_f = 0.03$ (lattice units), (b) $\mathrm{Re}_m = 20$, $\mathrm{Re}_T = 1.2$; $\mu_f = 0.03$ (lattice units), and (c) $\mathrm{Re}_m = 7$, $\mathrm{Re}_T = 0.6$; $\mu_f = 0.36$ (lattice units).

resolutions and extrapolated the fluid-particle drag to the infinite resolution case using a linear fit as illustrated in Figure 4. At higher fluid viscosities like $\mu_f = 0.36$, we have found that extrapolation of the fluid-particle drag results is unnecessary. It can be seen in Figure 4c that while the fluid-particle drag at any finite resolution differs between frozen and moving simulations, the fluid-particle drag results indeed approach one another in the limit of infinite resolution. Furthermore, if one focuses on the dependence of the fluid-particle drag from the *frozen* simulation case in Figure 4c (for a higher lattice viscosity) as a function of r_{h}^{-2} it can be seen that the fluid-particle drag changes by about 1.6% from the lowest resolution case to the extrapolated fluid-particle drag. Because of the decreased dependence of the fluid-particle drag on grid resolution at higher fluid viscosities, the drag results given at $\mu_f = 0.36$ were not extrapolated in an attempt to decrease the computational demand of the study.

Frozen Particle Simulation Results

Tables 1–3 give a list of the simulations performed at each volume fraction in this work. The fluctuation velocities of the particles were set to zero. The total force acting on the two types of particles and the pressure gradient required to maintain the average fluid velocity at zero were extracted from the simulations. The fluid-particle drag force on the

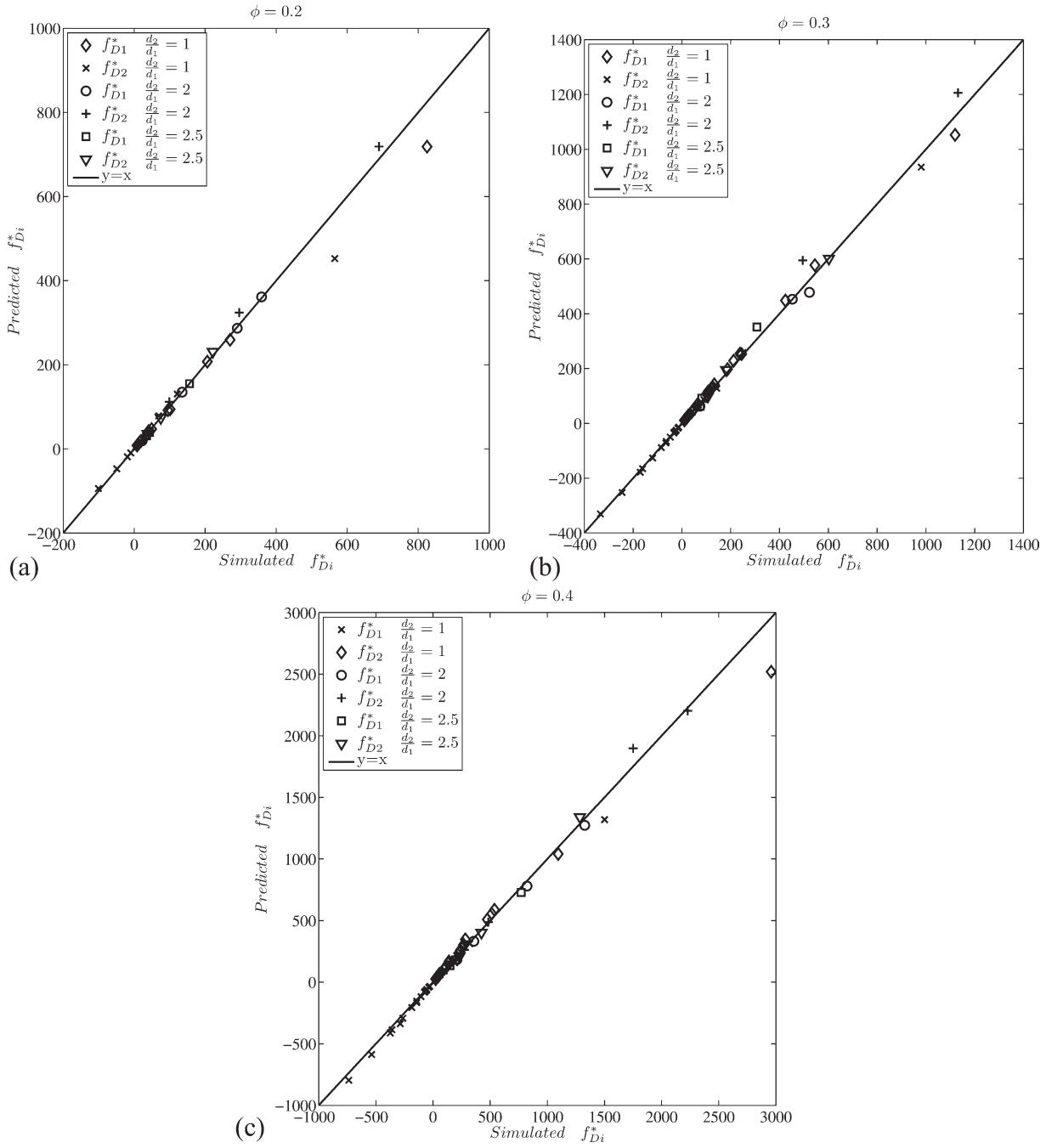

Figure 5. Parity plots showing the simulated fluid-particle drag force and that predicted by the proposed drag force model for bidisperse systems with different particle sizes, volume fraction ratios and Reynolds numbers summarized in Tables 1–3.

Results are shown for three different total volume fractions: (a) $\phi = 0.2$, (b) $\phi = 0.3$, (c) $\phi = 0.4$.

two particle types was then found using Eq. 10a and made dimensionless using the following relationship: $f^*_{\mathrm{Di}} = \rho_f \langle d \rangle^3 f_{\mathrm{Di}} / \mu_{\mathrm{f}}^2$. These drag results were then compared with values found from the drag force model given by Eqs. 2–4, 6, and 11–17. Figures 5a–c show parity plots comparing the model with simulation data; the proposed model fits the data reasonably well with an average deviation between model and simulation being about 5%, while the maximum deviations were about 25%.

To demonstrate that our proposed fluid-particle drag relation can be generalized to polydisperse mixtures of spheres with nonzero particle–particle relative motions, we performed two ternary suspension simulations at $\phi = 0.21$ and $\phi = 0.3$. Table 4 gives the ternary fluid-particle drag results obtained from lattice-Boltzmann simulations with the predicted fluid-particle drag obtained from Eqs. 2–4, 6, and 11–17. It can be seen that the proposed model captures the

Table 4. List of Ternary Suspension Results at $\phi = 0.21$ and $\phi = 0.3$

	$\phi = 0.21$	$\phi = 0.3$
$\phi_1/\phi_2\phi_3$	0.07/0.07/0.07	0.10/0.10/0.10
$d_1/d_2/d_3$	14.0/17.5/35.0	14.0/17.5/35.0
$N_1/N_2/N_3$	261/134/17	373/191/24
$\langle d \rangle$	19/1	19.1
Re_1/Re_2Re_3	6.8/9.1/28.3	8.3/10.6/29.9
$f^*_{D1}/f^*_{D2}/f^*_{D3}$ (simulation)	30.2/48.4/128.1	81.9/105.7/269.3
$f^*_{D1}/f^*_{D2}/f^*_{D3}$ (proposed model)	31.5/41.9/130.2	60.5/83.7/294.4

See Table 1 caption for definition of symbols.

fluid-particle drag results of the ternary suspension simulations with an average deviation of 12.5%.

Figure 6 illustrates that the fluid-mediated (hydrodynamic) particle–particle drag (namely, the second term on the right hand side of Eq. 11) accounts for 0–30% of the fluid-particle drag force in a bidisperse suspension depending on the magnitude of the relative velocity between particle species. From Figure 6, it can be seen that the importance of the fluid-mediated particle–particle drag increases as particle diameter ratio is increased, leading to the conclusion that increases in particle diameter ratio for a fixed Re_{mix} and Re_{12} increases the contribution of the fluid-mediated particle–particle drag to the total fluid-particle drag experienced by a particle of a given type.

The fluid-mediated particle–particle drag force can be compared with the particle–particle drag that results from direct collisions between particles of different types, for which Syamlal[30] proposed the following:

$$f^*_{i-j} = -6\phi_i\phi_j g_0 \mathrm{Re}^2_{ij} \mathrm{sgn}\left(\Delta U_i - \Delta U_j\right) \left(\frac{\left(\frac{\rho_i}{\rho_f}\right)\left(\frac{\rho_j}{\rho_f}\right)}{\frac{\rho_i}{\rho_f} + \frac{\rho_j}{\rho_f}} \right) \tag{19}$$

where g_0 is the radial distribution function (for the ij pair) at contact for a polydisperse hard sphere mixture. This leads to:

$$\frac{f^*_{D-i-j}}{f^*_{i-j}} = \frac{6\alpha(1-\phi)\left(F^*_{\text{Di-fixed}} F^*_{\text{Dj-fixed}}\right)}{g_0 \mathrm{Re}_{ij}\left(F^*_{\text{Di-fixed}} + F^*_{\text{Dj-fixed}}\right)} \left(\frac{\left(\frac{\rho_i}{\rho_f}\right) + \left(\frac{\rho_j}{\rho_f}\right)}{\left(\frac{\rho_i}{\rho_f}\right)\left(\frac{\rho_j}{\rho_f}\right)} \right). \tag{20}$$

Since $\frac{F^*_{Di-fixed}F^*_{Dj-fixed}}{F^*_{Di-fixed}+F^*_{Dj-fixed}}$ is only weakly dependent on Reynolds number, the most significant dependence on Reynolds number comes through Re_{ij}, and therefore as the difference between the Reynolds numbers of different particle species increases, the collisional particle–particle drag dominates the fluid-mediated particle drag term. The quantitative analysis of Yin and Sundaresan[7] about the relative importance of the fluid-mediated particle–particle drag and that due to collisions in the Stokes flow regime remains largely unchanged even in the presence of moderate inertia.

Summary

In this study, we combine the fluid-particle drag relation described by Yin and Sundaresan[7,8] for low Reynolds number flows and that for fixed beds under moderate fluid inertia given by Beetstra et al.[19] and construct a drag force model that applies to polydisperse, high-Stokes-number, and moderate-Reynolds-number suspensions of spherical particles, where the local average velocities of particles of different types are not the same. The proposed fluid-particle drag force model is summarized by Eqs. 2–4, 6, 11–17.

To test this model, a number of lattice-Boltzmann simulations of fluid flow in polydisperse assemblies of particles were carried out from which computational data on fluid-particle drag were gathered. The particle mixture Reynolds number was varied from $0 \leq \mathrm{Re}_{\mathrm{mix}} \leq 40$, over a particle volume fraction range of $0.2 \leq \phi \leq 0.4$, with volume fraction ratios of $1 \leq \phi_i/\phi_j \leq 3$, and particle diameter ratios varying from $1 \leq d_i/d_j \leq 2.5$. Within this parameter range, the proposed fluid-particle drag relation predicts the fluid-particle drag in bidisperse and ternary systems with an average deviation of 5% and 12.5%, respectively.

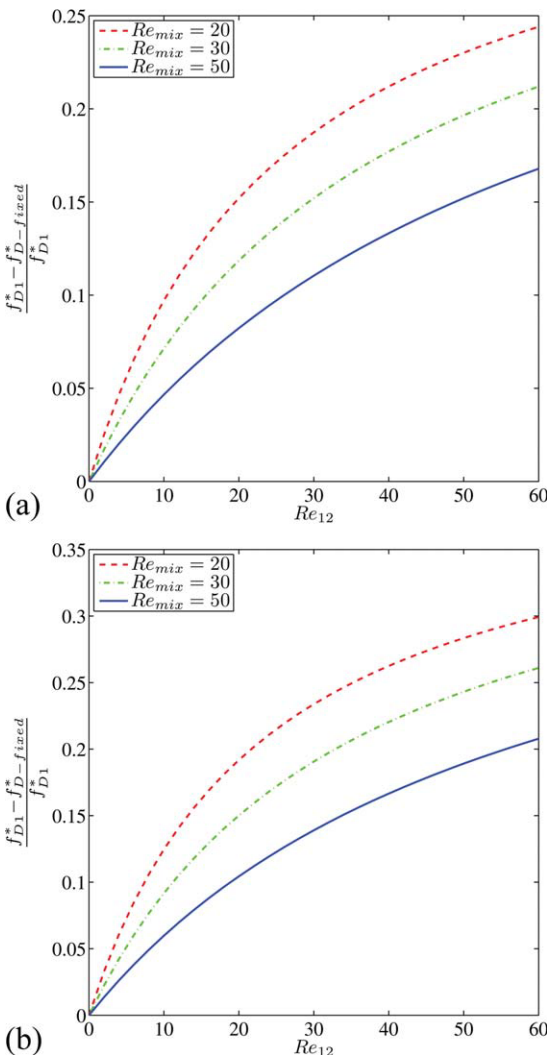

Figure 6. The fluid-mediated particle-particle drag force (normalized with the total fluid-particle drag force) as a function of Re_{12} for the proposed fluid-particle drag relation at two different diameter ratios: (a) d_1:d_2 = 1, (b) d_1:d_2 = 2.

[Color figure can be viewed in the online issue, which is available at www.interscience.wiley.com.]

Acknowledgments

This research was supported by, US Department of Energy (DE-FC26-07NT43098), ExxonMobil Research and Engineering Co. and ACS Petroleum Research Fund (43901-AC9).

Literature Cited

1. Fan LS, Zhu C. *Principles of Gas-Solids Flows*. New York: Cambridge University Press, 1998.
2. Jackson R. *The Dynamics of Fluidized Particles*. Cambridge: Cambridge University Press, 2000.
3. Gidaspow D. *Multiphase Flow and Fluidization: Continuum and Kinetic Theory Descriptions*. London: Academic Press, 1994.
4. Sangani A, Koch D. Particle pressure and marginal stability limits for a homogeneous monodisperse gas-fluidized bed: kinetic theory and numerical simulations. *J Fluid Mech*. 1999;400:229–263.
5. Ten Cate A, Sundaresan S. Analysis of unsteady forces in ordered arrays of monodisperse spheres. *J Fluid Mech*. 2006;552: 257–287.
6. Derksen JJ, Sundaresan S. Direct numerical simulations of dense suspensions: wave instabilities in fluidized beds. *J Fluid Mech*. 2007;587:303–336.
7. Yin X, Sundaresan S. Drag Law for Bidisperse Gas-Solid suspensions Containing Equally Sized Spheres. *Ind Eng Chem Res*. 2009;48:227–241.
8. Yin X, Sundaresan S. Fluid-particle drag in low-Reynolds-number polydisperse gas-solid suspensions. *AIChE J*. 2009;55:1352–1368.
9. Richardson JF, Zaki WN. The sedimentation of a suspension of uniform spheres under conditions of viscous flow. *Chem Eng Sci*. 1954;3:65–73.
10. Wen CY, Yu YH. Mechanics of fluidization. *Chem Eng Prog Symp Ser*. 1966;62:100–111.
11. Benyahia S, Syamlal M, O'Brien TJ. Extension of Hill-Koch-Ladd drag correlation over all ranges of Reynolds number and solids volume fraction. *Powder Technol*. 2006;162:166–174.
12. van der Hoef MA, Beetstra R, Kuipers JAM. Lattice-Boltzmann simulations of low-Reynolds-number flow past mono- and bidisperse arrays of spheres: results for permeability and drag force. *J Fluid Mech*. 2005;528:233–254.
13. Di Felice R. The voidage function for fluid-particle interaction systems. *Int J Multiphase Flow*. 1994;20:153–159.
14. Mazzei L, Lettieri P. A drag force closure for uniformly dispersed fluidized suspensions. *Chem Eng Sci*. 2007;62:6129–6142.
15. Geldart D, Baeyens J, Pope DJ, Van De Wijer P. Segregation in beds of large particles at high velocities. *Powder Technol*. 1981;30: 195–205.
16. Joseph GG, Leboreiro J, Hrenya CM, Stevens AR. Experimental segregation profiles in bubbling gas-fluidized beds. *AIChE J*. 2007; 53:2804–2813.
17. Hoffman AC, Janssen LPBM, Prins J. Particle segregation in fluidized binary mixtures. *Chem Eng Sci*. 1993;48:1583–1592.
18. Rowe PN, Nienow AW. Particle mixing and segregations in gas fluidised beds: a review. *Powder Technol*. 1976;15:141–147.
19. Beetstra R, Van Der Hoef MA, Kuipers JAM. Drag force of intermediate Reynolds number flow past mono- and bidisperse arrays of spheres. *AIChE J*. 2007;53:489–501.
20. Wylie JJ, Koch DL, Ladd AJC. Rheology of suspensions with high particle inertia and moderate fluid inertia. *J Fluid Mech*. 2003;480: 95–118.
21. Beetstra R, van der Hoef MA, Kuipers JAM. Erratum. *AIChE J*. 2007;53:3020.
22. Ladd AJC. Numerical simulations of particulate suspensions via a discretized Boltzmann equation. Part 1. Theoretical foundation. *J Fluid Mech*. 1994;271:285–309.
23. Ladd AJC. Numerical simulations of particulate suspensions via a discretized Boltzmann equation. Part 2. Numerical results. *J Fluid Mech*. 1994;271:311–339.
24. Ladd AJC, Verberg R. Lattice-Boltzmann simulations of particle-fluid suspensions. *J Stat Phys*. 2001;104:1191–1251.
25. Hill R, Koch DL, Ladd AJC. The first effects of fluid inertia on flows in ordered and random arrays of spheres. *J Fluid Mech*. 2001;448:243–278.
26. Hill R, Koch DL, Ladd A. Moderate-Reynolds-number flows in ordered and random arrays of spheres. *J Fluid Mech*. 2001;448:243–278.
27. Nguyen N-Q, Ladd AJC. Lubrication corrections for lattice-Boltzmann simulations of particle suspensions. *Phys Rev E*. 2002;66: 046708.
28. Valiveti P, Koch DL. The inhomogeneous structure of a bidisperse sedimenting gas-solid suspension. *Phys Fluids*. 1999;11:3283–3305.
29. Sundaresan S. Instabilities in fluidized beds. *Annu Rev Fluid Mech*. 2003;35:63–88.
30. Syamlal M. The particle-particle drag term in a multiparticle model of fluidization. Technical Report DOE/MC/21353–2373. US Department of Energy, NTIS/DE87006500, Washington D.C., 1987.

Manuscript received Aug. 24, 2009, and revision received Oct. 22, 2009, and final revision received Oct. 28, 2009.

Appendix E: Theory

A Lagrangian-Eulerian (LE) description is employed to describe the multiphase flow. The starting point for the LE description is the one-particle distribution function which evolves as:

$$\frac{\partial f}{\partial t}+\frac{\partial}{\partial x_i}\left(v_i f\right)+\frac{\partial}{\partial v_i}\left(\left\langle A_i \,|\mathbf{x},\mathbf{v},r;t\right\rangle f\right)=\dot{f}_{\text{coll}} \quad , \tag{E.1}$$

where, $\dot{f}_{\text{coll}}$ is the collisional term that depends on higher order statistics. The one-particle distribution function $f(\mathbf{x},\mathbf{v},r;t)$ can be expressed in terms of a number density and a joint probability density function of velocity and radius i.e.,

$$f(\mathbf{x},\mathbf{v},r;t)=n(\mathbf{x},t)\,f_{\mathbf{V}R}^{c}(\mathbf{v},r\,|\,\mathbf{x};t) \quad .$$

The joint pdf can be further expressed as

$$f_{\mathbf{V}R}^{c}(\mathbf{v},r\,|\,\mathbf{x};t)=f_{\mathbf{V}|R}^{c}(\mathbf{v}\,|\,r;\mathbf{x},t)\,f_{R}^{C} \tag{A.2}$$

and hence

$$f(\mathbf{x},\mathbf{v},r;t)=n(\mathbf{x},r,t)\,f_{\mathbf{V}|R}^{c}(\mathbf{v}\,|\,r\,,\mathbf{x};t) \quad .$$

where $n(\mathbf{x},r,t)$ characterizes the number density conditional on the particle size in the suspension and $f_{\mathbf{V}|R}^{c}(\mathbf{v}\,|\,r;\mathbf{x},t)$ describes the distribution of velocities in a particular size class. In a poly-disperse suspension with a continuous size distribution, f_R^c is specified and a size class in MFIX can be thought of as the integral of f_R^c over the interval $\left(r\,,r+\Delta r\right)$. If the particle size distribution is represented by discrete size classes, i.e., $f_R^c(r\,|\,\mathbf{x};t)=\sum_i p_i\delta\left(r-r_i\right)$, then,

$$n\left(\mathbf{x},r;t\right)=n_i\left(\mathbf{x},t\right)\delta\left(r-r_i\right)$$

$$n\left(\mathbf{x},t\right)=\int n\left(\mathbf{x},r;t\right)dr=\sum_i n_i\left(\mathbf{x},t\right).$$

Appendix F: Governing equations for freely evolving poly-disperse suspensions

Here we briefly show the relevant governing equations of motion in the accelerating frame of reference. The average velocity of the fluid phase denoted $\left\langle\mathbf{u}^{(f)}\right\rangle$ evolves according to the equation:

$$\frac{d}{dt}\left\langle\mathbf{u}^{(f)}\right\rangle=-\frac{1}{\rho_f}\left\langle\mathbf{g}\right\rangle-\frac{1}{\rho_f V_f}\sum_{\alpha=1}^{M}\mathbf{F}_{D-\alpha}-\mathbf{A}_f\,. \tag{F.1}$$

The above equation simply states that the average fluid velocity evolves because of the contribution of three forces acting because of: (i) the mean pressure gradient $\left\langle\mathbf{g}\right\rangle$; (ii) the total drag force acting on the particles and (iii) the pseudo force acting due to the frame acceleration. The procedure to derive the above equation from the governing Navier-Stokes equations can be found in Tenneti *et al.* (2010).

The governing equations of motion for the solid particles in the accelerating frame of reference can be derived similarly. For a poly-disperse suspension represented by M size classes, we can define a mean solid velocity for each size class as:

$$\left\langle \mathbf{v} \middle| r = R_\alpha \right\rangle = \frac{1}{N_\alpha} \sum_{n=1}^{N_\alpha} \mathbf{V}^{(n,\alpha)}$$

where, N_α is the total number of particles belonging to size class α and $\mathbf{V}^{(n,\alpha)}$ is the velocity of the n^{th} particle belonging to the size class α. The average solid velocity for each size class evolves because of the force exerted by the mean pressure gradient, the fluid-particle drag force, contact force due to collisions with particles belonging to other size classes and the pseudo force due to the frame acceleration. Mathematically this can be written as:

$$\frac{d}{dt}\left\langle \mathbf{v} \middle| r = R_\alpha \right\rangle = -\frac{1}{\rho_\alpha}\left\langle \mathbf{g} \right\rangle + \frac{1}{\rho_\alpha \phi_\alpha V}\left[\mathbf{F}_{D-\alpha} + \sum_{\substack{\beta=1 \\ \beta \neq \alpha}}^{M} \mathbf{F}^{C}{}_{\alpha-\beta} \right] - \mathbf{A}_f . \tag{F.2}$$

In the above equation $\mathbf{F}_{D-\alpha}$ is the drag force acting on the size class α and $\mathbf{F}^{C}{}_{\alpha-\beta}$ is the contact force acting on the size class α due to collisions with particles belonging to the the size class β. We can define a mass weighted mixture mean velocity whose evolution is not governed by the collision forces (similar to a mono-disperse suspension) as follows:

$$\left\langle \mathbf{u}^{(s)} \right\rangle = \frac{\sum_{\alpha=1}^{M} \rho_\alpha \phi_\alpha \left\langle \mathbf{v} \middle| r = R_\alpha \right\rangle}{\sum_{\alpha=1}^{M} \rho_\alpha \phi_\alpha} .$$

Using the above definition for the mixture mean solids velocity, its evolution equation can be derived from Eq. .2 as:

$$\frac{d}{dt}\left\langle \mathbf{u}^{(s)} \right\rangle = -\frac{\phi}{\sum_{\alpha=1}^{M} \rho_\alpha \phi_\alpha}\left\langle \mathbf{g} \right\rangle + \frac{1}{\sum_{\alpha=1}^{M} \rho_\alpha \phi_\alpha V} \sum_{\alpha=1}^{M} \mathbf{F}_{D-\alpha} - \mathbf{A}_f . \tag{F.3}$$

In this work we assume that the density of all the size classes is same and equal to ρ_p and this assumption simplifies the form of the above equation. Next, the evolution equation for the mean slip velocity can be derived by subtracting (F..1) from (F..3):

$$\frac{d}{dt}\left\langle \mathbf{W} \right\rangle = \left(\frac{1}{\rho_f} - \frac{1}{\rho_p} \right)\left\langle \mathbf{g} \right\rangle - \frac{1}{V}\left(\frac{1}{\phi \rho_p} - \frac{1}{(1-\phi)\rho_f} \right) \sum_{\alpha=1}^{M} \mathbf{F}_{D-\alpha} . \tag{F.4}$$

It is clear that a balance between the mean pressure gradient and fluid-particle drag force alone determines the mean slip velocity, i.e., the slip velocity is independent of the frame acceleration. From Eq. .3 we can see that for ploy-disperse suspensions the frame acceleration can be chosen such that the rate of change of mixture mean solids velocity is zero. Thus the reference frame moves with the mixture mean solids velocity.

Drag Law for Bidisperse Gas−Solid Suspensions Containing Equally Sized Spheres

Xiaolong Yin and Sankaran Sundaresan*

Chemical Engineering Department, Princeton University, Princeton, New Jersey 08543

In this study, we constructed from lattice-Boltzmann simulations a drag correlation for bidisperse gas−solid suspensions containing equally sized particles that are moving with different velocities relative to the interstitial fluid. Our analysis is limited to flows at low Reynolds numbers and high Stokes numbers, and the microstructure of the suspension is identical to that of a hard-sphere fluid. The Stokes drag forces acting on the two particle species are related to the fluid−particle relative velocities by a friction coefficient matrix, the off-diagonal components of which represent the particle−particle drag due to hydrodynamic interactions and were found to give important contributions to the net drag force. The off-diagonals exhibit a logarithmic dependence on the lubrication cutoff distance, a length scale on which the lubrication force between approaching particles begins to level off. In our simulations, the total particle volume fraction ϕ ranges from 0.1 to 0.4, and the volume fraction ratio ϕ_1/ϕ_2 ranges from 1:1 to 1:7. The results from these simulations are captured in explicit constitutive models, which can be readily generalized to multicomponent mixtures.

I. Introduction

Gas−solid suspensions are involved in many chemical engineering processes such as fluidizations and pneumatic conveying. In order to optimize design of these processes and reduce time and cost involved in experimentation, it has become increasingly popular to use computer simulations to study the dynamics of gas−solid flows. As it is impractical to solve the Navier−Stokes equations for the fluid and the Newton's equations of motion for large number of particles, most of the computational models for particulate flows in industrial scale devices treat a suspension as a mixture of two or more interpenetrating continua (the Euler−Euler approach). For suspensions with very much fewer particles, one can also choose to model the fluid phase as the only continuum and track the motions of particles explicitly (the Euler−Lagrange approach). In either approach, the model equations rely on constitutive relations to account for the various fluid−particle and particle−particle interactions. Of all the constitutive relations, the one for fluid−particle drag is particularly important; in many processes, fluid−particle drag is the primary force to overcome gravity, keep the particles suspended, and transport the particles to desired locations. It has a significant influence on the stability and heat/mass transfer characteristics of the flow. As a recent study by Bokkers et al.[1] exemplifies, the accuracy of fluid−particle drag correlations is critically important for an accurate prediction of the behavior of a gas fluidized bed. To date, the most accurate fluid−particle drag correlations are established from either carefully controlled experiments, or through direct numerical simulations of suspensions that contain hundreds to a few thousands of particles. In direct numerical simulations, one solves the full Navier−Stokes equations with the no-slip boundary condition applied between the fluid and the particles as the only interaction between the two phases. For fixed beds containing uniformly sized spheres (monodisperse), Hill et al.[2,3] conducted direct numerical simulations using the lattice-Boltzmann method, characterized the drag force as a function of volume fraction ϕ and particle Reynolds number, and computationally generated drag laws are now available in a variety of forms.[2–6] For fixed beds containing spheres of two different sizes (bidisperse), van der Hoef et al.[5] and Beetstra et al.[7] conducted lattice-Boltzmann simulations and proposed drag correlations based on their numerical results. Even though these drag formulas have been directly applied or adapted in ad hoc ways to study the dynamics of gas−solid flows, in particular fluidizations, it should be emphasized that a flowing suspension is different from a fixed bed in that the particles move constantly, and an accurate drag law for flowing suspensions should include the effect of particle velocity fluctuations when Reynolds number is not small,[8] and the effect of polydispersity when the suspension of interest contains particles of different sizes and/or different velocities. Among these challenges, the effect of polydispersity is particularly important, because it is a common practice to vary the amount of "fines" in reaction vessels to control the flow characteristics, yet polydisperse suspensions have not been studied systematically using direct numerical simulations.

In this study, we focus on gas−solid suspensions where the Reynolds number of the particles $Re = \rho_g U d/\mu$ is small, yet the Stokes number $St = (2\rho_p/9\rho_g)Re$ is large such that the relaxation time of a particle is longer than the average time between successive collisions. Here ρ_g and ρ_p are densities of the fluid and the particles, respectively, U is a characteristic velocity describing particle−fluid relative motion, d is particle diameter, and μ is the viscosity of the fluid. This dual limit is realistic for many gas−particle systems of practical interest, e.g. 50−100 μm particles suspended in air; it is also attractive in that it allows for efficient characterization of the drag forces. First, Re being small implies that the flow through particle assemblies is quasi-steady. Therefore, the drag forces can be characterized through static simulations as functions of particle positions and velocities. In addition, in Stokes suspensions the drag forces are linear functions of average particle velocities, and are independent of the velocity fluctuations.[8] One can thus assume that particles of the same type have identical velocities, which is very convenient for setting up the simulations. It is valid to compute the forces as functions of particle positions and velocities for gas−solid suspensions with high Stokes numbers, because in such suspensions the fluid forces usually

* To whom correspondence should be addressed. E-mail: sundar@princeton.edu. Phone: (609)258-4583. Fax: (609)258-0211.

10.1021/ie800171p CCC: $40.75
Published on Web 06/24/2008

do not balance particle weights due to the long relaxation time of the particles; the velocities of particles are controlled by collisions and obey Gaussian distributions.[9,10] In contrast, when particle Stokes number is low, which is less common for gas−solid suspensions but a reality for many liquid−solid colloidal suspensions, as the relaxation time is very short, a particle would adjust its velocity very quickly such that the fluid−particle force balances its own weight. In this limit, it is more appropriate to use particle positions and weights as input parameters.

Our objective is to establish a drag law for low-Reynolds-number polydisperse suspensions containing equally sized spheres that are moving with different velocities relative to the fluid. Such polydisperse suspensions are not as common in practice as those with unequally sized spheres, but the study of these simpler suspensions can give us insights and would pave way to future studies that include size differences. Due to the velocity difference between particle species, momentum will be transferred from one species to others through direct particle−particle collisions and indirect hydrodynamic interactions, yielding the so-called *particle−particle drag*. The momentum transferred through collisions can be estimated from kinetic theories of granular materials;[9] the momentum transferred through hydrodynamic interactions, on the other hand, is a part of the fluid−particle drag force that is often neglected in many ad hoc drag laws. Valiveti et al.[10] conducted a preliminary numerical study on this hydrodynamic particle–particle drag and showed that there is distinctive between difference high Stokes number gas–solid suspension and low Stokes number liquid–solid suspension. In this study, we have carried out more comprehensive lattice-Boltzmann simulations of bidisperse suspensions and examined the fluid−particle drag in detail. We conducted simulations in the volume fraction range $0.1 < \phi < 0.4$ and varied volume fraction ratio ϕ_1/ϕ_2 from 1:1 to 1:7. As will be exemplified in later sections of this paper, the particle−particle drag transmitted through the fluid is always an important part of the fluid−particle drag and should not be neglected; the Stokes drag forces, which depend on the volume fractions of particles and a lubrication cutoff distance that sets an upper limit on the lubrication forces, can be very well fit by a simple explicit drag law that can easily be generalized to polydisperse suspensions.

This paper is organized in the following order. In section II, we introduce the fluid−particle drag in the context of averaged continua equations for gas−solid flows, discuss common drag correlations used in past studies, and propose a new drag force expression for low-*Re*, high-*St* gas−solid suspensions of spheres with a binary velocity distribution. In section III, we present the lattice-Boltzmann method, the setup of the simulations, and test runs to validate the characteristics of our bidisperse gas−solid suspensions. In section IV, we characterize the dependence of the drag forces on the volume fractions of particles, velocities, and lubrication interactions and bring forth a simple drag correlation that can be easily generalized to polydisperse suspensions containing equally sized particles that are moving with three or more velocities relative to the fluid. In section V, we summarize and conclude the paper.

II. Fluid−Particle Drag in Polydisperse Suspensions

A. Drag in the Context of Averaged Equations. The Euler−Euler approach for monodisperse gas−solid suspensions treat the particles and the interstitial gas as two interpenetrating continua. The averaged equations governing the dynamics of these continua are discussed in many publications, for example, see the work of Jackson.[11] When a suspension contains more than one type of particles, the two-fluid model equations can be easily generalized to multifluid model equations (for examples see the works of Syamlal et al.[12] and Owoyemi et al.[13]). Assuming that the suspension of interest contains two different types of particles and there is neither aggregation nor breakup of particles, we can write down the continuity equation for the gas phase

$$\frac{\partial\left[\left(1-\sum_{i=1}^{2}\phi_i\right)\rho_g\right]}{\partial t}+\nabla\cdot\left[\left(1-\sum_{i=1}^{2}\phi_i\right)\rho_g\mathbf{U}_g\right]=0 \qquad (1)$$

and that for the particle phases ($i = 1$ and 2)

$$\frac{\partial(\phi_i\rho_i)}{\partial t}+\nabla\cdot(\phi_i\rho_i\mathbf{U}_i)=0 \qquad (2)$$

In eqs 1 and 2, ρ_g and $\mathbf{U}_g$ are the density and averaged velocity of the gas, ϕ_i, ρ_i, and $\mathbf{U}_i$ are the volume fraction, density, and average velocity of the ith particle phase. The averaged momentum equation for the gas is

$$\frac{\left[\left(1-\sum_{i=1}^{2}\phi_i\right)\rho_g\mathbf{U}_g\right]}{\partial t}+\nabla\cdot\left[\left(1-\sum_{i=1}^{2}\phi_i\right)\rho_g\mathbf{U}_g\mathbf{U}_g\right]=\nabla\cdot\mathbf{S}_g-\sum_{i=1}^{2}\mathbf{f}_{g-i}+\left(1-\sum_{i=1}^{2}\phi_i\right)\rho_g\mathbf{g} \qquad (3)$$

The momentum equations for the particle phases are

$$\frac{\partial(\phi_i\rho_i\mathbf{U}_i)}{\partial t}+\nabla\cdot(\phi_i\rho_i\mathbf{U}_i\mathbf{U}_i)=\nabla\cdot\mathbf{S}_i+\sum_{i=1}^{2}\mathbf{f}_{g-i}+\sum_{j=1}^{2}\mathbf{f}_{j-i}+\phi_i\rho_i\mathbf{g} \qquad (4)$$

In eqs 3 and 4, S_g and $\mathbf{S}_i$ are the stress tensors for the gas and the particle phases; $\mathbf{f}_{g-i}$ represent the interactive forces per unit volume of suspension between the gas and the ith particle phase; $\mathbf{f}_{j-i}$ represents the interactive forces per unit volume of suspension between particles phase j and particles phase i due to collisions and/or enduring contacts; finally, $\mathbf{g}$ is the gravity. $\mathbf{S}_g$ is usually expressed as $-P\mathbf{I}+\boldsymbol{\tau}_g$ with P being the pressure in the gas phase and $\boldsymbol{\tau}_g$ as the viscous stress. In order to solve eqs 1–4, one needs to supply constitutive models for $\boldsymbol{\tau}_g$, $\mathbf{f}_{g-i}$, $\mathbf{S}_i$, and $\mathbf{f}_{j-i}$.

Closures for $\mathbf{S}_i$ and $\mathbf{f}_{j-i}$ for high Stokes number systems are often sought through kinetic theories. Alternate simulation methods, such as the Euler−Lagrange approach (e.g., the work of Feng et al.[14]) or the multiphase particle-in-cell (MP-PIC) method,[15] circumvent the need to integrate eqs 2 and 4; instead, they track the motions of particles using Newton's equations of motion. Nevertheless, they still need constitutive models for the fluid−particle interaction force $\mathbf{f}_{g-i}$. In general, a complete description of $\mathbf{f}_{g-i}$ should include contributions from a variety of sources: the drag force resulted from the relative velocity between the fluid and the particles $\mathbf{f}_{Dg-i}$, the added mass force associated with the current relative acceleration, the history effect associated with the past history of relative acceleration, the generalized buoyancy, and the lift force, etc. In our simulations, we consider steady, low-*Re* flows with no bulk velocity gradient and focus on $\mathbf{f}_{Dg-i}$. The generalized buoyancy force is written as $\phi_i\nabla\cdot\mathbf{S}_g$, which in the absence of bulk velocity gradients (hence $\boldsymbol{\tau}_g = 0$), simplifies to $-\phi_i\nabla P$. Then, we write

$$\mathbf{f}_{g-i}=-\phi_i\nabla P+\mathbf{f}_{Dg-i} \qquad (5)$$

Drag defined this way is consistent with the majority of chemical engineering literature. An exception is the work by Hill et al.,[2,3] where they considered the entire $\mathbf{f}_{g-i}$ as the drag and did not subtract the bulk pressure gradient $-\phi_i\nabla P$ from $\mathbf{f}_{g-i}$.

B. Drag Correlations for Polydisperse Gas−Solid Suspensions. Owing to the growing interest in flows involving polydisperse suspensions, there have been a number of computational studies in the past few years on the mixing and segregation in fluidized polydisperse gas−solid suspensions.[1,13,14,16–21] In these studies, the closure for the fluid−particle drag $\mathbf{f}_{Dg-i}$ is usually a simple modification of the drag law for monodisperse suspensions with a general form

$$\mathbf{f}_{Dg-i} = \beta_i(\mathbf{U}_g - \mathbf{U}_i) \tag{6}$$

In this equation, the friction coefficient β_i depends on the volume fraction ϕ_i, the total volume fraction ϕ, and the relative velocity $\mathbf{U}_g - \mathbf{U}_i$. A common drag law of this type, which is used in refs 17, 18, 19, 1, 20, and 21, is a modification of the Gidaspow model,[22] which itself is a combination of the Ergun equation[23] at high volume fractions and the Wen−Yu drag law[24] at low volume fractions

$$\beta_i = \begin{cases} 150\dfrac{\phi_i\phi\mu}{(1-\phi)d_i^2} + 1.75\dfrac{\rho_g\phi_i}{d_i}|\mathbf{U}_g - \mathbf{U}|, & \phi \geq 0.2 \\ 0.75\dfrac{\rho_g\phi_i(1-\phi)^{-1.65}}{d_i}C_{Di}|\mathbf{U}_g - \mathbf{U}|, & \phi < 0.2 \end{cases} \tag{7}$$

with C_{Di} given by

$$C_{Di} = \begin{cases} \dfrac{24}{Re_i}(1 + 0.15Re_i^{0.687}), & Re_i < 1000 \\ 0.43, & Re_i \geq 1000 \end{cases} \tag{8}$$

and $Re_i = (1 - \phi)\,\rho_g|\mathbf{U}_g\text{-}\mathbf{U}_i|d_i/\mu$. The drag models used in the works of van Wachem et al.,[16] Feng et al.,[14] and Owoyemi et al.[13] are different from eqs 7 and 8, but they still conform with eq 6. These drag laws imply the drag acting on species i is independent of the velocities of other particle species $\mathbf{U}_g - \mathbf{U}_j$ ($j \neq i$), which is not physically sound because the presence of other particle species affects the drag not only by changing the total solid fraction but also through direct and indirect particle−particle momentum transfers (as discussed in the first section of the paper) that are proportional to the relative velocities between different particle species. In many Euler−Euler type studies, the momentum equations for particles contain a particle−particle drag term, the closure of which is originated from kinetic theories of dense granular materials.[25,26] While this particle−particle drag term can account for the interaction between different particle species due to direct collisions, the indirect particle−particle momentum transfer mediated by the interstitial fluid, which is an integrated part of the drag force, has not been considered and modeled in previous studies.

In order to assess the importance of the particle−particle drag due to hydrodynamic interactions, we propose to write the fluid−particle drag forces into a form that includes not only the velocity of species i but also the velocities of other species. For a bidisperse suspension where the relative velocities $\Delta\mathbf{U}_1 = \mathbf{U}_1 - \mathbf{U}_g$ and $\Delta\mathbf{U}_2 = \mathbf{U}_2 - \mathbf{U}_g$ are aligned in the same direction, we can consider a drag law in the following form

$$\begin{cases} F_{D1} = -B_{11}\Delta\mathbf{U}_1 - B_{12}\Delta\mathbf{U}_2 \\ F_{D2} = -B_{21}\Delta\mathbf{U}_1 - B_{22}\Delta\mathbf{U}_2 \end{cases} \tag{9}$$

where F_{Di} is the average drag force *per particle* of type i, and B_{ij} is the *particle-specific friction coefficient* which is a 2×2 matrix. Negative signs are placed before B_{ij} to reflect the fact that the drag forces are usually opposite to the direction of relative motion. In eq 9, the influence on the drag force on particles of type i due to the motion of particles of type j is reflected through the off-diagonal components of B_{ij}.

Because in two- and multifluid models fluid−particle drag forces are often averaged over a volume, it is useful to consider the drag forces per unit volume of suspension

$$\begin{cases} f_{D1} = -\beta_{11}\Delta\mathbf{U}_1 - \beta_{12}\Delta\mathbf{U}_2 \\ f_{D2} = -\beta_{21}\Delta\mathbf{U}_1 - \beta_{22}\Delta\mathbf{U}_2 \end{cases} \tag{10}$$

Here $f_{Di} = n_iF_{Di}$, n_i is the number density of the ith species in the suspension, and $\beta_{ij} = n_iB_{ij}$ is the *volume-specific friction coefficient*. We will present our simulation results in both particle-specific and volume-specific forms. Equation 9 can be nondimensionalized using $F_{Di}^* = \rho_gF_{Di}/\mu^2$ and $B_{ij}^* = B_{ij}/\mu d$

$$\begin{cases} F_{D1}^* = -B_{11}^*\Delta Re_1 - B_{12}\Delta Re_2 \\ F_{D2}^* = -B_{21}^*\Delta Re_1 - B_{22}\Delta Re_2 \end{cases} \tag{11}$$

Equation 10 can be nondimensionalized using $f_{Di}^* = \rho_gd^3f_{Di}/\mu^2$ and $\beta_{ij}^* = d^2\beta_{ij}/\mu$

$$\begin{cases} f_{D1}^* = -\beta_{11}^*\Delta Re_1 - \beta_{12}^*\Delta Re_2 \\ f_{D2}^* = -\beta_{21}^*\Delta Re_1 - \beta_{22}^*\Delta Re_2 \end{cases} \tag{12}$$

In the above two equations, the Reynolds numbers are defined as $\Delta Re_i = \rho_g\Delta\mathbf{U}_id_i/\mu$.

C. Drag Law for Polydisperse Liquid−Solid Suspensions in the Low-Reynolds-Number Limit. In the following discussion, we review the development of drag laws for polydisperse liquid−solid suspensions. A primary distinction between gas−solid suspensions and liquid−solid suspensions is that the Stokes number, a measure of the viscous relaxation time of particles, is usually on a similar order of magnitude as the Reynolds number in liquid−solid suspensions, whereas in gas−solid suspensions Re is usually smaller than St by several orders of magnitude. As a result, in low-Re liquid−solid suspensions, Stokes numbers are usually low as well, and particles would change their velocities very quickly such that the fluid−particle force acting on a particle balances its weight. For this reason, the drag laws for liquid−solid suspensions are usually written with the velocities on the left-hand side. The weights of particles, on the other hand, are placed on the right-hand side as input parameters. For example, the correlations for the hindered settling velocities in bidisperse liquid−solid suspensions are usually expressed as

$$\mathbf{U}_i = \mathbf{U}_i^0H_i(\phi_1, \phi_2, \rho_1, \rho_2, \rho_f, d_1, d_2, \mu, \mathbf{g}) \tag{13}$$

Here, $\mathbf{U}_i$ and $\mathbf{U}_i^0$ are the average sedimentation velocity and terminal velocity of type-i particles, respectively, ρ_f is the density of the fluid, and H_i is the *hindered settling function*. For monodisperse suspensions, it is well-known that H can be well fitted by $H = (1 - \phi)^n$ with n as a function of the terminal Reynolds number (based on $\mathbf{U}_i^0$)—the Richardson−Zaki formula.[27] Starting from the Richardson−Zaki formula, several authors proposed different modifications for polydisperse liquid−solid suspensions, for example, see the work of Mirza and Richardson,[28] Masliyah,[29] Selim et al.,[30] and Patwardhan and Tien.[31]

A particularly important result on the hindered settling functions for bidisperse liquid−solid suspensions was obtained by Batchelor[32] and Batchelor and Wen.[33] In the limit $Re \to 0$ and $St \to 0$, Batchelor developed a rigorous theory[32] to account for the hydrodynamic interactions in a dilute bidisperse suspen-

sion of spheres and found the leading order corrections to the hindered settling velocities

$$\begin{cases} \mathbf{U}_1 &= \mathbf{U}_1^0(1 + S_{11}\phi_1 + S_{12}\phi_2) \\ \mathbf{U}_2 &= \mathbf{U}_2^0(1 + S_{21}\phi_1 + S_{22}\phi_2) \end{cases} \tag{14}$$

where the coefficients S_{ij} are complex functions of the particle size ratio d_1/d_2, the reduced density ratio $\gamma = (\rho_1 - \rho_f)/(\rho_2 - \rho_f)$, the Péclet number based on the ratio between particle relative motion and Brownian diffusion, and interparticle forces. Numerical data for S_{ij} were given in Batchelor and Wen,[33] and they are in good agreement with experiments conducted in dilute polydisperse colloidal and noncolloidal suspensions.[34,36] In the limit of high Péclet number and with interparticle forces absent, for a suspension of same-size spheres, Batchelor's theory gives

$$S = \begin{bmatrix} -2.65 & -2.52 - 0.13\gamma^{-1} \\ -2.52 - 0.13\gamma & -2.65 \end{bmatrix} \tag{15}$$

Substituting eq 15 and $\mathbf{U}_i^0 = gd^2(\rho_i - \rho_f)/18\mu$ into eq 14 yields an explicit relation between the sedimentation velocities of the particles and the forces $F_i = 3\pi\mu d\mathbf{U}_i^0$

$$\begin{cases} 3\pi\mu d\mathbf{U}_1 &= (1 - 2.65\phi_1 - 2.52\phi_2)F_1 - 0.13\phi_2 F_2 \\ 3\pi\mu d\mathbf{U}_2 &= -0.13\phi_1 F_1 + (1 - 2.52\phi_1 - 2.65\phi_2)F_2 \end{cases} \tag{16}$$

in which the coefficients relating $\mathbf{U}_i$ and F_i are known as the *mobility matrix*.

In order to extend Batchelor's results to concentrated suspensions, Davis and Gecol[37] combined the Richardson−Zaki formula[27] with Batchelor's results and proposed an ad hoc drag law that agrees reasonably well with data obtained from bidisperse sedimentation experiments conducted in concentrated suspensions. More accurate numerical data for the mobility matrix are available in Revay and Higdon,[38] where the authors conducted a comprehensive numerical study in suspensions containing equally sized particles of two different densities for a wide range of volume fractions ($0.025 < \phi < 0.50$). Revay and Higdon's results can be summarized as

$$3\pi\mu d\mathbf{U}_i = M_0 F_i + (\bar{M} - M_0)\left(\frac{\phi_1}{\phi}F_1 + \frac{\phi_2}{\phi}F_2\right) \tag{17}$$

where M_0 and $\bar{M}$ only depend on the total volume fraction ϕ and can be fit by the following expressions

$$\begin{cases} M_0 &= 1 - 1.83\phi + 0.4084\phi^2 - 0.2108\phi^3 \\ \bar{M} &= (1 - \phi)^{6.55}(1 + 3.458\phi^2 + 8.990\phi^3) \end{cases} \tag{18}$$

In view of the fact that, in a sedimenting bidisperse suspension $\mathbf{U}_1\phi_1 + \mathbf{U}_2\phi_2 + \mathbf{U}_g(1 - \phi) = 0$ and $-\nabla P = n_1F_1 + n_2F_2$, it is easy to obtain a relation between the sedimentation velocities $\mathbf{U}_i$ and the relative velocities $\Delta\mathbf{U}_i$

$$\begin{cases} \Delta\mathbf{U}_1 &= \dfrac{1 - \phi_2}{1 - \phi}\mathbf{U}_1 + \dfrac{\phi_2}{1 - \phi}\mathbf{U}_2 \\ \Delta\mathbf{U}_2 &= \dfrac{\phi_1}{1 - \phi}\mathbf{U}_1 + \dfrac{1 - \phi_1}{1 - \phi}\mathbf{U}_2 \end{cases} \tag{19}$$

and a relation between the fluid−particle forces F_i and the drag forces F_{Di}

$$\begin{cases} F_{D1} &= (1 - \phi_1)F_1 - \phi_2 F_2 \\ F_{D2} &= -\phi_1 F_1 + (1 - \phi_2)F_2 \end{cases} \tag{20}$$

Thus, in low-*Re* bidisperse liquid−solid suspensions, the mobility matrix is all that is needed to fully describe the relation between fluid−particle relative velocities and the drag forces.

As one compares the drag law for bidisperse liquid−solid suspensions of equally sized spheres eqs 17 and 18 to the drag law that we hope to establish for bidisperse gas−solid suspensions eq 9, it is natural to ask the question: how different is the friction coefficient matrix B_{ij} from the inverse of the mobility matrix when the necessary transformations eqs 19 and 20 are taken into consideration? The mobility matrix formulation is established for the limit where both fluid and particle inertia are negligibly small. Particles thus have very short relaxation times and are always at a force balance, and direct collisions seldom occur due to the strong lubrication forces. The friction matrix formulation, on the other hand, is for gas−solid suspensions with zero fluid inertia but high particle inertia. Because of the large relaxation times, the particles are generally not at a force balance, and the stresses in the gas usually cannot prevent direct collisions. As a result, we will see that the drag forces acting on the particles, which include the particle−particle drag transmitted through the fluid, are strong functions of local lubrication interactions.

III. Simulation Method and Validations

We characterized the drag forces in bidisperse suspensions using a lattice-Boltzmann method developed by Ladd[39,40] for suspensions of spherical particles. It has been modified and improved over the years, and a complete review of the current version is available in Ladd and Verberg.[41] The lattice-Boltzmann method is different from conventional finite difference, finite volume, or finite element methods in that it does not solve the Navier−Stokes equations directly. Rather, it simulates the evolution of a simplified fluid molecular velocity distribution on a rectangular, space-filling lattice. The propagation and relaxation of this molecular velocity distribution are designed such that fluid density, momentum, and stresses, being the zeroth-, first-, and second-order moments of the velocity distribution, obey the Navier−Stokes equations on large length and time scales. Our lattice-Boltzmann method employs a 19-velocity model (commonly referred to as D3Q19 model to denote that the simulations are in three dimensions and that the continuous distribution of the fluid molecular velocity is discretized as a sum of 19 discrete velocity quadratures) in which the density of the fluid $\rho_g = 36$. The viscosity of the fluid was set to $\mu = 6.0$ which is a good choice for Stokes flows.

Since the drag forces contain particle−particle drag transmitted through the fluid due to the relative motion between particle species, we expect that they would be influenced by the lubrication forces between particles, and an accurate solution of the lubrication forces is needed. As capturing the lubrication forces from simulations requires a very fine lattice in the gaps between particles, in our lattice-Boltzmann method the lubrication interactions between spheres are solved analytically and imposed to the lattice solutions in an explicit manner. The detail of the implementation of the lubrication forces is supplied in the paper by Nguyen and Ladd.[42] They find that when the particles are separated by more than one lattice spacing, the lattice-Boltzmann method can fully resolve the hydrodynamic interaction between the particles; when the distance between particles is less than one lattice spacing, the lubrication forces obtained from the lattice-Boltzmann no longer increase with decreasing separation, and corrections must be applied to the forces so that they agree with the analytical solutions.[43] In our lattice-Boltzmann code, such corrections are applied to both normal and tangential motions.

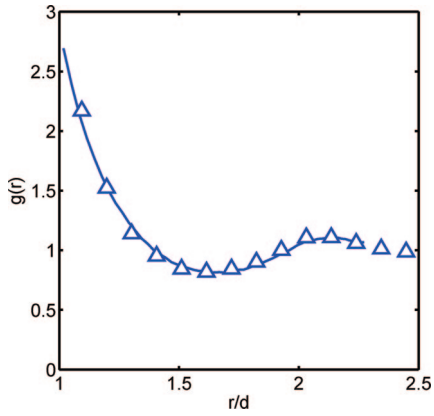

Figure 1. Radial distribution of particles in our initial configurations. $\phi_1 + \phi_2 = 0.34$. The triangles represent the radial distribution averaged from 18 configurations, each of which contains 1268 particles. The solid line represents the radial distribution in a hard-sphere fluid of the same volume fraction obtained from the work of Barker and Henderson.[49]

The lubrication forces between two spheres with different velocities diverge as the separation between the spheres approaches zero. In reality, this divergence may be removed by surface roughness, finite weight of particles, or noncontinuum effects. All of these effects may be approximated in our simulation by specifying a cutoff distance λ: when the separation between particles becomes less than λ, the lubrication forces no longer increase but remain as constants. In our simulations, we found that the particle−particle drag through hydrodynamic interactions increases with decreasing λ following a logarithmic scale. The breakdown of the lubrication force at λ thus plays an important role in limiting the magnitude of the particle−particle drag.

We began our simulations by first randomly distributing spherical particles in cubic, periodic domains. Then, we employed Monte-Carlo steps to ensure that the spatial distribution of particles satisfies the equilibrium hard-sphere distribution, as demonstrated in Figure 1. After that, the particles were randomly designated as being type-1 or type-2 such that the two types of particles are well mixed, and they were assigned velocities $\mathbf{U}_1$ and $\mathbf{U}_2$, respectively. These velocities generate a fluid flow within the particle assembly, the detail of which is solved by the lattice-Boltzmann method. Meanwhile, a pressure gradient was applied to the fluid to ensure that the net flow rate of the fluid through the particle assembly is zero. The velocities assigned to the particles $\mathbf{U}_1$ and $\mathbf{U}_2$ thus became equivalent to the relative velocities $\Delta\mathbf{U}_1$ and $\Delta\mathbf{U}_2$. Once the flow reached the steady state, the forces F_1 and F_2 acting on the particles were obtained by integrating the hydrodynamic stresses over particle surfaces and averaging over all particles of the same species. The drag forces F_{D1} and F_{D2} were then calculated from

$$F_{Di} = F_i + \frac{\pi d^3}{6}\nabla P \tag{21}$$

where ∇P is the bulk pressure gradient acting on the fluid that balances the total forces

$$-\nabla P = n_1 F_1 + n_2 F_2 \tag{22}$$

The accuracy of the lattice-Boltzmann simulation, as in any other type of fluid dynamic simulations, is affected by the choice of lattice resolution and system size L. To assess the influence of lattice resolution and system size, test simulations were conducted. As shown in Table 1, the results with $d = 9.6$ and $d = 12.48$ generally agree within 90% uncertainty levels. Here d denotes the number of lattice nodes across the diameter of the particle. Thus, $d = 9.6$ implies that the lattice spacing is 1/9.6 times the particle diameter. At the resolution of $d = 9.6$, the results obtained from $L/d = 15.6$ and $L/d = 20.8$ systems also agree within 90% uncertainty levels. (As L/d increases, the number of particles inside the simulation domain increases.) Therefore, we chose to use $d = 9.6$ and $L/d = 15.6$ for the majority of our simulations.

We first studied pressure driven flows through fixed beds with monodisperse spheres to check the accuracy of the method. This test is the same as those conducted by Hill et al.[2] and by van der Hoef et al.[5] As Figure 2 shows, our simulated drag forces were in excellent agreement with Koch and Sangani's formula[4]

$$F^*_{D-\text{fixed}} = \frac{F_{D-\text{fixed}}}{3\pi d\mu \mathbf{U}_s} = \begin{cases} \dfrac{(1-\phi)\left(1+\dfrac{3}{\sqrt{2}}\phi^{1/2}+\dfrac{135}{64}\phi\ln\phi+17.14\phi\right)}{1+0.681\phi-8.48\phi^2+8.16\phi^3}, & \phi<0.4 \\ \dfrac{10\phi}{(1-\phi)^2}, & \phi>0.4 \end{cases} \tag{23}$$

and van der Hoef et al.'s formula[5]

$$F^*_{D-\text{fixed}} = \frac{F_{D-\text{fixed}}}{3\pi d\mu \mathbf{U}_s} = \frac{10\phi}{(1-\phi)^2} + (1-\phi)^2(1+1.5\sqrt{\phi}) \tag{24}$$

for fixed beds containing randomly distributed monodisperse spheres under the Stokes flow condition. In eqs 23 and 24, $\mathbf{U}_s$ is the superficial gas velocity through the fixed bed and $\mathbf{U}_s = (1-\phi)\Delta\mathbf{U}$. Note that in eqs 23 and 24, the drag forces were nondimensionalized using the Stokes drag on isolated particles, which is a common choice for fixed bed simulations as there is only one velocity scale for fixed beds. In this study, as we are interested in polydisperse suspensions with multiple velocities, it is more convenient to use $F^*_{Di} = \rho_g F_{Di}/\mu^2$ to nondimensionalize the drag forces.

We then validated the linear dependence of the drag forces on the relative velocities. In this test, we set $\phi_1 = \phi_2 = 0.05$, $L/d = 15.6$, $\Delta Re_2 = 0$, and examined F^*_{Di} as functions of ΔRe_1. As shown in Figure 3, the drag forces can be fit very well by straight lines starting from the origin, proving that F^*_{Di} are linear functions of ΔRe_1. Due to this linearity, in our suspensions the friction coefficients B^*_{ij} and β^*_{ij} are independent of relative velocities and can be determined using two sets of simulations. In the first set of simulations, we let ΔRe_1 be 0.01 and ΔRe_2 be zero to determine B^*_{11} and B^*_{21}; in the second set, we let ΔRe_1 be zero and ΔRe_2 be 0.01 to determine B^*_{12} and B^*_{22}.

Finally, we confirmed that, in our suspensions, the velocity fluctuations of particles do not affect the drag. We conducted two sets of simulations: one with $\phi_1 = \phi_2 = 0.10$ and another with $\phi_1 = \phi_2 = 0.15$. The average velocities of the two particle species satisfy $\langle\Delta Re_1\rangle = 0$ and $\langle\Delta Re_2\rangle = 0.01$; the fluctuating velocities obey Gaussian distributions with standard deviations $Re_{\sigma 1} = Re_{\sigma 2} = 0.005$. As shown in Table 2, the drag forces found in suspensions with velocity fluctuations are nearly identical to those obtained from simulations without velocity fluctuations, which is consistent with the work of Wylie and Koch.[8] Because of this feature, in our simulations, we can assign same velocity to all particles of the same type and neglect the effect of velocity fluctuations.

Even though we can exploit the various features discussed above to make our computations efficient, a full characterization of B^*_{ij} and β^*_{ij} is still a nontrivial task that requires intensive computations. In order to study the dependence of B^*_{ij} and β^*_{ij} on the volume fractions, we varied the total volume fraction

Table 1. Test Simulations Showing the Effect of Lattice Resolution and System Size on the Fluid−Particle Drag Forces[a]

suspension size	fluid−particle drag force	$d = 5.84$	$d = 9.6$	$d = 12.46$
small	F^*_{D1}	0.0123 ± 0.0053	0.0200 ± 0.0025	0.0164 ± 0.0022
$L = d = 10.3$	F^*_{D2}	-0.2156 ± 0.0033 ($M = 8$)	-0.2266 ± 0.0030 ($M = 8$)	-0.2276 ± 0.0022 ($M = 6$)
intermediate	F^*_{D1}		0.0274 ± 0.0017	0.0304 ± 0.0027
$L = d = 15.6$	F^*_{D2}		-0.2352 ± 0.0016 ($M = 50$)	-0.2380 ± 0.0028 ($M = 12$)
large	F^*_{D1}	0.0258 ± 0.0025	0.02370 ± 0.0024	
$L = d = 20.8$	F^*_{D2}	-0.2226 ± 0.0020 ($M = 7$)	-0.2304 ± 0.0024 ($M = 5$)	

[a] For the simulations listed in this table, $\phi_1 = \phi_2 = 0.05$, $\Delta Re_1 = 0$, $\Delta Re_2 = 0.01$, and $\lambda/d = 0.001$. The numbers before the $\pm$ are the dimensionless drag forces $F^*_{Di} = \rho_g F_{Di}/\mu^2$; the numbers after the $\pm$ are the 90% uncertainty from M configurations.

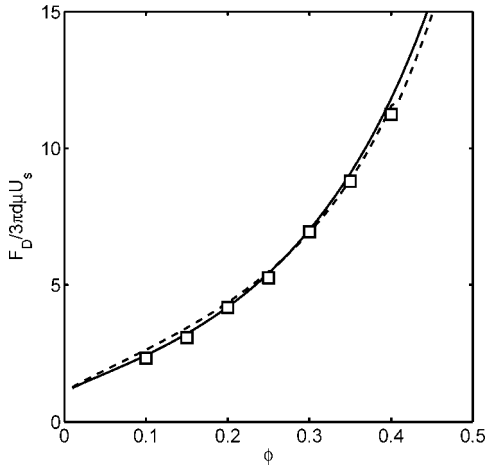

Figure 2. Normalized fluid−particle drag in a monodisperse fixed bed. The squares were obtained from our simulations. They agree very well with the drag law by Koch and Sangani[4] [eq 23, dashed line] and the drag law by van der Hoef et al.[5] [eq 24, solid line].

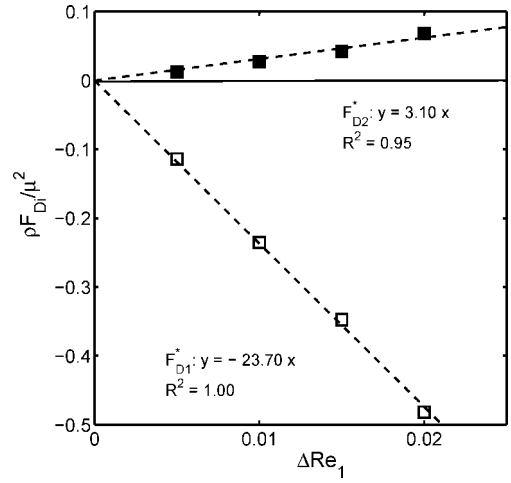

Figure 3. Linear dependence of F^*_{Di} (open symbols) and F^*_{D2} (filled symbols) on ΔRe_1 in a bidisperse suspension with $\phi_1 = \phi_2 = 0.05$. The size of the computational domain $L/d = 15.6$; the lubrication cutoff $\lambda/d = 0.001$; the velocity of the second particle phase $\Delta Re_2 = 0$. The dashed lines are the best linear fits with R^2 being the coefficient of regression.

from 0.1 to 0.4, and the volume fraction ratios of the particles from 1:1 to as high as 1:7. The number of particles in our systems ranges from 728 ($\phi = 0.1$) to 2914 ($\phi = 0.4$). For each combination of ϕ_1 and ϕ_2, we conducted 10−15 simulations with different particle configurations to obtain good statistics. In order to characterize the dependence of B_{ij} and β_{ij} on the lubrication cutoff distance λ, we subsequently varied λ/d from 0.001 to 0.01.

IV. Result and Discussion

In Tables 3–6, we list the numerical values of B^*_{ij} and β^*_{ij} found from simulations. The four tables correspond to $\lambda/d = 0.001$, 0.002, 0.005, and 0.01, respectively. It is clear that the off-diagonal components in B^*_{ij} and β^*_{ij}, which represent the particle−particle drag due to hydrodynamic interactions, are very important contributions to the net fluid−particle drag. In a relatively dilute suspension with $\phi_1 = \phi_2 = 0.05$, the size of the off-diagonals is more than 10% of the diagonals; when $\phi_1 + \phi_2 = 0.40$, the off-diagonals components are 20−30% of the diagonals. The importance of the off-diagonals thus grows rapidly with increasing volume fraction.

When we seek appropriate functions to fit the large amount of data presented in Tables 3–6, it is important to realize that the four entries in B^*_{ij} and β^*_{ij} are not totally independent of each other. In fact, they must satisfy two constraints and there is only one free parameter in B^*_{ij} and β^*_{ij} for us to fit.[10] The first constraint comes from the principle of action and reaction between the two types of particles that requires the volume-specific friction coefficient β^*_{ij} to be strictly symmetric. In the raw data listed in the tables, it can be observed that β^*_{ij} are indeed approximately symmetric. The condition $\beta^*_{12} = \beta^*_{21}$ leads to

$$\phi_1 B^*_{12} = \phi_2 B^*_{21} \tag{25}$$

In Figure 4 where we plotted the values of B_{12}/B_{21} as a function of ϕ_2/ϕ_1, the presence of this symmetry is evident. The second constraint comes from the fact that if we let the two particle species have identical velocities, our bidisperse suspension would become a monodisperse fixed bed. Thus, if $\Delta Re_1 = \Delta Re_2$, the drag forces F^*_{D1} and F^*_{D2} should both equal the drag force in a monodisperse fixed bed of the same volume fraction. This constraint requires

$$B^*_{11} + B^*_{12} = B^*_{21} + B^*_{22} = B^* \tag{26}$$

where B^* is the friction coefficient in a fixed bed. B^* satisfies $\rho_g F_{D-fixed}/\mu^2 = B^* \Delta Re$ and is related to $F^*_{D-fixed}$ in eqs 23 and 24 by

Table 2. Effect of Particle Velocity Fluctuations on the Fluid−Particle Drag[a]

		$Re_{\sigma i} = 0$	$Re_{\sigma i} = 0.005$
$\phi_1 = \phi_2 = 0.10$	F^*_{D1}	0.0769 ± 0.0040	0.0733 ± 0.0059
	F^*_{D2}	-0.3914 ± 0.0036	-0.3927 ± 0.0065
$\phi_1 = \phi_2 = 0.15$	F^*_{D1}	0.2120 ± 0.0099	0.1908 ± 0.0091
	F^*_{D2}	-0.6478 ± 0.0099	-0.6483 ± 0.0083

[a] The average velocities are $\langle \Delta Re_1 \rangle = 0$ and $\langle \Delta Re_2 \rangle = 0.01$. $Re_{\sigma i}$ is the Reynolds number based on the standard deviation of particle velocity distribution, which assumes the shape of a Gaussian. The lubrication cutoff $\lambda/d = 0.001$. The numbers after the $\pm$ are the 90% uncertainties from 10−14 simulations with different configurations.

Table 3. Friction Coefficient Matrix B^*_{ij} and the Volume Specific Friction Coefficient Matrix β^*_{ij} Obtained from Simulations with $\lambda/d = 0.001$[a]

ϕ_1	ϕ_2	B^*_{11}	B^*_{12}	B^*_{21}	B^*_{22}	β^*_{11}	β^*_{12}	β^*_{21}	β^*_{22}
0.05	0.05	23.5 (0.2)	−2.7 (0.2)	−2.7 (0.2)	23.5 (0.2)	2.24	−0.26	−0.26	2.24
0.05	0.10	32.6 (0.4)	−7.4(0.8)	−3.5 (0.2)	29.5 (0.4)	3.11	−0.71	−0.67	5.63
0.05	0.15	43.6 (0.8)	−11.7 (1.1)	−4.0 (0.3)	35.3 (0.4)	4.2	−1.1	−1.2	10.1
0.10	0.10	39.1 (0.4)	−7.7 (0.4)	−7.7(0.4)	39.1 (0.4)	7.5	−1.5	−1.5	7.5
0.05	0.20	56.8 (1.0)	−18.7 (1.0)	−4.9 (0.3)	42.5 (0.3)	5.4	−1.8	−1.9	16.2
0.10	0.15	52.7 (0.9)	−14.0(0.9)	−10.0 (0.6)	47.4 (0.5)	10.1	−2.7	−2.9	13.6
0.05	0.25	79.1 (0.9)	−35.2 (1.7)	−7.1 (0.2)	51.0 (0.4)	7.6	−3.4	−3.4	24.4
0.10	0.20	70.4 (0.6)	−25.3 (1.1)	−13.2(0.3)	56.8 (0.6)	13.4	−4.8	−5.0	21.7
0.15	0.15	64.8 (1.0)	−21.2 (1.0)	−21.2 (1.0)	64.8 (1.0)	18.6	−6.1	−6.1	18.6
0.05	0.30	101.3 (1.1)	−45.9(1.1)	−8.0 (0.2)	60.6 (0.2)	9.7	−4.4	−4.6	34.7
0.10	0.25	93.9 (1.6)	−40.2 (1.2)	−16.1 (0.6)	69.2 (0.5)	17.9	−7.7	−7.7	33.0
0.15	0.20	83.5 (1.4)	−31.6 (1.1)	−22.8(1.0)	76.8 (0.9)	23.9	−9.0	−8.7	29.3
0.05	0.35	127.1 (2.9)	−64.3 (3.9)	−9.2 (0.4)	73.0 (0.6)	12.1	−6.1	−6.2	48.4
0.10	0.30	119.3 (1.5)	−56.5(1.6)	−18.5 (0.5)	82.6 (0.5)	22.8	−10.8	−10.6	47.3
0.15	0.25	111.6 (1.8)	−49.6 (1.9)	−28.9 (1.2)	93.3 (1.1)	32.0	−14.2	−13.8	44.6
0.20	0.20	102.5 (1.6)	−38.8 (1.6)	−38.8(1.6)	102.5 (1.6)	39.2	−14.8	−14.8	39.2

[a] In the columns for B^*_{ij}, the numbers in parentheses are the 90% uncertainties. The uncertainties for β^*_{ij} are not shown for brevity.

Table 4. Friction Coefficient Matrix B^*_{ij} and the Volume Specific Friction Coefficient Matrix β^*_{ij} Obtained from Simulations with $\lambda/d = 0.002$[a]

ϕ_1	ϕ_2	B^*_{11}	B^*_{12}	B^*_{21}	B^*_{22}	β^*_{11}	β^*_{12}	β^*_{21}	β^*_{22}
0.05	0.10	31.5 (0.4)	−6.4 (0.7)	−2.9 (0.2)	29.1 (0.3)	3.01	−0.61	−0.55	5.55
0.10	0.10	37.8 (0.3)	−6.6(0.4)	−6.6 (0.4)	37.8 (0.3)	7.21	−1.26	−1.26	7.21
0.10	0.15	50.4 (0.7)	−11.6 (0.6)	−8.5 (0.4)	45.4 (0.4)	9.6	−2.2	−2.4	13.0
0.15	0.15	62.0 (1.0)	−18.5 (1.0)	−18.5(1.0)	62.0 (1.0)	17.8	−5.3	−5.3	17.8
0.10	0.25	86.7 (1.1)	−34.7 (1.2)	−13.2 (0.5)	67.1 (0.5)	16.6	−6.6	−6.3	32.1
0.20	0.20	95.7 (1.0)	−31.9(1.1)	−31.9 (1.1)	95.7 (1.0)	36.6	−12.2	−12.2	36.6

[a] The numbers in parentheses are the 90% uncertainties as in Table 3.

Table 5. Friction Coefficient Matrix B^*_{ij} and the Volume Specific Friction Coefficient Matrix β^*_{ij} Obtained from Simulations with $\lambda/d = 0.005$[a]

ϕ_1	ϕ_2	B^*_{11}	B^*_{12}	B^*_{21}	B^*_{22}	β^*_{11}	β^*_{12}	β^*_{21}	β^*_{22}
0.05	0.10	30.3 (0.3)	−4.8 (0.4)	−2.3 (0.2)	28.1 (0.2)	2.90	−0.46	−0.44	5.37
0.10	0.10	36.4 (0.3)	−4.9(0.2)	−4.9 (0.2)	36.4 (0.2)	6.95	−0.94	−0.94	6.95
0.10	0.15	47.5 (0.4)	−8.9 (0.3)	−6.5 (0.2)	43.6 (0.2)	9.1	−1.7	−1.9	12.5
0.15	0.15	58.3 (0.8)	−14.8 (0.8)	−14.8(0.8)	58.3 (0.8)	16.7	−4.2	−4.2	16.7
0.10	0.25	79.2 (0.8)	−26.9 (0.8)	−10.2 (0.3)	64.0 (0.3)	15.1	−5.1	−4.9	30.6
0.20	0.20	88.0 (0.5)	−24.3(0.6)	−24.3 (0.6)	88.0 (0.5)	33.6	−9.3	−9.3	33.6
0.05	0.35	103.6 (1.2)	−40.3 (1.6)	−5.8 (0.2)	69.5 (0.3)	9.9	−3.8	−3.8	46.5

[a] The numbers in parentheses are the 90% uncertainties as in Table 3.

Table 6. Friction Coefficient Matrix B^*_{ij} and the Volume Specific Friction Coefficient Matrix β^*_{ij} Obtained from Simulations with $\lambda/d = 0.01$[a]

ϕ_1	ϕ_2	B^*_{11}	B^*_{12}	B^*_{21}	B^*_{22}	β^*_{11}	β^*_{12}	β^*_{21}	β^*_{22}
0.05	0.10	29.4 (0.2)	−3.7 (0.4)	−1.8 (0.2)	27.7 (0.1)	2.80	−0.35	−0.35	5.29
0.10	0.10	35.2 (0.2)	−3.7(0.2)	−3.7 (0.2)	35.2 (0.2)	6.72	−0.71	−0.71	6.72
0.10	0.15	45.2 (0.2)	−6.8 (0.3)	−5.0 (0.2)	42.3 (0.1)	8.6	−1.3	−1.4	12.1
0.15	0.15	55.2 (0.7)	−11.7 (0.7)	−11.7(0.7)	55.2 (0.7)	15.8	−3.3	−3.3	15.8
0.10	0.25	73.6 (0.6)	−21.1 (0.6)	−8.0 (0.2)	61.7 (0.3)	14.1	−4.0	−3.8	29.4
0.20	0.20	82.6 (0.4)	−18.8(0.5)	−18.8 (0.5)	82.6 (0.4)	31.6	−7.2	−7.2	31.6

[a] The numbers in parentheses are the 90% uncertainties as in Table 3.

$$B^* = 3\pi(1-\phi)F^*_{\mathrm{D-fixed}} \tag{27}$$

In Figure 5, we show that $B^*_{11} + B^*_{12}$ and $B^*_{21} + B^*_{22}$ (with $\lambda/d = 0.001$), when plotted as functions of ϕ, agree very well with B^* for monodisperse fixed beds. In view of eqs 25 and 26, it is convenient to define a free parameter α to represent the off-diagonals

$$\alpha = -B^*_{12}/B^*\phi_2 \tag{28}$$

and the entire B^*_{ij} can then be expressed as a function of α

$$\begin{bmatrix} B^*_{11} & B^*_{12} \\ B^*_{21} & B^*_{22} \end{bmatrix} = 3\pi(1-\phi)F^*_{\mathrm{D-fixed}}\begin{bmatrix} 1+\phi_2\alpha & -\phi_2\alpha \\ -\phi_1\alpha & 1+\phi_1\alpha \end{bmatrix} \tag{29}$$

Here, we replaced B^* with $3\pi(1-\phi)F^*_{\mathrm{D-fixed}}$ to emphasize eq. 29's connection to the drag in monodisperse fixed beds. From eq 29, it is easy to obtain an expression for the volume-specific friction coefficient β^*_{ij}

$$\begin{bmatrix} \beta^*_{11} & \beta^*_{12} \\ \beta^*_{21} & \beta^*_{22} \end{bmatrix} = 18(1-\phi)F^*_{\mathrm{D-fixed}}\begin{bmatrix} (1+\alpha\phi_2)\phi_1 & -\alpha\phi_1\phi_2 \\ -\alpha\phi_1\phi_2 & (1+\alpha\phi_1)\phi_2 \end{bmatrix} \tag{30}$$

The dimensionless drag forces per unit volume of suspension thus are

$$\begin{cases} f^*_{\mathrm{D1}} &= -18(1-\phi)\phi_1F^*_{\mathrm{D-fixed}}[\Delta Re_1 + \alpha\phi_2(\Delta Re_1 - \Delta Re_2)] \\ f^*_{\mathrm{D2}} &= -18(1-\phi)\phi_2F^*_{\mathrm{D-fixed}}[\Delta Re_2 + \alpha\phi_1(\Delta Re_2 - \Delta Re_1)] \end{cases} \tag{31}$$

The first term on the right-hand-side of eq 31, $-18(1-\phi)\phi_iF^*_{\mathrm{D-fixed}}\Delta Re_i$, represents the drag acting on the ith species when all the particles have the same velocity ΔRe_i relative to the fluid; the second term on the right-hand-side of eq 31 represents the particle−particle drag transmitted through the fluid due to the velocity difference between particle species i

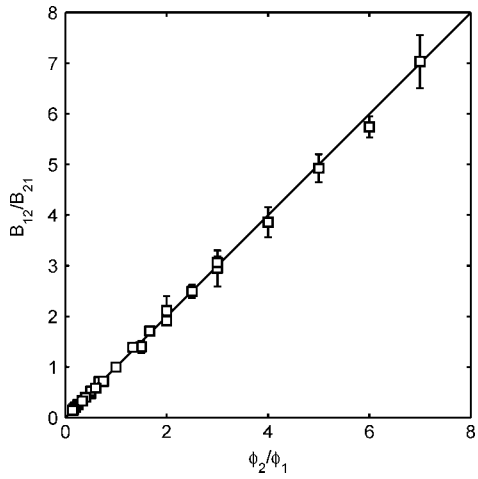

Figure 4. Symmetry in the off-diagonal components of B_{ij} due to $\beta_{12}^* = \beta_{21}^*$. The simulation data (symbols) shown in this figure are from Table 3. They fall unanimously on the solid line $y = x$, indicating that $\phi_1 B_{12}^* = \phi_2 B_{21}^*$. The error bars represent 90% uncertainties.

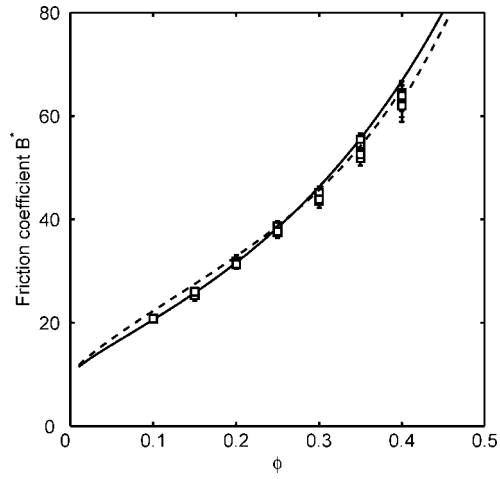

Figure 5. Recovery of B^* for monodisperse fixed beds from the friction coefficient B_{ij}^* under condition $\Delta Re_1 = \Delta Re_2$. The symbols represent $B_{11}^* + B_{12}^*$ and $B_{21}^* + B_{22}^*$ based on simulation data in Table 3. The dashed and solid lines were computed from eqs 24 and 25, respectively. The error bars represent 90% uncertainties.

and j. Clearly, existing ad hoc drag laws for bidisperse suspensions in the form of eq 6 only consider the first term; the second term that is proportional to α and represents the hydrodynamic particle−particle drag is neglected.

We will now characterize the dependence of α on the volume fractions ϕ_i and the lubrication cutoff λ/d. Because our bidisperse suspensions contain equally sized spheres, α must be symmetric about ϕ_1 and ϕ_2. As all symmetric combinations of ϕ_1 and ϕ_2 can be expressed as functions of two variables: the total volume fraction $\phi_1 + \phi_2$ and the product $\phi_1\phi_2$, we plotted α as a function of $\phi_1\phi_2$ in Figure 6 and as a function of $\phi_1 + \phi_2$ in Figure 7. Interestingly, α does not seem to have any systematic dependence on $\phi_1 + \phi_2$ and $\phi_1\phi_2$. Therefore, we propose to fit α as a single-variable function of λ/d as the first approximation. In Figure 8, we plotted the averages of α over ϕ_1 and ϕ_2 as a function of λ/d. It appears that the dependence of α on λ/d can be very well fitted by a logarithmic function of $(\lambda/d)^{-1}$

$$\alpha = 1.313 \log_{10}(d/\lambda) - 1.249 \qquad (32)$$

which implies that, in the limit of $\lambda \to 0$, the particle−particle drag terms in eq 31 would diverge to infinity. Therefore, λ/d is a very important parameter for bidisperse gas−solid suspensions, and a finite λ/d is necessary to keep the particle−particle drag due to hydrodynamic interactions finite.

The divergence of the particle−particle drag in the limit of $\lambda \to 0$ is a consequence of the assumption that the motion of the particles are not affected by the stresses in the gas. In a bidisperse suspension of equally sized spheres where the two types of particles are randomly mixed, there is a nonzero probability for two particles of different species to become very close. As these two particles have different velocities, there will be strong lubrication forces acting on the particles, and the net fluid−particle interactive forces would be very high. According to Kim and Karrila,[43] the squeezing motion of two spheres in the normal direction generates a lubrication force that is proportional to $d/2h$ where h is the distance between surfaces; the tangential motion of two spheres, on the other hand, produces a weaker lubrication force proportional to $\ln(d/2h)$. It is easy to show that integrating the normal lubrication forces over all possible particle orientations and over $0 < h < h_0$ yields a divergent integral proportional to $\int_0^{h_0} (d/2h)\, dh$. Here h_0 is the distance where the near-field solution in Kim and Karrila[43] starts to break down and is small compared to d. Clearly, in order to keep the net lubrication force finite, it is necessary to introduce a length scale λ—when $h < \lambda$, the lubrication force between the two particles saturate. The net lubrication force would then become a logarithmic function of d/λ, in excellent agreement with our numerical results in eq 32. Therefore, the normal lubrication forces are the leading order contributions to the net lubrication force; the tangential lubrication forces, on the other hand, are much weaker and are not as important as those in the normal direction.

In a real suspension, the lubrication forces between particles of different types can not diverge to infinity, either. The upper bound on the lubrication forces may be imposed by surface roughness of the particles, noncontinuum effects due to the mean free path of gas molecules, or finite Stokes number of the particles that stops the particles from approaching each other once the distance between the particles becomes small enough to produce a sufficiently large lubrication force. Therefore, the lubrication cutoff λ that is required to produce a finite net lubrication force does have a physical meaning.

Figure 9 shows the forces acting on the particles in a bidisperse suspension with $\phi_1 = \phi_2 = 0.10$ and $\Delta Re_1 = 0$, $\Delta Re_2 = 0.01$. It may be observed that the forces acting on certain particles are much higher, and for every positive "spike" in F_1^*, there is always a negative one in F_2^* having the same magnitude. When these force spikes are taken into the averages, they give rise to the logarithmic dependence of α on λ/d.

Our findings that the fluid−particle drag in a bidisperse gas−solid suspension has a logarithmic dependence on the lubrication cutoff is not unique. In the study of simple shear flows of gas−solid suspensions, Sangani et al.[44] made a similar discovery that the total energy dissipation due to particle−fluid friction is a logarithmic function of the lubrication cutoff, and a finite lubrication cutoff is needed to keep the net dissipation finite. In their simulations, they assumed that the particles have very high Stokes numbers and undergo hard-sphere molecular motions that are independent of the stresses in the fluid and solved the fluid equations using a multipole expansion method.[45,46] The relative velocities between pairs of particles in their study were produced by the random molecular motions of particles and the bulk shear, whereas in our study they are produced by the velocity difference related to the bidispersity of the suspension.

One can immediately extend eqs 29 and 30 to polydisperse suspensions of equally sized spheres. For example, for a ternary system one can write down the following expression for the volume-specific friction coefficient

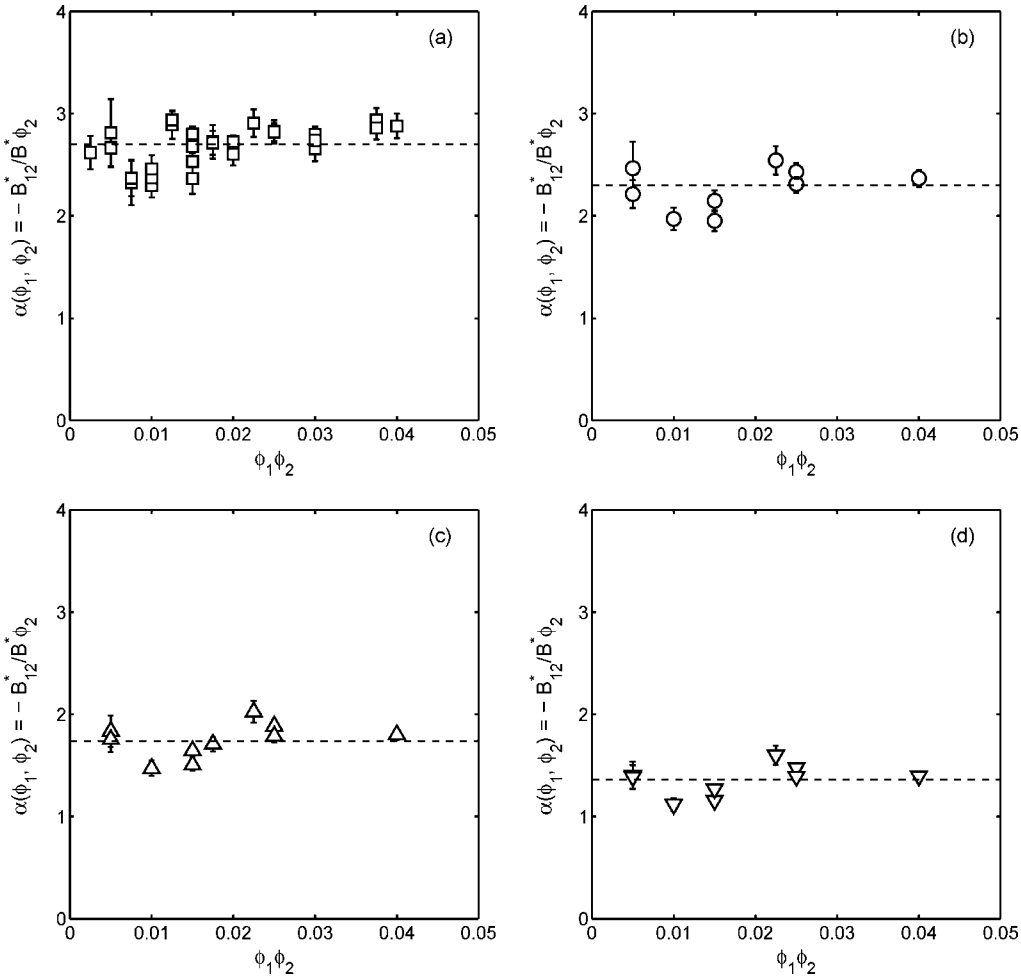

Figure 6. $\alpha(\phi_1, \phi_2, \lambda/d) = B^*_{12}/B^*\phi_2$ as functions of $\phi_1\phi_2$. Parts a−d correspond to λ/d values of 0.001, 0.002, 0.005, and 0.01, respectively. The error bars represent 90% uncertainties. The dashed lines at $y = 2.67$, 2.27, 1.74, and 1.36 correspond to the averages of $\alpha(\phi_1, \phi_2, \lambda/d)$ over ϕ_1 and ϕ_2.

$$\begin{bmatrix} \beta^*_{11} & \beta^*_{12} & \beta_{13} \\ \beta^*_{21} & \beta^*_{22} & \beta^*_{23} \\ \beta^*_{31} & \beta^*_{32} & \beta^*_{33} \end{bmatrix} = 18(1-\phi)F^*_{\mathrm{D-fixed}}$$
$$\begin{bmatrix} (1+\alpha\phi_2+\alpha\phi_3)\phi_1 & -\alpha\phi_1\phi_2 & -\alpha\phi_1\phi_3 \\ -\alpha\phi_1\phi_2 & (1+\alpha\phi_1+\alpha\phi_3)\phi_2 & -\alpha\phi_2\phi_3 \\ -\alpha\phi_1\phi_3 & -\alpha\phi_2\phi_3 & (1+\alpha\phi_1+\alpha\phi_2)\phi_3 \end{bmatrix} \quad (33)$$

To verify eq 33, we simulated the flow in a ternary suspension with $\phi_1 = \phi_2 = \phi_3 = 0.10$ and $\Delta Re_1 = 0.01$, $\Delta Re_2 = 0.02$, $\Delta Re_3 = 0.03$. The lubrication forces were assumed to be constant for distances less than $\lambda/d = 0.001$. For this suspension, eq 33 predicts the drag forces per unit volume of suspension acting on the three types of particles to be −0.017, −0.177, and −0.337. These numbers agree very well with the actual $f^*_{\mathrm{D}i}$ obtained from the simulations: −0.013, −0.177, and −0.330. The validity of the generalized form eq 33 is thus proved. For polydisperse suspensions of equally sized particles that are moving with M different velocities relative to the fluid, it is easy to show that the volume-specific fluid−particle drag acting on the ith species is

$$f^*_{\mathrm{D}i} = -18(1-\phi)\phi_i F^*_{\mathrm{D-fixed}}\left[\Delta Re_i + \alpha\phi\left(\Delta Re_i - \overline{\Delta Re}\right)\right] \quad (34)$$

where $\overline{\Delta Re}$ is the average velocity of all particle species relative to the fluid

$$\overline{\Delta Re} = \frac{1}{\phi}\sum_{k=1}^{M}\phi_k \Delta Re_k \quad (35)$$

Adding up all $f^*_{\mathrm{D}i}$ together, one sees that the total fluid−particle drag

$$\sum_{k=1}^{M} f^*_{\mathrm{D}i} = -18\phi(1-\phi)F^*_{\mathrm{D-fixed}}\overline{\Delta Re} \quad (36)$$

only depends on the average relative velocity of particles. It is independent of the higher-order moments of the velocity distribution and is not affected by α which is a measure of the internal interactions within a polydisperse suspension.

We now present a quantitative comparison between the new drag law [eq 34] and the modified Gidaspow drag law that is frequently used in previous studies of bidisperse suspensions [eqs 7 and 8] in Figure 10. In the Stokes limit $\Delta \mathrm{Re}_i \to 0$, eqs 7 and 8 are reduced to

$$(\beta^*_i)_{\mathrm{G}} = \begin{cases} 150\phi_i\phi/(1-\phi), & \phi \geq 0.2 \\ 18\phi_i(1-\phi)^{-2.65}, & \phi < 0.2 \end{cases} \quad (37)$$

The dimensionless fluid−particle drag force per unit volume of suspension according to eq 37 is thus

$$(f^*_{\mathrm{D}i})_{\mathrm{G}} = \begin{cases} -150\phi_i\phi/(1-\phi)\Delta Re_i, & \phi \geq 0.2 \\ -18\phi_i(1-\phi)^{-2.65}\Delta Re_i, & \phi < 0.2 \end{cases} \quad (38)$$

In Figure 10, $(f^*_{\mathrm{D}i})_{\mathrm{G}}$ obtained from eq 38 are represented by left-pointing (for type-1 particles) and right-pointing (for type-2 particles) triangles, and $f^*_{\mathrm{D}i}$ obtained from eq 34 are represented by upward (for type-1 particles) and downward (for type-2 particles) triangles. In Figure 10a−c, we specified the velocities

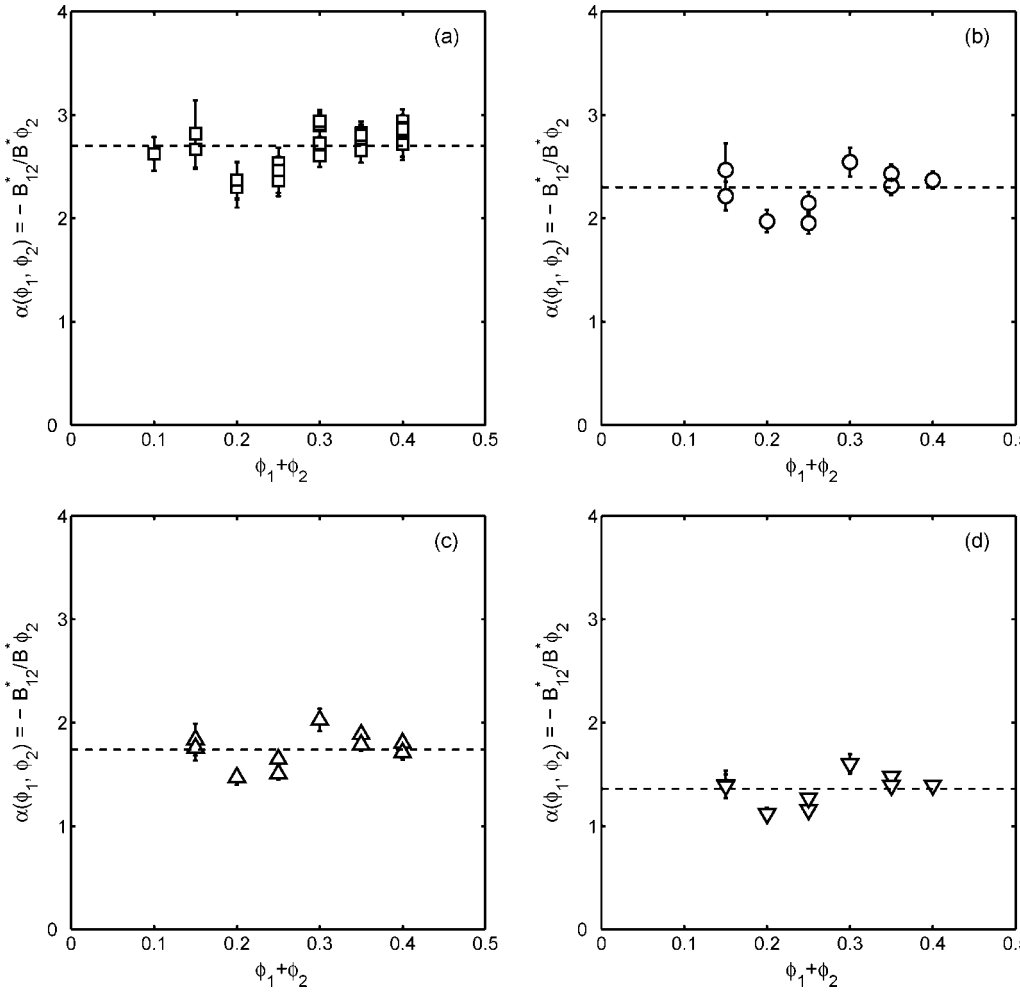

Figure 7. $\alpha(\phi_1, \phi_2, \lambda/d) = B^*_{12}/B^*\phi_2$ as functions of $\phi_1 + \phi_2$. Parts a−d correspond to λ/d values of 0.001, 0.002, 0.005, and 0.01, respectively. The error bars represent 90% uncertainties. The dashed lines at $y = 2.67$, 2.27, 1.74, and 1.36 correspond to the averages of $\alpha(\phi_1, \phi_2, \lambda/d)$ over ϕ_1 and ϕ_2.

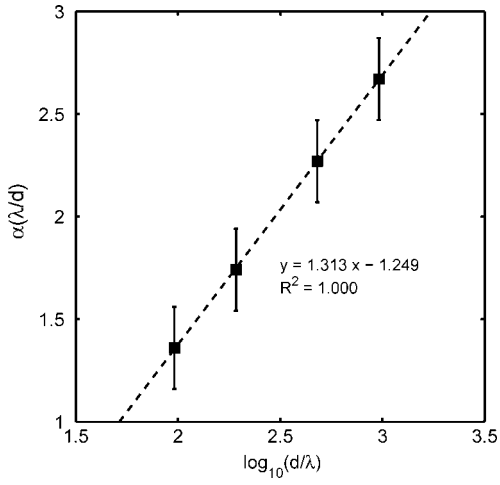

Figure 8. $\alpha(\lambda/d)$ as a function of $\log_{10}(d/\lambda)$. The error bars represent the standard deviations (approximately 0.2) in averaging $\alpha(\phi_1, \phi_2, \lambda/d)$ over ϕ_1 and ϕ_2. The dashed line is the best linear fit with R^2 being the coefficient of regression.

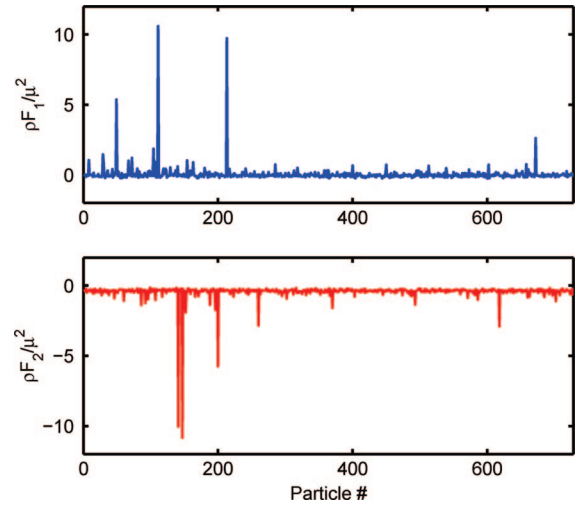

Figure 9. Demonstration of the force spikes in a bidisperse suspension with $\phi_1 = \phi_2 = 0.10$, $\Delta Re_1 = 0$, $\Delta Re_2 = 0.01$, and $\lambda/d = 0.001$. The size of the computational domain $L/d = 15.6$, and the total number of particles in this simulation is 1456.

of the particles $\Delta Re_1 = 0.05$ and $\Delta Re_2 = 0.1$ and set the volume fraction ratio ϕ_1/ϕ_2 to 4:1 (a), 1:1 (b), and 1:4 (c). The drag forces per volume f^*_{Di} were then plotted as functions of total volume fraction ϕ. It is clear from the first three graphs that the predictions from the new drag model differ substantially from those from the modified Gidaspow model, especially for the drag acting on the faster species f^*_{D2}. This comparison suggests that our new drag model, if applied to continuum simulations, would predict a higher drag on the faster (i.e., heavier) particle species, which would result in better mixing and less segregation in a fluidized polydisperse suspension. In Figure 10d, we show an interesting difference between the two drag models that for certain combination of parameters ($\phi_1/\phi_2 = {}^1/_4$, $\Delta Re_1 = 0.02$,

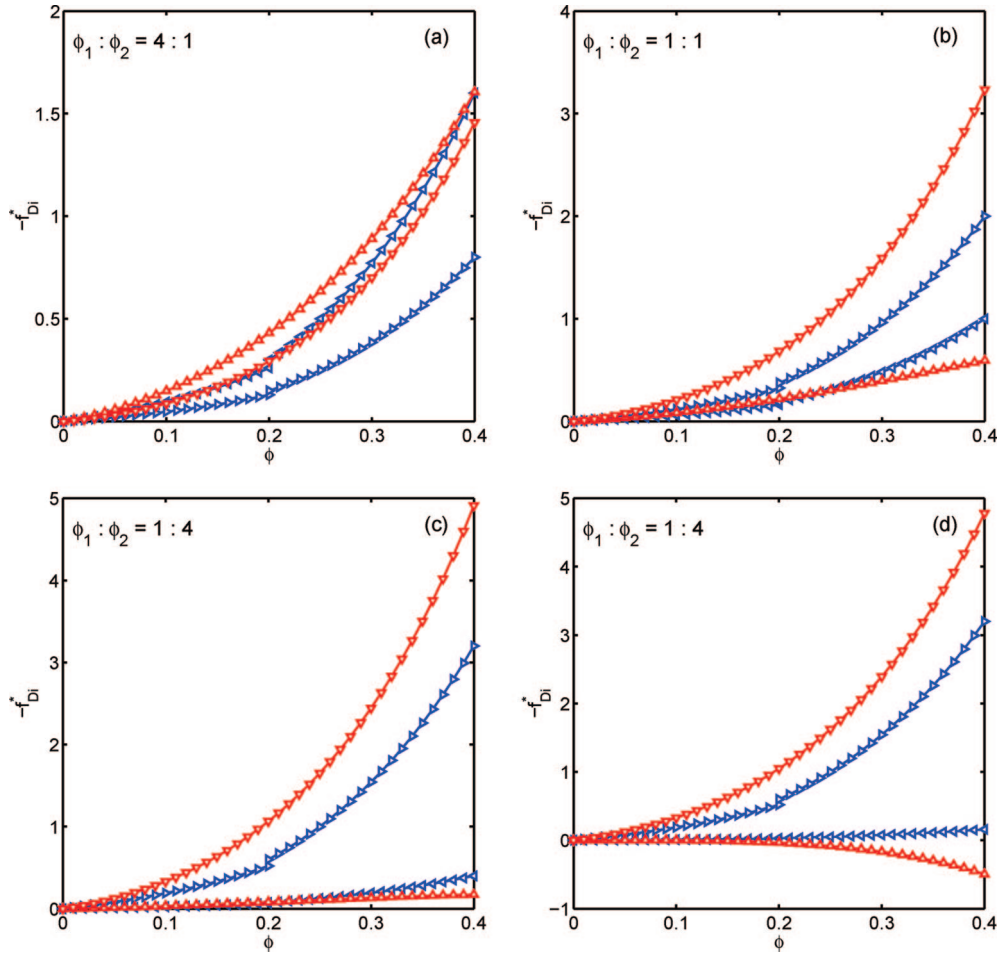

Figure 10. Comparison between the fluid−particle drag forces per unit volume of suspension calculated from the modified Gidaspow drag model in the low-Re limit [eq 38] and those calculated from the new drag model [eq 34] assuming $\lambda/d = 0.001$. In parts a−c, $\Delta Re_1 = 0.05$ and $\Delta Re_2 = 0.1$; in part d, $\Delta Re_1 = 0.02$ and $\Delta Re_2 = 0.1$: (upward triangle) $-f^*_{D1}$ based on the new drag model; (left-pointing triangle) $-f^*_{D1}$ based on the modified Gidaspow drag model; (downward triangle) $-f^*_{D2}$ based on the new drag model; (left-pointing triangle) $-f^*_{D2}$ based on the modified Gidaspow drag model.

$\Delta Re_2 = 0.1$ in this case) eq 34 could predict a negative f^*_{D1}, which implies that the strong interaction between two particle species makes the slower species move faster than it would by itself, i.e. in a suspension that contains exclusively the slower type particles. This phenomenon shows the importance of the particle−particle hydrodynamic drag term. In contrast, fluid−particle drag models in the form of eq 6 must be used in conjunction with particle−particle collisional drag models to capture this behavior.

In Figure 11, we compare the drag forces calculated from the new drag model [eq 34—upward and downward triangles] to those obtained from the mobility matrix formulation by Revay and Higdon[38] [eqs 17 and 18—left- and right-pointing triangles] that assumes instantaneous force balance on all particles. The comparison, again, reveals that there are significant differences between the two drag models. The drag forces acting on the faster species, in particular, appear to be very different: the new model always predicts a much higher drag than that obtained from Revay and Higdon's formulas. When we compare Figure 11 to Figure 10, it may be observed that the predictions of Revay and Higdon's formulas [eqs 17 and 18] are not very different from those from the modified Gidaspow model, especially for the slower particles where the two drag models give almost identical predictions. This similarity is probably because the Wen−Yu model[24] upon which the modified Gidaspow model was built was derived from liquid−solid fluidization and sedimentation experiments where the Stokes number of the particles are relatively low.

In Figure 12, we present the sensitivity of the drag forces $-f^*_{Di}$ on α. We include three values of α for comparison: $\alpha = 2.67$ ($\lambda/d = 0.001$: upward and downward triangles), $\alpha = 1.36$ ($\lambda/d = 0.01$: diamonds and squares), and $\alpha = 0$ (left- and right-pointing triangles). The limit of $\alpha = 0$, in particular, corresponds to the situation where we completely ignore the particle−particle hydrodynamic drag and only consider an ad hoc modification of the drag correlations for a monodisperse fixed bed [eq 23 or eq 24]. Figure 12 indicates that the drag acting on the slower species ($-f^*_{D1}$) decreases with increasing α, whereas the drag acting on the faster species ($-f^*_{D2}$) increases with increasing α. Therefore, the hydrodynamic particle−particle drag helps mixing and reduces segregation in a polydisperse suspension.

Finally, we would like to compare the particle−particle drag transmitted through the fluid [c.f. eq 31]

$$(f^*_{1-2})_{\text{fluid}} = -18(1-\phi)\alpha F^*_{\text{D-fixed}}\phi_1\phi_2(\Delta Re_1 - \Delta Re_2) \quad (39)$$

to the particle−particle drag due to collisions and frictions f^*_{1-2}. For the illustrative example discussed below, we consider a model presented by Syamlal.[25] Under conditions that the collisions are perfectly elastic, frictions are negligible, and particles are of the same size, Syamlal's expression for f^*_{1-2} is

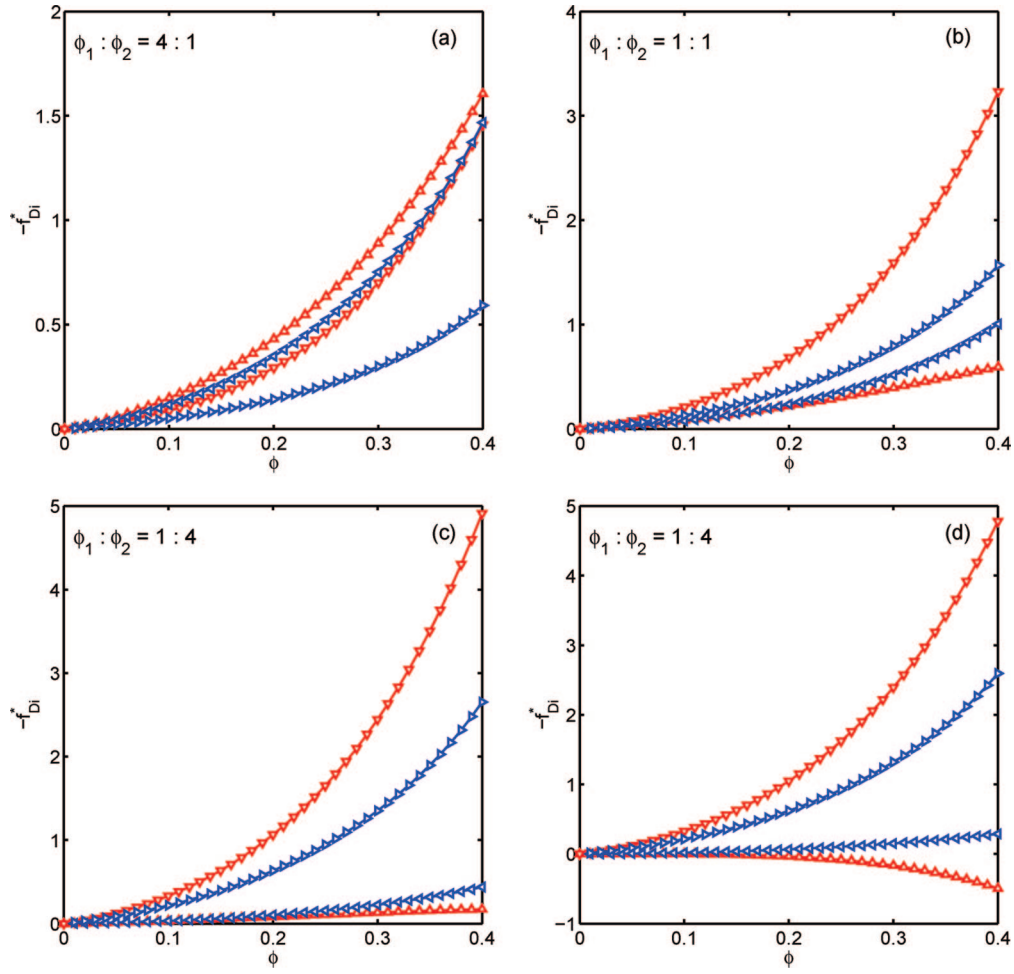

Figure 11. Comparison between the fluid−particle drag forces per unit volume of suspension calculated from Revay and Higdon[38] for bidisperse liquid−solid suspensions with low Reynolds numbers and low Stokes numbers [eqs 17 and 18] and those calculated from the new drag model [eq 34] for gas−solid suspensions with low Reynolds number but high Stokes numbers assuming $\lambda/d = 0.001$. In parts a−c, $\Delta Re_1 = 0.05$ and $\Delta Re_2 = 0.1$; in part d, $\Delta Re_1 = 0.02$ and $\Delta Re_2 = 0.1$: (upward triangle) $-f^*_{D1}$ based on the new drag model; (left-pointing triangle) $-f^*_{D1}$ based on the work of Revay and Higdon; (downward triangle) $-f^*_{D2}$ based on the new drag model; (right-pointing triangle) $-f^*_{D2}$ based on the work of Revay and Higdon.

$$f^*_{1-2} = -6\phi_1\phi_2 g_0 |\Delta Re_1 - \Delta Re_2|(\Delta Re_1 - \Delta Re_2)\frac{(\rho_1/\rho_g)(\rho_2/\rho_g)}{\rho_1/\rho_g + \rho_2/\rho_g} \tag{40}$$

where g_0 is the radial distribution of particles at contact. For a suspension of equally sized hard spheres, according to Lebowitz[47]

$$g_0 = \frac{1 + \frac{\phi}{2}}{(1-\phi)^2} \tag{41}$$

To estimate the relative importance of these two particle−particle drag terms, let us define δ to be the ratio of collisional particle−particle drag to hydrodynamic particle−particle drag

$$\delta = \frac{f^*_{1-2}}{(f^*_{1-2})_{\text{fluid}}} = \frac{g_0|\Delta Re_1 - \Delta Re_2|}{3(1-\phi)\alpha F^*_{\text{D-fixed}}}\frac{(\rho_1/\rho_g)(\rho_2/\rho_g)}{\rho_1/\rho_g + \rho_2/\rho_g} \tag{42}$$

We will now substitute some realistic numbers into this equation and calculate typical values of δ. As the density of fluidized particles is usually close to 1 g/cm^3, it is fair to assume $\rho_1 = 0.8$ g/cm^3 and $\rho_2 = 1.2$ g/cm^3. Under atmospheric conditions, the density and viscosity of air are $\rho_g = 0.0012$ g/cm^3 and $\mu = 1.81 \times 10^{-4}$ g/cm·s. For $d = 50$ μm particles suspended in air, with gravity $\mathbf{g} = 981$ cm/s^2, the terminal velocities of the particles are 6.0 and 9.0 cm/s, respectively. The corresponding Reynolds numbers are 0.20 and 0.30, and the Stokes numbers are 30 and 44. The dual limit of low Reynolds number and high Stokes number is thus satisfied. In very dilute suspensions, with $\phi \approx 0$, $|\Delta Re_1 - \Delta Re_2| = 0.1$, and $\alpha = 1.36$ ($\lambda = 0.5$ μm), $\delta = 9.8$, indicating that in the limit of $\phi \to 0$ the collisional particle−particle drag is more important than the hydrodynamic particle−particle drag. Nevertheless, the importance of the hydrodynamic particle−particle drag increases rapidly with increasing ϕ. When $\phi = 0.4$, if we allow the particles to settle freely, the average relative velocity between particle species will likely be much smaller than the relative velocity in a dilute suspension because of the hindrance in concentrated suspensions. As the Richardson−Zaki formula[27] for a monodisperse Stokes particle suspension, $\mathbf{U}/\mathbf{U}_t = (1-\phi)^{4.65}$, predicts a 90% decrease in the settling velocity at $\phi = 0.4$, we may take $|\Delta Re_1 - \Delta Re_2| \approx 0.01$ as an estimate for the relative velocity in our concentrated binary suspension. Substituting these numbers and $\alpha = 1.36$ into eq 42, one obtains $\delta \approx 0.45$. In a gas-fluidized bed operating at high pressure, δ becomes even smaller. It is thus clear that in more concentrated suspensions the particle−particle drag transmitted through the fluid is just as important as that transmitted by direct collisions.

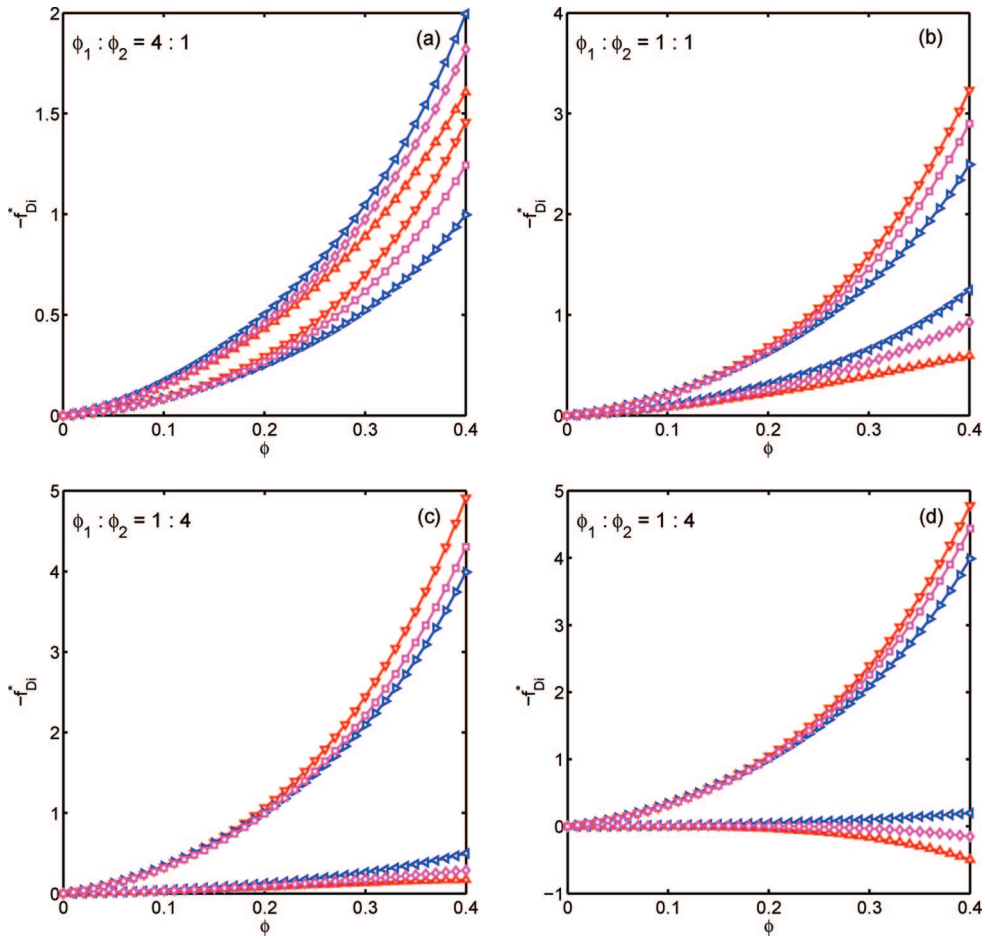

Figure 12. Comparison between the fluid−particle drag forces per unit volume of suspension calculated from eq 34 using $\alpha = 0$ and those calculated using $\alpha = 2.67$ ($\lambda/d = 0.001$). In parts a−c, $\Delta Re_1 = 0.05$ and $\Delta Re_2 = 0.1$; in part d, $\Delta Re_1 = 0.02$ and $\Delta Re_2 = 0.1$. Upward and downward triangles represent $-f^*_{D1}$ and $-f^*_{D2}$ for $\alpha = 2.67$; diamonds and squares represent $-f^*_{D1}$ and $-f^*_{D2}$ for $\alpha = 1.36$; left- and right-pointing triangles represent $-f^*_{D1}$ and $-f^*_{D2}$ for $\alpha = 0$.

V. Summary

In this numerical study, we have characterized the fluid−particle drag in low-Reynolds-number gas−solid suspensions containing two species of particles that are of the same size but are moving with different velocities relative to the fluid. This velocity difference may be resulted from a density difference, or from forces that are selectively applied to certain particles. These particles are spherical in shape, and they have high Stokes numbers such that their motions are not affected by the hydrodynamic forces between successive collisions. We found that the drag forces acting on the two particle species are linear functions of their relative velocities. The proportionality constants between the forces and the velocities, known as the friction coefficients, can be arranged into a matrix form, the off-diagonals of which are indicative of a particle−particle drag transmitted through the fluid. These off-diagonals have not been carefully studied in the past, and existing fluid−particle drag models for polydisperse gas−solid suspensions usually neglect them completely. Our numerical data, on the other hand, suggest that these off-diagonals produce sizable contributions to the drag forces and thus should not be neglected.

We have observed that the friction coefficients, once properly normalized, have relatively simple dependencies on the particle volume fractions and on the lubrication cutoff distance. The logarithmic dependence of the off-diagonals on the lubrication cutoff, in particular, indicates that the particle−particle hydrodynamic drag in a bidisperse suspension of spherical particles of infinite Stokes numbers would diverge to infinity due to the strong lubrication interaction between close pairs of particles. To suppress this nonphysical divergence, an extra length scale λ is needed to cut off the growth of the lubrication forces—it reflects the reality that the growth of the lubrication force between two approaching particles would be limited by surface roughness, noncontinuum effects, or finite weights of the particles.

On the basis of simulation data, we have proposed a new drag model for bidisperse gas−solid suspensions containing equally sized spheres. This drag model can easily be generalized to polydisperse suspensions of equally sized particles that possess three or more distinctive velocities. Compared with existing drag models for polydisperse gas−solid suspensions, our new drag model predicts higher drag on the particle species having a larger velocity relative to the fluid. Therefore, when applied to the continuum modeling of fluidizations of polydisperse gas−solid suspensions, this drag model is expected to predict better mixing and less segregation than existing drag models. Compared with collisional particle−particle drag forces, hydrodynamic particle−particle drag forces are generally of a similar magnitude and hence are equally important. Therefore, the averaged momentum equations in Euler−Euler models should include both terms.

This study assumes that particles of different species are intimately mixed, their spatial distributions are identical to that of a hard-sphere fluid, and the particle velocities are not

correlated to their local configurations. These assumptions are satisfied in the limit of very large Stokes numbers. As the Stokes number decreases, these assumptions become poor. However, for most gas-fluidized beds, the Stokes numbers are on the order of 100 or larger and hence our assumptions are expected to be good approximations. It is also noted that bidisperse gas−solid suspensions are known to be inherently unstable, and particles species will segregate in the direction perpendicular to the mean flow direction and form columns.[48] However, as the instability is usually manifested on large length scales, we expect that our drag law will apply on sufficiently small differential volumes where segregation and nonrandom distribution of particles are not critically important and that this segregation should naturally emerge as an instability mode of the Euler−Euler models.

Acknowledgment

The authors would like to acknowledge financial support from the ExxonMobil Corporation, US Department of Energy (DE-FC26-07NT43098), and ACS Petroleum Research Fund (43901-AC9). We are grateful to Professor Koch for sharing an unpublished manuscript by Valiveti and Koch that greatly assisted our initial research. We also thank Professor Derksen for the discussions and his particle configuration generator.

Literature Cited

(1) Bokkers, G. A.; van Sint Annaland, M.; Kuipers, J. A. M. Mixing and segregation in a bidisperse gas-solid fluidised bed: a numerical and experimental study. *Powder Tech.* **2004**, *140*, 176.

(2) Hill, R. J.; Koch, D. L.; Ladd, A. J. C. The first effects of fluid inertia on flows in ordered and random arrays of spheres. *J. Fluid Mech.* **2001**, *448*, 213.

(3) Hill, R. J.; Koch, D. L.; Ladd, A. J. C. Moderate-Reynolds-number flows in ordered and random arrays of spheres. *J. Fluid Mech.* **2001**, *448*, 243.

(4) Koch, D. L.; Sangani, A. S. Particle pressure and marginal stability limits for homogeneous monodisperse gas fluidized bed: kinetic theory and numerical simulations. *J. Fluid Mech.* **1999**, *400*, 229.

(5) van der Hoef, M. A.; Beetstra, R.; Kuipers, J. A. M. Lattice-Boltzmann simulations of low-Reynolds-number flow past mono- and bidisperse arrays of spheres. *J. Fluid Mech.* **2005**, *528*, 233.

(6) Benyahia, S.; Syamlal, M.; O'Brien, T. J. Extension of Hill-Koch-Ladd drag correlation over all ranges of Reynolds number and solid volume fraction. *Powder Tech.* **2006**, *162*, 166.

(7) Beetstra, R.; van der Hoef, M. A.; Kuipers, J. A. M. Drag force of intermediate Reynolds number flows past mono- and bidisperse arrays of spheres. *AIChE J.* **2007**, *53*, 489.

(8) Wylie, J. J.; Koch, D. L. Rheology of suspensions with high particle inertia and moderate fluid inertia. *J. Fluid Mech.* **2003**, *480*, 95.

(9) Kumaran, V.; Koch, D. L. Properties of a bidisperse particle-gas suspension, Part 1. Collision time small compared to the viscous relaxation time. *J. Fluid Mech.* **1993**, *247*, 623.

(10) Valiveti, P.; Koch, D. L.; Sangani, A. S. The effect of hydrodynamic interactions on sedimenting bidisperse particle-gas suspensions. Submitted to *J. Fluid Mech.* **2002**.

(11) Koch, D. L. Kinetic theory for a monodisperse gas-solid suspension. *Phys. Fluids A* **1990**, *2*, 1711.

(12) Jackson, R. Locally averaged equations of motion for a mixture of identical spherical particles and a Newtonian fluid. *Chem. Eng. Sci.* **1997**, *52*, 2457.

(13) Syamlal, M. ; Roger, W. A.; O'Brien, T. J. *MFIX documentation and theory guide*; Technical Report DOE/METC94/1004, NTIS/DE94000087, US Department of Energy: Washington, DC, 1993.

(14) Owoyemi, O.; Mazzei, L.; Lettieri, P. CFD modeling of binary-fluidized suspensions and investigation of role of particle-particle drag on mixing and segregation. *AIChE J.* **2007**, *53*, 1924.

(15) Feng, Y. Q.; Xu, B. H.; Zhang, S. J.; Yu, A. B. Discrete particle simulation of gas fluidization of particle mixtures. *AIChE J.* **2004**, *50*, 1713.

(16) Snider, D. M. An incompressible three-dimensional multiphase particle-in-cell model for dense particle flows. *J. Comp. Phys.* **2001**, *170*, 523.

(17) van Wachem, B. G. M.; Schouten, J. C.; van den Bleek, C. M.; Krishna, R.; Sinclair, J. L. CFD modeling of gas-fluidized beds with a bimodal particle mixture. *AIChE J.* **2001**, *47*, 1292.

(18) Huilin, L.; Yurong, H.; Gidaspow, D.; Lidan, Y.; Yukun, Q. Size segregation of binary mixture of solids in bubbling fluidized beds. *Powder Tech.* **2003**, *134*, 86.

(19) Fan, R.; Marchisio, D. L.; Fox, R. O. Application of the direct quadrature method of moments to polydisperse gas-solid fluidized beds. *Powder Tech.* **2004**, *139*, 7.

(20) Gera, D.; Syamlal, M.; O'Brien, T. J. Hydrodynamics of particle segregation in fluidized beds. *Int. J. Multiphase Flow* **2004**, *30*, 419.

(21) Cooper, S.; Coronella, C. J. CFD simulations of particle mixing in a binary fludized bed. *Powder Tech.* **2005**, *151*, 27.

(22) Dahl, S. R.; Hrenya, C. M. Size segregation in gas-solid fluidized beds with continuous size distributions. *Chem. Eng. Sci.* **2005**, *60*, 6658.

(23) Gidaspow, D. *Multiphase Flow and Fluidization*; Academic Press: Boston, 1994.

(24) Ergun, S. Fluid flow through packed columns. *Chem. Eng. Prog.* **1952**, *48*, 89.

(25) Wen, C. Y.; Yu, Y. H. Mechanics of fluidization. *Chem. Eng. Prog. Symp. Ser.* **1966**, *62*, 100.

(26) Syamlal, M. *The particle-particle drag term in a multiparticle model of fluidization*; Technical Report DOE/MC/21353−2373, NTIS/DE87006500, US Department of Energy: Washington, DC, 1987.

(27) Huilin, L.; Gidaspow, D.; Manger, E. Kinetic theory of fluidized bindary granular mixtures. *Phys. Rev. E* **2001**, *64*, 061301.

(28) Richardson, J. F.; Zaki, W. N. Sedimentation and fluidization: part I. *Trans. Inst. Chem. Eng.* **1954**, *32*, 35.

(29) Mirza, S.; Richardson, J. F. Sedimentation of suspensions of particles of two or more sizes. *Chem. Eng. Sci.* **1979**, *34*, 447.

(30) Masliyah, J. H. Hindered settling in a multi-species particle system. *Chem. Eng. Sci.* **1979**, *34*, 1166.

(31) Selim, M. S.; Kothari, A. C.; Turian, R. M. Sedimentation of multisized particles in concentrated suspensions. *AIChE J.* **1983**, *29*, 1029.

(32) Patwardhan, V. S.; Tien, C. Sedimentation and liquid fluidization of solid particles of different sizes and densities. *Chem. Eng. Sci.* **1985**, *40*, 1051.

(33) Batchelor, G. K. Sedimentation in a dilute polydisperse system of interacting spheres. Part 1. General theory. *J. Fluid Mech.* **1982**, *119*, 379.

(34) Batchelor, G. K.; Wen, C.-S. Sedimentation in a dilute polydisperse system of interacting spheres. Part 2. Numerical results. *J. Fluid Mech.* **1982**, *124*, 495.

(35) Davis, R. H.; Birdsell, K. H. Hindered settling of semidilute monodisperse and polydisperse suspensions. *AIChE J.* **1988**, *34*, 123.

(36) Bruneau, D.; Anthore, R.; Feuillebois, F.; Auvray, X.; Petipas, C. Measurement of the average velocity of sedimentation in a dilute polydisperse suspension of spheres. *J. Fluid Mech.* **1990**, *21*, 577.

(37) Al-Naafa, M. A.; Selim, M. S. Sedimentation of monodisperse and bidisperse hard-sphere colloidal suspensions. *AIChE J.* **1992**, *38*, 1618.

(38) Davis, R. H.; Gecol, H. Hindered settling function with no empirical parameters for polydisperse suspensions. *AIChE J.* **1994**, *40*, 570.

(39) Revay, J. M.; Higdon, J. J. L. Numerical simulation of polydisperse sedimentation: equal size spheres. *J. Fluid Mech.* **1992**, *243*, 15.

(40) Ladd, A. J. C. Numerical simulations of particulate suspensions via a discretized Boltzmann equation. Part 1. Theoretical foundation. *J. Fluid Mech.* **1994**, *271*, 285.

(41) Ladd, A. J. C. Numerical simulations of particulate suspensions via a discretized Boltzmann equation. Part 2. Numerical results. *J. Fluid Mech.* **1994**, *271*, 311.

(42) Ladd, A. J. C.; Verberg, R. Lattice-Boltzmann simulations of particle-fluid suspensions. *J. Stat. Phys.* **2001**, *104*, 1191.

(43) Nguyen, N.-Q.; Ladd, A. J. C. Lubrication corrections for lattice-Boltzmann simulations of particle suspensions. *Phys. Rev. E* **2002**, *66*, 046708.

(44) Kim, S.; Karrila, S. J. *Microhydrodynamics: Principles and Selected Applications*; Dover: New York, 2005.

(45) Sangani, A. S.; Mo, G.; Tsao, H.-K.; Koch, D. L. Simple shear flows of dense gas-solid suspensions at finite Stokes numbers. *J. Fluid Mech.* **1996**, *313*, 309.

(46) Mo, G.; Sangani, A. S. A method for computing Stokes flow interactions between spherical objects and its application to suspensions of drops and porous particles. *Phys. Fluids A* **1994**, *6*, 1637.

(47) Sangani, A. S.; Mo, G. Inclusion of lubrication forces in dynamical simulations. *Phys. Fluids A* **1994**, *6*, 1653.

(48) Lebowitz, J. L. Exact solution of generalized Percus-Yevick equation for a mixture of hard spheres. *Phys. Rev. A* **1964**, *133*, 895.

(49) Valiveti, P.; Koch, D. L. The inhomogeneous structure of a bidisperse sedimenting gas-solid suspension. *Phys. Fluids* **1999**, *11*, 3283.

(50) Barker, J. A.; Henderson, D. Theory of liquids. *Annu. Rev. Phys. Chem.* **1972**, *23*, 439.

Received for review January 30, 2008
Revised manuscript received March 27, 2008
Accepted April 1, 2008

IE800171P

Continuum Representation of a Continuous Size Distribution of Particles engaged in Rapid Granular Flow

J. A. Murray[a], S. Benyahia [b], P. Metzger[c], C. M. Hrenya[a]
[a]*Department of Chemical and Biological Engineering, University of Colorado, Boulder, CO 80309*
[b]*National Energy Technology Laboratory, Morgantown, WV 26507*
[c]*Granular Mechanics and Regolith Operations Lab, NE-S-1, NASA Kennedy Space Center, FL 32899*
(Dated: February 16, 2012)

Natural and industrial granular flows often consist of several particle sizes, approximately forming a *continuous* particle size distribution (PSD). Continuous PSDs are ubiquitous, though existing kinetic-theory-based models for rapid granular flows are limited to a discrete number of species. The objective of this work is twofold: (i) to determine the number of *discrete* species required to accurately approximate a *continuous* PSD, and (ii) to validate these results via a comparison with molecular dynamics (MD) simulations of continuous PSDs. With regard to the former, several analytic (Gaussian and lognormal) and experimental (coal and lunar soil simulants) distributions are investigated. Transport coefficients (pressure, shear viscosity, etc.) of the granular mixture given by the polydisperse theory of Garzó, Hrenya and Dufty [1, 2] are compared using an increasing number of species s to approximate the given PSD. These discrete approximations are determined by matching the first $2s$ moments of the approximation and the given continuous distribution. Relatively few species are required to approximate moderately wide distributions (Gaussian, lognormal), whereas even wider distributions (coal and lunar soil simulants) require a larger number of species. Regarding the second objective, a comparison between MD simulations and kinetic-theory predictions for a simple shear flow of both Gaussian and lognormal PSDs reveal essentially no loss of accuracy stemming from the polydisperse theory itself (as compared to theories for monodisperse systems) or from the discrete approximations of continuous PSDs used in the polydisperse theory.

I. INTRODUCTION

Granular materials are often comprised of particles of different sizes and/or material properties. Such polydispersity not only impacts the local flow patterns associated with changes in stresses of the solid phase, but also gives rise to a phenomenon with no monodisperse counterpart, namely species segregation or the de-mixing of unlike particles [3-6]. The vast majority of previous work on polydispersity has been limited to binary mixtures of particles. However, it is quite common that the distribution of particle sizes within a granular mixture is essentially continuous. Such continuous particle size distributions (PSDs) are prevalent in both nature (e.g., planetary rings, avalanches) and industry (e.g., pharmaceutical processing, coal gasification), though not well understood.

The focus of this work is on rapid granular flows of particles with a *continuous* distribution of sizes. Rapid flows are those in which particles engage in binary, instantaneous collisions. Such flows can be described mathematically via a kinetic-theory analogy, which shares the same assumptions. Although numerous kinetic-theory-based models for polydisperse systems exist which differ in assumptions related to the partition of energies (equipartition vs. non-equipartition), velocity distributions (Maxwellian vs. non-Maxwellian), solids concentration (dilute v. dense), etc. [see Ref. 6 for a recent review], a common feature of current models is their restriction to a *discrete* number, s, of particle species. This restriction stems from the

starting kinetic equations, which are cast as a single-particle velocity distribution function for a given particle species, where each species has a unique set of physical properties (i.e., size and/or material density and/or restitution coefficient). Consequently, current kinetic-theory-based models cannot be directly applied to a continuous PSD. Instead, the continuous PSD must first be approximated as a discrete distribution of s particle diameters and associated relative solids volume fractions (i.e., composition).

Collectively, this work introduces a universal methodology for representing a continuous PSD in models based on the kinetic theory analogy, which can be carried out prior to CFD simulation of a particular geometry. In particular, the mathematical technique developed and validated here uses as its foundation the explicit dependency of transport coefficients on the continuous PSD and its discrete approximation. From a physical standpoint, such information is critical for the prediction of practical flows, particularly since recent experiments exhibit qualitative differences between binary mixtures and continuous PSDs [7, 8].

Though several kinetic-theory-based models for rapid granular flows of s-component mixtures are available [1, 2, 9-11], studies involving the flow of mixtures containing 3 or more particle species are scarce, especially compared to their binary counterparts. Iddir, Arastoopour, and Hrenya [12] analyzed the kinetic-theory-based predictions of Iddir and Arastoopour [11] for both binary and ternary mixtures. Predictions of rheological behavior for binary mixtures were compared to both molecular dynamics (MD) and experimental data, but similar comparisons for the ternary system were not possible due to the lack of such data. With regard to continuous distributions, Remy, Khinast, and Glasser [13] investigated how the degree of polydispersity of a granular mixture within a bladed mixer affects flow and segregation. MD simulations were carried out for 4 different systems: binary, ternary, 5 particles, and 11 particles. Because this flow is not considered a rapid granular flow, a kinetic-theory-based model could not be included in the comparison. Dahl *et al*. [14-16] used MD simulations of simple shear flow and bounded conduction to analyze the behavior of rapid granular flows comprised of continuous PSDs, though to date no kinetic-theory predictions of this data have been performed.

To build on previous studies, the aim of the current work is to determine the suitability of polydisperse, kinetic-theory-based models to predict the flow behavior of a continuous size distribution of solids. In particular, the objective of this effort is twofold: (i) to determine the number of *discrete* species required to accurately approximate a *continuous* PSD, and (ii) to validate these results via a comparison with molecular dynamics (MD) simulations of continuous PSDs. The kinetic-theory-based model used in this study was proposed by Garzó, Hrenya, and Dufty [1, 2] and is applicable to any number of finite species (s). A review of existing kinetic-theory-based models of polydisperse flows is given in Ref. [6]. Hereafter, this model will be referred to as GHD theory.

With regard to the first objective, transport coefficients given by GHD theory are evaluated over a range of restitution coefficients and volume fractions (dilute to moderately dense). A discrete approximation for the continuous PSD (as is needed for use in the kinetic-theory-based model) is accomplished via the matching of moments of the given continuous distribution and its discrete approximation. As the number of species used to approximate a continuous PSD increases, the number of moments matched increases as well. To determine the appropriate number of species ($s_{\min}$) needed for the discrete approximation, both the desired accuracy and corresponding computational costs are considered. Specifically, transport coefficients of GHD theory are evaluated for increasing values of s until the desired accuracy is reached. The resulting $s_{\min}$ value is determined for a variety of Gaussian and lognormal PSDs of

various widths, as well as for two experimentally-obtained continuous PSDs, namely coal particles used for gasification and simulants of lunar regolith (i.e., lunar soil). Results of this effort indicate that wider continuous PSDs require a larger number of particle species for an accurate discrete approximation, though the appropriate number of species can be fairly low overall ($s_{\min} = 5$) for the widest lognormal PSD analyzed). With regard to the accuracy of GHD theory applied to continuous PSDs (objective 2), a comparison between previous MD simulations of continuous PSDs engaged in simple shear [14] and GHD predictions of granular pressure and shear viscosity is conducted. The results not only confirm the earlier determination of $s_{\min}$ for various Gaussian and lognormal PSDs, but also provide validation of the GHD theory as well as the use of a moment-based discrete approximation for continuous PSDs.

II. METHODS

As previously mentioned, a continuous PSD must be approximated as a discrete number of particle sizes (and associated volume fractions) in order to utilize existing kinetic-theory-based models. In the paragraphs below, the continuous PSDs examined in this work (Section A), the method used to obtain discrete approximation to continuous PSDs (Section B), as well as the technique used to evaluate the accuracy of the discrete approximations (Section C) are discussed.

A. Continuous PSDs investigated

In this work, four types of continuous size distributions are investigated: (i) Gaussian distributions, (ii) lognormal distributions, (iii) a bidisperse PSD of coal particles used for gasification provided by the Department of Energy National Energy Technology Laboratory (DOE NETL), and (iv) a simulant of lunar soil provided by National Aeronautics and Space Administration Kennedy Space Center (NASA KSC). Figure 1 shows the number-based frequency distribution, f_n, for each of these size distributions. For the Gaussian and lognormal distributions, a range of distribution widths, σ/d_{ave}, where σ denotes the standard deviation of the PSD and d_{ave} denotes its arithmetic mean, are examined. Accordingly, $\sigma/d_{ave} = 0$ corresponds to the monodisperse limit. For Gaussian distributions, the maximum distribution width is $\sigma/d_{ave} =$ 30% since a further increase would result in negative (unphysical) particle diameters [15]. Due to the extended right tail of lognormal distributions, a similar limit does not exist, and here lognormal distributions with $\sigma/d_{ave} =$ 0-90% are considered. Figures 1a and 1b show lognormal and Gaussian distributions, respectively, in which the average diameter (d_{ave} = 72.6 microns) is held constant, whereas Figures 1c and 1d show distributions with a constant root-mean-cube diameter (d_{rmc} = 72.6 microns). The former distributions were used in analyzing the discrete approximation of continuous PSDs (Sections III.A), and the latter were used for direct comparison with the MD simulations of Dahl *et al*. [14; see Section III.D]. The PSD of coal particles provided by DOE NETL was obtained via sieving and thus was provided in a mass-based form in Figure 1e. Note that the bidisperse nature of this distribution is no longer apparent when it is converted to a number-based distribution (Figure 1f), which is used to obtain a discrete approximation (see Section III.B). Lastly, the PSD of a simulant of lunar soil known as OB-1 and measured by NASA is shown, with the measured mass-based distribution in Figure 1g, and the associated number-based distribution in Figure 1h. For purposes of direct comparison, the bidisperse coal PSD (DOE NETL) and a lognormal distribution with the same average diameter

as the OB-1 and a distribution width of σ/d_{ave} = 90% are also shown on these log-log plots. Relative distribution widths are revealed in Figures 1g and 1h. The lognormal distribution exhibits a high frequency of particles with diameters near the average diameter (d_{ave} = 0.57); however, the frequency quickly approaches zero as the particle diameter is increased. On the other hand, the lunar soil simulant distribution (OB-1) and coal PSD exhibit moderate frequencies for a larger range of particle diameters. Thus, the experimental distributions contain a larger "width" of particle diameters. Because the OB-1 distribution and the coal PSD have different average diameters, the relative width of these distributions is not so obvious. However, by approximating each experimental PSD with a lognormal distribution of appropriate width, it was determined that the lunar soil simulant distributions are much wider than the coal PSD. For the sake of brevity, the OB-1 lunar soil simulant [17] is the only shown lunar PSD. It is worth noting that distributions of several other lunar soil simulants (OB-1, JSC-1a, LHT-2M, BP-1) and a sample of lunar soil were investigated; the resulting trends are similar to those of OB-1 and thus only the representative results of OB-1 are included below for the sake of brevity.

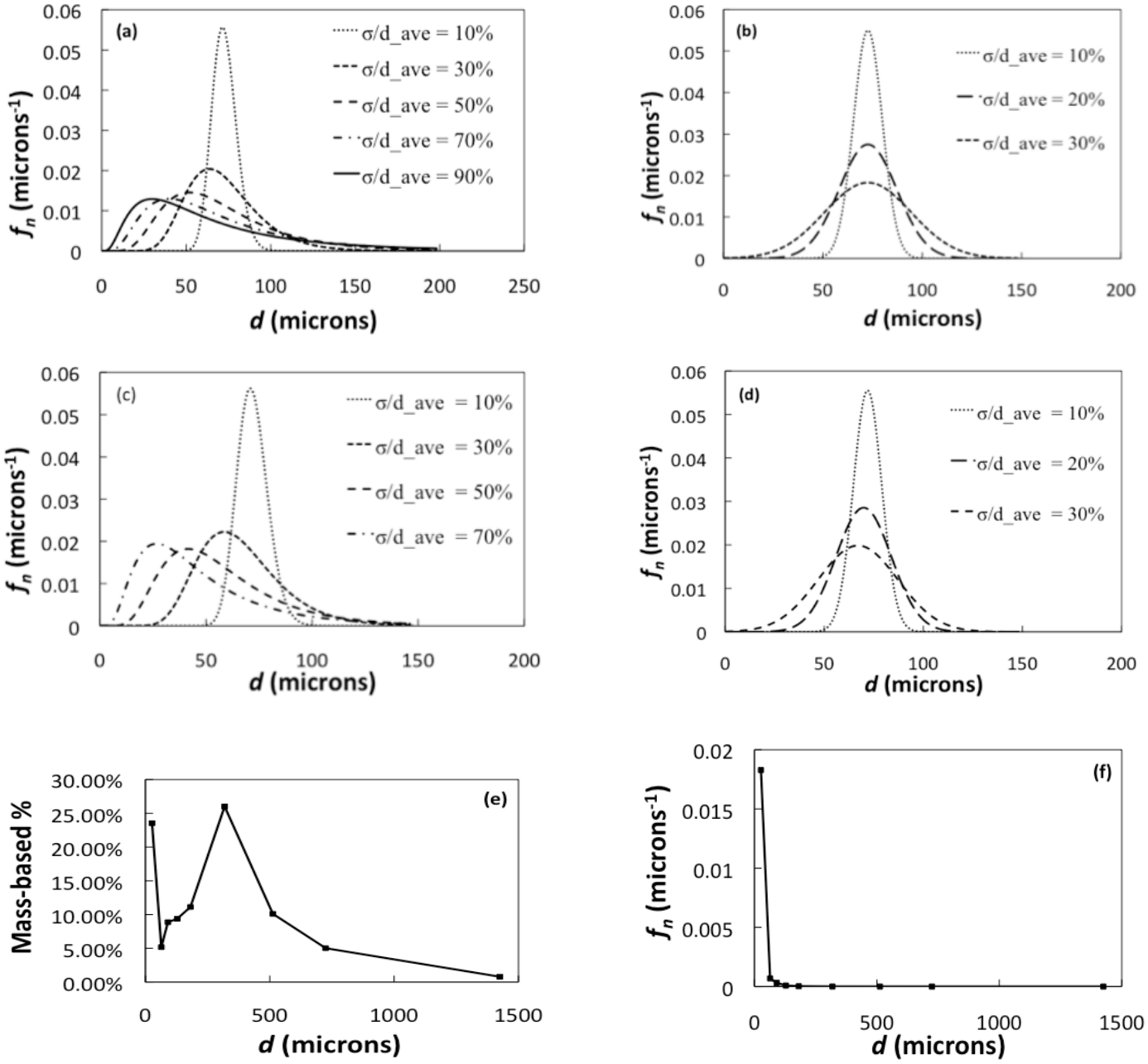

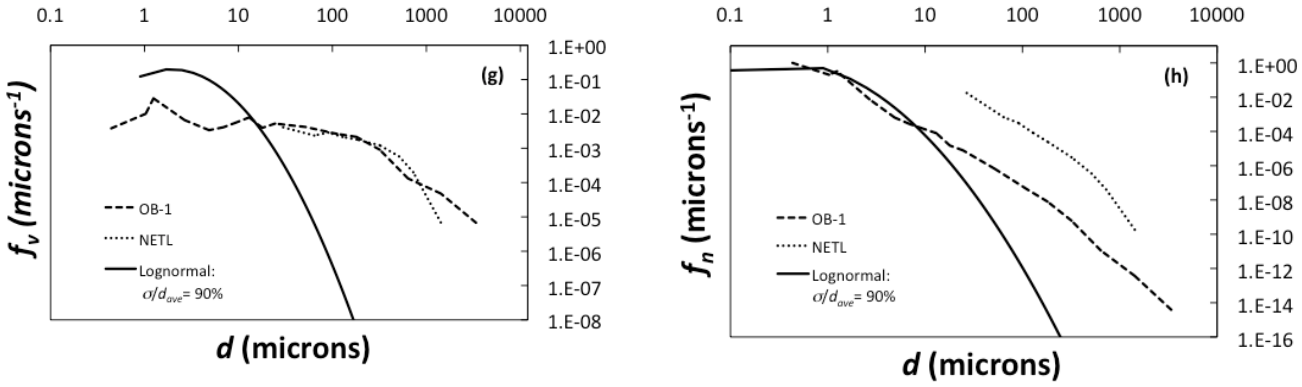

FIG. 1: Number-based frequency (f_n) for **(a)** lognormal PSD with constant d_{ave}, **(b)** Gaussian PSD with constant d_{ave}, **(c)** lognormal PSD with constant d_{rmc}, and **(d)** Gaussian PSD with constant d_{rmc}. Frequency distributions of coal particles in terms of a **(e)** mass and **(f)** number basis. Frequency distributions of lunar soil simulant (OB-1) in terms of a **(g)** mass and **(h)** number basis.

B. Discrete, moment-based approximation of continuous PSDs

Though continuous PSDs can be discretized using a variety of methods, a logical choice involves the matching of moments between the continuous PSD and its discrete approximation. The method of matching moments has been previously utilized by Fan and Fox [18] for application to fluidized beds. Specifically, the i^{th} moment of a continuous PSD (μ_i) is defined by:

$$\mu_i = \int_0^\infty d^i f_n d(d) \tag{1}$$

where f_n denotes the number-based frequency distribution of particle diameter (d). The first several moments are familiar quantities: the zeroth moment (μ_0) is equal to unity, the first moment (μ_1) is equal to the number-based average diameter, and the second and third moments are the variance and skewness, respectively.

For Gaussian and lognormal distributions, analytic expressions for the moments are available and take the following forms, respectively [18]:

$$\mu_{i,Gaussian} = \sum_{r=0}^{i} \sigma^{i-r} d_{ave}^{r} \frac{i! \cdot 1 \cdot 3 \cdots (i-r-1)}{(i-r)!r!} \tag{2}$$

$$\mu_{i,Lognormal} = d_{ave}^{i} \exp\left(\frac{i^2\sigma^2}{2}\right) \tag{3}$$

In these equations $r = 0,2,\ldots$ for even values of i and $r = 1,3,\ldots$for odd values of i.

Unlike Gaussian and lognormal distributions, analytic forms of the moments for the experimentally obtained distributions are not available. Accordingly, numerical means are

instead used to determine the moments of these continuous distributions, as given by Eq. (1). In other words, continuous PSDs can be divided into "bins" of width Δd, where smaller widths results in higher accuracy:

$$\mu_i \sim \sum_{b=1}^{k} d_b^i f_n \Delta d \tag{4}$$

where k is the number of bins and d_b is the diameter of particles associated with bin b.

Once the moments of a given *continuous* PSD have been obtained either analytically or numerically (via Eq. (3) or (4), respectively), a corresponding *discrete* approximation can be determined by matching the desired number of moments between the two distributions. The number of size species, s, contained in this discrete approximation is chosen independently, and with an increase in the number of species comes an increase in the number of moments matched. More specifically, for a discrete approximation with s species, the first $2s$ moments are matched between the distributions, where the moments of the discrete approximation are obtained via:

$$\mu_i = \sum_{j=1}^{s} d_j^i w_j \tag{5}$$

where d_j are the particle sizes and w_j are the corresponding number-based fractions or "weights" of particles with size d_j. Accordingly, the first $2s$ moments result a system of $2s$ equations, with s unknown diameters and s unknown weights. Furthermore, in order to relate the particle size and associated weight (number fraction) to the volume fraction of species j, the following relationship is used:

$$\frac{\phi_j}{\phi} = \frac{\phi_j}{\sum_{j=1}^{s} \phi_j} = \frac{d_j^3 w_j}{\sum_{j=1}^{s} d_j^3 w_j} \tag{6}$$

where the species volume fraction is denoted by ϕ_j and the overall volume fraction is denoted by ϕ. For example, for a discrete approximation using $s = 2$, the first four moments of the distribution are matched to that of the continuous distribution. Calculating the first four moments of the discrete approximation will allow for the determination of the two particle species diameters (d_1, d_2) and associated volume fraction ratios (ϕ_1/ϕ, ϕ_2/ϕ). Generally speaking, the resulting set of $2s$ nonlinear equations is quite stiff; therefore, a method known as the product-difference algorithm is used to solve for the s particle diameters and associated species weights [18, 19].

It is important to note that a tradeoff exists between the number of species s chosen for the discrete approximation and the computational power required to solve the resulting kinetic-theory-based equations (described below and presented in Table 1). Matching a greater number of moments (i.e., larger s) results in a more accurate approximation. Figure 2 shows an example of a continuous PSD (d_{ave} = 894 μm) that has been discretized using both two and four discrete species. Note that the discretization using $s = 4$ more accurately mimics the shape of the actual distribution than does the discretization using $s = 2$. However, because $s + 2$ governing

differential equations need to be solved for a mixture with s species (1 momentum, 1 granular energy, and s mass balances), choosing a larger number of species will increase the complexity of the resulting expressions given in Table 1 as well as the computational power required.

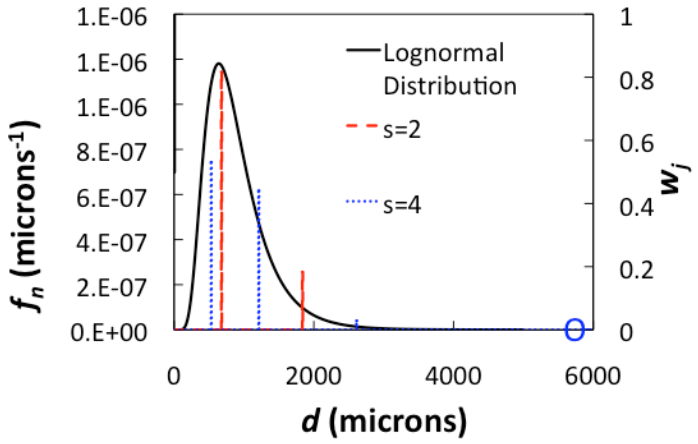

FIG. 2: Discrete approximation of lognormal distribution (d_{ave} = 894 microns, σ/d_{ave} = 50%) using two particle species (s = 2) and four particle species (s = 4), corresponding to the red and blue lines, respectively. The left hand y-axis corresponds to the number-based frequency of the lognormal distribution, whereas the right hand y-axis corresponds to the number-based fractions of the discrete approximations. The fourth particle species has such a low number-based fraction that the line is not visible at the given scale and its location is circled instead.

C. Evaluation of the discrete approximation to a continuous PSD

To determine the impact of the choice of s on the accuracy of the discrete approximations to continuous PSDs, such approximations are obtained for various values of s (Section B) for each of the PSDs considered here (Section A). Then, kinetic-theory predictions of transport coefficients are evaluated for each of the discrete approximations. By comparing predictions for discrete distributions at various values of s, the minimum number of species (s_{min}) needed to achieve the desired accuracy can be determined. Using these values, kinetic-theory predictions of discrete distributions are then compared to MD simulations of simple shear flows with continuous size distributions.

For purposes of this work, the kinetic-theory-based model considered here is that proposed by Garzó, Hrenya, and Dufty [1, 2]. This theory, referred to as GHD hereafter, is used since it contains the fewest assumptions of existing polydisperse theories; it accounts for non-equipartition and non-Maxwellian effects and is applicable up to moderately dense flows and over a wide range of restitution coefficients [see Ref. 6 for a review of various polydisperse, kinetic-theory-based models]. The mass, momentum, and granular energy balances for the GHD theory are cast in terms of the species number density (n_i), mass-based mixture velocity ($\underline{U}$), and number-based mixture granular temperature (T), as shown in Table 1. Each balance equation is expressed in terms of these hydrodynamic variables (n_i , $\underline{U}$, T) along with the following constitutive quantities: cooling rate (ζ), mass flux of species i ($\underline{j_{oi}}$), heat flux ($\underline{q}$), and pressure tensor ($\underline{P}$). Constitutive expressions for these quantities are also given in Table 1 in terms of the transport coefficients $\zeta^{(0)}$ (zeroth-order cooling rate), ζ_u (transport coefficient associated with first-order cooling rate), D_{ij} (mutual diffusivity), D_i^T (thermal diffusivity), D_{ij}^F (mass mobility), λ

(conductivity), $D_{q,i}$ (Dufour coefficient), L_{ij} (thermal mobility), p (pressure), η (shear viscosity), and κ (bulk viscosity). These transport coefficients depend on the particle properties (species diameters, species masses, species restitution coefficients) as well as the hydrodynamic variables, thereby resulting in a closed set of equations.

Table 1: Governing equations and constitutive relations of GHD theory. See Section V for nomenclature, and see Garzó, Hrenya, and Dufty [1, 2] for definitions of the following quantities: α_{ij} (coefficient of restitution between species i and j), χ_{ij} (pair correlation function relating species i and j), d_{ij} (average diameter of species i and j), D_{ij} (mutual (ordinary) diffusion coefficient relating species i and j, D_{ij}^F (mass mobility coefficient relating species i and j), D_i^T (thermal diffusion coefficient of species i), $D_{q,i}$ (dufour coefficient of species i), $e_{i,D}$ (quantity associated with the first-order contribution to the cooling rate), $\underline{F_i}$ (external force acting on species i, η (shear viscosity), η^c (collisional contribution to shear viscosity), η_j^k (kinetic contribution of species j to shear viscosity), $\underline{j_{oi}}$ (mass flux of species i), κ (bulk viscosity), λ (conductivity), L_{ij} (thermal mobility coefficient relating species i and j), m (average mass amongst particle species), m_i (mass of species i), μ_{ij} ($m_i/(m_i + m_j)$), n (number density of overall system), n_i (number-based density of species i), p (granular pressure), $\underline{\underline{P}}$ (pressure tensor), $\underline{q}$ (heat flux), θ_i ($m_i T/(m T_i)$), ρ (material density), T (number-based mixture granular temperature), T_i (granular temperature of species i), τ_{ij} (quantity associated with the shear viscosity of species i and j), $\underline{U}$ (mass-based mixture velocity), ζ (overall cooling rate), $\zeta^{(0)}$ (zeroth-order cooling rate), ζ_u (first-order cooling rate), $\zeta^{(1,1)}$ ((1,1) contribution to first-order cooling rate), $\zeta^{(1,0)}$ ((1,0) contribution to first-order cooling rate). It is important to note that GHD theory refers to restitution coefficient as α_{ij}, whereas this work refers to restitution coefficient as e.

Balance Equations

Mass	$\frac{Dn_i}{Dt} + n_i \underline{\nabla}\cdot \underline{U} = -\frac{1}{m_i}\underline{\nabla}\cdot \underline{j_{oi}}$
Momentum	$\rho \frac{D\underline{U}}{Dt} = -\underline{\nabla}\cdot \underline{\underline{P}} + \sum_{i=1}^{s} n_i \underline{F_i}$
Granular Energy	$\frac{3}{2} n \frac{DT}{Dt} = -\underline{\nabla}\cdot \underline{q} - \underline{\underline{P}} : \underline{\nabla U} - \frac{3}{2} nT\,\zeta + \frac{3}{2} T \sum_{i=1}^{s} \frac{1}{m_i} \underline{\nabla}\cdot \underline{j_{oi}} + \sum_{i=1}^{s} \frac{1}{m_i} \underline{F_i}\cdot \underline{j_{oi}}$

Flux Laws

Mass	$\underline{j_{oi}} = -\sum_{j=1}^{s} m_i m_j \frac{n_j}{\rho} D_{ij}\, \underline{\nabla}\ln(n_j) - \rho\, D_i^T\, \underline{\nabla}\ln T - \sum_{j=1}^{s} D_{ij}^F\, \underline{F}_j$
Heat	$\underline{q} = -\lambda \underline{\nabla} T - \sum_{i=1}^{s} T^2 D_{q,i} \underline{\nabla}\ln(n_i) - \sum_{i=1}^{s}\sum_{j=1}^{s} L_{ij} \underline{F_i}$
Pressure	$\underline{\underline{P}} = p\,\underline{\underline{\delta}} - \eta\left[\left(\underline{\nabla U} + (\underline{\nabla U})^T\right) - \frac{2}{3}(\underline{\nabla}\cdot \underline{U})\underline{\underline{\delta}}\right] - \kappa\,(\underline{\nabla}\cdot \underline{U})\underline{\underline{\delta}}$

Cooling Rate

$\zeta = \zeta^{(0)} + \zeta_U \underline{\nabla}\cdot \underline{U}$

Transport Coefficients Evaluated

Zeroth-Order Cooling Rate	$\zeta_i^{(0)} = \frac{8\sqrt{\pi}}{3}\sqrt{\frac{2T}{m}} \sum_{j=1}^{s} \chi_{ij}^{(0)} n_j \mu_{ji}\, d_{ij}^2 \left(\frac{\theta_i + \theta_j}{\theta_i \theta_j}\right)^{1/2} (1+\alpha_{ij})\left[1 - \frac{\mu_{ji}}{2}(1+\alpha_{ij})\left(\frac{\theta_i+\theta_j}{\theta_j}\right)\right]$	
Shear Viscosity	$\sum_{j=1}^{s}\left(\tau_{ij} - \frac{1}{2}\zeta^{(0)}\delta_{ij}\right)\eta_j^k = n_i T_i + \sum_{j=1}^{s} \frac{2\pi}{15} m_i n_i n_j \mu_{ji} d_{ij}^3 \chi_{ij}^{(0)} (1+\alpha_{ij})\left[\mu_{ji}(3\alpha_{ij} - 1)\left(\frac{T_i}{m_i} + \frac{T_j}{m_j}\right) - \frac{4(T_i - T_j)}{(m_i + m_j)}\right]$	
	$\eta^c = \left[\frac{4\pi}{15}\sum_{i=1}^{s}\sum_{j=1}^{s} n_j d_{ij}^3 \chi_{ij}^{(0)} \mu_{ji}(1+\alpha_{ij})\eta_i^k\right] + \frac{3}{5}\kappa^c$	$\eta = \eta^c + \sum_{j=1}^{s} \eta_j^k$
Pressure	$p = nT + \frac{2\pi}{3}\sum_{i=1}^{s}\sum_{j=1}^{s} \mu_{ji}(1+\alpha_{ij}) d_{ij}^3\, \chi_{ij}^{(0)} n_i\, n_j\, T_i$	
First-Order Cooling Rate	$\zeta^{(1,1)} = \frac{\sqrt{\pi}}{2}\frac{\left(2T/m\right)^{3/2}}{nT}\sum_{i=1}^{s}\sum_{j=1}^{s} e_{i,D} n_i n_j d_{ij}^2 \chi_{ij}^{(0)} m_j \mu_{ij}(1-\alpha_{ij}^2)\frac{\theta_j^{1/2}}{\theta_i^{3/2}(\theta_i+\theta_j)^{1/2}}$	
	$\zeta^{(1,0)} = \frac{-2\pi}{3nT}\sum_{i=1}^{s}\sum_{j=1}^{s} n_i n_j \mu_{ji} d_{ij}^3 \chi_{ij}^{(0)}(1-\alpha_{ij}^2) T_i$	$\zeta_u = \zeta^{(1,0)} + \zeta^{(1,1)}$
Bulk Viscosity	$\kappa = \kappa^c = \frac{2\sqrt{\pi}}{9}\sum_{i=1}^{s}\sum_{j=1}^{s} \mu_{ij}\, m_j\, n_i\, n_j \sqrt{\frac{2T}{m}} d_{ij}^4\, \chi_{ij}^{(0)}(1+\alpha_{ij})\left(\frac{\theta_i+\theta_j}{\theta_i\theta_j}\right)^{1/2}$	

To determine the number of species needed for the discrete approximation to accurately capture the given continuous PSD, the transport coefficients from the GHD theory are evaluated using the moment-based discrete approximation for increasing number of particle species (s). Namely, once the continuous PSD has been discretized for a given s (as described in Section II.B), the particle sizes and associated volume fractions ($\phi_i = n_i \pi d_i^3/6$) can be used in the GHD expressions of transport coefficients. More specifically, the transport coefficients $\zeta^{(0)}$, ζ_u, p, η, and κ given by GHD theory are compared for $s = 1$, $s = 2$, etc. over a range of restitution coefficients and overall solids fractions to determine at what value of s the predictions essentially collapse on one another (as detailed below). Results of this study provide a basis for using the least computational power (i.e., lowest value of s) while achieving an accurate approximation.

It is worthwhile to note that some transport coefficients (i.e., $\zeta^{(0)}$, ζ_u, p, η, κ, λ; see Table 1) are calculated as summations over each species, but exist as a single-valued quantity regardless of the number of species chosen. Because the remaining transport coefficients (i.e., D_{ij}, D_i^T, D_{ij}^F, $D_{a,i}$, L_{ij}) are calculated for each species (e.g., D_i^T) or for a species pairing (e.g., D_{ij}), a one-to-one comparison between approximations with different s is not possible. For instance, the prediction of D_1^T using an $s = 1$ approximation cannot be compared to the prediction of D_1^T for the $s = 2$ approximation since species 1 has a different size for each approximation. Though conductivity (λ) does not fall under this category, its summation includes D_i^T, a term that has been found to be discontinuous under certain conditions. Therefore, analyses of conductivity are omitted from this study.

The specific range of input parameters (solids fraction, restitution coefficient, etc.) used for each of the distributions considered here is given in Table 2. When three consecutive predictions of a transport coefficient, using increasing values of s (i.e., $s_{\min}$, $s_{\min}+1$, $s_{\min}+2$), lie within 2% of one another for the parameter space considered here (Table 2), the minimum number of discrete species is considered to be reached. An example of this methodology is displayed in Figure 3, which shows the dimensionless zeroth-order cooling rate as a function of restitution coefficient (e) for increasing values of s from 1-10. The zeroth-order cooling rate ($\zeta^{(0)}$) is non-dimensionalized by the average diameter of the distribution (d_{ave}), material density (ρ), and granular temperature (T). It is quite evident that the curves collapse when two or more discrete species are used in the approximation, which is a relatively small number. It is worthwhile to note that the minimum number of discrete species ($s_{\min}$) deemed necessary may be different depending on the specific transport coefficient analyzed.

As further verification of the $s_{\min}$ needed for the discrete approximation and for validation of the GHD theory itself, predictions from the theory for *discrete* approximations are also compared to molecular dynamics (MD) data of *continuous* size distributions undergoing simple shear flow [14]. The distributions examined in this MD-theory comparison are also contained in Table 2, along with the corresponding range of input parameters.

Table 2: Parameter space used to assess the number of discrete species needed to accurately represent a continuous PSD.

Type of Comparison	Continuous Distribution	Coefficient of Restitution	Volume Fraction	Distribution Width (σ/μ)
Kinetic-theory (GHD) predictions of $\zeta^{(0)}$, ξ_u, p, η, and κ for increasing values of s in the discrete approximation	Lognormal	0.50-0.99	10^{-8}-0.50	0, 0.1, 0.3, 0.5, 0.7, 0.9
	Gaussian	0.50-0.99	10^{-8}-0.50	0, 0.05, 0.1, 0.2, 0.3
	Coal Particles	0.50-0.99	10^{-8}-0.50	**N/A**
	Lunar Soil Simulant, OB-1	0.50-0.99	0.1	**N/A**
MD vs. kinetic-theory (GHD) predictions	Lognormal	0.85, 0.95	0.1, 0.3, 0.5	0, 0.1, 0.3, 0.5, 0.7
	Gaussian	0.85, 0.95	0.1, 0.3, 0.5	0, 0.05, 0.1, 0.2, 0.3

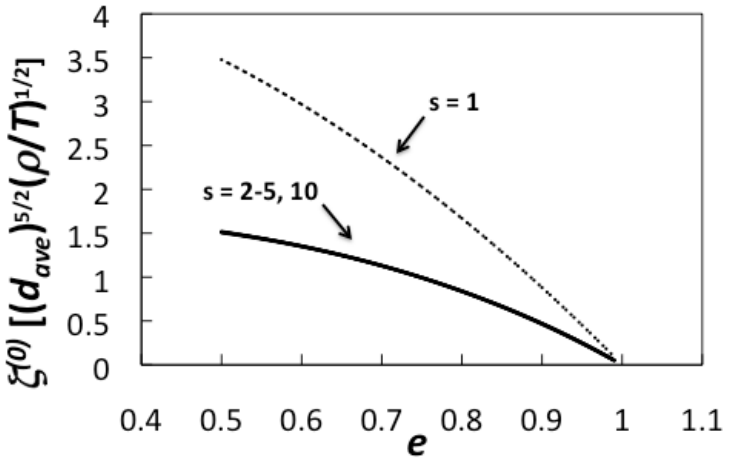

FIG. 3: GHD predictions of the dimensionless zeroth-order cooling rate as a function of restitution coefficient for various values of s. The discrete distributions shown here are approximations of a lognormal PSD with a distribution width σ/d_{ave} = 50% and an overall volume fraction $\phi = 0.3$.

III. RESULTS AND DISCUSSION

To determine the appropriateness of a (*discrete*) kinetic-theory-based prediction of a *continuous* PSD, the number of discrete species needed for the "collapse" of various transport coefficients ($\zeta^{(0)}$, ξ_u, p, η, and κ) over a range of parameters is first pursued for Gaussian and lognormal PSDs of different widths (Section III.A), as well as each experimentally-obtained PSD (Section III.B). A summary of the results is given in the following section (Section III.C).

Second, predictions of pressure and shear viscosity in a simple shear flow system obtained from (discrete) GHD theory is compared with MD simulations of continuous PSDs (Section III.D).

A. Discrete approximation of Gaussian and lognormal PSDs

To determine the number of species needed in kinetic-theory-based models to appropriately mimic continuous PSDs, the following transport coefficients were evaluated using GHD theory, the following transport coefficients are examined: zeroth-order cooling rate ($\zeta^{(0)}$), first-order cooling rate (ζ_u), pressure (p), shear viscosity (η), and bulk viscosity (κ). In particular, these quantities were evaluated for each continuous PSD using an increasing number of discrete species (s) to approximate the given PSD (as described in Section II.C). These evaluations were carried out over a range of restitution coefficients (e) and overall volume fractions (ϕ). Representative plots of the dimensionless pressure and shear viscosity are included in Figures 4-9; the remaining results are summarized in Table 3 for the sake of brevity. Both pressure and shear viscosity have been non-dimensionalized, where m is the particle mass associated with the average diameter of the distribution (d_{ave}).

Similar to Figure 3 for the dimensionless zeroth-order cooling rate, Figures 4 and 5 show how the pressure and shear viscosity vs. restitution coefficient, respectively, change with the number of species for *lognormal distributions* with $\phi = 0.3$ and distribution widths of $\sigma/d_{ave} = 10\%$ (Figures 4a and 5a) and $\sigma/d_{ave} = 70\%$ (Figures 4b and 5b). Expectedly, as the number of discrete species s used to approximate the continuous distribution increases, the curves begin to collapse on one another. As described in Section II.C, once a 2% or less error is established among three consecutive approximations (e.g., $s = 2, 3, 4$) of a transport coefficient over the entire range of restitution coefficients shown, the minimum number of species for desired accuracy ($s_{\min}$) has been determined. For instance, Figure 4a indicates that predictions of pressure using $s = 2$, 3, or 4 are extremely close to one another (< 2% change). Therefore, only 2 species are deemed necessary to approximate the pressure of a lognormal PSD with $\sigma/d_{ave} = 10\%$ and $\phi = 0.3$. Comparing Figure 4a to Figure 4b, it is evident that the number of species used in the discrete approximation of a lognormal PSD has a larger effect for wider distributions. Specifically, Figure 4a shows that the monodisperse prediction of pressure agrees qualitatively and quantitatively well with the polydisperse predictions (s = 1-10) for a narrow lognormal distribution ($\sigma/d_{ave} = 10\%$). However, for the wider continuous lognormal PSD ($\sigma/d_{ave} = 70\%$) of Figure 4b, the pressure predictions for $s > 1$ are quite different quantitatively than the monodisperse counterpart ($s = 1$). Moreover, Figure 4b shows that pressure predicted using s = 2-10 is slightly non-monotonic, whereas the monodisperse prediction increases monotonically with restitution coefficient. Nevertheless, both discretizations require 2 particles species for the established criterion to be met for granular pressure (i.e., $s_{\min} = 2$), regardless of vast differences in distribution width. Finally, as seen when comparing the shear viscosity of different distribution widths in Figures 5a and 5b, the trends are similar to those of pressure (Figures 4a and 4b), though $s_{\min} = 3$ for $\sigma/d_{ave} = 70\%$.

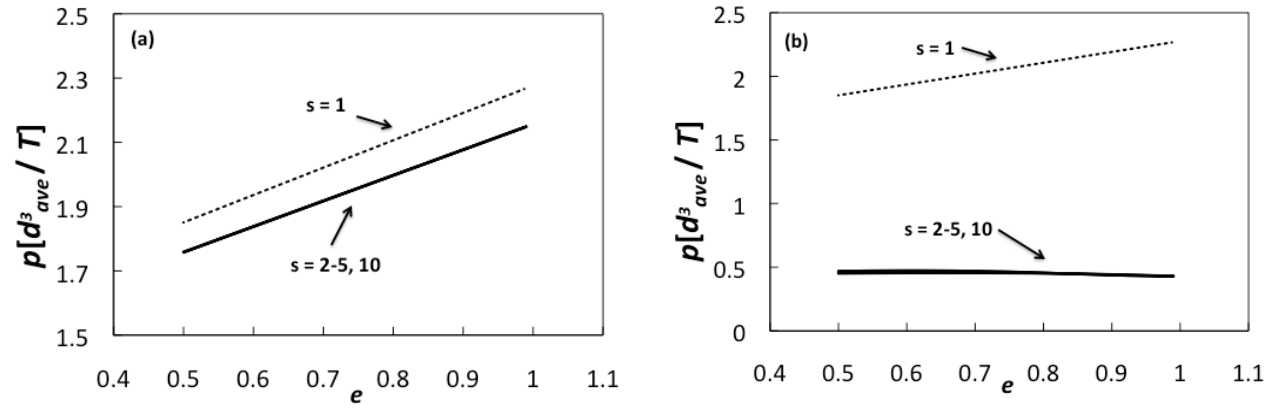

FIG. 4: Predictions of granular pressure as a function of coefficient of restitution for *lognormal* distributions with σ/d_{ave} of (a) 10% and (b) 70% using GHD theory. The overall volume fraction of the system is $\phi = 0.3$. See Tables A.3 and A.4 for discrete approximations.

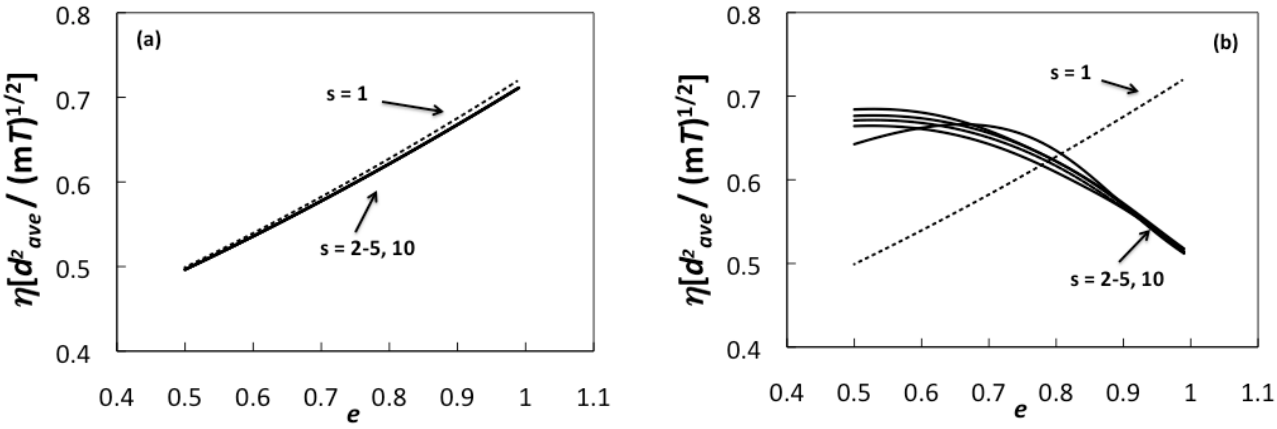

FIG. 5: Predictions of shear stress as a function of coefficient of restitution for *lognormal* distributions with σ/d_{ave} of (a) 10% and (b) 70% using GHD theory. The overall volume fraction of the system is $\phi = 0.3$. See Tables A.3 and A.4 for discrete approximations.

Analogous to Figures 4 and 5, Figures 6 and 7 show predictions of dimensionless pressure and shear viscosity for *Gaussian distributions* of σ/d_{ave} = 10% (Figures 6a and 7a) and σ/d_{ave} = 30% (Figures 6b and 7b). Lognormal and Gaussian distributions behave quite similarly for σ/d_{ave} = 10-30%, as the asymmetries of lognormal distributions are not prominent for such small distribution widths (see Figures 1a and 1c). Therefore, it is not surprising that Figures 4a and 6a for pressure and Figures 5a and 7a for shear viscosity are similar for the different distributions. Since Gaussian distributions are limited to a maximum σ/d_{ave} of 30% (otherwise unphysical negative diameters result), however, Figures 6b and 7b (σ/d_{ave} = 30%) do differ slightly from Figures 6a and 7a, respectively, though not nearly as much when comparing lognormal distributions over a wider range of distributions widths (e.g., comparing Figures 4a and 4b). It is also important to note that for pressure and shear viscosity, the widest Gaussian

distribution (σ/d_{ave} = 30%) requires only s_{min} = 2 and the widest lognormal distribution requires s_{min} = 3. In sum, very few particle species can be used to describe fairly wide continuous distributions.

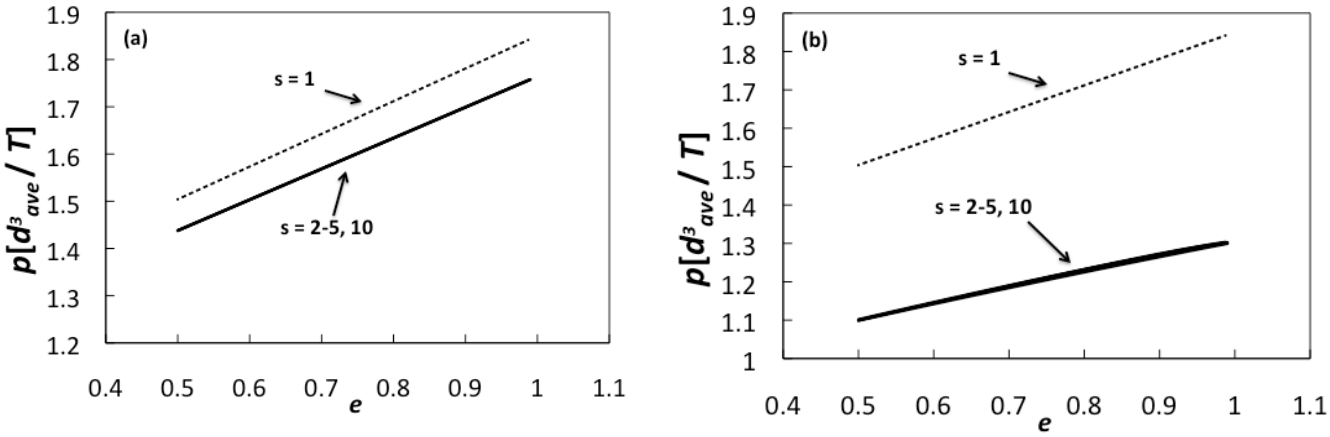

FIG. 6: Predictions of granular pressure as a function of coefficient of restitution for *Gaussian* distributions with σ/d_{ave} of (a) 10% and (b) 30% using GHD theory. The overall volume fraction of the system is ϕ = 0.3. See Tables A.1 and A.2 for discrete approximations.

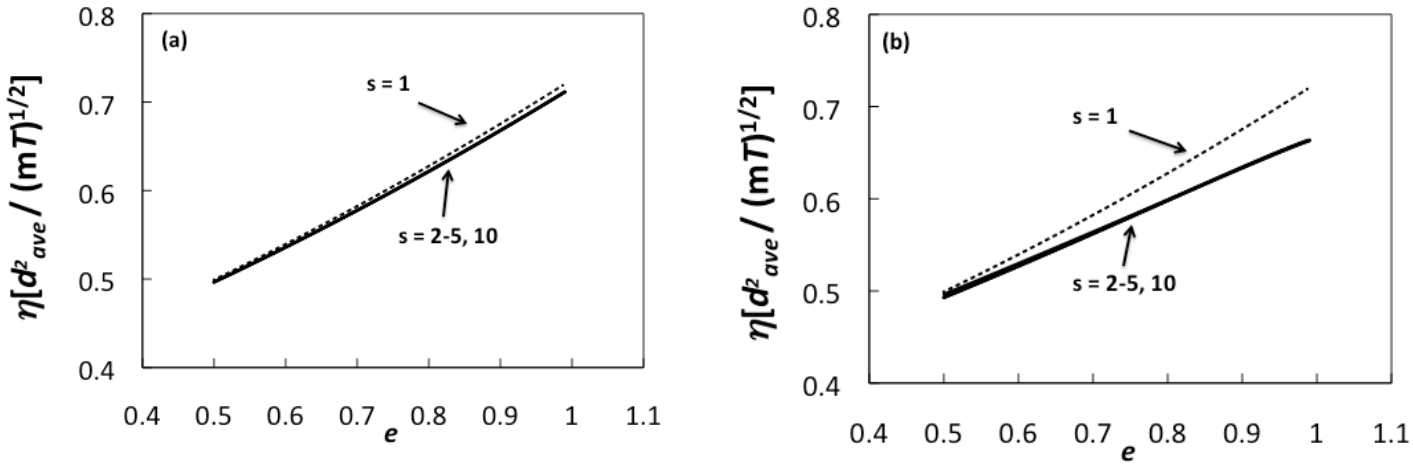

FIG. 7: Predictions of shear stress as a function of coefficient of restitution for *Gaussian* distributions with σ/d_{ave} of (a) 10% and (b) 30% using GHD theory. The overall volume fraction of the system is ϕ = 0.3. See Tables A.1 and A.2 for discrete approximations.

B. Discrete approximation of experimental PSDs

Results of dimensionless pressure and shear viscosity are also given for the *bidisperse NETL distribution of coal particles* (Figure 8). When the bidisperse mass-based distribution is converted to a number-based PSD, the resulting distribution is extremely right-skewed (Figure 1f), similar to a very wide lognormal distribution. Figure 8a shows that the monodisperse approximation (s = 1) of pressure is both qualitatively and quantitatively different than the polydisperse (s > 2) approximations. More notable is the discrepancy among discrete approximations for the shear viscosity (Figure 8b). The predictions using s = 3 and s = 4 are

almost indistinguishable; however, adding a fifth particle species causes a significant change in the prediction of shear viscosity. Predictions of this NETL distribution are obtained to $s = 10$ to ensure this pattern does not continue. Accordingly, the number of species required to accurately capture the pressure and shear viscosity of the NETL distribution is $s_{\min} = 6$ for both quantities. The need for a larger number of species to accurately approximate the NETL distribution comes about from the width of the PSD. Specifically, Figures 1g and 1h show the large width of the NETL distribution relative to a lognormal distribution with $\sigma/d_{ave} = 90\%$. Because the frequencies associated with the NETL distribution remains moderate over a larger range of particle diameters than those in the lognormal distribution, the coal PSD contains a larger width of particle diameters. Therefore, it is reasonable that the values of s_{min} for the NETL distribution are greater than or equal to the values of s_{min} for the Gaussian and lognormal distributions investigated here.

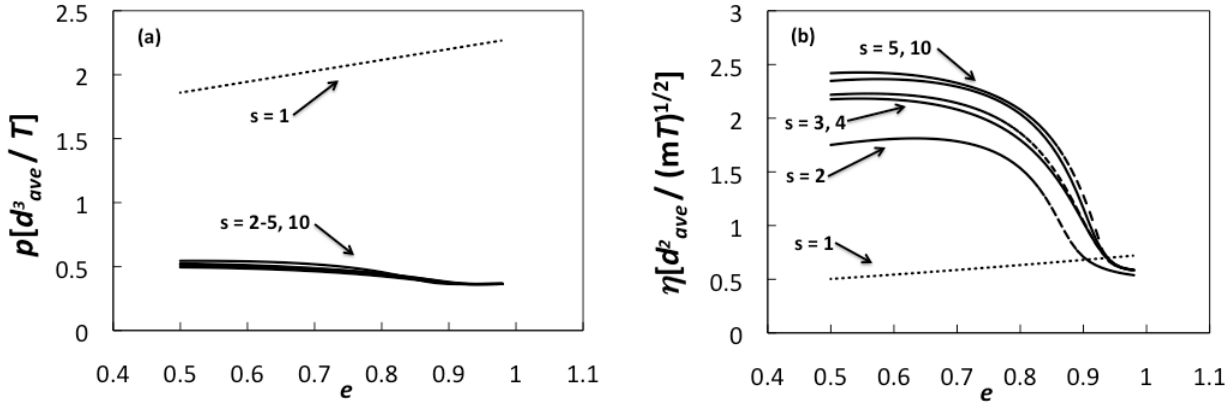

FIG. 8: Predictions of (a) granular pressure and (b) shear stress as a function of coefficient of restitution for *NETL distribution of coal feedstock* for gasification. The overall volume fraction of the system is $\phi = 0.3$. See Table A.5 for discrete approximations.

Referring back to Figures 1g and 1h, the width of the *NASA lunar soil simulant OB-1* is compared to that of a lognormal distribution with a similar arithmetic mean and a distribution width of $\sigma/d_{ave} = 90\%$, showing that OB-1 distribution is much wider than the lognormal distributions examined. Mimicking the lunar PSD with an extremely wide lognormal distribution, it was determined that the corresponding lognormal PSD has a width of about $\sigma/d_{ave} = 250\%$. For this lunar PSD, matching more than 9 moments does not change the discrete approximation; therefore, only predictions for $s = 1 – 9$ are shown in Figure 9. Due to the large width of lunar PSDs, a large number of species is required to accurately predict each of the transport coefficients compared to the other PSDs investigated here. The pressure predicted using only one particle species to approximate the lunar simulant OB-1 is orders of magnitude larger than the predictions for $s = 2 – 9$. Including the $s = 1$ prediction of dimensionless pressure in Figure 9a would cause the $s = 2 – 9$ predictions to be nearly indistinguishable, so it is omitted from the plot. Though only predictions up to $s = 9$ are reported, collapse of curves occurs at $s_{\min} = 7$ for pressure (Figure 9a) and begins at $s_{\min} = 8$ for shear viscosity (Figure 9b). Each transport coefficient examined here, with the exception of pressure, requires at least eight particle species to obtain an accurate prediction ($s_{\min} = 8$), as is the case for the lunar soil itself and other lunar soil simulants (figures not shown).

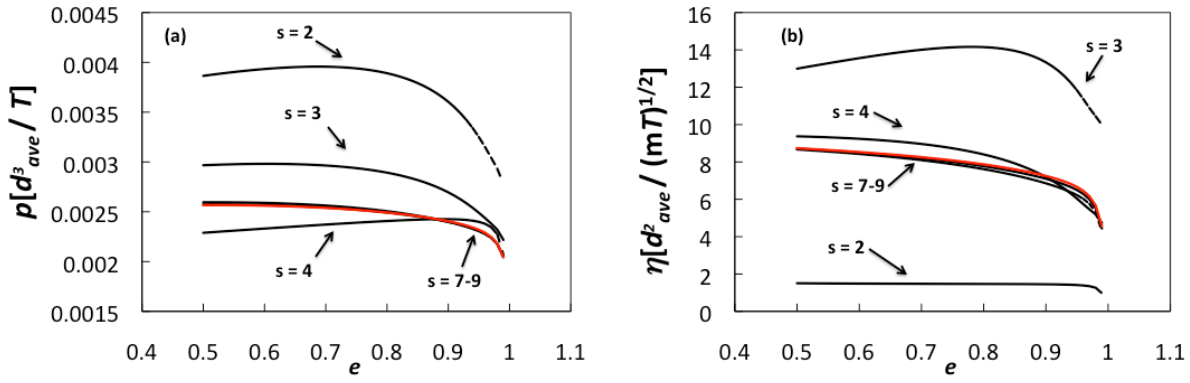

FIG. 9: Predictions of (a) granular pressure and (b) shear stress as a function of coefficient of restitution for the *OB-1* lunar PSD. The overall volume fraction of the system is $\phi = 0.1$. The $s = 9$ approximation is given by the solid red line, for color versions. See Table A.6 for discrete approximations.

C. Summary of discrete approximations

For the sake of brevity, only figures for pressure and shear viscosity were shown above for each of the continuous PSDs investigated. The results obtained for the remaining transport coefficients ($\zeta^{(0)}$, ζ_u, and κ) behave in a similar fashion. A summary of these results over the parameter space evaluated is given in Table 3. Each value in Table 3 corresponds to the minimum number of species ($s_{\min}$), as determined by the 2% criterion established in Section II.B. It is important to note that the number of species required to accurately represent a continuous PSD with σ/d_{ave} = 0-90% is generally quite low ($s_{\min}$ = 1 – 5). However, the much wider distributions (i.e., lunar soil simulant) may require as many as 8 particle species ($s_{\min}$ = 8).

Table 3: Summary of minimum number of species (s_{min}) required to accurately approximate Gaussian, lognormal, bidisperse coal (NETL), and lunar soil (OB-1) size distributions with a discrete number of species.

		Gaussian			Lognormal					NETL	OB-1
	σ/d_{ave}	10%	20%	30%	10%	30%	50%	70%	90%		
	ϕ										
Zeroth-Order Cooling Rate	0.05	2	2	3	2	2	3	4	4	5	
	0.1	2	2	2	2	2	3	4	4	5	8
	0.3	2	2	2	2	2	3	4	4	5	
	0.5	2	2	2	2	2	3	4	4	3	
First-Order Cooling Rate	0.05	1	2	2	2	2	2	4	4	6	
	0.1	1	2	2	2	2	2	4	4	6	8
	0.3	2	2	2	2	2	2	4	4	5	
	0.5	2	2	2	2	2	2	3	3	6	
Pressure	0.05	2	2	2	2	2	2	2	2	2	
	0.1	2	2	2	2	2	2	2	3	3	7
	0.3	2	2	2	2	2	2	3	4	5	
	0.5	2	2	2	2	2	2	3	4	6	
Shear Viscosity	0.05	1	2	2	1	2	4	5	5	5	
	0.1	1	2	2	1	2	4	4	4	5	8
	0.3	1	2	2	1	2	3	3	4	6	
	0.5	1	2	2	1	2	2	3	5	6	
Bulk Viscosity	0.05	2	2	2	2	2	2	4	4	5	
	0.1	1	2	2	1	2	2	4	4	5	8
	0.3	1	2	2	1	2	2	3	4	6	
	0.5	1	2	2	1	2	2	3	5	6	

Another notable trend that is revealed in Table 3 is that distribution width generally has a larger effect on the number of species required for an accurate discretization ($s_{\min}$) of a given continuous PSD than does the volume fraction. More specifically, the values in Table 3 increase more within rows (varying σ/d_{ave}) than within columns (varying ϕ). To better illustrate this trend, Figure 10 displays the dependency of number of discrete species required on both distribution width (Fig. 10a) and overall volume fraction (Fig. 10b). A sufficient increase in distribution width (σ/d_{ave} = 0-90%) always shows an increase to the number of species required, whereas the increases volume fraction may decrease (η) or not affect ($\xi^{(0)}$, ζ_u , p, κ) the number of species needed. For instance, Figure 10b shows that predictions for shear stress require fewer species at higher volume fractions, whereas the remaining transport coefficients require the same number of species regardless of the volume fraction ($\phi = 10^{-8}$ - 0.5). In sum, for all but one coefficient (η), s is independent of ϕ, though the same is not true for σ/d_{ave}.

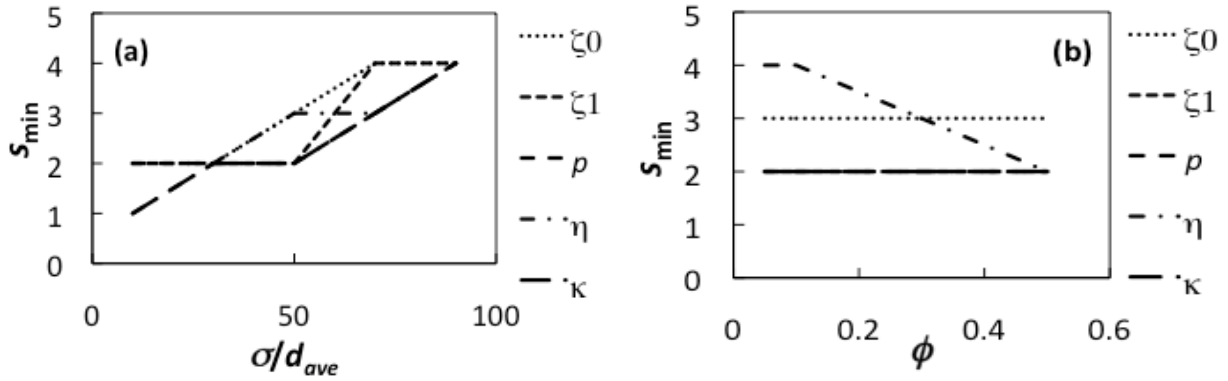

FIG. 10: Minimum number of species required ($s_{\min}$) for a (a) lognormal distribution with a volume fraction of $\phi = 0.3$ and varying σ/d_{ave} and (b) a lognormal distribution with σ/d_{ave} = 50% and varying ϕ.

Finally, Table 3 can be used as a guide for determining how many species are needed for a specific flow system. For instance, if a specific flow geometry is dominated by the granular pressure and contains a Gaussian PSD with σ/d_{ave} = 30% and the overall volume fraction is predominantly ϕ = 0.05, only two particle species are necessary for the level of accuracy described here (2%). However, if a different flow geometry with the same PSD and overall ϕ is dominated by the zeroth-order cooling rate, three particle species are necessary for a similarly accurate approximation. Thus, in order to use these results in a practical application, some information must be known about the dominating effects of a system *a priori*. Alternatively, the maximum value of $s_{\min}$ among all transport coefficients examined may be used as a guide. Further discussion on the pros and cons of the use of Table 3 (or a similar analysis for other distributions) as a guide for determining the appropriate number of discrete species for a given application is included in Concluding Remarks (Section IV).

D. Comparison with molecular dynamics (MD) simulations

Molecular dynamics (MD) simulations of lognormal and Gaussian distributions undergoing simple shear flow (SSF) have been performed by Dahl, Clelland, and Hrenya [14]. In the current work, the simulation data is used not only to confirm for the minimum number of species ($s_{\min}$) required for an accurate discrete approximation (as reported in previous section), but also to test the accuracy of the GHD theory. The parameters used as inputs for the MD simulations are included in Table 2; the outputs include both pressure and viscosity. This MD data is displayed in Figures 11 and 12 for lognormal and Gaussian distributions of various widths, respectively. Also shown in Figures 11 and 12 are the predictions obtained from GHD theory for several discrete approximations (various s) of the given continuous PSDs. Note that these predictions were obtained by first solving the energy equation (the only nontrivial equation for SSF) for granular temperature (T) using the appropriate discrete approximation, and then using this value of T to evaluate the pressure and shear viscosity. The DOE-based code MFIX (Multiphase Flow with Interphase Exchanges, www.mfix.netl.doe.gov), which contains the GHD theory, was used for these purposes.

The results displayed in Figures 11 and 12 demonstrate that the number of species required for an accurate approximation of pressure and shear viscosity is correctly predicted by the approach described in the previous section. More specifically, a value of $s = 3$ is sufficient in each case, as consistent with the values given in Table 3 (whereas smaller values of s do not achieve the desired accuracy). Figures 11 and 12 clearly show drastic differences between the monodisperse approximation and the ternary approximation ($s = 3$), where the ternary prediction using GHD theory is far more accurate. However, increasing the number of species to $s = 5$ in the discrete approximation shows little to no change at all, which further supports the predictions summarized in Table 3.

Though the monodisperse approximation of pressure and shear viscosity using GHD theory is appropriate in the monodispesre limit (i.e., $\sigma/d_{ave} = 0$), a larger number of particle species is required as the width of the PSD increases. Recall that for the MD data, the root mean cube of the continuous distribution was held constant ($d_{rmc} = 72.6$ microns). However, the dimensionless pressure and shear viscosity are plotted with respect to σ/d_{ave}. In order to maintain a constant d_{rmc} while increasing σ/d_{ave}, d_{ave} decreases accordingly, and thus the monodisperse approximations (i.e., $s = 1$) do not remain constant along the x-axis in Figures 11 and 12.

Regarding the validity of the GHD theory to predict properties of a continuous PSD, it is clear from Figures 11 and 12 that the GHD predictions using $s = 3$ and MD data are in close qualitative, as well as quantitative, agreement. From a qualitative perspective, the MD data displayed in Figures 11 and 12 indicate that the quantities behave non-monotonically with respect to the distribution width. This qualitative trend is captured by the polydisperse ($s = 3, 5$) GHD predictions, but not the monodisperse counterparts ($s=1$). Perhaps more importantly is the quantitative agreement between GHD predictions and MD data. For instance, Figure 12b shows a maximum percent difference between the $s = 3$ prediction and the MD data of 4%. For the widest distributions, GHD predictions have similar accuracy when compared to MD data as in the monodisperse limit ($\sigma/d_{ave} = 0$). Therefore, no loss of accuracy arises from the polydisperse theory itself (relative to monodisperse), nor due to the discrete approximations of continuous PSDs.

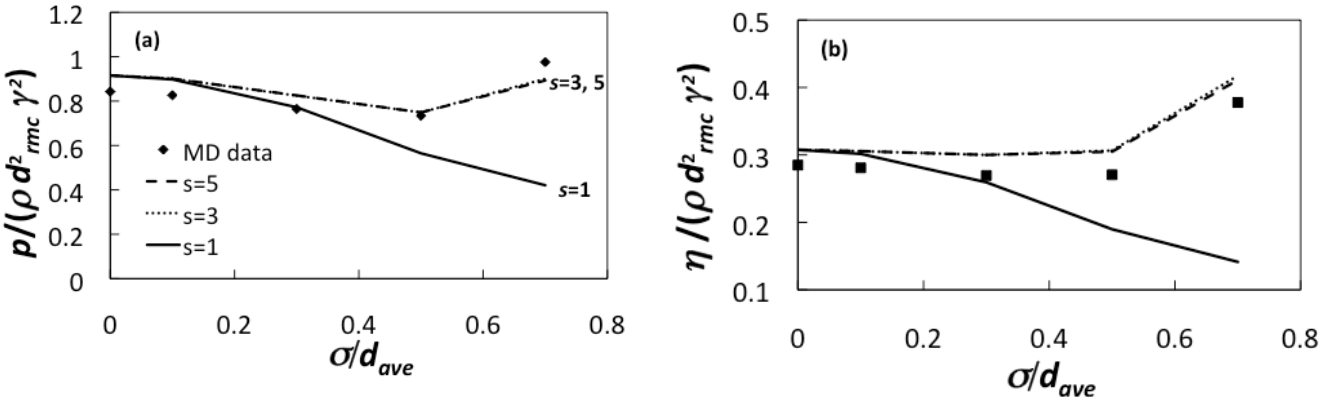

FIG. 11: Dimensionless (a) pressure and (b) shear stress as a function of σ/d_{ave} for *lognormal* distributions. Comparison of MD simulation data to GHD theory predictions using an increasing number of particle species. Overall volume fraction: $\phi = 0.3$, restitution coefficient: $\alpha = 0.85$.

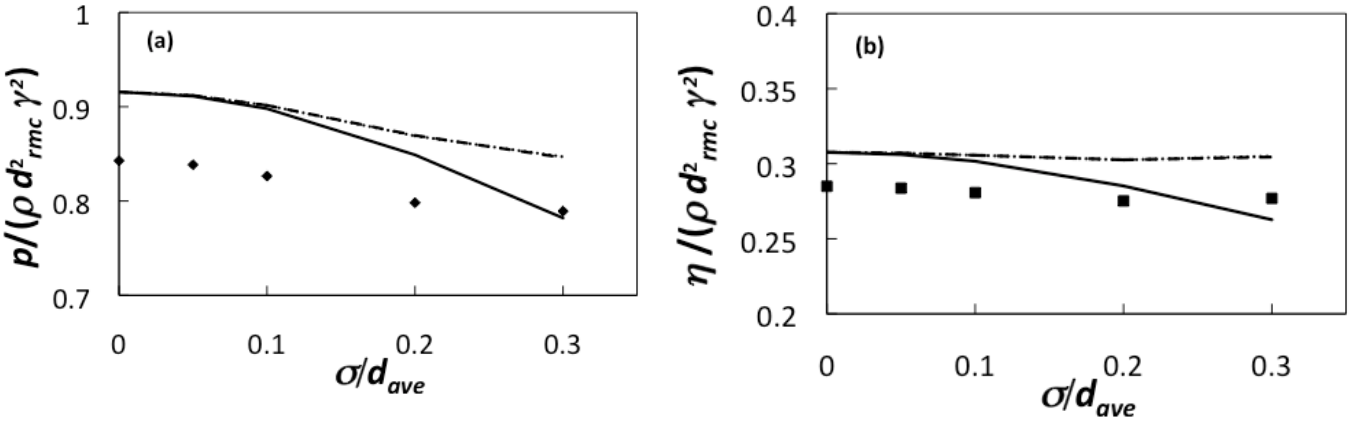

FIG. 12: Dimensionless (a) pressure and (b) shear stress as a function of σ/d_{ave} for *Gaussian* distributions. Comparison of MD simulation data to GHD theory predictions using an increasing number of particle species. Overall volume fraction: $\phi = 0.3$, restitution coefficient: $\alpha = 0.85$. See Figure 11a for legend.

IV. CONCLUDING REMARKS

The overall aim of this work is to assess the ability of polydisperse, kinetic-theory-based models to describe continuous size distributions. In particular, the objective of this effort is twofold: (i) to determine the number of *discrete* species (s) required to accurately approximate a *continuous* PSD, and (ii) to validate the theoretical predictions via a comparison with molecular dynamics (MD) simulations of continuous PSDs. With regards to the first objective, the moments of the discrete approximation are first matched with moments of the given continuous PSD. Next, five transport coefficients ($\xi^{(0)}$, ξ_u , p, η, κ) given by GHD theory [1, 2] are evaluated for the discrete approximations with various s, and the minimum number of species ($s_{\min}$) required to accurately capture the continuous PSD is identified via the "collapse" of these transport coefficients at higher values of s. It is worthwhile to note that this approach, unlike

previous works [20-23], does not involve the computational fluid dynamics (CFD) simulations of specific systems thereby making it more universal and computationally efficient than previous works. With regard to the second objective, a comparison between MD data [14] and theoretical predictions at $s = s_{\min}$ is presented to determine the validity of GHD predictions of pressure and shear viscosity.

Regarding the number of species required to accurately represent a continuous PSD, the transport coefficients $\zeta^{(0)}$, ζ_u , p, η, and κ given by GHD theory are examined over a range of coefficient of restitution (e), overall volume fraction (ϕ), and distribution width (σ/d_{ave}). Both ideal (Gaussian and lognormal) and experimental (bidisperse coal particles and lunar soil simulants) continuous PSDs are considered. The number of species required for an accurate approximation depends on the transport coefficient of interest. For the Gaussian distributions analyzed, the maximum number of species required is typically 2 regardless of transport coefficient. However, the wider lognormal distributions require more species for the same accuracy level. For example, $s_{\min} = 5$ for the shear and bulk viscosities of lognormal distributions with a width of $\sigma/d_{ave} = 90\%$. Because the number-based frequency distribution of the NETL distribution is wider than the lognormal distributions analyzed, it is found that a greater number of species is needed for an accurate approximation ($s_{\min} = 6$). Even wider than the NETL distribution are the distributions of the lunar soil simulants. An examination of the lunar PSD known as OB-1 shows that at least 8 particle species need to be considered in the discrete approximation for accurate predictions.

The aforementioned results indicate that an increase in distribution width leads to a corresponding increase in the number of species required to accurately approximate the PSD. However, the same is not true for volume fraction of the granular mixture. Increasing overall volume fraction may lead to a decrease or no change to the number of required species.

The second portion of this work focuses on the comparison of GHD predictions of pressure and shear viscosity with those given by previous MD simulations [14] for continuous PSDs. GHD predictions utilize a discrete approximation to the Gaussian and lognormal PSDs present in the MD simulations. Results indicate that the polydisperse prediction ($s = 3$) is qualitatively and quantitatively more accurate than the $s = 1$ counterpart, which is in agreement with the results of the former analysis on the discretization of continuous PSDs. The comparison also reveals that the level of accuracy (~5%) between MD and GHD predictions in distributions of increasing widths is similar to that of monodisperse systems. Accordingly, the results provide validation for both the moment-based approximation to continuous PSDs and the polydisperse theory itself. Furthermore, because the GHD theory uses the Enskog equation as its starting point, the good match obtained between MD and GHD theory displayed here provides support for the applicability of the Enskog equation to moderately dense flows.

Finally, a benefit of the current effort is that the analysis of some transport coefficients ($\zeta^{(0)}$, ζ_u, p, η, κ) is system-independent - i.e., it does not depend on the flow geometry under consideration since the most general form of the transport coefficients is utilized. Nonetheless, it is worthwhile to note that the analysis here is restricted to the transport coefficients that are not indexed to specific species or species pairs (ie., $\zeta^{(0)}$, ζ_u , p, η, κ). Because some transport coefficients are indexed to specific species or species pairs (ie., D_{ij}, D_i^T, D_{ij}^F, $D_{q,i}$, L_{ij}), a one-to-one comparison of these quantities for successive values of s is not possible. For example, the $s = 2$ prediction of D_{12} cannot be compared to the $s = 3$ approximation of D_{12} because species 1 and 2 have different sizes for each approximation. Accordingly, the results of this work may be used differently depending on the system under analysis. If the system is dominated by one or more of

the transport coefficients investigated here, then this analysis provides a method for determining the number of species needed for the discrete approximation. An example of such a system is simple shear flow, in which the only constitutive quantities that are included in the governing equations are $\zeta^{(0)}$, p, and η. Otherwise, results of this effort should be used as a guide until further work is done to determine the effects of the remaining transport coefficients. An example of such a system is one which segregates, since the governing equations of a segregating system would include D_{ij}. Nonetheless, because the discrepancy between the number of species required amongst the transport coefficients considered here is relatively small, it is possible that the same may be true for the transport coefficients not examined here (ie., D_{ij}, D_i^T, D_{ij}^F, $D_{q,i}$, L_{ij}). However, this matter remains to be tested and will be the focus of future work.

ACKNOWLEDGMENTS

The authors would like to thank Larry Shadle of DOE NETL for providing the bidisperse gasifier data, Rodney Fox for providing code to obtain the discrete approximations, and Vicente Garzó for fruitful discussions. Also, we are grateful for the funding support by the Department of Energy (DE-FC26-07NT43098) and the National Aeronautics and Space Administration (NNX09AD07A).

APPENDIX A: DISCRETE APPROXIMATIONS

Table A.1: Discrete approximations for a *Gaussian distribution of* $\sigma/d_{ave} = 10\%$ for s = 1-10. Values contained in the table correspond to the dimensionless diameters (d/d_{ave}).

		Species Number									
		1	**2**	**3**	**4**	**5**	**6**	**7**	**8**	**9**	**10**
Approximation	$s = 1$	1	0.9000	0.8268	0.7666	0.7143	0.6676	0.6249	0.5832	0.1946	0
	$s = 2$		1.1000	1.0000	0.9258	0.8644	0.8111	0.7633	0.7176	0.6091	0.5616
	$s = 3$			1.1732	1.0742	1.0000	0.9383	0.8845	0.8344	0.7408	0.6923
	$s = 4$				1.2334	1.1356	1.0617	1.0000	0.9442	0.8558	0.8050
	$s = 5$					1.2857	1.1889	1.1154	1.0522	0.9643	0.9103
	$s = 6$						1.3324	1.2366	1.1620	1.0711	1.0125
	$s = 7$							1.3750	1.2787	1.1800	1.1147
	$s = 8$								1.4130	1.2957	1.2200
	$s = 9$									1.4291	1.3327
	$s = 10$										1.4633

Table A.2: Discrete approximations for a *Gaussian distribution of* $\sigma/d_{ave} = 30\%$ for s = 1-10. Values contained in the table correspond to the dimensionless diameters (d/d_{ave}).

		Species Number									
		1	**2**	**3**	**4**	**5**	**6**	**7**	**8**	**9**	**10**
Approximation	$s = 1$	1	0.7000	0.4804	0.2997	0.1429	0.0027	0	0	0	0
	$s = 2$		1.3000	1.0000	0.7774	0.5933	0.4332	0.2900	0.1593	0.0384	0.0000
	$s = 3$			1.5196	1.2226	1.0000	0.8150	0.6537	0.5090	0.3769	0.2547
	$s = 4$				1.7003	1.4067	1.1850	1.0000	0.8383	0.6930	0.5602
	$s = 5$					1.8571	1.5668	1.3463	1.1617	1.0000	0.8545
	$s = 6$						1.9973	1.7100	1.4910	1.3070	1.1455
	$s = 7$							2.1251	1.8407	1.6231	1.4398
	$s = 8$								2.2434	1.9616	1.7453
	$s = 9$									2.3538	2.0745
	$s = 10$										2.4578

Table A.3: Discrete approximations for a *lognormal distribution of* $\sigma/d_{ave} = 10\%$ for s = 1-10. Values contained in the table correspond to the dimensionless diameters (d/d_{ave}).

		Species Number									
		1	**2**	**3**	**4**	**5**	**6**	**7**	**8**	**9**	**10**
Approximation	***s* = 1**	1	0.9139	0.8578	0.8156	0.7815	0.7530	0.7285	0.6885	0	0
	***s* = 2**		1.1162	1.0201	0.9565	0.9084	0.8696	0.8370	0.7909	0.7208	0.7208
	***s* = 3**			1.2131	1.1098	1.0406	0.9880	0.9453	0.8913	0.8256	0.8256
	***s* = 4**				1.3016	1.1920	1.1181	1.0615	0.9969	0.9290	0.9290
	***s* = 5**					1.3855	1.2703	1.1919	1.1125	1.0382	1.0382
	***s* = 6**						1.4669	1.3461	1.2436	1.1580	1.1580
	***s* = 7**							1.5466	1.3997	1.2943	1.2943
	***s* = 8**								1.6034	1.4570	1.4570
	***s* = 9**									1.6702	1.6702
	***s* = 10**										0

Table A.4: Discrete approximations for a *lognormal distribution of* $\sigma/d_{ave} = 70\%$ for s = 1-10. Values contained in the table correspond to the dimensionless diameters (d/d_{ave}).

		Species Number									
		1	**2**	**3**	**4**	**5**	**6**	**7**	**8**	**9**	**10**
Approximation	***s* = 1**	1	0.7500	0.6496	0.5979	0.5681	0.5500	0.5385	0.5311	0.5263	0.5231
	***s* = 2**		2.9601	2.2201	1.9179	1.7612	1.6708	1.6156	1.5806	1.5581	1.5434
	***s* = 3**			7.5872	5.7053	4.9288	4.5241	4.2900	4.1468	4.0562	3.9977
	***s* = 4**				18.3021	13.7936	11.9215	10.9425	10.3753	10.0279	9.8080
	***s* = 5**					42.7614	32.2804	27.9110	25.6216	24.2935	23.4794
	***s* = 6**						98.0689	74.1161	64.1054	58.8532	55.8040
	***s* = 7**							222.3586	168.1791	145.4994	133.5897
	***s* = 8**								500.5330	378.7733	327.7505
	***s* = 9**									1121.4452	848.9437
	***s* = 10**										2504.9058

Table A.5: Discrete approximations for the *coal gasifier distribution* (NETL) for s = 1-9. Values contained in the table correspond to the dimensionless diameters (d/d_{ave}).

		Species Number								
		1	**2**	**3**	**4**	**5**	**6**	**7**	**8**	**9**
Approximation	***s* = 1**	1	0.9612	0.9476	0.9395	0.9335	0.9309	0.9290	0.9284	0.9283
	***s* = 2**		7.6294	5.3369	4.2419	3.4859	3.1022	2.6657	2.3763	2.2416
	***s* = 3**			20.8009	14.7226	10.5194	7.7434	5.1838	3.8168	3.1689
	***s* = 4**				42.9550	22.0832	14.4580	10.9064	6.1549	4.4828
	***s* = 5**					49.5855	24.5743	17.7941	11.1512	6.3404
	***s* = 6**						49.9076	25.3766	17.9522	11.1572
	***s* = 7**							49.9185	25.3971	17.9532
	***s* = 8**								49.9185	25.3972
	***s* = 9**									49.9185

Table A.6: Discrete approximations for the *lunar soil simulant* (OB-1) for s = 1-9. Values contained in the table correspond to the dimensionless diameters (d/d_{ave}).

		Species Number								
		1	**2**	**3**	**4**	**5**	**6**	**7**	**8**	**9**
Approximation	***s* = 1**	1	0.9808	0.9762	0.9695	0.9575	0.9444	0.9244	0.8999	0.8788
	***s* = 2**		77.6791	62.5759	47.7713	32.6262	23.4533	15.7673	10.7574	8.1814
	***s* = 3**			2424.9892	929.0314	448.9339	276.6979	159.0545	93.5850	63.1384
	***s* = 4**				5440.3001	2323.1111	898.6763	505.5755	263.2646	172.0346
	***s* = 5**					5882.1552	2479.7679	1101.1664	552.0439	307.1937
	***s* = 6**						5890.8442	2487.2071	1112.5807	555.8081
	***s* = 7**							5890.8941	2487.2663	1112.7247
	***s* = 8**								5890.8941	2487.2664
	***s* = 9**									5890.8941

REFERENCES

1. Garzó, V., C.M. Hrenya, and J.W. Dufty, *Enskog theory for polydisperse granular mixtures. II. Sonine polynomial approximation.* Physical Review E, 2007. **76**(3): p. 031304.
2. Garzó, V., J.W. Dufty, and C.M. Hrenya, *Enskog theory for polydisperse granular mixtures. I. Navier-Stokes order transport.* Physical Review E, 2007. **76**(3): p. 031303.
3. Curtis, J.S. and B. van Wachem, *Modeling particle-laden flows: A research outlook.* AIChE Journal, 2004. **50**(11): p. 2638-2645.
4. Muzzio, F.J., T. Shinbrot, and B.J. Glasser, *Powder technology in the pharmaceutical industry: the need to catch up fast.* Powder Technology, 2002. **124**(1-2): p. 1-7.
5. Sundaresan, S., *Some outstanding questions in handling of cohesionless particles.* Powder Technology, 2001. **115**(1): p. 2-7.
6. Hrenya, C.M., *Kinetic theory for granular materials: Polydispersity*, in *Computational Gas-Solids Flows and Reacting Systems: Theory, Methods and Practice*, S.P., M. Syamlal, and T. O'Brien, Editor. 2011, IGI Global: Hershey, PA.
7. Chew, J. W., J. Wolz, and C. M. Hrenya, *Axial segregation in bubbling gas-fluidized beds with Gaussian and lognormal Distributions of Geldart group B particles*. AIChE Journal, 2010. **56**: p. 3049-3061.
8. Chew, J. W. and C. M. Hrenya, *Link between bubbling and segregation patterns in gas-fluidized beds with continuous size distributions*. AIChE Journal, 2011. **57**: p. 3003-3011.
9. Zamankhan, P., *Kinetic theory of multicomponent dense mixtures of slightly inelastic spherical particles.* Physical Review E, 1995. **52**(5): p. 4877-4891.
10. Mathiesen, V., et al., *Experimental and computational study of multiphase gas/particle flow in a CFB riser.* AIChE Journal, 1999. **45**(12): p. 2503-2518.
11. Iddir, H. and H. Arastoopour, *Modeling of multitype particle flow using the kinetic theory approach.* AIChE Journal, 2005. **51**(6): p. 1620-1632.
12. Iddir, H., H. Arastoopour, and C.M. Hrenya, *Analysis of binary and ternary granular mixtures behavior using the kinetic theory approach.* Powder Technology, 2005. **151**(1- 3): p. 117-125.
13. Remy, B., J.G. Khinast, and B.J. Glasser, *Polydisperse granular flows in a bladed mixer: Experiments and simulations of cohesionless spheres.* Chemical Engineering Science, 2011. **66**(9): p. 1811-1824.
14. Dahl, S., R. Clelland, and C.M. Hrenya, *Three-dimensional, rapid shear flow of particles with continuous size distributions.* Powder Technology, 2003. **138**(1): p. 7-12.
15. Dahl, S., R. Clelland, and C.M. Hrenya, *The effects of continuous size distributions on the rapid flow of inelastic particles.* Physics of Fluids, 2002. **14**: p. 1972.
16. Dahl, S. and C.M. Hrenya, *Size segregation in rapid, granular flows with continuous size distributions.* Physics of Fluids, 2004. **16**: p. 1.
17. Battler, M.M. and J.G. Spray, *The Shawmere anorthosite and OB-1 as lunar highland regolith simulants.* Planetary and Space Science, 2009. **57**(14-15): p. 2128-2131.17.
18. Fan, R. and R.O. Fox, *Segregation in polydisperse fluidized beds: Validation of a multi-fluid model.* Chemical Engineering Science, 2008. **63**(1): p. 272-285.
19. Gordon, R.G., *Error bounds in spectroscopy and nonequilibrium statistical mechanics.* Journal of Mathematical Physics, 1968. **9**: p. 1087-1092.

20. Fan, R., D.L. Marchisio, and R.O. Fox, *Application of the direct quadrature method of moments to polydisperse gas-solid fluidized beds.* Powder Technology, 2004. **139**(1): p. 7-20.
21. Isben, C.H., E. Helland, B.H. Hjertager, T. Solberg, L. Tadrist, and R. Occelli, *Comparison of multi-fluid and discrete particle modeling in numerical predictions of gas particle flow in circulating fluidized beds.* Powder Technology, 2004. **149**(1): p. 29-41.
22. Mathiesen, V., T. Solberg, and B.H. Hjertager, *Predictions of gas/particle flow with an Eulerian model including a realistic particle size distribution.* Powder Technology, 2000. **112**(1-2): p. 34-45.
23. Sanyal, J., D.L. Marchisio, R.O. Fox, and K. Dhanasekharan, *On the comparison between population balance models for CFD simulation of bubble columns.* Industrial & Engineering Chemistry Research, 2005. **44**(14): p. 5063-5072.

APPENDIX I

Table 14. *Key features and modeling techniques of the CFD model BFB1.*

Model Name:	**BFB1 MONO**	**BFB1 BI**	**BFB1 PB**	**BFB1 PB (R)**	**BFB1 DEM**
Model features	Euerian-Eulerian	Euerian-Eulerian	Eulerian-Eulerian + Population Balance	Eulerian-Eulerian + Population Balance	Euler-Lagrangian
No. of computational cells	198,000	198,000	198000	198000	237,000
Typical wall-clock time for fully developed conditions	15 hrs on eight processors	15 hrs on eight processors	18 hours on 8 processors	18 hours on 8 processors	24 hrs in a 4 processor machine
Time interval for time-averaged results	15 seconds	15 seconds	9 seconds	80 seconds	15s
Sub-models used					
- Wall boundary conditions	No-Slip for gas and solids				Reflect BC with a ew of 0.5
- Drag	Fluid/Solid only Gibilaro with c1=0.2-0.25				Wen-Yu
- Granular temperature	Algebraic, Syamlal				NA
- Collisional models	Kinetic Theory based, Granular Viscosity - Gidaspow, Solids pressure - Lun				DEM based
Treatment of the particle phase	Monodispersed spherical particles, particle diameter of 80 microns	Two particulate phases, 80 microns and 30 microns	Particle Size Distribution with Population Balance, Multi-velocity Discrete Method with 11 classes distributed over 2 phases.	Particle Size Distribution with Population Balance, Multi-velocity Discrete Method with 11 classes distributed over 2 phases. Granular Kinetic Theory based breakage and aggregation kernels	A PSD was used to represent each parcel in the Lagrangian model for the particulate phase. The particle diameters, for particles in a parcel where determined using the Rosin-Rammler fit for the given PSD

Table 15. *Key features and modeling techniques of CFD models BFB2 and BFB3.*

Model Name:	**BFB2**	**BFB2 (R)**	**BFB3, BFB3 (R)** *Same features except that solids close-pack volume fraction was 0.52 in BFB3 and 0.625 in BFB3 (R)*
Model features	Euerian-Eulerian		MP-PIC Eulerian-Lagrangian in the CPFD methodology
No. of computational cells	Case1 (7000), Case2 (7000), Case3 (8400), Case4 (-)	Case1 (27000), Case2 (27000), Case3 (428400), Case4 (42840)	187000
Typical wall-clock time for fully developed conditions	NA		1 day
Time interval for time-averaged results	30s - 40s	30 – 90 s	Last 10 seconds from each case
Sub-models used			
- Wall boundary conditions	Non-slip for air phase and Johnson-Jackson for granular phase (Restitution coefficient = 0.2)		LES turbulence. Large eddies resolved. Unresolved turbulence modeled by Smagarinsky model. Turbulent wall function at solid structures
- Drag	Syamlal-Obrien		Wen and Yu
- Granular temperature	Differential equation form		
- Collisional models	Syamlal et al. (Restitution coefficient = 0.9)		
Treatment of the particle phase	Single spherical particle, diameter calculated as Sauter mean diameter based on particle sized distribution		Over 1 million computational particles, with full particle size distribution matching that provided by PSRI.

AIChE

Fluid-Particle Drag in Low-Reynolds-Number Polydisperse Gas–Solid Suspensions

Xiaolong Yin and Sankaran Sundaresan
Chemical Engineering Dept., Princeton University, Princeton, NJ 08543

DOI 10.1002/aic.11800
Published online May 6, 2009 in Wiley InterScience (www.interscience.wiley.com).

Lattice-Boltzmann simulations of low-Reynolds-number fluid flow in bidisperse fixed beds and suspensions with particle–particle relative motions have been performed. The particles are spherical and are intimately mixed. The total volume fraction of the suspension was varied between 0.1 and 0.4, the volume fraction ratio ϕ_1/ϕ_2 from 1:1 to 1:6, and the particle size ratio d_1/d_2 from 1:1.5 to 1:4. A drag law with improved accuracy has been established for bidisperse fixed beds. For suspensions with particle–particle relative motions, the hydrodynamic particle–particle drag representing the momentum transfer between particle species through hydrodynamic interaction is found to be an important contribution to the net fluid-particle drag. It has a logarithmic dependence on the lubrication cutoff distance and can be fit as the harmonic mean of the drag forces in bidisperse fixed beds. The proposed drag laws for bidisperse fixed beds and suspensions are generalized to polydisperse suspensions with three or more particle species. © 2009 American Institute of Chemical Engineers *AIChE J,* 55: 1352–1368, 2009
Keywords: fluid-particle drag, gas-solid suspensions, low reynolds number, polydisperse, particle size distribution

Introduction

Gas–solid suspensions are involved in many chemical engineering operations. When simulating gas–solid suspension flows in large containers, as it is impossible to solve the Navier-Stokes equations for the fluid and the equations of motion for all the particles, the particles and the fluid are usually modeled as two or more inter-penetrating continua, the dynamics of which are governed by locally averaged equations (Euler-Euler approach). For suspensions with much fewer particles, one can also track the positions and velocities of all particles in an explicit manner and model the fluid phase as the only continuum (Euler-Lagrangian approach). In either approach, the model equations rely on various constitutive relations to account for the many unknown terms emerging from averaging—fluid-particle drag, added-mass, lift, history force, and particle and fluid phase stresses. Among all these terms, the fluid-particle drag is particularly important for gas–solid suspensions: it is usually the primary force to suspend and transport the particles; it has a significant influence on the bed expansion and stability of the suspension. In the past, closures for fluid-particle drag were generally based on experimental measurements, and were largely empirical in nature; in recent years, however, drag laws generated from direct numerical simulations have become available, and it was shown in several case studies that the drag law has a significant influence over the qualitative and quantitative nature of the flow,[1,2] and computationally generated drag laws in many occasions can indeed improve the accuracy of the continuum simulation.[3,4] To date, most of the computationally generated drag laws were derived from flows past fixed, random assemblies of spheres of the same size[5–7] or two different sizes.[8–10] Even though these drag formulas have been adapted in ad hoc ways to study the dynamics of mono- and polydisperse gas–solid suspensions, it should be emphasized that freely evolving suspensions are different from fixed beds in that the particles move constantly, and an accurate drag law should consider the effect of particle velocity fluctuation when the Reynolds number of the particles is not small,[11] and the effect of particle–particle relative motion when the suspension of interest contains particles of different densities and/or sizes. Among

Correspondence concerning this article should be addressed to S. Sundaresan at sundar@princeton.edu.

these challenges, the effect of polydispersity is particularly interesting, because suspensions with particle size distributions are very common, and one can vary the amount of "fines" to control the flow characteristics of a gas-fluidized bed.[12–17] In a previous study, we characterized by direct numerical simulations the fluid-particle drag in a special type of polydisperse suspension containing equally sized spheres with particle–particle relative motion.[18] It was found that particle–particle relative motion gave rise to a hydrodynamic particle–particle drag term that forms an important part of the total fluid-particle drag; in this study, we consider more general polydisperse fixed beds and suspensions containing spheres of different sizes. Our parameter space encompasses a total volume fraction range of $0.1 < \phi < 0.4$, in which the volume fraction ratio ϕ_1/ϕ_2 was varied from 1:1 to 1:6, and the particle size ratio d_1/d_2 from 1:1.5 to 1:4. We first revisit bidisperse fixed beds and propose a more accurate drag formula. Then, assisted by the new formula developed for fixed beds, we develop a fitting function for the hydrodynamic particle–particle drag and propose a drag law for low-Reynolds-number polydisperse suspensions with particle–particle relative motion.

In this study, we focus on suspensions with low Reynolds numbers $\mathrm{Re} = \rho_g U d/\mu$ and large Stokes numbers $\mathrm{St} = (2\rho_p/9\rho_g)\mathrm{Re}$. Here ρ_g and ρ_p are densities of the fluid and the particles, respectively, U is a characteristic velocity describing particle-fluid relative motion, d is a length scale for particle size, and μ is the viscosity of the fluid. Such a dual limit is realistic for many gas-particle systems of practical interest, e.g. 50–100 μm particles suspended in air; it is also attractive in that it allows for efficient characterization of the drag forces. First, low-Reynolds-number flows are quasi-steady, allowing us to characterize the drag forces as a function of particle positions and velocities. In addition, the drag forces are linear functions of average particle velocities and are independent of the velocity fluctuations.[11,18] One can thus assume that particles of the same type have identical velocities and simplify the setup of simulations. It is valid to compute the forces as functions of particle positions and velocities for gas–solid suspensions with high Stokes numbers, because in such suspensions the fluid-particle force on a particle usually does not balance the weight of the particle due to the long relaxation time; the velocities of particles are more readily changed by collisions and obey Gaussian distributions.[19,20] In contrast, when particle Stokes number is low, which is less common for gas–solid suspensions but a reality for many liquid–solid colloidal suspensions, as the relaxation time is very short, a particle would adjust its velocity very quickly such that the fluid-particle force always balances its own weight. In this limit, it is more appropriate to use the fluid-particle forces as input parameters, and use mobility matrices or hindered settling functions to relate the velocities of particles to the forces. For discussions on mobility matrices or hindered settling functions, see Batchelor,[21] Batchelor and Wen,[22] Davis and Gecol,[23] and Revay and Higdon.[24]

This article is arranged in the following order. We will first define the fluid-particle drag in the context of averaged continua equations for gas–solid suspensions, and discuss existing computationally generated drag formulas for mono- and polydisperse suspensions. We will then introduce the lattice-Boltzmann method and the setup of the simulations. After that, we present the drag forces in bidisperse fixed beds and propose a drag formula with improved accuracy. It is then followed by a study on suspensions with particle–particle relative motions. Assisted by the fixed-bed drag formula developed in this study, we were able to condense the volume fraction and particle size dependence of the drag forces obtained from simulations with particle–particle relative motion into a simple explicit drag formula that can easily be generalized to suspensions containing three or more particle species.

Fluid-Particle Drag in Mono- and Polydisperse Gas–Solid Suspensions

Drag in the context of averaged equations

The Euler-Euler approach for monodisperse gas–solid suspensions treat the particles and the interstitial gas as two interpenetrating continua. The averaged equations governing the dynamics of the suspension are discussed in many publications, e.g., Jackson,[25] and they can be easily generalized to multifluid model equations to describe polydisperse gas–solid suspensions.[26,27] Assuming that our suspension of interest contains two different types of particles and there is neither aggregation nor breakup of particles, we can write down the continuity equation for the gas phase

$$\frac{\partial\left((1-\phi)\rho_g\right)}{\partial t} + \nabla\cdot\left((1-\phi)\rho_g\mathbf{U}_g\right) = 0, \tag{1}$$

and those for the particle phases ($i = 1$ and 2)

$$\frac{\partial(\phi_i\rho_i)}{\partial t} + \nabla\cdot(\phi_i\rho_i\mathbf{U}_i) = 0. \tag{2}$$

In Eqs. 1 and 2, ρ_g and $\mathbf{U}_g$ are the density and average velocity of the gas phase, ϕ_i, ρ_i, and $\mathbf{U}_i$ are the volume fraction, density, and average velocity of the i-th particle species. $\phi = \sum_{i=1}^{2}\phi_i$. The averaged momentum equation for the gas phase is

$$\frac{\left((1-\phi)\rho_g\mathbf{U}_g\right)}{\partial t} + \nabla\cdot\left((1-\phi)\rho_g\mathbf{U}_g\mathbf{U}_g\right) = \nabla\cdot\mathbf{S}_g - \sum_{i=1}^{2}\mathbf{f}_{g-i} + (1-\phi)\rho_g\mathbf{g}. \tag{3}$$

The momentum equations for the particle phases are

$$\frac{\partial(\phi_i\rho_i\mathbf{U}_i)}{\partial t} + \nabla\cdot(\phi_i\rho_i\mathbf{U}_i\mathbf{U}_i) = \nabla\cdot\mathbf{S}_i + \mathbf{f}_{g-i} + \sum_{j=1,j\neq i}^{2}\mathbf{f}_{j-i} + \phi_i\rho_i\mathbf{g}. \tag{4}$$

In Eqs. 3 and 4, $\mathbf{S}_g$ and $\mathbf{S}_i$ are the stress tensors for the gas and the particle phases; $\mathbf{f}_{g-i}$ represent the interactive forces per unit volume of suspension between the gas and the i-th particle phase; $\mathbf{f}_{j-i}$ represent the interactive forces per unit volume of suspension between particles of phase j and particles of phase i due to collisions and/or enduring

contacts; finally, $\mathbf{g}$ is the gravity. $\mathbf{S}_g$ is usually expressed as $-P\mathbf{I}+\tau_g$ with P the pressure in the gas phase and τ_g the deviatoric stress. To solve Eqs. 1 through 4, one needs to supply constitutive models for τ_g, $\mathbf{f}_{g-i}$, $\mathbf{S}_i$, and $\mathbf{f}_{j-i}$.

Closures for $\mathbf{S}_i$ and $\mathbf{f}_{j-i}$ for high Stokes number systems are often sought through kinetic theories. Alternative simulation methods, such as the Euler-Lagrange approach (e.g. Feng et al.[28] and Beetstra et al.[4]) or the Multi-Phase Particle-in-Cell (MP-PIC) method (e.g. Snider,[29] Leboreiro et al.[2]), circumvent the need to solve the particle phase averaged equations by tracking the motions of particles or "clouds" of particles using Newton's equations of motion. Nevertheless, they still need constitutive models to account for the fluid-particle interaction $\mathbf{f}_{g-i}$. In general, a complete description of $\mathbf{f}_{g-i}$ includes contributions from a variety of sources: the drag force $\mathbf{f}_{Dg-i}$ resulting from the relative velocity between the fluid and the particles, the added mass force associated with the current relative acceleration, the history effect associated with the past history of relative acceleration, the generalized buoyancy, and the lift force, etc. As our simulations feature steady, low-Re flows with no bulk velocity gradient, the total fluid-particle force $\mathbf{f}_{g-i}$ only contains the drag $\mathbf{f}_{Dg-i}$ and the generalized buoyancy force $-\phi_i\nabla P$

$$\mathbf{f}_{g-i}=-\phi_i\nabla P+\mathbf{f}_{Dg-i}. \tag{5}$$

Drag defined this way is consistent with the majority of chemical engineering literature. It should be noted, however, that the work by Hill et al.[5,6] considered the entire $\mathbf{f}_{g-i}$ as the drag and did not subtract the bulk pressure gradient $-\phi_i\nabla P$. The readers should be aware of this difference when comparing expressions for drag forces from different sources.

Computationally generated drag laws for low-Re fixed beds

For monodisperse suspensions, the constitutive relations for the fluid-particle drag $\mathbf{f}_{Dg-i}$ are usually expressed as

$$\mathbf{f}_{D-\text{fixed}}=-\beta\Delta\mathbf{U}, \tag{6}$$

where $\Delta\mathbf{U}=(\mathbf{U}-\mathbf{U}_g)$ is the average slip velocity between particles and the fluid, and β is the volume-specific friction coefficient. In Eq. 6, we replaced the subscript $Dg-i$ with $D-$ fixed to emphasize that it is for fixed beds with only one particle species. In addition, we placed a negative sign before β_i to reflect the fact that the drag force is in the opposite direction of $\Delta\mathbf{U}$ and to make β positive. There exists several formulas for β that are based on direct numerical simulations of flow past fixed assemblies of spheres, e.g., Hill et al.[5,6] Koch and Hill,[30] Benyahia et al.[7] van der Hoef et al.[8,9] and Beetstra et al.[10] As the focus of this study is low-Re flows, here we pick among others the formula

$$\begin{aligned}F^*_{D-\text{fixed}}&=-\frac{F_{D-\text{fixed}}}{3\pi d\mu(1-\phi)\Delta U}\\&=\frac{10\phi}{(1-\phi)^2}+(1-\phi)^2\left(1+1.5\sqrt{\phi}\right)\end{aligned} \tag{7}$$

developed by van der Hoef et al.[8] for low-Re monodisperse fixed beds to compute $F^*_{D-\text{fixed}}$, the dimensionless average drag force per particle. It is easy to show that β is proportional to $F^*_{D-\text{fixed}}$ by

$$\beta=\frac{18\phi(1-\phi)\mu}{d^2}F^*_{D-\text{fixed}}. \tag{8}$$

For bidisperse fixed beds, each particle species would have its own drag correlation

$$\mathbf{f}_{Di-\text{fixed}}=-\beta_i\Delta\mathbf{U}. \tag{9}$$

Because of the added complexity due to particle size ratio d_1/d_2 and volume fraction ratio ϕ_1/ϕ_2, developing a closure for β_i in bidisperse fixed beds is very difficult, and it is only recently that van der Hoef et al.[8,9] were able to establish the first computationally based closure for β_i. In their study, it was recognized that the average drag per particle for phase i, $F_{Di-\text{fixed}}$, once properly normalized, can be expressed as a simple function of $F^*_{D-\text{fixed}}$, the drag in a monodisperse fixed bed of the same total volume fraction. The normalization procedure for $F_{Di-\text{fixed}}$ is as follow. First, a dimensionless drag force for phase i is defined

$$F^*_{Di-\text{fixed}}=-\frac{F_{Di-\text{fixed}}}{3\pi d_i\mu(1-\phi)\Delta U}. \tag{10}$$

Then, by using the Sauter mean diameter

$$\langle d\rangle=\frac{n_1d_1^3+n_2d_2^3}{n_1d_1^2+n_2d_2^2} \tag{11}$$

where n_i is the number density of phase i particles, a dimensionless particle size $y_i=d_i/\langle d\rangle$ is introduced. The numerical data by van der Hoef et al.[8,9] indicate that the ratio $F^*_{Di-\text{fixed}}/F^*_{D-\text{fixed}}$ can be well approximated by simple functions of the total volume fraction ϕ and the dimensionless size y_i. Van der Hoef et al.[8,9] proposed to use

$$F^*_{Di-\text{fixed}}=y_iF^*_{D-\text{fixed}} \tag{12}$$

as the first-order approximation of their numerical data. Note that Eq. 12 is different from the original expression in van der Hoef et al.[8] because of a later published erratum.[9] As in polydisperse fixed beds $f_{Di-\text{fixed}}=n_iF_{Di-\text{fixed}}$, it is easy to show that β_i is related to $F^*_{Di-\text{fixed}}$ by

$$\beta_i=\frac{18\phi_i(1-\phi)\mu}{d_i^2}F^*_{Di-\text{fixed}}. \tag{13}$$

We will see later that even though Eq. 12 is not very accurate for bidisperse fixed beds with large particle size ratios, the idea that $F^*_{Di-\text{fixed}}/F^*_{D-\text{fixed}}$ may be fit by simple functions of ϕ and y_i provides an excellent foundation for the construction of more accurate formulas. It is worth pointing out that for fixed beds with large particle size ratios, van der Hoef et al.[8] suggested to modify Eq. 12 with $O(y_i^3)$ corrections to improve the quality of fitting

$$\begin{cases}F^*_{D1-\text{fixed}}/F^*_{D-\text{fixed}} &= y_1+0.064y_1^3\left(1-\phi_1-\phi_2\frac{d_2}{d_1}\right)\\ F^*_{D2-\text{fixed}}/F^*_{D-\text{fixed}} &= y_2+0.064y_2^3\left(1-\phi_1\frac{d_1}{d_2}-\phi_2\right)\end{cases}. \tag{14}$$

The right-hand-side of Eq. 14, unlike Eq. 12, is no longer a simple function of y_i and ϕ.

Drag correlations for low-Re polydisperse gas–solid suspensions

Owing to the growing interest in the dynamics of polydisperse gas–solid suspensions, in particular, segregation and mixing, there have been a number of computational studies on polydisperse gas–solid suspensions in the past few years.[2–4,27,28,31–36] These studies employed ad hoc modifications of existing drag formulas with a general form

$$\mathbf{f}_{Di} = -\beta_i \Delta \mathbf{U}_i. \tag{15}$$

In this equation, $\Delta \mathbf{U}_i = (\mathbf{U}_i - \mathbf{U}_g)$ is the average velocity of particle phase i relative to the fluid. Equation 15 implies that the drag acting on species i is independent of the velocities of other particle species, which is not physically sound for polydisperse suspensions with particle–particle relative motion because the presence of one particle species affects the motion of other species not only by changing the total solid fraction, but also through collisional and hydrodynamical particle–particle momentum transfer. In many Euler–Euler models, the particle phase momentum equations contain particle–particle drag terms to account for direct particle–particle collisions, e.g. Syamlal[37] and Huilin et al.[38] The indirect particle–particle momentum transfer mediated by the interstitial fluid, or the hydrodynamic particle–particle drag, being an integrated part of the net fluid-particle drag, is not included in such drag models.

In order to assess the importance of the hydrodynamic particle–particle drag, we would like to develop a drag law that includes not only the velocity of species i but also the velocities of other species. For bidisperse suspensions with relative velocities $\Delta \mathbf{U}_1$ and $\Delta \mathbf{U}_2$ aligned in the same direction, we can use a scalar drag law of the following form

$$\begin{cases} F_{D1} &= -B_{11}\Delta U_1 - B_{12}\Delta U_2 \\ F_{D2} &= -B_{21}\Delta U_1 - B_{22}\Delta U_2 \end{cases}, \tag{16}$$

where F_{Di} is the average drag force per particle of type i, and B_{ij} is the particle-specific friction coefficient of a bidisperse suspension. The influence on the drag of particle phase i due to the motion of particle phase j is reflected in the off-diagonal components of the matrix. Multiplying Eq. 16 by the number densities of particles, one can obtain the drag forces per unit volume of suspension

$$\begin{cases} f_{D1} &= -\beta_{11}\Delta U_1 - \beta_{12}\Delta U_2 \\ f_{D2} &= -\beta_{21}\Delta U_1 - \beta_{22}\Delta U_2 \end{cases}. \tag{17}$$

Here $f_{Di} = n_i F_{Di}$, and $\beta_{ij} = n_i B_{ij}$ is the volume-specific friction coefficient of a bidisperse suspension.

In the aforementioned drag laws for fixed beds, the drag forces are nondimensionalized using the Stokes drag of an isolated particle (c.f. Eq. 10); in polydisperse suspensions, as there are more than one velocity scales available, it is best to nondimensionalize Eq. 16 using $F^*_{Di} = \rho_g F_{Di}/\mu^2$ and $B^*_{ij} = B_{ij}/\mu\langle d\rangle$

$$\begin{cases} F^*_{D1} &= -B^*_{11}\Delta \mathrm{Re}_1 - B^*_{12}\Delta \mathrm{Re}_2 \\ F^*_{D2} &= -B^*_{21}\Delta \mathrm{Re}_1 - B^*_{22}\Delta \mathrm{Re}_2 \end{cases}; \tag{18}$$

Equation 17 can be nondimensionalized using $f^*_{Di} = \rho_g \langle d\rangle^3 f_{Di}/\mu^2$ and $\beta^*_{ij} = \langle d\rangle^2 \beta_{ij}/\mu$

$$\begin{cases} f^*_{D1} &= -\beta^*_{11}\Delta \mathrm{Re}_1 - \beta^*_{12}\Delta \mathrm{Re}_2 \\ f^*_{D2} &= -\beta^*_{21}\Delta \mathrm{Re}_1 - \beta^*_{22}\Delta \mathrm{Re}_2 \end{cases}. \tag{19}$$

In the above two equations, the Reynolds numbers are defined as $\Delta \mathrm{Re}_i = \rho_g \Delta U_i \langle d\rangle/\mu$. In our previous study,[18] we characterized the friction coefficients B^*_{ij} and β^*_{ij} for bidisperse suspensions of equally sized spheres with particle–particle relative motion, i.e., $d_1 = d_2$ and $\Delta U_1 \neq \Delta U_2$. It was found that the off-diagonal components of the friction coefficient matrix are always important, and the size of the off-diagonals is influenced by the intensity of the lubrication interaction between particles. In this study, we use numerical simulations to characterize B^*_{ij} and β^*_{ij} for bidisperse suspensions of unequally sized spheres, and develop formulas to fit them.

Simulation Method and Setup

The numerical method used in this work is the Susp3D lattice-Boltzmann program developed by Ladd[39,40] for suspensions of spherical particles. It has been modified and improved over the years, and a complete review is available in Ladd and Verberg.[41] This program has been used to study many particle-laden flow problems, including the aforementioned studies on fluid-particle drag by Hill et al.[5,6] van der Hoef et al.[8] Beetstra et al.[10] and Yin and Sundaresan.[18] Because detailed information of this method are well available in the literature, here we will only provide a brief description.

The lattice-Boltzmann method is different from conventional finite difference, finite volume, or finite element methods in that it does not solve the Navier-Stokes equations directly. Rather, it simulates the evolution of a simplified fluid molecular velocity distribution on a rectangular, space-filling lattice. The propagation and relaxation of this molecular velocity distribution are designed such that fluid density, momentum, and stresses, being the zeroth, first and second order moments of the velocity distribution, obey the Navier-Stokes equations on large length and time scales. Our lattice-Boltzmann method employs a 19-velocity model (commonly referred to as D3Q19 model to denote that the simulations are in three dimensions and that the continuous distribution of the fluid molecular velocity is discretized as a sum of 19 discrete velocity quadratures) in which the density of the fluid $\rho_g = 36$. The viscosity of the fluid, which controls the relaxation rate of the non-equilibrium molecular velocity distribution, was set to $\mu = 6.0$, a good choice for low-Reynolds-number flows. The size of the smaller spheres was chosen to be 9.6 Δx where Δx is the lattice spacing. In our previous study,[18] we conducted grid resolution tests and found that the there is no significant difference between results obtained with $d = 9.6\ \Delta x$ and those with $d = 12.5\ \Delta x$. Therefore, 9.6 Δx was used to resolve the smaller spheres throughout this study.

In bidisperse gas–solid suspensions, because of the relative motion between particle species, lubrication interactions

between particles are very important. In our lattice-Boltzmann method, the lubrication interactions between spheres are solved analytically and imposed to the lattice solutions in an explicit manner. The detail of the implementation can be found in the paper by Nguyen and Ladd.[42] It was shown that when the particles are separated by more than one lattice spacing, the lattice-Boltzmann method can fully resolve the hydrodynamic interaction between the particles; when the distance between particles is less than one lattice spacing, the lubrication forces obtained from the lattice-Boltzmann no longer increase with decreasing separation, and corrections are applied to normal and tangential forces and torques so that they agree with the analytical solutions.[43]

The lubrication forces between two spheres with different velocities diverge as the separation between the spheres approaches zero. In reality, this divergence may be removed by surface roughness, finite weight of particles, or noncontinuum effects. All of these effects may be approximated in our simulations by specifying a cutoff distance λ: when the separation between particles becomes less than λ, the lubrication forces no longer increase but remain as constants. Our previous study[18] revealed that the particle–particle drag transmitted through the fluid increases with decreasing λ following a logarithmic scale, indicating that the lubrication forces in the normal direction is the primary contribution to the hydrodynamic particle–particle drag. In this study, we will also vary the values of λ to study the dependence of the drag forces on the lubrication cutoff distance.

We began our simulations by first randomly distributing spherical particles of different sizes in cubic, periodic domains, the size of which is typically 12–20 times the diameter of the smaller particles. Then, we employed Monte-Carlo steps to move the spheres in a random manner such that that all of our simulations began with the well-known microstructure of a binary hard-sphere fluid. This step is important because the drag forces would vary with the microstructure of the suspension. As there is no general knowledge on the microstructure of bidisperse gas–solid suspension, assuming all particles are intimately mixed and using a microstructure identical to that of a binary hard-sphere fluid provide a reasonable starting point. In Figure 1, we compared the structure factors of our initial particle configurations with the analytical solutions for a binary hard sphere fluid of the same composition.[44] The structure factors $S_{11}(k)$, $S_{22}(k)$, and $S_{12}(k)$ are measures of the microstructure of a bidisperse suspension, and are defined as the sums of particle relative positions in the Fourier space:

$$\begin{aligned} S_{11}(\mathbf{k}) &= \frac{1}{N_1}\left\langle \sum_{1-1\text{pairs}} e^{-i\mathbf{k}\cdot\mathbf{r}_{ij}} \right\rangle \\ S_{22}(\mathbf{k}) &= \frac{1}{N_2}\left\langle \sum_{2-2\text{pairs}} e^{-i\mathbf{k}\cdot\mathbf{r}_{ij}} \right\rangle \\ S_{12}(\mathbf{k}) &= \frac{1}{\sqrt{N_1 N_2}}\left\langle \sum_{1-2\text{pairs}} e^{-i\mathbf{k}\cdot\mathbf{r}_{ij}} \right\rangle. \end{aligned} \tag{20}$$

In Eq. 20, $\mathbf{k}$ is the wave number vector, and $\mathbf{r}_{ij}$ is the separation vector between a pair of particles. Unlike in previous discussions where i and j were used to index particle species, here i and j are indices to *individual* particles. S_{11} and S_{22} were calculated by summing r_{ij} over pairs consisting of identical particles, i.e., 1-1 pairs and 2-2 pairs; S_{12}, on the other hand, was calculated by summing r_{ij} over 1-2 pairs. These structure factors are functions of particle sizes, volume fractions, and the magnitude of the wave number vector $k = |\mathbf{k}|$ due to the isotropy of our suspensions. In Figure 1, the particle size ratio d_1:d_2 was 1:1.11, the volume fractions were $\phi_1 = 0.139$ and $\phi_2 = 0.285$. It may be observed that the structure factors calculated from ensemble averages of 260 configurations (750 particles in each configuration) agree very well with the analytical solutions provided by Ashcroft and Langreth.[44]

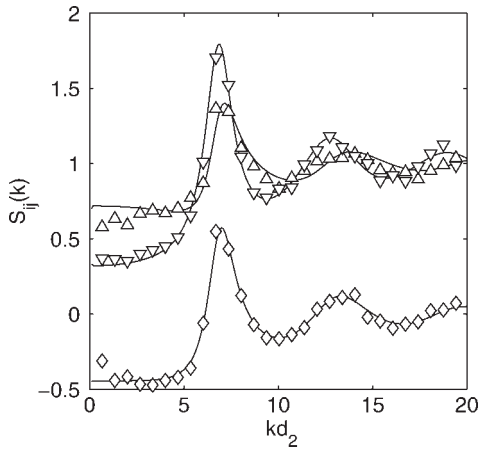

Figure 1. Structure factors $S_{11}(k)$ (upper triangles), $S_{22}(k)$ (downward triangles), and $S_{12}(k)$ (diamonds) calculated from 260 random configurations.

The particle sizes are: $d_1 = 9.6\Delta x$, $d_2 = 10.66\ \Delta x$; there are 301 particles of type 1 and 449 particles of type 2; the volume fractions are: $\phi_1 = 0.139$, $\phi_2 = 0.285$. The solid lines are based on the analytical solutions for S_{11}, S_{22}, and S_{12} in Ashcroft and Langreth.[44]

After obtaining initial particle configurations, we assigned a uniform velocity U to all particles if the configurations were for fixed-bed simulations, or velocities U_1 and U_2 to different particle species if they were for bidisperse suspension simulations with particle–particle relative motion. In both cases, the assigned velocities would generate a fluid flow within the particle assembly; meanwhile, a pressure gradient was applied to the fluid to ensure that the average fluid velocity U_g is zero. The velocities assigned to the particles thus became equivalent to the relative velocities to the fluid. Once the flow reached the steady state, the net fluid-particle interactive forces F_1 and F_2 acting on the particles were obtained by integrating the hydrodynamic stresses over particle surfaces and averaging over all particles of the same species. The drag forces F_{D1} and F_{D2} were then calculated from

$$F_{Di} = F_i + \frac{\pi d_i^3}{6}\frac{\mathrm{d}P}{\mathrm{d}x}, \tag{21}$$

where $\mathrm{d}P/\mathrm{d}x$ is the bulk pressure gradient acting on the fluid that balances the total forces

$$-\frac{\mathrm{d}P}{\mathrm{d}x} = n_1 F_1 + n_2 F_2. \tag{22}$$

Table 1. List of Bidisperse Fixed-Bed Simulations Conducted

Size Ratio	N_1/N_2	$\phi_1/\phi_2/M$	$F^*_{D1-\text{fixed}}$	$F^*_{D2-\text{fixed}}$
d_1:d_2 = 1:1.5	345/409	0.02/0.08/10	2.09 ± 0.01	2.64 ± 0.01
	863/256	0.05/0.05/10	2.34 ± 0.01	3.08 ± 0.04
	1382/102	0.08/0.02/10	2.23 ± 0.01	2.90 ± 0.03
	863/512	0.05/0.10/10	2.77 ± 0.01	3.69 ± 0.03
	1209/409	0.07/0.08/10	2.86 ± 0.01	3.83 ± 0.02
	1382/358	0.08/0.07/10	2.91 ± 0.01	3.94 ± 0.02
	1727/256	0.10/0.05/10	3.01 ± 0.01	4.11 ± 0.02
	863/768	0.05/0.15/10	3.43 ± 0.01	4.71 ± 0.03
	728/216	0.10/0.10/9	3.68 ± 0.01	5.20 ± 0.03
	863/1023	0.05/0.20/10	4.21 ± 0.01	6.02 ± 0.03
	1093/216	0.15/0.10/10	4.82 ± 0.02	7.02 ± 0.07
	728/432	0.10/0.20/10	5.56 ± 0.02	8.23 ± 0.06
	1457/216	0.20/0.10/10	6.24 ± 0.03	9.45 ± 0.06
	364/648	0.05/0.30/12	6.53 ± 0.05	9.83 ± 0.05
	728/648	0.10/0.30/10	8.70 ± 0.04	13.60 ± 0.09
	1457/432	0.20/0.20/10	9.55 ± 0.02	15.23 ± 0.10
	2186/216	0.30/0.10/10	10.45 ± 0.03	17.02 ± 0.14
d_1:d_2 = 1:2.5	728/47	0.10/0.10/4	3.31 ± 0.01	7.57 ± 0.56
	728/93	0.10/0.20/4	4.61 ± 0.09	11.29 ± 0.42
	1457/47	0.20/0.10/5	5.82 ± 0.02	15.75 ± 0.38
	728/140	0.10/0.30/5	6.71 ± 0.03	17.78 ± 0.70
	1457/93	0.20/0.20/4	8.18 ± 0.03	23.70 ± 0.45
	2186/47	0.30/0.10/5	9.84 ± 0.06	31.17 ± 1.55
d_1:d_2 = 1:4	863/27	0.05/0.10/14	2.26 ± 0.01	6.64 ± 0.24
	863/40	0.05/0.15/20	2.57 ± 0.01	7.63 ± 0.20
	1727/27	0.10/0.10/15	3.14 ± 0.01	11.41 ± 0.37
	863/54	0.05/0.20/20	2.98 ± 0.01	9.76 ± 0.26
	2590/27	0.15/0.10/16	4.19 ± 0.01	18.18 ± 0.45
	1727/54	0.10/0.20/14	4.15 ± 0.02	16.45 ± 0.38
	3454/27	0.20/0.10/15	5.51 ± 0.01	27.67 ±1.42
	863/81	0.05/0.30/9	4.04 ± 0.03	14.66 ± 0.62
	4317/27	0.25/0.10/8	7.20 ± 0.01	41.19 ± 1.74
	1727/81	0.10/0.30/13	5.72 ± 0.02	25.34 ± 0.83
	3454/54	0.20/0.20/9	7.52 ± 0.02	40.38 ± 2.04
	5180/27	0.30/0.10/10	9.42 ± 0.01	59.34 ± 3.12

The first column contains the numbers of particles in fixed beds; the second column contains the volume fractions and the number of configurations; the last two columns contain the normalized drag forces as defined in Eq. 10.

Note that all particles were frozen on the lattice, i.e., the positions of particles were not updated based on their velocities. This procedure is valid because of the quasi-steadiness of low-Re flows, and it ensures that the microstructure of the suspension remains unchanged in the course of a simulation.

We also exploited the linear characteristics of low-Re flows to characterize the friction coefficients for fixed beds and suspensions. For fixed beds, the friction coefficients β_i were obtained as $f_{Di-\text{fixed}}/\Delta U$; for suspensions, we first let $U_2 = 0$ and U_1 be a non-zero value and solve for the 11 and 21 components of B^*_{ij} and β^*_{ij}, then we ran another set of simulations with $U_1 = 0$ and non-zero U_2 to characterize the 12 and 22 components.

Drag in Polydisperse Fixed Beds

We now revisit the fluid-particle drag in bidisperse fixed beds. Because this problem has already been studied by van der Hoef et al.[8,9] it is an excellent opportunity for comparison and validation. In addition, an accurate drag law for bidisperse fixed beds is critically important for the development of a general drag law for bidisperse suspensions with particle–particle relative motion, because the general drag law must be able to recover the drag law for fixed beds when particle–particle relative motion is absent.

In order to characterize fluid-particle drag forces in bidisperse fixed beds, we conducted 361 simulations for 35 different combinations of $(\phi_1, \phi_2, d_1/d_2)$, listed in Table 1. The drag formula Eq. 12 developed by van der Hoef et al.[8,9] is good for bidisperse fixed beds with moderately different particle sizes (within a relatively narrow range of y_i in the vicinity of $y_i = 1$), and the agreement between Eq. 12 and the numerical data with large particle size ratios (1:4 in particular) was rather poor. For this reason, in our simulations we emphasized more on fixed beds with large particle size ratios and extended the range of y_i considerably. In Figure 2 where we plotted $F^*_{Di-\text{fixed}}/F^*_{D-\text{fixed}}$($F^*_{D-\text{fixed}}$ given by Eq. 7) as a function of y_i, an excellent agreement between our data and those by van der Hoef et al.[8,9] is observed over the range of y_i where the two data sets overlap. The extended range of y_i in our data sets confirmed that the simple linear relation $F^*_{Di-\text{fixed}}/F^*_{D-\text{fixed}} = y_i$ is only accurate in the vicinity of $y_i = 1$ and becomes rather poor when y_i becomes much larger than unity. Besides, Eq. 12 predicts $F^*_{Di-\text{fixed}} = 0$ when $y_i \to 0$, which does not agree with the general trend of the data in the low y_i limit. Even though the formula with $O(y_i^3)$ terms [Eq. 14] improved the quality of fitting for large y_i, the discrepancy in the low y_i limit is not addressed. Moreover, the additional dependence of $F^*_{Di-\text{fixed}}/F^*_{D-\text{fixed}}$ on the particle size ratio, in view of Figure 2,

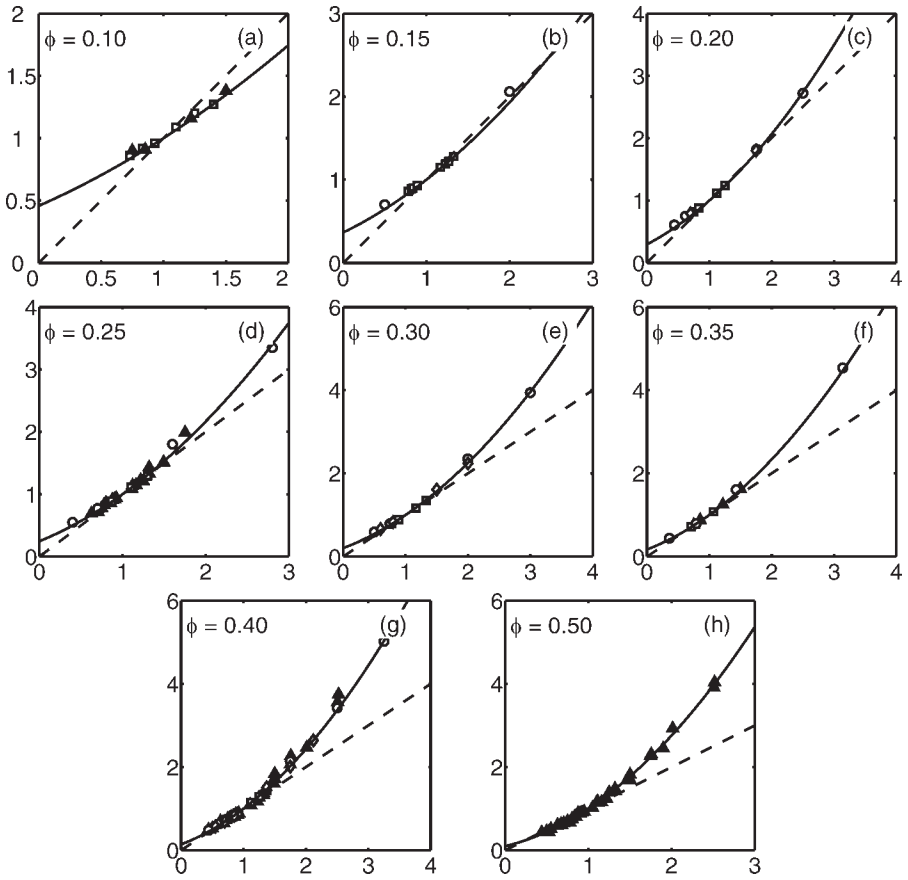

Figure 2. The vertical axis is the dimensionless drag in bidisperse fixed beds normalized by the dimensionless drag in monodisperse fixed beds of the same volume fraction $F^*_{Di-\text{fixed}}/F^*_{D-\text{fixed}}$; the horizontal axis is the dimensionless particle size ratio $y_i = d_i/\langle d\rangle$. $F^*_{D-\text{fixed}}$ was calculated based on Eq. 7.

This figure shows that (1) our simulation data, represented by the squares (d_1:d_2 = 1:1.5), diamonds (d_1:d_2 = 1:2.5), and circles (d_1:d_2 = 1:4), are in very good agreement with the data by van der Hoef et al.,[8,9] (solid triangles), and (2) $F^*_{Di-\text{fixed}}/F^*_{D-\text{fixed}}$ is only a function of ϕ and y_i. The dashed lines are based on van der Hoef et al.'s drag law Eq. 12[8,9]; the solid lines are based on our new drag law for bidisperse fixed beds Eqs. 23 and 25.

does not appear to be very necessary. Hence, we will assume that $F^*_{Di-\text{fixed}}/F^*_{D-\text{fixed}}$ can still be fit by a simple function of ϕ and y_i, and, in order to account for the nonlinear dependence of $F^*_{Di-\text{fixed}}/F^*_{D-\text{fixed}}$ on y_i, we will develop a quadratic function to fit the numerical data.

In view of the limitations of Eqs. 12 and 14 and the limiting behaviors of $F^*_{Di-\text{fixed}}$, we propose three conditions that $F^*_{Di-\text{fixed}}$ must satisfy to guide the design of the quadratic fitting function, and these conditions are listed below.

- $F^*_{Di-\text{fixed}}/F^*_{D-\text{fixed}} = 1$ when $y_i = 1$. This condition is needed such that the new drag law can reproduce the drag of a monodisperse fixed suspension when all d_i equal. While Eq. 12 satisfies this condition, Eq. 14 does not.
- $F^*_{Di-\text{fixed}} \to 1$ when $\phi \to 0$. This condition is needed because in the dilute limit every particle will be subjected to its respective Stokes drag, and it agrees with the trend observed in Figure 2. Neither Eq. 12 nor Eq. 14 satisfies this condition.
- $F^*_{Di-\text{fixed}} \to 1/(1-\phi)$ when $y_i \to 0$. In a bidisperse suspension, the scaled particle size y_1 would approach zero when $d_1 << d_2$ and $\phi_1 << \phi_2$. In this limit, because the average distance between smaller particles and larger particles and that between smaller particles themselves are much larger than d_1, the smaller particles can be treated as point particles and the fluid-particle drag force acting on a smaller particle is simply the Stokes drag based on the local fluid velocity. The average drag force $F_{D1-\text{fixed}}$ is therefore the Stokes drag based on the average fluid velocity relative to the particle assembly $3\pi\mu d_1\Delta U$, and $F^*_{D1-\text{fixed}} = 1/(1-\phi)$.

The simplest quadratic fitting function that satisfies the above conditions is

$$F^*_{Di-\text{fixed}} = \frac{1}{1-\phi} + \left(F^*_{D-\text{fixed}} - \frac{1}{1-\phi}\right)\left[ay_i + (1-a)y_i^2\right], \tag{23}$$

where a can be obtained from linear regression

$$\frac{F^*_{Di-\text{fixed}} - \frac{1}{1-\phi}}{F^*_{D-\text{fixed}} - \frac{1}{1-\phi}} - y_i^2 = a(y_i - y_i^2). \tag{24}$$

Figure 3 shows that $(F^*_{Di-\text{fixed}} - \frac{1}{1-\phi})/(F^*_{D-\text{fixed}} - \frac{1}{1-\phi}) - y_i^2$ can be very well approximated by linear functions of $y_i - y_i^2$. As indicated by Figure 4, the values of a generally decrease with increasing volume fraction, and can be fit by a third-order polynomial

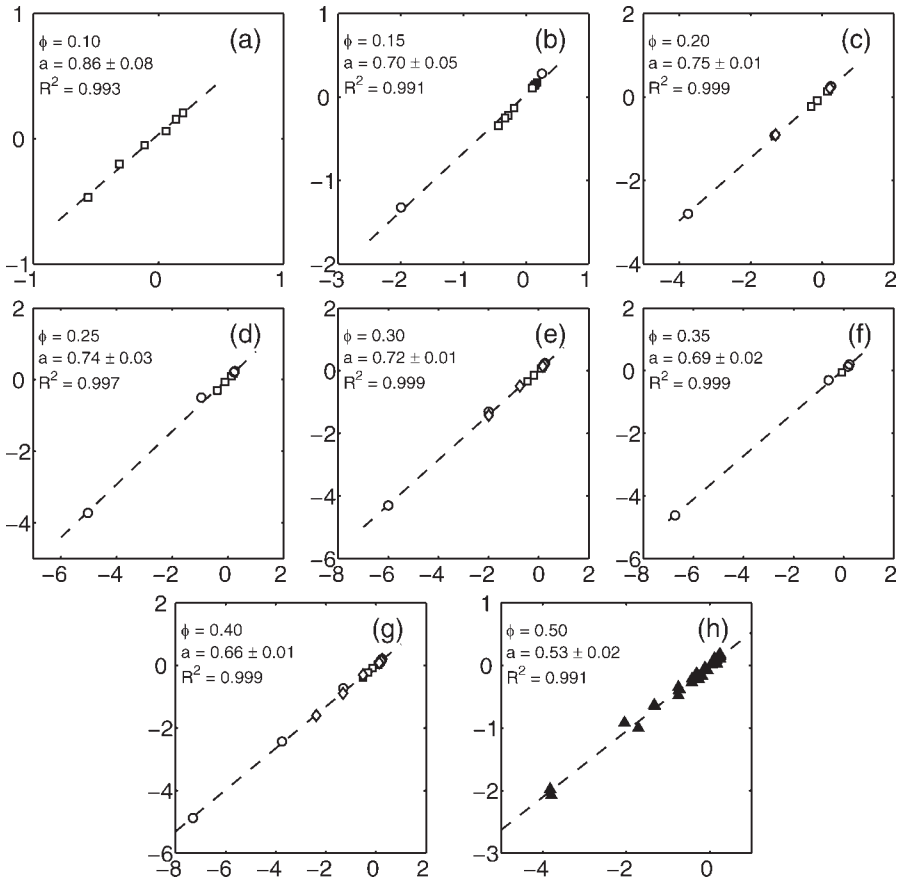

Figure 3. This figure shows the linear relation between $(F^*_{Di-\text{fixed}} - \frac{1}{1-\phi})/(F^*_{D-\text{fixed}} - \frac{1}{1-\phi}) - y_i^2$, the vertical axis, and $y_i - y_i^2$, the horizontal axis.

According to Eq. 24, the slopes of the best linear fits yield the values of $a(\phi)$, the fitting function in the new drag law for bidisperse fixed beds Eq. 23. In graphs (a) through (h), the symbols are the simulation data and the dashed lines are the best linear fits. The slopes of the lines and the R^2 values are included in the figure. The meanings of the symbols are identical to those in Figure (2).

$$a(\phi) = 1 - 2.660\phi + 9.096\phi^2 - 11.338\phi^3. \qquad (25)$$

In Figure 2, the predictions based on Eqs. 23 and 25 were included as solid lines. Compared with the predictions based on Eq. 12 (dotted lines), the solid lines are clearly better in the volume fraction range of $0.1 < \phi < 0.5$. The average deviation of this new drag law from the simulation data, defined as the square root of the mean square percentage deviations, is only 3.9%; the maximum deviation is 9.4%.

Equations 23 and 25 can be readily applied to polydisperse fixed beds with three or more sizes of particles. For general polydisperse suspensions and fixed beds, the Sauter mean $\langle d \rangle$ is defined as

$$\langle d \rangle = \frac{\sum_i (n_i d_i^3)}{\sum_i (n_i d_i^2)} \qquad (26)$$

We simulated a low-Re flow through a ternary fixed bed with $d_1 = 9.6\ \Delta x$, $d_2 = 12\ \Delta x$, and $d_3 = 14.4\ \Delta x$. The volume fractions are $\phi_1 = \phi_2 = \phi_3 = 0.07$. The size of the cubic computational domain is 15.6 times the size of the smallest particles (150 Δx). On the basis of these parameters, it is easy

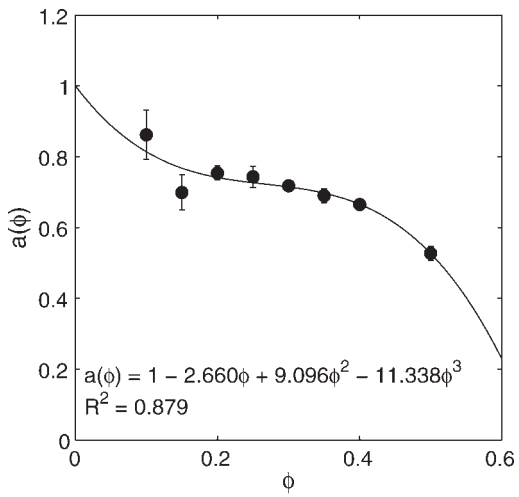

Figure 4. The slopes obtained in Fig. 3 are plotted here as a function of ϕ.

These data points can be fit by a third-order polynomial, which is Eq. 25. The error bars represent 95% confidence intervals of the linear fitting.

to obtain $y_1 = 0.822$, $y_2 = 1.028$, and $y_3 = 1.233$. Substituting y_i and ϕ_i into Eqs. 23 and 25, we obtained $F^*_{D1-\text{fixed}} = 3.94$, $F^*_{D2-\text{fixed}} = 4.64$, and $F^*_{D3-\text{fixed}} = 5.45$; $F^*_{Di-\text{fixed}}$ found from simulations (averaged over 10 runs with different particle configurations) are 3.74, 4.53, and 5.39 respectively for the three particle species, in good agreement with the predictions.

Even though Eq. 23 was developed to facilitate the development of a drag law for suspensions with particle–particle relative motions, an accurate drag law for polydisperse fixed beds has its own merits and can be useful for many practical applications. In addition, dense polydisperse fixed beds can be regarded as porous media with grain size distributions, and an expression for the overall permeability would be very informative for researchers and engineers interested in porous media flows. With this in mind, we invoke Eq. 13 and rewrite Eq. 23 into

$$\beta_i = \frac{18\phi_i(1-\phi)\mu}{d_i^2}\left[\frac{1}{1-\phi} + (F^*_{D-\text{fixed}} - \frac{1}{1-\phi})\left[ay_i + (1-a)y_i^2\right]\right], \tag{27}$$

The total drag force per unit volume is therefore

$$\begin{aligned}\sum_i f_{Di-\text{fixed}} &= -18(1-\phi)\mu\Delta U \sum_i \frac{\phi_i}{d_i^2} \\ &\quad\times\left[\frac{1}{1-\phi} + (F^*_{D-\text{fixed}} - \frac{1}{1-\phi})\left[ay_i + (1-a)y_i^2\right]\right] \\ &= -\frac{18\phi(1-\phi)\mu\Delta U}{\langle d\rangle^2} \\ &\quad\times\left[F^*_{D-\text{fixed}} + \frac{\langle d\rangle^2}{2\phi^2(1-\phi)}\sum_i\sum_j \phi_i\phi_j\left(\frac{1}{d_i} - \frac{1}{d_j}\right)^2\right]\end{aligned} \tag{28}$$

It is interesting to note that $a(\phi)$ disappeared in the summation. Since the total drag force is related to the pressure gradient by

$$\sum_i f_{Di-\text{fixed}} = (1-\phi)\frac{\mathrm{d}P}{\mathrm{d}x}, \tag{29}$$

one can obtain the relation between $\mathrm{d}P/\mathrm{d}x$ and the superficial velocity $U_s = (1-\phi)\Delta U$ of the fluid through the porous medium

$$\begin{aligned}\frac{\mathrm{d}P}{\mathrm{d}x} &= -\frac{18\phi\mu U_s}{(1-\phi)\langle d\rangle^2} \\ &\quad\times\left[F^*_{D-\text{fixed}} + \frac{\langle d\rangle^2}{2\phi^2(1-\phi)}\sum_i\sum_j \phi_i\phi_j\left(\frac{1}{d_i} - \frac{1}{d_j}\right)^2\right].\end{aligned} \tag{30}$$

Compared with the corresponding relation for a porous medium formed by monodisperse spheres

$$\frac{\mathrm{d}P}{\mathrm{d}x} = -\frac{18\phi\mu U_s}{(1-\phi)d^2}F^*_{D-\text{fixed}}, \tag{31}$$

Equation 30 clearly indicates that the permeability of a porous medium with grain size distribution is always *lower* than the permeability of a porous medium consisting of monodisperse spheres of the same volume fraction under the condition $d = \langle d\rangle$. For dense bidisperse fixed beds, it is straightforward to show that the change in the permeability due to bidispersity is usually small, and it is safe to neglect the $\phi_1\,\phi_2$ term in Eq. 30. However, at low volume fractions the difference becomes much more significant. As our fixed-bed drag law also serves as a stepping-stone for the subsequent development of the general drag law for fluidized bidisperse gas–solid suspensions with particle–particle relative motions, the accuracy in the dilute regime is also of critical importance to us.

Note that van der Hoef et al.[8,9] provided a seemingly opposite statement that the total drag force of a polydisperse fixed bed is lower than a monodisperse fixed bed of the same volume fraction, giving rise to a higher permeability. To understand this difference, it is important to realize that the comparison in van der Hoef et al.[8,9] is different and is between a polydisperse fixed bed and a monodisperse fixed bed with particle size $\bar{d}$ rather than $\langle d\rangle$. $\bar{d}$, being the number average of all particle sizes in the polydisperse fixed bed, is always smaller than the Sauter mean $\langle d\rangle$. Our drag law Eq. 30 is consistent with van der Hoef et al.[8,9] if we neglect the $\phi_i\phi_j$ terms and compare to a monodisperse fixed bed containing particles of size $\bar{d}$ rather than $\langle d\rangle$.

To develop a formula capable of handling a continuous size distribution, let $\sigma_i = n_i/\left(\sum_i n_i\right)$ be the fraction of the ith particle species and it is easy to obtain

$$\phi_i = \frac{\pi\sigma_i d_i^3}{6}\left(\sum_i n_i\right). \tag{32}$$

Because the sum of all ϕ_i yields ϕ, the total solid fraction of a porous medium, a relation between $\left(\sum_i n_i\right)$, the total number of particles per unit volume, and ϕ can be established

$$\phi = \frac{\pi}{6}\left(\sum_i \sigma_i d_i^3\right)\left(\sum_i n_i\right). \tag{33}$$

By substituting Eq. 33 into Eq. 32, we can write ϕ_i in terms of ϕ and σ_i

$$\phi_i = \phi\frac{\sigma_i d_i^3}{\sum_i \sigma_i d_i^3}. \tag{34}$$

Substituting Eq. 34 into Eq. 30, and using $\langle d\rangle = \left(\sum_i \sigma_i d_i^3\right)/\left(\sum_i \sigma_i d_i^2\right)$, we obtain

$$\frac{\mathrm{d}P}{\mathrm{d}x} = -\frac{18\phi\mu U_s}{(1-\phi)\langle d\rangle^2}\left[F^*_{D-\text{fixed}} + \frac{\sum_i\sum_j \sigma_i\sigma_j d_i d_j (d_i - d_j)^2}{2(1-\phi)\left(\sum_i \sigma_i d_i^2\right)^2}\right]. \tag{35}$$

Equation 35 can be further simplified to

$$\begin{aligned}\frac{\mathrm{d}P}{\mathrm{d}x} &= -\frac{18\phi\mu U_s}{(1-\phi)\langle d\rangle^2} \\ &\quad\times\left[F^*_{D-\text{fixed}} + \frac{1}{1-\phi}\left[\frac{\left(\sum_i \sigma_i d_i\right)\left(\sum_i \sigma_i d_i^3\right)}{\left(\sum_i \sigma_i d_i^2\right)^2} - 1\right]\right].\end{aligned} \tag{36}$$

Now, assume that the porous medium of interest is formed by grains whose size is described by a continuous size distribution $\sigma(d)$, let σ_I, σ_{II}, and σ_{III} denote the first, second, and third order moments of $\sigma(d)$, Eq. 36 indicates that the relation between the pressure gradient and superficial velocity of the fluid flowing through this porous medium is simply

$$\frac{dP}{dx} = -\frac{18\phi\mu U_s}{(1-\phi)\langle d\rangle^2}\left[F^*_{D-\text{fixed}} + \frac{1}{1-\phi}\left(\frac{\sigma_I\sigma_{III}}{\sigma_{II}\sigma_{II}} - 1\right)\right]. \quad (37)$$

Let us substitute two common particle size distributions—Gaussian and log-normal distributions—into Eq. 37 and examine the influence of the size distribution on the overall drag. If the size distribution is Gaussian

$$\sigma(d) = \frac{1}{\delta\sqrt{2\pi}}\exp\left(-\frac{(d-\bar{d})^2}{2\delta^2}\right), \quad (38)$$

then $\sigma_I = \bar{d}$, $\sigma_{II} = \bar{d}^2 + \delta^2$, and $\sigma_{III} = \bar{d}^3 + 3\delta^2\bar{d}$. It is easy to show that Eq. 37 becomes

$$\frac{dP}{dx} = -\frac{18\phi\mu U_s}{(1-\phi)\langle d\rangle^2}\left[F^*_{D-\text{fixed}} + \frac{1}{1-\phi}\,\frac{(\bar{d}/\delta)^2 - 1}{(\bar{d}/\delta)^4 + 2(\bar{d}/\delta)^2 + 1}\right]. \quad (39)$$

On the other hand, if the size distribution is log-normal

$$\sigma(d) = \frac{1}{d\delta^*\sqrt{2\pi}}\exp\left(-\frac{(\ln d - \ln\bar{d})^2}{2\delta^{*2}}\right), \quad (40)$$

then $\sigma_I = \bar{d}e^{\delta^{*2}/2}$, $\sigma_{II} = \bar{d}^2 e^{2\delta^{*2}}$, $\sigma_{III} = \bar{d}^3 e^{9\delta^{*2}/2}$, and Eq. 37 becomes

$$\frac{dP}{dx} = -\frac{18\phi\mu U_s}{(1-\phi)\langle d\rangle^2}\left[F^*_{D-\text{fixed}} + \frac{1}{1-\phi}\left(e^{\delta^{*2}} - 1\right)\right]. \quad (41)$$

Note that δ in Eq. 38 and δ^* in Eq. 40 have different meanings and units. In Eq. 38, δ represents the standard deviation of the distribution and has the unit of length; in Eq. 40, δ^* yields the shape of the distribution and is dimensionless and typically less than unity. When δ^* becomes less than about 0.25, the shape of the log-normal distribution becomes approximately Gaussian.

With these equations, we can now answer a practical question: how good the approximation would be if we neglect the second correction term on the right hand side of Eq. 37 and assume that the drag of a polydisperse fixed bed (or a porous medium with grain size distribution) equals the drag of a monodisperse fixed bed with $d = \langle d\rangle$? In Figure 5, we plotted $\sigma_I\sigma_{III}/\sigma_{II}^2 - 1$ as a function of $\bar{d}/\delta$ for Gaussian distributions and as a function of δ^* for log-normal distributions. For Gaussian distributions, the value of $\sigma_I\sigma_{III}/\sigma_{II}^2 - 1$ for all practical $\bar{d}/\delta$ never exceeds 0.13. Compared with the values of $F^*_{D-\text{fixed}}(1-\phi)$ which are typically 1–10 when $\phi < 0.5$, $\sigma_I\sigma_{III}/\sigma_{II}^2 - 1$ is indeed a small correction and can be neglected under most occasions. For log-normal distributions, however, $\sigma_I\sigma_{III}/\sigma_{II}^2 - 1$ can become comparable to $F^*_{D-\text{fixed}}(1-\phi)$ when δ^* becomes close to unity. When this happens, neglecting $\sigma_I\sigma_{III}/\sigma_{II}^2 - 1$ term would introduce rather significant errors and should not be practiced.

Drag in Polydisperse Gas–Solid Suspensions with Particle–Particle Relative Motion

We now consider the fluid-particle drag in suspensions where the two particle species have different velocities relative to the fluid, i.e. $\Delta U_1 \neq \Delta U_2$. In this case, the fluid-particle drag will contain a particle–particle drag term that represents the momentum transfer between particle species due to hydrodynamic interactions. In a preceding numerical study, Yin and Sundaresan[18] characterized the special case where the two particle species are of the same size, i.e., $d_1 = d_2$. In this study, we are interested in the more general situation of $d_1 \neq d_2$. We will show that the particle–particle drag due to hydrodynamic

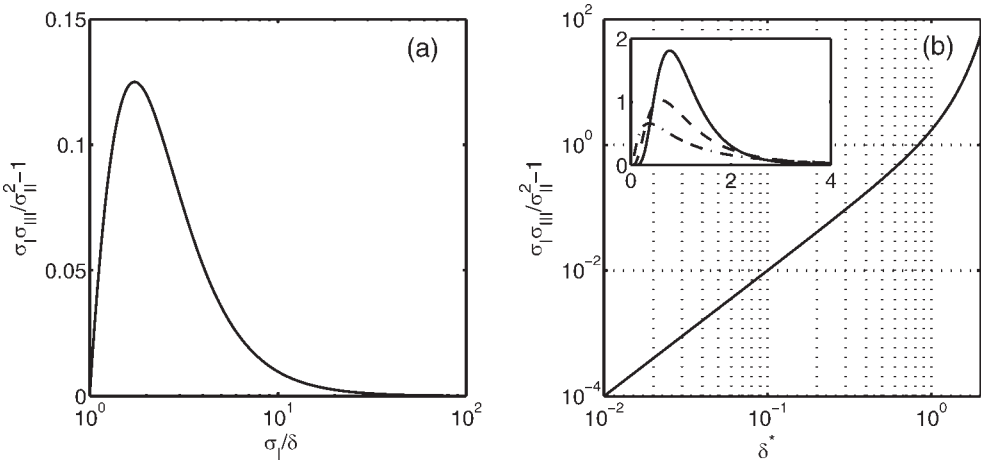

Figure 5. $\sigma_I\sigma_{III}/\sigma_{II}^2 - 1$ as a function of $\bar{d}/\delta$ for Gaussian particle size distributions (a), and as a function of δ^* for log-normal particle size distributions (b).

The lines were calculated base on Eq. 39 and Eq. 41. The small insert in (b) shows the log-normal size distribution $\sigma(d)\bar{d}$ as a function of $d/\bar{d}$ for three values of δ^*: 0.25 (solid line), 0.5 (dashed line), and 1.0 (dash-dot line).

Table 2. List of Polydisperse Suspension Simulations with Particle–Particle Relative Motions

Size Ratio	$\phi_1/\phi_2/M$	β^*_{11}	β^*_{12}	$-\beta^*_{12}/\beta^*_{11}$	β^*_{21}	β^*_{22}	$-\beta^*_{21}/\beta^*_{22}$
d_1:d_2 = 1:1.5	0.05/0.05/15	2.89 ± 0.04	−0.26 ± 0.04	0.09	−0.28 ± 0.04	1.77 ± 0.04	0.16
	0.05/0.10/15	4.25 ± 0.05	−0.73 ± 0.06	0.17	−0.75 ± 0.05	4.89 ± 0.09	0.15
	0.10/0.05/15	6.30 ± 0.04	−0.58 ± 0.05	0.09	−0.51 ± 0.04	2.35 ± 0.05	0.22
	0.05/0.15/12	5.61 ± 0.07	−1.33 ± 0.09	0.24	−1.23 ± 0.07	9.40 ± 0.10	0.13
	0.10/0.10/14	9.11 ± 0.15	−1.47 ± 0.13	0.16	−1.42 ± 0.13	6.25 ± 0.14	0.23
	0.05/0.20/12	7.50 ± 0.14	−2.09 ± 0.07	0.28	−2.18 ± 0.13	15.53 ± 0.07	0.14
	0.15/0.10/15	15.49 ± 0.16	−2.42 ± 0.15	0.16	−2.50 ± 0.14	8.04 ± 0.15	0.31
	0.10/0.20/12	16.08 ± 0.11	−4.18 ± 0.19	0.26	−4.48 ± 0.11	19.57 ± 0.18	0.23
	0.20/0.10/15	23.81 ± 0.21	−3.66 ± 0.24	0.15	−3.90 ± 0.23	10.40 ± 0.23	0.38
	0.05/0.30/12	12.09 ± 0.18	−4.75 ± 0.29	0.39	−4.57 ± 0.19	34.90 ± 0.31	0.13
	0.10/0.30/12	28.44 ± 0.56	−10.90 ± 0.59	0.38	−11.86 ± 0.56	45.74 ± 0.58	0.26
	0.20/0.20/12	42.80 ± 0.43	−12.83 ± 0.56	0.30	−13.10 ± 0.48	33.89 ± 0.52	0.38
	0.30/0.10/12	48.93 ± 0.31	−9.10 ± 0.31	0.18	−8.53 ± 0.32	18.86 ± 0.32	0.45
d_1:d_2 = 1:2.5	0.10/0.10/13	11.31 ± 0.21	−1.53 ± 0.22	0.14	−1.54 ± 0.22	5.03 ± 0.22	0.31
	0.10/0.20/12	20.06 ± 0.43	−4.61 ± 0.41	0.23	−3.91 ± 0.47	17.02 ± 0.42	0.23
	0.20/0.10/15	26.04 ± 0.27	−3.37 ± 0.22	0.13	−3.21 ± 0.24	8.50 ± 0.21	0.38
	0.10/0.30/10	37.27 ± 0.83	−12.30 ± 0.87	0.33	−13.39 ± 0.82	43.12 ± 0.89	0.31
	0.20/0.20/12	48.94 ± 0.37	−13.19 ± 0.23	0.27	−12.87 ± 0.41	29.95 ± 0.29	0.43
	0.30/0.10/15	51.78 ± 0.45	−7.69 ± 0.44	0.15	−7.74 ± 0.44	15.16 ± 0.43	0.51
d_1:d_2 = 1:4	0.05/0.10/22	7.68 ± 0.09	−0.61 ± 0.06	0.08	−0.72 ± 0.09	3.16 ± 0.06	0.23
	0.05/0.15/20	11.15 ± 0.15	−1.78 ± 0.16	0.16	−1.57 ± 0.17	7.06 ± 0.14	0.22
	0.10/0.10/20	12.65 ± 0.12	−1.12 ± 0.08	0.09	−1.03 ± 0.08	3.75 ± 0.07	0.27
	0.05/0.20/20	15.18 ± 0.26	−2.65 ± 0.31	0.17	−2.61 ± 0.28	12.79 ± 0.31	0.20
	0.15/0.10/25	19.07 ± 0.10	−1.71 ± 0.12	0.09	−1.74 ± 0.10	4.84 ± 0.12	0.36
	0.10/0.20/14	25.66 ± 0.27	−4.16 ± 0.21	0.16	−4.73 ± 0.35	14.54 ± 0.23	0.32
	0.20/0.10/23	27.37 ± 0.14	−2.58 ± 0.12	0.09	−2.66 ± 0.14	6.46 ± 0.13	0.41
	0.05/0.30/12	25.03 ± 0.65	−6.14 ± 0.69	0.24	−6.49 ± 0.66	31.56 ± 0.76	0.20
	0.25/0.10/24	37.96 ± 0.16	−3.99 ± 0.12	0.10	−3.84 ± 0.16	8.87 ± 0.14	0.43
	0.10/0.30/14	43.77 ± 0.73	−11.62 ± 0.88	0.26	−11.54 ± 0.70	38.50 ± 0.88	0.30
	0.20/0.20/19	52.40 ± 0.35	−11.04 ± 0.63	0.21	−10.70 ± 0.34	25.16 ± 0.67	0.42
	0.30/0.10/21	52.36 ± 0.19	−6.60 ± 0.19	0.13	−6.26 ± 0.18	12.79 ± 0.20	0.49

The first column contains the volume fractions and the number of configurations; the second, third, fifth, and sixth columns contain the dimensionless volume-specific friction coefficient β^*_{ij}. The ratio of the off-diagonals to the diagonals in the fourth and last columns indicate the importance of the hydrodynamic particle–particle drag. In all simulations $\lambda/d_1 = 0.01$.

interaction is always an important part of the total fluid-particle drag, and present a drag formula for polydisperse gas–solid suspensions with particle–particle relative motion.

As discussed previously, the dimensionless fluid-particle drag forces per particle and per volume in bidisperse gas–solid suspensions can be expressed as linear functions of fluid-particle relative velocities [c.f. Eqs. 18 and 19]. From now on, we will focus on the volume specific drag law Eq. 19 and report the values of the volume specific friction coefficient β^*_{ij} for different combinations of volume fractions, particle size ratios, and lubrication cutoff distances. The values for B^*_{ij} can be easily computed by invoking $n_i B^*_{ij} \langle d \rangle^3 = \beta^*_{ij}$.

In Table 2 through Table 5, we have listed all simulations conducted in this study with $\Delta U_1 \neq \Delta U_2$, including 504 simulations for the smallest lubrication cutoff $\lambda/d_1 = 0.01$, and 173 simulations for each of the higher lubrication cutoff values: $\lambda/d_1 = 0.02$, 0.05, and 0.10. Also listed in these tables are the friction coefficients β^*_{ij} and the ratios $-\beta^*_{12}/\beta^*_{11}$ and

Table 3. List of Polydisperse Suspension Simulations with Particle–Particle Relative Motions

Size Ratio	$\phi_1/\phi_2/M$	β^*_{11}	β^*_{12}	$-\beta^*_{12}/\beta^*_{11}$	β^*_{21}	β^*_{22}	$-\beta^*_{21}/\beta^*_{22}$
d_1:d_2 = 1:1.5	0.10/0.10/14	8.88 ± 0.11	−1.21 ± 0.09	0.14	−1.20 ± 0.10	5.99 ± 0.10	0.20
	0.10/0.20/12	15.39 ± 0.20	−3.95 ± 0.16	0.26	−3.67 ± 0.23	19.23 ± 0.18	0.19
	0.20/0.10/15	23.24 ± 0.16	−3.09 ± 0.18	0.13	−3.33 ± 0.18	9.83 ± 0.18	0.34
	0.10/0.30/12	26.91 ± 0.44	−9.55 ± 0.53	0.35	−10.33 ± 0.43	44.40 ± 0.54	0.24
d_1:d_2 = 1:2.5	0.10/0.10/12	11.12 ± 0.18	−1.26 ± 0.20	0.11	−1.36 ± 0.19	4.77 ± 0.20	0.28
	0.10/0.20/12	19.65 ± 0.27	−4.04 ± 0.26	0.20	−3.50 ± 0.31	16.45 ± 0.28	0.21
	0.20/0.10/15	25.75 ± 0.20	−2.96 ± 0.16	0.11	−2.91 ± 0.18	8.10 ± 0.15	0.36s
	0.10/0.30/10	35.66 ± 0.55	10.34 ± 0.55	0.29	−11.54 ± 0.57	41.17 ± 0.56	0.28
d_1:d_2 = 1:4	0.10/0.10/20	12.52 ± 0.07	−0.94 ± 0.04	0.08	−0.90 ± 0.07	3.57 ± 0.05	0.25
	0.10/0.20/14	24.88 ± 0.22	−3.73 ± 0.18	0.15	−3.95 ± 0.24	14.11 ± 0.19	0.28
	0.20/0.10/24	27.02 ± 0.10	−2.26 ± 0.08	0.08	−2.30 ± 0.09	6.14 ± 0.10	0.37
	0.10/0.30/14	42.41 ± 0.55	−10.54 ± 0.76	0.25	−10.18 ± 0.52	37.38 ± 0.78	0.27

The first column contains the volume fractions and the number of configurations; the second, third, fifth, and sixth columns contain the dimensionless volume-specific friction coefficient β^*_{ij}. The ratio of the off-diagonals to the diagonals in the fourth and last columns indicate the importance of the hydrodynamic particle–particle drag. In all simulations $\lambda/d_1 = 0.02$.

Table 4. List of Polydisperse Suspension Simulations with Particle–Particle Relative Motions

Size Ratio	$\phi_1/\phi_2/M$	β^*_{11}	β^*_{12}	$-\beta^*_{12}/\beta^*_{11}$	β^*_{21}	β^*_{22}	$-\beta^*_{21}/\beta^*_{22}$
d_1:d_2 = 1:1.5	0.10/0.10/14	8.61 ± 0.08	−0.94 ± 0.06	0.11	−0.93 ± 0.08	5.72 ± 0.07	0.16
	0.10/0.20/12	14.55 ± 0.15	−3.01 ± 0.11	0.21	−2.83 ± 0.18	18.29 ± 0.12	0.15
	0.20/0.10/15	22.46 ± 0.09	−2.41 ± 0.12	0.11	−2.53 ± 0.10	9.15 ± 0.12	0.28
	0.10/0.30/12	24.87 ± 0.39	−7.49 ± 0.43	0.30	−8.29 ± 0.36	42.3 ± 0.46	0.20
d_1:d_2 = 1:2.5	0.10/0.10/13	10.87 ± 0.13	−1.11 ± 0.15	0.10	−1.11 ± 0.14	4.62 ± 0.14	0.24
	0.10/0.20/12	18.99 ± 0.15	−3.29 ± 0.17	0.17	−2.84 ± 0.19	15.71 ± 0.18	0.18
	0.20/0.10/15	25.18 ± 0.14	−2.31 ± 0.10	0.09	−2.34 ± 0.12	7.44 ± 0.09	0.31
	0.10/0.30/10	33.14 ± 0.44	−8.28 ± 0.39	0.25	−9.25 ± 0.46	39.11 ± 0.40	0.24
d_1:d_2 = 1:4	0.10/0.10/20	12.36 ± 0.04	−0.74 ± 0.04	0.06	−0.74 ± 0.04	3.37 ± 0.03	0.22
	0.10/0.20/14	24.01 ± 0.18	−3.12 ± 0.15	0.13	−3.09 ± 0.19	13.50 ± 0.18	0.23
	0.20/0.10/24	26.56 ± 0.06	−1.85 ± 0.05	0.07	1.85 ± 0.06	5.71 ± 0.08	0.32
	0.10/0.30/14	40.69 ± 0.45	−8.62 ± 0.64	0.21	−8.46 ± 0.41	35.51 ± 0.68	0.24

The first column contains the volume fractions and the number of configurations; the second, third, fifth, and sixth columns contain the dimensionless volume-specific friction coefficient β^*_{ij}. The ratio of the off-diagonals to the diagonals in the fourth and last columns indicate the importance of the hydrodynamic particle–particle drag. In all simulations $\lambda/d_1 = 0.05$.

$-\beta^*_{21}/\beta^*_{22}$ representing the weight of the off-diagonals relative to the diagonals. It can be observed that the off-diagonals in the friction coefficient matrix are fairly significant compared to the diagonals, and they produce particle–particle drag forces that should not be neglected from the total fluid-particle drag force.

It may be observed from the data that the ratio $-\beta^*_{12}/\beta^*_{11}$ decreases with increasing particle size difference, and the ratio $-\beta^*_{21}/\beta^*_{22}$ increases with increasing particle size difference. These opposing trends, which are most obvious between the data obtained with d_1:d_2 = 1:1.5 and those with d_1:d_2 = 1:4 , can be explained as smaller particles would have fewer larger particle neighbors if the size difference between species increases, whereas the larger particles on average would find more smaller particles neighbors under the same situation. In addition, similar to what was reported in Yin and Sundaresan,[18] the off-diagonals decrease with increasing lubrication cutoff distance, indicating that the lubrication interaction between particles provides important contributions to the hydrodynamic particle–particle drag.

When we look for functions to fit β^*_{ij}, it is useful to recognize that the four components in β^*_{ij} are not independent of each other. Based on the principle of action and reaction between particle species, β^*_{ij} should always be symmetric, i.e., $\beta^*_{12} = \beta^*_{21}$. In addition, in order to reproduce the friction coefficients of bidisperse fixed beds when $\Delta U_1 = \Delta U_2$, β^*_{ij} must satisfy two constraints

$$\begin{aligned} \beta^*_{11} + \beta^*_{12} &= \beta^*_1 \\ \beta^*_{21} + \beta^*_{22} &= \beta^*_2, \end{aligned} \tag{42}$$

where $\beta^*_i = \beta_i \langle d \rangle^2/\mu$ is the dimensionless form of β_i that is related to $F^*_{Di-\text{fixed}}$ by Eq. 13. Our simulation data listed in Table 2 through Table 5 indicate that β^*_{ij} are indeed roughly symmetric. As shown in the left panel of Figure 6, $\beta^*_{12}/\beta^*_{21}$ as a function of ϕ were always close to unity. In the right panel of Figure 6, we show that the values of $(\beta^*_{11} + \beta^*_{12})/\beta^*_1$ and $(\beta^*_{21} + \beta^*_{22})/\beta^*_2$, where β^*_1 and β^*_2 were obtained from our fixed-bed simulations [c.f. Table 1], were also close to unity. Because of these constraints, the friction coefficient matrix can be written into the following form where β^*_{12} is the only free parameter

$$\begin{bmatrix} \beta^*_{11} & \beta^*_{12} \\ \beta^*_{21} & \beta^*_{22} \end{bmatrix} = \begin{bmatrix} \beta^*_1 - \beta^*_{12} & \beta^*_{12} \\ \beta^*_{12} & \beta^*_2 - \beta^*_{12} \end{bmatrix}. \tag{43}$$

Since we have already developed accurate fitting functions for β^*_1 and β^*_2 [Eqs. 23 and 25], it is our next task to look for appropriate functions to account for the dependence of β^*_{12} on ϕ_i, d_i, and λ.

Table 5. List of Polydisperse Suspension Simulations with Particle–Particle Relative Motions

Size Ratio	$\phi_1/\phi_2/M$	β^*_{11}	β^*_{12}	$-\beta^*_{12}/\beta^*_{11}$	β^*_{21}	β^*_{22}	$-\beta^*_{21}/\beta^*_{22}$
d_1:d_2 = 1:1.5	0.10/0.10/14	8.40 ± 0.07	−0.71 ± 0.04	0.08	−0.71 ± 0.06	5.50 ± 0.04	0.13
	0.10/0.20/12	13.88 ± 0.11	−2.34 ± 0.09	0.17	−2.17 ± 0.13	17.62 ± 0.10	0.12
	0.20/0.10/15	21.91 ± 0.06	−1.87 ± 0.08	0.08	−2.00 ± 0.07	8.62 ± 0.08	0.23
	0.10/0.30/12	23.37 ± 0.09	−5.95 ± 0.37	0.25	−6.74 ± 0.36	40.80 ± 0.40	0.16
d_1:d_2 = 1:2.5	0.10/0.10/13	10.71 ± 0.12	−0.94 ± 0.13	0.09	−0.94 ± 0.12	4.45 ± 0.12	0.21
	0.10/0.20/12	18.49 ± 0.08	−2.65 ± 0.13	0.14	−2.34 ± 0.14	15.07 ± 0.14	0.16
	0.20/0.10/15	24.72 ± 0.12	−1.83 ± 0.07	0.07	−1.87 ± 0.09	6.97 ± 0.07	0.27
	0.10/0.30/10	31.43 ± 0.34	−6.74 ± 0.35	0.21	−7.55 ± 0.35	37.56 ± 0.36	0.20
d_1:d_2 = 1:4	0.10/0.10/20	12.24 ± 0.03	−0.59 ± 0.04	0.05	−0.62 ± 0.03	3.23 ± 0.03	0.19
	0.10/0.20/14	23.40 ± 0.14	−2.54 ± 0.12	0.11	−2.47 ± 0.16	12.92 ± 0.16	0.19
	0.20/0.10/24	26.26 ± 0.05	−1.55 ± 0.05	0.06	−1.54 ± 0.05	5.40 ± 0.08	0.28
	0.10/0.30/14	39.26 ± 0.40	−7.11 ± 0.56	0.18	−7.08 ± 0.38	34.01 ± 0.61	0.21

The first column contains the volume fractions and the number of configurations; the second, third, fifth, and sixth columns contain the dimensionless volume-specific friction coefficient β^*_{ij}. The ratio of the off-diagonals to the diagonals in the fourth and last columns indicate the importance of the hydrodynamic particle–particle drag. In all simulations $\lambda/d_1 = 0.1$.

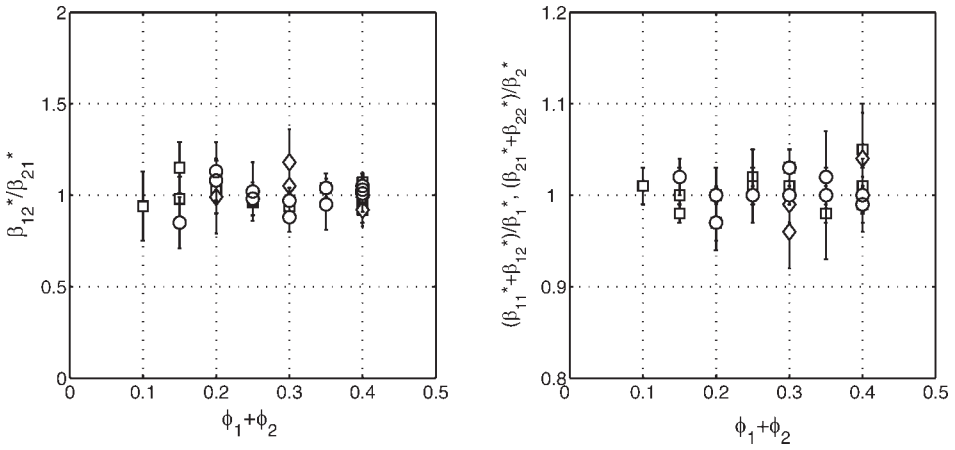

Figure 6. The left panel shows $\beta_{12}^*/\beta_{21}^*$ as a function of total volume fraction $\phi = \phi_1 + \phi_2$; the right panel shows the values of $(\beta_{11}^* + \beta_{12}^*)/\beta_1^*$ and $(\beta_{21}^* + \beta_{22}^*)/\beta_2^*$ as a function of ϕ.

The squares, diamonds, and circles represent simulation data with d_1:d_2 = 1:1.5, 1:2.5, and 1:4, respectively. The lubrication cutoff $\lambda/d_1 = 0.001$. This figure indicates that (1) the volume-specific friction coefficient matrix β_{ij}^* is nearly symmetric, and (2) the row summation of β_{ij}^* recovers the friction coefficients in bidisperse fixed beds of the particle composition. The error bars represent 90% confidence intervals due to variations in particle configurations.

In the process of seeking fitting functions for β_{12}^*, we were assisted by the insight gained from our previous study on polydisperse suspensions containing equally sized spheres.[18] In that study, it was found that for the special case of $d_1 = d_2 = d$, the friction coefficient matrix is simply

$$\begin{bmatrix} \beta_{11}^* & \beta_{12}^* \\ \beta_{21}^* & \beta_{22}^* \end{bmatrix} = 18(1-\phi)F_{D-\text{fixed}}^* \begin{bmatrix} (1+\alpha\phi_2)\phi_1 & -\alpha\phi_1\phi_2 \\ -\alpha\phi_1\phi_2 & (1+\alpha\phi_1)\phi_2 \end{bmatrix}, \tag{44}$$

where α is a logarithmic function of the distance on which the lubrication force between particles begins to saturate

$$\alpha = 1.313\log_{10}(d/\lambda) - 1.249, \tag{45}$$

and $F_{D-\text{fixed}}^*$ is the dimensionless drag of a monodisperse fixed bed of the same volume fraction [c.f. Eq. 7]. Comparing Eq. 44 with Eq. 43, one can see that for the case of $d_1 = d_2 = d$, β_{12}^* is proportional to β_1^* and β_2^*

$$\frac{\beta_{12}^*}{\phi_1\phi_2} = -\alpha\frac{\beta_1^*}{\phi_1} = -\alpha\frac{\beta_2^*}{\phi_2}. \tag{46}$$

Motivated by Eq. 46, we sought functions to relate $-\beta_{12}^*/\phi_1\phi_2$ to β_1^*/ϕ_1 and β_2^*/ϕ_2. Such functions should only contain symmetric combinations of β_1^*/ϕ_1 and β_2^*/ϕ_2, e.g., $\beta_1^*/\phi_1 + \beta_2^*/\phi_2$ or $\beta_1^*\beta_2^*/\phi_1\phi_2$, because a drag law should not depend on the way in which the particle species are indexed. After experimenting several different ways of combining β_1^*/ϕ_1 and β_2^*/ϕ_2, we found that $-\beta_{12}^*/\phi_1\phi_2$ can be approximated by a linear function of the harmonic mean of β_1^*/ϕ_1 and β_2^*/ϕ_2

$$\frac{\beta_{12}^*}{\phi_1\phi_2} = -\alpha\frac{2}{\phi_1/\beta_1^* + \phi_2/\beta_2^*}, \tag{47}$$

where α is given by

$$\alpha = 1.313\log_{10}(d_1/\lambda) - 1.249. \tag{48}$$

In Eq. 48, we used d_1, the size of the smaller particle species, to normalize λ. Eqs. 47 and 48 are reduced to Eqs. 46 and 45 for the special case of $d_1 = d_2$ and $\beta_1^*/\phi_1 = \beta_2^*/\phi_2$.

As Figure 7 shows, the expressions Eqs. 47 and 48 (the solid lines) provide good fittings for all β_{12}^* characterized from our numerical simulations (the symbols) regardless of volume fractions and particle size ratios. The average percentage deviation from Eqs. 47 and 48 with β_1^* and β_2^* determined from Eq. 27 to the numerical data is 13%; the maximum deviation is 31%. It may be observed from Figure 7 that most of the data points fall into the range of $\pm 13\%$ from the predictions of Eqs. 47 and 48 between the dashed lines sandwiching the center solid lines.

The fact that $-\beta_{12}^*/\phi_1\phi_2$ can be approximated by the product of a logarithmic function of λ/d_1 and the harmonic mean of β_1^*/ϕ_1 and β_2^*/ϕ_2, again, shows the importance of the local lubrication interactions between particles in the overall hydrodynamic particle–particle drag. In a random bidisperse suspension, the probability of finding a particle of species 2 right next to a particle of species 1—the probability of mutual contact—is known to be proportional to the harmonic mean of the two particle sizes.[45] As the overall lubrication force between particle species is proportional to the probability of mutual contact, it is not surprising that $-\beta_{12}^*/\phi_1\phi_2$ appeared to be proportional to the harmonic mean of β_1^*/ϕ_1 and β_2^*/ϕ_2. In fact, it was the above chain of thoughts that led us to Eq. 47, which turned out to be a simple yet excellent fitting function for our simulation data at all volume fractions and particle size ratios.

Equations 47 and 48 can easily be generalized to suspensions containing three or more species moving with different velocities relative to the fluid

$$\beta_{ij}^* = -\frac{2\alpha_{ij}\phi_i\phi_j}{\phi_i/\beta_i^* + \phi_j/\beta_j^*}. \tag{49}$$

In the above equation, α_{ij} is a logarithmic function of the ratio between the lubrication cutoff λ and the size of the smaller particle species of the two

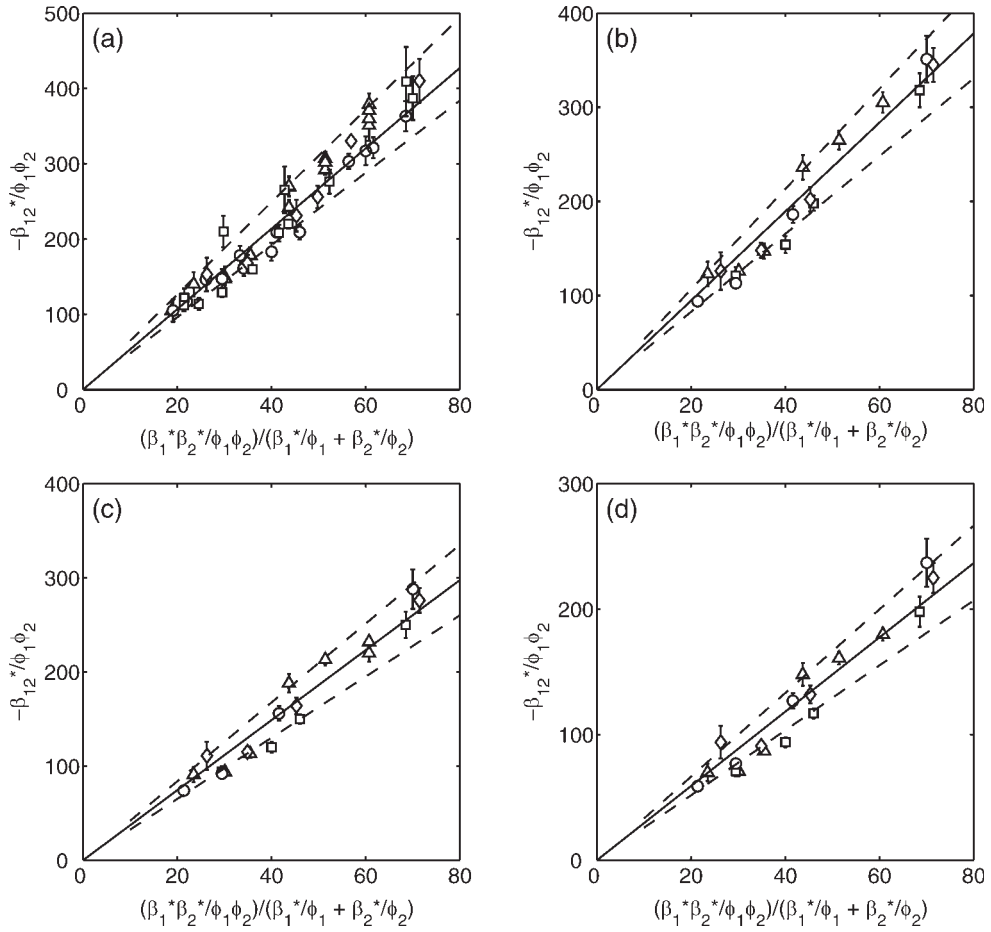

Figure 7. This figure shows the approximate linear dependence of $-\beta_{12}^*/\phi_1\phi_2$ on the harmonic mean of β_1^*/ϕ_1 and β_2^*/ϕ_2 for four different values of the lubrication cutoff: (a) $\lambda/d_1 = 0.001$, (b) $\lambda/d_1 = 0.002$, (c) $\lambda/d_1 = 0.005$, (d) $\lambda/d_1 = 0.01$.

The squares, diamonds, and circles represent, respectively, simulation data with $d_1{:}d_2$ = 1:1.5, 1:2.5, and 1:4. The upward triangles correspond to data from Yin and Sundaresan[18] where $d_1 = d_2$. The solid lines are based on the proposed fitting function Eq. 47 with α given by Eq. 48; the dashed lines represent the $\pm 13\%$ range of average deviations. The error bars represent 90% confidence intervals due to variations in particle configurations.

$$\alpha_{ij} = 1.313 \log_{10}(\min(d_i, d_j)/\lambda) - 1.249. \tag{50}$$

The net fluid-particle drag force per volume of suspension acting on species i is therefore

$$\begin{aligned} f_{Di}^* &= -\beta_i^* \Delta \mathrm{Re}_i - \sum_{j \neq i} \beta_{ij}^* (\Delta \mathrm{Re}_j - \Delta \mathrm{Re}_i) \\ &= -\beta_i^* \Delta \mathrm{Re}_i - \sum_{j \neq i} \frac{2\alpha_{ij}\phi_i\phi_j}{\phi_i/\beta_i^* + \phi_j/\beta_j^*} (\Delta \mathrm{Re}_i - \Delta \mathrm{Re}_j). \end{aligned} \tag{51}$$

One can substitute

$$\beta_i^* = \frac{18\phi_i(1-\phi)}{y_i^2} F_{Di-\mathrm{fixed}}^* \tag{52}$$

and

$$F_{Di}^* = \frac{\pi y_i^3}{6\phi_i} f_{Di}^* \tag{53}$$

into Eq. 51 to obtain the expression for the average fluid-particle drag per particle

$$\begin{aligned} F_{Di}^* &= -3\pi(1-\phi) \\ &\times \left[y_i \Delta \mathrm{Re}_i F_{Di-\mathrm{fixed}}^* + \sum_{j \neq i} \frac{2\alpha_{ij}\phi_j y_i^3 (\Delta \mathrm{Re}_i - \Delta \mathrm{Re}_j)}{y_i^2/F_{Di-\mathrm{fixed}}^* + y_j^2/F_{Dj-\mathrm{fixed}}^*} \right]. \end{aligned} \tag{54}$$

We constructed two ternary suspensions to test the applicability of Eq. 51 to general polydisperse gas–solid suspensions. Table 6 lists the volume fractions, sizes, and velocities of different particle species. It can be observed that the dimensionless drag forces calculated from Eq. 51 are very close to the actual drag forces obtained from simulations. Table 6 also shows that neglecting particle–particle hydrodynamic drag terms by setting α_{ij} to zero in Eq. 51 increases the differences between the calculated drag forces and the simulation data, proving that drag laws including hydrodynamic particle–particle drag terms are more accurate than the drag laws without such terms.

Table 6. Verification of the Drag Law Eq. 51 for Two Ternary Suspensions

	Suspension #1	Suspension #2
$\phi_{1,2,3}$	0.07 / 0.07 / 0.07	0.02 / 0.085 / 0.03
$d_{1,2,3}(\Delta x)$	9.60 / 12.0 / 14.4	7.60 / 9.60 / 11.6
$N_{1,2,3}$	510 / 261 / 151	84 / 180 / 36
M	20	19
$\langle d\rangle(\Delta x)$	11.7	9.60
$\Delta\mathrm{Re}_{1,2,3}$	0.0346 / 0.0485 / 0.0653	0.0252 / 0.0372 / 0.0466
$f^*_{D1,2,3}$ (simulation)	-0.085 ± 0.001 / -0.104 ± 0.001 / -0.133 ± 0.001	-0.0143 ± 0.0004 / -0.0686 ± 0.0004 / -0.0311 ± 0.0004
$f^*_{D1,2,3}$ (Eq. 50)	-0.083 / -0.103 / -0.127	-0.0132 / -0.0721 / -0.0315
$f^*_{D1,2,3}$ ($\alpha_{ij}=0$)	-0.095 / -0.103 / -0.115	-0.0155 / -0.0728 / -0.0285

Rows 1–4 contain the volume fractions, particle sizes in terms of lattice spacing Δx, numbers of particles in each simulation, and number of configurations. The fifth row contains the Sauter mean of the two suspensions, from which the Reynolds numbers in the sixth row were calculated. The last three rows compare the dimensionless drag forces obtained from simulations (the numbers after $\pm$ sign represent the 90% uncertainty levels) to those based on Eq. 51 using $\lambda = 0.01\Delta x$, and those based on Eq. 51 assuming zero hydrodynamic particle–particle drag ($\alpha_{ij}=0$).

Summary

Using the lattice-Boltzmann method, we characterized the fluid-particle drag forces in low-Reynolds-number bidisperse fixed beds and gas–solid suspensions with particle–particle relative motions. These particles are spherical in shape, and they are intimately mixed (the microstructure of our bidisperse suspensions is identical to that of a binary hard sphere fluid) and are assumed to have moderate-to-high Stokes numbers such that their fluctuating motions are not much affected by the hydrodynamic forces between successive collisions. This low-Re, high-St dual limit is realistic for many gas–solid suspensions containing 50–100 μm size particles under typical pressure conditions, and it allows for efficient characterization of the drag forces and the friction coefficients due to the linearity of the system.

For bidisperse fixed beds, our numerical data in the volume fraction range of $0.1 < \phi < 0.4$ agree very well with the existing data by van der Hoef et al.[8,9] Our data showed that the previously developed drag law by van der Hoef et al.,[8,9] for fixed beds is only accurate when the size difference between particles is moderate; in fixed beds with large size differences (1:4), our data confirmed that there is a systematic difference. By analyzing the general trend of existing data (both ours and those in van der Hoef et al.[8,9]) and the limiting behaviors of the drag forces, we developed a modified drag formula for polydisperse fixed beds

$$F^*_{Di-\mathrm{fixed}} = \frac{1}{1-\phi} + \left(F^*_{D-\mathrm{fixed}} - \frac{1}{1-\phi}\right)\left[a y_i + (1-a) y_i^2\right],$$

where a is a cubic polynomial of the total volume fraction of the suspension

$$a(\phi) = 1 - 2.660\phi + 9.096\phi^2 - 11.338\phi^3,$$

$F^*_{Di-\mathrm{fixed}}$ is the dimensionless drag force per particle of type i in a polydisperse fixed bed [c.f. Eq. 10], $F^*_{D-\mathrm{fixed}}$ is the dimensionless drag force in a monodisperse fixed bed [c.f. Eq. 7], and y_i is the dimensionless particle size ratio $d_i/\langle d\rangle$ with $\langle d\rangle$ the Sauter mean of the suspension [c.f. Eq. 26]. In the volume fraction range $0.1 < \phi < 0.5$, this new drag law fits the existing numerical data with an average percentage error of 3.9% and a maximum error of 9.4%; thus, it is a significant improvement over the existing drag formulas. On the basis of this drag formula, a relation between the overall pressure drop $\mathrm{d}P/\mathrm{d}x$ for a porous medium with a continuous grain size distribution $\sigma(d)$ and the superficial fluid velocity U_s through the medium is developed

$$\frac{\mathrm{d}P}{\mathrm{d}x} = -\frac{18\phi\mu U_s}{(1-\phi)\langle d\rangle^2}\left[F^*_{D-\mathrm{fixed}} + \frac{1}{1-\phi}\left(\frac{\sigma_I\sigma_{III}}{\sigma_{II}\sigma_{II}} - 1\right)\right],$$

where σ_I, σ_{II}, and σ_{III} are the first, second, and third order moments of $\sigma(d)$, and $\langle d\rangle = \sigma_{III}/\sigma_{II}$.

For bidisperse gas–solid suspensions with particle–particle relative motions, our objective is to characterize and develop fitting functions for the hydrodynamic particle–particle drag, a term that is not very well understood to date and is usually neglected in the existing drag formulas. Because of the linearity of low-Re flows, the drag forces acting on the two particle species in a bidisperse suspension with particle–particle relative motion may be expressed as linear functions of their respective velocities relative to the fluid. The proportionality constants between the forces and the velocities, known as the friction coefficients, is a matrix the off-diagonals of which are indicative of the size of the hydrodynamic particle–particle drag. Our numerical data for the friction coefficient matrix indicate that the off-diagonals produce sizeable contributions to the drag forces, and they are in fact linear functions of the harmonic means of the drags in bidisperse fixed beds [c.f. Eq. 49]. The net dimensionless fluid-particle drag force per volume of suspension acting on particles of type i in a polydisperse suspension where different particle types have different velocities relative to the fluid is

$$f^*_{Di} = -\beta^*_i \Delta\mathrm{Re}_i - \sum_{j\neq i} \frac{2\alpha_{ij}\phi_i\phi_j}{\phi_i/\beta^*_i + \phi_j/\beta^*_j}\left(\Delta\mathrm{Re}_i - \Delta\mathrm{Re}_j\right).$$

In the above equation, f^*_{Di} and $\Delta\mathrm{Re}_i$ are defined in Eq. 19, β^*_i is the volume-specific friction coefficient for type i particles in a polydisperse fixed bed of the same composition and is related to $F^*_{Di-\mathrm{fixed}}$ by Eq. 52, and α_{ij} is a logarithmic function of the ratio between the lubrication cutoff λ and the size of the smaller particle species of the two

$$\alpha_{ij} = 1.313\log_{10}(\min(d_i, d_j)/\lambda) - 1.249.$$

This drag formula fits our numerical data with an average percentage deviation of 13%, and a maximum deviation of

31%. The logarithmic dependence of the off-diagonals on the lubrication cutoff indicates that the hydrodynamic particle–particle drag in polydisperse suspensions of spherical particles of infinite Stokes numbers would diverge to infinity due to the strong lubrication interaction between close pairs of dissimilar particles. To suppress this nonphysical divergence, a length scale λ on which the lubrication force becomes saturated is needed—it reflects the reality that the growth of the lubrication force between two approaching particles would eventually be limited by surface roughness, non-continuum effects, or finite weights of the particles.

The difference between a freely evolving bidisperse suspension and a frozen bidisperse suspension is that the freely evolving suspension can develop instabilities, and the particle–particle momentum transfer will include an extra term due to direct collision and friction [c.f. Eq. 4]. In this study, we used frozen suspensions the microstructure of which is identical to that of a binary hard sphere suspension to isolate the particle–particle hydrodynamic momentum transfer under an idealized condition. Another study is underway to study the instability / microstructure and particle–particle collisional momentum transfer in high-St freely evolving binary suspensions. Allowing the particles to move also opens up possibilities to extend the formulas presented in this study to finite Reynolds number regime. Despite that binary gas–solid suspensions are usually unstable (e.g. see Valiveti and Koch[46]), as the instability is usually manifested on large length scales, we expect that our drag law will apply on sufficiently small differential volumes where segregation and nonrandom distribution of particles are not critically important and that this segregation should naturally emerge as an instability mode of the Euler-Euler model.

Acknowledgements

This research received supports from ExxonMobil Corporation, US Department of Energy (DE-FC26-07NT43098), and ACS Petroleum Research Fund (43901-AC9). The authors would like to acknowledge graduate student William Holloway for assisting in the verification of the applicability of the drag laws to ternary fixed beds and suspensions, and Professor Jos Derksen for supplying us a bidisperse particle configuration generator.

Literature Cited

1. Leboreiro J, Joseph GG, Hrenya CM. Revisiting the standard drag law for bubbling, gas-fluidized beds. *Powder Tech.* 2008;183:385–400.
2. Leboreiro J, Joseph GG, Hrenya CM, Snider DM, Banerjee SS, Galvin JE. The influence of binary drag laws on simulations of species segregation in gas-fluidized beds. *Powder Tech.* 2008;184:275–299.
3. Bokkers GA, van Sint Annaland M, Kuipers JAM. Mixing and segregation in a bidisperse gas–solid fluidised bed: a numerical and experimental study. *Powder Tech.* 2004;140:176–186.
4. Beetstra R, van der Hoef MA, Kuipers JAM. Numerical study of segregation using a new drag force correlation for polydisperse systems derived from lattice-Boltzmann simulations. *Chem Eng Sci.* 2007;62:246–255.
5. Hill RJ, Koch DL, Ladd AJC. The first effects of fluid inertia on flows in ordered and random arrays of spheres. *J Fluid Mech.* 2001; 448:213–241.
6. Hill RJ, Koch DL, Ladd AJC. Moderate-Reynolds-number flows in ordered and random arrays of spheres. *J Fluid Mech.* 2001;448:243–278.
7. Benyahia S, Syamlal M, O'Brien TJ. Extension of Hill-Koch-Ladd drag correlation over all ranges of Reynolds number and solid volume fraction. *Powder Tech.* 2006;162:166–174.
8. van der Hoef MA, Beetstra R, Kuipers JAM. Lattice-Boltzmann simulations of low-Reynolds-number flow past mono- and bidisperse arrays of spheres. *J Fluid Mech.* 2005;528:233–254.
9. van der Hoef MA. Erratum. *AIChE J.* 2007;53:3020.
10. Beetstra R, van der Hoef MA, Kuipers JAM. Drag force of intermediate Reynolds number flows past mono- and bidisperse arrays of spheres. *AIChE J.* 2007;53:489–501.
11. Wylie JJ, Koch DL. Rheology of suspensions with high particle inertia and moderate fluid inertia. *J Fluid Mech.* 2003;480:95–118.
12. Khoe GK, Ip TL, Grace JR. Rheological and fluidization behavior of powders of different particle-size distribution. *Powder Tech.* 1991;66:127–141.
13. Sun G, Grace JR. Effect of particle-size distribution in different fluidization regimes. *AIChE J.* 1992;38:716–722.
14. Gauthier D, Zerguerras S, Flamant G. Influence of the particle size distribution of powders on the velocities of minimum and complete fluidization. *Chem Eng J.* 1999;74:181–196.
15. Lin CL, Wey MY, You SD. The effect of particle size distribution on minimum fluidization velocity at high temperature. *Powder Tech.* 2002;126:297–301.
16. Lorences MJ, Patience GS, Diez FV, Coca J. Fines effects on collapsing fluidized beds. *Powder Tech.* 2003;131:234–240.
17. Shadle LJ, Spenik J, Sarra A, Ontko J. Factorial tests on process operating conditions and bed fines on the circulating fluid bed performance. *Ind Eng Chem Res.* 2004;43:4166–4173.
18. Yin X, Sundaresan S. Drag law for bidisperse gas–solid suspensions containing equally sized spheres. *Ind Eng Chem Res.* 2009;42:227–241.
19. Koch DL. Kinetic theory for a monodisperse gas–solid suspension. *Phys Fluids A.* 1990;2:1711–1723.
20. Kumaran V, Koch DL. Properties of a bidisperse particle-gas suspension, Part 1. Collision time small compared to the viscous relaxation time. *J Fluid Mech.* 1993;247:623–641.
21. Batchelor GK. Sedimentation in a dilute polydisperse system of interacting spheres. Part 1. General theory. *J Fluid Mech.* 1982; 119:379–408.
22. Batchelor GK, Wen CS. Sedimentation in a dilute polydisperse system of interacting spheres. Part 2. Numerical results. *J Fluid Mech.* 1982;124:495–528.
23. Davis RH, Gecol H. Hindered settling function with no empirical parameters for polydisperse suspensions. *AIChE J.* 1994;40:570–575.
24. Revay JM, Higdon JJL. Numerical simulation of polydisperse sedimentation: equal size spheres. *J Fluid Mech.* 1992;243:15–32.
25. Jackson R. Locally averaged equations of motion for a mixture of identical spherical particles and a Newtonian fluid. *Chem Eng Sci.* 1997;52:2457–2469.
26. Syamlal M, Roger WA, O'Brien TJ. MFIX documentation and theory guide. US Department of Energy: Technical Report DOE/METC94/1004, NTIS/DE94000087, 1993.
27. Owoyemi O, Mazzei L, Lettieri P. CFD modeling of binary-fluidized suspensions and investigation of role of particle–particle drag on mixing and segregation. *AIChE J.* 2007;53:1924–1940.
28. Feng YQ, Xu BH, Zhang SJ, Yu AB. Discrete particle simulation of gas fluidization of particle mixtures. *AIChE J.* 2004;50:1713–1728.
29. Snider DM. An incompressible three-dimensional multiphase particle-in-cell model for dense particle flows. *J Comp Phys.* 2001;170:523–549.
30. Koch DL, Hill RJ. Inertial effects in suspensions and porous media flows. *Annu Rev Fluid Mech.* 2001;33:619–647.
31. van Wachem BGM, Schouten JC, van den Bleek, CM, Krishna R, Sinclair JL. CFD modeling of gas-fluidized beds with a bimodal particle mixture. *AIChE J.* 2001;47:1292–1302.
32. Huilin L, Yurong H, Gidaspow D, Lidan Y, Yukun Q. Size segregation of binary mixture of solids in bubbling fluidized beds. *Powder Tech.* 2003;134:86–97.
33. Fan R, Marchisio DL, Fox RO. Application of the direct quadrature method of moments to polydisperse gas–solid fluidized beds. *Powder Tech.* 2004;139:7–20.
34. Gera D, Syamlal M, O'Brien TJ. Hydrodynamics of particle segregation in fluidized beds. *Int J Multiphase Flow.* 2004;30:419–428.
35. Cooper S, Coronella CJ. CFD simulations of particle mixing in a binary fludized bed. *Powder Tech.* 2005;151:27–36.
36. Dahl SR, Hrenya CM. Size segregation in gas–solid fluidized beds with continuous size distributions. *Chem Eng Sci.* 2005;60:6658–6673.

37. Syamlal M. The particle–particle drag term in a multiparticle model of fluidization. US Department of Energy: Technical Report DOE/MC/21353–2373, NTIS/DE87006500, 1987.
38. Huilin L, Gidaspow D, Manger E. Kinetic theory of fluidized bindary granular mixtures. *Phys Rev E*. 2001;64:061301.
39. Ladd AJC. Numerical simulations of particulate suspensions via a discretized Boltzmann equation. Part 1. Theoretical foundation. *J Fluid Mech*. 1994;271:285–309.
40. Ladd AJC. Numerical simulations of particulate suspensions via a discretized Boltzmann equation. Part 2. Numerical results. *J Fluid Mech*. 1994;271:311–339.
41. Ladd AJC, Verberg R. Lattice-Boltzmann simulations of particle-fluid suspensions. *J Stat Phys*. 2001;104:1191–1251.
42. Nguyen NQ, Ladd AJC. Lubrication corrections for lattice-Boltzmann simulations of particle suspensions. *Phys Rev E*. 2002;66:046708.
43. Kim S, Karrila SJ. *Microhydrodynamics: Principles and Selected Applications*. New York: Dover, 2005.
44. Ashcroft NW, Langreth DC. Structure of binary liquid mixtures. I. *Phys Rev*. 1967;156:685–692.
45. Lebowitz JL. Exact solution of generalized Percus-Yevick equation for a mixture of hard spheres. *Phys Rev A*. 1964;133:895–899.
46. Valiveti P, Koch DL. The inhomogeneous structure of a bidisperse sedimenting gas–solid suspension. *Phys Fluids*. 1999;11:3283–3305.

Manuscript received Sept. 7, 2008, and revision received Nov. 15, 2008.

Chemical Engineering Science 66 (2011) 4403–4420

Contents lists available at ScienceDirect

Chemical Engineering Science

journal homepage: www.elsevier.com/locate/ces

Meso-scale structures of bidisperse mixtures of particles fluidized by a gas

William Holloway [a], Sofiane Benyahia [b], Christine M. Hrenya [c], Sankaran Sundaresan [a,*]

[a] Department of Chemical and Biological Engineering, Princeton University, Princeton, NJ 08544, United States
[b] National Energy Technology Laboratory, Morgantown, WV 26505, United States
[c] Department of Chemical and Biological Engineering, University of Colorado, Boulder, CO 80309, United States

ARTICLE INFO

Article history:
Received 28 December 2010
Received in revised form
17 April 2011
Accepted 20 May 2011
Available online 1 June 2011

Keywords:
Fluidization
Fluid mechanics
Hydrodynamics
Multiphase flow
Suspension
Transport processes

ABSTRACT

Flow characteristics of bidisperse mixtures of particles fluidized by a gas predicted by the *mixture* based kinetic theory of Garzó et al. (2007a,b) and the *species* based kinetic theory model of Iddir and Arastoopour (2005) are compared. Simulations were carried out in two- and three-dimensional periodic domains. Direct comparison of the meso-scale gas-particle flow structures, and the domain-averaged slip velocities and meso-scale stresses reveals that both *mixture* and *species* based kinetic theory models manifest similar predictions for all the size ratios examined in this study. A detailed analysis is presented in which we demonstrate when the *species* based theory of Iddir and Arastoopour (2005) will reduce to a mathematical form similar to the *mixture* framework of Garzó et al. (2007a,b). We also find that the flow characteristics obtained for bidisperse mixtures are very similar to those obtained for monodisperse systems having the same Sauter mean diameter for the cases examined; however, the domain-averaged properties of monodisperse and bidisperse gas-particle flows do demonstrate quantitative differences. The use of filtered two-fluid models that average over meso-scale flow structures has already been described in the literature; it is clear from the present study that such filtered models are needed for coarse-grid simulations of polydisperse systems as well.

1. Introduction

Polydisperse (e.g. particles differing in size and/or density) gas-particle flows arise throughout the petrochemical, pharmaceutical, and energy conversion industries in fluidized beds, risers and pneumatic conveying devices. Despite the ubiquity of fluidized bed units in the chemical process industry the effect of polydispersity on the hydrodynamic behavior of fluidized beds remains poorly understood. The addition of a small amount of fine particles to an otherwise monodisperse fluidized bed is known to promote uniform fluidization (Squires et al., 1985; Yates and Newton, 1986). However, increasing the concentration of fine particles is known to result in macroscopic segregation between particles of different sizes when the superficial gas velocity is between the minimum fluidization velocity of the largest and smallest particle species (Rowe and Nienow, 1976; Geldart et al., 1981; Peeler and Huang, 1989; Hoffman et al., 1993; Joseph et al., 2007). There also exists a substantial amount of controversy on the role of bubbles in the mixing/segregation of different particle species in fluidized beds. Some argue that bubbles act as mixing agents in fluidized beds (Wu and Baeyens, 1998), while others argue that the bubbles tend to exacerbate the segregation of large particles (Rowe et al., 1972). Recent experimental work has demonstrated that segregation is correlated with the static height of the fluidized bed, but not the bubble parameters (Chew and Hrenya, in press).

Hydrodynamic (or continuum) model frameworks allow one to interrogate the physical mechanisms at play in the mixing/segregation phenomena in polydisperse gas-particle flows. These continuum model frameworks treat particle and fluid phases as interpenetrating continua (Gidaspow, 1994; Fan and Zhu, 1998; Jackson, 2000). Using the assumption of that particles in fluidized beds and risers interact predominantly through binary collisions, several researchers have developed kinetic theory based constitutive models for the stress in the particle phase and applied these models to the analysis of gas-particle flows (Lun et al., 1984; Sinclair and Jackson, 1989; Ding and Gidaspow, 1990; Koch and Sangani, 1999). There has been a considerable effort over the past 20 years devoted towards the extension of these monodisperse kinetic theories to account for polydispersity (for recent review, see Hrenya, 2011). Jenkins and Mancini (1989) constructed a model for binary particle mixtures assuming equipartition of granular energy. However, it was later shown via theory, experiments, and simulations that the assumption of equipartition of granular energy was invalid due to the fact that granular systems exhibit collisional dissipation of pseudothermal

* Corresponding author. Tel.: +1 609 258 4583; fax: +1 609 258 0211.
E-mail address: sundar@princeton.edu (S. Sundaresan).

0009-2509/$ - see front matter © 2011 Elsevier Ltd. All rights reserved.
doi:10.1016/j.ces.2011.05.037

energy unlike molecular systems (Garzó and Dufty, 1999; Wildman and Parker, 2002; Clelland and Hrenya, 2002). Several polydisperse kinetic theory models have since been derived without the constraint of equipartition of granular energy. Broadly speaking, these models adopt either a *species* or *mixture* based framework.

In the *species* based framework, evolution equations for *species* mass, momentum, and granular energy are formulated for each phase. Kinetic theories using this model framework have been derived for both binary (Huilin et al., 2001) and general polydisperse systems with many different components (Iddir and Arastoopour, 2005). Benyahia (2008) compared several *species* based polydisperse kinetic theories against molecular dynamics simulation results of Galvin et al. (2005) for simple shear flows and found the theory derived by Iddir and Arastoopour (2005) to match most closely the data.

In contrast, the *mixture* kinetic theory model framework only requires the solution of *mixture* momentum and fluctuating energy balance equations along with separate evolution equations for the individual species concentrations. The individual species velocities and granular temperatures are updated through algebraic constraints relating mixture properties to the constituent particle species. Kinetic theory models of this form are begin to appear in the literature (Garzó et al., 2007a,b; van Sint Annaland et al., 2009a,b). The number of differential balance equations in the *mixture* treatment is lower than that in the *species* treatment, and this difference in the number of equations increases with the number of species. It is reasonable to suspect that this difference would lead to lower CPU times for the *mixture* framework, which will be tested as a part of this study.

While there has been some work devoted to the simulation of segregation and bubbling phenomena of bidisperse gas-particle flows using the *mixture* and *species* based kinetic theory frameworks (Huilin et al., 2003; Owoyemi et al., 2007; Fan and Fox, 2008; van Sint Annaland et al., 2009b), there exists relatively few studies attempting to directly compare the predictions of the *species* and *mixture* based polydisperse kinetic theory model frameworks for a set of test cases.

The first objective of this work is to perform a direct comparison of the *mixture* based kinetic theory of Garzó et al. (2007a,b) (GHD theory) with the *species* based kinetic theory model of Iddir and Arastoopour (2005) (IA theory) for two different binary particle size distributions (PSDs). The PSDs used in this study are intended to span a wide range of particle size and particle volume fraction ratios. A direct comparison of the meso-scale gas-particle flow structures along with domain-averaged slip velocities and meso-scale stresses predicted by each kinetic theory framework will be presented. Furthermore, we follow an analysis similar to Goldman and Sirovich (1967) to establish a criteria where we expect the *species* based IA kinetic theory framework to have a similar mathematical form to the *mixture* based GHD kinetic theory model.

The second objective of this work is to compare the domain-averaged quantities obtained from bidisperse gas-particle flow simulations with those obtained for equivalent monodisperse systems having the same Sauter mean diameter. It will be shown that both monodisperse and bidisperse gas-particle flows manifest qualitatively similar flow structures.

The final objective of this study is to demonstrate the need for the development of sub-grid models to enable accurate coarse-grid simulation of continuum models for bidisperse gas-particle flows. It is known that *filtered* two-fluid model equations are necessary to perform coarse-grid simulations of monodisperse gas-particle flows without neglecting the consequences of the fine scale structures that occur on a sub-grid scale (Agrawal et al., 2001; Andrews et al., 2005; Igci et al., 2008). We present filtered statistics on the fluid-particle drag force in a bidisperse gas-particle flow, and illustrate that *filtered* models similar to what are required for the accurate simulation of monodisperse gas-particle flows on coarse numerical grids are indeed necessary for polydisperse systems as well.

2. Continuum model equations

In this work we seek to compare the predictions of *species* and *mixture* based polydisperse kinetic theories for two different polydisperse mixtures of particles. The two polydisperse kinetic theory models, the polydisperse fluid-particle drag model, and the numerical implementation used to solve the mono- and bi-disperse gas-particle flow problems are presented in this section.

2.1. Iddir–Arastoopour (IA) kinetic theory model

The Iddir–Arastoopour kinetic theory model consists of the following set of balance equations for particle species concentration, momentum, and fluctuating energy (Iddir and Arastoopour, 2005):

$$\frac{\partial(\rho_{s_i}\phi_i)}{\partial t}+\nabla\cdot(\rho_{s_i}\phi_i\mathbf{v_i})=0 \tag{1}$$

$$\frac{\partial(\rho_f\epsilon_f)}{\partial t}+\nabla\cdot(\rho_f\epsilon_f\mathbf{v_f})=0 \tag{2}$$

$$\frac{\partial(\rho_{s_i}\phi_i\mathbf{v_i})}{\partial t}+\nabla\cdot(\rho_{s_i}\phi_i\mathbf{v_i}\mathbf{v_i})=-\nabla\cdot\sigma_{s_i}+n_i\mathbf{F_i}+\sum_{m\neq i}^{s}\mathbf{I_{im}} \tag{3}$$

$$\frac{\partial(\rho_f\epsilon_f\mathbf{v_f})}{\partial t}+\nabla\cdot(\rho_f\epsilon_f\mathbf{v_f}\mathbf{v_f})=\epsilon_f\nabla\cdot\sigma_f-\sum_{i=1}^{s}\mathbf{f_{D_i}}+\rho_f\epsilon_f\mathbf{g} \tag{4}$$

$$\frac{3n_i}{2}\left(\frac{\partial T_i}{\partial t}+\mathbf{v_i}\cdot\nabla T_i\right)=-\nabla\cdot\mathbf{q_i}-\sigma_{s_i}:\nabla\mathbf{v_i}+\sum_{p=1}^{s}N_{ip} \tag{5}$$

where

$$\mathbf{F_i}=V_i\nabla\cdot\sigma_f+\mathbf{F_{D_i}}+m_i\mathbf{g} \tag{6}$$

Here, ρ_{s_i}, ϕ_i, n_i, m_i, $\mathbf{v_i}$, and T_i refer to the density, volume fraction, number density, mass, velocity and granular temperature of the ith particle species, respectively. The fluid density, velocity, and volume fraction are denoted by ρ_f, $\mathbf{v_f}$, and ϵ_f, respectively. In Eq. (3), σ_{s_i} represents the stress tensor of the ith particle species, $\mathbf{F_i}$ represents the sum of external forces experienced by particles of type i, and s is the number of particle species in the polydisperse mixture. In Eq. (4), $\mathbf{f_{D_i}}$ is the fluid-particle drag force *per unit volume suspension* experienced by a particle of type i, σ_f represents the gas phase stress tensor, and $\mathbf{g}$ is the gravitational acceleration. In all gas-particle flow simulations performed here, the Newtonian constitutive equation is assumed for the gas phase stress. The particle–particle collisional momentum exchange between types $\mathbf{I_{im}}$ defined in Eqs. (3) and (5) is given by

$$\mathbf{I_{im}}=\gamma_{im}\left\{\sqrt{\pi}R_2(\mathbf{v_m}-\mathbf{v_i})+\frac{d_{im}\pi R_0}{12}\left(\nabla\ln\frac{n_i}{n_m}-\frac{3}{2}\nabla\ln\frac{T_i}{T_m}\right)+\frac{d_{im}\pi}{16}[\mathbf{\Xi_{im}}+\mathbf{\Omega_{im}}+\mathbf{\Lambda_{im}}]\right\} \tag{7}$$

where

$$\gamma_{im}=\frac{d_{im}^2}{4}\frac{\rho_i\phi_i\rho_m\phi_m}{m_0}g_{im}(1+e_{im})\left(\frac{m_im_m}{T_iT_m}\right)^{3/2} \tag{8}$$

$$\mathbf{\Xi_{im}}=\left(\frac{m_m\nabla T_m}{T_m^2}-\frac{m_i\nabla T_i}{T_i^2}\right)R_{10} \tag{9}$$

$$\mathbf{\Omega_{im}} = \frac{5m_i m_m}{192(m_i+m_m)^2}\left(\frac{m_i\nabla T_m}{T_m^2} - \frac{m_m\nabla T_i}{T_i^2}\right)R_3 \tag{10}$$

$$\mathbf{\Lambda_{im}} = \frac{5m_i m_m}{96(m_i+m_m)}\left(\frac{\nabla T_m}{T_m^2} - \frac{\nabla T_i}{T_i^2}\right)R_4 \tag{11}$$

In Eq. (8) $m_0 = m_i + m_m$, e_{im} is coefficient of restitution for collisions between particles of type i and m, and g_{im} is the radial distribution function at contact for a bidisperse mixture of particles of types i and m. The terms R_0, R_2, R_3, R_4, and R_{10} in Eqs. (7), (9)–(11) are given as

$$R_0 = \frac{1}{A_{im}D_{im}^{5/2}} + \frac{15B_{im}^2}{A_{im}^{5/2}D_{im}^{7/2}} + \frac{175B_{im}^4}{A_{im}^{7/2}D_{im}^{9/2}} \tag{12}$$

$$R_2 = \frac{1}{2A_{im}^{3/2}D_{im}^2} + \frac{3B_{im}^2}{A_{im}^{5/2}D_{im}^3} + \frac{15B_{im}^4}{A_{im}^{7/2}D_{im}^4} \tag{13}$$

$$R_3 = \frac{1}{A_{im}^{3/2}D_{im}^{7/2}} + \frac{21B_{im}^2}{2A_{im}^{5/2}D_{im}^{9/2}} + \frac{315B_{im}^4}{8A_{im}^{7/2}D_{im}^{11/2}} \tag{14}$$

$$R_4 = \frac{3}{A_{im}^{5/2}D_{im}^{7/2}} + \frac{35B_{im}^2}{2A_{im}^{7/2}D_{im}^{9/2}} + \frac{441B_{im}^4}{8A_{im}^{9/2}D_{im}^{11/2}} \tag{15}$$

$$R_{10} = \frac{1}{A_{im}^{5/2}D_{im}^{5/2}} + \frac{25B_{im}^2}{2A_{im}^{7/2}D_{im}^{7/2}} + \frac{1225B_{im}^4}{8A_{im}^{9/2}D_{im}^{9/2}} \tag{16}$$

where

$$A_{im} = \frac{m_i T_m + m_m T_i}{2T_i T_m}, \quad B_{im} = \frac{m_i m_p (T_p - T_i)}{2m_0 T_i T_m} \tag{17}$$

$$D_{im} = \frac{m_i m_m (m_i T_i + m_m T_m)}{2m_0^2 T_i T_m} \tag{18}$$

In Eq. (5), $\mathbf{q_i}$ represents the granular energy flux term of a particle of type i, and N_{ip} is the collisional dissipation of granular energy due to inelastic collisions. In Eq. (6), V_i is the volume of the ith particle type and $\mathbf{F_{D_i}}$ is the fluid-particle drag force *per particle* experienced by a particle of type i. Constitutive relations for σ_{s_i}, $\mathbf{q_i}$, and N_{ip} can be found in Iddir and Arastoopour (2005) and Galvin (2007).

2.2. Garzó, Hrenya and Dufty (GHD) kinetic theory model

Mixture based kinetic theory models require the solution of individual species mass balance equations, and the balance equations for the mixture velocity and granular energy. Individual species velocities and temperatures are obtained from the mixture quantities and local composition using constitutive relations, which take the form of a set of non-linear algebraic equations. This allows one to simulate a polydisperse gas-particle flow with many different constituent particle species without having to solve an evolution equation for the momentum and fluctuating energy of each particle type. One such mixture framework was recently developed by Garzó et al. (2007a,b) for polydisperse granular flows with arbitrary levels of particle inelasticity. The GHD kinetic theory model has the following form:

$$\frac{\partial(\rho_{s_i}\phi_i)}{\partial t} + \nabla\cdot(\rho_{s_i}\phi_i\mathbf{v_i}) = 0 \tag{19}$$

$$\frac{\partial(\rho_s\mathbf{v})}{\partial t} + \nabla\cdot(\rho_s\mathbf{vv}) = -\nabla\cdot\sigma_s + \sum_{i=1}^{s} n_i\mathbf{F_i} \tag{20}$$

$$\frac{3n}{2}\left(\frac{\partial T}{\partial t} + \mathbf{v}\cdot\nabla T\right) = -\nabla\cdot\mathbf{q} - \sigma_s : \nabla\mathbf{v} - \frac{3n\zeta T}{2} + \frac{3T}{2}\sum_{i=1}^{s}\frac{\nabla\cdot\mathbf{j_{o_i}}}{m_i} + \sum_{i=1}^{N}\frac{\mathbf{F_i}\cdot\mathbf{j_{o_i}}}{m_i} \tag{21}$$

where ρ_s is the mixture density (given as $\rho_s = \sum_{i=1}^{s}\rho_{s_i}\phi_i$), $\mathbf{v}$ is the mixture velocity (given as $\mathbf{v} = \sum_{i=1}^{s}\rho_i\phi_i\mathbf{v_i}/(\sum_{i=1}^{s}\rho_i\phi_i)$), σ_s is the solid phase stress of the mixture, n is the mixture number density (defined as $n = \sum_{i=1}^{s} n_i$), T is the mixture granular temperature (defined as $T = \sum_{i=1}^{s} n_i T_i / \sum_{i=1}^{s} n_i$), $\mathbf{q}$ is the mixture granular energy flux, ζ is the cooling rate of the mixture, $\mathbf{F_i}$ is the sum of external forces given by Eq. (6), and $\mathbf{j_{o_i}}$ is the flux of a particle of type i relative to the mixture. In Eq. (21), the second term on the right-hand side represents the rate of production of pseudothermal energy due to shear, while the third term is the rate of dissipation of granular energy by inelastic collisions. The fourth and fifth terms in Eq. (21) represent the production of mixture granular energy due to gradients in the mass flux and products of external forces and mass fluxes of a particle of type i. Individual species velocities are obtained via algebraic constraints for the mass flux of a particle of type i which are given as follows:

$$\mathbf{j_{o_i}} = m_i n_i(\mathbf{v}_i - \mathbf{v}) = -\sum_{j=1}^{s}\frac{m_i m_j}{\rho_s}D_{ij}\nabla n_j - \rho_s D_i^T\nabla\ln(T) - \sum_{j=1}^{s} D_{ij}^F\mathbf{F_j} \tag{22}$$

where D_{ij} is the ordinary diffusivity of particles of type i in particles of type j, D_i^T is the thermal diffusivity of a particle of type i, and D_{ij}^F is the mass mobility of particles of type i in particles of type j. The cooling rate ζ is can be represented as follows:

$$\zeta = \zeta^0 + \zeta_U\nabla\cdot\mathbf{v} \tag{23}$$

where ζ^0 is the zeroth order cooling rate and ζ_u is the cooling rate transport coefficient. Individual species granular temperatures can be obtained by demanding equality of zeroth order cooling rates for each particle species (i.e. $\zeta_1^0 = \zeta_2^0 = \cdots = \zeta_s^0$). Constitutive relations for D_{ij}, D_i^T, D_{ij}^F, $\mathbf{q}$, σ_s, ζ^0 and ζ_U can be found in Murray et al. (in press).

2.3. Range of validity of the kinetic theory approach

Strictly speaking, kinetic theory models, be it *mixture* or *species* based, rely on the assumption that the particle phase Mach number is less than unity (Fox, 2008). This assumption arises due to the restrictions that are imposed when performing the Chapman–Enskog expansion that are used to derive kinetic theory based models of gas-particle flows (Garzó et al., 2007a). For monodisperse systems the condition of small particle phase Mach number is given as $Ma = v/\sqrt{T/m} < 1$ (here particle mass appears because both GHD and IA kinetic theories include particle mass in the definition of granular temperature). For bidisperse systems there is an additional constraint on the validity of the Chapman–Enskog expansion, namely that the Mach number based on particle velocity differences between each species ($Ma_{12} = |v_1 - v_2|/\sqrt{T_1/m_1 + T_2/m_2}$) is less than unity (Valiveti and Koch, 1999). From our simulations (to be presented later) we find that the particle phase Mach number can be greater than unity in our periodic domain simulations; however, these regions tend to have vanishingly small particle concentration. Moreover, we find that if we construct particle phase averages considering only regions where the particle phase Mach number is much smaller than unity (i.e. $Ma_{12} \leq 0.3$). There are only small ($\approx 2\%$) quantitative changes in our results for domain-averaged quantities. Therefore, we find that the effect of finite Mach number in our simulations is rather small for the domain-averaged particle volume fractions presented in this work. This can be rationalized by the fact that the clustered regions dictate the dynamics of the gas-particle flow, and in these regions the particle phase Mach number is less than unity. We suspect that as the

domain-averaged volume fraction decreases the violation of the finite Mach number condition will have a larger impact on the dynamics of the gas–solid flow.

2.4. Fluid-particle drag force model

In most gas-particle flows the fluid-particle drag force is the dominant term that balances the weight of the particles, and terms involving the divergence of the particle phase stress play a secondary role (Jackson, 2000; Ten Cate and Sundaresan, 2006). In fact recent studies reveal that drag models derived from direct numerical simulations predicted very different segregation profiles and bubble dynamics than models based on *ad-hoc* extensions of monodisperse drag models (Beetstra et al., 2006; Leboreiro et al., 2008). Beetstra et al. (2006) found that drag models derived from direct numerical simulations provided the best agreement with experimental observations of segregation in polydisperse fluidized bed simulations. With this in mind, a polydisperse fluid-particle drag model derived from direct numerical simulations has been used in all simulations presented here. The form of the polydisperse drag model is given as follows (Holloway et al., 2010; Yin and Sundaresan 2009a,b):

$$\mathbf{f_{D_i}} = \beta_i \mathbf{\Delta v_i} - \sum_{j \neq i}^{s} \beta_{ij}(\mathbf{\Delta v_j} - \mathbf{\Delta v_i}) \tag{24}$$

where $\mathbf{\Delta v_i}$ is the slip velocity between solid and fluid phases (defined as $\mathbf{\Delta v_i} = \mathbf{v_f} - \mathbf{v_i}$), β_i is the fixed bed friction coefficient for a particle of type i, and β_{ij} is the fluid-mediated particle–particle friction coefficient. The fixed bed friction coefficient can be written as follows (van der Hoef et al., 2005):

$$\beta_i = \frac{18\phi_i(1-\phi)\mu_f}{d_i^2} F^*_{Di-fixed} \tag{25}$$

where ϕ is the total particle volume fraction, μ_f is the dynamic viscosity of the fluid phase, d_i is the diameter of the ith particle species, and $F^*_{Di-fixed}$ is the *dimensionless* fixed bed fluid-particle drag force experienced by a particle of type i in a polydisperse assemblage of particles (here $F^*_{Di-fixed}$ is normalized by the Stokes drag $3\pi\mu_f d_i(1-\phi)\mathbf{\Delta v}$). $F^*_{Di-fixed}$ is given by Yin and Sundaresan (2009b) as follows:

$$F^*_{Di-fixed} = \frac{1}{1-\phi} + \left(F^*_{D-fixed} - \frac{1}{1-\phi}\right)(a y_i + (1-a) y_i^2) \tag{26}$$

where

$$y_i = \frac{d_i}{\langle d \rangle}, \quad \langle d \rangle = \frac{\sum_{i=1}^{N} n_i d_i^3}{\sum_{i=1}^{N} n_i d_i^2} \tag{27}$$

In Eq. (27), $\langle d \rangle$ is the Sauter mean diameter of the particle assembly. The parameter a in Eq. (26) is given as

$$a = 1 - 2.66\phi + 9.096\phi^2 - 11.338\phi^3 \tag{28}$$

Eq. (26) effectively relates the fluid-particle drag force of a particle of type i in a polydisperse fixed bed $F^*_{Di-fixed}$ to the fluid-particle drag force in a monodisperse fixed bed $F^*_{D-fixed}$ at the same volume fraction. In order to account for the effect of finite fluid inertia on the fluid-particle drag force in polydisperse suspensions Holloway et al. (2010) proposed:

$$F^*_{D-fixed} = \left(\frac{10\phi}{(1-\phi)^2} + (1-\phi)^2\left(1 + 1.5\sqrt{\phi}\right)\right)(1 + \chi^*_{BVK}) \tag{29}$$

where χ^*_{BVK} is a modified form of the inertial correction proposed by Beetstra et al. (2007):

$$\chi^*_{BVK} = \left(\frac{0.413 Re_{mix}}{240\phi + 24(1-\phi)^4\left(1 + 1.5\sqrt{\phi}\right)}\right) \times \left(\frac{(1-\phi)^{-1} + 3\phi(1-\phi) + 8.4 Re_{mix}^{-0.343}}{1 + 10^{3\phi} Re_{mix}^{-(1+4\phi)/2}}\right) \tag{30}$$

Here Re_{mix} is the mixture Reynolds number defined as

$$Re_{mix} = \frac{\rho_f |\Delta U_{mix}| (1-\phi)\langle d \rangle}{\mu_f}, \quad \Delta U_{mix} = \frac{\sum_{i=1}^{N} \phi_i \Delta v_i}{\sum_{i=1}^{N} \phi_i} \tag{31}$$

The fluid-mediated particle–particle friction coefficient β_{ij} can be written in terms of the fixed bed friction coefficient of particles of type i and j as

$$\beta_{ij} = -2\alpha_{ij} \frac{\phi_i \phi_j}{\frac{\phi_i}{\beta_i} + \frac{\phi_j}{\beta_j}} \tag{32}$$

where α_{ij} is written as

$$\alpha_{ij} = 1.313 \log_{10}\left(\frac{\min(d_i, d_j)}{\lambda}\right) - 1.249 \tag{33}$$

In Eq. (33), λ represents the lubrication cutoff distance. This distance corresponds to the point at which lubrication forces saturate between two approaching spheres as a result of either asparities on the particle surface or non-continuum effects. In all simulations performed in this work the default value of $\lambda = 1 \times 10^{-6}$ m was used.

2.5. Numerical implementation

The polydisperse kinetic theory model frameworks and the fluid-particle drag model outlined in the previous subsections were simulated using the Multiphase Flow with Interface eXchanges (MFIX) computational software (Syamlal, 1998). The MFIX software utilizes a variable time step, staggered grid, finite volume method for the solution of the continuum models for gas-particle flows. The numerical procedure in MFIX is based on the semi-implicit method with pressure-linked equations (SIMPLE) algorithm for the iterative solution of the continuum model equations. The partial elimination algorithm is used to effectively decouple the solution of the gas and solid phase momentum balances (Spalding, 1980). In order to minimize numerical diffusion in our simulations, we employ a second-order-accurate Superbee discretization of convective terms. Similar numerical approaches have been employed in the literature for the simulation of polydisperse gas-particle flows (Fan et al., 2004; Fan and Fox, 2008). In both kinetic theory models discussed above we added a frictional particle phase stress contribution given by Srivastava and Sundaresan (2003) to prevent the systems under investigation from over-packing.

The two- and three-dimensional simulations presented in subsequent sections were performed using doubly and triply periodic domains, respectively, to eliminate the effect of boundary conditions from consideration in the comparison of the *mixture* and *species* based kinetic theory approaches. In order to fluidize the systems under investigation, a vertical pressure gradient was imposed on the system to balance the weight of the suspension.

3. Results and discussion

Two different binary PSDs are used in the comparison of GHD and IA kinetic theory models. A detailed list of particle properties can be found in Table 1. The PSDs used in this study were chosen to mimic those used in the experiments of Chew et al. (submitted

for publication), and they span a wide range of particle size and volume fraction ratios.

3.1. Grid resolution studies

It is well known that continuum model simulations of monodisperse gas-particle flows manifest grid size dependent results until the grid size is on the order of 10 particle diameters (Agrawal et al., 2001). Therefore, grid resolution studies of both GHD and IA kinetic theory models were performed in order to determine at what point the simulated gas-particle flow behavior became independent of the grid size. Fig. 1 illustrates the grid size dependence of the gas-particle flow structures that are manifested by the GHD kinetic theory model framework for *Case D* (see Table 1). It is clear that as the grid resolution is increased, moving from left to right, the scale of the flow structures present in the simulation become finer. Analogous grid size dependent structures have been observed when performing continuum model simulations of monodisperse gas-particle flows (Agrawal et al., 2001; Igci et al., 2008). Similar grid size dependence was also obtained for the IA model (not shown).

Table 1
List of simulation cases. In all simulations presented here, a single coefficient of restitution was used to characterize collisions between particles of the same and different species.

Monodisperse cases	*Case A*	*Case B*
d	2.70×10^{-4} m	1.90×10^{-4} m
ρ_s	2.50×10^{3} kg/m^3	2.50×10^{3} kg/m^3
ρ_f	1.30 kg/m^3	1.30 kg/m^3
μ_f	1.80×10^{-5} kg/(m s)	1.80×10^{-5} kg/(m s)
e	0.99	0.99
ϕ	0.15	0.15
v_t	5.51 m/s	2.71 m/s
Bidisperse cases	*Case C*	*Case D*
d_1	6.50×10^{-4} m	2.13×10^{-4} m
d_2	1.70×10^{-4} m	1.28×10^{-4} m
$\langle d\rangle$	2.70×10^{-4} m	1.90×10^{-4} m
ρ_{s_1}	2.50×10^{3} kg/m^3	2.50×10^{3} kg/m^3
ρ_{s_2}	2.50×10^{3} kg/m^3	2.50×10^{3} kg/m^3
ρ_f	1.30 kg/m^3	1.30 kg/m^3
μ_f	1.80×10^{-5} kg/(m s)	1.80×10^{-5} kg/(m s)
e	0.99	0.99
ϕ_1	0.075	0.122
ϕ_2	0.075	0.028
ϕ	0.15	0.15
v_{t_1}	22.53 m/s	2.79 m/s
v_{t_2}	1.83 m/s	1.06 m/s
v_t	5.48 m/s	2.71 m/s

In order to determine what grid resolution was appropriate for the comparison of GHD and IA kinetic theory model frameworks, we examine the grid size dependence of the vertical component of the domain-averaged slip velocity, and the meso-scale vertical normal stress for different grid resolutions. To ensure that our simulations capture the detailed structure of the gas-particle flow, we also calculate and compare the energy spectra of the volume fraction fluctuations, mixture velocity fluctuations and mixture granular temperature fluctuations.

The vertical component of the domain-averaged slip velocity (hereafter referred to as the domain-averaged slip velocity) is defined as

$$\langle v_{slip}\rangle = \left\langle \frac{(1-\phi)v_f}{\langle 1-\phi\rangle} - \frac{\phi v}{\langle\phi\rangle}\right\rangle \tag{34}$$

where $\langle\cdot\rangle$ indicates a domain-averaged quantity. The domain-averaged meso-scale vertical normal stress is defined as

$$\left\langle \sum_i \phi_i v_i' v_i' \right\rangle = \sum_{i=1}^{s} \langle\phi_i v_i v_i\rangle - \langle\phi_i\rangle\langle v_i\rangle\langle v_i\rangle \tag{35}$$

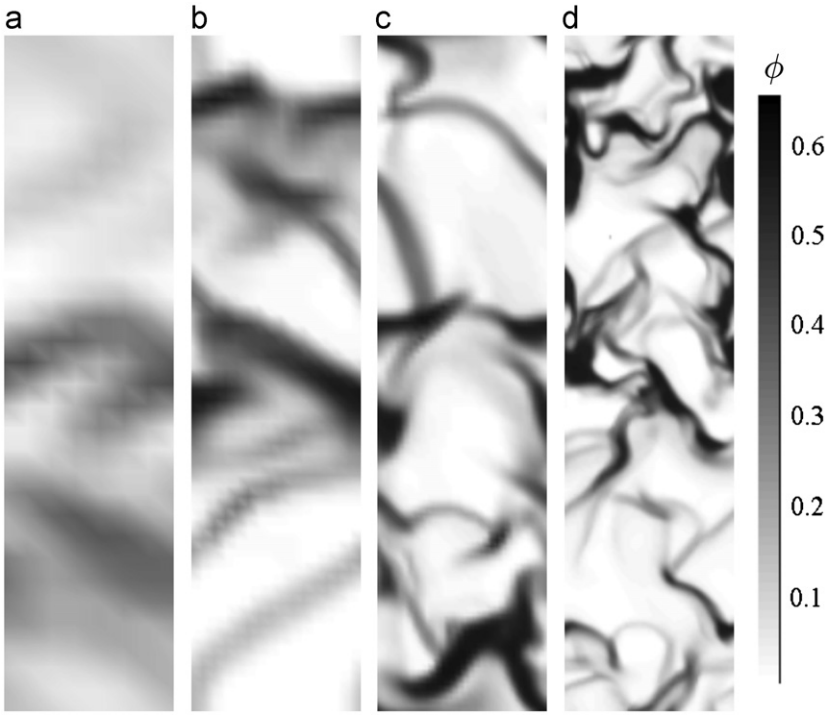

Fig. 1. Snapshots of the particle volume fraction obtained from two-dimensional simulations of the GHD model of *Case D* (see Table 1 for details). Finer gas-particle flow structures emerge as grid resolution is increased. Domain size: 16 cm $\times$ 64 cm. (a) 8 $\times$ 32, (b) 16 $\times$ 64, (c) 32 $\times$ 128, and (d) 64 $\times$ 256 grid cells. Similar grid size dependent structures were also found in simulations with the IA polydisperse kinetic theory model.

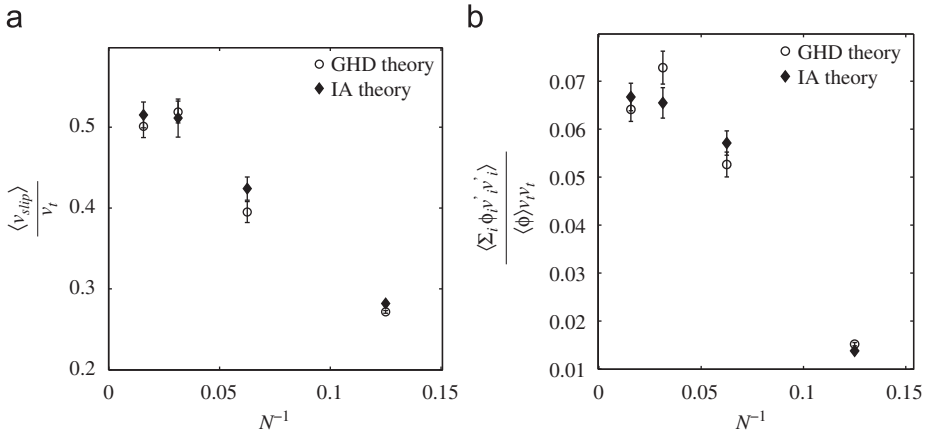

Fig. 2. Effect of grid resolution on domain-averaged properties as predicted by both GHD and IA theories for *Case D* (see Table 1). Dimensionless slip velocity (a) and dimensionless meso-scale vertical normal stress (b) are plotted against N^{-1}, where N is the number of grid cells in the horizontal direction. The terminal settling velocity v_t of an isolated particle with a diameter equal to the Sauter mean diameter of the bidisperse mixture is used for scaling.

Fig. 2 illustrates the grid size dependence of the scaled domain-averaged slip velocity and the domain-averaged meso-scale vertical normal stress for *Case D*. Both quantities are plotted against N^{-1} where N is the number of grids in the horizontal direction, and both are sensitive functions of N^{-1}. However, this dependence becomes very weak as $N^{-1} \to 0$. This indicates at sufficiently small values of N^{-1}, or equivalently, high grid resolution, the domain-averaged quantities do become grid independent for both GHD and IA kinetic theories.

In single phase turbulent flow research, grid independence in large eddy and direct numerical simulations is determined by examining how well the energy spectra of the velocity fluctuations in a turbulent flow collapse for different grid resolutions (Bose et al., 2010). In order to gauge the grid independence of our simulation results we define energy spectra of the volume fraction fluctuations E_ϕ, *dimensionless* mixture velocity fluctuations E_v, and *dimensionless* mixture granular temperature fluctuations E_T as follows:

$$\hat{\phi}(\mathbf{k},t) = \int (\phi(\mathbf{x},t) - \langle \phi \rangle) \exp(i\mathbf{k}\cdot\mathbf{x})\, d\mathbf{x}, \quad E_\phi(k) = \hat{\phi}\hat{\phi}^* \tag{36}$$

$$\hat{\mathbf{v}}(\mathbf{k},t) = \int \frac{(\mathbf{v}(\mathbf{x},t) - \langle \mathbf{v}(t) \rangle)}{v_t} \exp(i\mathbf{k}\cdot\mathbf{x})\, d\mathbf{x}, \quad E_v(k) = \frac{1}{2}(\widehat{v_x}\widehat{v_x}^* + \widehat{v_y}\widehat{v_y}^*) \tag{37}$$

$$\hat{T}(\mathbf{k},t) = \int \frac{(T(\mathbf{x},t) - \langle T(t) \rangle)}{m v_t^2} \exp(i\mathbf{k}\cdot\mathbf{x})\, d\mathbf{x}, \quad E_T(k) = \hat{T}\hat{T}^* \tag{38}$$

where m is the average particle mass based on the Sauter mean diameter, and $(\cdot)^*$ indicates a complex conjugate. In Fig. 3, we present E_ϕ, E_v, and E_T plotted against dimensionless scalar wavenumber $\hat{k}$ (here $\hat{k} = k v_t^2/g$) for four different grid resolutions for both GHD and IA theories. In Fig. 3(a) and (b), it is clear that the energy spectra of the particle volume fraction for the two highest grid resolutions (or smallest values of N^{-1}) collapse over a large range of *dimensionless* wavenumber $\hat{k}$ for both GHD and IA theories, respectively. The same collapse is clear by inspection of the energy spectra of *dimensionless* mixture velocity E_v and *dimensionless* mixture granular temperature E_T as is evidenced in Fig. 3(c)–(f).

From Figs. 2 and 3 we can conclude that both the domain-averaged quantities and the small scale variations are adequately resolved in our gas-particle flow simulations for two highest grid resolutions. In what follows, we present domain-averaged quantities that are obtained from the highest grid resolution case presented in Figs. 1–3.

3.2. Comparison of the predictions of GHD and IA kinetic theories

The meso-scale gas-particle flow structures that arise in simulations of GHD and IA theories are compared via juxtaposition of instantaneous grayscale plots of the volume fraction and volume fraction ratio fields in the periodic domain. In addition, probability distribution functions (PDF) of the mixture and species volume fractions are generated as a function of mixture and species volume fraction, respectively, in order to provide a more quantitative comparison of the meso-scale inhomogeneities admitted by each polydisperse kinetic theory model. The PDFs are obtained by binning the observed volume fraction in each cell based upon the observed value. Several instantaneous snapshots are used to generate a smooth distribution function of solids volume fraction. We also compare the energy spectra of total and species volume fraction admitted in GHD and IA theory simulations for each case.

Fig. 4(a) and (b) provides a side-by-side comparison of the instantaneous volume fraction fields obtained for *Case D* using GHD and IA theories, respectively. It is clear that both GHD and IA theory manifest qualitatively similar cluster and streamer formation throughout the periodic domain. Fig. 6(a) shows the PDF of ϕ as a function of mixture volume fraction for *Case D*. The distribution functions of mixture volume fraction for both GHD and IA theory manifest bimodal structure. The large peak at low volume fraction is a result of the fact that a large percentage of the periodic domain contains a very low concentration of particles. The small peak at high volume fractions corresponds to the dense clustered regions that cover a smaller percentage of the periodic domain. An additional quantitative comparison between the volume fraction fields predicted by the two kinetic theory model frameworks is given in Fig. 5(a) and (b) by comparing the energy spectra of ϕ for both GHD and IA theory for *Cases D* and *C*, respectively. Fig. 5(a) and (b) demonstrates that the energy spectrum is a strongly decreasing function of dimensionless wavenumber $\hat{k}$. Moreover, the energy spectra of ϕ admitted by the two different kinetic theory models collapse onto one another. The grayscale plots of total volume fraction obtained for *Case C* using GHD and IA kinetic theory in Fig. 4(c) and (d) reveal that even for binary mixtures with large size ratios, the volume fraction fields obtained by both *mixture* and *species* based kinetic theories are qualitatively similar. A more quantitative comparison

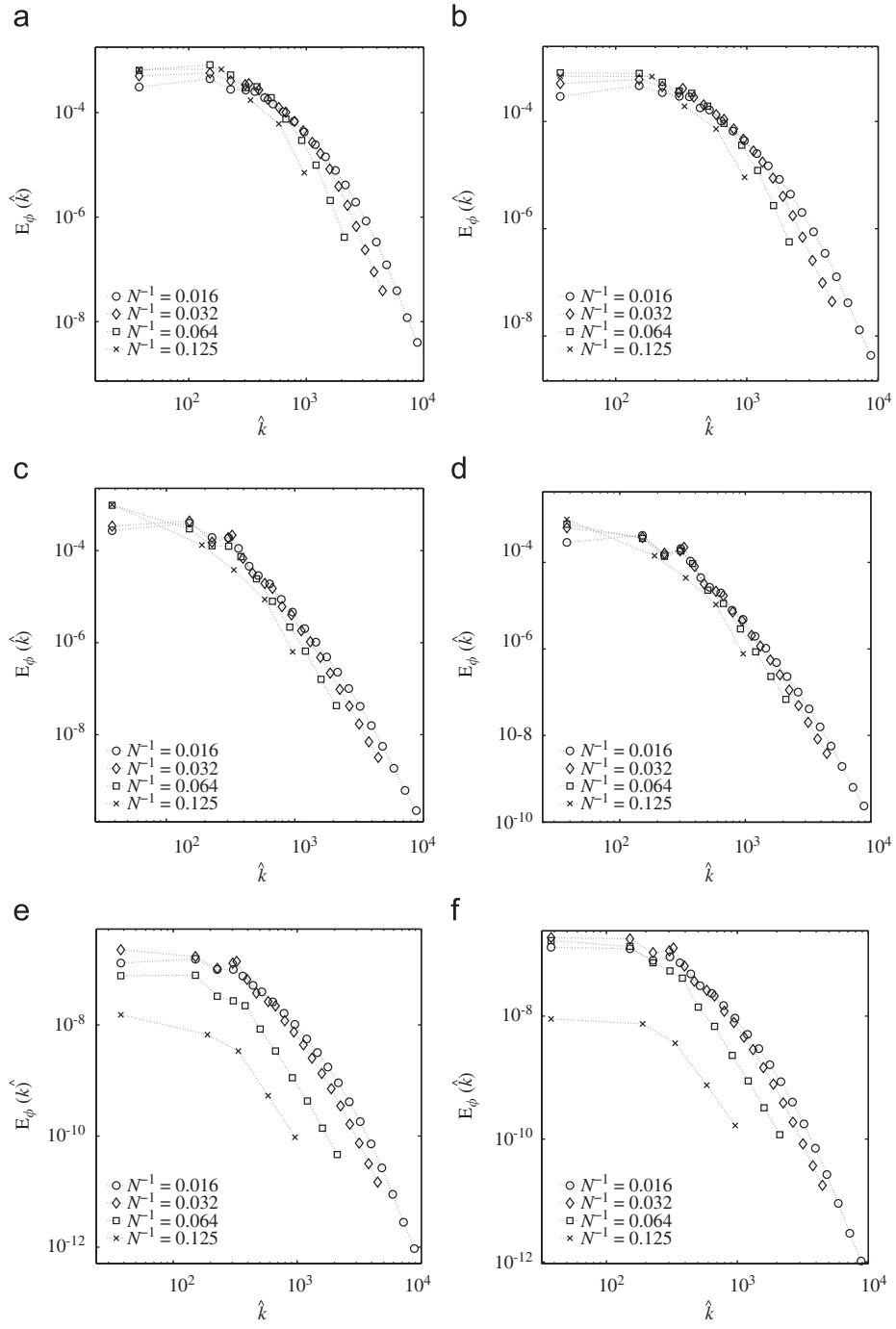

Fig. 3. Effect on grid resolution on the energy spectra of particle volume fraction E_ϕ, *dimensionless* mixture velocity E_v, and *dimensionless* mixture temperature E_T as predicted by GHD and IA theories for *Case D*. E_ϕ are plotted as a function of *dimensionless* wavenumber $\hat{k}$ for (a) GHD and (b) IA theories. E_v are plotted as a function of *dimensionless* wavenumber $\hat{k}$ for (c) GHD and (d) IA theories. E_T are plotted as a function of *dimensionless* wavenumber $\hat{k}$ for (e) GHD and (f) IA theories.

of the PDF of ϕ predicted by the kinetic theory models shows that there are more pronounced differences in the PDF of ϕ for the large size ratio bidisperse case (*Case C*) than in the smaller size ratio case (*Case D*). However, both kinetic theory frameworks still manifest nearly the same PDFs of ϕ.

Comparison of the grayscale plots of the volume fraction ratio field, shown in Fig. 4(e)–(h), reveals that both GHD and IA kinetic theory models manifest qualitatively similar predictions. The energy spectra of the volume fraction ratio field given in Fig. 5 show that while the energy spectra of the volume fraction ratio for both GHD and IA kinetic theories manifest a similar decay with increasing wavenumber, the energy associated with the volume fraction ratio fluctuations is consistently larger for IA kinetic theory. Direct comparison of the PDF of species volume fraction for *Case D* in Fig. 6(b) and (c) illustrates that both *mixture* and *species* kinetic theory frameworks have nearly identical PDFs for each particle as well. Fig. 6(e) and (f), corresponding to *Case C*, reveals that IA kinetic theory predicts slightly higher concentrations of larger particles in clustered regions than GHD theory. It is also noteworthy that the PDF of species volume fraction given in Fig. 6(b) and (c) for *Case D* is qualitatively different from the PDF of species volume fraction given in Fig. 6(e) and (f) for *Case C*.

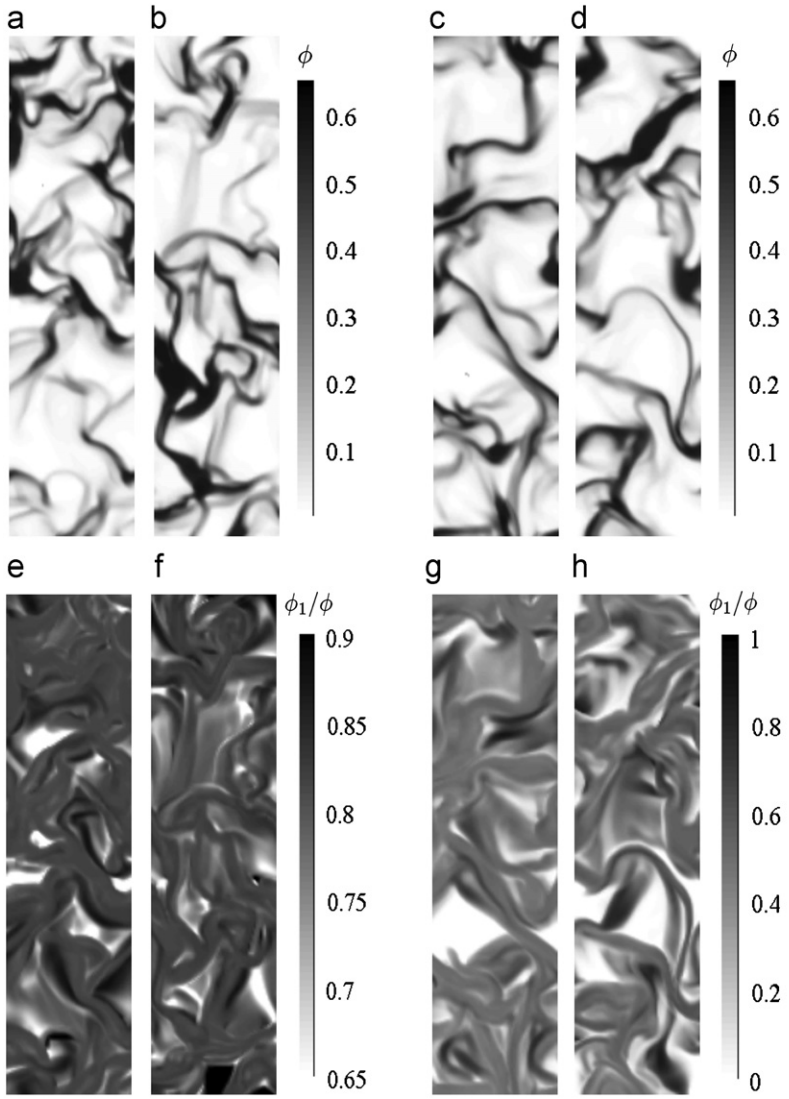

Fig. 4. Instantaneous snapshots of particle volume fraction and particle volume fraction ratio fields obtained from two-dimensional bidisperse gas-particle flow computations. The total volume fraction and volume fraction ratio fields are shown for four cases: *Case D* (see Table 1) using GHD theory —panels (a) and (e); *Case D* using IA theory—panels (b) and (f); *Case C* using GHD theory—panels (c) and (g); *Case C* using IA theory—panels (d) and (h).

The differences in the PDFs of species concentration in *Cases C* and *D* arise as a result of the fact that the domain-averaged species volume fractions are different between the two cases. For example, in *Case D* the domain-averaged volume fraction of particle species 2 is 0.028. Therefore, the range of the PDF of species 2 concentration given in Fig. 6(c) only varies from 0 to 0.20 reflecting the very low probability of finding regions have species concentrations higher than 0.20.

Fig. 7 shows the scaled domain-averaged mixture slip velocity, the domain-averaged slip velocity of particles of type 1, and the domain-averaged meso-scale vertical normal stress of the mixture as functions of *dimensionless* time, $\tau = tg/v_t$. As seen in Fig. 7(a) and (b), the domain-averaged mixture slip velocity and the domain-averaged slip velocity of a particle of type 1 in *Case D* predicted by GHD and IA kinetic theories oscillate about similar statistical steady state values. Fig. 7(c) shows that the same is true for the meso-scale vertical normal stress as well. The rather large fluctuations in the domain-averaged quantities given in Fig. 7 can be traced to the persistent fluctuations of the gas-particle flow structures that arise due to the instability of the uniformly fluidized state (Sundaresan, 2003). Time-averaged values of the domain-averaged slip velocity of mixture, the domain-averaged slip velocity of each particle species, and the domain-averaged meso-scale normal stress are given in Table 2.

Fig. 8(a) and (b) shows three-dimensional instantaneous snapshots of the total volume fraction field obtained by simulating *Case C* with GHD and IA kinetic theory models, respectively. The qualitative similarity between the snapshots of the total volume fraction is apparent. Furthermore, the *dimensionless* domain-averaged slip velocities for *Case C* obtained in simulations using GHD and IA theory were found to be 0.293 and 0.307, respectively; these are within 5% of each other. Here the domain-averaged slip velocities were scaled by v_t for the respective bidisperse particle mixture. Fig. 8(c) and (d) shows the volume fraction field obtained from the simulation of *Case D* using GHD and IA theory, respectively. Again the qualitative features of the volume fraction field obtained using either kinetic theory framework are similar. The *dimensionless* domain-averaged slip velocities for *Case D* were found to be 0.430 and 0.455 for GHD and IA theories, respectively.

To determine the similarity of the gas-particle flow structures in our three-dimensional simulations, PDFs of the total and

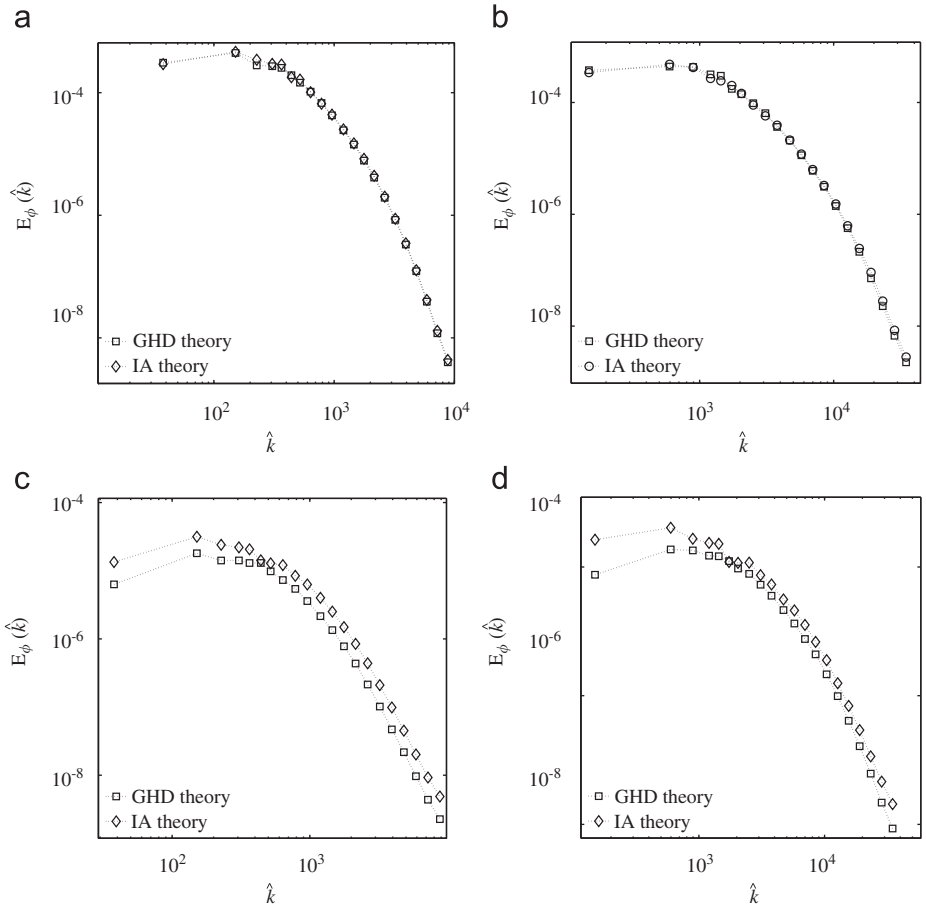

Fig. 5. Comparison of the energy spectra of ϕ for (a) *Case D* and (b) *Case C*. Comparison of the energy spectra of ϕ_1/ϕ for (c) *Case D* and (d) *Case C*.

species particle volume fraction were calculated and compared for both GHD and IA kinetic theories, and are given in Fig. 9. In Fig. 9(a) and (d) we show PDFs of the total particle volume fraction obtained from three-dimensional numerical simulations of *Cases D* and *C*, respectively. It is clear that for both GHD and IA kinetic theories the qualitative features of the PDF of total solid volume fractions are similar with small quantitative variations. The same feature can be noted by inspection of the PDF of species volume fractions given in Fig. 9(b) and (c) and Fig. 9(e) and (f) for *Cases D* and *C*, respectively.

It is interesting to note the qualitative differences in the PDFs of total and species volume fractions observed in two- and three-dimensional simulations for both particle size distributions examined in this study. The PDFs of species and total volume fraction obtained from three-dimensional simulations in Fig. 9 have very broad and monomodal shape, while the PDFs obtained from two-dimensional simulations show two sharp peaks in the PDFs corresponding to clustered and dilute regions. In two-dimensional simulations the ability of the gas to bypass the solid phase is inhibited by the lower dimensionality—this therefore induces more severe particle clustering than is present in three-dimensional simulations because it is generally easier for gas to bypass solid phase flow structures in three-dimensions than in two-dimensions.

A comparison of the computational times for GHD and IA kinetic theories is shown in Table 3 for the two binary particle size distributions used in this study. The *mixture* model framework is computationally less expensive than the *species* model framework; this can be attributed to the fact that GHD theory requires the solution of fewer time-dependent, non-linear, partial differential equations. However, the improvement in computational time appears to be a sensitive function the disparity in size between the smaller and larger particles.

In the *species* based model framework (adopted by IA theory), the momentum and granular energy of each particle phase are allowed to evolve separately. In contrast, in the *mixture* based model framework (adopted in GHD theory), the momentum and granular energy of the particle mixture are allowed to evolve, while it is postulated that the flux and granular energy of the individual particle species relax with respect to the mixture quantities rapidly. In Section 3.4, we develop an analysis to indicate when *species* velocities are slaved to the *mixture* velocity using an analysis similar to Goldman and Sirovich (1967) for binary molecular gases.

3.3. Comparison of monodisperse and bidisperse systems

It is common practice in the continuum modeling community to approximate a polydisperse gas–solid flow by an equivalent monodisperse gas–solid flow with a particle diameter given by the Sauter mean diameter (see Eq. (27a) for definition) of the polydisperse system (Neri and Gidaspow, 2000; Jiradilok et al., 2006, 2008). In order to understand the degree to which such an approximation is valid, the meso-scale flow structures, the domain-averaged slip velocities of the mixtures, and the meso-scale vertical normal stresses obtained from periodic domain simulations of bidisperse systems and equivalent monodisperse systems are directly compared.

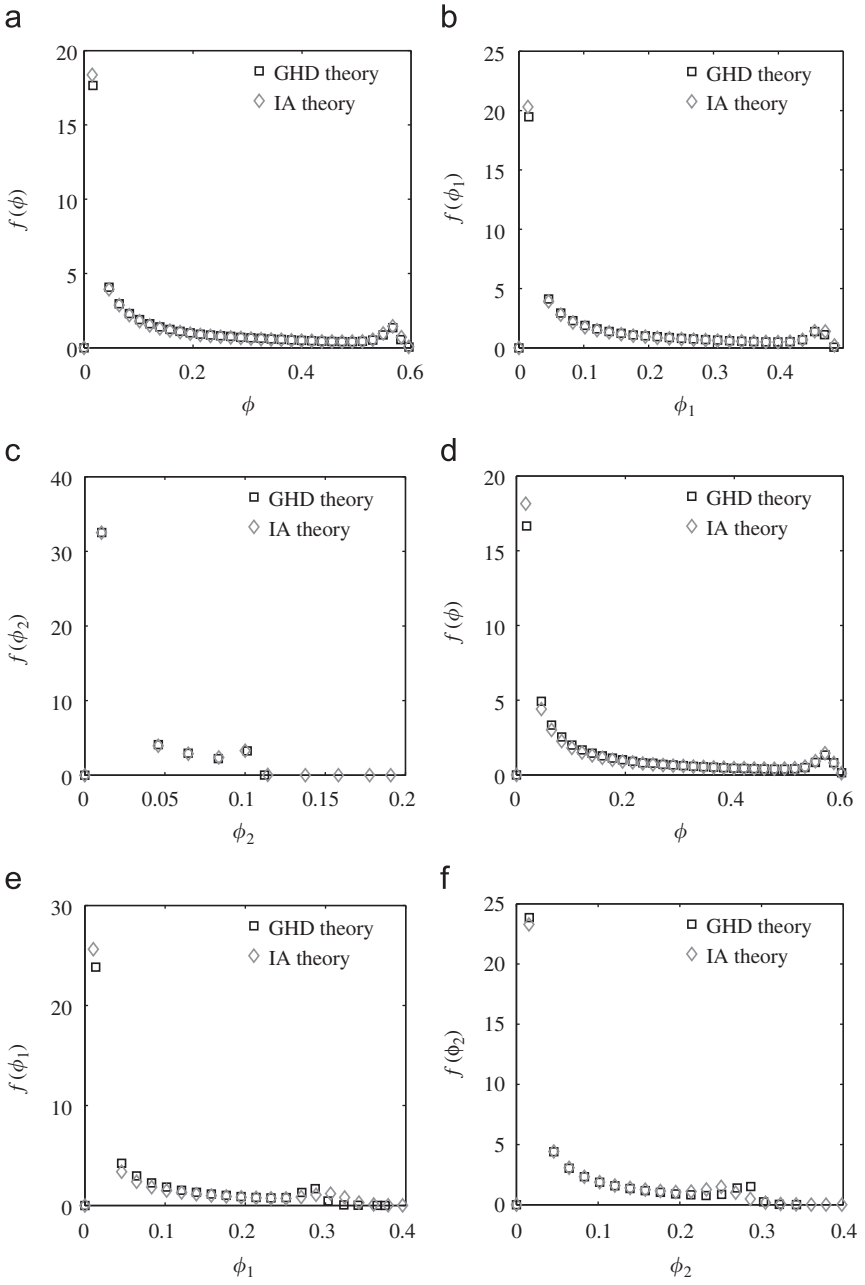

Fig. 6. Probability distribution function (PDF) of mixture and species volume fraction observed in two-dimensional bidisperse gas-particle flow simulations. The PDF of mixture volume fraction is given for *Case D* in (a), and for *Case C* in (d) as a function of mixture volume fraction. The PDF of the volume fraction of species 1 is given for *Case D* in (b), and for *Case C* in (e) as a function of the volume fraction of species 1. The PDF of the volume fraction of species 2 is given for *Case D* in (c), and for *Case C* in (f) as a function of the volume fraction of species 2.

Fig. 10 compares instantaneous snapshots of the particle volume fraction fields obtained from a bidisperse system (*Case C*) and a monodisperse system (*Case A*) with the same Sauter mean diameter. It is clear that the gas-particle flow structure is characterized by clusters and streamers in both cases. Comparison of the PDFs of the total particle volume fraction in Fig. 11 reveals that both monodisperse and bidisperse systems manifest similar distribution functions of solid volume fraction over the entire volume fraction range. However, the two peaks in the distribution appear to be slightly larger in the bidisperse case (*Case C*) than in the monodisperse case (*Case A*) indicating a slightly larger propensity of the bidisperse gas-particle flow to be heterogeneous. Fig. 12(a) and (b) shows the domain-averaged slip velocity of the mixture and the meso-scale vertical normal stress, respectively, for both monodisperse and bidisperse cases. It is clear that the domain-averaged quantities are fluctuating about similar statistically steady values for both the monodisperse and bidisperse systems. The time-averaged values of these domain-averaged quantities for the monodisperse (*Case A*) and bidisperse (*Case C*) cases are reported in Table 2. Approximating this bidisperse system with widely separated particle diameters with a monodisperse system having the same Sauter mean diameter leads to an underestimation of the mixture domain-averaged slip velocity by 15% while the domain-averaged vertical normal meso-scale stress is within 10% of that for the binary mixture (according to GHD theory). The predictions are similar for these cases according to IA theory as well; see Table 2. Comparison of the predictions for *Cases B* and *D* shows that the monodisperse

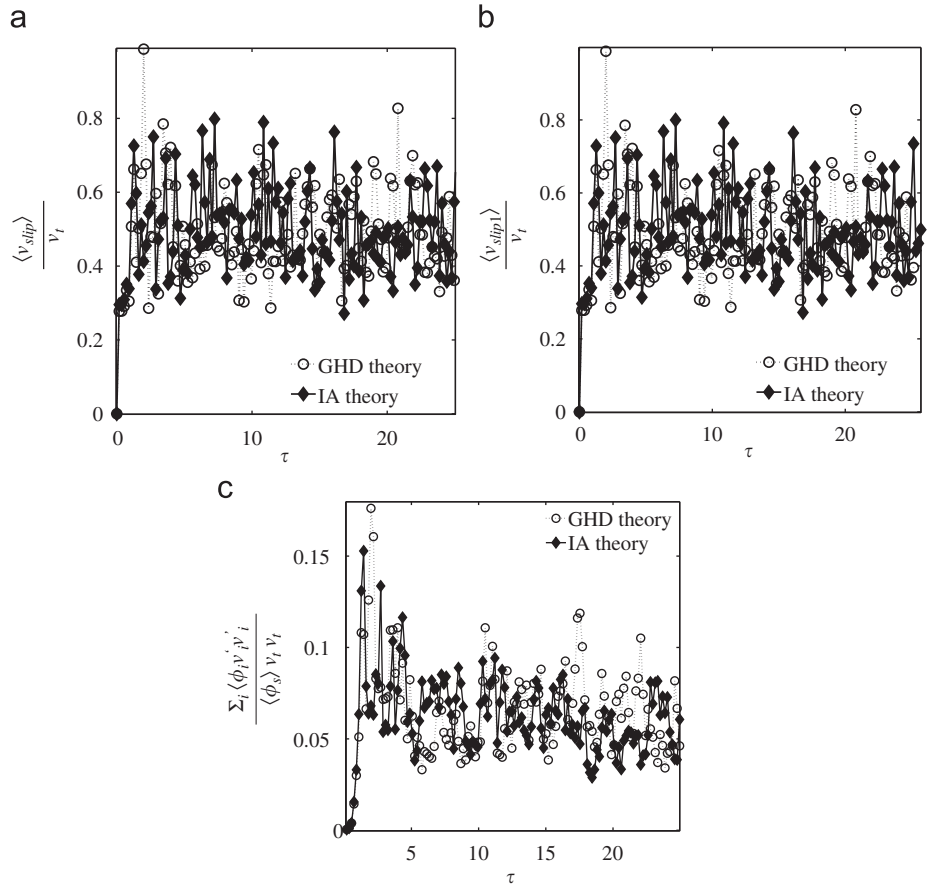

Fig. 7. The time progression of the (a) domain-averaged mixture slip velocity, (b) domain-averaged slip velocity of a particle of type 1, and (c) domain-averaged meso-scale normal stress obtained from two-dimensional periodic domain simulations of *Case D* are plotted for both GHD and IA theory. Table 2 shows the time-averaged results for each case listed in Table 1.

Table 2
Time-averaged results for the domain-averaged slip velocity and meso-scale vertical normal stress for all the simulated cases. The over-bar represents a time-averaged quantity.

Case	KT model	$\overline{\frac{\langle v_{slip}\rangle}{v_t}}$	$\overline{\frac{\langle v_{slip_1}\rangle}{v_{t_1}}}$	$\overline{\frac{\langle v_{slip_2}\rangle}{v_{t_2}}}$	$\overline{\frac{\langle \sum_i \phi_i v_i' v_i' \rangle}{\phi_i v_t^2}}$
A	GHD theory	$0.265 \pm 6.72 \times 10^{-3}$	–	–	$1.63 \times 10^{-2} \pm 4.98 \times 10^{-4}$
	IA theory	$0.244 \pm 5.11 \times 10^{-3}$	–	–	$1.17 \times 10^{-2} \pm 5.13 \times 10^{-4}$
B	GHD theory	$0.380 \pm 1.15 \times 10^{-2}$	–	–	$6.32 \times 10^{-2} \pm 2.35 \times 10^{-3}$
	IA theory	$0.392 \pm 1.07 \times 10^{-2}$	–	–	$5.96 \times 10^{-2} \pm 2.17 \times 10^{-3}$
C	GHD theory	$0.305 \pm 7.69 \times 10^{-3}$	$7.49 \times 10^{-2} \pm 1.88 \times 10^{-3}$	$0.911 \pm 2.29 \times 10^{-2}$	$1.51 \times 10^{-2} \pm 5.61 \times 10^{-4}$
	IA theory	$0.316 \pm 1.24 \times 10^{-2}$	$7.92 \times 10^{-2} \pm 3.09 \times 10^{-3}$	$0.924 \pm 3.64 \times 10^{-2}$	$1.57 \times 10^{-2} \pm 6.86 \times 10^{-4}$
D	GHD theory	$0.496 \pm 1.56 \times 10^{-2}$	$0.484 \pm 1.51 \times 10^{-2}$	$1.26 \pm 3.98 \times 10^{-2}$	$6.47 \times 10^{-2} \pm 2.85 \times 10^{-3}$
	IA theory	$0.526 \pm 1.82 \times 10^{-2}$	$0.513 \pm 1.77 \times 10^{-2}$	$1.33 \pm 4.59 \times 10^{-2}$	$7.06 \times 10^{-2} \pm 3.13 \times 10^{-3}$

approximation underestimates the domain-averaged slip velocity of a binary system by about 25%.

3.4. Mixture versus species kinetic theory frameworks

In Section 3.2, we emphasized that the GHD and IA kinetic theory model frameworks have similar gas-particle flow predictions in terms of both small scale and domain-averaged properties. However, it is of interest to develop a criteria upon which one might expect the *mixture* and *species* based kinetic theories to provide similar results. An approach was developed to compare the *mixture* and *species* based kinetic theory approaches for molecular systems (Goldman and Sirovich, 1967), and in this section we employ the same technique to examine when the *species* based kinetic theory model will reduce to a mathematical form consistent with the GHD *mixture* kinetic theory model. Simulation results presented in the previous section demonstrate that quantitative differences in the constitutive relations of each kinetic theory model have only a small quantitative effect domain-averaged quantities, so we will only develop a scaling analysis that indicates in what range we expect the species velocities to be slaved to the mixture velocity.

In order to directly compare the *species* kinetic theory model framework with that of a *mixture* kinetic theory model, we must construct a mixture momentum equation from the *species* momentum balance given in Eq. (3). Using the definition of the mixture velocity and species mass flux, it can readily be shown that one can construct an effective mixture momentum balance

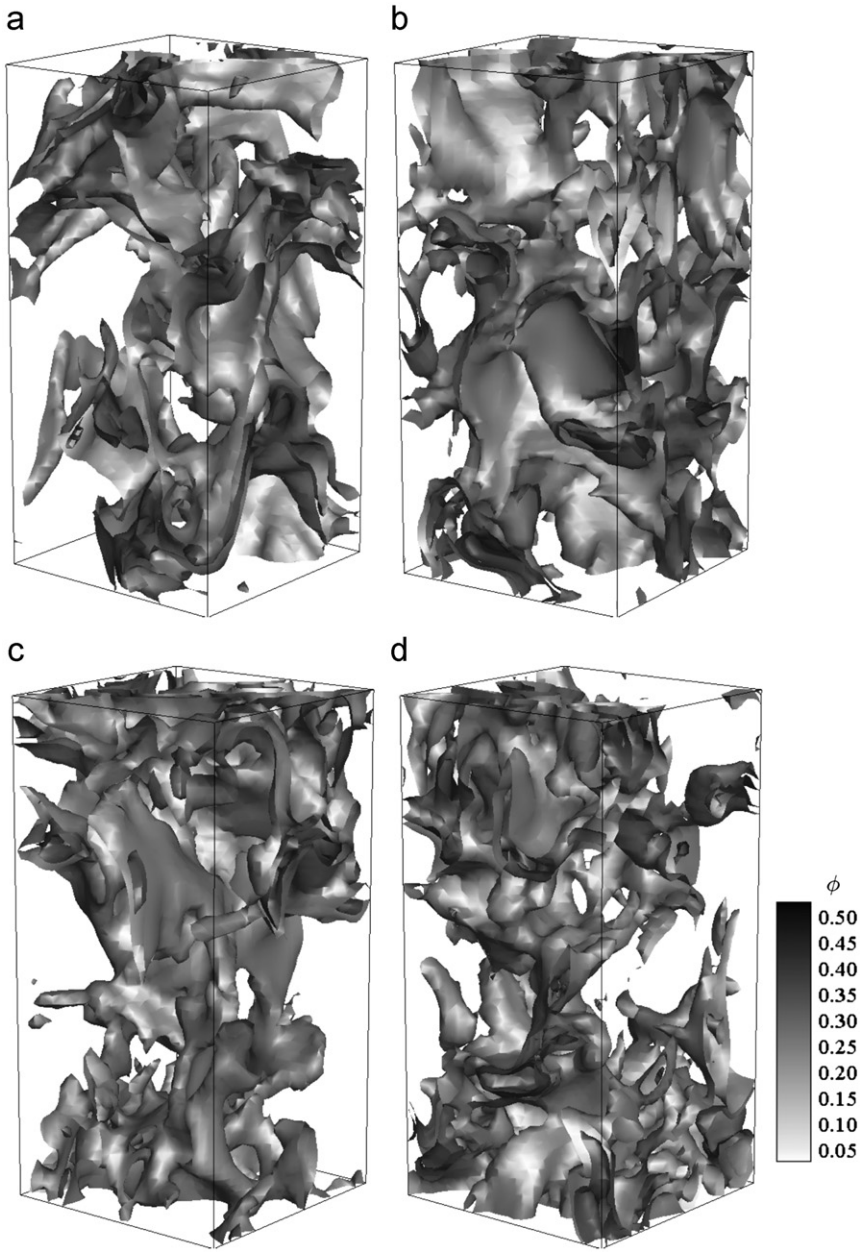

Fig. 8. Instantaneous snapshots of particle volume fraction fields obtained from three-dimensional bidisperse gas-particle flow simulations. Domain size: 8 cm $\times$16 cm $\times$8 cm; 32 $\times$64 $\times$32 grid cells. The total volume fraction fields is shown for the following four cases: (a) *Case C* using GHD theory; (b) *Case C* using IA theory; (c) *Case D* using GHD theory; and (d) *Case D* using IA theory.

equation from IA kinetic theory as follows:

$$\frac{\partial \mathbf{v}}{\partial t}+\mathbf{v}\cdot\nabla\mathbf{v}=-\frac{1}{\rho_s}\nabla\cdot\widehat{\sigma_s}+\frac{1}{\rho_s}\sum_i n_i\mathbf{F_i} \tag{39}$$

where

$$\widehat{\sigma_s}=\sum_i \sigma_{s_i}+\frac{\mathbf{j_{o_i}}\mathbf{j_{o_i}}}{\rho_i\phi_i} \tag{40}$$

If we restrict our attention to binary mixtures only, we can construct an evolution equation for the diffusion velocity of a particle of type 1 by subtracting Eq. (3) for particle species 1 from Eq. (39) to obtain

$$\frac{\mathbf{I_{12}}}{\rho_1\phi_1}=\frac{D(\mathbf{v_1}-\mathbf{v})}{Dt}+\frac{\mathbf{j_{o_1}}}{\rho_1\phi_1}\cdot\nabla\mathbf{v_1}+\left(\frac{1}{\rho_1\phi_1}\nabla\cdot\sigma_{s_1}-\frac{1}{\rho_s}\nabla\cdot\hat{\sigma}_s\right)-\frac{n_1}{\rho_1\phi_1}\mathbf{F_1}+\frac{1}{\rho_s}\sum_i n_i\mathbf{F_i} \tag{41}$$

where $D(\cdot)/Dt=\partial(\cdot)/\partial t+\mathbf{v}\cdot\nabla(\cdot)$ is the material derivative and $\mathbf{I_{12}}$ is the particle–particle collisional momentum transfer given in Eq. (7). Inserting Eq. (7) into Eq. (41) and using the definition of the mass flux in Eq. (22) we obtain

$$\begin{aligned}\frac{-\gamma_{12}\sqrt{\pi}R_2\rho_s(\mathbf{v_1}-\mathbf{v})}{\rho_1\phi_1\rho_2\phi_2}&=\frac{D(\mathbf{v_1}-\mathbf{v})}{Dt}+\frac{\mathbf{j_{o_1}}}{\rho_1\phi_1}\cdot\nabla\mathbf{v_1}\\&+\left(\frac{1}{\rho_1\phi_1}\nabla\cdot\sigma_{s_1}-\frac{1}{\rho_s}\nabla\cdot\hat{\sigma}_s\right)-\frac{n_1}{\rho_1\phi_1}\mathbf{F_1}\\&+\frac{1}{\rho_s}\sum_i n_i\mathbf{F_i}-\frac{\gamma_{12}d_{12}\pi R_0}{12\rho_1\phi_1}\left(\nabla\ln\frac{n_1}{n_2}-\frac{3}{2}\nabla\ln\frac{T_1}{T_2}\right)\\&-\frac{\gamma_{12}d_{12}\pi}{16\rho_1\phi_1}(\mathbf{\Xi_{12}}+\mathbf{\Omega_{12}}+\mathbf{\Lambda_{12}})\end{aligned} \tag{42}$$

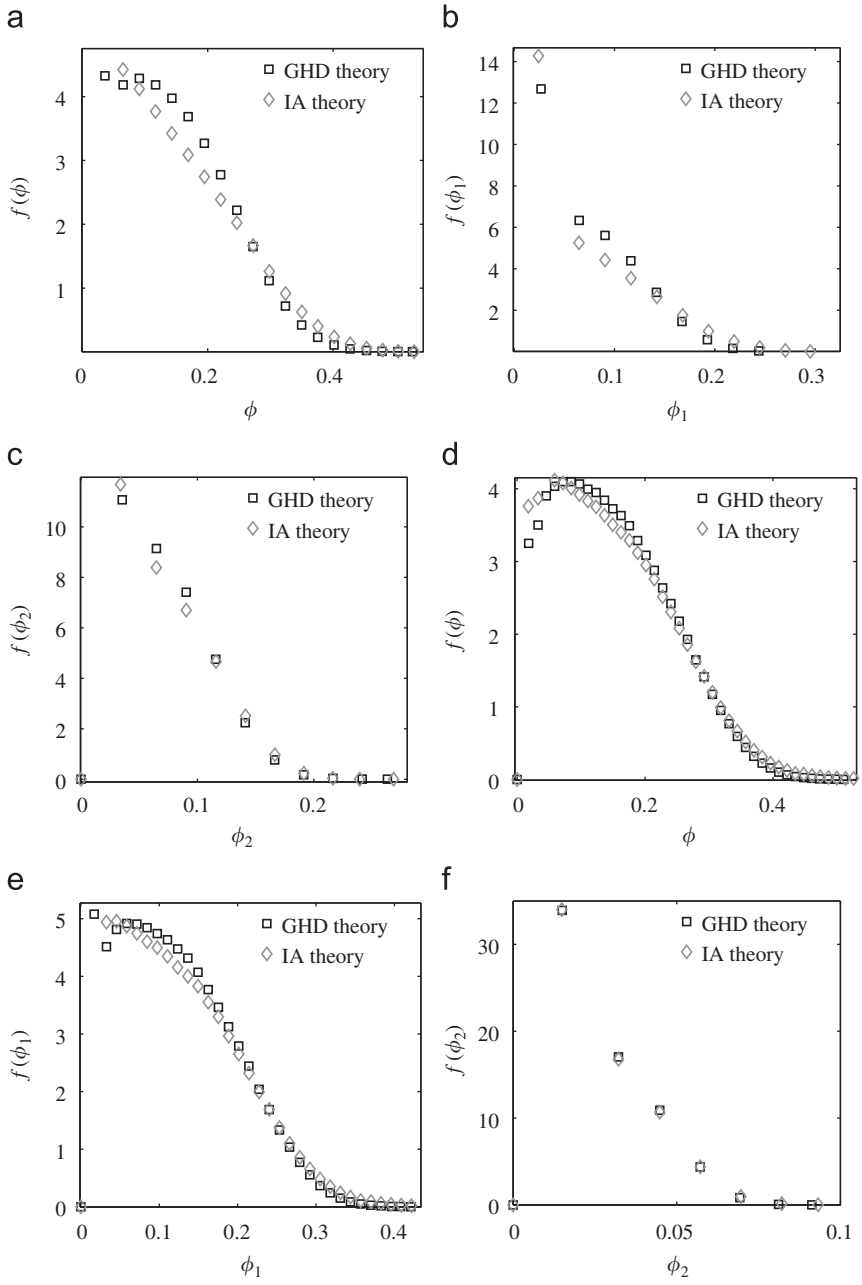

Fig. 9. Probability distribution function (PDF) of mixture and species volume fraction observed in three-dimensional bidisperse gas-particle flow simulations. The PDF of mixture volume fraction is given for *Case D* in (a), and for *Case C* in (d) as a function of mixture volume fraction. The PDF of the volume fraction of species 1 is given for *Case D* in (b), and for *Case C* in (e) as a function of the volume fraction of species 1. The PDF of the volume fraction of species 2 is given for *Case D* in (c), and for *Case C* in (f) as a function of the volume fraction of species 2.

Table 3
Computational times for both GHD and IA kinetic theories for the two different bidisperse PSDs simulated in this study. These computations were performed on 2.5 GHz Intel Xeon E5420 processors with all computational times given on a per processor basis.

Dimensionality	*Case*	GHD CPU time $(\frac{CPU\ hrs.\ used}{Sec.simulation})$	IA CPU time $(\frac{CPU\ hrs.\ used}{Sec.simulation})$	$\frac{IA}{GHD}$
2*D*	*C*	29.9	87.9	2.93
	D	25.8	41.6	1.61

In order for the species velocity to be slaved to the mixture velocity the first term on the right-hand side of Eq. (42) must be very small compared with to the left-hand side. In other words, the timescale associated with the relaxation of the diffusion velocity of species 1 must be much faster than the relaxation of the mixture velocity to its steady state value. From inspection of the mixture momentum balance expression given in Eq. (39), one can deduce that the timescale associated with the relaxation of the mixture velocity is be given as $t_{mix} = \rho_s/(\beta_1+\beta_2)$, and the characteristic timescale for the relaxation of the diffusion velocity of a particle of type 1 is the inverse of the prefactor of the diffusion velocity on the left-hand side of Eq. (41). Therefore, in order for the individual species velocity to be slaved to the mixture velocity the following inequality must hold:

$$Z = \frac{\sqrt{8\pi}\rho_s^2 d_{12}^2 g_{12} m_0^3 (1+e_{12})(T_1T_2)^2}{2(\beta_1+\beta_2)(m_1m_2)^{1/2}(m_1T_2+m_2T_1)^{3/2}(m_1T_1+m_2T_2)^2} \gg 1 \quad (43)$$

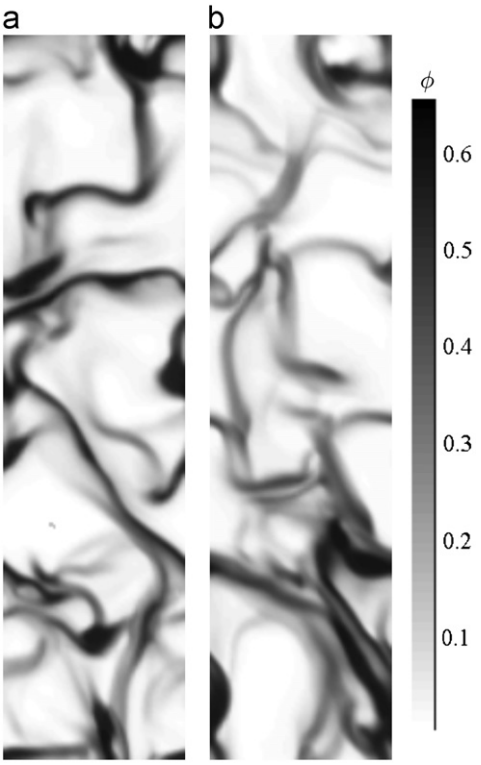

Fig. 10. Two-dimensional instantaneous snapshots of particle volume fraction fields obtained for (a) bidisperse (*Case C*) and (b) monodisperse (*Case A*) cases with the same Sauter mean diameter. The qualitative nature of the gas-particle flow structures in monodisperse and bidisperse is similar. Both snapshots illustrated above were obtained via GHD theory simulations.

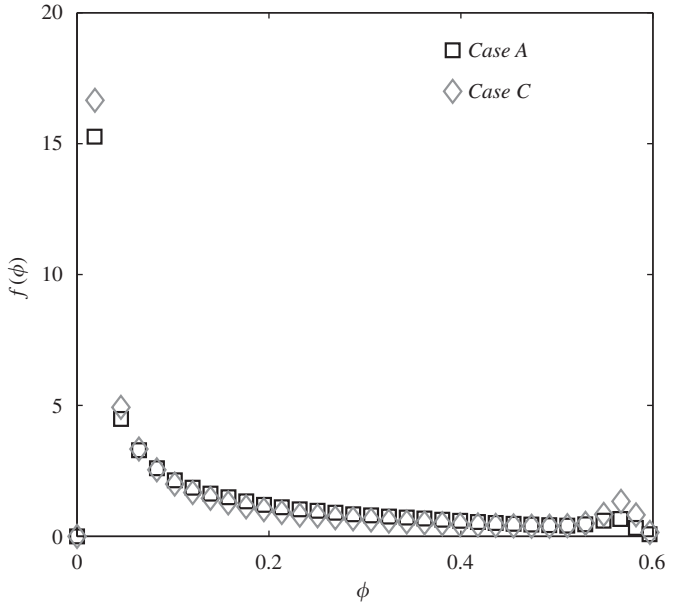

Fig. 11. Probability distribution of function of ϕ for monodisperse (*Case A*) and bidisperse (*Case C*) cases. The monodisperse system has the same Sauter mean diameter as the bidisperse system.

At this point it should be noted that the same inequality can be used for type 2 particles as well, due to the fact that $\gamma_{12}=\gamma_{21}$. In deriving Eq. (43) we have also only considered the first term in the expression for R_2 as it has been shown that the first term is dominant (Iddir and Arastoopour, 2005). Fig. 13 shows an instantaneous snapshot of Z obtained from IA theory simulations for both *Cases C* and *D*. It is clear that over a large percentage of the flow domain this value is much greater than unity. Therefore, the assumption that species velocities are slaved to the mixture is validated by our simulations to a good approximation. This analysis can be used to rationalize why the results obtained from GHD and IA kinetic theories are in quantitative agreement. However, it should be noted that these simulations were conducted at domain-average volume fractions of $\phi=0.15$, and as the domain-average volume fraction decreases the difference between the two kinetic theory approaches will increase. This is true because all of the regions where Z is $O(1)$ are regions where the particle concentration is very low. It is also worth noting that in Eq. (41), if all of the terms in the first row and third row of the right-hand side are very small compared to the terms in the second row, one will recover a similar form to the flux expression given by the GHD *mixture* theory given in Eq. (22).

3.5. On the need for sub-grid scale models for coarse-grid simulation of binary gas-particle flows

It is well known that continuum models of gas-particle flow manifest persistent density and velocity fluctuations that occur over a range of length scales. The length scale of the smallest inhomogeneities is known to be on the order of 10 particle diameters which necessitates prohibitively small grid sizes in order to fully resolve them (Agrawal et al., 2001). However, in order to simulate large scale gas-particle flows in fluidized beds and risers, grids much larger than 10 particle diameters are used in order to keep the total computational time within reasonable bounds (Sundaresan, 2000). Coarse-grid simulations which ignore the consequences of the sub-grid scale flow structures tend to overestimate the fluid-particle drag force (Agrawal et al., 2001; Andrews et al., 2005; Igci et al., 2008). In light of these observed differences between fine- and coarse-grid simulations of continuum models there has been a substantial amount of research devoted to the development of filtered two-fluid model equations, which are obtained by filtering the microscopic two-fluid model equations (Andrews et al., 2005; Igci et al., 2008). The *filtered* fluid-particle flow model requires constitutive relations for the *filtered* drag coefficient, particle phase viscosity, and particle phase pressure in terms of the *filtered* variables (Igci et al., 2008).

While a large effort has been focused on the development of filtered two-fluid models for the coarse-grid simulation of monodisperse gas-particle flows, polydisperse systems have not received any attention so far. As a first step in that direction, we have filtered the results of the highly resolved two-dimensional simulations carried out in this study and gathered statistics on the effective fluid-particle drag coefficient for each particle type for square filters of different sizes. The procedure follows that of Igci et al. (2008) for monodisperse systems. We define the effective drag force in a filtered multi-fluid model framework as follows:

$$\widetilde{\mathbf{f}_{\mathbf{D_i}}}=\widetilde{\beta_{i_{eff}}}(\widetilde{\mathbf{v}_{\mathbf{f}}}-\widetilde{\mathbf{v}_{\mathbf{i}}}) \tag{44}$$

where $\widetilde{\mathbf{f}_{\mathbf{D_i}}}$ is the *filtered* fluid-particle drag force, $\widetilde{\beta_{i_{eff}}}$ is the *filtered* drag coefficient, $\widetilde{\mathbf{v}_{\mathbf{f}}}$ is the *filtered* gas velocity, and $\widetilde{\mathbf{v}_{\mathbf{i}}}$ is the *filtered* velocity of a particle of species *i*. The right-hand side of Eq. (44) is the postulated form of a closure model for the *filtered* effective drag force. Using a closure of the form given in Eq. (44) we gathered filtered statistics for the filtered drag coefficient $\widetilde{\beta_{i_{eff}}}$

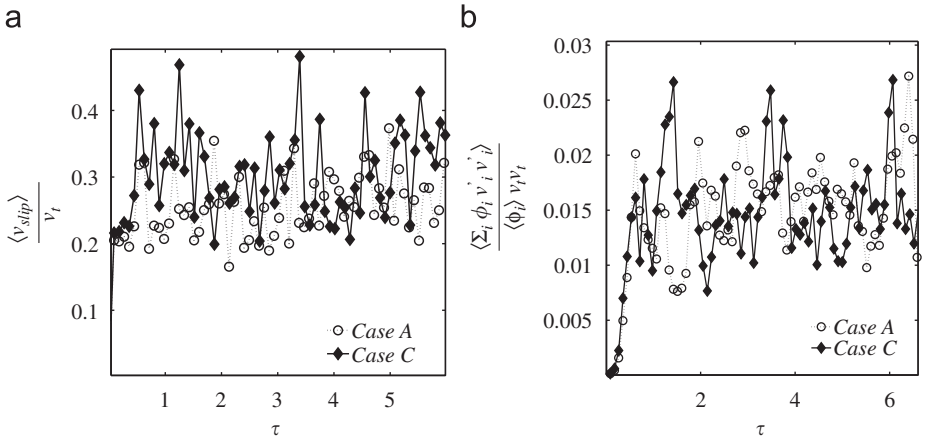

Fig. 12. Time progression of the (a) domain-averaged mixture slip velocity and (b) domain-averaged meso-scale vertical normal stress obtained from periodic domain simulations of bidisperse (*Case C*) and monodisperse (*Case A*) cases with the same Sauter mean diameter. All results presented in this plot were obtained from GHD theory simulations. Table 2 summarizes the time-averaged values for all cases examined in this study.

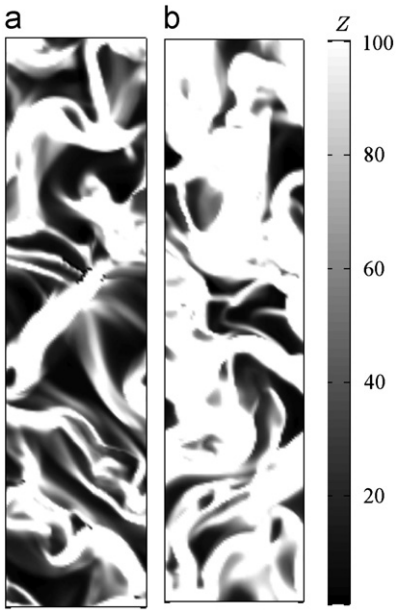

Fig. 13. (Color online) Instantaneous snapshot of the value of Z throughout the simulation domain obtained at statistical steady state for both (a) *Case C* and (b) *Case D* using IA kinetic theory. The color plots indicate that the value of Z is much greater than unity throughout the simulation both binary systems under investigation.

from high-resolution simulation results, and examined its dependence on filter size. Fig. 14(a) and (b) shows the *dimensionless* filtered drag coefficient $\widehat{\beta_{i_{eff}}}$ obtained by averaging the high-resolution simulation for *Case C* (using the GHD theory). Here $\widehat{\beta_{i_{eff}}} = \widetilde{\beta_{i_{eff}}} v_{t_i}/(\rho_{s_i} g)$. It is clear that the *dimensionless filtered* drag coefficient is a strong function of the filter size for both the large particle (type 1 particle) and small particle (type 2 particle) species. The same feature can be seen in Fig. 15(a) and (b), where the *filtered* drag coefficients for the two particle types are given for *Case C* using IA kinetic theory. For both models, the filtered drag coefficient decreases with increasing filter sizes, and this is exactly the same qualitative trend reported in the literature for monodisperse systems (Igci et al., 2008). So, one can readily anticipate that filtered constitutive relations must be developed for polydisperse systems as well, just as they are currently being done for monodisperse systems. This is true for both *mixture* and *species* based kinetic theory model frameworks.

4. Conclusions

In this work the predictions of two different polydisperse kinetic theory model frameworks have been compared for two different binary particle size distributions spanning a range of particle sizes and particle volume fraction ratios. Inspection of snapshots of the instantaneous particle volume fraction and volume fraction ratio fields revealed that the GHD and IA theories (representative of the *mixture* and *species* based modeling approaches, respectively) manifest qualitatively similar flow structures. Both models yields nearly identical probability distribution functions for the total particle volume fraction in a grid cell. Furthermore, the energy spectra of the particle volume fraction for both kinetic theory models are essentially the same; this serves as direct evidence that the nature of the gas-particle flow structures admitted by both kinetic theories are similar.

Direct comparison of bidisperse systems with equivalent monodisperse systems having the same Sauter mean diameters reveals that the qualitative nature of the gas-particle flow structures are similar for both monodisperse and bidisperse cases. More quantitative comparisons of the PDF of total volume fraction in a cell revealed a slightly higher probability of observing heterogeneous flow structures in the flow of the bidisperse systems; correspondingly, bidisperse flow simulations in periodic domains yielded larger slip velocities (or equivalently lower overall drag coefficients) than the equivalent monodisperse systems.

A systematic filtering of the high-resolution binary gas-particle flow simulation results revealed that the *filtered* drag coefficients decreased with increasing filter size. This filtering analysis clearly shows that filtered multi-fluid models are needed in order to reconcile the differences between coarse and highly resolved simulation results. While the need for filtered models for continuum model simulations of monodisperse gas-particle flows is well known, the present study provides the first demonstration of the need for filtered models for bidisperse gas-particle flows. It is expected that additional filtered models for the particle phase pressure and viscosity will also be necessary. The detailed form of the filtered multi-fluid models and the associated constitutive models will be the topic of future work within our group.

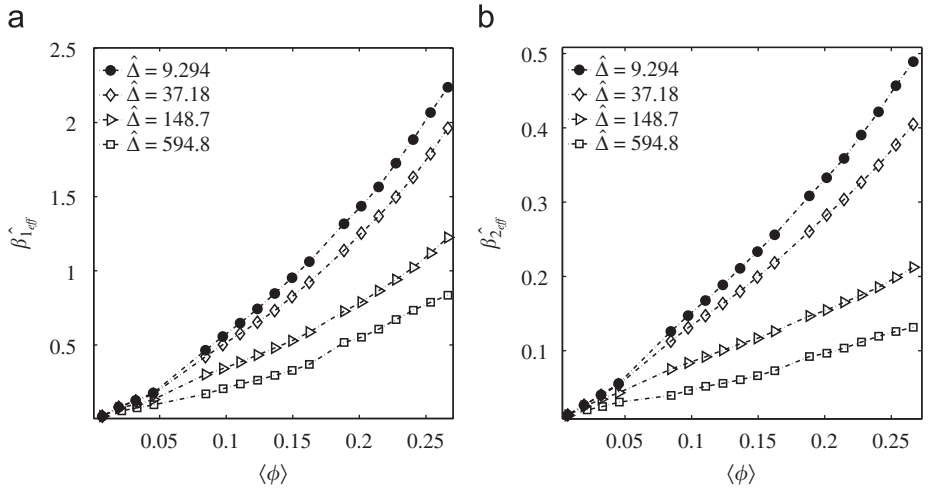

Fig. 14. *Filtered* drag coefficient for (a) particle of type 1 and (b) particle of type 2 for *Case C* obtained via continuum model simulations of GHD theory. The volume fraction ratio ϕ_1/ϕ_2 in the filtered region is unity in this plot. The simulation domain: 32 cm $\times$32 cm; 128 $\times$128 grid cells.

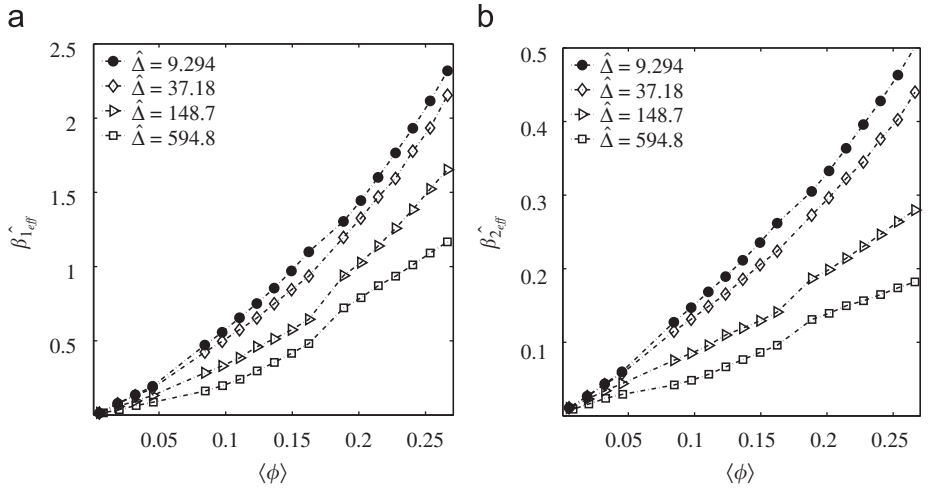

Fig. 15. *Filtered* drag coefficient for (a) particle of type 1, and (b) particle of type 2 for *Case C* obtained via continuum model simulations of IA theory. The volume fraction ratio ϕ_1/ϕ_2 in the filtered region is unity in this plot. The simulation domain: 32 cm $\times$32 cm; 128 $\times$128 grid cells.

Nomenclature

a	polynomial of particle volume fraction
$\langle d \rangle$	Sauter mean diameter of the mixture
d_i	diameter of a particle of species i
D_{ij}	ordinary diffusivity of particles of type i in particles of type j
D_{ij}^F	mass mobility of particles of type i in particles of type j
D_i^T	thermal diffusivity of particles of type i
e	coefficient of restitution
e_{ij}	coefficient of restitution between particles of types i and j
E_ϕ	energy spectra of volume fraction fluctuations
E_ϕ	energy spectra of *dimensionless* mixture velocity fluctuations
E_T	energy spectra of *dimensionless* mixture granular temperature fluctuations
$F^*_{D-fixed}$	*dimensionless* fluid-particle drag force in a monodisperse fixed bed
$\mathbf{f_{D_i}}$	fluid-particle drag force *per unit volume* experienced by a particle of type i
$\widetilde{\mathbf{f_{D_i}}}$	*filtered* fluid-particle drag force *per unit volume* experienced by a particle of type i
$\mathbf{F_{D_i}}$	fluid-particle drag force *per particle* experienced by a particle of type i
$F^*_{Di-fixed}$	*dimensionless* fixed bed fluid-particle drag force experienced by a particle of type i in a polydisperse assemblage of particles
$\mathbf{F_i}$	sum of external forces experienced by the ith particle type
$\mathbf{g}$	gravitational acceleration vector
g_{im}	radial distribution function at contact for a bidisperse mixture of particles of types i and m
$\mathbf{I_{im}}$	momentum exchanged between particles of types i and m due to collisions
$\mathbf{j_{o_i}}$	mass flux of a particle of type i relative to the mixture
k	wavenumber
$\hat{k}$	*dimensionless* wavenumber ($\hat{k} = k\nu_t^2/g$)
m	average particle mass based on the Sauter mean diameter of the mixture
m_i	mass of the ith particle type n mixture number density
N	number of horizontal grid points
n_i	number density of a particle of type i

N_{ip}	granular energy collisional dissipation term
$\mathbf{q}$	granular energy flux vector of the mixture
$\mathbf{q_i}$	granular energy flux vector of a particle of type i
Re_{mix}	mixture Reynolds number
s	number of particle types in a polydisperse mixture
t	time T mixture granular temperature
T_i	granular temperature of a particle of type i
$\mathbf{v}$	velocity vector of the particle mixture
$\mathbf{v_f}$	velocity vector of the fluid phase
$\widetilde{\mathbf{v_f}}$	*filtered* velocity vector of the fluid phase
$\mathbf{v_i}$	velocity vector of the ith particle phase
$\widetilde{\mathbf{v_i}}$	*filtered* velocity vector of the ith particle phase
V_i	volume of a particle of type i
v_i'	velocity fluctuation of a particle of type i
$\langle v_{slip} \rangle$	vertical component of the domain-averaged slip velocity
v_t	terminal settling velocity of an isolated particle with diameter given by the Sauter mean diameter of the system
v_{t_i}	terminal settling velocity of a particle of type i
y_i	ratio of the diameter of a particle of type i to the Sauter mean diameter of the mixture
Z	ratio of the timescale associated with mixture velocity relaxation to the timescale associated with the relaxation of the velocity species to the mixture velocity

Greek letters

α_{ij}	parameter in expression for the fluid-mediated particle–particle friction coefficient β_{ij}
β_i	fixed bed friction coefficient of a particle of type i
$\widetilde{\beta_{i_{eff}}}$	*filtered* effective drag coefficient of a particle of type i
$\widehat{\beta_{i_{eff}}}$	*dimensionless* effective drag coefficient of a particle of type i: $\widehat{\beta_{i_{eff}}} = \beta_{i_{eff}} v_{t_i}/(\rho_{s_i} g)$
β_{ij}	fluid-mediated particle–particle friction coefficient
Δ	filter size
$\hat{\Delta}$	*dimensionless* filter size; $\hat{\Delta} = \Delta/\langle d \rangle$
ΔU_{mix}	mixture velocity
ϵ_f	the void fraction of the fluid phase
ζ	cooling rate of the mixture
ζ^0	zeroth order cooling rate
ζ_U	cooling rate transport coefficient of the mixture
λ	lubrication cutoff distance
μ_f	viscosity of the fluid phase
ρ_f	density of the fluid phase
ρ_s	mixture density
ρ_{s_i}	density of the ith particle phase
σ_f	gas phase stress tensor
σ_s	solid phase stress tensor the particle mixture
σ_{s_i}	solid phase stress tensor of a particle of type i
τ	*dimensionless* time given as $\tau = tg/v_t$
ϕ	total volume fraction particle phase
ϕ_i	volume fraction of the ith particle phase
χ^*_{BVK}	inertial correction for fixed beds

Acknowledgments

The authors would like to acknowledge the financial support from Department of Energy NETL (Award DE-FC26-07NT43098), the National Science Foundation (Award CBET-0650893 to CMH), and the ExxonMobil Res. & Eng. Co (to S.S.).

References

Agrawal, K., Loezos, P.N., Syamlal, M., Sundaresan, S., 2001. The role of meso-scale structures in rapid gas–solid flows. Journal of Fluid Mechanics 445, 151–185.

Andrews, A.T.I., Loezos, P.N., Sundaresan, S., 2005. Coarse grid simulation of gas-particle flows in vertical risers. Industrial and Engineering Chemistry Research 44, 6022–6037.

Beetstra, R., Van Der Hoef, M.A., Kuipers, J.A.M., 2006. Numerical study of segregation using a new drag force correlation for polydisperse systems derived from lattice-Boltzmann simulations. Chemical Engineering Science 62, 246–255.

Beetstra, R., Van Der Hoef, M.A., Kuipers, J.A.M., 2007. Drag force of intermediate Reynolds number flow past mono- and bidisperse arrays of spheres. A.I.Ch.E. Journal 53, 489–501.

Benyahia, S., 2008. Verification and validation of some polydisperse kinetic theories. Chemical Engineering Science 63, 5672.

Bose, S.T., Moin, P., You, D., 2010. Grid-independent large-eddy simulation using explicit filtering. Physics of Fluids 22, 105103.

Chew, J.W., Hrenya, C.M. Link between bubbling and segregation patterns in gas-fluidized beds with continuous size distributions. A.I.Ch.E. Journal, in press. doi:10.1002/aic.12507.

Chew, J.W., Hrenya, C.M., Cocco, R.A., Hays, R., Findlay, J.G., Karri, S.B.R., Knowlton, T. Species segregation of binary mixtures and a continuous size distribution of group b particles in riser flow. Chemical Engineering Science, submitted for publication.

Clelland, R., Hrenya, C.M., 2002. Simulations of a binary-sized mixture of inelastic grains in rapid shear flow. Physical Review E 65, 031301.

Ding, J., Gidaspow, D., 1990. A bubbling fluidization model using kinetic theory of granular flow. A.I.Ch.E. Journal 36, 523–538.

Fan, L.S., Zhu, C., 1998. Principles of Gas–Solids Flows. Cambridge University Press, New York.

Fan, R., Fox, R.O., 2008. Segregation in polydisperse fluidized beds: validation of a multi-fluid model. Chemical Engineering Science 63, 272–285.

Fan, R., Marchisio, D.L., Fox, R.O., 2004. Application of the direct quadrature method of moments to polydisperse gas–solid fluidized beds. Powder Technology 139, 7–20.

Fox, R.O., 2008. A quadrature based third order moment method for dilute gas-particle flows. Journal of Computational Physics 227, 6313–6350.

Galvin, J.E., 2007. On the hydrodynamic description of binary mixtures of rapid granular flows and gas-fluidized beds. Ph.D. Thesis, University of Colorado, Boulder.

Galvin, J.E., Dahl, S.R., Hrenya, C.M., 2005. On the role of non-equipartition in the dynamics of rapidly flowing granular mixtures. Journal of Fluid Mechanics 528, 207–232.

Garzó, V., Dufty, J.W., 1999. Homogeneous cooling state for a granular mixture. Physical Review E 60, 5706–5713.

Garzó, V., Dufty, J.W., Hrenya, C.M., 2007a. Enskog theory for polydisperse granular mixtures. I. Navier–Stokes order transport. Physical Review E 76, 031303.

Garzó, V., Hrenya, C.M., Dufty, J.W., 2007b. Enskog theory for polydisperse granular mixtures. II. Sonine polynomial approximation. Physical Review E 76, 031304.

Geldart, D., Baeyens, J., Pope, D.J., Van De Wijer, P., 1981. Segregation in beds of large particles at high velocities. Powder Technology 30, 195–205.

Gidaspow, D., 1994. Multiphase Flow and Fluidization: Continuum and Kinetic Theory Descriptions. Academic Press, London.

Goldman, E., Sirovich, L., 1967. Equations for gas mixtures. Physics of Fluids 10, 1928–1941.

Hoffman, A.C., Janssen, L.P.B.M., Prins, J., 1993. Particle segregation in fluidized binary mixtures. Chemical Engineering Science 48, 1583–1592.

Holloway, W., Yin, X., Sundaresan, S., 2010. Fluid-particle drag in inertial polydisperse gas–solid suspensions. A.I.Ch.E. Journal 56, 1995–2004.

Hrenya, C.M., 2011. Kinetic theory for granular materials: polydispersity. In: Pannala, S., Syamlal, M., O'Brien, T. (Eds.), Computational Gas–Solid Flows and Reacting Systems: Theory, Methods and Practice. IGI Global, Hershey.

Huilin, L., Gidaspow, D., Manger, E., 2001. Kinetic theory of fluidized binary mixtures. Physical Review E 64, 61301–61309.

Huilin, L., Yurong, H., Gidaspow, D., Lidan, Y., Yukun, Q., 2003. Size segregation of binary mixture of solids in bubbling fluidized beds. Powder Technology 134, 86–97.

Iddir, H., Arastoopour, H., 2005. Modeling of multitype particle flow using the kinetic theory approach. A.I.Ch.E. Journal 51 (6), 1620–1632.

Igci, Y., Andrews, A.T., Sundaresan, S., Pannala, S., O'Brien, T., 2008. Filtered two-fluid models for fluidized gas-particle suspensions. A.I.Ch.E. Journal 54, 1431–1448.

Jackson, R., 2000. The Dynamics of Fluidized Particles. Cambridge Monographs on Mechanics. Cambridge University Press, Cambridge.

Jenkins, J.T., Mancini, F., 1989. Kinetic theory for binary mixtures of smooth, nearly elastic spheres. Physics of Fluids A: Fluid Dynamics 1, 2050–2057.

Jiradilok, V., Gidaspow, D., Breault, R.W., Shadle, L.J., Guenther, C., Shi, S., 2008. Computation of turbulence and dispersion of cork in the netl riser. Chemical Engineering Science 63, 2135–2148.

Jiradilok, V., Gidaspow, D., Damronglerd, S., Koves, W.J., Mostafi, R., 2006. Kinetic theory based CFD simulation of turbulent fluidization of FCC particles in a riser. Chemical Engineering Science 61, 5544–5559.

Joseph, G.G., Leboreiro, J., Hrenya, C.M., Stevens, A.R., 2007. Experimental segregation profiles in bubbling gas-fluidized beds. A.I.Ch.E. Journal 53, 2804–2813.

Koch, D.L., Sangani, A.S., 1999. Particle pressure and marginal stability limits for a homogeneous monodisperse gas-fluidized bed: kinetic theory and numerical simulations. Journal of Fluid Mechanics 400, 229–263.

Leboreiro, J., Joseph, G.G., Hrenya, C.M., Snider, D.M., Banerjee, S.S., Galvin, J.E., 2008. The influence of binary drag laws on simulations of species segregation in gas-fluidized beds. Powder Technology 184, 275–290.

Lun, C.K.K., Savage, S.B., Jeffrey, D.J., Chepurniy, N., 1984. Kinetic theories for granular flow: inelastic particles in Couette flow and slight inelastic particles in a general flowfield. Journal of Fluid Mechanics 140, 223–256.

Murray, J.A., Hrenya, C.M., Garzó, V. Enskog theory for polydisperse granular mixtures. III. Comparison of dense and dilute transport coefficients and equations of state for a binary mixture. Powder Technology, in press.

Neri, A., Gidaspow, D., 2000. Riser hydrodynamics: simulation using kinetic theory. A.I.Ch.E. Journal 46, 52–67.

Owoyemi, O., Mazzei, L., Lettieri, P., 2007. CFD modeling of binary-fluidized suspensions and investigation of role of particle–particle drag on mixing and segregation. A.I.Ch.E. Journal 53, 1924–1940.

Peeler, J.P.K., Huang, J.R., 1989. Segregation of wide size range particle mixtures in fluidized beds. Chemical Engineering Science 44, 1113–1119.

Rowe, P.N., Agbim, A.J., Nienow, A.W., 1972. Mechanisms by which particles segregate in gas fluidized-beds—binary-systems of near-spherical particles. Transactions of the Institution of Chemical Engineers and the Chemical Engineer 50, 310–323.

Rowe, P.N., Nienow, A.W., 1976. Particle mixing and segregations in gas fluidised beds: a review. Powder Technology 15, 141–147.

Sinclair, J.L., Jackson, R., 1989. Gas-particle flow in a vertical pipe with particle–particle interactions. A.I.Ch.E. Journal 35, 1473–1486.

Spalding, D.B., 1980. Numerical computation of multiphase flow and heat-transfer. In: Taylor, C. (Ed.), Recent Advances in Numerical Methods in Fluids. Pinbridge Press, Swansea.

Squires, A.M., Kwauk, M., Avidan, A.A., 1985. Fluid beds: at last, challenging two entrenched practices. Science 230, 1329–1337.

Srivastava, A., Sundaresan, S., 2003. Analysis of frictional-kinetic model for gas-particle flow. Powder Technology 129, 72–85.

Sundaresan, S., 2000. Perspective: modeling the hydrodynamics of multi-phase flow reactors: current status and challenges. A.I.Ch.E Journal 46, 1102–1105.

Sundaresan, S., 2003. Instabilities in fluidized beds. Annual Reviews of Fluid Mechanics 35, 63–88.

Syamlal, M., 1998. MFIX documentation: numerical techniques. Technical Report, Department of Energy, National Energy Technology Laboratory, see also www.mfix.org.

Ten Cate, A., Sundaresan, S., 2006. Analysis of unsteady forces in ordered arrays of monodisperse spheres. Journal of Fluid Mechanics 552, 257–872.

Valiveti, P., Koch, D.L., 1999. The inhomogeneous structure of a bidisperse sedimenting gas–solid suspension. Physics of Fluids 11, 3283–3305.

van der Hoef, M.A., Beetstra, R., Kuipers, J.A.M., 2005. Lattice-Boltzmann simulations of low-Reynolds-number flow past mono- and bidisperse arrays of spheres: results for permeability and drag force. Journal of Fluid Mechanics 528, 233–254.

van Sint Annaland, M., Bokkers, G.A., Goldscmidt, M.J.V., Olaofe, O.O., van der Hoef, M.A., Kuipers, J.A.M., 2009a. Development of a multi-fluid model for polydisperse dense gas–solid fluidised beds, part I: model derivation and numerical implementation. Chemical Engineering Science 64, 4222–4236.

van Sint Annaland, M., Bokkers, G.A., Goldscmidt, M.J.V., Olaofe, O.O., van der Hoef, M.A., Kuipers, J.A.M., 2009b. Development of a multi-fluid model for polydisperse dense gas–solid fluidised beds, part II: segregation in binary particle mixtures. Chemical Engineering Science 64, 4237–4246.

Wildman, R.D., Parker, D.J., 2002. Coexistence of two granular temperatures in binary vibrofluidized beds. Physical Review Letters 88, 064301.

Wu, S.Y., Baeyens, J., 1998. Segregation by size difference in gas fluidized beds. Powder Technology 98, 139–150.

Yates, J.G., Newton, G., 1986. Fine particle effects in a fluidized-bed reactor. Chemical Engineering Science 41, 801–806.

Yin, X., Sundaresan, S., 2009a. Drag law for bidisperse gas-solid suspensions containing equally sized spheres. Industrial and Engineering Chemistry Research 48, 227–241.

Yin, X., Sundaresan, S., 2009b. Fluid-particle drag in low-Reynolds-number polydisperse gas–solid suspensions. A.I.Ch.E. Journal 55, 1352–1368.

Effect of microstructural anisotropy on the fluid-particle drag force and the stability of the uniformly fluidized state

WILLLIAM HOLLOWAY[1]†, JIN SUN[2] AND SANKARAN SUNDARESAN[1]

[1]Department of Chemical and Biological Engineering, Princeton University, Princeton, NJ 08544

[2]School of Engineering, University of Edinburgh, Edinburgh, Scotland, UK

(Received 29 January 2012)

Lattice Boltzmann simulations of fluid flow through sheared assemblies of monodisperse spherical particles have been performed. The friction coefficient tensor extracted from these simulations is found to become progressively more anisotropic with increasing Peclet number, $Pe = \dot{\gamma}d^2/D$, where $\dot{\gamma}$ is the shear rate, d is the particle diameter, and D is the particle self-diffusivity. A model is presented for the anisotropic friction coefficient, and the model constants are related to changes in the particle microstructure. Linear stability analysis of the two-fluid model equations including the anisotropic drag force model developed in the present study reveals that the uniformly fluidized state of low Reynolds number suspensions is most unstable to mixed mode disturbances that take the form of vertically travelling waves having both vertical and transverse structures. As the Stokes number increases, the transverse-to-vertical wavenumber ratio decreases towards zero; i.e. the transverse structure becomes progressively less prominent.

1. Introduction

Fluidized beds where particles are kept in a suspended state by upward flowing fluid are common in chemical process industries. In most of these beds, the Stokes number, $St = mu_t/6\pi\mu_g a^2$, is usually much larger than unity. Here, m represents the particle mass, u_t is the terminal settling velocity of an isolated particle, μ_g represents the fluid viscosity, and a is the particle radius. Such beds are often unstable, with homogeneous suspensions giving way to persistent spatial and temporal inhomogeneities in particle volume fraction and the local average velocities of the fluid and particle phases. An inhomogeneous velocity field can be expected to lead to anisotropic microstructure of the particle assembly with the extent of anisotropy increasing with the Peclet number. In this communication, we examine the influence of this anisotropy on the fluid-particle interaction force. When the particle microstructure is anisotropic, the fluid-particle drag must be modeled via an anisotropic friction coefficient tensor; although this been recognized in soil mechanics for decades (for example, see Renard & Marsily (1997) and the references cited therein), to the best of our knowledge, the potential influence of this anisotropy on the dynamics of fluidized beds has not been studied in the literature. In the present study, we have first performed lattice Boltzmann simulations of fluid flow through anisotropic assemblies of spherical particles (at low Reynolds numbers) and determined the friction coefficient tensor for various volume fractions and degrees of anisotropy. The anisotropic

† Email address for correspondence: whollowa@princeton.edu

microstructures were created by shearing assemblies of elastic particles at different shear rates while maintaining them in a thermostat (i.e. fixed granular temperature). The friction coefficient anisotropy is then related to microstructural anisotropy and modeled in terms of Peclet number Pe.

We then present an analysis of the linear stability of the state of uniform fluidization to illustrate the influence of an anisotropic friction coefficient. The growth rate of instabilities in gas-fluidized beds of particles is too rapid to permit experimental observation of the initial stages of the formation of inhomogeneous structures. In contrast, the slower growth rates in liquid-solid systems permit observation of different structures in the hierarchy of instabilities. Convective instabilities in liquid fluidized beds that take the form of one-dimensional vertically traveling waves (Anderson & Jackson 1969; Ham *et al.* 1990; Nicolas *et al.* 1996; Duru & Guazzelli 2002) and two-dimensional structures (Duru & Guazzelli 2002) have been reported. Hydrodynamic models for fluidized beds that treat the fluid and particle phases as interpenetrating continua (the so-called two-fluid models) have been analyzed by several researchers to probe the emergence of the inhomogeneous structures; in all these studies, the friction coefficient contained in the fluid-particle drag force model is assumed to be isotropic, corresponding to a locally isotropic particle microstructure (for example, see Anderson & Jackson (1969); Batchelor (1988); Ham *et al.* (1990); Koch (1990); Koch & Sangani (1999); Jackson (2000)). These studies revealed that the state of homogeneous fluidization would first give rise to one-dimensional waves with no horizontal structures. These one-dimensional waves undergo subsequent bifurcations leading to the formation of bubble-like voids in dense fluidized beds, and particle clusters in dilute gas-solid systems (Anderson *et al.* 1995; Glasser *et al.* 1996, 1997, 1998; Agrawal *et al.* 2001). In the present study, we demonstrate that when anisotropic friction coefficient is taken into consideration the state of uniform fluidization is predicted to be unstable over a much wider parameter space and that in some regions of the parameter space the dominant mode has both vertical and lateral structures.

2. Continuum models for gas-particle flows

In order to place the objective of the work in more concrete terms, we begin with two-fluid model equations that are commonly used to describe the flow of uniformly sized particles and the interstitial (fluidizing) gas, which are given as

$$\frac{\partial\left(\rho_g(1-\phi)\right)}{\partial t} + \nabla\cdot\left(\rho_g(1-\phi)\boldsymbol{u}\right) = 0, \tag{2.1}$$

$$\frac{\partial\left(\rho_s\phi\right)}{\partial t} + \nabla\cdot\left(\rho_s\phi\boldsymbol{v}\right) = 0, \tag{2.2}$$

$$\frac{\partial\left(\rho_g(1-\phi)\boldsymbol{u}\right)}{\partial t} + \nabla\cdot\left(\rho_g(1-\phi)\boldsymbol{u}\boldsymbol{u}\right) = -(1-\phi)\nabla\cdot\boldsymbol{\sigma}_g - \boldsymbol{f_D} + \rho_g(1-\phi)\boldsymbol{g}, \tag{2.3}$$

$$\frac{\partial\left(\rho_s\phi\boldsymbol{v}\right)}{\partial t} + \nabla\cdot\left(\rho_s\phi\boldsymbol{v}\boldsymbol{v}\right) = -\phi\nabla\cdot\boldsymbol{\sigma}_g - \nabla\cdot\boldsymbol{\sigma}_s + \boldsymbol{f_D} + \rho_s\phi\boldsymbol{g}, \tag{2.4}$$

$$\frac{3\rho_s}{2}\left(\frac{\partial\left(\phi T\right)}{\partial t} + \nabla\cdot\left(\phi T\boldsymbol{v}\right)\right) = -\nabla\cdot\boldsymbol{q} - \boldsymbol{\sigma}_s : \nabla\boldsymbol{v} + \Gamma_{slip} - J_{coll} - J_{vis}, \tag{2.5}$$

where ϕ is the particle volume fraction; ρ_g and ρ_s are fluid and particle phase densities, respectively; $\boldsymbol{u}$ and $\boldsymbol{v}$ are fluid and particle phase velocities, respectively; $\boldsymbol{\sigma}_g$ and $\boldsymbol{\sigma}_s$ are fluid and particle phase stress tensors, respectively; $\boldsymbol{f_D}$ is the fluid-particle drag force per unit volume of suspension; $\boldsymbol{g}$ is the gravitational acceleration; T is the granular

temperature (defined as the root mean square of the particle velocity fluctuations); $\boldsymbol{q}$ is the granular energy flux vector; Γ_{slip} is the rate of production of granular energy through slip between particle and fluid phases per unit volume of suspension; J_{coll} is the rate of dissipation of granular energy due to inelastic collisions per unit volume of suspension; and J_{vis} is the rate of viscous dissipation of granular energy per unit volume of suspension. Eqs. (2.1) and (2.2) represent the continuity equations for particle and fluid phases; eqs. (2.3) and (2.4) are fluid and particle phase momentum balances; and eq. (2.5) is an evolution equation for the granular energy associated with particle velocity fluctuations. In this work a Newtonian closure is adopted for gas phase stress tensor. Several authors have derived constitutive models for $\boldsymbol{\sigma}_s$ and J_{col} using the kinetic theory of granular flow (for example, see Lun *et al.* (1984); Gidaspow (1994); Garzó & Dufty (1999)). For the purpose of the present study, we employ the model for $\boldsymbol{\sigma}_s$ and J_{col} derived by Lun *et al.* (1984), and use expressions for the role of the interstitial fluid on the granular energy production (Γ_{slip}) and dissipation (J_{vis}) described by Koch & Sangani (1999):

$$\boldsymbol{\sigma}_s = \left(p_s - \frac{(1+e_p)}{2}\mu_b \nabla\cdot\boldsymbol{v}\right) I - 2\mu_s \boldsymbol{S} \qquad \boldsymbol{S} = \frac{1}{2}\left(\nabla\boldsymbol{v} + \nabla\boldsymbol{v}^T\right) - \frac{1}{3}\left(\nabla\cdot\boldsymbol{v}\right) I, \tag{2.6}$$

$$p_s = \rho_s \phi \left(1 + 4\eta\phi g_0\right) T \qquad \mu_b = \frac{256}{96\sqrt{\pi}}\rho_s d\sqrt{T}\phi^2 g_0 \qquad \eta = \frac{1+e_p}{2}, \tag{2.7}$$

$$\mu_s = \left(\frac{5\rho_s d\sqrt{\pi T}}{96 g_0 \eta(2-\eta)}\left(1 + \frac{8}{5}\phi\eta g_0\right)\left(1 - \frac{8}{5}\phi\eta(3\eta-2)g_0\right) + \frac{3}{5}\eta\mu_b\right), \tag{2.8}$$

$$\Gamma_{slip} = \frac{81\phi\mu_g^2|\boldsymbol{u}-\boldsymbol{v}|^2\Xi}{g_0 d^3 \rho_s\sqrt{\pi T}}, \tag{2.9}$$

$$\Xi = \left\{ \begin{array}{cc} \left(\frac{1+3\sqrt{\phi/2}+(135/64)\phi\ln\phi+17.14\phi}{1+0.681\phi-8.48\phi^2+8.16\phi^3}\right)^2\left(\frac{1}{1+3.5\sqrt{\phi}+5.9\phi}\right) & \phi < 0.40 \\ \left(\frac{10\phi}{(1-\phi)^3}+0.7\right)^2\left(\frac{1}{1+3.5\sqrt{\phi}+5.9\phi}\right) & \phi \geq 0.40 \end{array} \right\}, \tag{2.10}$$

$$\boldsymbol{q} = -\kappa\nabla T, \tag{2.11}$$

$$\kappa = \frac{75\rho_s d\sqrt{\pi T}}{48 g_0 \eta\left(41-33\eta\right)}\left(\left(1 + \frac{12}{5}\eta\phi g_0\right)\left(1 + \frac{12}{5}\eta^2(4\eta-3)\phi g_0\right) + \frac{64}{24\pi}\left(41-33\eta\right)\eta^2\right)\phi^2 g_0^2\Big), \tag{2.12}$$

$$J_{vis} = \frac{54\phi\mu_g T}{d^2} R_{diss}, \tag{2.13}$$

$$R_{diss} = 1 + 3\sqrt{\frac{\phi}{2}} + \frac{135}{64}\phi\ln\phi + 11.26\left(1 - 5.1\phi + 16.57\phi^2 - 21.77\phi^3\right) - \phi g_0 \ln\epsilon_m, \tag{2.14}$$

$$J_{coll} = \frac{12}{\pi}\left(1-e_p^2\right)\frac{\rho_s\phi^2}{d} g_0 T^{3/2}, \tag{2.15}$$

where p_s is the particle phase pressure, μ_b is the bulk viscosity of the particle phase, μ_s is the particle phase viscosity, μ_g is the gas phase viscosity, e_p is the coefficient of

restitution, κ is the conductivity, R_{diss} is the coefficient associated with viscous granular energy dissipation, $\epsilon_m = 0.01$, and g_0 is the radial distribution function at contact for which we use the expression of Ma & Ahmadi (1988)

$$g_0(\phi) = \frac{1 + 2.5\phi + 4.5094\phi^2 + 4.515439\phi^3}{\left(1 - (\phi/\phi_m)^3\right)^{0.67821}}, \tag{2.16}$$

where $\phi_m = 0.64356$. This form of the radial distribution function was used by Koch & Sangani (1999) in their analysis of the stability of the uniformly fluidized state.

The fluid-particle interaction force $\boldsymbol{f_D}$ is usually written as

$$\boldsymbol{f_D} = \beta(\boldsymbol{u} - \boldsymbol{v}) \tag{2.17}$$

where the friction coefficient β is assumed to be isotropic; this is reasonable only if the particle microstructure is isotropic. However, the particle microstructure in fluidized beds is not isotropic (see Figure 8 (a)–(d)). Thus, in writing eq. (2.17), it is implicitly assumed that the microstructural anisotropy is unimportant in the drag force model. In fluidization problems, the weight of the particles is largely supported by the fluid-particle drag, and hence even a small change in the fluid-particle drag can have large influence on the dynamics. When the microstructural anisotropy is important, the drag force model should be modified as:

$$\boldsymbol{f_D} = \hat{\boldsymbol{\beta}} \cdot (\boldsymbol{u} - \boldsymbol{v}) \tag{2.18}$$

where $\hat{\boldsymbol{\beta}}$ is the friction coefficient tensor, whose diagonal elements will simply be β (eq. (2.17)) for isotropic systems. In this manuscript, we ask how significant the anisotropy of $\hat{\beta}$ is and what its consequence on the state of uniform fluidization is.

In the suspension rheology community, a substantial amount of work has been devoted toward describing the rheology of concentrated suspensions in terms of particle microstructure (for example, see Brady & Vicic (1995); Brady & Morris (1997); Stickel & Powell (2005)). The changes in particle microstructure upon simple shear deformation have been linked to nonlinear response properties like shear thinning, shear thickening, and normal stress differences (for example, see Phung *et al.* (1996)). The extent of deviation of the particle microstructure from an equilibrium state depends on the Peclet number

$$Pe = \frac{\dot{\gamma} d^2}{D} = \frac{\dot{\gamma} d}{\sqrt{T}} \frac{16\phi g_0(\phi)}{\sqrt{\pi}}, \tag{2.19}$$

where the shear rate $\dot{\gamma} = \sqrt{2(\boldsymbol{E} : \boldsymbol{E})}$, and the deformation rate tensor $\boldsymbol{E} = (1/2)\left(\nabla \boldsymbol{v} + \nabla \boldsymbol{v}^T\right)$. In eq. (2.19) we have used the expression for the self-diffusivity D that was derived by Savage and Dai using the fact that the particles in this study interact through elastic collisions (namely $e_p = 1$) (Savage & Dai 1993). If the Peclet number is substantially less than unity, the particle microstructure resembles that of an equilibrium configuration of spheres, however, as the Peclet number is increased beyond unity substantial anistropy develops in the particle microstructure.

In most gas-particle fluidized beds, the Reynolds number based on particle diameter and the fluid-particle slip velocity is O(1) or smaller; thus, the inertial correction to the fluid-particle drag force is quite small. With this in mind, we restrict our attention in this study to low Reynolds number flows. (In contrast, the Stokes number is much larger than unity, which is assumed in the present study.) In the low Reynolds number limit, we express the friction coefficients in eqs. (2.17) and (2.18) as:

$$\beta = 18\frac{\mu_g}{d^2}\phi(1-\phi)F(\phi) \qquad \hat{\boldsymbol{\beta}} = 18\frac{\mu_g}{d^2}\phi(1-\phi)\hat{\boldsymbol{F}}(\phi, Pe, \ldots). \tag{2.20}$$

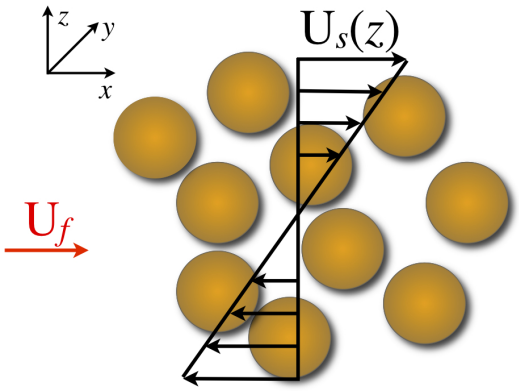

FIGURE 1. Schematic of homogeneous simple shear deformation of the particle phase. In this work, x is the mean flow direction, y is the vorticity direction, and z is the gradient direction associated with the simple shear deformation.

where $F(\phi)$ is a dimensionless friction coefficient, and $\hat{\boldsymbol{F}}(\phi, Pe, \ldots)$ is a dimensionless friction coefficient tensor. In section 4 we demonstrate the dependence of the elements of the friction coefficient tensor on Pe, and subsequently link the changes in the fluid-particle drag to the microstructure of the particle assembly.

3. Simulation Method

To isolate the effect of microstructural anisotropy on the fluid-particle drag force, our simulations were performed in two separate steps. First, we created anisotropic microstructures by performing constant volume simple shear simulations of a granular system using the large-scale atomic/molecular massive parallel simulator (LAMMPS) code that was developed at Sandia National Laboratories (Plimpton 1995). In order to ensure that the simple shear deformation of the particle assembly was homogeneous, the simulation domain was continuously deformed, and gravitational effects were not included. The simulations were initiated by depositing a number of elastic particles into a periodic box, and allowing the particle assembly to equilibrate to a random hard sphere microstructure. Subsequently, the particle assembly was sheared, as illustrated in Figure 1, for a strain in excess of unity in order to ensure that the particle microstructure had reached steady state. For all of the fluid-particle drag results presented in this work, the x-, y-, and z- components refer to the mean flow, vorticity, and gradient direction, respectively. The magnitude of the particle fluctuating velocity was controlled during the deformation using a thermostat, thus facilitating the creation of microstructures with different Pe associated with the deformation. These molecular dynamics simulations were repeated for 16 different realizations of each Peclet number Pe and volume fraction ϕ in order to provide a large number of microstructures from which good statistical averages of the elements of the friction coefficient tensor could be obtained.

The second step in the simulation procedure consisted of performing lattice-Boltzmann simulations of fluid flow through the anisotropic assembly of spheres. For our calculations we used the lattice-Boltzmann code developed by Tony Ladd for the simulation of particulate suspensions (Ladd 1994*a*,*b*; Ladd & Verberg 2001). The unique feature about the lattice-Boltzmann method is that it solves the evolution of a simplified particle velocity distribution function on a fixed lattice rather than solving the Navier-Stokes equations

directly (Chen & Doolen 1998; Ladd & Verberg 2001). The propagation and relaxation of the simplified particle velocity distribution function is designed such that the Navier-Stokes equations are reproduced on large length and time scales (Chen & Doolen 1998). In our simulations a 19 point quadrature in velocity space was used (D3Q19 method) giving a fluid density $\rho_g = 36$ in lattice units. In all simulations presented in this work the fluid viscosity $\mu_g = 6$ in lattice units. Previous work performed with the lattice-Boltzmann code of Ladd has shown that there is a substantial dependence of the fluid-particle drag results on the size of the particle used (van der Hoef *et al.* 2005). In order to obtain fluid-particle drag results that were independent of size of the particle (i.e. grid resolution) used, an extrapolation as a function of the hydraulic radius $r_h = d(1-\phi)/6\phi$ was performed (van der Hoef *et al.* 2005). In this study all simulations were performed with $d = 16.2$ lattice units in the cubic domain with 160^3 grid points. At such high grid resolutions and fluid viscosities we find our results to be independent of grid resolution, therefore we do not perform an extrapolation of our fluid-particle drag results. The Reynolds number $Re = \rho_g d|\boldsymbol{u} - \boldsymbol{v}|/\mu_g < 0.04$ in the results presented here.

Two types of simulations were performed. In the first type, snapshots of deformed particle microstructure and particle velocities in the periodic domain were imported from LAMMPS into the lattice Boltzmann simulation, fluid flow simulations were performed by freezing the positions of the particles (even though their velocities are non-zero) and applying a pressure gradient; this is a good approximation for large St and low Re systems. In the second type, only the particle positions were imported while setting their velocities to zero; fluid flow simulations were then performed in this fixed bed. The friction coefficient tensors obtained in these two types of simulations were virtually identical.

To determine the friction coefficient tensor, three simulations were performed with each snapshot, applying a pressure gradient in the three directions one at a time. The fluid-particle drag force from each realization was obtained by integrating the traction over the surface of all the particles in the simulation domain.

4. Fluid-particle drag in sheared assemblies

In assemblies subjected to simple shear as illustrated in Figure 1, the friction coefficient tensor was found to be essentially symmetric, and the $xy-$ and $yz-$ components were found to be zero within the uncertainty of the measured friction coefficient. Figures 2 (a)-(d) illustrate the variation of the remaining four components (scaled by the diagonal entries at $Pe = 0$) for a particle volume fraction of 0.45. (Simulations were also performed at volume fractions of 0.20, 0.30, 0.35 and 0.40; the same trends as shown in Figure 2 were obtained at all these volume fractions.) The xx-component manifests only a weak dependence on Pe, while the other three shown in Figure 2 reveal much larger variations. At $Pe > 100$, the friction coefficient tensor becomes essentially independent of Pe. The analysis discussed in Appendix A suggests $0 < Pe < 50$ as a reasonable range for fluidized beds, and hence further discussion is limited to only this range which is before the high Pe plateau.

In Figure 3 we show a montage of the two-dimensional projection of the radial distribution of particles in xy-, xz-, and yz-planes for three different values of Pe at a particle volume fraction $\phi = 0.45$. The change in the particle microstructure is apparent as Pe is increased. In the xz-plane a surplus of particles accumulate near the compressional axis of the simple shear deformation, while a depleted region is formed in the extensional axis of the shear flow. The depleted regions in the extensional axis of the simple shear deformation provide low resistance "channels" for the fluid to flow through, thereby decreasing the ensemble averaged β_{yy} value.

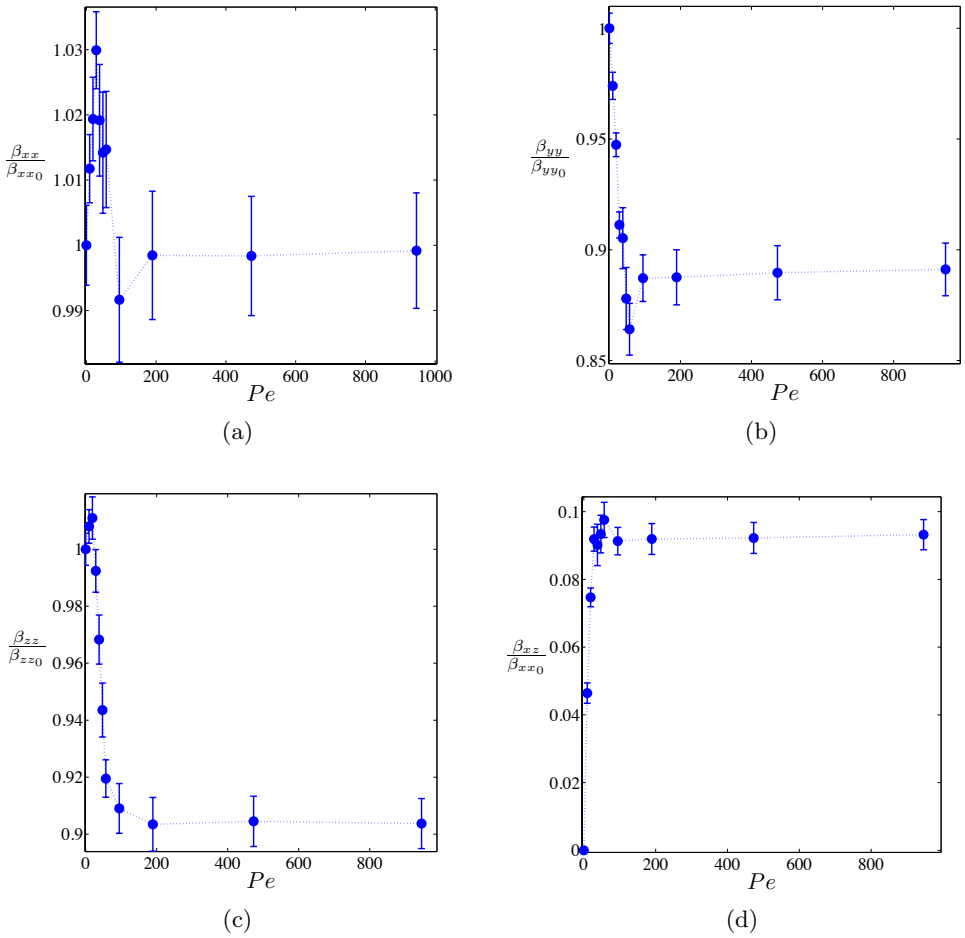

FIGURE 2. (Color online) The (a) β_{xx}, (b) β_{yy}, (c) β_{zz}, and (d) β_{xz} components of the friction coefficient tensor are given as a function of Pe for a particle volume fraction $\phi = 0.45$. In these simulations the domain size is 160^3 lattice units with 798 particles at a particle Reynolds number of $Re = 0.01$. The dotted lines are intended to guide the eye.

It is clear that the changes in the observed fluid-particle drag force arise from changes in the particle microstructure from an isotropic random array of spheres. The microstructure tensor, $\boldsymbol{Y}$, is written as (Stickel *et al.* 2006)

$$\boldsymbol{Y} = \zeta_s \boldsymbol{I} + \boldsymbol{Z}, \tag{4.1}$$

where $\boldsymbol{I}$ is the identity tensor, and

$$\zeta_s = \frac{1}{4\pi}\int_\Omega \frac{a}{l_{mf}(\hat{\boldsymbol{x}})} d\boldsymbol{\Omega} \qquad \boldsymbol{Z} = \frac{1}{4\pi}\int_\Omega \boldsymbol{X}(\hat{\boldsymbol{x}})\frac{a}{l_{mf}(\hat{\boldsymbol{x}})} d\boldsymbol{\Omega} \qquad \lambda = \zeta_s^{-1}. \tag{4.2}$$

In eq. (4.2), ζ_s is the particle radius scaled by the mean free path averaged over the solid angle Ω, $l_{mf}(\hat{\boldsymbol{x}})$ is the mean free path associated with a given direction $\hat{\boldsymbol{x}}$, λ is the mean free path averaged over all solid angles scaled by the particle radius, and $\boldsymbol{X}(\hat{\boldsymbol{x}})$ is the

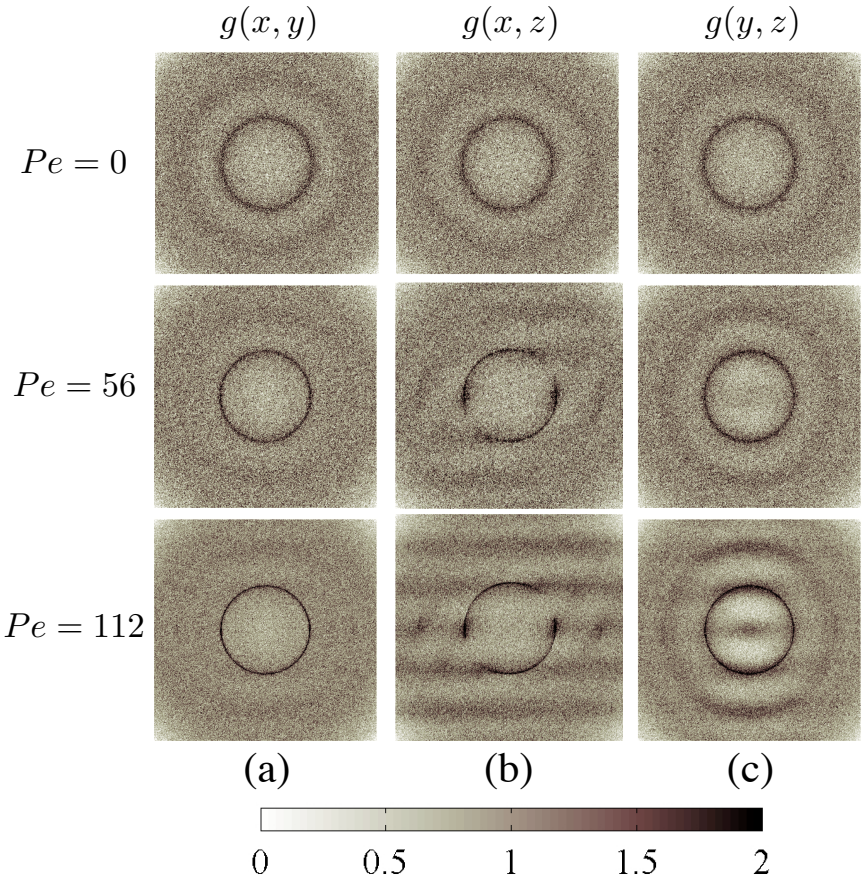

FIGURE 3. Grayscale plot of the two-dimensional projection of the radial distribution function in the (a) *xy*-plane, (b) *xz*-plane, and (c) *yz*-plane at three different values of Pe for a particle volume fraction of $\phi = 0.45$.

traceless dyadic product of $\hat{\boldsymbol{x}}$ given as

$$\boldsymbol{X}(\hat{\boldsymbol{x}}) = \sqrt{\frac{15}{2}} \begin{bmatrix} \hat{x}_x\hat{x}_x - 1/3 & \hat{x}_x\hat{x}_y & \hat{x}_x\hat{x}_z \\ \hat{x}_x\hat{x}_y & \hat{x}_y\hat{x}_y - 1/3 & \hat{x}_y\hat{x}_z \\ \hat{x}_x\hat{x}_z & \hat{x}_y\hat{x}_z & \hat{x}_z\hat{x}_z - 1/3 \end{bmatrix}. \tag{4.3}$$

Deviations of the angle-averaged mean free path from the isotropic value, and changes in the off-diagonal components of the microstructure tensor from zero are related to the level of anisotropy of the particle assembly, which is directly related to Pe. Here we define

$$\lambda_{res} = \lambda - \lambda_0, \tag{4.4}$$

where λ_0 is the mean free path scaled by the particle radius for an isotropic system. Figures 4 (a) and (b) illustrates that λ_{res} and Y_{xz}/ϕ for the deformed particle assembly can be expressed functions of Pe.

4.1. *Fluid-particle drag model*

We express the friction coefficient tensor

$$\begin{array}{cc} \hat{\boldsymbol{\beta}} = \beta\boldsymbol{I} + \boldsymbol{\beta_1} & \boldsymbol{\beta_1} = \hat{\beta}_1\boldsymbol{I} + \tilde{\boldsymbol{\beta}}_{\mathbf{1}} \\ \hat{\beta}_1 = 18\frac{\mu_g}{d^2}\phi(1-\phi)\hat{F}_1(\phi, Pe) & \tilde{\boldsymbol{\beta}}_{\mathbf{1}} = 18\frac{\mu_g}{d^2}\phi(1-\phi)\tilde{\boldsymbol{F}}_{\mathbf{1}}(\phi, Pe) \end{array} \tag{4.5}$$

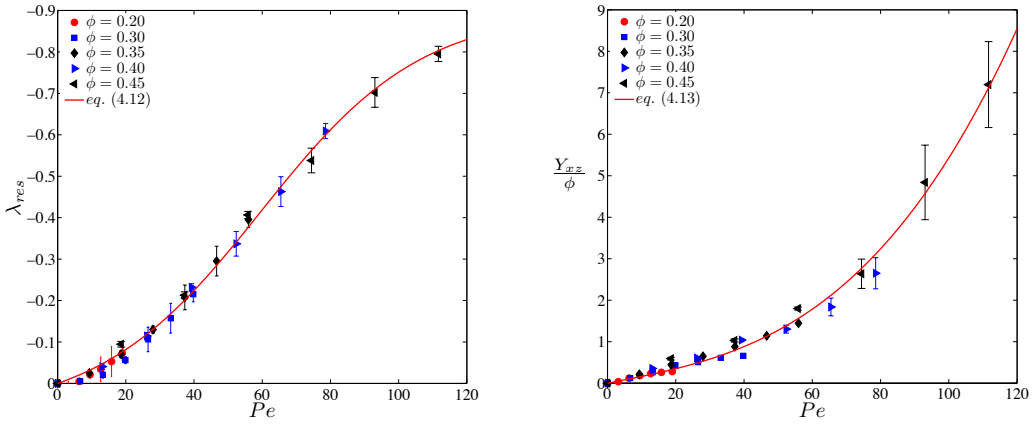

(a) (b)

FIGURE 4. (Color online) Connection between particle microstructure and changes in Pe is illustrated by (a) a plot of λ_{res} versus Pe, and (b) a plot of Y_{xz}/ϕ versus Pe.

where $\boldsymbol{\beta_1}$ represents the anisotropic friction coefficient tensor which is partitioned into an isotropic part $\hat{\beta}_1$, and a deviatoric part $\tilde{\boldsymbol{\beta}}_{\mathbf{1}}$. $\hat{F}_1(\phi, Pe)$ and $\tilde{\boldsymbol{F}}_{\mathbf{1}}(\phi, Pe)$ are dimensionless and must be modeled. We propose a model for $\tilde{\boldsymbol{F}}_{\mathbf{1}}$ as

$$\tilde{\boldsymbol{F}}_{\mathbf{1}}(\phi, Pe) = \chi_1(\phi, Pe)\hat{\boldsymbol{S}} + \chi_2(\phi, Pe)\left(\hat{\boldsymbol{S}}\cdot\hat{\boldsymbol{S}} - (1/3)(\hat{\boldsymbol{S}}:\hat{\boldsymbol{S}})\boldsymbol{I}\right) + \chi_3(\phi, Pe)\left(\hat{\boldsymbol{S}}\cdot\hat{\boldsymbol{W}} - \hat{\boldsymbol{W}}\cdot\hat{\boldsymbol{S}}\right), \tag{4.6}$$

where $\hat{\boldsymbol{S}}$ and $\hat{\boldsymbol{W}}$ are rate-independent traceless deformation rate, and vorticity tensors, respectively, which are given as

$$\hat{\boldsymbol{S}} = \frac{\boldsymbol{S}}{\sqrt{\frac{\boldsymbol{E}:\boldsymbol{E}}{2}}} \qquad \hat{\boldsymbol{W}} = \frac{\boldsymbol{W}}{\sqrt{\frac{\boldsymbol{E}:\boldsymbol{E}}{2}}}, \tag{4.7}$$

and are used to represent the kinematic effect of the shear deformation. In eq. (4.6), $\chi_1(\phi, Pe)$, $\chi_2(\phi, Pe)$, and $\chi_3(\phi, Pe)$ represent the three model constants that constitute the deviatoric part of anisotropic friction coefficient tensor. In this model, χ_1 and χ_2 are introduced to capture the β_{xz} and β_{yy}, respectively, in simple shear; $\hat{F}_1$ and χ_3 then allow us to model observed β_{xx} and β_{zz}. It should also be noted that in eq. (4.6) the second and third terms on the right hand side do not depend on the direction of shear deformation, while the first term does. This was deliberately done because the off-diagonal friction coefficient β_{xz} was observed to change sign upon reversing the direction of shear, while the diagonal components of the friction coefficient tensor remained unchanged.

Figure 5 shows the variation of model parameters with the microstructural parameters. Figures 5 (a) - (c) reveal that $\hat{F}_1\phi^3/F$, χ_2, and $\chi_3\phi^2$ correlate with λ_{res} and ϕ, while figure 5 (d) shows that χ_1 is a function of Y_{xz}/ϕ. Based on Figures 4 and 5, we arrive at the following correlations for the four model parameters

$$\hat{F}_1 = \frac{0.01}{\phi^3} F\lambda_{res}^2 \tag{4.8}$$

$$\chi_1 = 1.51\left(1 - \exp\left(-1.17 Y_{xz}/\phi\right)\right) \tag{4.9}$$

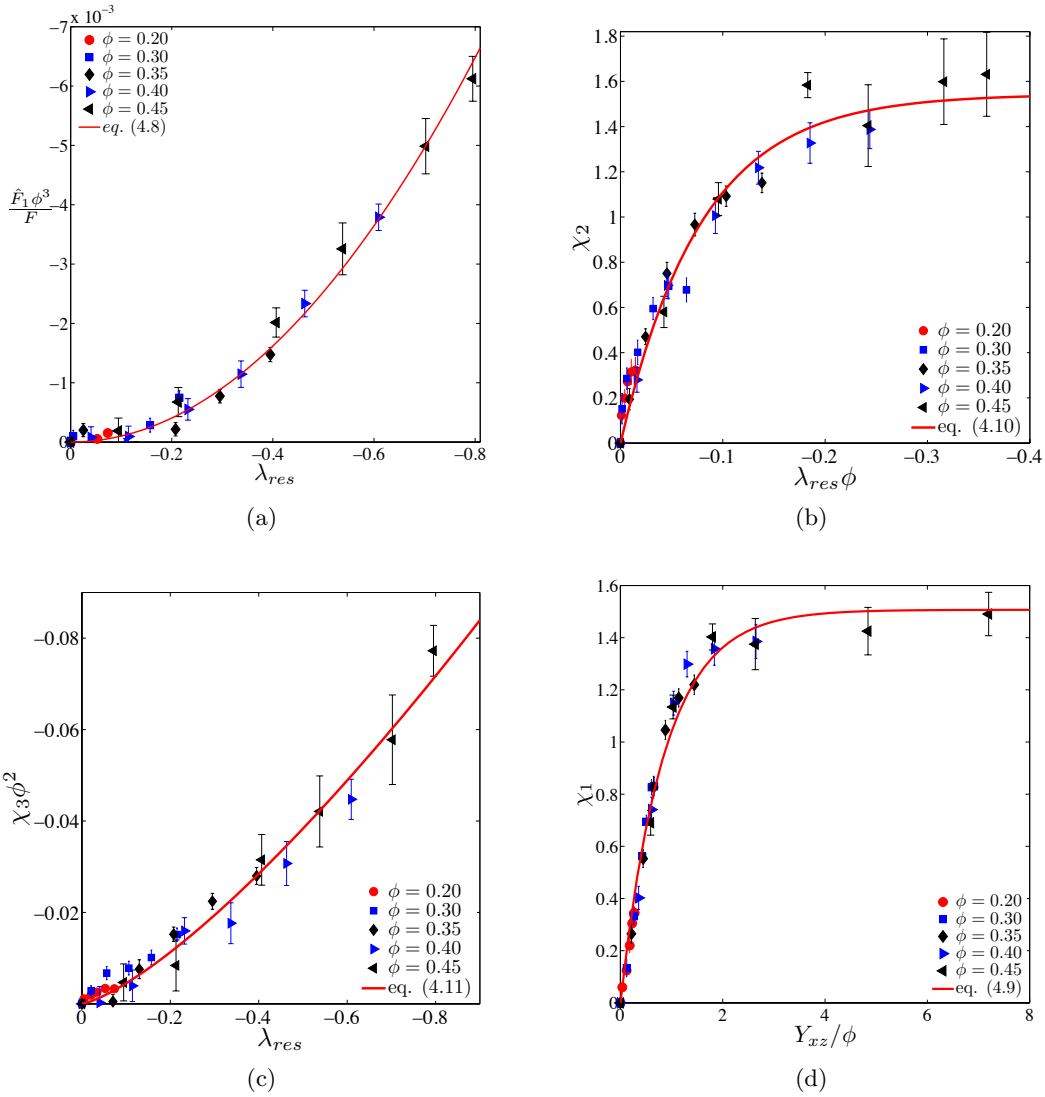

FIGURE 5. (Color online) Dependence of model constants on particle microstructure. (a) $\hat{F}_1\phi^3/F$ vs λ_{res}; (b) χ_2 vs. $\lambda_{res}\phi$; (c) $\chi_3\phi^2$ vs. λ_{res}; (d)χ_1 vs. Y_{xz}/ϕ.

$$\chi_2 = 1.54\left(1 - \exp\left(-12.67\lambda_{res}\phi\right)\right) \tag{4.10}$$

$$\chi_3 = -\frac{0.097}{\phi^2}\lambda_{res}^{4/3}. \tag{4.11}$$

The microstructural variables in Figure 4 can be related to Pe as follows

$$\lambda_{res} = 0.073\left(\frac{1}{1 + 0.925\left(\exp\left(-0.0422Pe\right) - 1\right)} - 1\right) \tag{4.12}$$

$$Y_{xz} = 0.016\phi\left(Pe + 2.13 \times 10^{-4}Pe^3\right). \tag{4.13}$$

Figures 4 and 5 also show the fits represented by eqs. (4.8)-(4.13). For small Pe, these expressions reduce to

$$\begin{array}{cc} \hat{F}_1 \sim \phi^{-3} Pe^2 & \chi_3 \sim \phi^{-2} Pe^{4/3} \\ \chi_1 \sim Pe & \chi_2 \sim \phi Pe. \end{array} \tag{4.14}$$

In eq. (4.8) any isotropic drag model can be used for F. We found that the relationship proposed by van der Hoef *et al.* (2005) for low-Reynolds number flows through random arrays given as

$$F(\phi) = \frac{10\phi}{(1-\phi)^2} + (1-\phi)^2\left(1 + 1.5\sqrt{\phi}\right), \tag{4.15}$$

agrees with our simulation results to within 1%. It should also be noted that the drag relation developed by Koch & Sangani (1999) describes our drag results equally well. Eq. (4.15) is invoked in the linear stability analysis presented in the next section.

5. Discussion

It can readily be seen from the sedimentation velocity of particles in a homogeneous suspension can be increased (by up to $\sim$ 10%) by subjecting the suspension to shear in the horizontal plane (so that the sedimentation is in the vorticity direction). In horizontal transport of non-neutrally buoyant suspensions, where velocity gradients naturally arise, the rates of sedimentation (or rise) of heavier (lighter) particles predicted by the isotropic and anisotropic drag models will differ. However, both of these effects are relatively small. In contrast, a more striking effect of the anisotropic drag model is observed in the classical problem of stability of uniform fluidization (sedimentation), which is discussed below.

We probe the effect of the anisotropic friction coefficient on the stability of uniformly fluidized state by performing a linear stability analysis in one and two dimensions, and comparing dispersion relations for both isotropic and the anisotropic drag models. Our analysis is based on eqs. (2.1)–(2.5). The governing equations are made dimensionless using u_t^2/g, u_t/g, u_t, u_t^2, and $\rho_s u_t^2$ as the characteristic length, time, velocity, temperature, and pressure scales, respectively. For a uniformly fluidized state, eqs. (2.1) – (2.5) reduce to the following set of equations for elastic particles

$$\phi = \phi_0 = constant \tag{5.1}$$

$$-2\phi_0(1-\phi_0)\frac{Fr}{St}F(\phi_0)\tilde{u}_0 - (1-\phi_0)\left(\frac{1}{\delta} - \frac{\partial \tilde{p}_0^f}{\partial \tilde{x}}\right) = 0 \tag{5.2}$$

$$2\phi_0(1-\phi_0)\frac{Fr}{St}F(\phi_0)\tilde{u}_0 - \phi_0\left(1 + \frac{\partial \tilde{p}_0^f}{\partial \tilde{x}}\right) = 0 \tag{5.3}$$

$$\tilde{T}_0 = \left(\frac{\Xi(\phi_0)}{16\sqrt{\pi} g_0 St(1-\phi_0)^2 F(\phi_0)^2 R_{diss}(\phi_0)}\right)^{2/3} \tag{5.4}$$

where the subscript zero refers to the base state, Fr is the Froude number based on particle diameter defined as $Fr = u_t^2/(gd)$, $\tilde{u}_0$ is the dimensionless slip velocity between solid and fluid phases at the base state, $\tilde{p}_0^f$ is the dimensionless base state fluid pressure, $\tilde{T}_0$ is the dimensionless base state granular temperature, and $\delta = \rho_s/\rho_g$. In this section the x-direction points vertically upward while the z-direction is in the horizontal plane. Note that for the low-Re number flows considered here, $Fr = (1 - 1/\delta)St/2$, and so the model parameters simply St, ϕ_0 and δ.

The perturbations to the particle volume fraction, particle and fluid phase velocities, fluid phase pressure, and the granular temperature have the following form

$$\psi = \psi_0 + \psi_1 \tag{5.5}$$

where ψ represents a generic field variable, ψ_0 is its value at the base state, and ψ_1 is a small perturbation variable of the form

$$\psi_1 = \hat{\psi}_1 \exp\left(i\boldsymbol{k}\cdot\boldsymbol{x}\right)\exp\left(\sigma t\right), \tag{5.6}$$

where $\hat{\psi}_1$ sets the amplitude, $\boldsymbol{k}$ is the wavenumber vector associated with the perturbation, and σ is the growth rate of the perturbation. Inserting these perturbations into eqs. (2.1)- (2.5), and simplifying we obtain a set of linear algebraic equations in the coefficients $\hat{\psi}_1$. The resulting characteristic equation takes the form of a fifth order polynomial for the growth rate σ as a function of the wavenumbers k_x and k_z. Note that while $Pe = 0$ in the base state, it will be nonzero in the perturbed state. Terms involving $(\partial\chi_1/\partial Pe)_0$ will appear in the characteristic equation, but $\hat{F}_1$, χ_2, and χ_3 and their derivatives with respect to Peclet number do not. As a result, identical dispersion relations are obtained with isotropic and anistropic drag models for one-dimensional perturbations in the vertical direction ($\hat{k}_x \neq 0$ and $\hat{k}_z = 0$, here $\hat{\boldsymbol{k}} = \boldsymbol{k}v_t^2/g$). It then follows that the region in the (St, ϕ_0, δ) space where the state of uniform fluidization is predicted to be unstable using an anisotropic friction coefficient will not be smaller than that afforded by the isotropic friction coefficient.

Figures 6 (a) and (b) show the real part of the maximum dimensionless growth rate $\hat{\sigma}_r(= \sigma_r v_t/g)$ as a function of St for three different particle volume fractions for the isotropic and anisotropic drag model, respectively. Figure 6 (c) and (d) compare the corresponding wavelengths in the vertical direction. When the isotropic friction coefficient is used in the analysis the uniformly fluidized state is unstable at large St values, but below a threshold value that depends on particle volume fraction the uniformly fluidized state is predicted to be stable. In contrast, the uniformly fluidized state is found to be unstable at all St values when the anistropic friction coefficient is used in the analysis. At very large St values, where both models predict instability, the growth rates and the dominant vertical wavelength predicted with the isotropic and anisotropic friction coefficients are quantitatively similar.

While the isotropic drag model predicts a one-dimensional traveling wave having no horizontal structure as the dominant mode of instability in a uniformly fluidized suspension, we find that the dominant instability mode has two-dimensional structure when an anistropic drag model is used. Figure 7 shows the ratio between $\hat{k}_z$ and $\hat{k}_x$ for the fastest growing instability predicted by the linear stability analysis with the anisotropic drag model developed in this study. At each of the three volume fractions shown in this figure, a vertically traveling wave having both transverse and vertical structures is dominant at lower St values and it transitions to a mode with little lateral structure at large St values. The St value at which this transition occurs increases with particle volume fraction.

In our stability analysis, the granular temperature has been assumed to be isotropic; Koch & Sangani (1999) allowed the mean-squared velocity fluctuations in the vertical direction to differ from that in the transverse direction and formulated a more elaborate set of equations, but employed an isotropic friction coefficient. The St value at which the uniformly fluidized state became stable for a given particle volume fraction was lower in the work of Koch & Sangani (1999) than what we report in figure 6 (a) as a result of their anistropic granular temperature formulation. The influence of the anisotropic granular

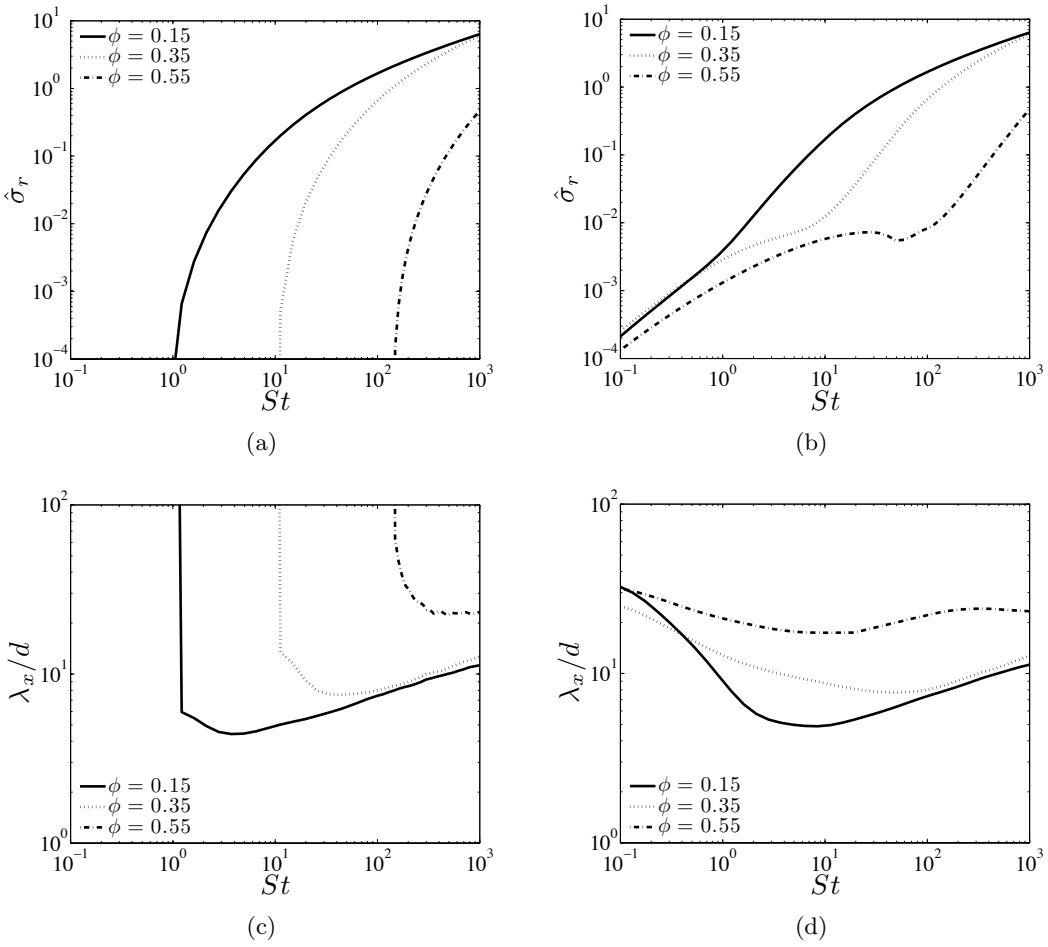

FIGURE 6. Dominant growth rate as a function of St for three different particle volume fractions using (a) the isotropic and (b) anisotropic drag models. The wavelength λ_x of the dominant instability mode (in the direction parallel to gravity) scaled by the particle diameter is also presented for both (c) isotropic and (d) anistropic drag models.

temperature, however, is only quantitative; in contrast, a qualitative change is seen in our studies upon introduction of anisotropic friction coefficient.

It should be noted that the model analyzed here is valid only for large Stokes numbers and hence the lower end of St values shown in these figures is outside the scope of the model. The impact of the anisotropic friction coefficient is, however, observed already at $St >> 1$ (see figures 6 (c), 6 (d) and 7); hence, we believe that our observation that the inclusion of anisotropic friction coefficient removes the stability predicted by the isotropic friction coefficient model remains valid.

Secondary circulation cells have been observed in low St sedimentation (Segre *et al.* 2001; Guazzelli & Hinch 2011). These have been rationalized in terms of particle volume fraction fluctuations that are always present in homogeneous sedimentation (Segre *et al.* 2001) and small gradients in vertical volume fraction (Mucha *et al.* 2004). It will be interesting to see if anisotropic friction coefficient has any role in inducing these circulation cells and/or the wavelength selection.

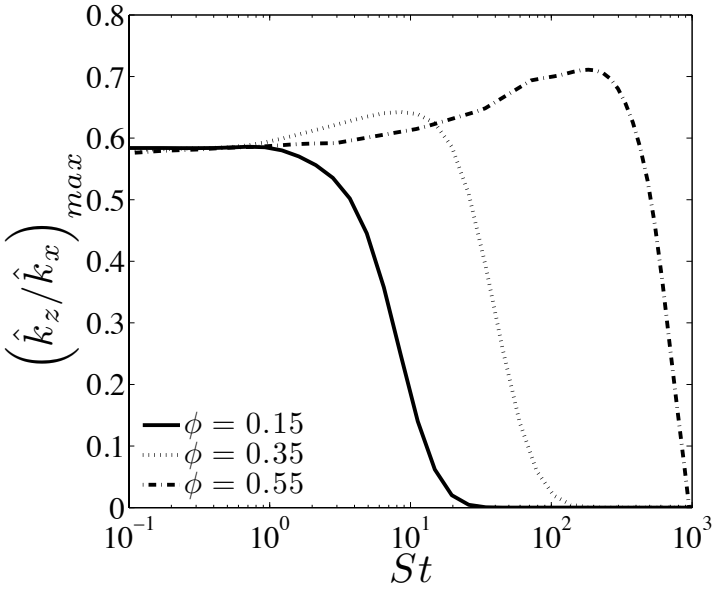

FIGURE 7. The ratio between dimensionless transverse ($\hat{k}_z$) and parallel ($\hat{k}_x$) wavenumbers of the dominant instability mode is plotted against St for three different particle volume fractions. Here, we illustrate the emergence of two-dimensional structure that arises due to anistropy in the fluid-particle drag force.

6. Summary

The results of a computational study of the anisotropy in the fluid-particle friction coefficient in sheared particle assemblies are described. A model for the anisotropic friction coefficient tensor under low Reynolds number conditions is presented (eq. (4.5)) and the model constants are connected to microstructural changes in the particle assemblies that arise due to the shearing of the particle assembly (eqs. (4.8)–(4.11)), which are in turn connected to the Peclet number associated with the deformation (eqs. (4.12)–(4.13)).

The influence of an anisotropic friction coefficient on the stability of the uniformly fluidized state was probed through linear stability analysis of the two-fluid model equations. When the friction coefficient anisotropy is not included, the uniformly fluidized state is most unstable at high Stokes numbers to vertically traveling disturbances having no transverse structure, but below some threshold St value which depends on the particle volume fraction it is predicted to be stable.

When the anisotropy is included, a qualitatively different result obtains, and the stability predicted at low St disappears. The uniformly fluidized state is now most unstable to vertically traveling disturbances having both vertical and transverse structures. The aspect ratio of the most dominant mode is a function of both St and particle volume fraction. At high Stokes numbers, the most dominant mode has very little transverse structure (and so, is nearly the same as that obtained with an isotropic friction coefficient), but at lower Stokes numbers the aspect ratio is predicted to be of the order of unity.

The authors would like to thank Professor James Gilchrist and his student Roy Xu for insightful conversations on particle microstructure and also Stefan Radl for carefully reading our manuscript.

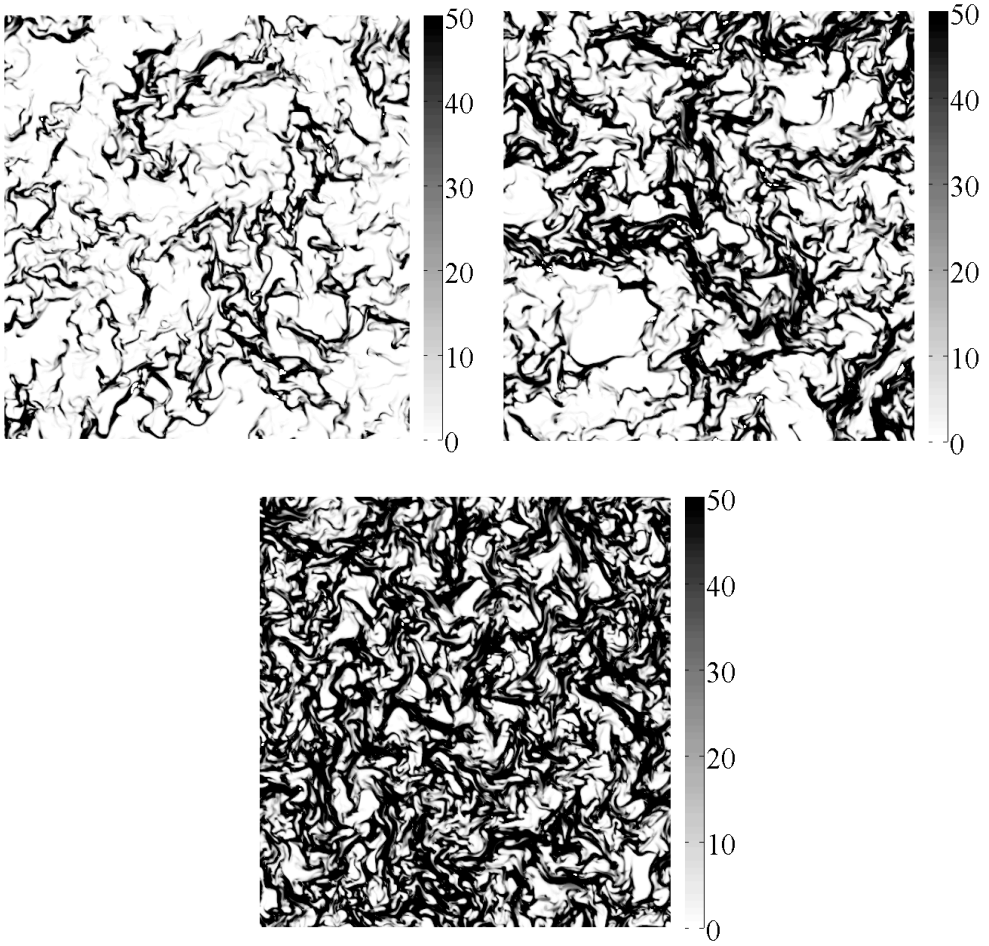

FIGURE 8. Three different colormaps of Pe are given for domain-averaged volume fractions of (a) ϕ = 0.20, (b) ϕ = 0.30, and (c) ϕ = 0.40. In these periodic domain simulations the particle and fluid phase properties are as follows: d = 75 μm, ρ_s = 1500 kg/m^3, ρ_g = 1.3 kg/m^3, and μ_g = 1.8×10^{-5} $kg/(m \cdot s)$. These particle and fluid phase properties give $St \approx 180$. These simulations were performed in a two-dimensional periodic domain measuring 64 $cm \times 64$ cm using 512×512 grid cells. The box size scaled by the particle diameter in this simulation is 8.53×10^5, and the Reynolds number based on the single particle terminal settling velocity is 1.4.

Appendix A

In section 2 the deformation of the particle microstructure was linked to the magnitude of the Peclet number Pe. Estimates of typical values of Pe for large Stokes number suspensions can be obtained by simulating eqs. (2.1)–(2.5) with constitutive relations given by eqs. (2.6)–(2.14) using finite volume methods. In Figures 8 (a)–(d) we show colormaps of the spatial variation of the Peclet number that were obtained from two-dimensional periodic domain simulations of the two-fluid model equations using the isotropic drag model. It is clear that the local Peclet number varies between $0 < Pe < 50$ throughout the periodic domain. Therefore, the microstructural anisotropy resulting at such large values of Pe could have a substantial impact on the predictions of these two-fluid model equations.

REFERENCES

Agrawal, K., Loezos, P. N., Syamlal, M. & Sundaresan, S. 2001 The role of meso-scale structures in rapid gas-solid flows. *J. Fluid Mech.* **445**, 151–185.

Anderson, K., Sundaresan, S. & Jackson, R. 1995 Instabilities and the formation of bubbles in fluidized beds. *J. Fluid Mech.* **303**, 327–366.

Anderson, T. B. & Jackson, R. 1969 A fluid mechanical description of fluidized beds. comparison of theory and experiment. *Ind. Eng. Chem. Fundam.* **8**, 137–144.

Batchelor, G. K. 1988 A new theory of the instability of a uniformly fluidized bed. *J. Fluid Mech.* **193**, 75–110.

Brady, J. F. & Morris, J. F. 1997 Microstructure of strongly sheared suspensions and its impact on rheology and diffusion. *J. Fluid Mech.* **348**, 101–139.

Brady, J. F. & Vicic, J. F. 1995 Normal stresses in colloidal dispersions. *J. Rheol.* **39**, 545–566.

Chen, S. & Doolen, G. D. 1998 Lattice-boltzmann method for fluid flows. *Annu. Rev. Fluid Mech.* **30**, 329–364.

Duru, P. & Guazzelli, E. 2002 Experimental investigation on the secondary instability of liquid-fluidized beds and the formation of bubbles. *J. Fluid Mech.* **470**, 359–382.

Garzó, V. & Dufty, J. W. 1999 Dense fluid transport for inelastic hard spheres. *Physical Review E* **59**, 5895–5713.

Gidaspow, D. 1994 *Multiphase Flow and Fluidization: Continuum and Kinetic Theory Descriptions*. London: Academic Press.

Glasser, B. J., Kevrekidis, I. G. & Sundaresan, S. 1996 One- and two-dimensional traveling wave solutions in gas-fluidized beds. *J. Fluid Mech.* **334**, 183–221.

Glasser, B. J., Kevrekidis, I. G. & Sundaresan, S. 1997 Fully developed travelling wave solutions and bubble formation in fluidized beds. *J. Fluid Mech.* **334**, 157–188.

Glasser, B. J., Sundaresan, S. & Kevrekidis, I. G. 1998 From bubbles to clusters in fluidized beds. *Phys. Rev. Lett.* **81**, 1849–1852.

Guazzelli, E. & Hinch, J. 2011 Fluctuations and instability in sedimentation. *Annu. Rev. Fluid Mech.* **43**, 97–110.

Ham, J. M., Thomas, S., Guazzelli, E., Homsy, G. M. & Anselmet, M.-C. 1990 An experimental study of the stability of liquid-fluidized beds. *Int. J. Multiphase Flow* **16**, 171–185.

van der Hoef, M. A., Beetstra, R. & Kuipers, J. A. M. 2005 Lattice-boltzmann simulations of low-reynolds-number flow past mono- and bidisperse arrays of spheres: results for permeability and drag force. *J. Fluid Mech.* **528**, 233–254.

Jackson, R. 2000 *The Dynamics of Fluidized Particles*. Cambridge: Cambridge University Press.

Koch, D. L. 1990 Kinetic theory for a monodisperse gas-solid suspension. *Phys. Fluids A.* **2**, 1711–1723.

Koch, D. L. & Sangani, A. S. 1999 Particle pressure and marginal stability limits for a homogeneous monodisperse gas-fluidized bed: kinetic theory and numerical simulations. *J. Fluid Mech.* **400**, 229–263.

Ladd, A. J. C. 1994*a* Numerical simulations of particulate suspensions via a discretized boltzmann equation. part 1: General theory. *J. Fluid Mech.* **271**, 285–309.

Ladd, A. J. C. 1994*b* Numerical simulations of particulate suspensions via a discretized boltzmann equation. part 2: Numerical results. *J. Fluid Mech.* **271**, 311–339.

Ladd, A. J. C. & Verberg, R. 2001 Lattice-boltzmann simulations of particle-fluid suspensions. *J. Stat. Phys.* **104**, 1191–1251.

Lun, C. K. K., Savage, S. B., Jeffrey, D. J. & Chepurniy, N. 1984 Kinetic theories for granular flow: inelastic particles in couette flow and slight inelastic particles in a general flowfield. *J. Fluid Mech.* **140**, 223–256.

Ma, D. & Ahmadi, G. 1988 A kinetic model for rapid granular flows of nearly elastic particles including interstitial fluid effects. *Powder Technol* **56**, 191.

Mucha, P. J., Tee, S. Y., Weitz, D. A., Shraiman, B. I. & Brenner, M. P. 2004 A model for velocity fluctuations in sedimentation. *J. Fluid Mech.* **501**, 71–104.

Nicolas, M., Chomaz, J. M., , Denis, V & Guazzelli, E. 1996 Experimental investigation on the nature of the first wavy instability in liquid fluidized beds. *Phys. Fluids* **8**, 1987–1989.

Phung, T. N., Brady, J. F. & Bossis, G. 1996 Stokesian dynamics simulation of brownian suspensions. *J. Fluid Mech.* **313**, 181–207.

Plimpton, S. 1995 Fast parallel algorithms for short-range molecular dynamics. *J. Comput. Phys.* **117**, 1–19.

Renard, Ph. & Marsily, G. D. 1997 Calculating equivalent permeability: a review. *Avd. Water Resour.* **20**, 253–278.

Savage, S. B. & Dai, R. 1993 Studies of granular shear flows: Wall slip velocities, 'layering', and self-diffusion. *Mechanics of Materials* **16**, 225–238.

Segre, P. N., Liu, F., Umbanhowar, P. & Weitz, D. A. 2001 An effective gravitational temperature for sedimentation. *Nature* **409**, 594–597.

Stickel, J. J., Phillips, R. J. & Powell, R. L. 2006 A constitutive model for microstructure and total stress in particulate suspensions. *J. Rheol.* **50**, 379–413.

Stickel, J. J. & Powell, R. L. 2005 Fluid mechanics and rheology of dense suspensions. *Annu. Rev. Fluid Mech.* **37**, 129–149.